

2011

Aminostratigraphy and luminescence dating of the Pleistocene Bridgewater formation, kangaroo island, South Australia: an archive of long term climate and sea-level change

Terry John Lachlan
University of Wollongong

Recommended Citation

Lachlan, Terry John, Aminostratigraphy and luminescence dating of the Pleistocene Bridgewater formation, kangaroo island, South Australia: an archive of long term climate and sea-level change, Doctor of Philosophy thesis, School of Earth & Environmental Sciences, University of Wollongong, 2011. <http://ro.uow.edu.au/theses/3503>

UNIVERSITY OF WOLLONGONG

COPYRIGHT WARNING

You may print or download ONE copy of this document for the purpose of your own research or study. The University does not authorise you to copy, communicate or otherwise make available electronically to any other person any copyright material contained on this site. You are reminded of the following:

Copyright owners are entitled to take legal action against persons who infringe their copyright. A reproduction of material that is protected by copyright may be a copyright infringement. A court may impose penalties and award damages in relation to offences and infringements relating to copyright material. Higher penalties may apply, and higher damages may be awarded, for offences and infringements involving the conversion of material into digital or electronic form.

**AMINOSTRATIGRAPHY AND LUMINESCENCE DATING OF THE
PLEISTOCENE BRIDGEWATER FORMATION, KANGAROO
ISLAND, SOUTH AUSTRALIA: AN ARCHIVE OF LONG TERM
CLIMATE AND SEA-LEVEL CHANGE**

A thesis submitted in fulfilment of the requirements for the award of the degree

DOCTOR OF PHILOSOPHY

from

The University of Wollongong

By

Terry John Lachlan

BSc (Hons), GradDipEd

School of Earth & Environmental Sciences

Faculty of Science

March 2011

Certification

I, Terry John Lachlan, declare that this thesis, submitted in fulfilment of the requirements for the award of Doctor of Philosophy, in the School of Earth & Environmental Sciences, Faculty of Science, University of Wollongong, is wholly my own work unless otherwise referenced or acknowledged. The document has not been submitted for qualifications at any other academic institution.

Terry John Lachlan

Date: 03/03/2011

“Neither smokes, nor other marks of inhabitants had as yet been perceived upon the southern land, although we had passed along seventy miles of its coast.”

Commodore Matthew Flinders observing the coast of Kangaroo Island, in 1802.

In Cumpston (1970: p. 9).

ABSTRACT

Kangaroo Island lies off the South Australian coast, in the Southern Ocean, between 35° 30' and 36° 30' south latitude, and 136° 30' and 138° 30' east longitude, on a broad expanse of continental shelf that extends southward from the mainland for approximately 100 km. The island itself lies adjacent to three peninsulas and two large gulfs (the Eyre Peninsula, Spencer Gulf, Yorke Peninsula, the Gulf of St. Vincent, and the Fleurieu Peninsula—proceeding in order to the south-east), and forms a boundary between the Lincoln Shelf in the northwest, and the Lacepede Shelf in the southeast.

Kangaroo Island is essentially a south-west extension of the Mount Lofty Ranges. The island is also part of the Adelaide Geosyncline, and forms the southern part of the Fleurieu Arc Segment, encompassing the Kanmantoo Trough. The sub-surface geology is dominated by clastic meta-sediments of Cambrian age. Kangaroo Island incorporates three distinct lithotectonic zones: the Northern Structural Zone comprising relatively unmetamorphosed platformal sediments, the Shear Zone Complex which follows the lines of the Snelling and Signet Faults, and the Southern Basinal Zone encompassing the Kanmantoo Group of metasediments. These rocks are generally poor in outcrop, as they are overlain in most areas by Tertiary laterites or Quaternary calcareous aeolianites. The island is essentially a dissected high lateritic plateau with lowland regions in the north-east and south. Dudley Peninsula is an isolated plateau connected to the island by Quaternary sediments.

This thesis focuses on developing an aminostratigraphical, and chronostratigraphical framework for Bridgewater Formation aeolianite deposition on Kangaroo Island. This required the development of new longer range dating methods, and the use and improvement of existing methods (such as amino acid racemization dating).

Amino acid racemization kinetic experiments were performed on molluscs, foraminifers, and (for the first time) whole-rock carbonate rich sediment, in order to compare the racemization forward rates of various amino acids (GLX in

particular) and the changes in the individual amino acid rates across material types, i.e., molluscs, foraminifers, and whole-rock. In the context of the Kangaroo Island samples, and the analysis methods employed, GLX was identified as the amino acid with the most utility (in terms of range, stability, and concentration). It was also revealed that for the Kangaroo Island samples the amino acid GLX was the most compatible (in terms of racemization rate) across many genera of molluscs, and two genera of foraminifers.

This thesis has used luminescence, U-series, ^{14}C , and independently calibrated amino acid racemization dating (for the first time using the amino acid GLX) to establish an aminostratigraphical and chronostratigraphical framework for carbonate deposition on Kangaroo Island. In order to do this a new long-range, single aliquot, luminescence dating method (SARTT-OSL: based upon the multiple-aliquot TTOSL method of Wang *et al*, 2006a) was developed and more comprehensive preparation treatments for amino acid racemization samples were established. A novel approach for the analysis of single grain AAR results was developed through the use of a statistical method (Ward [1963] hierarchical cluster algorithm). This allowed the identification of the youngest age population in a group of foraminifers (from the same sample) (for aminostratigraphical purposes) and also the identification of clusters of reworked tests within the sample.

The AAR chronology and morphostratigraphical position of raised shelly / cobble/ pebble beach deposits allowed the estimation of a Last Interglacial sea-level for Kangaroo Island, which supports similar sea-level estimates from the mainland (cf. Murray-Wallace and Belperio, 1991; Stirling *et al.*, 1998). The GLX D-L ratios for Last Interglacial marine molluscs, where available, were similar to those found on the South Australia mainland, in Glanville Formation shell-beds (cf. Firman, 1967; Cann, 1978; Belperio *et al.*, 1983, 1984; Hails *et al.*, 1984; Murray-Wallace *et al.*, 1988; Murray-Wallace and Belperio, 1991; Murray-Wallace *et al.*, 2010).

Aeolianite deposition has taken place on Kangaroo Island since at least the latter part of the Early Pleistocene (and in all likelihood some time before this),

with the oldest aeolianites recorded (WR AAR age 786 ± 181 ka) being from Stokes Bay on the north coast of the island, and Kelly Hill Caves (WR AAR age 835 ± 194 ka, and SARTT-OSL age 1.3 ± 0.1 Ma) on the south coast. The predominant aeolianites were of MIS 7 (Emu Bay, Pennington Bay, Baudin Beach) and MIS 5 (Pennington Bay, Bales Beach, Vivonne Bay, and Baudin Beach) age, with older aeolianites (MIS 11 and 9) being located on the bounding headlands of embayments (particularly on the south coast: Bales Beach and Pennington Bay). The location of the older sediments on headlands is hypothesized to be due to underlying geology acting as keystones or anchors for deposition, allowing the older sediments to build-up to the stage where younger sediments could begin to accrete in the lower topography in the central portions of embayments.

The indirect evidence of Last Interglacial (MIS 5e) raised beach deposits only being located within sediments older than the late Pleistocene points to regressive phase deposition rather than transgressive or highstand deposition of aeolianites (at least for late Pleistocene aeolianites). It is probable in this respect that late Pleistocene aeolianites were being deposited during the regressive phase just after MIS 5e (ca. 116 ka), and the regressive phases after MIS 5c (at Bales Beach ca. 97 ka—OSL age) and 5a.

The stratigraphical and geochronological findings presented in this thesis demonstrate that Kangaroo Island has a long record of the Quaternary coastal environment. This provides an important record that further increases understanding the complexities of carbonate deposition on Kangaroo Island, and its relevance to the broader issues of aeolianite development.

Acknowledgments

Writing this section of the thesis, for me, is of course a culmination, and represents the end of an interesting, and demanding task. I could not have progressed to this point without the help of many good people, and I would like to formally thank them all here.

Firstly I would like to thank my Supervisor Professor Colin Murray-Wallace for giving me the chance to undertake this PhD, and delve into a most interesting and rewarding area of research: amino acid racemization dating. Colin, thank you for your kindness and friendship, your inspiration, enthusiasm, guidance, your patience, your ready wit, and your encouragement. I would also like to thank Colin for the opportunity to work in the Amino Acid Racemization Dating Laboratory, and his confidence in letting me take care of the equipment. Without Colin's rapid and constructive reading of thesis drafts, this thesis would never have happened.

Many thanks are also due to Doctor Zenobia Jacobs and Professor Richard "Bert" Roberts whom, in their infinite patience, introduced me to the world of optical dating, and provided useful advice and support throughout the tenure of my PhD. I would also like to thank Bert, Zenobia, and Professor Allan Chivas for the opportunity to visit South Africa, and Caltech. Also, Professor Bob Bourman, Doctor Paul Hearty, and Doctor Paul Hesse, for advice and help during fieldwork, and especially Professor Darrell Kaufman who introduced me to the RP-HPLC.

There are many other people both members of staff and students that I would like to thank also. In particular: José Abrantes, for his friendship and willingness to help me out regardless, and for thin-sections, XRD and SEM; David Price for friendship, good advice, and some nice TL dates; Wendy Weeks for an always friendly face, and help with administrative matters; David Wheeler for his aura of calm (and interesting stories), and the PhD crew I 'grew up' with: Megan Williams, Paolo Abballe, Pamela Abouda, Martina Demuro, and in particular my AAR lab partner, Tony Nicholas. I also came to know a number of other PhD students in the twilight years of this thesis: Luke Gliganic, Nathan Jankowski,

Stephanie Kermode, Chrissie Neudorf, and Lili Yu; I thank them for their support.

There are so many others that I would like to include in these thanks—for helping in ways big and small: Professor Paul Carr, Doctor Adriana Garcia, Richard Miller, Brent Peterson, Sandra Chapman, Denise Alsop, Penny Williamson, Doctor Tim Cohen, Doctor Jan-Hendrik May, Doctor Michael Meyer, Professor Lesley Head, and Doctor Lee Arnold.

I would also like to remember here my friend and colleague Caroline Mitchell, who was taken from us in tragic circumstances. I only knew Carol for a short time, sadly. May she rest in peace.

This research would not have been possible without the support, and permission to sample in park and preserve areas on Kangaroo Island, provided by the South Australian Department of Environment and Natural Resources (formerly the Department for Environment and Heritage).

I would like to thank the University of Wollongong and Professor Colin Murray-Wallace for the provision of a Matching Scholarship. The field work and laboratory components of this project were financially supported by an Australia Research Council Large Grant to Professor Colin Murray-Wallace. I would also like to thank GeoQuEST for financial support to attend conferences and purchase field equipment.

Finally, I would like to thank my dear partner Janis, who ‘put up’ with me through this whole process, and without whom I would be lost.

Thesis Introduction

This study examines in detail the stratigraphy and age of Quaternary aeolianite and other carbonate deposits on Kangaroo Island, in the Southern Ocean off the South coast of South Australia. The investigations undertaken in the course of this study have revealed that aeolianite on Kangaroo Island was deposited as skeletal carbonate dune sands during periods of predominantly high sea-level. Dune formation is linked to phases of carbonate production and mobilisation occurring during sea-level highstands—in the case of this study, periods of slightly lower sea-level as may occur during the regressive phase of a highstand. Other deposits associated with aeolianite, usually in the form of raised beach sediments or shell beds, are associated with 2 phases of deposition: 1) during peak sea-level of the Last Interglacial (MIS 5e), and 2) during a possible high sea-level event that occurred in the early Pleistocene.

Previous studies on the deposition and formation types of sediments on Kangaroo Island are few, and the most notable studies are Ludbrook's (1983) investigation of the early Pleistocene Point Ellen Formation, and Milnes *et al.* (1983) examination of Cainozoic marine sedimentation on Kangaroo Island. Milnes *et al.* (1983) work focused broadly on many locations around the island and was concerned principally with describing marine sediments older than the Pleistocene.

This thesis has sourced a large range of geological, geomorphological, geochemical, geochronological, and geographical literature in order to provide a context for the interpretation of the Quaternary evolution of the Kangaroo Island study sites.

The thesis is organised as follows:

Chapter 1 examines the natural history of Kangaroo Island, its human occupation, geology, marine environment, modern climate, and vegetation. The environmental portion of this chapter is used to provide background for the interpretation of field and analytical data presented in later chapters, in terms of the Quaternary history of aeolianite formation.

Chapter 2 analyses the physical attributes of aeolianites and associated

palaeosols, their deposition, formation, and the implications for palaeoclimates and global eustasy. The final sections examine the global distribution of aeolianite, and previous studies of the aeolianite successions of Kangaroo Island.

Chapter 3 examines the stratigraphy of aeolianites, associated facies, and other near shore deposits from selected sites around Kangaroo Island. The sedimentary structures that are present in these deposits along with morphostratigraphical features are used to identify the depositional facies and architectural characteristics. Additionally, the petrographical aspects of a number of thin-sections sampled from representative facies found at the study sites are examined.

Chapter 4 examines the methods associated with the dating of the Kangaroo Island aeolianites and marine carbonate fossils: optically stimulated luminescence (OSL), thermoluminescence (TL), accelerator mass spectrometry carbon-14 (AMS¹⁴C), and Uranium-series (²³⁸U/²³⁰Th series) dating. The first section will outline the sampling and dating strategies for all dating methods (this does not include amino acid dating as this will be examined in Chapter 6). Following this, luminescence dating dosimetry techniques will be reviewed.

Chapter 5 describes the development and testing of a single aliquot (SAR) version of the multiple aliquot (MAR) TTOSL protocol developed by Wang *et al.* (2006a). The testing involves the comparison of known age samples with ages determined through the application of the single aliquot, regenerative dose, thermally transferred (termed SARTT) OSL method developed in this thesis. The initial testing of this SARTT-OSL protocol was presented at the 1st Asia Pacific Conference on Luminescence Dating, at Hong Kong University, during October of 2006. This technique was developed to enable long-range dating of quartz bearing sediments.

Chapter 6 examines the AAR reaction, and its application in stratigraphic studies (aminostratigraphy). The results of AAR age models (APK calibrations) and aminostratigraphic analyses are presented and evaluated.

Chapter 7 presents and evaluates the results derived from analyses using conventional OSL, TL, SARTT-OSL, AMS¹⁴C, ²³⁸U/²³⁰Th series, and AAR dating methods. The luminescence dosimetry results are also presented and discussed.

Chapter 8 is the final chapter and discusses the evolution of the Kangaroo Island near coastal sediments, at the sites examined in this thesis, in the context of the AAR and luminescence chronologies. This chapter also presents the main conclusions of the thesis and further research.

ABSTRACT.....	i
ACKNOWLEDGMENTS	iv
THESIS INTRODUCTION.....	vi
TABLE OF CONTENTS.....	ix
LIST OF FIGURES	xx
LIST OF TABLES.....	xlii

Chapter 1: Kangaroo Island: history and physical

environmental setting	1
1.1 Introduction	1
1.2 Kangaroo Island location	1
1.3 The history of human occupation of Kangaroo Island	2
1.3.1 Aboriginal occupation.....	2
1.3.2 European occupation	4
1.4 Geology and geomorphology	6
1.4.1 Geology.....	7
1.4.1.1 Precambrian to Mesozoic.....	9
1.4.1.2 Cainozoic	17
1.4.2 Geomorphology	19
1.5 Oceanography	20
1.5.1 Bathymetry.....	20
1.5.2 Tides	20
1.5.3 Ocean currents	22
1.5.4 Wave climate	23
1.5.5 Water temperature and salinity	23
1.6 Climate.....	24
1.6.1 Temperature	24
1.6.2 Winds	28
1.6.3 Rainfall.....	31
1.7 Vegetation.....	33
1.7.1 Low Open-Forest to Woodland or Open-Scrub (with heath understorey) 35	
1.7.2 Open-Scrub (with associated heath and dune vegetation along the coast)	
.....	37

1.7.3 Open-Scrub	37
1.7.4 Woodland to Open-Forest (with herbaceous understorey)	37
1.7.5 Salt Marsh.....	37
1.7.5 Other vegetation groups	38
1.8 Summary	38

Chapter 2: Aeolianite formation and distribution in the context of global sea-level change42

2.1 Introduction	42
2.1.1 Aeolianite research	42
2.2 Aeolianites and palaeosols	43
2.2.1 Aeolianites	43
2.2.2 Palaeosols	48
2.2.3 Aeolianites and palaeosols—sea-level and climate change	48
2.3 Production of coastal carbonate	52
2.3.1 Carbonate sedimentation.....	52
2.3.2 Heterozoan carbonate production.....	58
2.4 Distribution, stratigraphy, and age of major aeolianite tracts	60
2.4.1 Factors affecting the global distribution of aeolianite	60
2.4.2 Stratigraphy and age of the major aeolianite tracts.....	65
2.4.2.1 Western, southwestern, and southern Australia	65
2.4.2.2 South Africa	72
2.4.2.3 Bermuda and the Bahamas	73
2.5 Previous Kangaroo Island studies	77
2.6 Summary and conclusions.....	77

Chapter 3: Stratigraphy and petrology of carbonate aeolianites and other near-shore deposits on Kangaroo Island..... 79

3.1 Chapter introduction.....	79
Part I: Stratigraphical terms and sedimentary structures	82
3.2 Stratigraphic terminology used in this thesis.....	83
3.3 Sedimentary structures in beach and aeolian dune deposits.....	83
3.3.1 Modern beach environments	83

3.3.1.1 Shoreface.....	85
3.3.1.2 Foreshore.....	85
3.3.1.3 Backshore	86
Part II: South coast stratigraphy.....	87
3.4 Stratigraphy and facies of the Kangaroo Island study sites on the south coast	88
3.4.1 Introduction	88
3.4.2 Stratigraphy of aeolianite at Pennington Bay	88
3.4.2.1 Site PB1	94
3.4.2.2 Site PB2	105
3.4.2.3 Site PB3	110
3.4.2.4 Site PB4	114
3.4.2.5 Site PB5	121
3.4.3 Stratigraphy of aeolianite at Bales Beach	126
3.4.3.1 Bales1	129
3.4.3.2 Bales2	134
3.4.4 Stratigraphy of the Point Ellen Formation, aeolianite, and other near-shore deposits at Vivonne Bay	136
3.4.4.1 The Point Ellen Formation.....	136
3.4.4.2 Site PE 2 Vivonne Bay	146
3.4.4.3 Site PE 3 Vivonne Bay	150
3.4.4.4 Site PE 4 Vivonne Bay	156
3.4.5 Stratigraphy of the Hanson Bay near shore deposits	157
3.4.5.1 Basal calcarenite.....	158
3.4.5.2 Subaerial exposure surface	161
3.4.5.3 Washover (or sub-littoral or deflation?) facies.....	162
3.4.5.4 Back-barrier estuarine lagoon deposits.....	169
3.4.5.5 Laminar calcrete and the Holocene dunes.....	169
3.4.6 Kelly Hill Caves	170

Part III: Dudley Peninsula and east coast stratigraphy	172
3.5 Stratigraphy and facies of the Kangaroo Island study sites on Dudley Peninsula, and the east coast.....	173
3.5.1 Introduction	173
3.5.2 Stratigraphy of sediments at Rocky Point	173
3.5.3 Stratigraphy of sediments at Baudin Beach	176
3.5.3.1 Site BB1	181
3.5.3.2 Site BB2.....	183
3.5.3.3 Site BB3.....	187
3.5.4 Stratigraphy of sediments at American River.....	188
3.5.5 Stratigraphy of sediments at Kingscote Beach	191
 Part IV: North coast stratigraphy.....	196
3.6 Stratigraphy and facies of the Kangaroo Island study sites on north coast	197
3.6.1 Introduction	197
3.6.2 Stratigraphy of the North Cape sites (NC1 and NC2)	197
3.6.2.1 North Cape beach, Site NC1 (Figure 3.83; Figure 3.84)	200
3.6.2.2 North Cape beach, Site NC2 (Figure 3.83; Figure 3.84; Figure 3.87)	203
3.6.3 Stratigraphy of Emu Bay aeolianite.....	203
3.6.3.1 EB-a aeolianite	204
3.6.3.2 EB-c aeolianite.....	207
3.6.4 Stratigraphy of the Smith Bay near shore deposits	207
3.6.4.1 The uplifted cobble beach.....	208
3.6.5 Stratigraphy of the Stokes Bay aeolianite	210
3.6.5.1 Aeolianite unit	212
3.6.5.2 Calcrete unit.....	214
3.6.6 Summary and conclusions for stratigraphy sections	215
 Part V: Petrology of Kangaroo Island sediments.....	220
3.7 Petrology of Kangaroo Island sediments	221
3.7.1 Introduction	221
3.7.2 Petrological methods	221

3.7.3 Diagenesis of Pleistocene skeletal carbonate.....	227
3.7.3.1 Diagenetic processes.....	228
3.7.3.2 Meteoric vadose diagenesis.....	229
3.7.3.3 Meteoric phreatic diagenesis	231
3.7.3.4 Shallow marine diagenesis	232
3.7.3.5 Micritic sediments and micritisation.....	233
3.7.3.6 Carbonate sediment porosity	236
3.7.4 The texture and fabric of the Kangaroo Island carbonate sediments	237
3.7.4.1 The north coast.....	237
3.7.4.2 General characteristics of the north coast samples	240
3.7.5.1 The east coast and Dudley Peninsula.....	242
3.7.5.2 General characteristics of the east coast and Dudley Peninsula samples	243
3.7.6.3 The south coast	243
3.7.6.4 General characteristics of the south coast samples.....	252
3.7.7 Analysis of the compositional data and powder XRD data.....	253
3.7.7.1 Cluster analysis.....	254
3.7.7.2 Powder XRD analysis: CaCO ₃ mineral phases.....	256
3.7.8 Distinguishing petrological characteristics of the Kangaroo island sedimentary units examined in thin section, and conclusions	258

Chapter 4: Luminescence, accelerator mass spectrometry carbon-14 (AMS¹⁴C), and Uranium-series (²³⁸U/²³⁰Th series) dating methods..... 261

4.1 Introduction	261
4.2 Sampling and dating strategies.....	263
4.2.1 Luminescence sampling methods.....	265
4.2.2 ¹⁴ C sampling methods.....	267
4.2.3 Uranium series sampling methods.....	268
4.3 Luminescence dating: environmental radioactivity, the evaluation of the dose rate, and the luminescence signal.....	268
4.3.1 The external and internal dose rates.....	271
4.3.2 Dose rate determination.....	274
4.3.2.1 Laboratory based dosimetric methods	274

4.3.2.2 Field based dosimetric methods	278
4.3.4 Conventional OSL dating	279
4.3.4.1 Methods	280
4.3.4.2 Rejection Criteria	282
4.3.4.3 Experimental	290
4.4.5 Thermoluminescence dating methods	295
4.4.6 AMS ¹⁴ C dating methods	296
4.4.7 U-series dating methods	299
4.5 Summary	300

Chapter 5: Thermally transferred optically stimulated luminescence (TTOSL) dating: development and testing of a single aliquot regenerative dose (SAR) protocol..... 301

5.1 Introduction	301
5.2 Single aliquot thermally transferred OSL (SARTT-OSL) dating	301
5.3 Conventional luminescence dating background: samples of great antiquity from South Australia, and the choice of a long range luminescence dating method.....	304
5.4 The source of the thermally transferred OSL signal.....	307
5.5 Thermally transferred OSL dating	310
5.5.1 Accounting for inherent problems, and methods.....	310
5.5.1.1 Signal accumulation.....	311
5.5.1.2 Preheats	317
5.5.1.3 Bleachability.....	322
5.5.2 Testing the SARTT-OSL protocol: comparison to known age samples .	325
5.5.2.1 Known equivalent dose sample PB#2-18	325
5.5.2.2 Known equivalent dose sample PB#2b-3	326
5.5.2.3 SESA 145: a sample from the extreme edge of conventional luminescence technique	326
5.6 Discussion	328
5.7 Summary and Conclusions	330

Chapter 6: Amino acid racemization analysis methods, experiments, and age calibrations.....	332
6.1 Introduction	332
6.2 Amino acid racemization analysis	332
6.2.1 The AAR reaction.....	334
6.3 Applications of the AAR method in this thesis.....	343
6.3.1 Aminostratigraphy	343
6.4 AAR Methods.....	345
6.4.1 Instrumentation	345
6.4.2 Amino acid derivitisation	346
6.4.3 Stationary and mobile phases.....	346
6.4.4 Sample selection, strategy, and field criteria.....	347
6.4.4.1 Mollusc samples	349
6.4.4.2 Whole-rock samples.....	352
6.4.4.3 Foraminifer samples.....	354
6.4.5 Sample preparation and hydrolysis.....	355
6.4.6 Samples analysis numbers	359
6.4.7 AAR data screening—rejection criteria	360
6.4.7.1 Abundance of serine	361
6.4.7.2 Outlier D-L ratio values	366
6.4.7.3 Amino acid covariance	366
6.4.8 Data reduction.....	369
6.5 AAR kinetic studies	370
6.5.1 Pyrolysis experiments	370
6.5.1.1 Experiment #1: Isothermal pyrolysis of the marine mollusc <i>Katelsia scalarina</i>	370
6.5.1.2 Experiment #2: Isothermal pyrolysis of whole-rock modern beach sediment	372
6.5.1.3 Experiment #3: Isothermal pyrolysis of the foraminifer <i>Elphidium crispum</i>	374
6.5.1.4 Experiment #4: Isothermal pyrolysis of the foraminifer <i>Discorbis dimidiatus</i>	376
6.5.2 Pyrolysis results	377

6.5.2.1 Katelaysia scalarina	378
6.5.2.2 Whole-rock modern beach sediment	383
6.5.2.3 Elphidium crispum.....	386
6.5.2.4 Discorbis Dimidiatus	388
6.5.3 Pyrolysis discussion.....	389
6.6 AAR dating methods used in this study	394
6.6.1 Introduction	395
6.6.2 The apparent parabolic kinetic method.....	396
6.6.3 Sources of variation in the amino acid racemization numeric age determination	407
6.6.3.1 Uncertainty terms used in GLX AAR age calculation.....	407
6.6.4 Calibrating the amino acid GLX with an apparent parabolic kinetic model using ^{14}C , Uranium-series and conventional OSL dating methods	414
6.6.4.1 Mollusc GLX D-L ratio age calibration.....	418
6.6.4.2 Foraminifer GLX D-L ratio age calibration.....	422
6.6.4.3 Whole-rock sediment GLX D-L ratio age calibration	425
6.7 Summary and conclusions.....	433

Chapter 7: Kangaroo Island dating results..... 434

7.1 Introduction	434
PART I: Luminescence dosimetry	435
7.2 Dosimetry.....	436
7.2.1 Disequilibrium and the results from high resolution gamma spectrometry	436
7.2.1.1 The ^{238}U decay series	439
7.2.1.2 The ^{232}Th decay series	439
7.2.1.3 Implications for dose rate determinations	440
7.2.2 Determination of Uranium, Thorium, and Potassium via TSAC/GMBC, FGS, ICP-OES, and INAA	442
7.2.3 GM Beta counting and the beta dose rate	445
7.2.4 Cosmic ray dose rate	448
7.2.5 Dose rate summary and conclusions	448

PART II: South coast geochronology (and introduction)	449
7.3 Dating results introduction	450
7.3.1 Pennington Bay	450
7.3.1.1 Pennington Bay site PB1 geochronology	452
7.3.1.2 Pennington Bay site PB2 geochronology	476
7.3.1.3 Pennington Bay site PB3 geochronology	477
7.3.1.4 Pennington Bay site PB4 geochronology	481
7.3.1.5 Pennington Bay site PB5 geochronology	490
7.3.1.6 Discussion of the Pennington Bay geochronology	492
7.3.2 Bales Beach	496
7.3.2.1 Bales Beach site Bales1 geochronology	496
7.3.2.2 Bales Beach site Bales2 geochronology	502
7.3.2.3 Discussion of the Bales Beach geochronology	504
7.3.3 Point Ellen and Vivonne Bay	504
7.3.3.1 Point Ellen site PE1 geochronology	506
7.3.3.2 Vivonne Bay site PE2 geochronology	513
7.3.3.3 Vivonne Bay site PE3 geochronology	515
7.3.3.4 Vivonne Bay site PE4 geochronology	522
7.3.3.5 Discussion of the Point Ellen and Vivonne Bay geochronology	522
7.3.4 Hanson Bay	524
7.3.4.1 Hanson Bay site HB1 geochronology	527
7.3.4.2 Hanson Bay site HB2 geochronology	536
7.3.4.3 Discussion of the Hanson Bay geochronology	537
7.3.5 Kelly Hill Caves	537
7.3.5.1 Kelly Hill Caves geochronology	538
7.3.5.2 Discussion of the Kelly Hill Caves geochronology	544
 PART III: Dudley Peninsula and east coast geochronology	 545
7.3.6 Rocky Point	546
7.3.6.1 Rocky Point geochronology	548
7.3.6.2 Discussion of Rocky Point geochronology	548
7.3.7 Baudin Beach	551
7.3.7.1 Baudin Beach site BB1 geochronology	554

7.3.7.2 Baudin Beach site BB2 geochronology	560
7.3.7.3 Baudin Beach site BB3 geochronology	562
7.3.7.4 Discussion of the Baudin Beach geochronology	562
7.3.8 American River	565
7.3.8.1 American River geochronology	567
7.3.8.2 Discussion of the American River geochronology	575
7.3.9 Kingscote Conglomerate	577
7.3.9.1 Kingscote Conglomerate geochronology	578
7.3.9.2 Discussion of the Kingscote Conglomerate geochronology	587

PART IV: North coast geochronology (and Chapter summary).....589

7.3.10 North Cape	590
7.3.10.1 North Cape site NC1 geochronology	592
7.3.10.2 North Cape site NC2 geochronology	595
7.3.10.3 Discussion of the North Cape geochronology	600
7.3.11 Emu Bay	601
7.3.11.1 Emu Bay geochronology	601
7.3.11.2 Discussion of the Emu Bay geochronology	606
7.3.12 Smith Bay	607
7.3.12.1 Smith Bay geochronology	608
7.3.12.2 Discussion of the Smith Bay geochronological results	612
7.3.13 Stokes Bay	613
7.3.13.1 Stokes Bay Geochronology	613
7.3.13.1 Discussion of the Stokes Bay Geochronological results	617
7.4 Summary of dating results	617

Chapter 8: Kangaroo Island near-coastal Quaternary carbonate sediments: a synthesis 625

8.1 Introduction	625
8.2 Chronostratigraphical relationships of the Bridgewater Formation aeolianite sequences and other near-coastal carbonate sediment deposits around Kangaroo Island	625
8.2.1 Age determination methods	625

8.2.2 Time-stratigraphical relationships between Kangaroo Island study sites: aminozones.....	628
8.2.3 Chronostratigraphy of south coast Kangaroo Island near-coastal carbonate sediments.....	640
8.2.3.1 Pennington Bay.....	640
8.2.3.2 Bales Beach.....	642
8.2.3.3 Point Ellen and Vivonne Bay.....	644
8.2.3.4 Kelly Hill Caves.....	646
8.2.3.5 Hanson Bay.....	646
8.2.4 Chronostratigraphy of east coast Kangaroo Island and Dudley Peninsula near-coastal carbonate sediments.....	647
8.2.4.1 Rocky Point.....	647
8.2.4.2 Baudin Beach.....	648
8.2.4.3 American River.....	649
8.2.4.4 Kingscote.....	649
8.2.5 Chronostratigraphy of north coast Kangaroo Island near-coastal carbonate sediments.....	650
8.2.5.1 North Cape.....	650
8.2.5.2 Emu Bay.....	652
8.2.5.3 Smith Bay.....	653
8.2.5.4 Stokes Bay.....	654
8.2.5.5 Summary and conclusions.....	656
8.3 Sea-level controls on the evolution of the Bridgewater Formation aeolianite sequences and other near-coastal carbonate sediment deposits on Kangaroo Island.....	657
8.4 Comparisons with other near-coastal carbonate sediment chronologies from the southern and northern hemispheres.....	663
8.6 Conclusions of this study, and recommendations for further research.....	667
8.6.1 Further research.....	671
References.....	673
Appendices	
Appendix A.....	698
Appendix B.....	699

Appendix C	702
Appendix D	705
Appendix E	713

List of Figures

Chapter 1: Kangaroo Island: history and physical environmental setting

	Page
Figure 1.1: Location of Kangaroo Island. The island lies off the South Australian coast, adjacent to the Gulf of St. Vincent.	2
Figure 1.2: Location of sites mentioned in text.	4
Figure 1.3: Tectonic framework of Kangaroo Island and adjacent mainland (after Belperio and Flint, 1992).	8
Figure 1.4: Principal pre-Permian geological features of Kangaroo Island, illustrating the three lithotectonic zones, and the position of major and minor faults (modified from James and Clarke, 2002).	9
Figure 1.5: Kangaroo Island simplified geology map (compiled from Sprigg, 1954; Belperio and Flint, 1992; Belperio <i>et al.</i> , 2000).	12
Figure 1.6: Bathymetry off the South Australia coast.	21
Figure 1.7: Average monthly a) summer (Feb. 2007) and b) winter (Jul. 2007) sea-surface temperatures off the South Australian and Victorian coasts (CSIRO, 2007).	25
Figure 1.8: Kangaroo Island mean annual rainfall map, showing interpolated isohyets, locations of climate stations, and elevated land surface (modified from Schwerdtfeger, 2002).	27
Figure 1.9: Mean monthly minimum and maximum temperatures for stations around Kangaroo Island (from Bureau of Meteorology archived data in Table 1.4).	29
Figure 1.10: Mean diurnal temperature ranges for stations around Kangaroo Island (calculated from Bureau of Meteorology archived data – in Table 1.4).	29
Figure 1.11 Interpolated position of the Sub-Tropical Ridge, and high pressure systems, during summer and winter, over Australia (modified from BOM, 2007).	31
Figure 1.12: Bureau of Meteorology wind vector data for stations around Kangaroo Island.	32
Figure 1.13: Mean monthly wind speeds for stations around Kangaroo Island. Note that for all stations (excepting Kingscote in May) winds speeds are well above the sand...	33
Figure 1.14: Mean monthly rainfall for stations around Kangaroo Island (Bureau of Meteorology data: Table 1.4).	34
Figure 1.15: Kangaroo Island pre-European vegetation map based upon the Specht (1972) vegetation scheme with additional information from Ball (1998), Edwards (1987), Davies (1982), and. Bauer (1959).	36

Chapter 2: Aeolianite formation and distribution in the context of global sea-level change

Figure 2.1: World map (Robinson [1961] projection), showing locations mentioned in text.	44
Figure 2.2: Cross-section through an ideal transverse dune, showing bedding structures, and gross morphology (after Pye and Tsoar, 1990).	46
Figure 2.3: Hypothesised sequence of events that occur resulting in palaeosol and/or calcrete formation.	47
Figure 2.4: Continental margin of Australia illustrating the areas of cool-water versus warm-water carbonate deposition, and major oceanic current patterns (after James et al., 1999).	54
Figure 2.5: Predominantly Heterozoan carbonate associations deposited on southern Australian open shelves.	57
Figure 2.6: Warm and cold ocean currents and the distribution of shallow-marine carbonates...	59
Figure 2.7: Schematic ca. 90 km cross-section traversing the Coorong Coastal Plain (southeastern South Australia); showing the lateral separation of Pleistocene...	63
Figure 2.8: Geology of the Coorong to Mount Gambier coast plain (south-east South Australia), with inset cross-section and corresponding marine isotope stages for barrier dune deposition (from Belperio, 1995).	68

Chapter 3: Stratigraphy and petrology of aeolianite and other near-shore deposits on Kangaroo Island

Figure 3.1: Kangaroo location map for study sites described in this chapter (i.e. parts II, III, IV, and V).	89
Figure 3.2: Morphology and location of study sites at Pennington Bay, Kangaroo Island (Google Earth, 2008).	90
Figure 3.3: Vegetation and slumped dune sands obscuring aeolianite outcrops; site PB4 at the western segment of Pennington Bay. Note the Holocene platform formed in the basal calcarenite.	90
Figure 3.4: Aeolianite blocks broken from face of exposure. Site PB1 Pennington Bay, Kangaroo Island.	91
Figure 3.5: Wave cut notch and visor at base of aeolianite. Site PB1 Pennington Bay, Kangaroo Island.	91
Figure 3.6: Solutional crust left foreground, obscuring bedding in aeolianite, and transgressing dune sand ramp in mid-ground. Site PB1, Pennington Bay, Kangaroo Island.	92
Figure 3.7: Pervasive calcrete sheet draping the landscape around Pennington Bay: looking east from the top of the PB5 headland (see Figure 3.2).	94
Figure 3.8: Site PB1, displayed here as a composite 180 degree panorama; so there is distortion towards the edges of the image.	95

Figure 3.9: Stratigraphic columns for all sections measured at site PB1.	97
Figure 3.10: Western headland (looking west) section 1 at site PB1, Pennington Bay, Kangaroo Island.	98
Figure 3.11: Western headland section 1 PB1, Pennington Bay, Kangaroo Island—looking south-west from the top of the PB1 site. This image clearly shows the orientation of the aeolianite bedforms. Note the upper sea-caves undercutting the calcrete.	99
Figure 3.12: Section 2 at site PB1, Pennington Bay, Kangaroo Island. Cluffed exposure; note the “clean” face of the exposure and the broken blocks at the base of the deposit.	102
Figure 3.13: Section 3 of site PB1, Pennington Bay, Kangaroo Island, facing towards the north. There are 6 units in this section, 2 palaeosols, 2 aeolianites, a calcrete, and overlying modern/Holocene dunes.	103
Figure 3.14: Site PB1 section 4, facing towards the east. This section hosts 5 units: 2 aeolianites (1-4a, 1-4c), a palaeosol (1-4b), a calcrete (1-4d) and Modern/Holocene dunes (1-4e).	104
Figure 3.15: Site PB2, Pennington Bay, Kangaroo Island, immediately west of the PB1 western headland. Much of the upper portions of this section are obscured by overlying modern material and vegetation	106
Figure 3.16: Site PB3 is displayed here as a 180 degree composite panorama, and so there is distortion at the edges of the image.	107
Figure 3.17: Site PB3 generalized stratigraphic log. This outcrop exhibits 7 units: 3 aeolianites, 2 palaeosols, and the ubiquitous calcrete and backshore dunes. The upper aeolianite is karstified and the middle (3c) has some large solutional features.	108
Figure 3.18: An outcrop of unit 3a, site PB3, Pennington Bay, Kangaroo Island. Most of the upper section of this unit is obscured by solutional weathering. The unit dips steeply down into the plane of the beach. Hammer for scale (33 cm).	109
Figure 3.19: Displayed here are units 3b to 3f. Note the presence of solution pipes in unit 3c, and the laminae and rhizoliths in the upper bounding portions of unit 3d. Walking-stick for scale: 1.2 m.	112
Figure 3.20: Site PB4 section 1 is displayed here as a composite panorama (the image has some distortion towards the edges; however, it is minimal as the panorama is made up of only 3 components).	113
Figure 3.21: Bottom sets and cross-bed sets of unit 4-1a. Note the presence of solution pipe features in 4-1aii, and the erosional truncation surface bounding 4-1ai and 4-1aii. Note: dip azimuths of approximately 295°, with bedding dips of approximately 20°.	116
Figure 3.22a: Generalised stratigraphic log for section 1 of site PB#4.	117
Figure 3.22b: Site PB4 section 2 is displayed here as a merged panorama (the image has some distortion towards the edges).	120
Figure 3.23: Generalized stratigraphic log for section 2 at site PB4.	122
Figure 3.24: Generalized stratigraphic log for site PB5.	125
Figure 3.25: Site PB5 is displayed here as a merged panorama (the image has some distortion towards the edges)...	127

Figure 3.26: Satellite image of Bales Beach sites (Google Earth, 2008).	129
Figure 3.27: Generalised stratigraphical logs for Bales Beach site Bales1 (B) and Bales2 (A). The insets (C) are a satellite image (Google Earth, 2008), showing the location of the sites in the embayment, and a Kangaroo Island location map.	131
Figure 3.28: Units 1a and 1b at site Bales1. Note thin calcrete over palaeosol, and rhizomorphs in aeolian unit (rock hammer for scale 33 cm).	132
Figure 3.29: Units 1b, 1c, 1d, and 1e (unit 1g [backshore dunes] is not visible in this photograph). Note rhizomorphs in aeolian unit 1c (similar to the lower 1a), and abundant large casts in the upper calcrete (1f).	132
Figure 3.30: Site Bales2 is displayed here as a merged panorama (the image has some distortion towards the edges), with units marked in yellow. The...	133
Figure 3.31: Upper units at Bales2 site, note brecciated exposure surfaces, and karstified top calcrete (2i).	135
Figure 3.32: Location of sites around Vivonne Bay, and Point Ellen. The upper right inset shows the geographical location of the bay (small black arrow...	137
Figure 3.33: Conspicuous solution pipes running through the Point Ellen Formation at site A; the calcrete capping exhibits numerous small dolines or sink-holes. The...	137
Figure 3.34: Stratigraphic logs of the Point Ellen Formation at Point Ellen, and Vivonne Bay, Kangaroo Island. The logs illustrate the complexity of the formation and the approximate thickness of the units (inset satellite image courtesy of Google Earth, 2008).	138
Figure 3.35: Panorama of the Point Ellen Formation at site A, showing the positions of the various units outlined in Figure 3.2 Log A.	139
Figure 3.36: Basal shell unit in section from an exposed patch on the rock platform. Note pen for scale (15 cm).	141
Figure 3.37: Three large examples of <i>Elphidium rotatum</i> and one of <i>Marginopora vertebralis</i> extracted from the basal shell layer of the Point Ellen Formation...	141
Figure 3.38: Point Ellen rock platform; patches of the basal shell are evident mid-field; note the deformed Kanmantoo Group basement: left and right foreground. The background shows the base of the outcrop. The...	142
Figure 3.39: Unordered boulder/cobble unit at Point Ellen, site A; clast supported with upper shell matrix. Note pen for scale (15 cm).	143
Figure 3.40: Point Ellen Formation at site B.	145
Figure 3.41: Stratigraphic logs of the Bridgewater Formation at Vivonne Bay, Kangaroo Island. The logs illustrate the formation and the approximate thickness of the units at sites PE 2 and PE 3 (inset satellite image courtesy of Google Earth, 2008).	147
Figure 3.42: View south-east from the Vivonne Bay jetty; showing the location of site PE 2. Note the shallow cave structures ~3.5 m APSL, and the rock platforms (foreground and mid-ground). The...	148
Figure 3.43: Aeolianite unit at site PE 2 with overlying calcrete. Note abundant rhizoliths. The open ellipse denotes the rock-hammer set for scale (33 cm).	149

Figure 3.44: Clay pot karst running through the overlying calcrete into the aeolianite unit at site PE 2.	149
Figure 3.45: Shell and cobble unit at site PE 3. Note: rock-hammer for scale (41 cm); also note the smooth solutional sheath, upper left.	151
Figure 3.46: A scleractinian coral: <i>Plesiastrea versipora</i> , recovered from the shell rich cobble/pebble unit.	152
Figure 3.47: Collapsed blocks of aeolianite resting on cobble and shell, and the basal calcarenite. Note: the collapsed blocks are ~1.5-2 m thick; also note the solutional drape cementing calcrete gravel: upper right mid-ground.	153
Figure 3.48: A panoramic view of the isolated aeolianite outcrop at site PE 4. The outcrop is ~6.5 m APSL at its highest. Note the small pinnacle with notch and visor mid-right in the image. The...	155
Figure 3.49: Calcrete profile at PE 4, upper mid-ground. Note the rhizocretions weathered in relief, and the overlying well-vegetated Holocene/modern dunes: upper right back-ground.	156
Figure 3.50: Hanson Bay satellite digital photograph (edited); showing the location of the study site and bay morphology (unedited image from Google Earth, 2007).	157
Figure 3.51: The Hanson Bay site (bottom image) is displayed here as a composite 180 degree panorama, as such there is minor distortion towards the edges of the image. In the top graphic the individual units have been assigned different colours to make them more apparent. The...	159
Figure 3.52: Generalized stratigraphic logs for the Hanson Bay study site.	160
Figure 3.53: Basal calcarenite, note bedding structures. Also note the overlying calcrete unconformity on this section of the bench.	162
Figure 3.54: Top oblique view of basal platform; note isolated offshore remnant of the basal aeolianite (centre mid-ground).	163
Figure 3.55: Rear of aeolianite platform, showing the irregular exposed surface of the calcrete/palaeosol (note the large rhizomorph, possibly a large tree root—black arrow), washover...	164
Figure 3.56: Thick section of subaerial exposure surface; capped by laminar calcrete.	165
Figure 3.57: Back barrier estuarine lagoon sediments.	166
Figure 3.58: A Late Pleistocene barrier model hypothesized for the Hanson Bay site during a period of sea-level that was similar to the present—perhaps just before the peak of the Last Interglacial (MIS 5e), and at a time when the discharge of the South West River was possibly greater. The...	167
Figure 3.59: Estuarine lagoon facies; truncated by a shelly washover (or sub-littoral or deflation) deposit. LH mid-ground.	168
Figure 3.60: Relative abundance ($n=205$) of various foraminifer genera found in the Hanson Bay estuarine lagoon sediments; one of the most important species to note is <i>Ammonia beccarii</i> , a euryhaline species. It...	170
Figure 3.61: Location of Kelly Hill caves on the southern coast of Kangaroo Island. Upper LH inset shows the location on a regional map (black arrow) (image Google	171

Earth, 2009).

- Figure 3.62: Location of Rocky Point site (red circle upper LH inset) on the neck of the Dudley Peninsula (images Google Earth, 2009). 174
- Figure 3.63: Sample site location (red circle) at Rocky Point. Note the large broken calcrete block RH mid-ground, with carbonised calcrete clasts. Dashed lines denote limits of the shell bed, and the black ellipse shows the location of a rock-hammer set for scale (33 cm). 174
- Figure 3.64: Rocky Point stratigraphic log (C) for the sedimentary outcrops at the rear of the aeolianite headland. The top inset (A) is a merged panorama of the site outcrop. The... 175
- Figure 3.65: Location of Baudin Beach sites (red circles upper LH inset) on the western side of the Dudley Peninsula (images Google Earth, 2009). 177
- Figure 3.66: Collapsed calcrete/palaeosol blocks at site BB1, Baudin Beach, Kangaroo Island. 177
- Figure 3.67: Panorama near site BB3 (looking towards site BB2) showing the upper aeolianite and the alluvial fan sediments. The... 178
- Figure 3.68: Baudin Beach stratigraphic logs (B) for the sedimentary outcrops along a section of the north-west coast of the Dudley Peninsula. The... 179
- Figure 3.69: Site BB1 units, note large rhizomorphs running through the calcrete / palaeosol unit BB1-b (upper RH background). 181
- Figure 3.70: Calcrete / palaeosol (BB1-b) at sea-level (site BB1). 183
- Figure 3.71a,b: Units at site BB2. Blue dashed lines represent the limits of the sedimentary units. Note the faint level bedding in aeolianite BB2-a. This site is parallel to the coast. 184
- Figure 3.72: Location of units near site BB2. Note position of upper alluvial sediments in relation to the upper aeolianite unit (BB1a and BB3d) and calcrete (BB1b and BB3e). See person midfield for scale (~2 m). 185
- Figure 3.73: Sequence at site BB3. Note rock hammer (black ellipse) set for scale (33 cm). 188
- Figure 3.74: Location of American River sites (red circles upper LH inset) on the western side of the Dudley Peninsula (images Google Earth, 2009). 189
- Figure 3.75: St. Kilda Formation deposits at site AR1. Note sample pit lower LH foreground. 190
- Figure 3.76: St. Kilda Formation deposits at site AR2. Note sample pit midground. 190
- Figure 3.77: Extent in outcrop of the Kingscote Conglomerate, at sites KC1 and KC2, Kingscote, Kangaroo Island (courtesy of Google Earth, 2009). 191
- Figure 3.78: Kingscote Conglomerate near Rolls Point (site KC1). Note solution pipe middle background (knapsack for scale: 50 cm). 192
- Figure 3.79: Kingscote stratigraphic logs for the sedimentary outcrops near Rolls Point (KC1), and near "The Bluff" (KC2). The... 193

Figure 3.80: Close-up of the Kingscote Conglomerate unit (near Rolls Point). Note abundant basalt clasts (rock-hammer handle for scale: 20 cm).	194
Figure: 3.81: Kingscote Conglomerate at site KC2. Red dashed line shows approximate position of the unit (uppermost) (rock-hammer for scale: 33 cm).	195
Figure 3.82: Study site locations on the North Cape, Kangaroo Island. Inset upper left shows the geographical location (black arrow) of the North Cape region (unedited image courtesy of Google Earth, 2008).	197
Figure 3.83: Stratigraphic logs for the North Cape and Boxing Bay study sites (inset image courtesy of Google Earth, 2008).	198
Figure 3.84: Outcrop at site NC1, on North Cape, Kangaroo Island. The open ellipse indicates a rock-hammer set for scale (33 cm).	199
Figure 3.85: Shelly clay balls in the upper portion of the muddy sand unit; see text for possible explanations (pen for scale: 15 cm). The white flecks are broken shells.	201
Figure 3.86: Three examples of <i>Anapella cycladea</i> recovered from the muddy sand (intertidal/subtidal) unit. The bivalves in the dashed box are from 2 articulated individuals.	202
Figure 3.87: The Boxing Bay Conglomerate and beach facies (these could also be the bottomset beds of an aeolianite deposit (rock-hammer set for scale [black ellipse]: 33 cm).	204
Figure 3.88: Location map for study site on Emu Bay, Kangaroo Island. Inset (upper LH) shows the general location of site EB (red circle). The lower RH inset is a closer view of the EB study site; the red arrows indicate sample positions (unedited images courtesy of Google Earth, 2009).	205
Figure 3.89: Stratigraphic log (B) for the sedimentary outcrop at Emu Bay (EB). The...	206
Figure 3.90: Shingled cobbles and boulders at Smith Bay, Kangaroo Island. Clasts are generally flattened and range from pebbles and fist sized cobbles to large (>250 mm) boulders. Many...	207
Figure 3.91: Location of the Smith Bay study site.	208
Figure 3.92: Uplifted pebble beach over Permian till, Smith Bay, Kangaroo Island.	209
Figure 3.93: Stratigraphic log (A) for the sedimentary outcrop at Smith Bay (SB). The...	210
Figure 3.94: Location map for study site at Stokes Bay, Kangaroo Island. Inset (upper LH) shows the general location of site STB (red circle). The...	211
Figure 3.95: Stratigraphic logs of the Stokes Bay aeolianite, Stokes Bay Kangaroo Island. The log illustrates the approximate thickness of the units (inset satellite image courtesy of Google Earth, 2008).	212
Figure 3.96: Lower section of aeolianite unit, note the cavernous weathering, and also the bedding structures visible in this unit.	213
Figure 3.97: Calcrete unconformably overlying aeolianite at Stokes Bay.	213
Figure 3.98: Close view of the upper portions of the deposit, showing the nodule-like texture that may be due to pisoliths.	214

Figure 3.99: Evolution plot of the point count procedure for an example thin section (sample Bales#3-1) analysed using JMicroVision (Roudit, 2008). For this thin section 360 points were counted (although classes were reasonably stable after approximately 200 counts).	222
Figure 3.100: Schematic of simplified carbonate diagenetic environments for a rimmed shelf with unconfined aquifers (modified from Tucker, 1990).	227
Figure 3.101: Scanning electron microscope (SEM) image of micritic rind cement coating a foraminifer (<i>Elphidium rotatum</i>) recovered from the basal unit of the early...	234
Figure 3.102: Scanning electron microscope (SEM) image of anastomosing lines (blue arrow) created by boring algae in the surface of a foraminifer (<i>Peneroplis planatus</i> ...	235
Figure 3.103: Photomicrographs (note scale bars: 250 μ m) of point counted thin sections from Kangaroo Island, both in plane polarised light (PPL) and cross polarised light (CPL). A)...	238- 239
Figure 3.104: Ternary plots of various thin section (normalised) compositional data and CaCO ₃ mineral content of selected Kangaroo Island sediment thin sections (A, B, and C), and powder X-ray diffraction data (D) (processed into percentage weights using RockJock version 5). Blue...	241
Figure 3.105: Photomicrographs (note scale bars: 250 μ m) of point counted thin sections from Kangaroo Island, both in plane polarised light (PPL) and cross polarised light (CPL). A)...	245- 246
Figure 3.106: Photomicrographs (note scale bars: 250 and 500 μ m) of point counted thin sections from Kangaroo Island, both in plane polarised light (PPL) and cross polarised light (CPL). A)...	248
Figure 3.107: Skeletal grain cluster analysis (Ward Method) for Kangaroo Island thin section samples. Three clusters are apparent. Red shows (relatively) a low skeletal proportion, green a medium/high proportion, and blue a high proportion.	254
Figure 3.108: Mollusc grain cluster analysis (Ward Method) for Kangaroo Island thin section samples. Three clusters are apparent. Red shows (relatively) a low mollusc proportion, blue a medium/high proportion, and green a high proportion.	255
Figure 3.109: Cements cluster analysis (Ward Method) for Kangaroo Island thin section samples. Three clusters are apparent. Red shows (relatively) a high cement proportion, green a medium proportion, and blue a low proportion.	256
Figure 3.110: Location of XRD sample sites around Kangaroo Island, with accompanying mineral composition pie charts, and probable ages.	257
Figure 3.111: Pennington Bay sample PB#2-22 XRD trace with assay, and identified quartz, aragonite and calcite peaks.	259
Figure 3.112: Normalised percentage weights of CaCO ₃ mineral phases, showing changes in mineral chemistry over time. Note the almost complete alteration to calcite in the oldest sample (early Pleistocene).	259

Chapter 4: Luminescence, accelerator mass spectrometry carbon-14 (AMS¹⁴C), and Uranium-series (²³⁸U/²³⁰Th series) dating methods

Figure 4.1: Absolute dating sample sites for this study, on Kangaroo Island, South Australia.	262
---	-----

Figure 4.2: This schematic is adapted from Aitken (1985). It illustrates a sample pit with some of the sampling locations that should be avoided. The large black dots symbolize sample locations, and the dashed circles represent a 30 cm gamma sphere.	267
Figure 4.3: This is an energy level diagram of the OSL process; figure and caption based upon Aitken (1998). i) The ionization of the quartz crystal from exposure...	269
Figure 4.4: This is a schematic representation of a Risø TL/OSL machine heater plate which shows a) poor thermal contact of the sample disc to the heater plate caused by extraneous grains on the under-surface of the disc, b) poor thermal contact caused by a warped sample disc, and c) good thermal contact by way of a clean, flat disc.	283
Figure 4.5: Illustrated here are actual data from Kangaroo Island sample Bales#2-9, for an accepted disc and a disc rejected on the basis of poor thermal contact. These...	284
Figure 4.6: A dose response curve for an aliquot of Bales#2-9; the regeneration doses (R_x) given were 10, 20, 40, 60, and 100 Gy, with a 5 Gy test dose. The repeated dose point (R_1 and R_7) was 10 Gy. The...	285
Figure 4.7: A series of recycling ratios from Kangaroo Island Sample HB#3-4. The...	286
Figure 4.8: a) Dose response curve for an aliquot of Kangaroo Island sample BB#3-5, taken from an alluvial deposit, that is saturated for the 'natural' signal...	287
Figure 4.9: A recuperation plot for Kangaroo Island sample PB#2-18. The dashed line represents a 5% recuperation threshold. A second axis could also be included if one desired to compare the recuperation value with the D_e . 1σ error bars are within the data point.	290
Figure 4.10: Preheat plateau test for Kangaroo Island sample Bales#2-9. The ratios are relatively stable (1σ errors overlap unity) from 180° C to 280° C; it is likely that any PH within this range would yield reasonable results in a SAR dating run. Although...	291
Figure 4.11: Dose recovery test (50 Gy) for Bales#2-9; using the 260/220° C PH/CH combination for 6 aliquots (open circles), and the additional 300° C optical stimulation for the other 6 aliquots (filled circles). All...	293
Figure 4.12: Final modified SAR protocol used to determine the equivalent doses for the conventional OSL samples from Kangaroo Island.	294
Figure 4.13: The $N / (N + UV + \beta)$ plateau. Also displayed are the N, the dose $N + UV + \beta$, and bleached glow curves (modified from Aitken, 1985). The plateau represents the temperatures where the N TL can be compared to $N + UV + \beta$ TL.	295

Chapter 5: Thermally transferred optically stimulated luminescence (TTOSL) dating: development and testing of a single aliquot regenerative dose (SAR) protocol

Figure 5.1: SARTT-OSL dose response curve constructed to demonstrate high growth well beyond the conventional OSL range. Kangaroo Island sample Bales#2-9 was used in the experiment. This...	302
Figure 5.2: The Coorong to Mount Gambier coastal plain showing the location of various Pleistocene coastal barriers. Note the West Naracoorte dune range (from Murray-Wallace <i>et al.</i> , 1998).	303
Figure 5.3: Displayed here for the purposes of illustrating equation 5.3 are the L_{TTOSL} ,	309

L_{BTOSL} and corrected L_{ReOSL} signals from an aliquot of Kangaroo Island sample PB#2-18. The TTOSL and BTOSL signals are test dose corrected (L_x/T_x). The L_{ReOSL} signals are derived from the subtraction.

Figure 5.4: A typical SARTT-OSL dose response curve from an aliquot (3mm mask) of sample PB#2-18. The... 311

Figure 5.5: The dose dependent build-up of remnant recuperated signals that occur during each regenerative cycle (three decay curves from a typical aliquot of sample PB#2-18). Each... 312

Figure 5.6: A typical aliquot from the ReSAR run of PB#2-18 (6 x 3mm mask aliquots, 260° C PH, 220° C CH, 0.25 Gy test dose). A D_e of 135.3 ± 7.7 Gy... 313

Figure 5.7: Aliquots of sample Bales#2-9 (a known age sample from Kangaroo Island), subjected to different end cycle washes... 315

Figure 5.8: Example of a 300° C hot optical wash curve from the end of a regenerative dose cycle in the SARTT-OSL protocol (sample PB#2-18). 316

Figure 5.9a: A comparison between the TTOSL “natural” signal and the conventional OSL “natural” signal for sample PB#2-18 (log “Y” scale). 316

Figure 5.9b: Two TL curves from Kangaroo Island generated using KOPP-759 and HA-3 filters: a regenerative curve and a natural curve for sample Bales#2-9. 318

Figure 5.10: Equivalent dose comparisons using 240° C, 260° C and 280° C preheats on sample PB#2-18 from Kangaroo Island. Note the weak ($R^2 = 0.3281$) trend between increasing dose and preheat temperature. 319

Figure 5.11: Further preheat (in °C) comparisons for sample PB#2-18, the dashed lines represent the weighed means (central D_e) for each group. 320

Figure 5.12: Dose response curve comparisons for 240° C, 260° C and 280° C preheats (mean data of 3 aliquots for each preheat) for 3 mm mask aliquots of sample... 321

Figure 5.13a: A single aliquot of sample PB#2-18 was run through 6 x 100 Gy cycles of the SARTT-OSL protocol (240° C/10s PH, 220° C/5s CH); note the increasing sensitivity of the aliquot and the adequate correction by the test dose. The dashed line represents the average signal for 100 Gy. 321

Figure 5.13b: SARTT-OSL equivalent dose vs time for Kangaroo Island sample KPB#5-1. Eight weeks of sunlight bleaching were required to reduce the equivalent dose from ~250 Gy to ~37 Gy. It... 321

Figure 5.14: Results of the SARTT-OSL dose recovery performed on 7 aliquots of unbleached modern dune sample PB#2b-8. Four aliquots were within 10% of unity, and two overlapped 10% at 2σ . The solid line represents unity, and the two dashed lines are a 10% envelope around unity. 323

Chapter 6: Amino acid racemization analysis methods, experiments, and calibrations

Figure 6.1: Simplified general skeletal forms for L- and D-amino acids. The wedge-shaped bond implies protrusion above the plane of the paper. 335

Figure 6.2: Isoleucine structural configurations and racemization pathways (modified from Miller and Clarke, 2007). 336

Figure 6.3: Simplified skeletal structures for ASX and GLX showing the orientation change about the α -carbon that can occur after the abstraction and uptake of a proton. The solid wedge-shaped bonds imply protrusion above the plane of the paper, and the dashed implies protrusion below the plane of the paper. 337

Figure 6.4: The difference between effective diagenetic temperature (T_{eff}) and mean annual air temperature (MAT: 16.8° C) with depth based on multiyear instrumentation of a site in southern Arizona. The... 340

Figure 6.5: GLX (GLX) and CMAT data from various sources compiled to create a Last Interglacial (Last Interglacial—132-116 ka [from a variety of sources listed in Siddall *et al.*, {2007}]) envelope for GLX D-L ratios. The... 341

Figure 6.6: AAR subsample regions used in this study for both bivalves and gastropods. Shown here are examples of a Holocene *Eumarcia fumigata* (American River) and a modern *Nerita (Melanerita) atramentosa* (Point Ellen). Anatomical descriptions follow Ludbrook (1984). 348

Figure 6.7: Examples of modern and fossil marine shell analysed for amino acids in this study. These... 350

Figure 6.8: *Marginopora vertebralis* recovered from the Kingscote pebble/cobble beach deposit (sample KC#3-1) on Kangaroo Island (light microscope 100 x magnification). 351

Figure 6.9: Scanning electron microscope images of constituent grains and foraminifers commonly found in Kangaroo Island aeolianite and marine deposits. A. Calcareous algae. B. Bryozoan... 353

Figure 6.10: L-SER concentration characteristics and GLX D-L ratio data for *Mactra* sp., and *Irus* sp. recovered from a raised pebble/cobble beach at Smith Bay, Kangaroo Island. Two... 356

Figure 6.11: Total (D+L) amino acid enantiomer (ASX, GLX, SER and VAL) concentration data (pmol/mg carbonate⁻¹) for live-collected *Katylisia scalarina* used in an isothermal heating experiment. Note... 362

Figure 6.12: Total (D+L) amino acid enantiomer (ASX, GLX, SER and VAL) concentration data (pmol/mg carbonate⁻¹) for whole-rock modern beach sand from Emu Bay, Kangaroo Island, used in an isothermal heating experiment. SER... 362

Figure 6.13: (D+L) amino acid enantiomer (ASX, GLX, SER and VAL) concentration data (pmol/mg carbonate⁻¹) for Pleistocene whole-rock sediment samples recovered from the carbonate aeolian dune sequence on the Coorong coastal plain, mainland South Australia—see section 6.3. These... 363

Figure 6.14: Coorong coastal region showing the location of a series of Pleistocene dune barriers, that were the subject of the TL dating work undertaken by Huntley *et al.* (1993, 1994), Huntley and Prescott (2001), and the OSL work of and Banerjee *et al.* (2003) (from Murray-Wallace *et al.*, 2001). 364

Figure 6.15: Chromatogram traces for two individual *Discorbis dimidiatus* foraminifers recovered from a Mid-Pleistocene aeolianite (PB#2a-4) at Pennington Bay, Kangaroo Island. a)... 365

Figure 6.16: Bivariate plot of a group of single grain (*Elphidium* spp. recovered from raised pebble beach sediment at Pennington Bay) showing D-L ratios (ASX and GLX) that were subjected to a 2 σ filter, and the SER D-L rejection criterion. The... 367

- Figure 6.17: The covariant relationship between ASX and GLX is explored in plot a) and plot b) for the foraminifer *Elphidium* spp. and whole-rock sediment. Each... 368
- Figure 6.18: This plot is similar to those in Figure 6.15ab, and shows ASX and GLX D-L ratio data for molluscs recovered from Kangaroo Island sedimentary successions. The orange (freshwater) and mauve (marine) points are for gastropods and the green points are for bivalves (marine). The... 369
- Figure 6.19: Examples of pristine (transparent/translucent, unabraded individuals of *Elphidium crispum*. and *Discorbis dimidiatus*) benthic foraminifers, from... 374
- Figure 6.20: D-L ratio data from the set of pyrolysis experiments: a) Table 6.4 *Katelsia scalarina* D-L ratio data; these data clearly illustrate the rate differences between the amino acids SER, ASX, GLX, and VAL. All... 380
- Figure 6.21: Examples of representative RP-HPLC chromatograms for a) $t_{0 \text{ days}}$ and b) $t_{56 \text{ days}}$, from the *Katelsia scalarina* pyrolysis experiment (traces generated by Agilent Chemstation software Rev. A. 10.02 [1757] 1990-2003). 381
- Figure 6.22: Constrained power law transformations (exponent of 2) of pyrolysis D-L ratio data... 382
- Figure 6.23: Bivariate plot a) showing ASX and GLX D-L ratio results for two genera of foraminifer recovered from two units at Vivonne Bay, Kangaroo Island. The blue and green data points are from a Last Interglacial shell bed (sample PE#3-4, 3-5, and 3-6), and the red... 385
- Figure 6.24: Examples of *Elphidium rotatum* recovered from the basal unit of the Early Pleistocene Point Ellen Formation. Note the excellent preservation of the fine test morphology (light microscope 100 x magnification), this implies *in situ* deposition. 387
- Figure 6.25: Amino acid racemization forward rate “map” created using the forward rate data in Table 6.10. The map illustrates the rate differences between the different biomineral materials as well as the rate differences between the different amino acids that were examined. The arrows indicate the direction of rate decrease and hence the order. The... 392
- Figure 6.26: Conformity of ASX AAR to apparent reversible first-order kinetics (RFOK). The ASX D-L ratio data obtained from the total hydrolysable amino acids of *Katelsia scalarina* heated at 110° C are displayed (from this study). The data are transformed using the logarithmic term of the integrated rate equation and conform to RFOK where ASX D-L ratios are <0.450. 395
- Figure 6.27: GLX D-L ratio data vs. TL ages of Huntley *et al.* (1993; 1994) a) fit with a polynomial function b) A linear regression of GLX D-L ratio data vs. $\sqrt{\text{TL}}$ ages of Huntley *et al.* (1993; 1994). These... 403
- Figure 6.28: Calibration plot (GLX vs. $\sqrt{\text{Time [ka]}}$) for the Coorong GLX data (the open circle is GLX D-L vs. U-series; the black circle is the t_0 point... 404
- Figure 6.29: Comparison plots of the two chronologies vs. the GLX AAR ages a) TL vs. GLX (this study) and LEU AAR ages of Murray-Wallace *et al.* (2001); the open circles are GLX and the solid black circles are LEU; the black solid line represents unity, and the red dashed lines represent 10% either side of unity b) LEU AAR ages of Murray-Wallace *et al.* (2001) vs. the GLX AAR ages derived in this study. 406
- Figure 6.30: Comparison of GLX and ASX D-L ratios from various individual fossil molluscs and foraminifers recovered from Glanville Formation equivalent (Last Interglacial) sites around Kangaroo Island. Examined are 5 molluscan genera from 5 sites, and 2 genera of foraminifer (circles for ASX and triangles for GLX); red 410

(Pennington Bay)...

Figure 6.31: The analytical precision for GLX was determined by repeat measurements (injections) from single vials containing the interlaboratory comparison standards of Wehmiller (1984)... 411

Figure 6.32: Holocene study sites at American River, Kangaroo Island, incorporating coquina deposits (image courtesy of Google Earth, 2009). 418

Figure 6.33: Calibration curve for American River molluscs. This system can be described by apparent parabolic kinetics as the relationship between the D-L ratio and the square root of time is linear. Here... 419

Figure 6.34: Pleistocene study sites at Vivonne Bay, Kangaroo Island, incorporating a Last Interglacial shelly cobble/pebble deposit at site PE3 where the U-series dated coral (*Plesiastrea versipora*—PE#3-4) was recovered (image courtesy of Google Earth, 2009). 421

Figure 6.35: Calibration curve for AAR numerical age estimation of Pleistocene molluscs from Kangaroo Island. This... 421

Figure 6.36: Calibration curve for AAR age estimation of Pleistocene foraminifers from Kangaroo Island. This... 423

Figure 6.37: A comparison of all GLX data (Whole-rock sediment, *Katelsysia scalarina*, *Elphidium crispum*, and *Discorbis dimidiatus*) from the pyrolysis experiments; untransformed and plotted as linear regressions vs. $\sqrt{\text{Time}}$ (as in the apparent parabolic kinetic method). What this graph shows is the striking similarity between each of the heated materials in terms of slope (particularly in later diagenesis for *Katelsysia scalarina*), i.e., $9.0 \times 10^{-1} \sqrt{\text{yr}^{-1}}$ for whole-rock; $1.1 \sqrt{\text{yr}^{-1}}$ for *Katelsysia scalarina*, and $7.8 \times 10^{-1} \sqrt{\text{yr}^{-1}}$ for *Elphidium crispum* and *Discorbis dimidiatus*—hence the overlap of both regression lines. 424

Figure 6.38: Calibration curve for AAR age estimation of Pleistocene whole-rock sediment from Kangaroo Island. This... 427

Figure 6.39: D-L ratio data vs. luminescence ages from this study, fitted with an exponential function. This plot demonstrates the non-linear nature of GLX kinetics over time, and the appropriateness of the apparent parabolic kinetic calibration method in application to these data. 431

Figure 6.40: Calibration curve for AAR age estimation of Pleistocene whole-rock sediment from Kangaroo Island. This system can be described by apparent parabolic kinetics as the relationship between the D-L ratio and the square root of... 431

Figure 6.41: Direct comparison of the Kangaroo Island whole-rock sediment calibration (utilizing OSL ages) with the U-series calibration of the same data, and the Coorong whole-rock calibration (both of which used a single U-series age of 125 ± 20 ka [Schwebel, 1978; 1984] as a calibration point). The similarity between the three regressions is reasonably close. The defining factor that causes the deviation is the slight difference in the t_0 GLX D-L ratios; as all regressions pivot around 122-125 ka. 432

Chapter 7: Kangaroo Island dating results

Figure 7.1: Equilibrium plots for the 8 Kangaroo Island samples that underwent HRGS analysis. The... 441

Figure 7.2: Comparison plot of the 9 Kangaroo Island samples that had U and Th ppm 446

detected by INAA, TSAC, and FGS. Open triangles are Th and open circles are U, both with 1σ error bars. The solid line represents unity; the lighter dashed lines represent 20% around unity, and the heavy dashed lines 50%.

Figure 7.3: Comparison plot of %K as determined by a combination of TSAC and GMBC, and ICP-OES. The solid line is unity and the dashed lines are 20% around unity. 446

Figure 7.4: Kangaroo location map for study sites described in this chapter. 451

Figure 7.5: Morphology and location of study sites at Pennington Bay, Kangaroo Island (Google Earth, 2009). The centre inset shows the locations of the 4 sections examined at PB1. 451

Figure 7.6: Stratigraphic logs (B) for Pennington Bay aeolianite outcrop PB1; included are the geochronological data (blue boxes) and corresponding GLX D-L ratio data (red boxes—numbers in brackets are individuals or subsamples analysed), when a GLX AAR age. The... 463

Figure 7.7: Location of PB#2-22 SARTT-OSL (also AAR) sample (black dot) at site PB1: taken from a small sea-cave set into the aeolianite promontory at this site. The open ellipse denotes the rock-hammer (33 cm) set for scale. The lower right inset shows the morphology of the promontory and the position of the cave (white arrow): note the modern wave-cut notch. 464

Figure 7.8: Single-aliquot (SARTT-OSL) equivalent dose (D_e) distributions for PB#2-22, displayed as a radial plot. The... 465

Figure 7.9: Single-aliquot (OSL) equivalent dose (D_e) distributions for PB#3-2, displayed as a radial plot. The CAM D_e for this sample is 175 ± 8 Gy. 466

Figure 7.10a: Ward method hierarchical multivariate (cluster) analysis of the single foraminifer GLX D-L ratio data from Unit 2c (site PB1 section 2 aeolianite), inset within a bivariate plot (ASX vs. GLX). Three age populations are identified. The lowest set of D-L ratios is assumed to be representative of the “true” age. 467

Figure 7.10b: Location of PB#2-X and PB#3-2 OSL (and AAR) samples, and the PBTL#1-1 TL sample (blue dots) at site PB1, and stratigraphic designations for section 2 at site PB1... 467

Figure 7.11: Single-aliquot (OSL) equivalent dose (D_e) distributions for PB#2-X, displayed as a radial plot. The CAM D_e for this sample is 92 ± 3 Gy. 468

Figure 7.12: Location of WR AAR sample PB#2-24, and stratigraphic designations for section 3 at site PB1, Pennington Bay (the prefix represents the site number, i.e., PB1). 469

Figure 7.13: Location of PB#2-18 OSL (and AAR) sample (blue circle) at site PB1 (also shown are sample points for PB#2-24 and PB#2-16: red circles): taken from the uppermost aeolianite at this site. The open ellipse denotes a rock-hammer (33 cm) set for scale. The... 472

Figure 7.14: Single-aliquot (OSL) equivalent dose (D_e) distributions for PB#2-18, displayed as a radial plot. The CAM D_e for this sample is 76 ± 3 Gy. 472

Figure 7.15: Pennington Bay Glanville Formation equivalent, site PB2. Stratigraphic log (B) for the PB2 aeolianite outcrop... 473

Figure 7.16: Common fossil fauna from the Pennington Bay cobble/pebble beach deposit at site PB2. The molluscan assemblage is mixed, with representatives from rocky coast (*Turbo*, *Patella*, and *Patelloida*) and sandy shore (*Amesodesma*, and *Mactra*) habitats. Modern analogues of both habitats are present at Pennington Bay. 474

Figure 7.17a: Site PB2 showing position of cobble/pebble shell unit (dashed blue lines), and sample positions (red circles).	475
Figure 7. 17b: Ward method hierarchical multivariate (cluster) analysis of the single foraminifer GLX D-L ratio data from PB#2e-2 (site PB2 raised shell/pebble notch...	475
Figure 7.18: Pennington Bay site PB3 stratigraphic log (B), for the aeolianite outcrop in the centre of the bay; included are the geochronological data (blue boxes) and corresponding GLX D-L ratio data (red boxes—numbers in brackets are individuals or subsamples analysed), when a GLX AAR age. The...	478
Figure 7.19: Site PB3 showing OSL (blue) and AAR (red) sample points (AAR samples were also taken from the same holes as the OSL samples) and unit designations. The open ellipse denotes a rock-hammer (33 cm) set for scale.	479
Figure 7.20: Single-aliquot (OSL) equivalent dose (D_e) distributions for PB#2b-3, displayed as a radial plot. The CAM D_e for this sample is 63 ± 2 Gy.	479
Figure 7.21: Single-aliquot (OSL) equivalent dose (D_e) distributions for PB#2b-8, displayed as a radial plot. The CAM D_e for this sample is 0.09 ± 0.01 Gy.	481
Figure 7.22: Pennington Bay site PB4-1 stratigraphic log (B) for the aeolianite outcrop towards the western end of the bay; included are the geochronological data (blue boxes)...	483
Figure 7.23: Site PB4-1 showing AAR (red) sample point and unit designations. Note the broken blocks of aeolianite and the modern rock platform.	484
Figure 7.24: Wave-cut benches at site PB4, western Pennington Bay. Bench 1 is modern, bench 2 most likely formed during a slightly higher than present Holocene sea-level, and bench 3, at approximately +3 m APSL, possibly formed...	484
Figure 7.25: Single-aliquot (SARTT-OSL) equivalent dose (D_e) distributions for sample PB#2a-3, displayed as a radial plot. The CAM D_e for this sample is 138 ± 4 Gy.	485
Figure 7.26: Pennington Bay site PB4-2 stratigraphic log (B) for the aeolianite outcrop towards the western end of the bay; included are the geochronological data (blue boxes)...	487
Figure 7.27: Site PB4-2 showing OSL (blue) and AAR (red) sample points (AAR samples were also taken from the same hole as the OSL sample) and unit designations. The open ellipse below the OSL sample point denotes a rock-hammer (33 cm) set for scale.	488
Figure 7.28: Bivariate plot of <i>Elphidium</i> spp. and <i>D. dimidiatus</i> D-L ratios, from site PB4, unit PB4-2d, Pennington Bay. Each point on the plot represents multiple foraminifers.	488
Figure 7.29: Pennington Bay site PB5 stratigraphic log (B) for the aeolianite outcrop towards the western end of the bay; included are the geochronological data (blue boxes)...	489
Figure 7.30: Single-aliquot (SARTT-OSL) equivalent dose (D_e) distributions for sample KPB#5-1, displayed as a radial plot. The CAM D_e for this sample is 205 ± 4 Gy.	490
Figure 7.31: Single-aliquot (OSL) equivalent dose (D_e) distributions for sample PB#2c-1, displayed as a radial plot. The CAM D_e for this sample is 1.56 ± 0.02 Gy.	492
Figure 7.32: Morphostratigraphical interpretation of the Pennington Bay sites based upon recorded logs. The cross-section has a vertical exaggeration of 40, a vertical scale	494

of 1:200, and a horizontal scale of 1:8000.

- Figure 7.33: Chronostratigraphical interpretation of the Pennington Bay sites, based upon the derived AAR, and luminescence chronologies. The scales are different for some logs, therefore the heights are not directly comparable in this sense; however, this does not detract from the presentation. 495
- Figure 7.34: Satellite image of Bales Beach sites (Google Earth, 2008). 497
- Figure 7.35: Bales Beach sites Bales1 and 2 (stratigraphic logs E and C) for the aeolianite outcrops towards the western end of the bay; included are the geochronological data (blue boxes) and corresponding GLX D-L ratio data (red boxes... 500
- Figure 7.36: Single-aliquot (OSL) equivalent dose (D_e) distributions for sample Bales#2-9, displayed as a radial plot. The CAM D_e for this sample is 56 ± 1 Gy. 501
- Figure 7.37: Single-aliquot (SARTT-OSL) equivalent dose (D_e) distributions for sample Bales#3-1, displayed as a radial plot. The CAM D_e for this sample is 212 ± 3 Gy. 503
- Figure 7.38: Bivariate plot of Bales#3-1 foraminifer (*Elphidium* spp. + *Discorbis dimidiatus*) D-L ratio data. Here a hierarchical clustering... 503
- Figure 7.39: Location of sites around Vivonne Bay, and Point Ellen. The upper right inset shows the geographical location of the bay (small black arrow); the... 505
- Figure 7.40: Approximate extent (red line) of the Point Ellen Formation outcrop (~240 m laterally). 506
- Figure 7.41: Point Ellen sites PE1A and PE1B (stratigraphic logs) for the Point Ellen Formation outcrops in the eastern and western portions of the point. Included are the geochronological data (blue boxes)... 510
- Figure 7.42: Examples of marine molluscs and foraminifers found in the upper and basal portions of the Point Ellen Formation. 511
- Figure 7.43: Sample area at Point Ellen site PE1A. Several specimens of *Katelsysia scalarina* were recovered from this patch of the basal shell horizon overlying and infilling the irregular surface of the Kanmantoo Group bedrock (at ~sea-level). Whole... 512
- Figure 7.44: Sample area at Point Ellen site PE1B (see lower LH inset for detail). Several specimens of *Nerita milnesi* and *Katelsysia* sp. were recovered from this part of the upper shell horizon (red circle). Whole-rock sediment was also sampled. Note the small cave at approximately +3 m APSL. 512
- Figure 7.45: Location of PE#3-1 OSL sample (site PE2). Note that the sample was removed far enough from the calcrete contact to account for the gamma sphere. Also note the prominent calcrete visor. The... 513
- Figure 7.46: Vivonne Bay sites PE2 and PE3: stratigraphic logs for the aeolianite outcrops towards the southern end of the bay. Included are the geochronological data (blue boxes... 514
- Figure 7.47: Single-aliquot (OSL) equivalent dose (D_e) distributions for sample PE#3-1, displayed as a radial plot. The CAM D_e for this sample is 121 ± 4 Gy. 515
- Figure 7.48: Panorama looking east from Vivonne Bay, showing the location of PE2 and a series of Last Interglacial sea-caves. 516
- Figure 7.49: View south-east from Vivonne Bay site PE3, showing positions of units. 516

Figure 7.50: Single-aliquot (SARTT-OSL) equivalent dose (D_e) distributions for sample PE#3-2, displayed as a radial plot. The CAM D_e for this sample is 212 ± 4 Gy.	517
Figure 7.51: Ward method hierarchical multivariate (cluster) analysis of the single foraminifer GLX D-L ratio data from PE#3-2 (site PE3), inset within a bivariate plot (ASX vs. GLX). Two age populations are identified.	518
Figure 7.52: Ward method hierarchical multivariate (cluster) analysis of the single foraminifer GLX D-L ratio data from PE#3-4, 3-5 and 3-6 (site PE3 shell/pebble notch deposits), inset within a bivariate plot (ASX vs. GLX). Five age populations...	520
Figure 7.53: The stony coral <i>Plesiastrea versipora</i> (sample PE#3-4), recovered from unit b site PE3, Vivonne Bay, Kangaroo Island.	521
Figure 7.54: Vivonne Bay site PE4, an aeolianite outcrop towards the centre of the bay. Included are the geochronological data (blue boxes) and corresponding GLX D-L ratio data (red boxes—numbers in brackets are individuals or subsamples analysed). The top RH inset (B)...	523
Figure 7.55: Hanson Bay satellite digital photograph (edited); showing the location of the study sites (HB1 and HB2) and bay morphology (unedited image from Google Earth, 2009).	525
Figure 7.56: Common fossil fauna from the Hanson Bay shelly facies at site HB1. The molluscan assemblage is mixed, with representatives from rocky coast (F: <i>Turbo</i> [<i>Ninella</i>] <i>torquatus</i> , B: <i>Nerita</i> [<i>Melanerita</i>] <i>atramentosa</i> , and D: <i>Patella</i> [<i>Scutellastra</i>]...	526
Figure 7.57: Hanson Bay stratigraphic logs for the sedimentary outcrops towards the eastern end of the beach (HB1). Included are the geochronological data (blue boxes) and corresponding GLX D-L ratio data (red boxes—numbers in brackets are...	527
Figure 7.58: OSL sample point (blue circle) (TL sample was removed adjacent to this), and various facies at HB1, Hanson Bay (black ellipse denotes rock-hammer set for scale—33 cm). Top of shell rich unit is approximately +3 m APSL.	529
Figure 7.59: Single-aliquot (OSL) equivalent dose (D_e) distributions for sample HB#3-4, displayed as a radial plot. The CAM D_e for this sample is 96 ± 3 Gy.	530
Figure 7.60: Ward method hierarchical multivariate (cluster) analysis of the single foraminifer GLX D-L ratio data from the shell facies at HB1, inset within a bivariate...	530
Figure 7.61: Close view of shell facies at HB1, note that most shells in this photo are broken; it was difficult to find reasonably whole shell for AAR analyses in this unit. RH inset shows a closer view of the section outlined by the red rectangle (rock-hammer set for scale—33 cm).	533
Figure 7.62: Morphology of the lagoonal unit at site HB1. The red circles show the position of the whole-rock sediment AAR dating samples.	534
Figure 7.63: Ward method hierarchical multivariate (cluster) analysis of the single foraminifer GLX D-L ratio data from the backshore dunes at HB1, inset within a bivariate plot (ASX vs. GLX). Three age populations are identified. The mean of the lowest ...	535
Figure 7.64: Location of sample KHa#1 at site HB2, on the western end of Hanson Bay Beach (upper LH inset image Google Earth, 2009).	536
Figure 7.65: Location of Kelly Hill caves on the southern coast of Kangaroo Island. Upper LH inset shows the location on a regional map (black arrow) (image Google Earth, 2009).	538

- Figure 7.66: Map of main cavern at Kelly Hill, showing locations of various sample points. Cave map (modified) courtesy of G. Gartrell, P. Horne, and G. Pilkington of CEGSA (Cave exploration group of South Australia) (2007). Numbers in brackets are GLX D-L ratio means for AAR samples. 539
- Figure 7.67: Single-aliquot (SARTT-OSL) equivalent dose (D_e) distributions for sample KH#3-1, displayed as a radial plot. The CAM D_e for this sample is 227 ± 7 Gy. 542
- Figure 7.68: Location of AAR WR sample KH#1-1. See also Figure 7.64. Sample was removed from ~200 mm deep into relatively weakly cemented calcarenite. 542
- Figure 7.69: Location of Rocky Point site (red circle upper LH inset) on the neck of the Dudley Peninsula (images Google Earth, 2009). 546
- Figure 7.70: Rocky Point stratigraphic log (C) for the sedimentary outcrops at the rear of the aeolianite headland. Included are the geochronological data (blue boxes) and corresponding GLX D-L ratio data (red boxes...). 547
- Figure 7.71: Examples of marine shell recovered from the Rocky Point notch deposit. Found in the deposit are representatives from shallow water sand dwelling species (*Fulvia*), sublittoral rock dwelling species (*Conus*), and rocky coast species (*Diloma* and *Nerita*). 550
- Figure 7.72: Sample site location (red circle) at Rocky Point. Note the large broken calcrete block RH mid-ground, with carbonised calcrete clasts. Dashed lines denote limits of the shell bed, and the black ellipse shows the location of a rock-hammer set for scale (33 cm). 550
- Figure 7.73: Foraminifer (*Elphidium* spp. and *Discorbis dimidiatus*) bivariate plot for Rocky Point. Note the scatter in the D-L ratios. 551
- Figure 7.74: Location of Baudin Beach sites (red circles upper LH inset) on the western side of the Dudley Peninsula (images Google Earth, 2009). 552
- Figure 7.75: Collapsed calcrete/palaeosol blocks at site BB1, Baudin Beach, Kangaroo Island. 552
- Figure 7.76: Calcrete hardpan grading below sea-level (red dashed line) at site BB1, Baudin Beach, Kangaroo Island. 553
- Figure 7.77: Panorama near site BB3 showing the upper aeolianite and the alluvial fan sediments. The blue dashed line (middle background) demarks two apparently different alluvial units, and also the smooth contact between the alluvial sediments and the upper aeolianite (LH midground). 554
- Figure 7.78: Baudin Beach stratigraphic logs (B) for the sedimentary outcrops along a section of the north-west coast of the Dudley Peninsula. Included are the geochronological data (blue boxes) and corresponding GLX D-L ratio data... 555
- Figure 7.79: Single-aliquot (OSL) equivalent dose (D_e) distributions for sample BB#3-1, displayed as a radial plot. The CAM D_e for this sample is 103 ± 3 Gy. 556
- Figure 7.80: Ward method hierarchical multivariate (cluster) analysis of the single foraminifer GLX D-L ratio data from the upper aeolianite at site BB1 and BB3, inset within a bivariate plot (ASX vs. GLX). Two age populations are identified. The... 559
- Figure 7.81: Overlay of BB3a foraminifer D-L ratios (ASX vs. GLX) onto the BB1a and BB3d data. Note how the BB3a population overlies the higher D-L population from BB1a and BB3d. 559

Figure 7.82: Single-aliquot (OSL) equivalent dose (D_e) distributions for sample BB#3-5, displayed as a radial plot. The CAM D_e for this sample is 218 ± 15 Gy.	561
Figure 7.83: Freshwater gastropods (Family Hydrobiidae) extracted from the Pooraka Formation sediments at site BB2, Baudin Beach.	561
Figure 7.84: Location of units near site BB2. Note position of upper alluvial sediments in relation to the upper aeolianite unit (BB1a and BB3d) and calcrete (BB1b and BB3e). See person midfield for scale (~2 m).	563
Figure 7.85: Schematic representation of the units present along a 1000 m section of Baudin Beach encompassing the 3 examined sites (BB1, BB2 and BB3).	564
Figure 7.86: Pooraka Formation and overlying aeolianite near site BB3. Note clean contact (arrows) (Rock-hammer set for scale: 33 cm).	565
Figure 7.87: Long view looking north from Baudin Beach Jetty (near site BB1), showing the sequence at sites BB2 and BB3. Note the level upper surface (lower blue dotted line) of the Pooraka Formation...	566
Figure 7.88: Examples of marine molluscs analysed from sites AR1 and AR2 at American River.	567
Figure 7.89: Location of American River sites (red circles upper LH inset) on the western side of the Dudley Peninsula (images Google Earth, 2009).	568
Figure 7.90: Cambrian Tapanappa Formation outcropping at American River, north from Buicks Point.	568
Figure 7.91: AR1 and AR 2 sites at American River, with sample locations (red circles). The schematics are not to scale.	570
Figure 7.92: OxCal (V. 3.10) calibration plot for American River AMS ^{14}C sample AR#3-2AMS.	571
Figure 7.93: OxCal (V. 3.10) calibration plot for American River AMS ^{14}C sample AR#3-5AMS.	571
Figure 7.94: Bivariate plot of ASX vs. GLX for AR1 site marine molluscs (<i>Katelsysia scalarina</i> , <i>Katelsysia peronii</i> and <i>Katelsysia rhytiphora</i>). Cluster 1 represents a group of shells from +0.4 to +0.5 m APSL, cluster 2 from sea level, and cluster 4 from sea level (cluster 3 is present at site AR2) (see Table 7.26 for D-L ratios).	574
Figure 7.95: Bivariate plot of ASX vs. GLX for AR2 site marine molluscs (<i>Katelsysia scalarina</i> , <i>Katelsysia peronii</i> and <i>Katelsysia rhytiphora</i>). Inset is the Ward method multivariate plot used to differentiate the clusters.	575
Figure 7.96: Shell and sandy bands (layers) at site AR2, American River.	576
Figure 7.97: Bivariate plot of ASX vs. GLX for all shells analysed at American River. The ages were determined using a mean GLX D-L value (determined by Ward method...	576
Figure 7.98: Extent in outcrop of the Kingscote Conglomerate, at sites KC1 and KC2, Kingscote, Kangaroo Island (courtesy of Google Earth, 2009).	579
Figure 7.99: Kingscote Conglomerate exposed at surface, near Rolls Point (site KC1), Kingscote.	579

Figure 7.100: Kingscote Conglomerate near Rolls Point (site KC1). Note solution pipe middle background (knapsack for scale: 50 cm).	580
Figure 7.101: Close-up of the Kingscote Conglomerate unit (near Rolls Point). Note abundant basalt clasts (rock-hammer handle for scale: 20 cm).	580
Figure: 7.102: Kingscote Conglomerate at site KC2. Red dashed line shows approximate position of the unit (uppermost) (rock-hammer for scale: 33 cm).	581
Figure 7.103: Location of Kingscote study site. The upper LH inset shows GPS data points (yellow points) for extent in outcrop of the Kingscote Late Pleistocene raised basalt conglomerate. The...	581
Figure 7.104: Mollusc species analysed for AAR D-L enantiomers, from the Kingscote Conglomerate, Kingscote, Kangaroo Island.	584
Figure 7.105: Amino acid D-L ratio bivariate plot for <i>Katelsia scalarina</i> (N = 6) extracted from the Kingscote conglomerate (site KC1). The lower GLX D-L ratio population was used to determine the AAR age.	585
Figure 7.106: Kingscote stratigraphic logs for the sedimentary outcrops near Rolls Point (KC1), and near "The Bluff" (KC2). Included are the geochronological data...	586
Figure 7.107: Cobbles and pebbles (limestone, basalt, and quartz) on Kingscote Beach at the mid-tide level, south of Rolls Point.	588
Figure 7.108: Location map for study site on North Cape, Kangaroo Island. Inset (upper LH) shows the general locations of sites NC1 and NC2 (red circles) (unedited image courtesy of Google Earth, 2009).	591
Figure 7.109: Marine shell analysed for amino acid enantiomers. (A) <i>Anapella cycladea</i> , from site NC1, characteristic of tidal inlets, estuarine contexts and tidal flats. (B) <i>Tawera lagopus</i> and <i>Mactra australis</i> , from site NC2, characteristic of moderate to high energy beaches in shallow, sandy contexts.	591
Figure 7.110: Muddy sand unit (a1) at site NC1, near Point Marsden. Note rock-hammer for scale (33cm) (black ellipse).	592
Figure 7.111: Foraminifer bivariate plot (ASX vs. GLX) of <i>Elphidium</i> sp. recovered from the Boxing Bay Conglomerate. Note D-L ratio clustering in the highly racemized foraminifers.	595
Figure 7.112: North Cape stratigraphic logs for the sedimentary outcrops near Point Marsden (NC1), and Boxing Bay (NC2). Included are the geochronological data (blue boxes)...	596
Figure 7.113: The Boxing Bay Conglomerate and beach facies (these could also be the bottomset beds of an aeolianite deposit (rock-hammer set for scale [black ellipse]: 33 cm).	597
Figure 7.114: Closer view of the level bedded unit (b) overlying the Boxing Bay Conglomerate.	598
Figure 7.115: Closer view of the Boxing Bay Conglomerate, and thin sand layer (knapsack is 50 cm high).	598
Figure 7.116: Long view east from site NC2 of a Boxing Bay Conglomerate patch with a wave-cut Holocene (?) platform (blue dashed line). Note the large cemented boulders...	599
Figure 7.117: Location map for study site on Emu Bay, Kangaroo Island. Inset (upper	602

LH) shows the general location of site EB (red circle). The lower RH inset is a closer view of the EB study site; the red arrows indicate sample positions (unedited images courtesy of Google Earth, 2009).

Figure 7.118: Stratigraphic log (B) for the sedimentary outcrop at Emu Bay (EB). 603
Included are the geochronological data (blue boxes) and corresponding GLX D-L ratio...

Figure 7.119: Panorama of the Emu Bay site, showing sample locations, height of the 605
sequence (~14 m APSL), orientation of the site, and location of the stratigraphic units.

Figure 7.120: Location map for study site at Smith Bay, Kangaroo Island. Inset (upper 607
LH) shows the general location of site SB (red circle). The lower middle inset is a closer view of the SB study site; the red arrow indicates sample positions (unedited images courtesy of Google Earth, 2009).

Figure 7.121: The early Pleistocene Smith Bay Conglomerate, overlying Permian till at 609
Smith Bay, Kangaroo Island.

Figure 7.122: Stratigraphic log (A) for the sedimentary outcrop at Smith Bay (SB). 611
Included are the geochronological data (blue boxes) and corresponding GLX D-L ratio data (red boxes...

Figure 7.123: Wider view of the early Pleistocene Smith Bay Conglomerate (red dashed 612
lines), overlying Permian till at Smith Bay, Kangaroo Island. Note upper calcrete and talus slope over the Conglomerate.

Figure 7.124: Location map for study site at Stokes Bay, Kangaroo Island. Inset (upper 614
LH) shows the general location of site STB (red circle). The lower middle inset is a closer view of the STB study site; the red arrow indicates sample positions (unedited images courtesy of Google Earth, 2009).

Figure 7.125: Aeolianite at Stokes Bay. Note weathered condition of the calcarenite 614
(Rock-hammer set for scale: 33 cm).

Figure 7.126: Panorama of Stokes Bay outcrop (site STB), showing sample area, 615
position of calcrete and height of the units. Note the large collapsed blocks of aeolianite and calcrete at the seaward margin of the headland.

Figure 7.127: Stratigraphic log (A) for the sedimentary outcrop at Stokes Bay (STB). 616
Included are the geochronological data (blue boxes) and corresponding GLX D-L ratio data (red boxes...

Chapter 8: Kangaroo Island near-coastal Quaternary carbonate sediments: a synthesis

Figure 8.1: Ward (1963) method hierarchical clustering dendrogram (constructed in SAS 630
JMP) of whole-rock sediment GLX D-L ratio data from Kangaroo Island, and Coorong and Naracoorte on the southeast South Australia mainland...

Figure 8.2: Bivariate plot of mean whole-rock sediment AAR data from the Kangaroo 631
Island sites clustered using Ward (1963) method hierarchical dendrograms.

Figure 8.3: Bivariate plot of mean mollusc AAR data from the Kangaroo Island sites 631
clustered using Ward (1963) method hierarchical dendrograms.

Figure 8.4: Bivariate plot of mean foraminifer AAR data from the Kangaroo Island sites 631
clustered using Ward (1963) method hierarchical dendrograms.

Figure 8.5: Ward (1963) method hierarchical clustering dendrogram (constructed in SAS 632

JMP) of molluscan GLX D-L ratio data from Kangaroo Island; accompanied by the ^{14}C and U-series chronology and aminozones defined on the basis of 7 clusters. Amino acid D-L...

Figure 8.6: Ward (1963) method hierarchical clustering dendrogram (constructed in SAS JMP) of foraminifer GLX D-L ratio data from Kangaroo Island; accompanied by the ... 633

Figure 8.7: Holocene sea-level curve generated from 136 finite sea-level data points (compiled from southern Australia sites) fitted with a fourth-order polynomial. The sea-level curve is relative to present Low Water Datum (m LWD) (figure modified from Belperio *et al.*, 2002). The curve is overlain with GLX AAR ages, luminescence... 635

Figure 8.8: Quaternary oxygen isotope curve (modified from the Quaternary section of the Lisiecki and Raymo [2005] LR04 stack) with luminescence (SARTT-OSL), and amino acid racemization (AAR) chronologies, from this study, overlain. Note: only early... 636

Figure 8.9: Continuous sea-level estimates on the SPECMAP timescale (up to MIS 9) from a range of sources (coupled with other sea-level indicators), and compared with the benthonic oxygen isotope record of core V19-30 (Shackleton and Pisias, 1985) from the east equatorial... 637

Figure 8.10: Oblique view (200 m altitude) of Pennington Bay, facing north-east. Note position of small inner-bay headlands (centre and right mid-ground) (image is vertically exaggerated by 3—image and DEM courtesy of Google Earth, 2010). The high peak in the rear mid-ground is Prospect Hill (a vegetated, unconsolidated, large-scale dune). 640

Figure 8.11: Proposed chronostratigraphy for the south coast of Kangaroo Island based upon the luminescence and AAR chronologies. The y-axis and logs are to scale, however the x-axis is not. 643

Figure 8.12: Oblique view (241 m altitude) of Bales Beach, facing north-east (image is vertically exaggerated by 3—image and DEM courtesy of Google Earth, 2010). 644

Figure 8.13: Oblique view (452 m altitude) of Point Ellen and Vivonne Bay, facing north-west (image is vertically exaggerated by 3—image and DEM courtesy of Google Earth, 2010). 645

Figure 8.14: Oblique view (107 m altitude) of Hanson Bay section, facing north-east (image is vertically exaggerated by 3—image and DEM courtesy of Google Earth, 2010). 646

Figure 8.15: Oblique view (155 m altitude) of Baudin Beach sections, facing south-west (image is vertically exaggerated by 3—image and DEM courtesy of Google Earth, 2010). 648

Figure 8.16: Oblique view (144 m altitude) of North Cape site NC1, near Point Marsden, facing north-west (image is vertically exaggerated by 3—image and DEM courtesy of Google Earth, 2010). 651

Figure 8.17: Oblique view (163 m altitude) of North Cape site NC2, in Boxing Bay, facing south-west (image is vertically exaggerated by 3—image and DEM courtesy of Google Earth, 2010). 652

Figure 8.18: Oblique view (188 m altitude) of the Smith Bay site SB, facing south-west (image is vertically exaggerated by 3—image and DEM courtesy of Google Earth, 2010). 654

Figure 8.19: Oblique view (472 m altitude) of the Stokes Bay site STB, facing south-east (image is vertically exaggerated by 3—image and DEM courtesy of Google Earth, 655

2010).

Figure 8.20: Onshore and offshore profile for Pennington Bay (LH inset): upper RH inset shows orientation of the cross-section (image courtesy of Google earth, 2010), and the lower RH inset is a section of the scaled benthic oxygen isotope curve of Cutler *et al.* (2003)...

Figure 8.21: Onshore and offshore profile for Vivonne Bay (LH inset): upper RH inset shows orientation of the cross-section (image courtesy of Google earth, 2010), and...

Figure 8.22: Proposed model for aeolianite dune deposition, from the early Pleistocene to the Late Pleistocene and Holocene, in a headland bound embayment (similar to Pennington Bay).

Figure 8.23: Luminescence (some U-series and ^{14}C) ages from sites around the world, along with the Kangaroo Island ages, compared latitudinally and tuned to the...

List of Tables

Chapter 1: Kangaroo Island: history and physical environmental setting

Table 1.1: Kangaroo Island geology, after Tate (1883).	7
Table 1.2: Geological timescales and events for Kangaroo Island (after James and Clark, 2002).	11
Table 1.3: Kangaroo Island tidal data (after Short and Fotheringham, 1986).	22
Table 1.4: Archival climate averages for stations on Kangaroo Island (Bureau of meteorology [BOM], 2007).	26

Chapter 2: Aeolianite formation and distribution in the context of global sea-level change

Table 2.1: Influence of water temperature on carbonate sediment assemblages, constituent organism, and sedimentary characteristics (modified after James, 1997; Brooke, 2001).	56
--	----

Chapter 3: Stratigraphy and petrology of aeolianite and other near-shore deposits on Kangaroo Island

Table 3.1: Definitions of stratigraphic terms used in this thesis (modified from Brooke, 1999).	84
Table 3.2: Characteristics of PB1, section 1, lithostratigraphic units.	96
Table 3.3: Compiled bedding vector data for PB1 western headland (section 1a).	99
Table 3.4: Characteristics of PB1 section 2 lithostratigraphic units.	101
Table 3.5: Characteristics of PB1 section 3 lithostratigraphic units.	103
Table 3.6: Characteristics of PB1 section 4 lithostratigraphic units.	104
Table 3.7: Compiled bedding vector data for PB1 western headland (Unit 1-4ci).	105

Table 3.8: Compiled bedding vector data for PB3 headland (Units 3a and 3c.)	111
Table 3.9: Lithostratigraphic characteristics of site PB3.	114
Table 3.10: Lithostratigraphic characteristics of section 1 at site PB4.	116
Table 3.11: Compiled bedding vector data for the PB4 headland (section 1—units 4-1b and 4-1d).	118
Table 3.12: Lithostratigraphic characteristics of section 2 at site PB4.	119
Table 3.13: Compiled bedding vector data for PB4 headland section 2 (Units 4-2dii and 4-2fii).	121
Table 3.14: Lithostratigraphic characteristics of site PB5.	124
Table 3.15: Compiled bedding vector data for PB5 headland (units 5b, 5d, and 5f).	126
Table 3.16: Lithostratigraphic characteristics of sites Bales1 and Bales2.	128
Table 3.17: Characteristics of Baudin Beach lithostratigraphic units.	180
Table 3.18: Compiled bedding vector data for BB1 site (Unit BB1-a).	181
Table 3.19: Lithostratigraphic characteristics of site EB at Emu Bay.	205
Table 3.20: Compiled bedding vector data for site EB at Emu Bay.	205
Table 3.21: Thin section point-count compositional results for selected Kangaroo Island aeolianite, raised beach, and shelly deposits.	224
Table 3.22: Mineral composition of 13 various (age and facies) Kangaroo Island near-shore sediments. Data are percentages of 32 selected minerals, quantified from powder XRD analyses using USGS RockJock version 5 (Eberl, 2003).	225- 226

Chapter 4: Luminescence, accelerator mass spectrometry carbon-14 (AMS¹⁴C), and Uranium-series (²³⁸U/²³⁰Th series) dating methods

Table 4.1: List of absolute dating samples retrieved from Kangaroo Island, South Australia.	264
---	-----

Chapter 5: Thermally transferred optically stimulated luminescence (TTOSL) dating: development and testing of a single aliquot regenerative dose (SAR) protocol

Table 5.1: The Wang <i>et al.</i> (2006a) MAR TTOSL protocol.	306
Table 5.2: Comparison of conventional OSL to the MAR ReOSL method; all equivalent doses overlap at 2 σ .	314
Table 5.3: SARTT-OSL modification of the Wang <i>et al.</i> (2006a) MAR TTOSL protocol.	326
Table 5.4: Equivalent dose and age comparisons between SARTT-OSL, conventional OSL, single grain OSL, and TL.	327

Chapter 6: Amino acid racemization analysis methods, experiments, and calibrations

Table 6.1: Time Table for eluent gradient and flow rate.	348
Table 6.2: Pretreatment experiment results for Smith Bay molluscs.	357
Table 6.3: Pyrolysis experiment details for the marine cockle <i>Katelysia scalarina</i> .	371
Table 6.4: Pyrolysis experiment D-L ratio results for ASX, GLX, SER and VAL, for live-collected <i>Katelysia scalarina</i> from Kangaroo Island.	372
Table 6.5: Pyrolysis experiment details for whole-rock.	373
Table 6.6: Pyrolysis experiment D-L ratio results for ASX, GLX, SER and VAL, for biogenic carbonate modern beach sand (whole-rock) from Kangaroo Island.	373
Table 6.7: Pyrolysis experiment details for <i>Elphidium</i> sp. It should be noted that even though this experiment was started earlier than the whole-rock experiment; the whole-rock subsample used was removed prior to picking for foraminifer tests.	375
Table 6.8: Pyrolysis experiment D-L ratio results for ASX, GLX, and SER, for <i>Elphidium</i> sp. extracted from modern beach sand sample EB#2-7, from Emu Bay, Kangaroo Island.	375
Table 6.9: Pyrolysis experiment details for <i>Discorbis dimidiatus</i> . It should be noted that even though this experiment was started earlier than the whole-rock experiment; the whole-rock subsample used was removed prior to picking for foraminifer tests.	376
Table 6.10: Pyrolysis experiment D-L ratio results for ASX, GLX, and SER, for <i>Discorbis dimidiatus</i> . extracted from modern beach sand sample EB#2-7, from Emu Bay, Kangaroo Island.	376
Table 6.11: Constrained power law model composite forward rate constants (at 110° C) for selected amino acids, extracted from <i>Katelysia scalarina</i> , whole-rock modern beach sediment, <i>Elphidium crispum</i> and <i>Discorbis dimidiatus</i> .	379
Table 6.12: Some examples of middle and early Pleistocene THAA D-L ratios from Kangaroo Island.	392
Table 6.13: Calculated continental shelf to near-shore residence times estimated for Kangaroo Island biogenic carbonate sediments (these values do not account for the presence of reworked biomineral grains).	399
Table 6.14: D-L ratio comparison of near-shore and cliff face modern beach sediments, at two sites on Kangaroo Island.	400
Table 6.15: Calibration data for Coorong whole-rock aeolianite.	401
Table 6.16: A comparison of the extent of GLX racemization and numerical GLX AAR ages to the TL chronology of Huntley <i>et al.</i> (1993; 1994) (OSL of Banerjee <i>et al.</i> [2003] for Robe#1-1)	402
Table 6.17: Amino acid D-L ratios (. 1) derived from the interlaboratory comparative standards (ILC-A, B, and C) of Wehmiller (1984), and Kaufman and Manley (1998) (ILC-Z). Reported here are a set of comparisons to the original Wehmiller (1984) gas chromatography (GC) results and the Kaufman and Manley (1998) RP-HPLC ILC results.	413
Table 6.18: Calibration data for American River molluscs.	419

Table 6.19: Calibration data for Kangaroo Island Pleistocene molluscs.	420
Table 6.20: Calibration data for Kangaroo Island Pleistocene foraminifers.	423
Table 6.21: U-series calibration data for Kangaroo Island whole-rock aeolianite .	426
Table 6.22: Calibration data for Kangaroo Island Pleistocene whole-rock sediment samples.	430

Chapter 7: Kangaroo Island dating results

Table 7.2: HRGS radionuclide activities summary and daughter-to-parent ratios for the ^{238}U and ^{232}Th decay chains: used to calculate the environmental dose rates for 8 Kangaroo Island samples. Units are in Bq/kg^{-1} with associated 1σ uncertainties.	438
Table 7.2: Relative contributions to the beta and gamma dose rate from radionuclides, for aeolianite sample Bales#2-9. Conversions from Bq/kg^{-1} were performed using the program listed in Roberts <i>et al.</i> (1993). Note: not corrected for beta attenuation or moisture content.	440
Table 7.3: Concentrations in ppm of uranium, thorium and potassium for 7 Kangaroo Island samples; determined by TSAC (and GMBC for %K); using the methods of Aitken (1985) and Jacobs (2001).	443
Table 7.4: FGS results for 2 Kangaroo Island samples.	444
Table 7.5: INAA and ICP-OES analysis results of 9 Kangaroo Island dosimetry samples (INAA for U and Th; ICP-OES for K).	444
Table 7.6: Beta dose rate samples from Kangaroo Island, with sample water content; dry beta dose rate, and wet and attenuated (100 μm grain size) beta dose rate. The wet and attenuated dose rate is used for the age calculation.	445
Table 7.7: Total dose rate data for the Kangaroo Island OSL and SARTT-OSL samples (TL dose rate data is given in Table 7.13 in Part II of this Chapter, as they were determined independently).	447
Table 7.8: Kangaroo Island Pleistocene and Holocene (Holocene calibration molluscs only—American River mollusc dataset presented separately) marine and freshwater mollusc ASX and GLX AAR data, and AAR numerical ages.	453- 454
Table 7.9: Pleistocene and Holocene whole-rock (WR) sediment ASX and GLX AAR data, and AAR numerical age estimates for Pennington Bay.	455- 456
Table 7.10: Pennington Bay Pleistocene single foraminifer ASX and GLX AAR data, and numeric AAR age estimates.	457
Table 7.11: Conventional OSL ages for sediment samples from Kangaroo Island, together with supporting dose rate and equivalent dose data (place names in order: Bales Beach [Bales], Baudin Beach [BB], Hanson Bay [HB], Pennington Bay [PB], and Vivonne Bay [PE]).	458- 459

Table 7.12: Information on the number of 1 mm aliquots measured using the conventional OSL method. The table displays the rejection criteria used...	459
Table 7.13: SARTT-OSL ages for sediment samples from Kangaroo Island, together with supporting dose rate and equivalent dose data (place names in order: Bales Beach [Bales], Kelly Hill Caves [KH], Pennington Bay [PB], and Vivonne Bay [PE]).	460
Table 7.14: TL ages for sediment samples from Kangaroo Island, together with supporting dose rate and equivalent dose data (place names in order: Emu Bay [EB], Hanson Bay [HB], Pennington Bay [PB]).	461
Table 7.15: Pleistocene and Holocene whole-rock sediment ASX and GLX AAR data, and GLX AAR numerical ages for Bales Beach.	498
Table 7.16: Bales Beach Pleistocene single foraminifer ASX and GLX AAR data, and numeric AAR age estimates.	499
Table 7.17: Pleistocene whole-rock (WR) sediment ASX and GLX AAR data, and AAR numerical age estimates for Point Ellen and Vivonne Bay.	508
Table 7.18: Point Ellen and Vivonne Bay Pleistocene single foraminifer ASX and GLX AAR data, and numeric AAR age estimates.	509
Table 7.19: Uranium series analyses data (Australian National University geochronology), and calculated U-series age estimate for the stony coral <i>Plesiastrea versipora</i> (sample PE#3-4), recovered from unit b site PE3, Vivonne Bay.	521
Table 7.20: Pleistocene whole-rock (WR) sediment ASX and GLX AAR data, and AAR numerical age estimates for Hanson Bay.	531
Table 7.21: Hanson Bay Pleistocene single foraminifer ASX and GLX AAR data, and numeric AAR age estimates.	532
Table 7.22: Pleistocene whole-rock (WR) sediment ASX and GLX AAR data, and AAR numerical age estimates for Kelly Hill Caves.	541
Table 7.23: Rocky Point Pleistocene whole-rock (WR) sediment ASX and GLX AAR data, and AAR numerical age estimates.	549
Table 7.24: Rocky Point Pleistocene single foraminifer ASX and GLX AAR data, and numeric AAR age estimates.	549
Table 7.25: Baudin Beach Pleistocene whole-rock (WR) sediment ASX and GLX AAR data, and AAR numerical age estimates.	557
Table 7.26: Baudin Beach Pleistocene single foraminifer ASX and GLX AAR data, and numeric AAR age estimates.	558
Table 7.27: AMS 14C ages and sample details for American River mollusc samples.	569
Table 7.28: Holocene American River marine mollusc ASX and GLX AAR data, and AAR numerical ages.	573
Table 7.29: Kingscote Conglomerate Pleistocene marine mollusc ASX and GLX AAR data, and AAR numerical ages.	582
Table 7.30: Kingscote Conglomerate Pleistocene single foraminifer ASX and GLX AAR data, and numeric AAR age estimates.	583

Table 7.31: Height data (APSL) for Last Interglacial (MIS 5e) raised beach deposits, and raised shelly deposits on Kangaroo Island.	588
Table 7.32a: North Cape Pleistocene marine mollusc ASX and GLX AAR data, and AAR numerical ages.	593
Table 7.32b: North Cape Pleistocene single foraminifer ASX and GLX AAR data, and numeric AAR age estimates.	594
Table 7.33: Pleistocene (WR) sediment ASX and GLX AAR data, and AAR numerical age estimates for North Cape.	594
Table 7.34: Pleistocene whole-rock (WR) sediment ASX and GLX AAR data, and AAR numerical age estimates for Emu Bay.	604
Table 7.35: Smith Bay Conglomerate early Pleistocene marine mollusc ASX and GLX AAR data, and AAR numerical ages.	610
Table 7.36: Pleistocene whole-rock (WR) sediment ASX and GLX AAR data, and AAR numerical age estimates for Stokes Bay.	615

Chapter 8: Kangaroo Island near-coastal Quaternary carbonate sediments: a synthesis

Table 8.1: GLX D-L ratio data (whole-rock sediment, mollusc, and foraminifer) for Last Interglacial raised deposits for Kangaroo Island Sites Pennington Bay, Vivonne Bay, Hanson Bay, Rocky Point and Kingscote.	629
Table 8.2: Mollusc and whole-rock sediment GLX D-L ratio data for selected, predominantly Last Interglacial, sites on Kangaroo Island (this study), the South Australia mainland, and the cape region of South Africa.	664-665

Chapter 1: Kangaroo Island: history and physical environmental setting

1.1 Introduction

The following review examines the natural history of Kangaroo Island, its human occupation, geology, marine environment, modern climate, and vegetation. The environmental portion of this chapter will be used to provide background for the interpretation of field and analytical data presented in later chapters, in terms of the Quaternary history of aeolianite formation.

This chapter begins with a short description of the geography of Kangaroo Island, then a brief review of the history of human occupation, which describes both Aboriginal and European occupation. This is followed by a assessment of the literature on the geology and geomorphology of Kangaroo Island, and finally the present-day environments of the island (i.e. marine environment, climate and vegetation) are examined.

1.2 Kangaroo Island location

Kangaroo Island lies off the South Australian coast, in the Southern Ocean, between 35° 30' and 36° 30' south latitude, and 136° 30' and 138° 30' east longitude, on a broad expanse of continental shelf that extends southward from the mainland for approximately 100 km. The island itself lies adjacent to three peninsulas and two large gulfs (the Eyre Peninsula, Spencer Gulf, Yorke Peninsula, the Gulf of St. Vincent, and the Fleurieu Peninsula—proceeding in order to the south-east), and forms a boundary between the Lincoln Shelf in the northwest, and the Lacepede Shelf in the southeast (Figure 1.1).

Kangaroo Island is closest to the mainland from Dudley Peninsula to the Fleurieu Peninsula, at 14.5 km distance across the Backstairs Passage. To the north is the Yorke Peninsula, at 50 km distance across Investigator Strait, whereas the Eyre Peninsula is approximately 100 km distance to the northwest of the island.

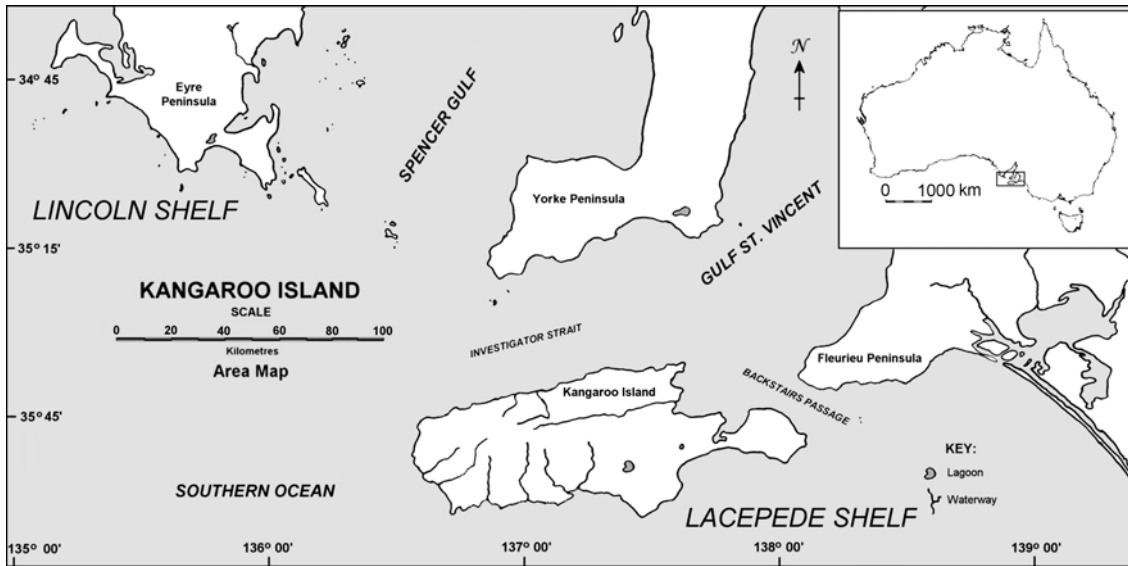


Figure 1.1: Location of Kangaroo Island. The island lies off the South Australian coast, adjacent to the Gulf of St. Vincent.

1.3 The history of human occupation of Kangaroo Island

1.3.1 Aboriginal occupation

The original inhabitants of Kangaroo Island no longer exist, having passed into prehistory long before the incursion of Europeans into southern Australia. The oldest date thus far for human occupation of Kangaroo Island is 16 ka (Bowdler, 1995). At this time sea-levels were lower due to the last glaciation and Kangaroo Island was part of the Australian mainland, surrounded by a large expanse of exposed continental shelf. The human population would have been scattered all around this region not just on Kangaroo Island; probably concentrating around the Murray delta (Lampert, 1981).

The precise timing of human occupation of Kangaroo Island is unknown; however, Lampert (1981) suggests that it is possible that occupation reached as far back as 30 ka, perhaps even further. It was first thought that Aborigines abandoned Kangaroo Island and the surrounding shelf region as the sea-level rose towards the end of the Last Glacial Maximum (LGM). Facing this "impending isolation" (Lampert, 1981, p. 170), the population migrated to what would become the mainland of South Australia, as Kangaroo Island was "cut-off" at around 9.5 ka due to the marine transgression (Bowdler, 1995). Nevertheless, later radiocarbon evidence from various sites around the island showed human occupation after this time at ca. 8 ka, ca. 6 ka, ca. 5.2 ka and

ca. 4.3 ka. There was also proxy evidence, in the form of fossil charcoal particles from pollen cores that suggested occupation for a further 2000 years after the youngest radiocarbon age (Lampert, 1981). Therefore, this new evidence meant a change in the original view of abandonment; nonetheless the island very likely became depopulated sometime between ca. 4.3 ka to ca 2.3 ka.

There are two hypotheses for the human occupation of Kangaroo Island after ca. 9.5 ka. One hypothesis states that the island may have been frequently visited by Aborigines by way of water craft, either across the Backstairs Passage or Investigator Strait: thus there was a sporadic population. However, due to the difficulty in negotiating the sometimes un-navigable Backstairs Passage (because of wind, weather and current regimes) and the low probability that water-craft technology extant at the time would be able to negotiate the much longer (although less dangerous trip across Investigator Strait), this suggestion may not be viable. The second and most likely reasoning, according to Lampert (1981), is that there was a permanent, albeit, small population of humans stranded on the island after the marine transgression. Small populations by their very nature are vulnerable to a number of internal and external factors. Some examples of internal factors would include change in age/sex demographics, and small gene pools which could lead to re-enforcement of undesirable or contra-survival traits. External factors such as long term environmental change could decrease the availability of natural resources over time, and short term natural disasters could literally destroy a small population overnight (Lampert, 1981). As humans reproduce relatively slowly the probability of these factors being able to affect a given population increases. Therefore, the likely scenario that arises on Kangaroo Island is that there may have been a stranded population that was vulnerable, because of a number of internal factors that could be related to its small size, encountering an environmental change (i.e. the increasing aridity that took place during the middle Holocene). Thus, subsequently, this small population underwent attrition over approximately 2000 years, and was eventually, in all probability, pushed over the survival threshold into extinction (Lampert, 1981).

1.3.2 European occupation

The discovery of Kangaroo Island is generally attributed to Commander Matthew Flinders, on His Majesty's sloop *Investigator* in 1802; however, an American ship the *Fairy* may have made contact with the island just before 1800 (Cumpston, 1970). Another American ship the *Elligood* may have also stopped at Kangaroo Island sometime in 1800, before possibly being wrecked off King Island during an attempt to pass through Bass Strait. Flinders did find signs of forest fires that led him to consider the possibility that the island had been visited relatively recently (Cumpston, 1970). Nevertheless, Flinders was the first to carry the news of its discovery to Port Jackson, Sydney (Cumpston, 1970). The island was also mapped and explored by a French expedition under the command of Nicholas Baudin, in 1803.

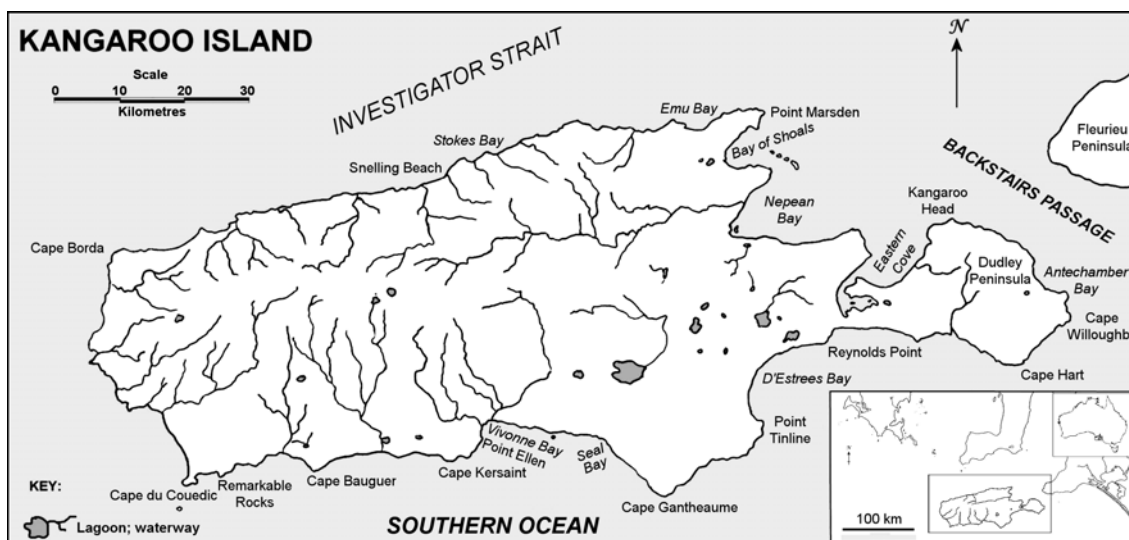


Figure 1.2: Location of sites mentioned in text.

Kangaroo Island was first sighted from the decks of the *Investigator* on 20th March 1802 and was approached on the morning of 21st March, the crew of the *Investigator* finally making landfall near Kangaroo Head (Figure 1.2: Dudley Peninsula) on 22nd March. Due to a preponderance of Kangaroos - being that many were shot and skinned by the men of the *Investigator* with little trouble, as their "extraordinary tameness" (Flinders in Cumpston, 1970: p. 9) allowed them to be easily approached - Flinders named the island "Kanguroo" [sic] Island. The "tameness of the kanguroos [sic] and the presence of seals on the shore" (Flinders in Cumpston, 1970: p. 9) led Flinders to conclude that the island was uninhabited.

It was soon after this time, around 1803, that Kangaroo Island once again became populated, albeit sporadically, with the advent of the sealing industry in the first two decades of the 19th century. Sealers would stay for months, sometime years, at a time on the island where there were abundant seals and plenty of natural salt deposits that could be used to cure the skins (Cumpston, 1970). The island soon began to build up a more permanent population as European sailors, sealers and convicts escaped from passing ships to become more or less permanent residents of the island. According to Captain George Sutherland (Cumpston, 1970: p. 51) of the brig *Governor Macquarie*, who was dispatched to Kangaroo Island in 1819 to procure salt, seal and kangaroo skins: these men had become "complete savages, living in bark huts like the [mainland] natives, not cultivating anything, but living entirely on kangaroos, emus, and small porcupines, and getting spirits and tobacco in barter for the skins which they lay up during the sealing season". Also, according to Sutherland (Cumpston, 1970: p. 51), these men would use ships to raid the mainland to seize "natives, particularly the women", "keeping them in a state of slavery, cruelly beating them on every trifling occasion". Aboriginal women were forcibly removed from as far away as Tasmania as well, and it is probable that these were among the first women taken, since Van Diemen's Land was a regular stop off point for sealers and whalers. The view may also be taken that, despite their poor treatment of Aboriginal women, what may also have been happening was a cross-cultural adaptation by the sealers, in terms of their dress, occupation and use of the landscape (Clarke, 1996; Taylor, 2000). It is most likely that life on Kangaroo Island would not have been possible for these men without the survival skills, and cultural influence of the Tasmanian and Mainland Aboriginal women. The sealers also played a role, albeit forcibly so, in the preservation of some Tasmanian Aboriginal culture and lineage, as the descendants of these women still survive today on Kangaroo Island (Cumpston, 1970; Taylor, 2000).

The sealing industry was still booming into the third decade of the 19th century. Around this time the island had the beginnings of a colony with a stable population of approximately 200 people, consisting of Tasmanian and Mainland Aborigines, and European sealers, sailors and runaways (Clarke, 1996). However, the official colonization of Kangaroo Island, instituted by the South

Australia Company, started in 1836, with the first of five colony ships from Britain reaching the island on 27th July. Initially these colonists relied heavily on the 'original' inhabitants—especially the Aboriginal women—in order to obtain a foothold on the island. However, they quickly became independent of this reliance as land was developed for agriculture and the colony's social structure was established (Clarke, 1996).

1.4 Geology and geomorphology

The first description of the geology of Kangaroo Island came from Matthew Flinders's expedition, which arrived off the coast of the Island in 1802. Flinders gave some cursory descriptions of the superiority of the soil and the calcareous nature of the cliffs near his anchorage at Kangaroo Head on the Dudley Peninsula (Figure 1.2). He also noted horizontal strata at the base of these cliffs that appeared to be some form of brown slate deposited in layers with interstitial quartz laminations (Cumpston, 1970). However, it is not known precisely what Flinders was looking at as the observation was made in passing without it seems further investigation.

Slightly more detailed examinations were made recently after Commander Flinders' voyage. Soon after Flinders' encounter with Kangaroo Island a French expedition commanded by Captain Nicholas Baudin made landfall from his anchorage at Nepean Bay (Figure 1.2) in 1803, and the expedition's zoologist, François Péron, made several observations regarding the island's geology. He noted recent sand dunes; Pleistocene calcareous (calciferous sandstone) deposits on the south coast that contained fossils; Tertiary limestones at Rolls Point and pre-Silurian schists, sandstones and quartzites that dominated the northern areas around Dudley Peninsula (Tate, 1883). The southern coastal "calciferous sandstone" as Péron called it, was given a detailed examination, and he attempted to explain its formation describing it as marine produced, initially wind blown then consolidated deposits.

Professor Ralph Tate of the University of Adelaide (1883) devoted a portion of his study on the botany of Kangaroo Island to describing the geology of some areas of the Island; he also included observations from Péron's "Voyage de

Découvertes aux Terres Australes" (1817) as iterated above. Tate created a table from his personal observations classifying Tertiary and Palaeozoic deposits (Table 1.1):

Table 1.1: Kangaroo Island geology, after Tate (1883).

Tertiary	
1	Recent sand dunes. Lacustrine deposits
2	Pleistocene. Calciferous sand-rock of the south coast and marine beds
3	Pliocene. Pluvial drifts
4	Miocene. Bryozoa limestone of Roll's Point
Palaeozoic	
5	Diorite and intrusive granite
6	Pre-Silurian schists and associated strata

1.4.1 Geology

In terms of structural geology Kangaroo Island is essentially the south-west extension of the Mount Lofty Ranges. These, together with the Flinders Ranges, are a remnant of a mid-Palaeozoic fold mountain belt known as the Delamerides which formed (i.e. deformation of existing sediments) sometime between the Cambrian and the Ordovician periods in the Palaeozoic (known as the Cambro-Ordovician Delamerian Orogeny) (Daily *et al.*, 1980). The island is also a part of the Adelaide Geosyncline—a fold-thrust belt that consists of a succession of Neoproterozoic to Cambrian metasediments (Flottmann *et al.*, 1995; Haines *et al.*, 2001)—and represents the southern continuation of the Fleurieu arc-segment of the Geosyncline; encompassing the Kanmantoo Trough (Figure 1.3).

The subsurface geology of Kangaroo Island is dominated by clastic metasediments of Cambrian age, belonging to the Kanmantoo Group, with an underlying succession of Adelaidean metasediments and a crystalline basement rock (James and Clarke, 2002) (See Table 1.2 for a timescale and details of Kangaroo Island geologic events). The island is located on the southern edge of the Gawler Craton—with the Cygnet and Snelling fault lines being geographically coincident with the southern-most land bound edge of the craton (Belperio and Flint, 1992)—and incorporates three distinct lithotectonic zones (Flottmann *et al.*, 1995) (Figure 1.4). The rocks of these zones are poorly exposed in most areas due to overlying younger sediments, however, they can

be observed in coastal platform and cliff areas, and the dissected areas of the plateau region. The zones are (Flottmann *et al.*, 1995):

- i) The Northern Structural Zone: encompassing the Kangaroo Island group of relatively unmetamorphosed platformal sediments.
- ii) The Shear Zone Complex: following the approximate line of the Snelling and Cygnet Faults, and the Gawler Craton; branching south into an arc through Dudley Peninsula. The fault lines also topographically separate the lower northern coastal plateau from the southern tablelands.
- iii) The Southern Basinal Zone: encompassing the dominant Kanmantoo Group of metasediments.

The major east-west path of the shear zone complex forms a boundary between the two distinctively different depositional realms of the Kangaroo Island Group and the Kanmantoo Group (Flottmann *et al.*, 1995) (Figure 1.4).

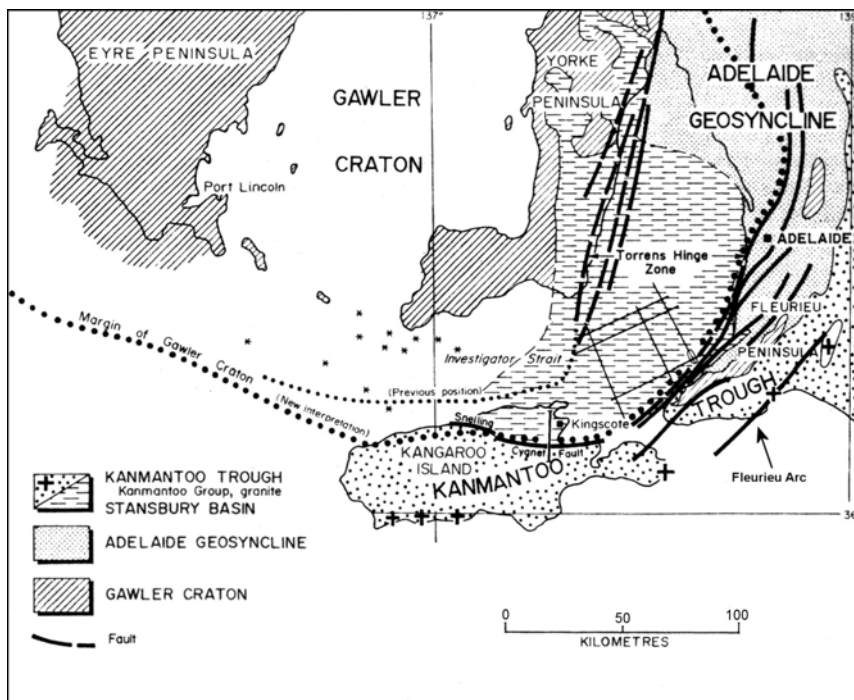


Figure 1.3: Tectonic framework of Kangaroo Island and adjacent mainland (after Belperio and Flint, 1992).

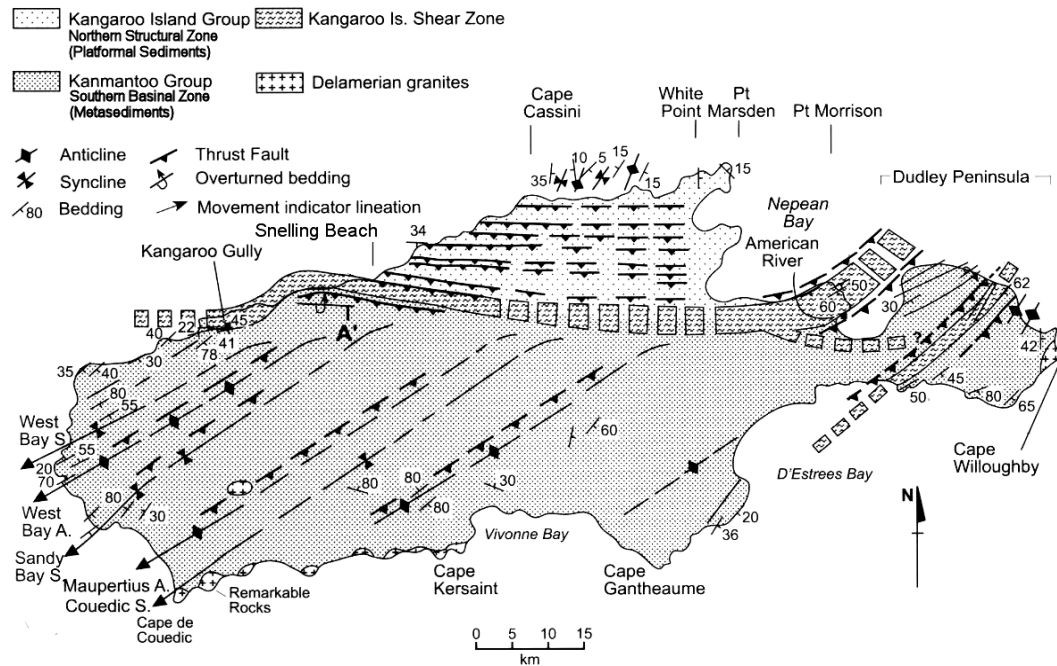


Figure 1.4: Principal pre-Permian geological features of Kangaroo Island, illustrating the three lithotectonic zones, and the position of major and minor faults (modified from James and Clarke, 2002).

The following sections will discuss the large-scale geology of Kangaroo Island, dealing with each geological zone in turn. Sediments of the Quaternary and the laterites of the Tertiary will be examined in their own sections as they are in most cases found overlying the formations inherent to each zone. However, Quaternary sediments will be discussed only briefly in this chapter, as they will be examined in detail in later chapters, and represent the principal focus of this thesis.

1.4.1.1 Precambrian to Mesozoic

Northern Structural Zone

This area is located in the north-eastern quadrant of Kangaroo Island and is host to several richly fossiliferous Cambrian formations of shale, conglomerate and sandstone, collectively called the Kangaroo Island Group (James and Clarke, 2002) (Figure 1.4). There are also Permian glaciogene sediments and Jurassic basalts that overlie this group in the region. The rocks of the Kangaroo Island group unconformably overlie a Proterozoic basement of deformed granulites and gniesses that form the structure of the Gawler Craton (Belperio and Flint, 1992).

Cambrian

There are six formations in the Kangaroo Island Group, they are listed and described in ascending order here (Sprigg, 1955; Flottmann *et al.*, 1995; Marshak and Flottmann, 1996; James and Clark, 2002):

- i) Mt. McDonnell Formation: finely laminated dark brown silt-shale with a basal siltstone and sandstone on the top.
- ii) Stokes Bay Sandstone: a pale brown arkose.
- iii) Smith Bay Shale: a basal shale unit capped by red-brown sandstone.
- iv) White Point Conglomerate: a poorly sorted matrix conglomerate, interbedded with siltstone and basal sandstone.
- v) Emu Bay Shale: mudstones and shale.
- vi) Boxing Bay Formation: a micaceous, feldspathic, conglomerate sandstone.

All of the units described above are exposed in cliffs and on shore platforms along the north-coast of the island from Snelling Beach in the west to Point Marsden in the east (Flottmann *et al.*, 1995; James and Clark, 2002) (Figure 1.5). The sediments are middle to early Cambrian in age and overlie a Proterozoic basement rock, with the Boxing Bay Formation representing the youngest unit. Deposition of this formation commenced in the early Cambrian due to the evolution of a shallow marine shelf on the margins of the Gawler Craton (James and Clarke, 2002). The sediments themselves are interpreted to be the remnants of intertidal and alluvial deposits laid down as a result of shoreline migration and fault uplift, sourced presumably from the northern areas of the basin (Flottmann *et al.*, 1995). The rock types of this group have been displaced northwards by a series of imbricate thrusts and are geometrically and sedimentologically (in part) distinct from other groups on the island—and on the Fleurieu Peninsula. They represent a region that was uplifted, strained, and intensely deformed (particularly in those areas nearest the Shear Zone—the deformation tends to be less intense to the north) in places during the Cambro-Ordovician Delamerian Orogeny (Flottmann *et al.*, 1995; Flottmann *et al.*, 1998; James and Clark, 2002).

Table 1.2: Geological timescales and events for Kangaroo Island (after James and Clark, 2002).

ERA	Period	Time in years before the present and Kangaroo Island events	
Cainozoic	QUATERNARY	2.6 Ma	Aeolianite deposition during this period
	TERTIARY	50 Ma 65 Ma	Australia-Antarctica separate Laterite plateau forms
Mesozoic	CRETACEOUS	140 Ma	
	JURASSIC	205 Ma	Flood basalt north-eastern KI
	TRIASSIC	251 Ma	
Palaeozoic	PERMIAN	298 Ma	Glaciation: deposits north-east KI and Dudley Peninsula
	CARBONIFEROUS	354 Ma	
	DEVONIAN	410 Ma	
	SILURIAN	434 Ma	
	ORDOVICIAN	490 Ma	South coast granite crystallizes
	CAMBRIAN	545 Ma	Mountain building Cambrian and
Precambrian	PROTEROZOIC	800 Ma	Adelaidean sediments
		2.5 Ga	
	ARCHAEAN	4.0 Ga	

Permian

During the Late Palaeozoic, when Australia was still attached to Antarctica, the Gulfs region of South Australia and the land mass what was to become Kangaroo Island were covered by ice sheets and glaciers (Twidale, 2000). Evidence for this exists in the form of glacial till deposits and glacially striated bedrock surfaces from northern Kangaroo Island.

The most extensive of these deposits is located in the north-east margin of the Northern Structural Zone, with another large deposit immediately south of the Cygnet Fault, near Nepean Bay and a small deposit near Kangaroo Head (Figure 1.5).

According to Bourman and Alley (1999) the melt water erosional surfaces and abundance of ice transported sediments led to the conclusion that these glaciers were temperate to sub-polar wet based rather than polar, during the

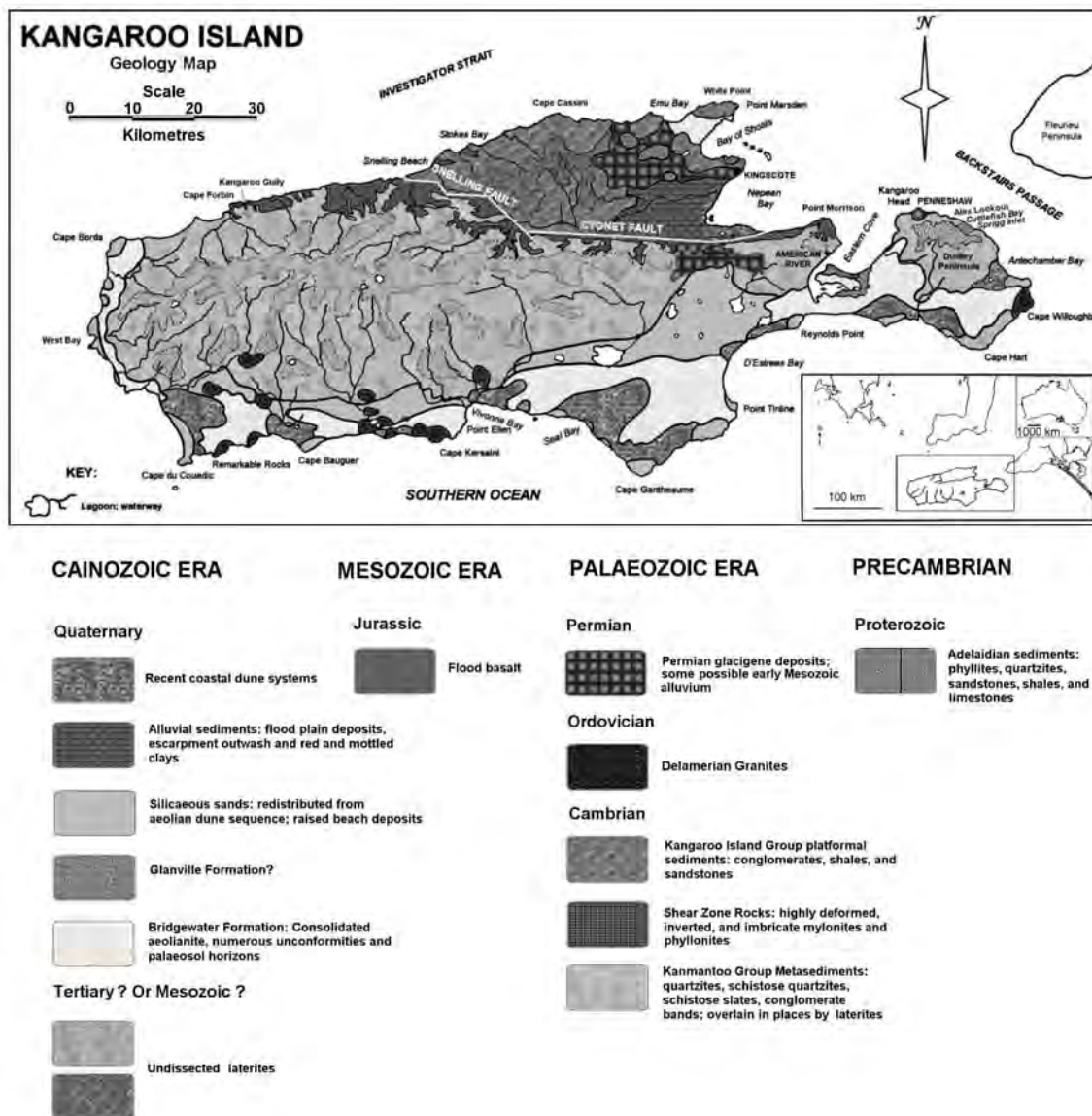


Figure 1.5: Kangaroo Island simplified geology map (compiled from Sprigg, 1954; Belperio and Flint, 1992; Belperio *et al.*, 2000).

Permian. The form of erosional surfaces on the basal rocks indicate that the ice was at the pressure or near pressure melting point and the glacier was sliding over the substrate rather than shearing it within the ice. The glaciogene sediments consist of interbedded sands, clays, silts, and conglomerates. The clasts are locally sourced and some of the erratics show striated surfaces in keeping with glacial deposition (Bourman and Alley, 1999).

Jurassic

In the north eastern corner of Kangaroo Island in an area known as the Gap Hills there are eroded remnants of a mid-Jurassic flood basalt cap—called the

Wisanger Basalt. The basalt crops out as fragmented surficial sheets that unconformably overlie possible early Mesozoic alluvial and ferruginous sediments, and late Palaeozoic glaciogene deposits (Milnes *et al.*, 1982; Bourman and Alley, 1999) (Figure 1.5). There are also related outcrops near Kingscote, and an isolated deposit on Dudley Peninsula (Alex Lookout) (Figure 1.5).

The scattered outcrops of these rocks indicate a previously more extensive basalt sheet that originally flowed over a weathered late Palaeozoic to early Mesozoic landscape and was subsequently deeply eroded and dissected over time. However, evidence of this erosion only directly exists as an occurrence of abundant basalt clasts and pebbles in late Pleistocene and Eocene deposits that are found in the area (Milnes *et al.*, 1982).

The most likely reason, according to Milnes *et al.* (1982), for the survival of these remnant outcrops of basalt is that they were covered soon after extrusion by other younger Jurassic sediments, which were subsequently eroded away. This erosion must have happened comparatively recently, as there is a distinct lack of deep weathering on the surfaces of the basalt outcrops. Some of the outcrops exhibit overlying layers of sediment which may be the remnants of this protective covering.

The Shear Zone Complex

According to James and Clark (2002) the Kangaroo Island Shear Zone is now recognized as a major tectonic boundary and zone of crustal deformation in South Australia. The strata found along this discontinuity have an imbricate morphology, being compressionally directed to the northwest, or are overturned and structurally juxtaposed. They appear to be an amalgamation of formations found in the Northern Structural Zone and those found in the Southern Basinal Zone (Flottmann *et al.*, 1995).

Cambrian

The precincts of this zone essentially follow the southern edge of the Gawler Craton, and the Snelling and Cygnet faults, and represent what may be an ancient crustal plate margin (Flottmann *et al.*, 1995; James and Clarke, 2002).

As one moves south from the Northern Structural Zone towards the discontinuity there is an increase in the level of deformity and folding in the Kangaroo Island Group of rocks. A similar trend is evident north from the Southern Basinal Zone, where there is an increase in shear stress nearer the Zone and the rocks become more crenulated and cleaved. The Shear Zone itself is a mylonized combination of rocks from the two depositional areas of the island and records the most intense strain and deformation (Flottmann *et al.*, 1995; Marshak and Flottmann, 1996).

The westernmost outcrops of Shear Zone rocks occur at Cape Forbin and Kangaroo Gully (Figure 1.4 and 1.5). These outcrops are of intensely deformed country rock surrounded by highly strained mylonitic and schistose rocks. The easternmost portions of the Shear Zone are represented by outcrops in the Point Morrison / American River area (Figure 1.4 and 1.5). These outcrops differ slightly from the western rocks, having less intensely developed phyllonites and mylonites and a more broadly dispersed strain zone (Flottmann and James, 1997; James and Clark, 2002). The Shear zone branches just before American River and arcs across Dudley Peninsula where Cuttlefish Bay and Sprigg Inlet form the easternmost extension of the branch (Figure 1.4 and 1.5) - called the Sprigg Inlet Shear Zone. This portion of the Zone is characterized by highly strained rocks that have been subject to variably intense folding and shearing. The Sprigg Inlet Shear Zone separates the less deformed Kanmantoo Group in the south from the overturned rocks of the Cuttlefish Bay anticline to the north. These rocks are considered to be Adelaidean, however, the strata are extremely deformed, foliated, sheared, and moderately metamorphosed; hence lithostratigraphic classification is at best tentative (Flottmann *et al.*, 1995; James and Clark, 2002).

The Southern Basinal Zone

The tectonic structure of the Southern Basinal Zone is dominated by northeast-southwest trending folds and thrusts with southeast dipping axial surfaces (Flottmann *et al.*, 1995; Marshak and Flottmann, 1996). However, along the Shear Zone the basinal sediments show northwest directed compressional displacement and form an overturned anticline against the rigid boundary posed by the Gawler Craton (Flottmann *et al.*, 1995) (Figure 1.4).

Proterozoic

The only outcrops on Kangaroo Island of what are deemed to be Proterozoic sediments are located on the Dudley Peninsula as a narrow wedge in the core of the Cuttlefish Bay anticline (Figure 1.5). As iterated previously it is difficult to reconcile the stratigraphy of these sediments with those on the mainland due to the severe deformation and metamorphism of the formations. Some formations appear so lithologically similar to the highly deformed Kanmantoo rocks within the Sprigg Inlet Shear Zone that they are extremely difficult to distinguish. Nevertheless, as outlined above, they have been tentatively equated with an underlying and mainland Adelaidean succession (James and Clark, 2002).

There are 4 Adelaidean metasediments recorded at Cuttlefish Bay. In descending order they are:

- i) Sturt Tillite: deformed conglomerates
- ii) Tapley Hill Formation: Laminated shales
- iii) Brighton: Limestone
- iv) Marino: Arkose

Cambrian

The Southern Basinal Zone is the most extensive depositional region of Kangaroo Island, and appears to be dominated by a single group of rocks (mainly meta siltstones and sandstones) called the Kanmantoo Group, though much of this is poorly exposed due to younger overlying lateritic, aeolian, and alluvial sediments (Figure 1.5).

The Kanmantoo Group consists of a series of metasediments that deposited in a short lived basin during early- to middle-Cambrian; they overlie another assemblage called the Normanville Group which in turn overlies Adelaidean sediments of the Neoproterozoic and a crystalline basement rock (a nearly complete sequence of the Normanville Group is exposed on Dudley Peninsula, near Antechamber Bay) (James and Clark, 2002). This depositional basin is not limited to Kangaroo Island; it extends through the Fleurieu Peninsula and is part of the Adelaide Fold-Thrust Belt (Figure 1.3). Sedimentation in the basin terminated at around 510 Ma with the onset of the Delamerian Orogen. This

compressional event included many phases of mountain building which ended at a around 480 Ma (Belperio *et al.*, 1998).

There are eight formations associated with the Kanmantoo Group of metasediments on Kangaroo Island (listed in ascending order) (from Daily *et al.*, 1979; Flottmann *et al.*, 1995; Belperio *et al.*, 1998; James and Clark, 2002):

- i) *Carrickalinga Head Formation*: metasiltstones, metasandstones and schist. Thin calcareous metasandstone.
- ii) *Backstairs Passage Formation*: grey metasandstones and minor phyllite interbeds.
- iii) *Talisker Calc-Siltstone*: calcareous and non-calcareous phyllite, and minor marble. Metasandstone and metasiltstone interbeds.
- iv) *Tapanappa Formation*: grey metasandstone, minor metasiltstone, phyllite and schist. Lenticular pebble and cobble conglomerates, commonly in metasandstone.
- v) *Tunkilla Formation*: highly deformed blue-grey phyllites.
- vi) *Balquhiddy Formation*: phyllite interbedded in grey metasandstone
- vii) *Petrel Cove Formation*: grey metasiltstone, schist and phyllite with lesser metasandstone often with shale-chip conglomerates.
- viii) *Middleton Sandstone*: dark to pale grey metasandstone with shale-chip conglomerates.

These units are poorly exposed along the south coast of the island with limited inland outcrop, because of a covering of Tertiary and Quaternary sediments. Until recently this lack of contiguous outcrop hindered the association of the Kangaroo Island Kanmantoo Group with that on the Fleurieu Peninsula (Flottmann *et al.*, 1995). However, stratigraphic correlation with all Kanmantoo formations found on the Fleurieu Peninsula has now been presented by Belperio *et al.* (1998) (Figure 1.5). The Carrickalinga; Backstairs Passage formations and thin overlying layers of Talisker Calc-Siltstone can be found outcropping south of the Sprigg Inlet Shear Zone. The remainder of the Kanmantoo metasediments of Dudley Peninsula is generally comprised of the Tapanappa Formation. The blue-grey phyllites of the Tunkilla Formation crop out at Middle River and Castle Gully on the north coast. Antechamber Bay,

Middle River, and Snelling Beach are host to examples of the Balquhider Formation. The North East River on the central plateau of Kangaroo Island hosts the only known outcrop of the Petrel Cove Formation, showing fine-grained laminae of sandstone and siltstone. The uppermost and youngest layer of the Kanmantoo Group, the Middleton Sandstone, is the most common outcrop over the southern parts of the Dudley Peninsula and the southern and western portions of the island. It is characterized by an orange coloured crust, formed during weathering (Belperio *et al.*, 1998; James and Clark, 2002).

Ordovician

The granitic rocks of southern Kangaroo Island were extruded during the Delamerian Orogeny (Table 1.2), and are confined to the Southern Basinal Zone. These rocks which crop out in various places along the southern coastal and near coastal regions of the island; primarily concentrating between Vivonne Bay and Remarkable rocks (with an isolated outcrop on Dudley Peninsula) (Figure 1.5), were created from partial melts of *in situ* early Cambrian sediments, and intrusion of either mafic magmas or granitic magmas. The intrusive magmas also provided the heat source for the crustal melts (Foden *et al.*, 2002; James and Clark, 2002).

1.4.1.2 Cainozoic

Tertiary laterites

The laterites of Kangaroo Island are pervasive in that they overlie much of the older successions in almost every depositional realm of Kangaroo Island, excluding where they have been eroded or in turn overlain by younger sediments (Figure 1.5).

The laterite for all intents and purposes forms a protective cap over the sediments on the plateau regions of the island. This high plain exhibits broad, rolling hills, and valleys on the dissected margins. The laterite is comprised of a sandy A-horizon up to a metre thick which overlies a ferruginous zone of one to two metres thickness, consisting of pisolites or irregular spheres of iron oxide. Underneath these covering layers is a kaolinised zone, where ferruginous red, brown and yellow mottling and siliceous bands are common. This zone can be tens of metres thick and merges with the underlying country rock. Laterite forms

as a result of rock weathering, usually in humid, tropical areas (Twidale and Bourne, 2002). This is the traditional view; however, it is likely that parameters of formation are more complex than this. According to Bourman (1993) the climatic control over laterite formation is in question, as laterites are still forming outside of the traditionally accepted conditions.

Exactly when the laterites of Kangaroo Island formed is under contention. Some workers attribute its age as Tertiary (Belperio *et al.*, 1992; Northcote, 2002) whilst others, Daily *et al.* (1974) for example, assign a much older age, and argue that the laterites were formed sometime during the early Mesozoic and are of late Triassic or early Jurassic age. Daily *et al.* (1974) base this assumption on the existence of truncate possibly relict laterite profiles found beneath the Wisanger Basalt, and the further assumption that this laterite was developed over the top of Permian glaciogene sediments. Northcote (2002), in an argument against a late Triassic age, cites oxygen isotope studies on kaolinised profiles from beneath the basalt and from beneath the plateau. The isotopic values for the sub-basalt profile indicated early Mesozoic weathering conditions; however, those from the plateau layer were characteristic of middle Tertiary times. On the basis of this evidence, the Tertiary may be the more likely formation period.

Other tertiary sediments

According to James and Clark (2002), very little is known about Tertiary conditions on Kangaroo Island. The major event of the Tertiary in this region was the separation of Australia and Antarctica, which led to the onset of the marine transgressions and the deposition of large amounts of marine carbonate on the coast of South Australia (James and Clark, 2002). Remnants of these deposits can be found in the form of limestone and calcareous sandstone outcrops. Some examples of limestones can be found at Kingscote, Vivonne Bay, and at Cape Willoughby on the Dudley Peninsula overlying the Delamerian granites. Tertiary calcareous sandstone deposits are to be found in various places along the south coast of the island, and on the north coast at Gum Creek, near Stokes Bay. Some outcrops of Tertiary limestone occur in areas 120 meters above sea level, indicating that large portions of Kangaroo Island

were inundated by transgressive episodes during the Tertiary (James and Clark, 2002).

Quaternary sediments

Much of the southern and western coastal areas of Kangaroo Island have a covering of Quaternary sediments which were deposited as a result of marine transgression / regression, aeolian processes, and probable tectonic uplift (Daily *et al.* 1979). In most cases these are marine derived skeletal carbonate sediments which have been consolidated by meteoric water percolating through the profiles (Daily *et al.* 1979). However, there are areas on the eastern side of the island surrounding the Cygnet River that have an extensive covering of alluvial; floodplain deposits (Figure 1.5). The origin of these coastal aeolian sediments and the formation of the Quaternary coastal landforms will be examined in detail in Chapter 2.

1.4.2 Geomorphology

Kangaroo Island is dominated by a high lateritic plateau that encompasses the central, western and northern portions of the island. The plateau ranges between 50 m above present sea-level (APSL) in the east and south to 250 m in the north and west. The highest point on the island is in the central-west at 320 m (Twidale and Bourne, 2002), and the central region is tilted from the west to the south and east due to uplift. The plateau is deeply dissected by streams forming steep rocky gullies in places, and the margins of the plateau are dominated by convex, dissected, bedrock hills. A scarp formed by the Cygnet-Snelling fault-line separates the central plateau from a lowland region in the north-east. The northern coastal areas are characterised by hills, slopes, and cliffs eroded out of the bedrock, interspersed with pocket beaches; however, there are isolated patches of aeolianite along this coast at Emu Bay, Smith Bay, Stokes Bay, and Cape Dutton (Belperio and Flint, 1992). Dudley Peninsula in the far east of the island is really an isolated plateau that is connected to the rest of the island by a low lying area of Quaternary aeolian sediments. The peninsula may have formed a separate island during times of higher sea-level.

The southern and western coastal areas are dominated by sequences of consolidated, calcareous aeolianite (consisting of wind deposited, consolidated,

skeletal carbonate grains) laid down at various times during the Quaternary. Episodes of dune migration are evident in the succession of calcrete horizons which are visible in the deposits. Karst features are also well developed; with sea caves, dolines, and limestone caves evident in places. Erosion and weathering has formed precipitous cliffs and well developed shore platforms. Holocene transgressive dune fields are also characteristic of the southern coastal areas; these dunes are comprised predominantly of re-worked Pleistocene aeolian material, and may be mobile or stabilized by vegetation (Belperio and Flint, 1992).

1.5 Oceanography

This section examines the marine environment of Kangaroo Island; this will encompass bathymetry, tides, ocean currents, wave climate, water temperature and salinity. This is relevant to later chapters as these parameters have directly affected the formation and deposition of the biogenic carbonate (aeolianite, calcarenite) successions which blanket large areas of Kangaroo Island.

1.5.1 Bathymetry

Kangaroo Island lies on a broad expanse of continental shelf, surrounded by shallow waters which have a depth range between 30 and 90 m. The greatest depth gradient lies off the north-western cape area of the island where a steep shoreline dips sharply to a depth of 100 m (Figure 1.6). The implications of this are that Kangaroo Island at various times in the past, during periods of low sea-level, must have been connected to the mainland. During the Last Glacial Maximum (LGM) the sea-level was so low (approximately -140 m in some areas of the globe [Lambeck and Chappell, 2001]) that the continental shelf would have been exposed and the edge of the shelf would have probably formed the coastline. Kangaroo Island at this time would have been discrete only as a large plateau, bordered by cliffs, swallowed in the immensity of the exposed continental shelf.

1.5.2 Tides

Kangaroo Island experiences a mixed tide system with diurnal and semidiurnal phases. The northern coastal areas and the American River inlet are characterised by dodge tides (two tides of unequal height occurring in 24 hr

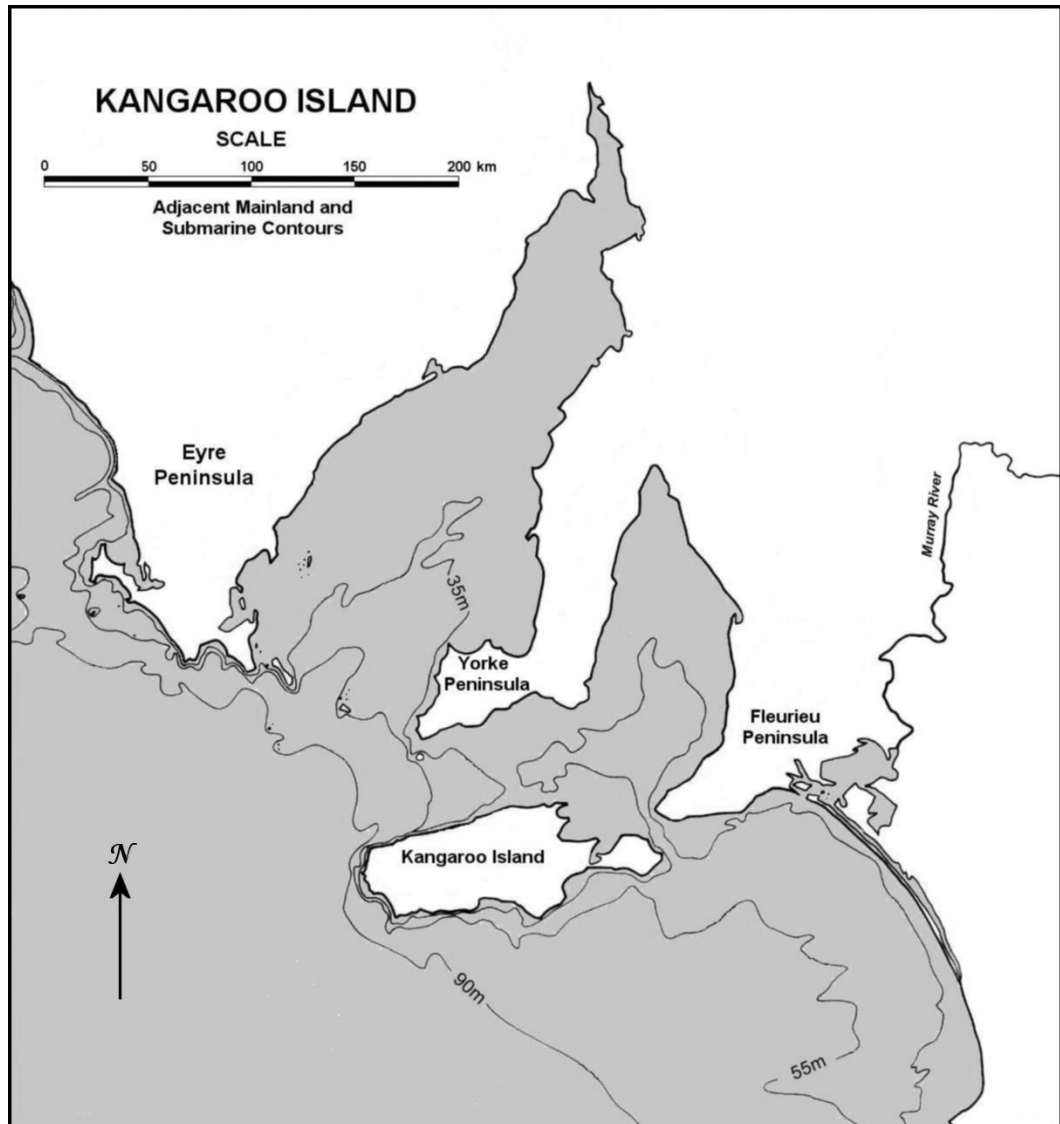


Figure 1.6: Bathymetry off the South Australia coast.

during a neap period—the sun and moon are pulling at right angles to each other) where the water remains at mid-tide for 24 hr or more. The southern coast also experiences a mixed tide system, although the tides have a slightly lower range than the northern coast (Table 1.3) (Edwards, 1987).

Actual tides can differ from predicted levels due the effects of barometric pressure, and winds. Storm events can also change predicted tides, some extreme events have caused tidal ranges from 1 to 1.2 m above the predicted level.

There are also long term oscillations in tides which are linked to the west to east movement of pressure systems and interactions of the Southern Ocean with the continental shelf (Edwards, 1987).

Table 1.3: Kangaroo Island tidal data (after Short and Fotheringham, 1986).

MHHW =	mean high, high water		MHLW =	Mean high, low water	
MLHW =	mean low, high water		MLLW =	Mean low, low water	
MSR =	Mean spring range				
Location	MHHW (m)	MLHW (m)	MHLW (m)	MLLW (m)	MSR (m)
Emu Bay	1.3	0.8	0.6	0.5	0.8
Kingscote	1.4	0.9	0.6	0.5	0.9
American River	1.2	0.9	0.6	0.4	0.8
Hog Bay	1.0	0.5	0.5	0.4	0.6
Antechamber Bay	1.0	0.5	0.5	0.4	0.6
Vivonne Bay	0.9	0.6	0.5	0.4	0.5

1.5.3 Ocean currents

Kangaroo Island experiences surface currents that flow from west to east on both sides of the island. These currents are at their strongest during the period of May to July. The currents that dominate the northern coast of the island flow through the Backstairs passage and are largely derived from tidal activity (Edwards, 1987).

The Leeuwin Current is a strong, slow flowing, shallow depth current of low salinity (35.7-35.8‰ [per mil]) warm water (17-19 °C). The current flows south from the north-west of Western Australia. It may have its origins in the South Equatorial Current, via the Indonesian Throughflow, or via the Eastern Gyral Current (Cann and Clarke, 1993; McGowran *et al.*, 1997; Domingues, 2006). It flows south along the Western Australia coastline to Cape Leeuwin, then turns east and flows along the southern coastal margin to the Great Australian Bight (GAB). The current is stronger during winter and reaches across the GAB, as far as the Spencer and St. Vincent Gulfs (McGowran *et al.*, 1997; Li *et al.*, 1998). Although, according to McGowran *et al.* (1997), the current loses its identity in the GAB waters, and continues to flow south-east towards Tasmania as the “East Bight Current”. The warm waters of the Leeuwin Current allow tropical marine species to exist along the western and southern Australian coastal margins as far as the GAB. There is evidence to suggest that the current has turned off and on in the past in concert with glacial and interglacial

periods; this evidence is in the form of planktonic foraminifer faunal successions that have been recorded in sediments from the GAB (McGowran *et al.*, 1997). There is also evidence to suggest that the current was stronger than today during the Last Interglacial (LIG), and possibly during other interglacial periods as well. The Glanville Formation shell beds and their equivalents found on the South Australian and Kangaroo Island coasts contain warm water species of mollusc and foraminifera, such as *Anadara trapezia* (Deshayes) 1839, and *Marginopora vertebralis* (Blainville) 1830, respectively, that are normally found at lower latitudes. This indicates that the water must have been warmer in these regions during the LIG than it is today (Cann and Clarke, 1993; McGowran *et al.*, 1997; Murray-Wallace *et al.*, 2000). The Leeuwin Current is clearly an important factor in carbonate production and the faunal distribution around Kangaroo Island; the implications of this will be examined in detail in Chapter 2.

1.5.4 Wave climate

The west and south coast of Kangaroo Island experience year round high energy west to south-westerly swells from the Southern Ocean. The swell is less than 2 m for approximately 50% of the year; however, for 30-45% of the year the swell is between 2 and 4 m, and for 10% of the year it can exceed 4 m. These swell conditions are most persistent between March and October. Coastal processes, in particular beach-surf zone dynamics, are dominated by a high energy wave environment; also wind generated sea conditions are an additional source of wave energy. The southern and western coasts are characterised by high calcarenite cliffs, massive Pleistocene and Holocene dune transgression, and eroded barriers (Edwards, 1987; Short and Fotheringham, 1986). The northern and eastern coastal areas experience moderate to low wave energy conditions respectively. The eastern coast is characterised by tidal inlets and mudflats, and the northern coast by moderately high bedrock cliffs and isolated pocket beaches (Short and Fotheringham, 1986).

1.5.5 Water temperature and salinity

Sea surface temperatures around Kangaroo Island fluctuate with the seasons. These range from 4 to 6 °C between summer and winter. Summer maxima are

around 20 °C and in winter the maxima is around 14 °C. Near shoreline temperatures can vary even more (Edwards, 1987). These temperatures are undoubtedly influenced by water depth, wave action, and the ocean current systems that flow around the island. Figure 1.7 illustrates the seasonal variations in sea surface temperatures (SSTs) around Kangaroo Island.

The salt concentration in waters around the island is in the range of 35.4 to 35.9‰. In protected low energy, shallow areas, such as lagoons and inlets the salt concentrations can be significantly higher: The salinity in Pelican Lagoon (Dudley Peninsula: Figure 1.2) can be as high as 37‰ in summer, and the waters in the Kingscote embayment can range from 35.7 to 37.5‰ (Edwards, 1987). The effect of variations in water temperature and salinity on carbonate production will be discussed in the Chapter 2.

1.6 Climate

In this section the climatic characteristics of Kangaroo Island are examined, particularly the islands temperature, rainfall and wind regimes. Data from 7 stations situated around the island are used to illustrate the various factors that influence the climate of Kangaroo Island.

1.6.1 Temperature

The island has relatively low topography, with no elevation exceeding 320 m, and only 16% of the land surface above 200 metres. In light of this it is assumed that altitudinal differences in temperature contribute little to overall temperature variation (Schwerdtfeger, 2002).

The locations of climate stations (Gum Ridge only has rainfall data) described in this section are shown in Figure 1.8. The data used is derived from between 13 and 139 years of Bureau of Meteorology observations (Table 1.4). Kangaroo Island experiences a Mediterranean climate, with its highest temperatures during summer (the warmest months being January and February) and its lowest temperatures in winter (the coolest months being July and August). The monthly maximum and minimum temperatures are illustrated in Figure 1.9. What is immediately evident is the notable difference in temperature ranges

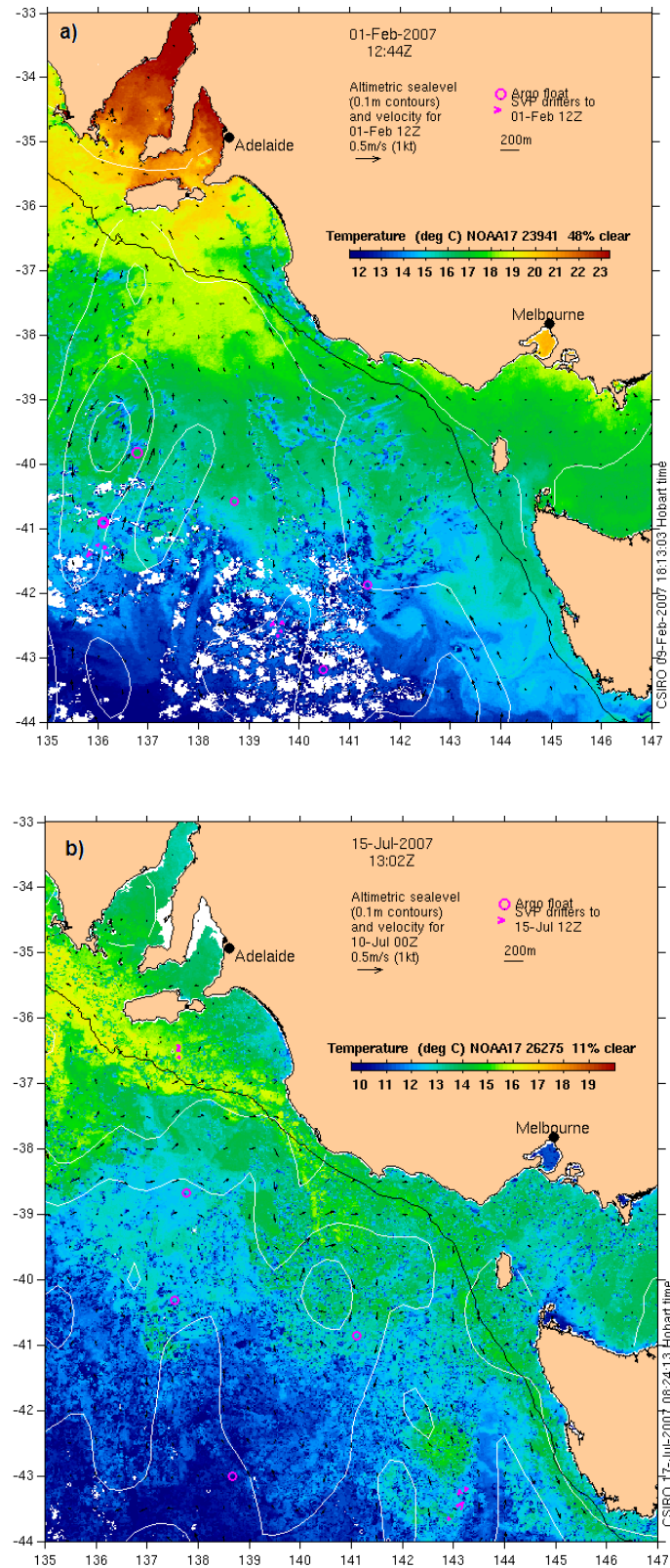


Figure 1.7: Average monthly a) summer (Feb. 2007) and b) winter (Jul. 2007) sea-surface temperatures off the South Australian and Victorian coasts (CSIRO, 2007).

Table 1.4: Archival climate averages for stations on Kangaroo Island (Bureau of meteorology [BOM], 2007).

KINGSCOTE	Jan	Feb	Mar	Apr	May	Jun	Jul	Aug	Sep	Oct	Nov	Dec	Annual	C.M.A.T.	No. Years	Record Years
Mean maximum temperature (°C)	23.7	23.6	22.1	19.8	17.5	15.4	14.6	15.1	16.5	18.5	20.5	22.3	19.1	15.4	88	1914-2002
Mean minimum temperature (°C)	15	15.5	14.4	12.5	10.8	9.4	8.4	8.4	9.2	10.4	12.1	13.7	11.6		88	1914-2002
Mean diurnal temperature range (°C)	8.7	8.1	7.7	7.3	6.7	6	6.2	6.7	7.3	8.1	8.4	8.6				
Mean rainfall (mm)	14.7	17	18.4	35.1	58.7	72.7	77.7	65.2	47.4	37.1	23	19.2	483.8		124	1877-2002
CAPE WILLOUGHBY																
Mean maximum temperature (°C)	21.5	21.9	20.6	19.1	16.9	14.9	14.1	14.4	15.7	17.5	19	20.5	18	15.4	39	1967-2007
Mean minimum temperature (°C)	15.6	16.2	15.5	14.1	12.5	10.7	9.7	9.6	10.3	11.4	12.9	14.3	12.7		40	1967-2007
Mean diurnal temperature range (°C)	5.9	5.7	5.1	5	4.4	4.2	4.4	4.8	5.4	6.1	6.1	6.2				
Mean rainfall (mm)	18.9	17.9	21.2	39.7	61.9	75.6	81.5	73.9	56.5	42.8	28.3	22.7	540		126	1881-2007
CAPE DE COUEDIC																
Mean maximum temperature (°C)	21.6	21.2	20.8	18.9	16.8	15.2	14.4	14.6	15.9	17.3	18.4	20.4	18	14.9	23	1939-1973
Mean minimum temperature (°C)	14.2	14.7	14.3	13.1	11.5	10.4	9.3	9.1	9.6	10.5	11.5	12.9	11.8		23	1939-1973
Mean diurnal temperature range (°C)	7.4	6.5	6.5	5.8	5.3	4.8	5.1	5.5	6.3	6.8	6.9	7.5				
Mean rainfall (mm)	16.3	24.9	23.6	48.2	75.2	105	110.5	82.7	56.8	40.2	30.1	24.8	639.2		55	1907-1973
CAPE BORDA																
Mean maximum temperature (°C)	23	23.3	21.3	18.7	16.4	14.6	13.9	14	15.1	16.9	19.4	21.2	18.2	14.8	59	1925-1007
Mean minimum temperature (°C)	13.8	14.3	13.6	12.4	11.2	9.8	9.1	8.9	9.3	10	11.2	12.5	11.3		59	1925-2007
Mean diurnal temperature range (°C)	9.2	9	7.7	6.3	5.2	4.8	4.8	5.1	5.8	6.9	8.2	8.7				
Mean rainfall (mm)	15.4	16.9	23.7	45.2	79.6	106	104.4	86.5	55.3	41.7	26.1	21	621.2		139	1865-2007
PARNDANA EAST RESEARCH STATION																
Mean maximum temperature (°C)	25	25.2	22.7	20.1	16.6	14.2	13.5	14.1	15.4	17.7	20.5	23.1	19	14.2	26	1954-1984
Mean minimum temperature (°C)	12.5	13.3	12.2	10.6	8.9	7.3	6.5	6.5	7	8.1	9.3	11	9.4		26	1954-1984
Mean diurnal temperature range (°C)	12.5	11.9	10.5	9.5	7.7	6.9	7	7.6	8.4	9.6	11.2	12.1				
Mean rainfall (mm)	16.5	21.1	29	49.2	76	87.9	101.5	86.1	63.9	45.4	28.7	23.6	632.2		31	1954-1984
KINGSCOTE AIRPORT																
Mean maximum temperature (°C)	26	26.5	24	21.3	18.4	16.1	15.3	15.9	17.6	19.6	22.4	24.5	20.6	14.7	13	1994-2007
Mean minimum temperature (°C)	13.2	13.4	10.9	8.5	7.7	6.7	5.8	5.7	6.4	7.1	9.4	10.6	8.8		13	1994-2007
Mean diurnal temperature range (°C)	12.8	13.1	13.1	12.8	10.7	9.4	9.5	10.2	11.2	12.5	13	13.9				
Mean rainfall (mm)	17.6	14.6	22	24.8	48.6	66.8	68.2	57.9	46.5	37.3	22.9	14.4	438.2		14	1993-2007

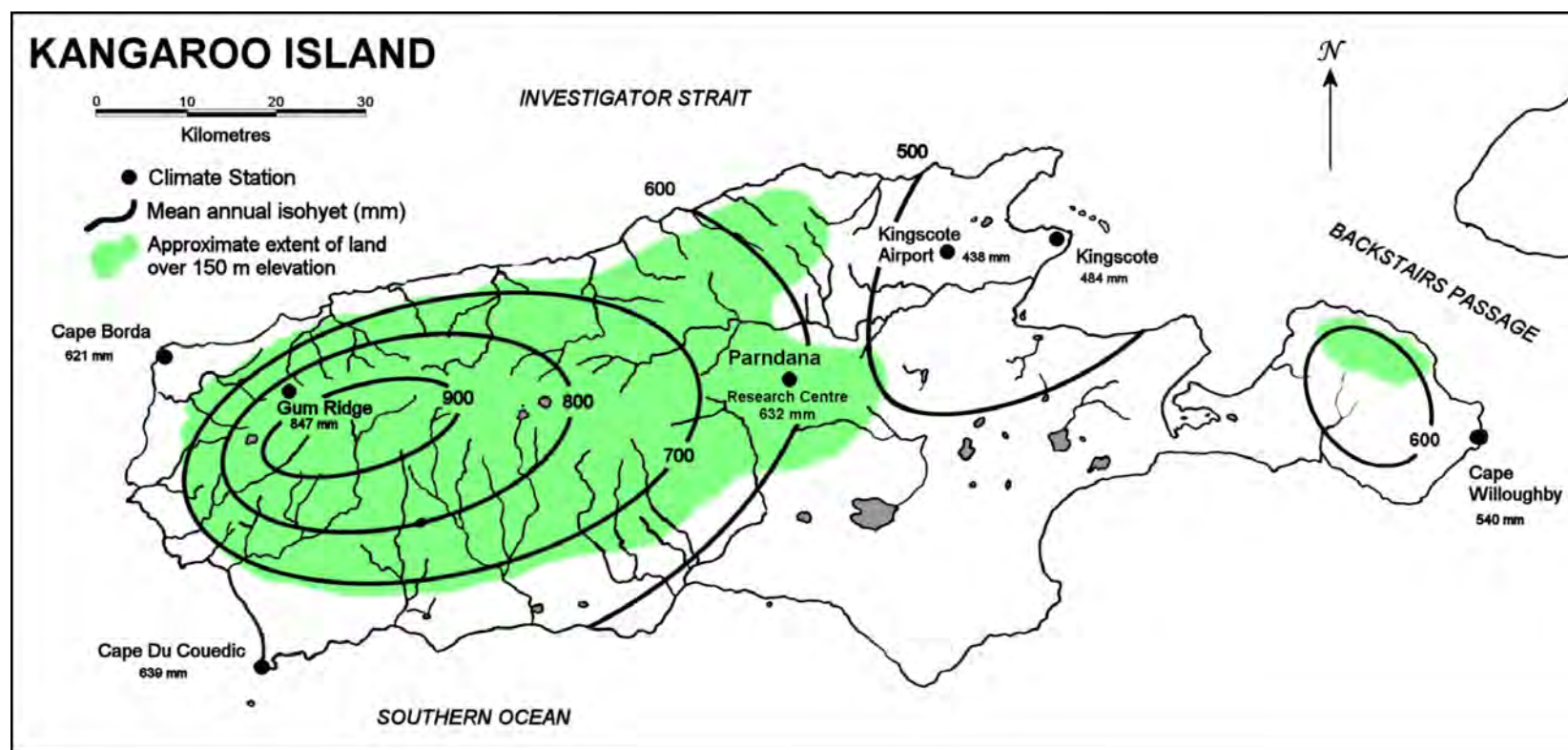


Figure 1.8: Kangaroo Island mean annual rainfall map, showing interpolated isohyets, locations of climate stations, and elevated land surface (modified from Schwerdtfeger, 2002).

when comparing inland and coastal stations. Parndana and Kingscote Airport exhibit the lowest minimum temperature ranges throughout the year, and also have the highest summer temperature maxima. Parndana also has the lowest maxima during winter; Kingscote Airport is less extreme, possibly due to its proximity to the coast. The town of Kingscote is approximately 13 km from the airport on the eastern coast (Figure 1.8). Kingscote experiences a much milder temperature range as the town is situated adjacent to a thermally moderating sheltered embayment (Schwerdtfeger, 2002).

Cape Willoughby (Figure 1.8 and Figure 1.9) exhibits the most moderate temperature variations showing the least differences between minima and maxima; this is due to buffering oceanic influences. Cape Du Couedic shows similar trends for summer and winter maxima; although overall the minima are lower. In contrast, the summertime thermal features exhibited by Cape Willoughby and Cape Du Couedic are not shared by Cape Borda. The reason for this lies in the proximity of the heated land mass of the Eyre Peninsula, and intermittent north-westerly winds; however, summer easterlies that travel over the length of the island picking up heat as they traverse the landscape contributing most to the difference in temperature (Schwerdtfeger, 2002).

Figure 1.10 illustrates the mean diurnal temperature range (the difference between minima and maxima) for all stations. Parndana and Kingscote Airport show the extreme differences between minima and maxima that are characteristic of sites that experience a continental thermal regime. Cape Willoughby and Cape Du Couedic both share maritime characteristics; although Cape Willoughby is the most maritime. Cape Borda is subject to continental influences during summer, however, during winter it is similar to Cape Willoughby and Cape Du Couedic. The diurnal data for Kingscote reflects its sheltered position.

1.6.2 Winds

According to Schwerdtfeger (2002) the coastal environments of South Australia all share similar wind regimes in winter, due to their location within a narrow latitudinal band. The sub-tropical ridge (which is characterised by eastward moving high pressure systems) drifts southward so that in summer it is situated

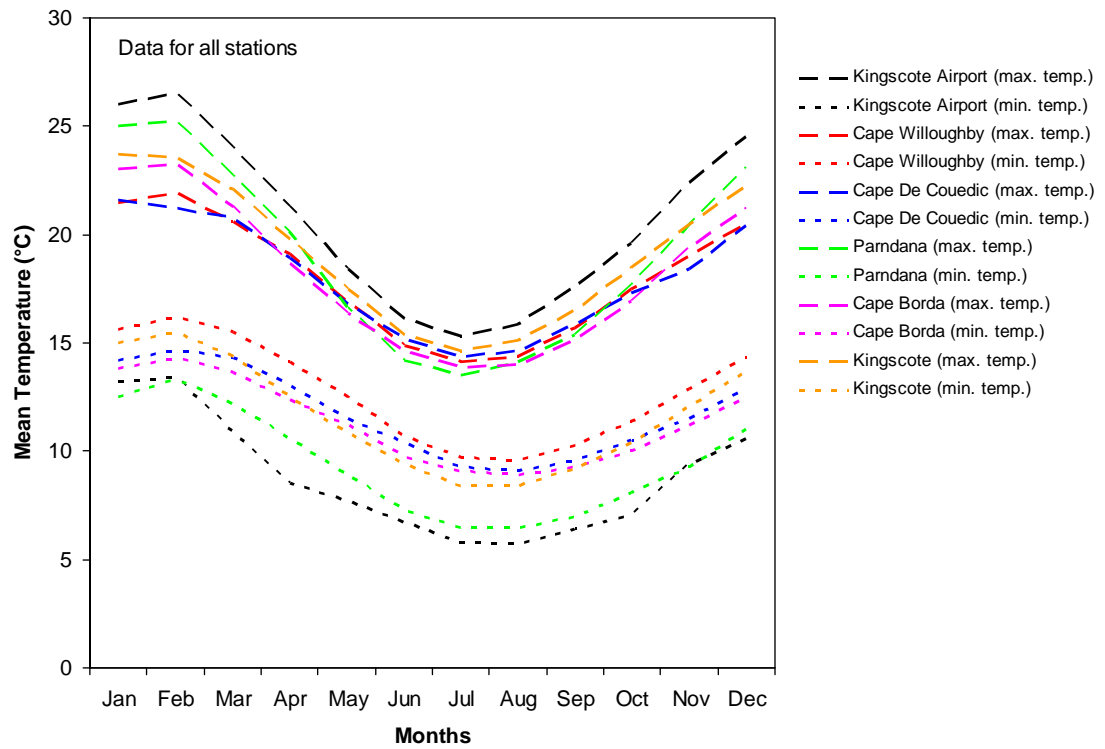


Figure 1.9: Mean monthly minimum and maximum temperatures for stations around Kangaroo Island (from Bureau of Meteorology archived data in Table 1.4).

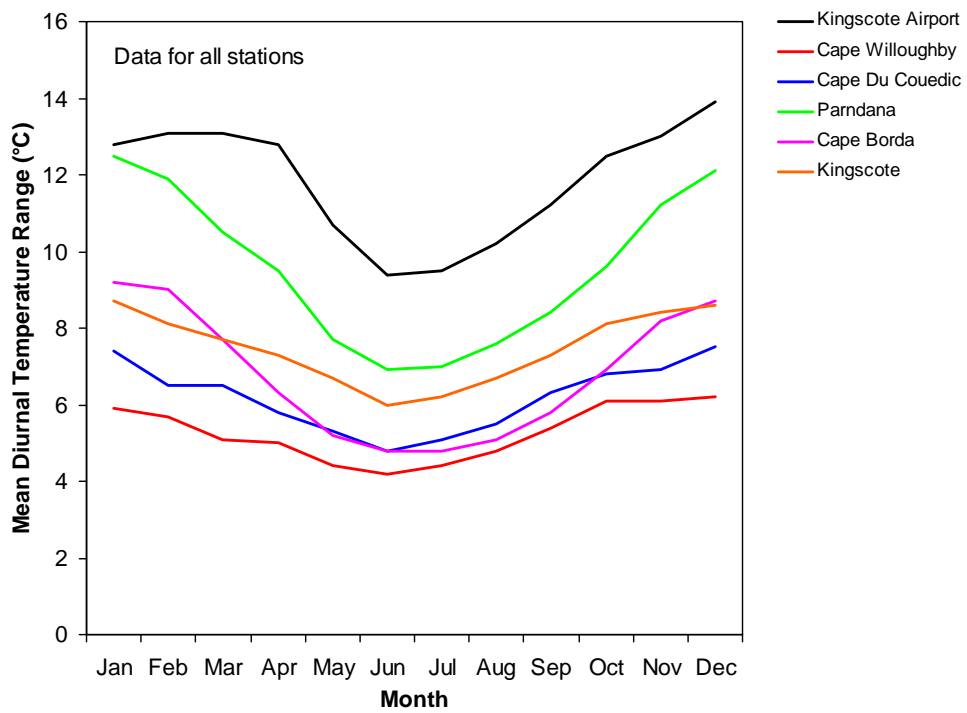


Figure 1.10: Mean diurnal temperature ranges for stations around Kangaroo Island (calculated from Bureau of Meteorology archived data – in Table 1.4).

below Kangaroo Island over the Southern Ocean. As the ridge migrates south the winds shift from a north-westerly winter pattern to a summer south-easterly pattern (Figure 1.11). The Kangaroo Island summer wind pattern is strengthened by afternoon south to south-east sea breezes, drawn by the landmass to the north as well as to the prevailing high pressure systems situated over the Great Australian Bight area (Schwerdtfeger, 2002; Edwards, 1987). The wind systems for all stations are similar during summer; however, at Cape Borda the sea breeze effect is somewhat reduced due to elevation in topography towards the western part of the island. There is also a stronger summer north and south westerly component at Cape Borda. The winter wind regime is again similar for all stations with winds coming predominantly from the north-west. It can be seen from Figure 12 that for all stations the highest wind velocities tend to occur during the warmest period of the day, in both summer and winter. The most exposed coastal stations (on the Capes) experience the highest wind velocities and overall windier conditions in both winter and summer. Cape Willoughby experiences the highest wind velocities in summer, where the wind can exceed 50 km/hr^{-1} on 5% of all occasions (Schwerdtfeger, 2002) (Figure 1.12), although the mean wind velocities are higher in winter. High wind velocities have implications for the entraining and deposition of sand; hence, mobilization for dune and barrier formation.

Mean monthly winds speeds plotted in Figure 1.13 show that for inland stations the highest mean wind velocities occur during the summer months, the same is apparent for the town of Kingscote although due to its sheltered position wind speeds are lower overall. The exposed coastal stations of Cape Borda and Cape Willoughby show the highest mean wind velocities during the winter months. All stations except Kingscote have similar summer mean wind speeds, showing the dominance of the south-easterlies. The exposed coastal stations have high winter wind speeds as they are more exposed to the northerly and north-westerly components than their inland counterparts. Parndana and Kingscote Airport may be sheltered to a degree by intervening topography and vegetation stands. According to Schwerdtfeger (2002) the Kangaroo Island wind system is influenced little by topography as most areas are below 200 m; which is too low to greatly modify the synoptic system. Land surface irregularities generally decrease overland wind speed when compared with the

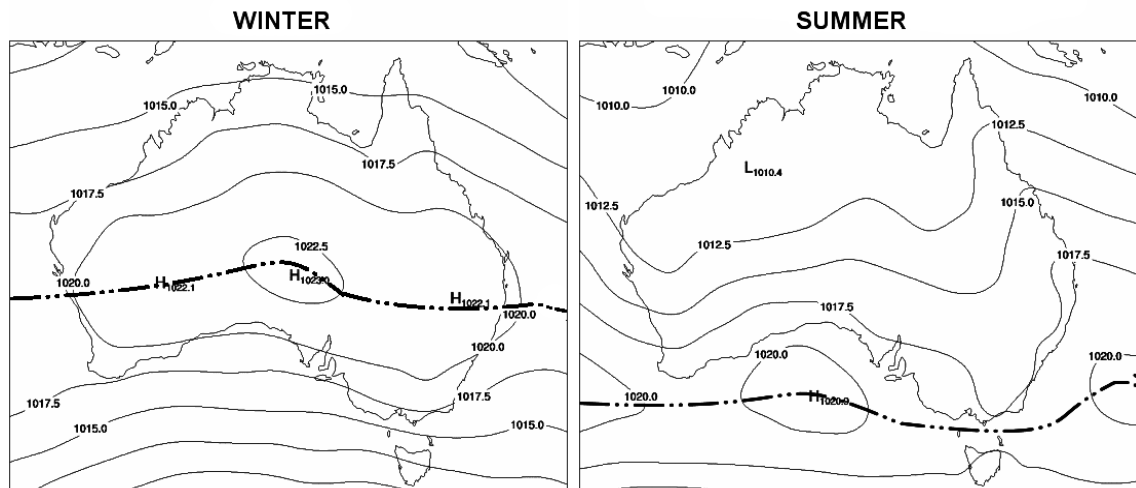


Figure 1.11 Interpolated position of the Sub-Tropical Ridge, and high pressure systems, during summer and winter, over Australia (modified from BOM, 2007).

ocean; however, due to the proximity of the mainland the land and sea winds generated by this proximity have a tendency to overshadow the smaller scale effects that develop on the island. Nonetheless, it is apparent from Figure 1.13 that topography is a factor in controlling wind velocities on the island.

In summary, the Kangaroo Island wind regime is dominated by the northerly mainland that draws air masses from the south as part of a large scale oceanic wind system. The system is reversed during winter and the island is exposed to north-westerly winds.

1.6.3 Rainfall

Kangaroo Island experiences a Mediterranean rainfall climate as most rain falls during the winter months with a pronounced minimum rainfall during summer. June and July are the wettest months and January and February are the driest (Figure 1.14). Topography tends to control the distribution of rainfall over the island with the highest rainfall levels occurring in the areas of increased elevation on the western and central parts of the island (Figure 1.8). This is an orographic effect that extracts moisture from frontal lows that move across the region—as the air rises due to the topography it cools and releases moisture as rain. Cape Willoughby receives somewhat increased rainfall for this reason also. There is a slight elevation immediately west that orographically increases the amount of rain received in the area. Rainfall is lower at Kingscote Airport

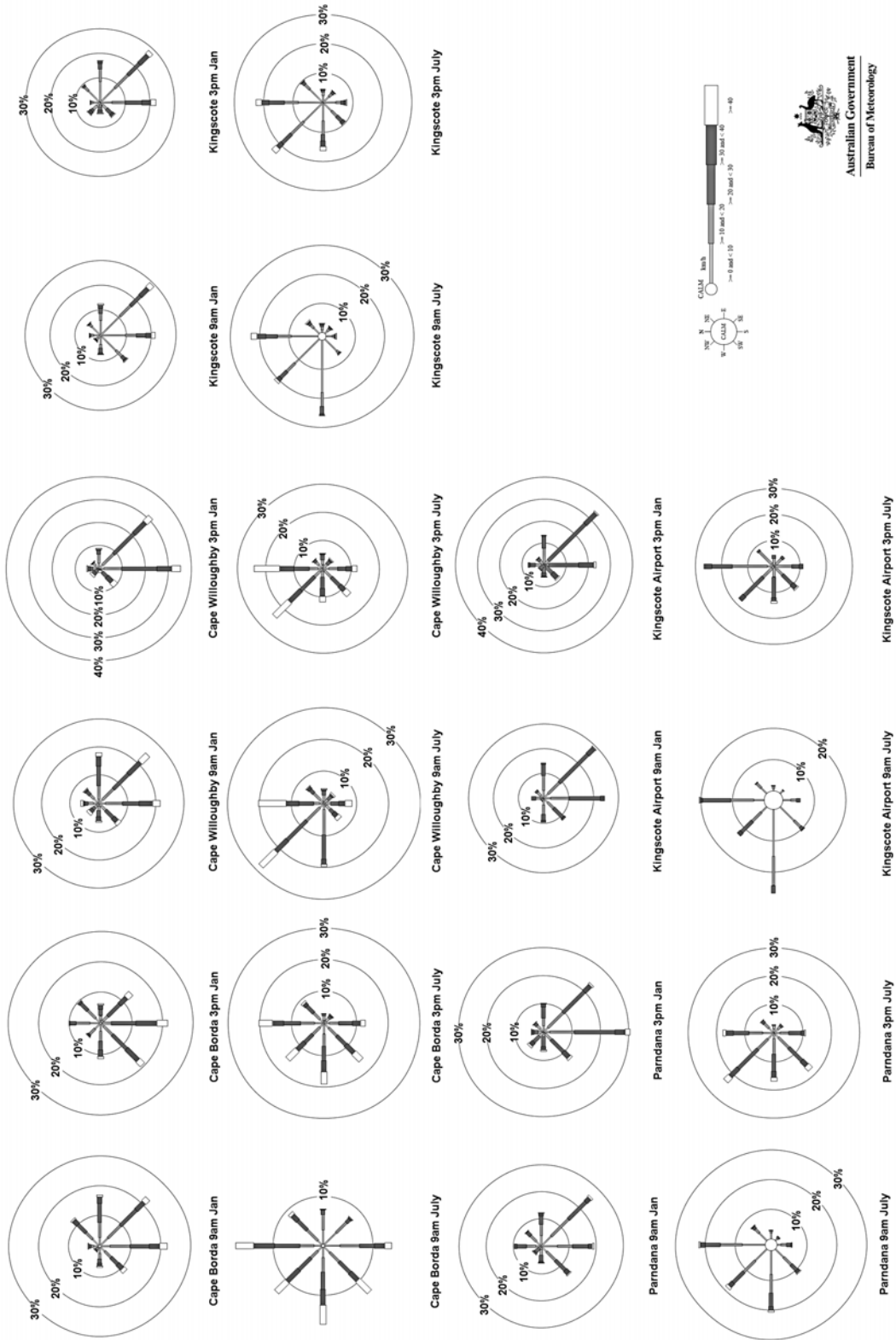


Figure 1.12: Bureau of Meteorology wind vector data for stations around Kangaroo Island.

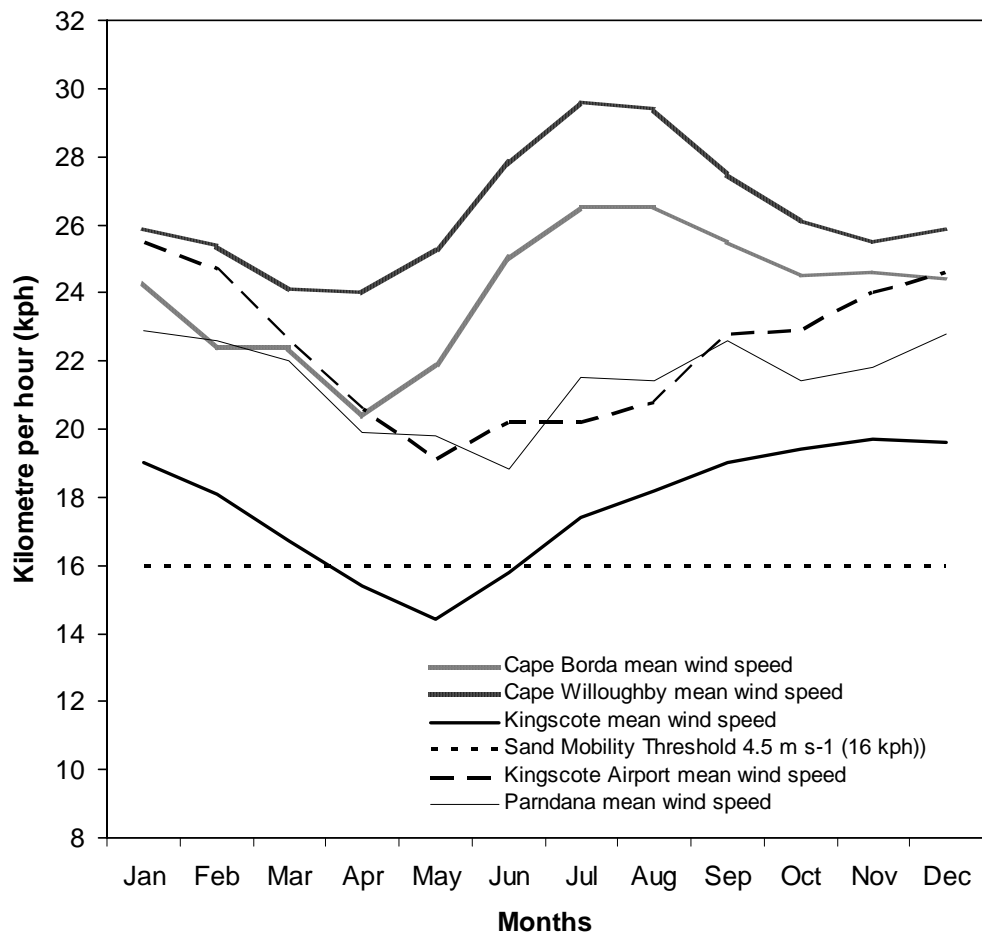


Figure 1.13: Mean monthly wind speeds for stations around Kangaroo Island. Note that for all stations (excepting Kingscote in May) winds speeds are well above the sand mobility threshold of Bagnold (1941) (Bureau of Meteorology).

and Kingscote as both are within the rain shadow created by the highlands in the west (Schwerdtfeger, 2002; Edwards, 1987).

1.7 Vegetation

The first botanical collections were undertaken on Kangaroo Island in 1802 by Robert Brown, the naturalist to Flinders' expedition aboard the *Investigator*. Brown managed to collect 29 new species under unfavorable conditions from littoral areas at Kangaroo Head, American River, Pelican Lagoon, and from the isthmus connecting Dudley Peninsula (Tate, 1883). Various other collections and surveys took place during the second half of the 19th century (detailed in Tate, 1883). Of these the most comprehensive was that of Professor Ralph Tate (1883). He classified 415 species (404 continental and 11 endemic) into 4 prominent vegetation groups:

- 1) Heathy Scrub Lands (covering the majority of the island; classed as the most characteristic)
- 2) Sylvan Vegetation (confined to the borders of waterways)
- 3) Savanna Vegetation (grassy areas with scattered *Casuarina* and *Eucalyptus*)
- 4) Vegetation of the Littoral Tracts (confined to mud flats, and coastal areas)

This survey extended as far as the Stun 'sail-boom River in the south-west quadrant of the island.

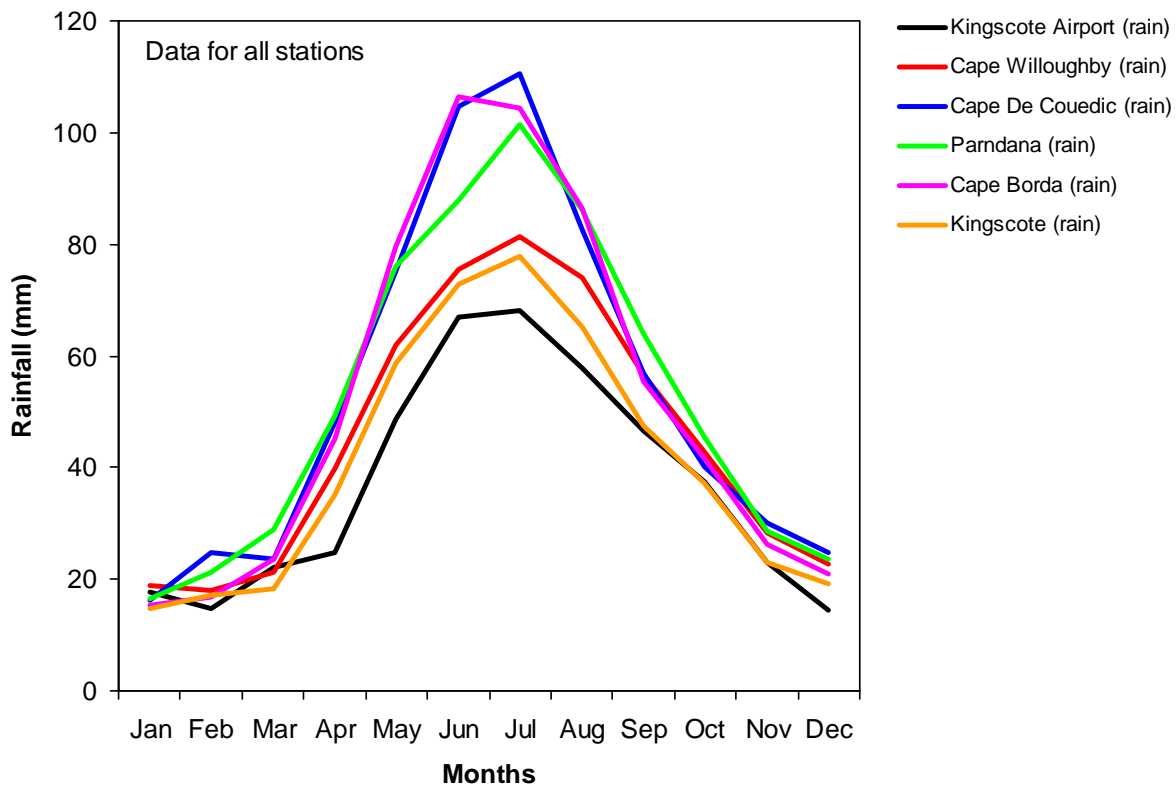


Figure 1.14: Mean monthly rainfall for stations around Kangaroo Island (Bureau of Meteorology data: Table 1.4).

Bauer (1959) as part of his PhD thesis in Geography undertook a survey of Kangaroo Islands vegetation describing 13 broad vegetation associations and formations, and up until recently this work was considered to be the most comprehensive undertaken (Edwards, 1987). Recently detailed vegetation

mapping has been undertaken by the South Australia Department for Environment and Heritage on Kangaroo Island, describing 37 different groups in which 132 sub-groups have been identified. However, for this section of the thesis a broad approach is all that is required, therefore the much simpler Specht (1972) scheme (see vegetation map: Figure 1.15) has been adopted, and modified with some additional information from Ball (1998), Edwards (1987); Davies (1982), and. Bauer (1959).

It should be pointed out that approximately half of the native vegetation extant on Kangaroo Island has been cleared since European settlement, particularly in the central and eastern parts of the island, and particularly during post World War II settlement. Therefore, some associations now exist only as pockets. For example 93% of the Open-Scrub association (*E. cneorifolia* and *Melaleuca uncinata*) has been cleared and the remnants now only exist as isolated islands (Ball, 1998; Edwards, 1987). The vegetation map in Figure 1.15, in this case, represents a pre-European distribution.

Five environmental factors control the distribution of vegetation on the island, these are the underlying geology, rainfall, the influence of wind and saline drift along the coast, historical legacy (past land clearing and burning regimes), and geomorphology. The most important of these being underlying geology (clay and soil formation), geomorphology (which controls drainage patterns), and rainfall (Ball, 1998).

1.7.1 Low Open-Forest to Woodland or Open-Scrub (with heath understorey)

This mixture of groups and associations is the most extensive on the island and is confined to higher rainfall areas in the highlands of Kangaroo Island. Low Open Forest to Woodland associations (*Eucalyptus obliqua*, *E. baxteri*, *E. fasciculosa*) are found in the central regions of the upland areas, whereas the Open Scrub associations with heath understorey (*E. baxteri*, *E. fasciculosa*, *E. cosmophylla*, *E. remota*, *E. diversifolia*) are characteristic of the western portions and lower margins of the plateau, abutting the northern coast in areas (Edwards 1987; Bauer, 1959).

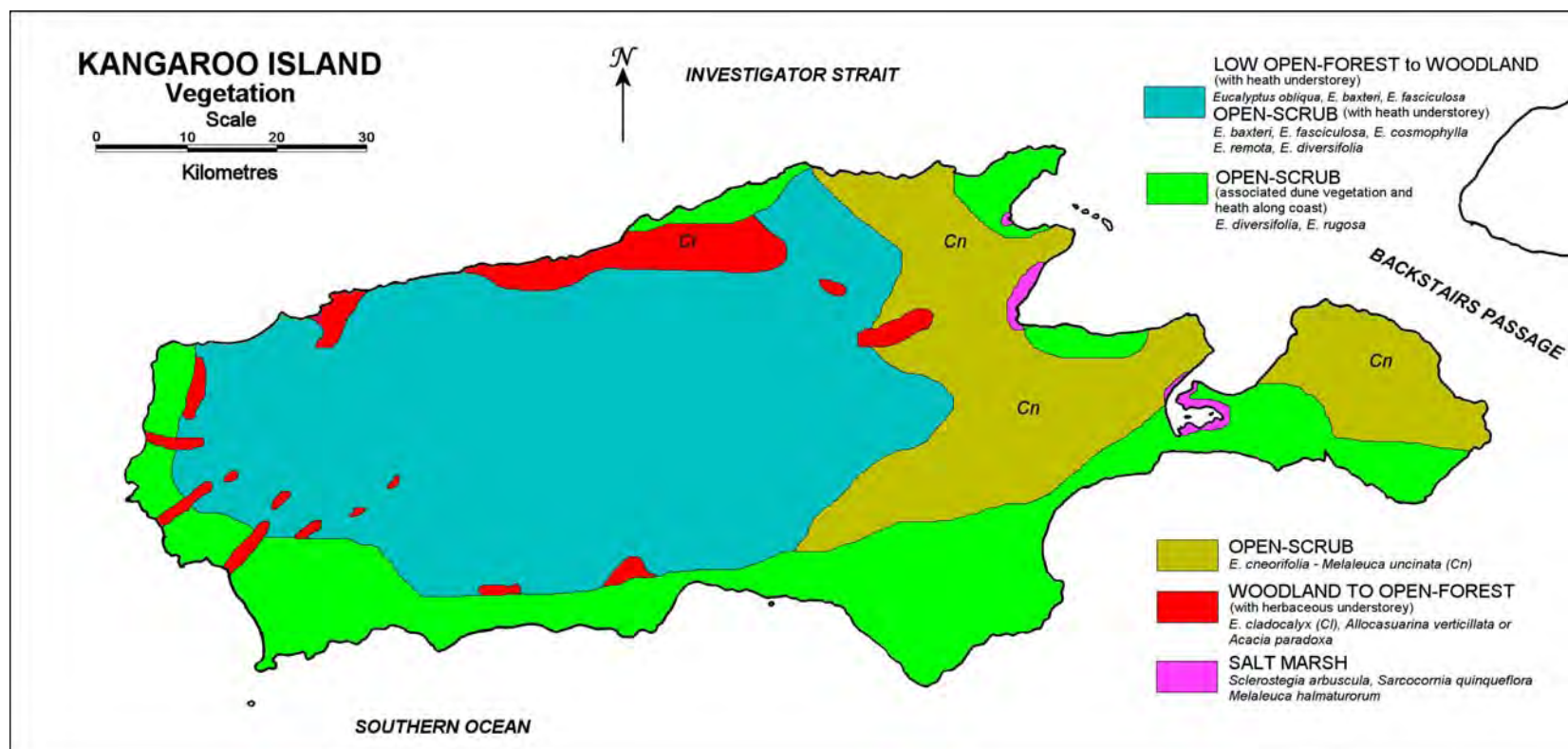


Figure 1.15: Kangaroo Island pre-European vegetation map based upon the Specht (1972) vegetation scheme with additional information from Ball (1998), Edwards (1987), Davies (1982), and Bauer (1959).

1.7.2 Open-Scrub (with associated heath and dune vegetation along the coast)

This formation is found in coastal and near coastal situations primarily along the southern and western portions of the island. The aeolianite cliff tops are dominated by coastal heath and shrublands which can extend 200-700 m landward. As the wind sheer reduces these give way to *E. diversifolia* and *E. rugosa* associations. *E. rugosa* associations are also characteristic of unlithified Holocene cliff top dunes and transgressive dunes. These dunes are found in large sometimes isolated lobes overlying Pleistocene aeolianite largely along the southern coast (Edwards, 1987; Bauer, 1959).

1.7.3 Open-Scrub

The eastern side of Kangaroo Island and much of Dudley Peninsula is dominated by this formation, which is characterised by *E. cneorifolia* and *Melaleuca uncinata*. This formation occurs on fertile, sandy loams, and hence most has been cleared for agriculture (Edwards, 1987; Davies, 1982; Bauer, 1959).

1.7.4 Woodland to Open-Forest (with herbaceous understorey)

This group features *E. cladocalyx*, associated with *Allocasuarina verticillata* or *Acacia paradoxa* as part of the understorey. These associations are patchily distributed along the coast in the northern, southern and western portions of Kangaroo Island, occurring along mid and lower gully slopes, and in riparian situations on alluvial soils. Within this group there are sometimes dense nonspecific stands of *A. verticillata*, often located at the bases and slopes of rocky gorges, sometimes abutting the coast. Major stands of *A. verticillata* occur along the northern coast west of Cape Cassini (Edwards, 1987; Bauer, 1959).

1.7.5 Salt Marsh

Saline marsh associations occur in the small number of areas that experience low energy conditions and tidal inundation. Associations of *Sclerostegia arbuscula*, *Sarcocornia quinqueflora* with or without the presence of *M. halmaturorum* shrubs occur at Pelican Lagoon, American River tidal inlet, Bay of Shoals, Nepean Bay, and the mouth of the Cygnet River (Edwards, 1987; Bauer, 1959).

1.7.5 Other vegetation groups

There is also a number of vegetation groups on Kangaroo Island that were not mapped by Specht (1972) or Bauer (1959). These groups are mainly extant along the coast and are often small and scattered with specialized habitat preferences (Edwards, 1987).

Modern beach dunes

Beach foredunes can be stabilized by colonizing species such as *Atriplex cinerea*, *Cacille maritime*, *Myoporum insulare*, *Acacia longifolia*, *Oleria axillarius*, and *Leucopogon parviflorus*. Blow out inland dune areas are often colonized by low shrubs such as *Ixodia archillaeoides*, *Festuca litteralis*, *Senecio lautus* and *Spyridium phyliciodes* (Edwards, 1987).

1.8 Summary

The history and physical environment of Kangaroo Island can be summarised with the following points:

- 1) Kangaroo Island lies off the South Australian coast, between 35°30' and 36°30' south latitude, and 136°30' and 138°30' east longitude, on the continental shelf which extends southward from the mainland for approximately 100 km.
- 2) The earliest age for Aboriginal occupation is 16 ka, but may have been as early as 30 ka. A small population of Aboriginal people may have been isolated on the island due to the marine transgression, at approximately 9.5 ka. Proxy evidence suggests that the island may have been occupied up until around 2.3 ka, after this the island was probably depopulated. This could have happened for a number of reasons; however, the most likely scenarios are migration or natural disaster.
- 3) The discovery of Kangaroo Island is attributed to Matthew Flinders, in 1802. The island was also explored by Nicholas Baudin's French expedition soon after this. Kangaroo island became sporadically populated after 1803, as a lay over, or desertion point for sailors, sealers and convicts. Sealers began

to steal aboriginal women from Tasmania and the mainland, taking them to Kangaroo Island, where their skills contributed to the survival of the sealers. By the time official colonization began in 1836, with the arrival of 5 ships from Britain, there was a stable population on the island of approximately 200 individuals. The colonists relied heavily on these 'original' inhabitants of the island to gain a foothold.

- 4) Kangaroo Island is essentially a south-west extension of the Mount Lofty Ranges. The island is also part of the Adelaide Geosyncline, and forms the southern part of the Fleurieu Arc Segment, encompassing the Kanmantoo Trough. The sub-surface geology is dominated by clastic meta-sediments of Cambrian age. Kangaroo Island incorporates three distinct lithotectonic zones: the Northern Structural Zone comprising relatively unmetamorphosed platformal sediments, the Shear Zone Complex which follows the lines of the Snelling and Signet Faults, and the Southern Basinal Zone encompassing the Kanmantoo Group of metasediments. These rocks are generally poor in outcrop, as they are overlain in most areas by Tertiary laterites or Quaternary calcareous aeolianites. The island is essentially a dissected high lateritic plateau with lowland regions in the north-east and south. Dudley Peninsula is an isolated plateau connected to the island by Quaternary sediments.
- 5) Kangaroo Island is surrounded by the shallow waters of the continental shelf with a depth range between 30 and 90 m. The greatest depth gradient lies of the north-west cape where it dips sharply to 100 m. The island experiences a mixed tide system with diurnal and semidiurnal phases; it also experiences surface currents that flow from west to east on both sides of the island, and is influenced by the warm waters of the Leeuwin and East Bight Currents. The west and south coasts of Kangaroo Island experience year round high energy west to south-westerly swells from the southern ocean, and these sections of coast, particularly, can be subject to extensive erosion during high-magnitude storm events. During such events shelf sediments can also be mobilised onshore, and to the deeper ocean (Richardson *et al.*, 2005). The northern and eastern coastal areas experience moderate to low wave energy conditions respectively. Sea surface temperatures around Kangaroo

Island fluctuate with the seasons. These range from 4 to 6° C between summer and winter. The salt concentration in waters around the island is in the range of 35.4 to 35.9‰. In protected low energy, shallow areas, such as lagoons and inlets the salt concentrations can be significantly higher.

- 6) Because of its relatively low elevation Kangaroo Island temperatures are little influenced by altitudinal differences. The island experiences its highest temperatures during summer; the warmest months being January and February, and its lowest temperatures in winter; the coolest months being July and August. The wind systems of the island are controlled by the southern drift of the Sub-Tropical Ridge (eastward moving high pressure systems). As the ridge migrates south the winds shift from a north-westerly winter pattern to a summer south-easterly pattern. The summer wind pattern is strengthened by afternoon south to south-east sea breezes, drawn by the landmass to the north as well as to the prevailing high pressure systems situated over the Great Australian Bight area. Most rain falls on the island during the winter months with a pronounced minimum rainfall during summer. June and July are the wettest months and January and February are the driest. Hence, Kangaroo Island experiences a Mediterranean rainfall climate.

- 7) Kangaroo Island has a rich vegetation heritage, classified here using the Specht (1972) scheme. The central and northern regions of the island are characterised by low open forest to woodland (*Eucalyptus obliqua*, *E. baxteri*, *E. fasciculosa*), and open scrub (*E. baxteri*, *E. fasciculosa*, *E. cosmophylla*, *E. remota*, *E. diversifolia*) associations. The southern coastal margins are characterized by open scrub and heath associations dominated by *E. diversifolia* and *E. rugosa*. The eastern lowland areas exhibit open scrub associations dominated by *E. cneorifolia* and *Melaleuca uncinata*, although most of this group has been removed due to land clearing. Portions of the northern coast and some areas around waterways are host to woodland and open forest associations. These feature *E. cladocalyx*, associated with *Allocasuarina verticillata* or *Acacia paradoxa* as part of the understorey. Saline marsh associations occur in the small number of areas that experience low energy conditions and tidal inundation.

This chapter has illustrated important background information for the palaeoenvironmental interpretations that will follow in later chapters. The next chapter, Chapter 2, will explore the formation of Quaternary calcareous aeolianite with respect to changes in sea level, in a global context.

This chapter has illustrated important background information for the palaeoenvironmental interpretations that will follow in later chapters. The next chapter, Chapter 2, will explore the formation of Quaternary calcareous aeolianite with respect to changes in sea level, in a global context.

Chapter 2: Aeolianite formation and distribution in the context of global sea-level change

2.1 Introduction

Coastal aeolianites are distinctive wind deposited sedimentary formations found in the coastal areas of many continents and islands in the mid-latitudes (typically between 20° and 40° north and south latitude) (Fairbridge and Johnson, 1978; Brooke, 2001; Price *et al.*, 2001). They form as a result of onshore winds, marine processes, and continental shelf carbonate production, and are generally in the form of consolidated stacked units or discrete (consolidated) barrier complexes. Parts of the South Australian coast have large deposits of skeletal carbonate aeolianite. For example, the Coorong to Mount Gambier Coastal Plain (southeast South Australia) preserves one of the world's most extensive records of aeolianite deposition (Murray-Wallace *et al.*, 1999; Brooke, 2001), representing a record of sea-level change, in the form of stranded aeolianite dune sequences that extend deep into Pleistocene time.

This chapter first analyses the physical attributes of aeolianites and associated palaeosols, their deposition, formation, and the implications for palaeoclimates and global eustasy. The final sections examine the global distribution of aeolianite, and previous studies of the aeolianite successions of Kangaroo Island.

2.2 Aeolianite research

Aeolianites have been studied for a variety of reasons. The common themes relate particularly to the timing of aeolianite deposition in relation to sea-level change during the Pleistocene, and reconstruction of marine, and terrestrial palaeoenvironments (e.g. from species mix of skeletal grains, groundwater movement, palaeowind regimes, position of palaeobarriers). For example reconstruction of past sea-levels, recorded as stranded dune barriers (formed during past interglacial and interstadial periods; preserved due to gentle epeirogenic uplift [Sprigg, 1952; Huntley *et al.*, 1993; Murray-Wallace *et al.*, 1998; Murray-Wallace *et al.*, 2001]) on the Coorong coastal plain, southeastern South Australia, (see Figure 2.1), has been undertaken by many researchers,

most notably by Sprigg (1952) Schwebel (1984), Huntley *et al.* (1993), and Murray-Wallace *et al.* (2001). Amino acid racemization (AAR) and uranium series (U-series) chronologies developed by Hearty *et al.* (2007), using samples recovered from the Bahamas, Hawaii, and Western Australia (i.e. aeolianite, beach deposit, marine shell, and coral samples) have revealed significant fluctuations in sea-level during Marine Isotope Stage 5e (MIS 5e) (+2 m to >+6 m above present sea-level [APSL]). In another study Kindler and Hearty (2000) used petrographical analysis (in conjunction with AAR and U-series chronologies) of aeolianites and palaeosols, from the Bahamas and Bermuda, to reveal deglaciation events that occurred during the middle Pleistocene.

2.2 Aeolianites and palaeosols

The following sections outline the general characteristics of aeolianites and palaeosols in terms of structure, morphology, and stratigraphic arrangement. The relationship of aeolianites and palaeosols to fluctuating environments is also explored.

2.2.1 Aeolianites

Aeolianite—also termed eolianite in the North American literature (the term first coined by Sayles [1931])—in the strictest sense refers to deposits of *any* wind blown sediments that have been lithified by diagenetic processes. Over time, however, this term has become more focused, and tends to be used to describe the lithified, coastal marine carbonate sequences that have been deposited during the Quaternary (Fairbridge and Johnson, 1978).

Aeolianite is also known as calcareous dune rock and dune calcarenite (McKee and Ward, 1983), and occurs on carbonate banks, isolated mid-ocean islands and continental shelf coastlines—most commonly between 20° and 40°, north and south of the equator (Brooke, 2001; Woodroffe, 2002). The sediment is derived from accumulations of skeletal, and depending upon location, precipitated carbonate (ooids for example) that forms within continental environments, and is subsequently moved onshore by marine processes to be deposited as (initially) beach sediment, then barrier, backshore, cliff-top, or possibly inland dunes (eventually undergoing diagenesis to form aeolianite).

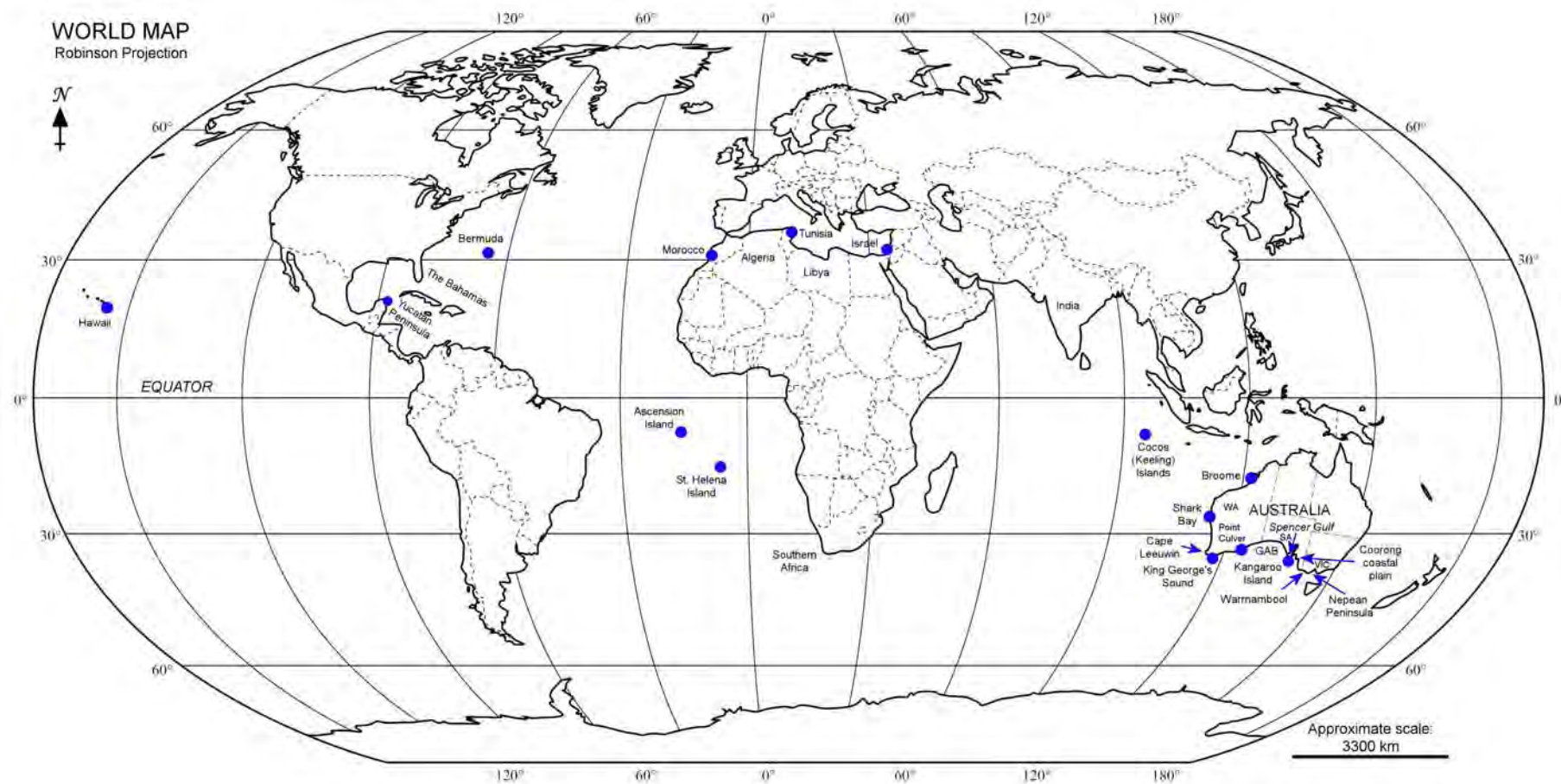


Figure 2.1: World map (Robinson [1961] projection), showing locations mentioned in text.

Morphostratigraphically, where such morphology and depositional architecture has been clearly preserved, the deposits are generally in the form of elongate, shore parallel, transverse dune ridges, and shore parallel ridges commonly cut into by wave action (if neotectonic uplift is occurring, as on the Coorong to Mount Gambier coast plain [southeast South Australia—see Figure 2.1], then the ridges are commonly preserved as discrete, shore parallel, barrier dune formations extending inland—as a response to the uplift, and fluctuating sea-level [Murray-Wallace *et al.*, 2001]), and bounded by headlands.

These deposits may comprise stacked or consolidated complexes of smaller dunes. In stable tectonic environments dune successions are superimposed (rather than being discrete dunes), and characteristically separated by intercalated palaeosols, protosols, calcretes, or other subaerial exposure surfaces.

The major implication of stacked sequences of aeolianite relates to the recording of environmental change. The stacked units act as archives, chronicling fluctuating sea-levels over time, with depositional hiatuses generally represented by intercalated palaeosols or calcretes. Micromorphologically the sediments also can record changes in depositional environment (i.e. alteration of groundwater levels, types of water [vadose, phreatic—marine or meteoric]), continental shelf or near-shore environments, and sea-water temperature (e.g. foraminifer species diversity, and indicator species). The gross morphology of the units (e.g. cliff collapses, sea-caves, wave-cut notches) can also allude to past sea-level.

The dunes that aeolianites form from are generally present as barchan, parabolic and blowout dunes: morphologies that can be observed as common contemporary features of many beaches globally (McKee and Ward, 1983; Brooke, 2001) (see Figure 2.2 for an ideal dune cross-section). Dune configuration depends upon a number of factors, the most important being sediment supply and the prevailing wind conditions. Stratigraphically the deposits show alternating coarse and fine laminae, which are associated with

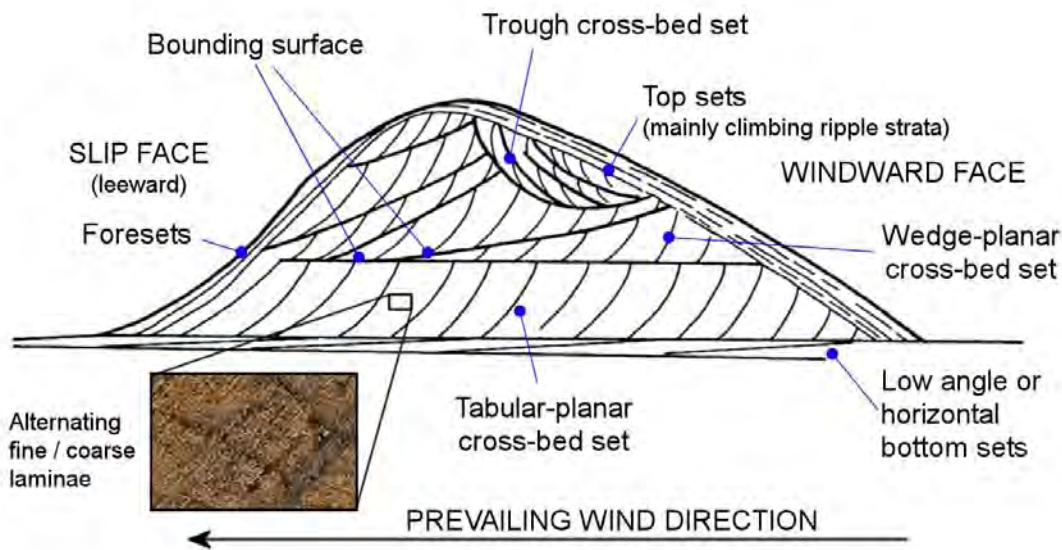


Figure 2.2: Cross-section through an ideal transverse dune, showing bedding structures, and gross morphology (after Pye and Tsoar, 1990).

multiple cycles of dune formation. They tend to be considerably cross-stratified with high angle dune foresets dipping landward (see Figure 2.2). Furthermore, (as mentioned above) there may be discontinuities in the strata distinguished by layers of pedogenically-altered sediments called calcretes, palaeosols and protosols. These indicate a hiatus from a marine dominated depositional regime (Woodroffe, 2002), and contrast the lengths of time that sediments undergo pedogenesis. Other facies in association with the aeolianite may be in the form of sublittoral shell beds, pebble beds, near shore sands, beach deposits, and landward lagoonal, swamp, and cave deposits (McKee and Ward, 1983). The term aeolianite refers then to, taking into account the above factors, not only coastal carbonate dune sediments, but the range of facies associated with them as well.

Structurally aeolianites may be made up of a mixture of siliceous sands, broken shell, bryozoans, echinoderm spines, ooids, pellets; sand grain sized skeletal fragments, and whole foraminiferal tests. These grains can be, depending on the level of diagenesis, lithified by meniscus, pendulous, or needle fibre carbonate cements. The deposits may also exhibit trace fossils in the form of animal burrows, root-hair sheaths, rhizoliths, and rhizcretions (McKee and Ward, 1983).

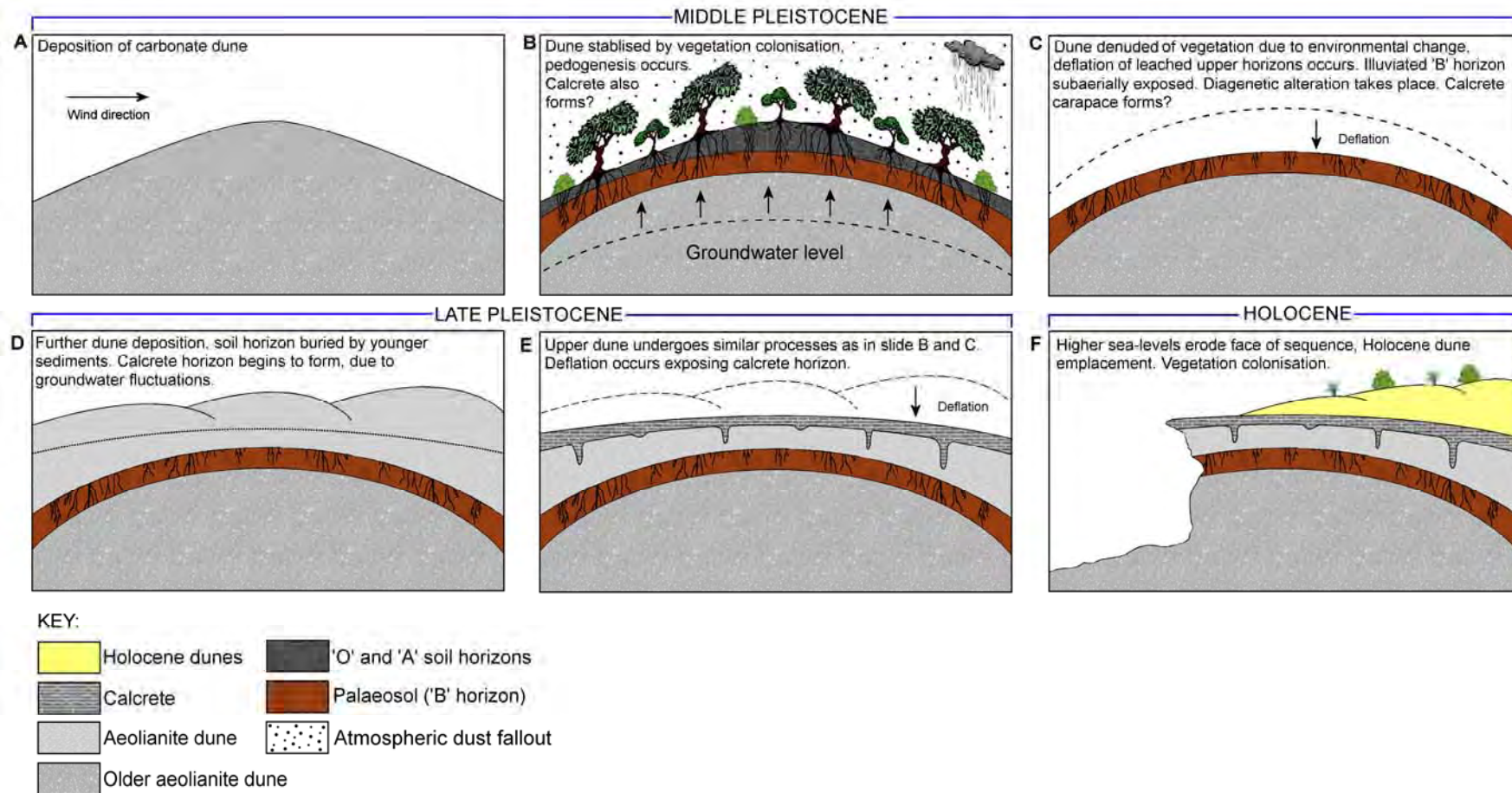


Figure 2.3: Hypothesised sequence of events that occur resulting in palaeosol and/or calcrete formation.

2.2.2 Palaeosols

Palaeosols (to paraphrase Flügel [2004]: pg 10) are described as *buried soil horizons of the geological past*; they are strong indicators of past subaerial exposure surfaces. In reference to aeolianite deposits palaeosols may stratigraphically represent long pauses in carbonate deposition (Land *et al.*, 1967; Boardman *et al.*, 1995; Woodroffe, 2002). Essentially palaeosols are the remnant illuviated 'B' horizons of carbonate rich soils (the upper portions lost due to dissolution and deflation) that formed with the accretion of wind deposited carbonate sediments, stabilised by vegetation occupation. The sediment becomes vegetated and biologically active, and subsequently undergoes pedogenesis. Figure 2.3 proposes a sequence of events leading to palaeosol and/or calcrete formation.

How well the soil is developed may depend upon the length of the depositional pause, and (or) the environment (i.e. rainfall, groundwater, for example). Therefore, these fossil soils range from embryonic protosols (incipient, pale, structureless layers), and calcretes, that show little evidence of pedogenesis to strongly-coloured, well developed *terra rossa* (red-earth) soils, that may have taken many tens of thousands of years to form (*terra rossa* soils can also develop purely as a result of dissolution and *in situ* calcrete pedogenesis, however, there is generally some input from the atmosphere and biosphere [Land *et al.*, 1967; Zhou *et al.*, 1994, Boardman *et al.*, 1995; Brooke, 2001]). The remnant soil horizon (usually 0.3 m to 1.5 m thick) is subsequently buried (and preserved) by overlying sediments (i.e. carbonate dune sands) once the depositional pause ends. More weakly developed soils may represent short depositional pauses within an interglacial highstand, whereas well-developed *terra rossa* soils may represent the entire depositional pause related to a glacial lowstand (Carew and Mylroie, 1997). The term palaeosol has also been used in a more general sense, embracing other horizon features associated with aeolianites, such as caliche crusts, duricrusts, calcareous laminated crusts and calcrete (Boardman *et al.*, 1995).

2.2.3 Aeolianites and palaeosols—sea-level and climate change

The potential for aeolianites as indicators of past environmental change has long been recognised. François Péron, the zoologist aboard the French

exploration vessel *Le Geographe* in 1803, noted the presence of many deposits of 'calciferous sandstone' along the southern coastal areas of Kangaroo Island (off the coast of South Australia—see Figure 2.1). Upon closer examination Péron (1817) described this calciferous sandstone as consisting of marine produced skeletal fragments, wind blown from the shoreline into dune structures that were subsequently consolidated. However, Péron (1817) did not draw any conclusions with regard to environmental change, his observations were mainly concerned with the mechanical nature of the deposition and the chemistry that produced the many examples of 'petrified' vegetation remnants (rhizocretions) found in the consolidated dunes. However, when Péron (1817) encountered marine shells in similar calcareous deposits well above the present coastline on the South Australian mainland, he suggested that the deposits were from a time when the coastline was lower.

Decades later (in 1836) during the voyages of the HMS *Beagle*, Charles Darwin observed coastal deposits on the mid-Atlantic Islands of St. Helena, and Ascension (see Figure 2.1), and also later at King George's Sound on the southwest coast of Australia (see Figure 2.1). In comparing the deposits on St Helena and Ascension, Darwin (1844) was puzzled over the absence of modern equivalents for the calcareous deposits on St. Helena. He noted that there were no shell beach deposits on any part of the coastline, and hence no visible calcareous source material for dune creation. Darwin stated that:

'..we must, therefore, look back to a former period, when, before the land was worn into the present day great precipices, a shelving coast, like that of Ascension [Island], was favourable to the accumulation of shelly detritus. Some of the beds of limestone are between 600 and 700 feet above the sea; but part of this height may possibly be due to elevation of the land, subsequent to the accumulation of the calcareous sand.' (Darwin, 1844: p. 69).

Darwin's interpretation, on the basis of his observations, was that the coastal depositional environment must have been considerably different in the past. At

an earlier period in St. Helena's history lower sea-level allowed for the formation of a shallow shelf around the island. This resulted in the accumulation of calcareous material which was subsequently deposited into dunes that eventually formed the bed like structures of the present precipitous coastline.

According to Brooke (2001) the work of Daly (1927) on St. Helena brought to light the existence of large stores of skeletal carbonate offshore of the aeolianite units. Daly (1927) noted that the deposits were located between 20 and 30 meters depth and suggested that even a small regressive movement of sea-level, rather than a large drop associated with glaciation, could result in the shoreward migration of the sediments.

When Darwin visited King George's Sound he commented upon the apparent vast scale of coastal calcareous deposits along the southern Australian margin, in relation to those he found on the mid-Atlantic islands. He compared the extent of these deposits with those of '...the great coral reefs of the Indian and Pacific Oceans...' (Darwin, 1844: p. 117), noting that the process of formation was similar to that taking place contemporaneously in Bermuda and the Keeling Atoll (see Figure 2.1).

Bald Hill (King George's Sound) was of particular interest to Darwin (1844: pg 114), as the calcareous deposits of this area displayed high angle cross-bedding features, commonly showing massive bedforms. According to Darwin (1844: p. 114) these structureless features were examples of some form of subaerial weathering. Darwin equated the calcareous material from the deposits of Bald Hill with skeletal grains from St Helena, stating a similar marine origin. Based upon the structure of the Bald Hill deposits, and the morphology of the present coastline, Darwin (1844: p. 115) suggested that the materials comprising the Bald Hill deposits were derived from a '...period when the land stood lower...' from a shoreline that is now submerged.

The early observations of Darwin and Péron anticipated the significance of aeolianites as records of coastline change due to uplift and eustasy, marine carbonate production, changing depositional volumes, and sediment reworking. According to Brooke (2001) it was not until a comprehensive investigation,

undertaken by Sayles (1931), of the aeolianite deposits on Bermuda that it became apparent there was a connection between the palaeosols that separated the dune units and alterations in the depositional environment due to glacially induced sea-level change. Sayles (1931) interpreted the aeolianite as reworked shelf sediments that were wind deposited as dunes during periods of low sea-level, when the platform surrounding the islands was exposed. Accordingly he interpreted the palaeosols as representing the diagenetic products of warm-wet interglacial periods. However, subsequent studies of aeolianite on Bermuda have shown that aeolianite was predominantly deposited during periods of high sea-level (Bretz, 1960; Land *et al.*, 1967; Harmon *et al.*, 1981; Hearty *et al.*, 1992; Vacher *et al.*, 1995). Conversely, it was discovered that the palaeosol layers could be equated with the sea-level lowstands of glacial periods, when the surrounding platform would be exposed, and rapidly vegetated (Barwis and Tankard, 1983), and there would be negligible influx of marine carbonate because of stabilisation. These hiatuses in carbonate deposition allowed the activation of subaerial weathering and pedogenic processes.

Studies from other locations around the world, most notably from the western Mediterranean (Brückner, 1986; Engelmann *et al.*, 2001) the Caribbean (Land *et al.*, 1967; Harmon *et al.*, 1981; Hearty *et al.*, 1992; Vacher *et al.*, 1995; Hearty, 2002), Lord Howe Island (Brooke, 1999; Brooke *et al.*, 2003), and the Coorong coastal plain of southeastern Australia (Huntley *et al.*, 1993, 1994; Murray-Wallace *et al.*, 1996, 1998, 2001; Huntley and Prescott, 2001), support the premise of sea-level highstand deposition of aeolianites.

However, according to Brooke (2001), in some regions aeolianite deposition appears to coincide with intervals of lower than present sea-level. For example, there are various studies of aeolianites in the Mediterranean (e.g. Porat and Wintle, 1995; Frechen *et al.*, 2001) and some Californian islands (e.g. Johnson, 1977) as well as some sites in Africa (e.g. Coetzee, 1975), southern Victoria (e.g. Zhou *et al.*, 1994) and Western Australia (e.g. Playford *et al.*, 1976, Playford, 1988, 1997; Price *et al.*, 2001) that suggest that the aeolianites were, at times, deposited during sea-level lowstands, during glacial cycles. According to Brooke (2001) these glacial age deposits are in all probability the result of

aeolian reworking of unlithified carbonate that was deposited on the shelf or shoreline during an interglacial; or carbonate produced offshore on a narrow shelf during the glacial period, and moved from the distant shoreline. It is difficult to reconcile the most likely event, although, arid glacial conditions and vegetation colonisation, may have been conducive to the lithification, and/or stabilisation of exposed shelf carbonates.

2.3 Production of coastal carbonate

Several environmental variables that control the production and deposition of biogenic marine carbonate have a bearing on successive episodes of aeolianite deposition, and the inferred record of environmental change. Parameters that influence the production of bioclastic carbonate include: water temperature, carbonate concentration, wind direction, salinity levels, tectonic settings, and terrigenous input.

2.3.1 Carbonate sedimentation

Traditionally shelf carbonate production was regarded as low latitude phenomenon, restricted to the warm-water areas of the tropics. However, subsequent studies by many researchers (e.g. Lees and Buller, 1972; Lees, 1975; Fuller *et al.*, 1994; James, 1997; James *et al.*, 1999; Knoerich and Mutti, 2003; Saxena and Betzler, 2003) show that this is not the case and sites for large-scale production and sedimentation of carbonate exist well outside of these areas (Lees and Buller, 1972). The submerged continental margin of southern Australia, for example, is one of the largest cool-water carbonate provinces in the world (Fuller *et al.*, 1994).

Sediment associations have a tendency to vary over a geographical gradient, i.e., degrees of latitude north and south of the equator. Strictly speaking carbonate production occurs, on open shelf areas, between 60° south latitudes and 60° north, and different sediment associations occur over this gradient. The Brooke (2001) database of aeolianite deposition shows that most aeolianite study sites are concentrated between 20° and 40° north and south latitude, with 82% of sites falling within these zones. According to Lees (1975) the apparent reason for these latitudinal associations is a result of the variations in temperature and salinity that occur due to the change in latitude.

An important factor in determining the distribution of carbonate provinces is the rate of terrigenous (siliciclastic) input, which is related to fluvial discharge (Chave, 1967; Mount, 1984; James, 1997). According to Chave (1967) rivers control the distribution of carbonate sediments, not chemistry, water temperature, or biological production. Terrigenous sediments can, in sufficient quantities, increase the turbidity of the water (reducing insolation), and decrease the feeding efficiency of carbonate producing organisms (McKinney, 1984). Hence, in order for carbonate to accumulate on shelves it is critical that the rate at which carbonate is produced is greater than the influx of terrigenous sediment (Rao, 1996; James, 1997). For example the low percentage of terrigenous clastic components in the southern Spencer Gulf (part of a major carbonate province on the shelf off the coast of southern Australia—see Figure 2.1) sediments can be attributed to the regional semi-arid climate, and the absence of perennial streams (Fuller *et al.*, 1994).

Originally three main carbonate sedimentary associations were described (on the basis of biological components of the sediments rather than the geographical factors of latitude and temperature—however, as explained above these factors alone do not fully explain the distribution of skeletal associations [Lees and Buller, 1972; Brooke, 2001]) (Figure 2.4 illustrates the distribution of warm- and cool-water carbonate associations around Australia):

- i) *The Chlorozoan Association* (a warm-water association [0°-30° latitude]; near-surface minimum temperatures of 14-15 °C, with a mean of at least 23 °C): skeletal clastic composition comprising mainly calcareous green and red algae (or just green algae), hermatypic corals (green algae and hermatypic corals [reef-building corals {cf. Schuhmacher and Zibrowius, 1985}] are characteristic of this association), molluscs and foraminifers (and a component derived from ostracods, sponge spicules, worm tubes, and ahermatypic corals [non-reef-building corals {cf. Schuhmacher and Zibrowius, 1985}]), with small contributions from bryozoans and barnacles (Lees and Buller, 1972; Lees, 1975).
- ii) *The Foramol Association* (a cool-water association [latitudinal

variability is greater than Chlorozoan, ranging from 0° to >60° of latitude—eastern continental margin ocean currents influence the wider distribution of Foramol sediments, to an extent, into lower latitudes]; mean near-surface temperatures <20 °C): skeletal clastic composition comprising mainly calcareous red algae, molluscs, foraminifers, and a component derived from ostracods, sponge spicules, worm tubes, and ahermatypic corals) and characterised by major bryozoan and barnacle components (Lees and Buller, 1972; Lees, 1975).

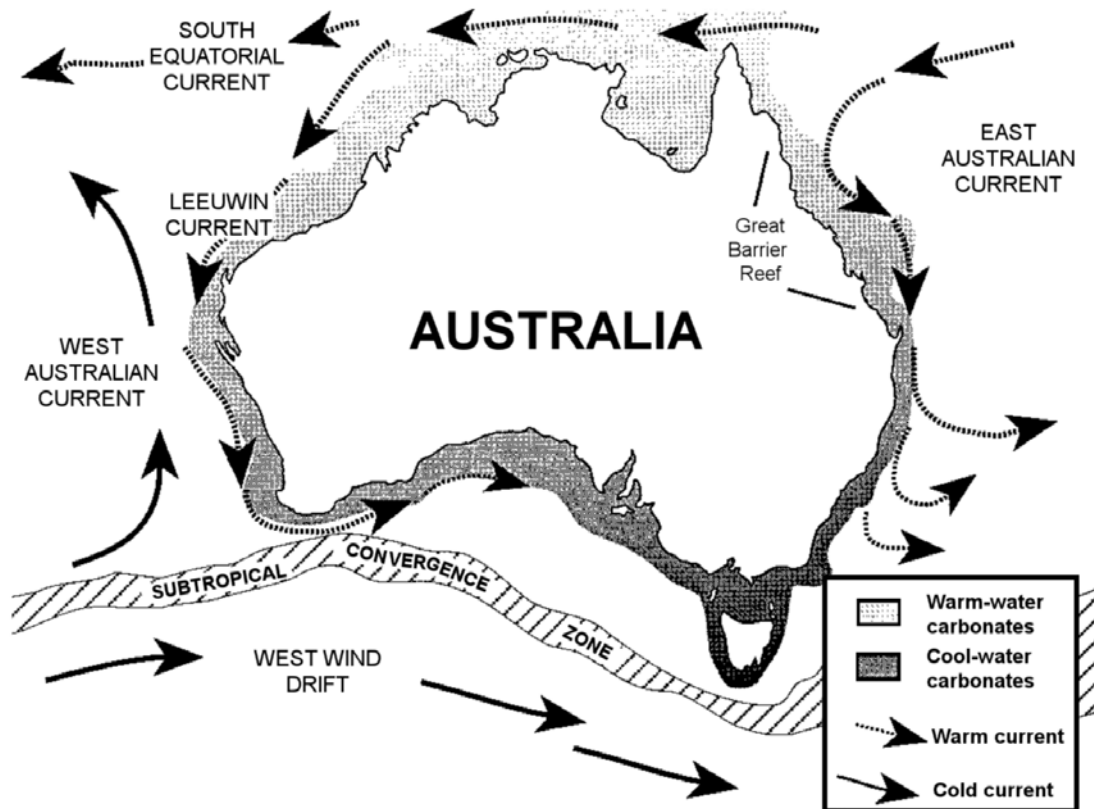


Figure 2.4: Continental margin of Australia illustrating the areas of cool-water versus warm-water carbonate deposition, and major oceanic current patterns (after James *et al.*, 1999).

- iii) *The Chloralgal Association.* Lees (1975) distinguished this association based upon the influence of salinity levels on the composition of the Chlorozoan Association. The Chloralgal Association is deposited in regions of high salinity (43 ‰ to >45 ‰), or regions of lower salinity (<33 ‰) with corresponding high water

temperature (>30 °C). Because of the extreme salinity range these sediments are characterised by green algae and an absence of corals, with non-skeletal grains such as ooids and aggregate particles being present in high salinity regions.

Later, in a study on cool-water carbonate deposition, James (1997) revised these classifications, by combining the Chlorozoan and Chloralgal associations (along with other Cenozoic and pre-Cenozoic skeletal assemblages such as Coralgall, Oopeloid, Fusilinalgal, and Rudist), and also by redefining the Foramol Association. This new Chlorozoan-Chloralgal combination was designated 'Photozoan', '[emphasizing] *the light-dependant nature of the major biotic constituents*' (James, 1997: pg 3) (e.g. zooxanthellate corals, and calcareous algae, which are photosynthetic autotrophs [carbon fixing]—although most zooxanthellate corals are also heterotrophic [utilise organic carbon] to a degree, preying on zooplankton [Barnes and Hughes, 1999]).

The Foramol Association was redefined primarily because of the use of taxa in the name—given that foraminifers, and molluscs, do not always represent dominant components of the association, in particular areas (in both Cenozoic and pre-Cenozoic carbonate sediments) (James, 1997). The term 'Heterozoan' was adopted for the association reflecting the diversity of the skeletal components. The dominant biotas of the Heterozoan Association are heterotrophic (not including red algae), benthic organisms, existing in most marine environments from the poles to the equator (intertidal to deep-ocean)—although only where the supply of other sediment types (e.g. siliciclastic and Photozoan) is limited by environmental conditions (James, 1997). For example the Heterozoan Association is typical of marine environments that exist below the photic zone in warm water. Figure 2.5 illustrates the different Heterozoan assemblages, and their dominant components, found along the grading cross-section of an open shelf, on the southern margin of Australia. The Heterozoan Association will also develop at low latitudes in warm-water when nutrient levels encourage plankton abundances dense enough to reduce water transparency; thereby preventing the development of the Photozoan Association (James, 1997; Flügel, 2004; Perry *et al.*, 2008). This means that while cool-water

Table 2.1: Influence of water temperature on carbonate sediment assemblages, constituent organism, and sedimentary characteristics (modified after James, 1997; Brooke, 2001).

Bottom water temperature	Sediment provinces	Approximate latitude (N and S) range of provinces	TROPH: Carbonate assemblages	ASSOCIATION: Sedimentary attributes
Warm >22° C	Tropical	0°-20°	AUTOTROPHIC: Coral and or green algae; ooids, red algae, other Heterozoan	PHOTOZOAN: shallow rimmed shelves, open shelves, ramps, reefs; abundant carbonate mud, marine cementation, micritisation, bioerosion; aragonite and Mg-calcite mineralogies.
~18–22° C	Subtropical	20°-40°	AUTOTROPHIC / HETEROTROPHIC: Abundant red algae, minor coral and / or green algae; other Heterozoan	HETEROZOAN and minor Photozoan elements: open shelves and ramps, few reefs; minor carbonate mud, marine cementation, bioerosion; aragonite and calcite mineralogies.
Cool ~10–18° C	Temperate	40°-60°	HETEROTROPHIC / AUTOTROPHIC: Abundant or dominant foraminifera or mollusc or bryozoan; red algae, other Heterozoan	HETEROZOAN: open shelves and ramps, no reefs, slope mounds; minor carbonate mud, minor cementation, extensive bioerosion and maceration; calcite minerals dominant.
~5–10° C	Sub-polar	50°-70°	HETEROTROPHIC: Abundant molluscs and or barnacles; brachiopods, other Heterozoan	HETEROZOAN: open shelves and ramps; extensive maceration and boring, no cementation; calcite mineralogies.
Cold <5° C	Polar	>70°	HETEROTROPHIC: Sponges (siliceous); bryozoans, barnacles	HETEROZOAN: open shelves and ramps; gigantism, biogenic siliceous facies; no cementation; calcite mineralogies.

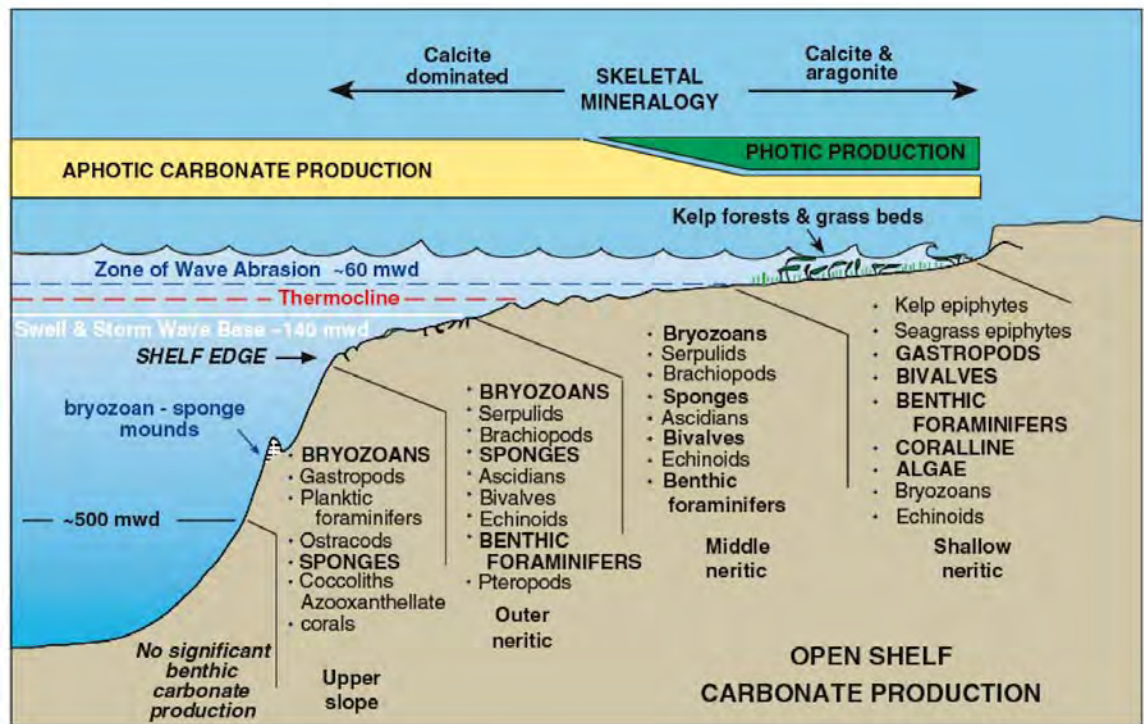


Figure 2.5: Predominantly Heterozoan carbonate associations deposited on southern Australian open shelves. Bold capitalized text indicates dominant sediment components (diagram from James and Bone, 2011). Photic (autotrophic) components in this association are kelp, seagrass and coralline (red) algae, rather than zooxanthellate corals. The Heterozoan Association is aphotic (heterotrophic) past the shallow neritic zone.

carbonates are always Heterozoan, the presence of the Heterozoan Association (in fossil sediment for example) does not necessarily imply that the sediment developed in cool-water (James, 1997).

Table 2.1 illustrates the characteristics of the James (1997) reclassification, and the division into 5 sediment provinces on the basis of water temperature; the table also lists the main attributes and depositional regions (i.e. rimmed shelves, open shelves, ramps and reefs). Hence, since there is a link between water temperature and sediment associations, it is possible that any temperature alteration could affect the sedimentary attributes. For example, associations located on shelves or platforms that are adjacent to the thermal boundary of a carbonate province may be altered by changes in sea-surface temperatures (SST) associated with glacioeustatic cycles (Brooke, 2001). This may be recorded as changes in the assemblages preserved in shelf and coastal deposits (Brooke, 2001). For example warmer sea temperatures experienced along the South Australian coast during the Last Interglacial period (MIS 5e: ca.

116 ka to ca. 132 ka—Siddall *et al.*, 2007), as a result of a strengthened Leeuwin current (McGowran *et al.*, 1997) (see Figure 2.4), have been recorded in South Australian, and Kangaroo Island coastal sediments. This is in the form of warm-water foraminifer and molluscan species such as *Marginopora vertebralis* (Blainville) 1830, and *Anadara trapezia* (the Sydney cockle) (Deshayes) 1840, which are no longer extant in these regions (Milnes *et al.*, 1983; Cann and Clarke, 1993; McGowran *et al.*, 1997; Murray-Wallace *et al.*, 2000).

2.3.2 Heterozoan carbonate production

The shelf along the southern portion of Australia is a major cool-water carbonate province, and represents the world's largest cool-water carbonate sedimentary system (Fuller *et al.*, 1994; Saxena and Betzler, 2003). Indeed the shelf area is a vast carbonate factory where carbonate producing organisms (dominated by molluscs and foraminifers, with red algae, bryozoans, and echinoid components) provide large accumulations of carbonate detritus (Gostin *et al.*, 1988; James *et al.*, 1993). The slow rate of terrigenous sediment inputs, because of the semi-arid regional climate and the absence of perennial streams (Fuller *et al.*, 1994), contributes to the high rate of carbonate production. This is similar to South Africa (near Cape Agulhas—see Figure 2.1) where the wide expanse of continental shelf (characterised by a low gradient), low terrigenous input, and the mixing of the warm Agulhas current with the nutrient rich cold waters of the Benguela current (see Figure 2.6), facilitates a high rate of heterozoan carbonate production (Bateman *et al.*, 2011). Similar to the Heterozoan Association found in south Australian coastal carbonate sediments, shelf and near-shore sediments from the Agulhas region are dominated by molluscs, with foraminifers, coralline (red) algae, and echinoids contributing (Siesser, 1970; Malan, 1990; Bateman *et al.*, 2011).

In the past carbonate production along southern Australia must have been similar to, or of greater magnitude than, the present. Particularly during climatic optimums when there may have been a strengthened Leeuwin current (McGowran *et al.*, 1997). The southern and southwestern coastlines of Australia have the world's most extensive tracts of aeolianite, with deposits ranging from tens of metres to over 150 m in thickness (Brooke, 2001). For example, the

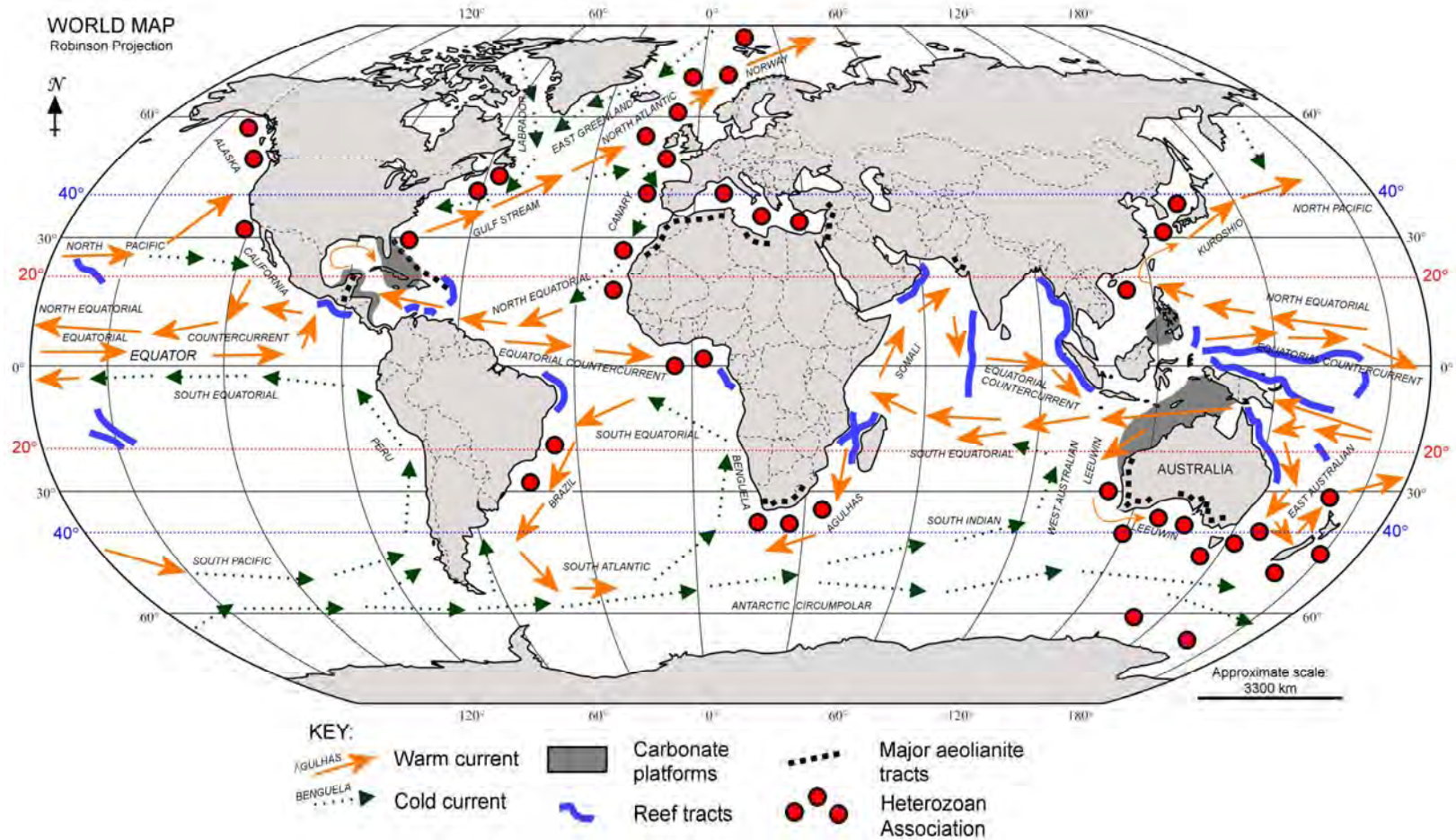


Figure 2.6: Warm and cold ocean currents and the distribution of shallow-marine carbonates and aeolianite (modified after James, 1997; Brooke, 2001). Major aeolianite tracts are often marginal to major Heterozoan carbonate provinces (i.e. southern Africa, the Mediterranean, Bermuda and the Bahamas, Yucatan [Mexico], and southern and southwestern Australia). Photozoan provinces (reef tracts and carbonate platforms) are concentrated predominantly in regions with warm-water currents.

Tamala Limestone Formation (Playford *et al.*, 1976) (found along the western Australian coastline from the North West Cape to Cape Leeuwin, and across the Great Australian Bight to South Australia) and Bridgewater Formation aeolianites (Boutakoff and Sprigg, 1953; Boutakoff, 1963) (South Australia and Victoria), are vast deposits representing onshore carbonate accumulation that has taken place during the Pleistocene. The aeolianite sequences (with intercalated palaeosols and calcretes) within the formations record multiple eustatic sea-level events (as many as 12 stacked sequences at Cape Spencer, southern Yorke Peninsula, and southern Kangaroo Island [Belperio, 1995]). The great thickness of the deposits is a testament to the production capability of the offshore Heterozoan carbonate factory.

In contrast to the above, the eastern continental shelf areas of Australia are characterised by high terrigenous input from fluvial sources, which has mantled the inner shelf areas. Below 20° of latitude onshore dune, beach, and inner shelf sediments along the eastern Australian coast are predominantly siliciclastic (Brooke, 2001). Further north inside the boundary of the Great Barrier Reef, the sediments are muddier, with relatively low percentages (<30%: Marshall and Davies, 1978; Marshall, 1980; Belperio, 1983) of carbonate (Brooke, 2001).

2.4 Distribution, stratigraphy, and age of major aeolianite tracts

Excellent reviews on the global distribution of carbonate aeolianite are given in Brooke (2001) and in the Jacobs (2008) database of luminescence dated coastal and marine sediments. Nevertheless, the following sections briefly outline the distribution, stratigraphy, and age of the major global aeolianite tracts, as a framework to contextualize the significance of the Kangaroo Island aeolianite successions

2.4.1 Factors affecting the global distribution of aeolianite

In his global database that reviewed over 80 sites hosting Quaternary carbonate aeolianites, Brooke (2001), established that aeolian carbonate sediments, although found over a wide range of latitudes, were primarily deposited between 20° and 40° of latitude (see Figure 2.6)—with the bulk of the

world's aeolianite being found in southwestern and southern Australia, and southern Africa (in terms of lateral extent and thickness of units). Subsequent statistical testing showed that this geographical distribution was the same across both hemispheres. Brooke (2001) concluded that this reflected the global nature of the controls on aeolianite formation.

The primary controls on aeolianite formation relate principally to climate and eustatic sea-level change, and to a degree the topography of the coastline in relation to the tectonic setting. The morphology of the aeolianite deposits is also influenced by the tectonic setting. According McKee and Ward (1983) the requisite conditions for aeolianite formation are a warm climate (i.e. subtropical, temperate) conducive to carbonate production, and onshore winds to move the sediment inland from the beach to depositional areas (e.g. barrier, backshore, cliff-top, and inland dunes). Another important factor is the mechanism for the mobilisation of sediment from the highly productive shelf to onshore. Particularly as the vast Pleistocene deposits of southern Africa and Australia attest to past periods of large-scale mobilisation. Many studies suggest that these periods of mobilisation and deposition are related to sea-level highstands (e.g. Land *et al.*, 1967; Harmon *et al.*, 1981; Brückner, 1986; Hearty *et al.*, 1992; Vacher *et al.*, 1995; Brooke, 2001; Engelmann *et al.*, 2001; Murray-Wallace *et al.*, 2001; Hearty, 2002;) and there is also some evidence that implies a relationship to regressive and transgressive phases of highstands (rather than peak sea-level), in the activation of sediment mobilisation (e.g. Brooke *et al.*, 2003; Bateman *et al.*, 2004; Butzer, 2004; Gardner *et al.*, 2006; Carr *et al.*, 2010).

Ocean currents are another important factor that influences carbonate production. The rate of carbonate production is much higher in warm water than in cool. Hence, the distribution of carbonate is related to major ocean currents, which move bodies of cool water towards the equator, and bodies of warm water towards the poles (Brooke, 2001) (see Figure 2.6). Deep-ocean upwelling, controlled by ocean-atmosphere interactions (i.e. differential heating and evaporation between the low and high latitudes causes ocean density contrasts, forming zones of upwelling), also influences carbonate production. Upwelling zones can provide high levels of nutrients (primarily in the form of nitrate flux moved from cold deep-water) to carbonate producing organisms

(Eppley and Peterson, 1979; James, 1997; Saenko and Weaver, 2003). For example the large carbonate provinces of southern Africa and southern Australia are located near zones of upwelling. Coastal upwelling is common in the Southern Ocean, particularly when the prevailing winds are from a southeasterly direction (Wells, and Okada, 1996). In contrast, for example, according to Wells and Okada (1996) (in their study of planktonic and benthic foraminifers extracted from a Vema ocean core [VI8-222] recovered from southern Australia) this upwelling strengthens during glacial periods, as a result of the northward migration of the subtropical convergence zone (see Figure 2.4). Based upon the absence of tropical and subtropical nannoflora in core sections equated with the last glacial period Wells and Okada (1996) also suggest that the Leeuwin Current ceased to flow during glacial periods. In this instance then, the strengthened upwelling of cold water, and the absence of the warm Leeuwin Current, acted to reduce carbonate producing species diversity. This, coupled with the subaerial exposure of the continental shelf that occurs during glacial intervals, would have caused the further reduction of carbonate production off southern Australia. Hence, strengthened upwelling, in this case, would *not* have enhanced carbonate production.

The tectonic setting of coastlines can influence the formation, volume, stratigraphy, and morphology of aeolianites (Brooke, 2001). The Coorong coastal plain in southeast South Australia demonstrates the effect of gentle epeirogenic uplift on the stratigraphy and morphology of aeolian dune deposits. Here relatively low (ranging from ca. 5 m to ca. 30 m high) aeolianite dune ridges are separated laterally with the youngest ridges near the coast (see Figure 2.7). The ridges, which can be kilometres apart, increase successively in age and elevation further inland. Conversely aeolian carbonate sediments deposited on tectonically stable coastlines, such as those found along southwest Western Australia, southwest South Australia (i.e. Cape Spencer, southern Yorke Peninsula, and southern Kangaroo Island) (Belperio, 1995; Hearty, 2003; Hearty and O'Leary, 2008), and Bermuda (Hearty *et al.*, 1992; Kindler and Hearty, 2000) and the islands of the Bahamas (Hearty, 1998; Hearty and Kaufman, 2000; Kindler and Hearty, 2000), are stratigraphically more complex and may be characterised by superimposed and stacked units of aeolianite, which are subject to erosion during times of higher sea-level.

Lithification (by secondary carbonate) and pedogenesis also plays an important role in the preservation of carbonate sediments (and in maintaining the integrity of radionuclide concentrations for dating purposes—Prescott and Hutton, 1995). Carbonate sediments, as a response to a semi-arid/arid climate, subaerial exposure, and near-surface vadose diagenesis (also evapotranspiration induced precipitation); tend to undergo lithification quite rapidly (Ward, 1973; Dravis, 1996). These processes, and the pedogenic formation of calcretes and palaeosols (which can mantle sediment deposits) (stabilisation by vegetation colonisation also plays an important role), act to preserve the underlying units, by retarding any reworking by wind or water (Dravis, 1996).

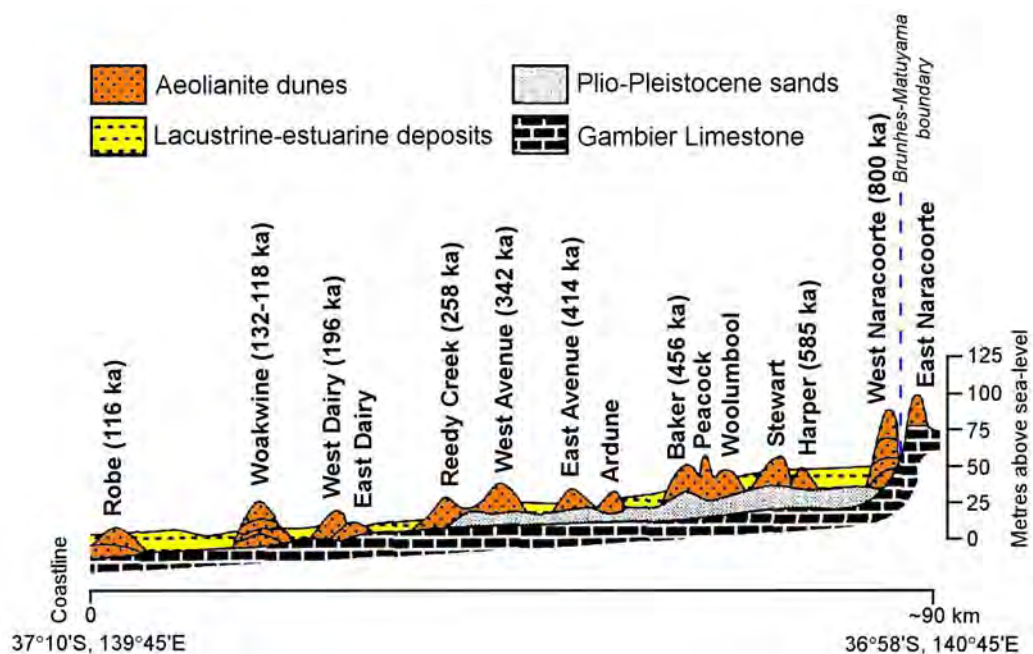


Figure 2.7: Schematic ca. 90 km cross-section traversing the Coorong Coastal Plain (southeastern South Australia); showing the lateral separation of Pleistocene barrier dunes as a consequence of epeirogenic uplift (due to Quaternary volcanism). Also shown are the dune unit thermoluminescence ages of Huntley *et al.* (1993, 1994) (modified after Schwebel, 1984; Huntley *et al.*, 1993; Murray-Wallace *et al.*, 2001). See also Figure 2.8.

The topography of a coastline can influence the volume of carbonate sediment deposited or act to prevent sedimentation. Tectonically active coastlines are characterised by rugged erosional landforms, such as rocky headlands, and precipitous cliff-lines (Lajoie, 1986); such relief is unsuitable for the formation of coastal dune systems (Brooke, 2001). The western coast of South America geomorphically reflects regional crustal uplift, and is characterised by a mountainous coast (Lajoie, 1986). Subsequently, aeolianite formations are rare

in this region of South America. This is similar to the north-western coastline of Kangaroo Island where the shear zone associated with the Snelling Fault (which is coincident with the margin of the Gawler Craton) (see Chapter 1, section 1.4.1: Figures 1.3 and 1.4) has controlled the formation, orientation and rugged relief of this section of the coast (Belperio and Flint, 1999). Because of the high relief of the deformed bedrock coastline, in conjunction with the steep offshore profile, aeolianite formation has not taken place. As such there are no substantial outcrops along this section of the Kangaroo Island coast.

Climatic factors that affect the timing of eustatic sea-level change and hence, carbonate deposition and aeolianite formation can be related to changes in the Earth's orbital and rotational parameters. Orbital cycling is regarded as being one of the major forcing functions for global climate change (Imbrie and Imbrie, 1979; Dodson, 1998). An astronomical or orbital theory of climate change was first proposed by Croll (1875); however, it was not until the work of Milutin Milankovitch (1941)—*Canon of Insolation and the Ice Age Problem*—was extensively publicised that the theory gained some acceptance (Pillans *et al.*, 1998). It was not until the 1970s that the theory gained firm support with the application of $^{230}\text{Th}/^{234}\text{U}$ dating to raised coral terraces, and the periodicity evident in faunal, sediment and isotopic changes in deep-sea cores (Pillans *et al.*, 1998). The changes wrought to the Earth's environment can be attributed to changes in insolation due to variation in orbital and rotational parameters.

There are three major components that contribute to changes in the planetary insolation budget. Orbital eccentricity which operates on a cycle of around 100,000 years, axial tilt which cycles at around 41,000 years, and the precession of the equinoxes which exhibits a cycle of approximately 21,000 years (Dodson, 1998). There is also a larger overlying cycle of around 400,000 years, which modulates precess and either weakens or strengthens the 100,000-year eccentricity (Ruddiman, 2003). The values for these cycles are averages, and the overall effect varies geographically (Dodson, 1998). According to the Milankovitch theory these long-term, quasi-periodic variations in the earth's orbital parameters (axial tilt, precession and eccentricity), control the global ice volume and thus, sea-level fluctuation (Pillans *et al.*, 1998).

2.4.2 Stratigraphy and age of the major aeolianite tracts

The stratigraphical and chronological characteristics of selected major aeolianite tracts (i.e. from southern and southwestern Australia, southern Africa, the Bahamas and Bermuda) (see Figures 2.1 and 2.6) are briefly examined in the following sections. There are of course other less significant (in terms of scale) regions of aeolianite deposition; however, they will not be covered here.

2.4.2.1 Western, southwestern, and southern Australia

The southern and southwestern Australian coastlines host the world's most extensive aeolianite formations, in both volume and lateral extent. Aeolianite outcrops from Broome to Cape Leeuwin (Western Australia—WA), and across the Great Australian Bight (GAB) (along the Roe Plains) to South Australia (SA), and Victoria (VIC) (see Figure 2.1 and 2.6).

Aeolianites along the coast of Western Australia have been the subject of numerous past studies (Brooke, 2001) (e.g. Fairbridge, 1948, 1950; Teichert, 1947, 1950; Fairbridge and Teichert, 1953). The aeolianites, which are exposed in the form of stacked units in coastal cliffs, can exceed 300 m in height (Hocking and Mory, 2006). This formation of aeolianite and associated shallow-marine units is formally known as the 'Tamala Limestone' (Playford *et al.*, 1976); named for Tamala Station (a pastoral station) located near the type section on the Zuytdorp Cliffs, at Shark Bay (Hearty and O'Leary, 2008) (see Figure 2.1). Originally considered to be of Late Pleistocene age (Teichert, 1947, 1950; Playford *et al.*, 1976), the age range was later broadened to include accumulation during (multiple) Pleistocene glacial periods or periods of lowered sea-level (during the Pleistocene) (Playford, 1990, 1997). Extensive work undertaken by Hearty and O'Leary (2008) suggests that the type section is of much greater antiquity than other 'Tamala' aeolianites along the west Australian coast. In general most of the aeolianites in the formation along the west Australian coast can be correlated with interglacial and interstadial periods (rather than glacial periods, as interpreted by Playford, 1990, 1997) ranging from the Holocene to ca. 500 ka (Hearty and O'Leary, 2008). However amino acid racemization (AAR) work undertaken by Hearty and O'Leary (2008), on the Tamala Limestone type section at Shark Bay, suggests that this is a much older early Pleistocene sequence, ranging between ca. 800 ka to ca. 1.4 Ma. Much further south of the type section, thermoluminescence (TL) dating undertaken by Price *et al.* (2001) on Rottnest Island (Figure 2.1) and the adjacent

Fremantle coastline yielded a TL chronology for the Tamala Limestone aeolianites that ranged from ca. 20 ka to >422 ka. Most of the ages in this chronology were consistent with either interglacial or interstadial deposition. There were two TL ages for dune units from Rottnest Island, however, that indicated a last glacial maximum (LGM) deposition (i.e. 19 ± 3 ka and 20 ± 2 ka). Hearty (2003) discounts glacial timing of aeolianite deposition along western Australian coastlines and found that the developed Rottnest whole-rock sediment (WR), alioisoleucine/isoleucine (A/I), AAR chronology was inconsistent with the Price *et al.* (2001) TL chronology. Regardless, glacial deposition of carbonate material on Rottnest Island is conceivable, given the Island's proximity to a glacial coastline, and the relatively large expanse of low gradient shelf between ca. -120 m (the glacial shore at the LGM—Yokoyama *et al.*, 2000, 2001a, 2001b) and the -200 m isobath (see Myers and Hocking, 1998; James *et al.*, 1999)—which may have remained relatively productive during the LGM, in terms of carbonate. Note: Glacial conditions in southern Australia (during the LGM [21 ± 2 ka]—Williams *et al.* [2009]) were accompanied by a drier, windier climate, with possibly a 50% reduction in rainfall. Temperatures may have been reduced by as much as 8 °C (Williams *et al.*, 2001; Williams *et al.*, 2009; Luly *et al.*, 2010).

Glacial shore deposited carbonate may have migrated landward to be deposited on Rottnest Island, if there were appropriate onshore winds, and minimum interference to mobilisation by shelf occupying vegetation and lithification. Conversely, there could have been aeolian reworking of existing carbonate deposited during an interglacial, now exposed. For example Pleistocene dunes on Kangaroo Island migrated, in some areas, over 10 km inland, prior to lithification. Hence, the very precise LGM TL ages for the dune units described by Price *et al.* (2001) should not be too easily discounted.

Tamala Limestone Formation aeolianite also crops out sporadically along the western portion of the southern coast from Cape Leeuwin to Point Culver (see Figure 2.1 and 2.6). Further east on the Roe Plains (in the Eucla Basin), adjacent to the GAB (see Figure 2.1), is an extensive calcarenite deposit characterised by late Pliocene to early Pleistocene (minimum upper age) marine fauna (Ludbrook, 1973, 1978; Murray-Wallace, 1995; James *et al.*, 2006). Known as the Roe Calcarenite, this deposit is also present on the eastern side of the GAB, cropping out at the base of aeolianite cliffs composed of the early to late Pleistocene Bridgewater Formation (Boutakoff, 1963;

Belperio, 1995; Brooke, 2001).

Boutakoff (1963) formally defined the Bridgewater Formation at Bridgewater Bay, Victoria. Bridgewater Bay lies at the eastern extremity of the Mount Gambier coastal plain (Belperio, 1995). This formation, interspersed with calcrete and palaeosol unconformities, comprises three main carbonate facies types; these are shallow subtidal, littoral, and dune. Often the Last Interglacial Glanville Formation lagoonal facies (or equivalents), and Padthaway Formation lacustrine sediments (which commonly overlie the lagoonal facies) are found in association, particularly within the Bridgewater Formation interdune corridors of the Coorong coastal plain (Belperio, 1995) (see Figure 2.8). Although, the Padthaway Formation sediments are not necessarily coeval with the formation of adjacent dune barriers (Belperio, 1995).

Aeolianites of this formation crop out extensively on the western and southern portions of the Eyre Peninsula, as far as Thistle Island. At Fowler's bay and the head of the GAB, aeolianite barriers of the Bridgewater Formation and associated lagoonal sediments (the Last Interglacial Glanville Formation) were mapped by Belperio (1988). Present are barriers equated with sea-level highstands of the late, middle (the penultimate interglacial), and early Pleistocene (Belperio, 1995). Further southeast Bridgewater Formation aeolianites crop out as stacked sequences, rather than relatively discrete onlapped barriers as found at Fowler's Bay on the western part of the Eyre Peninsula. At Cape Spencer (southern Yorke Peninsula) and southern Kangaroo Island these form precipitous cliff lines with as many as 12 stacked sequences of aeolianite, separated by pedogenic horizons (palaeosols and calcretes). The sequences consist not only of barrier shoreline complexes, but also transgressive dunes and sand sheets that extend a large distance inland (over 10 km in places on Kangaroo Island) (Belperio 1995). Bateman (1987) undertook magnetostratigraphic measurements along southern Yorke Peninsula which indicated a middle to late Pleistocene age for these cliffed sequences. A TL chronology that ranged from ca. 630 ka to ca. 180 ka was developed by Wilson (1991) for stacked sequences on southern and western Eyre Peninsula, and at Point Reynolds on southern Kangaroo Island a

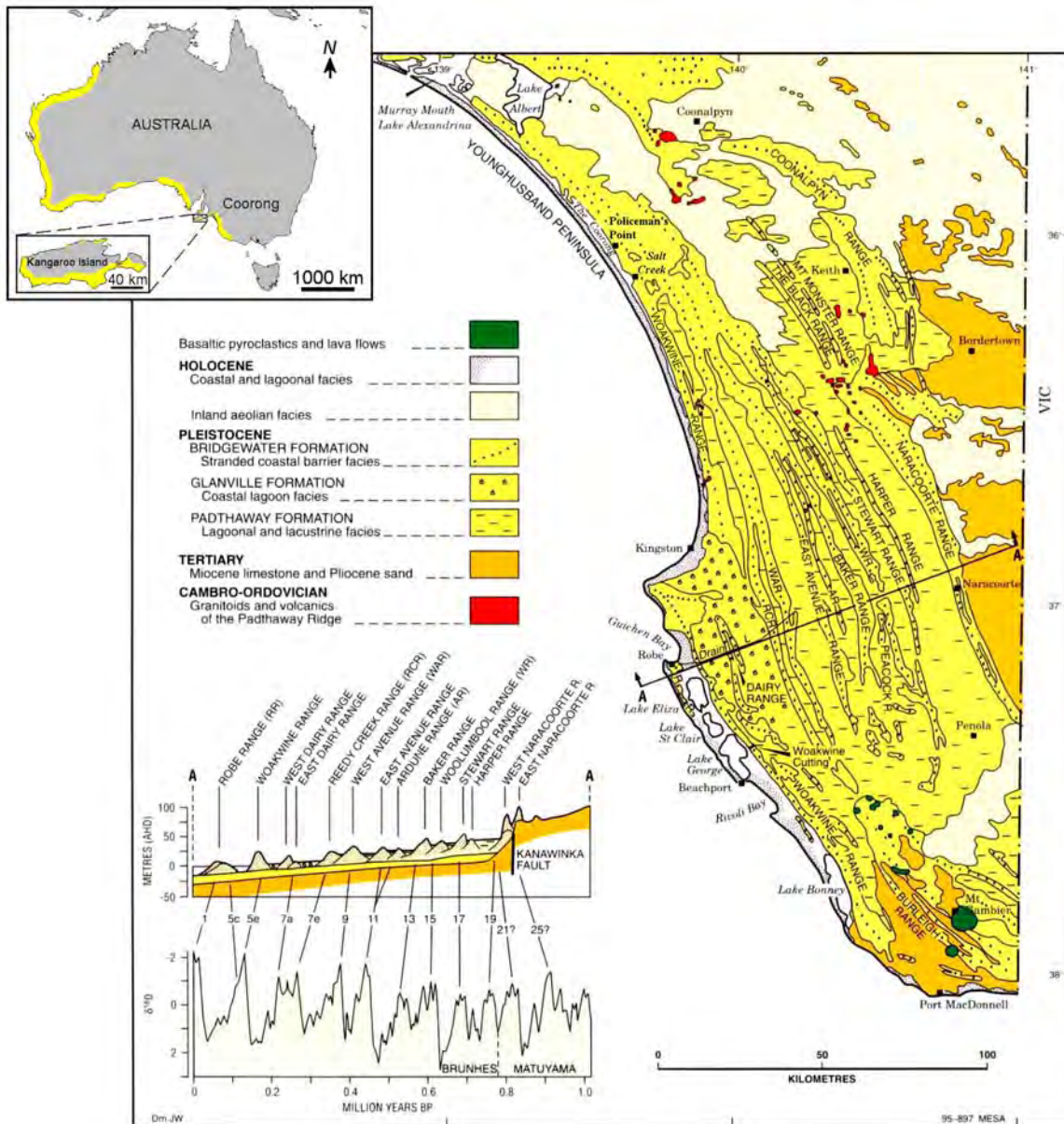


Figure 2.8: Geology of the Coorong to Mount Gambier coast plain (south-east South Australia), with inset cross-section (lower LH) and corresponding marine isotope stages for barrier dune deposition (modified from Belperio, 1995). Upper LH inset shows approximate extent of Pleistocene aeolianite (yellow) along the Australian coast, and Kangaroo Island (inland extent not to scale)—aeolianite outcrops intermittently along the coast of western and southern Australia, and almost continuously along the southern coast of Kangaroo Island.

strontium (Sr) isotope age of ca. 520 ka was obtained for a basal marine unit, overlain by Bridgewater Formation aeolianite (Belperio, 1995). These age estimates suggest Bridgewater Formation aeolianite deposition at these sites spans the middle to late Pleistocene.

The 'stacked' morphology of the Bridgewater Formation in these regions is a testament to the relative tectonic stability of the coastlines along southern Kangaroo Island and southern Yorke Peninsula. By way of a simplified explanation dune material accumulated during a sea-level highstand is covered by dune material from subsequent highstands (with pedogenesis occurring during depositional hiatuses). The superimposed and lithified sequence is later undercut by wave action (during the Holocene for example) causing failure of overlying material (thereby exposing the internal structure of the stack) thus forming a cliff. Alternatively, coastal palaeobarriers formed in areas that experience tectonic uplift are physically separated, being preserved as a lateral sequence of discrete barriers that increase in age further inland—such as those found along the Coorong to Mount Gambier coastal plain. The separation occurs as the gentle uplift causes barriers emplaced during sea-level highstands to become elevated in relation to barriers formed in subsequent highstands (Brooke, 2001). As such stacked sequences are inherently more complex than lateral stranded sequences. For example, where there is no lateral separation units can become superimposed, or units can even be removed during high sea-level events.

The discrete series of relict barriers on the coastal plain in the southeast of South Australia extends from near Hindmarsh Island (the beginning of the Woakwine range: see Figure 2.8) to near Discovery Bay in Western Victoria. The barrier separation is at its most apparent from Robe to Naracoorte (see Figure 2.8). Thirteen barriers which are related to specific sea-level highstands during the Pleistocene are preserved between Robe and Naracoorte. The barriers, which have been preserved because of epeirogenic uplift and the formation of calcrete mantles, are on average up to 30 m high, and are spaced up to 10 km apart, running sub-parallel to the modern coastline (Belperio, 1995; Murray-Wallace *et al.*, 2001). The dune ranges have been the subject of several significant studies in the past (e.g. Sprigg, 1952, 1959, 1979; Sprigg and

Boutakoff, 1953), and relatively recently (i.e. Huntley *et al.*, 1993, 1994; Huntley and Prescott, 2001; Murray-Wallace *et al.*, 2001; Banerjee *et al.*, 2003). A TL chronology for the lateral sequence was developed by Huntley *et al.*, (1993, 1994), and Huntley and Prescott (2001), with an age range between ca. 116 ka for the Robe III Range and ca. 800 ka for the West Naracoorte Range. Figure 2.7 shows the lateral positions of the barriers and the corresponding TL chronology of Huntley *et al.* (1993, 1994). This chronology was found to be in broad agreement with the independent age estimates, for the dune ranges, of Schwebel (1983, 1984) and Belperio and Cann (1990). The oxygen isotope (OI) alignment of the dunes to sea-level highstands is given in Figure 2.8.

The East Naracoorte range was TL dated to 720 ± 70 ka by Huntley *et al.* (1993); however, as the sediment is geomagnetically reversed the age should be greater than 780 ka (the Bruhnes / Matuyama boundary)—which it could be, when taking into account the uncertainty term, although Huntley and Prescott (2001) prefer a >900 ka age. A later attempt by Huntley and Prescott (2001) (using an improved TL method) to further date the East Naracoorte dune was unsuccessful due to failure of the new method to yield matching dose response curves. Nevertheless, the Huntley and Prescott (2001) study also provided ages for the East Dairy Range (292 ± 25 ka), and the Stewart Range (725 ± 100 ka) (see Figure 2.7), and for a younger unnamed dune bordering the Coorong near Policeman's Point (95 ± 6 ka) (Figure 2.8)—which possibly relates to a marine isotope stage (MIS) 5a or 5c deposition.

In order to critically assess the whole-rock method of amino acid dating using a parabolic kinetic calibration Murray-Wallace *et al.* (2001) compared their calibrated Leucine (LEU) AAR chronology (derived from the extent of LEU racemization in whole-rock sediment samples taken from 8 of the dune ranges, and calibrated using the Schwebel [1978, 1984] uranium series age of 125 ± 20 ka, obtained from the back-barrier lagoon facies [Glanville Formation] of the Woakwine Range) with the Huntley *et al.* (1993, 1994) TL chronology. The AAR chronology was, in the case of many AAR ages, in excellent agreement with the Huntley *et al.* (1993, 1994) TL chronology, even deriving a more realistic age estimate for the East Naracoorte Range, i.e., 935 ± 178 ka. In a more recent

study undertaken by Banerjee *et al.* (2003) a single aliquot (SAR) optically stimulated luminescence (OSL) method was used to date sediments from 4 of the dune ranges: Robe II and II, Woakwine I and II, Reedy Creek, and West Naracoorte. The OSL ages derived were also in reasonable agreement with the corresponding TL ages of Huntley *et al.* (1993, 1994).

All of these studies have provided a good chronostratigraphical framework for the depositional timing of the stranded dune sequence, particularly for those dunes younger than ca. 600 ka. As such, the dunes have been shown to increase in age inland matching the highstands of oxygen isotope stages 5a, c, and e, 7, 9, 11, 13, ca. 19 and between oxygen isotope stages 21 and 25 (Brooke, 2001).

The lateral structure of the Coorong dunes coalescences into a single composite sequence towards Lake Alexandrina in the northwest, and in western Victoria the older dunes merge, and only those barriers sea-ward of the Avenue Range are discernable as discrete barriers. These in turn merge towards Cape Bridgewater. This is because of gradual reduction in the rate of uplift the further one moves from the centre of the tectonic disturbance, i.e., the Mount Burr-Mount Gambier volcanic province (Belperio, 1995; Murray-Wallace *et al.*, 1998, 2001).

Bridgewater Formation aeolianites in western, southern, and southeastern Victoria have also been TL and OSL dated. Aeolianites at Warrnambool (east of Cape Bridgewater) were TL dated to Last Interglacial age (Brooke, 2001), as were aeolianites on the Nepean Peninsula (southern Victoria) (TL age ca. 118 ka), with ages for upper (overlying) aeolianites that correspond to MIS 3 (TL age ca. 47 ka) and MIS 2 (LGM) (TL age ca. 23 ka) deposition (Zhou *et al.*, 1994). Further east at Cape Liptrap an extensive study undertaken by Gardner *et al.* (2006), using OSL to date Bridgewater Formation aeolianites showed that, on the basis of the OSL chronology, deposition began immediately *after* the Last Interglacial highstand (MIS 5e), during the regression. Deposition continued sporadically after this, during the regressive phases of interstadials (although not apparently during the regressive phase of MIS 5c), until the beginning of MIS 4 (i.e. ca 68 ka to ca. 112 ka).

2.4.2.2 South Africa

Similar to southern Australia, stacked aeolianite sequences are widely distributed along the western, southern, and eastern cape regions of South Africa (see Figure 2.6) (Bateman *et al.*, 2004; Bateman *et al.*, 2011). The deposits include the Pleistocene aeolian-derived Waenhuiskrans Formation of the Cainozoic Bredasdorp Group, and the late/middle Pleistocene Klein Brak Formation (Malan, 1987; Bateman *et al.*, 2004). The Waenhuiskrans Formation, which has been correlated with similar formations on the western and eastern capes region coastlines, is characterised by large-scale cross-bedded aeolianite sequences that are in excess of 100 m thickness in some areas. These are formed into high coastal cliffs due to erosion at higher sea-level (Bateman *et al.*, 2004). An exposed section of this formation was dated by Bateman *et al.* (2004), using OSL. The OSL ages for a lower and upper unit (i.e. 88 ± 4 ka and 80 ± 3 ka) indicated a MIS 5b deposition and deposition during the MIS 5a to 5b transition.

Bateman *et al.* (2004) also undertook OSL dating on 2 other exposed sections of aeolianite, at Soetendals Valley ridge (209 ± 15 ka, 283 ± 11 ka, and 176 ± 7 ka), and Agulhas ridge (159 ± 6 ka and 179 ± 7 ka) these ages were correlated with a MIS 7/6 transition for deposition. Bateman *et al.* (2004) combined their OSL chronology with ages from numerous other studies along the South African coastline in order to correlate regional aeolian activity (i.e. from Illenberger and Verhagen, 1990; Illenberger *et al.*, 1997; Roberts and Berger, 1997; Vogel *et al.*, 1999; Shaw *et al.*, 2001; Henshilwood *et al.*, 2002; Ramsay and Cooper, 2002). This enabled Bateman *et al.* (2004) to define 5 phases of aeolianite deposition for South Africa, ranging from the middle to late Pleistocene: ca. 67–80 ka, ca. 88–90 ka, ca. 104–128 ka, ca. 160–189 ka and >200 ka. This work was further supplemented by Carr *et al.* (2006), where OSL dating of aeolianites at the Swartvlei and Groot Brak estuaries, and Cape Agulhas, revealed a similar *late* Pleistocene depositional range: ca 95 ka to 122 ka. OSL dating of aeolianite barriers along the Wilderness embayment undertaken by Bateman *et al.* (2011) defined a similar chronological depositional scheme to that originally proposed by Bateman *et al.* (2004). Here, on the basis of 62 individual OSL ages, Bateman *et al.* (2010) delineated 4 Pleistocene phases of

barrier construction from ca. 241-221 ka, ca. 159-143 ka, ca. 130-120 ka, and ca. 92-87 ka, and included a post 6 ka Holocene depositional phase.

2.4.2.3 Bermuda and the Bahamas

Bermuda consists of a one large island and a proximal group of smaller islands, situated in the North Atlantic Ocean (see Figure 2.1). The islands, which have cores of pre-Quaternary volcanic rocks derived from the mid-Atlantic Ridge, are constructed of Quaternary carbonates (Muhs *et al.*, 2002)—predominantly aeolianites. The islands experience a warm-temperate to subtropical climate due to the influence of the warm Gulf Stream (see Figure 2.6) (Brooke, 2001).

The near-shore dunes on islands of Bermuda represent the most studied aeolianite sedimentary successions in the northern hemisphere (Brooke, 2001; Hearty, 2002), indeed the geology of the islands has been the subject of study since the early 19th century (e.g. Nelson, 1837; Thompson, 1873; Heilprin, 1888; Agassiz, 1894) (from Land *et al.*, 1967). A later study by Sayles (1931) linked carbonate deposition with glacioeustatic cycles, suggesting that carbonate accumulation and aeolianite formation occurred during glacial low sea-levels, when carbonate sources on the continental shelf would be exposed, and wind-formed dunes would migrate inland (Land *et al.*, 1967). Conversely, palaeosol formation, according to Sayles (1931), took place during periods of high sea-level when the carbonate source would be cut-off and pedogenesis could occur. In a significant and subsequent examination of the Bermuda carbonates, Bretz (1960) accepted the Sayles (1931) premise of eustatic control over palaeosol / aeolianite sequential formation; however Bretz (1960) did not agree with the timing order of formation (Land *et al.*, 1967). Bretz (1960) found many sites where carbonate dunes had been deposited adjacent to beaches of the time. For example, the examination of aeolianite deposits at Whalebone Bay led Bretz (1960) to conclude that these dunes were deposited immediately upslope of the beach when the lagoon floor was submerged. Hence, it was surmised that carbonate deposition and aeolianite formation was occurring at high sea-level rather than low. Bretz (1960) also concluded that, due to the high carbonate content of the dunes, cementation and consolidation would have been rapid, preventing any significant inland transport. Because of observations like these Bretz (1960) reversed the Sayles (1931) scheme,

favouring carbonate accumulation during interglacial sea-level highstands and soil formation during glacial lowstands.

Later studies have firmly established a lithostratigraphic and chronostratigraphic framework for Bermudian aeolianites, and supported the views of Bretz (1960) on the highstand timing of carbonate deposition and aeolianite formation (e.g. McKenzie, 1964; Land *et al.*, 1967; Hearty *et al.*, 1992; Hearty and Vacher, 1994; Vacher *et al.*, 1995; Vacher and Rowe, 1997; Hearty, 2002; Hearty *et al.*, 2007). Five lithostratigraphic formations (consisting of marine and aeolian carbonate, and intercalated palaeosols) have been thoroughly mapped around Bermuda (see Hearty *et al.*, 1992; Hearty and Vacher, 1994; Vacher *et al.*, 1995; Hearty, 2002); these are:

- i) The Southampton Formation: the youngest formation, deposited during MIS 5a (ca. 85 ka: coral U-series of Harmon *et al.*, 1983). The formation contains both aeolian and marine units.
- ii) The Rocky Bay Formation: deposited during MIS 5e (ca. 125 ka: coral U-series of Harmon *et al.*, 1983, and ca. 170 ka: A/I AAR age estimate of Hearty and Vacher, 1995). This formation has 3 members: Pembroke, Harrington, and Rocky Bay.
- iii) The Belmont Formation: which has both aeolian and marine units, and dates from early to late MIS 7 (ca. 200 ka: coral U-series of Harmon *et al.*, 1983, to ca. 265 ka: AAR WR age of Hearty *et al.*, 1992). Although, Hearty *et al.* (2007) recently revised the age estimate for the raised Belmont shoreline to MIS 5e.
- iv) The Town Hill Formation, consisting of 2 widely distributed members: the MIS 9 upper Town Hill (ca. 350 ka), and the MIS 11 (ca. 450 ka) lower Town Hill members (Hearty *et al.*, 1992; Hearty and Vacher, 1994; Vacher *et al.*, 1995).
- v) The early Pleistocene Walsingham Formation: >880 ka (WR A/I AAR age estimate of Hearty *et al.* [1992]).

Similar to southern Australia, Bermuda has experienced extensive carbonate deposition and aeolianite formation over much of the Pleistocene; with preserved sequences of MIS 5, 7, 9, and 11, and early Pleistocene aeolianites

(i.e. the Walsingham Formation). Thus, Bermuda is an important northern hemisphere site recording long-term Quaternary sea-level fluctuation, and coastal environmental change.

The Bahamas consists of an extensive archipelago of carbonate islands and shallow banks (generally <10 m deep) in the western North Atlantic, and covers approximately 300,000 km², including the shallow bank areas (Carew and Mylroie, 1997) (see Figure 2.1 and 2.6). The climate ranges from subtropical-temperate in the northern part of the archipelago to semi-arid in the south (Carew and Mylroie, 1997).

Because of the relative tectonic stability of the Bahamian platforms the study of aeolianites and marine deposits in this region is crucial to the understanding of sea-level and global ice-volume fluctuations (Hearty and Kaufman, 2000) (as the position of particular deposits [or morphologies] can be related directly to sea-level at the time of deposition [or formation], e.g., raised beach deposits, beach facies, flank margin caves, sea-caves, notches, etc.). As with Bermuda, southern Africa, and southern Australia, the Quaternary evolution of the Bahamian islands and banks has been primarily controlled by glacioeustatic sea-level fluctuations (Carew and Mylroie, 1997). Aeolianite successions on the Bahamian islands, as with Bermuda, are generally in the form of elongate coastal ridges. The coastal morphology is commonly in the form of headland bound catenary beaches (Garrett and Gould, 1984). The headlands are generally constructed of older aeolianite, with younger aeolianite deposits between the boundaries, in that the headlands have acted as keystones or anchors for later deposition of carbonate (Brooke, 2001) (this is similar to the coastal morphology of aeolianite successions on Kangaroo Island). The Bahamian aeolianite successions are not always in the form of superimposed or stacked sequences, they can also be found as lateral deposits (Carew and Mylroie, 1997).

Similar to Bermuda the Bahamian aeolianite successions can be correlated to the sea-level highstands associated with MIS 5, 7, 9, and 11. Unlike Bermuda, however, the Bahamian islands have a prevalent Holocene succession (Vacher *et al.*, 1995; Kindler and Hearty, 1996; Hearty and Kindler, 1997). Also, the

Bahamian islands do not exhibit early Pleistocene sequences. Three major lithostratigraphic formations (consisting of marine and aeolian carbonate, and intercalated palaeosols) have been mapped around the Bahamas (Carew and Mylroie, 1995; Carew and Mylroie, 1997; Hearty, 1998); these are:

- i) The Holocene Rice Bay Formation, consisting of 2 members: the late Holocene aeolian Hanna Bay Member and the beach and aeolian facies of the middle Holocene North Point Member.
- ii) The MIS 5 Grotto Beach Formation which has 2 members also: the MIS 5e Cockburn Town Member which consists of subtidal (reefal), beach and aeolian dune facies, and the MIS 5e beach and aeolian dune facies of the French Bay Member.
- iii) The middle Pleistocene Owl's Hole Formation, which may represent one or more of the interglacial highstands associated with MIS 7, MIS 9, or MIS 11.

Although the type sections for these major lithostratigraphical units are located on the Bahamian island of San Salvador, the stratigraphy is applicable throughout the Bahamas (Carew and Mylroie, 1997), and is supported by a range of other studies (e.g. Curran and White, 1991; Carew and Mylroie, 1995; Kindler, 1995; Hearty, 1998). Hearty and Kindler (1993) also recognized formations additional to those described by Carew and Mylroie (1995) and Carew and Mylroie (1997), on San Salvador:

- i) The late Pleistocene Almgreen Cay Formation, a MIS 5a aeolianite.
- ii) The late Pleistocene Fernandez Bay Member (additional to the Grotto Beach Formation), a MIS 5e oolite.
- iii) The middle Pleistocene Fortune Hill Formation, a MIS 7 calcarenite.

There are also other unrecognised units (see Kindler and Hearty, 1996; Kindler and Hearty, 1997; Hearty, 1998) on Eleuthera that, on the basis of the extent of racemization in whole-rock carbonate samples, are of MIS 9/11 and \geq MIS 13 in age. The MIS 9/11 units are oolitic-peloidal limestones and the \geq MIS 13 unit is a bioclastic calcarenite located at the base of cliffs comprised of the oolitic-peloidal limestone.

2.5 Previous Kangaroo Island studies

Research into the Quaternary carbonate deposits on Kangaroo Island, South Australia, is still in its infancy. As such there is a lack of extensive geochronological data. Few studies have been undertaken in the past 100 years, and those that examine the islands coastal carbonate deposits in any detail are virtually non-existent, except perhaps as small sections within larger studies. For example Bauer (1959) undertook—as part of his PhD thesis on the geography of Kangaroo Island—a study of the coastal deposits. However, the thesis was primarily concerned with the island in a geographical context. The chapters devoted to coastal calcarenites were concerned with delineating raised marine terraces, and examining the morphology and the extent of the Pleistocene aeolianite. The most notable studies that attempted at least partial interpretations of Quaternary deposits on the island are Ludbrook's (1983) investigation of the early Pleistocene Point Ellen Formation, and Milnes *et al.* (1983) examination of Cainozoic marine sedimentation on Kangaroo Island. Milnes *et al.* (1983) work focused broadly on many locations around the island and was concerned principally with describing marine sediments older than the Pleistocene. However, Milnes *et al.* (1983) included a section in their paper devoted to Pleistocene formations on Kangaroo Island, detailing the molluscan and sometimes foraminiferal assemblages. A later work by Belperio (1995) broadly covered carbonate sedimentation along the southern Australian coast as part of the compilation, including the south coast of Kangaroo Island. The Sprigg (1954) Kingscote geological sheet and the Belperio *et al.* (2000) Kingscote geological sheet also give good regional coverage of the geology of the island, but of course these media do not provide a detailed chronology or stratigraphy for Quaternary Kangaroo Island sediments.

2.6 Summary and Conclusions

This chapter has briefly reviewed the distribution of major aeolianite tracts, and the palaeoenvironmental implications of carbonate deposition. Conclusions and summaries follow:

- 1) Aeolianites are formed from wind deposited skeletal carbonate and are generally found on the coastal areas of many continents and islands in

the mid-latitudes (typically between 20° and 40° north and south latitude).

- 2) Carbonate production on continental shelves and banks is the primary controlling factor for aeolianite formation, with most carbonate derived from the Heterozoan Association, in subtropical and temperate (cool-water) environments, with low rates of terrigenous influx.
- 3) Most aeolianite has formed in large tracts in the southern hemisphere (i.e. southwestern and southern Australia, and southern Africa) with the largest volume and lateral extent in southwestern and southern Australia.
- 4) Tectonic stability and coastal morphology can affect the volume of deposited carbonate, and also the morphology of aeolianite deposits (i.e. stacked or lateral units).
- 5) In southern Australia carbonate deposition and aeolianite formation has taken place throughout most of the Pleistocene (early to late), with the most prevalent deposits occurring during the Last Interglacial (116-132 ka). Carbonate deposition has been shown to happen predominantly during sea-level highstands; although some studies suggest that deposition during glacial periods, and the transgressive/regressive phases of interglacials, has also occurred.
- 6) Southern Africa aeolianites follow a similar pattern of deposition and formation to southern Australia, with barrier construction occurring from ca. 241-221 ka, ca. 159-143 ka, ca. 130-120 ka, and ca. 92-87 ka, and post 6 ka.
- 7) Bermuda and the Bahamas have aeolianite units that correlate with MIS 1, 5, 7, 9, 11, and possibly 13. The early Pleistocene is also represented on Bermuda.
- 8) Studies of the aeolianite formations on Kangaroo Island are few, and are generally only represented as small sections in examinations of larger scope.

Chapter 3: Stratigraphy and petrology of carbonate aeolianites and other near-shore deposits on Kangaroo Island

3.1 Chapter introduction

This chapter will examine the stratigraphy of aeolianites, associated facies, and other near shore deposits from selected sites around Kangaroo Island. The sedimentary structures that are present in these deposits along with morphostratigraphical features are used to identify the depositional facies and architectural characteristics. Additionally, the petrographical aspects of a number of thin-sections sampled from representative facies found at the study sites are examined.

The previous chapter described in detail the formation and morphology of aeolianite sequences along with associated facies, also various case studies were also examined in detail. This chapter will apply what was discussed in Chapter 2 to the deposits of Kangaroo Island.

Kangaroo Island has been the subject of very few detailed palaeoenvironmental studies. As such there is a dearth of detailed stratigraphic work in terms of facies architecture and sequence stratigraphy. This is particularly noticeable when dealing with carbonate grainstones, palaeosols and other such deposits that are apparently of the Quaternary period.

As stated in Chapter 1, one of the first encounters with the Quaternary carbonate geology of Kangaroo Island occurred on the south coast of the island in 1803. François Peron (Tate, 1883), a zoologist onboard *Le Geographe*—a French expedition corvette—instituted the first examination of these calcareous deposits. He examined recent sand dunes, “petrified trees”, and sediments on the south coast that contained fossils. The southern coastal “calciferous sandstone” as Peron called it was given a detailed examination. He attempted an explanation for its formation, suggesting that it was a marine produced, initially wind blown series of deposits that were then consolidated over time. Much later Tate (1883) undertook a study of the botany of Kangaroo Island and as part of this work he examined what he coined as “calciferous sand-rock”—

referring to the aeolianite sequences. Tate (1883) assigned a Pleistocene age for these formations; however, this section of his work was on the whole a re-iteration of François Peron's original observations.

Bauer (1959) undertook a study of the coastal deposits as part of his PhD thesis on the geography of Kangaroo Island. However, Bauer's thesis was primarily concerned with the island in a geographical context. The chapters devoted to coastal calcarenites were concerned with delineating raised marine terraces, and examining the gross morphology and extent of the Quaternary aeolianite.

The most notable studies containing at least partial interpretations of Quaternary deposits on the island are Ludbrook's (1983) investigation of the Early Pleistocene Point Ellen Formation, and Milnes *et al.* (1983) work on Cainozoic marine sedimentation on Kangaroo Island.

Milnes *et al.* (1983) work examined many locations around the island and was concerned principally with describing marine sediments older than the Quaternary. Nonetheless, Milnes *et al.* (1983) included a section in their paper devoted to Pleistocene formations on Kangaroo Island, detailing the molluscan and sometimes foraminiferal assemblages. This was an important study regardless, giving the locations and compositions of relevant sedimentary units (e.g. Last Interglacial [MIS 5e] raised shell beds, beach deposits).

The Sprigg (1954) Kingscote geological sheet and the Belperio *et al.* (2000) Kingscote sheet also give good regional coverage of the geology of the island, but of course these media do not provide a detailed stratigraphy for Quaternary Kangaroo Island. However, they provide useful information on the location of relevant sediments.

Therefore, the main focus of this chapter is a detailed examination of the morphology and facies architecture of the aeolianite successions. The stratigraphic relationships between the units exposed in numerous outcrops around the island are collated. The identification of depositional facies, the number and succession of discrete units of carbonate grainstone, and fossil soil horizons (palaeosols) preserved in the aeolianite, and the presence of pebble beach deposits and shell beds, is used to infer an environmental history for

Kangaroo Island, during the Quaternary. Establishing such a stratigraphic framework for these deposits is essential for testing the geochronological data presented in Chapter 7.

The aeolianite at numerous sites around Kangaroo Island exhibits, in many cases, good exposure of internal architecture. This is particularly evident along headlands perpendicular to the coast, and cliff lines where the face of the deposit has been cut into by wave action, and there has been large-scale collapse of undercut structures. The distinctive higher-order sedimentary structures (bedding structures, assemblages of beds and morphostratigraphical forms) exposed in these outcrops are potent tools which can be used to identify facies types, and depositional environments (Brooke, 1999). Shell deposits exposed either as discreet layers or as notch deposits within aeolianite and pebble beach deposits are also examined. These can be useful indicators for parameters such as palaeosea-level and depositional environment.

The subsequent section outlines the basic definitions of the stratigraphic terms adopted for this study. Following this are detailed examinations of the stratigraphy at each Kangaroo Island study site. Interpretations of the morphostratigraphical characteristics of the outcrops examined in this study are offered in these sections, and where possible palaeoenvironmental interpretations, and stratigraphical correlation between sites as well.

Descriptions of the methods used to map the stratigraphical units, and the theoretical framework adopted in this study, are given in Appendix A. This chapter concludes with a summary of the stratigraphical results.

This chapter will help formulate an evolutionary history for these deposits, and will contribute to the chronostratigraphical framework that is developed in Chapters 7 and 8.

This Chapter is broken into 5 parts to better present a very large stratigraphical database: Part I: Stratigraphical terms; Part II: South coast stratigraphy; Part III: Dudley Peninsula and east coast stratigraphy; Part IV: North coast stratigraphy, and Part V: Petrology of Kangaroo Island sediments.

Part I: Stratigraphical terms and sedimentary structures

3.2 Stratigraphic terminology used in this thesis

The stratigraphic terminology used in this thesis is that of the North American Stratigraphic Code published in the AAPG Bulletin (volume 89, number 11, 2005), and the Field Geologist's Guide to Lithostratigraphic Nomenclature in Australia (Staines, 1985). Descriptions used for aeolianite bedding are taken from Nordstrom *et al.* (1990), Pye and Tsoar (1990), Tucker and Wright (1990), Collinson and Thompson (1989), Davis (1985), Allen (1982a, 1982b). The descriptions are summarised in Table 3.1; modified from Brooke (1999).

3.3 Sedimentary structures in beach and aeolian dune deposits

As shown in Chapter 2 the few studies that have been undertaken on Kangaroo Island involving marine and aeolian deposits have identified a range of depositional environments, such as aeolian, palaeosol, shell beds and pebble beaches, and also including alluvial. Diverse bedding forms are characteristic of those deposits extant within the beach environment, and aeolian dune forms can vary dramatically depending upon the conditions existing in the shore and marine environments.

This section briefly examines the literature on modern beach and aeolian environments. This is useful in defining a set of criteria which can be applied to stratigraphical interpretations of the sedimentary structures described in this study on Kangaroo Island.

3.3.1 Modern beach environments

There is no universally accepted definition for the term "beach"; however, it is generally accepted that it is an accumulation of unconsolidated sand, be it siliciclastic, bioclastic or volcanic in nature, or coarser material such as pebbles, cobbles or boulders, or some other sediment that extends from the uppermost limit of wave action to the lowest tide level (Trenhaile, 1997). The backshore portion of the beach is usually subaerial and extends from the high tide level to the landward margin of the beach. The intertidal foreshore or beachface extends from the berm crest to the low tide level, and the nearshore zone is an

Table 3.1: Definitions of stratigraphic terms used in this thesis (modified from Brooke, 1999).

Term	Definition
Lithostratigraphical unit^{1,2}	Bodies of rocks, bedded or unbedded, defined on the basis of lithologic properties, and stratigraphic relations. These are the basic units in geological mapping.
Group	Successions of two or more associated formations with significant lithological properties in common.
Formation	The primary formal unit of lithostratigraphic classification. Formations are the only formal units into which the stratigraphic column everywhere should be divided completely on the basis of lithology.
Member	Named body of rock within a formation which is lithologically distinct from adjacent portions of the formation.
Bed (s)	The smallest formal unit in the hierarchy; for example a single stratum that is lithologically distinct from layers above and below. Generally only key/marker beds are named and considered formal lithostratigraphic units.
Allostratigraphical unit¹	A mappable body of rock that is defined and identified on the basis of its bounding discontinuities.
Alloformation	The fundamental unit in allostratigraphic classification; may be completely or partly divided into members.
Allomember	An allostratigraphic unit next in rank below an alloformation.
Structural terms³	
Bed	A sedimentary unit greater than 1cm thick, that is distinguishable from units above and below by composition, texture, and internal structure; with planar bounding surfaces.
Composed of:	
Lamina	Unit < 1 cm thick
Stratum/layer	Unit > 1 cm thick
Bedset	Groups of beds representing a continuous period of sedimentation.
Coset	Two or more bedsets in vertical sequence with similar composition and structure.
Bed dip	
True dip	Dip of the bounding plane of a bed usually a low angle, < 5°
Apparent dip	Dip of structural planes within a bed
Low angle	3 - 18°
Moderate angle	19 - 25°
High angle	26 - 35°
Bedding types	
Backset	Low angle ripple laminations on the stoss side of dune form.
Topset	Low angle ripple laminations in dune crest
Brinkset	Ripple strata in upper leeward section of dune form.
Foreset	The inclined or cross-laminae or strata produced by grain fall and grain flow down the steep (lee) side of the dune form.
Toeset	Low angle ripple strata in front of foreset beds
Bed internal features	
Cross-sets/cross bedding	Strata or laminae with an apparent dip.
Parallel, wavy, curved	Stratified, rolling or sinuous strata or laminae
Continuous	Strata or laminae unbroken over several tens of metres.
Troughed	Highly curved, concave up strata.

¹ North American Stratigraphic Code (NASCN, 2005)² Staines (1985)³ Pye and Tsoar (1990), Collinson and Thompson (1989), Allen (1982a, 1982b)

area of undefined width that extends seawards from the shoreline to beyond the breaker boundary (Trenhaile, 1997). The range of bedforms, bedding types, sequences, and morphologies observed across various beach types is explored in Tucker and Wright (1990, pp 101-112), and Reineck and Singh (1980, pp. 339-350). Depositional facies characteristic of these beach types are summarised below.

3.3.1.1 Shoreface

The Shoreface of a beach is always submerged, and is usually made up of longshore bars with landward side channels. The number of longshore bars is related to the wave energy experienced on the coastline; generally the weaker the wave energy the fewer the number of longshore bars. The bedding structures that form within the sediments of the shoreface (fairweather wave-base (FWB) to low tide), can vary depending upon the depth of the water and wave strength. The upper portion of the shoreface specifically the breaker/surf zone can be characterised by asymmetric wave ripples, and dunes formed as a result of turbulence. Large-scale bars may also form; giving rise to onshore directed planar cross-bedded sediments; whereas in the deeper water areas cross-bedding is rare and laminated sand becomes the dominant bedding structure. Bioturbation also increases with water depth. In high energy systems, onshore directed lunate dunes (mega-ripples) may form, that exhibit trough crossbedding. When identifying fossil shoreface deposits it is considered that truncated wave ripple laminae are the characteristic bedform (Tucker and Wright, 1990; Reineck and Singh, 1980; Campbell, 1966, 1971).

3.3.1.2 Foreshore

The foreshore extends from the berm crest to the low tide level, and encompasses the swash-backwash zone. The main type of bedding formed is low angle sand laminations that have been deposited from suspension clouds, carried by the incoming wave trains. The swash and backwash produces characteristic sorting evident in the individual laminae, and the angle of dip is strongly controlled by the grain size. The larger the grain size the higher the angle of the beach slope, and thus, the higher the angle of dip in the sediment

bedsets (Reineck and Singh, 1980). The slope of the foreshore may be inclined as little as 1 to 3° , or it could be as high as 30° (Davis, 1985).

Low beach berms and washover sediments are found in the upper portions of the foreshore, leading to onshore directed planar cross-beds, and the lower portions of the foreshore exhibit low ridges covered in dunes and ripples, and runnels floored by ripples produce cross-bedding, cross-lamination and shallow scours (Tucker and Wright, 1990). Beachrock may be another common feature of the foreshore, particularly at lower latitudes in areas with abundant carbonate, such as the Bahamas (Tucker and Wright, 1990).

3.3.1.3 Backshore

The backshore represents the uppermost portion of the beach, and normally remains dry, except when there are anomalously high water levels; which can occur during storm events for example. When this happens the sediments can be acted upon by waves and currents, and the upward growth of the backshore takes place. Apart from events such as these the backshore is normally only exposed to wind activity. The dominant bedding structures evident in backshore deposits are near-horizontally laminated sands, although this may be broken by small-scale cross-bedding produced by current ripples. Shell beds can sometime be present as deflation deposits, when the wind removes finer sediments, thereby concentrating the coarser, heavier components (Otvos, 2000; Reineck and Singh, 1980).

Backshore dunes form from sand that has accumulated through deflation of the beach by wind and storm; conversely they are also a source of sediment used to replenish the beach during and after storms. Dunes can form on both barriers and beach ridges. A variety of aeolian dune forms can develop but the most common are transverse dunes with high angle landward faces. These dunes can be tens of metres in height and can cover areas up to two kilometres in width. The common bedforms are typical of aeolian deposition: cross-bedding, tabular-planar and wedge-planar with high dip angles, up to 34° ; invariably directed onshore. The bedforms will also exhibit alternating fine to medium-coarse sand laminae (Otvos, 2000; Trenhaile, 1997; Tucker and Wright, 1990).

Part II: South coast stratigraphy

3.4 Stratigraphy and facies of the Kangaroo Island study sites on the south coast

3.4.1 Introduction

The stratigraphic features of the Kangaroo Island Bridgewater Formation carbonate sequences (and other associated facies) found along the southern coast are examined in the following sections. Pennington Bay is examined first, then Bales Beach, Point Ellen and Vivonne Bay, Hanson Bay and finally Kelly Hill Caves. Pennington bay is a small embayment with extensive aeolianite outcrops; Bales Beach is similar. Point Ellen and Vivonne Bay host the Point Ellen Formation (a richly fossiliferous coquinite), 3 apparent aeolianite sequences, and a discontinuous, raised shelly pebble/cobble notch deposit. At Hanson Bay a lagoonal/estuarine unit crops out at sea-level, and a raised shelly, carbonate sand unit rests on and older aeolianite/marine platform. Kelly Hill Caves is also discussed briefly as some calcarenite was sampled for luminescence measurements—in order to estimate a time of deposition for the parent material.

3.4.2 Stratigraphy of aeolianite at Pennington Bay

Pennington Bay is a small high energy embayment located on the south coast of Kangaroo Island, near the western end of the Dudley Peninsula (Figure 3.1). The bay is approximately 1.5 km wide and is delimited by two large aeolianite headlands, with a series of smaller headlands located in between. In effect this breaks the embayment up into a group of smaller bays that are isolated from each other during high tide (Figure 3.2). The region experiences strong, predominantly south-south easterly winds in summer and is exposed to westerly and northerly winds during winter (Schwerdtfeger, 2002). The aeolianite sequences and their associated facies on Kangaroo Island, as discussed in the previous chapter, are classified as Bridgewater Formation (Sprigg, 1954; Boutakoff, 1963; Belperio, 1995; Belperio *et al.*, 2000). The sites at Pennington Bay comprise a series of aeolianite sequences that possibly overlie early/middle Pleistocene calcarenites (although the calcarenites only

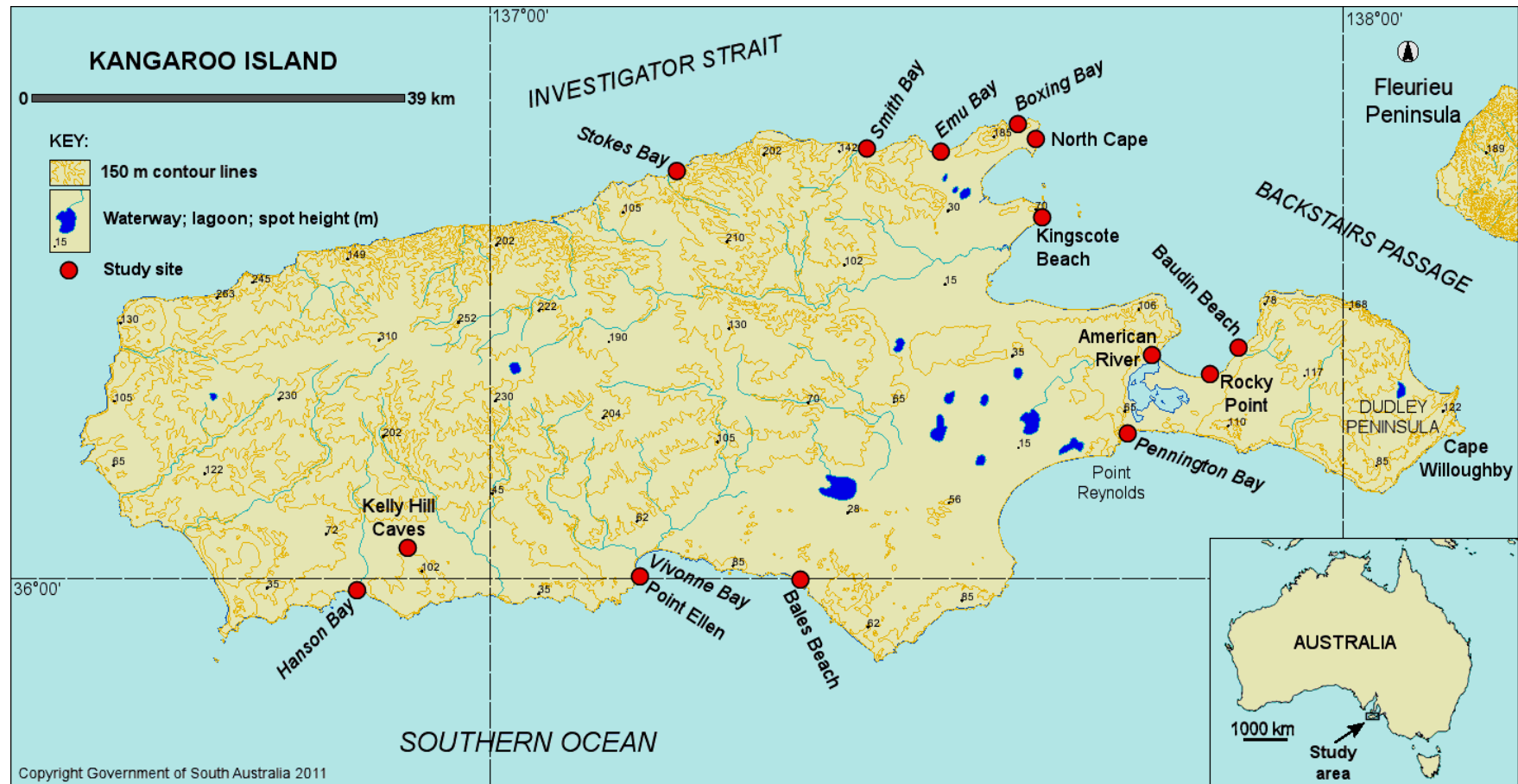


Figure 3.1: Kangaroo Island location (and topographic) map for study sites described in this chapter (i.e. parts II, III, IV, and V) (modified from the online atlas of South Australia [2011]).

Third party source; Images redacted at request of thesis author

Figure 3.2: Morphology and location of study sites at Pennington Bay, Kangaroo Island (Google Earth, 2009).



Figure 3.3: Vegetation and slumped dune sands obscuring aeolianite outcrops; site PB4 at the western segment of Pennington Bay. Note the Holocene platform formed in the basal calcarenite.



Figure 3.4: Aeolianite blocks broken from face of exposure. Site PB1 Pennington Bay, Kangaroo Island.



Figure 3.5: Wave cut notch and visor at base of aeolianite. Site PB1 Pennington Bay, Kangaroo Island.



Figure 3.6: Solutional crust left foreground, obscuring bedding in aeolianite, and transgressing dune sand ramp in mid-ground. Site PB1, Pennington Bay, Kangaroo Island.

crop out extensively past the western end of the bay near Point Reynolds [Figure 3.1], and are only present as a basal unit, or are totally obscured by overlying Quaternary sediments, or stripped off, in other areas around the bay) and Kanmantoo Group basement rocks. The aeolianites are subdivided by intercalated palaeosols; occasional laminar / blocky calcretes, and brecciated exposure surfaces. These units crop out discontinuously around the bay. Over time storm events and wave action have undercut the base of some of these deposits leading to failure of the upper units; this has allowed the overlying Holocene and Modern dunes to slump, obscuring large swathes of the deposits (Figure 3.3). Evidence in the form of broken blocks of aeolianite on the beach and wave cut notches at the base of headlands and strandline parallel exposures, found in various places around the bay, are obvious indicators of this (Figure 3.4 and 3.5). Vegetation cover, solutional weathering, re-precipitation of carbonate (solutional crusts), debris slopes, and transgressing modern dunes are also a problem and have obscured or obliterated bedding in

places (Figure 3.6), making it difficult and sometimes impossible to follow particular beds. Due to these issues only 5 areas at Pennington Bay were examined; this is illustrated in Figure 3.2.

The section of the bay that lies approximately between PB3 and the headland to the west of PB2 (Figure 3.2) is an area of relatively low topography that has only modern and Holocene barrier dunes evident, with no outcropping aeolianite. It is suggested by Belperio (1995) that this region of the bay may have hosted a channel or seaway that connected the bay to northern side of the isthmus; bisecting the neck of Dudley Peninsula (Figure 3.1) during periods of higher than present sea-level (e.g. the Last Interglacial). The channel, if it existed, would have been filled in with dune sands during periods of lower sea-level (glacial periods). The morphology of this section of the bay and the lack of Pleistocene formations may support this.

The five sites examined in this section of Chapter 3 have exposures that are either located on headlands, perpendicular to the coast, or cliffed outcrops that run parallel with the shoreline. The headland exposures are particularly useful given that the dip azimuths of the internal bedding structures in the aeolianite units can be used to estimate palaeowind directions (McKee and Ward, 1983). The cliffed exposures and headlands range from approximately 5–22 m APSL, and generally host 2 well-developed palaeosol units, although site PB5 has 3; sometimes thinner more weakly developed palaeosols are also present. A pervasive, commonly blocky, calcrete sheet of varying thickness drapes the landscape in a spectacular fashion; this is overlain in many areas by well-vegetated, unconsolidated Holocene or modern dunes (Figure 3.7). Site PB2 has the remnant of a raised pebble beach deposit. The deposit is in a notch approximately 3.2 m above sea-level (ASL) and contains pebbles and cobbles of various sizes as well as many sub-fossil shells; the bivalve *Amesodesma angusta* being the most common species present. This bivalve is characteristic of sands in the foreshore swash-backwash zone (Ludbrook, 1984).

The following sections examine the mapped aeolianite sequences around Pennington Bay at PB1, PB2, PB3, PB4, and PB5 (Figure 3.2).



Figure 3.7: Pervasive calcrete sheet draping the landscape around Pennington Bay: looking east from the top of the PB5 headland (see Figure 3.2).

3.4.2.1 Site PB1

PB1 is a small unnamed embayment (Figure 3.8) enclosed by two aeolianite headlands. The embayment is approximately 36 metres wide across the mouth and approximately 63 metres around the circumference. It has been carved out by wave action which has exposed the internal structure of the palaeodunes, although in many places this is obscured by slump, vegetation, and solutinal crusts (precipitated secondary carbonate). The bedding where visible is often typical of aeolian deposition, exhibiting high-angle cross-bedding features dipping landward (foresets, see Table 3.1, Part: I), the directional vectors of which can be used to estimate palaeowind directions (McKee and Ward, 1983). Four sections have been measured at this site, one from the western headland, two from the backshore cliff, and one from the rear of the eastern headland. A basal unit, depicted in the foreground of Figure 3.8, which has been cut into a platform, exhibits low angle landward dipping beds that may represent the bottom sets of an older, possibly middle-Pleistocene, dune system.

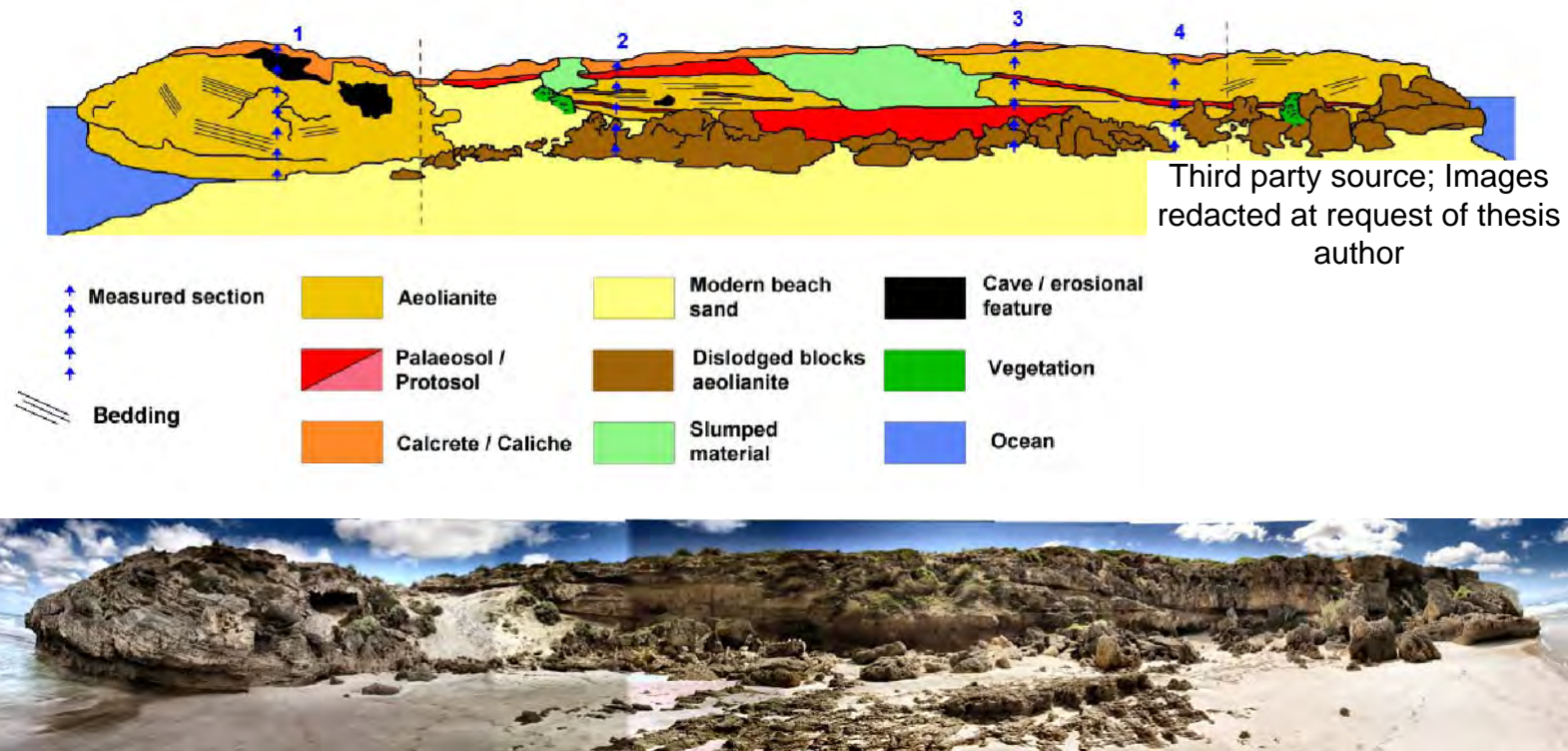


Figure 3.8: Site PB1, displayed here as a composite 180 degree panorama; so there is distortion towards the edges of the image. The top image depicts the individual units which have been assigned different colours to make them more apparent. The black dotted lines show approximate landward margins of the headlands and the blue arrowed lines and red squares (on the inset satellite image of the embayment [Google Earth, 2008]), show the position of measured sections for the site. This site is relatively low, at approximately 5-8m ASL.

Table 3.2: Characteristics of PB1, section 1, lithostratigraphic units.

Unit number	Lithostratigraphic unit	Description	Munsell colour	Grain size	Grain sphericity	Grain sorting
1-1b	Calcrete	Indurated blocky calcrete of varying thickness. Occasionally incorporating angular calcrete clasts in matrix cement.	7.5YR 8/2 Pinkish white	Very Fine	--	--
1-1aii	Aeolianite	Consolidated bioclastic carbonate sand with prominent tabular cross-beds (foresets). Dipping predominantly landwards.	10YR 8/1 White	Fine	Sub-angular to subrounded	Well sorted
1-1ai	Aeolianite	Consolidated bioclastic carbonate sand with prominent low angle beds (bottomsets). Level or dipping seaward. The lower portions of this unit are strongly cemented and riddled with fenestrae; the upper portions are much softer – possibly due to leaching.	10YR 8/1 White	Fine	Sub-angular to subrounded	Well sorted

PB1 Section 1

This section was measured on the western aeolianite headland (Figure 3.8 and 3.9 inset) and consists of two lithostratigraphic units: an aeolianite (1-1ai and 1-1aii), approximately 4 m thick, overlain unconformably by a calcrete that is approximately 0.4 m thick; although this varies considerably around the site (Figure 3.9, Table 3.2). The aeolianite bedding is predominantly tabular planar, dipping landward towards the north-west (1-1aii) (Figures 3.10 and 3.11). The dip angles range between 18 and 30°, typical of aeolian foreset beds. The lower portion of the aeolianite unit (1-1ai) is characterised by a series of level beds, and landward intersecting these, are some low angle seaward dipping beds (dipping 7-10° to the south-west). Both sets of beds are interpreted here as bottomsets. The foreset beds dip primarily towards the north-west, with mean vector trends of $327 \pm 6^\circ$ at the 95% confidence interval (Table 3.3), indicating that the wind direction would have been predominantly from the south-east during deposition.

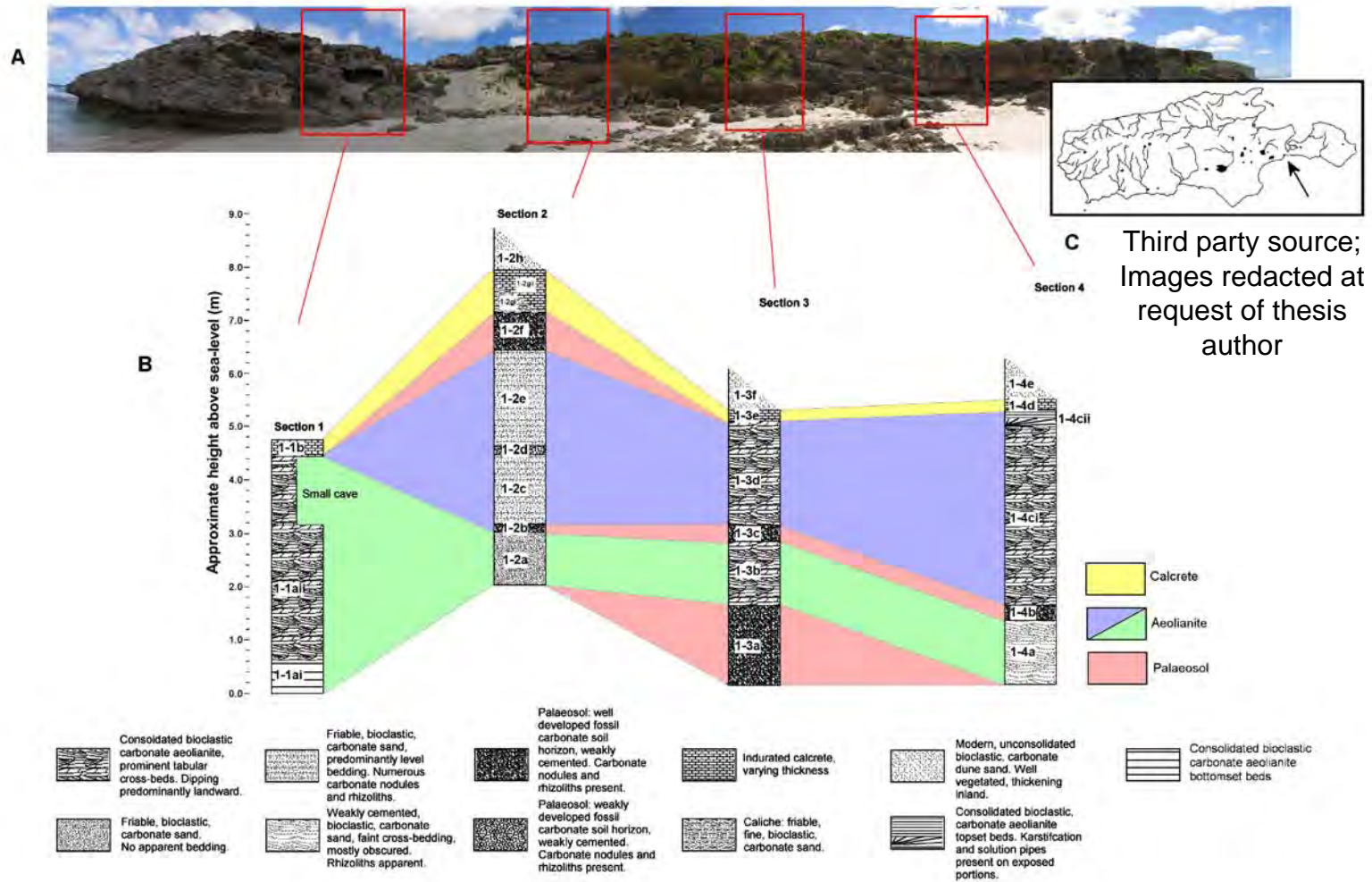


Figure 3.9: Stratigraphic columns for all sections measured at site PB1 (RH inset satellite image Google Earth, 2010).

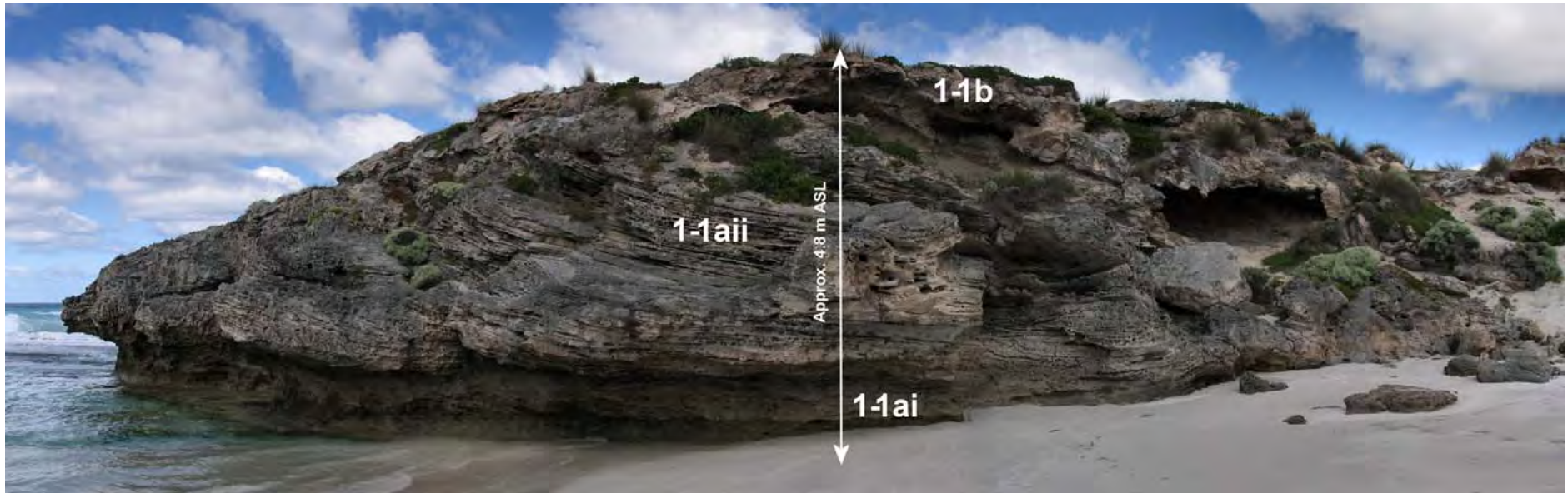
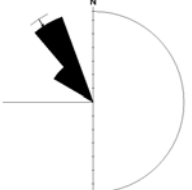


Figure 3.10: Western headland (looking west) section 1 at site PB1, Pennington Bay, Kangaroo Island. This is an aeolianite unit with high angle cross-bed sets (1-1aii), and low angle bottom-sets (1-1ai), with an overlying blocky calcrete (1-1b). The greyish colour of the units is due to a coating produced by weathering and possibly fungus or lichen. Note the well-developed notch and visor formed by wave erosion. Also note that this is a merged image; therefore there is a degree of distortion that adds some curvature to otherwise planar surfaces.



Figure 3.11: Western headland section 1 PB1, Pennington Bay, Kangaroo Island—looking south-west from the top of the PB1 site. This image clearly shows the orientation of the aeolianite bedforms. Note the upper sea-caves undercutting the calcrete.

Table 3.3: Compiled bedding vector data for PB1 western headland (section 1a).

Lithostratigraphic unit	Number of measurements	Sector angle (degrees)	Mean direction (degrees)	Rose diagram
Aeolianite (1-1a _{ii})	6	20	327 ± 6	

PB1 section 2

A section (2) of the cliffed exposure running parallel to the shore was measured at the area indicated in Figure 3.8. Section 2 is a relatively recently exposed cliff face, as evidenced by the broken aeolianite blocks littered about the base of the deposit and the clean colour of the exposure face: unblemished by either weathering or fungal growth. Section 2 is more complicated than section 1; the stratigraphic columns, and site morphology are illustrated in Figure 3.9 and Figure 3.12. The bottom-most visible unit in this section is approximately 2 m

ASL, as the lower portion of the deposit to near sea-level is obscured by broken blocks and modern beach sand. There is a “basal” sand unit (1-2a) unconformably overlain by a thin palaeosol (1-2b); this bottom unit may be the continuation of the 1a aeolianite from the western headland; however, it shows little bedding and is weakly cemented in comparison. Above the thin palaeosol (1-2b) lies another aeolianite (1-2c) with almost level bedding (there is a slight dip in the beds of approximately 3° at 60° azimuth); however, the perpendicular dip of the beds into the face of the deposit, as can be seen from the interior of the small cave in the face of the unit, is high angled at approximately 22° . It was difficult to determine dip direction, but it was approximately north-west. Another thin palaeosol (1-2d) forms a bounding surface for the aeolianite unit (1-2e) above. Unit 1-2e exhibits similar bedding to 1-2c. A thicker more developed palaeosol (1-2f) unconformably overlies aeolianite unit 1-2e, and is characterised by a thin laminar calcrete on its upper bounding surface. The topmost unit (1-2gi and 1-2gii) is a blocky calcrete that, in this section, grades towards the west into less indurated carbonate sediment that has abundant rhizoliths, and is capped by cemented cobbles of calcrete. Above the calcrete is a modern and Holocene dune system that is well vegetated; these dunes are present as a relatively thin covering at the cliff-face; however, they thicken considerably inland (ranging from bare calcrete and <1 m at the cliff-face to >70 m inland). The thin palaeosol 1-2d may represent a relatively short hiatus in carbonate deposition, given that the aeolianite units 1-2c and 1-2e share the same general characteristics (Table 3.4). However, the thin palaeosol 1-2b appears to be the distal edge of a much thicker well developed palaeosol that has apparently formed in a dune swale in section 3.

PB1 section 3

This section (section 3) of the cliffed exposure running parallel to the shore was measured at the area indicated in Figure 3.8. Section 3 is approximately 10 m from section 2, and is comprised of 6 discrete units (Figure 3.9 and Table 3.5). The bottom-most unit is a well-developed thick (up to 1.6 m) palaeosol (1-3a). This unit is essentially featureless (massive) through the profile; however, the upper portions below contact have abundant carbonate nodules and rhizcretions.

Table 3.4: Characteristics of PB1 section 2 lithostratigraphic units.

Unit number	Lithostratigraphic unit	Description	Munsell colour	Grain size	Grain sphericity	Grain sorting
1-2h	Modern / Holocene backshore dunes	Unconsolidated dune sand, abundant vegetation cover	2.5Y 7/1 Pale brown	Coarse/medium	rounded	Moderately sorted
1-2gii	Calcrete	Indurated blocky calcrete of varying thickness. Occasionally incorporating angular calcrete clasts in matrix cement.	7.5YR 8/2 Pinkish white	Very fine	--	--
1-2gi	Calcrete / protosol	Weakly cemented carbonate sand, with abundant rhizoliths, overlain by cemented calcrete cobbles and blocks.	10YR 8/2 very pale brown	Fine	Sub-rounded to rounded	Poorly sorted
1-2f	Palaeosol	Thick well-developed palaeosol	7.5YR 5/3 brown	Fine	rounded	Very well sorted
1-2e	Aeolianite	Weakly cemented carbonate sand, friable, abundant rhizocretions in upper sections.	10YR 7/4 very pale brown	Medium/fine	Sub-rounded to rounded	Moderately to poorly sorted
1-2d	Palaeosol	Thin weakly developed palaeosol, abundant rhizocretions.	7.5YR 5/3 Brown	Fine	--	--
1-2c	Aeolianite	Weakly cemented carbonate sand, friable, abundant rhizocretions in upper sections.	10YR 7/4 very pale brown	Medium/fine	Sub-rounded to rounded	Moderately to poorly sorted
1-2b	Palaeosol	Thin palaeosol, abundant rhizocretions.	5YR 7/2 Pinkish grey	Fine	--	--
1-2a	Aeolianite	Weakly cemented carbonate sand, relatively featureless.	10YR 8/2 very pale brown	Medium/fine	Sub-angular to sub-rounded	Moderately sorted

Upon examination of the morphology at this section it is apparent the 1-3a palaeosol has formed in a dune swale and has been exposed as the face of the deposit (an older sequence of dunes) was removed. Since the palaeosol is much softer than the overlying aeolianite it has eroded more rapidly, leading to failure in the overlying units; hence the abundant debris about the base of the deposit (Figure 3.13). Unit 3a is overlain by an aeolianite (1-3b); that exhibits level bedding, however, the “true dip” perpendicular to the face of the deposit is likely to be high angled and landward, as it is in 2c. A palaeosol unconformity (1-3c) separates another aeolianite unit (1-3d); the 3c palaeosol is interpreted to be the same as the uppermost palaeosol in section 2 (1-2f). It is quite thin (<300 mm) here but thickens and grades upward towards section 2. The aeolianite unit 1-3d exhibits level bedding as well (0-3°), although a protruding section of aeolianite allowed the perpendicular dip to be determined. The dip is 16° at approximately 330° azimuth. Unit 1-3e is the pervasive blocky calcrete

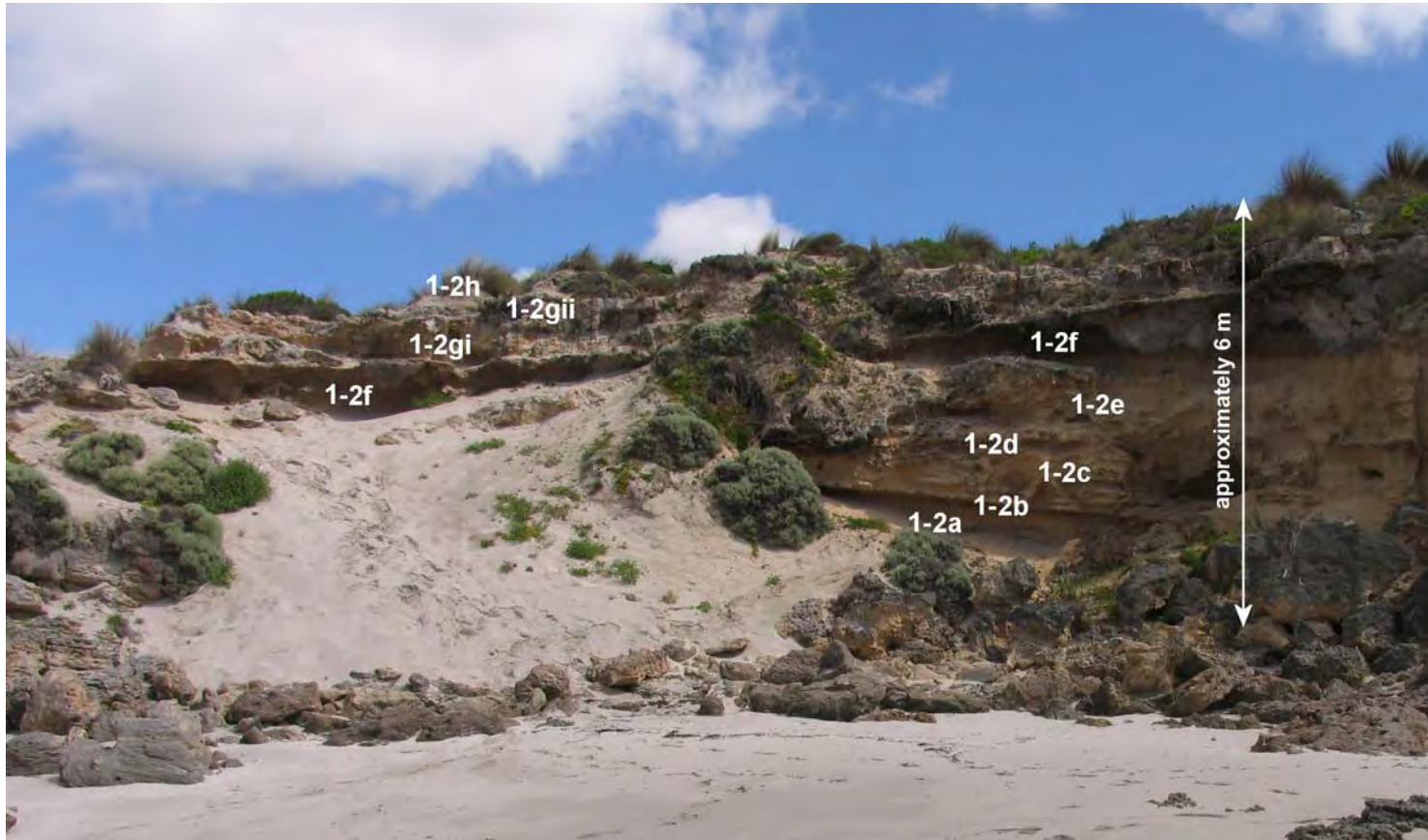


Figure 3.12: Section 2 at site PB1, Pennington Bay, Kangaroo Island. Cluffed exposure; note the “clean” face of the exposure and the broken blocks at the base of the deposit. Some time in the past (possibly quite recently) this series of units was undercut very probably by storm wave action and has subsequently collapsed, leaving a fresh exposure. There are 8 recognisable units in this section: 3 aeolianites (1-2a, 1-2c, and 1-2e), 3 Palaeosols (1-2b, 1-2d, and 1-2f), a calcrete (1-2gi and 1-2gii), and modern dunes (1-2h). Note the transgressive sand ramp LH mid-field.



Figure 3.13: Section 3 of site PB1, Pennington Bay, Kangaroo Island, facing towards the north. There are 6 units in this section, 2 palaeosols, 2 aeolianites, a calcrete, and overlying modern/Holocene dunes.

Table 3.5: Characteristics of PB1 section 3 lithostratigraphic units.

Unit number	Lithostratigraphic unit	Description	Munsell colour	Grain size	Grain sphericity	Grain sorting
1-3f	Modern / Holocene backshore dunes	Unconsolidated dune sand, abundant vegetation cover	2.5Y 7/1 Pale brown	Coarse/medium	Rounded	Moderately sorted
1-3e	Calcrete	Indurated blocky calcrete of varying thickness.	7.5YR 8/2 Pinkish white	Very fine	--	--
1-3d	Aeolianite	Consolidated bioclastic carbonate sand, predominantly landward dipping beds	10YR 7/4 Very pale brown	Medium/fine	Sub-rounded to rounded	Moderately to poorly sorted
1-3c	Palaeosol	Thin palaeosol, abundant rhizcretions.	7.5YR 5/3 Brown	Medium/fine	Sub-rounded to rounded	Moderately to poorly sorted
1-3b	Aeolianite	Consolidated bioclastic carbonate sand, level bedding.	10YR 8/3 Very pale brown	Fine/medium	Sub-rounded to rounded	Well sorted
1-3a	Palaeosol	Thick well developed palaeosol, abundant rhizcretions, and carbonate nodules in upper portions.	5YR 5/2 Reddish grey	Fine	Rounded	Very well sorted

Table 3.6: Characteristics of PB1 section 4 lithostratigraphic units.

Unit number	Lithostratigraphic unit	Description	Munsell colour	Grain size	Grain sphericity	Grain sorting
1-4e	Modern / Holocene backshore dunes	Unconsolidated dune sand, abundant vegetation cover	2.5Y 7/1 Pale brown	Coarse/medium	rounded	Moderately sorted
1-4d	Calcrete	Indurated thin, laminar calcrete.	7.5YR 8/2 Pinkish white	Very fine	--	--
1-4cii (b) upper	Aeolianite	Consolidated bioclastic carbonate sand, predominantly level beds. Bedding obscured in places by solutional crusts. Upper portions karstified.	10YR 8/3 Very pale brown	Fine/medium	Sub-rounded to rounded	Well sorted
1-4cii (a) lower	Aeolianite	Consolidated bioclastic carbonate sand, predominantly wedge planar bedding. Bedding obscured in places by solutional crusts.	10YR 8/3 Very pale brown	Fine/medium	Sub-rounded to rounded	Well sorted
1-4ci	Aeolianite	Consolidated bioclastic carbonate sand, predominantly landward dipping beds. Bedding obscured in places by solutional crusts.	10YR 8/3 Very pale brown	Fine/medium	Sub-rounded to rounded	Moderately to poorly sorted
1-4b	Palaeosol	Thin palaeosol, abundant rhizocretions.	7.5YR 5/3 Brown	Medium/fine	Sub-rounded to rounded	Moderately to poorly sorted
1-4a	Aeolianite	Consolidated bioclastic carbonate sand, bedding obscured by crusts and rhizocretions.	10YR 8/3 Very pale brown	Fine/medium	Sub-rounded to rounded	Well sorted

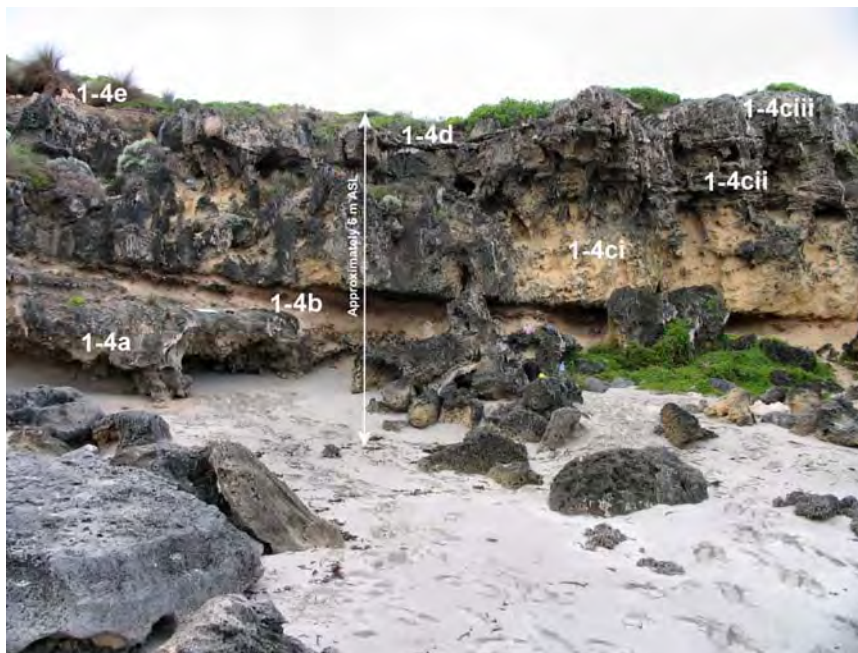
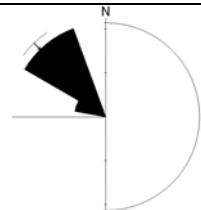


Figure 3.14: Site PB1 section 4, facing towards the east. This section hosts 5 units: 2 aeolianites (1-4a, 1-4c), a palaeosol (1-4b), a calcrete (1-4d) and Modern/Holocene dunes (1-4e).

Table 3.7: Compiled bedding vector data for PB1 western headland (Unit 1-4ci).

Lithostratigraphic unit	Number of measurements	Sector angle (degrees)	Mean direction (degrees)	Rose diagram
Aeolianite (1-4ci)	7	20	316 ± 9	

described above, and this is overlain by the Modern/Holocene backshore dunes (1-3f).

PB1 section 4

This section (section 4) is approximately 10 m from section 3 at the eastern headland (see Figure 3.9 and Table 3.6). It is comprised of 5 units: 2 aeolianites, a palaeosol, a calcrete and the covering of modern / Holocene dunes. The basal aeolianite (1-4a) is weakly cemented and unfortunately the bedding is difficult to discern due to the presence of numerous rhizoliths. This unit is unconformably overlain by a thin palaeosol (1-4b) that grades upwards to the east, and can be traced through sections 3 and 2 (1-3c and 1-2f). The unit above this is an aeolianite (1-4ci) exhibiting prominent tabular cross-beds that dip landward in the lower portions. There is a sharp bounding surface separating the upper portions of this unit, which can be characterised by wedge planar cross-bedding (1-4cii) and above a series of level bedsets (1-4ciii) that contact the overlying calcrete unconformity (1-4d). The level beds are interpreted as top sets. The Modern/Holocene dunes are present as thin sands back from the edge of the headland, and the calcrete is quite thin and laminar. The foreset beds in unit 1-4ci dip primarily towards the north-west, with mean vector trends of $316 \pm 9^\circ$ at the 95% confidence interval (Table 3.7); this indicates that the wind direction would have been predominantly from the south-east during deposition. The dip angles range between 15 and 20° .

3.4.2.2 Site PB2

Only a single section at site PB2 was measured, this section is approximately 5 m west of the western side the PB1 headland (inset Figure 3.8). This site hosts

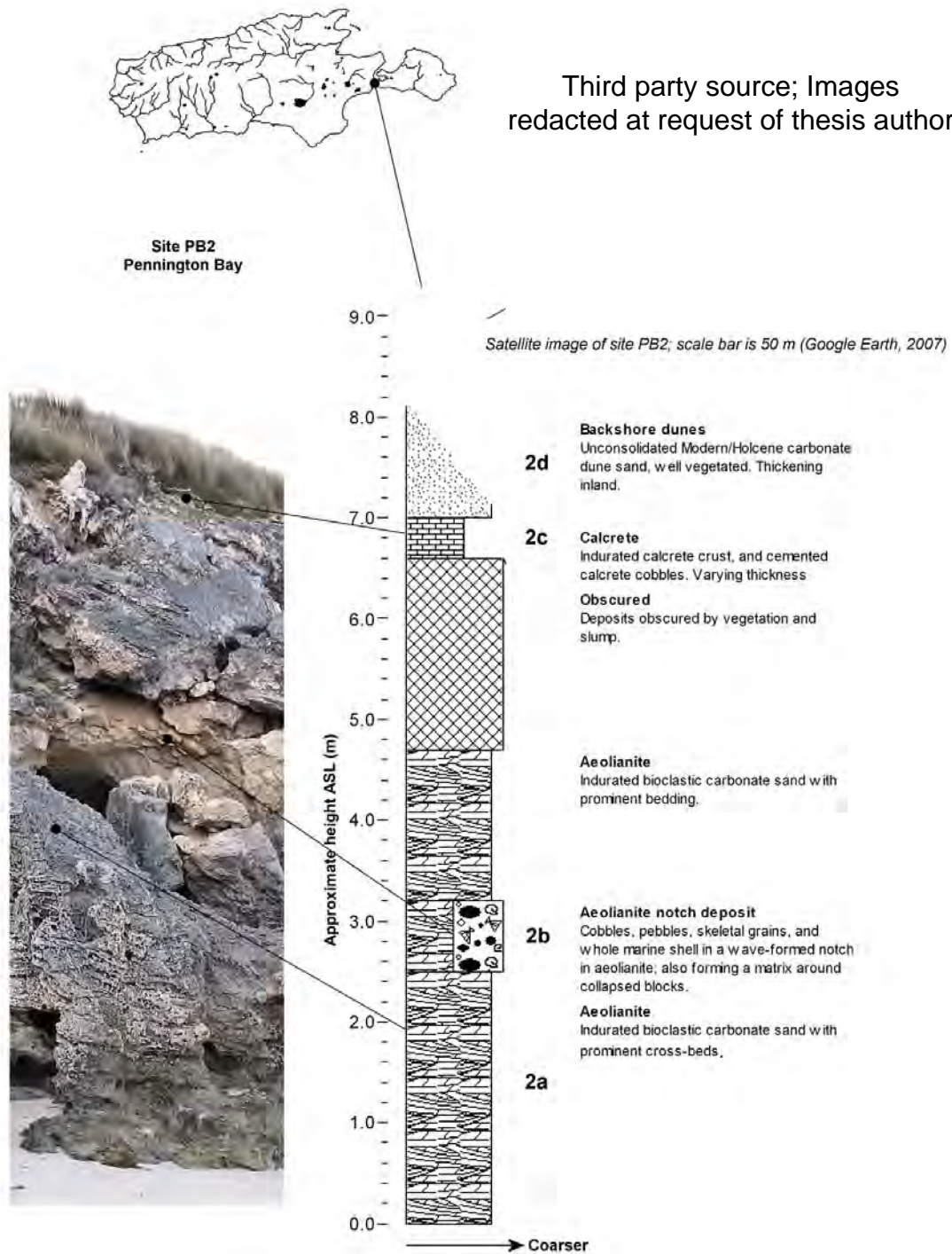


Figure 3.15: Site PB2, Pennington Bay, Kangaroo Island, immediately west of the PB1 western headland. Much of the upper portions of this section are obscured by overlying modern material and vegetation. However, 4 units can be observed: a lower aeolianite (2a), a shelly notch deposit in the aeolianite (2b), the pervasive upper calcrete (2c), and the overlying modern/Holocene dunes (2d).

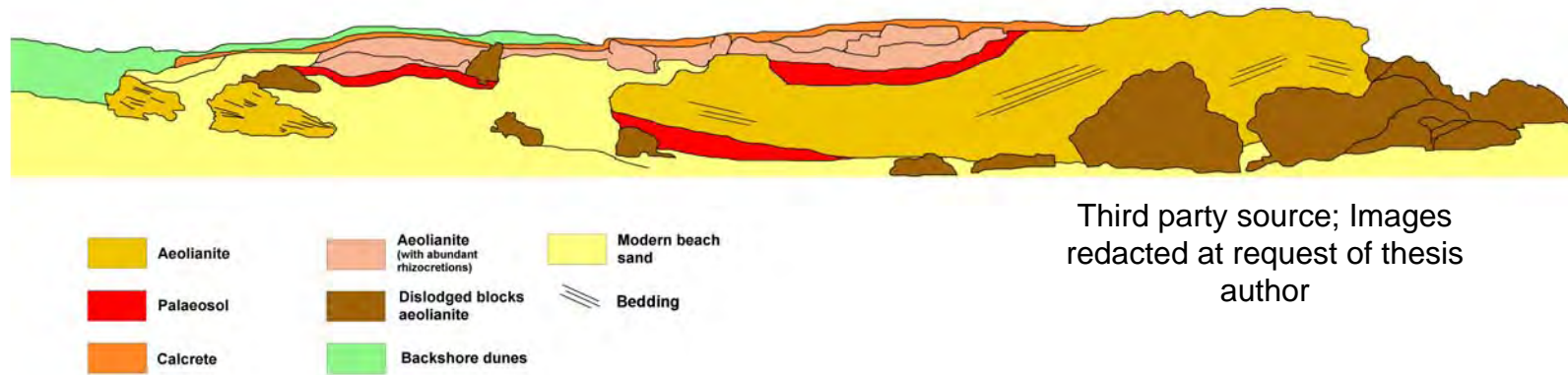


Figure 3.16: Site PB3 is displayed here as a 180 degree composite panorama, and so there is distortion at the edges of the image. The top image depicts individual units which have been assigned different colours to make them more apparent. The red line on the satellite image (inset) shows the approximate extent of the measured section (Google Earth, 2010). This site is relatively low, at approximately 6 m ASL.

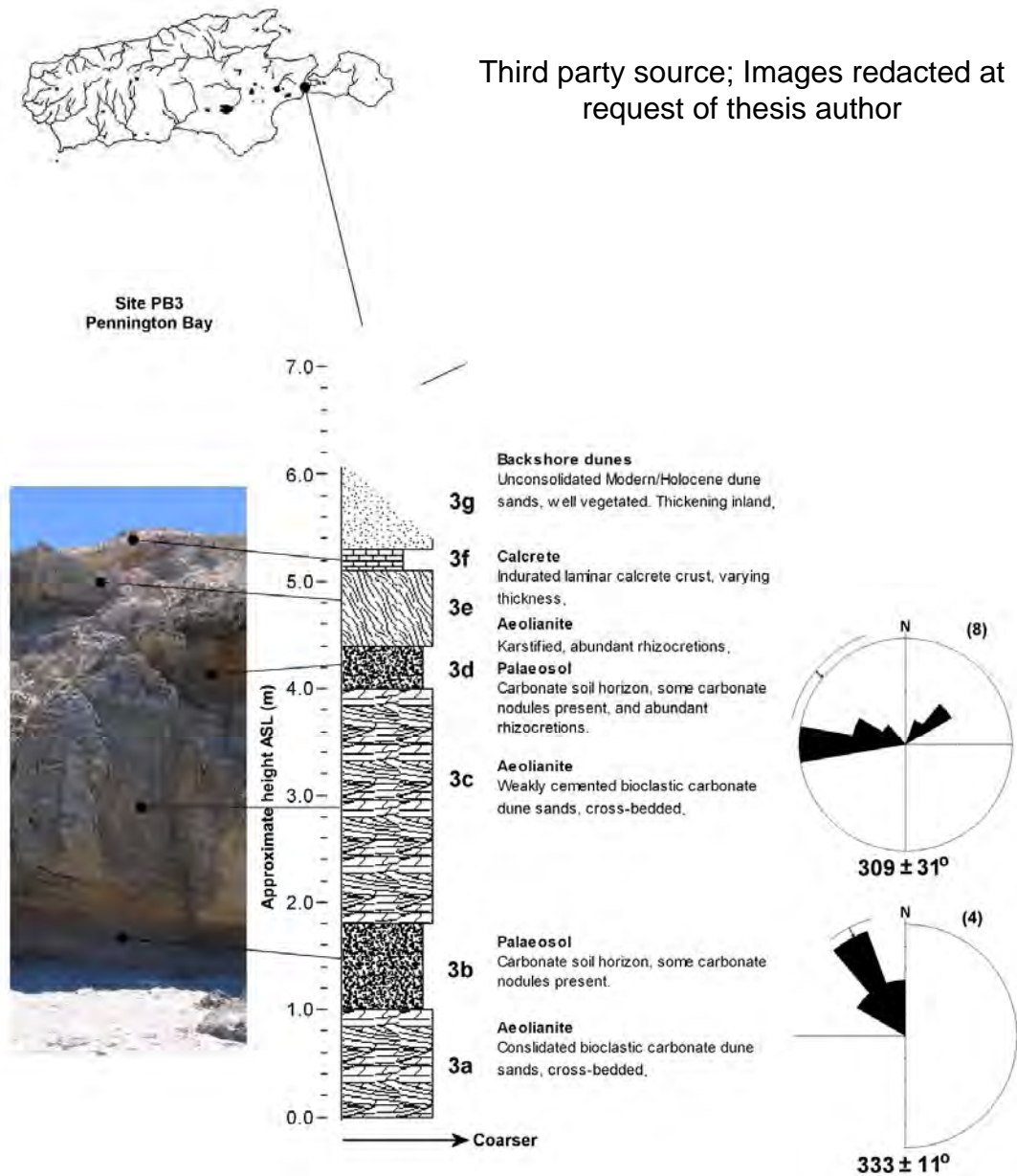


Figure 3.17: Site PB3 generalised stratigraphic log. This outcrop exhibits 7 units: 3 aeolianites, 2 palaeosols, and the ubiquitous calcrete and backshore dunes. The upper aeolianite is karstified and the middle (3c) has some large solutional features (inset satellite image Google Earth 2010).



Figure 3.18: An outcrop of unit 3a, site PB3, Pennington Bay, Kangaroo Island. Most of the upper section of this unit is obscured by solutional weathering. The unit dips steeply down into the plane of the beach. Hammer for scale (33 cm).

a wave cut notch that formed during a past sea-level highstand (interpreted as MIS 5e, based upon morphostratigraphy, i.e., height APSL); the top of the notch is approximately 3.2 m ASL. Wave action has cut into the face of the aeolianite and, subsequently, the overhanging visor has collapsed into a series of blocks. The gaps between blocks and the remnants of the notch have been filled with cobbles, pebbles, sand sized skeletal grains, and marine shell washed in during the highstand. This forms a matrix that has cemented in place over time. The aeolianite may have been deposited during the transgressive phase of the highstand—possibly MIS 5e; although, it is very likely that the aeolianite is much older than MIS 5e. Based upon the position of the aeolianite and the level of induration it is possibly MIS 7 or 9 in age. This site is very similar to one at Vivonne Bay, which has morphology that bears a close resemblance to PB2. This site will be described later in this chapter. Figure 3.15 illustrates the general stratigraphy for the site.

3.4.2.3 Site PB3

This site is similar to the sections described from PB1, exhibiting what are in all probability the same aeolianite/palaeosol couplets. PB3 is around 600 m west of PB2, and borders the low topography area inferred to be a Pleistocene sea-way (Figure 3.2, and 3.16).

This site comprises 7 units: 3 aeolianites, 2 palaeosols, the upper calcrete and the overlying modern / Holocene backshore dunes (see Table 3.9). Unit 3a is an aeolianite that underlies the lowest palaeosol (3b). Unit 3a is only apparent as a few sections of dune rock, jutting out of the beach at around 5-10 metres to the west of the main deposits (Figure 3.16 and 3.18). This unit can be characterised by prominent bedding that dips landward at approximately 30° . The dip azimuth $333 \pm 11^{\circ}$ at the 95% confidence interval (Table 3.8); this indicates that the palaeowind direction was predominantly from the south to south-east during deposition. Stratigraphically unit 3a is almost certainly the same unit as 1-2a at site PB1.



Overlying the 3a aeolianite is unit 3b (Figure 3.19); a well developed palaeosol that formed in a dune swale as in section 3 at site PB1. It is also very likely that

unit 3b is contemporaneous with the 1-3a palaeosol. The palaeosol is essentially featureless (massive), and there are a few carbonate nodules and some broken rhizoliths scattered throughout the unit. Above 3b is another aeolianite; this unit (3c) is approximately 2.2 m thick and exhibits some steeply dipping beds ($24 - 31^\circ$) running almost parallel to the shore. The dip direction is towards the north-east ($40 - 60^\circ$ azimuth). As the unit curves around the headland the predominant dip direction is towards the north-west at around $270 - 285^\circ$ azimuth). This would indicate that portions of this dune formed under two palaeowind regimes; south-westerly and east-south-easterly. The mean dip azimuth for the unit is $309 \pm 31^\circ$ at the 95% confidence interval (Table 3.8). Characteristically this unit shows abundant rhizocretions, especially in the upper contact, and there are also many large solution pipes present.

Another palaeosol (3d) overlies this aeolianite, although it is not as well developed as palaeosol 3b (i.e. having weaker colour: 7.5YR 5/3 Brown); its upper sections are thick with rhizocretions that emerge from a thin laminar calcrete. In turn, overlying this is the uppermost aeolianite (3e); unfortunately this unit is so altered by solutional crusts, karstification, and webs of rhizocretions that bedding is almost impossible to discern (Figures 3.16, 3.17 and 3.19). The pervasive calcrete (3f) drapes over this aeolianite and is quite thin and laminar, although thickness varies. The modern / Holocene dunes are thin near the edge of the cliff, although they thicken moving inland.

The deposits are obscured further along the beach to the west as transgressing beach sands with vegetation cover have buried them.

Table 3.8: Compiled bedding vector data for PB3 headland (Units 3a and 3c.)

Lithostratigraphic unit	Number of measurements	Sector angle (degrees)	Mean direction (degrees)	Rose diagram
Aeolianite (3c)	8	20	309 ± 31	
Aeolianite (3a)	4	20	333 ± 11	

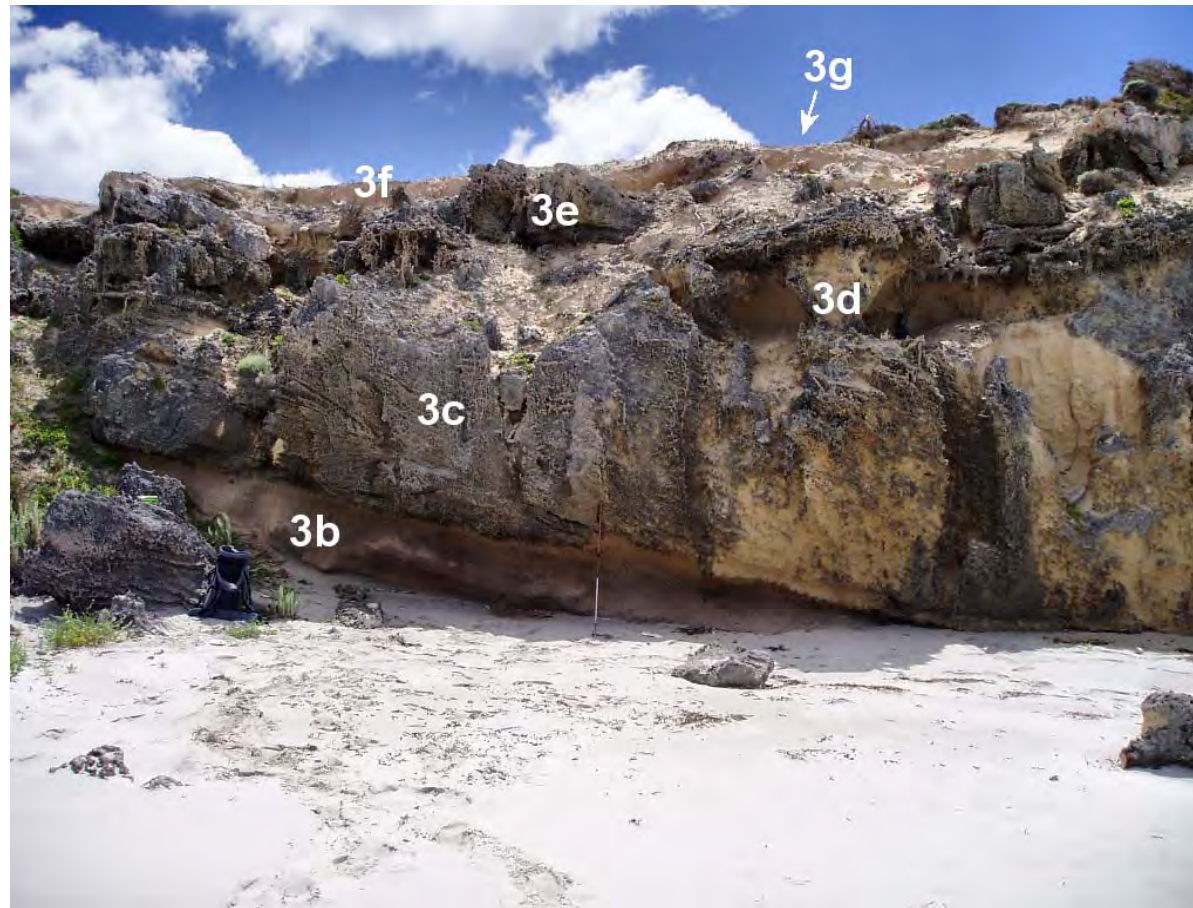


Figure 3.19: Displayed here are units 3b to 3f. Note the presence of solution pipes in unit 3c, and the laminae and rhizoliths in the upper bounding portions of unit 3d. Walking-stick for scale: 1.2 m.

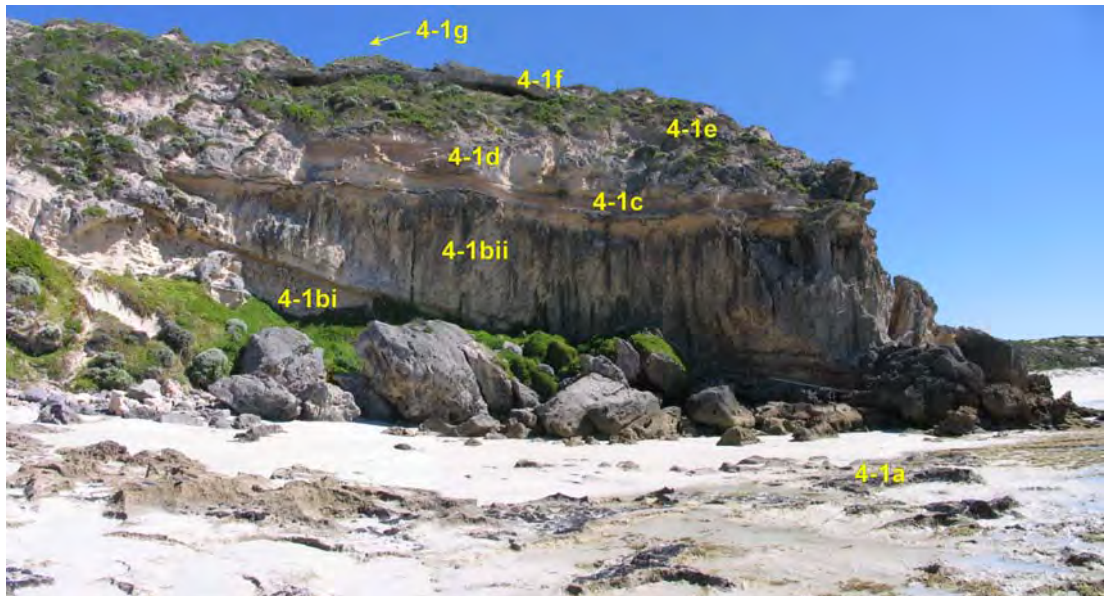
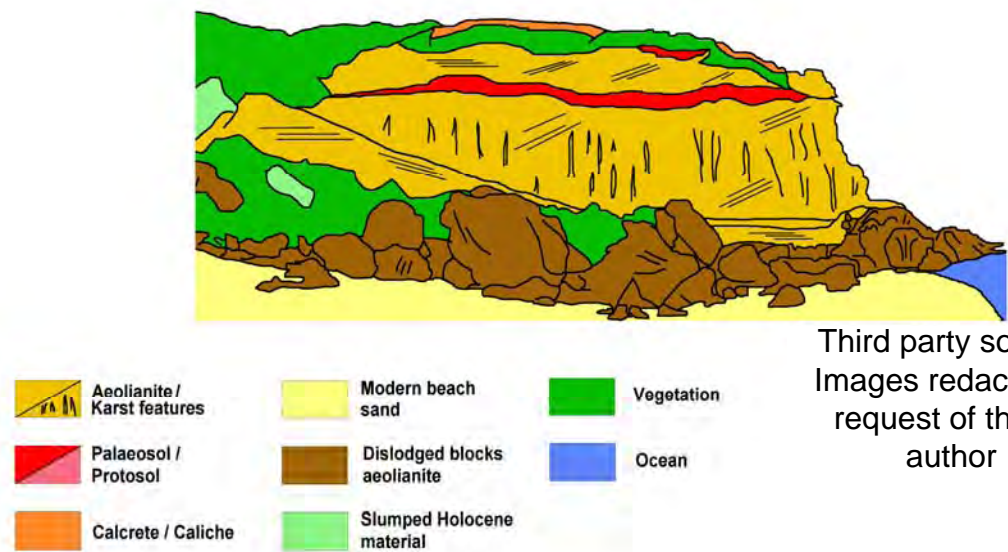


Figure 3.20: Site PB4 section 1 is displayed here as a composite panorama (the image has some distortion towards the edges; however, it is minimal as the panorama is made up of only 3 components). The top image depicts the individual units which have been assigned different colours to make them more apparent. The red line on the satellite image (inset) shows the approximate extent of the measured section (Google Earth, 2010). The section is relatively tall, at approximately 15 m ASL

Table 3.9: Lithostratigraphic characteristics of site PB3

Unit number	Lithostratigraphic unit	Description	Munsell colour	Grain size	Grain sphericity	Grain sorting
3g	Modern / Holocene backshore dunes	Unconsolidated dune sand, abundant vegetation cover	2.5Y 7/1 Pale brown	Coarse/medium	rounded	Moderately sorted
3f	Calcrete	Indurated thin, laminar calcrete.	7.5YR 8/2 Pinkish white	Very fine	--	--
3e	Aeolianite	Consolidated bioclastic carbonate sand. Bedding mostly obscured by solutional crusts, rhizocretions and karstification. Weakly developed palaeosol. Upper bounding surface characterised by thin laminae and abundant rhizocretions.	10YR 8/3 Very pale brown	Fine/medium	Sub-rounded	Well sorted
3d	Palaeosol	Consolidated bioclastic carbonate sand, predominantly landward dipping beds. Bedding obscured in places by solutional crusts. Solution pipes present. Thick palaeosol with scattered carbonate nodules and broken rhizoliths.	7.5YR 5/3 Brown	Fine	Rounded	Very well sorted
3c	Aeolianite	Consolidated bioclastic carbonate sand, prominent steep landward dipping beds.	10YR 8/3 Very pale brown	Medium/fine	Sub-rounded	Well sorted
3b	Palaeosol		5YR 5/2 Reddish grey	Fine	Rounded	Very well sorted
3a	Aeolianite		10YR 8/4 Very pale brown	Fine	Sub-rounded	Well sorted

3.4.2.4 Site PB4

Site PB4 is located at the far western end of Pennington Bay (Figure 3.2, 3.2) and is large headland where two sections have been measured: section 1 (Figure 3.20) is the western side of the headland and section 2 is the eastern side. Both sections exhibit essentially the same units, which is to be expected; although, the thickness of some of the units is dissimilar. The sections are characterised by 3 aeolianite units intercalated by two palaeosols. The lower aeolianites on both sections have low angle bedding, interpreted here as being bottom set beds—although at section 2 these bottom beds are less distinct. These are conformably overlain by high angle cross-bed sets. Section 2 also clearly shows what is probably an older set of aeolianite beds, in the basal portions at the front of the headland; there is no unconformity and the contact with the upper aeolianite is quite sharp. The basal aeolianite is strongly cemented and may represent the remnants of a middle / early-Pleistocene dune system that has been planed off; acting as a “keystone” or an anchor for later

deposition. The upper palaeosol (section 1) is less distinct than section 2, most of the unit is obscured by vegetation, as is the upper aeolianite at section 1.

PB4 Section 1

Section 1 is the western side of the PB4 headland. This section comprises 8 discernable units (Table 3.10, Figure 3.20 and 3.21) and 1 obscured unit – the upper section of the deposit under the calcrete probably hosts an aeolianite (as it does in section 2), but this is completely obscured by low coastal vegetation. Therefore this unit is missing from the section 1 log. The units are: 1 basal calcarenite (1-4a), 2 aeolianites (1-4bi, 1-4bii, and 1-4d), 2 palaeosols (1-4c, and 1-4e), a calcrete (1-4f) and the overlying Holocene dunes (1-4g) (Table 3.10). Unit 4-1b consists of two bed sets: 4-1bi which is a series of low angle beds ($\sim 10^\circ$ dip at 050° azimuth) that form the bottom sets of this dune unit, and 4-1bii characterised by high angle cross-beds that dip landward ($\sim 20^\circ$ at $294 \pm 5^\circ$ azimuth; indicating south-easterly winds during deposition) (Table 3.11). Between 4-1bi and 4bii is a truncation surface that indicates a period of short period of subaerial exposure and erosion. 4-1bii has numerous exposed karst features (or possibly tree casts) in the form of solution pipes (up to 200 mm in diameter); these would indicate an extended period of subaerial exposure (Figure 3.22). This is also recorded in the form of a thick, although poorly developed (pale colouring) palaeosol overlying the dune unit. The upper portions of 4-1bii are essentially featureless (except for some scattered rhizoliths) where they contact the overlying palaeosol (4-1c). The palaeosol has several thin, continuous calcrete laminae or solutional rinds running through it (Figure 3.22a). Unit 4-1d is another aeolianite that has landward dipping cross-bed sets. These beds dip approximately 18° with an azimuth of $295 \pm 5^\circ$, at the 95% confidence interval (Table 3.11); hence, they have shared a similar depositional wind regime with unit 4-1bii. Unconformably overlying this is a palaeosol unit (4-1e); although only a small section of this unit is visible, and it is difficult to discriminate. Most of the upper areas of this outcrop are obscured by low coastal vegetation, and so identifying this upper unit that overlies the palaeosol (4-1e) and underlies the calcrete (4-1f) is not possible; however, it is



Figure 3.21: Bottom sets and cross-bed sets of unit 4-1a. Note the presence of solution pipe features in 4-1aii, and the erosional truncation surface bounding 4-1ai and 4-1aii. Note: dip azimuths of approximately 295°, with bedding dips of approximately 20°.

Table 3.10: Lithostratigraphic characteristics of section 1 at site PB4

Unit number	Lithostratigraphic unit	Description	Munsell colour	Grain size	Grain sphericity	Grain sorting
4-1g	Holocene cliff top dunes	Unconsolidated dune sand, abundant vegetation cover	2.5Y 7/1 Pale brown	Coarse/ medium	rounded	Moderately sorted
4-1f	Calcrete	Indurated thick, blocky calcrete.	7.5YR 8/3 Pinkish white	Very fine	--	--
4-1e	Palaeosol	Weakly developed palaeosol.	--	--	--	--
4-1d	Aeolianite	Consolidated bioclastic carbonate sand, prominent steep landward dipping beds.	10YR 8/2 Very pale brown	Fine/ medium	Sub-rounded/ rounded	Well sorted
4-1c	Palaeosol	Thick, weakly developed palaeosol characterised by thin calcrete or solutional laminae.	--	--	--	--
4-1bii	Aeolianite	Consolidated bioclastic carbonate sand, prominent, steep landward dipping beds.	10YR 8/1 White	Fine	Sub-rounded	Well sorted
4-1bi	Aeolianite	Consolidated bioclastic carbonate sand, prominent low angle beds.	10YR 8/1 White	Fine	Sub-rounded	Well sorted
4-1a	Aeolianite (?)	Indurated basal calcarenite, extremely hard.	--	--	--	--

Third party source; Images redacted at request of thesis author

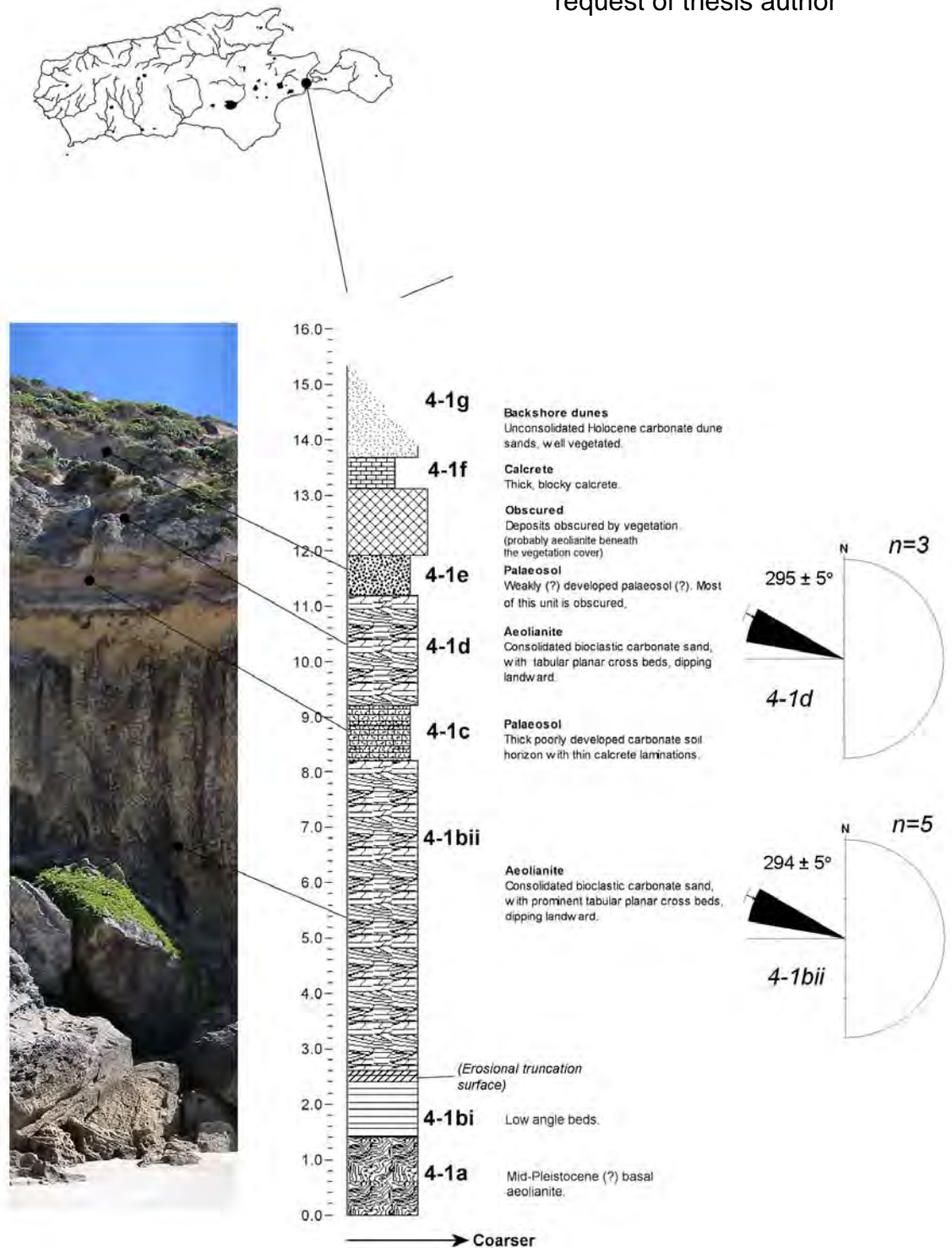


Figure 3:22a: Generalised stratigraphic log for section 1 of site PB#4 (RH inset satellite image Google Earth, 2010).

likely that—based upon observations undertaken on the eastern side of this headland—the obscured unit is an aeolianite. A thick blocky calcrete (4-1f) caps the underlying units, and this in turn is overlain by vegetated Holocene cliff top dunes. Figure 3.22a details the general stratigraphy for the section.

PB4 Section 2

Section 2 is the eastern side of the PB4 headland. This section comprises 8 discernable units (Table 3.12, Figure 3.22b and 3.23), and although this is a prominent site much of the bedding in the aeolianite units is obliterated or covered by solutional crusts or vegetation. The basal unit (4-2a) is an extremely hard, indurated calcarenite that may be a remnant of an older dune sequence, possibly Mid- or Early-Pleistocene; most of which has removed by erosion. These beds may have acted as an anchor point for later aeolian deposition. Above this unit there are a series of low angle beds (4-2bi) that form the bottom sets of unit 4-2b; the upper beds (4-2bii), although mostly hidden by slump and vegetation, dip landward. These beds are unconformably overlain by palaeosol 4-2c. This unit is a weakly developed palaeosol which is approximately 1 m thick in places; it is quite featureless and makes clean sharp contact with the underlying and overlying units. Above the palaeosol is unit 4-2d, an aeolianite that has low angle bottom set beds (4-2di) and high angle cross-bed sets (4-2dii). Again, most of the bedding is concealed by crusts, slump or vegetation; however, some bedding orientations could be measured (Table 3.13). Bedding tended to dip at approximately 31° with an azimuth of $330 \pm 7^{\circ}$, at the 95% confidence interval, signifying a south-easterly wind regime for deposition.

Table 3.11: Compiled bedding vector data for the PB4 headland (section 1—units 4-1b and 4-1d).

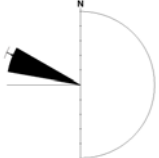
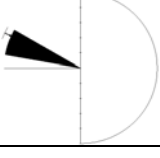
Lithostratigraphic unit	Number of measurements	Sector angle (degrees)	Mean direction (degrees)	Rose diagram
Aeolianite (4-1bii)	5	20	294 ± 5	
Aeolianite (4-1d)	3	20	295 ± 5	

Table 3.12: Lithostratigraphic characteristics of section 2 at site PB4

Unit number	Lithostratigraphic unit	Description	Munsell colour	Grain size	Grain sphericity	Grain sorting
4-2h	Holocene cliff top dunes	Unconsolidated dune sand, abundant vegetation cover	2.5Y 7/1 Pale brown	Coarse/medium	rounded	Moderately sorted
4-2g	Calcrete	Indurated thick, blocky calcrete.	7.5YR 8/3 Pinkish white	Very fine	--	--
4-2fii	Aeolianite	Consolidated bioclastic carbonate sand, landward dipping beds.				
4-2fi	Aeolianite	Consolidated bioclastic carbonate sand, low angle beds				
4-2e	Palaeosol	Weakly developed palaeosol.	--	--	--	--
4-2dii	Aeolianite	Consolidated bioclastic carbonate sand, landward dipping beds.	10YR 8/2 Very pale brown	Fine/medium	Sub-rounded/rounded	Well sorted
4-2di	Aeolianite	Consolidated bioclastic carbonate sand, low angle beds	10YR 8/2 Very pale brown	Fine/medium	Sub-rounded/rounded	Well sorted
4-2c	Palaeosol	Thick weakly developed palaeosol characterised by thin calcrete or solutional laminae.	--	--	--	--
4-2bii	Aeolianite	Consolidated bioclastic carbonate sand, prominent steep landward dipping beds.	10YR 8/1 White	Fine	Sub-rounded	Well sorted
4-2bi	Aeolianite	Consolidated bioclastic carbonate sand, prominent low angle bottom set beds.	10YR 8/1 White	Fine	Sub-rounded	Well sorted
4-2a	Aeolianite	Indurated basal aeolianite, extremely hard.	--	--	--	--

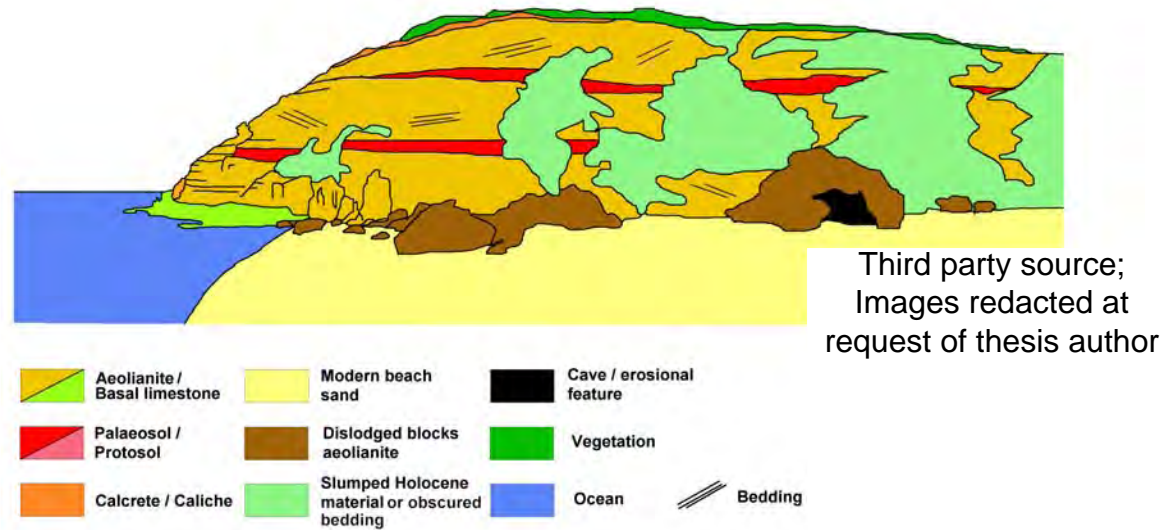


Figure 3.22b: Site PB4 section 2 is displayed here as a merged panorama (the image has some distortion towards the edges). In the top graphic the individual units have been assigned different colours to make them more apparent. The red line on the satellite image (inset) shows the approximate extent of the measured section (Google Earth, 2010). This site is relatively high, at approximately 17 m ASL.

Unit 4-2e is a poorly developed palaeosol that has an abundance of broken carbonate clasts (gravel and cobble sized) scattered through the horizon. The unit is obscured in places; however, it can be traced part the way around the headland. The clasts may have originated from a covering calcrete crust that broke up as a result of subaerial weathering, and were incorporated into the underlying material during pedogenesis. Conformably overlying the palaeosol is the uppermost aeolianite (4-2f); this unit contrary to that found in the lower aeolianites has a bed dip direction (where such bedding can be discerned) predominantly towards the south-east, rather than the north-west. The unit also exhibits low angle bottom set beds (4-2fi) contacting the palaeosol. The upper high angle cross-beds (4-2fii) have a dip angle of approximately $20\text{--}25^\circ$, with an azimuth of $148 \pm 26^\circ$, at the 95% confidence interval (Table 3.13). There are also present some high angle beds that dip towards the north-west; although the relationship between these beds and the ones that dip in the opposite direction is unknown. This is due to the presence of obscuring crusts, slumped material or vegetation.

Table 3.13: Compiled bedding vector data for PB4 headland section 2 (Units 4-2dii and 4-2fii).

Lithostratigraphic unit	Number of measurements	Sector angle (degrees)	Mean direction (degrees)	Rose diagram
Aeolianite (4-2fii)	8	20	148 ± 26	
Aeolianite (4-2dii)	5	20	$330 \pm 7^\circ$	

3.4.2.5 Site PB5

Site PB5 is located on the far eastern end of Pennington Bay and forms the bounding headland for the embayment (Figure 3.2). This is a high site at around 20-23 m at the highest point. Deeply dissected, unconsolidated Holocene dunes cover the top of the headland; these are well vegetated and quite thick in places

Third party source; Images
redacted at request of thesis
author

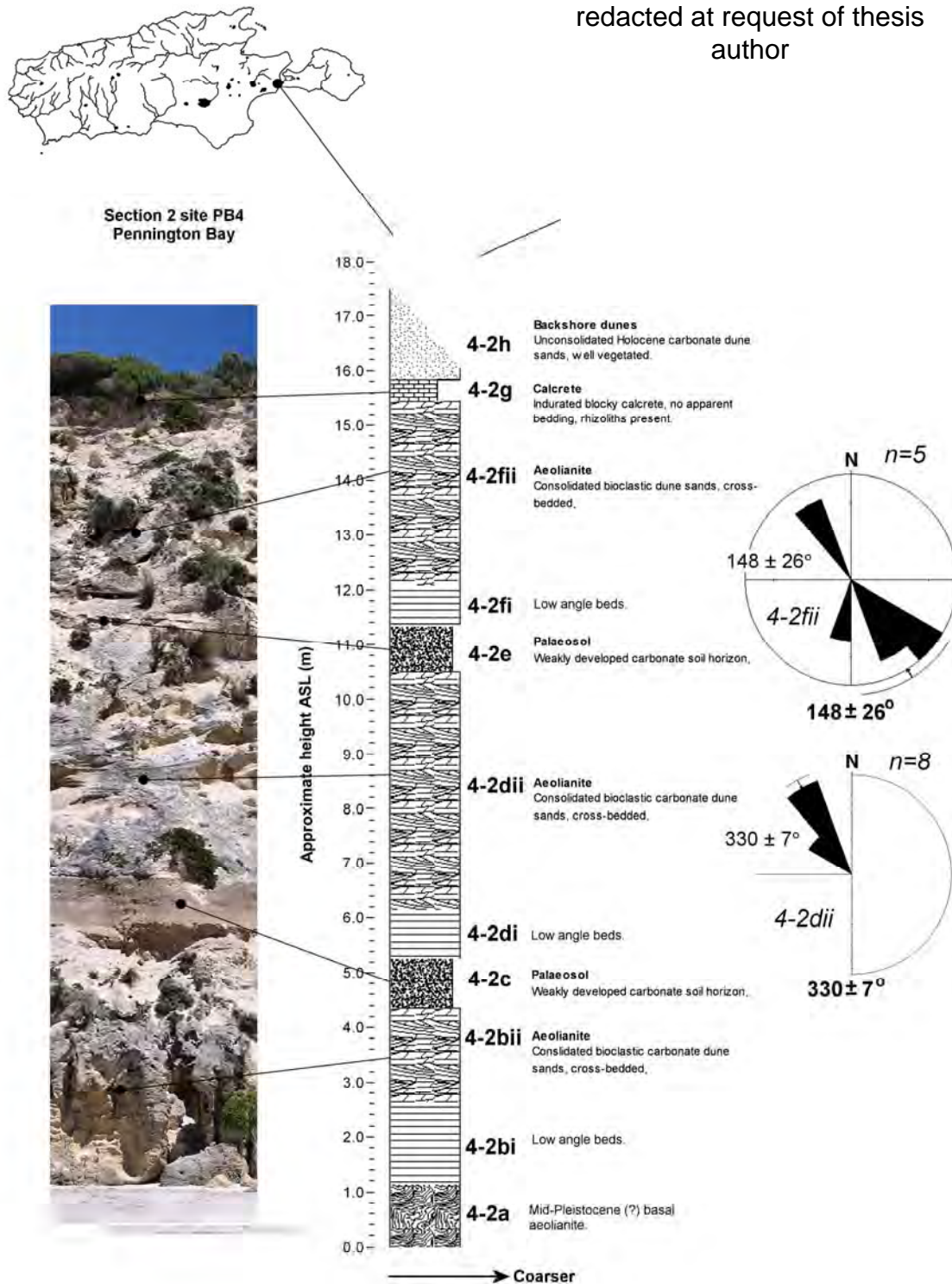


Figure 3.23: Generalized stratigraphic log for section 2 at site PB4 (RH inset satellite image Google Earth, 2010).

at 3-4 m. The site comprises apparently 11 or possibly 12 different units (see Table 3.14, Figure 3.24 and 3.25)—the unit under the uppermost calcrete (5j) is obscured by vegetation and slumping sediment. There are 4 discernable aeolianite units, 3 palaeosols, 3 calcretes (the middle calcrete is discontinuous and indeed may be a palaeosol (pink colouring); although its height and inaccessibility made this difficult to establish. The lower calcrete is laminated and weathered), and the cliff top Holocene dunes. The lowest unit (below sea-level) in the sequence (5a) is an extremely hard calcarenite which is pervasive around the bay. This calcarenite as iterated previously may be the remnant of an older dune or marine sequence, possibly middle or early-Pleistocene. At this site it also forms a broad Holocene rock platform arcing around the front of the headland. Unit 5a is overlain by a weathered low angle bedded aeolianite (5b). Above 5b is a thick palaeosol (5c) that is divided through the middle by calcrete laminae. This unit is classified into three sub-units: 5ci has broken pieces of rhizolith disseminated throughout; 5cii a very weathered calcrete characterized by thin laminae and 5ciii the upper part of the palaeosol. The portions of 5ciii which contact with the overlying aeolianite exhibit abundant carbonate nodules and rhizocretions. Unit 5d is a cross-bedded aeolianite unit that is characterised by many solutional features in the form of solution pipes; in this respect it is very similar to unit 4-1bii at site PB4 (Figures 3.20, 3.21, and 3.22a). It is plausible to assume that this is indeed the same unit. A relatively thin palaeosol (5e) unconformably overlies the aeolianite; this palaeosol unit was inaccessible and lacks detailed description. Above this is another aeolianite, unit 5f. This unit exhibits some of the most complex bedding of any of the aeolianite units discussed in this section; although, this may be more to do with its scale than anything else. Unit 5f is the thickest unit examined at Pennington Bay, and ranges up to 8 m thick in places.

The most striking observation that can be made at this site is the planar nature of the lower palaeosol units (5c and 5e). Certainly the planation of the aeolianite underlying the 5c palaeosol can be explained by wave cutting at a time of similar sea-level to the present (i.e. the formation of a rock platform). However, given that the 5d aeolianite is on average ~7 m APSL, its mode of planation is a more difficult to explain. It may be attributable to the position of the water table

during the period of soil formation; however, this is conjecture. These units as with their counterparts on the western bounding headlands (site PB4) probably represent the oldest sequences in Pennington Bay.

Where possible observations of bedding vectors were recorded. This was undertaken for 3 of the aeolianite units: 5b, d, and f. Unit 5b exhibited predominantly level beds, although there were some landward dipping beds that averaged at approximately 5° of dip, with an azimuth of $343 \pm 9^\circ$, at the 95% confidence interval (Table 3.15). This indicates a south-southeasterly wind direction during deposition. Because of the difficulty in accessing unit 5d only a few observations could be recorded ($n=3$); nevertheless these data ($331 \pm 10^\circ$ at $\sim 5^\circ$ of dip) indicate a southeasterly wind direction during deposition. Unit 5f

Table 3.14: Lithostratigraphic characteristics of site PB5

Unit number	Lithostratigraphic unit	Description	Munsell colour	Grain size	Grain sphericity	Grain sorting
5k	Cliff-top dunes	Unconsolidated carbonate dunes, well vegetated, thickening inland	2.5Y 8/1 White	Fine	Rounded	Very well sorted
5j	Calcrete	Blocky calcrete, with rhizoliths	--	--	--	--
5i	Calcrete	Thin discontinuous calcrete, with possible palaeosol at contact with 5h	--	--	--	--
5h	Aeolianite	Consolidated bioclastic carbonate sand, predominantly low angle beds, upper portions often obscured	--	--	--	--
5g	Palaeosol	Thin palaeosol, with carbonate clasts throughout	--	--	--	--
5f	Aeolianite	Consolidated bioclastic carbonate sand, with complex cross-bedding	10YR 8/1 White	Very fine / fine	Sub-rounded/ rounded	Very well sorted
5e	Palaeosol	Thin palaeosol	--	--	--	--
5d	Aeolianite	Consolidated bioclastic carbonate sand, predominantly landward dipping beds.	10YR 8/3 Very pale brown	Very fine	Sub-rounded/ rounded	Very well sorted
5ciii	Palaeosol	Carbonate palaeosol, abundant calcrete clasts	7.5YR 6/3 Light brown	Fine	--	--
5cii	Calcrete	Thick, weathered, blocky calcrete, lower portions laminated	7.5YR 8/3 Pinkish white	Very fine	--	--
5ci	Palaeosol	Carbonate palaeosol, broken fragments of rhizolith disseminated	7.5YR 6/3 Light brown	Fine	--	--
5b	Aeolianite	Weathered, weakly consolidated bioclastic carbonate sand, low angle beds.	10YR 8/4 Very pale brown	Medium/ fine	Sub-rounded/ rounded	moderately sorted
5a	Aeolianite / marine (?)	Indurated basal calcarenite, extremely hard.	2.5YR 7/4 Pale yellow	Medium/ fine	Sub-angular / sub-rounded	moderately sorted



Third party source;
Images redacted at
request of thesis author

A



C

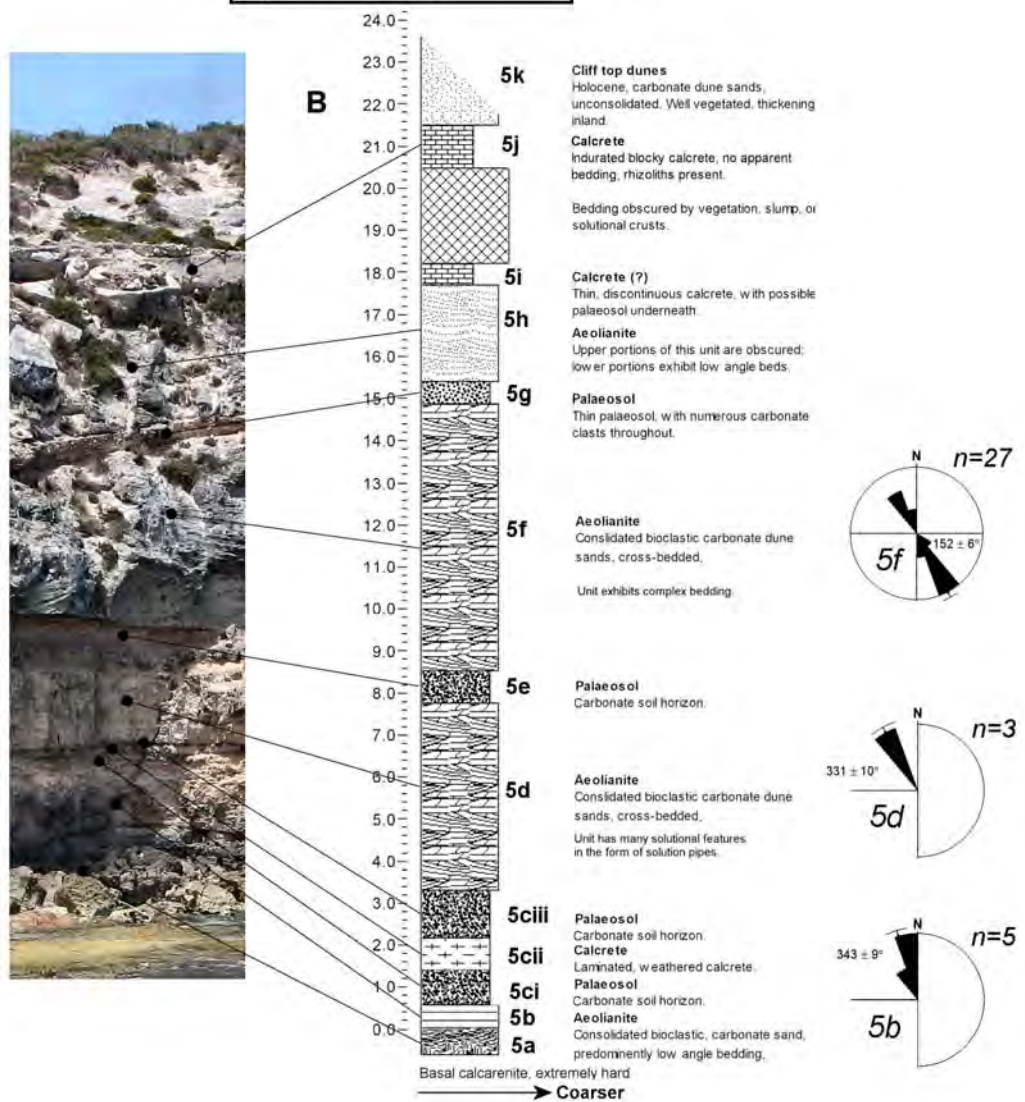

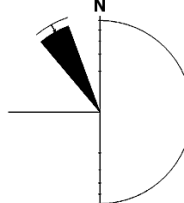
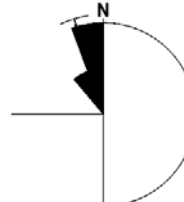


Figure 3.24: Generalized stratigraphic log for site PB5 (RH inset satellite image Google Earth, 2010).

Table 3.15: Compiled bedding vector data for PB5 headland (units 5b, 5d, and 5f).

Lithostratigraphic unit	Number of measurements	Sector angle (degrees)	Mean direction (degrees)	Rose diagram
Aeolianite (5f)	27	20	152 ± 6	
Aeolianite (5d)	3	20	$331 \pm 10^\circ$	
Aeolianite (5b)	5	20	343 ± 9	

exhibited the most complex bedding of all units in this section, and 27 observations were recorded. The mean azimuth was $152 \pm 6^\circ$, indicating winds from a northwesterly direction; however, several observations ($n=9$, at vector $\sim 330^\circ$) show wind directions also from the southeast. The complex bedding in this thick (~ 6 m) unit may then be due to, not only high carbonate production (i.e. the very thick unit), but also to deposition under two wind direction regimes. Dip angles for unit 5f ranged from 3 to 25° .

3.4.3 Stratigraphy of aeolianite at Bales Beach

Bales Beach lies on the south-coast of Kangaroo Island, approximately 38 km straight-line distance from Pennington Bay (Figure 3.1), in the Seal Bay Conservation Park. This site is similar to Pennington Bay, hosting strandline-parallel aeolianite / palaeosol couplets, and high headland outcrops. Two sections were examined at Bales Beach (Figure 3.26): Bales1, a length of low, scarped, complex aeolianite / palaeosol units that run parallel to the shoreline (which may represent a single MIS deposition) and Bales2 a large, high headland at the western end of the bay.

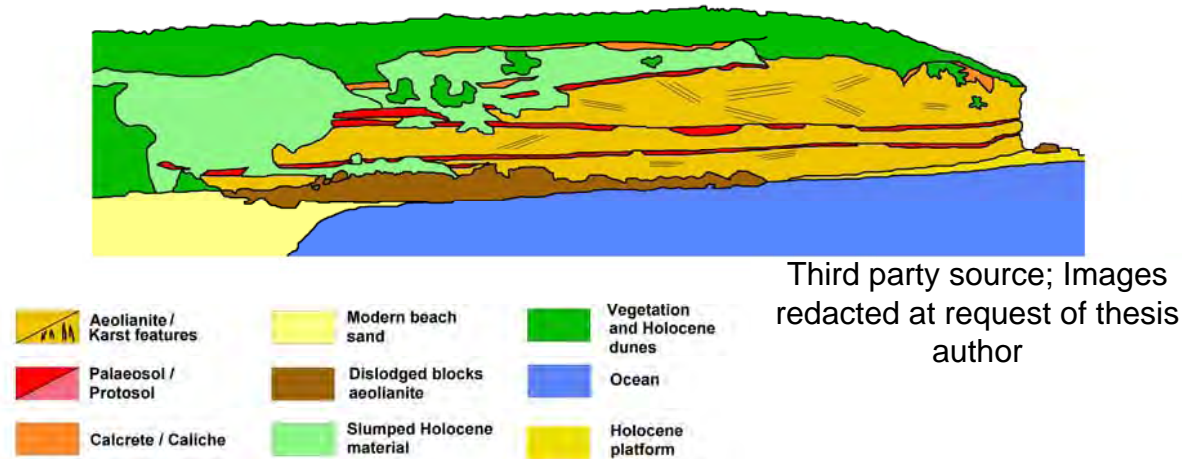


Figure 3.25: Site PB5 is displayed here as a merged panorama (the image has some distortion towards the edges), with units marked in yellow, white, and black. In the top graphic the individual units have been assigned different colours to make them more apparent. The satellite image (inset) shows the approximate extent of the measured section (Google Earth, 2010). This site is relatively high, at approximately 23 m ASL.

Table 3.16: Lithostratigraphic characteristics of sites Bales1 and Bales2

Unit number	Lithostratigraphic unit	Description	Munsell colour	Grain size	Grain sphericity	Grain sorting
BALES1						
1g	Backshore dunes	Modern/Holocene unconsolidated carbonate dunes, well vegetated	2.5Y 7/1 Pale brown	Coarse/ medium	rounded	Moderately sorted
1f	Calcrete	Blocky calcrete, with rhizoliths	7.5YR 8/2 Pinkish white	Very Fine	--	--
1e	Aeolianite	Weakly cemented carbonate dune sands	10YR 8/2 Very pale brown	Medium/ fine	sub- rounded / rounded	moderately sorted
1d	Palaeosol	Thin carbonate soil horizon, weakly cemented, with abundant calcrete clasts	7.5YR 6/3 Light brown	Fine	Sub- rounded to rounded	Moderately to poorly sorted
1c	Aeolianite	Weakly cemented carbonate dune sands	2.5YR 7/1 Light gray	Medium/ fine	sub- rounded / rounded	Poorly sorted
1b	Palaeosol	Thin carbonate soil horizon, weakly cemented, with abundant calcrete clasts	7.5YR 6/3 Light brown	Fine	Sub- rounded to rounded	Moderately to poorly sorted
1a	Aeolianite	Weakly cemented carbonate dune sands	10YR 7/3 Very pale brown	Medium/ fine	sub- rounded	moderately sorted / well sorted
BALES2						
2j	Backshore dunes	Holocene unconsolidated carbonate dunes, well vegetated	--	--	--	--
2i	Calcrete	Thick, blocky calcrete, with rhizoliths	--	--	--	--
2h	Aeolianite	Cemented carbonate dune foresets with prominent cross-bedding Brecciated exposure	--	--	--	--
2g	Subaerial exposure surface	surface, angular calcrete rubble, pedogenically modified matrix	--	--	--	--
2f	Aeolianite	Cemented carbonate dune foresets with prominent cross-bedding Brecciated exposure	--	--	--	--
2e	Subaerial exposure surface	surface, angular calcrete rubble, pedogenically modified matrix	--	--	--	--
2d	Aeolianite	Cemented carbonate dune foresets with prominent cross-bedding	--	--	--	--
2c	Palaeosol	Thin discontinuous carbonate soil horizon, weakly cemented, with abundant calcrete clasts	--	--	--	--
2b	Aeolianite	Cemented carbonate dune foresets with prominent cross-bedding	10YR 7/3 Very pale brown	Medium/ fine	sub- rounded	Well sorted
2a	Aeolianite / marine (?)	Indurated basal calcarenite, extremely hard.	2.5YR 7/4 Pale yellow	Medium/ fine	Sub- angular / sub- rounded	moderately sorted

3.4.3.1 Bales1

The Bales1 site is a low (<4 m high) series of aeolianite / palaeosol couplets that grade at around 6° towards the east. The calcrete mantle which covers the units grades downward (as do all units) and enters the modern beach sand below sea-level. The aeolianite scarp in this area of the bay is complex and the presented stratigraphic log (B) in Figure 3.27 is a composite of three large sections along the scarp—as most units do not present along the total length of the outcrop. Units at Bales1 may be present also as the uppermost units at the Bales2 site. However, it was not possible to reach these upper units to confirm this (see Table 3.16 for lithostratigraphical descriptions).

Third party source; Images redacted at request of thesis author

Figure 3.26: Satellite image of Bales Beach sites (Google Earth, 2008).

This site is characterised by 7 discrete units, that crop out discontinuously for approximately 300 m along the western end of the embayment. The succession is scarped due to undercutting by wave action. This has most likely occurred during the Holocene high sea-level (~+2 m APSL, Belperio *et al.*, 2002), and later storm surge.

The lowest unit in the succession (1a) is a weakly cemented aeolianite sand with little discernable bedding; the upper portions of this unit have abundant rhizocretions, and the lower portions can be characterised by occasional large rhizomorphs (i.e. large tree and root moulds) (see Figure 3.28). Unconformably overlying this is a relatively thin (approximately 0.3 to 0.4 m thick), weakly

developed palaeosol (unit 1b), characterised by a thin laminated calcrete carapace, and small clasts of calcified broken root disseminated throughout (see Figure 3.28). This unit grades down towards sea-level in an easterly direction, becoming more indurated, and strengthening in colour (see Figure 3.29). Above this is another weakly cemented carbonate sand, unit 1c; this unit has some faint bedding, although it is mostly obliterated. Present also at the overlying palaeosol (1d) boundary are numerous calcrete clasts and thin crusts. The 1d palaeosol is similar to the 1b palaeosol, although it is much thinner in section (approximately 0.2 m thick, and thinner in places). The overlying dune unit (1e) is weakly cemented and resembles units 1a and 1c, although it does not exhibit bedding (see Figure 3.29).

The sequence is mantled by a thick (0.3 m to 0.6 m thick) blocky calcrete, and the entire sequence dips or grades towards the east at approximately 6°. All units, including the mantle, disappear beneath the modern beach sediment. Well vegetated backshore dunes overlie the succession; these are unconsolidated carbonate dunes that thicken considerably inland: similar to dunes overlying Pleistocene successions at Pennington Bay.

The comparatively low height of the sequence (~4 m to 5 m ASL), in relation to the large number of thin units, alludes to a relatively slow rate of deposition during a single MIS: in all probability MIS 5. It is possible the dune units (1a, 1c, and 1e) represent the Last Interglacial, and subsequent interstadials (i.e. MIS 5e, c, and a), and the thin palaeosols indicate short hiatuses in deposition that may have occurred during the stadials (i.e. MIS 5d and b). It is also possible that the sequence is representative only of MIS 5e, and short depositional pauses that may have occurred during *that* substage.

Bedding was not generally apparent in the dune units; this is most likely due to disruption by vegetation roots and rootlets during hiatuses. The morphology of the soil unconformities is consistent with formation as a root-zone horizon (i.e. a 'B' horizon) during a depositional pause, with roots and rootlets sometimes extending into the underlying dune.

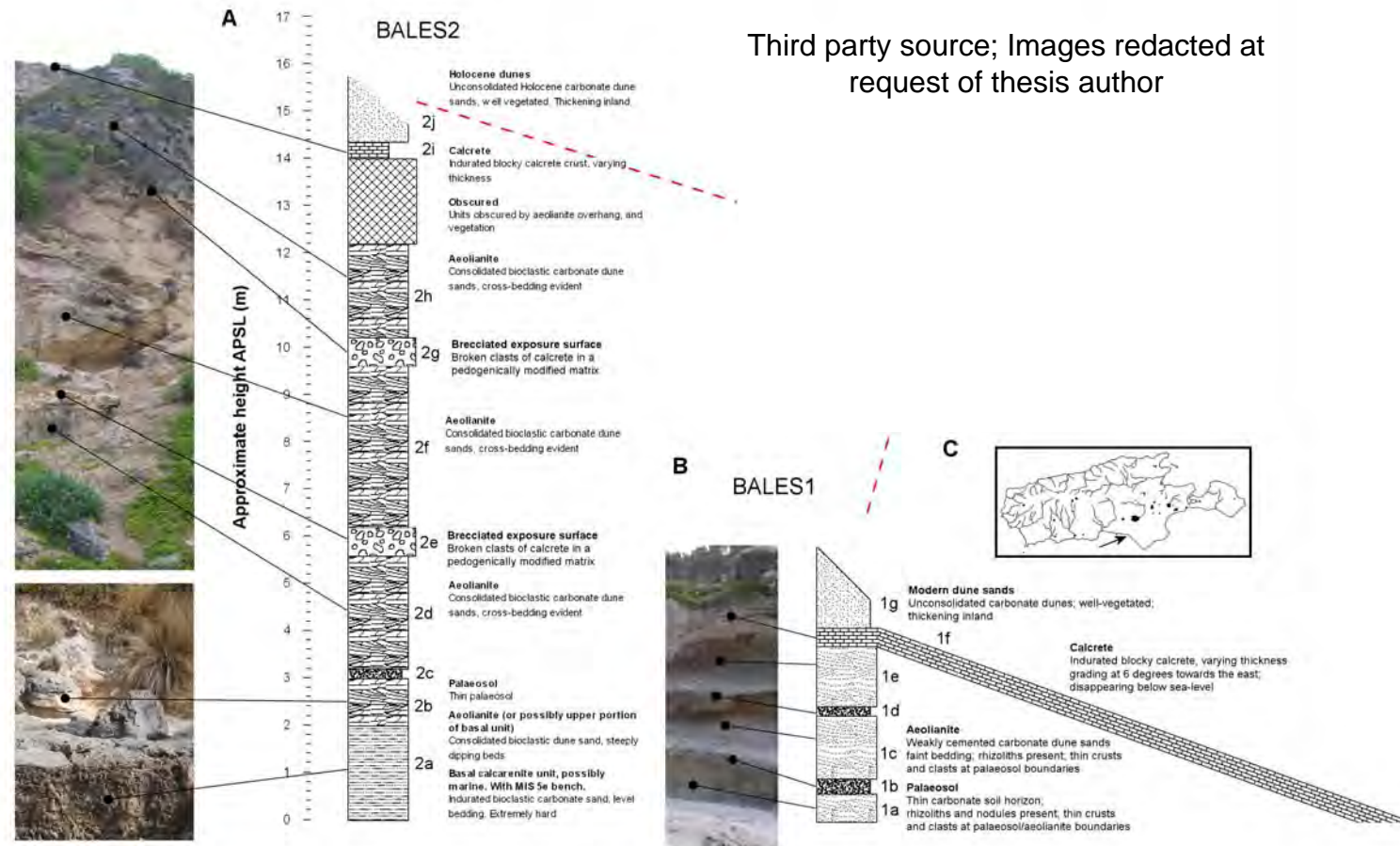


Figure 3.27: Generalised stratigraphical logs for Bales Beach site Bales1 (B) and Bales2 (A). The insets (C) are a satellite image (Google Earth, 2008), showing the location of the sites in the embayment, and a Kangaroo Island location map.



Figure 3.28: Units 1a and 1b at site Bales1. Note thin calcrete over palaeosol, and rhizomorphs in aeolian unit (rock hammer for scale 33 cm).

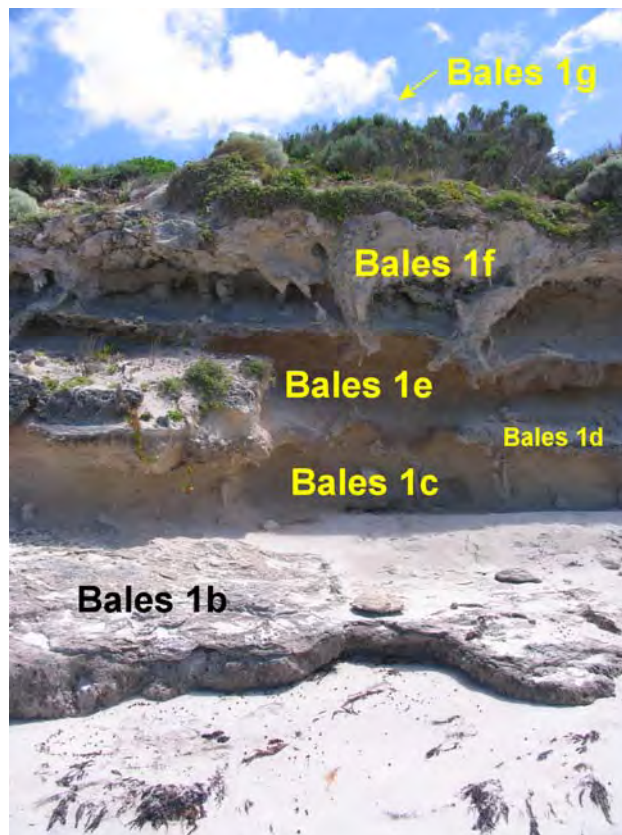


Figure 3.29: Units 1b, 1c, 1d, and 1e (unit 1g [backshore dunes] is not visible in this photograph). Note rhizomorphs in aeolian unit 1c (similar to the lower 1a), and abundant large casts in the upper calcrete (1f).

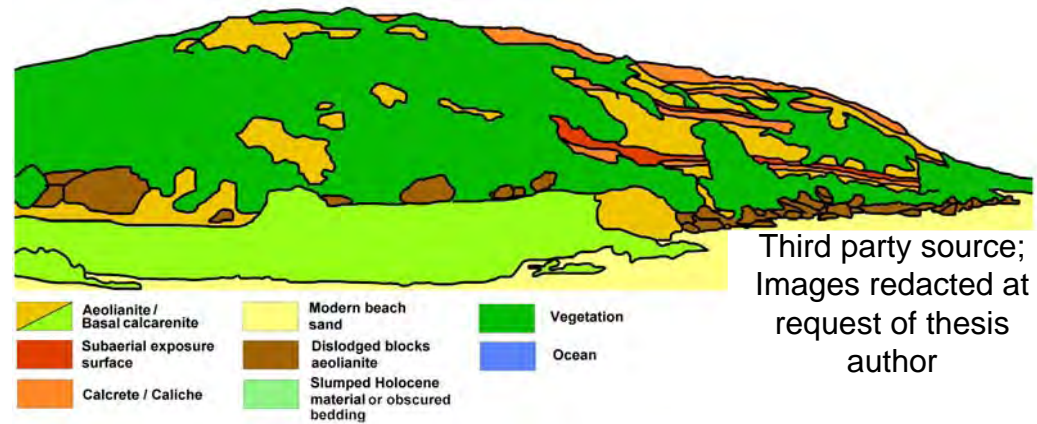


Figure 3.30: Site Bales2 is displayed here as a merged panorama (the image has some distortion towards the edges), with units marked in yellow. The top image depicts the individual units which have been assigned different colours to make them more apparent. The satellite image (inset) shows the approximate extent of the measured section (Google Earth, 2008). This site was mostly obscured by vegetation and slumping material. Note, this site is relatively high, at approximately 16 m ASL.

3.4.3.2 Bales2

As with the Pennington Bay western and eastern headlands the Bales2 site is a high, complex sequence of aeolianites, and palaeosols, and also brecciated exposure surfaces. This site lies at the western end of the Bales Beach bay and forms the beginning of a high cliffed section of coast (see Figure 3.26). The basal portion of the sequence is an extremely hard indurated calcarenite (unit 2a), most likely of the same or similar antiquity (early or perhaps middle Pleistocene in age) to that found as the lowest unit at the Pennington Bay headland outcrops (see Figure 3.27 and 3.30). A bench has formed in the unit at approximately +2 m APSL, suggesting erosion during a higher sea-level, probably the Last Interglacial highstand (MIS 5e). Site Bales2 was largely inaccessible and only the lower aeolianite was able to be sampled (unit 2b). Little could be sampled from this site as it was quite precipitous, and not possible at the time to scale; much of the outcrop is concealed by a thick covering of vegetation, as can be seen in Figure 3.30.

Unit 2b, a moderately cemented aeolianite (see Table 3.16), conformably overlies the basal calcarenite. This unit was sampled for both AAR and luminescence dating purposes. A thin, rubbly palaeosol unconformity (unit 2c) overlies this, and is mostly obscured by vegetation. There are two other couplets above this: 2d/2e, an aeolianite (2d) similar to 2b, and a brecciated exposure surface (2e), that grades to what appears to be a thick, massive calcrete, and 2f/2g which is the same (see Figure 3.31). Above 2g is another aeolianite (2h) which is mostly obscured in the upper portions. The entire sequence is capped by a blocky/laminar calcrete (2i), with a covering of unconsolidated cliff-top dunes (2j) further back from the precipice (Figure 3.27 and 3.30). The upper calcrete is characterised by solutional features (karst and caves), and what appear to be laminations surrounding calcified root or tree columns (see red arrow, and lower RH inset in Figure 3.31). The lower margins of the 2i calcrete may have undergone weathering associated with the presence of a past water table at this level, i.e., at the meteoric vadose/phreatic boundary.

Few dip and azimuth directions in the aeolianite bedding were recorded at this site. The lower aeolianite (2b) had dip angles at approximately 20° at 107°

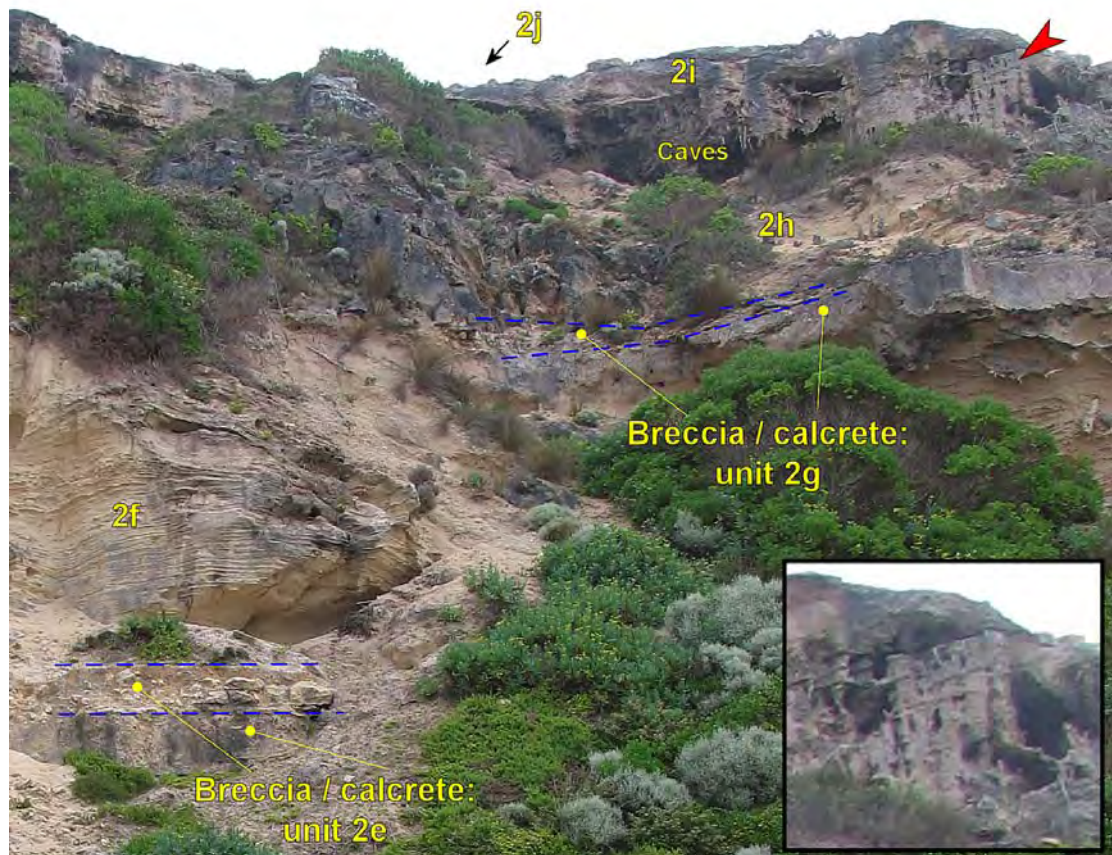


Figure 3.31: Upper units at Bales2 site, note brecciated exposure surfaces, and karstified top calcrete (2i).

azimuth, indicating a west-north-westerly wind direction during deposition. The 2d aeolianite unit had predominantly low angle seaward dipping beds (4° - 6°) with azimuths ranging around 190° . This would indicate a possible north-north-easterly wind direction. Unit 2f was similar to 2d, and 2h, where discernable had predominantly level beds, although there were some high angled beds ($\sim 30^{\circ}$ of dip) with azimuths at around 65° —indicating a south-westerly wind regime. The azimuthal data were not very good at this site as the orientation of the outcrop was not perpendicular to the plane of the beach, i.e., the bedding planes were probably not being viewed laterally.

The Bales2 succession is interpreted to represent several marine isotope stages, in all likelihood ranging from the middle to late Pleistocene. The lack of distinct palaeosol horizons is unusual; the brecciated surfaces may be an indication of short pauses in carbonate deposition. This could mean that the sequence may only represent 1 or 2 marine isotope stages, with the

breccia/calcretes representing stadial pauses, and the lower thin palaeosol (2c) perhaps representing a longer glacial pause.

The Bales2 site is difficult to reconcile with the Pennington Bay sites, which have often well-developed palaeosol units. The variations could be due to local differences in depositional and groundwater dynamics between the two areas, with also, perhaps, more rapid accretion occurring at Bales Beach. Regardless, this is all conjecture until the upper units at Bales2 can be comprehensively sampled and dated.

3.4.4 Stratigraphy of the Point Ellen Formation, aeolianite, and other near-shore deposits at Vivonne Bay

Vivonne Bay and Point Ellen are located on the southern coast of Kangaroo Island (Figure 3.1). The bay is host to a variety of Pleistocene deposits; in particular it hosts the type section of the Point Ellen Formation—a small outcrop exhibiting a richly fossiliferous set of shell beds. The following discussions examine the stratigraphy of the Point Ellen Formation and also some of the aeolianite deposits found around the south-western end of Vivonne Bay. There are 3 areas examined around the bay (PE2, 3 and 4), as well as a complete mapping of the Point Ellen Formation (PE1), at Point Ellen (Figure 3.32).

This formation is considered to be the equivalent of the richly fossiliferous Roe Calcarenite (on the basis of faunal comparisons) found in Western Australia (these molluscs were first described by Ludbrook in 1978) in the western portion of the Eucla Basin, and the Burnham Limestone which outcrops along the Fleurieu Peninsula, in southern South Australia.

3.4.4.1 The Point Ellen Formation

Located on the western point of Vivonne Bay (Figure 3.32), Point Ellen hosts a spectacular series of weakly to strongly cemented shell beds (coquinite) that are interpreted to be early Pleistocene in age (Ludbrook, 1983; Milnes *et al.*, 1983; Ludbrook, 1984). The formation, first defined by Milnes *et al.* (1983), crops out to a limited extent at 'Table Rock' Point Reynolds, Pennington Bay and at Cape Willoughby; however, the largest and most extensive outcrop is at

Third party source; Images redacted at request of thesis author

Figure 3.32: Location of sites around Vivonne Bay, and Point Ellen. The upper right inset shows the geographical location of the bay (small black arrow); the red spots are mapped areas, and the numbered blue spots (inset) are the locations of 1) the Point Ellen type site for the Point Ellen Formation, 2) the Point Ellen Formation at Point Reynolds, Pennington Bay, and 3) the Point Ellen Formation at Cape Willoughby (image courtesy of Google Earth, 2008). Note the north-easterly alignment of Holocene parabolic dunes in the upper right of the image.

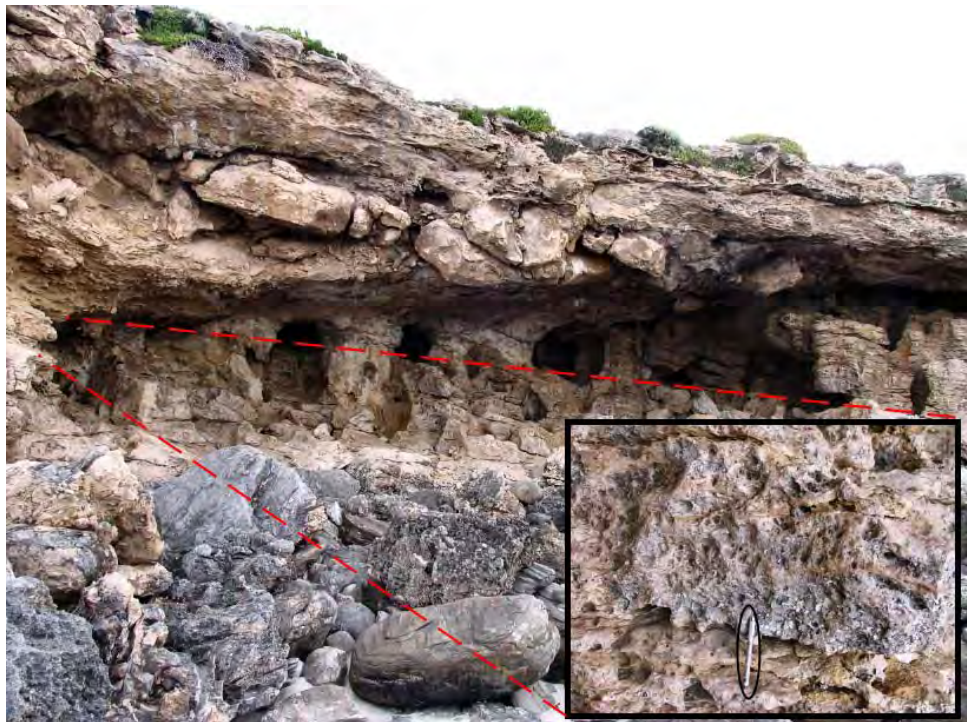


Figure 3.33: Conspicuous solution pipes running through the Point Ellen Formation at site A; the calcrete capping exhibits numerous small dolines or sink-holes. The expanded lower right inset shows the fenestrate-like texture of the shelly unit, as gastropods have been weathered out of the face, leaving behind depressions.

Third party source;
Images redacted at
request of thesis
author

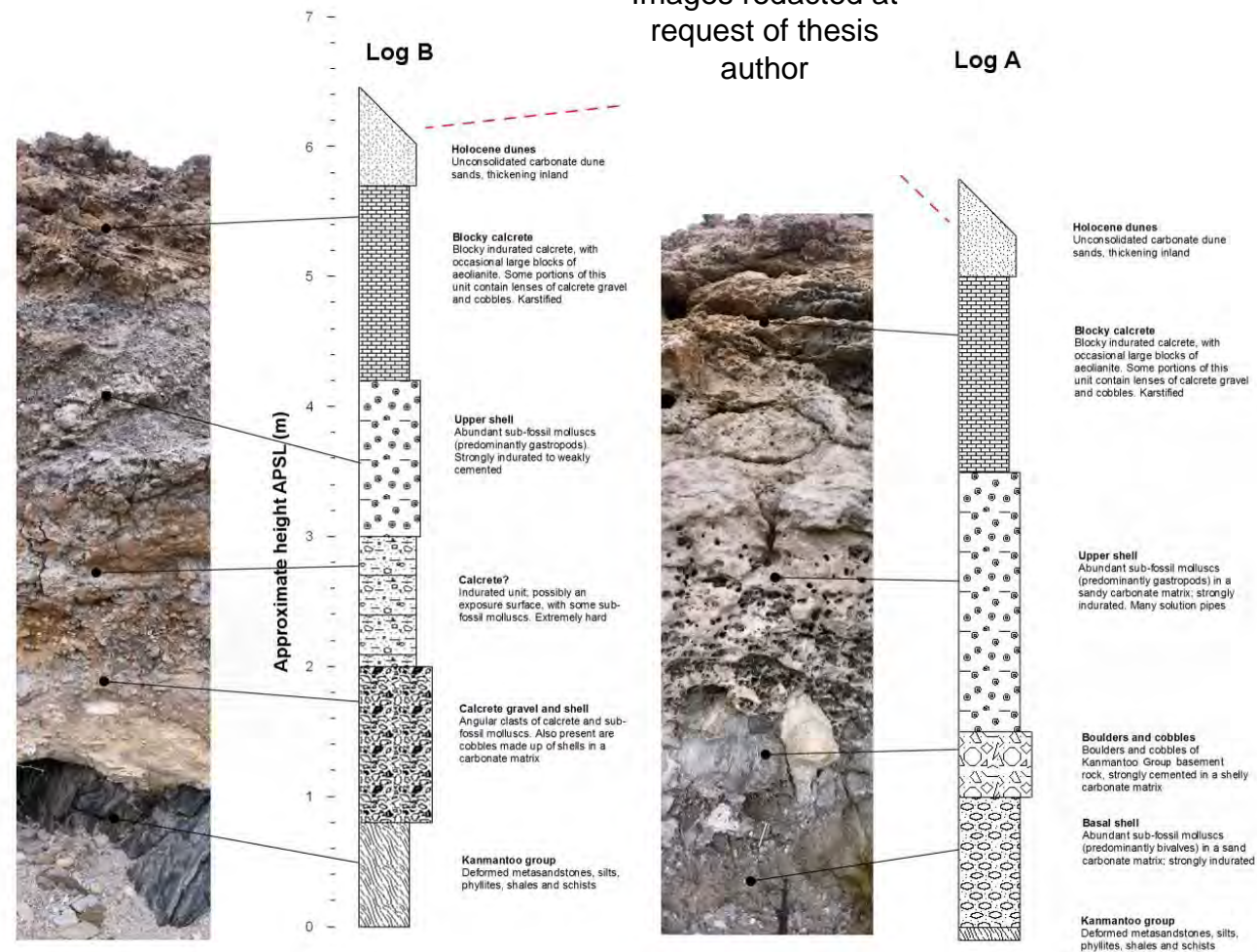


Figure 3.34: Stratigraphic logs of the Point Ellen Formation at Point Ellen, and Vivonne Bay, Kangaroo Island. The logs illustrate the complexity of the formation and the approximate thickness of the units (inset satellite image courtesy of Google Earth, 2008).



Figure 3.35: Panorama of the Point Ellen Formation at site A, showing the positions of the various units outlined in Figure 3.2 Log A.

Point Ellen (Figure 3.32 inset). The Point Ellen Formation is also present on the mainland at Cape Jervis and Naracoorte (Ludbrook, 1983; 1984). A strontium isotope ($^{87}\text{Sr}/^{86}\text{Sr}$) age of 1.2 Ma (no uncertainties were reported) was obtained for the upper portion of the formation (3 m APSL) at Point Reynolds, Pennington Bay by Belperio (1995), supporting the early Pleistocene age assigned to the formation. The formation infills the irregular surface of a basin in the bedrock and has a lateral extent of approximately 300 m at Point Ellen, and ranges from up to ~2 to ~4 m in thickness (thicker than originally reported in Milnes *et al.*, 1983). It unconformably overlies the Cambrian Kanmantoo Group (Section 1.4.1, Chapter 1) and consists, generally, of three discrete units (Figure 3.34 and 3.35): a basal shell unit, a cobble unit, and an upper shell unit; capped by a thick, blocky, karstified calcrete. The entire area is host to many sink-holes and solution pipes that extend through the formation (Figure 3.33 and 3.35).

Basal shell unit (Figure 3.34 Log A)

This unit ranges up to ~1 m thick. It unconformably overlies the Kanmantoo Group basement rocks (metasandstones) and consists of marine shell (Figure 3.36)—mainly large bivalves (e.g. *Miltha hamptonensis* [Ludbrook] 1969, *Anodontia sphericula* [Ludbrook] 1959, and *Tellina* sp. [Linnaeus] 1758)—weakly to strongly cemented in a very pale brown (Munsell 10YR 8/2) coarse-fine biogenic carbonate grain matrix (Figure 3.34, log A). The matrix is composed predominantly of comminuted shell, foraminifer tests, bryozoan and echinoid debris, and calcareous algae; with a small fraction of quartz and heavier minerals (~11% by dry mass).

The generally excellent condition of the foraminifers (in particular *Elphidium rotatum* [Howchin and Parr] 1938, *Marginopora vertebralis* [Blainville] 1830 [Figure 3.37], *Discorbis dimidiatus* [Jones and Parker] 1862, and *Triloculina trigonula* [Lamarck] 1804) found in this unit indicate *in situ* deposition, with little or no movement after the event. The basal shell unit is also present as discrete patches on the rock platform surrounding the outcrop; this indicates the possibility that the formation may have been far more extensive in the past (Figure 3.38). The upper units may have been scoured during later highstands.



Figure 3.36: Basal shell unit in section from an exposed patch on the rock platform. Note pen for scale (15 cm).

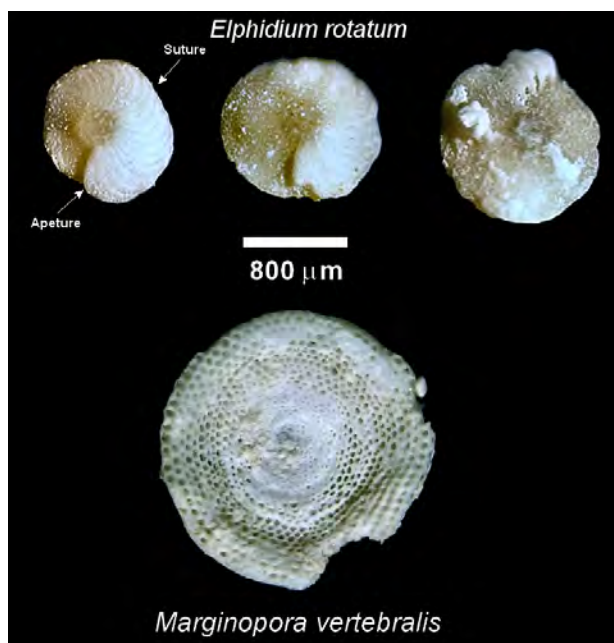


Figure 3.37: Three large examples of *Elphidium rotatum* and one of *Marginopora vertebralis* extracted from the basal shell layer of the Point Ellen Formation; note the excellent state of preservation for specimens that are probably in excess of 1 million years old. Note in particular the preservation of the fine morphology of the sutures and the apertures on the *Elphidium* examples.

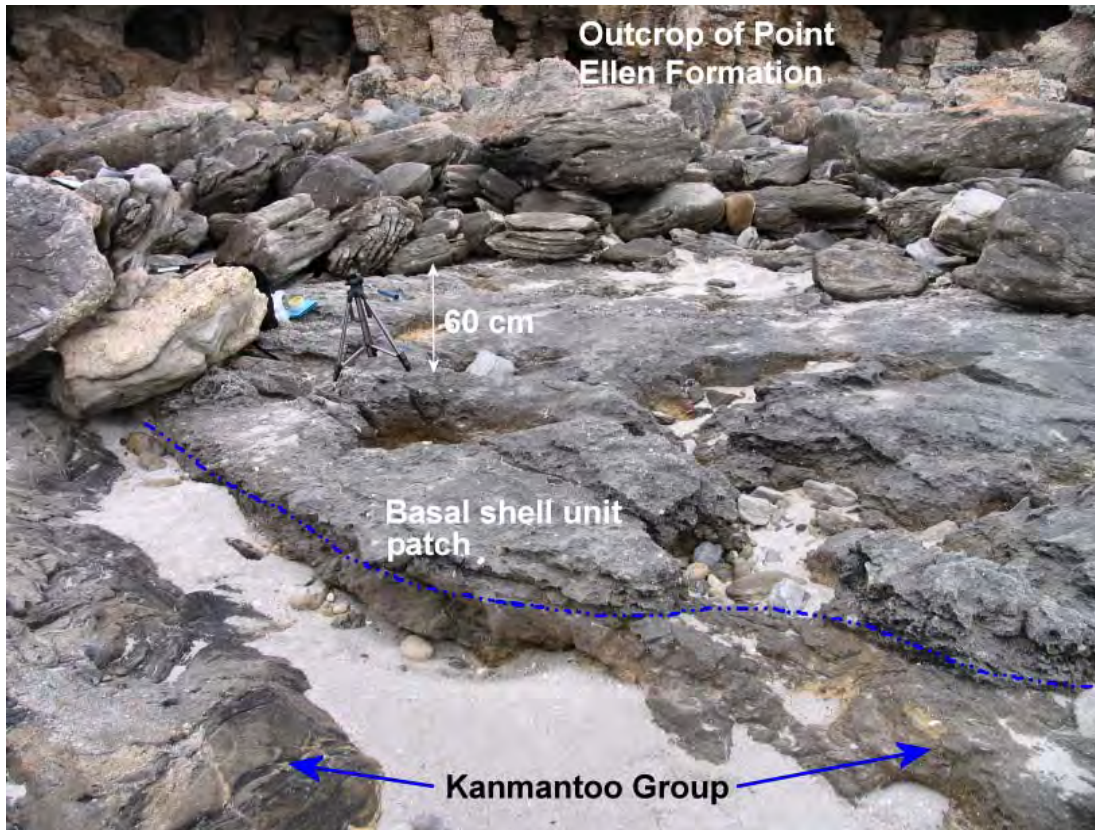


Figure 3.38: Point Ellen rock platform; patches of the basal shell are evident mid-field; note the deformed Kanmantoo Group basement: left and right foreground. The background shows the base of the outcrop. The rubble far mid-field may be derived from the cobble unit situated above the basal shell in the formation. Note: the camera tripod is 60 cm high.

This unit is only present at site B as a thin remnant at the sea-ward side of the section.

The basal shell unit was deposited under sea-level conditions higher than present; however, lower than when the deposition of the upper portions of the formation took place. This is supported by the observed absence of the basal shell layer at site B, at least in the section of the formation that is farthest from shore.

Cobble/boulder unit (Figure 3.34 Log A)

Boulders and cobbles of the Kanmantoo Group basement rock are cemented in a shelly carbonate matrix, consistent with the overlying unit (upper shell). This layer is approximately 0.5 m thick and is absent from the Formation at site B (as is the basal shell unit). This is most likely due to the shape of the basin and the sea-level at time of deposition (Figure 3.39).

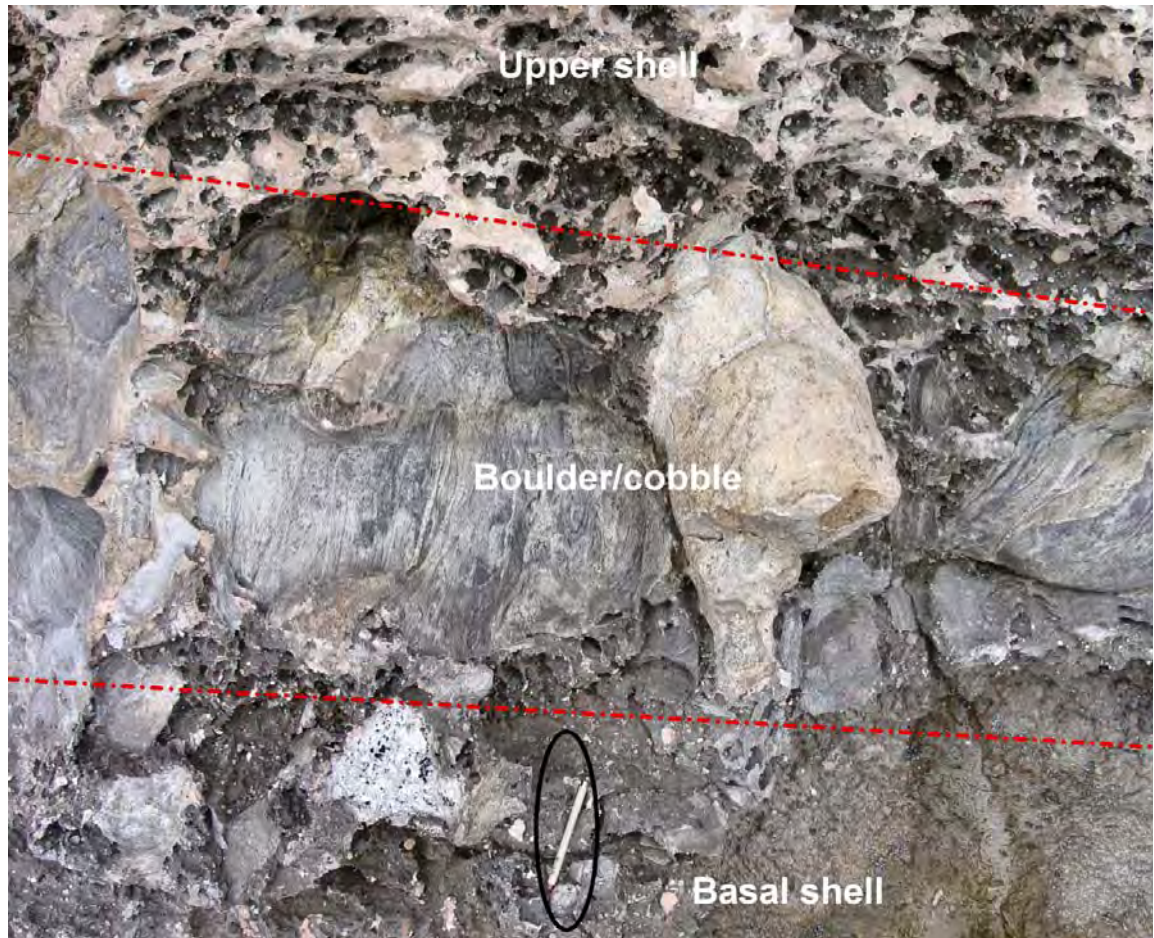


Figure 3.39: Unordered boulder/cobble unit at Point Ellen, site A; clast supported with upper shell matrix. Note pen for scale (15 cm).

This unit may have formed as a cobble / boulder beach, represent similar sea-level to the present, or it could be the result of storm deposition (where cobbles and boulders were pushed up above the high-tide mark during extreme events). Hence, It is possible that this unit formed under lower sea-level conditions than either the underlying or overlying shell beds.

As the boulders and cobbles are apparently cemented by a matrix comprised of the overlying shell bed sediments, the implication is that this unit is not contemporaneous with the underlying beds. It is likely the boulders and cobbles were later submerged and then buried when the upper shell unit was deposited during a higher stand of sea-level (Figure 3.34 Log A). This presupposes that tectonic uplift has not occurred since deposition (which is not entirely certain); although, at Cape Willoughby gentle warping has raised the Formation to around 10 m APSL.

Upper shell unit (Figure 3.34 Log A and B)

This unit is a variably cemented coquinite dominated by marine gastropod subfossils (bivalves are also represented). The most common being *Nerita milnesi* (Ludbrook) 1983 and a pelagic species *Hartungia dennanti chavani* (Ludbrook) 1978—the assemblage, which includes representatives from over 50 species, is indicative of a sheltered embayment on a rocky coast. According to Ludbrook (1983) *Hartungia* must have been moved onshore by winds and concentrated along with the rocky coast species. The unit overlies and cements the boulder/cobble layer at site A. At site B (Figure 3.34; Figure 3.40) the upper shell unit is more complex showing a lower gravelly section and a strongly indurated section (molluscs are relatively sparse in both), with a more weakly cemented and crowded upper section (it is from this section that the most accessible and best preserved gastropods are found). The gravelly, brecciated section may be talus derived from failing upper portions (due to wave-cutting during highstands) of the formation re-cemented in place; hence, the presence of angular shelly carbonate cobbles in the matrix.

The upper portion of the shell unit is densely crowded with gastropods suspended in a weakly cemented coarse-medium yellow (Munsell 10YR 7/6) carbonate grain matrix. The matrix is predominantly comminuted shell; foraminifera are poorly represented.

It is difficult to interpret what this part of the formation actually represents in terms of sea-level; particularly if tectonic uplift has taken place. Given that Nerites (which live in the littoral or supralittoral zones on rocky shores) dominate the molluscan species assemblage of the deposit, and the existence of modern equivalent shelly sands at the high-tide level, it is probable that the upper limit of this unit represents (if we discount uplift) something close to sea-level at the time of deposition: around 3-4 m APSL.

Calcrete (Figure 3.34 Log A and B)

The calcrete unit overlies the upper shell unit at both sites; it is variable up to ~1.8 m thick in places. It is blocky and dissected and is also deeply weathered in places; at these sites it is karstified with solution pipes running right through



Figure 3.40: Point Ellen Formation at site B.

to the lower units of the formation. At site B it is brecciated and rubbly near the contact with the upper shell unit—this could be scree from slope failure or evidence of extensive re-working of the profile. The calcrete may be derived from an aeolian unit deposited sometime after the formation; although, it is probably not of late Pleistocene origin, it is likely to have been deposited earlier than this given its current state.

3.4.4.2 Site PE 2 Vivonne Bay

Site PE 2 is located on the western edge of Vivonne Bay, south-east of the jetty (Figure 3.32 and 3.41), and is interpreted here to be representative of the Pleistocene Bridgewater Formation (see Chapter 2, and Boutakoff, 1963). The outcrop is cliffed indicating failure in the upper units due to undercutting at higher sea-level. Indeed, the aeolianite unit below the topmost calcrete has been eroded into a series of shallow caves at various places along the outcrop (Figure 3.42). This has happened, in all probability, during the Last Interglacial (LIG) highstand (on the basis that the caves are $\sim +3.5$ m APSL: approximate LIG sea-level). The base of the outcrop is strewn with broken boulders of aeolianite and calcrete derived from the upper units.

The formation at this site has three distinct units (although much of the middle section is obscured by vegetation and rubble): a basal calcarenite that is extremely hard and has been eroded into a raised edge platform in places, a moderately cemented aeolianite, and a topmost laminar to blocky calcrete.

Basal calcarenite (Figure 3.41 PE 2)

The basal calcarenite is a very strongly cemented limestone of marine or aeolian origin which varies greatly in thickness along outcrop (<1 m to ~ 2 m). Bedding is obliterated therefore it is difficult to classify the unit (this unit is probably related to similar basal calcarenites located at Pennington Bay, Bales Beach and Hanson Bay, and may be of middle Pleistocene age or older); although, at many locations these units extend offshore, which may lend strength to an aeolian origin of the deposit (i.e. deposition during a lower stand of sea-level). Conversely, uplift or higher sea-level could also account for the position of the basal calcarenite units if they are of marine origin.

Third party source; Images
redacted at request of thesis
author

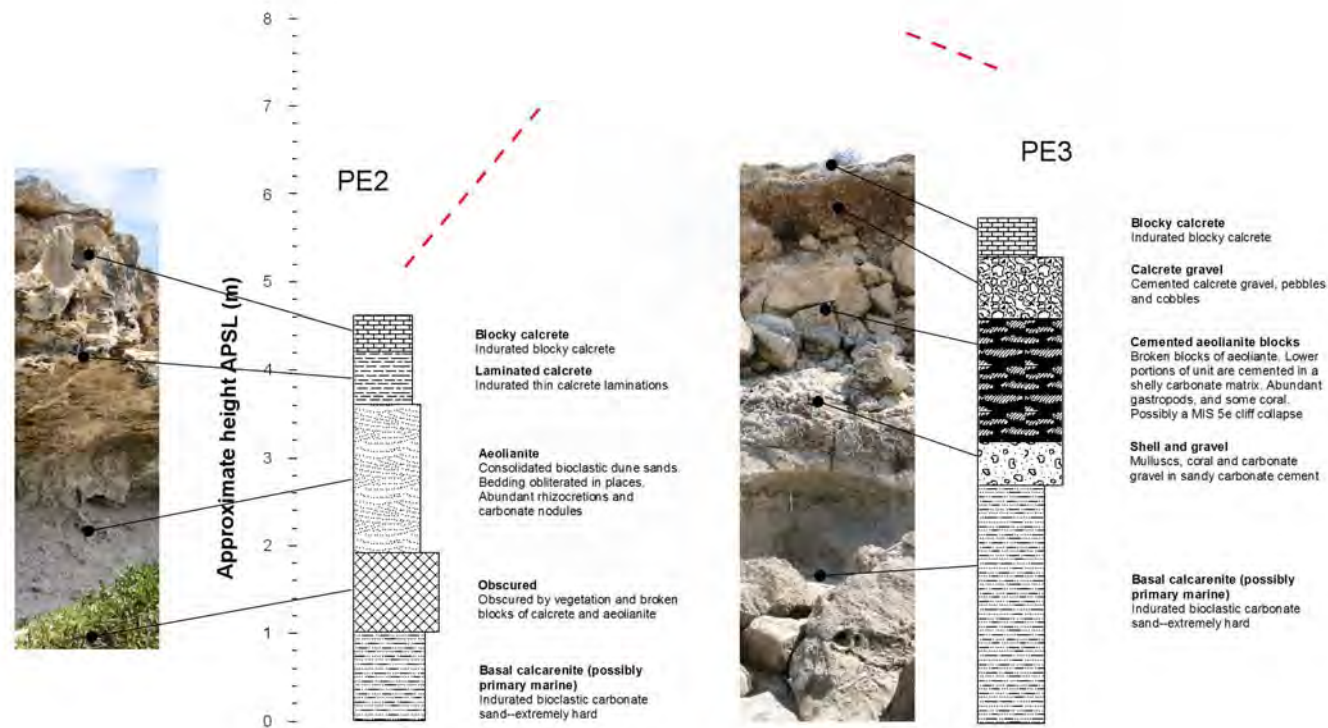


Figure 3.41: Stratigraphic logs of the Bridgewater Formation at Vivonne Bay, Kangaroo Island. The logs illustrate the formation and the approximate thickness of the units at sites PE 2 and PE 3 (inset satellite image courtesy of Google Earth, 2008)



Figure 3.42: View south-east from the Vivonne Bay jetty; showing the location of site PE 2. Note the shallow cave structures ~3.5 m APSL, and the rock platforms (foreground and mid-ground). The grey coloured layer at the base of outcrop is constructed of broken blocks of calcrete and aeolianite resting on the basal calcarenite.

Aeolianite unit (Figure 3.41 PE 2)

This unit may rest directly upon the basal calcarenite—the lower portions of the aeolianite unit are obscured continuously along outcrop; so contact cannot be observed (Figure 3.43). The unit is a very pale brown (Munsell 10YR 8/2) moderately cemented aeolian dune sand, consisting primarily of biogenic carbonate grains (~10% by dry mass quartz and other inorganic minerals) such as bryozoan and echinoid particles, foraminifer tests, and comminuted shell. The grain size ranges from medium to fine subrounded; the grains are generally well-sorted. Rhizoliths weathered in relief and carbonate nodules were prevalent throughout the unit and bedding structures were not very obvious; although some faint crossbedding was visible (Figure 3.43). Clay pot karst features and solution pipes also occasionally occur through the overlying calcrete and this unit (Figure 3.44). This unit was dated using optically stimulated luminescence (the results of which are presented in Chapter 7);



Figure 3.43: Aeolianite unit at site PE 2 with overlying calcrete. Note abundant rhizoliths. The open ellipse denotes the rock-hammer set for scale (33 cm).



Figure 3.44: Clay pot karst running through the overlying calcrete into the aeolianite unit at site PE 2.

the results suggest deposition within the range of MIS 5e-7. This will be discussed further in Chapter 7.

Calcrete unit (Figure 3.41 PE 2)

A ubiquitous calcrete sheath or carapace covers most of the coastal landscape of southern Kangaroo Island; whether or not this covering is contemporaneous at various sites is uncertain as no attempt has yet been made to establish a chronology for its formation. Certainly in the elevated south-west of the island the calcrete may be of greater antiquity than the more south-eastern deposits of much lower elevation. It is certain; nonetheless, for the Kangaroo Island sites in the south and south-east that have underlying geochronology, the calcretes are younger than the Last Interglacial.

At this site (PE2) the calcrete is characterised by a laminated lower portion, where dissolved secondary carbonate has precipitated and cemented along bedding planes, with a blocky, dissected upper portion (Figure 3.41 and 3.43). The unit *is* karstified although not to as large a degree as the calcrete overlying the Point Ellen Formation. Some meteoric pedogenic features such as soil filled solution pipes (clay pots) are occasionally found (Figure 3.44). The top of the unit also exhibits a thin mantle of soil infilling the irregular surface.

3.4.4.3 Site PE 3 Vivonne Bay

PE 3 is located on the western margin of Vivonne Bay, approximately 330 m north-west of site PE 2. At this site the aeolian facies from PE 2 are absent; the stratigraphic log in Figure 3.41 illustrates the 5 discrete units found along outcrop: the basal calcarenite (described in section 3.4.4.2), a cemented cobble and shell layer, collapsed large scale aeolianite blocks, cemented *in situ*, a calcrete gravel, and a calcrete mantle.

Cobble and shell unit (Figure 3.41 PE 3)

This unit varies in thickness along outcrop from just a few tens of cm to ~1.3 m thick. It lies on or within hollows on the basal calcarenite, and also infills the gaps in the lower sections of the aeolianite block unit directly above (Figure 3.45). The unit is relatively rich in molluscan fauna; dominated by rock dwelling

species, in particular the supralittoral-littoral species *Nerita* (*Melanerita*) *atramentosa* (Reeve) 1855—several of these gastropods were sampled for amino acid racemization dating purposes.



Figure 3.45: Shell and cobble unit at site PE 3. Note: rock-hammer for scale (41 cm); also note the smooth solutional sheath, upper left.

The unit also contains (as well as broken shell and whole shell) abundant boulders and cobbles of aeolianite, rounded pebbles of calcrete and Kanmantoo Group metasandstone. The unit is on the whole clast supported; clasts are moderately cemented in a very pale brown (Munsell 10YR 8/4) coarse-medium biogenic carbonate matrix, consisting of comminuted shell, abundant foraminifera (including *Elphidium crispum* [Linnaeus] 1767 and *Discorbis dimidiatus* [Jones and Parker] 1862), echinoid and bryozoan fragments, and calcareous algae, with around 17% quartz and heavier minerals (by dry mass). Also found within the unit (although rare) were some specimens of scleractinian or ‘stony’ corals—a reasonably well-preserved (the fine structures of the corallites have been weathered) example of a scleractinian, hermatypic, temperate coral was recovered from this unit for uranium series dating: *Plesiastrea versipora* (Lamarck) 1816 (Figure 3.46). This species can thrive in cool waters (Howe and Marshall, 2002), and currently exists in a range of marine habitats distributed throughout Australasia—including the South Australian gulfs region (Burgess *et al.*, 2006).

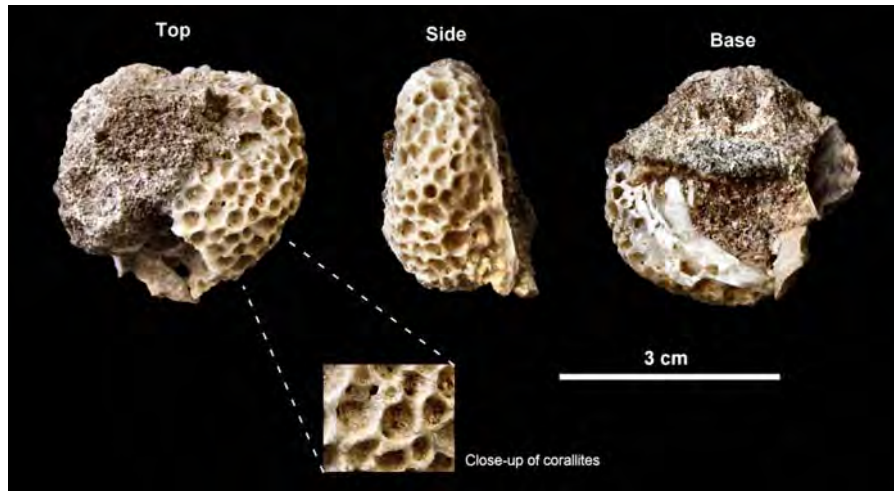


Figure 3.46: A scleractinian coral: *Plesiastrea versipora*, recovered from the shell rich cobble/pebble unit.

This unit is unlikely to be related to the Point Ellen Formation as the presence of particular diagnostic species e.g. *Nerita milnesi* (Ludbrook) 1983, *Hartungia dennanti chavani* (Ludbrook) 1978, and *Anodontia sphericula* (Basedow) 1902, is not apparent.

The unit may not continue far into the face of the deposit, and may only be a few metres deep (horizontally), plastered as lenses and stringers of material into gaps and notches in the face of the outcrop—as it was during deposition. The morphology and height of the unit suggests high-energy deposition (energetic enough to plaster cobbles and boulders into the irregular face of the deposit) during a period of higher sea-level. This unit is characteristic of notch type deposits found at Pennington Bay, and Rocky Point, although it is larger in extent. These deposits, including the Vivonne Bay unit, are considered to be of Last Interglacial (MIS 5e) origin, given their position above sea-level (+2.5 to +3.5 m APSL), and the results of amino acid racemisation and U-series dating (discussed in Chapters 7 and 8). These types of deposits are also regarded here as equivalents to the South Australian Glanville Formation shell-beds (cf. Firman, 1967; Cann, 1978; Belperio *et al.*, 1984; Hails *et al.*, 1984a, 1984b; Murray-Wallace *et al.*, 1988; Murray-Wallace and Belperio, 1991). This assumption is based upon morphostratigraphical (and later biostratigraphical) evidence, i.e., the heights APSL of the Kangaroo Island units were comparable to Last Interglacial Glanville Formation sites on the South Australia (SA) mainland (+2 to +3 m) (e.g. Eyre Peninsula, Spencer Gulf, Port Wakefield, Port

Adelaide) (cf. Belperio *et al.*, 1984; Murray-Wallace *et al.*, 1988). Although they lack the presence of *Anadara trapezia* (Deshayes) 1839 (the Sydney cockle), a large bivalve that is a prevalent constituent of the SA Last Interglacial (MIS 5e) deposits. However, other species commonly found in SA Last Interglacial (MIS 5e) deposits are also sometimes found in the Kangaroo Island units, e.g. *Katelsia scalarina* (Lamarck) 1818, *Amesodesma angusta* (Reeve) 1854, *Nerita (Melanerita) atramentosa* (Reeve) 1855, *Diloma concamerata* (Wood) 1828, *Fulvia tenuicostata* (Lamarck) 1819, *Thais orbita* (Gmelin) 1791, and *Macra australis* (Lamarck) 1819.

Aeolianite block unit (Figure 3.41 PE 3)

Broken and collapsed blocks of aeolianite form a spectacular structure that essentially rests upon the basal calcarenite (Figure 3.47). The blocks are the remnants of what is apparently a cliff collapse. This was in all likelihood an aeolianite unit deposited as a barrier dune sometime before the Last Interglacial (MIS 5e) (luminescence chronology suggests MIS 9), that has been undercut by wave processes during a later sea-level highstand. There is no bedding discernable in the blocks as most are covered in solutional crusts and sheaths



Figure 3.47: Collapsed blocks of aeolianite resting on cobble and shell, and the basal calcarenite. Note: the collapsed blocks are ~1.5-2 m thick; also note the solutional drape cementing calcrete gravel: upper right mid-ground.

(Figure 3.45) derived from dissolved secondary carbonate in meteoric waters running over the precipice and cascading down the face of the outcrop.

Based upon the oxygen isotope sea-level database presented in Siddall *et al.* (2007), MIS 5e is the most likely MIS for this to have occurred as the earlier highstand at MIS 7 was not of the same magnitude (-5 to -15 m APSL as opposed to +2 to +4 m APSL for MIS 5e). The cobble and shell unit appears to be underneath the blocks in places suggesting undercutting, deposition of the shelly unit, then collapse of the overlying blocks, and subsequent infilling during the highstand.

The aeolianite itself is a strongly cemented very pale brown (Munsell 10YR 8/3) medium-fine biogenic carbonate grainstone, consisting of comminuted shell, abundant foraminifera (including *Elphidium crispum* [Linnaeus] 1767 and *Discorbis dimidiatus* [Jones and Parker] 1862), echinoid and bryozoan fragments, and calcareous algae, with around 3% quartz and heavier minerals (by dry mass). The solutional sheaths and crusts are generally a pink to pinkish white (Munsell 5YR 7/3-8/2) colour.

Calcrete units (Figure 3.41 PE 3)

The calcrete gravel unit that is apparently underlying the topmost blocky calcrete may represent either an older calcrete that has been severely weathered, or scree derived from earlier deposits, and cemented in place. Subsequently, a dune unit has been deposited over this, undergone downward leaching, forming the uppermost calcrete carapace. Alternately, both 'units' may also be part of a single older calcrete profile where pedogenesis has broken down the calcrete into cobbles and nodules in the lower layer. The calcrete profile at PE 2 is of different character than at this site; there is no suggestion of gravelly calcrete layer.



Figure 3.48: A panoramic view of the isolated aeolianite outcrop at site PE 4. The outcrop is ~6.5 m APSL at its highest. Note the small pinnacle with notch and visor mid-right in the image. The upper right inset image (courtesy of Google Earth, 2008) shows the geographical position of PE 4, and also the location of submerged structures (see in text). Note the transgressing beach sands left mid-ground, and the modern analogue of a pebble beach notch deposit: lower left inset (rock-hammer for scale: 33 cm).

3.4.4.4 Site PE 4 Vivonne Bay

The morphostratigraphy of this site is relatively uncomplicated when compared to that of the other sites examined around the embayment. This site exhibits an isolated aeolianite unit which crops out at sea-level (forming a small promontory) that is mantled by a thin calcrete (~0.3 m), and extensive well-vegetated Holocene / modern backshore dunes. The height of the outcrop, not including the overlying dunes is approximately 6.5 m APSL; large scale crossbedding is plainly visible (Figure 3.48). The beds (on average) dip 6° bearing 117° east-south-east, towards the centre of the bay; however they also dip (~15°) to the north-north-east, into the face of the unit. When considering the alignment of the Holocene parabolic dunes (NE) illustrated in Figure 3.31, this may be indicating a palaeowind direction from the south-west that prevailed during deposition. The offshore remnant of the aeolianite (note the well-formed notch and visor) and submerged structures allude to a larger barrier complex being present in the past at this location. Given the location of the Harriet and Eleanor rivers (Figure 3.32), large barrier estuaries may have been present during a period of slightly-lower-than-present sea-level—similar to Hanson Bay. This isolated outcrop may be contemporaneous with the aeolianite at site PE 2. The calcrete (Figure 3.49) is comparable; however, at this site it lacks the laminated lower portion. Although, it does exhibit a well developed rhizomorph horizon, weathered in relief, below the carapace; similar to PE 2.



Figure 3.49: Calcrete profile at PE 4, upper mid-ground. Note the rhizocretions weathered in relief, and the overlying well-vegetated Holocene/modern dunes: upper right back-ground.

3.4.5 Stratigraphy of the Hanson Bay near shore deposits

Hanson Bay lies on the south coast of Kangaroo Island, between Cape Younghusband and Cape Bouguer, at approximately S36°01' and E136°51' (Figure 3.1, Part I).

Hanson Bay is approximately 8 km wide and is broken into a series of smaller embayments, with moderate to high-energy beaches, by small headlands; similar to Pennington Bay. The beaches are characterised for the most part by unconsolidated, skeletal carbonate, long-walled, parabolic backshore dunes (Holocene/modern), and actively eroding Pleistocene calcarenite cliffs (Figure 3.50).

The study site (HB1) is located in a small embayment towards the centre of the main bay. It lies east of the entrance to South West River; at the rear of a small aeolianite headland. Large submerged calcarenite structures nearshore reduce incoming wave energy, forming a steep, reflective beach at this site (Short and Fotheringham, 1986).

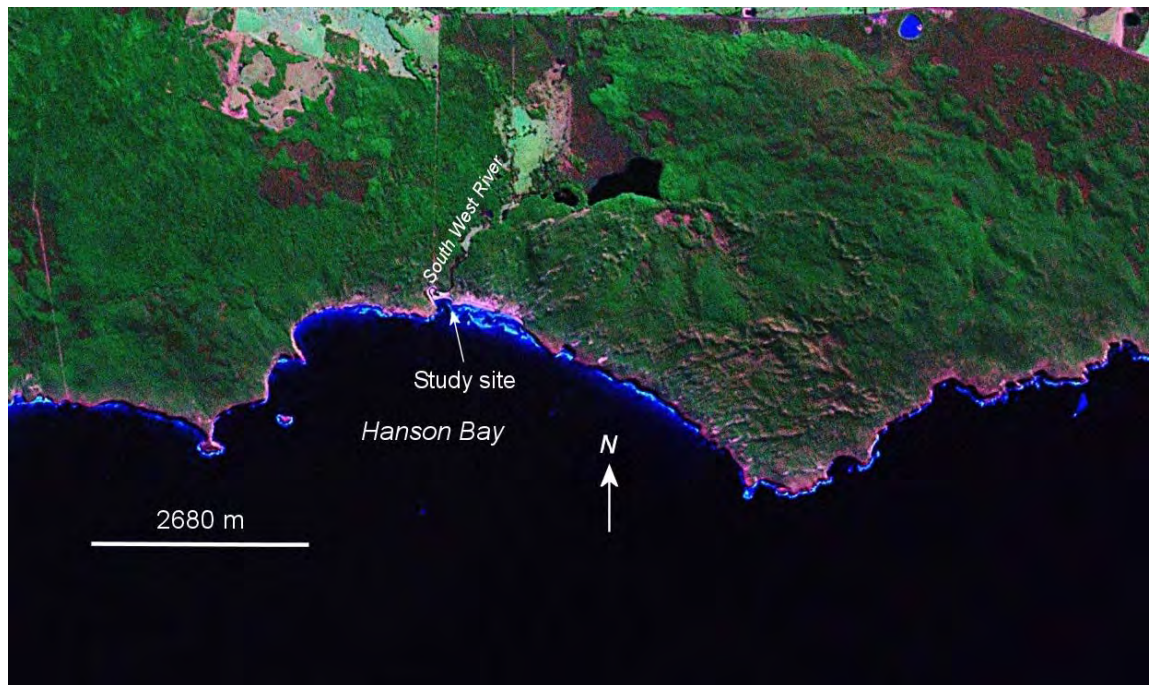


Figure 3.50: Hanson Bay Landsat ETM image (edited); showing the location of the study site and bay morphology (NASA Landsat program, 2001).

The study site is a series of deposits overlying an old calcarenite platform (Figure 3.50). The basal portion of the platform consists of outcropping aeolian / marine carbonate of unknown age extending offshore—although it is possibly early to middle Pleistocene in age. The platform has an overlying subaerial exposure surface which shows evidence of scouring by wave action. The exposure surface is an indurated calcrete / palaeosol much of which has been removed; there are now only thin patches remaining scattered around the platform. These patches are dense with rhizomorphs, and there are examples of insect burrows. Much of this surface was scoured during sea-level highstands, when sea-level was high enough for wave action to cause erosion. Some of these patches are overlain by remnants of what is apparently a shelly washover or sub-littoral deposit (or deflation deposit, it is difficult to interpret)—the main part of this unit is on the eastern portion of the platform. Evidence of higher sea-level can be seen on some of the washover patches in the form of small notch and visor structures. Much of this unit, barring that on the eastern part of the platform, was removed as well. Overlying all units at this site are a calcrete and thick Holocene/modern dunes. The shelly deposit appears to truncate a set of what have been interpreted here to be back-barrier estuarine lagoon sediments.

The deposits of interest extend from the aeolianite platform inland for approximately 10 m, where they vanish into overlying Holocene dunes. The following sections will examine the deposits at the Hanson Bay study site in detail.

3.4.5.1 Basal calcarenite

The basal calcarenite underlies all other sediments at this site (HB1); forming a platform on which the other units were deposited (Figure 3.51 and 3.52). Bedding structures are plainly visible in this unit, although whether they are the result of aeolian or marine sedimentation is not easy to interpret. The stratigraphic superposition and level of induration (characteristic of older

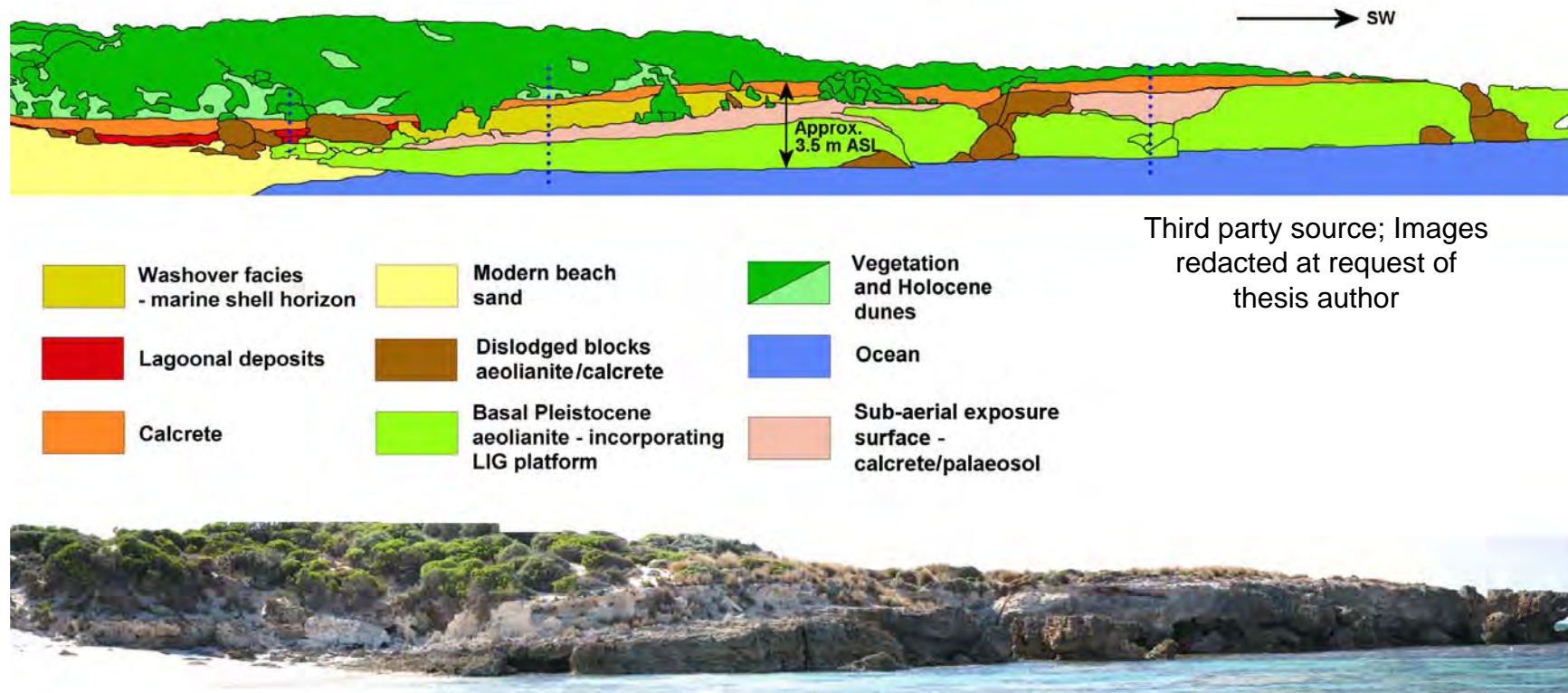


Figure 3.51: The Hanson Bay site (bottom image) is displayed here as a composite 180 degree panorama, as such there is minor distortion towards the edges of the image. In the top graphic the individual units have been assigned different colours to make them more apparent. The black box in the inset satellite image of the site (Google Earth, 2007) illustrates the approximate extent of the deposits. The top of the calcrete is approximately 3.5 m ASL. The blue dashed lines show the approximate positions of the measured sections as shown in Figure 3.51.

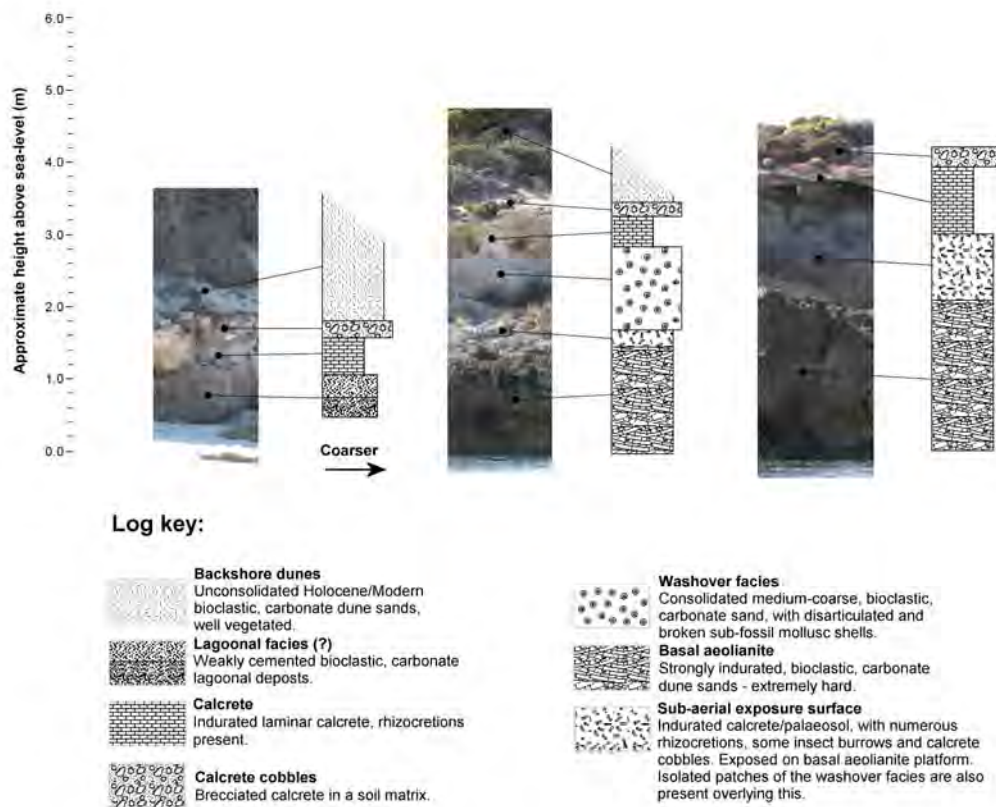


Figure 3.52: Generalized stratigraphic logs for the Hanson Bay study site.

aeolianites [Hearty, pers. comm., 2006]), led to the conclusion that this unit is early to middle Pleistocene in age. This is a regional unit that is present as the lowest visible stratum at most of the sites examined along the southern coast of Kangaroo Island. At Hanson Bay, as discussed above, this unit has been etched into a platform during an earlier MIS of higher sea-level possibly MIS 5e, although, MIS 9 or 11 would more appropriately explain the platform evolution in light of the overlying sediments—the top of the platform is on average 2 m APSL (Figure 3.53). This unit was probably much larger in lateral extent as evidenced by the isolated offshore stack illustrated in Figure 3.54. The sediment is a strongly cemented, well sorted, sub-angular to sub-rounded, medium-fine, bioclastic carbonate sand. The platform dips 5° landward towards the north. The basal calcarenite was sampled for AAR analysis on the western side of the beach, as it was softer and more easily sampled than the unit on the eastern side of the beach.

3.4.5.2 Subaerial exposure surface

This unit (Figure 3.52) is present as a patchy, relatively thin (~0.2 m) unconformity exposed on the platform surface (Figure 3.52; Figure 3.55); although, at the sea-ward section of the platform it is quite thick at ~0.9 m (possibly filling hollows in the platform) and is capped by a younger laminar calcrete (Figure 3.52, 3.53, 3.55 and 3.56). This unit has undergone some pedogenesis as indicated by a weak red colouring (5YR 7/2 Pinkish grey Munsell colour); the numerous rhizoliths are also evidence for long-term exposure and vegetation growth. It is hypothesized that the calcrete / palaeosol is derived from aeolian sands that were deposited perhaps during MIS 7 or 9 that underwent a period of pedogenesis and diagenetic alteration, after stabilization. Subsequent deflation led to the exposure of the 'B' horizon. This would have happened during a later depositional hiatus—this is likely to have been a glacial phase. During the hiatus vegetation colonised the dune, and over time meteoric waters concentrated calcium carbonate in the root zone ('B' horizon), forming casts and moulds (existing carbonate grains within the root zone would also have been cemented); eventually the upper portions of the soil were deflated leaving behind a cemented calcium carbonate horizon. Destabilization and removal of the leached (carbonate), unconsolidated upper soil/sand layers occurred due to the elimination of vegetation cover. This could have happened for a number of reasons; the most likely being fire, climate change, ground water dynamics, inundation by active dunes, rising sea-levels or a combination of factors (Cullen and Bird, 1980; Seppälä, 1995). For example a rise in sea-level would mean that the environment would change from inland to coastal; the implication being that the vegetation communities present would not adapted to coastal conditions; hence, die off due to stress could occur. This scenario would depend upon both the rapidity of the transgression, and on how swift the colonization of more salt tolerant species would be. During a later sea-level highstand much of this unit was removed by wave scouring. The sediment is strongly cemented, dominated by fine-medium, bioclastic carbonate grains and threaded with abundant rhizoliths and insect burrows.



Figure 3.53: Basal calcarenite, note bedding structures. Also note the overlying calcrete unconformity on this section of the bench.

3.4.5.3 Washover (or sub-littoral or deflation?) facies

The washover facies are overlain by a thick, laminated calcrete and well-vegetated Holocene aeolian dunes (Figure 3.51; Figure 3.52). These facies are characterised by a cemented shelly horizon, approximately 1 m thick in places (increasing in thickness towards the shore) comprising several molluscan and foraminiferal species. The unit also exhibits numerous thin calcrete laminae or solutional rinds, and rhizocretions. The sediment is a consolidated, very pale brown (10YR 8/2), medium-coarse, carbonate sand with abundant coarse skeletal fragments, occasional whole foraminiferal tests, and some whole shells: although these are rare. Most gastropod shells were broken and bivalves were disarticulated and commonly broken—an indication, in this case, of high-energy deposition. However, foraminiferal tests were generally well-preserved (although *Marginopora vertebralis* ([Blainville] 1834) tests were fragmented, which is not surprising, given their delicate structure). The most common molluscs found in this unit were *Turbo* (*Ninella*) *torquatus* (Gmelin) 1791, *Thais orbita*, *Haliotis* (*Padollas*) *scalaris* (Reeve) 1846, *Patella* (*Scutellastra*) *laticostata* (Blainville) 1825, *Spisula* (*Notospisula*) *trigonella* (Lamarck) 1819, and *Nerita* (*Melanerita*) *atramentosa*.



Figure 3.54: Top oblique view of basal platform; note isolated offshore remnant of the basal aeolianite (centre mid-ground).

Many molluscan species in this unit are of unrecognisable affinity due to fragmentation. *Turbo (Ninella) torquatus* is characteristic of limestone platforms, from the lower littoral to the sub-littoral zone, *Thais orbita* is found on rocky shores, and on rock platforms at low tide. *Haliotis (Padollas) scalaris* is found along rocky coasts, generally in the subtidal region, and *Patella (Scutellastra) laticostata* is another inter-tidal mollusc common on rock platforms. *Nerita (Melanerita) atramentosa* is also a common gastropod found on rock platforms in the supralittoral and littoral zones (Ludbrook, 1984). However, the bivalve *Spisula (Notozospisula) trigonella* is not characteristic of rock platforms, being found more commonly in muddy/sandy estuarine and river mouth environments (Ludbrook, 1984); nevertheless, this is in keeping with the close proximity of the entrance to the South West River which is around 200 metres to the west (Figure 3.49). All of these molluscan species are characteristic of the late Pleistocene Glanville Formation (Firman, 1966; Ludbrook, 1984; Cann, 1978)—based upon this and dating results (OSL and AAR: discussed in Chapter 7) this unit is therefore correlated with the late Pleistocene Glanville Formation.



Figure 3.55: Rear of aeolianite platform, showing the irregular exposed surface of the calcrete/palaeosol (note the large rhizomorph, possibly a large tree root—black arrow), washover patch (mid-ground) with notch and visor, washover facies, and upper calcrete (left mid-ground). The water-bottle mid-ground is 250 mm high.

The dominant species of foraminifers found were *Discorbis dimidiatus*, *Elphidium crispum* and *Elphidium macelliforme* (McCulloch) 1981 (there were also fragments of *Marginopora vertebralis*). These are benthic foraminifers characteristic of intertidal and subtidal environments (Cann *et al.*, 2002). *Discorbis dimidiatus* is commonly found in subtidal environments, in seagrass meadows, whereas both *Elphidium crispum* and *Elphidium macelliforme* are characteristic of the intertidal zone (Cann *et al.*, 2002). The foraminifers were generally in good condition, with some abrasion present, and little diagenetic modification (e.g. recrystallization, oxidation). The morphology of the site, sediment structure, and height APSL (approximately +3.0 m at the top of the unit) suggests that this unit is a high energy washover deposit that may have been deposited after a coastal barrier had been breached, during the Last Interglacial (MIS 5e), or a sub-littoral (subtidal) shell deposit. The deposit also appears to truncate back-barrier estuarine lagoon sediments, at the rear of the site (Figure 3.51, 3.52 and 3.57). The original extent of the barrier



Figure 3.56: Thick section of subaerial exposure surface; capped by laminar calcrete.

can only be surmised: the schematic in Figure 3.58 illustrates a barrier model based upon the underwater structures present in the embayment. The model suggests that this embayment may have once been semi-enclosed as a small-scale estuarine lagoon. The model for deposition proposed here is that the barrier was breached during the Last Interglacial (MIS 5e)—this is supported by OSL dating for the washover sediment which suggests a MIS 5e age for deposition (as do the AAR results for molluscs, foraminifers, and whole-rock; this will be discussed in chapter 7). The barrier was breached and the lagoon scoured, flushing much of the estuarine sediment, and laying down a coarse, shelly facies. Later, as sea-level regressed the washover was covered by aeolian processes in finer carbonate sand and subaerial exposure, during a depositional hiatus, formed a calcrete mantle over the sediments (washover, lagoonal, and the older subaerial exposure surface described above). This is just one possible hypothesis; it is also possible that the sediments are derived from a sub-littoral deposit formed during higher sea-level or from a deflated shelly dune (although this is the least likely event).



Figure 3.57: Back barrier estuarine lagoon sediments.

Third party source; Images redacted at request of thesis author

Figure 3.58: A Late Pleistocene barrier model hypothesized for the Hanson Bay site during a period of sea-level that was similar to the present—perhaps just before the peak of the Last Interglacial (MIS 5e), and at a time when the discharge of the South West River was possibly greater. The barrier dune location is interpreted from submarine structures visible in the image; the boundaries for the estuarine lagoon are defined here by existing morphology. The extent of the Pleistocene lagoon could have been larger than has been interpreted as the lagoonal deposits (red marker) underlie the Holocene dunes to the north and east. The western headland boundaries too may have hosted barrier dunes. Note the light blue water with dark margins (centre bottom) forming the precincts of what appears to be a channel. This may have been the path that the South West River travelled during periods of low sea-level. The barrier formation may well have been initiated as a result of rising-sea-levels before MIS 5e, and the barrier could have been breached (deposition of the washover facies) and scoured by an event when the MIS 5e sea-level was at its peak height of 2-4 m APSL (Siddall *et al.*, 2007). Thus, the barrier may have been removed instantly, if the event was a storm surge or tsunami. However, a smaller event or series of events could have resulted in damage that weakened the barrier which subsequently deflated and was, eventually, removed (unedited image from Google Earth, 2007). Image edited in Map Maker, version 3.5 (Dudley, 1995).



Figure 3.59: Estuarine lagoon facies; truncated by a shelly washover (or sub-littoral or deflation) deposit. LH mid-ground.

3.4.5.4 Back-barrier estuarine lagoon deposits

This unit is located at the rear of the platform and represents what has been interpreted as a lagoonal deposit. These facies appear to have been truncated by the washover unit described above (Figure 3.51, 3.52, 3.57 and 3.59). However, the truncation surface has been obscured by collapsed blocks of the overlying calcrete and slumping Holocene dune sands.

The numerical distribution of species of foraminifera within a carbonate sediment sample can yield clues as to the origin of the sediment. The analysis for the lagoonal sediments at Hanson Bay supports the hypothesis that this unit is estuarine lagoonal in origin (Figure 3.60).

The presence of significant numbers of *Ammonia beccarii* is indicative of restricted waters (Yassini and Jones, 1995; Cann *et al.*, 1999). At first it may appear that the sediment is dominated by the shallow marine species *Discorbis dimidiatus* and *Elphidium* spp.; however, it is possible that these and other marine foraminifers were winnowed from the barrier dune that once existed, and consequently do not have the same origins as *Ammonia beccarii*.

3.4.5.5 Laminar calcrete and the Holocene dunes

This is the same persistent calcrete present at all sites examined along the southern coast. It varies in thickness at this site from 0.5-1 m and is predominantly laminar. The unit is threaded with numerous rhizcretions. The top portions of the unit host a breccia of angular calcrete clasts in a soil matrix; this may be a deflation deposit. The sediment is a strongly indurated, very fine, pinkish white (7.5YR 8/2 Munsell colour) carbonate sand. This unit would have formed during a depositional hiatus; in this case it is likely that the calcrete evolved during one or more glacial and stadial periods sometime after MIS 5e—possibly MIS 4 and MIS 2. This unit would have evolved in a similar mode to that described for the subaerial exposure surface above: from dunes formed after the deposition of the washover facies (MIS 5e).

Holocene dunes overlie the calcrete to a height of around 6 m APSL near shore (getting higher inland); they are long-walled parabolics aligned to the north-east

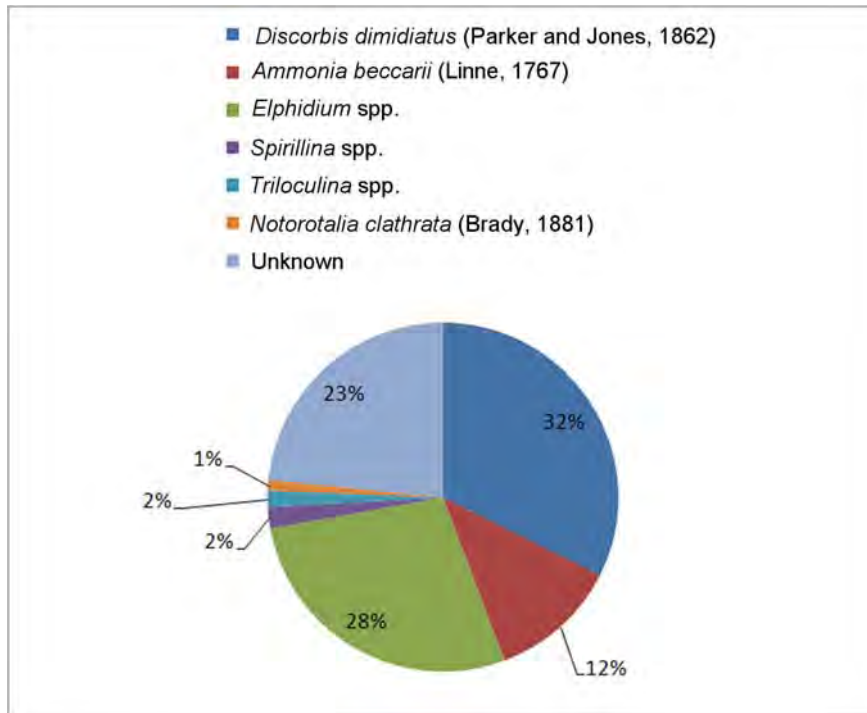


Figure 3.60: Relative abundance ($n=205$) of various foraminifer genera found in the Hanson Bay estuarine lagoon sediments; one of the most important species to note is *Ammonia beccarii*, a euryhaline species. It is indicative of restrictive conditions, and hence is characteristic of lagoons, open estuaries and inlets.

(Figure 3.50). The dunes are unconsolidated, well vegetated, and are predominantly composed of bioclastic carbonate grains; with abundant foraminifers, echinoid spines, bryozoans, calcareous algae, ostracods, and comminuted shell. Amino acid analyses performed on foraminifers (see Chapter 7) from this unit indicate a Holocene age for these dunes.

3.4.6 Kelly Hill Caves

The Kelly Hill caves sediments are examined very briefly here as the study at the caves was primarily a dating exercise. A comprehensive examination of the site is given in the dating chapter (Chapter 7), section 7.3.5.

There are numerous underground drainage features on Kangaroo Island with at least two large systems, the largest and most extensive being Kelly Hill caves (Bauer, 1959). The Kelly Hill Cave system is located on the southern portion of Kangaroo Island approximately 6 km from the coast (Figure 3.61). The caves are formed in calcarenite that may be between Miocene and Late Pleistocene in age. Bauer (1959) surmised that the basal calcarenite was of Pliocene age and

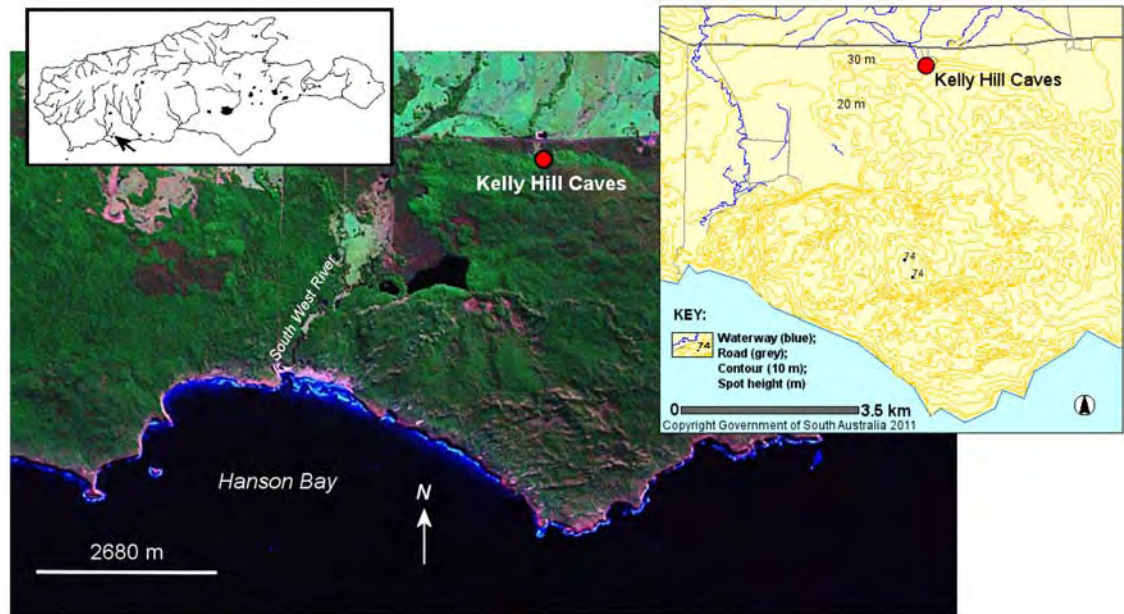


Figure 3.61: Location of Kelly Hill caves on the southern coast of Kangaroo Island. Upper LH inset shows the location on a regional map (black arrow) (main image is a Landsat ETM: NASA Landsat program, 2001). Upper RH inset is a topographic map of the Kelly Hill cave area, the cave entrance lies between the 30 m and 40 m contour lines (Atlas of South Australia, 2011).

may have been covered by Pleistocene calcarenites, as the surface topography around the caves region was precisely the same as along the southern coast. The caverns formed by solutional weathering as groundwater flowed through and into the basal portions of the deposits; chambers becoming larger as there was an upward migration of cavern roofs due to mass collapse (Bauer, 1959; Hill, 1957). Hill (1957) in an unpublished draft also discusses the origin of the cave system, and Bauer (1959) supported Hill's speculations on the formation of the caves. Other researchers have sampled from the caves, for example Major and Vitols (1973) collected samples from within the caves, and Milnes *et al.* (1983) included a small section in their Cainozoic study of the island discussing these samples with regard to the depositional age of the Kelly Hill Caves calcarenite. They preferred a Miocene age on the basis of the foraminifera found. Belperio (1995) suggested rather that the Kelly Hill caves were formed in Pleistocene calcarenites; similar to karst features found on the west coast of the Eyre Peninsula, and the south-western end of the Yorke Peninsula. Indeed the caves were actively forming prior to 500 ka (Heath, pers. Comm., 2007), as suggested by uranium series dating undertaken on the base of a flowstone sequence, located near the main cave entrance (see Chapter 7, section 7.3.5 for detail).

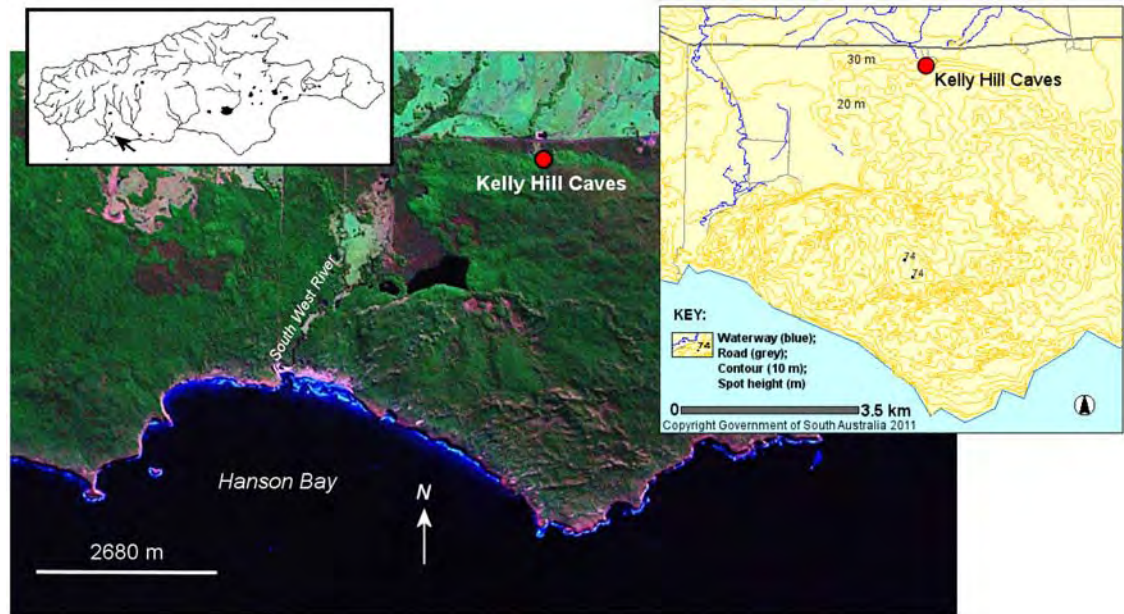


Figure 3.61: Location of Kelly Hill caves on the southern coast of Kangaroo Island. Upper LH inset shows the location on a regional map (black arrow) (main image is a Landsat ETM: NASA Landsat program, 2001). Upper RH inset is a topographic map of the Kelly Hill cave area, the cave entrance lies between the 30 m and 40 m contour lines (Atlas of South Australia, 2011).

may have been covered by Pleistocene calcarenites, as the surface topography around the caves region was precisely the same as along the southern coast. The caverns formed by solutional weathering as groundwater flowed through and into the basal portions of the deposits; chambers becoming larger as there was an upward migration of cavern roofs due to mass collapse (Bauer, 1959; Hill, 1957). Hill (1957) in an unpublished draft also discusses the origin of the cave system, and Bauer (1959) supported Hill's speculations on the formation of the caves. Other researchers have sampled from the caves, for example Major and Vitols (1973) collected samples from within the caves, and Milnes *et al.* (1983) included a small section in their Cainozoic study of the island discussing these samples with regard to the depositional age of the Kelly Hill Caves calcarenite. They preferred a Miocene age on the basis of the foraminifera found. Belperio (1995) suggested rather that the Kelly Hill caves were formed in Pleistocene calcarenites; similar to karst features found on the west coast of the Eyre Peninsula, and the south-western end of the Yorke Peninsula. Indeed the caves were actively forming prior to 500 ka (Heath, pers. Comm., 2007), as suggested by uranium series dating undertaken on the base of a flowstone sequence, located near the main cave entrance (see Chapter 7, section 7.3.5 for detail).

Part III: Dudley Peninsula and east coast stratigraphy

3.5 Stratigraphy and facies of the Kangaroo Island study sites on Dudley Peninsula, and the east coast.

3.5.1 Introduction

The following sections describe the stratigraphy and facies of carbonate deposits at 4 sites located on the west coast of the Dudley Peninsula and the east coast of the main body of Kangaroo Island (see Figure 3.1). The sediments include not only Bridgewater Formation aeolianites (Boutakoff, 1963), but also Pooraka Formation alluvial sediments (Firman, 1967; Milnes and Hutton, 1983; Bourman *et al.*, 1997; Bourman *et al.*, 2010), Glanville Formation equivalent raised shell beds (Firman, 1967; Cann, 1978; Belperio *et al.*, 1984; Hails *et al.*, 1984a, 1984b; Murray-Wallace *et al.*, 1988; Murray-Wallace and Belperio, 1991), and St. Kilda Formation equivalent coquinite (Firman, 1966). The sites are examined in the order of: Rocky Point, Baudin Beach, American River, and Kingscote.

3.5.2 Stratigraphy of sediments at Rocky Point

Rocky Point lies on the northern coast of the neck of Dudley Peninsula, in Eastern Cove (see Figure 3.1 and 3.62). The site is a wave eroded notch in an aeolianite outcrop which forms a small headland, surrounded by low energy beaches. The aeolianite, which is surmised to be of middle Pleistocene age, is capped by a blocky calcrete that has been undercut. This has resulted in quantities of broken blocks scattered about the site. The calcrete has lenses of diagenetically modified sediments (indicated by a pinkish hue: Munsell 2.5YR 8/1 pinkish white) characterised by pebble-sized angular clasts of carbonised (black in colour) calcrete in a strongly cemented matrix. These lenses may represent sediments and clasts washed into dune swales after bushfires (i.e. palaeofires; hence the carbonization) (examples can also be seen at Point Ellen on the south coast).

Towards the rear of the headland at approximately +2 m APSL is a wave eroded notch filled with poorly preserved (chalky) fossiliferous carbonate sediment (see Figure 3.63). The white coloured sediment (Munsell 10YR 8/1)

Third party source; Images
redacted at request of thesis
author

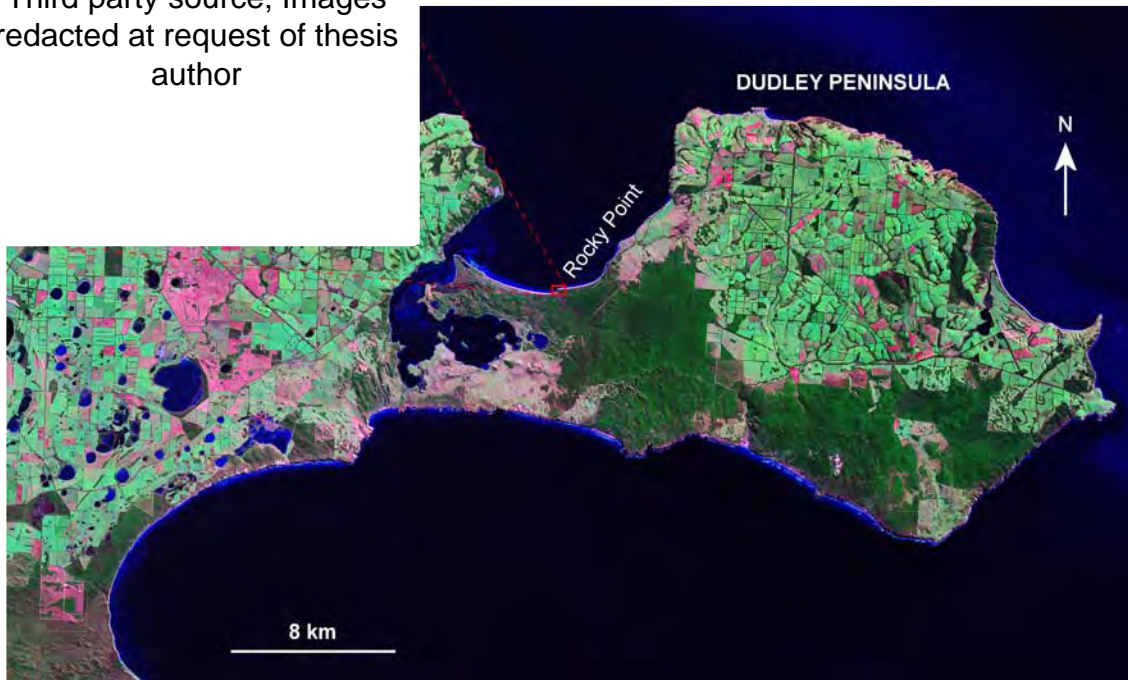


Figure 3.62: Location of Rocky Point site (red circle upper LH inset) on the neck of the Dudley Peninsula (main image is a Landsat ETM: NASA Landsat program, 2001; upper LH image Google Earth, 2010).



Figure 3.63: Sample site location (red circle) at Rocky Point. Note the large broken calcrete block RH mid-ground, with carbonised calcrete clasts. Dashed lines denote limits of the shell bed, and the black ellipse shows the location of a rock-hammer set for scale (33 cm).

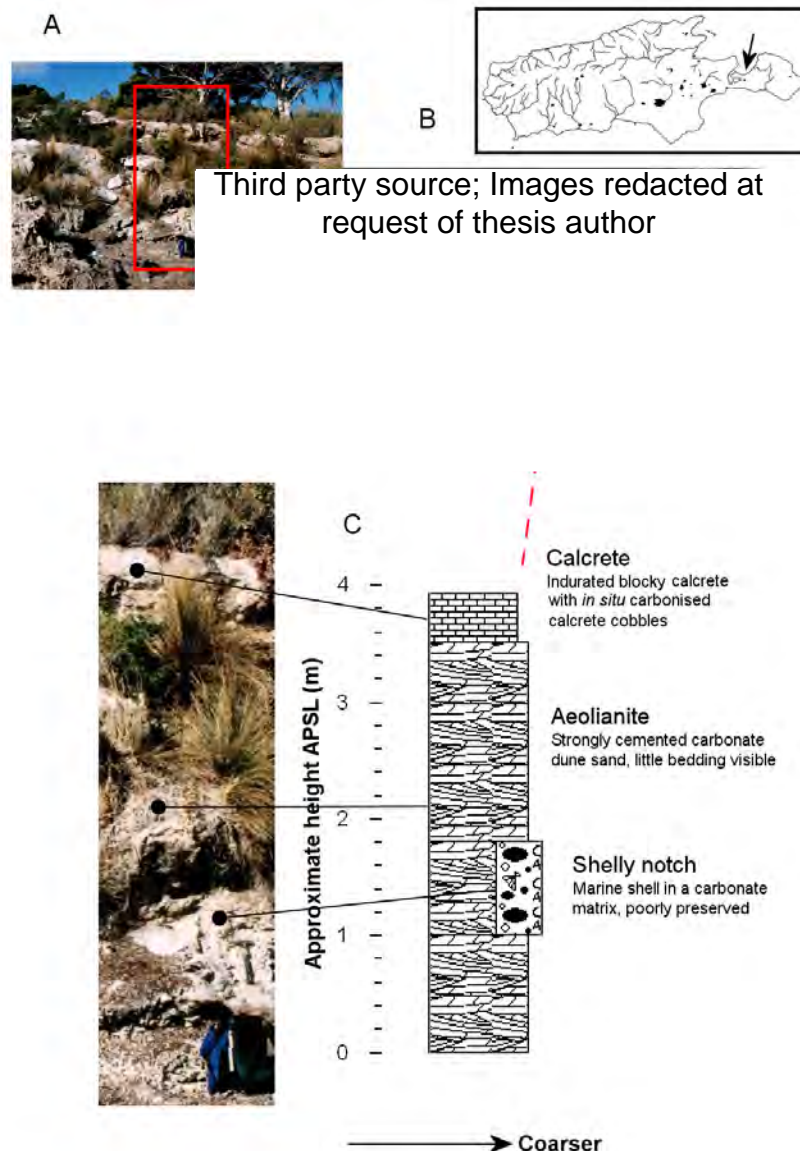


Figure 3.64: Rocky Point stratigraphic log (C) for the sedimentary outcrops at the rear of the aeolianite headland. The top inset (A) is a merged panorama of the site outcrop. The middle LH inset (B) comprises a satellite image (Google Earth, 2007) showing indicated log and sample sites, and a Kangaroo Island location map (with the site indicated by a black arrow).

which has coarse/medium, sub-rounded grains is very poorly sorted, and comprises primarily molluscan fragments and some rare whole shell, in a skeletal carbonate matrix. Few shells could be recovered that were in suitable condition for amino acid analysis. Common foraminifers found in the deposit were *Elphidium* spp. and *Discorbis dimidiatus*, and also fragments of *Marginopora vertebralis*. Common marine shell species were *Fulvia tenuicostata* (Lamarck) 1819, *Conus (Floraconus) anenome* (Lamarck) 1810, *Diloma (Fractarmilla) concamerata* (Wood) 1828, and *Nerita (Melanerita) atramentosa* (Reeve) 1855; representing shallow water sand dwelling species

(*Fulvia*), sublittoral rock dwelling species (*Conus*), and rocky coast species (*Diloma* and *Nerita*).

Similar to site PB2 at Pennington Bay the shelly sediments are packed into what appears to be a notch in older aeolianite (Figure 3.64). These sediments are considered equivalent to the South Australia mainland Glanville Formation (a Last Interglacial highstand lagoonal deposit (cf. Firman, 1967; Cann, 1978; Belperio *et al.*, 1983, 1984; Hails *et al.*, 1984; Murray-Wallace *et al.*, 1988; Murray-Wallace and Belperio, 1991), given their morphostratigraphical position (~+2 m APSL) and the presence of the biostratigraphical indicator fossil *Marginopora vertebralis*, common in South Australian marine sediments of Last Interglacial age.

The height mAPSL of the Rocky Point shelly deposit is comparable to Last Interglacial Glanville Formation sites on the South Australia mainland (+2 to +3 m) (e.g. Eyre Peninsula, Spencer Gulf, Port Wakefield, Port Adelaide) (cf. Belperio *et al.*, 1984; Murray-Wallace *et al.*, 1988) and, during later microscopic examination of the sediments, the presence of an indicator fossil: the foraminifer *Marginopora vertebralis* (typically found in tropical waters) (Milnes *et al.* 1983; Ludbrook, 1984; Belperio, 1995; Cann and Clarke, 1993) , supported this assumption.

3.5.3 Stratigraphy of sediments at Baudin Beach

Baudin Beach is located on the western side of the Dudley peninsula (Figure 3.1 and 3.65), and the entire sequence examined here extends for approximately 2 km along a north-east/south-west line. The morphology of the sites can be characterised by low aeolianite cliffs (approximately 7 m high) with narrow carbonate sand beaches (low energy) dominated by broken (often jagged) blocks of calcrete and indurated palaeosol of various sizes (i.e. cobbles to large boulders) (Figure 3.66). The blocks are derived from cliff collapses caused by wave undercutting during periods of higher sea-level (i.e. during a storm surge for example) (the aeolianite units at Baudin Beach are only weakly cemented hence any subsequent collapse is soon dispersed or removed—only indurated material remains). The overlying calcrete / palaeosol hardpan grades below sea-level at site BB1. This is where the south-western portion of the

Third party source; Images
redacted at request of thesis
author

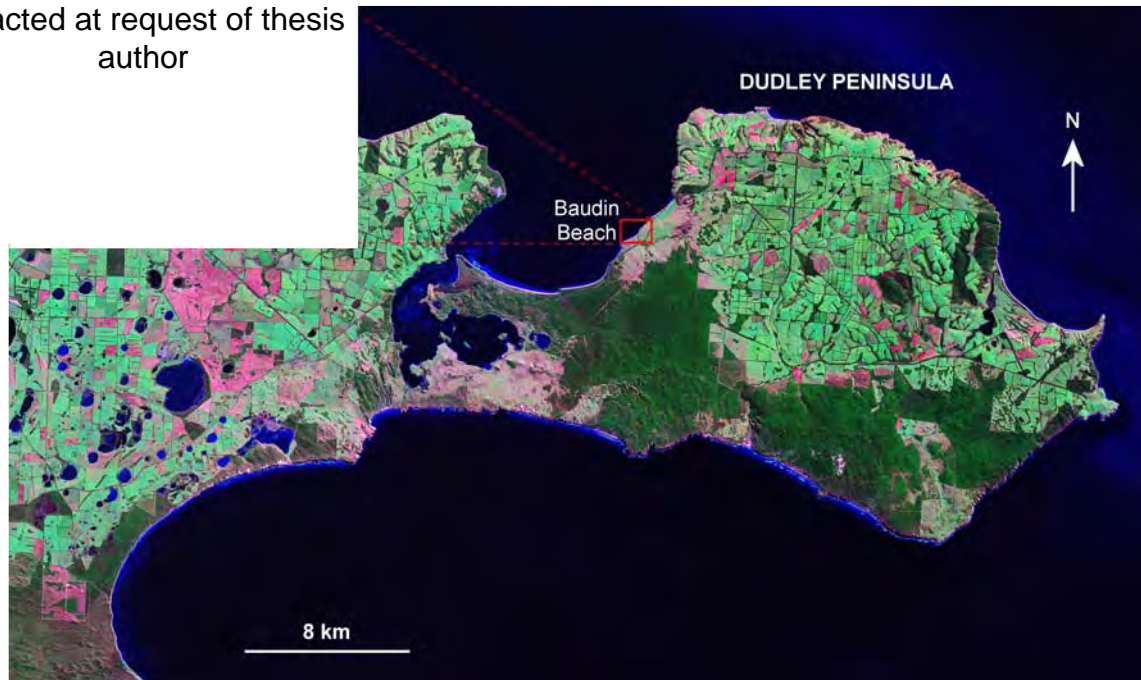


Figure 3.65: Location of Baudin Beach sites (red circles upper LH inset) on the western side of the Dudley Peninsula (main image is a Landsat ETM: NASA Landsat program, 2001; upper LH image Google Earth, 2010).



Figure 3.66: Collapsed calcrete/palaeosol blocks at site BB1, Baudin Beach, Kangaroo Island.

Pleistocene sequence terminates. Modern/Holocene dunes dominate from this point on (until Rocky Point).

The Pleistocene aeolian units are truncated by a large alluvial fan deposit (equivalent to the South Australian Pooraka Formation: Firman, 1967; Bourman *et al.*, 1997; Bourman *et al.*, 2010) at site BB2 (Figure 3.67), and alluvial sediment that is apparently a constituent of this large fan underlies the upper Pleistocene aeolianite at site BB3. There are two alluvial units (see Figure 3.68 for details of the stratigraphy at each log site):

- i) A lower unit (BB2b and BB3c), which is of course older, truncates the lower aeolianite (BB3a and BB2a) at BB2 and overlies it at BB3; this is in turn overlain at BB3 by the upper aeolianite unit (BB3d).
- ii) A younger upper alluvial unit (BB2d) which overlies the upper aeolianite (BB3d).



Figure 3.67: Panorama near site BB3 (looking towards site BB2) showing the upper aeolianite and the alluvial fan sediments. The blue dashed line (middle background) demarks two apparently different alluvial units, and also the smooth contact between the alluvial sediments and the upper aeolianite (LH midground).

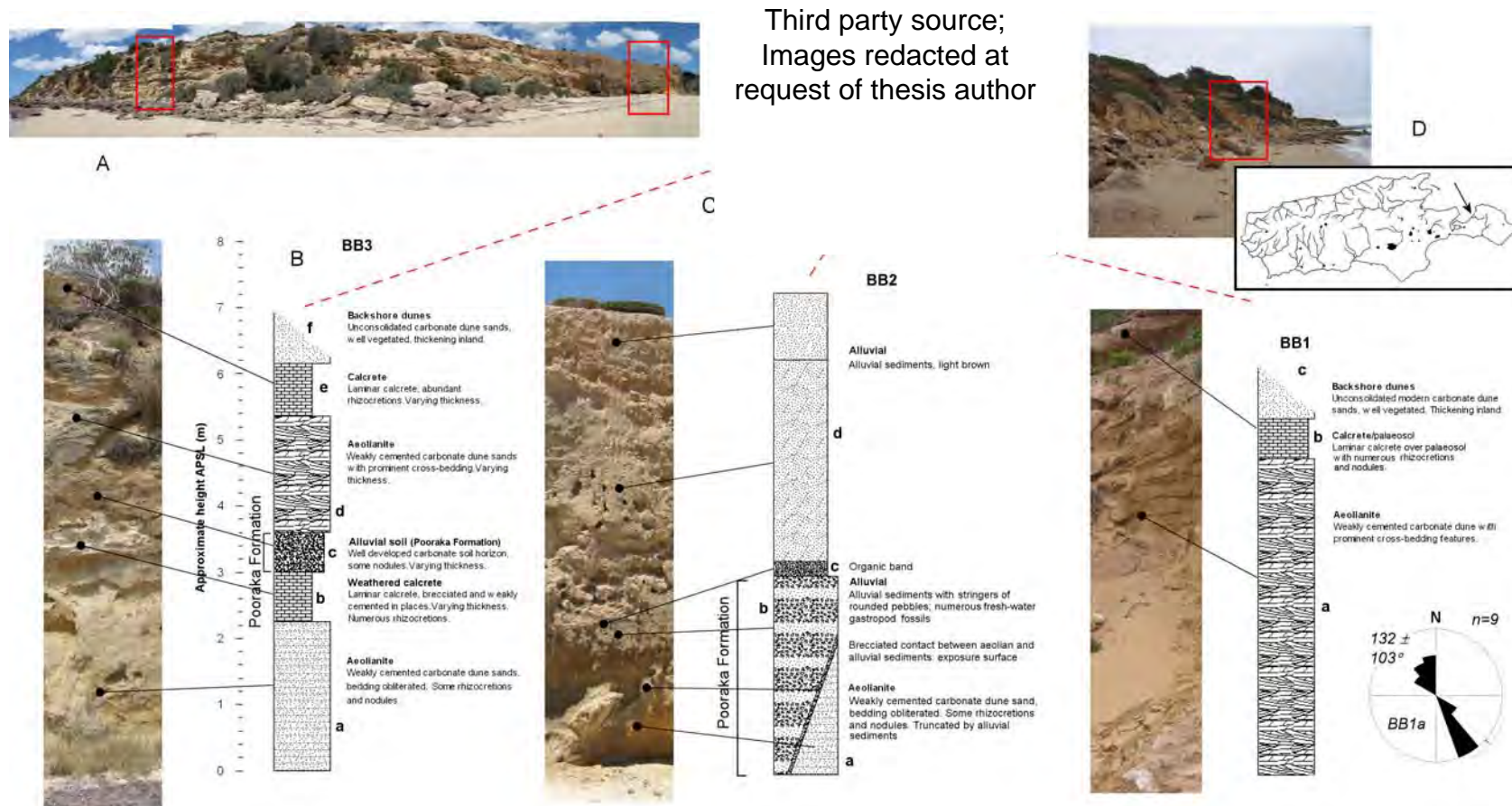



Figure 3.68: Baudin Beach stratigraphic logs (B) for the sedimentary outcrops along a section of the north-west coast of the Dudley Peninsula. The top LH inset (A) is a merged panorama (there is some distortion towards the ends of the image) of the BB2 and BB3 site outcrop. The middle top inset (C) comprises a satellite image (Google Earth, 2007) showing indicated log and sample sites, and the RH top inset (D) is a panorama of site BB1 outcrop, and a Kangaroo Island location map (with the site indicated by a black arrow).

Table 3.17: Characteristics of Baudin Beach lithostratigraphic units.

Unit number	Lithostratigraphic unit	Description	Munsell colour	Grain size	Grain sphericity	Grain sorting
BB1						
BB1-c	Modern / Holocene backshore dunes	Unconsolidated dune sand, abundant vegetation cover	2.5Y 7/1 Pale brown	Coarse/medium	rounded	Moderately sorted
BB1-b	Calcrete / palaeosol	Laminar calcrete over palaeosol, abundant rhizocretions and rhizomorphs, brecciated in places	5YR 7/4 Pink	--	--	--
BB1-a	Aeolianite	Weakly cemented bioclastic carbonate sand, prominent, low angle foresets.	10YR 7/4 Very pale brown	Medium/fine	Sub-rounded to rounded	Well sorted
BB2						
BB2-d	Alluvial sediment	Weakly cemented alluvial sediment	10YR 7/4 Very pale brown	--	--	--
BB2-c	Organic band	Thin band of dark organic sediment.	2.5YR 4/2 Dark grayish brown	--	--	--
BB2-b	Alluvial sediment	Weakly cemented Alluvial sediments (sandy silty) of the Pooraka Formation, with stringers of rounded pebbles, and numerous fresh-water gastropod fossils	10YR 5/3 Brown	Medium/very fine	Sub-angular to sub-rounded	Moderately sorted
BB2-a	Aeolianite	Weakly cemented bioclastic carbonate sand, bedding obliterated, some rhizocretions and carbonate nodules (truncated by alluvial sediments)	2.5YR 8/6 Yellow	Medium/fine	Sub-rounded to rounded	Well sorted
BB3						
BB1-f	Modern / Holocene backshore dunes	Unconsolidated dune sand, abundant vegetation cover	2.5Y 7/1 Pale brown	Coarse/medium	rounded	Moderately sorted
BB3-e	Calcrete / palaeosol	Laminar calcrete over palaeosol, abundant rhizocretions and rhizomorphs, brecciated in places	5YR 7/4 Pink	--	--	--
BB3-d	Aeolianite	Weakly cemented bioclastic carbonate sand, prominent, low angle foresets.	10YR 7/4 Very pale brown	Medium/fine	Sub-rounded to rounded	Well sorted
BB3-c	Alluvial sediment	Weakly cemented Alluvial sediments of the Pooraka Formation, with numerous fresh-water gastropod fossils	10YR 5/3 Brown	Medium/fine	Sub-angular to sub-rounded	Well sorted
BB3-b	Calcrete	Weathered laminar calcrete, brecciated and weakly cemented in places, varying thickness, abundant rhizocretions	10YR 8/1 White	--	--	--
BB3-a	Aeolianite	Weakly cemented bioclastic carbonate sand, bedding obliterated, some rhizocretions and carbonate nodules	2.5YR 8/6 Yellow	Medium/fine	Sub-rounded to rounded	Well sorted

Table 3.18: Compiled bedding vector data for BB1 site (Unit BB1-a).

Lithostratigraphic unit	Number of measurements	Sector angle (degrees)	Mean direction (degrees)	Rose diagram
Aeolianite (BB1-a)	9	20	132 ± 103	

3.5.3.1 Site BB1

There are 3 units present at this site (see Table 3.17 and Figure 3.68 for lithostratigraphical details), a basal aeolianite unit that appears underlie the modern beach (although the lower parts of the unit are obscured by sand ramps and numerous broken blocks of calcrete and consolidated palaeosol); a thick calcrete / palaeosol that contains numerous rhizocretions (i.e. rootlets and root mats) and large rhizomorphs (i.e. calcified tree trunks and large roots) (Figure 3.69), and overlying unconsolidated Holocene / modern dunes, as often found at sites on the south coast.



Figure 3.69: Site BB1 units, note large rhizomorphs running through the calcrete / palaeosol unit BB1-b (upper RH background).

BB1-a aeolianite

This is a weakly cemented aeolianite (Figure 3.68 and 3.69) that exhibits prominent, though low angle, cross-bedding. Carbonate content for this aeolianite ranged from 82% to 77% by dry mass, which may be part of the reason for weak cementation (south coast aeolianites, of similar age, which are more strongly cemented averaged at around 95% CaCO₃ by dry mass). The unit has apparently formed under 2 wind regimes (south-south-east and north-north-west), however, the dominant wind direction was from the north-north-west during deposition. The mean wind vector was $132 \pm 103^\circ$ at the 95% confidence interval (Table 3.18). This unit which crops out almost continuously for over 2 km along this section of the coast is thought to be of late Pleistocene age, given its stratigraphical position. This initial assumption is supported by later OSL and AAR dating (see Chapter 7). The unit undulates towards the north becoming thinner in places where the presence of older underlying units has restricted deposition to a degree (near BB3 for example).

BB1-b calcrete / palaeosol

As with the above aeolianite this unit crops out almost continuously for over 2 km of the western coast of Dudley Peninsula. Unit BB1-b unconformably overlies the BB1-a aeolianite, and comprises an upper laminar / brecciated section and a lower more pedogenically modified section that resembles an indurated palaeosol. The unit has formed when the upper regions of the BB1-a aeolianite were stabilized by vegetation colonization, and subaerially exposed during a depositional hiatus (hiatuses) sometime after MIS 5. Rhizomorphs and rhizcretions are a dominant feature of the unit with some large and spectacular examples (see Figure 3.69). At site BB1 the calcrete / palaeosol mantles the large aeolianite dune (BB1-a) dropping to sea-level in the swales to either side of the aeolianite (Figure 3.70).

BB1-c Holocene / modern backshore dunes

These dunes overlie most of the sediments along this section of the coast, except at site BB2 (Figure 3.68) near Deep Creek, where the larger alluvial fan deposit is situated. The dunes which are similar to those found at Pennington



Figure 3.70: Calcrete / palaeosol (BB1-b) at sea-level (site BB1).

Bay, Bales Beach, Vivonne Bay, and Hanson Bay, on the south coast of the island, are unconsolidated and have a thick covering of vegetation.

3.5.3.2 Site BB2

This site has possibly 4 discrete units (the organic band may not be a unit in its own right, rather it may represent a horizon within the Pooraka Formation sediment): an aeolianite unit (BB2-a), alluvial sediment equated with the Pooraka Formation (BB2-b), a thin organic (darkly coloured Munsell 2.5YR 4/2) band (BB2-c), and an upper distinct (from BB2-b) alluvial deposit, much younger than the underlying Pooraka Formation (Figure 3.68).

BB2-a aeolianite

This unit crops out intermittently along the coast and should not be confused with the bottom aeolianite at BB1-a. It is an older unit which underlies the BB1-a aeolianite at site BB3 (here unit BB3-d) (see Figure 3.68, 3.71a, b). At site BB2 unit BB2-a is truncated by alluvial sediments, and exhibits a thin remnant of a brecciated calcrete carapace, which can be seen in more complete form at site BB3 (BB3-b). BB2-a is only weakly cemented and is lightly coloured with a

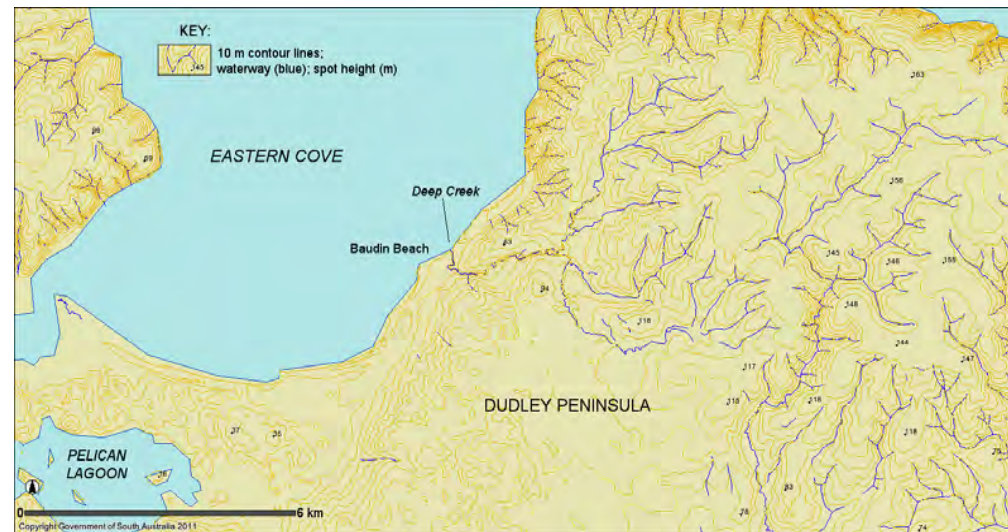


Figure 3.71a: Location of Pooraka Formation and other alluvial sediments at Deep Creek (site BB2), Baudin Beach, and surrounding topography (modified from the online atlas of South Australia [2011]).



Figure 3.71b: Units at site BB2. Blue dashed lines represent the limits of the sedimentary units. Note the faint level bedding in aeolianite BB2-a. This site is parallel to the coast.

yellowish cast (Munsell 2.5YR 8/6) (Table 3.17). Bedding has been mostly obliterated although there are some structures visible at this site (Figure 3.71b). BB2-a is the lowest aeolianite in the sequence at Baudin Beach, and may have been formed during the penultimate interglacial (MIS 7), or MIS 9.

BB2-b alluvial sediments of the Pooraka Formation

Overlying the BB2-a aeolianite is a thick body of massive alluvial fan sediments which have been interpreted as being representative of the South Australian mainland Pooraka Formation (Firman, 1967; Bourman *et al.*, 1997; Bourman *et al.*, 2010) (see Table 3.17 and Figure 3.68, 3.71a, b and 3.72) (Figure 3.71a illustrates the surrounding topography of the BB sites). The depositional timing for the Pooraka Formation has recently been equated with the Last Interglacial (MIS 5e), on the basis of luminescence dating measurements (Bourman *et al.*, 2010).



Figure 3.72: Location of units near site BB2. Note position of upper alluvial sediments in relation to the upper aeolianite unit (BB1a and BB3d) and calcrete (BB1b and BB3e). See person midfield for scale (~2 m).

The sediment is relatively rich in small, freshwater gastropod fossils (Family: Hydrobiidae—see Chapter 7, section 7.3.7.2), which all may be of the same genus. Many of these were collected from AAR dating purposes, as was a sample of the sediment for luminescence dating.

The site is incised by a small waterway called Deep Creek (Figure 3.71a), which must have been much more extensive, with greater output and a wider spread deltaic system during the Last Interglacial (MIS 5e).

The unit also exhibits a thin organic band (BB2-c) where it contacts the upper alluvium (BB2-2d). The band is probably a pedogenic accumulation of organic material concentrated by water movement. Slightly north of BB2 BB2-b is overlain by the late Pleistocene aeolianite BB1-a (which is also BB3-d at site BB3) (see Figure 3.72). This indicates that, even though both units may be late Pleistocene in age, the aeolianite is a younger unit than the Pooraka Formation sediments (BB2-b). As can be seen in Figure 3.72 the upper alluvial sediment (BB2-d) clearly overlies the upper calcrete / palaeosol (BB1-b and BB3-e), an indication that the upper alluvial sediments were deposited much later than the Pooraka Formation sediments (i.e. the aeolianite/calcrete forms the limits of a smaller palaeochannel formed sometime after the deposition of Pooraka Formation sediments—the BB2-d alluvium was later deposited over both, when a larger palaeochannel formed).

BB2-d upper alluvial sediments

The upper alluvial sediment is of a different character to the Pooraka alluvium (BB2-b) (Table 3.17 and Figure 3.68, 3.71a, b and 3.72). It overlies both the upper calcrete and aeolianite (BB1-a and BB1-b, and BB3-d and BB3-e) near site BB2, and directly overlies the Pooraka Formation where the palaeochannel truncates these units (see Figure 3.72). Bourman *et al.* (2010) described a “sub-pluvial” alluvial unit (at Burra Creek, South Australia) aligned with MIS 3 that overlies the Pooraka Formation. This unit, which contains *Diprotodon* bones, was dated at 43 ± 3 ka using OSL. The thick alluvial unit (~4 m: BB2-d) overlying the Pooraka Formation at Baudin Beach may be equivalent to this sub-pluvial unit described above (given that it overlies the upper calcrete [BB1-b and BB3-e] [see Figure 3.72], and must be therefore be younger than MIS 5).

3.5.3.3 Site BB3

This site unites most units (barring BB2-d) into one continuous sequence. There are 6 units: a lower aeolianite (BB3-a, the same as BB2-a) unconformably overlain by a weathered calcrete (BB3-b), Pooraka Formation alluvial sediment (BB3-c), an upper aeolianite (BB3-d, the same as BB1a) unconformably overlain by a laminar calcrete / palaeosol (BB3-e, the same as BB1-b), and well-vegetated Holocene / modern dunes (BB3-f, the same as BB1-c).

BB3-a lower aeolianite

This unit is the same unit as described at BB2a, although bedding structures are not visible (Table 3.17, Figure 3.68 and 3.73). This unit (and the associated calcrete [BB3-b] unconformity) crops out sporadically along this section of the coast; the uneven surface thus formed is infilled by Pooraka Formation sediments, which have a remarkably level upper surface.

BB3-b weathered calcrete

This unit unconformably overlies the aeolianite, and can be characterised by thin crumbly laminations, with abundant rhizocretions at lower contact (Table 3.17, Figure 3.68 and 3.73). The unit also resembles a featureless protosol in places along outcrop. BB3-b is very weathered and weakly cemented; as such the sediment readily crumbles. This may be a remnant horizon of a thicker deposit, much of which may have been removed by fluvial processes during Pooraka Formation deposition.

BB3-c alluvial sediments of the Pooraka Formation

These are the same sediments as described at BB2-b. Here they are much thinner as they are topping the underlying dune (BB3-a); however, in the swales either side of the dune the unit is much thicker (similar to site BB2) (Table 3.17, Figure 3.68 and 3.73). As mentioned above the upper surface of BB3-c is very level, and it infills the irregular topography formed by the lower aeolianite. Viewed from a distance the consistency of this level upper surface over a >2 km section of the coast is visually striking.

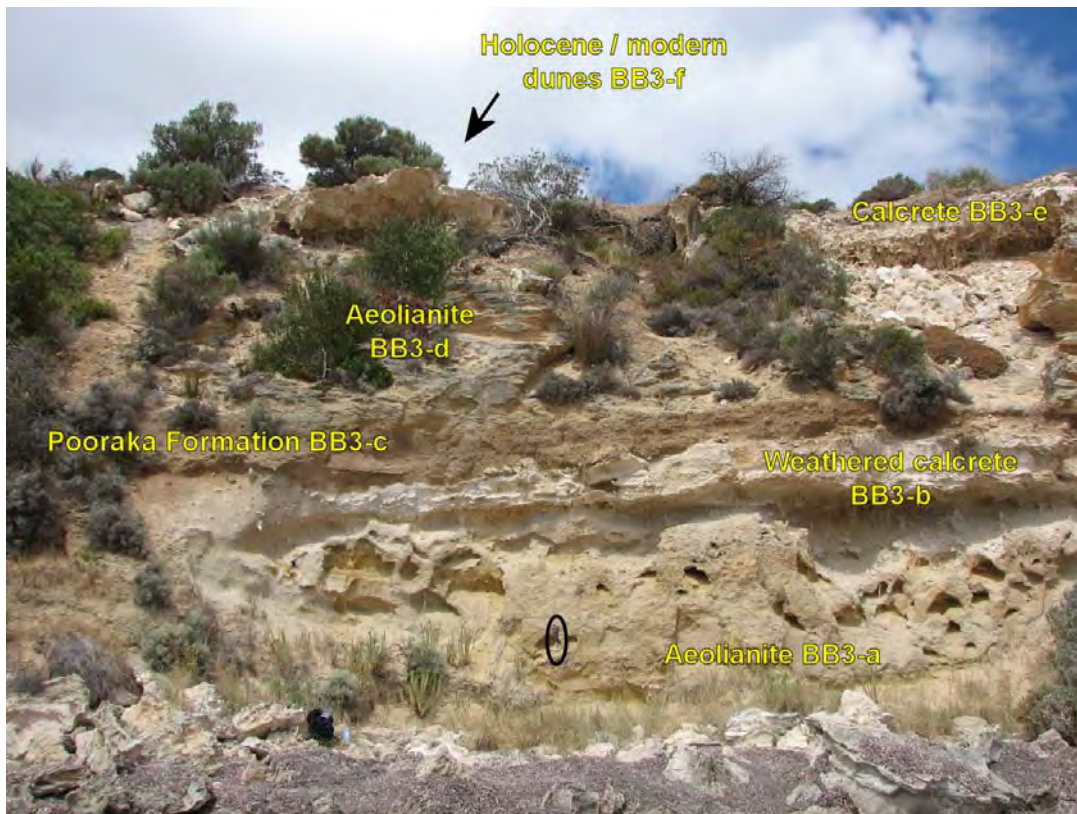


Figure 3.73: Sequence at site BB3. Note rock hammer (black ellipse) set for scale (33 cm).

BB3-d aeolianite, BB3-e calcrete / palaeosol, and BB3-f Holocene / modern dunes

These are the same sediments as described at BB1-a (Table 3.17, Figure 3.68 and 3.73). The aeolianite unit (BB3-d) is not as thick as it is at site BB1, this may be due to the presence of underlying sediments limiting deposition somewhat.

3.5.4 Stratigraphy of sediments at American River

This site is an extensive Holocene marine shell deposit on the shores of American River, south-west of Buicks Point, on Kangaroo Island. The sites consist of a series of extensive unconsolidated coquina beds, characterized by a hash of whole shells, comminuted shell, and other skeletal fragments in a loose, primarily carbonate, matrix (although not including foraminifers). American River is a large channel that almost bisects the Dudley Peninsula (Figure 3.1 and 3.74), and broadens to form Pelican Lagoon. In the past the channel may have formed a seaway that isolated the Peninsula from the rest of

the island (see Chapter 7, section 7.7.1.6). The study site is an extensive tidal flat deposit consisting of densely packed unconsolidated shell layers overlying Tapanappa Formation metasandstones of the Kanmantoo Group (these outcrop extensively north of Buicks Point).

The sediment contains numerous species of bivalves, and gastropods, typical of lagoonal, tidal flat, sand flat and estuarine contexts. These extensive shell deposits are regarded as St. Kilda Formation equivalents. The St. Kilda Formation on the South Australian mainland refers to Holocene deposits of unconsolidated shell, and shelly samphire and tidal flat sediments (cf. Firman, 1966; Ludbrook, 1984).

The deposits at American River cover a large area, and are characterised by low arcuate features which have similar morphology to beach ridges. Two sites were examined: AR1 on samphire flats and AR2, a scarped beach ridge closer to the shore (see Figure 3.74, 3.75 and 3.76). Common marine shells (bivalves and gastropods) found in these deposits were: *Katelysia scalarina* (Lamarck) 1818, *Katelysia rhytiphora* (Lamy) 1937, *Katelysia peronii* (Lamarck) 1818, *Eumarcia fumigata* (Sowerby) 1853, and *Battilaria* spp. (Benson) 1842. The American River deposits are discussed in more detail in the dating chapter (Chapter 7, section 7.3.8).

Third party source; Images redacted at request of thesis author

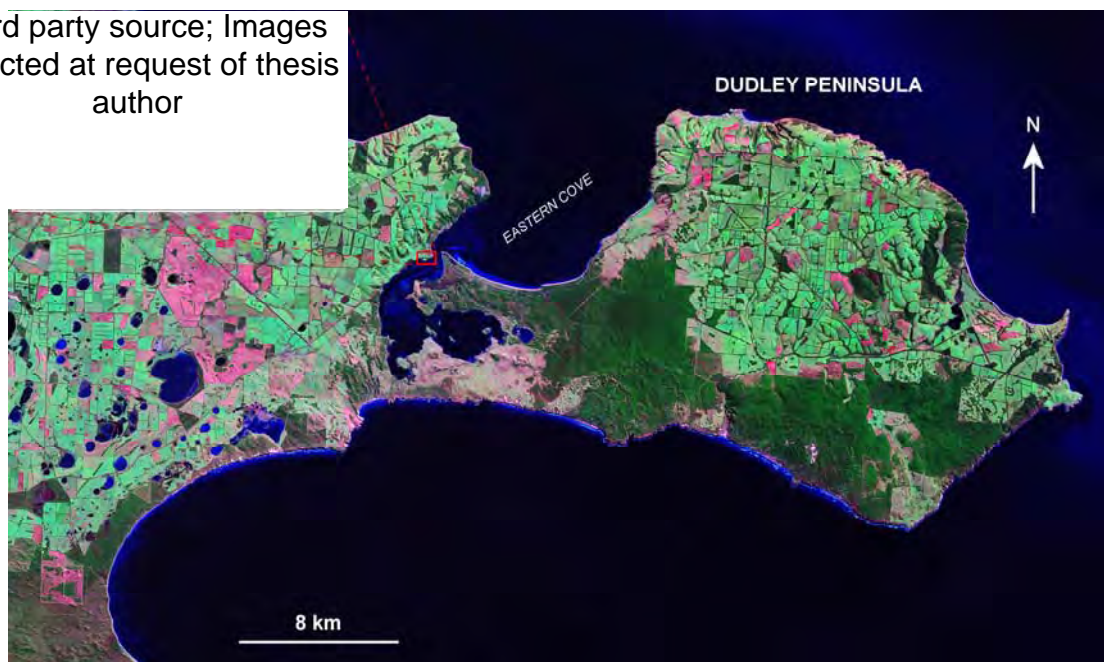


Figure 3.74: Location of American River sites (red circles upper LH inset) on the western side of the Dudley Peninsula (main image is a Landsat ETM: NASA Landsat program, 2001; upper LH image Google Earth, 2010).



Figure 3.75: St. Kilda Formation deposits at site AR1. Note sample pit lower LH foreground.



Figure 3.76: St. Kilda Formation deposits at site AR2. Note sample pit midground.

3.5.5 Stratigraphy of sediments at Kingscote Beach

The Kingscote study site (located at Kingscote: see Figure 3.1, and 3.77) is an extensive raised (+3.5 to +3.0 m APSL—top of unit) basalt cobble/pebble (Jurassic Wisanger Basalt is the most common cobble, with occasional limestone and quartz cobbles) conglomerate beach deposit, strongly cemented in a fine carbonate matrix, with relatively abundant whole and broken shell. The beach in the area is well protected and as such is of low-energy, and can be characterised by a shallow profile. Areas to the north and south have broad sand flats.

The thickness of the unit varies in conjunction with the undulations in the karstified underlying Kingscote Limestone (Late Eocene to early Late Oligocene: Milnes *et al.* [1983]); it ranges from a few 10s of cm to over 1 m in thickness. The lateral extent exposed sporadically in outcrop is approximately 680 m (Figure 3.77). The unit is usually unconformably overlain by a thin calcrete, and soil mantle, although the conglomerate is sometimes exposed at the surface. Clay pot Karst features are also present. Good outcrop of the unit can be found south of Beare Point, near Rolls Point (see Figure 3.77) and there is a small unconsolidated and pedogenically modified exposure near the boat ramp south-east of “The Bluff” (see Figure 3.77).



Figure 3.77: Extent in outcrop (red marker lines) of the Kingscote Conglomerate, at sites KC1 and KC2, Kingscote, Kangaroo Island (image is a Landsat ETM: NASA Landsat program, 2001).

The Kingscote Conglomerate unit was first described by Howchin (1899) who regarded it as a Recent coastline deposit. Bauer (1959) suggested a Pleistocene age based upon molluscs found in the unit. Further examination of the molluscan and foraminiferal assemblages led Milnes *et al.* (1983) to consider a Late Pleistocene age, equating the Conglomerate with the south Australian Glanville Formation (cf. Firman, 1967; Cann, 1978; Belperio *et al.*, 1984; Hails *et al.*, 1984a, 1984b; Murray-Wallace *et al.*, 1988; Murray-Wallace and Belperio, 1991). The AAR dating work completed (see Chapter 7, section 7.3.9) on the Kingscote conglomerate agrees with Milnes *et al.* (1983) chronological interpretation.



Figure 3.78: Kingscote Conglomerate near Rolls Point (site KC1). Note solution pipe middle background (knapsack for scale: 50 cm)

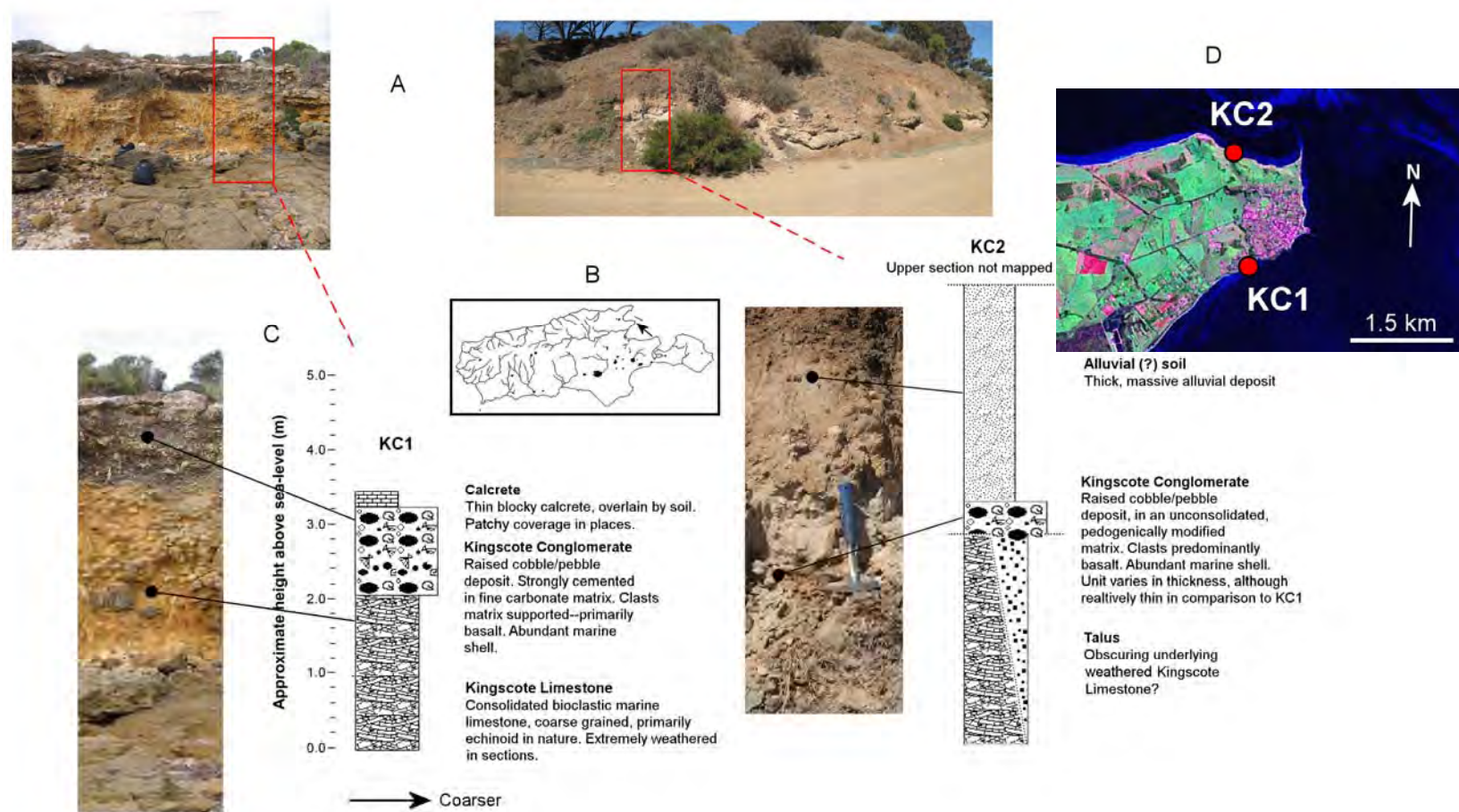


Figure 3.79: Kingscote stratigraphic logs for the sedimentary outcrops near Rolls Point (KC1), and near “The Bluff” (KC2). The top LH insets (A) are panoramas of site KC1 and site KC2 example outcrops. The middle inset (B) is a Kangaroo Island location map (with the location indicated by a black arrow). The site logs are C, and RH inset D comprises a satellite image (Landsat ETM: NASA Landsat program, 2001) showing indicated log and sample sites.

KC1: the Kingscote Conglomerate

At this section of the KC1 outcrop the conglomerate (depicted in Figure 3.78) is approximately 1 m in thickness (see also Figure 3.79). It overlies a very weathered section of the Kingscote Limestone. The unit is characterised by abundant basalt clasts, predominantly of pebble size (although some larger cobbles are present) (Figure 3.80), strongly cemented in a white carbonate matrix (10YR 8/1). Marine molluscs (bivalves and gastropods) are relatively abundant, however, not to the same extent as the clasts. No articulated bivalves were recovered from the sediment. Three species of marine shell were recovered from the unit for AAR analysis, and appeared to be among the most abundant, these were: *Katelsia scalarina*, *Amesodesma angusta* (Reeve) 1854, and *Nerita* (*Melanerita*) *atramentosa*. These represent sand dwelling, shallow water / tidal species (*Katelsia* and *Amesodesma*), and a rocky coast species (*Nerita*); both of these environments are characteristic of the modern Kingscote coast. Fragments and whole tests of the foraminifer *Marginopora vertebralis* were also found in the conglomerate: an indication of a probable MIS 5e age for the unit.



Figure 3.80: Close-up of the Kingscote Conglomerate unit (near Rolls Point). Note abundant basalt clasts (rock-hammer handle for scale: 20 cm).

KC2: the Kingscote Conglomerate

At this site the matrix is soft and unconsolidated (very pale brown colouring—10YR 8/4), with flat basalt pebbles and marine shell (similar species mix to KC1) falling out of the exposure. The unit is overlain by a massive, thick red-brown soil, which is possibly alluvial in origin (see Figure 3.77, 3.79 and 3.81). This soil may possibly be equated with the upper alluvial unit at Baudin Beach. Talus from the disintegrating conglomerate has formed a small scree slope which may be obscuring the underlying Kingscote Limestone at this site.

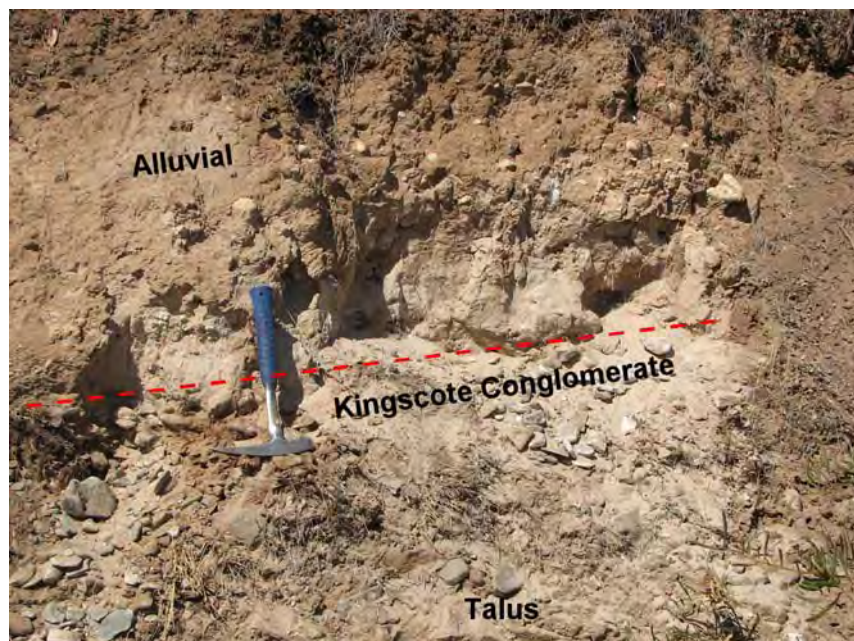


Figure: 3.81: Kingscote Conglomerate at site KC2. Red dashed line shows approximate position of the unit (uppermost) (rock-hammer for scale: 33 cm).

KC2: the Kingscote Conglomerate

At this site the matrix is soft and unconsolidated (very pale brown colouring—10YR 8/4), with flat basalt pebbles and marine shell (similar species mix to KC1) falling out of the exposure. The unit is overlain by a massive, thick red-brown soil, which is possibly alluvial in origin (see Figure 3.77, 3.79 and 3.81). This soil may possibly be equated with the upper alluvial unit at Baudin Beach. Talus from the disintegrating conglomerate has formed a small scree slope which may be obscuring the underlying Kingscote Limestone at this site.

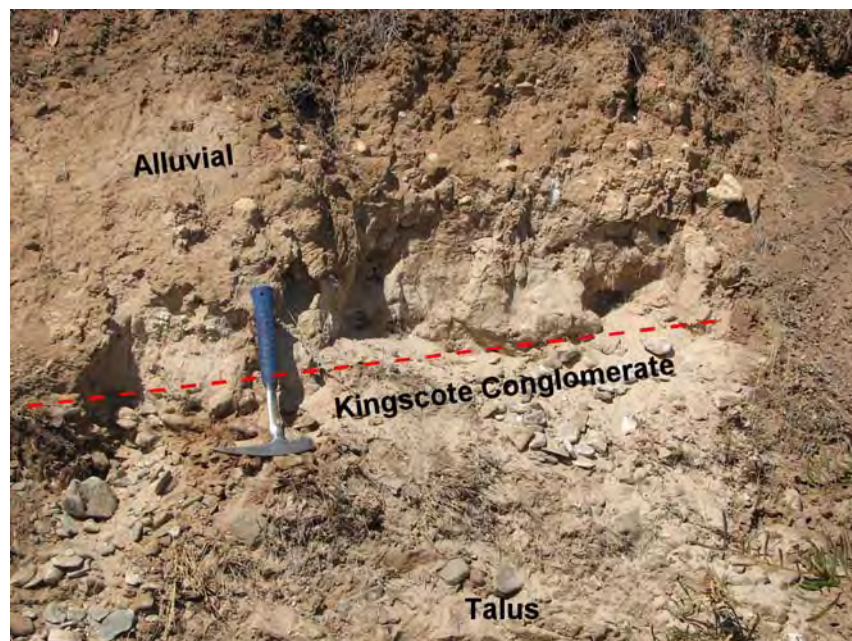


Figure: 3.81: Kingscote Conglomerate at site KC2. Red dashed line shows approximate position of the unit (uppermost) (rock-hammer for scale: 33 cm).

PART IV: North coast stratigraphy (and
summary and conclusions for chapter
stratigraphy sections)

3.6 Stratigraphy and facies of the Kangaroo Island study sites on the north coast

3.6.1 Introduction

The following sections examine the stratigraphy and facies present at sites examined along the north coast of Kangaroo Island. Sites represented host shelly tidal flat muds (NC1), raise beach facies (NC2), aeolianites (Emu Bay and Stokes Bay), and raised cobble beach facies (Smith Bay).

3.6.2 Stratigraphy of the North Cape sites (NC1 and NC2)

Two sites were examined on North Cape, Kangaroo Island: Site A (NC1), south of Point Marsden, and Site B (NC2), situated in Boxing Bay. The sites are located on the North Cape, a large cape on the northern coast (Figure 3.1; Figure 3.82).

As a result of its leeward location, and the refraction of the predominant south-west swell into the Backstairs Passage before it reaches the eastern portions of the coast (Short and Fotheringham, 1986; Short, 2006), the eastern face of the cape where Site A is located is of low wave energy. The protrusion below Point Marsden may also afford some protection to these eastern beaches.

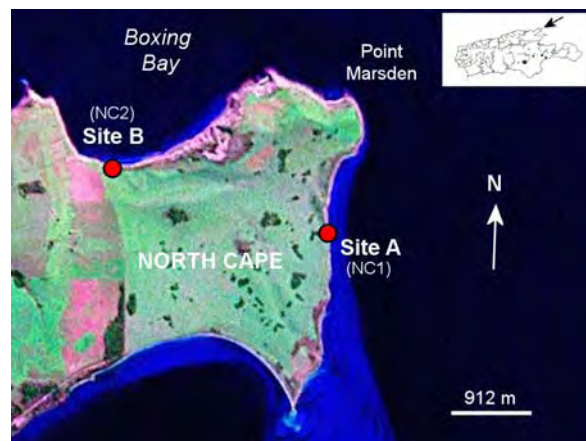


Figure 3.82: Study site locations on the North Cape, Kangaroo Island. Inset upper left shows the geographical location (black arrow) of the North Cape region (Landsat ETM image: NASA Landsat program, 2001).

The coast along this area is characterised by broad tidal flats (~100 m wide) and sandy/cobble high-tide beaches. The beach at the study site is bordered by low cliffs cut into what are possibly Early Pleistocene calcareous sediments; the base of the cliff is strewn with broken blocks, and the upper sediments are

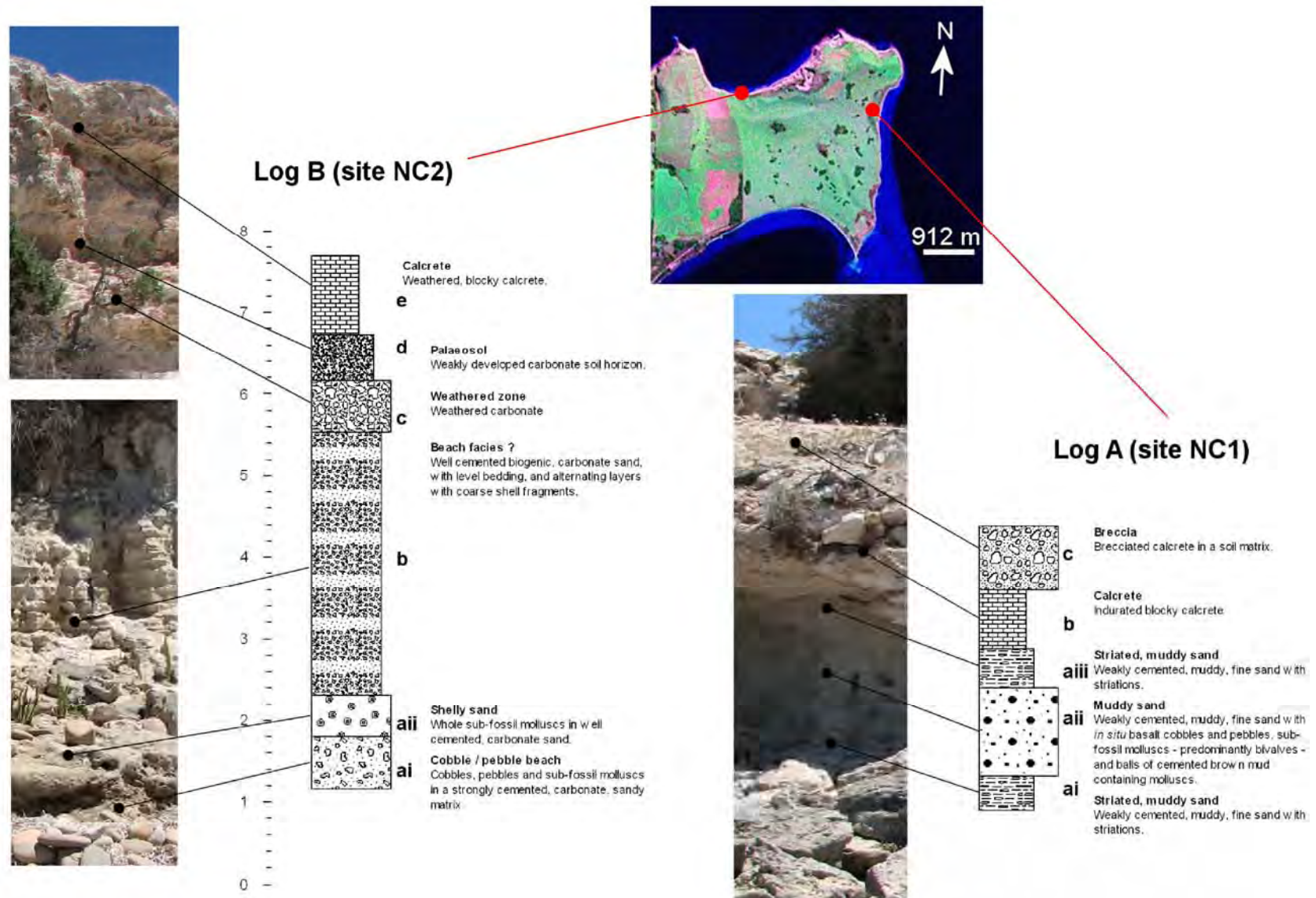


Figure 3.83: Stratigraphic logs for the North Cape and Boxing Bay study sites (upper RH inset image Landsat ETM: NASA Landsat program, 2001)



Figure 3.84: Outcrop at site NC1, on North Cape, Kangaroo Island. The open ellipse indicates a rock-hammer set for scale (33 cm).

undercut. These sediments form a large platform (above the cliff-line) that grades towards the north at $\sim 3^\circ$ of dip, and to the east, at least in the region traversed around the study site. The top of the cliff-line near the shore is approximately +4 m APSL. This site has what are probably 2 discrete units: a muddy or clayey sand with *in situ* marine shell, and an overlying calcrete crust.

The beach at Site B (NC2), in Boxing Bay, is of moderate wave energy; characterised by a sandy beach with some storm deposited cobbles and boulders at the high-tide mark. The rear of the beach hosts high calcarenite cliffs (~ 8 m APSL) that overlie cemented shelly sands and a cemented cobble/pebble beach. The cobble/pebble beach extends to below sea-level at the eastern end of the beach, this would indicate that the cobble/pebble beach was of greater extent in the past and was subsequently eroded sometime after deposition and cementation.

3.6.2.1 North Cape beach, Site NC1 (Figure 3.83; Figure 3.84)

Muddy sand unit

This unit may be an Early Pleistocene (suggested by amino acid dating: Chapter 7) shallow subtidal or (more likely) intertidal facies (marl) equivalent to the modern sand flat sediments (particularly in morphology, given the extent of the upper platform). The facies is characterised by a sparsely shelled very-fine light reddish grey (Munsell 2.5YR 7/1), muddy/clayey moderately cemented carbonate sand (17% non-organic minerals) striated or laminated at the upper and lower bounding surfaces, with few fossils. Basalt cobbles occur occasionally in the unit, as do grayish brown (Munsell 10YR 5/2) balls (~ 100 to 200 mm in diameter) of cemented shelly mud or clay (Figure 3.85). These balls show abundant fragments of marine gastropod and bivalve fossils. Their formation can only be speculated upon; they may have been clots of sticky clay washed into the shallows during rainstorms; rolled around on the sea-bed by storm waves and currents, picking up broken shell in the process, prior to deposition. Although, a local supply for the clay is not immediately obvious; it could have been sourced from riverine environments farther afield however. Equally, a simpler (and more



Figure 3.85: Shelly clay balls in the upper portion of the muddy sand unit; see text for possible explanations (pen for scale: 15 cm). The white flecks are broken shells.

plausible) explanation would be that they are merely solution pipe infills (clay pots) that protruded through the calcrete into the underlying unit and were subsequently exposed as the upper calcrete was undercut during storm surge or higher sea-level (Figure 3.85). The marine shell in the mix could have been sourced from sea-bird middens on the upper surface. In the central portion of the unit there were occasional marine shells apparently all bivalves; most were poorly preserved and broken. Nevertheless, there were the rare unbroken (although disarticulated) shells; there were also a few examples of articulated shells in the unit (Figure 3.86). All of the marine shell sampled for amino acid dating purposes were of the species *Anapella cycladea* (Lamarck) 1818. This species is common in low-energy contexts, in the intertidal to shallow subtidal zone, for example mud and sand flats in enclosed bays, inlets, and estuaries (Ludbrook, 1984; James *et al.*, 2006). Given the articulated condition of some of the shells it is likely that these represent a sparse biocenosis.

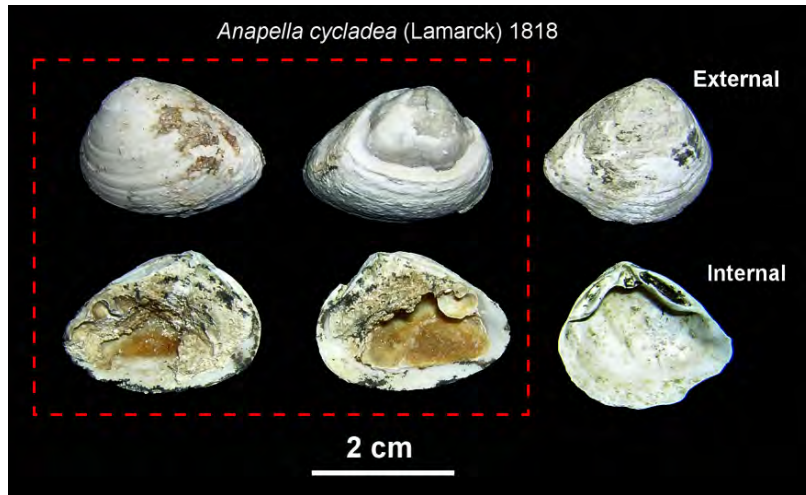


Figure 3.86: Three examples of *Anapella cycladea* recovered from the muddy sand (intertidal/subtidal) unit. The bivalves in the dashed box are from 2 articulated individuals.

This unit was only accessible in a few areas along the approximate 400 m length of shore investigated; most of its length was obscured by collapse. The Site A outcrop was the best example of the facies with some of the best preserved fossils.

It is difficult to assess whether this unit should be associated with the Bridgewater Formation (or indeed the Point Ellen Formation). The Bridgewater Formation is often not only comprised of aeolianite intercalated with palaeosols and calcretes, but occasionally is also associated with shallow subtidal, littoral, lagoonal (Glanville Formation and equivalents), and lacustrine (Padthaway Formation) facies (Belperio, 1995). There is no aeolianite present at this site other than a remnant calcified 'B' horizon—the calcrete mantle. In light of this, and the probable age of the facies; its faunal content [i.e. too old to be a Glanville Formation equivalent (MIS 5e), and the absence of indicator fossils to tie it to the Point Ellen Formation], it should be considered apart. Given this, the units comprising the outcrop at North Cape beach are informally designated in this thesis as the North Cape Beds. At least until further investigation can be undertaken, including detailed mapping of the full extent of the outcrop.

Calcrete unit

This calcrete may be an older example of this sediment type than that found on the southern side of the island. It is blocky and weathered and the upper

portions are extremely brecciated, and infilled with thin soil (Figure 3.84). The upper surface forms a large platform around 4 to 5 m APSL, this implies that the carbonate dunes that the calcretes formed from were deposited onto a large relatively level body of sediments, in this case the underlying intertidal facies which were probably present originally as sand flats or mud flats similar to the present. These would have extended much farther inland during a time of higher than present sea-level—conversely, these units could also have been uplifted during the Pleistocene, then cut back to their current margins at the rear of the shore.

3.6.2.2 North Cape beach, Site NC2 (Figure 3.83; Figure 3.84; Figure 3.87)

The beach at NC2, in Boxing Bay, is of moderate wave energy, and is characterised by a sandy beach with some storm deposited cobbles and boulders at the rear of the berm. The backshore of the beach hosts high calcarenite cliffs (~8 m APSL) that overlie cemented shelly sands and a cemented cobble/pebble beach. The cobble/pebble beach extends to below sea-level at the eastern end of the bay. This would indicate that the cobble/pebble beach was of much greater extent in the past and was subsequently eroded sometime after deposition and cementation. The cobble/pebble beach and thin shelly sands are informally designated here as the Boxing Bay Conglomerate (this should not be confused with the conglomerate facies associated with the Cambrian Boxing Bay Formation [cf. Daily *et al.*, 1980], which are located further east and west near Point Marsden and White Point). It was difficult to make an initial age estimate at this site; however, later amino acid analysis suggested early / middle Pleistocene. This section is examined in more detail in the chronology chapter (Chapter 7).

3.6.3 Stratigraphy of Emu Bay aeolianite

Emu Bay is a large embayment on the northern coast of Kangaroo Island, at the neck of the North Cape isthmus (see Figure 3.1 and 3.88). The study site (EB) is an isolated outcropping of an aeolianite sequence located towards the eastern end of the embayment. The outcrop protrudes to sea-level forming a small headland, similar to those at Pennington Bay. The beach is of moderate



Figure 3.87: The Boxing Bay Conglomerate and beach facies (these could also be the bottomset beds of an aeolianite deposit (rock-hammer set for scale [black ellipse]: 33 cm).

energy and most of the embayment is dominated by well-vegetated modern and Holocene backshore dunes. The sequence (see Figure 3.89 and Table 3.19) consists of 2 aeolianite units (a and c) separated by a palaeosol unconformity (b), and capped by a calcrete mantle (d) and cliff-top dunes (e).

3.6.3.1 EB-a aeolianite

This is a thick (~8 m) consolidated unit characterised by prominent cross-bedded and troughed dune foresets (Figure 3.89). The sediment is a well-cemented, fine carbonate sand with some solutional weathering features (karst) (Table 3.19). Rhizocretions are few, and the site presents a clean face that has recently been eroded.

Luminescence dating (see Chapter 7) suggests a middle Pleistocene age for this unit (MIS 7). Bedding vector data implies a predominantly north-westerly wind direction during deposition of the sediment at $169 \pm 78^\circ$ azimuth (Table 3.20). The aeolianite is unconformably overlain by a weakly cemented, poorly developed, pinkish palaeosol (EB-b) (Table 3.19). This may represent a relatively short depositional hiatus.

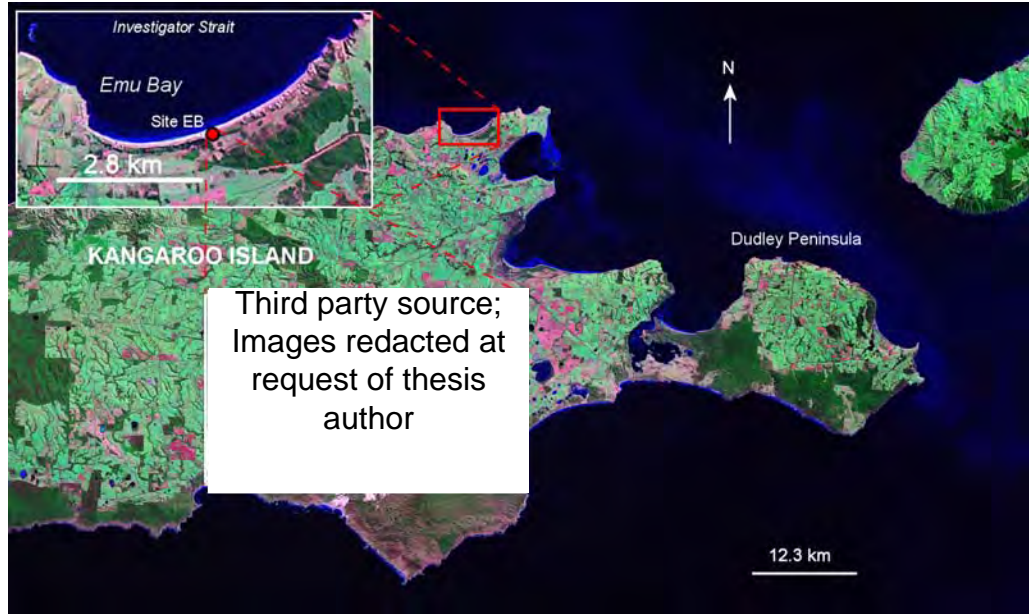
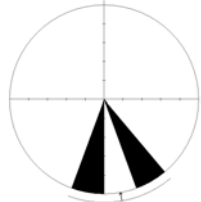
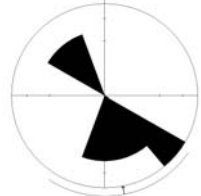


Figure 3.88: Location map for study site on Emu Bay, Kangaroo Island. Inset (upper LH) shows the general location of site EB (red circle). The lower LH inset is a closer view of the EB study site; the red arrows indicate sample positions (Google Earth, 2010) (main image is a Landsat ETM: NASA Landsat program, 2001).

Table 3.19: Lithostratigraphic characteristics of site EB at Emu Bay.

Unit number	Lithostratigraphic unit	Description	Munsell colour	Grain size	Grain sphericity	Grain sorting
e	Backshore dunes	Modern/Holocene unconsolidated carbonate dunes, well vegetated	2.5Y 7/1 Pale brown	Coarse/medium	rounded	Moderately sorted
d	Calcrete	Blocky calcrete	--	--	--	--
c	Aeolianite	Consolidated carbonate dune sands, some karst	10YR 8/1 White	Fine	Sub-angular / sub-rounded	Very well sorted
b	Palaeosol	Carbonate soil horizon, weakly cemented, carbonate nodules, and rhizoliths present	7.5YR 7/3 Pink	Fine	Sub-rounded to rounded	Moderately to poorly sorted
a	Aeolianite	Consolidated carbonate dune sands, some karst	10YR 8/1 White	Fine	Sub-angular / sub-rounded	Very well sorted

Table 3.20: Compiled bedding vector data for site EB at Emu Bay.

Lithostratigraphic unit	Number of measurements	Sector angle (degrees)	Mean direction (degrees)	Rose diagram
Aeolianite (c)	2	20	170 ± 20	
Aeolianite (a)	7	20	$169 \pm 78^\circ$	

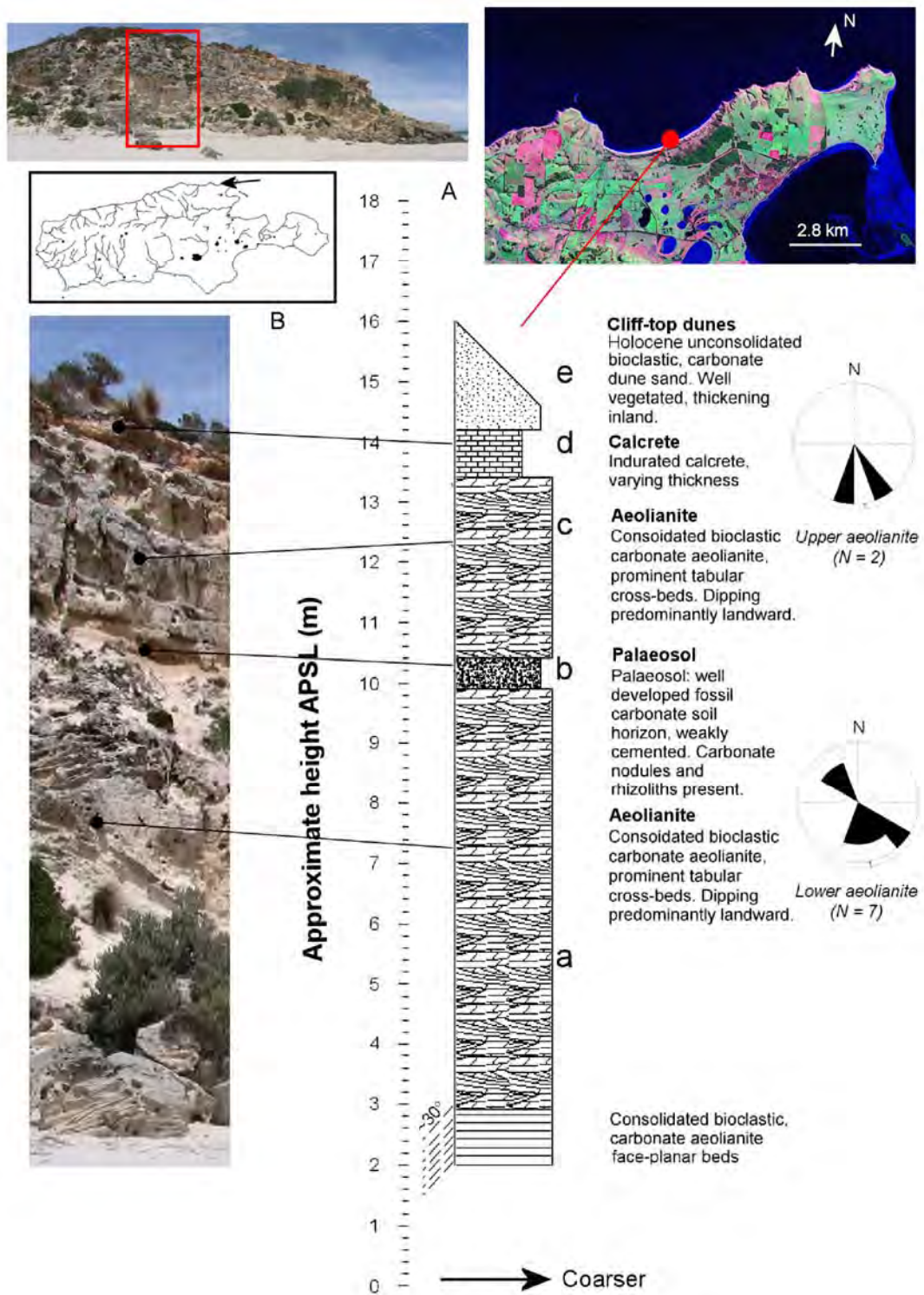


Figure 3.89: Stratigraphic log (B) for the sedimentary outcrop at Emu Bay (EB). The top LH, lower LH, and RH insets (A) are a panorama of site EB outcrop, a satellite image (Landsat ETM: NASA Landsat program, 2001) showing indicated log and sample sites, and a Kangaroo Island location map (with the location indicated by a black arrow). Rose diagrams are given for the upper and lower aeolianite units, showing bedding orientations attributable to wind vector.

3.6.3.2 EB-c aeolianite

This unit is very similar to the lower aeolianite (see Table 3.19 and Figure 3.89), although it is less exposed than the lower unit (i.e. much of the face is covered by solutional carbonate sheaths). Bedding vector data (only 2 were recorded) suggest a similar wind regime to the lower unit—north to north-westerly winds during deposition.

This unit is unconformably overlain by a blocky calcrete (EB-d) that varies in thickness along outcrop. The sequence is topped by well-vegetated, unconsolidated Holocene cliff-top dunes (EB-e).

3.6.4 Stratigraphy of the Smith Bay near shore deposits

Smith Bay is located on the northern coast of Kangaroo Island, approximately 23 km east of Stokes Bay (Figure 3.1). The study site at Smith Bay hosts an uplifted pebble/cobble beach that rests unconformably on Permian glacialine sediments.



Figure 3.90: Shingled cobbles and boulders at Smith Bay, Kangaroo Island. Clasts are generally flattened and range from pebbles and fist sized cobbles to large (>250 mm) boulders. Many of the clasts may be reworked glacial erratics from a Permian succession, as some boulders have deep scratches and striations on their surfaces (the gray cobble in the left foreground, for example—see inset). The boulders and cobbles are predominantly red Cambrian sandstone, Kanmantoo Group metasediments, with some granites, and quartzites. The dark brown laminated sediments in the background exposed at the shore are Cambrian micaceous siltstones of the Smith Bay shale.

Smith Bay is a wide (~4 km) shallow bay (in terms of coastal morphology, not water depth—Figure 3.91), characterised by high-angled (~20°) shingled cobble/boulder beaches (Figure 3.90) with a sandy margin at the shore, resting on Cambrian Kangaroo Island Group platformal sediments, in this case the Smith Bay Shale (Chapter 1, section 1.4.1.1).

3.6.4.1 The uplifted cobble beach

The cobble beach unit is located near the top of a broad headland towards the eastern side of the embayment (Figure 3.90). The base of the unit is approximately 18 m APSL, and ranges up to ~2 m thick. It is overlain by a

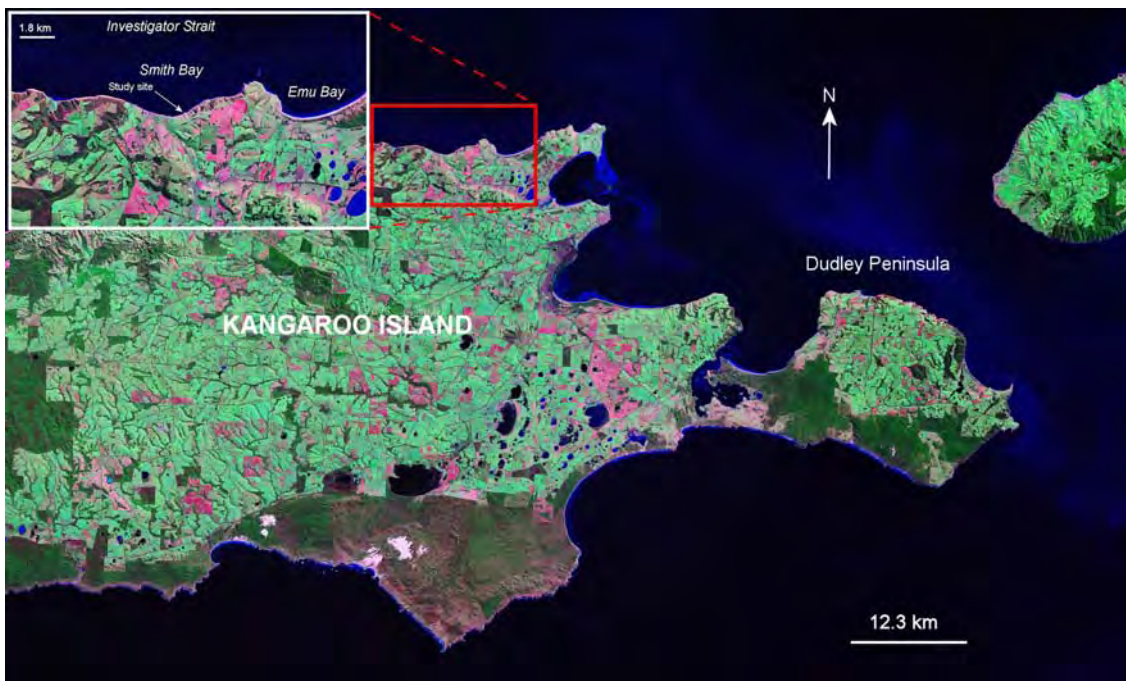


Figure 3.91: Location of the Smith Bay study site (image is a Landsat ETM: NASA Landsat program, 2001).

blocky, weathered calcrete. The upper surface of the calcrete over the entire ridgeline is broken and dissected, and strewn with calcrete rubble. A thin soil infills the broken surface, and the lower portions of the calcrete are commonly powdery and loose.

The beach (Figure 3.92 and 3.93) overlies ~18 m of Permian glacial till, first described in detail by Bourman and Alley (1999). The pebbles, cobbles and boulders that make up the beach are strongly cemented in a white (Munsell 10YR 8/1) subangular/subrounded fine carbonate matrix, that is well sorted. The matrix is composed primarily of unidentifiable carbonate bioclasts, rare foraminifers and calcareous algae, and a high proportion of quartz grains (~31%

by dry mass—along with other non-organic minerals). Also cemented in the matrix were rare, poorly preserved marine molluscs, which were difficult to remove from the sediment matrix (no intact entire molluscs were identified). Nevertheless, some fragments of shell were large enough to permit identification to the genus level; although only two were identified, these were: *Mactra* sp. (Linnaeus) 1767 and *Irus* sp. (Linnaeus) 1758. Both genera have species that live in a range of environments, from sandy beaches to tidal inlets and mangrove swamps (Ludbrook, 1984).

The beach deposit formed under similar conditions to that of its modern counterpart. This unit is interpreted to be of early Pleistocene age, based upon amino acid racemization work undertaken on the recovered fragments of marine shell (see Chapter 7). In this case then the height of the beach unit implies that tectonic uplift must have taken place sometime later in the Pleistocene. If the beach is of similar antiquity to the Point Ellen Formation (given the condition of the fossils and level of induration), which implied a sea-level of around 3-4 m APSL during deposition (uplift notwithstanding), then the Smith Bay cobble beach may have been uplifted by as much as 15 m. Neotectonic uplift must be considered as according to the Oxygen Isotope record (Lisiecki and Raymo, 2005) it is unlikely that any instances of interglacial sea-levels reached the current height of the unit during the Quaternary period. Indeed, according to Siddall *et al.* (2007) interglacial sea-levels prior to MIS 11 were similar to or lower than present.



Figure 3.92: Uplifted pebble beach over Permian till, Smith Bay, Kangaroo Island.

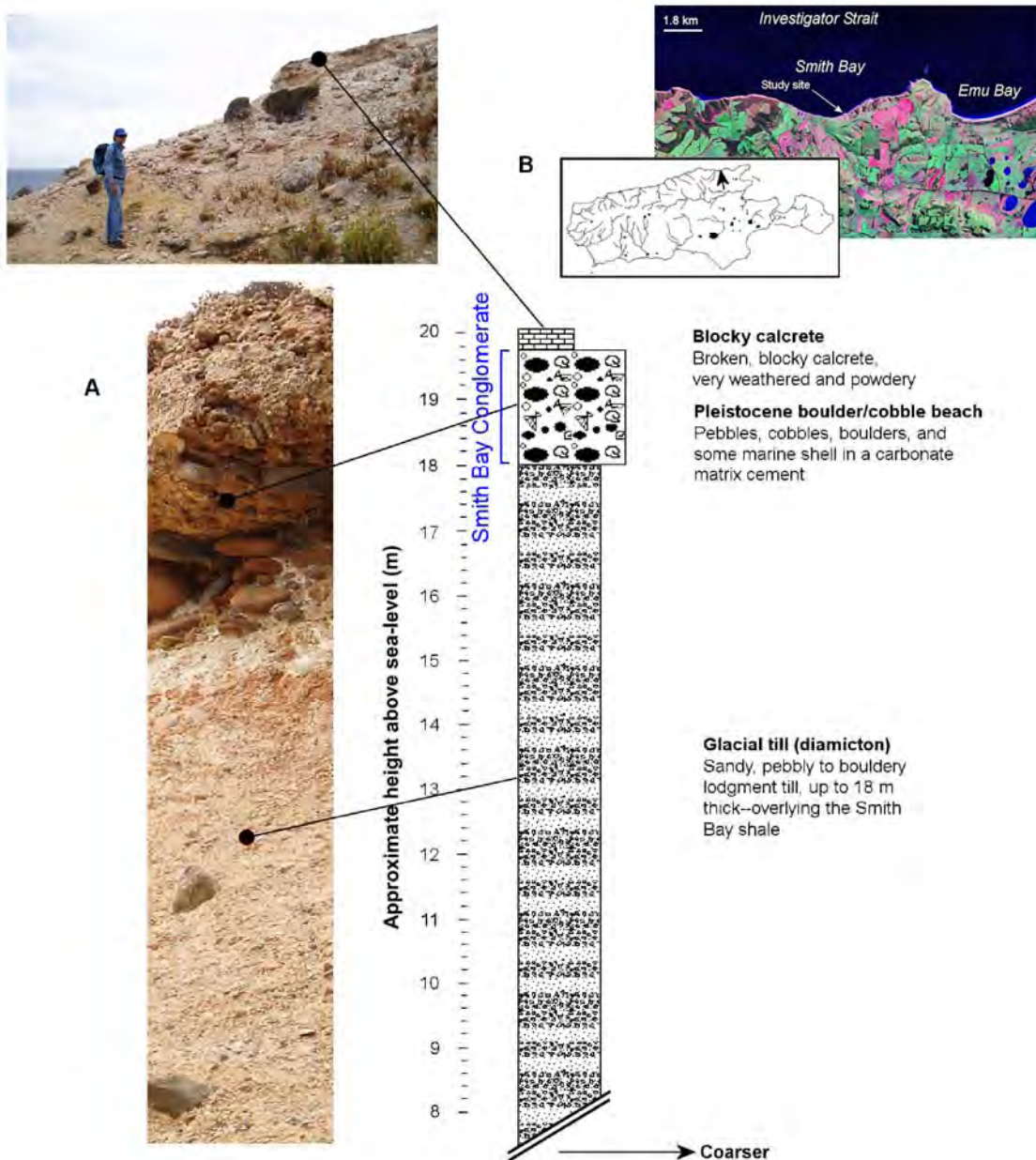


Figure 3.93: Stratigraphic log (A) for the sedimentary outcrop at Smith Bay (SB). The top LH, top middle, and top RH insets (B) are a panorama of site SB outcrop, a Kangaroo Island location map (with the location indicated by a black arrow), and a satellite image (Landsat ETM: NASA Landsat program, 2001) showing indicated log and sample sites.

Although not the principal focus of this thesis, this is a rare site that warrants in depth study; the neotectonic implications should prove to be of great importance in furthering the understanding of Quaternary sedimentary deposition on Kangaroo Island.

3.6.5 Stratigraphy of the Stokes Bay aeolianite

Stokes bay is a small embayment located on the northern coast of Kangaroo Island, approximately 22 km west of Smith Bay. The bay hosts a sandy

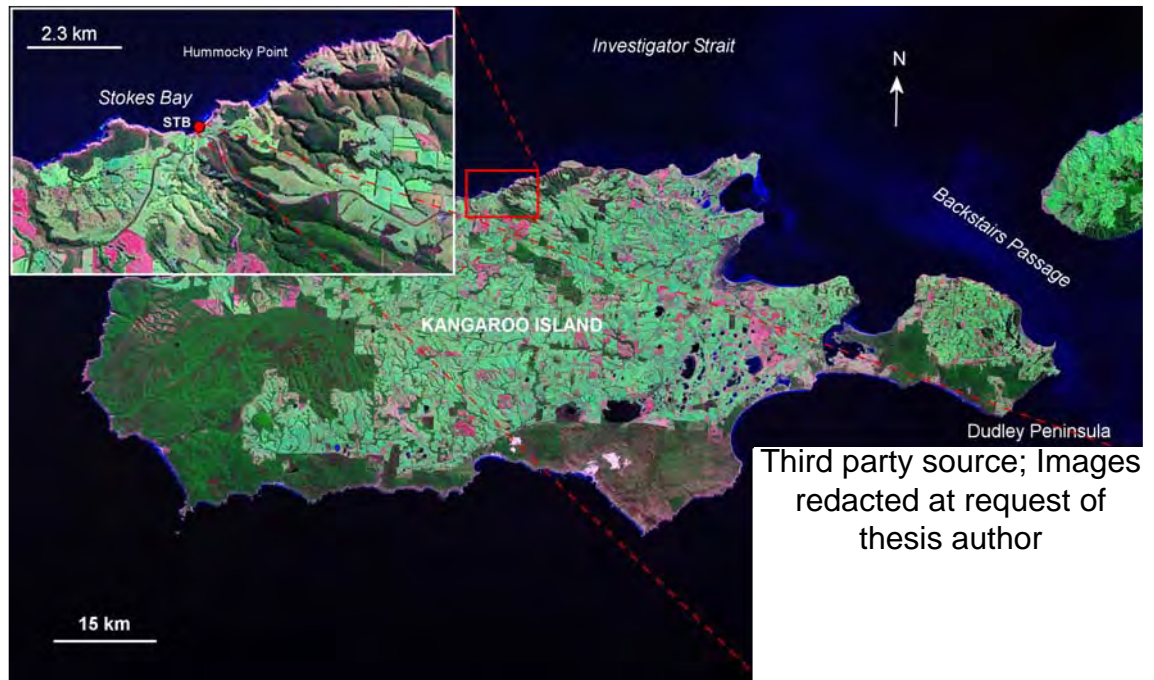


Figure 3.94: Location map for study site at Stokes Bay, Kangaroo Island. Inset (upper LH) shows the general location of site STB (red circle) (Landsat ETM images: NASA Landsat program, 2001). The lower RH inset is a closer view of the STB study site; the red arrow indicates sample positions (Google Earth, 2010).

moderate energy beach backed by ~8 m high aeolianite cliffs, with scree slopes and large dislodged blocks of aeolianite and calcrete at the base.

The study site is the bounding western calcarenite headland (see Figure 3.94). The headland is a single aeolianite unit, overlain by a blocky calcrete that is weathered and brecciated. The aeolianite is karstified, very weathered and leached, and although the sediment is indurated it is quite friable and “foamy” (of low density) in places. Most of the bedding is obliterated, although some is visible in patches along the outcrop. The unit was initially interpreted to be of early Pleistocene age, and this was based on the appearance of the sediments, in terms of the weathered and leached facade. The base of the outcrop is strewn with broken blocks and boulders of aeolianite, and calcrete. The site is high at ~13 m APSL, and no cliff-top Holocene dunes are evident; although, a vegetated sandy soil is present.

The site is located in a small embayment, approximately 750 m wide; bounded by headlands. The beach is of moderate energy (Short, 2006); certainly less energetic than beaches of the southern coast.

3.6.5.1 Aeolianite unit

This unit averages at approximately 8 m thick (Figure 3.95); it is extremely weathered and karstified; although bedding is not entirely obliterated (Figure 3.96). The upper portions of the unit are blocky and dissected (Figure 3.97), rich with what appear to be pisoliths (Figure 3.98); however, close observation could not be made because of the height of the unit. These nodules could also be gravel derived from the overlying calcrete, cemented in place. Given that it was

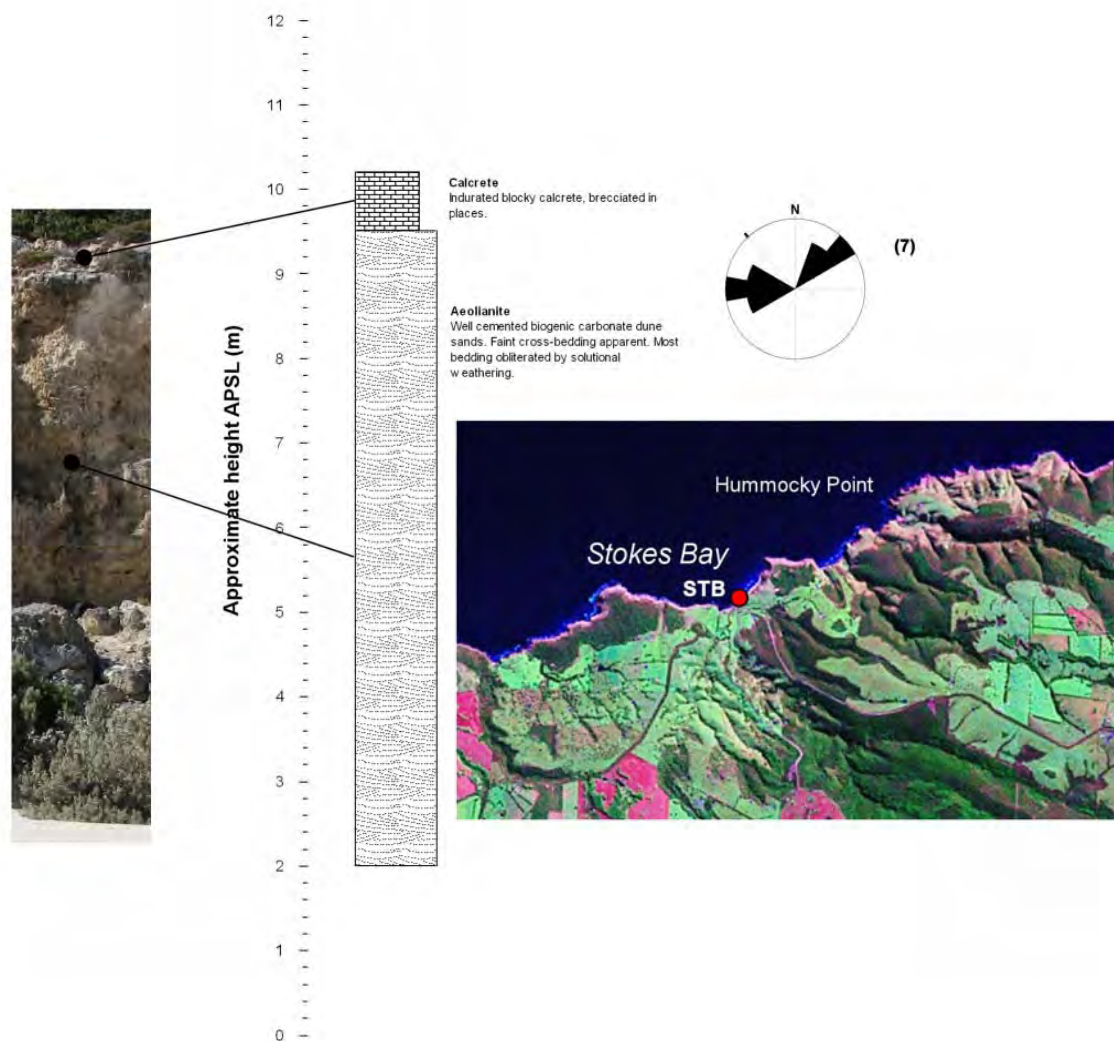


Figure 3.95: Stratigraphic logs of the Stokes Bay aeolianite, Stokes Bay Kangaroo Island. The log illustrates the approximate thickness of the units (inset satellite image is a Landsat ETM: NASA Landsat program, 2001).



Figure 3.96: Lower section of aeolianite unit, note the cavernous weathering, and also the bedding structures visible in this unit.



Figure 3.97: Calcrete unconformably overlying aeolianite at Stokes Bay.



Figure 3.98: Close view of the upper portions of the deposit, showing the nodule-like texture that may be due to pisoliths.

hard to discern where contact between the aeolianite and the calcrete began, it may be that this pisolitic (if indeed that is what the nodules are) section is the lower portion of a very thick complex calcrete profile.

The aeolianite is a yellow (Munsell 10YR 8/6) medium-fine biogenic carbonate grainstone composed primarily of unidentifiable carbonate bioclasts: some shell particles and foraminifers can be found; however, most clasts are too diagenetically altered to be identified. The sediment is moderately cemented but is friable and foamy (light). It is almost pure carbonate with only ~1.2% quartz and other non-carbonate minerals by dry mass.

The bedding dip and orientations (where observable) suggest that this aeolianite was deposited under wind regimes blowing from the east and the south-west.

3.6.5.2 Calcrete unit

The calcrete is very weathered, blocky and massive (Figure 3.96). The upper surface is deeply dissected and rubbly; it is unlikely that this calcrete is of similar age to that found covering some of the southern coastal deposits, it is probably much older. It varies in thickness to around 1.5 m, and is infilled by a

thin, vegetated sandy soil. The upper part of the aeolianite where it makes contact with the calcrete appears to be pisolitic (Figure 3.97); although, as iterated in the previous section this may also be the lower portion of a more complex calcrete profile.

3.6.6 Summary and conclusions for stratigraphic sections

This section will discuss the stratigraphy and facies analyses detailed in the previous stratigraphical sections of this chapter.

The Pennington Bay study area (south coast) was the largest examined on the island, in terms of the number of sections that were logged and sampled. The site is dominated by Quaternary aeolianite and palaeosol couplets; this does not mean this was an uncomplicated site to interpret. In itself, the position of the units in relation to each other across the geographical space of the study area was extremely complicated, and the sections examined may not be adequate to give more than a cursory overview of the environmental history of this site implied by the Quaternary geology.

Chapter 2 outlined various case studies that infer that the timing of coastal aeolian dune deposition is linked to periods of high sea-level; not necessarily higher than, or as high as present, and rarely during periods of extreme low sea-level (as experienced during a glacial for example). Their position, orientation, and internal structure suggests that they were barrier dunes which were immediately adjacent to the strandline, but also probably spread for hundreds of metres or even many kilometres inland from the coast.

The position of the Kangaroo Island aeolianites at Pennington Bay suggests that many of the units were laid down at a time when sea-level was lower than present, possibly many meters lower. This conclusion is reached by observation of the aeolianite outcrops: all are wave-cut into cliffs and there are many stacked headlands that protrude below current sea-level. All this would require is that during deposition the coast was a few tens of metres or hundreds of meters south of its current position, as it would be during a transgressive or regressive phase of an interglacial, or interstadial for example. This is in keeping with the modern / Holocene analogue (the modern / Holocene

backshore and cliff top dunes) of the Pleistocene dunes. The modern / Holocene dunes extend inland for hundreds of metres, and in some areas many kilometres. For example, if modern sea-level were to rise by just a few metres the inland backshore dunes (if consolidated) would be cut into and cliffed by the higher water level. So, protrusion *below* sea-level does not necessarily imply deposition during *extreme* low sea-level, as would be experienced during a glacial period. These periods of slight higher or slightly lower sea-level could be termed as 'intermediate sea-levels'. The aeolianite sites at Bales Beach had similar morphostratigraphy to that of Pennington Bay, and it is suggested that these too are possibly regressive or transgressive phase aeolianites. Both Pennington Bay and Bales Beach aeolianite successions range from the middle to late Pleistocene. This is suggested by luminescence and amino acid racemization dating in Chapter 7, section 7.3). The aeolianite successions in Vivonne Bay have a similar age range as well.

Underlying all of these successions is a strongly cemented calcarenite that may be of early to middle Pleistocene age. This unit may have acted as an anchor point for subsequent deposition.

Overlying a similar unit at Hanson Bay is a shell-rich, coarse sandy unit that probably represents a (~+3.0 m APSL) washover event or sub-littoral deposition (or possibly deflation of a shelly dune, although this is considered to be less likely) during the Last Interglacial (MIS 5e). These facies truncate older lagoonal sediments (this interpretation is supported by the presence of the foraminifer: *Ammonia beccarii*, a euryhaline species, common in estuarine and lagoonal contexts) at the rear of the basal calcarenite platform. The lagoonal facies are hypothesised as being deposited during a period of lower sea-level, possibly during MIS 7, as they appear to pre-date the washover / sub-littoral / deflation facies (this is examined in more detail in Chapter 7).

The Kelly Hill Caves are formed in what is interpreted to be strongly cemented dune calcarenite. This site was only discussed briefly in this chapter; an in depth examination, including previous geochronology, is given in Chapter 7.

On the western coast of Dudley Peninsula, Baudin Beach hosts a sequence of aeolianites that is interspersed with alluvial deposits, palaeosols and calcretes. The oldest unit in the sequence is a weathered aeolianite that is truncated and

removed in places along outcrop being overlain by alluvial sediment correlated with the Last Interglacial South Australian Pooraka Formation. The upper portion of the sequence (overlying the Pooraka Formation) is an aeolianite unit equated with MIS 5, this overlain by a calcrete/palaeosol and modern / Holocene dunes. The alluvial fan deposits at Baudin Beach infill the irregular surface of a middle Pleistocene dune complex present along most of the northwestern portion of the west coast of Dudley Peninsula (see topographic map: Figure 3.71a). The alluvial sediments were laid down during MIS 5e, and were later overlain by Late Pleistocene aeolianites (possibly during the regressive phase *after* MIS 5e) along most of the section. A later episode of alluvial deposition (possible during MIS 3) occurred in an isolated section near Deep Creek. These sediments overlie the Late Pleistocene aeolianite. During the Late Pleistocene Deep Creek must have been larger with a more extensive deltaic system, as evidenced by the wide ranging presence of Pooraka Formation sediments along the northwest coast of Dudley Peninsula.

The Kingscote Conglomerate at Kingscote Beach is an example (although very extensive in outcrop) of a Last Interglacial (MIS 5e) raised beach deposit. This interpretation is supported by the morphostratigraphical and biostratigraphical evidence (i.e. the presence of the indicator fossil *Marginopora vertebralis*) recovered from the study sites. The average height of the unit indicated a Last Interglacial sea-level of approximately +3.0 m (this agrees with palaeosea-levels from Pennington Bay, Vivonne Bay, Hanson Bay and Rocky Point [to a degree]).

Two study sites were examined at North Cape. Site NC1, near Marsden Point, is a large carbonate platform, of probable early Pleistocene age. The sediments are the remnants of an early Pleistocene sand/mud flat, which accumulated under a palaeosea-level of between +2.0 m to +4.0 m. The age estimate for the sediments is early Pleistocene. Site NC2 is located on the northern side of the cape in Boxing Bay, and hosts a widespread beach conglomerate (designated in this thesis as the Boxing Bay Conglomerate) that crops out at +2.0 m APSL down to present sea-level. AAR analysis of marine shell, whole-rock sediments and foraminifers recovered from the conglomerate allowed the assignment of an

early/middle Pleistocene age. Overlying the conglomerate are consolidated dune sands of similar antiquity.

Emu Bay hosts an isolated aeolianite unit, located towards the eastern side of the embayment. The sequence consists of two aeolianite units, separated by a palaeosol. The sequence possibly represents a single MIS (possibly MIS 7). Problems with AAR dating at this site (see Chapter 7) made this difficult to resolve.

An extensive raised cobble/boulder beach is present at Smith Bay (the Smith Bay Conglomerate) on the north coast of the island. The beach is approximately +18 m APSL and rests unconformably on a thick deposit of Permian glaciogene sediments. An AAR age estimate, derived using marine molluscs (*Macra* spp. and *Irus* spp.) (Chapter 7), suggest an early Pleistocene deposition. The site is interesting not only for its probable antiquity, but also for the neotectonic implications of its current height above sea-level.

Stokes Bay, the final site examined on the north coast of Kangaroo Island, hosts an extensive aeolianite outcrop that consists of a single unit unconformably overlain by a blocky, weathered calcrete. It must be noted that the aeolianite sediment at Stokes Bay was in generally poor condition. Given this it was considered to be an old unit, of possibly early to middle Pleistocene age.

The north coast sites were few, and no aeolianites that were apparently younger than the middle Pleistocene were present at any site examined. Along the northwest portion of this coast there are no substantial aeolianite deposits at all. This is in contrast to the southern coastal areas of the island which have an abundance of aeolianites that are of likely MIS 5 age. These reasons for this may be related to the topography of the precipitous, predominantly bedrock north coast, in conjunction with a relatively steep offshore profile, which have prevented extensive carbonate deposition (particularly in the northwest). It is hypothesized that the few available basins for deposition have been filled by

older, early / middle Pleistocene aeolianite, thereby preventing a late Pleistocene overprint.

Bedding azimuths were recorded, when possible, at each site along the south coast, Dudley Peninsula, and the north coast. These azimuths suggest that, for middle Pleistocene aeolianite units on the south-coast, deposition took place under predominantly southeasterly winds. Late Pleistocene palaeowind directions were similar. On the west coast of Dudley Peninsula at Baudin Beach late Pleistocene wind direction were generally from the northwest. On the north coast (Emu Bay) middle Pleistocene palaeowinds were predominantly from the north, and early / middle Pleistocene from the west and northeast. This is indicating deposition was (predominantly) occurring during periods of onshore wind. This agrees reasonable well with contemporary wind regimes given in Chapter 1, section 1.6.2).

This concludes the stratigraphical section of Chapter 3. The results presented here, and insights gained in the previous chapter, that examined aeolianite deposition and global sea-level change, are evaluated and discussed in Chapter 7 and Chapter 8. Following this Part IV of Chapter 3 is Part V: Petrology of Kangaroo Island sediments.

The subsequent chapter (Chapter 4) evaluates the radiometric dating methods used in this thesis.

older, early / middle Pleistocene aeolianite, thereby preventing a late Pleistocene overprint.

Bedding azimuths were recorded, when possible, at each site along the south coast, Dudley Peninsula, and the north coast. These azimuths suggest that, for middle Pleistocene aeolianite units on the south-coast, deposition took place under predominantly southeasterly winds. Late Pleistocene palaeowind directions were similar. On the west coast of Dudley Peninsula at Baudin Beach late Pleistocene wind direction were generally from the northwest. On the north coast (Emu Bay) middle Pleistocene palaeowinds were predominantly from the north, and early / middle Pleistocene from the west and northeast. This is indicating deposition was (predominantly) occurring during periods of onshore wind. This agrees reasonable well with contemporary wind regimes given in Chapter 1, section 1.6.2).

This concludes the stratigraphical section of Chapter 3. The results presented here, and insights gained in previous chapter, that examined aeolianite deposition and global sea-level change, are evaluated and discussed in Chapter 7 and Chapter 8. Following this Part IV of Chapter 3 is Part V: Petrology of Kangaroo Island sediments.

The subsequent chapter (Chapter 4) evaluates the radiometric dating methods used in this thesis.

PART V: Petrology of Kangaroo Island sediments

3.7 Petrology of Kangaroo Island sediments

3.7.1 Introduction

Petrology is the classification and description of rocks or sediments. This also embraces their composition, origin and geological history (Moorehouse, 1959). In the context of sediments that are predominantly carbonate (such as aeolianites, shelly deposits, or shelly beach deposits), analysis of the texture and fabric can provide insight into the depositional and diagenetic history of these types of sediments (James and Choquette, 1989a; Flügel, 2004). These insights can also be applied to test the interpretation of megascopic field observations of the sediment outcrops (those described in Parts II, III, and IV of this Chapter, for example).

This part (Part V) of the stratigraphy Chapter broadly examines the petrological aspects of selected Kangaroo Island aeolianites, shelly deposits, and raised beach deposits. Carbonate diagenetic processes (phreatic, vadose, marine, and micritisation) will be discussed, following this a representative selection of sediment thin sections, and powder X-ray diffraction data are examined, and the texture and fabric of the sediments are described. This Chapter part (Chapter 3: part V) will conclude with a description of the petrological characteristics of the Kangaroo Island sediments, and the analysis of the compositional data.

3.7.2 Petrological methods

Thin sections (ground optically flat to 30 μm and sealed under glass cover-slips on microscope slides) of representative samples of Kangaroo Island sediments were produced using standard methods (cf. Miller, 1988). Seventeen (of a total of 34) thin sections (2 from the north coast, 1 from the east coast, 1 from Dudley Peninsula, and 13 from various south coast samples) were selected for analysis, 6 of these were of unconsolidated samples (due either to disaggregation during sampling or preparation, or the natural state of the sediment). Compositional data were estimated using a point count method (cf. Flügel, 2004 pg: 254-262). Here digital photographs of the microfacies of each thin section were point counted in JMicroVision (a software toolbox for

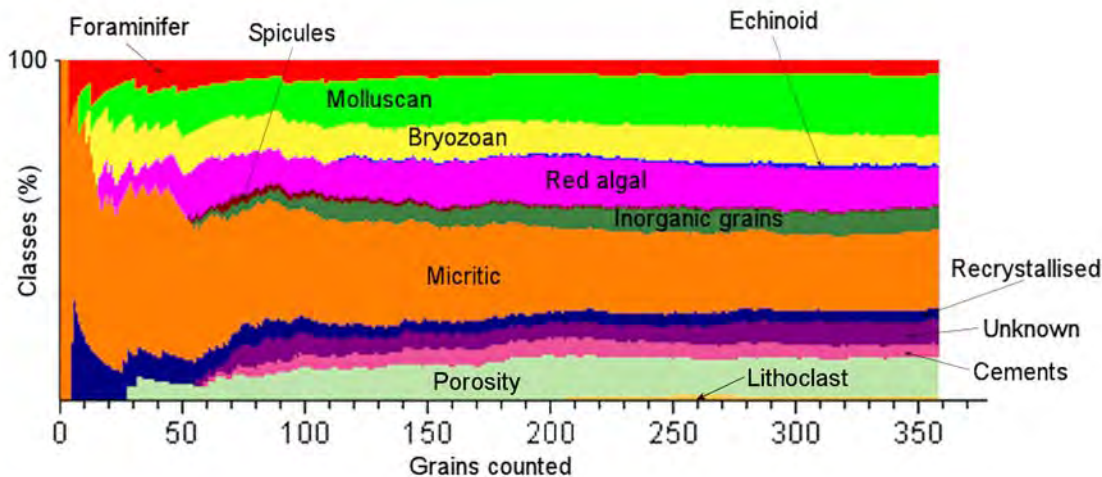


Figure 3.99: Evolution plot of the point count procedure for an example thin section (sample Bales#3-1) analysed using JMicroVision (Roduit, 2008). For this thin section 360 points were counted (although classes were reasonably stable after approximately 200 counts).

measuring and quantifying high-definition image components, developed by Roduit [2008])—using a random grid. Between 250 and 400 points were counted per thin section; counting was terminated when the evolution plot for the section revealed stable component percentages (see Figure 3.99).

Thirteen compositional classes were defined for each thin section (Table 3.21): foraminifer, molluscan, bryozoan, echinoid, red algal, sponge spicules, micritic, lithoclast, recrystallised, inorganic minerals, unknown carbonate grains, cement, and porosity. Grain proportion classes (%) followed Brooke (1999): >20 (dominant), >15-20 (major), >10-15 (abundant), >5-10 (common), >2-5 (minor), and ≤ 2 (rare). The compositional data for all 17 thin sections are given in Table 3.21.

For the purposes of comparison carbonate grains were also more broadly classified into a skeletal class (i.e. biogenic structural remains) and a peloidal class, which included micritic and faecal grains (Table 3.21). The diagnostic and structural features used to identify skeletal grains (foraminifers, molluscan, bryozoan, echinoid, red algal, and sponge spicules [which can be calcareous or siliceous]), and peloidal grains are given in Appendix B. The skeletal class also included unknown carbonate grains (probably comprised mainly of molluscan and bryozoan fragments), which could not be confidently identified because of a lack of defining internal microstructures or structural morphology.

The inorganic mineral class was defined by those grains that were of metamorphic or igneous origin (for example quartz, feldspar, rutile, ilmenite, biotite, smectite, muscovite, basalt particles etc.). These grains, however, were not specifically identified to rock species, as defining a non-biogenic non-carbonate class for comparative purposes was the only objective here (see Appendix B and Table 3.21).

Skeletal grains that were diagenetically altered by replacement with calcite cements, had undergone dissolution (i.e. only moulds remaining) or had undergone complete or partial recrystallisation were classified as “recrystallised” grains (features of these grains are described in Appendix B, see also Table 3.21).

Discrete conglomerations of skeletal (and sometimes inorganic) grains in micritic cement were classified as “lithoclasts” (see Appendix B and Table 3.21).

The compositional data (Table 3.21) were also statistically analysed, using Ward method hierarchical cluster analysis (Ward, 1963), in JMP 5.1. The Ward method uses an analysis of variance approach in order to evaluate distances between clusters, using an agglomerative clustering algorithm (i.e. the sum of squared deviations [uncertainties] from the mean of a particular cluster as the clustering criterion). This method was used to define clusters of similarity in the thin section compositional data.

In order to make direct comparisons between groups of 3 compositional classes ternary plots were also used.

A series of powder X-ray diffraction (XRD) analyses were undertaken in order to quantify the proportion of aragonite, Mg-calcite and calcite, and other minerals present in various samples of aeolianite and raised beach sediments from Kangaroo Island (see Table 3.22). The United States Geological Survey (USGS) software package RockJock (version 5) (Eberl, 2003) was used to quantify the XRD traces, using a “standardless” analysis (i.e. without using an

Table 3.21: Thin section point-count compositional results for selected Kangaroo Island aeolianite, raised beach, and shelly deposits. Data are percentages, and between 250 and 400 points were counted per sample.

Sample code	Facies	Skeletal grains							Peloidal grains		Diagenetic				Total (%)
		Foraminifer	Molluscan	Bryozoan	Echinoid	Red algae	Spicules	Unknown grains	Micritic ¹	Inorganic minerals ²	Lithoclast	Recrystallised grains	Cements ³	Porosity ⁴	
KMAR#3-2	Aeolianite	0.3	14.2	2.0	0.3	0.7	0.0	4.6	13.5	19.8	1.3	12.5	21.5	9.2	100
EBTL#1-1	Aeolianite	1.5	11.5	6.7	0.0	3.0	0.7	4.1	27.4	5.9	0.0	6.3	10.0	23.0	100
BB#2-1	Aeolianite	7.9	11.0	12.2	0.0	7.9	0.8	11.8	23.2	15.8	0.0	7.5	2.0	0.0	100
KC#1-1	Raised beach	0.8	6.7	0.8	0.0	0.8	0.0	6.7	6.7	54.2	14.2	4.2	5.0	0.0	100
Bales#3-1	Aeolianite	5.0	18.1	8.1	1.4	10.9	0.6	7.2	22.8	6.7	0.6	3.3	4.2	11.1	100
HB#1-3	Dune	6.7	33.3	11.1	1.1	10.0	0.0	5.9	10.7	17.8	0.0	3.0	0.4	0.0	100
HBTL#1-1	Shelly sand	8.7	29.6	6.3	1.5	8.7	0.5	3.4	10.7	3.9	0.0	1.9	14.6	10.2	100
KH#3-1	Cave calcarenite	5.9	38.2	5.4	0.5	2.5	0.0	10.8	7.8	3.9	0.0	4.9	13.7	6.4	100
KPB#5-1	Aeolianite	7.4	25.7	8.3	0.9	12.6	0.0	7.4	7.0	8.3	0.0	2.2	6.1	14.4	100
KVIV#3-1	Aeolianite	2.3	19.5	6.2	0.0	10.4	0.0	11.0	11.4	15.3	0.0	1.6	8.4	14.0	100
PB#1-5	Raised beach	2.0	37.8	1.0	0.0	1.0	0.0	4.5	13.9	4.0	5.5	5.0	25.4	0.0	100
PB#2-18	Aeolianite	2.8	40.0	4.7	0.4	12.2	1.2	13.3	7.5	5.9	0.0	2.4	9.8	0.0	100
PB#2-22	Aeolianite	3.3	14.2	3.8	0.0	10.4	0.0	10.4	23.6	2.8	0.0	4.3	17.0	10.4	100
PE#2-7	Upper shell	3.9	17.8	2.3	0.0	3.1	0.0	1.6	10.1	8.5	2.3	6.2	28.7	15.5	100
PE#3-1	Aeolianite	4.1	21.8	5.5	1.1	8.3	0.3	3.6	11.0	12.1	0.3	6.9	13.2	11.9	100
PE#3-2	Aeolianite	4.9	17.9	6.7	0.6	17.3	0.0	5.8	14.9	4.2	0.3	3.9	14.5	9.1	100
PE#3-4	Raised beach	4.8	29.3	7.6	1.2	16.1	0.0	3.6	10.8	15.3	4.0	4.4	2.8	0.0	100

¹ Also includes a faecal pellet component

² Includes quartz, feldspars, and other minerals.

³ May include matrix particles.

⁴ Several samples were unconsolidated prior to (or as a result of) thin section preparation; hence, porosity was not an available parameter (i.e. 0.0%).

Grain proportion classes (%) : >20 (dominant), >15-20 (major), >10-15 (abundant), >5-10 (common), >2-5 (minor), and ≤2 (rare)

Table 3.22: Mineral composition of 13 various (age and facies) Kangaroo Island near-shore sediments. Data are percentages of 32 selected minerals, quantified from powder XRD analyses using USGS RockJock version 5 (Eberl, 2003). The most common minerals are quartz, calcite, Mg-calcite, and aragonite. Light grey cells are the common calcium based minerals; dark grey cells are the clay minerals.

Geographical location	North coast			Dudley Peninsula		South coast							
Probable age	Early Pleistocene	Late Pleistocene	Middle Pleistocene	Late Pleistocene	Middle Pleistocene		Late Pleistocene	Modern	Middle Pleistocene	Holocene	Late Pleistocene		
Facies	Aeolianite	Calcrete	Aeolianite	Aeolianite	Aeolianite	Aeolianite	Aeolianite	Modern Beach	Palaeosol	Holocene dune	Aeolianite	Aeolianite	Lagoonal
Sample code	¹ STB#3-1	² EB#2-5	² EB#2-2	³ BB#3-1	⁴ PB#2-22	⁴ PB#2a-3	⁴ PB#2b-3	⁴ PB#2-29	⁴ PB#1-2	⁵ LS#1-1	⁶ Bales#2-3	⁷ PE#3-1	⁸ HB#1-2b
Mineral	Weight (%)	Weight (%)	Weight (%)	Weight (%)	Weight (%)	Weight (%)	Weight (%)	Weight (%)	Weight (%)	Weight (%)	Weight (%)	Weight (%)	Weight (%)
Quartz	4.7	12.4	29.0	21.9	9.3	4.3	5.7	14.5	29.6	1.7	28.7	4.4	27.2
Ordered microcline feldspar	1.3	1.2	1.3	0.5	0.0	0.0	0.0	0.6	0.3	1.9	0.0	0.0	0.0
Intermediate microcline feldspar	0.0	2.0	0.7	1.4	3.4	0.3	0.5	0.4	0.1	1.7	1.1	1.3	1.0
Orthoclase feldspar	1.2	0.9	2.6	1.4	0.0	0.7	0.3	4.0	0.1	1.8	0.5	0.2	3.3
Calcite	86.9	28.5	55.7	29.4	54.1	73.0	57.3	27.9	59.8	33.5	27.1	27.6	29.7
Mg-calcite	0.0	25.5	4.9	18.6	6.3	9.2	8.1	23.8	3.6	22.1	17.9	28.3	13.7
Aragonite	0.3	19.4	1.4	19.9	25.2	8.2	26.8	24.5	4.3	29.4	19.9	26.2	10.6
Dolomite	0.0	0.0	0.0	0.0	0.1	0.0	0.0	0.0	0.0	0.0	0.0	0.3	0.0
Fe-Dolomite	0.0	3.3	0.0	0.0	0.0	0.0	0.0	0.0	0.0	0.6	0.8	1.2	0.5
Magnesite	0.0	0.0	0.0	0.0	0.1	0.0	0.0	0.0	0.0	0.0	0.1	0.0	0.0
Halite	2.9	0.5	0.6	0.1	0.7	1.1	0.0	0.1	0.1	0.0	0.2	0.3	3.8
Amphibole	0.4	1.0	0.2	1.9	0.4	0.7	1.0	0.9	0.2	2.4	1.2	2.4	1.1
Pyrite	0.0	0.0	0.0	0.0	0.0	0.0	0.0	0.0	0.1	0.0	0.0	0.0	0.0
Gypsum	0.0	2.4	0.2	1.8	0.1	0.8	0.0	1.0	0.0	0.7	0.6	1.2	0.0
Magnetite	0.0	0.0	0.0	0.0	0.0	0.1	0.1	0.0	0.0	0.0	0.0	0.0	0.0
Apatite	0.0	0.0	0.0	0.0	0.0	0.0	0.0	0.0	0.0	0.4	0.1	0.1	0.0
Rutile	0.3	0.0	0.3	0.0	0.0	0.0	0.0	1.9	0.1	1.5	0.0	0.1	0.5

Table 3.22: (Cont.)

Grossular garnet	0.0	0.0	0.0	0.0	0.0	0.0	0.0	0.4	0.0	0.0	0.1	0.0	0.0
Almandine garnet	0.0	0.0	0.0	0.0	0.0	0.0	0.2	0.0	0.2	0.0	0.0	0.0	0.0
Epidote	0.0	0.0	0.5	0.6	0.0	0.7	0.0	0.0	0.2	1.0	0.9	1.9	1.0
Sillimanite	0.2	0.0	0.0	0.0	0.2	0.0	0.0	0.0	0.0	0.0	0.0	0.0	0.0
Ilmenite	0.1	0.2	0.0	0.0	0.0	0.0	0.0	0.0	0.1	0.0	0.0	0.0	0.6
Charcoal	0.2	0.0	0.3	0.0	0.0	0.0	0.0	0.0	0.7	0.0	0.1	3.5	3.1
Diatoms	0.0	0.3	0.3	0.6	0.0	0.0	0.0	0.0	0.0	0.3	0.0	0.7	1.0
Tourmaline	0.0	0.0	0.0	0.0	0.0	0.0	0.0	0.0	0.4	0.0	0.0	0.3	0.0
Ordered Kaolinite	0.0	0.0	0.0	0.0	0.0	0.0	0.0	0.0	0.0	0.4	0.0	0.0	0.0
Ferruginous smectite	0.0	0.3	1.1	0.7	0.0	0.7	0.0	0.0	0.0	0.1	0.4	0.0	0.5
Biotite (1M)	0.2	0.5	0.4	0.7	0.0	0.0	0.0	0.0	0.0	0.5	0.0	0.0	0.3
Biotite (2M1)	0.2	0.0	0.0	0.4	0.0	0.0	0.0	0.0	0.0	0.0	0.0	0.0	0.0
Phlogopite (2M1)	0.2	0.0	0.0	0.0	0.0	0.0	0.0	0.0	0.0	0.0	0.3	0.0	0.2
Gibbsite	0.7	0.0	0.0	0.0	0.0	0.0	0.0	0.1	0.0	0.0	0.0	0.0	0.0
Muscovite (2M1)	0.0	1.5	0.6	0.1	0.0	0.0	0.0	0.0	0.0	0.0	0.0	0.0	1.8
TOTAL (%)	100.0	100.0	100.0	100.0	100.0	100.0	100.0	100.0	100.0	100.0	100.0	100.0	100.0

¹Stokes Bay²Emu Bay³Baudin Beach⁴Pennington Bay⁵Little Sahara⁶Bales Beach⁷Vivonne Bay⁸Hanson Bay

internal standard during analysis) (through comparison to a set of stored pure standard XRD traces).

3.7.3 Diagenesis of Pleistocene skeletal carbonate

Diagenesis of carbonate sediments (through contact with surface and sub-surface waters) occurs in three major diagenetic environments (see Figure 3.100): marine, near-surface, and burial (James and Choquette, 1989; Tucker, 1990; Flügel, 2004). Marine diagenesis occurs on the sea-floor and just below, on tidal flats and on beaches, through contact with shallow marine phreatic and mixed shallow phreatic (below the water table) and vadose (above the water table) waters (Longman, 1982; James and Choquette, 1989; Tucker, 1990; Flügel, 2004)—this contact with mixed waters occurs at the strandline. Near surface diagenesis occurs through contact with meteoric vadose (pore spaces filled with freshwater and air) and meteoric phreatic waters (pore spaces filled with freshwater). Burial diagenesis occurs in the deep sub-surface where pores are filled with waters that were once marine (although modified by diagenesis, i.e. varying salinities from brackish to highly saline), and the sediments are progressively acted upon by pressure and temperature during and after lithification (Longman, 1982; James and Choquette, 1989; Tucker, 1990; Flügel, 2004).

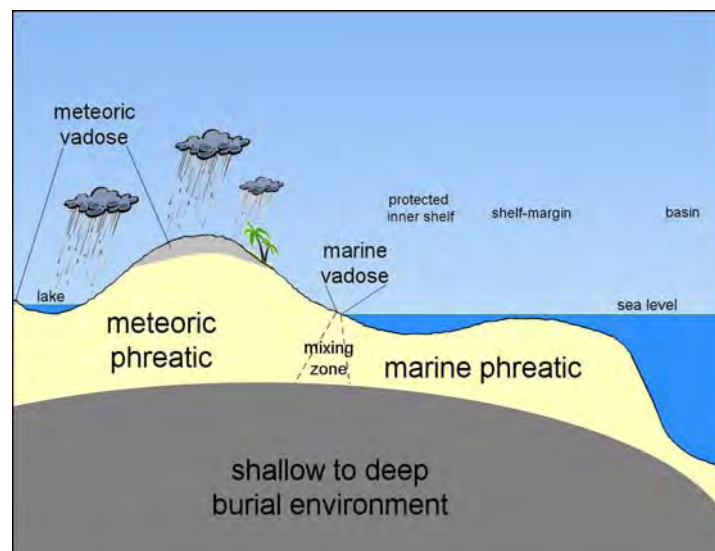
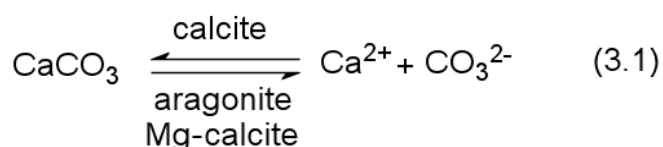


Figure 3.100: Schematic of simplified carbonate diagenetic environments for a rimmed shelf with unconfined aquifers (modified from Tucker, 1990).

3.7.3.1 Diagenetic processes

Dissolution and precipitation (i.e. cementation [e.g. micritisation, formation of sparite], and recrystallisation) are the main processes affecting the diagenesis of calcium carbonate minerals (particularly in the marine and near-surface environments).

Previously lithified carbonate grainstones may undergo dissolution when pore fluids are undersaturated with respect to the carbonate mineralogy and the flux of carbon dioxide (CO₂) in solution (James and Choquette, 1989; Tucker, 1990). However, dissolution factors are not equally applicable across all CaCO₃ variants (i.e. aragonite, magnesium [Mg]-calcite and [low Mg] calcite). Aragonite and Mg-calcite are more soluble phases of CaCO₃, particularly in freshwater (they are stable in high ionic strength sea water, but metastable in freshwater). Calcite is less soluble in comparison (although calcite becomes progressively more soluble with increasing concentrations of Mg in the lattice). Because of these differences in solubility (in freshwater) generally only aragonite and Mg-calcite will undergo dissolution, leading to the replacement of these metastable minerals by calcite. For example:



In this simple model (Equation 3.1) calcite is not dissolved and oversaturation is achieved from the dissolution of aragonite and Mg-calcite; as such this reaction leads eventually to the replacement of metastable carbonates with calcite (James and Choquette, 1989).

The rate at which these processes occur, and how they occur, is governed principally by contact with fluids (i.e. freshwater, saline, mixed). Other important factors in relation to this are extrinsic thermodynamic factors such as fluid temperature and fluid pH (which can also be altered intrinsically by organic decomposition) (Walter *et al.*, 1993), and environmental and geographical

factors, i.e., climate, region and stratigraphical position (James and Choquette, 1989) (these will determine, to some extent, the amount and types of waters contacted). Grain size, porosity and permeability of the sediments are important intrinsic factors which can also govern the rate at which diagenetic processes occur (James and Choquette, 1989).

The following sections focus upon processes related to dissolution and precipitation in the meteoric vadose, meteoric phreatic, and shallow marine zones. The process of micritisation and porosity in calcareous sediments will also be examined briefly.

3.7.3.2 Meteoric vadose diagenesis

The meteoric vadose zone is located near-surface (Figure 3.100) above the water table. Rainwater (or meltwater) will enter a carbonate sequence either through direct contact with the surface of the sequence (i.e. bare carbonate rock or unconsolidated carbonate sediment), or by percolation through an overlying soil profile. This can result in compositional alteration of the water (e.g. lowering the pH—humic acids—inducing carbonate dissolution). Because this near-surface zone is subject to evaporation and evapotranspiration, downward percolated waters can also be drawn back to the surface, resulting in precipitation. Pores within the sediment will periodically contain water or air, or a mixture of both; the water, when present, exists as thin films between and surrounding the sediment grains (Tucker, 1990). This non-uniformity will tend to constrain the formation of cement; hence, vadose cements tend to be irregularly distributed.

In subaerially exposed, unconsolidated carbonate sediments the water moves through a network of pores via diffuse flow. However, as lithification occurs in the sediment water movement alters to a conduit flow, moving through joints and fractures that have developed. This also results in the formation of caves and karst features as the joints and fractures are enlarged by dissolution (Tucker, 1990).

The diagenetic processes that occur in the meteoric vadose zone are the loss of Mg-calcite, the gradual replacement of aragonite by low Mg calcite, and diverse forms of cementation (Flügel, 2004). The rapidity and extent of these occurrences will depend upon the permeability of the carbonate sediment, the availability of water (e.g. rainfall), the saturation (with respect to the particular mineral phase) and pH characteristics of the water, and the level of evaporation, evapotranspiration, and CO₂ degassing that the sediments experience (Tucker, 1990; Flügel, 2004). For example rates of dissolution and cementation can vary greatly depending upon the climate (i.e. rapid in tropical climates and slower in an arid climate). For example Kindler and Mazzolini (2001) described rapid cementation in dredged carbonate sands that were pumped onto Stocking Island (the Bahamas). These sands (modern subtidal sediments) were transferred from a nearby lagoon and subsequently subaerially exposed (i.e. transferred from a marine phreatic to a meteoric vadose environment, thus simulating a drop in sea-level). The sands (the allochems were predominantly peloidal) underwent rapid cementation over a period of 60 years, exhibiting meniscus, pendant, and isopachous calcite fabrics.

The formation of several different types of cements can occur in the meteoric vadose zone (these are detailed in McKee and Ward [1983]; McLaren [1993], and Flügel [2004]); some are described in brief here:

- i) *Contact and meniscus cements*: these are cements that are preferentially precipitated at grain contact points. As crystal growth continues the contacts form a concave meniscus that surrounds the grain, rounding the pore at the convex contact points. Calcite crystals making up these cements can be large (5-25 μm) and bladed or “dog toothed”; however, this depends upon the rapidity of precipitation. When precipitation is rapid (i.e. because of evaporation and desiccation) the cements can have a finer less-defined crystalline structure. These are more typical of the vadose zone (Tucker, 1990).
- ii) *Rim cements*: large (10-50 μm) dog-toothed calcite crystals in a discontinuous layer around grains.

- iii) *Pendulous cements (also known as “dripstone” or “pendant” cements)*: these are calcite crystals that are preferentially precipitated at the base of grains. This is a response to the “gravitational” collection of water as drainage occurs (i.e. water collects at the base of grains).
- iv) *Needle-fibre cements*: needle-like crystals (up to 200 μm long and 4 μm wide) of calcite that can occur in the vadose zone as unoriented fibres around grains, in the pore spaces between grains, and within voids created by dissolution.
- v) *Pore-occluding cements*: these are cements that totally fill pore spaces. These cements have a wide range of crystal sizes and shapes, ranging from large single crystals and blocky sparite, to fine microcrystalline structures. Finer cements are more common in the upper vadose zone which is subject to frequent evaporation and desiccation.
- vi) *Microcrystalline (micrite) rind cement*: small-grained (1-2 μm) cement that can form thin coatings (rinds) around grains, bridge grains, and line or occlude pore-spaces. This type of cement is also common in the phreatic zone.

3.7.3.3 Meteoric phreatic diagenesis

The meteoric phreatic zone is located under the meteoric vadose zone, below the water table; as such all pore spaces are filled with fluid. The extent of the meteoric phreatic lens can vary depending upon setting (Tucker, 1990). For example in near-marine settings the meteoric phreatic zone may be bordered or even underlain by marine waters, or the lens may be thin or brackish in areas of low relief. If hydrostatic pressure is sufficient the interface (the mixing zone: see Figure 3.100) between meteoric and marine phreatic waters may be displaced seawards many kilometres (Tucker, 1990).

Sediments in the phreatic zone are always saturated with freshwater. In the upper part of this zone there is a diverse range of cementation, and dissolution.

Deeper in the zone the water is stagnant, as such aragonite and Mg-calcite are stabilised and little cementation occurs (Flügel, 2004). In the saturated upper zone environment crystal growth is unimpeded, and the cements that form are generally rinds, well-developed isopachous rim layers and pore filling blocky or granular (sparry) calcite (Flügel, 2004). The sizes of calcite crystals grown in the phreatic environment are usually larger than those of the vadose zone (James and Choquette, 1989). This is related to the rapid crystal formation that can take place when desiccation occurs in the vadose zone.

3.7.3.4 Shallow marine diagenesis

Shallow marine diagenesis occurs in the marine vadose zone, the mixing zone, and the marine phreatic zone (see Figure 3.100). The marine vadose zone is located in the near-surface land/sea interface (marine beaches, the shore-face, tidal flats, etc.). The diagenetic criteria for this zone are similar to those of the meteoric vadose zone. Rapid cementation here may result in the formation of beachrock (Tucker, 1990; Flügel, 2004). Aragonite and Mg-calcite cemented beachrocks have been observed to form, for example, on the Hawaiian island of Maui in skeletal rich beach sediments (Meyers, 1987), on the Red Sea and Mediterranean coasts (Holail and Rashed, 1992), and the Grand Cayman (in the Caribbean) (Moore, 1973). Beachrock formation is not limited to the tropics or subtropics, for example Kneale and Viles (2000) observed high latitude beachrock formation in North Uist, Scotland. This was a result of argonitic and Mg-calcite cementation initiated by the remobilisation of Mg-calcite from micritic rinds already present on skeletal grains and lithoclasts (in combination with additional argonitic cementation).

The mixing zone is an interface where both meteoric and marine phreatic waters mix together. Aragonite and dolomite precipitation may occur here, and dissolution in carbonate rocks may be extensive because of “mixing corrosion”. The strength of this effect is controlled by the saturation characteristics of the mixing waters with regard to the mineral phase and the partial pressure of CO₂ at the interface (hence, the flux of CO₂ in solution).

The marine phreatic zone is located on the shallow sea-floor or just below (see Figure 3.100), all pore spaces are filled with fluid; in this zone the fluid is sea water. Because of saturation there can be diverse cementation (Flügel, 2004). However, in temperate latitudes extensive cementation is atypical due to undersaturation with respect to CaCO_3 (Tucker, 1990). Contrary to a freshwater environment cements that do form in the marine phreatic zone are of aragonite and Mg-calcite, rather than (low Mg) calcite. This is because of ionic stabilisation of the metastable mineral phases in sea water. A variety of cements can form in this environment, for example: Mg-calcite micritic rinds and isopachous bladed cements, blocky equant cements (similar to sparite), and argonitic acicular fringes, botryoidal fans, and needle meshes, and also peloidal cements (peloids in an Mg-calcite matrix) (Tucker, 1990; Flügel, 2004).

Vollbrecht and Meischner (1996) correlated diagenetic alteration in carbonate sediments (in Bermuda) with eustatic sea-level changes (i.e. by developing a diagenetic stratigraphy). This was accomplished by identifying shallow marine diagenetic (i.e. phreatic) signatures and meteoric signatures in the lithified Pleistocene shoreline sediments. These sediments would be periodically inundated and subaerially exposed during periods of higher and lower sea-level; this was recorded as diagenetic oscillations (i.e. marine cementation/meteoric alteration, for example) within the sediment fabric. This Bermuda research demonstrated the utility of the petrographical study of carbonate microfacies with regard to identifying diagenetic changes or signatures that relate to particular diagenetic environments.

3.7.3.5 Micritic sediments and micritisation

Micrite is an abbreviation of the term “microcrystalline calcite” (Flügel, 2004). Generally the term describes the fine-grained matrix of carbonate rocks and the fine-grained constituent of carbonate grains (see Figure 3.101). Crystal sizes

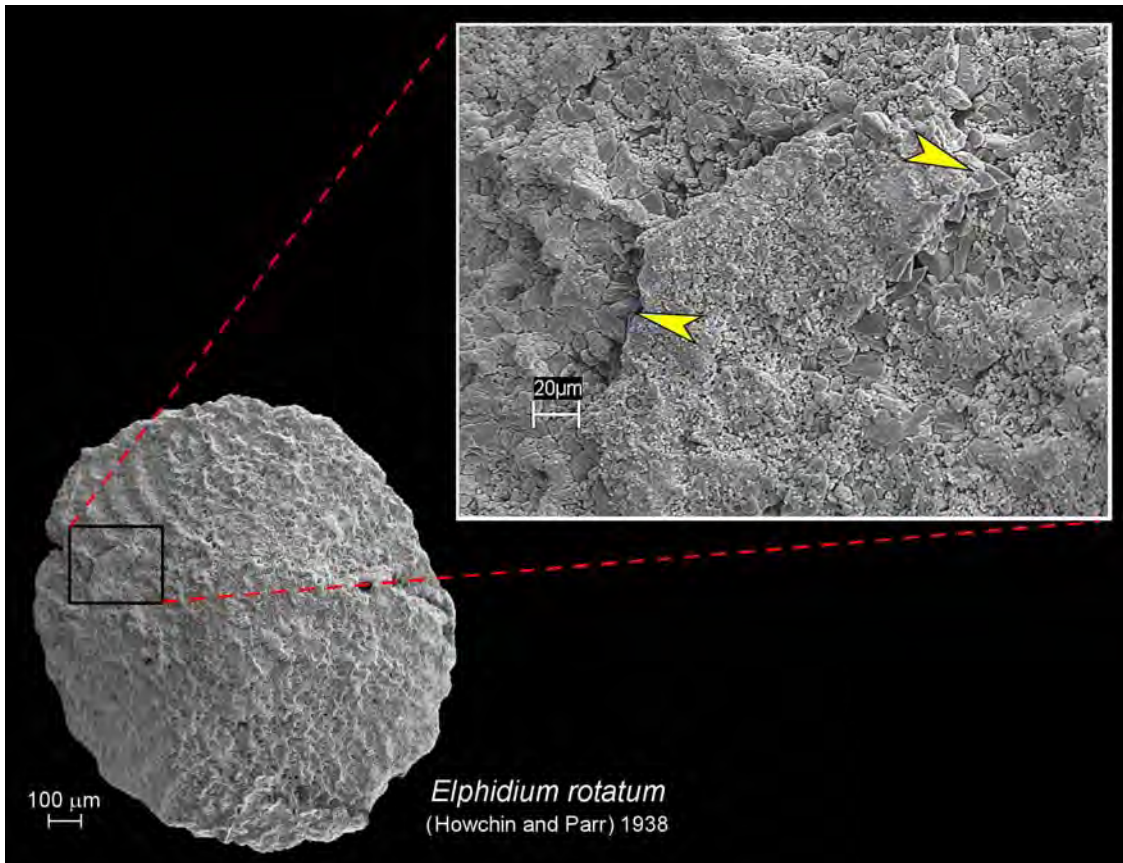


Figure 3.101: Scanning electron microscope (SEM) image of micritic rind cement coating a foraminifer (*Elphidium rotatum*) recovered from the basal unit of the early Pleistocene Point Ellen Formation, Point Ellen, Kangaroo Island. Note the ~15 µm rhombic micrite crystals (see arrows for examples) in the expanded view.

range from cryptocrystalline (<4 µm) to microcrystalline (4-30 µm) (Wright, 1990; Flügel, 2004). According to Flügel (2004) there are 5 main hypotheses that endeavour to explain the origin of microcrystalline calcite in carbonate cements:

- i) In place formation as a result of biochemical and physiochemical factors.
- ii) Post mortem breakdown of calcareous algae.
- iii) The abrasion (physical or biological) of skeletal material (see Figure 3.102)
- iv) The accumulation of pelagic calcareous plankton
- v) A direct result of diagenetic processes, i.e., cementation and recrystallisation.

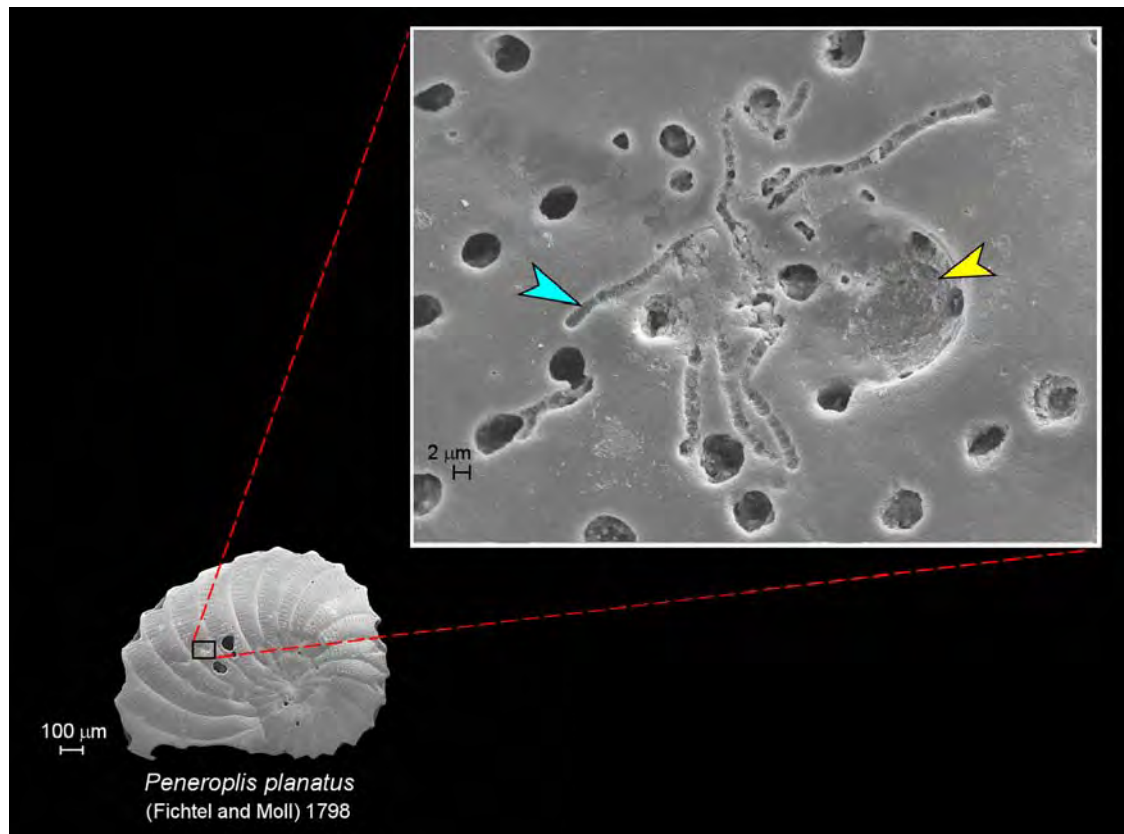


Figure 3.102: Scanning electron microscope (SEM) image of anastomosing lines (blue arrow) created by boring algae in the surface of a foraminifer (*Peneroplis planatus*: recovered from modern beach sediment at Emu Bay, Kangaroo Island). The large semicircular depression (RH field: yellow arrow) is the work of colonial unicellular algae.

To expand upon the above hypotheses micrite can be differentiated into primary and secondary micrite. Primary micrite is that produced by precipitation (which can be assisted by algal boring activities: cf. Margolis and Rex [1971]) (Figure 3.101) related to changes in fluid chemistry (i.e. CaCO_3 saturation, CO_2 flux, salinity, algal and cyanobacterial respiration, and organic decomposition), and also by the accumulation and disintegration of benthic and pelagic biota (i.e. calcareous algae and invertebrate skeletons, foraminifers, faecal pellets, coccolithophorids and other nanofossils), bioerosion (algal boring: Figure 3.102), and mechanical erosion (at the shoreface) (Flügel, 2004). Secondary micrite is classified as diagenetic micrite where there is recrystallisation (via a dissolution/cementation process) of the primary mineral and grain diminution (i.e. the replacement of large crystals with smaller crystals of cryptocrystalline or microcrystalline size) (Wolf, 1965; Wright, 1990; Flügel, 2004).

3.7.3.6 Carbonate sediment porosity

According to Flügel (2004) the porosity of sedimentary rock falls within two major groups:

- i) Primary porosity in skeletal carbonate sediment forms during both the pre-depositional phase, and the post-depositional phase. Pre-depositional porosity is the intragranular pores already present in the morphology of foraminifer, algal or coral bioclasts for example. Post-depositional porosity is created by the interstices within the initial self-supporting grain framework (Choquette and Pray, 1970; Flügel, 2004).
- ii) Secondary porosity forms during diagenesis, which can take place at anytime after deposition. Choquette and Pray (1970) further divided this into three substages:
 - *Eogenetic* (near surface): pore modification processes related to the meteoric vadose, meteoric phreatic and mixing zone diagenetic environments.
 - *Mesogenetic* (burial): pore modification processes related to the deep burial diagenetic environment.
 - *Telogenetic* (unconformity related diagenesis): exhumation of long-buried (mesogenetic) sediments, hence exposure to meteoric processes. This can result in the formation of unconformities as seen in palaeokarst systems and overprinting of eogenetic and mesogenetic signatures.

The time scales at which these processes take place may be extremely long (Flügel, 2004).

Choquette and Pray (1970) also classified pore types into three groups, i.e., fabric selective types (where pores are defined by fabric elements in the rock), for example inter- and intragranular pores, mouldic pores, and framework pores; not fabric selective types (where pores cross-cut through the rock fabric), for

example, fractures, vugs, channels (micro and macro scale) and caverns (macro scale), and the third group which may or may not display fabric control, for example, borings (micro and macro scale), burrows (micro and macro scale), and shrinkage (tidal flat mud cracks) (Wright, 1990; Flügel, 2004).

3.7.4 The texture and fabric of the Kangaroo Island carbonate sediments

The following sections will describe the petrological characteristics of the Kangaroo Island sample thin sections. Seventeen (of a total of 34) thin sections (2 from the north coast, 1 from the east coast, 1 from Dudley Peninsula, and 13 from various south coast samples) were selected for analysis. The main features of the thin section samples are described, and are compared with field observations of the particular sample sites.

The north coast thin section samples were both taken from older aeolianites of possibly middle and early Pleistocene age. The east coast sample is carbonate matrix material from a Last Interglacial raised cobble/pebble beach deposit at Kingscote Beach. The sample from Dudley Peninsula is weakly cemented upper aeolianite (of possibly Last Interglacial age), taken from Baudin Beach. The other 13 thin section samples are a mixture of aeolianites (7), unconsolidated dune sands (1), raised shelly beach deposits (3), coquina (1), and cave calcarenite (1), that were recovered from a range of sites, with a range of probable ages, located along the southern coast of Kangaroo Island. Sample details and compositional data are outlined in Table 3.21. Samples were chosen for thin section analyses that were representative (where possible) of the main lithological units identified in megascopic field observations, at particular sites.

3.7.4.1 The north coast

Two thin sections were examined from the north coast of the island: sample KMAR#3-2 was recovered from a consolidated aeolianite unit (of probable early

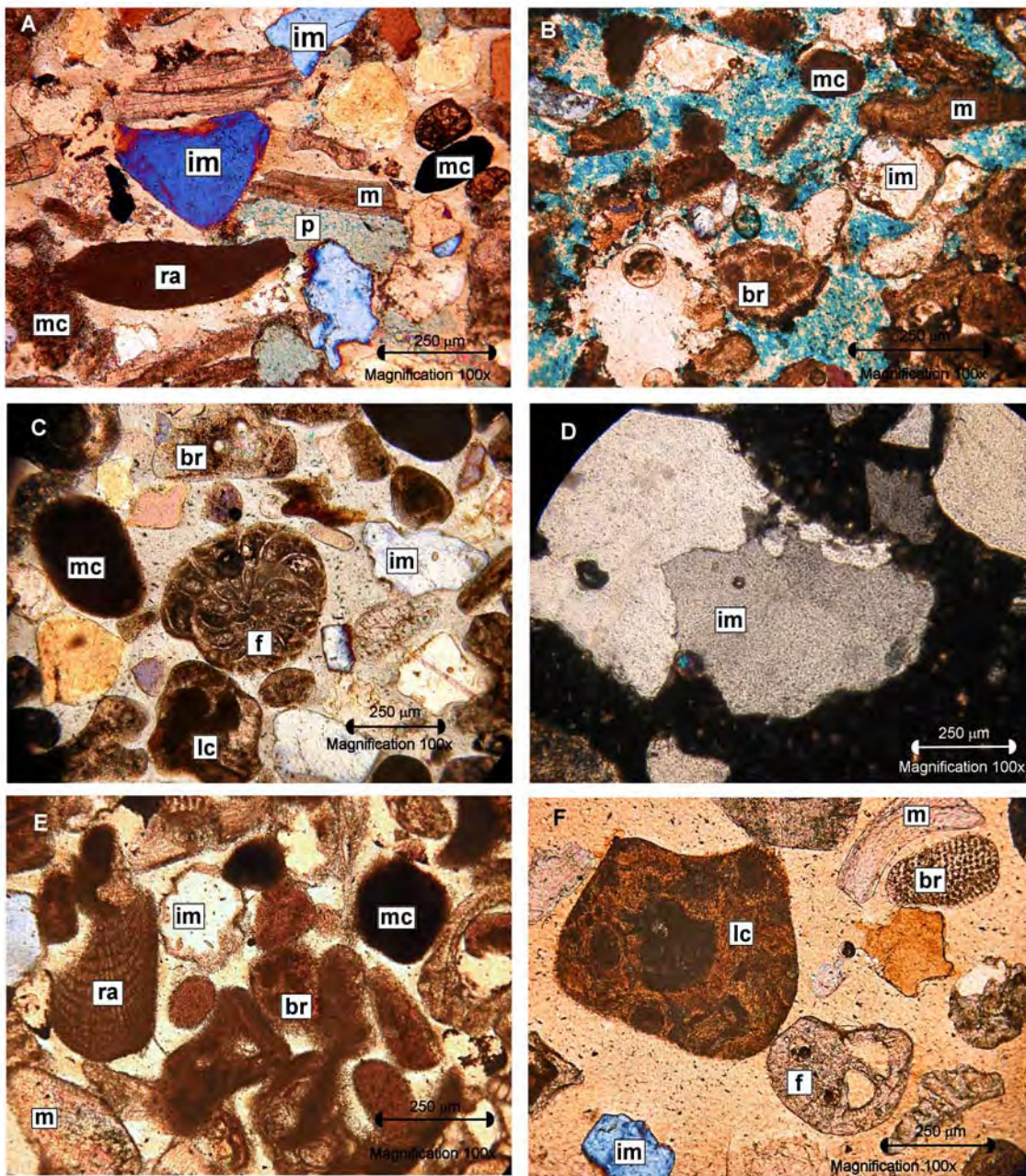


Figure 3.103: Photomicrographs (note scale bars: 250 μm) of point counted thin sections from Kangaroo Island, both in plane polarised light (PPL) and cross polarised light (CPL). A) Thin section field of view (FOV) from sample KMAR#3-2 (PPL) (aeolianite recovered from the North Cape region); this sample exhibits major proportions of molluscan grains (m), peloidal grains (mc), and inorganic mineral grains (im); cements are also an abundant class, and pore spaces (p) are common. The image also features red algal grains (ra) and a patch of micritic cement (lower LH). The grains are imbedded in sparry cement (sparite). B) Thin section FOV from sample EBTL#1-1 (PPL) (aeolianite recovered from Emu Bay); this sample is dominated by peloidal grains (mc) with abundant proportion of molluscan grains (m), and common inorganic minerals (im), and cements. The sediment is also very porous, and bryozoans (br) are also common. Many grains have micritic rinds. C) Thin section FOV from sample BB#2-1 (PPL) (aeolianite recovered from Baudin Beach); this sample is also dominated by peloidal grains (mc) with a major proportion of inorganic minerals (im) (in this case quartz). Foraminifers (f) (in this FOV a Rotaliida, probably *Elphidium*), and red algal grains are common, and molluscan (m) and bryozoan (br) fragments are abundant. This FOV also shows a rare lithoclast (lc) (none were encountered during the point count). D) Thin section FOV from sample KC#1-1 (CPL) (raised pebble/cobble beach matrix sediment recovered from Kingscote Beach); this sample is dominated by inorganic mineral grains (predominantly large quartz grains) (im), with abundant

[cont.]

lithoclasts (featuring imbedded feldspar crystals). Molluscan and peloidal grains are also common. E) Thin section FOV from sample Bales#3-1 (PPL) (aeolianite recovered from Bales Beach); this sample is dominated by peloidal grains (mc) with major proportions of molluscan grains (m), abundant red algal grains (ra) and pore spaces. Foraminifer and bryozoan (br) fragments, and inorganic minerals (im) are also common. F) Thin section FOV from sample HB#1-3 (PPL) (Holocene dune sediment recovered from Hanson Bay); this sample is dominated by molluscan grains (m), with a major proportion of inorganic mineral grains (im), and abundant bryozoan (br), red algal, and peloidal grains. Foraminifers (f) are common, and this FOV shows a large but extremely rare lithoclast (lc).

Pleistocene age) that overlies a cobble beach deposit at Boxing Bay (the Boxing Bay Conglomerate), and sample EBTL#1-1 was recovered from the consolidated lower aeolianite unit of an isolated outcrop (of probable middle Pleistocene age) at Emu Bay (see location map Figure 3.1).

Sample KMAR#3-2

This thin section (see Figure 3.103A and Table 3.21) was taken from sample KMAR#3-2 at site NC2 (North Cape site 2), unit b (see Figure 3.83 Part IV). The section exhibits major proportions of molluscan grains, peloidal grains, and inorganic mineral grains (predominantly quartz). Cements, largely pore filling sparite, bladed rim cements and micrite (note the large patch of micrite cement at the lower LH FOV), are a dominant class; although pore spaces are still common. Recrystallised grains are an abundant class, with outlining micritic envelopes, filled in many cases with sparry cement. These features would suggest a meteoric environment with both vadose and phreatic characters. The sample was located at the base of cliff (~+3.0 m APSL) so the dual character could indicate a fluctuating water table over time. The image (Figure 3.103A) features a large red-algal grain; however, these are very rare. Bryozoans are a minor grain component, and foraminifers, echinoids, and lithoclasts are rare.

Sample EBTL#1-1

This thin section (see Figure 3.103B and Table 3.21) was taken from sample EBTL#1-1 at Emu Bay, unit a (see Figure 3.89 Part IV). This sample is dominated by peloidal grains with abundant proportion of molluscan grains, and common inorganic minerals (mainly quartz), and cements. The cements are generally micritic rinds and menisci, and some bladed, discontinuous rim

cements. The sediment is dominated by pore spaces, and bryozoans and recrystallised grains are common. Red algal grains are of minor representation, and foraminifers and sponge spicules are rare. This sample was removed at +4.0 m APSL from the lowest aeolianite in a ~16 m high cliffed sequence. The aeolianite is of probable middle Pleistocene age, and the diagenetic characteristics of this sample would advocate a meteoric vadose environment, given the level of porosity and cement types. Powder XRD analysis (see Table 3.22 and Figure 3.104D) of this sample (EBTL#1-1 = EB#2-2) suggests that it is diagenetically mature with a high percentage of calcite, in comparison to Mg-calcite and aragonite.

3.7.4.2 General characteristics of the north coast samples

Both stratigraphical units appear to have evolved under a meteoric environment; although the older sample (KMAR#3-2) has apparently experienced both vadose and phreatic diagenesis. Differences are to be expected as these units do not represent age equivalents.

Ternary plots of thin section compositional data and CaCO_3 powder XRD data are given in Figure 3.104. Ternary plot 3.104A is a comparison of inorganic grains, peloidal grains, and skeletal grains for all thin section samples. The north coast samples are quite different in this respect: KMAR#3-2 has a higher proportion of inorganic grains (mainly quartz), and less peloidal grains than EBTL#1-1. However, they do have similar proportions of skeletal grains. Ternary plot 3.104B is a comparison of mollusc grains, foraminifer grains and red algal grains for all thin section samples. Both samples are very similar with regards to skeletal grain proportions, although KMAR#3-2 shows a greater abundance of molluscan grains. Ternary plot 3.104C is a comparison of recrystallised grains, porosity and cementation for all thin section samples. KMAR#3-2 and EBTL#1-1 are quite different when comparing diagenetic traits. EBTL#1-1 is more porous, while KMAR#3-2 is more cemented and shows a higher proportion of recrystallised grains than EBTL#1-1. Although both samples are diagenetically mature, these characteristics reveal the greater maturity of KMAR#3-2. However, as stated above KMAR#3-2 may have experienced prolonged contact

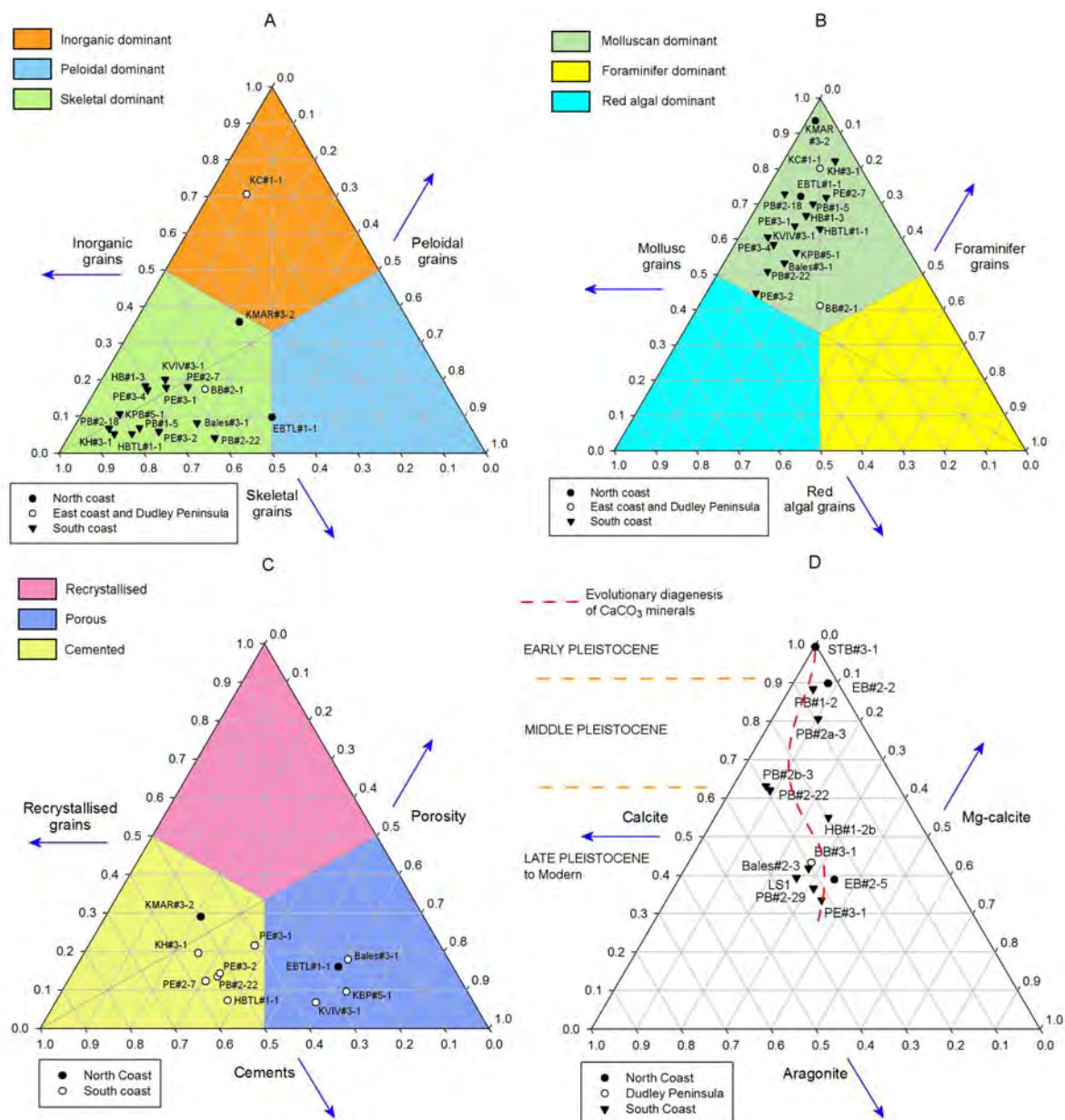


Figure 3.104: Ternary plots of various thin section (normalised) compositional data and CaCO_3 mineral content of selected Kangaroo Island sediment thin sections (A, B, and C), and powder X-ray diffraction data (D) (processed into percentage weights using RockJock version 5). Blue arrows show orientation of axis intersection for plotted data. Solid circles represent north coast data, open circles represent east coast and Dudley Peninsula data (except in plot C—open circles represent south coast), and solid triangles represent south coast data. A) Compositional classes: Peloidal (X), inorganic (Y), and skeletal grains (Z), showing a predominant skeletal content for the selected Kangaroo Island samples. B) Compositional classes: Foraminifer (X), molluscan (Y), and red algal grains (Z), showing a predominant molluscan content for the selected Kangaroo Island samples. C) Compositional classes: Pore spaces (X), recrystallised grains (Y), and cements (Z), showing a strong inverse relationship between porosity and cementation, and a weaker relationship between cementation and recrystallised grains. D) CaCO_3 minerals: Mg-calcite (X), calcite (Y), and aragonite (Z). Diagenetically mature sediments show the lowest relative concentrations of Mg-calcite, and aragonite, in comparison to calcite (low Mg). The dashed red line shows the interpolated evolutionary pathway for carbonate diagenesis in these samples. Also note the relationship between diagenesis and the proposed age for the sediments (i.e. younger sediments [in most cases] have higher concentrations of [particularly] Mg-calcite and aragonite than sediments that are proposed to be older).

with freshwater in the phreatic environment, which could have accelerated diagenesis.

3.7.5.1 The east coast and Dudley Peninsula

Two thin sections were examined from the eastern portion of Kangaroo Island, 1 from the east coast at Kingscote Beach, and 1 from Baudin Beach on the western side of Dudley Peninsula (see location map Figure 3.1). These are very different sample types: KC#1-1 is unconsolidated matrix material from a raised cobble/ pebble beach deposit, and BB#2-1 is from a weakly cemented upper aeolianite (although this sample disaggregated during thin section preparation). Both sites are proposed to be of Last Interglacial age.

Kingscote sample

KC#1-1

This thin section was taken from sample KC#1-1 at site KC1, Kingscote Beach (see Figure 3.79, Part III). This sample (Figure 3.103D and Table 3.21) is dominated by inorganic mineral grains (predominantly large [~500 μ m] quartz crystals), with abundant large lithoclasts (featuring imbedded feldspar crystals). Cements are common, being mainly micritic envelopes, and microcrystalline, possibly pore-filling Mg-calcite cements. Recrystallised grains are of minor representation. Since this sample was disaggregated it was difficult to assign a diagenetic environment. However, given the morphology and current position (+3.0 m APSL) of the unit (and its position relative to sea-level at the Last Interglacial, i.e., 0 m ASL, intertidal), the most likely environments would have been meteoric and marine vadose. Molluscan and peloidal grains are also common in this sample, and foraminifers, bryozoans, and red algal grains are rare.

Baudin Beach sample

BB#2-1

This thin section (Figure 3.103C and Table 3.21) was taken from sample BB#2-1, an upper aeolianite (unit a, site BB1) recovered from Baudin Beach (see Figure 3.68, Part III); this sample is also dominated by peloidal grains with a

major proportion of inorganic minerals (predominantly quartz). Foraminifers (in this image [Figure 3.103C] a Rotaliida, probably *Elphidium*), and red algal grains are common, and molluscan and bryozoan grains are abundant. This image also shows a very rare lithoclast. Recrystallised grains are common, being mainly moulds filled with sparite, and cements are a minor component comprising thin micrite envelopes and rare discontinuous rim cements. These characters would imply a meteoric vadose diagenetic environment. The position of the unit (i.e. an upper unit with an overlying calcrete unconformity and a thin covering of Holocene dunes), and the level of induration in the sediments is in accordance with this. Powder XRD analysis (see Table 3.22 and Figure 3.104D) of this sample suggests that it is not as diagenetically mature as, for example, EBTL#1-1, as it still has high proportions of aragonite and Mg-calcite in comparison. This is in good agreement with the proposed age differences between the two samples (i.e. Last Interglacial for BB#2-1 and middle Pleistocene for EBTL#1-1).

3.7.5.2 General characteristics of the east coast and Dudley Peninsula samples

These units have evolved under different diagenetic environments (which is expected as they are from very different depositional environments). The pebble beach sample indicates a marine vadose environment (although this would have changed to meteoric vadose after the Last Interglacial), and the aeolianite would have been subject to meteoric vadose conditions for most of its evolution. Ternary plot 3.104A shows the predominantly inorganic mineral character of sample KC#1-1, as opposed to BB#2-1 which is dominated by skeletal and peloidal grains. Plot 3.104B shows major differences between the samples: BB#2-1 has almost equal proportions of molluscan, foraminiferal, and red algal grains, while KC#1-1 is predominantly molluscan. Because both of these samples were unconsolidated in thin section, porosity could not be estimated; therefore they were not included in the diagenesis plot (Figure 3.104C).

3.7.6.3 The south coast

As there were a greater number of sites that could be accessed on the southern coast of Kangaroo Island a larger number of thin sections were chosen for

examination. Thirteen thin sections were selected to represent major units (where possible) from this part of the island and they are described here in geographical order (from east to west) (see location map Figure 3.1). Four samples were examined from Pennington Bay: PB#2-18, taken from an upper aeolianite of possible late Pleistocene age; PB#1-5, from a Last Interglacial shelly/cobble raised beach (notch) deposit; PB#2-22, from a lower aeolianite of possible middle Pleistocene age and KPB#5-1, from a weathered lower aeolianite unit of possible middle Pleistocene age. One sample was examined from Bales beach: Bales#3-1, taken from a lower aeolianite of possible middle Pleistocene age. Five samples were examined from Vivonne Bay and Point Ellen: KVIV#3-1 taken from a possible late Pleistocene aeolianite; PE#3-4, from a Last Interglacial raised pebble beach deposit; PE#3-2, from a lower possibly middle Pleistocene aeolianite; PE#3-1, from an upper possibly late Pleistocene aeolianite and PE#2-7, from a strongly indurated upper coquinite unit of early Pleistocene age (the Early Pleistocene Point Ellen Formation). One sample was examined from Kelly Hill Caves: KH#3-1, taken from a (depth -15 m) limestone cave calcarenite (caves formed in aeolianite) of possible early Pleistocene age. Two samples were examined from Hanson Bay: HB#1-3, taken from an unconsolidated Holocene dune and HBTL#1-1, from a shelly sand unit possibly late Pleistocene in age.

Pennington Bay samples

PB#2-18

This thin section (Figure 3.105F and Table 3.21) is dominated by molluscan grains, with abundant red algal grains. Peloidal and inorganic mineral grains are common, and foraminifers and bryozoans are of minor abundance. Echinoid grains and spicules are rare. Cements are generally in the form of thin micritic rinds (many molluscan shards were partly coated by micrite), with some pendulous cements, and grain moulds filled with sparite. The cement types described are indicative of the meteoric vadose zone, and the position of the unit (i.e. see Figure 3.9 Part II: an upper aeolianite [unit 4ci, site PB1], in a cliffed sequence [6.0 m high], with an overlying thin calcrete), would also support this. Porosity was not estimated as the sample was unconsolidated in thin section.

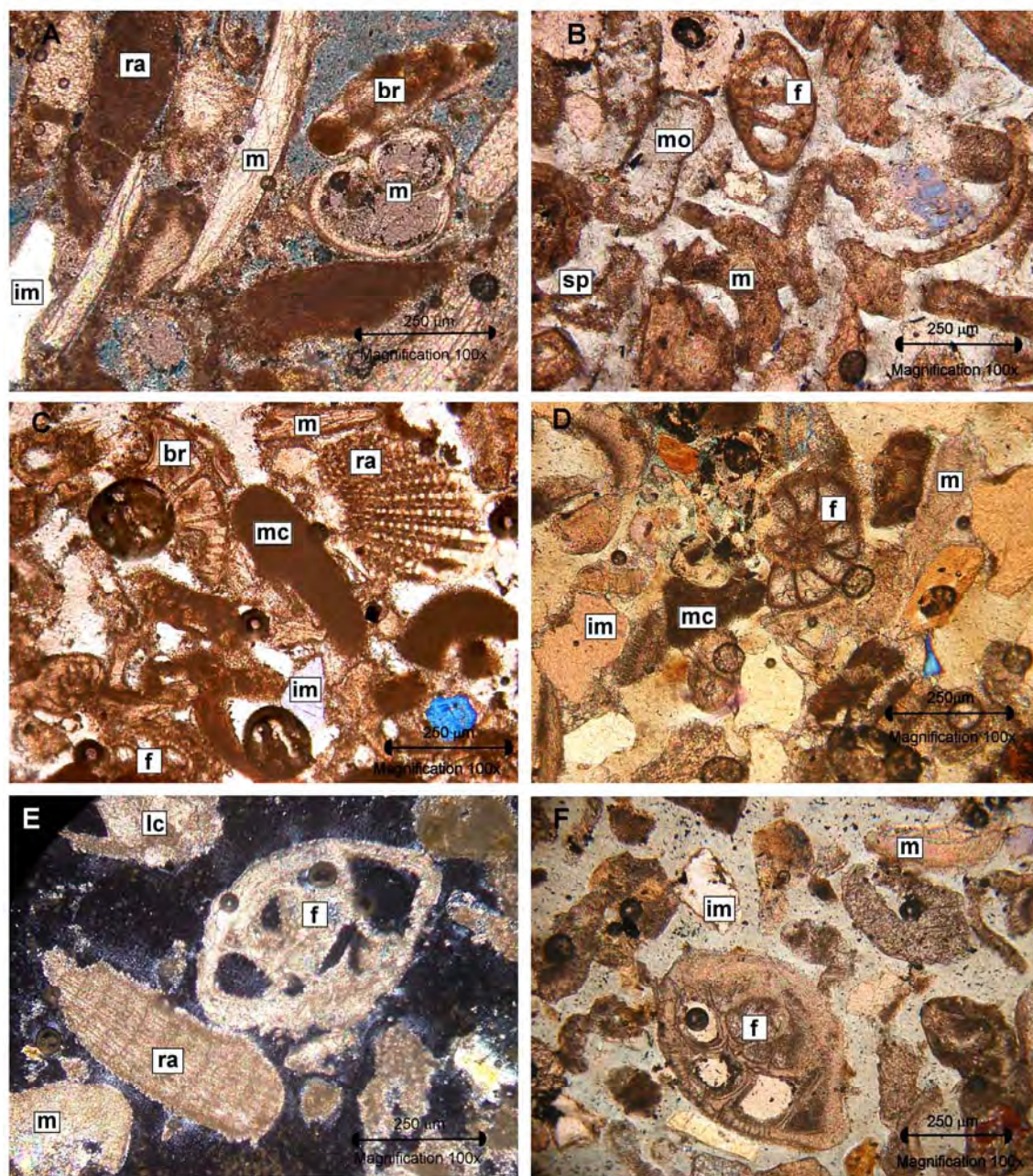


Figure 3.105: Photomicrographs (note scale bars: 250 µm) of point counted thin sections from Kangaroo Island, both in plane polarised light (PPL) and cross polarised light (CPL). A) Thin section FOV from sample HBTL#1-1 (PPL) (shelly sand sample recovered from Hanson Bay); this sample is dominated by molluscan grains, with abundant peloidal grains, cements (note the arcuate molluscan grains [A—left] surrounded by micritic cements) and pore spaces. Foraminifer, bryozoan, and red algal grains are common. B) Thin section FOV from sample KH#3-1 (PPL) (cave calcarenite sample recovered from Kelly Hill Caves); this sample is dominated by molluscan grains (m), and foraminifer (f), bryozoan, and micritic grains are common. Pore spaces and grain moulds (mo) are sometimes filled with abundant sparry cement (sp—sparite). C) Thin section FOV from sample KPB#5-1 (PPL) (aeolianite sample recovered from Pennington Bay); this sample is dominated by molluscan grains (m) with abundant red algal grains (ra), and pore spaces. Foraminifer (f), bryozoan (br), micritic, and inorganic mineral grains (im) are common. Most grains exhibited a micritic rind, and some pore spaces are filled with sparite. D) Thin section FOV from sample KVIV#3-1 (PPL) (aeolianite sample recovered from Vivonne Bay); molluscan (m) and inorganic grains (im) are a major component of this sample. Red algal, peloidal grains (mc) and pore spaces are abundant. Note the central foraminifer grain (Rotaliida); this grain exhibits a micritic rind and the test chambers are filled

[Cont.]

with sparry calcite cement (sparite). E) Thin section FOV from sample PB#1-5 (CPL) raised pebble/cobble beach matrix sediment recovered from Pennington Bay); this sample is dominated by molluscan grains (m) with abundant peloidal grains and lithoclasts (lc). Foraminifers (f), red algal (ra), and inorganic mineral grains are common components. F) Thin section FOV from sample PB#2-18 (PPL) (aeolianite sample recovered from Pennington Bay); this sample is dominated by molluscan grains (m), with abundant red algal grains. Peloidal and inorganic mineral grains (im) are common.

PB#1-5

This thin section (Figure 3.105E and Table 3.21) is dominated by molluscan grains and cements. The cements are predominantly micritic rinds, and patches of fine rhombic grains. There are abundant peloidal grains and lithoclasts are common. Foraminifers and inorganic mineral grains are minor components. Bryozoans and red algal grains are rare. Porosity was not estimated as this sample was unconsolidated in thin section. Given the abundant micritic cements it is likely that the sediments evolved in a marine vadose environment; however, for a major part of their history these sediments may have been subjected to a meteoric vadose environment. This is likely as the sediments (see Figure 3.15 Part II: a cobble/pebble/shell notch deposit [unit 2-2b, site PB2], in a cliffed sequence [~8.0 m high], with an overlying aeolianite, thin calcrete and modern/Holocene dunes) were deposited at sea-level during the Last Interglacial, and were subsequently subaerially exposed as sea-level regressed. The notch deposit is now at +3.0 m APSL.

PB#2-22

This thin section (Figure 3.106A and Table 3.21) is dominated by peloidal grains, with abundant molluscan, red algal grains and pore spaces. Cements are a major component and are principally micritic rinds, pendulous and meniscus cements, with some sparite. These diagenetic characters suggest a vadose environment, probably meteoric. However, this unit is thought to be middle Pleistocene in age and its current position (near sea-level: see Figure 3.9 Part II: unit 1a_{ii}, site PB1) means that it was partially or totally submerged during the Last Interglacial. Hence, it would have been exposed to a shallow marine environment for several thousand years, and some overprinting would be expected. Nevertheless, the thin section does not exhibit any acicular or fibrous aragonite cement which would be an indicator of exposure to this environment. Powder XRD analysis (see Table 3.22 and Figure 3.104D) of this

sample suggests that it is more diagenetically mature than aeolianite sample BB#3-1, for example, based upon the comparative proportion of calcite present in PB#2-22. This is in good agreement with the proposed ages for these two samples (middle and late Pleistocene).

KPB#5-1

This thin section (Figure 3.105C and Table 3.21) is dominated by molluscan grains with abundant red algal grains, and pore spaces. Foraminifer, bryozoan, peloidal and inorganic mineral grains are common, and echinoids are rare. Most grains exhibited micritic rinds, and meniscus cements, and some pore spaces and grain moulds are occluded with sparite. These cement types indicate a meteoric environment, probably both phreatic and vadose (possibly marine also as the unit is close the shoreface—it is the lowest aeolianite unit [see Figure 3.24, Part II: unit 5b, site PB5] in an 18 m high sequence—and would have been submerged during periods of higher sea-level).

Bales Beach sample

Bales#3-1

This thin section (Figure 3.103E and Table 3.21) is dominated by peloidal grains with major proportions of molluscan grains, abundant red algal grains and pore spaces. Foraminifer and bryozoan fragments and inorganic minerals are also common. Cements are predominantly micritic rinds and meniscus, with some pendulous. Many molluscan shards are mouldic (defined by a micrite envelope) with fillings of sparite. There were no large patches of pore occluding sparite, however, or examples of needle fibre cements. The diagenetic characters would suggest a meteoric vadose environment. Echinoid, sponge spicules and lithoclasts are rare.

Vivonne Bay, and Point Ellen samples

KVIV#3-1

This thin section (Figure 3.105D and Table 3.21) is dominated by molluscan grains, and inorganic grains are a major component of this sample. Red algal,

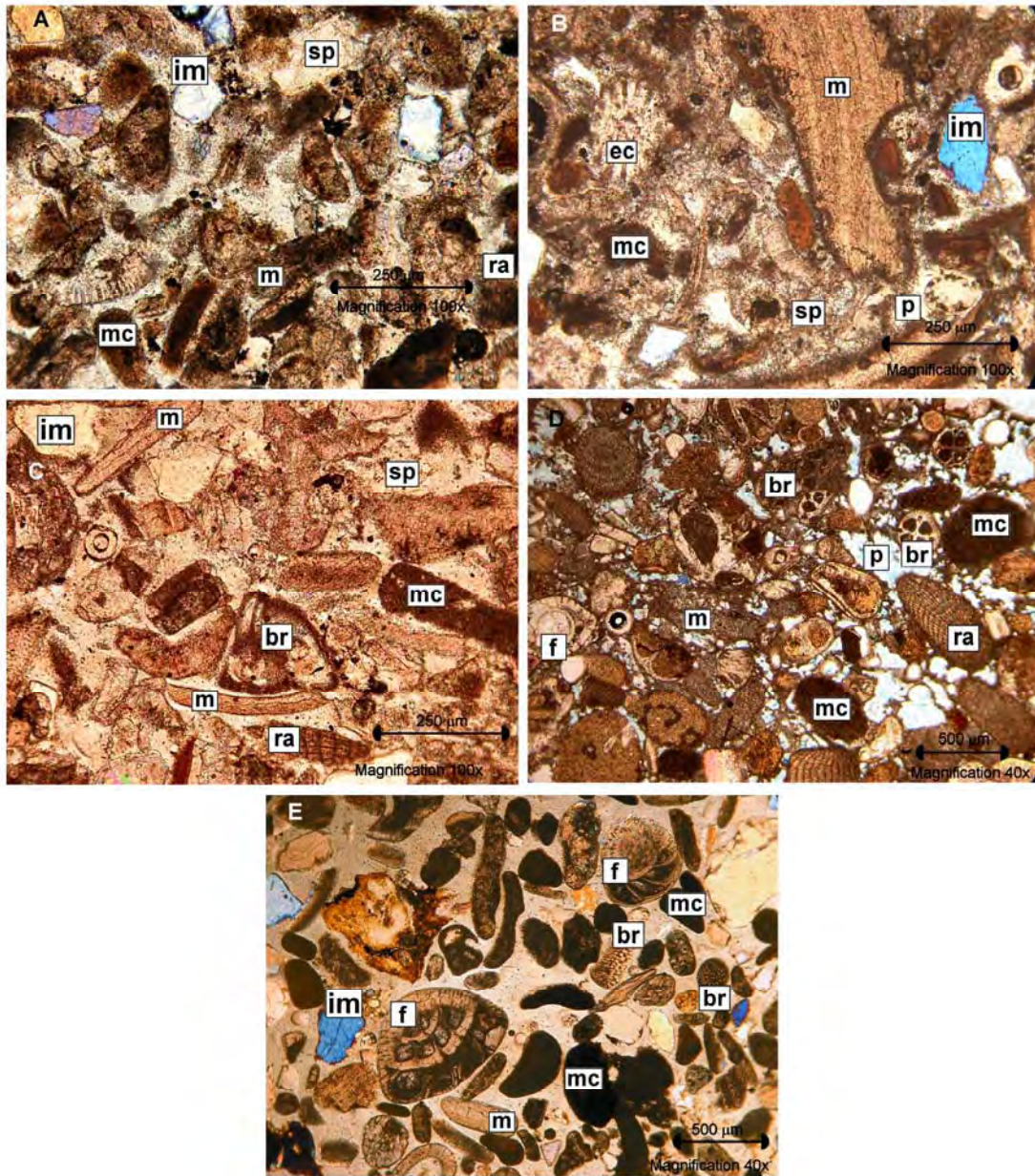


Figure 3.106: Photomicrographs (note scale bars: 250 and 500 μm) of point counted thin sections from Kangaroo Island, both in plane polarised light (PPL) and cross polarised light (CPL). A) Thin section FOV from sample PB#2-22 (PPL) (aeolianite sample recovered from Pennington Bay); this sample is dominated by peloidal grains (mc), with abundant molluscan (m), red algal grains (ra) and pore spaces. Grains are imbedded within sparry cement (sp—sparite). B) Thin section FOV from sample PE#2-7 (PPL) (upper shell unit sample recovered from Point Ellen); a major proportion of grains are molluscan (m) with abundant peloidal grains (mc) and pore spaces. Inorganic minerals (im) are common, and the sample is dominated by micritic and microsparite (sp) cements. C) Thin section FOV from sample PE#3-1 (PPL) (aeolianite sample recovered from Vivonne Bay); this sample is dominated by molluscan grains (m), with abundant peloidal (mc), inorganic mineral grains (im), and pore spaces. Bryozoan (br) and red algal (ra) grains are common. Grains are cemented in sparite (sp). D) Thin section FOV from sample PE#3-2 (PPL) (aeolianite sample recovered from Vivonne Bay); this sample has a major proportion of molluscan (m), red algal (ra), and peloidal grains (mc), and foraminifer (f), bryozoan grains (br), and pore spaces (p) are common constituents. The grains are mainly supported by micritic cements. E) Thin section FOV from sample PE#3-4 (PPL) (raised shelly pebble beach sample recovered from Vivonne Bay); this sample is dominated by molluscan grains (m), with red algal (ra), and inorganic mineral grains (im) as a major component. Peloidal grains (mc) are abundant, and foraminifer (f) (the foraminifer top right is partially recrystallised in its upper portions) and bryozoan grains (br) are common.

peloidal grains and pore spaces are abundant, and foraminifers are minor. Note the central foraminifer grain in Figure 3.104D (Rotaliida); this grain exhibits a micritic rind and the test chambers are filled with sparry calcite cement (sparite). Cements are common and many pore spaces are occluded by sparite and microsparite, and numerous grains had well-developed isopachous rim layers. Micritic rinds are also visible. These characters point toward a meteoric phreatic environment. This sample site (PE4) is a single 6.0 m thick aeolianite unit, with an overlying unconformity, and a covering of Holocene dunes (Figure 3.48, Part II).

PE#3-4

This thin section (Figure 3.106E and Table 3.21) is dominated by molluscan grains, with red algal and inorganic mineral grains as a major component. Peloidal grains are abundant, and foraminifer (the foraminifer top right of Figure 3.105E is partially recrystallised in its upper portions) and bryozoan grains are common. Lithoclasts are a minor component and echinoids are rare. Cements are generally micritic rinds, and many grains are partially recrystallised, with portions being replaced by sparry calcite or micrite. This unit (see Figure 3.41, part II: unit b, site PE3) is a shelly, cobble/pebble, raised notch deposit in a middle Pleistocene aeolianite. The notch was created and sediments deposited during the Last Interglacial, and as such would have experienced a marine vadose environment for part of their history. After the Last Interglacial terminated and the regression of sea-level, the sediments would have been exposed to a meteoric environment.

PE#3-2

This thin section (Figure 3.106D and Table 3.21) has a major proportion of molluscan, red algal, and peloidal grains. Foraminifer, bryozoan grains, and pore spaces are common constituents. The grains are mainly supported by abundant micritic, and meniscus cements, and many pore spaces are totally occluded with micrite. Numerous molluscan grains exhibit bored surfaces also infilled with micrite. Sparite was not common, and was usually only found in moulds. The abundant fine cements (which point to rapid crystallization probably via desiccation) would indicate an evolution dominated by a meteoric

vadose diagenetic environment. The sample was taken from unit c (of proposed middle Pleistocene age), site PE3 (see Figure 3.41, part II).

PE#3-1

This thin section (Figure 3.106C and Table 3.21) is dominated by molluscan grains, with abundant peloidal grains, inorganic mineral grains, and pore spaces. Bryozoan and red algal grains are common. Foraminifers are minor and echinoids, spicules and lithoclasts are rare. Similar to sample PE#3-2 grains are mainly supported by abundant micritic, and meniscus cements, and many pore spaces are totally occluded with micrite. Sparite was mainly present as an infill in grain moulds. The abundant fine cements (which point to rapid crystallization probably via desiccation) would indicate an evolution dominated by a meteoric vadose diagenetic environment. The sample was taken from unit b (of proposed late Pleistocene age), site PE2 (see Figure 3.41, part II). Powder XRD analysis (see Table 3.22 and Figure 3.104D) of this sample suggests that it is of similar diagenetic maturity as, for example, sample BB#3-1, as it still has high proportions of aragonite and Mg-calcite. This would be expected as both samples are of probable late Pleistocene age.

PE#2-7

This thin section (Figure 3.106B and Table 3.21) has a major proportion of molluscan grains with abundant peloidal grains and pore spaces. Inorganic minerals are common, and the sample is dominated by micritic cements. Pore spaces are often occluded by fine cements, and isopachous rim cements, and needle fibre cements are common. Foraminifers, bryozoans, red algae, and lithoclasts are minor components of the sample. This sample was the most heavily cemented sample examined. The sample was taken from a strongly indurated upper coquinite (see Figure 3.34, part II: unit d, site PE1A) of early Pleistocene age (the early Pleistocene Point Ellen Formation). This unit may have been a subtidal deposit, and the cements would indicate a shallow marine diagenetic environment. However, the unit is also heavily karstified and perforated by solution pipes in places; as such much of the unit's evolution would have been spent in the meteoric vadose zone.

Kelly Hill Caves sample***KH#3-1***

This thin section (Figure 3.105B and Table 3.21) is dominated by molluscan grains, and foraminifer, bryozoan, and peloidal grains are common. Red algal grains and inorganic minerals are minor, and echinoids are rare. Grains generally had a micritic coating rather than isopachous cements. Pore spaces are sometimes filled with abundant blocky/sparry calcite cement and grain moulds with sparite. KH#3-1 was taken from a limestone cave at 15 m depth: the material that the caves formed in is of aeolian origin. The cements would appear to indicate, at least in the case of the intergranular cements, a meteoric phreatic environment, probably at the interface between vadose and phreatic where cavern formation occurs.

Hanson Bay samples***HB#1-3***

This thin section (Figure 3.103F and Table 3.21) is dominated by molluscan grains, with a major proportion of inorganic mineral grains, and abundant bryozoan, red algal, and peloidal grains. Foraminifers are common, and this image (Figure 3.103F) shows a large and extremely rare lithoclast. This sample was taken from an unconsolidated modern/Holocene dune (see Figure 3.52, Part II), and so cements are rare. Nevertheless, some skeletal particles (mainly molluscan) did exhibit discontinuous rinds of micrite, and there are also some pellet-like shards of sparite—these may have been re-worked older cements from adjacent units.

HBTL#1-1

This thin section (Figure 3.104A and Table 3.21) is dominated by molluscan grains, with abundant peloidal grains, cements (note the large arcuate molluscan shards [Figure 3.105A—left] surrounded by micritic cements) and pore spaces. Foraminifer, bryozoan, and red algal grains are common. Inorganic minerals are a minor component and echinoid, and spicules are rare. Some pore spaces are occluded with fine cements (microsparite?) and micrite, and grains exhibited micritic rinds, meniscus and sometimes isopachous cements. Grain moulds are filled with either sparite or microsparite. HBTL#1-1 was taken from a raised shelly facies that was probably deposited in the Late

Pleistocene (possibly the Last Interglacial), it may be an intertidal marine deposit, but could also be the result of dune deflation. Some of the diagenetic characters (fine pore occluding cements) point to a marine (vadose) origin, while others (meniscus, isopachous) may point to a meteoric origin. This may be a reflection (due to overprinting) of time spent in both marine and meteoric environments. This is in agreement with the possible position of the unit in terms of sea-level during the Last Interglacial (i.e. in the intertidal zone), and the units subsequent position after regression (i.e. +2.5 m APSL, subaerial exposure).

3.7.6.4 General characteristics of the south coast samples

The sediments examined under thin section from the south coast of Kangaroo Island have evolved under a range of diagenetic environments. This has occurred through being exposed to one type of environment at, during and sometime after deposition, then subsequently after a time being exposed to another (due to a change in sea-level for example). The Last Interglacial beach deposits at Pennington Bay, Vivonne Bay, and Hanson Bay are examples of this, having been initially deposited in a marine environment (under higher-than-present sea-level), then after a drop in sea-level experiencing a meteoric environment for the rest of their history. Conversely, those sediments deposited by aeolian processes may have experienced an initial meteoric vadose environment, and over time due to burial and compaction, or changes in the location of the water table, main processes may have changed from vadose to phreatic (or aeolianite located close to shore may have been submerged during a sea-level rise, or exposed to an intertidal environment, thus a change from meteoric vadose to shallow marine or marine vadose diagenetic processes would occur). Aeolianite samples such as PB#2-22 and KPB#5-1 from Pennington Bay which are located quite close to the modern shoreline may have experienced inundation during the Last Interglacial (although not during previous interglacial periods as sea-level was not high enough—see Siddall *et al.*, 2007), and thus would have been exposed to both meteoric and marine processes. However, these units would have had greater exposure to a meteoric diagenetic environment for most of their history. Regardless,

diagenetic signatures found in this set of thin section samples show predominant meteoric influences on aeolianites, and marine and meteoric influences on raised beach deposits.

Ternary plots of thin section compositional data and CaCO_3 powder XRD data are given in Figure 3.104. Ternary plot 3.104A is a comparison of inorganic grains, peloidal grains, and skeletal grains for all thin section samples. The south coast samples are predominantly skeletal in nature, although some of the apparently older samples (PE#3-2, Bales#3-1, and PB#2-22) have higher proportions of peloidal grains, reflecting perhaps extensive micrite formation. Ternary plot 3.104B is a comparison of mollusc grains, foraminifer grains and red algal grains for all thin section samples. The dominant skeletal grains for the south coast samples are molluscan, particularly in the raised beach samples. Some of the aeolianite sediments have higher proportions of red algal and foraminifer grains. Ternary plot 3.104C is a comparison of recrystallised grains, porosity and cementation for all thin section samples. The south coast samples are all very similar in terms of recrystallised grains; however, there are major differences between samples in terms of porosity and cementation. There are two groups of samples, one with a higher proportion of cements (i.e. PE#2-7, PE#3-2, KH#3-1, PB#2-22, and HBTL#1-1), and another with greater porosity (i.e. PE#3-1, Bales#3-1, KPB#5-1, and KVIV#3-1). This may reflect those sediments that spent a longer period of time in a saturated environment (i.e. more cementation), and those that did not (i.e. less cementation).

3.7.7 Analysis of the compositional data and powder XRD data

The following discussion examines the thin section compositional data (see Table 3.21) using Ward Method hierarchical cluster analysis (Ward, 1963). This was undertaken to reveal clusters of similarity in different compositional classes. A range of sediment samples from various locations (see Table 3.22) around Kangaroo Island and various depositional environments were also analysed for mineral content using powder XRD, and USGS RockJock (version 5) (Eberl, 2003). The percentage proportions of CaCO_3 minerals in the samples were normalised and plotted in a ternary diagram.

3.7.7.1 Cluster analysis

Non-normalised (to better reflect proportional differences across the range of compositional classes) compositional data for skeletal grains, mollusc grains, and cements were examined using cluster analysis. These classes were chosen to reflect differences in skeletal composition and diagenetic maturity. Figure 3.107 shows the differences in skeletal grains for each thin section. It is apparent from this plot that the north coast and east coast samples are broadly different to the south coast samples, as they have lower proportions of skeletal grains in comparison (however more north and east coast samples would be required to truly ascertain this.).

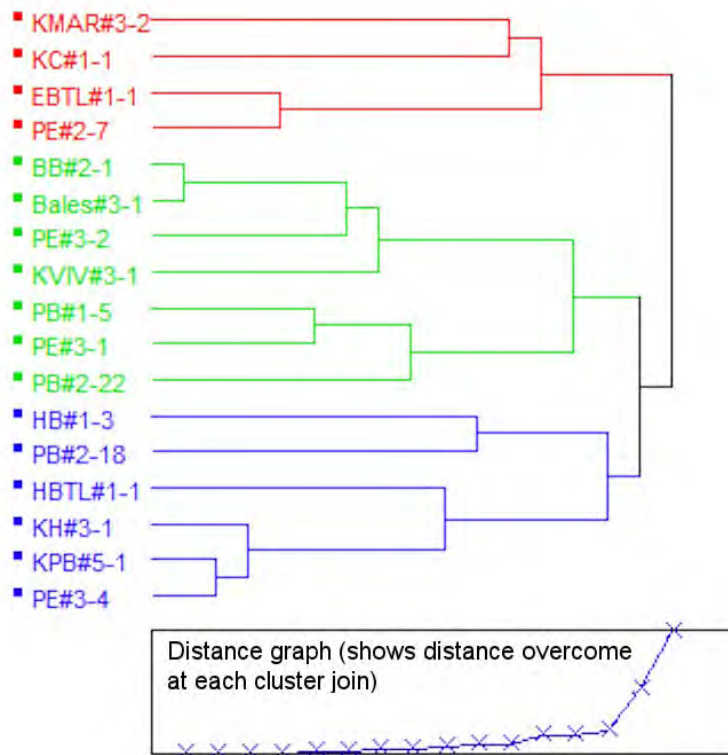


Figure 3.107: Skeletal grain cluster analysis (Ward Method) for Kangaroo Island thin section samples. Three clusters are apparent. Red shows (relatively) a low skeletal proportion, green a medium/high proportion, and blue a high proportion.

This is also reflected in Figure 3.108; here mollusc grain proportions are compared. Again, the north coast and east coast (and Dudley Peninsula) samples are clustered together, showing overall low proportions of mollusc grains in comparison. The reasons for the differences possibly relate to

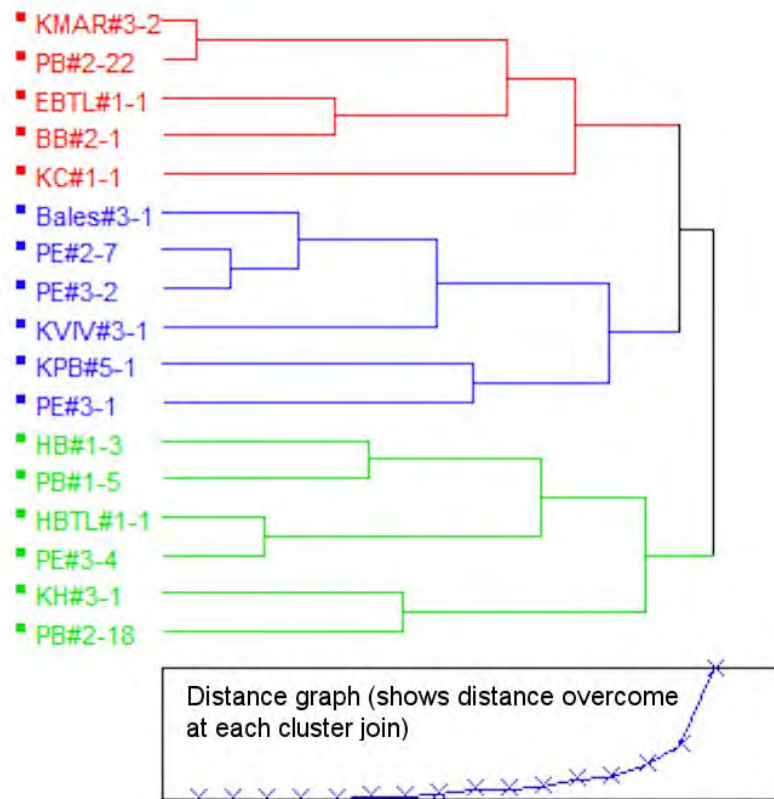


Figure 3.108: Mollusc grain cluster analysis (Ward Method) for Kangaroo Island thin section samples. Three clusters are apparent. Red shows (relatively) a low mollusc proportion, blue a medium/high proportion, and green a high proportion.

carbonate productivity (particularly for molluscs) in each region, i.e., lower production in the north and east, and higher production in the south. However, more thin section analyses from the north and east coast (including Dudley Peninsula) would be required to further support this hypothesis. Cement proportions were also examined in order to determine patterns in diagenetic maturity. This was plotted in Figure 3.109. Unfortunately, relationships in terms of geographical location or probable age are not really apparent in the clusters. Even though the level of cementation may to a degree reflect diagenetic maturity, it does not necessarily reflect age. The data may also be skewed as some samples were unconsolidated prior to thin section preparation, hence, cements that were point counted were only rim cements (these were BB#2-1, KC#1-1, HB#1-3, PB#1-5, PB#2-18, and PE#3-4). Regardless, the relationship between diagenetic maturity and age is better illustrated in the next section.

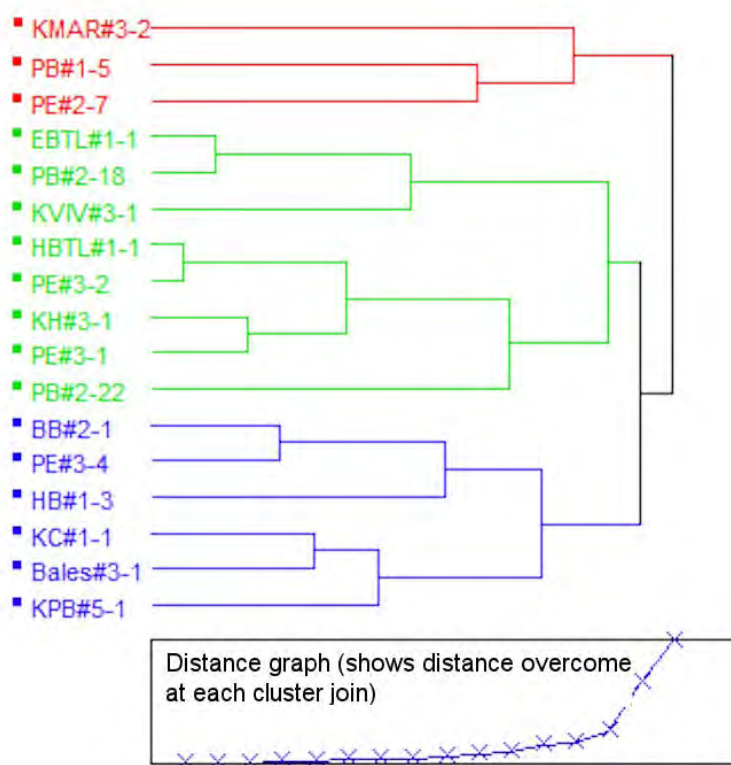


Figure 3.109: Cements cluster analysis (Ward Method) for Kangaroo Island thin section samples. Three clusters are apparent. Red shows (relatively) a high cement proportion, green a medium proportion, and blue a low proportion.

3.7.7.2 Powder XRD analysis: CaCO_3 mineral phases

The percentage weights of the 3 common mineral phases of CaCO_3 (aragonite, Mg-calcite, and calcite) were determined for a variety of samples recovered from the north, east and south coasts of Kangaroo Island (see Table 3.22). The proposed age ranges for the samples were from the early Pleistocene to modern, with an array of facies from aeolianite and calcrete to dune, palaeosol and lagoonal. Figure 3.110 displays the location of the samples sites and mineral compositions for each sample in the form of pie charts (see also Table 3.22 for numerical data). Figure 3.111 displays a sample XRD trace and assay for Pennington Bay middle Pleistocene sample PB#2-22, identified are the peaks for quartz, aragonite and calcite.

The 3 mineral phase percentage weights were normalised and placed into a ternary plot (see Figure 3.104D) and a stacked area plot (see Figure 3.112).

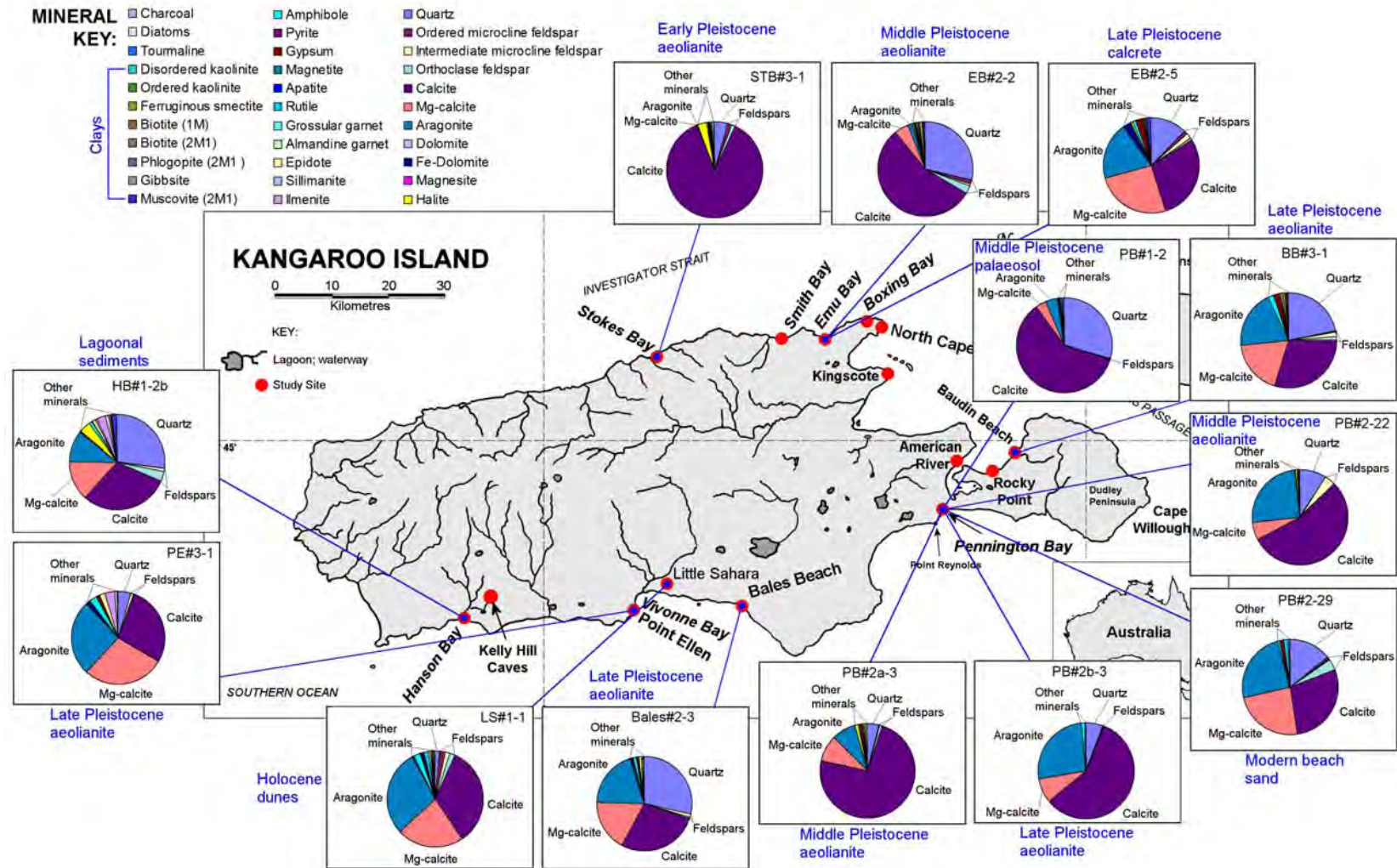


Figure 3.110: Location of XRD sample sites around Kangaroo Island, with accompanying mineral composition pie charts, and probable ages.

These plots illustrate very well the relationship between diagenetic maturity and probable sample age. As such there is a reasonably good relationship between increasing calcite concentration and increasing age in this group of samples, i.e., the oldest sample (STB#3-1), recovered from Stokes Bay (Figure 3.110) has, essentially, only calcite remaining. It should be noted that even the youngest group of samples has quite high concentrations of calcite (~30-40% weight). This is in all probability reflecting the high level of sediment reworking (from actively eroding, older, adjacent skeletal carbonate units) that is experienced by Kangaroo Island coastal carbonate sediments.

3.7.8 Distinguishing petrological characteristics of the Kangaroo island sedimentary units examined in thin section, and conclusions

The granular compositions of almost all of the samples examined in this chapter part are quite distinctive in two respects: they are dominated by a skeletal component (see Figure 3.104A), and the granular components of this broad skeletal class are dominated by molluscan grains (see Figure 3.104B) (although KC#1-1 and KMAR#3-1 have high proportions of inorganic grains in comparison). In this respect most of the analysed sediments can be classified as molluscan skeletal sands or molluscan skeletal grainstones-packstones, depending upon cement types.

No real patterns emerged in the diagenetic (i.e. porosity, recrystallised grains, and cements) compositional data that were related to the age of the sediments. There was, however, an inverse relationship between the sediment porosity and proportions of cements (see Figure 3.104C), which may be related to diagenetic maturity (hence, age is not necessarily the whole “equation”, environment is also key).

The powder XRD results (see Figure 3.104D and Table 3.22) provide good evidence for a relationship between the level of diagenetic maturity and age. Looking quantitatively at the carbonate mineral phases is a more direct method of determining diagenesis rather than the qualitative estimation of diagenetic factors. These results show increasing concentrations of calcite (low Mg) with

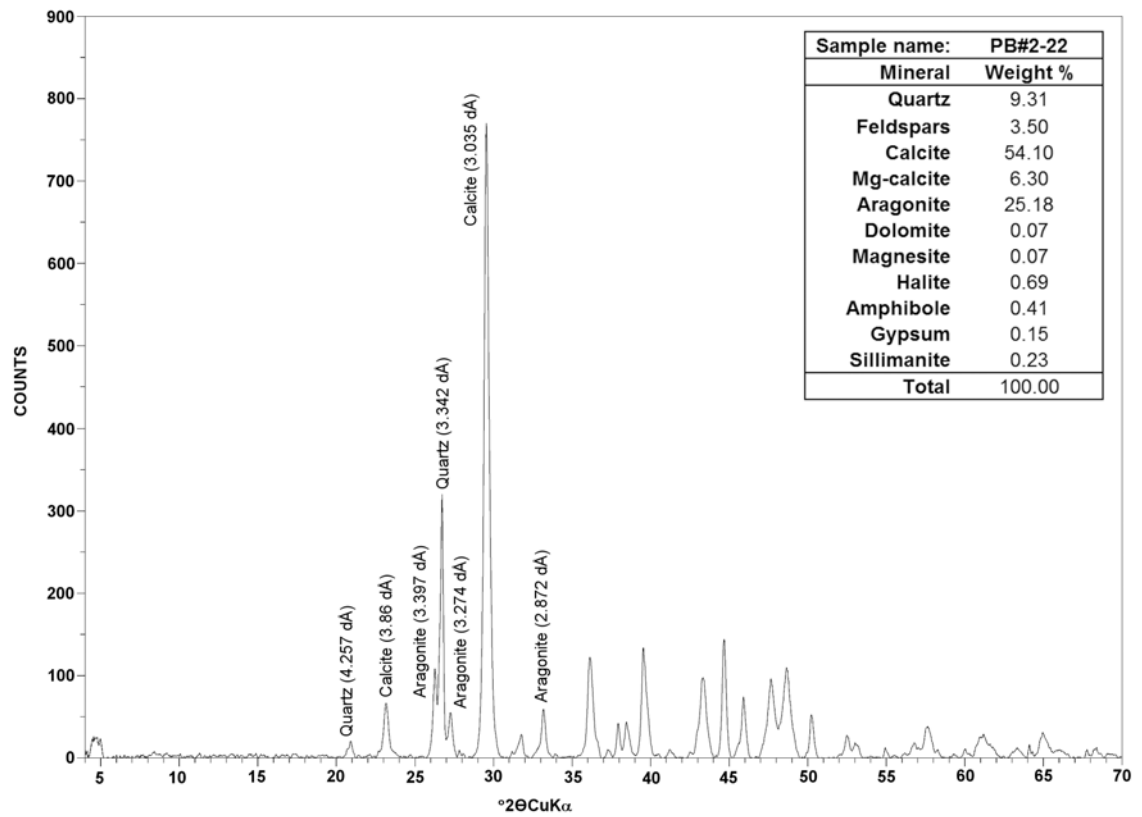


Figure 3.111: Pennington Bay sample PB#2-22 XRD trace with assay, and identified quartz, aragonite and calcite peaks.

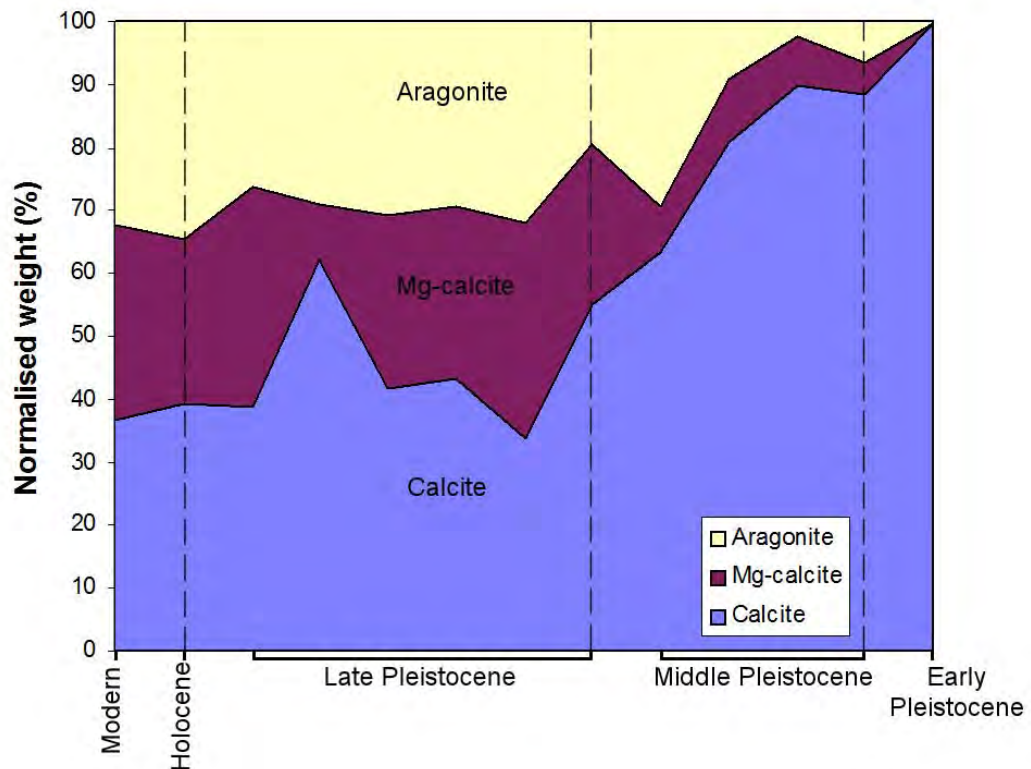


Figure 3.112: Normalised percentage weights of CaCO_3 mineral phases, showing changes in mineral chemistry over time. Note the almost complete alteration to calcite in the oldest sample (early Pleistocene).

age (proposed ages initially based upon morphostratigraphical and biostratigraphical features [see previous stratigraphy sections]—which are quantified in the later geochronology chapter [Chapter 7]), in concert with decreasing concentrations of aragonite and Mg-calcite. This is a good indicator of the level of maturity.

Overall, the petrographical data indicates that (at least for the examined samples) the Kangaroo Island aeolianites evolved under a predominantly meteoric-vadose environment. The raised beach deposits sometimes exhibited both marine and meteoric characters, attributable to subaerial exposure after sea-level regression.

Chapter 4: Luminescence, accelerator mass spectrometry carbon-14 (AMS¹⁴C), and Uranium-series (²³⁸U/²³⁰Th series) dating methods

4.1 Introduction

This chapter will examine the methods associated with the dating of the Kangaroo Island aeolianites and marine carbonate fossils (specifically molluscs and coral), i.e., optically stimulated luminescence (OSL), thermoluminescence (TL), accelerator mass spectrometry carbon-14 (AMS¹⁴C), and Uranium-series (²³⁸U/²³⁰Th series) dating. Luminescence is a ‘trapped’ charge dating method and accelerator mass spectrometry carbon-14 (AMS¹⁴C) and uranium series (U-series or ²³⁸U/²³⁰Th) dating (using multi-collector-inductively coupled plasma mass spectrometry [MC-ICPMS]), involves the comparison of the abundance of different isotopes in a sample.

The first section outlines the sampling and dating strategies for all dating methods (this does not include amino acid dating as this is examined in Chapter 6). Following this, luminescence dating dosimetry techniques are reviewed (the discussion and assessment of the dosimetry results for the Kangaroo Island luminescence samples are presented in Chapter 7: Part I).

The proceeding sections examine each dating method in turn; beginning with luminescence dating. OSL dating, termed ‘conventional’ OSL dating in this thesis is investigated first, followed by thermoluminescence (TL).

An assessment of the relatively new ‘long-range’ multiple aliquot (MAR) technique of thermally transferred OSL dating (TTOSL or recuperated OSL) is undertaken in the next chapter (Chapter 5). A single aliquot regenerative dose (SAR) TTOSL protocol (termed SARTT-OSL in this thesis) is developed in this thesis; hence, this method and its application to some test samples will be evaluated

The closing sections of the chapter briefly outline the ¹⁴C and U-series methods used to determine ages for Holocene marine shell and a Late Pleistocene stony coral, respectively. The chapter concludes with a summary of the dating methods examined in this chapter.

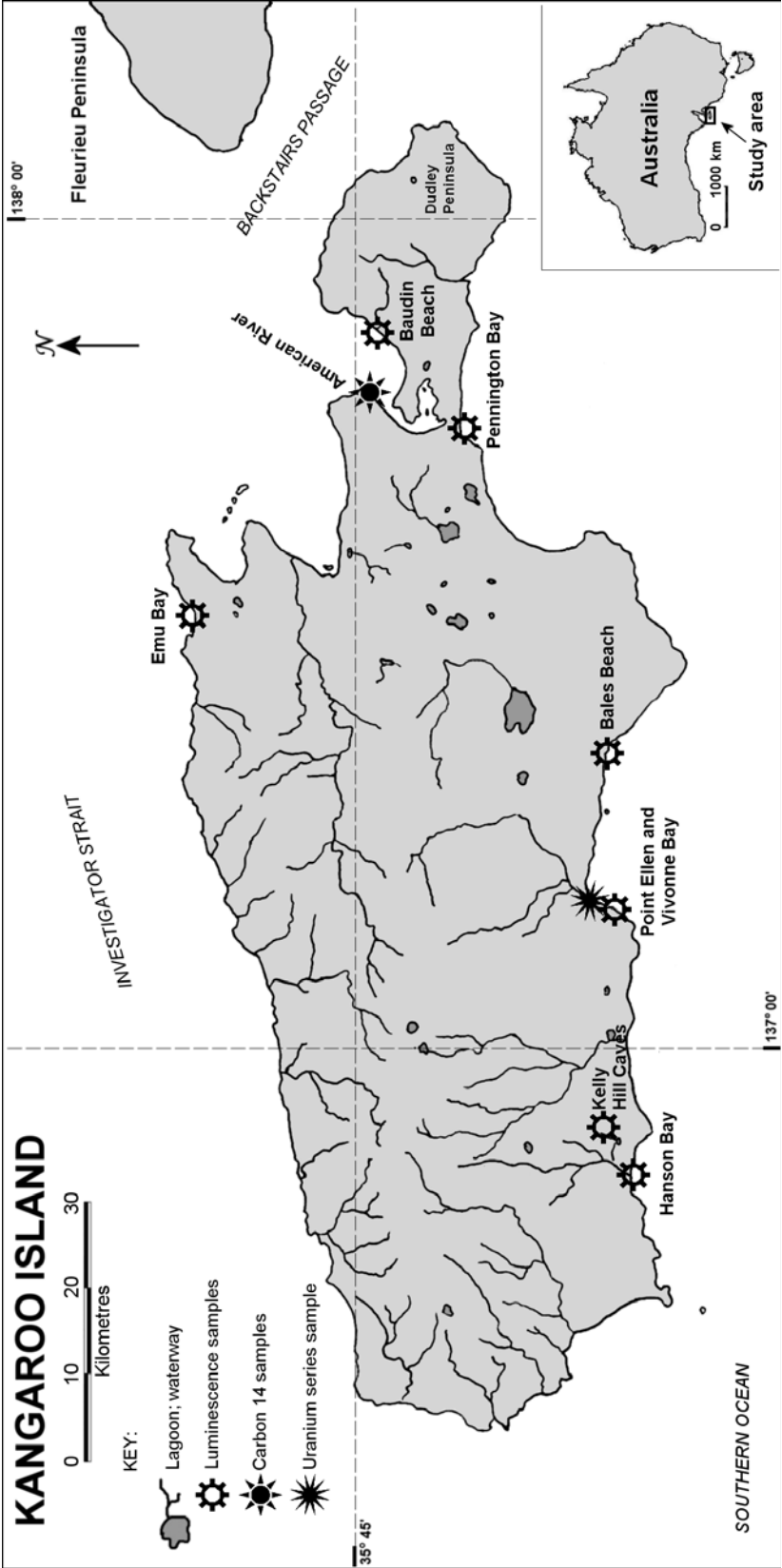


Figure 4.1: Radiometric dating sample sites for this study, on Kangaroo Island, South Australia.

The dating results derived from the application of these methods to the Kangaroo Island samples will be presented in Chapter 7.

4.2 Sampling and dating strategies

Radiometric dating samples were removed from a variety of locations, and sediment settings around Kangaroo Island (aeolian, marine, and estuarine). The map in Figure 4.1 shows the locality of the sites examined on the island where dating samples.

Only 23 samples were taken for radiometric dating purposes, though a larger number would have been preferred, it was not possible in light of resource restrictions. In the case of OSL samples, these were taken from (wherever possible) ‘fresh’ exposures in stratigraphic units that were in easily accessible positions. The units sampled had sediment that was appropriately homogeneous; lacking pedogenic features and were also of key importance stratigraphically and chronologically. For example, upper most and lower most aeolianite units, where accessible, and units that were considered to be significant in terms of sea-level, where suitable. At most only one or two samples were taken from each site. Since so few of these samples could be taken, they were also used to provide calibration for amino acid racemization (AAR) data; allowing other aeolianite units in the sequence to be age estimated (using the amino acids found in subfossils and the organic component of the sediment). This will be discussed in the dating results chapter (8).

Two ^{14}C samples (marine shell) were removed from a Holocene site at American River (Figure 4.1). These were also used to provide calibration points for AAR data—in this case it was direct calibration, since only half of each shell was used for ^{14}C ; the other half was analyzed for amino acid enantiomers.

A scleractinian coral recovered from a shelly matrix surrounding aeolianite boulders at Vivonne Bay (Figure 4.1) was dated using the U-series method; this too was also used for calibration purposes. This was an important sample to date as the upper limits of the matrix material the coral was found in could be used as a proxy sea-level indicator.

Table 4.1: List of radiometric dating samples retrieved from Kangaroo Island, South Australia.

Lab code	Location	Sample code	Facies type	Material dated	Absolute dating method	Event dated
Wk21538 Wk21537	American River	AR#3-2	Shell hash (coquina)	Marine shell	^{14}C (AMS)	Death of organism
	American River	AR#3-5	Shell hash (coquina)	Marine shell	^{14}C (AMS)	Death of organism
	Bales Beach	Bales#2-9	Aeolian (dune calcarenite)	Quartz	SAR OSU/SARTT OSL	Last exposure to sunlight
	Bales Beach	Bales#3-1	Aeolian (calcarenite)	Quartz	SARTT OSL	Last exposure to sunlight
	Baudin Beach	BB#3-1	Aeolian sand	Quartz	SAR OSL	Last exposure to sunlight
W3792 W3790	Baudin Beach	BB#3-5	Aluvial	Quartz	SAR OSU/SARTT OSL	Last exposure to sunlight
	Emu Bay	EBTL#1-1	Aeolian (dune calcarenite)	Quartz	TL	Last exposure to sunlight
	Hanson Bay	HBTL#1-1	Shelly coarse sands	Quartz	TL	Last exposure to sunlight
	Hanson Bay	HB#3-4	Shelly coarse sands	Quartz	SAR OSL	Last exposure to sunlight
	Kelly Hill Caves	KH#3-1	Cave (calcarenite)	Quartz	SARTT OSL	Last exposure to sunlight
W3791	Pennington Bay	KPB#5-1	Aeolian (dune calcarenite)	Quartz	SARTT OSL	Last exposure to sunlight
	Pennington Bay	PB#2-18	Aeolian (dune calcarenite)	Quartz	SAR OSU/SARTT OSL	Last exposure to sunlight
	Pennington Bay	PB#2-22	Aeolian (dune calcarenite)	Quartz	SARTT OSL	Last exposure to sunlight
	Pennington Bay	PB#2a-3	Aeolian (dune calcarenite)	Quartz	SAR OSU/SARTT OSL	Last exposure to sunlight
	Pennington Bay	PB#2b-3	Aeolian (dune calcarenite)	Quartz	SAR OSL	Last exposure to sunlight
	Pennington Bay	PB#2b-8	Aeolian (modern dune)	Quartz	SAR OSL	Last exposure to sunlight
	Pennington Bay	PB#2c-1	Aeolian sand	Quartz	SAR OSL	Last exposure to sunlight
	Pennington Bay	PBTL#1-1	Aeolian (dune calcarenite)	Quartz	TL	Last exposure to sunlight
	Pennington Bay	PB#2-x	Aeolian sand	Quartz	SARTT OSL	Last exposure to sunlight
	Pennington Bay	PB#3-2	Aeolian sand	Quartz	SARTT OSL	Last exposure to sunlight
ANU01-07-08	Vivonne Bay	PE#3-1	Aeolian (dune calcarenite)	Quartz	SAR OSL	Last exposure to sunlight
	Vivonne Bay	PE#3-2	Aeolian (dune calcarenite)	Quartz	SARTT OSL	Last exposure to sunlight
	Vivonne Bay	PE#3-4	Shelly matrix	Coral	UTh	Death of organism

4.2.1 Luminescence sampling methods

A total of 20 luminescence samples (Table 4.1) were collected from Kangaroo Island (10 were analyzed for OSL, 7 for SARTT OSL, and 3 for TL). Half of these were taken from Pennington Bay, one of the most representative sites on the island with many easily accessible outcrops. Sample collection procedure depended upon whether the sediment was consolidated or unconsolidated. Since Kangaroo Island coastal sediments (aeolianite dune sands) have high biogenic calcium carbonate (CaCO_3) content (sometimes as high as 98% carbonate by mass) most are consolidated (particularly the older aeolianites) due to dissolution and re-precipitation of some of the carbonate as interstitial cements, by meteoric and vadose waters (this also has implications for radionuclide mobility). This is problematic as sampling becomes much more difficult. Most of the sites that were sampled exist in national park and reserve areas, so the use of powered coring tools was not an option, as the permit acquired for this study required a minimum impact when sampling. Therefore, when the unit to be sampled was indurated, a block of sediment material was removed from the cleaned face of the unit by chipping out a section (around 10x10x10 cm) with a rock hammer then carefully breaking this off. A reasonably large sample was required because of (as iterated above) the relatively low quartz content of the sediment (luminescence methods date the last exposure of mineral (quartz; feldspars) grains to sunlight or heating). Surprisingly this sampling method is very low impact as the hole left behind is reasonably shallow and virtually invisible against the relief the rock face. The block sample could then be wrapped in foil and sealed in plastic to preserve the existing water content.

Sections of the block could be used for laboratory dosimetry and luminescence analysis (sample preparation and processing is discussed in Appendix C). Conversely, if the sediment was unconsolidated the tube sample method was used: a section was cleaned flat and a 65 mm diameter steel tube 150 mm in length was hammered into the face of the unit. The outside end of the tube was packed with plastic to ensure that, once the tube was hammered completely in, the contents would be tight and could not move about during transport. Once the tube was completely imbedded the packed end of the tube was capped;

then the tube could be carefully dug out. The inside end of the tube was capped in turn, and both ends were tightly taped. Samples of sediment from the same hole were also collected for laboratory dosimetry. At two sites *in situ* field gamma spectrometry (FGS) was used to determine concentrations of radionuclides for gamma dose rate estimation. The FGS detector was placed in the same hole that the luminescence sample was taken from; after this was completed the hole could then be filled in. FGS will be explained in section 4.3.2.2 of this chapter. Before a unit was sampled it was scrutinized to locate the most appropriate portion to sample. It is important to take luminescence samples from the most homogeneous section of a given unit. Heterogeneous sediments can give rise to problems with dosimetry, as the proximity of pebbles, cobbles, or boulders can introduce non-uniformity in dose rate. Near surface contexts should be avoided as this will lead to uncertainties in the gamma sphere—a quartz grain will receive ionizing gamma radiation from a sphere of surrounding sediment approximately 30 cm in diameter. For example if an OSL sample is taken from just below the surface, then only one half of the gamma dose is being received by the sample. Therefore, at least 20-30 cm of homogeneous sediment should envelop the sample section (Aitken, 1985; Forman *et al.*, 2000).

Sampling proximal to stratigraphic boundaries or weathering bedrock should be avoided, not only because of non-uniformity in the dose rate, but also because there may have been translocation of younger sediment grains from the overlying unit, or unbleached grains from the weathered rock. This can happen as a result of factors like ground water movement and bioturbation: sediment churning due to the action of small vertebrates, invertebrates and plant roots. Additionally, since a stratigraphic boundary may have once been an old surface, proximal quartz grains would have received a different level of radiation than those more deeply buried (Aitken, 1985). Units that have been weathered post-deposition have undergone pedogenesis and exhibit accumulations of clay, carbonate, silt or silica should also be avoided (Forman *et al.*, 2000). These weathering processes can alter radionuclide concentrations, disrupt the crystal structure of mineral grains and can also translocate in younger grains (Forman

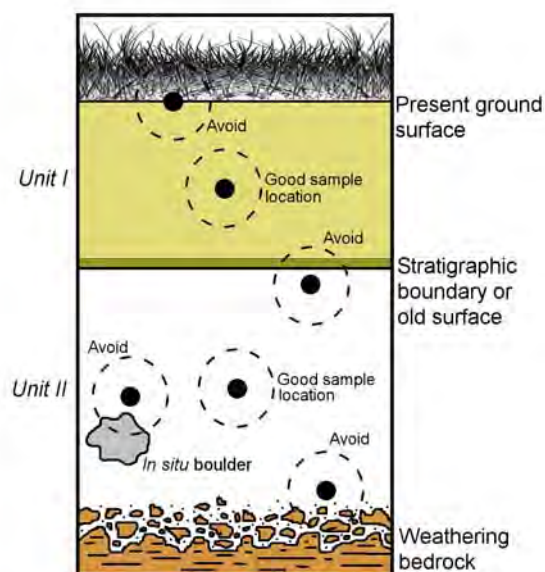


Figure 4.2: This schematic is adapted from Aitken (1985). It illustrates a sample pit with some of the sampling locations that should be avoided. The large black dots symbolize sample locations, and the dashed circles represent a 30 cm radius gamma sphere.

et al., 2000). Figure 4.2 outlines some of the sampling strategies that should be avoided. Uncertainties relating to gamma sphere dosimetry must be considered; in light of this, when sampling from exposures (such as coastal aeolianite) samples should be taken at a minimum of 20 cm depth (into the face of the unit); sediment should be scraped back for at least 20 cm to expose a clean face (Aitken, 1985; Forman *et al.*, 2000). This was not always practical at some sites on Kangaroo Island for the reason that a number of aeolianite units studied were strongly cemented; thus, cutting back into the face to the appropriate depth was often difficult. Wherever possible, at these sites, samples were taken from recently (relatively) exposed sediment faces, i.e. from faces exposed as a consequence of cliff collapses attributable to undercutting by wave action. However, for two samples collected this was not possible; at these sites then, some additional uncertainty in the gamma dose must be accepted. This will be evaluated in the sections relating to these particular samples in chapter 7.

4.2.2 ^{14}C sampling methods

In order to be appropriate for ^{14}C dating a sample *must* contain carbon that was fixed originally from the atmosphere (atmospheric CO_2) when the organism was living (Trumbore, 2000). In light of this one must sample carbonaceous material, in this case marine molluscs that are in a good state of preservation. There is

less chance of isotopic contamination by non-indigenous carbon if shells that exhibit diagenetic modification features, such as recrystallization (shells will have a powdery or chalky texture), cementation, dissolution, and oxidation, are avoided. Or, if some of these features are unavoidable, then care must be taken to remove the affected portions if possible. Much of this pretreatment is done by the dating laboratory; however, choosing shells in the field that are in a good state of preservation is advantages in gaining high-quality results. Sample analysis methods will be discussed later in this chapter.

4.2.3 Uranium series sampling methods

As with ^{14}C sample collection, care must be taken to choose a sample, in this case a nodule of coral, which is free from diagenetic modification features, particularly recrystallization of the primary aragonite, and also precipitated calcitic cements. These non-indigenous minerals can act as pathways for thorium into a closed system. Sample analysis methods will be discussed later in this chapter.

4.3 Luminescence dating: environmental radioactivity, the evaluation of the dose rate, and the luminescence signal.

The following sections will discuss in detail the various luminescence methods used in this thesis. However, first, the methods used for dose rate determination for the Kangaroo Island samples will be briefly reviewed, then the luminescence methods: OSL, the new TTOSL method (its modification in this thesis to operate as a single aliquot protocol), and TL will follow this.

OSL, TTOSL, and TL are ‘trapped’ charge or radiometric techniques; therefore, dosimetry represents the other ‘half’ of the luminescence equation. Dosimetric methods determine the concentration of radionuclides in sediment, and from this the rate (termed: dose rate) at which ionizing radiation is delivered to the mineral (quartz in this instance) sample (the unit of absorbed radiation is termed ‘Gray’—Gy: 1 Gy = the absorption of 1 joule of energy, in the form of ionizing radiation, by 1 kg of matter) can be determined. Hence, in the simplest terms,

when the equivalent dose (D_e : the radiation dose absorbed by the mineral grain, as measured in the laboratory) is divided by the total dose rate (the dose rate is most often expressed in terms of Gy per thousand years (ka); the *total* dose rate is the alpha (α) + beta (β) + gamma (γ) + cosmic rates with corrections for water content, attenuation, location, elevation and depth), an age estimate for the sample can be calculated.

Luminescence dating has its foundation in the fact that certain crystalline minerals (principally quartz and feldspar) in sediment have defects in the crystal structure which can store electrons for long periods of time; in this way these minerals can act as natural dosimeters (Fleming, 1979; Aitken, 1985; Duller, 1995; Aitken, 1998).

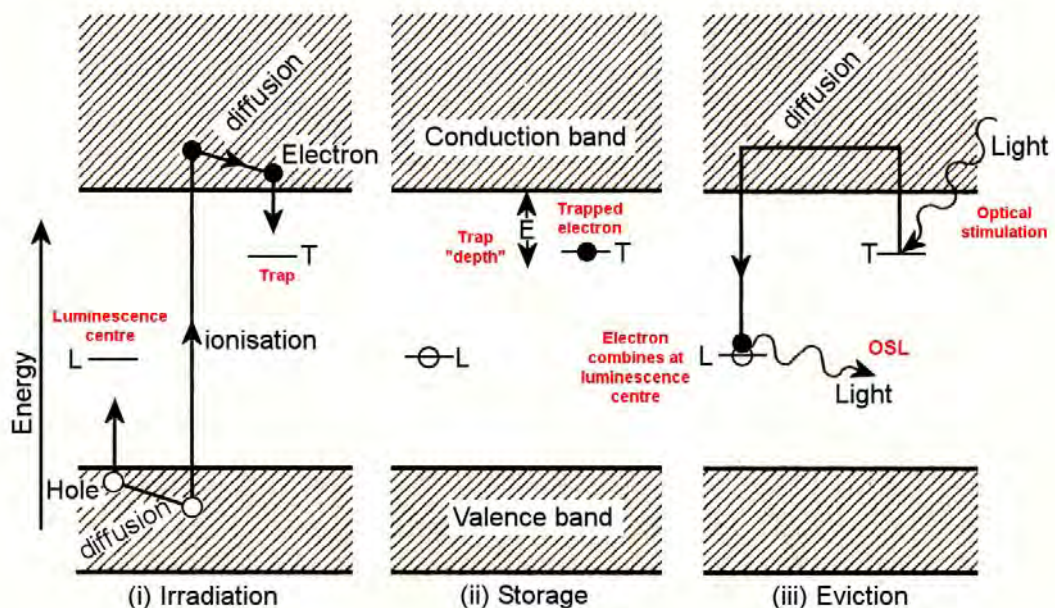


Figure 4.3: This is an energy level diagram of the OSL process; figure and caption based upon Aitken (1998). i) The ionization of the quartz crystal from exposure to environmental radiation, and the trapping of electrons and holes at defects T and L. ii) Electron storage during antiquity; the lifetime of the electrons in the trap needs to be longer than the age span of the sample. The depth of the trap (E) below the conduction band (the range of electron energy higher than the valence band—the highest electron energy band that can be filled with electrons) denotes trap lifetime. For dating purposes only traps that are 'deep' enough (around 1.6 eV or greater) to give lifetimes in the range of millions of years are useful. iii) The exposure to light of the appropriate wavelength evicts the electrons, and a portion of these reach luminescence centres (L); photons are emitted (OSL) in the process of combining with these centres. Also, some electrons may combine at non-luminescence centres, or be re-captured in the same type of trap or other types of traps. The process for TL is similar, excepting that heat is the stimulus (from Aitken, 1985; Aitken, 1998).

Ionizing radiation can evict electrons from their stable ground state, where they can become 'trapped' within these defects; a portion of this population may become fixed and remain stable for millions of years (Stokes, 1999). Upon the addition of energy in the form of either optical or thermal stimulation, the electrons can combine with holes at recombination centres, and return to their ground state. If the recombination centres are of the luminescent type, then there is a corresponding release of energy in the form of photons (Aitken, 1998; Stokes, 1999): this is the luminescence signal which can be measured in the laboratory. For a detailed discussion of this see Aitken (1985; 1998); however, Figure 4.3 summarises the OSL process.

The electron populations will continue to accumulate at these metastable defect sites throughout the period of burial; at a rate proportional to the level of natural background radioactivity. The purpose of OSL dating is to determine the length of time that has passed since the 'traps' were last 'emptied' of electrons: this can be attributable to an event such as transport and deposition, when the mineral grains were exposed to sunlight and the luminescence signal was reset. The intensity of this luminescence is proportional to the amount of trapped charge and hence to the radiation dose that the sample received during burial. It is possible to measure this luminescence in the laboratory by exposing the mineral grains to an artificial narrow wavelength light source (e.g. blue light emitting diodes [BLEDs], blue-green light from a halogen lamp, a green or an IR laser, or infra-red emitting diodes [IRLEDs]); the intensity of measured luminescence is in proportion to the quantity of stored electrons, and hence to the radiation dose acquired during burial. The total burial dose or palaeodose can be quantified by determining the equivalent dose (D_e): where the initial luminescence signal or 'natural' is calibrated against the signals obtained from a series of known laboratory doses (Murray and Roberts, 1998). When the D_e is combined with the environmental dose-rate (calculated from the concentrations of radionuclides in the surrounding sediment, and determined by appropriate dosimetric methods), as in equation 4.1, the luminescence age estimate can be calculated (Aitken, 1985):

$$\text{Luminescence age (ka)} = \frac{\text{Equivalent dose (Gy)}}{\text{Total dose rate (Gy ka}^{-1}\text{)}} \quad (5.1)$$

To reiterate: the energy (ionizing radiation) required to evict electrons from their stable ground state comes from radioactive elements in the surrounding sediments, and also cosmic radiation from space. To paraphrase Aitken (1985: pg 61):

"the role that radioactivity plays [in luminescence dating] is in providing a constant dose-rate for the production of [luminescence]"

Thus, the following sections will examine dosimetry for luminescence dating in detail, and discuss the various methods used, in this thesis, to derive α , β , γ , and cosmic dose rates for the Kangaroo Island samples.

4.3.1 The external and internal dose rates

The amount of radiation received by the mineral grain depends mainly upon the radioactive decay of the isotopes uranium-238 (^{238}U), uranium-235 (^{235}U), thorium-232 (^{232}Th); their daughter products, and potassium-40 (^{40}K), found in the surrounding sediment. Most of the natural uranium is composed of ^{238}U ; ^{235}U only represents around 0.7% of the natural abundance. ^{238}U , ^{235}U , ^{232}Th (their progeny), and ^{40}K , deliver α , β , and γ radiation. Alpha particles are a massive (2 protons and 2 neutrons: He^{2+} ions) highly ionizing form of short range (travelling only around 25 μm in sediment) radiation arising from the decay of radioisotopes in the nuclide chains of U and Th. Beta particles are derived from the decay chains of U, Th, K (and also Rubidium [Rb]); these are generally high-energy, high-speed electrons and positrons that have a range of approximately 2 mm. Naturally occurring ^{87}Rb , however, is a *low energy* β emitter that contributes only a small amount to the total external dose rate. With an assumed average K to Rb ratio of 200:1 (Aitken, 1985), the dose from Rb would be an estimated 2.9% of the total β dose as derived from K. Any contribution from Rb to quartz is considered negligible in the light of both this low concentration and attenuation of the low energy β particles (Warren, 1978). Equally, the same can be assumed for any internal contribution from Rb. Therefore, no allowance for a dose rate contribution from Rb has been included in the age calculation for the Kangaroo Island samples.

Gamma rays are a form of high-energy electromagnetic radiation (without mass or charge, i.e. photons) derived from the decay chains of U, Th, and K. They are much more penetrating than α and β particles, and can penetrate up to 30cm into sediment (Aitken, 1985).

Beta particles and gamma radiation contribute the most to the external dose rate applied to quartz.

Additionally, there is also cosmic radiation which is composed of highly energetic relativistic particles—most are protons (~90%), with a small percentage of α and β particles—that originate in space and encroach upon the Earth's atmosphere (Munyikwa, 2000). The portion of the dose rate that cosmic radiation contributes depends upon geographical location (geomagnetic latitude, due to interaction with Earth's magnetic field), height APSL and depth of the sample in relation to overburden. This contribution is generally small compared to the β and γ from the radionuclides. Nevertheless, it can be a significant contributor if the overall dose rate received from the radionuclides is low. Cosmic rays reach the Earth's surface as a shower or cascade of lighter particles that formed as a result of collisions with molecules in the upper atmosphere (Munyikwa, 2000; Ridky and Travnicek, 2003). This shower of particles has a 'soft' component and a 'hard' component. The soft component (mainly electrons) is absorbed by the first ~60cm of sediment; however, the hard component, composed primarily of muons (muons are negatively charged elementary particles similar to electrons, although significantly more massive), is unusually penetrative, and can pass through metres of sediment before attenuation starts to occur (Alexeenko *et al.*, 2002; Prescott and Hutton, 1994). Thus, for the purposes of determining the cosmic dose rate for a buried sample, it is this muon flux that is most important (Prescott and Hutton, 1994; Munyikwa, 2000). In determining the cosmic dose rates for the Kangaroo Island OSL samples calculations were made with regard to the sediment depth below surface, the geomagnetic latitude, and altitude APSL, using the procedures and equations of Prescott and Hutton (1994). Corrections for water content were also applied.

The majority of this radiation is delivered as an external dose to the mineral grain of interest, in this case quartz. Nevertheless, there is also a small internal α , β , and γ dose principally derived from the decay of U and Th (and K) contained within the quartz crystal; although, only the α contribution is relevant due to the much larger range of β and γ radiation (Aitken, 1985). A combination of the low alpha efficiency (0.04 ± 0.01 for Australian quartz from Lake Mungo) of quartz and the low internal concentrations of radionuclides (rarely $> 10^{-4}$ ppm) mean that little effective dose rate arises from this internal activity (Fleming, 1979; Aitken, 1985; 1998; Thorne *et al.*, 1999).

For the purposes of this study an effective internal α dose rate of 0.030 Gy/ka (Bowler *et al.*, 2003) is applied to the final dose rate estimation for all Kangaroo Island samples. This value is essentially negligible in comparison to the external β and γ dose rates, in most cases (ranging from 2 to 6% of the total dose rate). However, there are instances where the internal α dose rate is not an insignificant contributor: when the external β and γ dose rates are very low, for example. In this situation a more specific determination of the internal α dose rate would be desirable (Aitken, 1985). The cosmic contribution becomes more important as well. This set of circumstances arises for one of the Kangaroo Island samples: KH#3-1, where the combination of the assumed internal alpha and cosmic dose rates is ~39% of the total dose rate. This is discussed in the relevant sections in chapter 7.

There is also an external alpha contribution to the total dose rate; however, this is considered unimportant as most of the influence is removed during sample processing. Due to the low penetration capability of α particles only a thin outer layer of the quartz grain is irradiated. Therefore, a hydrofluoric (HF) acid etch can remove the α exposed 'rind' of the quartz grain ($\sim 10\mu\text{m}$) leaving an inner 'core' that has only been externally irradiated by β , γ , and cosmic radiation. This avoids the additional uncertainty that would be associated with the estimation of an α dose rate resulting from the partial penetration of the quartz grain. Even if some α irradiated rind remains after etching, the low α efficiency of quartz still allows for the assumption of an insignificant contribution to the total dose rate.

4.3.2 Dose rate determination

A range of techniques can be used to estimate the concentrations of U, Th, K, in the sediments surrounding the sample. They can be divided into two methods:

i) Those based upon measuring the emission of α and β particles, and γ rays from a sediment sample over a period of time (counting); such as Geiger-Müller beta counting (this study used a Risø GM-25-5 beta-counter (GMBC)), thick source alpha counting (TSAC: measures daughter activities), *in situ* field gamma spectrometry (FGS: measures daughter activities), and high resolution gamma spectrometry (HRGS: yields parent *and* daughter activity concentrations; useful for delineating equilibrium in a decay series). For TSAC and FGS it is assumed that the dose rate as measured at time of sampling has remained the same throughout the period of burial; without necessarily implying secular equilibrium (Olley *et al.*, 1996).

ii) Those that determine the elemental concentration of the *parent* nuclides directly; for example, instrumental neutron activation analysis (INAA), inductively coupled plasma mass spectrometry (ICP-MS), and X-ray fluorescence (XRF). These methods assume that the decay chains have *always* been in secular equilibrium (Olley *et al.*, 1996).

The above are predominantly laboratory based methods; however, the field based method, *in situ* or field gamma spectrometry (FGS) was also used to determine the concentrations in parts per million (ppm) of U, Th, and % K for two Kangaroo Island OSL samples. This technique measures (*in situ*) the γ emissions from the surrounding sediment to quantify the radionuclides (though, when determining the dose rates it should be coupled with GMBC for the beta dose rate: as GMBC (if sampled directly from, or adjacent to, the OSL sample) gives a more accurate assessment because of the shorter range of β particles.

4.3.2.1 Laboratory based dosimetric methods

Most of the dose rate quantification undertaken for this thesis was done in the laboratory, as often it was not possible to measure in the field, either because of

sample position; strongly indurated sediments that prevented the proper placement of the FGS, or instrument availability.

Laboratory based methods are used to determine both beta and gamma dose rates. Beta dose rates measured in the laboratory will generally give an accurate representation of the 'true' or 'natural' beta dose rate, as β particles only penetrate approximately 2 mm into the sediment (this presupposes that beta-microdosimetry is not an issue). Gamma radiation, in contrast, can penetrate up to 30cm into the surrounding sediment; hence, a true representation of the gamma dose rate is not possible using laboratory methods. However, all Kangaroo Island samples (except one which was fluvial in origin) that utilised laboratory based methods for dose rate determination in this study were removed from homogenous aeolian dune matrices. The assumption can be made, then, that the gamma sphere is effectively homogeneous as well, and that laboratory gamma dose rate determinations, in these cases, are appropriate.

This study utilised both emission and direct measurement methods: TSAC, GMBC, HRGS, FGS, INAA, and inductively coupled plasma-optical emission spectrometry (ICP-OES: used to determine % ^{40}K). Although, the INAA results were not used to calculate the final beta and gamma dose rates, for reasons relating to disequilibrium in the ^{238}U decay chain. Rather, for the 17 OSL samples a combination of TSAC, GMBC and ICP-OES were used for 7 samples; HRGS was used for 8 samples, and FGS and GMBC were used for 2 samples. The 2 TL samples were analysed at the University of Wollongong's commercial thermoluminescence laboratory (by D. Price), and used a combination of TSAC and atomic emission spectrometry (AES), to determine U, Th, and K respectively. The various dose rate determination methods will be outlined in the following sections.

Thick source alpha counting (TSAC)

TSAC has been in use since the inception of luminescence dating as a relatively simple and inexpensive dose rate determination method; it measures the (combined) contribution of α particles from U and Th. If the 'pairs' counting technique (this is where the paired counts—counts that occur within ~0.2 sec of

each other—resulting from the successive α decays of ^{220}Rn to ^{216}Po ($T_{1/2} = 0.15$ sec) in the ^{232}Th decay chain are recorded and compared to the total α count: the pairs rate is a measure of the Th activity in the sample) is applied an estimate of the concentrations (ppm) of U and Th in a sediment sample can easily be established (Huntley and Wintle, 1981; Aitken, 1985). Using the conversion factors of Adamiec and Aitken (1998), the *contribution* of U and Th to the beta and gamma dose rates can be estimated, and when the technique is used in conjunction with an independent method for determining %K (for example, flame photometry, XRF, AES, or ICP-OES), both beta and gamma dose rates can be calculated. It is also possible to combine TSAC with GMBC to calculate an estimate of %K: an even less expensive approach to determine beta and gamma dose rates (Jacobs, 2004).

Alpha counting was undertaken on a calibrated Daybreak 583 thick source alpha counter. The method used to determine U and Th for 7 samples in this thesis follows that described in Aitken (1985): Appendix J, and Jacobs (2004): Appendix C. Percentage K was also calculated using the TSAC-GMBC combination method (above), as a comparison to the ICP-OES determination of %K.

Kangaroo Island dosimetry samples were prepared for TSAC by first being oven dried at 100°C , then milled in a Retsch grinder (ball-mill) to $<20\mu\text{m}$ (a flour-like consistency) (Jacobs, 2004), in order to ensure that the total alpha activity would be recorded; this is related to the short range of α particles. The samples were left for several weeks to allow progeny ingrowth, and were then counted placed ‘alpha-thick’ (>1 mm) on a 14.79 cm^2 (when the surface area of the retaining ring edge is subtracted) zinc sulphide (ZnS) scintillation screen. Prior to this, however, two screens are counted ‘face-to-face’ (the side that has ZnS powder imbedded) in the Daybreak 583 in a Perspex sample holder to determine a background count for the screens; half of this count is used in the final calculation. Once the background check was completed one of the pre-counted ZnS screens was positioned (face up) in a Perspex sample holder, held in place with a stainless steel retaining ring, and sample was packed on top: firmly, to a thickness of >1 mm. The Perspex holder was then capped; however,

spacers were put in place so that the holder was left unsealed. The holder was then placed in the Daybreak 583, and counted until the total counts reached 2000.

An Excel spreadsheet was created to derive the concentrations of U and Th, and also K (in combination with the GMBC data) using the equations, and methods of Aitken (1985): Appendix J, and Jacobs (2004): Appendix C. The concentrations were then converted to beta and gamma dose rates using the conversion factors of Adamiec and Aitken (1998).

Geiger-Müller beta counting (GMBC)

For several OSL samples from Kangaroo Island GM beta counting (GMBC) was used to determine the beta dose rate. Beta radiation has a short ionization range of approximately 2mm, so the most accurate estimation of the external beta dose rate will come from sub-samples taken directly from, or adjacent to, the OSL sediment samples themselves: the Kangaroo Island beta sub-samples were taken directly from the OSL samples. The external beta dose rates for these sub-samples were determined by a Geiger-Müller multi-counter, Risø model GM-25-5 (Bøtter-Jensen and Mejdahl, 1988). The dried sub-samples were finely ground in a Retsch grinder (ball-mill) to ensure homogeneity and were left for several weeks to allow for Radon (Rn) progeny ingrowth. Then three aliquots of each sub-sample (approximately 4-5 grams each) were packed firmly into plastic beta counting pots and sealed under polyethylene film with a retaining ring. The three aliquots were then 'counted' in the GM-25-5 for 24 hours, along with a blank sample (magnesium oxide), and a standard sample (loess sample NUSSI). The background subtracted count rates were calibrated against the known beta dose rate of the NUSSI standard (1.49 Gy/ka) to calculate the final dose rates. This was undertaken following the methods of Bøtter-Jensen and Mejdahl (1988) and Ankjærgaard and Murray (2007).

High resolution gamma spectrometry (HRGS)

HRGS provides the opportunity to evaluate the equilibrium condition of the radionuclide decay chains of ^{238}U , and ^{232}Th . Eight Kangaroo Island samples were analysed at the Black Mountain Radionuclide Laboratories, in Canberra.

Approximately 150 g of each sample was submitted for analysis. Prior to counting the samples are ground to a fine powder, pressed into sealed containers, and are left for 23 days to allow for progeny ingrowth (equilibrium of Rn and its daughters). Subsequently, each sample was counted in a high-purity germanium (Ge) coplanar γ detector (a large volume semiconductor); the detector is shielded against background interference by aged lead blocks, and is operated at cryogenic temperatures, using liquid nitrogen (N₂) (see Hancock and Pietsch [2008] for further details).

Instrumental neutron activation analysis (INAA) and inductively coupled plasma-optical emission spectrometry (ICP-OES)

Nine Kangaroo Island dosimetry samples were commercially analysed at Activation Laboratories Ltd. (2006), in Ontario, Canada; using a combination of INAA (to determine U and Th ppm), and ICP-OES to determine % K₂O, which is converted to %K (a range of other oxides were determined as well). Methods used for these analyses are detailed at the Activation Laboratories website: <http://www.actlabs.com/page.aspx?menu=72&app=239&cat1=602&tp=2&lk=no>

4.3.2.2 Field based dosimetric methods

In situ (field) gamma spectrometry (FGS)

There were only 2 sample sites examined on Kangaroo Island that had the contribution from γ radiation to the external dose rate estimated by FGS. Many other sites either had sediment layers that were too strongly cemented for its use to be practicable; or could not be visited during the field season when the FGS was available. This was unfortunate as FGS would have been the preferred method for determining gamma dose rates, in that any spatial variability in the 30 cm γ ray ionization sphere can be accounted for.

The field gamma measurements for the two samples (Table 4.4) were made with an Exploranium (model GR 320) portable, field γ spectrometer with a GPX-21A sodium iodide (thallium doped) [NaI (TI)] detector crystal of 0.35 L volume; calibrated at the CSIRO North Ryde calibration pads. The instrument was set to 256 channels; with three regions of interest corresponding to the energy windows for the radionuclide peaks of ⁴⁰K (at 1.46 MeV), ²¹⁴Pb (at 1.76 MeV) in

the ^{238}U decay series and ^{208}Tl (at 2.61 MeV) in the ^{232}Th decay series. The energy window for ^{40}K is 1.38-1.53 MeV; for ^{214}Bi is 1.69-1.84 MeV, and for ^{208}Tl is 2.46-2.76 MeV (Aitken, 1985). The measured activities of ^{214}Bi and ^{208}Tl were re-calculated by the instrument into U and Th concentrations (ppm), respectively; assuming secular equilibrium in the decay chains. The ^{40}K activity was given as %K.

After the OSL sample was removed from the sedimentary unit to be dated, the sample hole created in the process was then made large enough to accommodate the 115 mm diameter GR 320 detector housing, which was buried to its complete length (406 mm) in the sediment; any gaps were infilled with sediment removed from the hole. The γ radiation flux was then counted for three successive 300 sec periods. The three sets of results provided a check on reproducibility, and after (2π) geometric correction and dose rate conversion factors were applied (4.2), a gamma contribution (in Gy/ka) could then be calculated for each of U, Th, and K. Thus, after summing and correction for moisture content, the mean total gamma dose rate, and standard error could then be estimated for the sample.

$$\gamma \text{ contribution (Gy/ka}^{-1}\text{)} = \left(\frac{\text{Radionuclide conc.}}{2.11} \right) \times \text{DR conversion factor} \quad (4.2)$$

4.3.4 Conventional OSL dating

Optically stimulated luminescence (OSL) dating, first proposed by Huntley *et al.* (1985), has its foundations in the premise that certain naturally occurring minerals, such as quartz and feldspar, found in sediments, act as dosimeters that record the amount of ionizing radiation received during continuous periods of burial (Wintle, 1997; Aitken, 1998). This radiation exposure results in the eviction of electrons from their stable ground state and the subsequent accumulation of this liberated charge at localised metastable defect sites within the crystal lattices of silicate mineral grains. These 'trapped' charge populations will continue to accumulate throughout the burial period at a rate proportional to the level of natural background radioactivity. The aim of the OSL method is to determine the timing of the particular event or events that last emptied these electron traps and hence, reset the luminescence signal. Usually the event of

interest is the last exposure to sunlight that occurred during transport and deposition. In the laboratory it is possible to measure the amount of trapped charge that has accumulated since a mineral grain was last exposed to daylight via artificial illumination with a narrow-wavelength light source. The intensity of light (OSL) emitted is proportional to the amount of trapped charge, and thus the radiation dose received by the sample during burial. The total burial dose or 'palaeodose' can then be quantified by calculating an equivalent dose (D_e), which involves calibrating this natural OSL signal against that obtained from a series of known laboratory doses. In order to calculate a depositional age for a sample it is also necessary to determine the rate at which the sample was exposed to radiation in the environment, or the 'environmental dose rate' (determined by measuring the elemental concentrations of the radioisotopes U, Th and K, in the surrounding sediment). When the D_e estimate is combined with the environmental dose rate for the sample, this equation can be used to determine time since burial (Equation 4.1):

In this study, the equivalent dose is determined by subjecting silicate mineral grains, in this case quartz, to a single aliquot regenerative dose (SAR) protocol (Murray and Wintle, 2000). In brief, D_e is determined by measuring the natural OSL signals from a series of sample aliquots; giving those same aliquots a series of different laboratory radiation doses and then measuring the OSL response after each dose. Sensitivity changes are corrected for by measuring the OSL signal response to a small test dose (T_x) given immediately after the natural (L_n) or regenerated (L_x) OSL signals have been measured. Sensitivity-corrected luminescence responses are then determined by dividing the natural and regenerated OSL intensities by their respective test-dose OSL intensities (L_n/T_n and L_x/T_x , respectively). By measuring a number of sensitivity corrected responses to different laboratory doses it is possible to construct a sensitivity corrected dose response, or 'growth curve'. D_e values can be derived by interpolation of the sensitivity corrected natural signal onto this growth curve.

4.3.4.1 Methods

Quartz grains of 90-125 μm in diameter were isolated from the samples and prepared for OSL dating using standard procedures (Aitken, 1998): this

procedure is detailed in Appendix C. The prepared grains were mounted as a monolayer onto stainless-steel discs, using Silkospray (silicone oil spray) and then optically stimulated for 40 s at 125 °C using blue (470 ± 30 nm) light from blue LEDs, or a broad-band halogen lamp (green light) (420-550 nm)—in this instance a 100 sec stimulation was used. The resulting ultraviolet emissions were detected by an Electron Tubes 9235B photomultiplier tube on a Risø TL-DA-20 (Risø 4), and on a TL-DA-15 (Risø 2), or by a Thorn-EMI 9235 QA photomultiplier tube on a Risø TL-DA-12 (Risø 1); all machines were fitted with two 3 mm Hoya U-340 filters. Laboratory irradiations were performed using a calibrated $^{90}\text{Sr}/^{90}\text{Y}$ beta source, on all dating machines

For each sample between 15 and 48 multi-grain 1 mm mask aliquots (each composed of ~80 grains) were measured, using a modified single-aliquot regenerative-dose (SAR) protocol to determine the D_e (Wintle and Murray, 2006). Small aliquot masks were used to permit an assessment of the adequacy of sediment exposure to sunlight before deposition (Olley *et al.*, 1999); although, this was not expected to be a significant problem, with the Kangaroo Island samples being predominantly from aeolian barrier dunes. Standard tests of protocol performance were performed, including checks for thermal transfer (resulting from the heat treatment applied to each aliquot before optical stimulation) and for the sufficiency of the test-dose correction procedure used to compensate for any changes in OSL sensitivity between successive regenerative-dose cycles (Wintle and Murray, 2006). Dose recovery tests (in which grains are bleached and then given a known dose) were also performed to determine the most appropriate experimental conditions for each sample. As a result of these tests, aliquots were heated to 260°C (and held at this temperature for 10 s) before measuring the natural and regenerative-dose signals, and the test doses were heated to 220°C (for 5 sec) before optical stimulation. OSL dose-response curves were constructed for each aliquot. The regeneration dose points in all aliquots were fitted with an exponential plus linear term (Jacobs *et al.*, 2003):

$$I = I_0 + L_{\max} \left(1 - e^{-\frac{D}{D_0}} \right) + k \cdot D \quad (4.3)$$

Where I is the sensitivity corrected luminescence intensity; D is the given laboratory dose and D_o and k are constants. All data were fitted using this function, generating a fit as shown in Figure 3. Using the above function the corresponding D_e values were determined from the first 0.32 s of OSL signal, using the count rate over the final 8 s of stimulation as background. Methods of data analysis and error estimation follow Yoshida *et al.* (2003). The rejection criteria used, and the standard tests performed are outlined in the following sections (4.3.4.2 and 4.3.4.3).

4.3.4.2 Rejection Criteria

The validity of equivalent doses determined via a particular SAR protocol must be evaluated prior to calculating the final age estimate for the sample. Single aliquot analysis yields a series of D_e s, and some may be affected by behavioural, compositional, and/or analytical problems; therefore, not all of these results will be useable. In order for a single aliquot result to be accepted, it must first pass a series of ‘tests’ i.e. be filtered through a set of rejection criteria. In the case of the Kangaroo Island studies 5 routine criteria were used to filter the single aliquot data: poor thermal contact (110 °C peak shift), poor recycling ratio, no L_n/T_n intersection with the dose response curve (saturation), poor infra-red (IR) depletion ratio, and poor recuperation. Pre-heat plateau tests, and dose recovery tests were also used to identify and evaluate the veracity of the particular heating regime undertaken—these, however, are global tests and do not examine individual aliquots.

Thermal contact

Poor thermal contact can be observed during analysis as a positive shift in the 110 °C TL peak. That is to say the peak plotted by the Sequence Pro and Analyst software packages does not lie over 110 °C; rather it will lie at a temperature above this, for example 130 °C, on the graph. The shift (actually a thermal lag) can be caused by two easily controlled factors: i) warped or bent sample discs, or ii) mineral grains on the base or sides of the sample disc. In order for the sample disc to be heated to the correct temperature (for a preheat or cutheat, for example) during analysis it needs to be in complete contact with the heater plate. If a disc is warped or bent, or has grains adhering to the base,

contact with the heater plate will be limited (heating efficiency will be reduced), and so thermal lag and/or a lower heating rate may occur (Figure 4.4). This

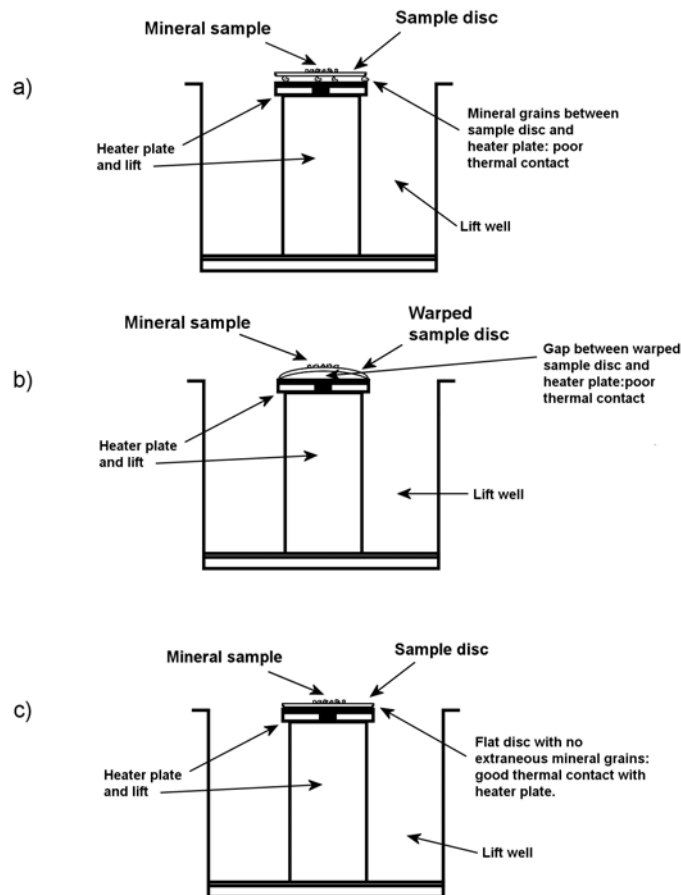


Figure 4.4: This is a schematic representation of a Risø TL/OSL machine heater plate which shows a) poor thermal contact of the sample disc to the heater plate caused by extraneous grains on the under-surface of the disc, b) poor thermal contact caused by a warped sample disc, and c) good thermal contact by way of a clean, flat disc.

means that the disc may not be heating at the same rate as the heater plate; or the disc temperature may lag behind the heater plate temperature. Therefore, since the thermocouple reads the temperature of the heater plate *not* the sample disc, the photomultiplier tube receives the thermoluminescence from the sample at an apparent higher temperature, as the disc 'arrives late' at 110 °C: thus a positive shift in the peak is observed. In itself this is not a problem. However, *if* the thermal lag does not allow the correct preheat or cutheat temperature to be achieved by the sample disc it will be inconsistent with other

aliquots that did not experience thermal contact problems. *The aliquot can then be rejected on this basis.* Figure 4.5 illustrates the effect of thermal lag on the position of the 110 °C TL peak. The lag may not be problematic when using preheats with a 10 sec hold (the sample disc may ‘catch up’; this will of course depend upon the magnitude of the lag); however, for 0 or 5 sec cutheats the correct temperature may not be reached for the sample disc. Accordingly, for this particular aliquot sensitivity correction is inconsistent with the other aliquots.

In light of this scrupulous care was taken to ensure that all discs used were in good condition, and—after sample placement—were also cleaned of any quartz grains adhering to the bottom and sides before loading into the Risø. Nevertheless, a few discs still exhibited shifting 110° C peaks (probably due to slight warping that went unnoticed), and were, hence, rejected. This level of care is necessary, especially since an entire dating run could potentially be ruined by a few clusters of quartz grains gathering on the heater plate.

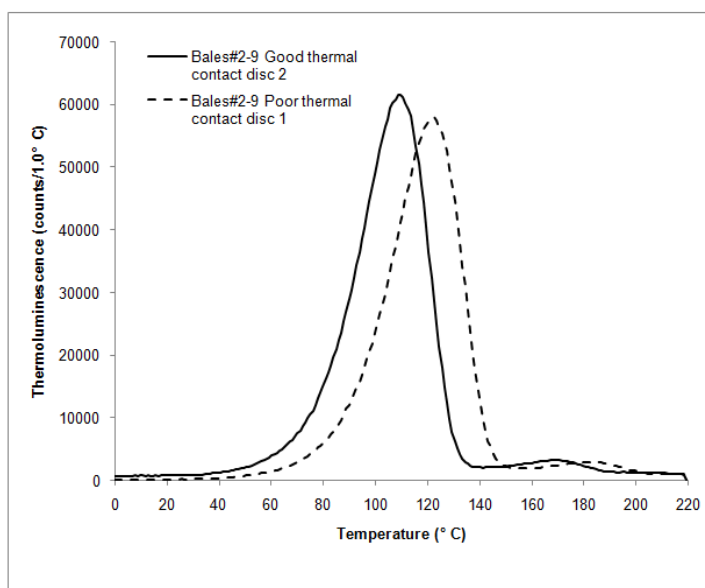


Figure 4.5: Illustrated here are actual data from Kangaroo Island sample Bales#2-9, for an accepted disc and a disc rejected on the basis of poor thermal contact. These are from 220 °C/5 sec cutheats; the disc with apparent poor contact with the heater plate shows a difference of +13 °C on the 110 °C TL peak; this aliquot may not have reached the required temperature even with the 5 sec hold. Factors such as the thermal diffusivity of the atmosphere and extraneous mineral grains between the stainless steel sample disc and the heater plate, and how much direct contact the sample disc has with the heater plate would control the magnitude of the thermal lag. The ‘poor thermal contact’ aliquot showed a much lower D_e (38 Gy—average was 56 Gy) than others in the run. It should be noted that the recycling ratio was also quite poor for this aliquot (1.13).

This effect is of particular importance in thermoluminescence dating where heating to very high temperatures is required, and isothermal TL dating. Detailed discussions of the physics and quantification of thermal lag, and associated problems can be found in Betts *et al.* (1993); Betts and Townsend (1993), and Jain *et al.* (2007).

Thermal lag should not be confused with the temperature offset experienced by some Risø TL/OSL dating machines.

Recycling ratio test

As part of the construction of sensitivity corrected dose response curves, a repeat dose point is included in order to monitor adequate correction for sensitivity change (Murray and Wintle, 2000; Wintle and Murray, 2006).

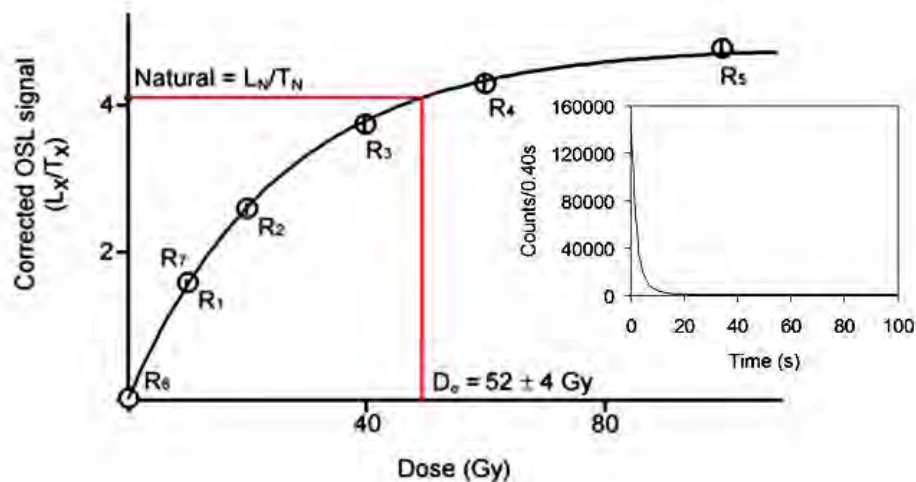


Figure 4.6: A dose response curve for an aliquot of Bales#2-9; the regeneration doses (R_x) given were 10, 20, 40, 60, and 100 Gy, with a 5 Gy test dose. The repeated dose point (R_1 and R_7) was 10 Gy. The recycling ratio (R_7/R_1) for this aliquot was 0.98. The error bars for each regeneration dose lie within the point symbol. The dose points are fit with an exponential plus linear function (Equation 4.3). The RH inset is the 'natural' OSL decay curve for this aliquot.

Since sensitivity usually increases through the measurement cycles, the first and last measurements will show the widest spread in sensitivity change (Wintle and Murray, 2006). Therefore, the first dose given is repeated in the last measurement cycle (Figure 4.6). The difference between the sensitivity corrected OSL signals from the repeat dose (also known as the recycled dose) and the first dose is expressed as a ratio—called the recycling ratio (in the case of the example from figure 4: $[L_7/T_7]/[L_1/T_1]$). If the protocol is successfully

correcting for sensitivity change then the ratio will be at or near unity. It was suggested by Murray and Wintle (2000) that an acceptable range for the ratio should lay between 0.90 and 1.10: 10% either side of unity. Alternatively, a ratio could also be considered acceptable if the value overlapped unity at 2σ . Nonetheless, in this study the recommendations of Murray and Wintle (2000) were followed. Figure 4.7 illustrates a recycling ratio plot which visualizes the distribution of ratios for a sample from Kangaroo Island [HB#3-4]).

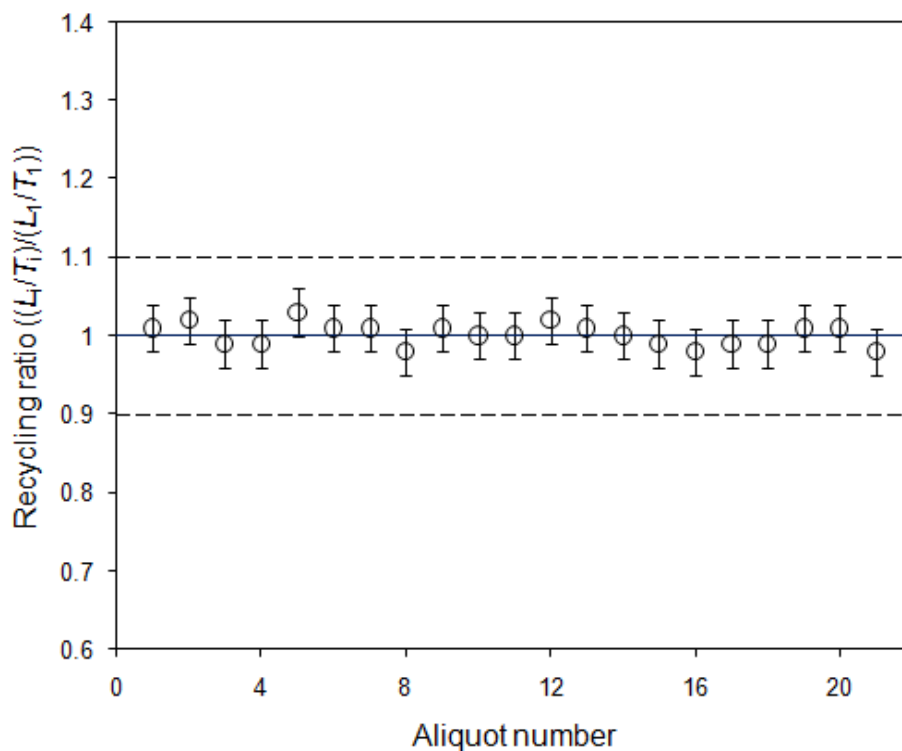


Figure 4.7: A series of recycling ratios from Kangaroo Island Sample HB#3-4. The solid line represents unity, and the two dashed lines correspond to 10% either side of unity. Note that all aliquots fall within the prescribed range of Murray and Wintle (2000); it is pleasing to also note that, for this sample, all aliquots overlap unity at 1σ .

No L_n/T_n intersection with the dose response curve (saturation)

This criterion is not a test; it is simply a category of unusable aliquots that in one case have no response curve intersection (i.e. the sensitivity corrected natural signal lies above the asymptote of the dose response curve: Figure 4.8a. In the other case there are aliquots that *do* intersect the response curve; however, the intersection is beyond the final regeneration dose point, along a line forecast by the Analyst software (Figure 4.8b).

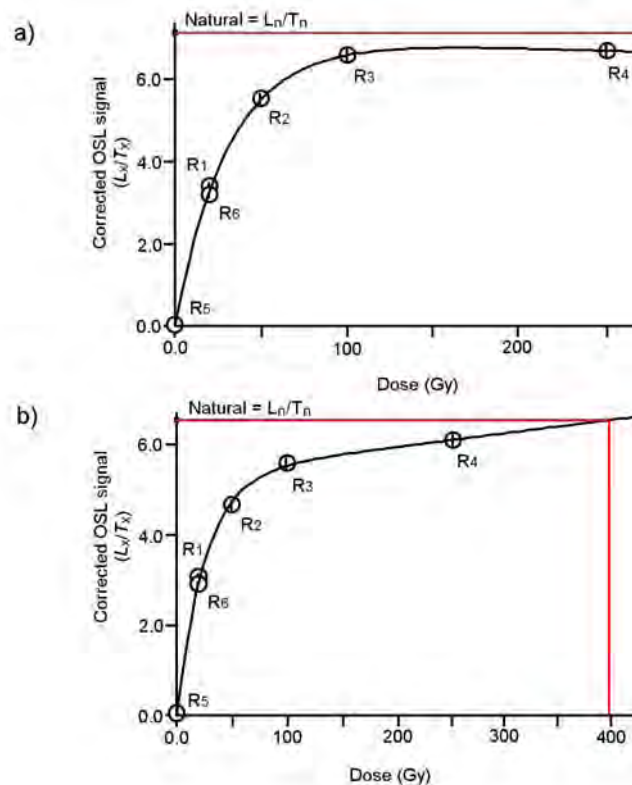


Figure 4.8: a) Dose response curve for an aliquot of Kangaroo Island sample BB#3-5, taken from an alluvial deposit, that is saturated for the ‘natural’ signal, i.e. the sensitivity corrected ‘natural’ signal (L_n/T_n) has no intersection with the dose response curve and lies above the asymptote. Plot b) is for an aliquot of the same sample where the natural does intersect the response curve; however, the intersection is beyond the last regeneration point, along the software forecast line.

In this instance another regeneration point can be added to the aliquot in an attempt to ‘verify’ or bracket the intersection; often, however, the extra point will only shape the curve so it lies below the natural. In many instances it may be desirable to reject these aliquots outright as they possibly contain a significant proportion of poorly bleached grains—this is particularly applicable to fluvial samples.

The IR depletion ratio

It is essential that in determining equivalent doses for aliquots of quartz that *only* the OSL signal from quartz is observed. Feldspathic contamination can be problematic for many quartz OSL samples (ref). Even after extensive pre-treatment of the mineral sample to remove feldspars there may still be some residual contamination. This can be in the form of either individual feldspar

grains that were not separated during heavy liquid treatment, that also survived HF etching, or as inclusions within grains of quartz (Fragoulis and Readhead, 1991; Jain and Singhvi, 2001; Wintle and Murray, 2006; Thompson *et al.*, 2008). Feldspars have greater intrinsic luminescence than quartz grains (which may manifest as a slower decay curve); this in addition to the possibility of anomalous fading could cause underestimation of D_e , if this luminescence is included as part of the quartz OSL signal. Additionally, the presence of ^{40}K in some feldspar minerals may induce locally significant changes in beta dosimetry (Jacobs *et al.*, 2003; Thompson *et al.*, 2008).

Routine methods used to mitigate the effect of feldspathic contamination involve:

i) The use of an additional optical stimulation, using IR diodes, before the blue LED stimulation in both the L_x and T_x portions of the Murray and Wintle (2000) SAR protocol.

This usually involves IR stimulation at ambient temperature for 100 sec, as a means of 'cleaning out' any signal derived from feldspar contaminants. However, there also exists a post-IR blue stimulated feldspar signal which can still interfere with quartz OSL (Duller and Bøtter-Jensen, 1993; Wallinga *et al.*, 2002; Thompson *et al.*, 2008). Accordingly, this signal can be depleted by IR stimulation at elevated temperatures; although, there is some risk that the quartz OSL may be depleted as well (Thompson *et al.*, 2008). Nonetheless, according to Zhang and Zhou (2007) this risk may only be significant if the duration of the IR stimulations is >1000 sec.

ii) The addition of a further replicate dose point at the end of the regeneration cycle, given prior to ambient temperature IR stimulation (50 °C for 100 sec); then followed by the preheat and measurement sequence. This allows the detection of signal depletion following exposure to IR.

This modification of the SAR protocol was proposed by Duller (2003). A ratio is derived from the sensitivity corrected luminescence of the recycled point with no

prior IR (L_x/T_x), and the post IR (L_y/T_y) recycled point (Jacobs *et al.*, 2003). This ratio—called the IR depletion ratio ($[L_y/T_y]/[L_x/T_x]$)—is used to reject any aliquots that lie outside of a 10% envelope surrounding unity, much in the same way as the recycling ratio. This modification is very easy to implement, and involves no risk with regards to the integrity of the quartz OSL signal; it eliminates the need for additional stimulations within the SAR cycle—shortening runtime—and allows the quick detection of aliquots that have significant feldspathic contamination, either as grains or inclusions.

For most of the OSL analyses in this study the Duller (2003) IR depletion ratio was employed; however, some analyses undertaken in the early stages of this study utilised the within cycle IR stimulation at room temperature. It should be noted that none of the Kangaroo Island samples had substantial feldspathic contamination; either in terms of the IR depletion ratio or significant IR decay curves.

Recuperation

Recuperation is the transfer of charge from relatively light insensitive deep traps (refuge traps), to OSL traps, that occurs as a result of irradiation, optical stimulation, and preheating (Aitken, 1998; Wintle and Murray, 2006). Electrons that were stored in OSL traps at the beginning of an optical stimulation are evicted; a portion of these move into refuge traps for the duration of the stimulation. Later, preheating thermally transfers some of these electrons in the refuge traps back into the OSL traps (Aitken, 1998). For recuperation to have a deleterious effect then, the refuge traps need to have accumulated an appreciable charge at the termination of stimulation; therefore, they need to be relatively light insensitive in comparison to the OSL traps. They also need to be of sufficient depth that thermal leakage is minimal during optical stimulation; yet not so deep that thermal transfer to the OSL traps is insignificant (Aitken, 1998).

If this process is happening, then, when the zero dose is measured in the SAR protocol, the signal will be greater than zero. High recuperation can cause overestimation in the regenerative dose signals which will lead to

underestimation of the equivalent dose (Murray and Wintle, 2000; Ward *et al.*, 2003; Wintle and Murray, 2006). Recuperation in an aliquot is expressed either as the zero dose (sensitivity corrected signal) percentage of the natural signal; or as a percentage of the D_e . It is recommended that this value should not exceed 5% (Wintle and Murray, 2006).

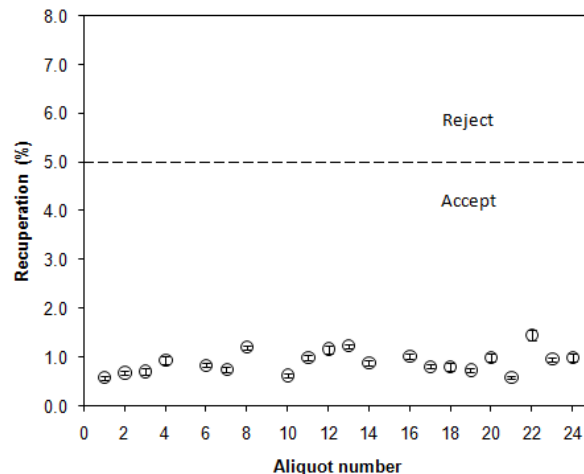


Figure 4.9: A recuperation plot for Kangaroo Island sample PB#2-18. The dashed line represents a 5% recuperation threshold. A second axis could also be included if one desired to compare the recuperation value with the D_e . 1σ error bars are within the data point.

These percentage values can be plotted vs. aliquot number to make a visual assessment of the level of recuperation across all aliquots (Figure 4.9).

Recuperation was not a significant contributor to aliquot rejection for the Kangaroo Island samples; a modern dune sample (PB#2b-8) was the only sample that experienced a high level of recuperation. This will be discussed in the section pertaining to this sample in chapter 7.

4.3.4.3 Experimental

Before proceeding with an OSL dating run (and implementing the rejection criteria: section 4.3.4.1) two very important things need to be ascertained with regards to the behaviour of the OSL sample:

- i) The ideal preheat (PH) and cutheat (CH) temperatures for the sample (or range of samples) need to be established.
- ii) The protocol (using the established PH/CH combination) must be able to recover a given laboratory dose to within experimental error.

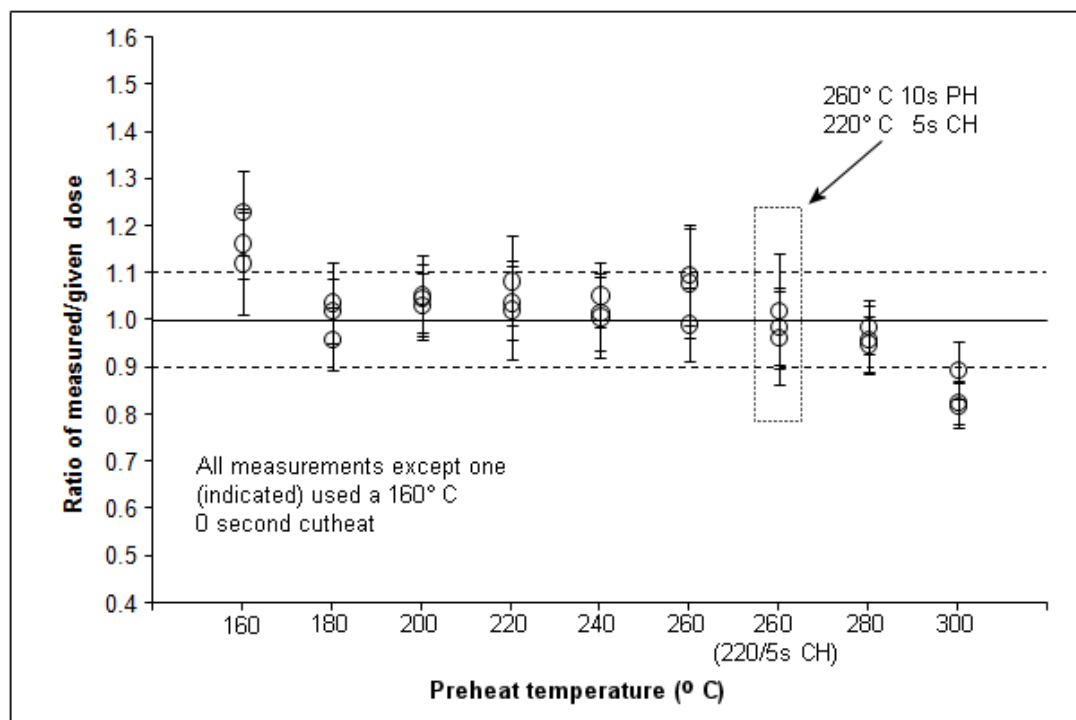


Figure 4.10: Preheat plateau test for Kangaroo Island sample Bales#2-9. The ratios are relatively stable (1σ errors overlap unity) from 180 °C to 280 °C; it is likely that any PH within this range would yield reasonable results in a SAR dating run. Although, the 260 °C/10 sec PH 220 °C/5 sec CH was the PH/CH combination of choice—for reasons discussed in the text. The wide range of stable ratios indicates that this sample is relatively insensitive to variation in PH. The aliquots used in this test were sunlight bleached for 24 hours, and then given a laboratory dose of 50 Gy; 3 x 1 mm mask aliquots were run for each PH. The solid line represents unity, and the dashed lines border a 10% envelope around unity.

The accepted method of detecting the ‘best’, as it were, PH to derive equivalent doses in a given sample is to carry out a ‘preheat plateau’ (PHP) test. This test can be undertaken in several ways. A common version of the PHP test involves analysing unbleached sample aliquots using the SAR protocol at varying PHs (keeping a common CH—usually at 160 °C for 0 sec): from 160 to 300 °C in 20 °C increments; with 3 or more aliquots for each PH (Wintle, 1997; Murray *et al.*, 1997; Aitken, 1998). This test will reveal (ideally) a range of PHs where the aliquot D_e s stabilise (plateau). Thus, one is given a choice of PHs to use. Another method is to employ (rather than unbleached sample aliquots) sunlight or laboratory bleached aliquots; give them a laboratory dose, and vary the PHs as above. A PHP plot can be constructed on the basis of the given dose to recovered dose ratio versus the PH temperature (Figure 4.10). This offers some improvement over the first method as the dose is not an unknown, and if the PH temperature for the sample is effective this will manifest as a ratio at or close to unity. Hence, for this version of the PHP test an actual ‘plateau’ is not essential.

In the first method, if the PH was specific, then it would be difficult to establish the 'correct' PH, since the plateau region would be uncertain. Furthermore, the second method essentially removes variability in the aliquot due to, for example, partial bleaching, or grain mixing, and focuses on variation that occurs as a consequence of PH temperature, as the aliquots are 'zeroed' during the sunlight or laboratory bleach. In the first method (which uses the equivalent dose); however, partial bleaching or grain mixing are very much part of the equation.

A more complete version of the dose ratio PHP test is to not only vary the PH but also the CH; in this way a more comprehensive range of responses to heating can be examined. Although, this is a sample and time consumptive method requiring that large numbers of aliquots are used for the test (depending upon the range of CHs explored). For reasons of time, and instrument availability, this comprehensive test was not run; however, it was adapted down to a more economical version.

Preheat plateau tests were not performed on all Kangaroo Island samples; they were only undertaken on one sample: Bales#2-9, a representative aeolian dune sample (this was also an abundant sample so it was chosen for much of other the OSL experimental work in this thesis). The decision to use results from the one sample to determine PHs and CHs for the global SAR protocol was predominantly based upon instrument time. Hence, it was assumed that the responses of Bales#2-9 would reflect all other samples; this also leads to the additional assumption that the quartz in all of the Kangaroo Island samples was derived from the same regional source.

The dose ratio PHP test was used on sunlight bleached aliquots of Bales#2-9 with a range of PHs from 160-300 °C employing a 160/0 sec CH (three 1 mm mask aliquots per PH), excepting that an additional 260 PH was run with a 220 CH (really a short PH: held for 5 sec to stabilise the temperature) (Figure XX). Prior to analysis the aliquots were given a 50 Gy laboratory dose. The reasons for running additional 260 °C PH aliquots with the 220 °C CH relates to the discussions in Murray and Wintle (2003), and Wintle and Murray (2006). Certain samples may be problematic due to the presence of shallow, less thermally stable OSL traps where thermal transfer at ambient temperatures could occur;

or the presence of an ultra-fast component in the luminescence signal. In these instances the traditional 160 °C/0 sec CH may be inappropriate; however, a higher cutheat temperature may reduce problematic behaviour (Jacobs *et al.*, 2006; Wintle and Murray, 2006). Typically a 260 °C PH, 220 °C CH (or PH) combination (first suggested by Bailey (2000)) has been used to mitigate behavioural problems associated with heating (Ward *et al.*, 2003; Jacobs *et al.*, 2006). Jacobs *et al.* (2006) for example, showed that the 260/220 PH/CH combination was ideal for problematic samples.

Figure 4.10 clearly shows that for sample Bales#2-9 the dose recovery ratio is relatively stable from 160 to 280 °C. This sample would in all probability behave well at any PH temperature in this range. However, to account for possible behavioural problems, as described above, the 260 °C, 220 °C PH/CH combination was utilized in the SAR protocol that was applied to further samples (Figure 4.11).

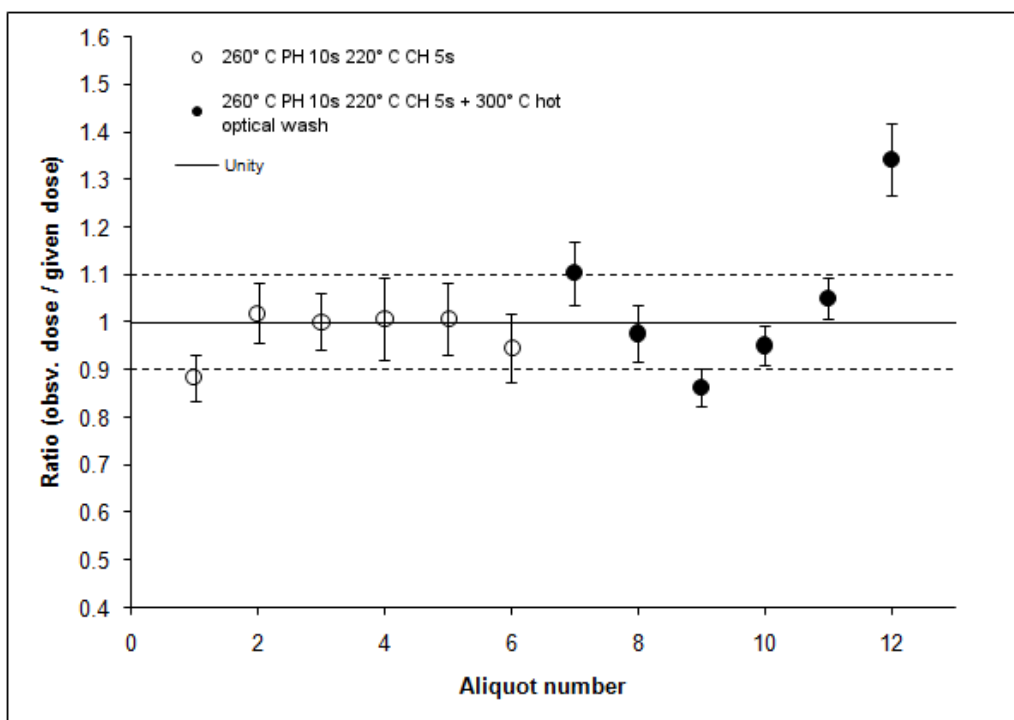


Figure 4.12: Dose recovery test (50 Gy) for Bales#2-9; using the 260/220 °C PH/CH combination for 6 aliquots (open circles), and the additional 300° C optical stimulation for the other 6 aliquots (filled circles). All aliquots were 1 mm mask size, using the 90-125 μ m quartz fractions. With the exception of one aliquot the 260/220 C PH/CH combination worked well. The hot optical wash aliquots showed reasonable recovery of the given dose too; however, there is clearly more scatter in the data.

Before proceeding into implementation of the modified protocol, it was first tested again by running a larger number of aliquots: here 12 sunlight bleached aliquots were analysed using 1 mm mask sizes after being given a 50 Gy laboratory dose (Figure 4.12). Six of the aliquots were subject to the 260/220° C PH/CH; the other 6, whilst also using this combination, had an additional modification applied to the end of each regenerative cycle: a 40 sec 300 °C optical stimulation. This step was suggested by Murray and Wintle (2003) as a method of reducing the effect of recuperation (section 4.3.4.1.4 of this chapter); the aim being to thermally induce and optically remove any accumulated charge from the main OSL traps that was derived from optically insensitive traps during preheat. Experimentally the additional step introduced more scatter into the Bales#2-9 data (Figure 4.12), and hence, was not used in the final global, modified, SAR protocol.

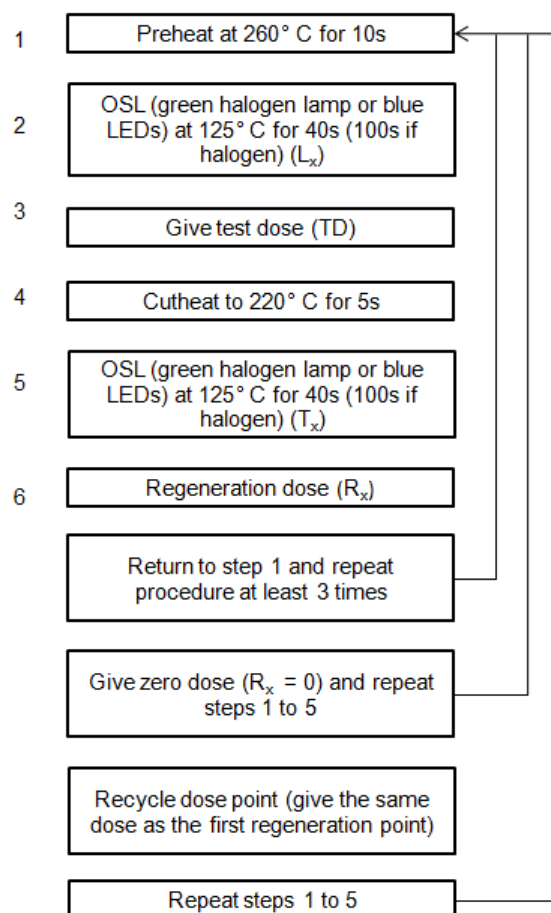


Figure 4.11: Final modified SAR protocol used to determine the equivalent doses for the conventional OSL samples from Kangaroo Island.

4.4.5 Thermoluminescence dating methods

Three samples (2 carbonate aeolianite and 1 shelly sand sample) were submitted to the University of Wollongong's commercial TL dating laboratory (Table 4.1). The two aeolianite samples were from Pennington Bay and Emu Bay, and the shelly sand sample was taken from Hanson Bay (Figure 4.1). The preparation and dating work was undertaken by D. Price. The analysis methods will be outlined briefly here, and the results will be presented in Chapter 8.

The TL samples were prepared under subdued yellow light. Detailed descriptions of laboratory procedures and sample analysis techniques used for the Kangaroo Island samples can be found in Shepherd and Price (1990), Nanson *et al.* (1991), Price *et al.* (1999), and Murray-Wallace *et al.* (2002). However, in brief, the University of Wollongong TL laboratory determines a palaeodose for each extracted quartz sample based upon a modified version of the regenerative additive dose technique developed by Readhead (1984; 1988). An Appropriate analysis temperature for each sample is determined by observing the relationship between a natural (N) glow curve and a laboratory irradiated curve.

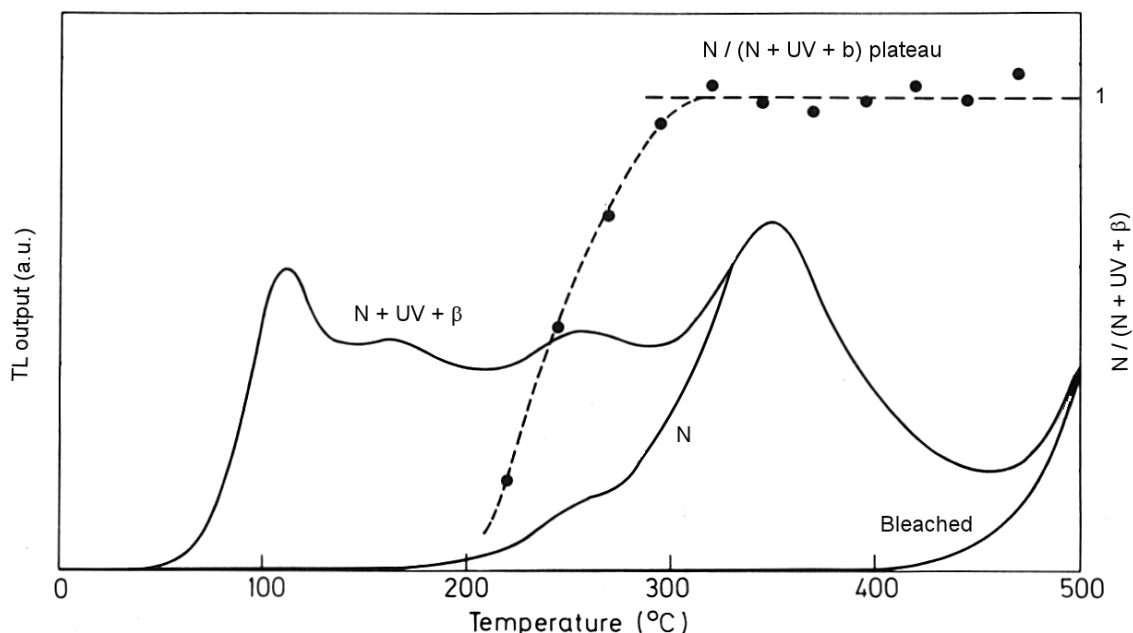


Figure 4.13: The $N / (N + UV + \beta)$ plateau. Also displayed are the N, the dose $N + UV + \beta$, and bleached glow curves (modified from Aitken, 1985). The plateau represents the temperatures where the N TL can be compared to $N + UV + \beta$ TL.

The ratio of natural/artificial TL is plotted and shows a plateau when all lower temperature unstable traps have been emptied of electrons. The plateau region identifies peak temperatures where trap lifetime is sufficient to exceed the burial period (Figure 4.13). In the case of the Kangaroo Island samples the most appropriate analysis temperature was 375 °C.

Once the analysis temperature was established a D_e is interpolated by plotting the normalised (using a second glow procedure) TL output of a series of 8 (N) aliquots (90-125 μm quartz) onto a dose response curve constructed of 24 laboratory bleached (24hr under a Philips MLU300W UV lamp) aliquots given a series of regenerative doses ($N + \text{UV} + \beta$) using a ^{90}Sr plaque β source. The appropriateness of the D_e is checked through the use of the additive dose method ($N + \beta$). The combination of the two techniques (regenerative and additive) provides an assessment of sensitivity change that can occur as a result of laboratory procedures. The mean natural TL output is fitted to the regenerative dose curve; then the $N + \beta$ data is plotted with respect to this value. If the two plots coincide then sensitivity change is not an issue (Murray-Wallace *et al.*, 2002).

During analysis samples were heated at 5 °C/s in high purity N_2 and TL output was measured using an EMI 9635QB photomultiplier tube coupled with a Corning 7-57 blue filter. Annual radiation dose was determined by a combination of TSAC (U and Th), and AES (%K), for beta and gamma contributions. Final dose rates also included a cosmic component, and corrections for sample water content.

4.4.6 AMS ^{14}C dating methods

AMS ^{14}C was used to estimate the age of two marine bivalves (*Katelysia scalarina* [Lamarck] 1818 and *Katelysia rhytiphora* [Lamy] 1937) recovered from American River (Figure 4.1). The analyses were performed commercially at Waikato Dating Laboratory, University of Waikato, New Zealand. The core strategy for dating these shells was to provide a Holocene calibration point for amino acid data; however, through ^{14}C the middle to late Holocene age of the coquina (marine shell hash) that the shells were removed from was also established. One half of each shell was submitted for AMS ^{14}C ; the

corresponding other halves were analysed for amino acid enantiomers at the University of Wollongong AAR geochronology laboratory.

The analysis methods and background are described briefly below. More detailed explanations of AMS ^{14}C and ^{14}C methodology and applications can be found in Berger *et al.* (1964), Gillespie *et al.* (1984), Ajie *et al.* (1990), Aitken (1990), Bard *et al.* (1993), Finkel and Suter (1993), Taylor and Aitken (1997), Gove (1998), Tuniz *et al.* (1998) and Noller *et al.* (2000).

There are three naturally occurring isotopes of carbon. The most abundant are the two stable isotopes ^{12}C (98.89%) and ^{13}C (1.11%); the third, ^{14}C , has an abundance of less than $10^{-10}\%$. Carbon 14 is unstable and undergoes β decay to ^{14}N . It has a half life of 5730 years, and only exists because it is continually produced by the interaction of cosmic radiation with the upper atmosphere (Trumbore, 2000). The ^{14}C is rapidly oxidised to ^{14}CO and eventually to $^{14}\text{CO}_2$. Because of the rapid cycling of carbon between the atmosphere and biosphere ^{14}C is incorporated into the tissues of living plants and animals, and is maintained at a relatively constant level of activity; almost equal to that of the atmosphere (Trumbore, 2000). After the death of the organism, the ^{14}C is no longer replenished through the carbon cycle and it decays to ^{14}N . If the organic material remains protected from any further exchange with the environment, the decrease in ^{14}C content through decay, when compared to living organisms (expressed as the ratio of ^{14}C to ^{12}C), can be used to estimate the time since death. This is the basis of the ^{14}C dating method (Trumbore, 2000).

AMS ^{14}C dating allows the direct measurement of the ^{14}C atoms; this means that much smaller sample masses can be analysed. Samples massing around 1 mg of carbon are routinely analysed, and smaller amounts of 100-200 μg in certain circumstances can also be analysed.

In the case of shell samples isotopic carbon is recovered in the form of CO_2 by reaction with phosphoric acid. This then reduced to graphite by heating with zinc (Zn) at 600 $^{\circ}\text{C}$ in the presence of an iron (Fe) catalyst. The pressed graphite pellet is then analysed in an AMS. The AMS analyses for the graphite pellets recovered from the American River bivalves were undertaken at the Keck Radiocarbon Dating Laboratory at the University of California, Irvine. A full

explanation of the theory and operation of AMS systems can be found in Finkel and Suter (1993).

Corrections need to be made to ^{14}C activity. Isotopic fractionation will cause the $^{14}\text{C}/^{12}\text{C}$ ratios of organic carbon and CO_2 , in the atmosphere, to differ. This can be corrected by measuring the magnitude of the effect this fractionation has on ^{13}C content, and assuming that the fractionation will be doubled in ^{14}C (Trumbore, 2000). There is also the problem that ^{14}C content in the atmosphere has changed over time. The variation is because of changes in cosmic radiation flux and the distribution of carbon throughout the various reservoirs, e.g. the biosphere, ocean, and atmosphere. These variations have been deduced by the study of annual tree ring growths. Corrections for the variation are based upon the observed ^{14}C content of independently dated tree ring cellulose, macrofossils from lake sediments, and coral terraces. These corrections yield 'calibrated' ^{14}C ages (Trumbore, 2000).

Dating marine shell presents a further complication. The carbon content in marine shell is predominantly inorganic in nature, being derived from carbonate (CO_3^{2-}) anions in ocean waters. There is an observed difference between the ^{14}C concentration of the atmosphere and the oceans; this is because of a delay in the exchange rates, and the mixing of near surface waters with older deeper waters derived from upwelling (Mangerud, 1972). In comparing ^{14}C ages for coeval terrestrial and marine samples the difference can be in the order of 400 years (Stuiver and Braziunas, 1993); although, it may differ significantly from this regionally. The apparent difference in age is called the marine reservoir effect. The magnitude of the effect is expressed as a regional offset value (ΔR) (Stuiver *et al.*, 1986) which reflects the difference to the global model for ^{14}C activity.

There are several software packages available to calibrate ^{14}C ages, and global databases for obtaining marine reservoir offsets, for example, Reimer and Reimer (2001). For the American River bivalves age calibrations were established using OxCal v3.10 (Bronk Ramsey, 2005), and correction for reservoir effect was undertaken with marine data from Hughen *et al.* (2004), using a ΔR value of 62 ± 63 .

4.4.7 U-series dating methods

A scleractinian ‘stony’ coral (*Plesiastrea versipora*: [Lamarck] 1816) recovered from an elevated shelly, cemented, carbonate matrix (see Chapter 3, section 3.4.4.3) infilling a series of collapsed aeolianite blocks at Vivonne Bay, Kangaroo Island (Figure 4.1 and Table 4.1), was dated by ^{238}U - ^{230}Th series disequilibrium, via MC-ICPMS. This coral was an important find as the upper margins of the matrix cement it was recovered from are a good proxy indicator of sea-level. The age on the coral was also used as a calibration point for the molluscan and foraminifer AAR data (Chapter 8).

The sample preparation and analyses were undertaken at the Research School of Earth Sciences, Australian National University, by Dr. G. Mortimer. Preparation and sample analysis methods can be found in McCulloch and Mortimer (2008). Uranium series dating background is discussed briefly below.

If ^{238}U , in a closed system, remains undisturbed for millions of years a state of secular equilibrium arises between the parent ^{238}U and its daughter nuclides in the decay series (e.g. in the case of the radionuclides of interest: the activity concentrations of $^{238}\text{U} = ^{234}\text{U} = ^{230}\text{Th}$). However, there are processes (nuclear and chemical—solutional) that can disrupt this equilibrium by separating members of the decay series; this can happen through partial melting, weathering, transport, and deposition (Ku, 2000).

For example when an organism, such as a coral polyp, precipitates aragonite from an aqueous solution that contains, among other ions and anions, uranyl ($[\text{UO}_2]^{2+}$, a product of the relatively low ionic potential of uranium and an oxidising environment, e.g. natural waters), some uranium is incorporated into the matrix. Conversely, thorium is relatively insoluble because of its high ionic potential (Th^{+4}); however, even if some Th is ionized in solution, it is quickly precipitated out. Therefore the precipitated aragonite crystal will contain some U but effectively no Th. From time zero ^{238}U is decaying; therefore, if over time the coral calcite remains as a closed system, with respect to isotopes of U and Th, the extent of daughter ingrowth, in this case ^{230}Th , can be used to calculate the age (Ku, 2000). What is being dated here is the time since precipitation of the aragonite.

Two important assumptions are made with respect to this method:

- i) At $t = 0$ there is no Th, and:
- ii) The system remains closed in deference to the isotopes of interest.

Corals are particularly good for dating purposes because of the very low Th/U ratios found in oceanic waters; in this case the first assumption can be held in confidence. It is somewhat different in terrestrial settings, where many deposits are not free of Th, and contain initial ^{230}Th derived from allochthonous sources. This effectively negates the first assumption.

For the purposes of dating coral, with regard to the second assumption, it is important that the primary aragonite has not undergone re-crystallisation. If it has then the second assumption is not valid, and the coral may have been leached of, or contaminated by, isotopes of interest.

4.5 Summary

The preceding sections have outlined the various methods used to determine dose rates for luminescence sample dating. Described were the methods of TSAC, GMBC, INAA, FSG, and HRGS, used to determine gamma and beta dose rates. The optically stimulated luminescence (OSL) method was examined in detail, describing the sampling strategies, preparation methods, and types of instruments used to determine an equivalent dose. Also examined in brief were the dating methods of U-series, ^{14}C , and thermoluminescence, as these methods were used infrequently.

The next chapter (Chapter 5) details a relatively new long-range method of luminescence dating, called thermally transferred OSL, or TT-OSL. A new dating protocol (SARTT-OSL), based upon this method, was created in this thesis, in order to estimate ages of aeolian quartz samples extracted from Kangaroo Island aeolianites (that were beyond the range of conventional OSL dating).

Chapter 5: Thermally transferred optically stimulated luminescence (TTOSL) dating: development and testing of a single aliquot regenerative dose (SAR) protocol

5.1 Introduction

This Chapter will describe the development and testing of a single aliquot (SAR) version of the multiple aliquot (MAR) TTOSL protocol developed by Wang *et al.* (2006a). The testing involves the comparison of known age samples with ages determined through the application of the single aliquot, regenerative dose, thermally transferred (termed SARTT) OSL method developed in this thesis. The initial testing of this SARTT-OSL protocol was presented at the 1st Asia Pacific Conference on Luminescence Dating, at Hong Kong University, during October of 2006.

5.2 Single aliquot thermally transferred OSL (SARTT-OSL) dating

Luminescence dating work on quartz from the Pleistocene aeolian sediments on Kangaroo Island is hampered by the age range limitations of conventional OSL. The conventional OSL D_0 (dose at break of slope, from equation 5.3, Chapter 5) for many of the Kangaroo Island samples is around 25 Gy, and some of these samples experience saturation (saturation of luminescence centres: Chapter 5, section 5.3.4.2) in the region of 100-120 Gy. Environmental dose rates for the Kangaroo Island samples range between 0.182 and 1.644 Gy/ka⁻¹, in the extreme. The average dose rate across all sites is 0.716 Gy/ka⁻¹, so broadly speaking the upper age range using conventional OSL is in the order of 175 ka—of course it may be higher or lower at the individual level. Bearing this in mind, many of the Pleistocene aeolianite successions of Kangaroo Island are significantly older than 175 ka; this is based on independent geological and palaeontological evidence (Ludbrook, 1983; Milnes *et al.*, 1983). The multiple aliquot (MAR) TTOSL protocol, developed by Wang *et al.* (2006a), allows for a dramatic extension of the OSL dating range.

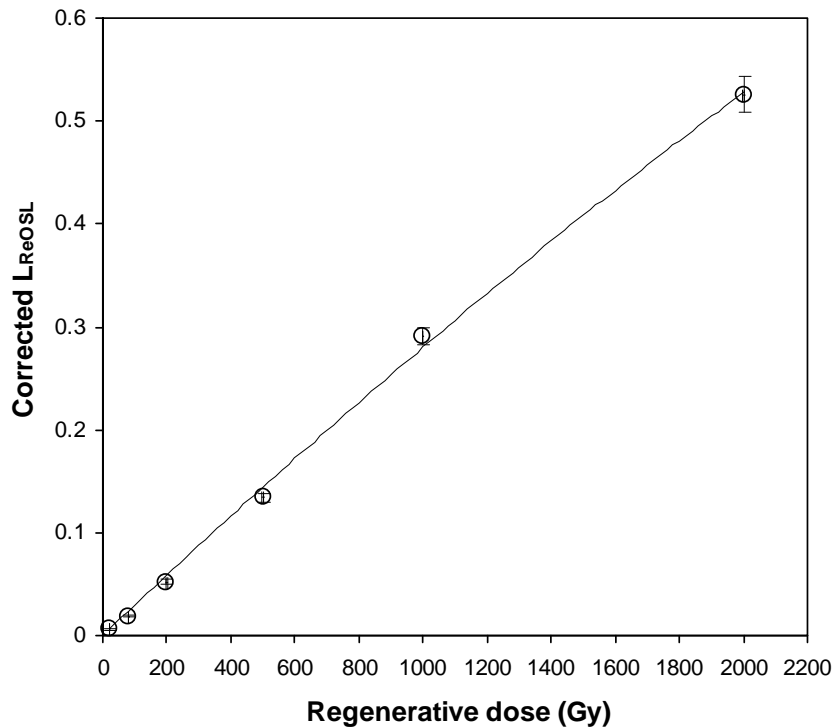


Figure 5.1: SARTT-OSL dose response curve constructed to demonstrate high growth well beyond the conventional OSL range. Kangaroo Island sample Bales#2-9 was used in the experiment. This was a sunlight bleached aliquot (24 hr); the regenerative doses were 20, 80, 200, 500, 1000 and 2000 Gy. A 2 Gy test dose was used (later versions of the protocol used a 0.25 Gy test dose, in order to reduce signal build-up).

This new procedure, according to Wang *et al.* (2006a), accesses a recuperated OSL signal that grows with dose well beyond the region where the conventional OSL signal begins to saturate. The original work of Aitken (1998) on ambient temperature thermal transfer states that this is a signal made up of two parts: recuperated or thermally transferred OSL (TTOSL) and basic transfer OSL (BTOSL). Wang *et al.* (2006a) adopted this viewpoint and put forward a MAR TTOSL protocol to extract these signal components.

Many aliquots of the samples examined in this Chapter, using the SARTT-OSL protocol, have a TTOSL D_0 in the order of 1600 Gy. In light of this, using the SARTT-OSL modification, it may be possible to realize an optical dating range for Kangaroo Island that extends back to Pliocene time. Figure 5.1 illustrates a dose response curve constructed using the SARTT-OSL method developed in this thesis. The highest regenerative dose point is 2000 Gy; it is apparent from the shape of the curve that much greater regenerative doses would be possible.

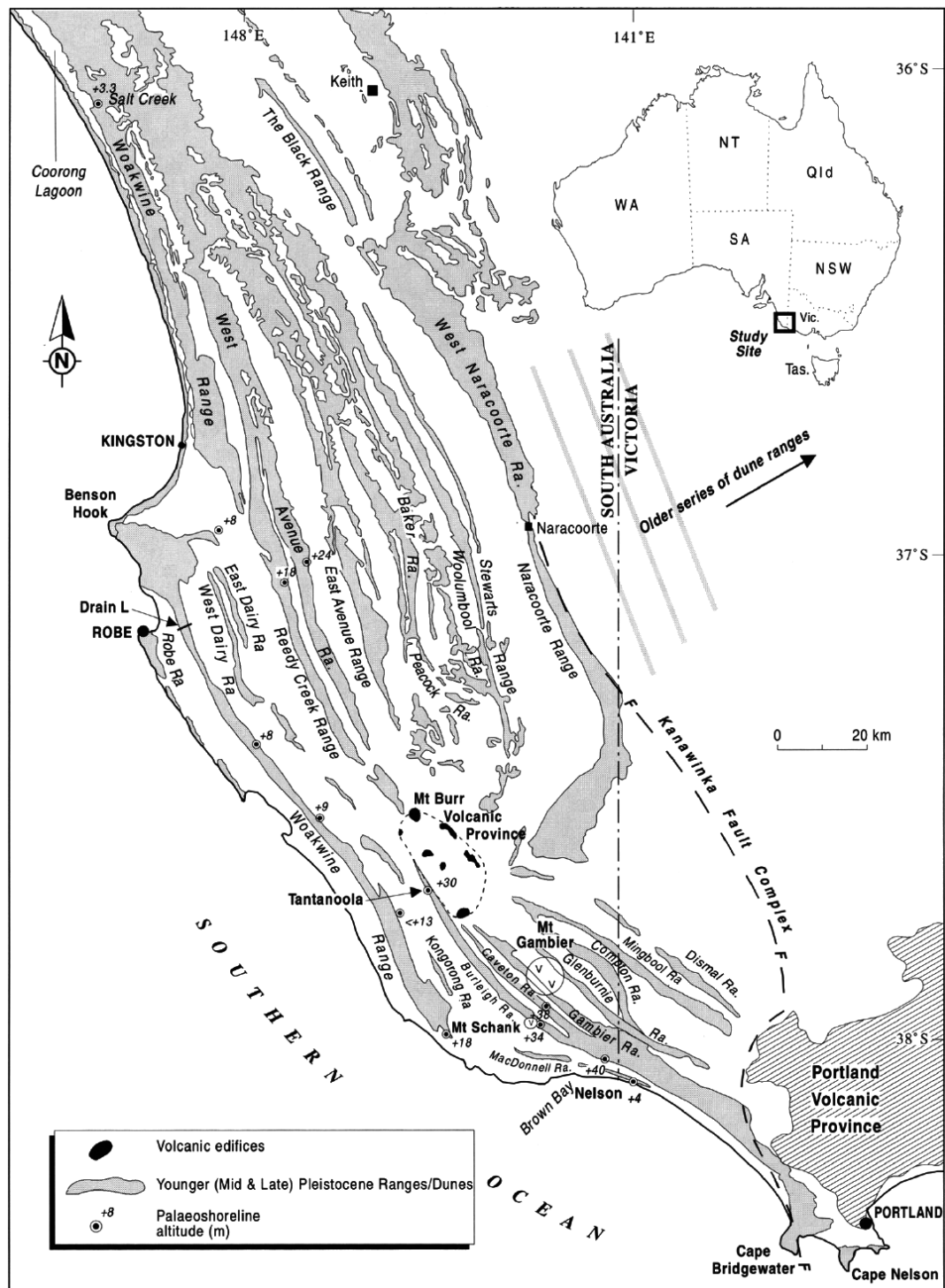


Figure 5.2: The Coorong to Mount Gambier coastal plain showing the location of various Pleistocene coastal barriers. Note the West Naracoorte dune range (from Murray-Wallace *et al.*, 1998).

Hence, there is potential to date suitable material of great antiquity (possibly >1 Ma, provided there is secure dosimetry). The following sections describe the steps that were undertaken in an attempt to date Kangaroo Island aeolianite sediments that were beyond the range of the conventional OSL dating method. It primarily describes the method developed for a SAR version of the Wang *et al.* (2006a) MAR protocol.

5.3 Conventional luminescence dating background: samples of great antiquity from South Australia, and the choice of a long range luminescence dating method

The south-eastern coast of South Australia has a preserved sequence of carbonate aeolian dunes that have recorded variations in sea-level for at least the past 800,000 years (Huntley *et al.*, 1993; Murray-Wallace *et al.*, 1998) (Figure 5.2). Quartz fractions of sediments taken from this sequence of dunes were extensively dated by thermoluminescence (TL) using the 325° C TL peak (Huntley *et al.*, 1993, 1994; Huntley and Prescott, 2001). Several TL ages were estimated in the course of the three studies mentioned above that enabled a succession of sea-level highstands to be determined. The dunes become older moving inland and TL ages range from 95 ± 6 ka near Policeman's Point and Salt Creek (Figure 5.2); bordering the Coorong coastal plain, to 800 ± 100 ka on a sample taken from the West Naracoorte range (approximately 60 km NE of the coast, Figure 5.2), although Huntley *et al.* (1994) were concerned about this age.

Banerjee *et al.* (2003) revisited these sites using conventional SAR OSL with the aim of testing the accuracy of this procedure over an extended age range. This study produced a series of OSL ages that were generally consistent with the TL chronologies of Huntley *et al.* (1993, 1994), and Huntley and Prescott (2001). Again samples from the West Naracoorte range were the oldest materials dated. Based upon the assumption of Huntley and Prescott (2001) that the top dune was deposited during the Matuyama reversed epoch (even though it shows normal magnetization; however, the post-depositional chemical process of magnetization takes place on a 10^4 to 10^5 year time scale), it is

expected to have a depositional age somewhere between 780 and 880 ka. Banerjee *et al.* (2003) obtained a post-IR OSL age of 710 ± 62 ka for this site, which was within 2σ of the expected age.

Samples taken from sites in south-eastern South Australia are generally characterised by low environmental dose rates, with most being in the order of $0.4\text{-}0.6 \text{ Gy/ka}^{-1}$ (Huntley *et al.*, 1993, 1994; Huntley and Prescott, 2001; Banerjee *et al.*, 2003). This means comparatively large time spans can be dealt with using luminescence dating methods provided the luminescence signal is saturating at a high level. For example the West Naracoorte samples have an estimated equivalent dose (D_e) of 327 ± 30 Gy determined by Huntley *et al.* (1994) using TL, and 302 ± 21 Gy as determined by Banerjee *et al.* (2003) using OSL. It should be noted that these equivalent doses represent values close to the upper limits for these samples and their respective methods.

Since luminescence age is determined by equation 4.1 (section 4.3, Chapter 4), the combination of low dose rate and high saturation is essential for the long-range luminescence dating of quartz.

Kangaroo Island is in the same geographical region as the studies above, and the samples used in this study are taken from comparable aeolian sediments, and although dose rates are similarly low, the saturation characteristics of the Kangaroo Island samples are apparently different to those from the south-east South Australia dune sequence. If we look at the Banerjee *et al.* (2003) study for example, saturation was much higher. Using the conventional OSL method the Kangaroo Island samples exhibit, in many cases, response curves that saturate at around 100-120 Gy. In combination with low dose rates the age range is still very good; nevertheless, as mentioned above many areas on Kangaroo Island comprise aeolian sediments that are in all probability much older than the limit imposed by this luminescence behaviour.

The challenge then, for this thesis, was to apply a geochronological method that could circumvent the saturation 'barrier'. In the course of the investigation alternative luminescence methods to conventional OSL were considered. Initially TL using the 375 °C peak was experimented with, because of its high

saturation characteristics. However, due to efficiency concerns this approach was not continued. Bailey (2004) and Bailey *et al.* (2005) proposed a modified SAR method which incorporated pulsed delivery of the regenerative dose. It is suggested in Bailey (2004) that the shape of the dose response curve is affected by the filling state of non-radiative recombination centres. Some of these centres are thermally unstable and would remain relatively empty during

Table 5.1: The Wang *et al.* (2006a) MAR TTOSL protocol.

STEP	TREATMENT	RESULT	NOTES
<i>Part 1. Detection of thermally-transferred OSL signals</i>			
1-1	Dose, D_i		For natural $D_i = 0$
1-2	Preheating at 260° C for 10s		Removing electrons in unstable TL traps
1-3	Blue LED at 125° C for 270s		Bleaching OSL signals
1-4	Preheating at 260° C for 10s		Thermally inducing TT-OSL signals
1-5	Blue LED at 125° C for 90s	L_{TTOSL}	Detecting TT-OSL signals
1-6	Give test dose, D_t		Monitoring OSL production
1-7	Preheating at 220° C for 20s		Removing electrons in unstable TL traps
1-8	Blue LED at 125° C for 90s	T_{TTOSL}	Test dose response
<i>Part 2. Detection of basic-transferred OSL signal</i>			
2-1	Annealing to 300° C for 10s		Thermally inducing remnant recuperated OSL signals
2-2	Blue LED at 125° C for 90s		Removing recuperated OSL signals
2-3	Preheating at 260° C for 10s		Thermally inducing basic-transferred OSL signals
2-4	Blue LED at 125° C for 90s	L_{BTOSL}	Measuring basic-transferred OSL signals
2-5	Give test dose, D_t		Monitoring OSL production
2-6	Preheating at 220° C for 20s		Removing electrons in unstable TL traps
2-7	Blue LED at 125° C for 90s	T_{BTOSL}	Test dose response

burial; however, they would be filled and saturated during laboratory irradiation. It is suggested that this competition for charge affects the dose response causing D_e overestimation by around 10%, particularly for equivalent doses between 40 and 100 Gy (Bailey, 2004; Bailey *et al.* 2005; Wintle and Murray, 2006). Simply delivering the regenerative dose at elevated temperature would serve to keep these unstable centres empty, but this would also alter electron trapping probability, which would no longer be the same as it was during environmental irradiation (Wintle and Murray, 2006). This problem could be solved by delivering the regenerative dose in pulses interspersed with a preheat to empty the unstable centres. The models proposed by Bailey (2004) and Bailey *et al.* (2005) indicate that a 10 Gy pulse with an intervening preheat to 240° C would be adequate for most samples. Delivering the regenerative doses in such a way reduces charge competition which changes the dose response

lifting the response curve. This means the natural signal intercepts on a higher angled slope giving a significantly lower D_e value for the aliquot compared with to that derived from a non-pulsed curve. The curve deviation only becomes significant when regeneration doses exceeding 20 Gy are delivered, and is effective for equivalent doses over 30 Gy (Bailey *et al.*, 2005). This method subsequently should have the capability to increase the apparent saturation level of a sample. Nonetheless, for the Kangaroo Island samples that were considered to be beyond the conventional OSL range this method would still not be applicable.

The Wang *et al.* (2006a) MAR TTOSL method was also investigated, and became the method of choice owing to the order of magnitude (possibly greater) difference in saturation when compared to conventional OSL. It was decided to apply an adaptation of this method to Kangaroo Island samples that were likely to be beyond the conventional OSL range.

5.4 The source of the thermally transferred OSL signal

When an irradiated aliquot of quartz is heated and subsequently exposed to light to remove the OSL signal; then heated and exposed to light again, a smaller signal arises: the recuperated OSL signal. It is assumed that this signal consists of electrons that have been transferred into relatively light-insensitive, less thermally stable refuge traps by exposure to light. The recuperation effect can be described thus (Wang *et al.*, 2006a; 2006b):

- i) When an aliquot of quartz is preheated and is then subject to optical stimulation as in step 1-3 of the Wang *et al.* (2006a) protocol (Table 5.1), the main OSL traps are emptied and a portion of these electrons become trapped in a refuge trap.
- ii) A further preheating, at 260° C for example, will thermally transfer these electrons into the conduction band and they become re-trapped in the main OSL trap.
- iii) These re-trapped electrons will give rise to the TTOSL signal upon subsequent optical stimulation as in step 1-5 of the protocol (Table 5.1).

This is a 'double transfer' mechanism, as electrons are optically transferred during stimulation, and thermally transferred during heating (Wang *et al.*, 2006b). This recuperated (TTOSL) signal is a dose dependent signal as it is associated with the electrons from the main OSL trap prior to the initial stimulation. These electrons have accumulated since the quartz was last exposed to sunlight, and consequently the recuperated signal should also be zeroed by exposure to light. This renders it suitable for dating appropriate sediments (Wang *et al.*, 2006a).

Conversely the basic transferred signal (BTOSL) is apparently derived from light-insensitive traps that have no potential mechanism for zeroing. These traps contain populations of electrons that were trapped before deposition, and they may even continue to accrue electrons after deposition; as such these traps are not suitable for use in dating. Any signal arising from these traps would be in addition that derived from the light-sensitive traps associated with recuperated OSL (Wang *et al.*, 2006a). The basic transfer signal is outlined here (Wang *et al.*, 2006a; 2006b; 2007):

- i) When an aliquot of quartz is preheated as described above, a very small portion of the electrons trapped in the light-insensitive traps will be moved into the conduction band, even though these traps are apparently more thermally stable than the main OSL traps. They become re-trapped in the main OSL traps as well.
- ii) The re-trapped electrons from the light-insensitive traps will give rise to a signal that is in addition to the recuperated signal. Thus, this portion must be excluded when dating sediment.

The BTOSL signal is isolated by part 2 of the Wang *et al.* (2006a) protocol (Table 5.1). After sensitivity correction is applied with the addition of a test dose (T_{TTOSL} and T_{BTOSL}) to both parts of the protocol the separation of the useful signal is performed using equation (5.1).

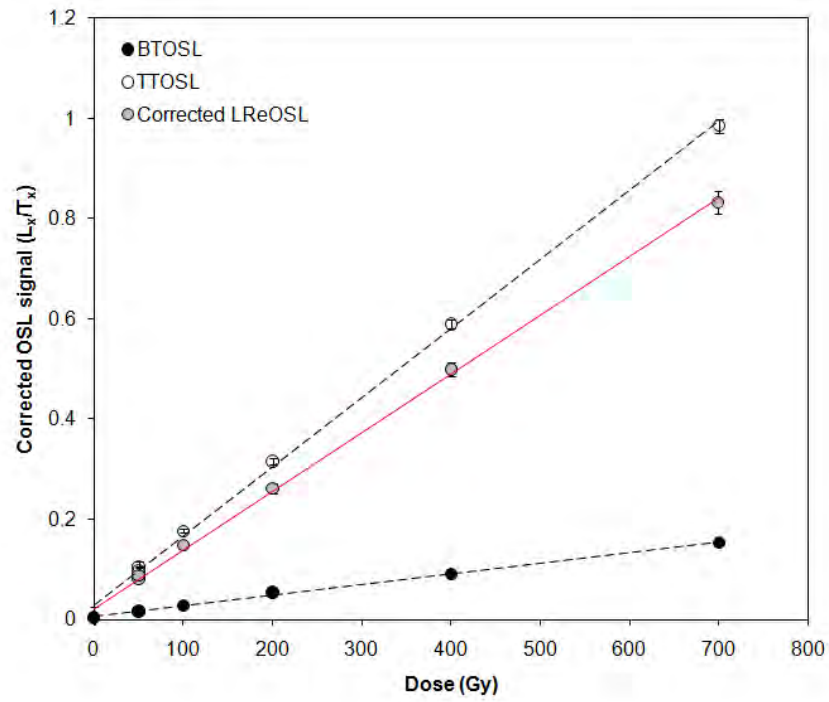


Figure 5.3: Displayed here for the purposes of illustrating equation 5.3 are the L_{TTOSL} , L_{BTOSL} and corrected L_{ReOSL} signals from an aliquot of Kangaroo Island sample PB#2-18. The TTOSL and BTOSL signals are test dose corrected (L_x/T_x). The L_{ReOSL} signals are derived from the subtraction.

The results are used to construct a response curve by plotting the corrected recuperated value against the regenerative dose (Wang *et al.*, 2006a; 2007); the ‘natural’ L_{ReOSL} intercept giving the R_eOSL D_e (Figure 5.3):

$$\text{Corrected } L_{ReOSL} = [L_{TTOSL}/T_{TTOSL}] - [L_{BTOSL}/T_{BTOSL}] \quad (5.1)$$

The ‘double transfer’ mechanism described here requires that the observed saturation in main OSL traps is due to saturation of the luminescence centres, and that the charge population continues to grow even after this. Wang *et al.* (2007) also propose a ‘single transfer’ mechanism for the recuperated signal, which is related to the Slow 3 (S3) OSL component (Jain *et al.*, 2003); however, they were unable to identify which is the more appropriate.

If the TTOSL signal is derived from the S3 component then this has implications for the range of sediment types that can be used with the method, limiting it only to quartz that has experienced long light exposure. This is discussed later.

5.5 Thermally transferred OSL dating

5.5.1 Accounting for inherent problems, and methods

The samples used to develop this modified protocol were derived from two sites along the southern coast of Kangaroo Island: Pennington Bay and Bales Beach—both are described in detail in chapter 4—and one sample taken from the south-east South Australia dune sequence: SESA 145. The 2 comparative samples (PB#2-18 and PB#2b-3) were taken from Late Pleistocene aeolianites dated successfully using conventional OSL in this study. The third comparative sample (SESA 145) is from a stranded aeolianite dune unit on the South Australian mainland, at West Naracoorte (Figure 5.2); this dune has been dated with varying levels of success by Huntley *et al.* (1994), Yoshida *et al.* (2000), and Banerjee *et al.* (2003). A fourth sample, KPB#5-1 was used in sunlight bleached and pre-annealed SARTT-OSL dose recovery experiments. This sample was chosen for its assumed high D_e , and possible great age (based upon morphostratigraphical position). A fifth sample, PB#2b-8 (a modern dune sample) was used in unbleached SARTT-OSL dose recovery experiments. This sample was chosen for SARTT-OSL experiments because of its very low equivalent dose (0.09 ± 0.01 Gy), as determined in previous conventional OSL analyses.

Much of the initial experimental work on the protocol modification was performed using Kangaroo Island samples Bales#2-9 and PB#2-18 (Bales#2-9 was depleted in the process unfortunately). Once the conditions for the protocol were established it was then used to estimate SARTT-OSL equivalent doses for three known D_e samples. The results derived from the application of the SARTT-OSL protocol to the other Kangaroo Island samples considered to be beyond conventional OSL are given in Chapter 7).

Sample preparation and instrumentation is the same as presented in section 4.3.4.1 of Chapter 4, and Appendix C, for conventional OSL. Analyses of the TTOSL results were made using Risø Analyst software and Microsoft Excel. The Risø Sequence Pro TTOSL sequences were configured in such a way that the resulting BIN files could be analysed using Risø Analyst software;

generating the test dose corrected values of L_{TTOSL} and L_{BTOSL} and associated errors. As iterated previously the BTOSL signal represents a light-insensitive portion of the two part signal (Wang *et al.*, 2006b). This portion must be subtracted from the thermally transferred signal in order to calculate recuperated OSL (corrected L_{ReOSL}). This was calculated using equation 5.1. The data were analysed in Microsoft Excel, the regenerative dose response curves were fit with exponential plus linear functions (Equation 4.3, Section 4.3.4.1, of Chapter 4), and uncertainties were estimated using a Monte Carlo simulation (Figure 5.4 shows an example SARTT-OSL dose response curve).

5.5.1.1 Signal accumulation

In order to test the robustness of the MAR TTOSL protocol the known age sample Bales#2-9 was run using this method. Table 5.2 compares the conventional OSL and MAR TTOSL equivalent doses; it can be seen that

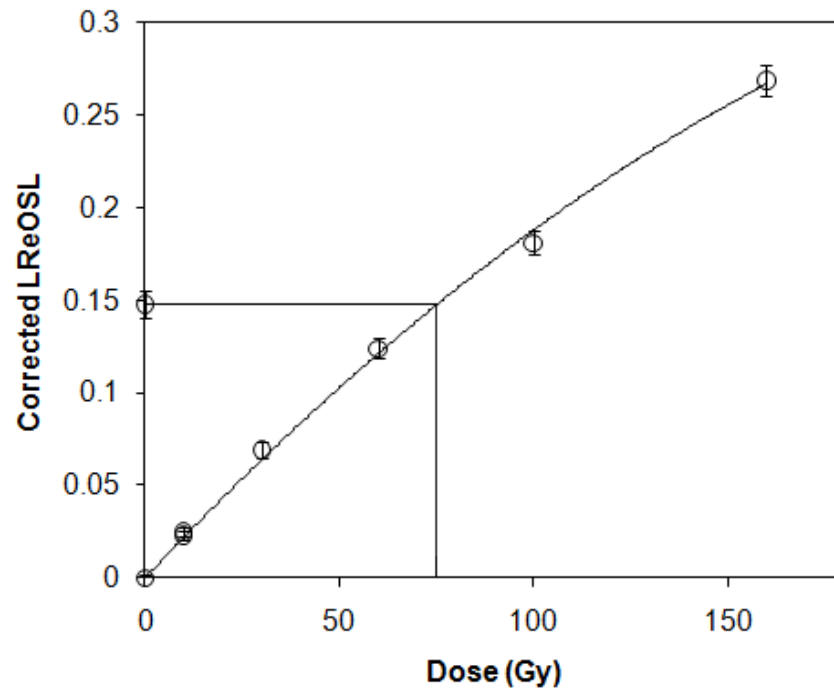


Fig. 5.4. A typical SARTT-OSL dose response curve from an aliquot (3mm mask) of sample PB#2-18. The aliquot was subjected to 7 cycles of the SARTT-OSL protocol, i.e. given 5 regenerative doses (10, 30, 60, 100, and 160 Gy), a zero dose, and a recycled dose (10 Gy). The recovered SARTT-OSL D_e for this aliquot was 76 ± 5 Gy. Note: preheat was 240 °C, test dose was 0.25 Gy, and the recycling ratio was 1.08.

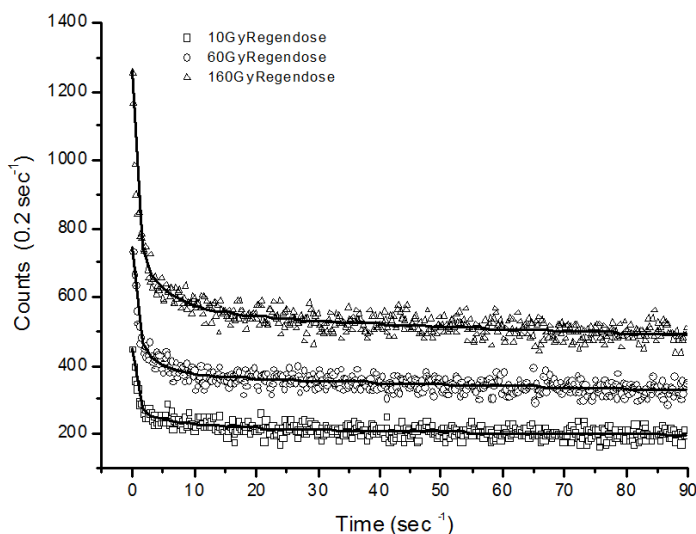


Figure 5.5. The dose dependent build-up of remnant recuperated signals that occur during each regenerative cycle (three decay curves from a typical aliquot of sample PB#2-18). Each curve was generated from an optical stimulation at 125 °C after preheating to 240 °C to thermally induce any remnant signals. This was performed after the part 2 test dose measurement of the initial SAR version of the Wang *et al.* (2006a) MAR protocol (only three regenerative doses are illustrated here. The 30 Gy and 100 Gy curves were left out to emphasize the signal build-up). The curves are fit with exponential decays. It should also be noted that the level of the build-up is, in all likelihood, reduced here because of the preheat and stimulation used to observe the signals; therefore, the level of remnant signal accumulation would of course be larger if unobserved.

there is reasonable agreement with conventional OSL at 2σ , even though MAR TTOSL does appear to overestimate the D_e . The MAR protocol, while surprisingly effective in this instance (considering the low D_e to be detected), was troublesome and time consuming to implement.

In a later study, Wang *et al.* (2007) proposed a single aliquot modification to their MAR protocol. This recuperated single aliquot method (ReSAR) was essentially the repetition of their MAR protocol on a single aliquot with a series of different regenerative doses and the addition of a repeat dose and a zero dose, as in conventional SAR. They used an empirical correction involving the zero dose to account for the problem of signal build-up (from the test dose in the second part of their protocol) that occurs over each successive regenerative cycle. The build-up occurs because the pre-heats and stimulations used in the second part of each cycle are not sufficient to release all of the trapped electrons related to the measured signal; therefore the portion of the signal not released will accumulate through a SAR protocol. This will affect the value of

each successive measured TTOSL signal. The experiments on signal accumulation in this thesis reflect this (Figure 5.5). Wang *et al.* (2007) also found that the effect was more pronounced when a larger test dose was used. The ReSAR protocol was tested on sample PB#2-18 using the same parameters of Wang *et al.* (2007); however, a small test dose was used (0.25 Gy) rather than a test dose that was 10% of the known dose (Wang *et al.*, 2007). This was done with the aim of reducing the magnitude of signal build. As evident in Figure 5.6 the ReSAR protocol significantly overestimated the equivalent dose in comparison to that derived from conventional OSL. The dose response curve in Figure 5.6 exhibits apparent exponential growth when the zero dose correction is applied. This can be explained by the summing of remnant signals through each cycle. The subtraction of the zero dose signal will not be applicable to each regeneration cycle since the amount of the remnant signal increases through each dose point and is not constant. This indicates that the ReSAR method is not appropriate for the Kangaroo Island samples.

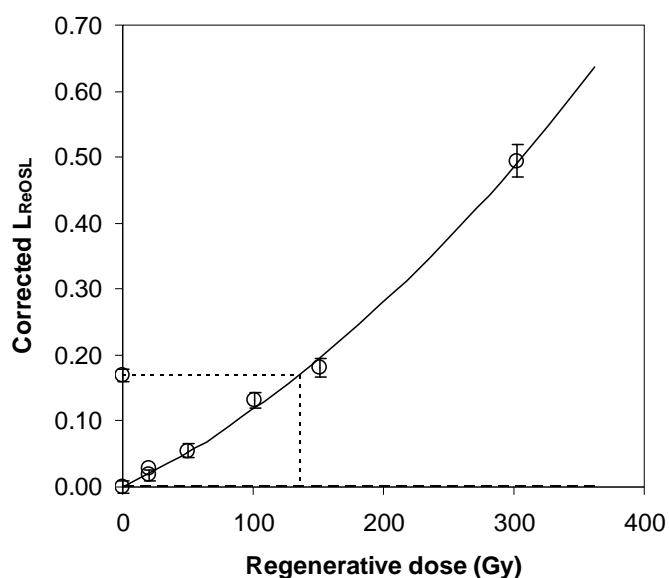


Figure 5.6: A typical aliquot from the ReSAR run of PB#2-18 (6 x 3mm mask aliquots, 260 °C PH, 220 °C CH, 0.25 Gy test dose). A D_e of 135.3 ± 7.7 Gy was obtained from this aliquot, the central value for all 6 aliquots was 113.0 ± 6.3 Gy; the overdispersion was 11.5 %, the average recycling ratio for the 6 aliquots was 2.18. The conventional SAR central value for this sample is 76 ± 3 Gy, and the SARTT-OSL central value is 73 ± 4 Gy. Note the apparent exponential increase in the curve indicating the inadequate removal of remnant recuperated signals from each cycle, even after the zero dose correction is applied.

Table 5.2: Comparison of conventional OSL to the MAR ReOSL method; all equivalent doses overlap at 2σ .

Sample Code	OSL Method	No. aliquots	Over-dispersion (%)	D _e (Gy)
Bales#2-9	Conventional OSL	25	4.4 ± 3.9	56 ± 1
Bales#2-9	MAR TTOSL	6	--	69 ± 7

The signal accumulation problem that occurs when using a TTOSL SAR protocol; the need for a zero dose correction to account for the build-up in ReSAR, and the results produced using the ReSAR method, supplied the impetus for the creation of an alternative and more robust SAR TTOSL approach. One that removes the remnant signals at the end of each cycle. Hence, there is no requirement for an empirical correction.

It was reasoned that in order to rework the MAR TTOSL dating method into a SAR method, the ReSAR method notwithstanding, it was important that a means of removing the build-up of signal (that would inevitably happen as a result of laboratory dosing and recuperation) through the protocol. The logic behind this was that since the very nature of the protocol revolves around the transfer of charge via heating, there would be remnant re-trapped signals at the end of each regenerative cycle, particularly from part 2 of the protocol. This is not a problem *per se* with a MAR protocol as each regeneration is performed on a different set of aliquots; therefore charge can be not carried over. With a SAR version however, any remnant charge would be carried into the next cycle. It was also reasoned that the use of a very small test dose would also reduce the magnitude of any remnant recuperated signals.

Jacobs *et al.* (2006) and Murray and Wintle (2003) suggested the use of an additional hot optical wash using blue LEDs at the end of each cycle in conventional SAR to remove recuperated signals, and Bailey (2000) suggested the use of a high temperature thermal wash. In light of this a thermal wash (280 °C) at the end of each cycle in the SARTT-OSL protocol was experimented with; however, this apparently induced but did not remove remnant signals resulting in a significant increase in the slope of the dose response curve (Figure 5.7). Wang *et al.* (2006a) show that a 300 °C anneal for 10 seconds

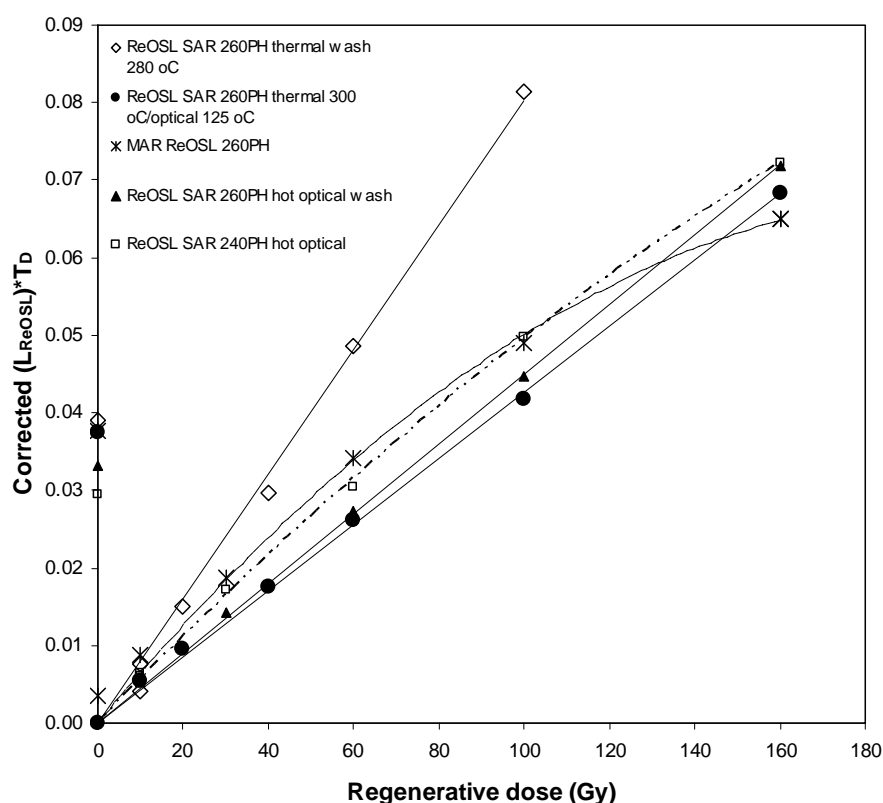


Figure 5.7: Aliquots of sample Bales#2-9 (a known age sample from Kangaroo Island), subjected to different end cycle washes, compared with a dose response curve derived from a sample of Bales#2-9 run using the MAR ReOSL protocol of Wang *et al.* (2006a). All samples except one used a 260° C PH, 220° C CH; the response curves were normalised to the test dose.

followed by an optical stimulation at 125 °C will thermally induce and then remove remnant recuperated signals from Part I of their MAR TTOSL protocol. Consequently, later SARTT-OSL experiments included a 300 °C thermal treatment in addition to a long 125 °C optical stimulation at the end of each regeneration cycle; which gratifyingly produced a growth curve similar to that derived from MAR TTOSL (Figure 5.7) (the MAR curve was less linear however).

To increase efficiency and reduce the number of steps in the protocol the thermal/optical treatment was combined into one long end cycle hot optical wash (Figure 5.7) similar to that used by Jacobs *et al.* (2006). Jacobs *et al.* (2006) implemented an end cycle 280 °C (40 s) hot optical wash in their modified conventional SAR protocol to remove recuperated signals. In the SARTT-OSL protocol the hot optical wash (here a 300 °C hot optical wash for 400 s was used) simultaneously thermally transfers and removes any remnant

signals (Murray and Wintle, 2003). The 400 s duration for this wash allowed the counts to be reduced to a near background level (see Figure 5.8); a longer wash could also be used. Note that with the Kangaroo Island samples a shorter wash duration would not be sufficient for remnant signal reduction to background (Figure 5.8).

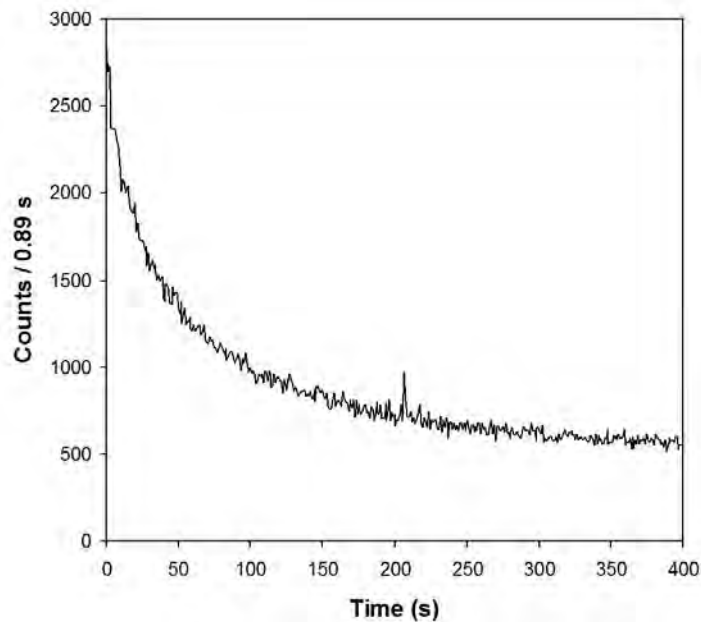


Figure 5.8: Example of a 300° C hot optical wash curve from the end of a regenerative dose cycle in the SARTT-OSL protocol (sample PB#2-18).

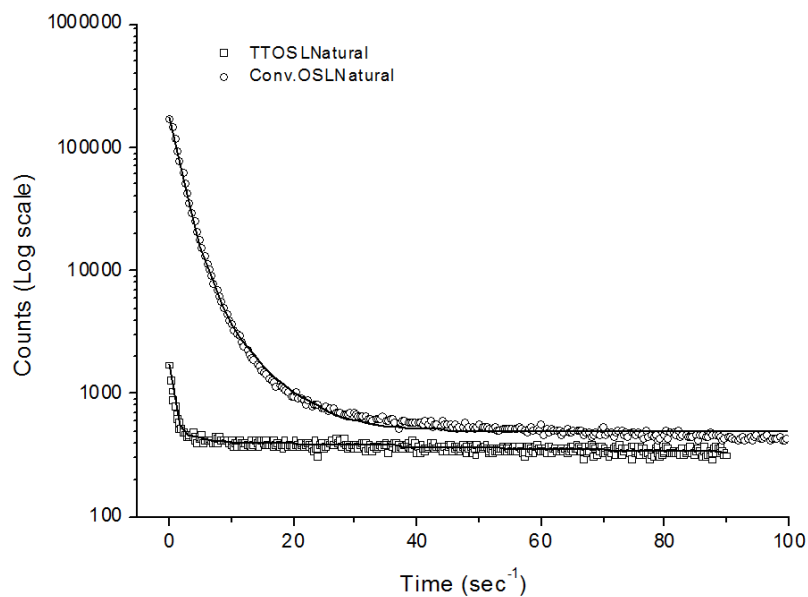


Figure 5.9a: A comparison between the TTOSL “natural” signal and the conventional OSL “natural” signal for sample PB#2-18 (log “Y” scale).

Any build-up of signal could significantly affect SARTT-OSL results as the thermally transferred signal is relatively small compared with the conventional OSL signal (Figure 5.9a). As stated above, to reduce the magnitude of any signal build-up very small test doses were chosen for the protocol: 5 Gy, 2Gy, and 0.5 Gy initially, then finally 0.25 Gy became the standard. Figure 5.5 demonstrates the signal build-up that happens within cycles from regenerative doses and test doses; this shows the necessity of removing these signals. If these remnants are not removed the signal will continue to build through each cycle; this will alter the slope of the response curve resulting in an incorrect estimation of the equivalent dose.

5.5.1.2 Preheats

It is evident that just as in conventional OSL samples analysed for TTOSL can be sensitive to changes in preheat temperature. Initial experiments, outlined in previous sections, were on the whole conducted according to the preheat prescribed by Wang *et al.* (2006a) and Wang *et al.* (2007). However, it was found that this temperature was not the most favourable for the Kangaroo Island samples. In order to unearth the possible reasons for this, and to determine what the optimum preheat temperatures may be, the TL curves of sample Bales#2-9 from Kangaroo Island were analysed (Figure 5.9b).

The natural TL curve in Figure 5.9b was generated by first bleaching 7 mm mask aliquots with blue LEDs at 125 °C for 100 seconds, using U-340 filters then changing to KOPP-759 and HA-3 filters, preheating to 280 for 10 s and measuring the TL by heating to 450 °C at 5 °/sec⁻¹. The aliquot used for the regenerative curve was bleached for 24 hours under a Philips MLU 300W mercury-discharge sunlamp, which emits both UV and visible wavelengths, and given an 800 Gy dose. The heating rate and filters were the same as for the 'natural' aliquot, although this aliquot was heated up to 500 °C. The Kangaroo Island sample exhibits a very smooth TL curve without any apparent lower temperature shoulders.

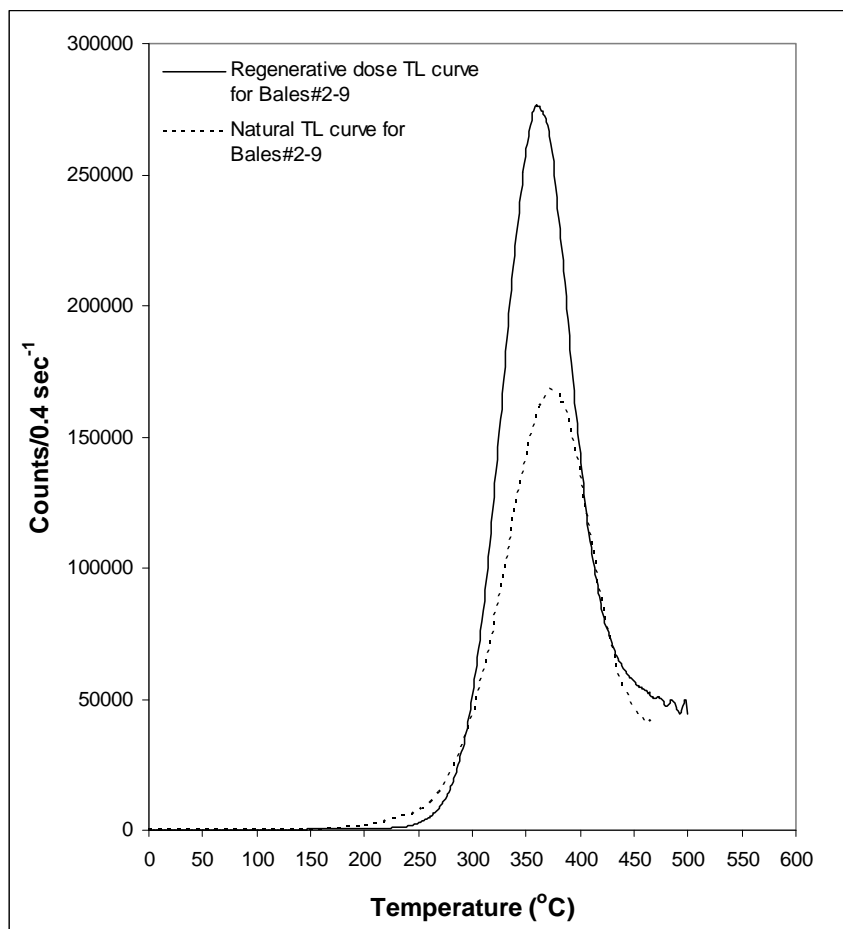


Figure 5.9b: Two TL curves from Kangaroo Island generated using KOPP-759 and HA-3 filters: a regenerative curve and a natural curve for sample Bales#2-9.

Even though the TL curve showed no obvious anomalies, it was decided to bracket the 260 °C preheat prescribed by Wang *et al.* (2006a; 2007) with 240 °C and 280 °C in a preheat comparison test—essentially a preheat plateau test (Figures 5.10 and 5.11). The choice of preheat to use with the Kangaroo Island samples was qualitatively made on the basis of equivalent doses determined from the preheat comparisons; which were then compared to the known conventional D_e for sample PB#2-18. Figures 5.10 and 5.11 display the results of a preheat comparison test for sample PB#2-18. Eighteen aliquots of this sample were subjected to 240 °C, 260 °C and 280 °C preheats, 6 aliquots of each (a later batch of 6 x 240 °C aliquots were added to the graph, and all aliquots used a 3 mm mask size and were subjected to a 220 °C cutheat). Unfortunately, 3 aliquots were lost from the 280 °C preheat analysis; although, the remaining 3 yielded a D_e (97 ± 7 Gy) much higher than the central D_e (76 ± 3 Gy) from the conventional OSL analysis. The 260 °C preheat apparently

delivers a tighter D_e distribution (Figure 5.10), and although the central D_e at 86 ± 4 Gy was not significantly different at 2σ to that derived from conventional OSL (76 ± 3 Gy); the central D_e derived from the aliquots that experienced a 240°C preheat (73 ± 4 Gy) was in better agreement, overlapping at 1σ .

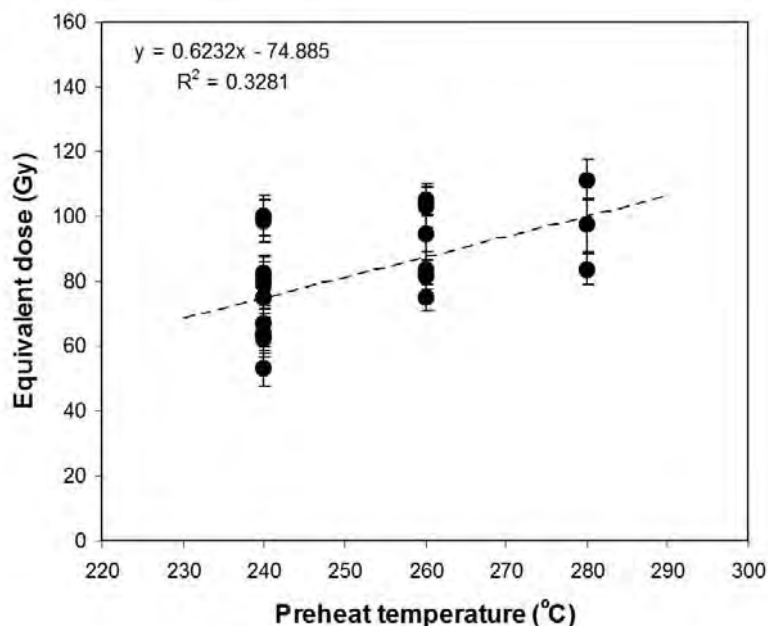


Figure 5.10: Equivalent dose comparisons using 240°C , 260°C and 280°C preheats on sample PB#2-18 from Kangaroo Island. Note the weak ($R^2 = 0.3281$) trend between increasing dose and preheat temperature.

The over-dispersions for each were 17%, 10% and 11% respectively. It must be noted that there may be no real difference between the 240°C and 260°C preheats (see Figures 5.10 and 5.11). The apparent difference may be an artefact of the small number of aliquots used for the preheat comparisons, or it may be related to greater spread in the data because of the signal to noise ratio, i.e., the small size of the TTOSL signal in samples that have a relatively low equivalent dose. At this early stage of experimentation 240°C became the preheat of preference for the Kangaroo Island SARTT-OSL samples, and as such, all SARTT-OSL samples used in this thesis were analysed for TTOSL using 240°C preheats, and 0.25 Gy test doses (using the SARTT-OSL modification of the Wang *et al.* [2006a] protocol). Table 5.3 illustrates the final modified protocol.

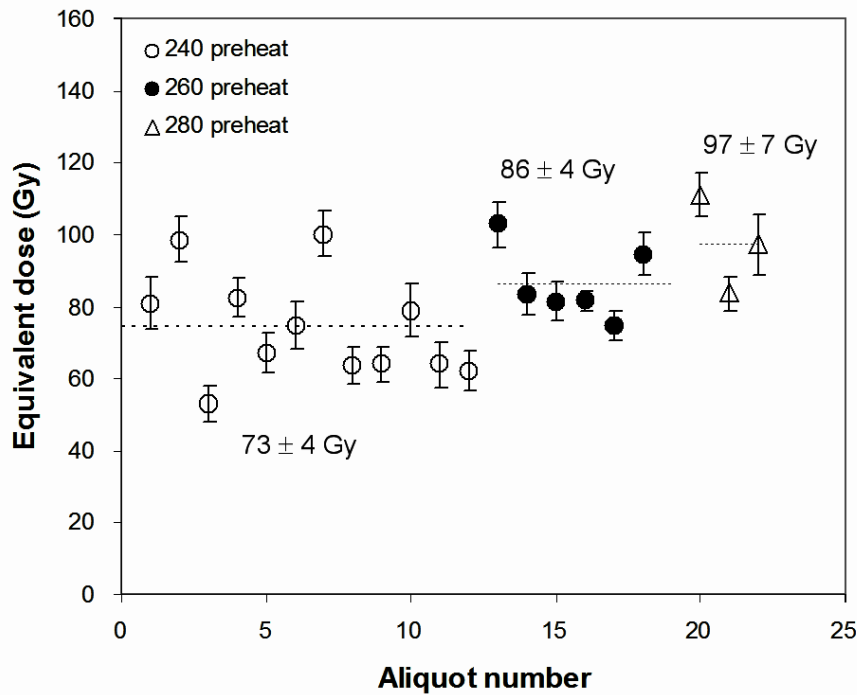


Figure 5.11: Further preheat (in °C) comparisons for sample PB#2-18, the dashed lines represent the weighed means (central D_e) for each group.

To provide a further test of the SARTT-OSL protocol a sensitivity correction test was carried out using a 240 °C preheat on several aliquots of PB#2-18. Figure 5.13a illustrates the results; the SARTT-OSL protocol was successful in correcting for any change in sensitivity. This indicated by the reproducibility of the signal from a series of 100 Gy regenerative doses.

The most important aspect of the experiments in this section is the realization that the choice of preheat temperature for thermally transferred OSL may be sample dependent, just as in conventional OSL. Even though, it seems that the Kangaroo Island samples may be relatively insensitive to preheat temperature in terms of the dose response curve. Conversely, choice of preheat temperature may affect the natural L_{ReOSL} signal. This can be seen in Figure 5.12. Here 3 aliquots of each preheat (240 °C, 260 °C, and 280 °C) were compared (data averaged); the response curves are all similar but the naturals are significantly different at 1σ when comparing to the 240 °C preheat. Choice of cutheat temperature may also be important for these samples; however, this was not tested.

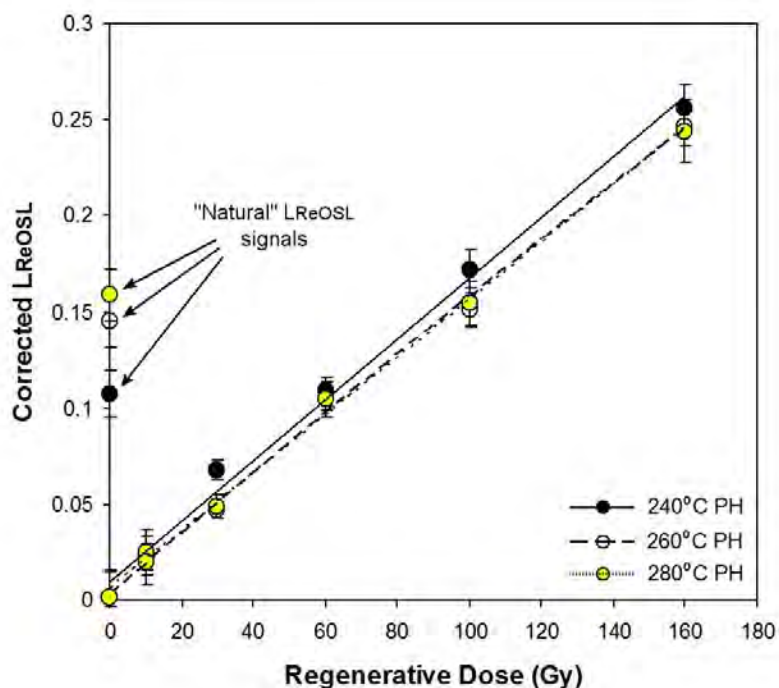


Figure 5.12: Dose response curve comparisons for 240° C, 260° C and 280° C preheats (mean data of 3 aliquots for each preheat) for 3 mm mask aliquots of sample PB#2-18 (regeneration doses of 10, 30, 60, 100, and 160 Gy, test dose 0.25 Gy, 300° C hot optical wash for 400 s). Note the similarity of all dose response curves, and the differences between the L_{ReOSL} natural signals of the 260° C, 280° C preheats and the 240° C preheat.

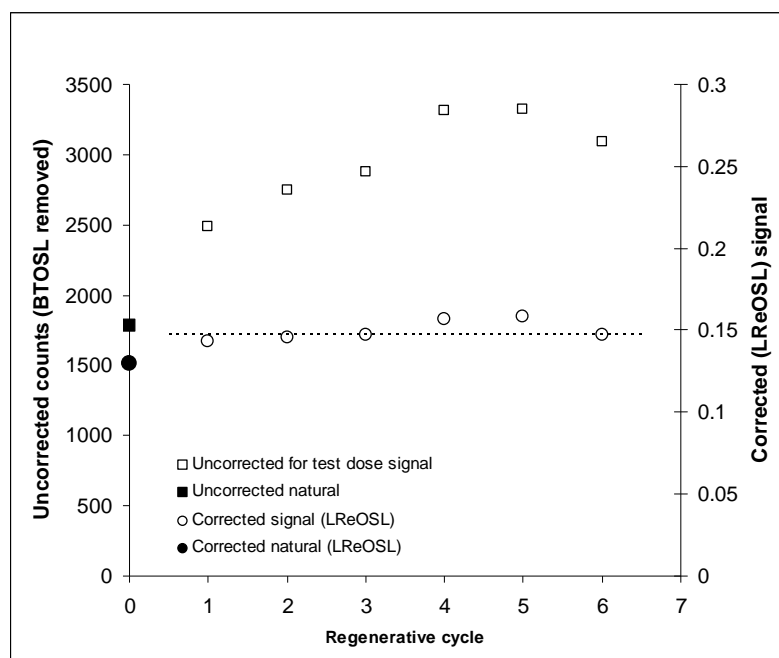


Figure 5.13a: A single aliquot of sample PB#2-18 was run through 6 x 100 Gy cycles of the SARTT-OSL protocol (240° C/10s PH, 220° C/5s CH); note the increasing sensitivity of the aliquot and the adequate correction by the test dose. The dashed line represents the average signal for 100 Gy.

In light of these experiments it is recommended that users of any SAR TTOSL method should examine the TL curves for some of their samples, and perform similar bracketing, and comparative tests prior to analysis, to determine if there may be sensitivity to preheat temperature.

5.5.1.3 Bleachability

Dose recovery experiments using the SARTT-OSL protocol were first performed on sample KPB#5-1. The first experiment was undertaken on 3 sunlight-bleached (24 hr) 3 mm mask aliquots, which were given a 300 Gy laboratory dose. The results were unsatisfactory as the mean dose recovered was 509 ± 34 Gy. The over-estimation was in the order of 209 Gy. This indicates that little TTOSL signal was eroded by the 24 hr sunlight bleach; seeing that the central D_e for this sample was 205 ± 4 Gy (from later SARTT-OSL dating work), this would appear to account for the residual. To test this lack of (or very slow) optical depletion further, several aliquots of KPB#5-1 were bleached for 0, 1, 4, 6 and 8 weeks in sunlight (two for each time-slice). The results are displayed in Figure 5.13b.

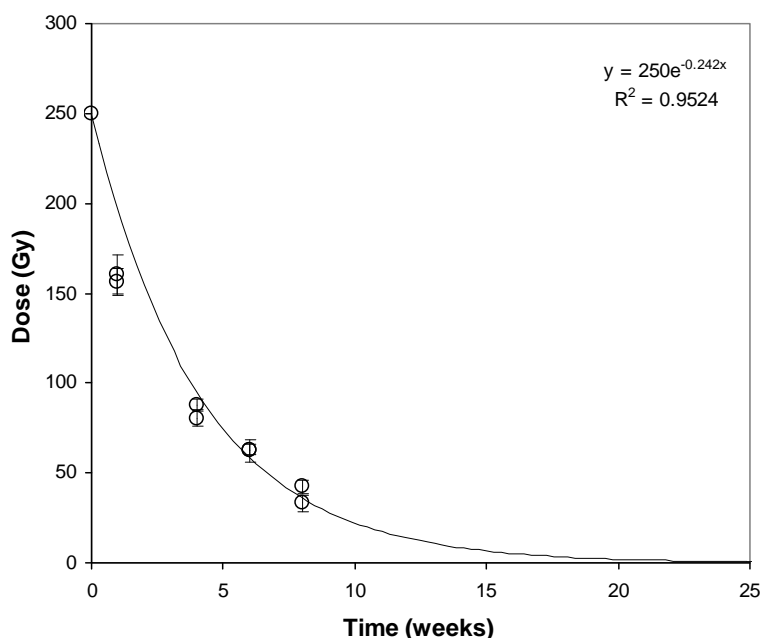


Figure 5.13b: SARTT-OSL equivalent dose vs time for Kangaroo Island sample KPB#5-1. Eight weeks of sunlight bleaching were required to reduce the equivalent dose from ~250 Gy to ~37 Gy. It would take around 20 weeks at this rate of decay for the dose to be reduced to negligible levels (the fit was extended to extrapolate this estimate), if at all, as past a certain point an unbleachable component may become evident; although, this was not tested.

The difficulty in eroding the natural signal from this sample is perturbing, as is the possibility that there may also be an unbleachable component within the signal. From this point, in order to test the internal consistency of the SARTT-OSL protocol (Table 5.3), a 300 Gy dose recovery was performed on 3 pre-annealed aliquots (i.e. spent discs from a SARTT-OSL run) of KBP#5-1. The mean recovered dose from these aliquots was 299 ± 18 Gy, which is an excellent recovery. The ability of the SARTT-OSL protocol to demonstrate this internal consistency was an important step. One further dose recovery experiment was performed on an unbleached series of aliquots from a modern backshore dune sample (PB#2b-8: Pennington Bay, Kangaroo Island). This sample has a low conventional OSL D_e of 0.09 ± 0.01 Gy; making it an excellent candidate for an unbleached SARTT-OSL high dose recovery test. The implicit assumption for this experiment was that these grains would have experienced sufficient sunlight exposure (i.e. >20 weeks?) prior to deposition to ensure total (?) optical depletion of the natural TTOSL signal (the small environmental dose

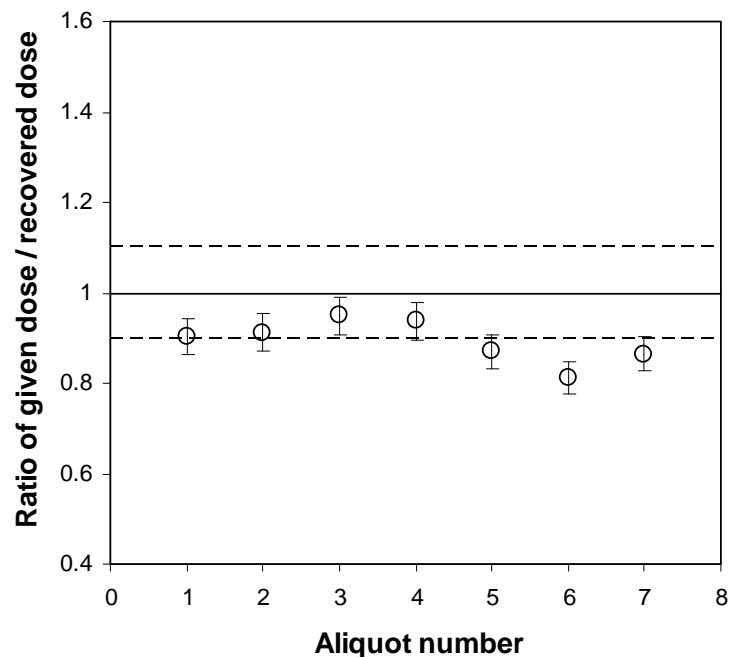


Figure 5.14: Results of the SARTT-OSL dose recovery performed on 7 aliquots of unbleached modern dune sample PB#2b-8. Four aliquots were within 10% of unity, and two overlapped 10% at 2σ . The solid line represents unity, and the two dashed lines are a 10% envelope around unity.

received during the relatively short burial period notwithstanding). Seven 3 mm mask aliquots of PB#2b-8 were given a laboratory dose of 300 Gy (without being sunlight or blue LED bleached) and were subjected to the SARTT-OSL protocol (Table 5.3). The weighted mean dose recovered from PB#2b-8 was 336 ± 6 Gy, and 4 of the aliquots fell within 10% of unity (Figure 5.14). A reasonable recovery; however, it is evident that there may be some form of additional residual signal present that prevents better recovery of the given dose. The presence of a small residual signal (equivalent to 10-30 Gy for example) in most samples may be of little importance, as the SARTT-OSL protocol will only be used when dating very old aeolianite sequences (>middle Pleistocene?) that have substantial equivalent doses, e.g. >200 Gy. In light of this the overall effect on the age determination may be small. For example if a sample has a “true” D_e of 300 Gy, then the inclusion of a 30 Gy residual may effect the final age estimate by <10%.

From the experiments undertaken in this section it is apparent that extended (up to 8 weeks) sunlight bleaching will remove much of the natural TTOSL signal from samples with substantial equivalent doses. The lengths of time normally used to remove signals from samples employed for conventional OSL (e.g. 24 hr sunlight) are not long enough for application to TTOSL, at least in the case of samples used in this study.

Wang *et al.* (2007) suggest that, alternatively, rather than a double transfer mechanism, a single transfer mechanism related to the slow (S3) OSL component (Jain *et al.*, 2003) may be the source of the TTOSL signal. If this is the case then it would explain the difficulty in eroding the natural signal from the Kangaroo Island samples. Importantly, the slow rate of optical depletion of this component has implications for the type of sediment which can be dated with the SARTT-OSL and MAR TTOSL protocols, limiting the application to sediments that have undergone long bleaching times, such as aeolian dune sediments.

For the purposes of dating the Kangaroo Islands samples considered to be beyond the range of conventional OSL, the possibility of an unbleachable

component that is in addition to the natural TTOSL signal is not accounted for in this study.

5.5.2 Testing the SARTT-OSL protocol: comparison to known age samples

The various parameters for a workable SARTT-OSL protocol have been established through a series of experiments to determine the most efficient way to:

- i) remove signal build-up throughout the regenerative cycles
- ii) establish an appropriate preheat temperature
- iii) recover a dose (i.e. bleaching the sample)

The SARTT-OSL protocol is further tested in this section by comparing SARTT-OSL equivalent doses from samples that had their D_e previously determined by conventional OSL, single grain OSL, and thermoluminescence. Three samples are compared here, 2 from Kangaroo Island and 1 from the south-east South Australia dune sequence (the West Naracoorte dune) (Huntley *et al.*, 1993, 1994; Murray-Wallace *et al.*, 1998; Huntley and Prescott, 2001; Banerjee *et al.*, 2003). The samples are PB#2-18 (used for many of the experiments on TTOSL), and PB#2b-3 from Kangaroo Island, and SESA 145 from the South Australia dune sequence. All of the equivalent doses for these samples were derived from the 90-125 μm quartz fractions isolated from carbonate aeolian dune sediment. The SESA 145 SARTT-OSL D_e is compared to results from three other luminescence studies of this dune.

5.5.2.1 Known equivalent dose sample PB#2-18

Twenty four aliquots (3 were rejected on the basis of saturation) of this sample were analysed with the conventional OSL protocol. The conventional OSL central value of 76 ± 3 Gy derived from this analysis was used for comparison to the SARTT-OSL results. Twelve aliquots of the sample produced a SARTT-OSL central value of 73 ± 4 Gy which is in excellent agreement with conventional OSL. The over-dispersion for this analysis was 17% (Table 5.4).

5.5.2.2 Known equivalent dose sample PB#2b-3

Forty eight aliquots (9 were rejected following criteria set out in the previous chapter) of this sample were analysed with the conventional OSL protocol. The conventional OSL central value of 63 ± 2 Gy derived from this analysis was used for comparison to the SARTT-OSL results. Six aliquots of sample PB#2b-3 produced a SARTT-OSL central value of 65 ± 5 Gy which is again in excellent agreement with the conventional OSL. The over-dispersion for this analysis was 16% (Table 5.4).

Table 5.3: SARTT-OSL modification of the Wang *et al.* (2006a) MAR TTOSL protocol.

STEP	TREATMENT	RESULT	NOTES
<i>Part 1. Detection of thermally-transferred OSL signals</i>			
1-1	Dose, D_i		For natural $D_i = 0$
1-2	Preheating at 240° C for 10s		Removing electrons in unstable TL traps
1-3	Blue LED at 125° C for 270s		Bleaching OSL signals
1-4	Preheating at 240° C for 10s		Thermally inducing TTOSL signals
1-5	Blue LED at 125° C for 90s	L_{TTOSL}	Detecting TTOSL signals
1-6	Give test dose, D_t		Monitoring OSL production
1-7	Preheating at 220° C for 5s		Removing electrons in unstable TL traps
1-8	Blue LED at 125° C for 90s	T_{TTOSL}	Test dose response
<i>Part 2. Detection of basic-transferred OSL signal</i>			
2-1	Annealing to 300° C for 10s		Thermally inducing remnant recuperated OSL signals
2-2	Blue LED at 125° C for 90s		Removing recuperated OSL signals
2-3	Preheating at 240° C for 10s		Thermally inducing basic-transferred OSL signals
2-4	Blue LED at 125° C for 90s	L_{BTOSL}	Measuring basic-transferred OSL signals
2-5	Give test dose, D_t		Monitoring OSL production
2-6	Preheating at 220° C for 5s		Removing electrons in unstable TL traps
2-7	Blue LED at 125° C for 90s	T_{BTOSL}	Test dose response
<i>Part 3. Hot optical wash</i>			
3-1	Blue LED at 300° C for 400s		Thermally inducing and optically removing remnant signal accumulation
<i>For SAR repeat parts 1 to 3 using different regenerative doses 4-5 times, include also a zero dose and repeat dose for a recycling ratio.</i>			

5.5.2.3 SESA 145: a sample from the extreme edge of conventional luminescence technique

The West Naracoorte dune range, as part of the south-east South Australia dune sequence, has been the subject of several luminescence studies in the past two decades, as iterated above. It was decided to analyse a sample from this dune as not only is it extremely old (possibly in excess of 800 ka) and therefore would be a good test for the SARTT-OSL protocol, but it has also

Table 5.4: Equivalent dose and age comparisons between SARTT-OSL, conventional OSL, single grain OSL, and TL

Sample Site	Sample	N ^a	Single grain (SG) and SAR OSL D _e (Gy)	Over-dispersion (%)	TL D _e (Gy)	N ^a	SARTT-OSL D _e (Gy)	Over-dispersion (%)	Total dose rate (Gy/ka ⁻¹)	SG*, SAR OSL ^o , TL age (ka)	SARTT-OSL age (ka)
Kangaroo Island	PB#2-18 ^{b,c}	21	76 ± 3	12	--	12	73 ± 4	17	0.622 ± 0.028	122 ± 7 ^o	119 ± 8
Kangaroo Island	PB#2b-3 ^{b,c}	39	63 ± 2	17	--	6	65 ± 5	16	0.652 ± 0.030	97 ± 6 ^o	99 ± 9
West Naracoorte	SESA 145 ^{b,d}	--	400 ± 15 390 ± 15	--	--	11	392 ± 15	11	0.461 ± 0.023	870 ± 50* 860 ± 70*	850 ± 57
West Naracoorte	SA023 ^e	--	302 ± 21	--	--	--	--	--	0.430 ± (?)	710 ± 62 ^o	--
West Naracoorte	SESA 74 ^f	--	--	--	327 ± 30	--	--	--	0.410 ± 0.030	800 ± 100	--

^a Number of useable aliquots (for OSL and SARTT-OSL from this study)

^b SARTT-OSL this study

^c Conventional SAR this study

^d Single 'supergrains' (Yoshida *et al.*, 2000)

^e Conventional SAR (Banerjee *et al.*, 2003)

^f TL (Huntley *et al.*, 1994)

been dated relatively successfully in a number of different studies (Huntley *et al.*, 1994; Yoshida *et al.*, 2000; Banerjee *et al.*, 2003). Analysed here were 11 aliquots of SESA 145 using the SARTT-OSL protocol; a central D_e value of 392 ± 15 Gy was derived from the results. The over-dispersion was 11%. This result is somewhat higher than some of the previous equivalent doses determined in other studies; however, the differences may be because the Huntley *et al.* (1994), and Banerjee *et al.* (2003) equivalent doses were in all likelihood obtained close to the upper limits of the respective methods. Nevertheless the D_e (392 ± 15 Gy) and SARTT-OSL age (850 ± 57 ka), using the dosimetry of Yoshida *et al.* [2000]) derived here fall within the 370-400 Gy range prescribed by Yoshida *et al.* (2000) in their 'supergrain' study, and the age range 820-870 ka for the sea-level highstand correlated with this dune sequence (Yoshida *et al.*, 2000; Huntley and Prescott, 2001) (Table 5.4 delineates the D_e values and luminescence ages for all of the West Naracoorte studies).

5.6 Discussion

This modified SAR version of the MAR protocol has performed quite well within the dose ranges experimented with here. The apparent consistency of equivalent doses recovered using the modified protocol on the known D_e samples is encouraging, and the successful recovery of an equivalent dose for SESA 145 is particularly encouraging. This would also indicate that the presence of a residual signal (if any), at least in these instances, did not have a significant effect on the recovery of comparable equivalent doses. It is felt that the demonstrated consistency validates the use of the SARTT-OSL protocol for use on samples of (presumed) old *aeolian* quartz with unknown D_e values.

The preheat used in the Wang *et al.* (2006a) protocol is apparently unsuitable for application to the samples from Kangaroo Island, as there was overestimation of the equivalent dose in comparison to equivalent doses derived from conventional OSL. A lower preheat of 240 °C gives results that are closer to expected values, although the reason for this can only be speculated upon until further investigations are undertaken. However, for reasons explained in previous sections, the Kangaroo Island samples examined may not *really* be particularly sensitive to the choice of preheat when

constructing a dose response curve. When comparing data from 260 and 240 °C preheats, it is observed that the key difference between the two preheats is in the natural signal. There are small differences in the response curves (Figure 5.12) but the most significant difference is in the corrected “natural” L_{ReOSL} signals. It is possible that the observed effect is due to:

- i) An initial change in sensitivity during measurement of the natural signal, related to the preheat temperature used, that is not adequately corrected for by the test dose in part 2 of the protocol.
- ii) Significant inter-aliquot variation in the natural that the small number of aliquots (i.e. 6-12) being analysed do not adequately account for. Consequently, the ‘differences’ in the natural TTOSL signals using the different preheats are the result of a statistically inadequate number of subsamples. This could potentially be resolved by analysing larger numbers of aliquots (48 for example) from a given sample.
- iii) The 300 °C anneal (part 2 of the protocol) and the hot optical wash at the end of each regenerative cycle are causing sensitivity changes that are not effectively normalized by the test dose (in the case of the anneal), thereby depressing the response curve, and giving higher than expected D_e values. The reason that the 240 °C preheat *appears* to work, in this set of circumstances, is that there is a reduction in the thermal transfer of signal due to the lower temperature which decreases the natural and compensates for the response curve depression. Giving what is apparently the correct D_e . However, this is probably not the case as it would be unlikely that dose response curves constructed with different preheats would be comparable, which they are (see Figure 5.12).

It is plausible that point i) above describes the most likely scenario. What is happening is in all probability specific to the samples being analysed, and that

for these samples there is some form of initial sensitivity alteration related to preheat temperature, which affects the 'natural' TTOSL signal. It is also possible that the differences between the two preheats will become less significant when dealing with larger equivalent doses, or greater numbers of aliquots; however, this was not tested in this study.

The failure of the SARTT-OSL protocol to successfully recover a laboratory dose from samples with substantial environmental doses is troubling. It is believed that this may be due to a component that contributes to the TTOSL signal. As iterated in previous sections, Wang *et al.* (2007) suggested that, alternatively, a single transfer mechanism related to the S3 component could also be the source of the TTOSL signal. The slow rate of optical depletion of the S3 component has implications for the type of sediment which can be dated with the SARTT-OSL and MAR TTOSL protocols. Fortunately the sediments used for this study are all of aeolian origin so it can be reasonably expected that they have had sufficient sunlight exposure before burial to reset the thermally transferred signal (the presence of an unbleachable component notwithstanding). If the S3 component is the source of the TTOSL signal then this would also explain the failure of the protocol to recover a given dose from samples with substantial environmental doses. The bleaching times used in this study for dose recovery were almost certainly insufficient to significantly erode the S3 signal. According to Singarayer *et al.* (2000) between 17 hours and one week of white light bleaching may be required to reduce the slow component to background levels; the length of time would be related to the size of the environmental dose. This would also explain why it is possible to recover a laboratory dose using a sample that has a negligible D_e . Dose recovery experiments based upon this slow component and residual component assumption will be carried out in later investigations of the SARTT-OSL protocol.

5.7 Summary and Conclusions

This chapter has detailed the methodology development and testing of a modified version the Wang *et al.* (2006a) MAR ReOSL protocol. This protocol was modified as a result of this research to operate as a SAR protocol by the

introduction of a 300 °C blue LED optical stimulation at the end of each regenerative cycle. The modified protocol was then used to estimate SARTT-OSL equivalent doses for samples that have known D_e estimates (from conventional OSL and TL), and to obtain recovered doses that were generally within experimental error.

SARTT-OSL equivalent doses and age estimates were determined for Kangaroo Island sample unknowns that were deemed beyond the conventional OSL range. Based upon the empirical evidence presented in this chapter these equivalent doses and ages should be reliable estimates (the caveat being that the method is considered experimental at this early stage of protocol development). The results derived through the use of this modified protocol are presented and discussed (along with the conventional OSL and amino acid dating results) in Chapter 7.

introduction of a 300 °C blue LED optical stimulation at the end of each regenerative cycle. The modified protocol was then used to estimate SARTT-OSL equivalent doses for samples that have known D_e estimates (from conventional OSL and TL), and to obtain recovered doses that were generally within experimental error.

SARTT-OSL equivalent doses and age estimates were determined for Kangaroo Island sample unknowns that were deemed beyond the conventional OSL range. Based upon the empirical evidence presented in this chapter these equivalent doses and ages should be reliable estimates (the caveat being that the method is considered experimental at this early stage of protocol development). The results derived through the use of this modified protocol are presented and discussed (along with the conventional OSL and amino acid dating results) in Chapter 7.

Chapter 6: Amino acid racemization analysis methods, experiments, and age calibrations

6.1 Introduction

The research undertaken in this thesis has employed a variety of methods to investigate the Quaternary history of aeolian deposition on Kangaroo Island. This chapter examines the amino acid racemization (AAR) reaction to determine stratigraphic relationships and estimate the age of aeolian and marine deposits investigated (see Chapter 6). Amino acid D-L ratios, when modelled using ^{14}C , U-series, and OSL dating methods, allow numeric and relative ages for stratigraphic units of unknown age to be estimated. Additionally the D-L ratios can be used to identify relationships between bioclastic units that are separated in space or where lateral continuity has been disturbed or obscured by erosion, vegetation growth, or there is non-deposition due to a lack of key underlying geology.

The AAR reaction, and its application in stratigraphic studies (aminostratigraphy) are examined in this chapter, and the results of AAR age models and aminostratigraphic analyses are presented and evaluated.

6.2 Amino acid racemization analysis

Amino acid racemization analysis is a technique for examining amino acids that are the constituents of protein residues remaining in biologically produced calcium-based minerals (biominerals), i.e., calcium phosphate: specifically hydroxylapatite $[\text{Ca}_{10}(\text{PO}_4)_6(\text{OH})_2]$, and calcium carbonate: specifically aragonite and calcite (CaCO_3). Examples of biological materials constructed of these minerals are bone and teeth (calcium phosphate), marine, freshwater and terrestrial molluscan shell (calcite and aragonite), and protistan (foraminifer) tests (calcite) (Weiner *et al.*, 1983; Ludbrook, 1984; Yassini and Jones, 1995; Koch *et al.*, 1997; Skinner and Jahren, 2007; Dobberstein *et al.*, 2008). The proteins in fossil biominerals once acted as substrates (crystal nucleation sites) and frameworks for mineralization, and regulated crystal growth when the organism was living (in molluscs the proteins may also be involved with cell signalling and interactions with other matrix macromolecules) (Lowenstam and

Weiner, 1989; Marin and Luquet, 2004; Skinner and Jahren, 2007). This organic component in fossils exists as diagenetically (diagenesis refers to the series of reactions that result in the loss, degradation and alteration of the organic component of biominerals during the period of burial, i.e., leaching, decomposition, decarboxylation, deamination, racemization and epimerization, and hydrolysis) modified residues that lie between the crystallites (of apatite, aragonite, or calcite) making up the bone, shell, or test, and as very small amounts of organic matter “trapped” within the crystals themselves (Sykes *et al.*, 1995). These are termed as the *intercrystalline* and *intracrystalline* fractions of the organic residue respectively.

The intracrystalline fraction, which may be present at domain boundaries (orientation interfaces) of crystallites or within fluid inclusions, can represent between 0.001 and 0.01% by mass of the biomineral (Sykes *et al.*, 1995). The intercrystalline fraction, by definition, represents a much larger percentage by mass. The intracrystalline fraction may be effectively in a closed-system, and thereby less prone to diagenetic processes such as leaching which can remove the more “exposed” (located in the interstices between crystallites—those located at the outer portions of the shell are particularly susceptible) intercrystalline residues (principally lower molecular weight macromolecules and free amino acids) (Wehmiller and Hare, 1971; Lajoie *et al.*, 1980; Miller and Mangerud, 1985; Sykes *et al.*, 1995; Collins and Riley, 2000; Penkman *et al.*, 2008). A closed system should also protect against the introduction of non-indigenous peptide residues, provide a consistent chemical environment, and allow for predictable diagenetic reactions, in addition to retaining the original molecules and their degradation products (Sykes *et al.*, 1995; Collins and Riley, 2000; Penkman *et al.*, 2008). The geochronological utility of the intracrystalline organic residue has been investigated in Penkman (2005) and Penkman *et al.* (2007, 2008). The intracrystalline isolation method of Sykes *et al.* (1995) and Penkman (2005) was not employed in this study; however, part of the methodology was adapted for the preparation of older marine shell and whole-rock samples where contamination was suspected. This is outlined in the methods section of this chapter and detailed in Appendix D.

The presence of amino acids in fossils was first demonstrated by Abelson (1954) in his work on the organic constituents of fossil molluscs. The potential application of the amino acid reaction, involving the interconversion of amino acid optical isomers in fossils, was anticipated by P. E. Hare (1962). Hare also completed further research, i.e., Hare (1969), Miller and Hare (1980), Hare *et al.*, (1984), for example. Successive generations of researchers have expanded upon Abelson and Hare's original studies, and good reviews of methodology and application can be found in Goodfriend *et al.* (2000), Wehmiller and Miller (2000), and Miller and Clarke (2007).

The main geochronological advantages of the method are the relatively small sample masses required for analysis, the array of sample types and the age range of the method (~ 1 year to $\sim 3 \times 10^6$ years) as a function of the diagenetic temperature history. The foremost disadvantage of the technique is the temperature dependence of the reaction (Wehmiller and Miller, 2000), and in geological contexts the uncertainty relating to diagenetic temperature variation over the period of burial—this may be of particular significance when dealing with very old samples (e.g. early Pleistocene) which have experienced multiple periods of cooling and warming. However, Wehmiller (1982), and Wehmiller *et al.* (1988) demonstrated that thermal histories could be estimated for late Pleistocene locations (and by extrapolation up to Marine Isotope Stage [MIS] 19). This was done using aminostratigraphical data (LEU D-L ratios), and kinetically modelled isochrons constructed over a latitudinal temperature gradient (see Wehmiller, 1982 and Wehmiller *et al.*, 1988 for an in depth discussion).

6.2.1 The AAR reaction

Amino acids are molecules that lack an internal plane of symmetry (this is called chirality) and may exist in either of two forms in nature. These forms are designated by the way that the molecules in solution rotate plane polarized light. The L-form (lævorotatory) rotates polarized light counterclockwise (also known as a left handed amino acid), and the D-form (dextrorotatory) rotates polarized light clockwise (also known as a right handed amino acid) (an exception to this is glycine which is symmetrical, as the central carbon atom is bonded to two hydrogen atoms, and therefore has no D-L configuration). The D- and L-forms of amino acids are essentially mirror images (Figure 6.1)—these are known as stereoisomers or enantiomers—and exhibit the same chemical composition. Biological systems contain small amounts of amino acids in the D-configuration (this is particularly evident in the long-lived proteins that are

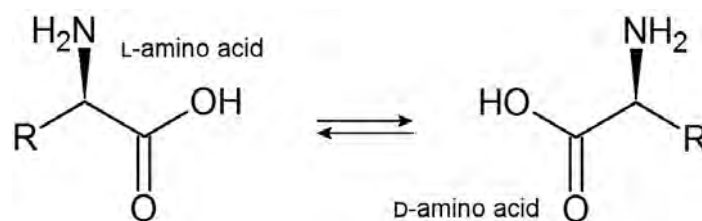


Figure 6.1: Simplified general skeletal forms for L- and D-amino acids. The wedge-shaped bond implies protrusion above the plane of the paper.

constituent in dentine and eye-lenses, and in unusually long-lived molluscs such as *Tridacna* spp.). Nevertheless, the proteins that make up the majority of constituents in a *living* organism are composed of amino acids that are almost *exclusively* in the L-configuration (Kvenvolden, 1975; Schroeder and Bada, 1976).

Systems that contain only L-amino acids are thermodynamically unstable (Bada, 1985), and these D- and L-forms can reversibly convert with time, due either to catalyzed chemical reactions or arbitrary thermal inputs. When an organism dies there is no longer any metabolic or enzymatic support (i.e. no protein “turnover”), accordingly the L-forms begin to change configuration and the D-forms start to accumulate; this happens until equilibrium conditions are attained. In the case of aspartic acid (ASX) and glutamic acid (GLX) for example, which have one chiral centre (this is the $[\alpha]$ carbon atom at the stereogenic centre—also termed the centre of asymmetry), the equilibrium state is achieved when there are 50% L and 50% D, i.e., $D/L = 1$. This progressive alteration from one form to another is known as racemization (Wehmiller and Miller, 2000; Robins *et al.*, 2001). If the measured D-form to L-form ratio is <1 then this ratio (when calibrated or modelled) can be used to estimate the time passed since the cessation of protein formation (which in short-lived organisms essentially equates with death), or provide a means to link coeval individuals (or stratigraphic units) across geographical space.

Epimerization involves amino acids with two chiral centres (e.g., isoleucine [ILE] which is extensively used for amino acid dating, is one of these amino acids). Here it is possible for racemization to occur about either the α -carbon or the β -carbon centre (which has a side chain), *or both*. There are 4 structural

configurations for these amino acids, with 4 possible diastereomeric pathways—Figure 6.2 illustrates the structural configurations for ILE. In nature L-isoleucine racemizes almost exclusively about the α -carbon forming D-alloisoleucine; the

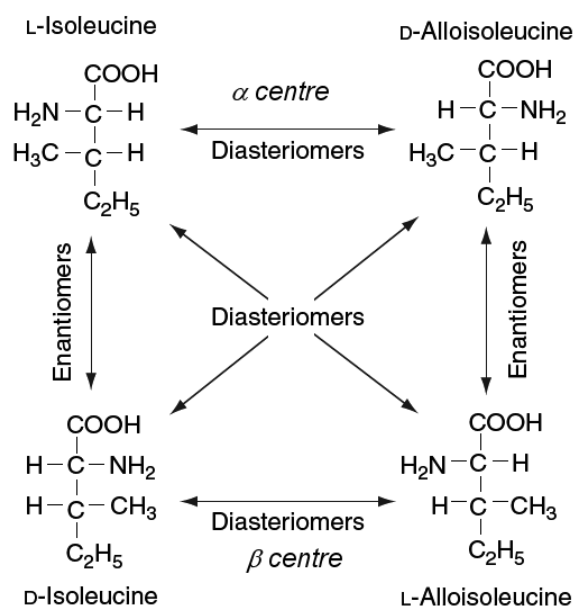


Figure 6.2: Isoleucine structural configurations and racemization pathways (modified from Miller and Clarke, 2007).

D-L ratio of these two isomers, i.e., the A/I ratio (D-alloisoleucine / L-isoleucine), is used for dating purposes (Miller and Clarke, 2007; Pizzarello *et al.*, 2008). Reaction about the β -carbon centre seldom occurs on Earth; this is generally a signature of n chiral amino acids that are extraterrestrial in origin, e.g., found in organic material extracted from meteorites (Pizzarello *et al.*, 2008).

The rate at which at which interconversion proceeds depends upon several factors, for example, the capacity of the radical (R) group of the particular amino acid to stabilize the intermediate planar carbanion (Figure 6.3), whether the amino acid is peptide bound or unbound (“free”), the position of the amino acid within the protein or peptide—terminal amino acids tend to have a higher racemization rate than those internal to the protein (Kriausakul and Mitterer, 1978; Kriausakul and Mitterer, 1983; Goodfriend and Weidman, 2001; Clarke and Murray-Wallace, 2006; Miller and Clarke, 2007)—the nature of adjacent amino acids (Kriausakul and Mitterer, 1978), and the conformational constraints

imposed by the peptide backbone (Van Duin and Collins, 1998). The rate order for isoleucine, for example, was found to be: N-terminal > C-terminal » interior > free (Kriausakul and Mitterer, 1978); although this may not be exactly the same for all amino acids, it does serve to stress the importance of the effect that amino acid position (in relation to the peptide or protein) has on rate. N-terminal amino acids are those at the start of a peptide sequence (i.e., the start of the sequence is terminated by an amino acid with an unbound amino group). The end of the sequence is terminated by an amino acid with an unbound carboxyl group, i.e., the C-terminus. To clarify, proteins are synthesized by RNA in biological systems starting at the N-terminus and ending at the C-terminus.

As stated above the conversion of L-amino acids into D-amino acids is temperature dependant and as such the time required for equilibrium to be reached can vary from thousands of years to millions of years. The age range for equilibrium is dependent upon the effective diagenetic temperature (T_{eff}).

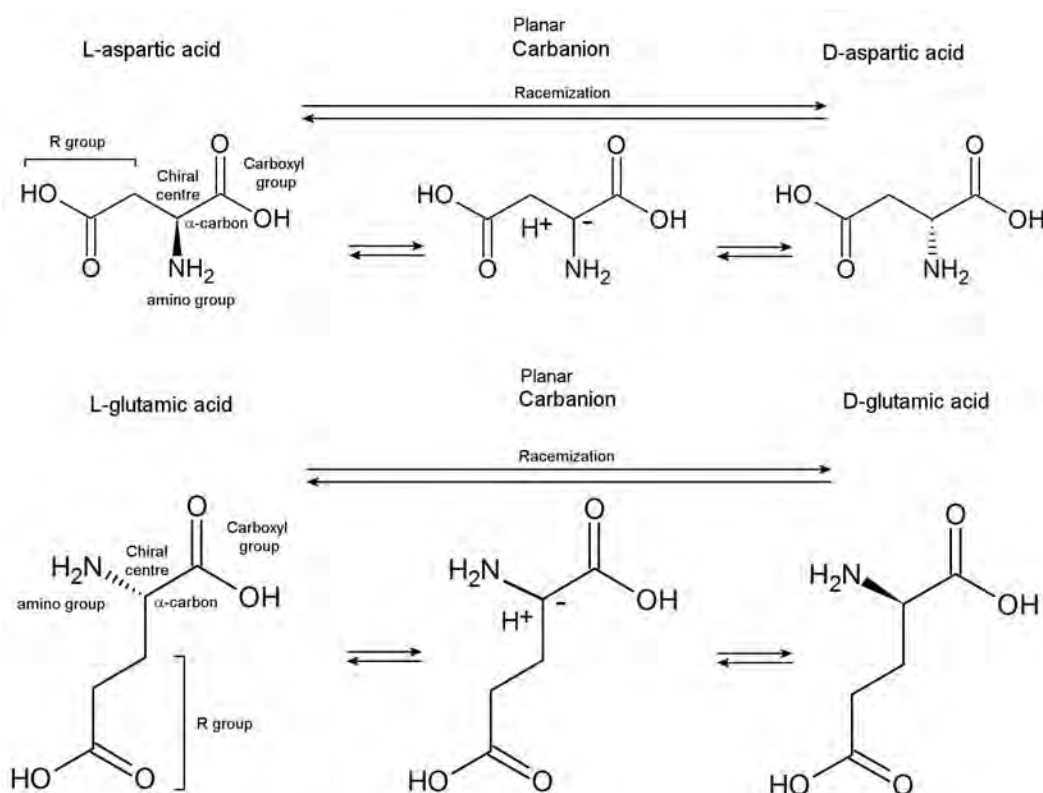


Figure 6.3: Simplified skeletal structures for ASX and GLX showing the orientation change about the α -carbon that can occur after the abstraction and uptake of a proton. The solid wedge-shaped bonds imply protrusion above the plane of the paper, and the dashed implies protrusion below the plane of the paper.

This is the temperature the biomineral experiences over the period of burial. Different effective diagenetic temperatures affect the rate of amino acid interconversion (i.e. higher temperatures = faster rates, and lower temperatures = slower rates of interconversion). This translates as: lower temperatures = greater age range and higher temperatures = shorter age range (in terms of equilibrium achievement). Age range until equilibrium is also dependent upon the amino acid, as the numerous amino acids that can be used for aminostratigraphy have differing rates of racemization (Miller and Mangerud, 1985; Wehmiller and Miller, 2000; Goodfriend and Weidman, 2001; Miller and Clarke, 2007).

The different isomers of amino acids can be detected and quantified via several chromatography techniques (gas chromatography [GC], ion exchange high-performance liquid chromatography [IE-HPLC] and reverse phase high-performance liquid chromatography [RP-HPLC]). Therefore, a comparison of the concentrations of D- and L- enantiomers in the form of a D-L ratio can be made (Wehmiller and Miller, 2000; Miller and Clarke, 2007).

In order to employ AAR as a geochronological tool, two important assumptions must first be made. The first is that the mixture of amino acids in a given fossil sample reacts in an orderly and predictable fashion during the course of diagenesis (Wehmiller and Miller, 2000). However, given that there are now many thousands of AAR analytical results available in the literature which have highlighted the geochronological applicability of different fossil taxa, the first is more than just a simple assumption. Researchers now have a large database from which to draw comparisons, contrast their own results, and make choices related to the shell genera (for example) that would be best to use for analyses, if a large selection is available.

The “assumption” of predictability allows the calibration of racemization reactions through the use of “known age” samples, and also allows the use of observed rates of reaction to estimate the age of samples that are of unknown age (Wehmiller and Miller, 2000). The phenomenon of taxonomic differences in rates of racemization—where different genera of marine bivalves *can* exhibit

different rates for the same amino acid (*Anadara trapezia* and *Katelaysia scalarina* for example) (Murray-Wallace and Kimber, 1987)—suggests that only amino acid D-L ratios derived from a single genus should be used as relative age indices. There can also be interspecies variation; however, this is not as pronounced as the disparity encountered when differing genera are used (Murray-Wallace and Kimber, 1987). ASX in different genera of foraminifera, for example *Discorbis dimidiatus* and *Elphidium* spp. from this study, has also shown differences in rates of reaction (Section 6.5). Conversely, GLX from analyses undertaken in the course of this research is demonstrated to be reasonably stable across molluscan genera and also foraminiferal genera from coeval deposits. Nevertheless, wherever possible assumptions about the predictability and consistency of AAR reactions should not be applied uniformly to all samples, only to specific types of samples (those of at least the same genera of mollusc or foraminifera for example)—although this can also depend upon whether multiple individuals of the same genus are available across samples, which is not always the case.

The second assumption is related to the temperature histories of the samples of interest. As explained above AAR is a temperature-dependent reaction, hence an estimation of the diagenetic temperature for the sample needs to be obtained; although, Miller and Mangerud (1985) suggested that regional or local palaeoclimatic data will have, generally, insufficient resolution to assess this. Hence, it is commonly assumed that the effective temperatures experienced by a set of samples, over their diagenetic history, are equivalent when collected from a region of equal present temperatures (Wehmiller and Miller, 2000)—this is also assuming that latitudinal gradients of temperature have not changed significantly over time (Wehmiller, 1984b). As part of a sampling strategy, and in order to lessen the effect of historical temperature variation, it is usual to sample from a minimum depth of >1 m (preferably >2 m) (Miller and Clarke, 2007). At depths >1 m the temperature changes experienced by the fossil material are those of longer-term seasonal change and variation associated with climate change, rather the short-term often extreme daily variations. Figure 6.4 (from Miller and Brigham-Grette, 1989; Miller and Clarke, 2007) models decreasing amplitudinal temperature change with increasing

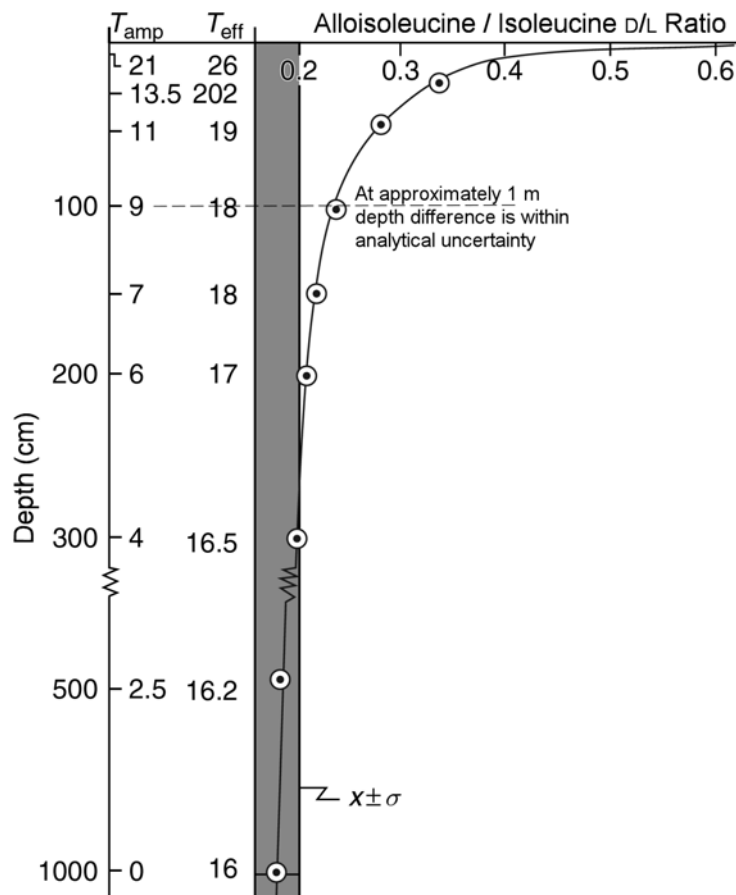


Figure 6.4: The difference between effective diagenetic temperature (T_{eff}) and mean annual air temperature (MAT: 16.8 °C) with depth based on multiyear instrumentation of a site in southern Arizona. The high amplitude of the annual temperature cycle near the surface (T_{amp} ¼ 21 °C) results in an T_{eff} 9° C above the MAT. The predicted A/I in a molluscan fossil held at particular depths for 14 k yr is plotted on the right. By a depth of approximately 1 m, the difference between the predicted and the expected A/I D-L ratio is within analytical uncertainty, but at shallow burial depths the predicted A/I D-L ratio deviates markedly from that expected based on the site MAT. At >2 m depth the difference between T_{eff} and MAT is negligible: <1 °C (caption and figure modified from Miller and Clarke, 2007).

depth and its effect on the alloisoleucene/isoleucine (A/I) D-L ratio. Therefore the advantage of sampling at depth is highlighted. This simple approach may, of course, mask complications in the thermal history of the sample, and so is not without problems (Miller and Mangerud, 1985); particularly with samples that may have experienced several glacial cycles, or samples that have been buried, exhumed, and subsequently re-buried. These periods of cooling and warming, or exposure and re-burial may have affected the rate of racemization, possibly quite significantly, since the relationship between temperature and racemization rate (and thus D-L ratio) is exponential in nature. The relationship

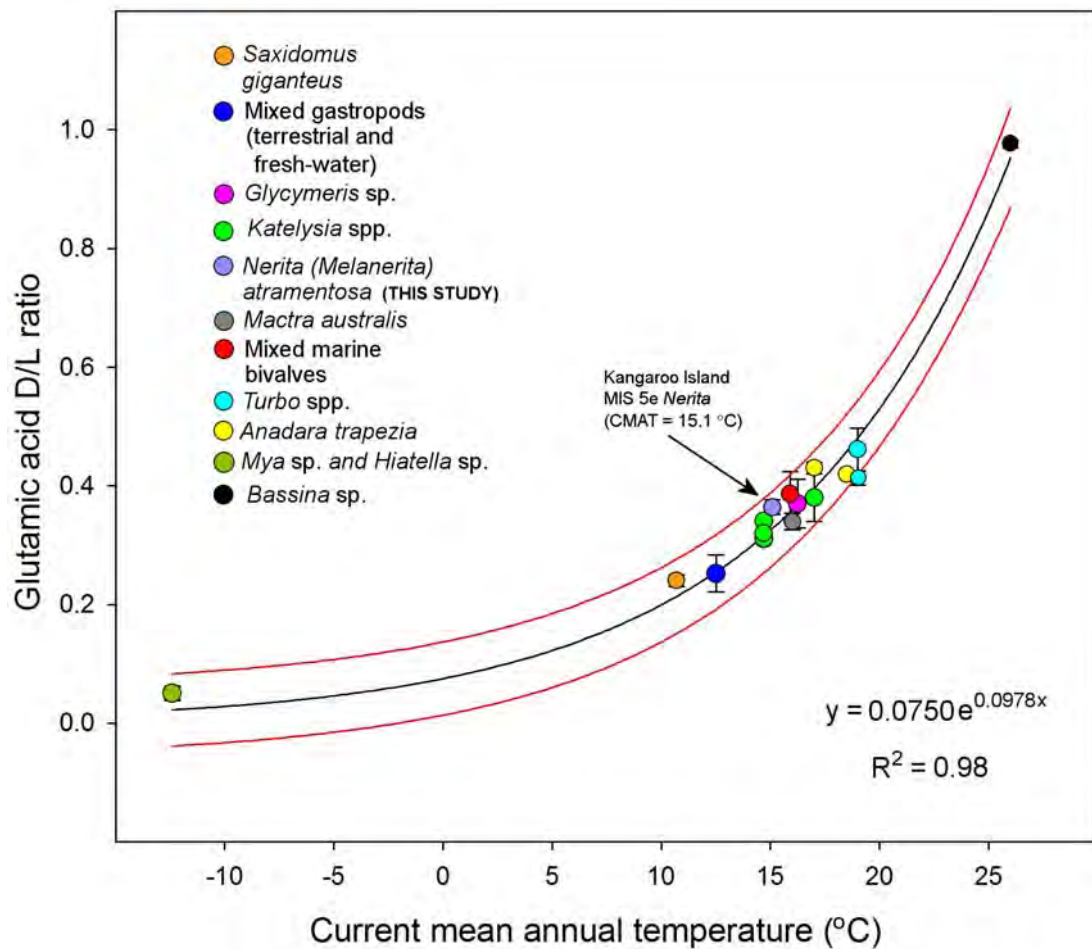


Figure 6.5: Glutamic acid (GLX) and CMAT data from various sources compiled to create a Last Interglacial (MIS 5e—132-116 ka [from a variety of sources listed in Siddall *et al.*, {2007}]) envelope for GLX D-L ratios. The data prescribe an excellent exponential fit (2-parameter) ($R^2 = 0.98$), and the envelope is formed by a 95% prediction band (bordered in red). Any GLX D-L ratio and its corresponding CMAT, from a Last Interglacial site, should fall within the limits of this envelope. These data were compiled from Kvenvolden and Blunt (1978); Murray-Wallace and Kimber (1987); Torres *et al.* (1997); Kaufman and Manley, (1998); Murray-Wallace *et al.* (1999); Torres *et al.* (2000); Chivas *et al.* (2001); Murray-Wallace and Bourman (2002); Carr *et al.* (2010); Murray-Wallace *et al.* (2010), and this research. The plot relies on molluscan D-L ratios from a range of genera, since a good GLX database does not exist for a single genus of shells across a range of CMATs. It is expected therefore that there may be some additional uncertainty related this mixing of genera. This plot is also limited by the underrepresentation in the literature of GLX examples from CMATs higher than 19 °C and below 10.7 °C. The molluscs were all recovered from Last Interglacial deposits, both in Australia and other countries. These data represent many individuals from the genera *Anadara*, *Bassina*, *Glycymeris*, *Hiatella*, *Kataysia*, *Mactra*, *Mya*, *Nerita*, *Saxidomus*, and *Turbo* (and a mixed assemblage of terrestrial and freshwater gastropods, see Torres *et al.* [1997], and a group of marine molluscs: *Anadara*, *Donax*, *Notospisula*, *Nuculana*, *Polinices*, see Murray-Wallace *et al.* [2010]). The lowest GLX data point was sourced from RP-HPLC analyses of *Mya* sp. and *Hiatella* sp. (undertaken by Kaufman and Manley [1998]) recovered from the Kogalu aminozone on Baffin Island (Canada) (CMAT = -12.4 °C) and is assigned a MIS 5 age (Andrews and Miller, 1984; Miller, 1985; Kaufman and Manley, 1998). This aminozone is also equated with the Thule aminozone of Greenland (North America/Europe) which spans 136-69 ka (Funder, 1989; Funder *et al.*, 1991). The highest GLX data point represents AAR analyses of Last Interglacial *Bassina* sp. recovered from the Gulf of Carpentaria (Northern Australia) (CMAT = 26 °C) (Chivas *et al.*, 2001). Y-scale uncertainty bars are 1 σ .

of D-L ratio to temperature is demonstrated in Figure 6.5. This plot reveals the exponential nature of GLX D-L ratios (from a range of Last Interglacial fossil molluscan taxa) versus the mean annual temperature (MAT) at each locality. Taken from a variety of AAR studies these data represent sites located around the world and in Australia, i.e., Africa, South Australia, Northern Australia, Canada, Spain and the United States (Kvenvolden and Blunt, 1978; Murray-Wallace and Kimber, 1987; Torres *et al.*, 1997; Kaufman and Manley, 1998; Murray-Wallace *et al.*, 1999; Torres *et al.*, 2000; Chivas *et al.*, 2001; Murray-Wallace and Bourman, 2002; Carr *et al.*, 2010; Murray-Wallace *et al.*, 2010).

Despite the inherent necessity to make these assumptions, models used to describe the behaviour of amino acids over time can be effective in numerical and relative age estimation. Racemization relationships to temperature can also be quantified by laboratory heating experiments (which allow the Arrhenius parameters to be determined when using several pyrolysis temperatures) (cf. Kaufman, 2000; Manley *et al.*, 2000; Miller *et al.*, 2000), and used to produce age equations for particular genera. Applications of these types of equations are reviewed in Goodfriend *et al.* (2000) (i.e. Kaufman, 2000; Miller *et al.*, 2000; Manley *et al.*, 2000; Wehmiller *et al.*, 2000) and Clarke and Murray-Wallace (2006). Additionally, there are other key questions that must be considered when using amino acids as geochronological tools. Two important questions are:

- i) The degree of diffusive loss of amino acid residues from fossils during diagenesis. Accordingly, are the concentrations of amino acids left after processing sufficient to yield reliable analytical results (diffusive loss may also involve the preferential loss of lower molecular weight more highly racemized residues, resulting in a lower D/L value [largely weighted by the degree of racemization in the remaining higher molecular weight residues])?
- ii) Has the sample been contaminated with younger (non-indigenous) amino acids?

These are variables commonly associated with the location and condition of the sample upon collection. For example weathered, exposed, recrystallised or poorly preserved shells and oxidized, recrystallised or poorly preserved foraminifera should be avoided as, for example, most of the organic residue may have been leached, there may have been selective leaching of larger less racemized macromolecules, or there may have been incorporation of “non-indigenous” amino acids. The incorporation of younger (or older) non-indigenous (also termed allochthonous) amino acids may be less problematic when the concentration of the indigenous amino acids is much greater, as their contribution to the final result is negligible. However, when the sample is of great antiquity (early Pleistocene for example) the concentration of indigenous amino acids can be lower (as a result of leaching, decomposition, and destruction, i.e., deamination, decarboxylation, recrystallisation, and microbial digestion) (Walton, 1998; Wehmiller and Miller, 2000; Penkman *et al.*, 2008); therefore, the non-indigenous amino acids become a greater problem, as they can now contribute significantly to the final result giving lower than expected D-L ratios. This is assuming that the contaminant is younger than the indigenous peptide residue; the opposite can also occur (but the former is almost always the case). To some extent this can be assessed based on various indices, e.g., concentration of L-serine (L-SER), and D-amino acids characteristic of bacterial cell walls (D-alanine [D-ALA] for example).

This study employed a set of both field and laboratory criteria, and methodology, in order to reject materials or mitigate (or remove) contamination. This is detailed in the following sections.

6.3 Applications of the AAR method in this thesis

The primary use of the amino acid racemisation reaction in this thesis was to generate numerical age estimates for unknown age aeolianite units, and marine deposits, and to define the aminostratigraphical subdivisions of these coastal sedimentary successions.

6.3.1 Aminostratigraphy

Aminostratigraphy is a chemostratigraphical method (based on chronostratigraphical principles) that utilises the AAR reaction that takes place

in the protein fraction of biominerals to classify strata (in this case aeolianite units, and marine units such as raised beach deposits) into chronostratigraphical units or *aminozones* that are concordant with intervals of time (Murray-Wallace, 1995; Murray-Wallace, 2000). These are termed *geochronological units* and AAR calibration by independent geochronological methods (here ^{14}C , U-series, and luminescence dating), as well as litho-, bio-, and morphostratigraphical evidence, is used to support these chronostratigraphical defined units (Murray-Wallace, 2000). The *aminozone* is the fundamental unit of aminostratigraphy and refers to a single time-stratigraphical unit. This unit represents a well-defined interval of time delineated by the clustering of amino acid D-L ratios from replicate analyses of fossils (generally molluscs or foraminifers) or whole-rock skeletal carbonate sediments recovered from a single, mappable lithostratigraphical unit (Murray-Wallace, 2000). Hence, aminostratigraphy provides a means to:

- i) estimate the time passed since the death of the constituent organism (i.e., marine shell, foraminifers or an average if using whole-rock samples).
- ii) define the stratigraphic relationships between contiguous and discontinuous skeletal deposits (carbonate aeolian/marine deposits primarily made up of comminuted shell, whole shell, echinoderm and bryozoan fragments, calcareous algae, and foraminifers).

Not only can aminostratigraphy be used to differentiate stratigraphic layers; it can also be used to match discontinuous skeletal carbonate units which are contemporaneous but isolated in geographical space. For example bedding and contact can be obscured by slumping of overlying material, or solutional crusts. The lateral continuity can also be disturbed or removed by erosion, weathering, or human activities. There are also examples of deposits that are contemporaneous but are isolated due to the requirement of key underlying geology or morphology; such as basement rocks that are “anchors”, “keystones” or basins for deposition, or dune swales that act as receptacles for large palaeosol lenses, and also wave-cut notch deposits.

Aminostratigraphy is one of the least ambiguous applications of amino acid geochronology, as it to some extent overcomes the uncertainties associated with diagenetic thermal histories, and racemization kinetic models (Miller and Hare, 1980; Murray-Wallace, 2000). This is provided that it is used over limited geographical regions that are characterized by similar palaeoclimatic regimes, and annual and seasonal temperature changes (Miller and Hare, 1980).

6.4 AAR Methods

All samples collected for amino acid racemization analysis in this study were analysed using reverse phase high-performance liquid chromatography (RP-HPLC). While not a new method for organic analysis (cf. Lindroth and Mopper, 1979), the novel use of the technique in order to determine D-L ratios of fossil amino acids is relatively new. This method was developed by Kaufman and Manley (1998); based upon the previous work of Brückner *et al.* (1991) in food chemistry. RP-HPLC, using the particular instrumentation and configuration at the University of Wollongong AAR laboratory, also has the advantage of automation, where sample injection, mobile phase/solvent mixing, and flow rates are controlled by Chemstation software. The capacity of RP-HPLC to detect amino acids in the picomole range, from sample masses in sub-milligram amounts, is the reason single grain analysis of carbonate sediment has become possible. Whole marine and freshwater shell can also be analysed by sub-sampling a small portion from a particular area (for consistency) of the shell—usually from the umbo or hinge region, or the aperture in the case of gastropods. Skeletal carbonate whole-rock sediment can also be analysed.

This study followed closely the RP-HPLC methods developed in Kaufman and Manley (1998) and the modification of those methods in Kaufman (2000). Detail on these methods can be found therein; however, they are briefly described below.

6.4.1 Instrumentation

All AAR analyses reported in this thesis were performed on an integrated Agilent 1100 series liquid chromatograph incorporating the following modules:

- i) a vacuum degasser and quaternary pump
- ii) a thermostatted combination autosampler/autoinjector
- iii) a thermostatted column compartment
- iv) an Agilent G1321A fluorescence detector

The detector utilizes a 20 w xenon flash lamp (296 Hz and 74 Hz modes) with a 280 nm cut-off filter operated at an excitation wavelength of 230 nm, and an emission wavelength of 445 nm, during sample analysis. Agilent Chemstation software (Rev. A. 10.02 [1757] 1990-2003) was used to calibrate and integrate the fluorescence signal. The software also controlled the eluent gradient, and the sample derivitisation and injection method programs (macros). Other macros also developed by Kaufman and Manley (1998) were used to determine D-L ratios based upon the calculated and recognized peak areas, and peak heights.

6.4.2 Amino acid derivitisation

The sample D- and L-amino acids are derived prior to injection into the RP-HPLC column using *o*-phthaldialdehyde (OPA) in conjunction with the chiral thiol, *N*-isobutyl-L-cysteine (IBLC). This yields fluorescent diastereomeric derivatives of the chiral primary amino acids (Kaufman and Manley, 1998). The sample solution and the OPA/IBLC derivitising reagent are drawn up into an offline sample loop via the autosampler needle, mixed in the needle seat by a motorized plunger, and allowed to react at room temperature. This mixture is then injected from the needle seat into the online RP-HPLC column. Mixture assembly, needle washing (before and after reagent and sample draws), mixing and injection are controlled automatically by the autosampler/autoinjector macro.

6.4.3 Stationary and mobile phases

Separation of the D and L amino acid derivatives occurs on a C₁₈ stationary phase. During the course of this study two brands of reverse phase C₁₈ stainless steel column were used:

- i) Thermo Scientific Hypersil BDS-C18, 5 µm particle size, 250 mm L x 3.0 mm ID

- ii) Sigma Aldrich Supelcosil LC-18-DB, 5 μm particle size, 250 mm L x 3.0 mm ID

Both have endcapped, base deactivated packings (BDS and LC-DB) with 120 Å pore size. Column temperature was controlled in a thermostatted compartment, set at 30° C for sample analysis and 25° C for end-run flush. The amino acid elution order for these columns is: L and D-aspartic acid (ASX), L and D-glutamic acid (GLX), L and D-serine (SER), L-threonine (THR), glycine (GLY), D-THR, L and D-arginine (ARG), L-alanine (ALA), L-Homo-Arginine (L-hARG), D-ALA, L and D-tyrosine (TYR), L and D-valine (VAL), L-phenylalanine (PHE), L-isoleucine (ILE), D-PHE, L-leucine (LEU), D-alloisoleucine (AILE), and D-LEU. The amino acids THR, ARG, and TYR were not monitored in this study; there were other compounds (most likely produced during fossil diagenesis), indicated by small unknown peaks, that also elute, these too were not monitored.

Three mobile phase channels (A, B, and C) deliver eluent to the column in a linear gradient. Eluent A is a 23 mM sodium acetate ($\text{CH}_3\text{COONa} \cdot 3\text{H}_2\text{O}$) solution, with 1.5 mM of sodium azide (NaN_3) to inhibit bacterial growth, adjusted to pH 6.00 with 10% acetic acid. This solution degrades so it must be prepared at least weekly. Eluent B is 100% HPLC grade methanol, and eluent C is 100% HPLC grade acetonitrile (Kaufman and Manley, 1998). The gradient (upon sample injection) for BDS and LC-DB columns is initially 95% eluent A to 5% eluent B, grading to 45% B and 5% C after 88 min. (at a flow rate of $0.560 \text{ ml/min}^{-1}$). At the end of a sample run the column is flushed with 95% B and 5% C for 15 min, at a flow rate of $0.600 \text{ ml/min}^{-1}$, in order to remove excess sample and reagents. This is followed by an equilibration step (for 10 min.) of 95% A and 5% B, prior to the next sample injection (see Table 6.1).

6.4.4 Sample selection, strategy, and field criteria

These sections will detail field sample selection and the strategies behind the types of samples used in this study; the types of field criteria used will also be examined. Before proceeding into the discussions the terms “sample” and “subsample”, in the context of this study need to be defined. An amino acid racemization sample and subsample are defined below.

Table 6.1: Time Table for eluent gradient and flow rate.

Time (min. ⁻¹)	Eluent A (%)	Eluent B (%)	Eluent C (%)	Flow rate (ml/min. ⁻¹)
0	95	5	0	0.560
31	76.6	23	0.4	0.560
88	50	45	5	0.600
89	0	95	5	0.600
104	0	95	5	0.600
105	95	5	0	0.600
115	95	5	0	0.560

- i) A sample is a collection of whole individual molluscs (bivalve or gastropod, freshwater or marine) taken from a single stratigraphic unit in the field or:
- ii) An amount of whole-rock sediment, i.e., either free-flowing carbonate sediment, or consolidated carbonate aeolianite, or carbonate matrix material taken from a single stratigraphic unit in the field.
- iii) A subsample is either a section of a mollusc(s) (see Figure 6.6 for subsample diagram) taken from a single stratigraphic unit sample for AAR analysis, or a whole mollusc(s), taken from a single stratigraphic unit sample for AAR analysis.
- iv) A subsample of whole-rock sediment is an amount taken from the main whole-rock sample (usually a few hundred mg) for AAR analysis.
- v) Foraminifers are taken as a subsample (i.e., usually 5-10 single foraminifers) from the main whole-rock sample.

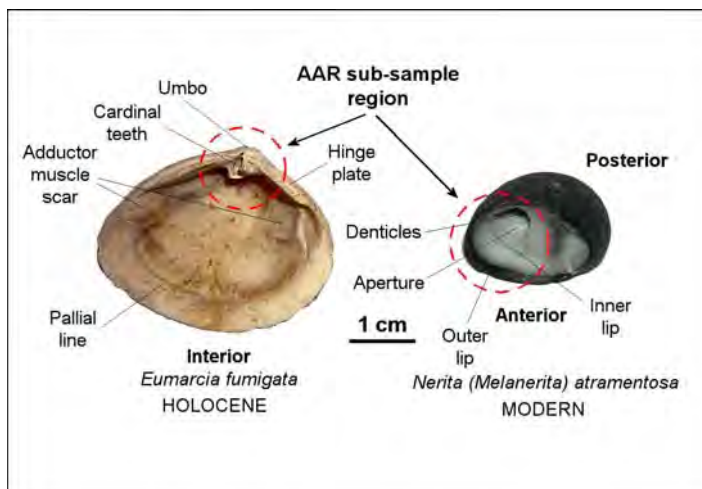


Figure 6.6: AAR subsample regions used in this study for both bivalves and gastropods. Shown here are examples of a Holocene *Eumarcia fumigata* (American River) and a modern *Nerita (Melanerita) atramentosa* (Point Ellen). Anatomical descriptions follow Ludbrook (1984).

To simplify: a sample is that material which is removed in the field from a single stratigraphic unit, and a subsample is a subset of that particular sample which is removed in the laboratory for AAR analysis.

6.4.4.1 Mollusc samples

A set of field criteria were used in the selection of fossil molluscan shells for AAR analysis. In most cases shells were sampled from deeply buried contexts, i.e., not less than 1 m (preferably > 2 m) below the surface. However, in some instances it was unavoidable, particularly with Last Interglacial (or older) exposed shell beds. Nevertheless, sampling from these sites was essentially not problematic as it is likely from a morphological perspective that the shell beds were buried for much of their history, having been exposed relatively recently due to an actively eroding coastline—particularly during the past 7 ka, since the attainment of the Holocene sea-level highstand (Belperio, *et al.*, 2002). Shell material was always sampled unambiguously and scrutinized on site for any obvious signs of re-crystallization or poor preservation (powdery or chalky surfaces), and contamination (algae growths for example). Articulated individuals were sampled preferentially or at least single valves or gastropods that were not broken or damaged (articulation was rare), again at some sites it was unavoidable and the only available shell was fragmented (Smith Bay for example). These deposits are often a diverse thanatocenose of biocenose faunal assemblages. To qualify this: the shells in (most of) these deposits have undergone thanatocenosis, and so do not represent a *life assemblage*; they were transported, and consequently deposited as part of the sedimentation process, undergoing mixing, disarticulation, and often mechanical abrasion and breakage. The attempt was also made to select individuals from the same genus across sites; however, this was rarely possible (see Figure 6.7 for examples of Kangaroo Island modern and fossil molluscs).

To summarise the field criteria for sampling molluscs:

- i) Sample from deeply buried contexts.
- ii) Establish an unambiguous association with the sedimentary unit.
- iii) Reject shell that was poorly preserved or obviously contaminated.
- iv) Wherever possible sample only undamaged shell.



Figure 6.7: Examples of modern and fossil marine shell analysed for amino acids in this study. These are representatives from modern (modern rock platform *Nerita* [A] from Point Ellen, and live-collected *Katelsysia* [B] from Kingscote beach), Holocene (*Katelsysia* [C,D,E] and *Eumarcia* [F] from shell beds at American River), Late Pleistocene (*Nerita* [G] from a raised pebble notch at Vivonne Bay; *Fulvia* [H] from a notch deposit at Rocky Point; *Katelsysia* [I] from the Kingscote raised pebble/cobble beach *Amesodesma* [J] from raised beach deposits at Pennington Bay; *Spisula* [K] from a shelly deflation deposit at Hanson Bay), Mid-Pleistocene (*Mactra* [L] and *Tawera* [M] from a raised cobble beach at Boxing Bay), and early Pleistocene deposits (*Nerita* [N], *Glycymeris* [O], and *Katelsysia* [P] from the Point Ellen Formation at Point Ellen, and *Anapella* [Q] from a raised shelly mud at North Cape). Also, freshwater gastropods (Family Hydrobiidae [R]) were recovered from a Late Pleistocene fluvial deposit at Baudin Beach.

- v) Try to sample from a single genus to ensure consistent rates of racemization.

The strategy behind the collection of fossil marine shell was to establish the age or timing of periods of higher than present sea-level on Kangaroo Island. Many shell/pebble beach units at the time of sampling were considered to be of Last Interglacial age (*sensu stricto*: Marine Isotope Substage 5e; Riss-Würm; Sangamonian, Eemian, Ipswichian) (Kingscote Beach, Rocky Point, Pennington Bay, Vivonne Bay, and Hanson Bay) (Chapter 3: Figure 3.1). This initial (at the time of sampling) assumption of a Last Interglacial age for these deposits was based on morphostratigraphical evidence (i.e. the heights APSL of the Kangaroo Island units were comparable to Last Interglacial Glanville Formation sites on the South Australia mainland [+2 to +3 m] [e.g. Eyre Peninsula, Spencer Gulf, Port Wakefield, Port Adelaide]) (Belperio *et al.*, 1984; Murray-Wallace, 1987; Murray-Wallace *et al.*, 1988) and, during later microscope examination, the presence of the indicator fossil (the foraminifer *Marginopora vertebralis*—typically found in tropical waters) (Milnes *et al.* 1983; Ludbrook, 1984; Belperio, 1995; Cann and Clarke, 1993). Whole tests of *Marginopora vertebralis* were found at the Kingscote site (see Figure 6.8), but it was only found as fragments at other sites (Hanson Bay, Pennington Bay, Vivonne Bay, and Rocky Point).



Figure 6.8: *Marginopora vertebralis* recovered from the Kingscote pebble/cobble beach deposit (sample KC#3-1) on Kangaroo Island (light microscope 100 x magnification).

Other sedimentary successions considered to be much older (shell/pebble/cobble beach deposits most likely of early Pleistocene age) were also examined, i.e., at Smith Bay, Boxing Bay, North Cape, and Point Ellen. The considered antiquity of these units was based on not only morphostratigraphy, but also on the condition of recovered fossil molluscs and foraminifers, and previous studies of some of the sites (e.g. Point Ellen, and Smith Bay: Ludbrook, 1983; Milnes *et al.*, 1983; Ludbrook, 1984; Bourman and Alley, 1999). See Figures 3.1 (Chapter 3) and 6.7 for site locations and examples of modern and fossil shells sampled for AAR analysis.

These shelly units were originally deposited at or near sea-level at the time of deposition, and so their height-above-present-sea-level (APSL) is a good proxy indicator of these palaeosea-levels. Neotectonic uplift has probably occurred at least one of the early Pleistocene sites, namely Smith Bay, as this unit is +18 m APSL (see Chapter 3: section 3.6.4).

6.4.4.2 Whole-rock samples

Whole-rock sediment samples are defined here as either being consolidated biogenic carbonate grainstone (e.g. carbonate aeolianite or carbonate matrix) or unconsolidated biogenic carbonate sediments (e.g. modern beach sand). A whole-rock AAR analysis involves measurement of the extent of AAR in a representative population of grainstone or unconsolidated sediment; the D-L ratios represent the “averages” (the integrated effect of the amino acid D/L enantiomers and amino acid concentrations across a range of biominerals contained therein) of the amino acid contributions from *all* biominerals contained within the sample. Figure 6.9 illustrates some of the many constituent grains found in a carbonate whole-rock sample.

Whole-rock sediment samples in this study were usually recovered at depth (as above) from recently exposed carbonate aeolianite units. Samples were collected by cutting into the surface of the exposure and sampling approximately 100-200 mm into the face (similar to an OSL sampling strategy), depending upon the level of induration in the aeolianite outcrop. This was done

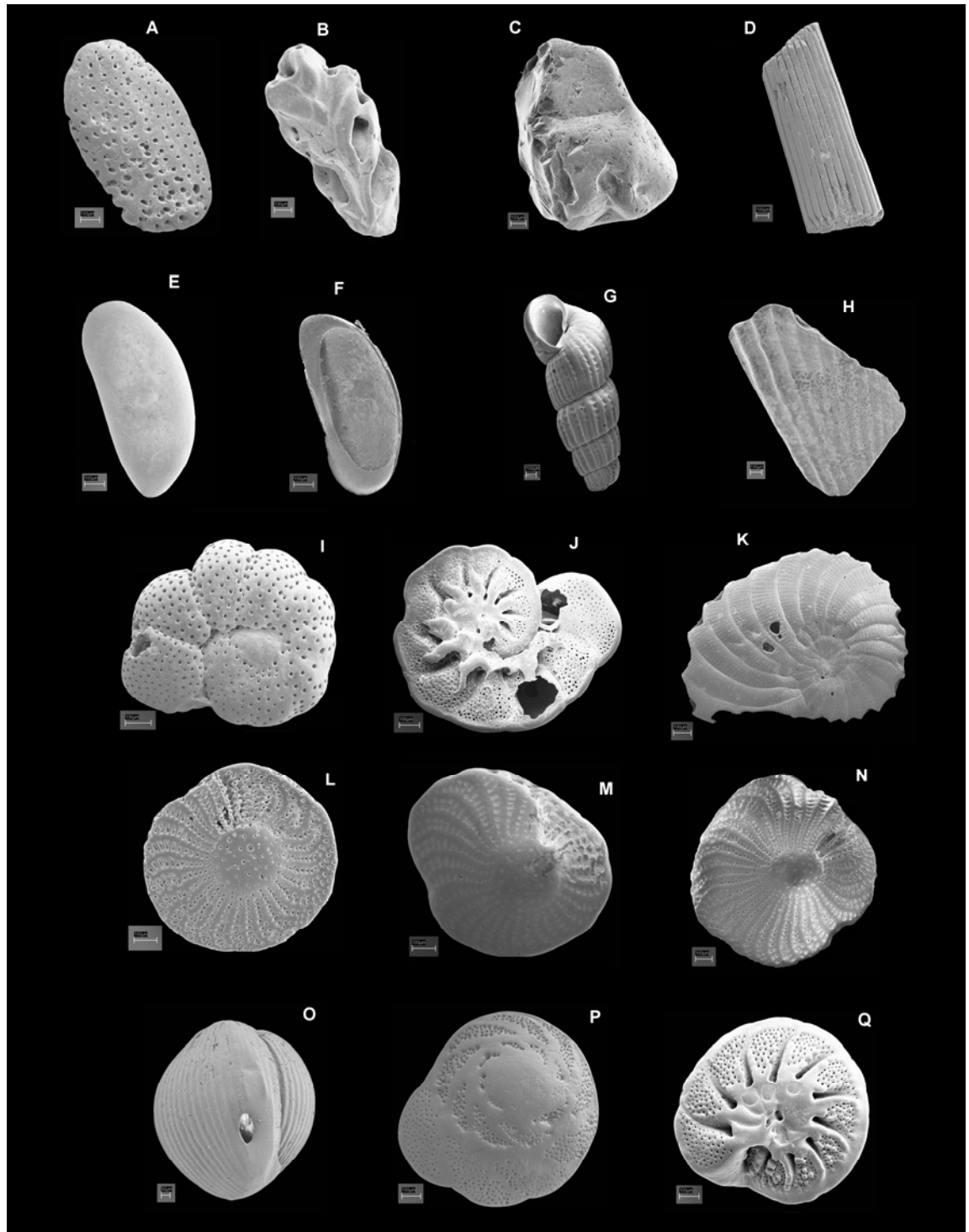


Figure 6.9: Scanning electron microscope images of constituent grains and foraminifers commonly found in Kangaroo Island aeolianite and marine deposits. A. Calcareous algae. B. Bryozoan fragments. C. Quartz grains. D. Echinoderm fragments. E and F. Ostracoda (interior and exterior). G. Small gastropods (*Batillaria* spp. [Benson] 1842). H. Comminuted shell. I and J. *Ammonia Beccarii* (dorsal and ventral) (Linne') 1758. K. *Peneroplis planatus* (Fichtel and Moll) 1798. L and M. *Elphidium macelliforme* (McCulloch) 1981. N. *Elphidium crispum* (Linne') 1758. O. *Triloculina* spp. (d'Orbigny), 1826. P and Q. *Discorbis dimidiatus* (dorsal and ventral) (Parker and Jones) 1862. The grayed bars represent 100 μm .

to ensure that an unexposed sample would be collected. Usually a few hundred grams of sediment was taken from each unit—foraminifers were also picked from these samples for single grain AAR analysis.

Aeolianite whole-rock samples were strategically selected to establish the timing of aeolianite deposition around the island (using OSL numerical ages and the degree of racemization in amino acids as a framework for relative age), and to distinguish depositional aminozones within the stacked units.

6.4.4.3 Foraminifer samples

Field criteria are not applicable to foraminifers given the difficulty of identifying them at the genus level. Foraminifers were, however, carefully selected for analysis using the following laboratory criteria. Although it was not always possible to unambiguously identify well-preserved individuals from given samples:

- i) Poorly preserved individuals, those that were obviously contaminated, or those that exhibited a yellow-brown colouring (possibly due to tannin or iron oxide [FeO] and iron sulphide [FeS₂] staining) were not selected for analysis.
- ii) Individuals that were characterised by extensive surficial cements were also excluded from analysis (or if nothing else was available a 2 M HCl etch was used to remove cements coating the surfaces of the tests—this was done in a batch).
- iii) Intact entire individuals, with little or no abrasion, or dissolution (wherever possible) were favoured for analysis.
- iv) Preference was given to samples from a single genus where possible (in this study *Elphidium* spp. and sometimes *Discorbis dimidiatus* were utilized—Figure 6.9). These are both benthic foraminifers that were present in almost every whole-rock sample. Although, *Discorbis dimidiatus* was generally the most abundant and the most common. Nevertheless, *Elphidium* spp. were preferred for their more robust test structure.

The strategies for analysing foraminifers were essentially the same as for whole-rock samples, i.e., to establish the depositional timing of aeolianite deposits. Additionally, the single grain analyses would also shed light on the mixing characteristics of aeolian and marine sediments, in terms of reworked materials.

6.4.5 Sample preparation and hydrolysis

Preparation of molluscan shells, whole-rock samples, and foraminifers for AAR analysis is given in Appendix D and generally follows procedures (with some modifications) outlined by Kaufman and Manley (1998), Hearty and Kaufman (2000), Kaufman (2000), and Hearty *et al.* (2004). In summary, however, molluscs were placed either in small beakers or culture tubes filled with purified (Millipore) water (H_2O) and initially cleaned in a sonic bath for 10 min. Then, using a dental drill, adhering impurities and diagenetically altered surfaces were removed. Large specimens were selectively subsampled from the umbo or hinge region (bivalve), or the aperture (gastropod) (Figure 6.6). For small specimens commonly the entire individual was processed. The individual or subsample shell was then cleaned further in a sonic bath for 10 min, washed in 3-4 volumes of purified (Millipore) water (H_2O), then air dried in sterile plastic dishes. The dried shells were then subjected to a 2 M hydrochloric acid (HCl) etch (to remove modified or leached carbonate). This is stoichiometric in that 33% of outer shell was dissolved.

The remaining shell was subsequently washed again then immersed in either 3% hydrogen peroxide (H_2O_2) for 2 hr or 12.5% sodium hypochlorite ($NaClO$) for 24 hr, depending upon the condition and probable age of the shell. This step removed the non-indigenous organic fraction.

A 12.5% $NaClO$ oxidation step was introduced when AAR analyses performed on *some* of the older samples (e.g. considered to be of early Pleistocene age) of shell and whole-rock sediments were found to return anomalously low D-L ratios, with corresponding high concentrations of L-SER. Clearly the conventional pretreatment step was not effective in removing contaminants in these samples, as indicated by the presence of significant quantities of L-SER,

which should have been degraded in shells and sediments of such antiquity. Following Sykes *et al.* (1995) and Penkman *et al.* (2007, 2008), a bleach step was trialed on whole shell fragments (rather than powdered shell, as the object was not to isolate an intracrystalline organic fraction but to remove adsorbed non-indigenous residues) recovered from a raised pebble/cobble beach at Smith Bay (see Chapter 3, section 3.6.4). The experiment used 6 x *Mactra* sp. (3 x NaClO and 3 x H₂O₂) and 10 x *Irus* sp. (5 x NaClO and 5 x H₂O₂). The results of the trial are presented in Figure 6.10. Replacement of the peroxide bath with an extended strong bleach soak had unambiguous, beneficial results: lower concentrations of L-SER (between 50% to 90% lower), and more stable (and realistic) D-L ratios (ranging from [individual fragment D/L results] 0.809 to 0.953 for GLX in both genera: see Table 6.2 for compiled

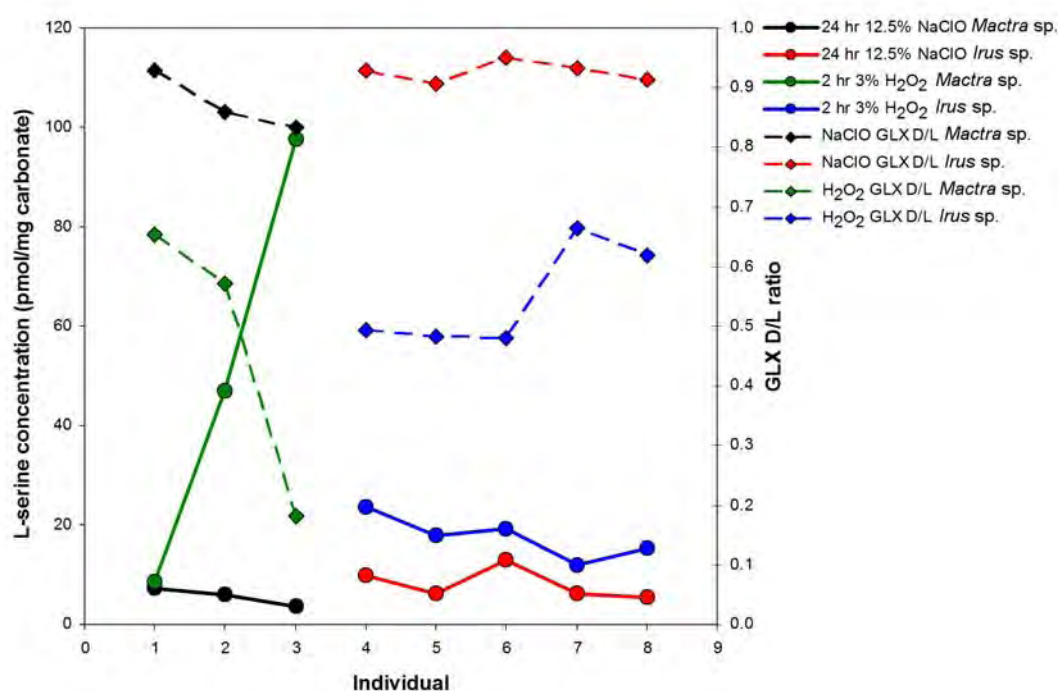


Figure 6.10: L-SER concentration characteristics and GLX D-L ratio data for *Mactra* sp., and *Irus* sp. recovered from a raised pebble/cobble beach at Smith Bay, Kangaroo Island. Two pretreatments were used (5 x *Irus* sp., and 3 x *Mactra* sp. for each treatment), 2 hr 3% H₂O₂, and 24 hr 12.5% NaClO. These treatments are designed to oxidise non-indigenous organic material adsorbed onto the shell structure (or foraminifer test, or whole-rock grains). The object of this experiment was to test the hypothesis that, based upon the work of Sykes *et al.* (1995) and Penkman *et al.* (2007, 2008), a 24 hr 12.5% NaClO soak (on solid shell, not powdered) would be a superior pretreatment (for older material) to a 2 hr H₂O₂ soak, for removing non-indigenous organic material. This plot demonstrates that shell material treated with NaClO yields a higher (considering the probable early Pleistocene age of the Smith Bay deposit, this is expected) and more stable set of GLX D-L ratios, and much lower concentrations of L-SER, when compared with the H₂O₂ treatment. The dashed lines with diamond symbols correspond to the RH y-axis (D-L ratio), and the solid lines with circles correspond to the LH y-axis (concentration).

Table 6.2: Pretreatment experiment results for Smith Bay molluscs.

Lab number	Site / sample code	Genus / species (N) ^a	GLX D-L ratio $\pm 1\sigma$ (H ₂ O ₂) ^b [CV] ^c	GLX D-L ratio $\pm 1\sigma$ (NaClO) ^b [CV] ^c
UWGA 5027, 7000	Smith Bay / SB#1-3	<i>Mactra</i> sp. (3, 3)	0.469 \pm 0.252 [54]	0.874 \pm 0.046 [5]
UWGA 5028, 7001	Smith Bay / SB#1-4	<i>Irus</i> sp. (5, 5)	0.548 \pm 0.087 [16]	0.926 \pm 0.019 [2]

^a Number of individual fragments used in each experiment

^b Pretreatment method

^c Coefficient of variation (%)

results). Conversely, the H₂O₂ oxidised shell results show higher concentrations of L-SER and unstable (*Mactra* sp. particularly so) D-L ratios (ranging from [individual fragment D/L results] 0.182 to 0.665 for GLX in both genera).

These data reveal a correlation (and covariance) between high concentrations of L-SER and lowered D-L ratios. The results of this trial suggest that an extended strong bleach step can be used to improve AAR reproducibility. This alternative was also used on marine shell and whole-rock samples from the type section of the Point Ellen Formation at Point Ellen (Vivonne Bay), and whole-rock samples from Kelly Hill Caves with similar results. Since the use of this oxidation step produced such encouraging results, it was henceforth used on all sample materials where there was suspected contamination and/or the material was of possible great antiquity.

After the oxidation step shell samples were washed in 4 volumes of purified (Millipore) water (H₂O) and air dried once more (if a 12.5% bleach step was used then there was a subsequent wash in 100% methanol to remove any remaining bleach from the sample). Shell mass was determined (mg), then the shells were placed in reaction vials and dissolved in an appropriate amount of 8 M HCl; again the amount used was a stoichiometric volume which yielded a 7 M HCl solution upon complete dissolution of the shell carbonate. This solution contains the liberated shell organic residues, and free amino acids (FAA). The vials were sealed under an N₂ atmosphere (to prevent oxidation of the organic components during hydrolysis) and the solution hydrolysed in an oven for 22 hr at 110 °C. The hydrolysis step induces a small amount of racemization as can be seen in hydrolysed live-collected (*t*₀) *Katelsia scalarina* (e.g., GLX D/L:

0.046 \pm 0.004), detailed in the section on pyrolysis (Section 6.5). After hydrolysis the whole solution was either dried *in vacuo*, or subsampled (50 μ L) and dried *in vacuo*, then rehydrated in a 0.01 M HCl solution, with 1.5 mM NaN₃, and 0.01 mM L-Homo-Arginine (used as an internal standard to quantify amino acid concentrations, if required) at 0.02 ml per mg of shell, or the subsample volume. The rehydrated solute was subsequently placed in chromatography vials for analysis in the RP-HPLC.

The preparation process for foraminifers was similar, except the acid etch step was generally omitted, as it was difficult to weigh small single foraminifers accurately, and dispense the appropriate volume of 2 M HCl. Even a small error could result in sample destruction. Nevertheless, multiple foraminifers can be batch etched (as an accurate mass can be determined for the 2 M etch by weighing and etching many individuals in a batch) if deemed necessary. The cleaned single foraminifers were then placed individually in 100 μ L micro-reaction vials for hydrolysis (using a high-purity 6 M HCl solution—Sigma 84429) and subsequent RP-HPLC analysis.

Whole-rock sediment samples are processed in a similar fashion as shell, although there are some additional steps required:

- i) The whole-rock sediment sample if indurated was first gently disaggregated using a mortar and pestle. In this study samples were sieved to isolate the 250-500 μ m grain size fraction, which was used for analysis—the fall through fraction contains interstitial and surficial cements, and grains which may be representative of an older extensively comminuted component. Disaggregation was often a long process, requiring repeated gentle grinding and sieving, in order to ensure clean (free of cement) grains. The 250-500 μ m fraction was also inspected under a light microscope to determine the condition of the grains, and to check for the presence of “false grains” that may represent cement. The fraction was subsequently cleaned in a sonic bath, washed and air dried.

- ii) Before either etching or hydrolysis the percentage carbonate (by mass) for the 250-500 μm fraction was determined by acid digestion. This ensured the correct volumes of 2 M and 8 M HCl were added for etching and hydrolysis, as the whole-rock would not normally be 100% carbonate. The carbonate content of aeolianites and marine deposits examined from Kangaroo Island ranged from ~50-98% carbonate by mass, as they also contain varying amounts of quartz, feldspar, and heavy mineral grains. The mass based calculations used to determine etch and hydrolysis volumes were modified to account for the non-carbonate content, and to optimize the concentration of the organic components.

After the completion of hydrolysis although prior to vacuum drying, rehydration, and injection into the RP-HPLC, the samples were filtered (using 0.45 μm porosity, regenerated cellulose, syringe filters) to remove undissolved solids such as quartz, feldspar, and heavy mineral grains, and other inorganic particles. Filtering helps to avoid fouling of the HPLC injection needle, sample loop, and column.

6.4.6 Samples analysis numbers

The number of analyses performed on given samples was determined by:

- i) the amount of sample material, i.e., the number of high quality shells able to be collected from a site; useable foraminifers in the sample, for example, and:
- ii) RP-HPLC availability (available runtime because of high instrument demand)

For whole-rock samples no less than 2 analyses (more typically 3 or 4) were performed on each sample. This involved the processing of at least 2 subsamples (~100 mg each) for analysis. If extra runtime was available, each subsample was injected into the RP-HPLC twice. Older (early Pleistocene for example) whole-rock sediment subsamples were sometimes rehydrated at half of the hydrolysis volume. This slight method change boosts amino acid

concentrations, thereby increasing chromatogram peak resolution (i.e., greater peak area and height).

Foraminifer samples were harder to analyze as test abundances and quality were not uniform across all samples. Nevertheless, where foraminifers were present at least 5 individual tests were analysed from a sample—typically 10 or more (sometimes as many as 50) were analysed. Occasionally, in older samples where low amino acid concentration was demonstrated (and when foraminifer numbers were abundant), multiple tests (5-10) were processed in each microvial, rather than just one. This yielded a diagenetic average set of D-L ratio results from each injection. Generally it was more efficient to forgo this and just analyze a whole-rock sample.

Fossil marine mollusc shell was not exceptionally abundant at many of the raised beach sites described in this thesis, and preservation of shell was often poor, particularly at the Rocky Point, Hanson Bay, Smith Bay, and North Cape sites. Point Ellen and American River, however, were the exception to this, having some of the largest exposed, well preserved, marine shell deposits on Kangaroo Island (see Chapter 3). With shell samples at least 2 individuals were analysed, where possible. More typically 5-10 (80 were analysed from American River) individuals were analysed; although occasionally only 1 individual was available for analysis. When this occurred the subsample was injected into the HPLC several times to obtain a random uncertainty. However, between shell D-L ratio variations in the deposit is an unknown in these cases. Generally all shell subsamples were injected into the RP-HPLC twice.

6.4.7 AAR data screening—rejection criteria

Several rejection criteria were established and used to screen the RP-HPLC D-L ratio data. These screening methods were used to exclude data points that may not be representative of the “true” D-L ratio.

6.4.7.1 Abundance of serine

Serine (SER) is a rapidly racemizing, thermodynamically unstable amino acid which decomposes relatively quickly during the early diagenetic history of fossils (Wehmiller and Miller, 2000; Miller and Clarke, 2007; Kosnik and Kaufman, 2008). This is evident in the pyrolysis experiments discussed in the following sections, and empirical comparisons of amino acid concentrations made over time. Given that SER breaks down rapidly, leaving only comparatively small amounts, the presence of significant quantities in Pleistocene fossil shell, whole-rock sediments or foraminifer subsamples is indicative of contamination with non-indigenous peptide residues. SER decomposes over time via dehydration, aldol cleavage, and decarboxylation pathways into a complex series of products, i.e., other amino acids: ALA, GLY, and a suite of organic molecules: ammonia, formaldehyde, ethanolamine, and propanolamine (Bada *et al*, 1978; Walton, 1998). Because of this it is rapidly 'lost' from the system, and is only 'replaced' when there is an introduction and adsorption of non-indigenous proteins. This can happen through a number of pathways including microbial and algal growth, introduction via solution during burial (Davies and Treloar, 1977; Williams and Smith, 1977; Schroeder and Bada, 1976), and laboratory contamination.

Figure 6.11 and 6.12 demonstrate the loss of various amino acids over time in an isothermal heating experiment: in *Katelsia scalarina* the concentration of SER (D+L) decreases by ~98% over 56 days at 110° C; in whole-rock (modern beach sediment) it decreases by ~81%. This decrease is initially extremely rapid in *Katelsia scalarina* as SER concentration drops by ~52% in the first 24 hours of the experiment. It is not as "rapid" in the whole-rock as a major component of the beach material is reworked, and SER in the reworked component has already degraded to a degree prior to pyrolysis. Figure 6.13 shows a similar set of results derived from a set of whole-rock samples recovered from the south-east South Australia dune sequence which extends inland from the Coorong coastal lagoon (Figure 6.14). These samples were removed proximal to the original TL sample locations of Huntley *et al.* (1993, 1994) and Huntley and Prescott (2001); hence, the TL chronologies were used

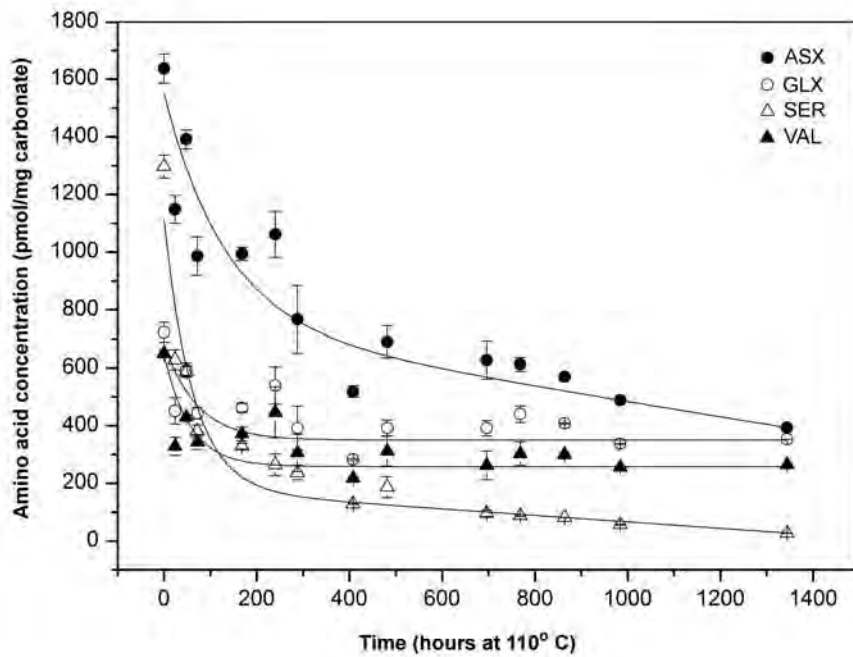


Figure 6.11: Total (D+L) amino acid enantiomer (ASX, GLX, SER and VAL) concentration data ($\text{pmol/mg carbonate}^{-1}$) for live-collected *Katelaysia scalarina* used in an isothermal heating experiment. Note the rapid decay in the concentration of both ASX and SER, although SER is considerably more rapid initially. GLX and VAL are relatively stable however. All data are fitted with exponential decay functions.

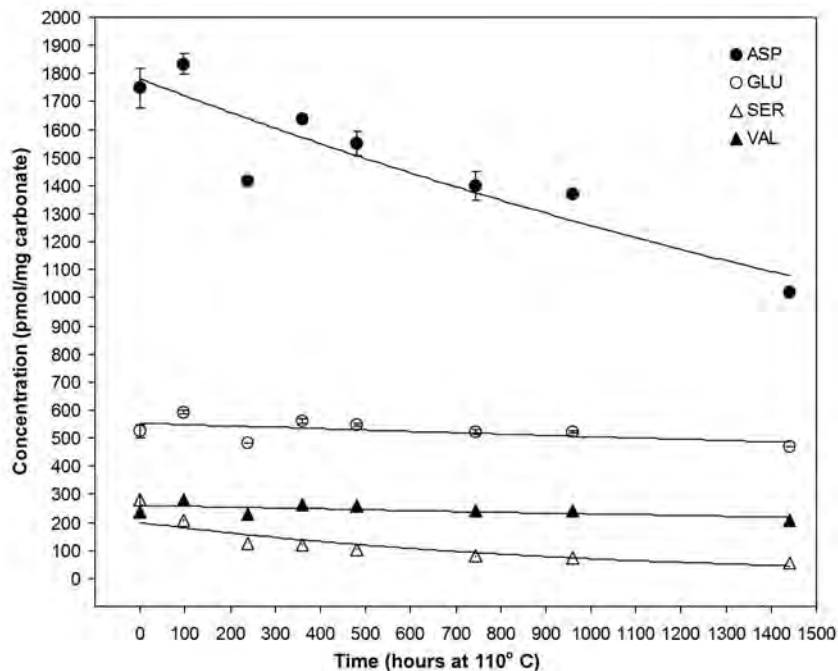


Figure 6.12: Total (D+L) amino acid enantiomer (ASX, GLX, SER and VAL) concentration data ($\text{pmol/mg carbonate}^{-1}$) for whole-rock modern beach sand from Emu Bay, Kangaroo Island, used in an isothermal heating experiment. SER concentrations are initially quite low as a significant component of the beach sand is reworked older material. All data are fitted with exponential decay functions.

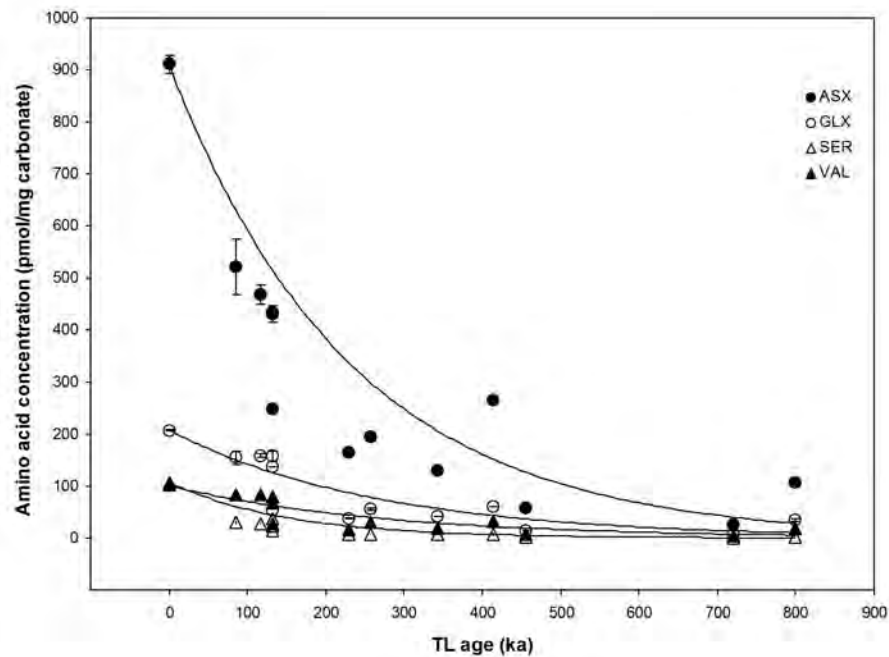


Figure 6.13: (D+L) amino acid enantiomer (ASX, GLX, SER and VAL) concentration data ($\text{pmol/mg carbonate}^{-1}$) for Pleistocene whole-rock sediment samples recovered from the carbonate aeolian dune sequence on the Coorong coastal plain, mainland South Australia—see section 6.3. These data were matched with the TL chronologies of Huntley *et al.* (1993, 1994) and Huntley and Prescott (2001) in order to examine changes in amino acid concentrations over long periods of time. All data are fitted with exponential decay functions.

to define the x-axis for Figure 6.13. The concentration values of the whole-rock sediment subsamples analysed and presented in Figure 6.13 will be slightly different to the “true” values because of the inclusion of relict grains in the sediment. Also, the TL chronology is representative of the time of deposition, and not the cessation of protein metabolism, as with AAR. Therefore, the two events do not necessarily coincide. Section 6.6, later in this chapter, fully explains this. This should be kept in mind when interpreting Figure 6.13. Nevertheless, amino acid loss over time is demonstrated. A whole-rock sediment sample from the modern beach at Guichen Bay was used to represent a t_0 concentration of amino acids. Similar to the pyrolysis experiments (Figure 6.11 and 6.12) the concentration of SER in the 800 ka sample from the Coorong (Figure 6.13) is less than 2% of the modern concentration.

In light of the relatively rapid decomposition of serine, a simple cutoff method was adopted for use as a rejection criterion. Given that any modern

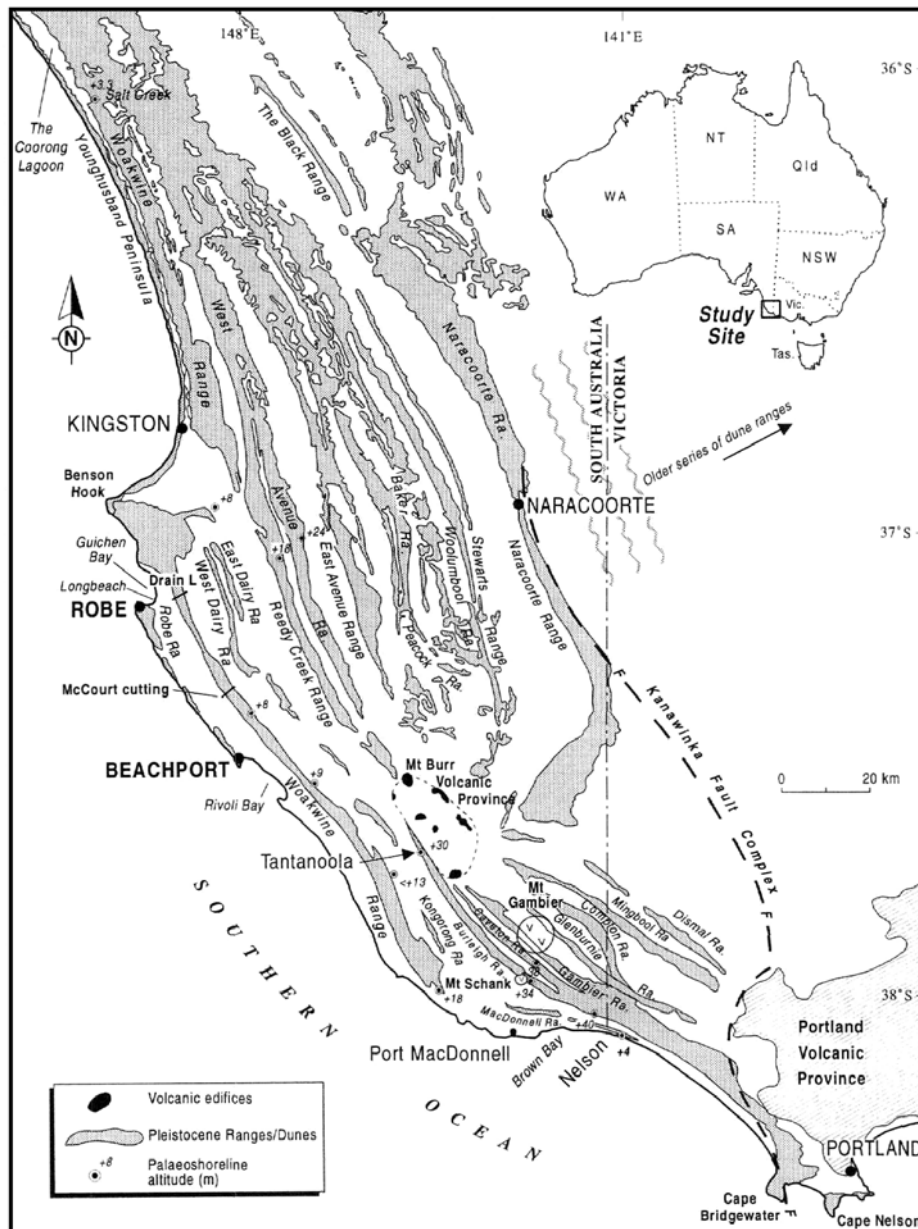


Figure 6.14: Coorong coastal region showing the location of a series of Pleistocene dune barriers, that were the subject of the TL dating work undertaken by Huntley *et al.* (1993, 1994), Huntley and Prescott (2001), and the OSL work of and Banerjee *et al.* (2003) (from Murray-Wallace *et al.*, 2001).

non-indigenous residues introduced into a system would be composed primarily of L-amino acids, a very low SER D-L ratio (in Pleistocene materials: molluscs, foraminifers, or whole-rock sediment) will be indicative of contamination. Here a cutoff SER D-L ratio of 0.100 is used for sediment expected to be older than the Holocene (i.e. a SER ratio below 0.100 is rejected and a SER ratio over 0.100 is accepted) this is a tolerant value, a higher cutoff can be used for lower tolerance; however, the 0.100 value is effective in filtering anomalously low D-L

ratios (here GLX)—generally the incidences of sample contamination observed during this research exhibited SER D-L ratios much lower than 0.100. In combination with the cutoff criterion, chromatograms were inspected for each subsample (or single foraminifer) and a large L-SER peak in an older (Pleistocene) subsample chromatogram is an effective indicator of contamination. Figure 6.15 (a and b) shows chromatograms from a contaminated foraminifer subsample, and an uncontaminated subsample (both are individual *Discorbis dimidiatus* from the same Pleistocene aeolianite deposit at Pennington Bay, Kangaroo Island), note the L-SER peak in the contaminated subsample, and also note the covariance of ASX and GLX with a low SER D-L ratio.

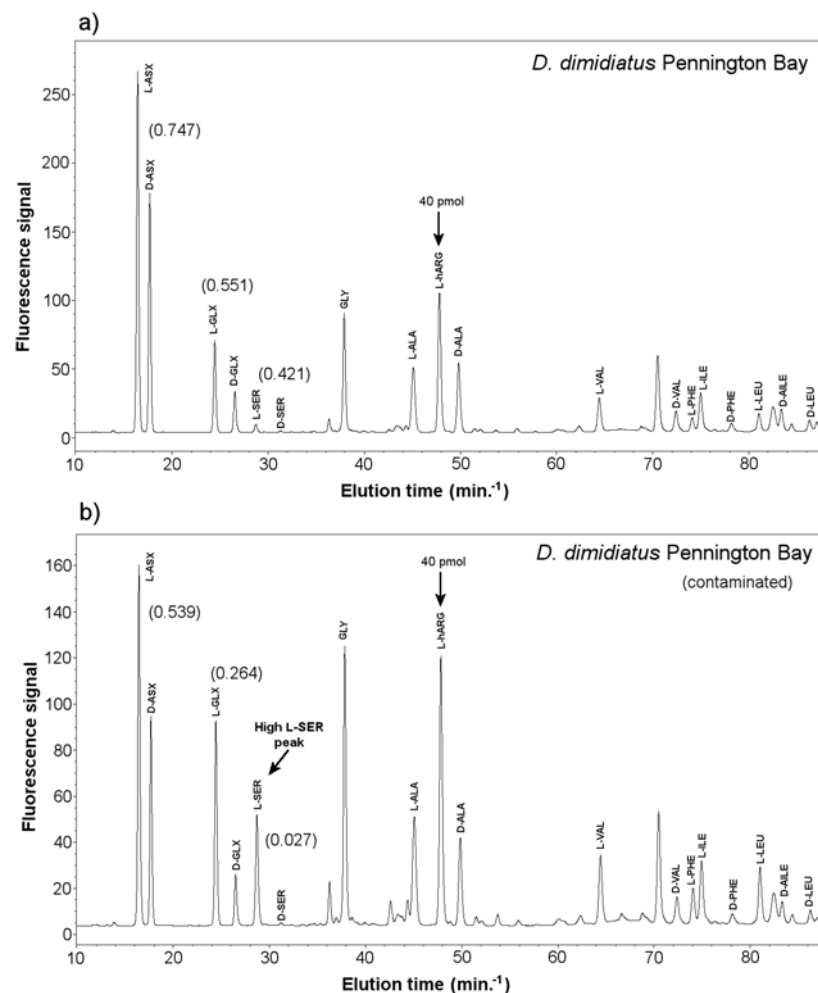


Figure 6.15: Chromatogram traces for two individual *Discorbis dimidiatus* foraminifers recovered from a middle Pleistocene aeolianite (PB#2a-4) at Pennington Bay, Kangaroo Island. a) A relatively uncontaminated sample and b) a sample considered to be contaminated because of the area and height of the L-SER peak, and the corresponding very low SER D-L ratio. The decimals in parenthesis are the D-L ratios (area integration) for ASX, GLX and SER (traces generated by Agilent Chemstation software Rev. A. 10.02 [1757] 1990-2003).

Holocene molluscs and foraminifers exhibit generally high SER D-L ratios (ranging from 0.6 to 0.8 in molluscs from American River, and 0.2 to 0.5 in foraminifers from Hanson Bay), this is due to rapid SER racemization. In combination with this there are still high concentrations of both L- and D-SER enantiomers, as much of the SER has not degraded. In relatively uncontaminated Pleistocene samples most of the SER *has* degraded. Sometimes the inclusion of insignificant amounts of non-indigenous residues results in a somewhat low SER D-L ratio; however, this rarely results in a D-L ratio lower than 0.100, and the SER peaks are still comparatively small. Nonetheless, the cutoff criterion should always be used in conjunction with a chromatogram inspection.

6.4.7.2 Outlier D-L ratio values

The general aim of aminostratigraphic studies is to resolve the central tendency of a group of D-L ratios in order to determine the best age estimate for a stratigraphic unit (Kosnik and Kaufman, 2008). Hence, in this study, when any D-L ratios from a given sample group fell outside of 2σ of the mean of the group they were excluded from the dataset (Figure 6.16). This can account for (in the case of single grain and shell analysis when many individual foraminifers or molluscs from the same stratigraphic unit were analysed) the presence of reworked (very high D-L ratios) or even contaminated materials (very low D-L ratios) that fall within the acceptable L-SER criterion. However, sometimes sample groups show D-L ratio clustering, exhibiting two or more distinct populations. Where this was identified, Ward (1963) method cluster analysis was employed to define the 'youngest' (lowest D-L ratio cluster) population in the sample; the mean of this population was then used in the numeric age calculation. The outlier rejection criterion was used only on foraminifer datasets and was not used to filter whole-rock sediment D-L ratios because only small sets of subsamples were analysed.

6.4.7.3 Amino acid covariance

There is a mutually consistent covariance in the increasing extent of racemization with increasing fossil age across the range of amino acids resolved using the RP-HPLC method. This cohesive nature is demonstrated in

the ASX/GLX relationship, illustrated in Figures 6.17a,b and 6.18. These foraminifers, whole-rock sediments, and mollusc subsamples were collected from an array of sites around Kangaroo Island and represent ages that range from modern to early Pleistocene. The covariant trend demonstrated by these data can be used to discard individual foraminifer D-L ratios, whole-rock sediment D-L ratios or mollusc D-L ratios, derived in later analyses, that fall outside of the trends—in this case outside of the 95% predictive bands (cf. Laabs and Kaufman, 2003).

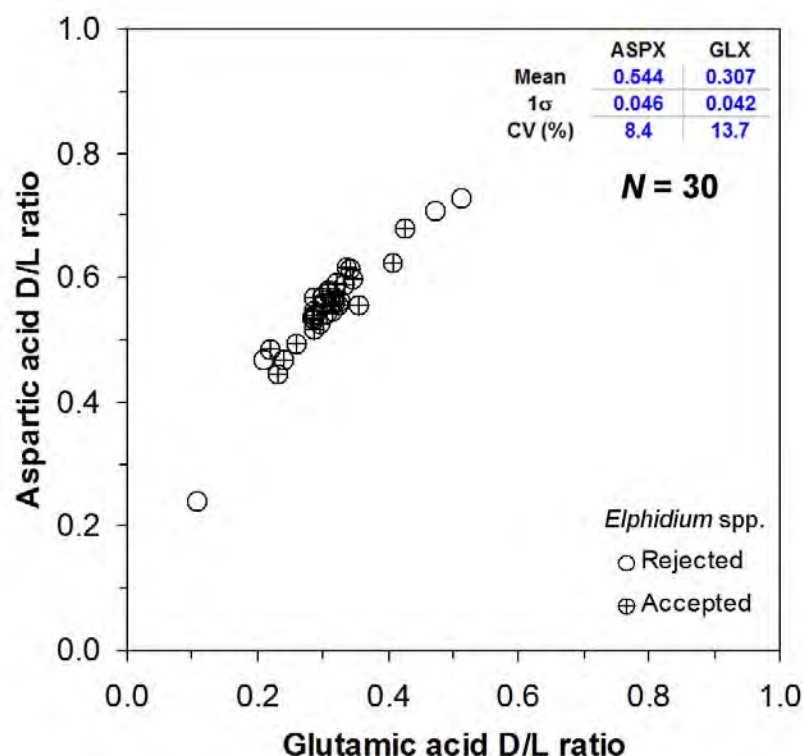


Figure 6.16: Bivariate plot of a group of single grain (*Elphidium* spp. recovered from raised pebble beach sediment at Pennington Bay) showing D-L ratios (ASX and GLX) that were subjected to a 2σ filter, and the SER D/L rejection criterion. The central group is designated by crossed circles (the upper right inset are the statistical data for the D/L set). Those data points that lay outside of the 2σ range, or were rejected on the basis of L-SER, are designated by open circles. In this set of D-L ratios 4 data points were rejected from the original 34. The higher and lower D-L ratios may represent reworked grains and contaminated grains respectively. The unfiltered results yielded very similar means for the sample set (ASX 0.554 and GLX 0.311); however, the errors were not as low, e.g., ASX and GLX CVs of 15% and 23%, as opposed to 8% and 14% for the filtered set. This dataset seems to have at least 3 populations of grains; in this instance Ward method cluster analysis may be the better option for determining the age.

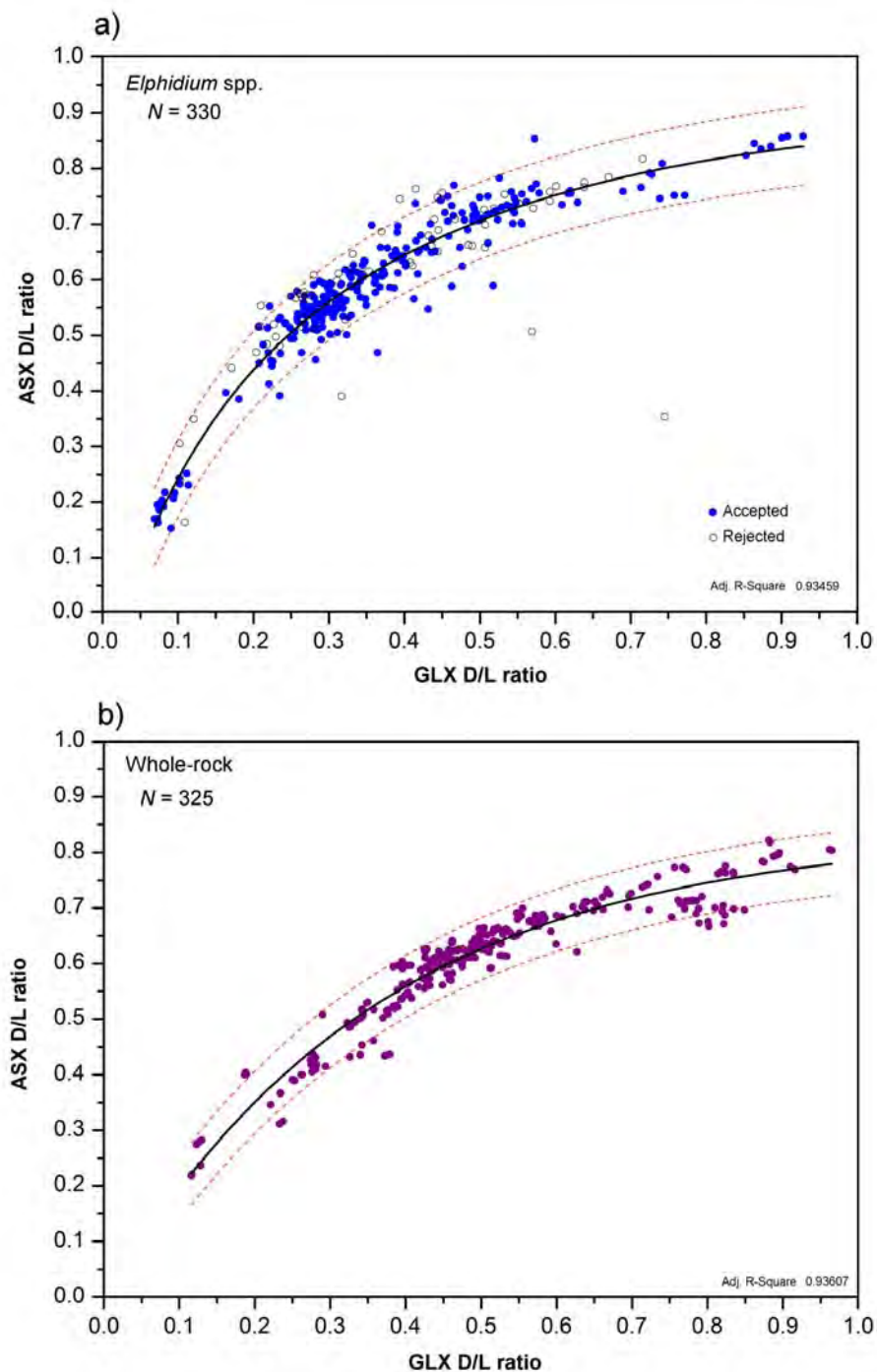


Figure 6.17: The covariant relationship between ASX and GLX is explored in plot a) and plot b) for the foraminifer *Elphidium* spp. and whole-rock sediment. Each dataset contains all individual analyses (+repeat injections) for the particular material recovered from Kangaroo Island sedimentary successions. Both datasets are fitted with exponential functions; the red dashed lines represent 95% predictive bands. In plot a) the open circles signify data points that were rejected on the basis of i) very low SER D-L ratios (<0.100) or ii) being positioned 2σ outside of the group mean. These data points were not included in the exponential fit. R^2 values are 0.93459 for a) and 0.93607 for b).

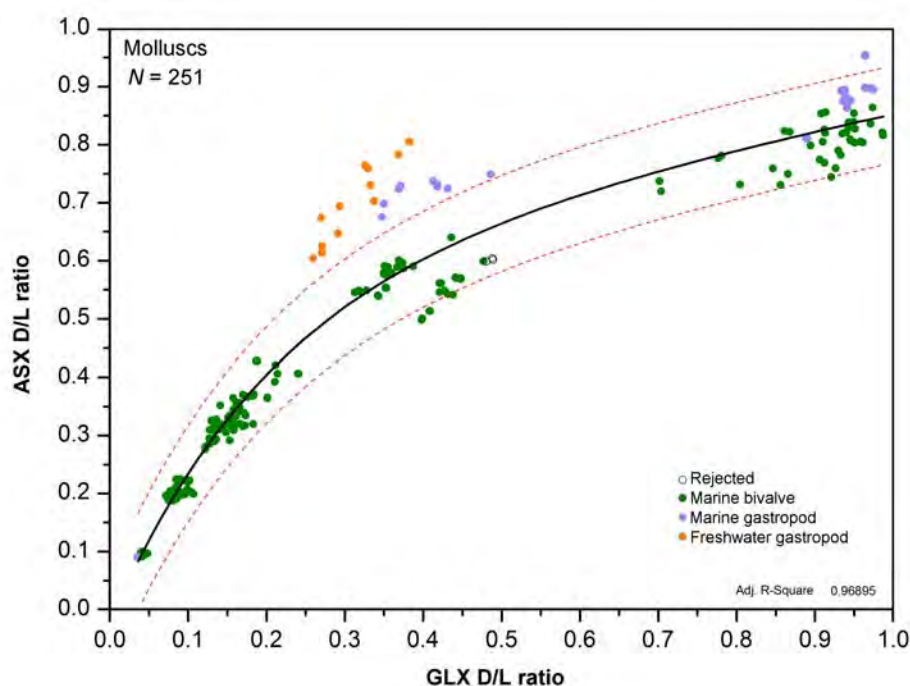


Figure 6.18: This plot is similar to those in Figure 6.15a,b, and shows ASX and GLX D-L ratio data for molluscs recovered from Kangaroo Island sedimentary successions. The orange (freshwater) and mauve (marine) points are for gastropods and the green points are for bivalves (marine). The gastropods exhibit a slightly different trend to the bivalves, as ASX appears to racemize faster in this class (at least for early diagenesis). In contrast GLX, in the gastropods, racemizes at similar rates to that of the bivalves. Represented in this dataset are all of the molluscan genera displayed in Figure 6.7. The dataset is fitted with an exponential function, and the red dashed lines signify a 95% predictive band. The R^2 value for the exponential fit is 0.96895.

6.4.8 Data reduction

The fluorescence signals derived from the various amino acids resolved using the RP-HPLC method are calibrated (based upon elution times) and integrated using Chemstation software (Rev. A. 10.02 [1757] 1990-2003) and the appropriate macros (section 6.4.1). The software displays the amino acid “signals” as peaks above a baseline (which represents the threshold “noise” level). The software integrates both peak-areas and peak-heights, and automatically defines the baseline limits of the integrations—these limits can also be adjusted manually if required—each peak base on the chromatograms generated for this study was inspected to ensure correct integration. Accordingly, the strength of the fluorescence signal (related to amino acid concentration) for a given amino acid enantiomer is an important factor when deciding whether to use either peak-area or peak-height for reporting. Since small peaks are subject to larger errors (uncertainty related to the effect of

baseline “noise” on the beginning and end of the peak) when using peak-area integration it may be prudent to use peak-height integration in this instance, as it is not as susceptible to this problem (Wehmiller and Miller, 2000). In this study peak-height integration was generally reported when the L-amino acid height was lower than 50 fluorescence (lux) units (LU) (see Figure 6.13 for scale). This was qualitative as the choice was related to observations of peak-height D-L ratio consistency in repeat injections when compared to peak-area at this level, i.e., when peak-height delivered consistently lower uncertainties (at 1σ) compared to peak-area. However, as the amino acid GLX was being used for aminostratigraphy, which was on the whole present in relatively high concentrations (i.e., >50 LU), peak-area integrations of the signals represent the greatest proportion of reported D-L ratios.

6.5 AAR kinetic studies

These following sections outline a range of pyrolysis (heating) experiments (also known as simulated aging experiments) undertaken to illustrate the kinetic behaviour of several of the suite of amino acids resolvable with RP-HPLC.

6.5.1 Pyrolysis experiments

Before deciding which amino acid was most appropriate for aminostratigraphic studies on Kangaroo Island, a range of kinetic experiments and amino acid comparisons were undertaken using marine molluscs, modern beach sediment (whole-rock sediment) and benthic foraminifers:

6.5.1.1 Experiment #1: Isothermal pyrolysis of the marine mollusc *Katelsysia scalarina*

This was an isothermal pyrolysis experiment (run at 110 °C) using live-collected marine mollusc shells (*Katelsysia scalarina*: Figure 6.7). This experiment was undertaken to compare the kinetic behaviour of several total hydrolysable amino acids (THAA—composed of “free” amino acids [FAA], and inter- and intracrystalline amino acids): ASX, GLX, SER, and VAL (all found in the carbonate matrices of marine molluscs). Several shell specimens were first

cleaned of adhering organic material and sediment, using a scalpel and dental tools, and subjected to an ultrasonic bath for 10 minutes. They were then air-dried and all of the whole-shells were ground to a medium powder using an agate mortar and pestle and mixed together thoroughly (this was to average any intershell variation [although this would be minimal as the shells were live-collected] and intrashell variation). The powder was then portioned into 42 pyrolysis tubes in 175 mg lots (mixed with 1 g of roasted [at 450 °C] quartz sand—as a substrate), moistened with purified (Millipore) water and sealed with cap and septa. The tubes were paired into 21 (Table 6.3) and heated in an oven at 110 °C for varying times prior to processing (Appendix D) and analysis. Unfortunately several samples were lost through drying (drying halts hydrolysis), due to seal failures on the pyrolysis tubes during heating. Only 13 sets were usable; however, these were enough for a viable experiment (Table 6.4).

Table 6.3: Pyrolysis experiment details for the marine cockle *Katelysia scalarina*.

Tube number	Heating time (days at 110 °C)	Oven removal date at 3.00pm on the day.
*1 a and b	0	01-08-06
*2 a and b	1	02-08-06
*3 a and b	2	03-08-06
*4 a and b	3	04-08-06
5 a and b	4	05-08-06
6 a and b	5	06-08-06
*7 a and b	7	08-08-06
*8 a and b	9	10-08-06
*9 a and b	12	13-08-06
*10 a and b	16	17-08-06
*11 a and b	20	21-08-06
12 a and b	24	25-08-06
*13 a and b	28	29-08-06
14 a and b	32	02-09-06
*15 a and b	36	06-09-06
*16 a and b	40	10-09-06
17 a and b	48	18-09-06
*18 a and b	56	26-09-06
19 a and b	64	04-10-06
20 a and b	96	05-11-06
21 a and b	128	07-12-06

*Denotes usable tubes

Table 6.4: Pyrolysis experiment D-L ratio results for ASX, GLX, SER and VAL, for live-collected *Katelsysia scalarina* from Kangaroo Island.

Sample tube	ASX D/L ¹	Uncertainty ²	GLX D/L ¹	Uncertainty ²	SER D/L ¹	Uncertainty ²	VAL D/L ¹	Uncertainty ²	Time (hrs ⁻¹)
Tube 1	0.093	0.002	0.046	0.004	0.038	0.001	0.010	0.001	0
Tube 2	0.324	0.025	0.144	0.018	0.663	0.057	0.022	0.002	24
Tube 3	0.450	0.020	0.214	0.015	0.798	0.026	0.038	0.002	48
Tube 4	0.485	0.002	0.279	0.002	0.847	0.007	0.065	0.002	72
Tube 7	0.565	0.015	0.322	0.018	0.887	0.014	0.091	0.003	168
Tube 8	0.600	0.010	0.376	0.035	0.842	0.056	0.116	0.003	240
Tube 9	0.631	0.008	0.333	0.013	0.960	0.017	0.131	0.020	288
Tube 10	0.673	0.002	0.379	0.002	0.943	0.001	0.169	0.001	408
Tube 11	0.718	0.006	0.424	0.006	1.007	0.019	0.222	0.007	482
Tube 13	0.766	0.006	0.502	0.004	1.019	0.010	0.331	0.005	696
Tube 15	0.811	0.002	0.540	0.004	1.003	0.001	0.353	0.002	864
Tube 16	0.804	0.001	0.536	0.001	0.968	0.022	0.345	0.001	984
Tube 18	0.808	0.002	0.583	0.001	0.879	0.005	0.445	0.003	1344

¹ Mean D/L value of two subsamples, injected into the RP-HPLC twice

² Uncertainty terms are 1 σ (standard deviation)

The D-L ratio results are tabulated in Table 6.3. These data were then plotted versus time in order to emphasize the differences in observable rates of reaction at 110° C, between the various amino acids. Fifty six days was the longest heating time attained, and although longer times would have been desirable the heating times up to and including this were sufficient to resolve composite forward rates of reaction for *Katelsysia scalarina* amino acids.

6.5.1.2 Experiment #2: Isothermal pyrolysis of whole-rock modern beach sediment

An isothermal heating experiment (run at 110 °C) was undertaken using whole-rock to compare amino acid kinetics as in experiment #1. This experiment was set up in a similar manner to experiment #1, although fewer time-slices were used (Table 6.5). Approximately 400 mg of thoroughly mixed modern beach sediment was added to each tube, covered with purified (Millipore) water (H₂O) and sealed with cap and septa, prior to heating at 110 °C as in Table 6.3. Modern beach sample EB#2-7 from Emu Bay was chosen for this experiment as it has the lowest set of D-L ratios of any of the modern beach samples collected on Kangaroo Island. Ideally a whole-rock sediment pyrolysis sample would contain only biogenic grains from (relatively) recently deceased

organisms; however, even modern beach sand has older, reworked, biomineral components. Hence the moderately high set of t_0 D-L ratios (Table 6.6) when compared to live-collected molluscs, for example (Table 6.4). This essentially means that the early rapid rates of interconversion (observed in *Katelsia scalarina*) are tempered by the presence of older biomineral components; nevertheless, the later slower rates which dominate during burial and diagenesis are still observed. In light of this the experiment is still useful.

Table 6.5: Pyrolysis experiment details for whole-rock.

Tube number	Heating time (days at 110 °C)	Oven removal date at 12.20pm on the day.
1 a and b	0	19/12/2007
2 a and b	4	23/12/2007
3 a and b	10	29/12/2007
4 a and b	15	3/01/2008
5 a and b	20	8/01/2008
6 a and b	30	18/01/2008
7 a and b	40	28/01/2008
8 a and b	60	17/02/2008

Table 6.6: Pyrolysis experiment D-L ratio results for ASX, GLX, SER and VAL, for biogenic carbonate modern beach sand (whole-rock) from Kangaroo Island.

Sample tube	ASP D/L ¹	error ²	GLX D/L ¹	error ²	SER D/L ¹	error ²	VAL D/L ¹	error ²	Time (hrs ⁻¹)
Tube 1	0.262	0.001	0.170	0.001	0.306	0.003	0.179	0.002	0
Tube 2	0.392	0.001	0.227	0.001	0.551	0.005	0.227	0.001	96
Tube 3	0.494	0.002	0.313	0.001	0.663	0.016	0.324	0.003	240
Tube 4	0.526	0.001	0.341	0.001	0.695	0.000	0.355	0.001	360
Tube 5	0.559	0.001	0.374	0.001	0.714	0.005	0.390	0.002	480
Tube 6	0.621	0.003	0.459	0.004	0.676	0.023	0.496	0.006	720
Tube 7	0.622	0.002	0.458	0.002	0.664	0.004	0.507	0.000	960
Tube 8	0.663	0.002	0.503	0.005	0.581	0.072	0.569	0.022	1440

¹ Mean D/L value of two injected subsamples

² Uncertainty terms are 1 σ (standard deviation)

6.5.1.3 Experiment #3: Isothermal pyrolysis of the foraminifer *Elphidium crispum*

A single temperature heating (pyrolysis) experiment using foraminifers recovered from the remaining EB#2-7 modern beach sample—in this case *Elphidium crispum*—to compare amino acid kinetics as in experiment #1 and #2. This experiment was set up in a similar manner to experiment #2; although here 3 foraminifers were placed in each tube and a substrate was not used. Duplicate tubes were also not used as the species had a relatively low abundance in the sediment. As a result only 3 per pyrolysis tube were used. However, each specimen was chosen carefully on the basis of clarity and condition, i.e., only transparent/translucent and unabraded individuals were used (see Figure 6.19 for examples).

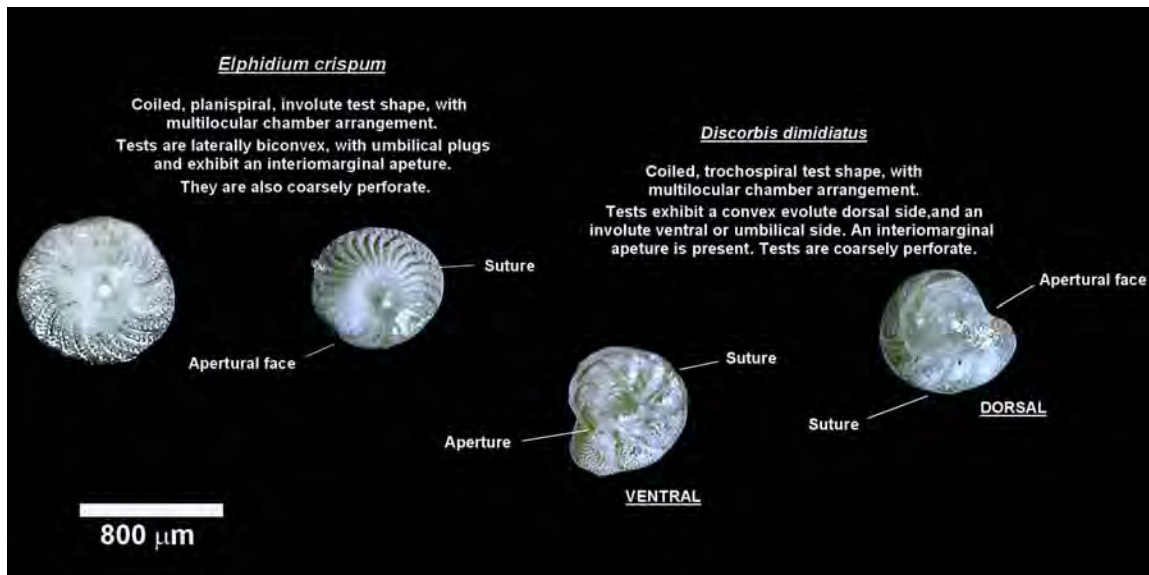


Figure 6.19: Examples of pristine (transparent/translucent, unabraded individuals of *Elphidium crispum* and *Discorbis dimidiatus*) benthic foraminifers, from modern beach sample EB#2-7, used for heating experiments and t_0 values in age calibration (photographed through a light microscope at 100x magnification).

The reasoning for this was that these pristine foraminifers would most likely be modern, relatively recently deceased individuals. Hence, the results, on this taphonomic basis, should be of high quality. The specimens were then pyrolyzed as in experiment #2 (Table 6.7). The results for this pyrolysis experiment are given in Table 6.8. Due to runtime constraints, this set of foraminifers was analysed using a “short” RP-HPLC method which only resolves ASX, GLX and SER (the method only allows for a 30 min elution time).

When using this RP-HPLC method it is also not possible to quantify amino acid concentrations as the elution time is insufficient to capture the L-Homoarginine internal standard peak (~45 min. elution time) (Figure 6.15). Quantification was not entirely the object of these experiments, and those experiments that did determine the full suite of amino acids were sufficient in resolving questions concerning amino acid concentrations (this will be discussed later in this section).

Table 6.7: Pyrolysis experiment details for *Elphidium* sp. It should be noted that even though this experiment was started earlier than the whole-rock experiment; the whole-rock subsample used was removed prior to picking for foraminifer tests.

Tube number	Heating time (days at 110°C)	Oven removal date at 10.40am on the day.
1	0	08/12/2007
2	4	12/12/2007
3	10	18/12/2007
4	15	23/12/2007
5	20	28/12/2007
6	30	07/01/2008
7	40	17/01/2008
8	60	06/02/2008

Table 6.8: Pyrolysis experiment D-L ratio results for ASX, GLX, and SER, for *Elphidium* sp. extracted from modern beach sand sample EB#2-7, from Emu Bay, Kangaroo Island.

Sample tube	ASP D/L ¹	error ²	GLX D/L ¹	error ²	SER D/L ¹	error ²	Time (hrs-1)
Tube 1	0.184	0.041	0.098	0.021	0.257	0.046	0
Tube 2	0.266	0.016	0.130	0.001	0.271	0.041	96
Tube 3	0.337	0.001	0.182	0.000	0.356	0.034	240
Tube 4	0.426	0.042	0.232	0.004	0.350	0.099	360
Tube 5	0.463	0.025	0.244	0.008	--	--	480
Tube 6	0.521	0.023	0.281	0.013	0.417	0.033	720
Tube 7	0.578	0.032	0.346	0.006	0.390	0.083	960
Tube 8	0.698	0.027	0.393	0.033	0.548	0.040	1440

¹ Mean D/L value of 3 injected samples

² Uncertainty terms are 1 σ (standard deviation)

6.5.1.4 Experiment #4: Isothermal pyrolysis of the foraminifer *Discorbis dimidiatus*

This experiment was essentially the same as experiment #3, except the foraminifers used were *Discorbis dimidiatus* (Table 6.9). Also, given that *Discorbis dimidiatus* was found to be more abundant than *Elphidium crispum* in sample EB#2-7, more could be used per pyrolysis tube. There were enough usable (same criteria as with *Elphidium crispum*) specimens to place 5 individuals per tube. Again, as with experiment 3, time constraints and high RP-HPLC demand meant that the pyrolyzed samples could only be run in the RP-HPLC using the short method. Therefore, only SER, ASX and GLX were resolved. This is acceptable since one of the main objectives of the set of experiments was to compare GLX racemization rates across marine shell, whole-rock and foraminifers (results are given in Table 6.10).

Table 6.9: Pyrolysis experiment details for *Discorbis dimidiatus*. It should be noted that even though this experiment was started earlier than the whole-rock experiment; the whole-rock subsample used was removed prior to picking for foraminifer tests.

Tube number	Heating time (days at 110°C)	Oven removal date at 12.30pm on the day.
1	0	5/12/2007
2	4	9/12/2007
3	10	15/12/2007
4	15	20/12/2007
5	20	25/12/2007
6	30	4/01/2008
7	40	14/01/2008
8	60	3/02/2008

Table 6.10: Pyrolysis experiment D-L ratio results for ASX, GLX, and SER, for *Discorbis dimidiatus*. extracted from modern beach sand sample EB#2-7, from Emu Bay, Kangaroo Island.

Sample tube	ASP D/L ¹	error ²	GLX D/L ¹	error ²	SER D/L ¹	error ²	Time (hrs-1)
Tube 1	0.156	0.068	0.057	0.015	0.205	0.074	0
Tube 2	0.322	0.020	0.167	0.036	0.623	0.049	96
Tube 3	0.387	0.009	0.187	0.013	--	--	240
Tube 4	0.434	0.012	0.244	0.003	0.616	0.013	360
Tube 5	0.445	0.017	0.256	0.024	0.528	0.311	480
Tube 6	0.509	0.042	0.291	0.018	0.550	0.057	720
Tube 7	0.507	0.017	0.324	0.023	0.505	0.113	960
Tube 8	0.578	0.026	0.382	0.013	0.537	0.097	1440

¹ Mean D/L value of 5 injected samples

² Uncertainty terms are 1 σ (standard deviation)

6.5.2 Pyrolysis results

The following sections will examine the results of the pyrolysis experiments and discuss the implications of rates of reaction in relation to particular amino acids, in this case ASX, GLX, SER, and VAL. Furthermore, through comparing changes in amino acid concentrations over time (by means of the pyrolysis experiments), the implications of amino acid loss during diagenesis will be evaluated. Each amino acid resolved for the different materials (i.e., molluscs, whole-rock sediments and foraminifers), was subjected to a model to derive the different *composite* (the rates of reaction for different amino acids change over time due to a complex of chemical reactions that take place, e.g., conversion, and decomposition) forward rates of reaction. Here a constrained power law model (cf. Goodfriend *et al.*, 1996; Kaufman, 2000; Manley *et al.*, 2000; Clarke and Murray-Wallace, 2006) is used with an exponent of 2 to define the various rates of reaction for all materials. The 2 exponent was the most consistent (through trial and error), and was applied to all pyrolysis D-L ratio data. While the 2 exponent may not have produced the best linear correlation for *all* amino acids analysed, the use of different exponents for different amino acids would not allow direct comparisons because the magnitude of the rate constant is dependent upon the exponent value used in the transformations.

Manley *et al.* (2000) prescribed the omission of ASX D-L ratios >0.500 from the power law transformation as they found that the functions fit the data better (in terms of the R^2 value) within the D-L ratio range 0.0-0.5 (deviation from first-order kinetics [particularly for ASX] complicates the linear fit when ratios are over ~0.500). However, in this study the full ranges of pyrolysis D-L ratios were included in the functions. Thus, the expected D-L ratio ranges of the Holocene to Pleistocene age material encountered on Kangaroo Island would be reflected. In all cases the fits were very good, giving R^2 values generally >0.95 (mean $R^2 = 0.96 \pm 0.04$). The D-L ratios were transformed, and forward rates were determined using the following equations (cf. Kaufman, 2000; Manley *et al.*, 2000):

$$\left(\frac{1 + D/L}{1 - D/L} \right)^n \quad (6.1)$$

and

$$\left(\frac{1+D/L}{1-D/L}\right)^n - C \quad (6.2)$$

and

$$\left(\frac{1+D/L}{1-K'D/L}\right)^n = (1+K')kt + C \quad (6.3)$$

Where K' is the reciprocal of the equilibrium constant (1.0); k is the *composite* forward rate constant (yr^{-1}) at a given temperature (here 110°C); t is time (yr); n is the exponent that produced the best *overall* linearization (R^2) of the data, and C is a constant that is equivalent to the left side of the equation (6.3) at t_0 . Here C is the unheated subsample D-L ratio (transformed using equation 6.1) of live-collected *Katelsysia scalarina*, modern whole-rock sediment, *Elphidium crispum*, or *Discorbis dimidiatus*.

The slope of the least squares linear regressions performed on equation 6.2 versus t (yr) is equivalent to $2(k)$ (equation 6.3). Hence, 0.5 by the slope gives the forward rate constant (k in yr^{-1}) at 110°C (Table 6.11).

The forward rate constants are designated as *composites* because some of the modelled amino acids have an initial period of rapid racemization prior to an inflection (a break in slope), whereby the rate of increase in D-L ratio is considerably reduced. This is particularly evident in *Katelsysia scalarina* (see Figure 6.20a) for ASX, GLX, and SER: ASX inflects at a D-L ratio of ~ 0.500 , GLX at ~ 0.300 , and SER at ~ 0.900 (SER is mostly degraded at this point and is essentially at equilibrium shortly after this)—VAL has a slight inflection at ~ 0.100 . Hence, the forward rate constant (derived from least squares regression of a constrained power law model) is a *composite* of the “step” or “steps” in racemization rate that can occur. It is, in simpler terms, an average rate.

6.5.2.1 Katelsysia scalarina

The marine cockle *Katelsysia scalarina* (Lamarck) 1818, is a bivalve mollusc of the Family Veneridae (Rafinesque, 1815); the shell is obliquely oval, with a straight posterior dorsal margin (Figure 6.7). The surface of the shell is

Table 6.11: Constrained power law model composite forward rate constants (at 110 °C) for selected amino acids, extracted from *Katelsysia scalarina*, whole-rock modern beach sediment, *Elphidium crispum* and *Discorbis dimidiatus*.

Amino acid	Pyrolysis temperature (°C)	Forward rate constant (<i>k</i>) (yr ⁻¹)*			
		<i>Katelsysia scalarina</i>	Whole-rock sediment	<i>Elphidium crispum</i>	<i>Discorbis dimidiatus</i>
ASX	110	3.37 x 10 ²	6.46 x 10 ¹	8.35 x 10 ¹	3.39 x 10 ¹
GLX	110	4.23 x 10 ¹	2.25 x 10 ¹	1.17 x 10 ¹	1.05 x 10 ¹
SER	110	7.52 x 10 ³	3.00 x 10 ²	2.30 x 10 ¹	7.39 x 10 ²
VAL	110	1.79 x 10 ¹	3.51 x 10 ¹	--	--

*Calculated from the slope of a linear regression generated for a constrained power law model (exponent of 2) transformation of D-L ratio data (Figure 6.22). Note that the magnitude of the rate constant is dependent upon the exponent used in the transformation; hence, the same exponent value was used for each fit in order to allow direct comparisons of amino acid rates across each type of material (mollusc, whole-rock, and foraminifers). The 2 exponent yielded R² values that were in most cases higher than 0.95. SER rates represent the stable initial rate—see text. These fits were not forced through the origin.

sculptured with concentric lamellae that are slightly recurved (Ludbrook, 1984). *Katelsysia scalarina* generally inhabits sandy shores in the lower littoral zone (Ludbrook, 1984). This species was chosen for use in the pyrolysis experiments for its ready abundance and its frequent use in other aminostratigraphic studies (Murray-Wallace, 1995; Murray-Wallace, 2000)

The definition and separation of the amino acid D-L ratios for this mollusc was extremely good (see Figure 6.20a), and the differences in rate are quite plain, particularly during the early (up to 7 days) part of the experiment. Later, however, past the inflection points rate differences are small, relatively speaking (when compared using an apparent parabolic kinetic method for example). Figure 6.21 illustrates the D- and L-concentration differences (i.e. peak height) between *t*₀ and *t*₅₆ pyrolysis days for *Katelsysia scalarina*, particularly for L-SER, and also demonstrates diffusive loss of amino acids that occurs over time.

SER was the fastest racemizing amino acid examined in *Katelsysia scalarina*, becoming almost racemic after around 3-7 days of heating at 110° C—the lowest SER concentrations (pmol/mg carbonate⁻¹) are recorded after this point also (Figure 6.11). It remained stable at a D-L ratio of around 1.00 for the remainder of the experiment (up to 56 days) (Figure 6.20a). The forward rate for

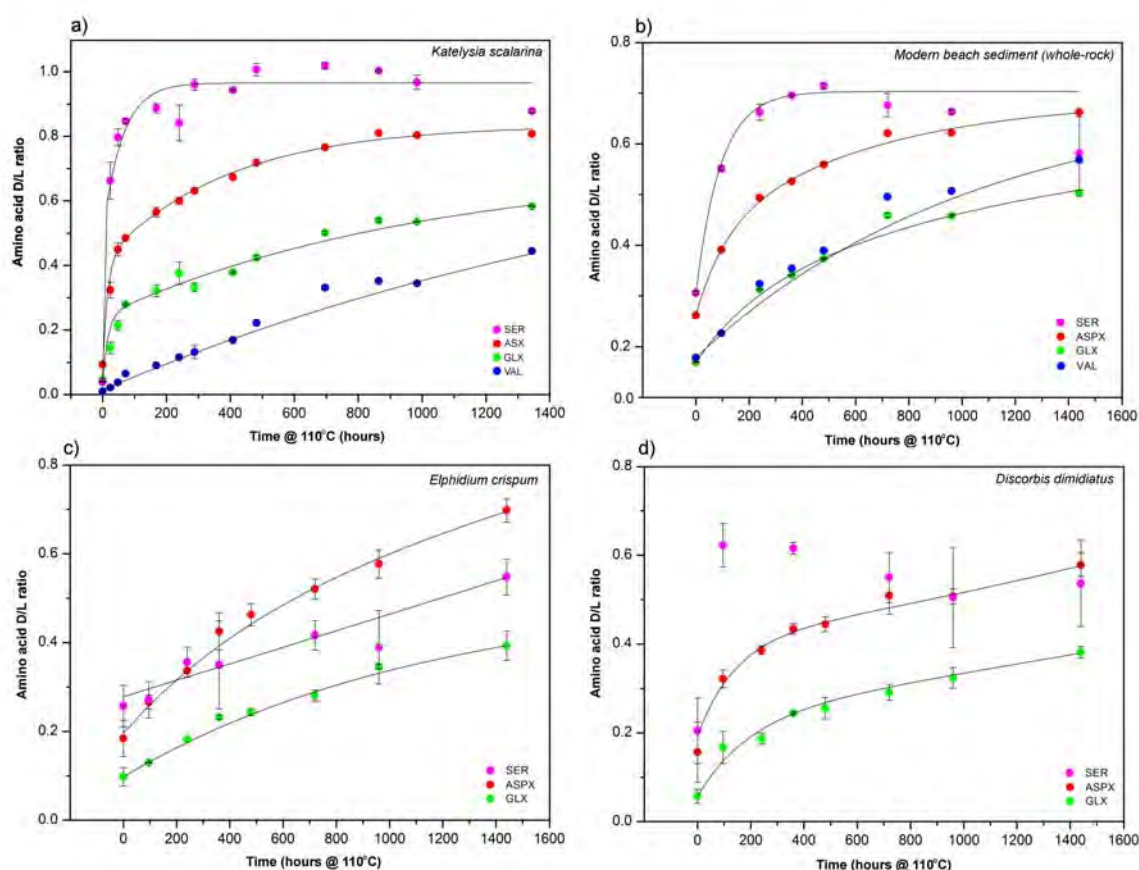


Figure 6.20: D-L ratio data from the set of pyrolysis experiments: a) Table 6.4 *Katelsysia scalarina* D-L ratio data; these data clearly illustrate the rate differences between the amino acids SER, ASPX, GLX, and VAL. All data are fit with 2-parameter exponential functions. All curves follow apparent parabolic kinetics, with a rapid initial rate of racemization, followed by a slower rate, forming an inflection point. This was a single temperature experiment set at 110° C. b) D-L ratio data from Table 6.6. Whole-rock amino acid rate differences are illustrated for SER, ASPX, GLX, and VAL. For these samples GLX and VAL have similar rates initially; however, after around 700 hr GLX apparently slows. c) D-L ratio data from Table 6.8. *Elphidium crispum* amino acid rate differences are illustrated for SER, ASPX, and GLX. The rates are slower for ASPX and GLX, in comparison to *Katelsysia scalarina*, and the curves lack the well defined inflection point. However, the absence of an inflection point may be because these foraminifers were racemized past this point prior to pyrolysis (most must have been somewhat older than modern), rather than being due to kinetic behavioral differences; although, this cannot be ruled out. All data are fit with 2 parameter exponential functions. d) D-L ratio data from Table 6.10. *Discorbis dimidiatus* rate differences are illustrated for SER, ASPX, and GLX; GLX in *Discorbis dimidiatus* is similar to *Elphidium crispum*, however, the ASPX rate is much slower.

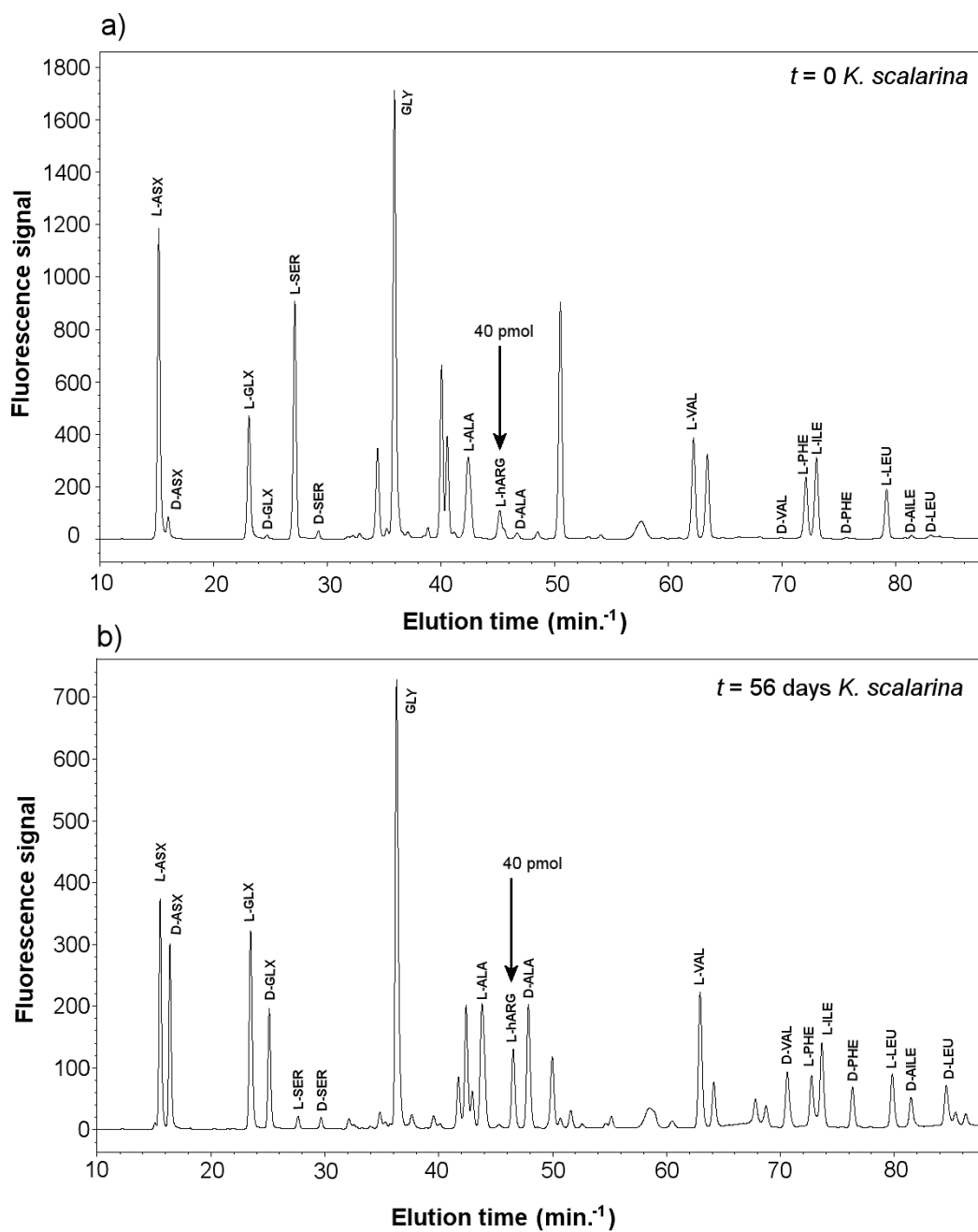


Figure 6.21: Examples of representative RP-HPLC chromatograms for a) t_0 days and b) t_{56} days, from the *Katylisia scalarina* pyrolysis experiment (traces generated by Agilent Chemstation software Rev. A. 10.02 [1757] 1990-2003).

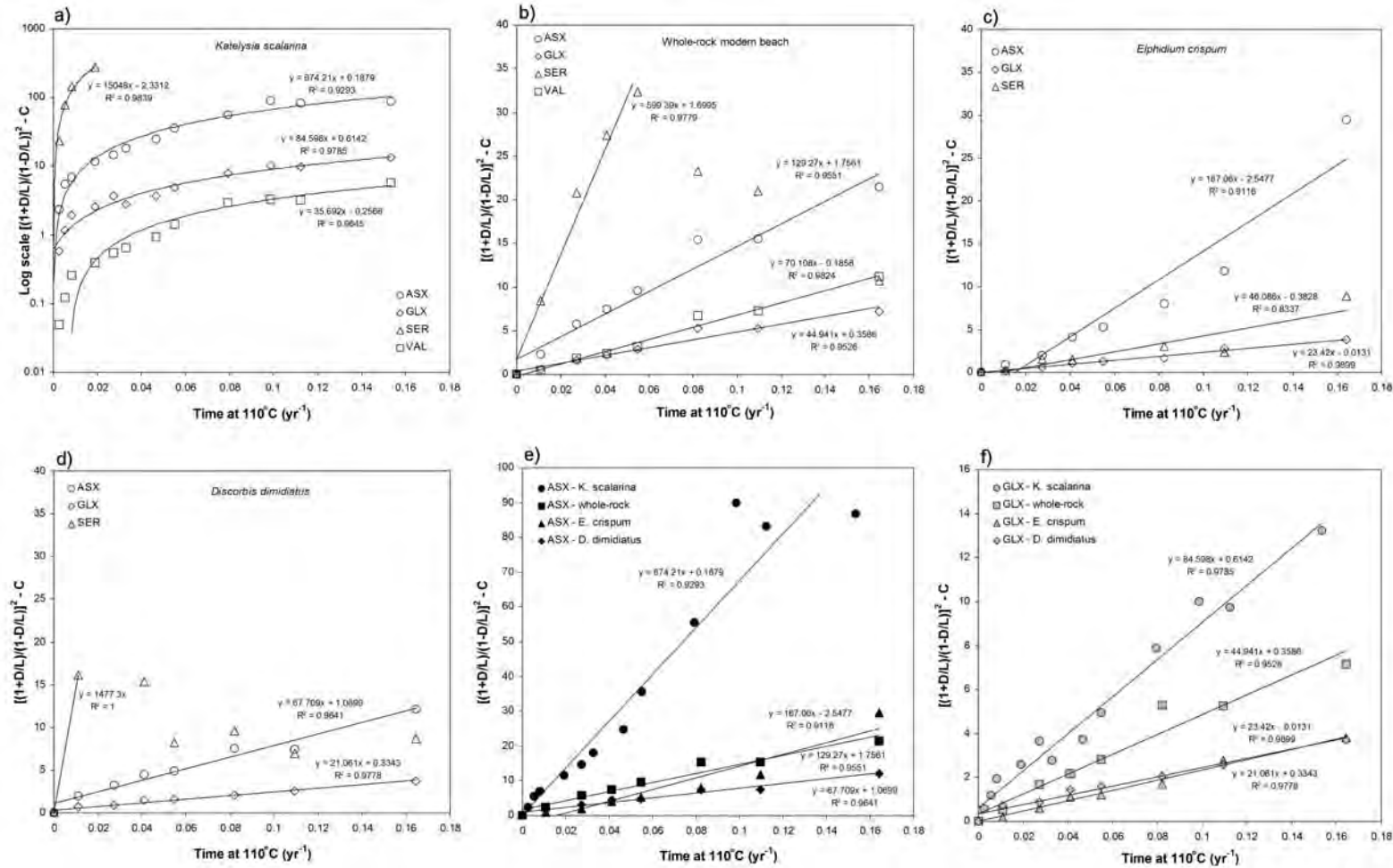


Figure 6.22: Constrained power law transformations (exponent of 2) of pyrolysis D-L ratio data: a) ASX, GLX, SER, and VAL from *Katelsia scalarina*; b) ASX, GLX, SER, and VAL from whole-rock modern beach sediment; c) ASX, GLX, and SER from *E. crispum*; d) ASX, GLX, and SER from *Discorbis dimidiatus*; e) a comparison of all ASX data, and f) a comparison of all GLX data. Explanations are in text. Pyrolysis hours were converted to years⁻¹ for forward rate convention. Plot a) uses a log y-scale for curve separation purposes.

SER was calculated from the initial 7 days of rapid racemization. The rate, from Table 6.11, is $7.52 \times 10^3 \text{ yr}^{-1}$ (Figure 6.22a illustrates the constrained power law regressions for *Katelsia scalarina*—this plot uses a log y-scale for better curve separation).

The amino acid ASX also exhibited an initial fast rate of racemization that inflected, at around 3-7 days of heating at 110 °C, to a slower rate of D-L ratio increase. The calculated forward rate constant (using all data points) was $3.37 \times 10^2 \text{ yr}^{-1}$; this is an order of magnitude slower than SER (Table 6.11).

GLX was an order of magnitude slower than ASX with a forward rate constant of $4.23 \times 10^1 \text{ yr}^{-1}$ (GLX also has an initial fast racemization rate). VAL was of the same magnitude as GLX but approximately half as fast, i.e., $1.79 \times 10^1 \text{ yr}^{-1}$ (Table 6.11)

The slower racemizing amino acids GLX and VAL were also reasonably stable chemically, in comparison to SER and ASX (see Figure 6.11). The concentration (pmol/mg carbonate⁻¹) of GLX and VAL, over the course of the pyrolysis experiment, dropped by 51% and 59% respectively (comparing the first and last concentration values), as opposed to 98% and 76% for SER and ASX. GLX and VAL remained at stable concentrations from approximately 200 hours into the experiment, whereas SER and ASX continually decrease.

Based upon these observations, the rate order for *Katelsia scalarina* amino acids examined is: SER>>ASX>>GLX>VAL.

6.5.2.2 Whole-rock modern beach sediment

Whole-rock modern beach sediments from Kangaroo Island are comprised of various biomineral grains (as well as other organic and lithic components), most of which (not including the lithic components) probably contain amino acids (see Figure 6.9). The grains are not all from recently deceased organisms, there is also a component that has been reworked from local sources (e.g. from actively eroding near-shore aeolianite deposits of various antiquities). Furthermore, the grains are not all from the same source organism, they can be a mixture of

foraminifer tests, comminuted marine shell, small whole-shells (gastropods and bivalves), echinoid fragments, calcareous algae fragments, ostracod valves, comminuted crustacean shell, bryozoans, and even vertebrate skeletal particles. Each of these types of grains will undoubtedly have characteristic amino acid kinetic behaviours. Hence, the amino acid “signals” from a whole-rock beach sediment AAR subsample will represent an integration of this range of behaviours, and an average of the age populations represented in the mixture—in terms of D-L ratios, racemization rates, and amino acid concentrations. For example, if the t_0 whole-rock modern beach sediment GLX D-L ratio (Table 6.6) is compared with the t_0 GLX D-L ratio of *Katelsysia scalarina* (Table 6.4) it can be seen that the whole-rock D-L ratio is much higher (0.170 as opposed to 0.046 for *Katelsysia scalarina*). If the biomineral constituents of the whole-rock sediment were all derived from recently dead organisms, then the D-L ratios would very probably be similar. This is clearly not the case. Reworked grains can represent a significant proportion of the constituent grains in a whole-rock sample. For example the foraminifers in a subsample of Last Interglacial (MIS 5e) sediment recovered from Vivonne Bay were found to be approximately 75% reworked (from nearby older [MIS 9] aeolianite), and this was only the foraminifers that were examined (the overall effect of the presence of reworked grains on a whole-rock sediment D-L ratio will also depend on the retention level of indigenous organic residues within the older grains) (Figure 6.23). The whole-rock modern beach sediment pyrolysis results should then be interpreted in the light of these characteristics.

SER in whole-rock sediment racemized at a much slower rate than in *Katelsysia scalarina*: $3.00 \times 10^2 \text{ yr}^{-1}$ as opposed to $7.52 \times 10^3 \text{ yr}^{-1}$ (Table 6.11, Figure 6.20b and 6.22b). This may be due to the influence of a significant proportion of older more racemized grains being present in the whole-rock sediment (i.e. SER in the older grains has in all probability racemized past the inflection point). Evidence for older grains is also present in the form of low initial concentrations of SER (279 pmol/mg carbonate⁻¹—it was 1637 pmol/mg carbonate⁻¹ in *Katelsysia scalarina*) (Figure 6.11 and 6.12); this is consistent with much of the SER in the older grains being degraded prior to heating. Only the first 5 data

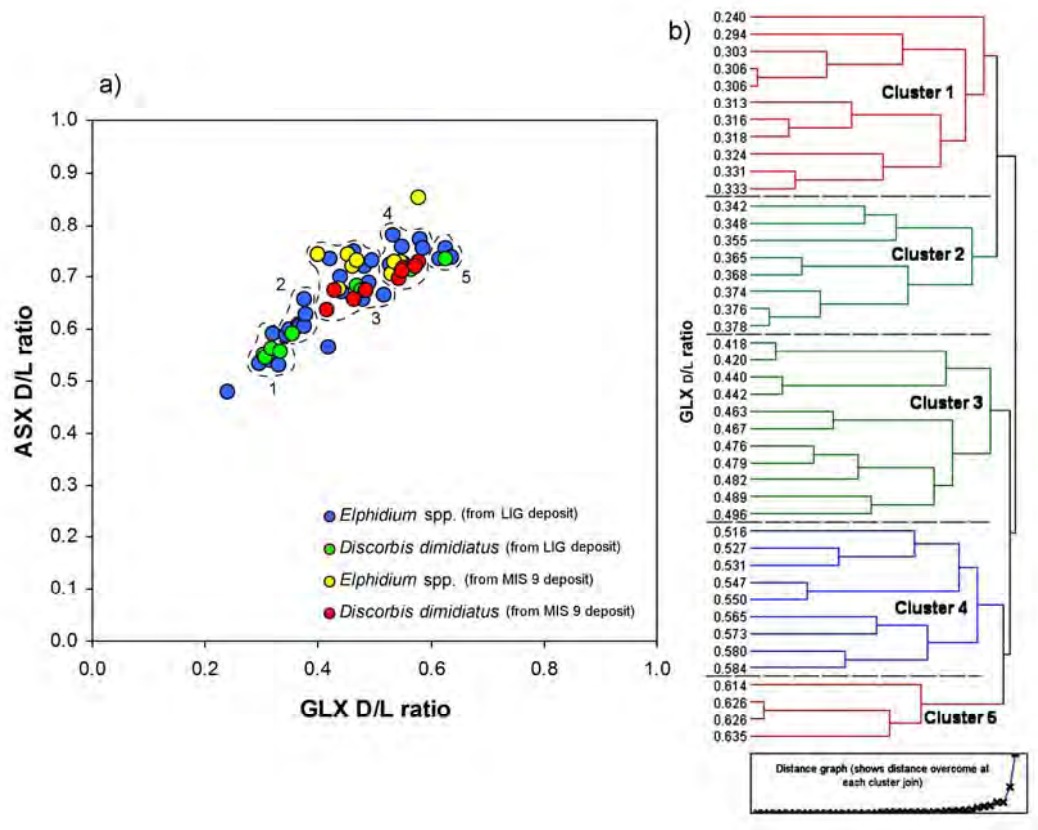


Figure 6.23: Bivariate plot a) showing ASX and GLX D-L ratio results for two genera of foraminifer recovered from two units at Vivonne Bay, Kangaroo Island. The blue and green data points are from a Last Interglacial shell bed (sample PE#3-4, 3-5, and 3-6), and the red and yellow data points are from a MIS 9 (based upon a SARTT-OSL age estimate—Chapter 7) aeolianite (sample PE#3-2). The shell beds (see Chapter 3) are plastered as stringers and lenses into gaps and notches in the lower portions of the MIS 9 aeolianite unit. The shell bed is also rich in cobbles, pebbles, and foraminifers. What is special about this site is the clear evidence that mixing of biomineral grains has occurred. Older foraminifers from the MIS 9 aeolianite have been weathered out of the face; have been mixed with younger near-shore sediments (also containing foraminifers), and have been re-deposited into wave-cut notches during the Last Interglacial. The mixing of the populations is rendered unambiguous when the MIS 9 data (red and yellow) is overlaid onto the Last Interglacial data (blue and green). The MIS 9 data clearly overlies the more racemized populations from the Last Interglacial sample. It is patent from these data that at least 5 populations of grains are present in the Last Interglacial sample, and 2 corresponding populations in the MIS 9 sample (see dashed polygons). Plot b) is a hierarchical clustering dendrogram (Ward method) used to define the different D-L ratio populations displayed in plot a). Cluster 1 in the dendrogram was also used as the calibration D/L set for the foraminifer calibration plot—see section 6.6.4.2 of this chapter.

points were used to calculate the forward rate constant for SER (up to 480 hours) as after this point SER was unstable.

The forward rate constant for whole-rock ASX was $6.46 \times 10^1 \text{ yr}^{-1}$, an order of magnitude slower than *Katelsia scalarina* ASX (Table 6.11). ASX in this sample of modern beach sediment was also more stable and in higher concentrations than in *Katelsia scalarina* (initially $\sim 1800 \text{ pmol/mg carbonate}^{-1}$ as opposed to ~ 1600 in *Katelsia scalarina*), decreasing in concentration by only $\sim 42\%$ after 60 days of heating at 110°C (Figure 6.11 and 6.12).

VAL had a slightly faster forward rate than GLX, i.e., $3.51 \times 10^1 \text{ yr}^{-1}$ and $2.25 \times 10^1 \text{ yr}^{-1}$, respectively (Table 6.11; Figure 6.20b and 6.22b). Contrary to this GLX was around twice as fast as VAL in *Katelsia scalarina*. This difference in order may be due to the integration of various kinetic behaviours manifest from the different grain types in the whole-rock modern beach sample. Also contributing to this would be the variation in D- and L-amino acid concentration across the various grain types.

The rate order for whole-rock modern beach sediment amino acids that were examined is: SER>>ASX>VAL>GLX. The position of VAL in the rate order is consistent with AAR analysis (for aminostratigraphy) results observed in whole-rock samples on Kangaroo Island: in Pleistocene samples VAL D-L ratios were generally similar to, or slightly higher than GLX.

6.5.2.3 Elphidium crispum

Elphidium crispum (Linne') 1758, is a robust foraminifer of the Family Elphidiidae (Galloway) 1933; it has a coiled, planispiral involute test shape with a multilocular chamber arrangement. The tests are laterally biconvex exhibiting umbilical plugs and an interiomarginal aperture; tests are also coarsely perforate (Figure 6.9 and 6.19) (Yassini and Jones, 1995). *Elphidium crispum* is a foraminifer that inhabits the benthic zone and is distributed in open estuaries, inlets, sheltered embayments and the intertidal zone (Yassini and Jones, 1995). This foraminifer was used in the single grain pyrolysis experiments (and for aminostratigraphic studies) because of the following two attributes:

- i) The genus was often an abundant component in Kangaroo Island whole-rock samples, and
- ii) of the many genera of foraminifer examined, the genus *Elphidium* is one of the most robust and durable, being recognizable in even the older Kangaroo Island carbonate sediments (the Early Pleistocene Point Ellen Formation for example: Figure 6.24).



Figure 6.24: Examples of *Elphidium rotatum* recovered from the basal unit of the Early Pleistocene Point Ellen Formation. Note the excellent preservation of the fine test morphology (light microscope 100 x magnification), this implies *in situ* deposition.

SER does not apparently racemize as fast in *Elphidium crispum*, as it does in *Katelsia scalarina* and whole-rock (Figure 6.20c). However, there was a large amount of spread in the D-L ratio data for SER which can probably be attributed to low relative concentrations (as “short” RP-HPLC runs were used for the foraminifer analyses concentrations could not be quantified; however, relative concentrations could be estimated from observations of peak height and area) later in the experiment. This may be a contributing factor in the resultant low rate, or SER could be more stable in *Elphidium crispum*, or this may be in part related to the integrity of the test structure in *Elphidium*. Nevertheless, despite the scatter there is still a consistent increase in SER D/L over time. The calculated forward rate constant for SER in *Elphidium crispum* was $2.30 \times 10^1 \text{ yr}^{-1}$ (Table 6.11; Figure 6.22c).

The forward rate constant for ASX in *Elphidium crispum* was $8.35 \times 10^1 \text{ yr}^{-1}$; this was similar to whole-rock, although slightly faster, and an order of magnitude

slower than in *Katelsia scalarina* (Table 6.11). This type of behaviour was noted by Murray-Wallace and Kimber (1987), when comparing Last Interglacial *Marginopora vertebralis* ASX D-L ratios to Last Interglacial marine molluscs (indicated by comparatively lower D-L ratios in *Marginopora vertebralis*). This was originally termed as the “species effect” (Murray-Wallace and Kimber, 1987; Murray-Wallace, 2000). Although, these effects are predominantly at the genus level and will be referred to as such (i.e. the “genus effect”) from this point on. The D/L versus time (hr at 110 °C) curve for ASX was also similar to the whole-rock curve, although, the *Elphidium crispum* curve was more linear and lacked a definite point of inflection (Figure 6.20c).

The GLX forward rate constant ($1.17 \times 10^1 \text{ yr}^{-1}$) was in the same order of magnitude as both *Katelsia scalarina* and whole-rock, although it was slower than both (Table 6.11; Figure 6.22). This is in all likelihood due to the genus effect as well. The rate order for *Elphidium crispum* is ASX>SER>GLX.

6.5.2.4 Discorbis Dimidiatus

Discorbis dimidiatus (Parker and Jones) 1862, is another robust, benthic foraminifer, from the Family Discorbidae (Ehrenberg, 1838); it has a coiled, trochospiral test shape with a multilocular chamber arrangement. The tests exhibit a convex evolute dorsal side, and an involute ventral, or umbilical side; an interiomarginal aperture is present and the tests are also coarsely perforate (Figure 6.9 and 6.19) (Yassini and Jones, 1995). *Discorbis dimidiatus* also inhabits the benthic zone and is distributed in open estuaries, inlets, sheltered embayments, and the intertidal and subtidal zone (Yassini and Jones, 1995). It is commonly associated with shallow subtidal *Posidonia* sea-grass beds (Li *et al.*, 1998; Cann *et al.*, 2002).

This foraminifer was selected for use in both the pyrolysis experiments, and amino stratigraphic studies for the same reasons that *Elphidium crispum* was chosen (although, *Discorbis dimidiatus* was more widespread than *Elphidium crispum* and *Elphidium* spp. in general).

SER in *Discorbis dimidiatus* followed a similar kinetic behaviour to *Katelsia scalarina* and whole-rock modern beach sediment (i.e., it exhibited a rapid initial

rate of racemization up to an inflection point at approximately 7-10 days, becoming relatively unstable after this) (Figure 6.20d). The forward rate constant for SER ($7.39 \times 10^2 \text{ yr}^{-1}$) was of the same magnitude as whole-rock (though faster), and was an order of magnitude slower than *Katelsia scalarina* (Figure 6.22; Table 6.11). The rate was calculated from the initial rapid period of racemization (Figure 6.20d).

The forward rate constant for ASX from *Discorbis dimidiatus* was $3.39 \times 10^1 \text{ yr}^{-1}$. This is around half as fast as in *Elphidium crispum* and whole-rock (but in the same magnitude); however, ASX from *Discorbis dimidiatus* was an order of magnitude slower than *Katelsia scalarina* (Table 6.11; Figure 6.22).

GLX in *Discorbis dimidiatus* has, within 1σ uncertainty, essentially the same forward rate constant ($1.05 \pm 0.07 \times 10^1 \text{ yr}^{-1}$) as *Elphidium crispum* ($1.17 \pm 0.05 \times 10^1 \text{ yr}^{-1}$). This is gratifying in the sense that *Elphidium* spp. D-L ratio data could be used together with *Discorbis dimidiatus* for aminostratigraphic purposes, particularly when only one or the other genus is present in a sediment sample (Figure 6.22; Table 6.11).

The forward rate order for *Discorbis dimidiatus* is: SER>>ASX>GLX.

6.5.3 Pyrolysis discussion

This set of experiments has highlighted the differences in rates of racemization across a range of biomineral materials: marine shell, whole-rock sediment, and foraminifers. Two of the pyrolysis experiments (using marine molluscs and whole-rock sediments) have also revealed the changes in the concentration of amino acids that occur over time.

The main purpose of these experiments was to determine which of the examined amino acids extracted from Kangaroo Island fossil shell, whole-rock sediment and fossil foraminifers would be most suitable for aminostratigraphical application. The desired characteristics of a suitable amino acid are:

- i) The concentration of the amino acid (D+L) should be high relative to other amino acids and be stable over a long period of time (i.e. for the Kangaroo Island samples an amino acid that remains in useful concentrations in samples that are of early Pleistocene age would be desirable).
- ii) The amino acid should exhibit stable behaviour (i.e. not be subject to kinetic reversal, or behave unpredictably) over a range of biomineral materials (e.g. molluscan shell, whole-rock sediment, and foraminifers).
- iii) The amino acid should be *non-racemic* within the desired age range (which is also dependent upon the effective diagenetic temperature), and the amino acid should be able to be effectively modelled over the desired age range (i.e. for the Kangaroo Island samples be able to be used to estimate relative ages for shells, sediments, or foraminifers ranging from the Holocene to the early Pleistocene).
- iv) The fossil taxa should be able to maintain D-L ratio equilibrium once the racemic state is attained (Wehmiller, 1984).

Of the 3 amino acids examined (as useful for this application, i.e., ASX, GLX, and VAL—not including SER), GLX and VAL both showed the greatest geochronological applicability. Both of these amino acids exhibit relatively stable concentrations over time. However, GLX concentrations were marginally more stable than VAL, and GLX was also present in higher concentrations. This is demonstrated in Figures 6.11, 6.12 and 6.13. Figure 6.13 is a plot of amino acid (ASX, GLX, SER and VAL) concentrations (extracted from Pleistocene whole-rock aeolianite collected from the Coorong Coastal Plain) versus TL age. These samples were collected from as near as possible to the original TL sample sites of Huntley *et al.* (1993, 1994) and Huntley and Prescott (2001) in order to match the D-L ratio data (and concentration data) to the TL chronology. The loss of whole-rock amino acids, shown in Figure 6.13, is somewhat more dramatic in the Pleistocene samples than it is in the simulated aging (Figure 6.12) that takes place during pyrolysis (particularly for ASX); however, GLX and VAL are characteristically stable in both. Nevertheless, in the oldest Pleistocene samples (700-800 ka) the concentrations for all amino acids examined are

almost equally low; indeed the amino acids remaining at this later stage of diagenesis may be only representative of the intracrystalline fraction of the organic residue (i.e. the intercrystalline fraction may be almost entirely leached or degraded). The difference between the “initial” Pleistocene sample concentrations and the simulated aging concentrations is due to the characteristics of the whole-rock samples used for each (i.e. the Kangaroo Island sample (EB#2-7) used for the pyrolysis experiment was richer in amino acids than the Guichen Bay sample used for t_0 on the Pleistocene whole-rock plot). ASX is present in very high concentrations; however the loss over time of this amino acid is quite dramatic in most of the biominerals examined. ASX can also be subject to kinetic reversal (Kimber *et al.*, 1986; Kimber and Griffin, 1987); where the D-L ratio increases for a period; then there is an observed decrease in D-L ratio.

Both GLX and VAL exhibit stable kinetic behaviour over time; although GLX does have an initial rapid rate of racemisation. It does slow down to a relatively stable rate similar to VAL over the course of the pyrolysis experiments. GLX rates of interconversion are of the same order of magnitude over the range of biominerals examined here; other amino acids such as ASX and SER show order-of-magnitude rate differences between biomineral materials. The rate differences in GLX across materials (molluscs, whole-rock sediment, and foraminifers) are mainly defined by the initial short period of comparatively faster racemization during early pyrolysis (hence early diagenesis in fossil material), i.e., rates during later pyrolysis (later diagenesis in fossil material) are similar. Regardless, the rate order for GLX also proceeds as would be expected (see Table 6.11, Figure 6.22f and 6.25): GLX is faster in *Katelaysia scalarina* than in whole-rock sediment, and whole-rock is faster than the foraminifers. The GLX rate for whole-rock sediment lies between that of *Katelaysia scalarina* and the foraminifers; this is predictable as the material analysed has both molluscan and foraminiferal components. VAL too exhibits the same forward rate order of magnitude for *Katelaysia scalarina* and whole-rock sediment; however, VAL has an apparent higher rate in whole-rock when compared to *Katelaysia scalarina*. The rate for GLX, in later diagenesis, appears to decrease slightly (in comparison to VAL: this can be observed experimentally in Figure 6.22a and

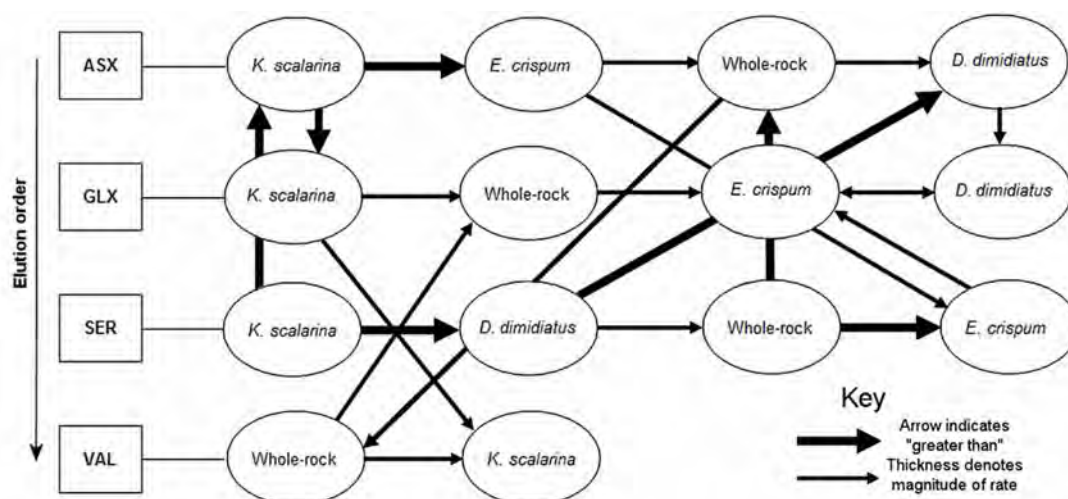


Figure 6.25: Amino acid racemization forward rate “map” created using the forward rate data in Table 6.11. The map illustrates the rate differences between the different biomineral materials as well as the rate differences between the different amino acids that were examined. The arrows indicate the direction of rate decrease and hence the order. The thick arrows designate an order of magnitude rate difference; the thinner arrows designate the same magnitude.

Table 6.12: Some examples of middle and early Pleistocene THAA D-L ratios from Kangaroo Island

Location / site code: genus / species (N) ^a	GLX D/L $\pm 1\sigma$	VAL D/L $\pm 1\sigma$
Smith Bay / SB#1-4: <i>Irus</i> sp. (5)	0.926 \pm 0.019	0.985 \pm 0.067
Boxing Bay / KMAR#3-3: <i>Tawera lagopus</i> (1)	0.782 \pm 0.003	0.814 \pm 0.03
Boxing Bay / KMAR#3-3: <i>Mactra</i> sp. (1)	0.706 \pm 0.001	0.759 \pm 0.023
North Cape / KMAR#3-1: <i>Anapella cycladea</i> (2)	0.978 \pm 0.015	0.997 \pm 0.030
Point Ellen / PE#1-1: <i>Katylusia scalarina</i> (2)	0.938 \pm 0.029	1.163 \pm 0.046
Point Ellen / PE#2b-2: <i>Nerita milnesi</i> (8)	0.958 \pm 0.016	1.171 \pm 0.031
Point Ellen / PE#2b-2: <i>Elphidium rotatum</i> (10)	0.830 \pm 0.074	0.937 \pm 0.095
Point Ellen / PE#1-2b: <i>Elphidium rotatum</i> (10)	0.853 \pm 0.068	0.958 \pm 0.016
Stokes Bay / STB#3-1: Whole-rock aeolianite (7)	0.779 \pm 0.010	0.923 \pm 0.126
Pennington Bay / KPB#5-1: Whole-rock aeolianite (4)	0.578 \pm 0.010	0.820 \pm 0.016

^a Number of subsamples analysed

6.22b); this would account for the observation of VAL D-L ratios that are higher than GLX in Pleistocene marine shell, whole-rock sediment and foraminifers. For instance, middle / early Pleistocene VAL D-L ratios from (the same) Kangaroo Island molluscs, whole-rock sediments, and foraminifers are generally higher than GLX; this is illustrated in Table 6.12. The uncertainties are usually quite large for VAL; this is possibly because of the lower concentrations of this amino acid in older samples, i.e., there are additional uncertainties (contamination notwithstanding) when undertaking integration that are linked to the amount of baseline noise (in relation to peak area and height—explained in

section 6.4.8). Hence, the VAL D-L ratio may not be a good representation when dealing with very old samples where the concentrations of the amino acid are low. The situation is marginally better with GLX, as concentrations are always higher in comparison to VAL; uncertainties are generally smaller as well (Table 6.12). Nevertheless, care must be taken when interpreting the geochronological implications of samples that exhibit low concentrations of amino acids.

Glutamic acid was selected for geochronological purposes in this research, even though VAL would have been a good choice as well. However, GLX was the better option given the anomalous behaviour of VAL in the modern whole-rock sample pyrolysis experiment.

Amino acids other than GLX (or VAL) could also have been used, although those with similar or slower rates of racemization were often not present in sufficient concentration for a confident D/L determination (LEU or ILE for example [particularly with samples mid- to early Pleistocene in age]). ASX was generally the most abundant amino acid found in all forms of fossil biomineral analysed from Kangaroo Island; it is also one of the fastest racemizing amino acids (Sloss *et al.*, 2004). It is for this reason that ASX was not used, even though it yields in high concentrations—as an aside Penkman (2005) advocates the use of multiple amino acids combined into a single index to derive amino acid ages. However, this should only be recommended where there are high concentrations of *all* amino acids to be used in the index (in Holocene samples for example). In the case of the Kangaroo Island samples this would not be practical as in older Pleistocene samples amino acids with geochronological utility that elute after GLX, have comparatively low concentrations. ASX racemization is too rapid for application to middle to early Pleistocene deposits, at the T_{eff} (CMATs for Kangaroo Island coastal regions range from 14.7 °C to 15.4 °C) experienced by the Kangaroo Island samples; being more suited to late Pleistocene, Holocene and modern applications—ASX concentrations derived from AAR analysis are actually “signals” that are a composite of aspartic acid (ASP) and asparagine (ASN); ASN decomposes to ASP during acid hydrolysis. This composite (ASP + ASN) is referred to as ASX. It was

suggested by Goodfriend (1991) that ASN may contribute to the initial rapid phase of racemization that occurs during early diagenesis.

Many of the Kangaroo Island sites have aeolianite and shell rich sediments that range from late to early Pleistocene (and possibly much older); therefore, a slower racemizing amino acid is more appropriate for these deposits. Numerous studies undertaken on the South Australian mainland (e.g., Murray-Wallace and Kimber, 1987; Belperio *et al.*, 1995; Murray-Wallace *et al.*, 2001; Murray-Wallace *et al.*, 2010) also utilized LEU, A/I, VAL, and GLX for aminostratigraphical purposes. These amino acids are all suitable for older deposits. GLX was chosen for the Kangaroo Island deposits as it is one of the more easily resolvable amino acids (in addition to ASX) using RP-HPLC (isomers eluting at approximately 25 and 28 minutes). It is a slowly racemizing amino acid, only slightly faster than VAL (although it is apparently slower in later diagenesis), and in the Kangaroo Island samples it is *always* present in greater concentrations than either LEU, A/I, or VAL. GLX also exhibited stable and predictable behaviour in all of the pyrolysis experiments examined in this section. Additionally, due to its generally high concentration and an initial rapid period of racemization, it can also be used to provide Holocene amino acid age estimates. The GLX “signal” (as with ASX) is a composite of both glutamic acid (GLU) and glutamine (GLN), and is referred to as GLX. GLN decomposes to GLU during the acid hydrolysis stage of RP-HPLC preparation. Finally, in many of the early Pleistocene samples examined GLX remained in useful concentrations and exhibited D-L ratios of <1.

6.6 AAR dating methods used in this study

The following sections will detail the methods used to calibrate and develop GLX AAR age models for AAR numerical and relative ages for the Kangaroo Island AAR samples. The types of uncertainty encountered when AAR calibration is undertaken are also defined and discussed; since little confidence should be placed in an age determination that is unconstrained by an uncertainty term.

6.6.1 Introduction

Age models that describe the behaviour of amino acids over time have been in use for decades. Some of the pioneering work was undertaken on fossilised bone, and marine sediments, using the extent of epimerization and racemization in ILE and ASX to model AAR ages (e.g. Bada *et al.*, 1970; Bada, 1972; Bada and Protsch, 1973; Bada, 1981). For example Bada and Protsch (1973) utilised an integrated rate equation to date hominin bones recovered from Olduvai Gorge, in Tanzania. This was accomplished by substituting an ASX D-L ratio from a ^{14}C dated bone sample into the equation along with the corresponding ^{14}C age to derive a first-order forward rate constant. The forward rate constant could then be used to estimate amino acid ages on other pieces of bone by substituting in an unknown D-L ratio. This is an early example of age estimation by calibration with a numerical age. While not a particularly sound study as one of the bone samples had an ASX D-L ratio of 0.720, which is beyond the point of conformation to reversible first order kinetics (RFOK—Figure 6.26) for this amino acid. Hence, Bada and Protsch (1973) were assuming first order kinetics for ASX would apply during later diagenesis.

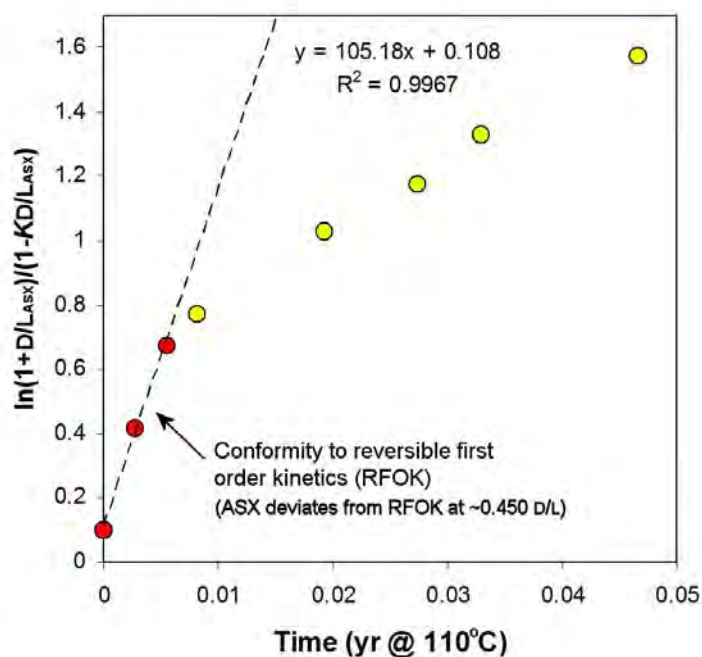


Figure 6.26: Conformity of ASX AAR to apparent reversible first-order kinetics (RFOK). The ASX D-L ratio data obtained from the total hydrolysable amino acids of *Katetylsia scalarina* heated at 110 °C are displayed (from this study). The data are transformed using the logarithmic term of the integrated rate equation and conform to RFOK where ASX D-L ratios are <0.450.

Regardless, Bada and Protsch (1973) used this calibration to age estimate hominin bones that were beyond the range of ^{14}C . They also speculated that the ILE reaction could be calibrated in a similar fashion to extend the age resolving power of the method. Indeed using this amino acid would have been a better choice. Good reviews of other early studies are available in Schroeder and Bada (1976), and Bada (1985).

A range of other equations used for amino acid age estimation are reviewed in Clarke and Murray-Wallace (2007); this paper discusses the application of several forms of expression used to estimate AAR ages for a range of biomineral samples types. The equations that are discussed and evaluated include integrated rate equations, linear, logarithmic, power law and parabolic. The parabolic method was selected for this research because of its simplicity and its utility over an extensive D-L ratio range (potentially modern to early Pleistocene [or older depending upon T_{eff}]). This model can be used to estimate ages for unknowns provided it can be confidently assumed or demonstrated that both the unknown dating samples and calibration samples share the same or similar diagenetic temperature history; the model also precludes potential uncertainties related to non-linear racemization kinetics (Mitterer and Kriausakul, 1989; Clarke and Murray-Wallace, 2007). The integrated rate model (with multiple k_1 values) would also be suitable; however, it is not as easy to apply, and it can be difficult to estimate ages for D-L ratios that hover near racemization transitional points (inflection points) (Clarke and Murray-Wallace, 2007).

6.6.2 The apparent parabolic kinetic method

The age model of choice for the Kangaroo Island AAR data calibration is the apparent parabolic kinetic model prescribed by Mitterer and Kriausakul (1989), accordingly numeric GLX AAR ages were estimated using the equation:

$$t = \left[\frac{(D/L)_s - (D/L)_{t_0}}{Mc} \right]^2 \quad (6.4)$$

Where t is the AAR age estimate, $(D/L)_s$ is the mean extent of racemization from multiple analyses of biomineral sediment, fossil foraminifers or molluscs of unknown age; $(D/L)_{t_0}$ is the time = 0 (t_0) D-L ratio (y-intercept) (either from whole-rock modern beach sediment, modern beach foraminifers, or live-collected

Katelsia scalarina and modern *Nerita (Melanerita) atramentosa*) which is subtracted from $(D/L)_s$, in order to account for various factors which are explained below, and Mc is the slope of the linear regression defined as:

$$\left[= \frac{\Delta(D/L)}{\Delta\sqrt{t}} \right] \quad (6.5)$$

The amino acid D-L ratios must be calibrated by independent methods in order to validate the AAR derived numerical ages, and to determine the slope of the linear regression that is used for the age calculations of sample unknowns. The slope of the linear regression was determined on the basis of the extent of racemization of various whole-rock sediments, foraminifers, and molluscs plotted against the corresponding square root of U-series, ^{14}C , or OSL ages (although using OSL in calibration has issues related to the event being dated, i.e., OSL dates last exposure to sunlight; AAR cessation of protein metabolism—this will be discussed later in this chapter). The y intercept in each calibration was based upon the extent of racemization in either ‘modern’ shoreface beach sediments, ‘modern’ (pristine) foraminifers (recovered from ‘modern’ beach sediments) (Figure 6.19) or live-collected *Katelsia scalarina* (Figure 6.9). The y intercept is the t_0 D/L value. Accordingly, this degree of racemization (particularly in whole-rock) is *assumed* to be representative of the time passed (in the case of live-collected or modern molluscs, the t_0 D/L value is mainly indicative of the level of induced racemization as a consequence of sample processing and hydrolysis) since:

- i) The cessation of protein metabolism (which in short-lived organisms equates with death).
- ii) Subsequent comminution (in the case of whole-rock sediments).
- iii) Incorporation within the continental shelf or near-shore sediments (as well as mixing with any reworked older sediments).
- iv) Final deposition.

For molluscs it is assumed that death and deposition are relatively contemporaneous (especially in the context of infaunal or semi-infaunal molluscs). For example the difference between mollusc (*Amesodesma angusta*) GLX D-L ratios and the matrix sediment GLX D-L ratios, recovered from a Last

Interglacial (see section 6.4.4.1 of this chapter for the reasons for initially assigning this age) cobble/pebble beach deposit at Pennington Bay, is 0.103; at Hanson Bay the difference between Last Interglacial molluscs (*Spisula* [*Notospisula*] *trigonella*) and matrix sediment GLX D-L ratios is also 0.103; at Vivonne Bay (*Nerita* [*Melanerita*] *atramentosa*) it is 0.180; at Rocky Point (*Fulvia tenuicostata*) it is 0.083. These are all similar to the differences between the GLX D-L ratio of live-collected shells and modern host near-shore (beach) sediments (differences ranging from 0.078 to 0.201—northern and southern Kangaroo Island respectively).

NOTE: This comparability to modern analogues suggests reasonably rapid post-mortem deposition of molluscs (and also comparable sediment residence times). In light of these differences sediment shelf residence time to deposition as near-shore modern beach deposits is (using the D-L ratio difference values above as a proxy measure of residence time) estimated to be between 1.7 ka and 17 ka (this was calculated using the ^{14}C calibrated parabolic equation for molluscs: section 6.6.4.1) (see Table 6.13). For Last Interglacial deposits the shelf residence (based on the D-L ratio difference values) ranges between 7 ka and 51 ka (this was calculated using the *U-series* calibrated parabolic equation for molluscs: section 6.6.4.1; the upper range is in all probability greatly over estimated as the Vivonne Bay matrix sediment has a very high percentage of reworked grains), which is comparable to the range calculated for modern beach sediments on Kangaroo Island (Table 6.13). This measure of residence time, however, is influenced to a great extent by the intermixing of older Pleistocene biomineral components. Therefore, these represent *maximum* residence times. A study by Stride *et al.* (1999), conducted on continental shelf biogenic sediments between northern Scotland and western France, suggested that the age (using a series of 51 ^{14}C dates on bulk carbonate sediment and marine molluscs) of the sediments studied ranged from the early Holocene to the late Pleistocene in age; with most of the sediment ages being in the order of 5000 years. This is comparable to the estimates for the Kangaroo Island shelf to near-shore residence times given above and in Table 6.13.

Table 6.13: Calculated continental shelf to near-shore residence times estimated for Kangaroo Island biogenic carbonate sediments (these values do not account for the presence of reworked biomineral grains).

Location / facies: <i>age</i>	Whole-rock sediment GLX D/L $\pm 1\sigma$ (N) ^a	Mollusc GLX D/L $\pm 1\sigma$ (N) ^a	Difference between whole-rock and mollusc GLX D-L ratios $\pm 1\sigma$	Residence estimate (ka) $\pm 1\sigma$
Point Ellen / modern beach: <i>modern</i>	0.245 \pm 0.016 (7)	0.045 \pm 0.004 ^b (9)	0.201 \pm 0.016	14 \pm 3
Hanson Bay / modern beach: <i>modern</i>	0.215 \pm 0.001 (2)	0.045 \pm 0.004 ^b (9)	0.170 \pm 0.004	10 \pm 2
Bales Beach / modern beach: <i>modern</i>	0.235 \pm 0.003 (2)	0.045 \pm 0.004 ^b (9)	0.191 \pm 0.005	12 \pm 2
Emu Bay / modern beach: <i>modern</i>	0.122 \pm 0.007 (4)	0.045 \pm 0.004 ^b (9)	0.078 \pm 0.008	2.1 \pm 0.4
Pennington Bay / raised cobble-pebble notch deposit: <i>LIG*</i>	0.463 \pm 0.007 (8)	0.360 \pm 0.008 ^c (8)	0.103 \pm 0.011	14 \pm 2
Hanson Bay / raised shelly deposit: <i>LIG*</i>	0.462 \pm 0.010 (8)	0.359 \pm 0.025 ^d (6)	0.103 \pm 0.027	14 \pm 3
Rocky Point / raised shelly deposit: <i>LIG*</i>	0.401 \pm 0.005 (4)	0.318 \pm 0.007 ^e (3)	0.083 \pm 0.009	9 \pm 2
Vivonne Bay / cobble-pebble notch deposit: <i>LIG*</i>	0.543 \pm 0.006 (2)	0.364 \pm 0.012 ^f (4)	0.180 \pm 0.013	43 \pm 8

* *LIG* = Last Interglacial

^a Number of subsamples analysed

^b Live collected *Katelysia scalarina* and modern *Nerita* (*Melanerita*) *atramentosa*

^c *Amesodesma angusta*

^d *Spisula* (*Notospisula*) *trigonella*

^e *Fulvia tenuicostata*

^f *Nerita* (*Melanerita*) *atramentosa*

The t_0 D-L ratios were subtracted from the D-L ratios of the unknowns, in each calibration, to account for the duration or effect of these processes (and also hydrolysis induced racemization). This will be explained to a greater degree in the sections of this chapter related to the specific calibrations (sections 6.6.4.1, 6.6.4.2, and 6.6.4.3).

The large differences between whole-rock modern beach sediment D-L ratios and live-collected or modern shells are not unexpected when the proximity of older near-shore sediment deposits to erosive elements such as onshore winds and wave action is considered. Erosion of coastal aeolianites provides a ready supply of various biomineral grains to be reworked into younger sediments at the shoreface; as discussed previously there is also a period of residence time on the continental shelf and near-shore prior to deposition on the shoreface and barrier formation. As a point of interest it is notable that modern beach D-L ratios can also vary with proximity to the aeolianite cliff face. For example, samples of modern beach sediments recovered from the base of Bridgewater Formation

aeolianite cliffs at Pennington Bay exhibited higher D-L ratios when compared to that recovered from the shore face: GLX 0.315 from the cliff base, and GLX 0.279 from the shore face. Also, from sediment recovered from the base of the Point Ellen Formation and the shore face: GLX 0.277 from the base of the Formation and GLX 0.228 from the shore face (see Table 6.14 for details). The reason for the higher D/Ls near the outcrops of older material is due to local spall as grains are eroded from the face; the increased concentration of older grains is reflected as a higher D-L ratio. Grain mixing can be more clearly seen in the graph from section 6.5.2.2 (Figure 6.23) that illustrates several populations of single-grains within Last Interglacial (MIS 5e) sediment from Vivonne Bay.

Table 6.14: D-L ratio comparison of near-shore and cliff face modern beach sediments, at two sites on Kangaroo Island.

Laboratory code	Location/Site code	Modern beach cliff face whole-rock GLX D/L $\pm 1\sigma$	Modern beach shore face whole-rock GLX D/L $\pm 1\sigma$
UWGA	Pennington Bay / PB#2a-b PB#2-29	0.315 \pm 0.023	0.279 \pm 0.003
UWGA	Point Ellen / PE#2-8 and PE#2-4	0.277 \pm 0.004	0.228 \pm 0.009

In order to test the robustness of the parabolic method when using the amino acid GLX, a series of aminostratigraphical analyses that were first carried out by Murray-Wallace *et al.* (2001) using the amino acid LEU to estimate numeric ages, were repeated in this study using GLX. Here, Murray-Wallace *et al.* (2001) completed an aminostratigraphic analysis of the Pleistocene dune barrier sequence located on the Coorong Coastal Plain (specifically the Robe, Woakwine, Reedy Creek, West Avenue, East Avenue, Harper, West Naracoorte, and East Naracoorte dune ranges—Figure 6.14). This was undertaken using whole-rock sediment collected from the dunes (these dunes were preserved via a combination of epeirogenic uplift and the pedogenic formation of a protective calcrete mantle). The samples were taken wherever possible from the same auger holes made by Huntley *et al.* (1993; 1994) when collecting thermoluminescence (TL) samples. The object of Murray-Wallace *et al.* (2001) study was to assess the TL chronology obtained by Huntley *et al.* (1993; 1994)—particularly for the oldest dune barriers—and the efficacy and veracity of their whole-rock sediment AAR dating method. The AAR dating was

undertaken by calibrating the extent of racemization in the amino acid LEU through an apparent parabolic kinetic calibration method. A sample of modern beach sediment from Guichen Bay was collected for a t_0 sample, and a U-series age of 125 ± 20 ka (Schwebel, 1978; 1984), for fossil molluscs recovered from the back-barrier lagoon facies of the Woakwine I range, was used as the calibration point.

A similar set of samples was collected from the Coorong Coastal Plain for this comparative study, again wherever possible the samples were taken from, or near, the original sample sites of Huntley *et al.* (1993; 1994). The purpose was to compare a calibrated GLX chronology with the TL chronology and also to compare with the LEU chronology of Murray-Wallace *et al.* (2001). A series (with some duplicates) of whole-rock aeolianite samples was collected from the Robe, Woakwine, Reedy Creek, West Avenue, East Avenue, Baker, West Naracoorte, and East Naracoorte ranges (a sample was not collected from the Harper range). A t_0 sample was also collected for this study from the modern beach at Guichen Bay. The U-series age of Schwebel (1978; 1984) was also used as the calibration point in this study (Table 6.15 and 6.16). All samples (except the t_0 sample) were recovered from >2 m depth.

Table 6.15: Calibration data for Coorong whole-rock aeolianite

Biom mineral	Sample Code	U-series age $\pm 1\sigma$ (ka)	$\sqrt{\text{U-series age}} \pm 1\sigma$	GLX D-L ratio $\pm 1\sigma$ (N) ^b
Whole-rock aeolianite	WW#1-1	125 ± 20^a	$11.18^{+0.86}_{-0.93}$	0.454 ± 0.017 (6)
Whole-rock modern beach sediment	GB#1-1	0	0	0.273 ± 0.004 (4)

^a Calibration point (U-series age for the Last Interglacial Woakwine I dune [Schwebel, 1978; 1984])

^b No. individuals analysed

Figure 6.27a demonstrates the parabolic nature of GLX racemization kinetics by comparing the extent of racemization in GLX (THAA) to the TL chronology of Huntley *et al.* (1993; 1994). In Figure 6.27b the GLX data from 10 dune ranges is compared to the square root of the TL ages, in order to assess conformity to the apparent parabolic kinetic method of Mitterer and Kriausakul (1989). The least-squares linear regression (R^2 value of 0.9431) suggests that the GLX D-L ratio dataset derived from the extent of GLX racemization in aeolianite whole-

rock sediment recovered from the Coorong Coastal Plain conforms appropriately to the apparent parabolic kinetic model (there is particularly good agreement with the GLX results from the Robe III, Reedy Creek, West Avenue, and Baker ranges).

Table 6.16: A comparison of the extent of GLX racemization and numerical GLX AAR ages to the TL chronology of Huntley *et al.* (1993; 1994) (OSL of Banerjee *et al.* [2003] for Robe#1-1)

Laboratory code	Location/ site code	Luminescence age $\pm 1\sigma$ (ka) ^a	LEU AAR ages $\pm 1\sigma$ (ka) ^d	Whole-rock GLX D-L ratio $\pm 1\sigma$ (N) ^e	GLX AAR ages $\pm 1\sigma$ (ka)
UWGA 6539	Guichen Bay / GB#1-1	Modern ^b	Modern	0.273 ± 0.004 (4)	Modern
UWGA 6522	Robe Range II / Robe#1-1	61 ± 3.6 ^c	—	0.455 ± 0.005 (3)	127 ± 28
UWGA 6523	Robe Range III / Robe#1-3	116 ± 6	127 ± 24	0.463 ± 0.005 (4)	139 ± 30
UWGA 6519, 6521, 6525	Woakwine I / WW#1-1, WC#1-1, WC#1-3	132 ± 9	(125 ± 20) ^f	0.454 ± 0.017 (6)	(125 ± 20) ^f
UWGA 6529	Reedy Creek / RC#1-1	258 ± 25	251 ± 48	0.554 ± 0.017 (4)	302 ± 67
UWGA 6518	West Avenue / WA#1-1	342 ± 32	382 ± 73	0.560 ± 0.005 (2)	315 ± 69
UWGA 6520	East Avenue / EA#1-1	414 ± 29	—	0.539 ± 0.016 (4)	271 ± 60
UWGA 6527	Baker Range / BR#1-1	456 ± 37	438 ± 83	0.598 ± 0.033 (4)	405 ± 91
UWGA 6526	East Naracoorte / EN#1-1	720 ± 70	935 ± 178	0.740 ± 0.028 (2)	837 ± 185
UWGA 6524	West Naracoorte / WN#1-1	800 ± 100	543 ± 103	0.700 ± 0.034 (2)	700 ± 156

^a TL chronology of Huntley *et al.* (1993; 1994)

^b t_0 sample

^c OSL age from Banerjee *et al.* (2003)

^d LEU AAR chronology of Murray-Wallace *et al.* (2001)

^e Number of whole-rock subsamples analysed

^f Calibration point (U-series age for the Last Interglacial Woakwine I dune [Schwebel, 1978; 1984])

The parabolic method, using the calibration in Table 6.15 (the linear regression of this calibration data was plotted in Figure 6.28: note the similarity of the slope of the calibration regression to the slope of the GLX vs. TL age regression in Figure 6.27b [1.6 and $1.5 \times 10^{-2} \sqrt{k \text{ yr}}$ respectively]), was applied to the GLX AAR results in Table 6.16. This produced a set of AAR numeric ages comparable to the TL chronology of Huntley *et al.* (1993; 1994) and the LEU AAR ages of Murray-Wallace *et al.* (2001). The GLX ages are associated with a large but sensible uncertainty term of 22% (the coefficient of variation [CV]) derived from the square root of the sum of the squares of all uncertainty terms (as a CV) (i.e. uncertainty in the independently determined U-series age [16%], uncertainty in the quantitation of the GLX D-L ratios [0.9–6%], random instrumental error [2%],

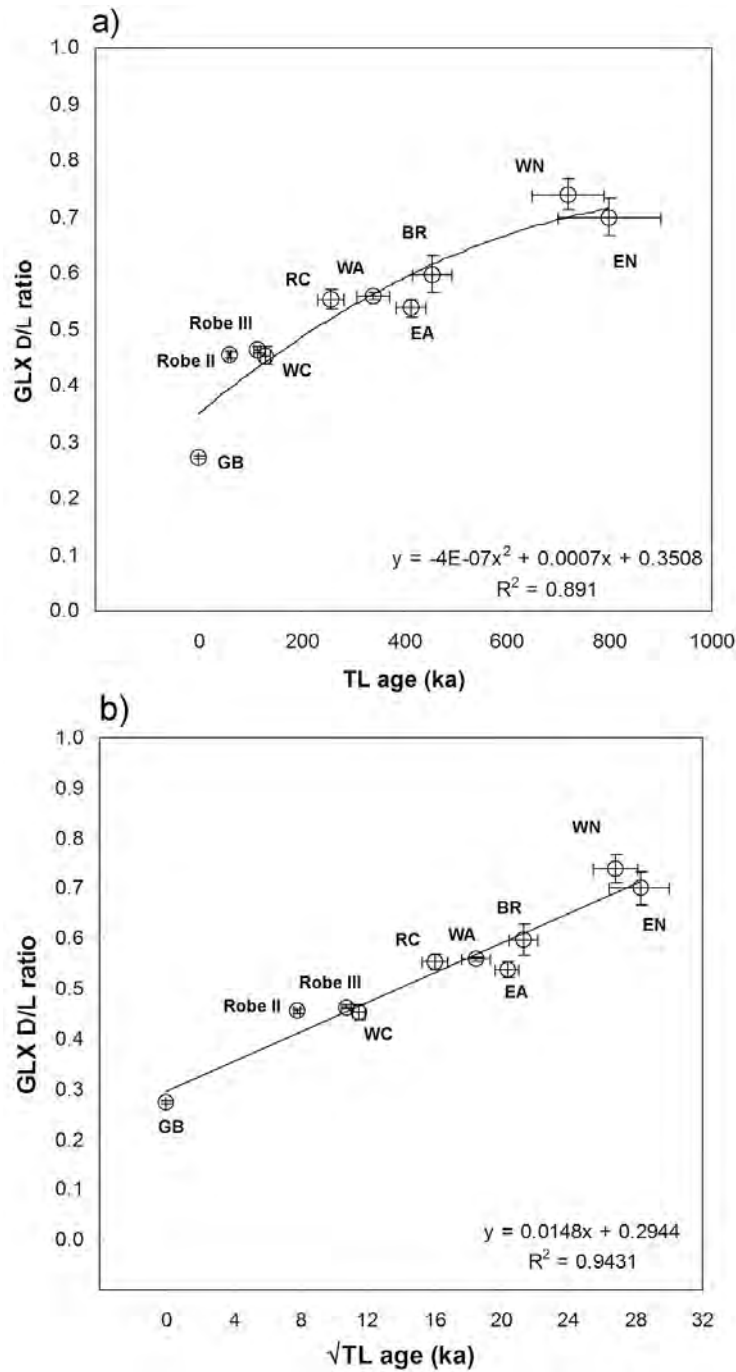


Figure 6.27: GLX D-L ratio data vs. TL ages of Huntley *et al.* (1993; 1994) a) fit with a polynomial function b) A linear regression of GLX D-L ratio data vs. $\sqrt{\text{TL age}}$ of Huntley *et al.* (1993; 1994). These plots demonstrate the non-linear nature of GLX kinetics over time, and the appropriateness of the apparent parabolic kinetic calibration method in application to these data. Abbreviations: GB, Guichen Bay; Robe II, Robe Range II; Robe III, Robe Range III; WC, Woakwine Range I; RC, Reedy Creek Range; WA, West Avenue Range; EA, East Avenue Range; BR, Baker Range; WN, West Naracoorte Range; EN, East Naracoorte Range.

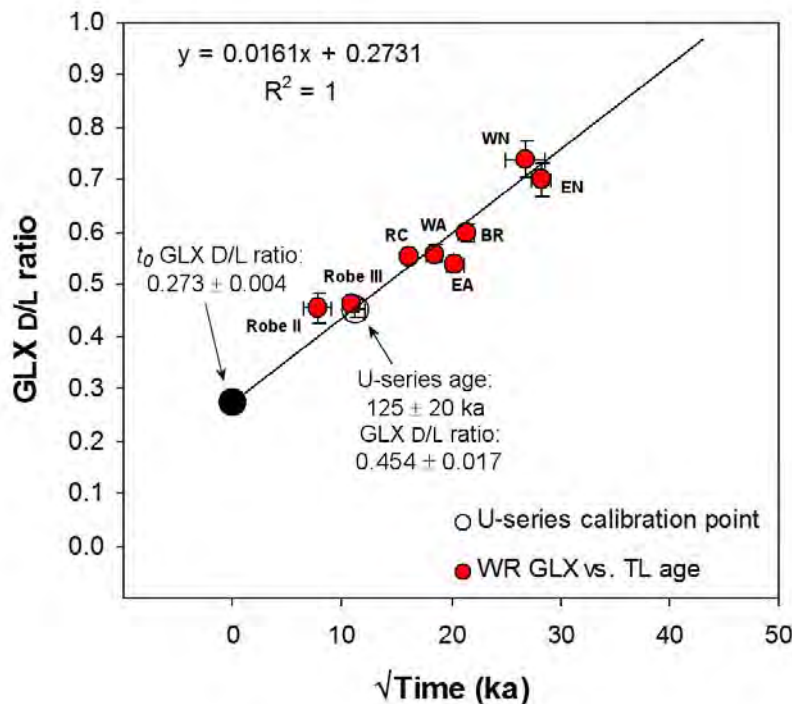


Figure 6.28: Calibration plot (GLX vs. $\sqrt{\text{Time [ka]}}$) for the Coorong GLX data (the open circle is GLX D/L vs. U-series; the black circle is the t_0 point—uncertainties are inside the point). The slope of the linear regression is required as an integral part of the apparent parabolic kinetic (APK) method (in this case the slope is: $1.6 \times 10^{-2} \sqrt{\text{k yr}}$) (see equations 6.4 and 6.5). The red circles are the whole-rock sediment GLX D/L data vs. $\sqrt{\text{TL age}}$ (which were not part of the regression); these data demonstrate conformity to the calibration. $R^2 = 1$ as only two data points in the regression. Note: no t_0 subtractions are required on the calibration curves—the subtraction is undertaken in the APK age equation.

and also an assumed ± 1 °C diagenetic temperature variation [10%]). The derivation of these uncertainty terms [and others] is explained in later sections of this chapter.

The TL ages and the LEU AAR ages were plotted against the GLX AAR ages in Figure 6.29 a) and b). The GLX AAR ages agree quite well with both the TL and LEU chronologies; particularly with ages younger than ~400 ka. There are, however, some GLX AAR results that deviate from the trends displayed in Figure 6.27; principally Robe II, East Avenue, and West Naracoorte. The discrepancy for the Robe II GLX result, in terms of a D-L ratio that deviates from the trend (Figure 6.27), may be due to the presence of a high percentage (comparatively) of reworked biomineral grains, derived from the underlying older calcrete and aeolianite units at the site (this needs to be investigated further with a single-grain AAR analysis). The East Avenue range GLX results reflect the LEU D-L ratio results of Murray-Wallace *et al.* (2001); here Murray-

Wallace *et al.* (2001) proposed (on the basis recrystallization, dissolution, and carbonate leaching observed in thin-section and binocular microscopy) that the reason for a lower than expected LEU D-L ratio was due to *in situ* leaching of lower molecular weight, more highly racemised peptide residues, and free amino acids. This is also supported by field observations of the East Avenue range aeolianite unit, which is very weathered and friable, suggesting leaching of carbonate. The West Naracoorte range GLX D-L ratio results are again reflected in the LEU results; with the D-L ratios being lower than expected with regards to the linear trend (Figure 6.27).

The reasons for this are again probably due to selective leaching of lower molecular weight, highly racemized peptide residues (Murray-Wallace *et al.*, 2001). Contamination with younger non-indigenous amino acids is unlikely because of the extremely low concentrations of L-SER present in the West Naracoorte sub-sample. All of the older dune ranges (>400 ka [TL]) have very low overall concentrations of amino acids (see Figure 6.13) and so the D-L ratio results may have been influenced to a greater or lesser degree by preferential loss of amino acids.

Nevertheless, as can be seen in Figure 6.29 and Table 6.16, the GLX numeric age results compare favourably and are rarely significantly different to the TL and LEU AAR chronologies at 1 σ —at 2 σ all results (except Robe III) overlap.

The comparison of GLX AAR numeric ages, derived in this preliminary study, to the TL and LEU chronologies of Huntley *et al.* (1993; 1994), and Murray-Wallace *et al.* (2001) (for the Coorong Coastal Plain dune ranges) was an important step in verifying the appropriateness of the apparent parabolic kinetic method to model the behaviour of the amino acid GLX over time. This study supports the application of this calibration method using GLX D-L ratios to the Kangaroo Island samples.

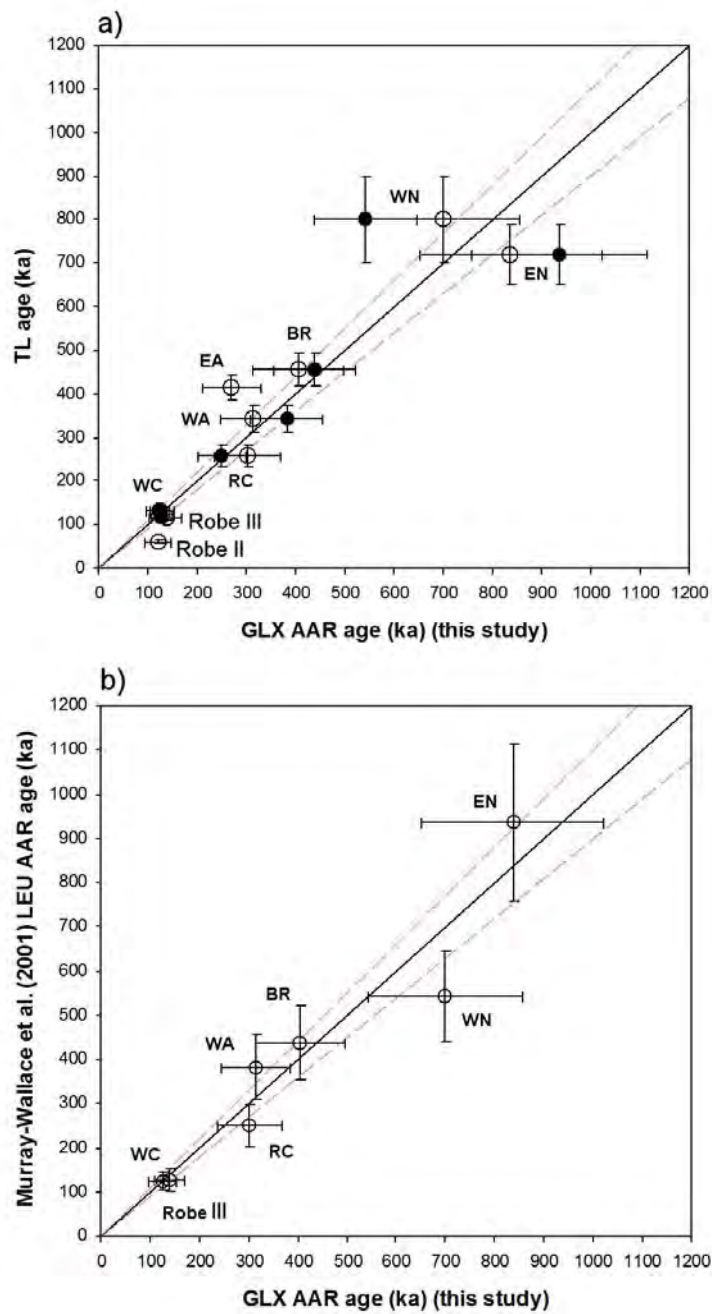


Figure 6.29: Comparison plots of the two chronologies vs. the GLX AAR ages a) TL vs. GLX (this study) and LEU AAR ages of Murray-Wallace *et al.* (2001); the open circles are GLX and the solid black circles are LEU; the black solid line represents unity, and the red dashed lines represent 10% either side of unity b) LEU AAR ages of Murray-Wallace *et al.* (2001) vs. the GLX AAR ages derived in this study.

6.6.3 Sources of variation in the amino acid racemization numeric age determination

In order to obtain an overall uncertainty term for amino acid numeric ages (calculated using an apparent parabolic kinetic model) determined for the unknowns, several sources of uncertainty were considered. These sources of uncertainty (i.e. diagenetic temperature variation, within deposit variation, species [genus] effect, independent [calibration] age uncertainties, x-variable, and instrument reproducibility) were propagated into the final uncertainty term when calculating an AAR age estimate.

6.6.3.1 Uncertainty terms used in GLX AAR age calculation

Six sources of uncertainty were considered for the Kangaroo Island AAR samples in order to define a final uncertainty term for the age calculation. All of these terms were propagated into the final uncertainty estimate for the calibrated GLX AAR ages.

i) *Diagenetic temperature variation.* The diagenetic temperature is that experienced by the fossil or biominerals over the period of burial: deeply buried sediments experience less variation in this temperature when at depth (>1 m, preferably >2 m [Miller and Clarke, 2007]). The sub-surface temperature is close to or the same as the *mean* annual air temperature (MAT) experienced in the region, since seasonal temperature fluctuations are averaged by the insulating overburden. AAR data are interpreted in the context of the current mean annual temperature (CMAT) for the region that the AAR sample was recovered from, as AAR is predominantly a temperature dependent reaction. The postulation is that fossils, when collected from regions of equal present temperatures (i.e. CMATs), will have experienced equivalent effective temperatures (T_{eff}): the integrated temperature experienced over the period of burial (also see section 6.2.1 of this chapter, and Figure 6.4). The assumption is also made that little change in latitudinal temperature gradients has occurred over time (Wehmiller, 1984b; Wehmiller and Miller, 2000). For the Kangaroo Island samples the magnitude and complexities in the deviation from the CMAT over the period of burial is an unknown, although, generally, all samples were removed from deeply buried contexts so variation should be minimal. AAR samples removed from shallow depths (<1 m) may have experienced large temperature fluctuations (due not only to seasonal changes but day to day

changes as well) where racemization has both increased and decreased in rate at various times (e.g. a +4 °C increase in temperature can effectively double the rate of racemization for a given amino acid [Miller and Clarke, 2007]). These shallow contexts can provide unreliable AAR results because the biominerals, fossil molluscs, or fossil foraminifers may have experienced longer periods of time at higher or lower temperatures, in contrast to those residing at greater depths.

In an attempt to account for small variations in the diagenetic temperature a $\pm 1^\circ\text{C}$ uncertainty (Belperio *et al.*, 1995) over the period of burial was assumed. This translates as approximately $\pm 10\%$ deviation from the “true” D-L ratio (not taking into account other uncertainties). This is estimated from the exponential in Figure 6.5, within the mean annual temperature range experienced by the coastal regions of Kangaroo Island (14.7 °C to 15.4 °C).

ii) *Within deposit variation (or intershell, intersample variation)*. For marine shell and foraminifers there is a within deposit variation in D-L ratio related to the depositional, weathering and exposure, and contamination histories of each individual. In molluscs of \geq Last Interglacial age (MIS 5e) this variation tended to be small. Foraminifers, conversely, showed the greatest variation. Where possible at least 4 individual molluscs, and 5-10 foraminifers were used to determine an average GLX D-L ratio for a stratigraphic unit; although, it was not always possible to recover this many suitable shells or tests from a sample. These data were also exposed to a set of rejection criteria (section 6.4.7) before the mean D-L ratio and 1σ uncertainties were calculated for the samples.

Whole-rock sediment samples (approximately 200-500 g) were taken for analysis, when possible, from different outcrops or different areas of the same unit. This was done to account for the effect of any variability in the relative proportion of reworked grains along the unit, as a single sample may not necessarily yield a representative D-L ratio if the proportion of reworked grains within the sediment is heterogeneous. Undertaking several measurements from different areas or outcrops of the same unit may define a more meaningful mean D-L ratio for the particular sedimentary unit.

The deviation from the mean D/L, expressed as a CV, was used as part of the total uncertainty sum in the AAR age calculation.

iii) *Genus specific differences in rates of racemization for marine shell (genus effect)* For the Kangaroo Island samples a set of marine shells representing various genera were recovered from 5 different Last Interglacial sites around Kangaroo Island (Figure 6.30). The differences in the GLX D-L ratios were used to estimate uncertainty associated with differing rates of racemization in different genera. The deviation in the GLX D/L means of 5 molluscan genera from 5 different sites was used to calculate an uncertainty estimate for the genus effect. This was done because if the overall CV for all the molluscs was used then it would also include “within deposit variation” which has already been accounted for. The comparison of the 5 means yielded a CV of 5%, which was included in the total uncertainty sum for the AAR age calculation.

iv) *Error associated with dating methods used for calibration.* This study utilized ^{14}C , U-series, and OSL dating as a means of geochronological calibration of the GLX D-L ratio data. Therefore, the errors associated with uncertainty in the dating results were also included in the final uncertainty estimate for the AAR ages.

v) *Standard error in the x-variable (if more than 2 data points are used)*

The x-variable (i.e. the slope $[M_c]$ of the regression line) in the calibration regression has an associated uncertainty (when there are more than two data points in the regression), this was also included as part of the uncertainty sum. However, it was always very small at $<1\%$ (because of the small number of calibration points used, i.e., 2 in the ^{14}C calibration and 4 in the OSL calibration).

vi) *Instrument reproducibility and laboratory error.* The random uncertainties associated with instrument reproducibility and laboratory procedures were estimated by running several repeat injections of each of the interlaboratory comparative standards ILC-A, B, and C (Wehmiller, 1984) across three batch runs. This gave an indication of the analytical uncertainty across a range of

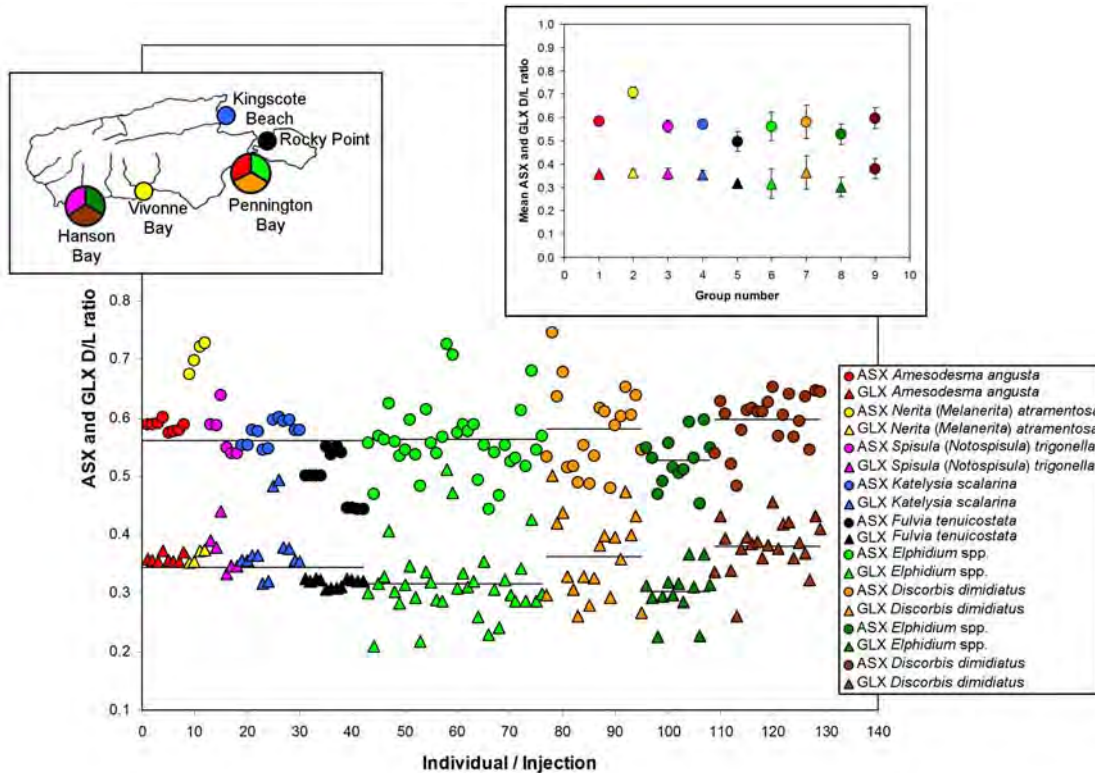


Figure 6.30: Comparison of GLX and ASX D-L ratios from various individual fossil molluscs and foraminifers recovered from Glanville Formation equivalent (Last Interglacial) sites around Kangaroo Island. Examined are 5 molluscan genera from 5 sites, and 2 genera of foraminifer (circles for ASX and triangles for GLX): red (Pennington Bay) for *Amesodesma angusta*, yellow (Vivonne Bay) for *Nerita (Melanerita) atramentosa*, pink (Hanson Bay) for *Spisula (Notospisula) trigonella*, blue (Kingscote Beach) for *Katylsia scalarina*, black (Rocky Point) for *Fulvia tenuicostata*, light green (Pennington Bay) and dark green (Hanson Bay) for *Elphidium* spp., and orange (Pennington Bay) and brown (Hanson Bay) for *Discorbis dimidiatus*; the colours also correspond to the locations on the inset map of Kangaroo Island. It is apparent that, even though 5 different molluscan genera are compared, the differences in D-L ratios from site to site are quite small, particularly for GLX (the overall CV is <7% and the CV of the means for each genus is ~5%—not including the foraminifera). There is also generally good covariance. However, the D-L ratios for ASX recovered from *Nerita* are quite different than in the other 4 molluscs; they are much higher, possibly indicating a faster rate of racemization for ASX in this genus. The foraminifer data suggest that both *Elphidium* and *Discorbis* racemize at a slower rate than molluscs (also supported by the pyrolysis experiments), more so for GLX than ASX. This is similar to that found by Murray-Wallace and Kimber (1987) for the foraminifer *Marginopora vertebralis*. Overall these data suggest that it is possible to utilise GLX across molluscan genera; however, foraminifer and mollusc AAR data should probably not be used together (even though all means generally overlap at 1σ (particularly for GLX)—the uncertainties are large for the foraminifer means as the data are raw and have not been subjected to rejection criteria, i.e., there is a large degree of scatter in the data). The horizontal black lines represent means for each dataset, and the RH inset graph displays the mean data + 2σ error bars (note that some error bars are within the symbol; the symbols and colours correspond to the lower RH legend).

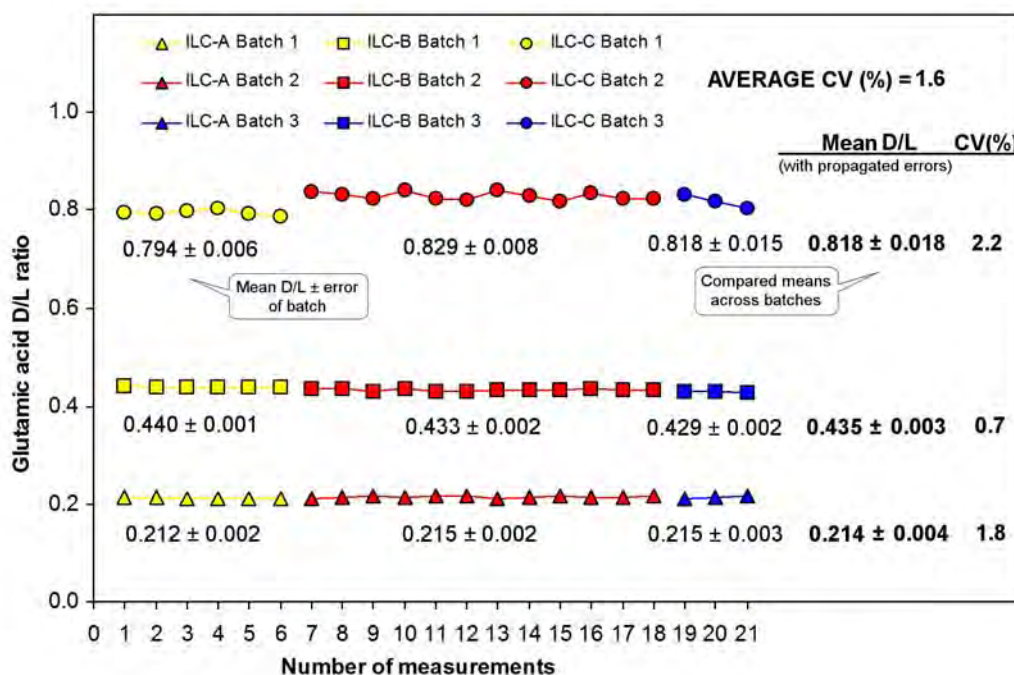


Figure 6.31: The analytical precision for GLX was determined by repeat measurements (injections) from single vials containing the interlaboratory comparison standards of Wehmiller (1984) (ILC-A, B, and C). All CVs from each batch were <2% (most were <1%) indicating that there is high precision when using RP-HPLC to determine GLX D-L ratios. The plot shows D-L ratios from three batches of ILCs: each batch was run at a different time using different lots of reagents and glassware. The batch to batch comparisons (weighted to the number of injections) give an estimate of laboratory error (disparities between different lots of reagent, and also possible contamination during preparation). The average of the CVs is 1.6%; this value (which is a combination of random instrumental uncertainty [analytical precision] and laboratory uncertainty) was used when calculating the total uncertainty term for the amino acid age determinations. Note that some batches were injected more or less frequently—this was due to available RP-HPLC time; however, the results were weighted to account for this source of variability. It is also notable that ILC-C (the oldest of the standards at ~ 1 Ma) had the most variability; this may be because of comparatively low concentrations of GLX introducing increased baseline uncertainty (attributable to smaller peak areas and heights).

GLX D-L ratios, and amino acid concentrations. The mean of these uncertainties (1.6%—rounded to 2%) was also used in the final uncertainty estimates for the AAR ages (Figure 6.31). Table 6.17 illustrates a range of ILC analyses performed over many months (usually ILC standards were run with every batch of samples). These analyses (ILC-A, B, C, and Z), undertaken using the University of Wollongong RP-HPLC, are compared with the original series of Wehmiller (1984a), and Kaufman and Manley (1998). Generally (from Table 6.17), all are comparable at 1 standard deviation.

The total uncertainty in the GLX AAR numeric ages (calculated for the unknowns) was estimated using the following equation:

$$\Delta z = \sqrt{\sum_{y=1}^n (\Delta x_y)^2} \quad (6.6)$$

Where Δx is the uncertainty in n terms, and Δz is the total uncertainty in the GLX AAR age calculation. In summary this equation was used to calculate the square-root of the sum of the squares of six uncertainty terms viz., diagenetic temperature variation (CV = 10%), within deposit variation of GLX D-L ratios (for both calibration samples and unknowns) (average CV of 2-15%), the genus effect (CV = 5%), uncertainty in the independently determined numerical ages of the calibration samples (average CV of 3-16%), uncertainty in the x-variable (CV <1%), and the random uncertainty associated with instrument reproducibility of GLX D-L ratios, sample processing, and analysis (CV = 2%).

The simple propagation method used here returned large but realistic AAR age uncertainties of 17-22% for molluscs, 30-40% for foraminifers (depending upon scatter in the D-L ratio data), and 22-24% for whole-rock sediments. Also, foraminifers and whole-rock sediment subsamples did not include a genus effect uncertainty component, as the whole-rock subsamples represent a diagenetic average, and the two genera of foraminifer used had similar racemization kinetics for the amino acid GLX.

Table 6.17: Amino acid D-L ratios ($\pm 1\sigma$) derived from the interlaboratory comparative standards (ILC-A, B, and C) of Wehmiller (1984), and Kaufman and Manley (1998) (ILC-Z). Reported here are a set of comparisons to the original Wehmiller (1984) gas chromatography (GC) results and the Kaufman and Manley (1998) RP-HPLC ILC results.

Amino Acid*	Wehmiller (1984) ^a			Kaufman and Manley (1998) ^b				This study ^b			
	ILC-A	ILC-B	ILC-C	ILC-A	ILC-B	ILC-C	ILC-Z	ILC-A ^c	ILC-B ^c	ILC-C ^c	ILC-Z ^c
ASX	0.378 \pm 0.028	0.705 \pm 0.028	0.894 \pm 0.079	0.393 \pm 0.006	0.684 \pm 0.011	0.824 \pm 0.028	0.171 \pm 0.002	0.399 \pm 0.005	0.701 \pm 0.009	0.873 \pm 0.037	0.181 \pm 0.002
GLX	0.203 \pm 0.011	0.432 \pm 0.017	0.849 \pm 0.035	0.205 \pm 0.009	0.424 \pm 0.009	0.849 \pm 0.010	0.037 \pm 0.002	0.207 \pm 0.002	0.416 \pm 0.004	0.857 \pm 0.004	0.040 \pm 0.001
SER	--	--	--	0.430 \pm 0.046	0.308 \pm 0.018	0.208 \pm 0.019	0.112 \pm 0.003	0.428 \pm 0.087	0.407 \pm 0.034	0.229 \pm 0.086	0.123 \pm 0.001
ALA	0.364 \pm 0.017	0.725 \pm 0.034	0.946 \pm 0.029	0.397 \pm 0.024	0.766 \pm 0.018	1.019 \pm 0.019	0.038 \pm 0.004	0.379 \pm 0.018	0.781 \pm 0.007	1.070 \pm 0.007	0.051 \pm 0.005
VAL	0.159 \pm 0.030	0.449 \pm 0.068	0.868 \pm 0.084	0.164 \pm 0.017	0.425 \pm 0.012	0.906 \pm 0.034	0.013 \pm 0.003	0.162 \pm 0.004	0.429 \pm 0.003	0.952 \pm 0.013	0.023 \pm 0.002
PHE	0.239 \pm 0.020	0.583 \pm 0.059	0.873 \pm 0.089	0.256 \pm 0.014	0.601 \pm 0.021	0.923 \pm 0.069	0.029 \pm 0.007	0.241 \pm 0.021	0.541 \pm 0.009	0.812 \pm 0.060	0.033 \pm 0.013
A/I	0.212 \pm 0.036	0.540 \pm 0.081	1.215 \pm 0.015	0.176 \pm 0.018	0.509 \pm 0.062	1.124 \pm 0.066	0.021 \pm 0.003	0.168 \pm 0.012	0.654 \pm 0.034	1.125 \pm 0.089	--
LEU	0.196 \pm 0.021	0.497 \pm 0.049	0.833 \pm 0.043	--	--	--	--	--	--	--	--

* Abbreviations are as follows: ASX = aspartic acid; GLX = glutamic acid; SER = serine; ALA = alanine; VAL = valine; PHE = phenylalanine; A/I = alioisoleucene/isoleucine; LEU = leucine

^a Analysis of powdered marine shell using GC

^b Analysis of powdered marine shell using RP-HPLC

^c Numbers of usable analyses for each sample solution of ILC were: ILC-A x 18, ILC-B x 17, ILC-C x 14, and ILC-Z x 16

6.6.4 Calibrating the amino acid GLX with an apparent parabolic kinetic model using ^{14}C , Uranium-series and conventional OSL dating methods

This study used AMS ^{14}C , U-series, and OSL dating to directly calibrate GLX D-L ratios, using an apparent parabolic kinetic model. The D-L ratios are derived from whole-rock sediment, single grain (single foraminifer), and mollusc AAR analyses. In all cases specimen averaged D-L ratio data were used in the calibration.

For the Holocene study site at American River (Chapter 3: Figure 3.1) direct calibration, utilising AMS ^{14}C , was applied to determine the ages on a range of marine shells recovered from various depths within two profiles. Calibration involved the AAR analysis of marine molluscs that were split prior to analysis (i.e. one half of an individual marine shell was dated using ^{14}C , and the other half was analysed for amino acid D-L ratios). Another method involves the AAR analysis of the ^{14}C HCl residue (Murray-Wallace and Bourman, 1990); although, preparation and analysis can be complicated somewhat by the low concentrations of amino acids present in the residue.

A specimen of a scleractinian coral (*Plesiastrea versipora*) extracted from a raised shelly cobble/pebble deposit at Vivonne Bay (Figure 3.45; Chapter 3, section 3.4.4.3), was dated by Uranium-series at the Australian National University (ANU) using the methods described in McCulloch and Mortimer (2008) (the sample was over-spiked during analysis [because of low uranium concentration: ~50 ppb] [Eggins and Mortimer pers. comm., 2008, 2009] and so some caution is warranted as the uncertainty is larger than expected; although, it is still reasonable). The U-series age for the coral was estimated to be 114.3 ± 3.0 ka (ANU lab code: TU 235, 236), which was close to what was expected for the unit (i.e., Last Interglacial in age [MIS 5e]).

The initial assumption (at the time of sampling) of a Last Interglacial age for this deposit was based on morphostratigraphical evidence, and later biostratigraphical evidence, i.e., the height APSL of this unit (+3 m) was comparable to Last Interglacial Glanville Formation sites on the South Australia mainland (+2 to +3 m) (e.g. Eyre Peninsula, Spencer Gulf, Port Wakefield, Port

Adelaide) (cf. Belperio *et al.*, 1984; Murray-Wallace, 1987; Murray-Wallace *et al.*, 1988), and the presence of fragmented *Marginopora vertebralis*: a Glanville Formation indicator fossil (Milnes *et al.* 1983; Ludbrook, 1984; Belperio, 1995; Cann and Clarke, 1993). This deposit is almost certainly a thanatocenosis; therefore it is not surprising that the delicately constructed *Marginopora vertebralis* tests were fragmented.

The ANU U-series age (114.3 ± 3.0 ka) was used to calibrate single foraminifer GLX D-L ratios and molluscan GLX D-L ratios. The foraminifers (*Elphidium* spp. and *Discorbis dimidiatus*) and molluscs (*Nerita* [*Melanerita*] *atramentosa*) used to provide the dependent GLX D-L ratios for the calibration were recovered from the same unit as the coral. As such the implicit assumptions are:

- i) The coral is the same age as the other biomineral components analysed for amino acid racemization, from the same sedimentary deposit.
- ii) All components have similar diagenetic temperature histories. This is a reasonable assumption as marine shell recovered from three different areas along the deposit yielded similar GLX D-L ratios.

In order to calibrate the whole-rock sediment D-L ratio data the original intention was to use the U-series age of the coral *Plesiastrea versipora* and the corresponding GLX D-L ratio recovered from the matrix material that the coral was found in. Unfortunately, the matrix material was found to have a very high proportion of reworked grains, which accounted for the anomalously high matrix D-L ratio (WR GLX D/L 0.543 ± 0.006). If this ratio was used then the calibration would not be representative. Because of this the decision was made to use the U-series age of Schwebel (1978, 1984) (125 ± 20 ka), determined for the Last Interglacial Woakwine I range (see previous section 6.6.2) (cf. Murray-Wallace *et al.*, 2001). The corresponding GLX D-L ratio (0.454 ± 0.017), determined for sediment extracted from various points along this dune range (in this study), was used as the calibration point for the unknown age GLX whole-rock sediment D-L ratios from Kangaroo Island. Diagenetic temperature variation between the Coorong and Kangaroo Island regions should be minimal as both experience similar mean annual temperatures: 14.7°C to 15.4°C for Kangaroo

Island coastal sites, and 14.7° C and 14.5° C for Robe and Naracoorte, respectively. Furthermore, in order to reflect sedimentation processes in operation on Kangaroo Island an average whole-rock GLX D-L ratio (0.238 ± 0.017) determined from a range of modern beach sediments was used as the t_0 (y-intercept) point in the calibration. This D-L ratio was also subtracted from the D-L ratios of the unknowns to account for the contribution of residence time and sediment reworking to the extent of racemization in Kangaroo Island whole-rock sediments.

As a comparison to the U-series calibration of the whole-rock sediment D-L ratios, OSL was also used to calibrate whole-rock sediment D-L ratios. However, in this instance greater caution was exercised in the interpretation of results derived from this application, compared with those methods that date events that coincide with the death of the organism, as with AAR (in terms of cessation of protein metabolism [AAR]; cessation of carbon fixing [^{14}C], and cessation of uranium uptake [U-series]).

To explain: OSL and AAR are essentially “dating” two different events: AAR quantifies the time of cessation of protein formation (and hence the cessation of protein metabolism) which for short-lived organisms essentially equates with death (the two are indistinguishable in terms of the resolution of the amino acid method) of the organism. In contrast, OSL defines the timing of depositional events, i.e., the deposition (and burial) of an inorganic mineral grain. The two events may not coincide.

It is likely that the organism analysed using AAR may have perished some time before (undergoing comminution) being washed up on the beach and subsequently deposited in a dune barrier (or some other near-shore deposit—along with the inorganic minerals dated via OSL). Therefore, this continental shelf to beach to barrier (or other near-shore deposit) “residence time” experienced prior to deposition should be taken into consideration. Nevertheless, with increasing age the residence time is of less importance when deriving an age through OSL calibration of AAR data (if it is assumed that residence is relatively consistent over time), as the uncertainties increase progressively. For example a residence time of several hundred or several

thousand years is of less importance in an AAR age estimate when the calculated uncertainty may be in several tens of thousands of years. For example, when dealing with a sample that has an AAR numerical age estimate of 270 ± 60 ka, then a timing delay (as a result of continental shelf residence) of 2, 5 or even 10 ka that may have been experienced by the organisms skeletal remains prior to deposition is of less importance. It can even be considered negligible in some cases; especially when the uncertainty term may easily encompass the possible offset caused by the delay. However, residence time prior to deposition is not the only adverse issue for this form of calibration: incorporation of reworked sediments also occurs.

This means that a given whole-rock sediment sample will not only contain a single age population of constituent biomineral grains—a portion of the grains *must* also be derived from reworked older sediments. Because of this whole-rock sediment D-L ratios represent an integration of the age populations in the mix (as well as a range of kinetic behaviours and diagenetic histories), and are generally higher in value than either single grain D-L ratios or marine shell D-L ratios extracted from the same sediment. This may not be the case for very dynamic depositional systems such as those found in the Bahamas and Bermuda (Hearty and Kaufman, 2000; Kindler and Hearty, 2000; Hearty and Neumann, 2001). In an Australian context (particularly South Australia), however, there is no doubt that the skeletal carbonate grains, or at least a proportion of the grains, in whole-rock sediment are demonstrably older (Murray-Wallace *et al.*, 2001; Murray-Wallace *et al.*, 2010).

Because of the above characteristics the use of OSL to calibrate whole-rock sediment D-L ratios must be qualified in order for the age estimations to be considered reasonable. This can be done in two ways:

- i) By accounting for the offset in OSL and AAR dating events.
- ii) Qualification by comparison to similar studies.

This will be discussed in the relevant sections later in this chapter.

6.6.4.1 Mollusc GLX D-L ratio age calibration

Two forms of calibration were used to create models that enabled the derivation of amino acid numerical ages for marine molluscs sampled from Kangaroo Island sites.

For Holocene shell samples recovered from American River (Chapter 3: Figure 3.1) AMS ^{14}C ages were used. The ^{14}C dating was undertaken on two individual molluscs (*Katelysia scalarina* [AR 1], and *Katelysia rhytiphora* [AR 2]) one from each site that was examined at American River (Figure 6.32). The age model was developed from these radiocarbon ages, live-collected *Katelysia scalarina* and modern rock-platform *Nerita (Melanerita) atramentosa* (combined as the t_0 GLX D-L ratio). An apparent parabolic kinetic model was used to fit the calibration data with excellent correlation ($R^2 = 0.9957$). The following Table (6.18) and Figure (6.33) illustrate the calibration data. Note that the slope of the linear regression ($5.4 \times 10^{-2} \sqrt{\text{k yr}}$) is much steeper for the molluscs than it is for the Coorong whole-rock sediment calibration ($1.6 \times 10^{-2} \sqrt{\text{k yr}}$) (see Figure 6.28). This is in keeping with overall faster rates of racemization in molluscs, and an initial faster period during early diagenesis—as demonstrated in section 6.5.2.1 (AAR kinetics). AAR ages and uncertainties for the unknowns were calculated using equations 6.4 and 6.6, after the t_0 D-L ratio was subtracted to account for induced racemization from the hydrolysis preparation step. These will be presented and discussed in Chapter 7.

Third party source; Images redacted at request of thesis author

Figure 6.32: Holocene study sites at American River, Kangaroo Island, incorporating coquina deposits (image from Google Earth, 2009).

Table 6.18: Calibration data for American River molluscs.

UOW AAR lab. code	Genus/species	site / sample code	Cal. ^{14}C age $\pm 1\sigma$ (ka BP) ^a	$\sqrt{^{14}\text{C}}$ age $\pm 1\sigma$	GLX D-L ratio $\pm 1\sigma$ (N) ^b
UWGA 5879, 6514	<i>Katelsia scalarina</i>	AR2 / AR#3-5	2.50 ± 0.12 (Wk-21537) ^c	1.58 ± 0.04	0.137 ± 0.010 (1)
UWGA 5878, 6515	<i>Katelsia rhytiphora</i>	AR1 / AR#3-2	5.46 ± 0.11 (Wk-21538) ^c	2.34 ± 0.02	0.170 ± 0.007 (1)
UWGA 5489, 5490	<i>scalarina</i> and <i>Nerita</i> (<i>Melanerita</i>) <i>atramentosa</i>	Live-collected and modern rock-platform	0	0	0.047 ± 0.004 (4)

^a Marine data from Hughen *et al.* (2004); ΔR 62 \pm 63; calibrated using OxCal v3.10 Bronk Ramsey (2005); cub r:5 sd:12 prob usp [chron]

^b Number of individuals or powdered subsamples analysed

^c Waikato Radiocarbon Dating lab code

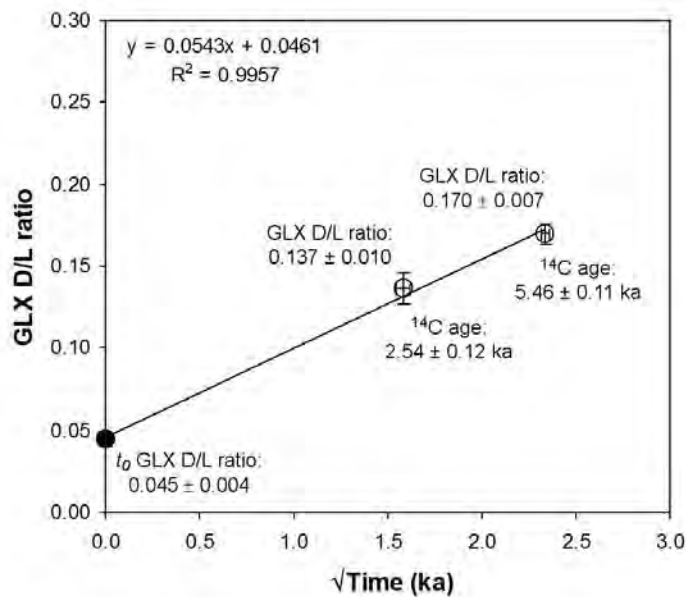


Figure 6.33: Calibration curve for American River molluscs. This system can be described by apparent parabolic kinetics as the relationship between the D-L ratio and the square root of time is linear. Here the fit is excellent, with an R^2 value of 0.9956. This model was generated using two ^{14}C ages (and their corresponding GLX D-L ratios) derived from two mollusc specimens: *Katelsia scalarina* (2495 ± 115 cal. a BP); *Katelsia rhytiphora* (5455 ± 105 cal. a BP), and live-collected *Katelsia scalarina* and modern rock-platform *Nerita* (*Melanerita*) *atramentosa* (for t_0 GLX D/L). Note: no t_0 subtractions are required on the calibration curves—the subtraction is undertaken in the APK age equation.

In order to calibrate the Kangaroo Island Pleistocene mollusc D-L ratios the two ^{14}C ages, and the t_0 point were combined with the U-series age estimate (114.3 ± 3.0 ka) (Table 6.19) for the scleractinian coral *Plesiastrea versipora* recovered from a Last Interglacial shelly cobble/pebble unit at Vivonne Bay (Chapter 3: Figure 3.1, and Figure 6.34). Here the supralittoral-littoral gastropod species *Nerita* (*Melanerita*) *atramentosa*, recovered from the same unit, was used to provide the GLX calibration D-L ratio for the U-series age. The calibration data are given in Table 6.19, and the plot for the linear regression is shown in Figure 6.35. The regression is not as concordant as the fit in Figure 6.33. This is in all likelihood due to the initial rapid phase of GLX racemization, that occurs during early diagenesis in marine molluscs (Wehmiller, 1984b), not being adequately accounted for by the apparent parabolic kinetic method used for calibration. Nonetheless, the regression is still good ($R^2 = 0.9597$), and its proximity to the Point Ellen Sr isotope data point is notable. The slope of the regression was determined to be $2.7 \times 10^{-2} \sqrt{\text{k yr}}$. AAR numerical ages and associated uncertainties were calculated as with the American River molluscs (equations 6.4 and 6.6). These results will be presented and discussed in Chapter 7.

Table 6.19: Calibration data for Kangaroo Island Pleistocene molluscs.

UOW AAR lab. code	Genus/species	Site / sample code	U-series and ^{14}C age $\pm 1\sigma$ (ka)	$\sqrt{\text{Age}} \pm 1\sigma$ (ka)	GLX D-L ratio $\pm 1\sigma$ (N) ^b
UWGA 5872	<i>Plesiastrea versipora</i> (U-series) and <i>Nerita</i> (<i>Melanerita</i>) <i>atramentosa</i> (AAR)	Vivonne Bay / PE#3-4 & 3-5	114.3 ± 3.0 (TU 235, 236) ^c	10.69 ± 0.14	0.364 ± 0.012 (3)
UWGA 5879, 6514	<i>Katelsysia scalarina</i>	AR2 / AR#3-5	2.50 ± 0.12^a (Wk-21537) ^d	1.58 ± 0.04	0.137 ± 0.010 (1)
UWGA 5878, 6515	<i>Katelsysia rhytiphora</i>	AR1 / AR#3-2	5.46 ± 0.11^a (Wk-21538) ^d	2.34 ± 0.02	0.170 ± 0.007 (1)
UWGA 5489, 5490	<i>Katelsysia scalarina</i> and <i>Nerita</i> (<i>Melanerita</i>) <i>atramentosa</i>	Live-collected and modern rock-platform	0	0	0.045 ± 0.004 (8)

^a Marine data from Hughen *et al.* (2004); ΔR 62 ± 63 ; calibrated using OxCal v3.10 Bronk Ramsey (2005); cub r:5 sd:12 prob usp [chron]

^b Number of individuals or powdered subsamples analysed

^c ANU U-series dating lab code

^d Waikato radiocarbon dating lab code

Third party source; Images redacted at request of thesis author

Figure 6.34: Pleistocene study sites at Vivonne Bay, Kangaroo Island, incorporating a Last Interglacial shelly cobble/pebble deposit at site PE3 where the U-series dated coral (*Plesiastrea versipora*—PE#3-4) was recovered (image from Google Earth, 2009).

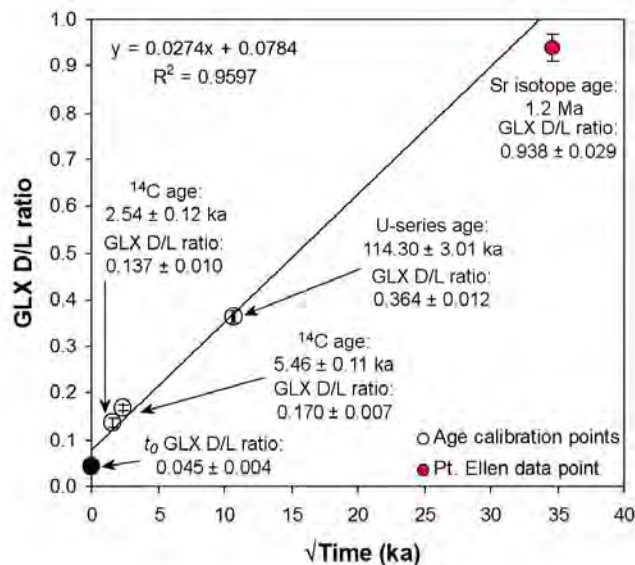


Figure 6.35: Calibration curve for AAR numerical age estimation of Pleistocene molluscs from Kangaroo Island. This system can be described by apparent parabolic kinetics as the relationship between the D-L ratio and the square root of time is relatively linear. The fit of the regression to the data is good, with an R^2 value of 0.9597. This model was generated using a U-series age (and the corresponding mean GLX D-L ratio from *Nerita (Melanerita) atramentosa* fossils found in the same unit) derived from a scleractinian coral: *Plesiastrea versipora* (114.3 ± 3.0 ka); two ^{14}C ages (and their corresponding GLX D-L ratios) derived from two mollusc specimens: *Katylsia scalarina* (2495 ± 115 cal. a BP); *Katylsia rhytiphora* (5455 ± 105 cal. a BP), and live-collected *Katylsia scalarina* and modern rock-platform *Nerita (Melanerita) atramentosa* (for t_0 GLX D/L). The red circle is the mean GLX D-L ratio (0.938 ± 0.029) for *Katylsia scalarina* fossils recovered from the basal unit of the Early Pleistocene Point Ellen Formation, at Point Ellen, Kangaroo Island. This D-L ratio was plotted against the $\sqrt{{}^{87}\text{Sr}/{}^{86}\text{Sr}}$ isotope age (1.2 Ma) of the unit (Belperio, 1995). The point is not part of the linear regression, and is placed for comparison purposes only—the fit is extended for this purpose too. Note: no t_0 subtractions are required on the calibration curves—the subtraction is undertaken in the APK age equation.

In reference to the Point Ellen Sr isotope age mentioned above and in Figure 6.35: Strontium isotope ages are relative ages derived from a marine strontium isotope reference curve (generated from the isotopic composition of planktonic foraminifers) and a corresponding “look-up” table. The method uses variations in the $^{87}\text{Sr}/^{86}\text{Sr}$ ratio of biogenic carbonates that record the strontium isotope composition of ambient sea-water, over Phanerozoic time (Hodell *et al.*, 1991; Oslick *et al.* 1994; McArthur *et al.*, 2001). The uncertainties associated with strontium isotope ages can be very large. There are not only uncertainties associated with the measurement of the $^{87}\text{Sr}/^{86}\text{Sr}$ ratios and age assignments used to construct the reference curves, but also uncertainties related to the measurement of the $^{87}\text{Sr}/^{86}\text{Sr}$ ratio of the unknowns, the slope of the reference curve section, and the extent of preservation of the original isotopic composition of both the control and the unknown samples (Banner, 2004). For example the Farrell *et al.* (1995) Sr seawater curve and the Hodell *et al.* (1991) Sr seawater curve have a stratigraphic resolution of ± 0.6 Ma for the early Pleistocene. The Point Ellen $^{87}\text{Sr}/^{86}\text{Sr}$ age of 1.2 Ma from Belperio (1995) was quoted without an accompanying uncertainty term; therefore if the Farrell *et al.* (1995) or Hodell *et al.* (1991) reference curves are used to define the uncertainty for the Point Ellen age, the age could lie somewhere between 0.6 Ma and 1.8 Ma (this is assuming that the central age is good). In light of this, caution should be exercised when referring to this numerical age for the Point Ellen Formation. Furthermore, the $^{87}\text{Sr}/^{86}\text{Sr}$ age data point is only included in the calibration graphs in this study as a comparison, and is not meant to be used as any type of confirmation for the validity of the AAR calibrations. Although, it is interesting to note that the $^{87}\text{Sr}/^{86}\text{Sr}$ age and its corresponding material GLX D-L ratios conform quite well to each of the calibration regressions.

6.6.4.2 Foraminifer GLX D-L ratio age calibration

Kangaroo Island Pleistocene foraminifers were calibrated with the U-series age estimate (114.3 ± 3.0 ka) and the t_0 point. Here a combination of the foraminifers *Elphidium* spp. and *Discorbis dimidiatus* (expressed as a mean)—extracted from the matrix material of the Last Interglacial deposit at Vivonne Bay (also the matrix surrounding the U-series coral [*Plesiastrea versipora*]) and the modern beach whole-rock sediment sample EB#2-7—were used to provide

Table 6.20: Calibration data for Kangaroo Island Pleistocene foraminifers.

UOW AAR lab. code	Genus/species	Site / sample code	U-series and ^{14}C age \pm 1 σ (ka)	$\sqrt{\text{Age}} \pm 1\sigma$ (ka)	GLX D-L ratio $\pm 1\sigma$ (<i>N</i>) ^b
UWGA 5871, 6587, 6588	<i>Plesiastrea versipora</i> (U-series) and <i>Elphidium</i> spp. and <i>Discorbis dimidiatus</i> (AAR)	Vivonne Bay / PE#3-4 (coral), 3- 4a, 3-5, 3-6	114.3 ± 3.0 (TU 235, 236) ^a	10.69 ± 0.14	0.308 ± 0.025 (11)
UWGA 6550, 6586, 6588	<i>Elphidium crispum</i> and <i>Discorbis</i> <i>dimidiatus</i>	Emu Bay / EB#2-7 modern beach ^c	0	0	0.076 ± 0.018 (17)

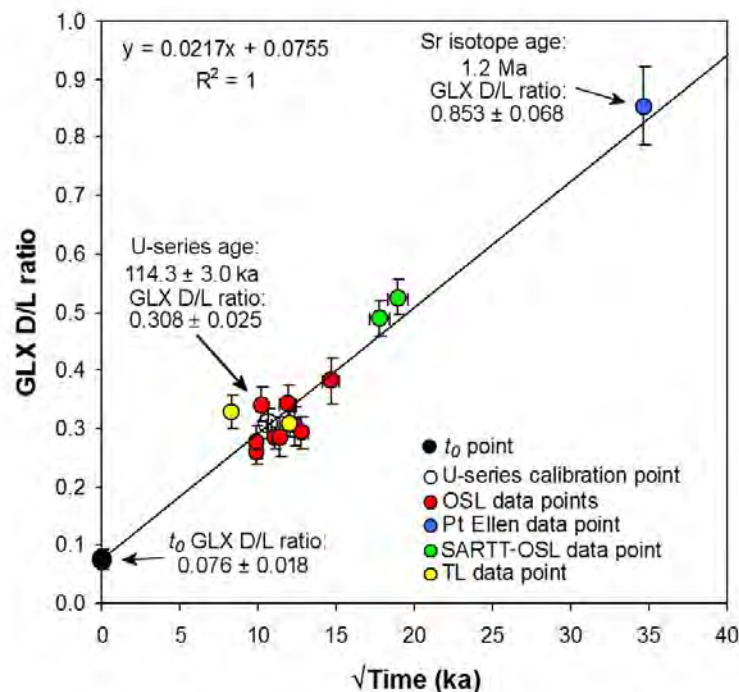
^a ANU U-series dating lab code^b Number of individual foraminifers^c The sample was used for t_0 as it had the lowest GLX D-L ratio of all modern beach sediments examined

Figure 6.36: Calibration curve for AAR age estimation of Pleistocene foraminifers from Kangaroo Island. This system can be described by apparent parabolic kinetics as the relationship between the D-L ratio and the square root of time is linear. The fit of the regression to the data is $R^2 = 1$, as there are only 2 points. This model was generated using a U-series age (and the corresponding mean GLX D-L ratio from *Elphidium* spp. and *Discorbis dimidiatus* fossil foraminifers found in the same unit) derived from a scleractinian coral: *Plesiastrea versipora* (114.3 ± 3.0 ka). The blue circle is the mean GLX D-L ratio (0.853 ± 0.068) for *E. rotatum* fossils recovered from the basal unit of the Early Pleistocene Point Ellen Formation, at Point Ellen, Kangaroo Island. This D-L ratio was plotted against the $\sqrt{^{87}\text{Sr}/^{86}\text{Sr}}$ isotope age (1.2 Ma) of the unit (Belperio, 1995). The red circles are the mean GLX D-L ratios for all of the OSL dated units (where foraminifers could be recovered) plotted against the corresponding $\sqrt{\text{OSL age}}$ (ka), the green circles are the mean GLX D-L ratios for all of the SARTT-OSL dated units (where foraminifers could be recovered) plotted against the corresponding $\sqrt{\text{SARTT-OSL age}}$ (ka), and the yellow circles are the mean GLX D-L ratios for the TL dated units, plotted against the corresponding TL age. These points (red, blue, green, and yellow) are not part of the linear regression, and are placed for comparison purposes only—the fit is extrapolated for this purpose too. Note: no t_0 subtractions are required on the calibration curves—the subtraction is undertaken in the APK age equation.

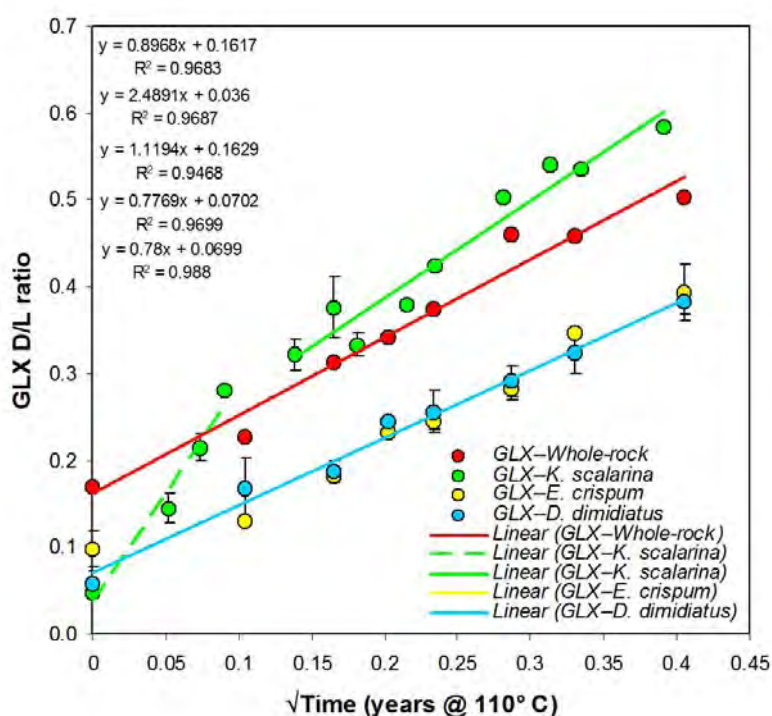


Figure 6.37: A comparison of all GLX data (Whole-rock sediment, *Katelaysia scalarina*, *Elphidium crispum*, and *Discorbis dimidiatus*) from the pyrolysis experiments; untransformed and plotted as linear regressions vs. $\sqrt{\text{Time}}$ (as in the apparent parabolic kinetic method). What this graph shows is the striking similarity between each of the heated materials in terms of slope (particularly in later diagenesis for *Katelaysia scalarina*), i.e., $9.0 \times 10^{-1} \sqrt{\text{yr}^{-1}}$ for whole-rock; $1.1 \sqrt{\text{yr}^{-1}}$ for *Katelaysia scalarina*, and $7.8 \times 10^{-1} \sqrt{\text{yr}^{-1}}$ for *Elphidium crispum* and *Discorbis dimidiatus*—hence the overlap of both regression lines.

calibration GLX D-L ratios for the regression (Table 6.20 and Figure 6.36). Figure 6.36 also includes GLX D-L ratios vs. their corresponding $\sqrt{\text{OSL}}$ and $\sqrt{\text{SARTT-OSL}}$ ages and the $^{87}\text{Sr}/^{86}\text{Sr}$ isotope age (1.2 Ma), as a comparison to the calibration regression (these are not included in the fit). The comparison points all conform quite well to the regression; the slope is $2.2 \times 10^{-2} \sqrt{\text{k yr}^{-1}}$. This is not quite as steep as with the Pleistocene molluscs ($2.7 \times 10^{-2} \sqrt{\text{k yr}}$), which is expected, and it is marginally steeper than the Coorong whole-rock calibration ($1.6 \times 10^{-2} \sqrt{\text{k yr}}$). The comparative similarity of each of these slopes is not unanticipated as the amino acids (here GLX) examined in the previous pyrolysis sections, when plotted as time transformed linear regressions (as with the apparent parabolic kinetic method), show similar comparative slopes (Figure 6.37). GLX in *Katelaysia scalarina* has a dramatic inflection point; prior to this point the slope is approximately twice as steep as it is after the inflection, showing an initial rapid period of racemization. The other biomineral materials

too have inflection points; however, they are much less obvious than in the molluscs (particularly for whole-rock sediment and *Elphidium crispum*: see Figure 6.20 in the pyrolysis section [6.5]), and are masked by the time transformation. Figure 6.37 demonstrates that, after a period of time (i.e., during later diagenesis), the differences in racemization rates between molluscs, whole-rock sediment and foraminifers, at least for the amino acid GLX, become less pronounced.

AAR numerical ages and associated uncertainties for the Pleistocene foraminifer samples were calculated with equations 6.4 and 6.6. These results will be presented and discussed in Chapter 7.

6.6.4.3 Whole-rock sediment GLX D-L ratio age calibration

Two calibrations were undertaken on the Kangaroo Island whole-rock sediments:

- i) Calibration using the U-series age of Schwebel (1978, 1984) (125 ± 20 ka), determined for the Last Interglacial Woakwine I range (see previous section: 6.6.2) (cf. Murray-Wallace *et al.*, 2001).
- ii) Calibration using a series of OSL ages and their corresponding GLX D-L ratios.

The validity of an AAR calibration method using luminescence ages and corresponding GLX D/L ratios is tested by comparison to the U-series calibration. Before this, however, the U-series calibration will be described.

As with the Kangaroo Island marine molluscs and benthic foraminifers, whole-rock sediments were age estimated using the apparent parabolic kinetic method of Mitterer and Kriausakul (1989), see section 6.62. This method allows the calculation of numerical ages by directly calibrating the extent of racemization (here GLX) in a sediment sample with an independently determined age for that same sediment. In this study the U-series age determined by Schwebel (1978, 1984) for the Woakwine I range (125 ± 20 ka) on the Coorong Coastal plain in south-east South Australia (Figure 6.14) was used in conjunction with the mean

GLX D-L ratio (0.454 ± 0.017) of whole-rock sediments collected from different locations within the Woakwine I dune unit (Table 6.21 and Figure 6.38).

The Kangaroo Island whole-rock sediment subsamples were also calibrated using a series of OSL dated whole-rock sediment samples and their corresponding GLX D-L ratios (along with a t_0 sample). Murray-Wallace (2000) advised caution when using luminescence methods to calibrate amino acid D-L ratios; this is because it is not normally the same event that is being dated, as stated previously.

Table 6.21: U-series calibration data for Kangaroo Island whole-rock aeolianite

UOW AAR lab code	Material	Site / sample code	U-series age $\pm 1\sigma$ (ka)	\sqrt{U} -series age $\pm 1\sigma$	GLX D-L ratio $\pm 1\sigma$ (N) ^b
UWGA 6519, 6521, 6525	Whole-rock aeolianite sediment	Woakwine I range / WW#1-1, WC#1-1, WW#1-3	125 ± 20^a	$11.18^{+0.86}_{-0.93}$	0.454 ± 0.017 (6)
UWGA 6541, 6542, 6543	Whole-rock modern beach sediment	Point Ellen, Bales Beach and Hanson Bay / PE#2-4, PE#2-5, Bales#1-2 and HB#3a (AAR) ^c	0	0	0.238 ± 0.017 (11)

^a Calibration point (U-series age for the Last Interglacial Woakwine I dune [Schwebel, 1978; 1984])

^b Number of subsamples analysed

^c The mean GLX D-L ratio of these samples was used for t_0 ; they represent the lowest set of modern beach D-L ratios from the south coast of Kangaroo Island.

The slope of the regression (via the apparent parabolic kinetic equation, as with the other calibrations) can be used to determine ages for unknowns (i.e. unknown age GLX D-L ratios). However, before this it must be qualified that the differences in the timing of the two events (OSL: deposition and burial; AAR: cessation of protein metabolism) are adequately taken into account. Marine organisms that can be used for amino acid D-L ratio determination are not normally deposited in dune barriers immediately after death. Nevertheless, there are exceptions: Murray-Wallace *et al.* (1996) found fossils of molluscs (*Katelysia rhytiphora*) that asphyxiated after failing to keep pace with rapid sediment accumulation (i.e. transgressive coastal dunes) cascading into the (late Pleistocene) back-barrier coastal lagoonal environment. In this case the timing of the death of the organism could be regarded as being equivalent to the time of deposition and burial of the surrounding sediment. In this study, however, OSL is being used to calibrate *whole-rock sediment* D-L ratios, and so a similar scenario does not really exist.

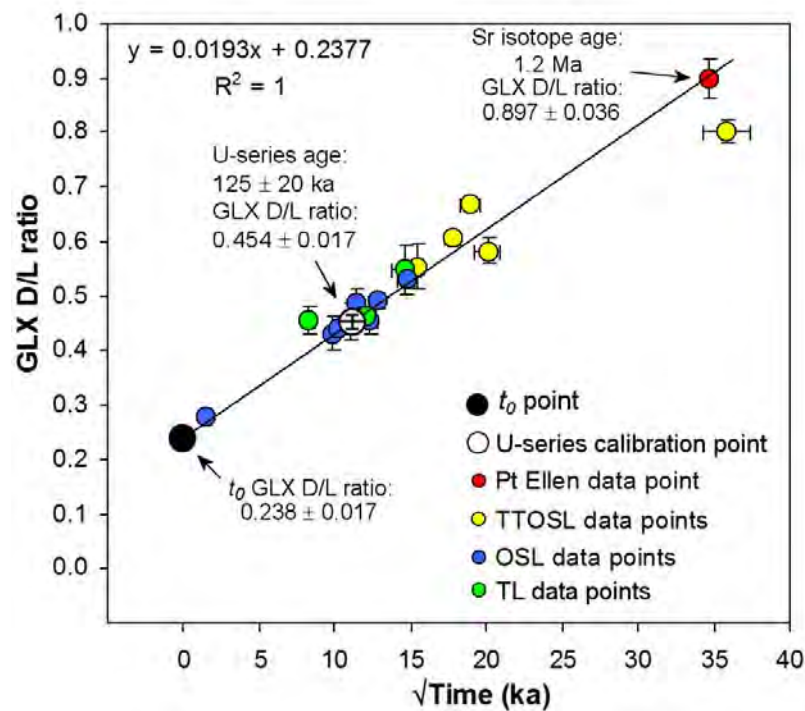


Figure 6.38: Calibration curve for AAR age estimation of Pleistocene whole-rock sediment from Kangaroo Island. This system can be described by apparent parabolic kinetics as the relationship between the D-L ratio and the square root of time is linear. The fit of the regression to the data is $R^2 = 1$, as there are just two data points in the regression. This model was generated using U-series age determined by Schwebel (1978, 1984) for the Woakwine I range (125 ± 20 ka) (and the corresponding mean GLX D-L ratios) and a t_0 point. The red circle is the mean GLX D-L ratio (0.897 ± 0.036) for whole-rock sediment recovered from the basal unit of the Early Pleistocene Point Ellen Formation, at Point Ellen, Kangaroo Island. This D-L ratio was plotted against the $\sqrt{{}^{87}\text{Sr}/{}^{86}\text{Sr}}$ Sr isotope age (1.2 Ma) of the unit (Belperio, 1995). The blue circles are the mean GLX D-L ratios for all of the OSL dated units (these are not part of the regression) plotted against the corresponding $\sqrt{\text{OSL age (ka)}}$, and the yellow circles are the mean GLX D-L ratios for all of the SARTT-OSL dated units (also not part of the regression) plotted against the corresponding $\sqrt{\text{SARTT-OSL age (ka)}}$. The green circles are the TL ages. These points (red, blue, yellow, and green) are not part of the linear regression, and are placed for comparison purposes only—the fit is extrapolated for this purpose too. Note: no t_0 subtractions are required on the calibration curves—the subtraction is undertaken in the APK age equation.

Biogenic marine sediments will generally experience lengthy periods of time (i.e. hundreds or thousands of years) on the continental shelf (see section 6.6.2 of this chapter) and on the near-shore undergoing comminution and mixing, prior to incorporation within a dune barrier or a similar deposit. During this time racemization of the constituent amino acids residing in the organic component of the biomineral grain is also occurring. Once the sediment is deposited (along with other [inorganic] grains, i.e., quartz) and the grains are buried, the $t = 0$ event for OSL dating is defined. Hence, the time lag denoted by the racemization that took place before deposition, burial and the initialization of the

OSL signal, should be taken into account. Additionally, whole-rock sediment will rarely consist of a single time-population of biomineral grains; there will generally be older component populations reworked into the younger sediment from proximal near-shore deposits. Reworked components notwithstanding, the mix of grains will still represent a continuum (i.e. the sample will still represent a time-series of D-L ratios).

One way to account for the shelf to near-shore residence time of fossil biomineral grains (in a carbonate aeolianite for example) is to make the implicit assumption that the extent of racemization in a modern equivalent of these sediment grains—modern beach sediments—is comparable to, or representative of, this residence time (cf. Murray-Wallace *et al.*, 2001). Continuing in this vein, the further assumption is made that inclusive in this degree of racemization is the contribution from reworked biomineral grains as well. In this instance then, one performs an empirical “correction” of the subsample D-L ratio result by subtracting the extent of racemization in a modern equivalent (the t_0 whole-rock modern beach sediment D-L ratio) (Murray-Wallace *et al.*, 2001) (Equation 6.4). Thus, in this way the time-lag (and reworked components) can be somewhat accounted for, at least the portion attributable to shelf and near-shore residence. This is not a perfect solution; however, it is not without merit as was shown in section 6.6.2 of this chapter. Here the differences between live-collected mollusc D-L ratios and host modern beach sediment D-L ratios were shown to be similar to that of Last Interglacial (MIS 5e) molluscs and their host sediments.

The other portion of the time-lag: near-shore to deposition (in a dune barrier for example), is more difficult to quantify. However, the time-scale on which this takes place may be sufficiently short that the consequential effect of *not* accounting for its duration will be minimal. If the sediment takes decades or even centuries to move from the beach and arrive at its burial “destination”; the resultant effect on the AAR age estimate, particularly in Pleistocene sediments, would be relatively insignificant. It should be noted here that the apparent age of the modern back-shore dunes at Pennington Bay is approximately 100 years

(OSL age $[0.10 \pm 0.01 \text{ ka}]$ of modern dune sample PB#2b-8); this would indicate a relatively short beach-to-dune lag-time.

This study employs an empirical subtraction of the t_0 whole-rock modern beach sediment D-L ratio from the whole-rock subsample D-L ratio, prior to calibration using the slope of a linear regression derived from the alignment of the Schwebel (1978, 1984) \sqrt{U} -series age (along with its corresponding GLX D-L ratio) and in a separate calibration, $\sqrt{\text{OSL}}$ ages and their corresponding D-L ratios. The reason for not utilizing the Vivonne Bay U-series age as a calibration point (rather than OSL) in this instance was that, unfortunately, the whole-rock sediment that the U-series coral (*Plesiastrea versipora*: $114 \pm 3 \text{ ka}$) was recovered from had a disappointingly high set of D-L ratios. This was attributable to the fact that the host sediment has a large older reworked component (75% or more of older grains), derived from adjacent, actively eroding, middle-Pleistocene aeolianites (SARTT-OSL dated). Conversely, it was acceptable to use the U-series age as a calibration point for the foraminifer subsamples as single-grain AAR analysis allows different populations of D-L ratios to be resolved; hence, the representative population can be identified (see Figure 6.23).

The whole-rock sediment calibration data are presented in Table 6.22. Here 4 OSL ages and their corresponding D-L ratios were used, along with a t_0 whole-rock D-L ratio (compiled as a mean of the D/L results from 3 modern beaches along the southern coast of Kangaroo Island: Point Ellen, Bales Beach, and Hanson Bay).

The luminescence dating portion of this study consisted of 20 luminescence age determinations (11 OSL, 6 SARTT-OSL, and 3 TL), it would have been possible to use all of these (or at least the non-experimental methods) as calibration points; however, to do so would mean a further inflation of the uncertainty associated with the AAR age estimates, as each of the age errors would need to be propagated. As such I chose a series of 4 ages that I had high confidence in; based upon OSL samples that exhibited good luminescence behaviour (i.e. relatively low overdispersion, and a high ratio of useable

aliquots). The SARTT-OSL ages are not used in any calibration as this is an experimental method, and conversely the calibrations are also used as a proxy form of validation for these data. In that these SARTT-OSL ages and their corresponding D-L ratios would be expected to conform to the regression.

Table 6.22: Calibration data for Kangaroo Island Pleistocene whole-rock sediment samples.

UOW AAR lab. code	Material	Site / sample code	OSL age \pm 1 σ (ka)	$\sqrt{\text{OSL Age}}$ \pm 1 σ (ka)	GLX D-L ratio \pm 1 σ (N) ^a
UWGA 6551	Whole-rock cliff-top unconsolidated dune sediment	Pennington Bay / PB#2c-1 (OSL) and PB#2c-4 (AAR)	2.09 \pm 0.15	1.45 \pm 0.05	0.279 \pm 0.003 (4)
UWGA 6493	Whole-rock aeolianite sediment	Bales Beach / Bales#2-9 (OSL) and Bales#2-5 (AAR)	105 \pm 7	10.25 ^{+0.34} -0.35	0.439 \pm 0.007 (4)
UWGA 6553, 6564	Whole-rock aeolianite sediment	Pennington Bay / PB#2-18 (OSL and AAR)	122 \pm 7	11.05 ^{+0.31} -0.32	0.454 \pm 0.035 (5)
UWGA 6502, 6556	Whole-rock aeolianite sediment	Pennington Bay / PB#3-2 (OSL and AAR)	217 \pm 16	14.73 ^{+0.53} -0.55	0.530 \pm 0.002 (4)
UWGA 6541, 6542, 6543	Whole-rock modern beach sediment	Point Ellen, Bales Beach and Hanson Bay / PE#2-4, PE#2-5, Bales#1-2 and HB#3a (AAR) ^b	0	0	0.238 \pm 0.017 (11)

^a Number of subsamples of whole-rock sediment analysed

^b The mean of all of these samples was used for t_0 ; they represent the lowest set of modern beach D-L ratios from the south coast of Kangaroo Island.

Figure 6.39 demonstrates the non-linear nature of GLX racemization kinetics in the Kangaroo Island whole-rock sediments by comparing the extent of racemization in GLX (THAA) with the corresponding luminescence chronology (OSL, TL, and SARTT-OSL).

The GLX D-L ratio vs. $\sqrt{\text{OSL age}}$ regression is plotted in Figure 6.40. The plot shows excellent conformation ($R^2 = 0.997$) to parabolic kinetics as the relationship to the $\sqrt{\text{time}}$ is linear. Other variables on this plot (and matching GLX D-L ratios) include $\sqrt{\text{OSL}}$ ages that were not part of the regression (blue), and $\sqrt{\text{SARTT-OSL}}$ ages (green). The $\sqrt{{}^{87}\text{Sr}/{}^{86}\text{Sr}}$ isotope age (1.2 Ma) of the Point Ellen Formation is also included (Belperio, 1995) (red). These were plotted for comparative purposes only, and it can be seen that these points conform relatively well with the regression. The slope of the OSL calibrated whole-rock sediment regression (used in the apparent parabolic kinetic

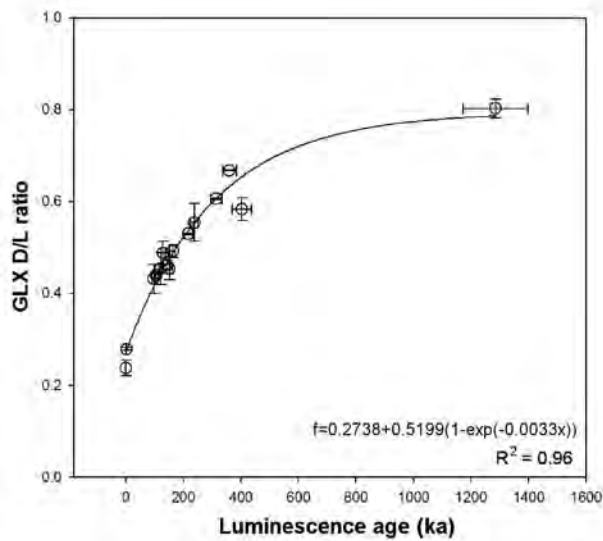


Figure 6.39: D-L ratio data vs. luminescence ages from this study, fitted with an exponential function. This plot demonstrates the non-linear nature of GLX kinetics over time, and the appropriateness of the apparent parabolic kinetic calibration method in application to these data.

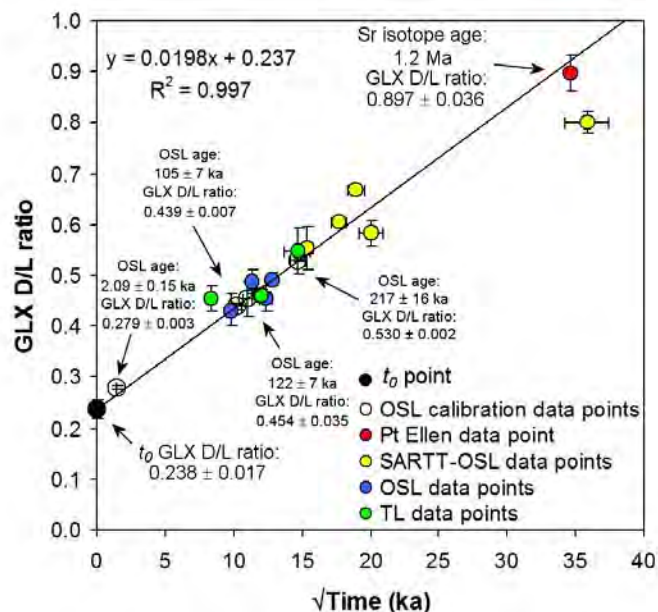


Figure 6.40: Calibration curve for AAR age estimation of Pleistocene whole-rock sediment from Kangaroo Island. This system can be described by apparent parabolic kinetics as the relationship between the D-L ratio and the square root of time is linear. The fit of the regression to the data is $R^2 = 0.997$. This model was generated using 4 OSL ages (and the corresponding mean GLX D-L ratios) and a t_0 point. The red circle is the mean GLX D-L ratio (0.897 ± 0.036) for whole-rock sediment recovered from the basal unit of the Early Pleistocene Point Ellen Formation, at Point Ellen, Kangaroo Island. This D-L ratio was plotted against the $^{87}\text{Sr}/^{86}\text{Sr}$ isotope age (1.2 Ma) of the unit (Belperio, 1995). The blue circles are the mean GLX D-L ratios for all of the OSL dated units (that were not part of the regression) plotted against the corresponding $\sqrt{\text{OSL age}}$ (ka), the yellow circles are the mean GLX D-L ratios for all of the SARTT-OSL dated units (also not part of the regression) plotted against the corresponding $\sqrt{\text{TTOSL age}}$ (ka), and the green circles are the mean GLX D-L ratios for all of the TL dated units (not part of the regression) plotted against the corresponding $\sqrt{\text{TL age}}$ (ka). These points (red, blue, yellow, and green) are not part of the linear regression, and are placed for comparison purposes only—the fit is extended for this purpose too. Note: no t_0 subtractions are required on the calibration curves—the subtraction is undertaken in the APK age equation.

equation [6.4, 6.5] to estimate AAR ages for unknowns) is $2.0 \times 10^{-2} \sqrt{k} \text{ yr}^{-1}$. This is very similar to that derived from the Schwebel (1978, 1984) U-series calibration of the Kangaroo Island whole-rock ($1.9 \times 10^{-2} \sqrt{k} \text{ yr}^{-1}$) and the Coorong calibration ($1.6 \times 10^{-2} \sqrt{k} \text{ yr}^{-1}$), in this section and section 6.6.2 of this chapter, respectively. The similarity of these regressions (as demonstrated in Figure 6.41), where two different forms of calibration were used (U-series for the Coorong whole-rock sediments, and U-series and OSL for the Kangaroo Island whole-rock sediments), further qualifies the use of OSL ages and corresponding GLX D-L ratios as a form of apparent parabolic kinetic calibration.

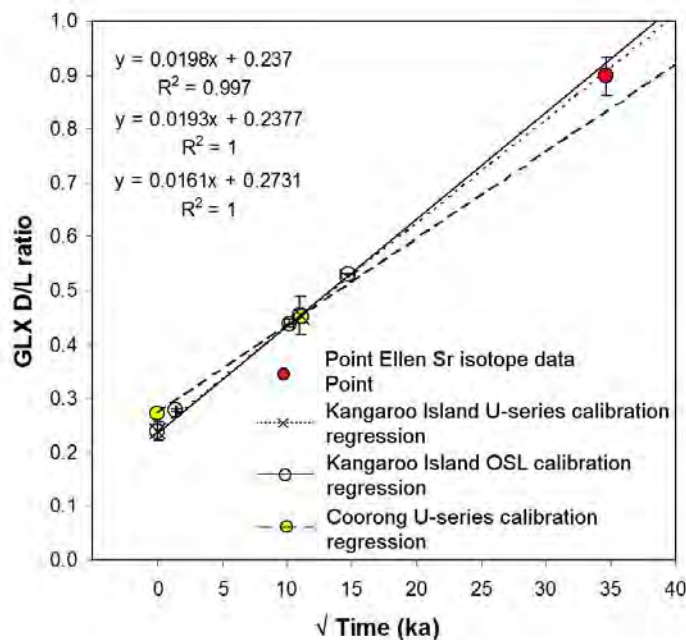


Figure 6.41: Direct comparison of the Kangaroo Island whole-rock sediment calibration (utilizing OSL ages) with the U-series calibration of the same data, and the Coorong whole-rock calibration (both of which used a single U-series age of $125 \pm 20 \text{ ka}$ [Schwebel, 1978; 1984] as a calibration point). The similarity between the three regressions is reasonable. The factor that causes the deviation is the slight difference in the t_0 GLX D-L ratios; as all regressions pivot around 122-125 ka. Note: no t_0 subtractions are required on the calibration curves—the subtraction is undertaken in the APK age equation.

AAR numerical ages and associated uncertainties for the Pleistocene whole-rock samples were calculated with equations 6.4 and 6.6. The dating results for both the U-series, and OSL calibrations are presented and discussed in the following results chapter (Chapter 7). The U-series calibration was preferentially used to provide AAR ages; although, the differences between the two

calibrations are shown to be small. Both sets of results are presented side by side in the dating tables in Chapter 7.

6.7 Summary and conclusions

This chapter has examined in detail the application of the amino acid racemization method to fossil molluscs, foraminifers, and whole-rock sediments, and has explained the instrumental derivitisation of D-L ratios. Sampling strategies for the various materials, and sample preparation were also outlined. In order to ensure good quality data various rejection criteria, preparation strategies, and data reduction methods were also employed.

Through a series of pyrolysis experiments the kinetic behaviour of ASX, GLX, and VAL was explored, and the results of these experiment led to the choice of GLX as the amino acid with the most utility (in terms of range and stability), for the Kangaroo Island samples.

The final portion of the chapter explored the apparent parabolic calibration of amino acid D-L ratio data using the apparent parabolic kinetic method (APK) and corresponding numerical ages (i.e. derived from U-series, AMS ^{14}C , and OSL). The estimation of uncertainties, and the sources of uncertainties in AAR numerical age estimation were also examined in detail.

Several calibration curves were generated (using APK) for molluscan, foraminifer, and whole-rock sediment D-L ratio data, which have allowed the creation of an aminostratigraphy, and numerical amino acid racemization ages for Kangaroo Island stratigraphical units. An APK calibration was also generated for a series of samples taken from the stranded dune sequence on the Coorong Coastal Plain, which allowed the estimation of a set of numerical ages comparable to the TL and LEU chronologies of Huntley *et al.* (1993; 1994), and Murray-Wallace *et al.* (2001).

These calibrations have been applied in Chapter 7 (the dating results chapter) (along with luminescence ages) to generate a relatively comprehensive set of ages for a range of carbonate sediments located around Kangaroo Island.

calibrations are shown to be small. Both sets of results are presented side by side in the dating tables in Chapter 7.

6.7 Summary and conclusions

This chapter has examined in detail the application of the amino acid racemization method to fossil molluscs, foraminifers, and whole-rock sediments, and has explained the instrumental derivitisation of D-L ratios. Sampling strategies for the various materials, and sample preparation were also outlined. In order to ensure good quality data various rejection criteria, preparation strategies, and data reduction methods were also employed.

Through a series of pyrolysis experiments the kinetic behaviour of ASX, GLX, and VAL was explored, and the results of these experiment led to the choice of GLX as the amino acid with the most utility (in terms of range and stability), for the Kangaroo Island samples.

The final portion of the chapter explored the apparent parabolic calibration of amino acid D-L ratio data using the apparent parabolic kinetic method (APK) and corresponding numerical ages (i.e. derived from U-series, AMS ^{14}C , and OSL). The estimation of uncertainties, and the sources of uncertainties in AAR numerical age estimation were also examined in detail.

Several calibration curves were generated (using APK) for molluscan, foraminifer, and whole-rock sediment D-L ratio data, which have allowed the creation of an aminostratigraphy, and numerical amino acid racemization ages for Kangaroo Island stratigraphical units. An APK calibration was also generated for a series of samples taken from the stranded dune sequence on the Coorong Coastal Plain, which allowed the estimation of a set of numerical ages comparable to the TL and LEU chronologies of Huntley *et al.* (1993; 1994), and Murray-Wallace *et al.* (2001).

These calibrations have been applied in Chapter 7 (the dating results chapter) (along with luminescence ages) to generate a relatively comprehensive set of ages for a range of carbonate sediments located around Kangaroo Island.

Chapter 7: Kangaroo Island dating results

7.1 Introduction

The previous three chapters have explained the methods and background of the various dating techniques (and where associated, dosimetry techniques) utilised in this thesis.

This chapter will present the results derived from analyses using conventional OSL, TL, SARTT-OSL, AMS¹⁴C, ²³⁸U/²³⁰Th series, and AAR dating methods. However, before describing the results of the geochronological analyses, the luminescence dosimetry results are presented and discussed.

This chapter is divided into 4 parts for the sake of convenience:

Part I: Luminescence dosimetry

Part II: South coast geochronology

Part III: East coast and Dudley Peninsula geochronology

Part IV: North coast geochronology

This chapter concludes with a summary of the geochronological results. A detailed evaluation and a set of conclusions, in relation to the formation and evolution of Quaternary carbonate deposits on Kangaroo Island (using insights gained in all previous Chapters) is presented in the final chapter: Chapter 8.

PART I: Luminescence dosimetry

7.2 Dosimetry

Eight luminescence samples were analysed from Kangaroo Island for radionuclides using HRGS (high resolution gamma spectrometry). This method can delineate both parents and progeny (or daughters) in the decay chains of interest, e.g. ^{238}U and ^{232}Th . The strength of the method really being the capacity to compare the activity concentrations of parent and daughter radionuclides directly, in order to not only calculate dose rates, but also to identify any significant disequilibrium in the decay chains.

A combination of thick-source alpha counting (TSAC), Geiger-Müller beta counting (GMBC), field gamma-spectrometry (FGS), inductively coupled plasma-optical emission spectrometry (ICP-OES), and instrumental neutron activation analysis (INAA) was used to determine β and γ dose rates for remaining Kangaroo Island luminescence samples (12 samples). While direct determination of equilibrium conditions was not possible for these samples, a comparison of TSAC and INAA U and Th does allow for the detection of disequilibrium: as one method derives the concentrations from the activity of daughters and the other directly from the parents. A difference between the two could indicate a state of disequilibrium. This was done for 9 of the Kangaroo Island samples.

7.2.1 Disequilibrium and the results from high resolution gamma spectrometry

When a parent nuclide has a much longer half-life than its daughters (i.e. the activity of the parent does not decrease markedly over many half lives of the daughters). Concentration of a particular daughter nuclide can build up until the rate at which it is being produced (by the parent) equals the rate at which it decays. In this case the activity concentrations of daughter nuclides remain constant as they are 'supported' by a decaying parent. This state is called 'secular equilibrium'. In the case of the longer-lived daughters in the ^{238}U decay series, secular equilibrium is reached when the activity concentrations of $^{238}\text{U} = ^{234}\text{U} = ^{230}\text{Th} = ^{226}\text{Ra} = ^{222}\text{Rn} = ^{210}\text{Pb}$ (Olley *et al.* 1996). If parent or daughter nuclides are moved into or out of the system then activity concentrations can

alter, this is called *disequilibrium*. The use of a dosimetry method that will delineate the parents *and* the daughters in a decay series is desirable to verify that the sediments are in secular equilibrium, or if not, determine the level of disequilibrium. Some methods, for example INAA, ICP-MS and XRF, typically will only reveal the concentration of the parent nuclides. Hence, when utilising these methods the assumption is made that the decay chains have always been in equilibrium, however, the true equilibrium state is unknown. Other methods such as TSAC and FGS measure nuclides in the lower portions of the decay series, and so allow for a better evaluation of the dose rate, this is assuming that it is the parent that has been altered (the ^{238}U decay chain is of particular importance, as disequilibrium in this chain is commonplace in many depositional environments, owing to the high solubility of U isotopes). For example any net increase or deficit in U may not have had time to influence activity concentrations in the lower parts of the series, of course this will also depend upon sediment age. In this instance these techniques (TSAC and FGS) allow for a superior estimate that may be based upon something close to the original equilibrium state, i.e. before the addition of allochthonous U or leaching of parent U for example: the assumption of a constant dose rate notwithstanding. Thorium is not as mobile as U because of its high ionic potential, i.e. it does not go easily into solution, and so is less prone to leaching for example. This is reflected in the HRGS results from Kangaroo Island (Table 7.1). Even if disequilibrium occurs the relatively short half lives of its progeny (^{228}Ra has the longest at $\tau_{1/2} = 5.75$ a) means that, for samples older than around 20 years, any disequilibrium in this chain is relatively unimportant anyway (Olley *et al.*, 1997). Upon examination of the HRGS results it can be seen most of the samples (except Bales#2-9, and possibly PB#2b-8) in the ^{238}U series are in disequilibrium, in that ^{238}U is in deficit with respect to ^{226}Ra . Additionally, the activity concentrations of ^{210}Pb are in deficit with respect to ^{226}Ra ; this is, in all probability, due to diffusive loss of ^{222}Rn to the atmosphere. Following Olley *et al.* (1997) the assumption is made here that this has prevailed since deposition, in all samples. Geochemical sorting can act to move radionuclides (both parent and progeny) into or out of a system, establishing disequilibria. According to Olley *et al.* (1996) there are three main processes that facilitate this:

Table 7.1: HRGS radionuclide activities summary and daughter-to-parent ratios for the ^{238}U and ^{232}Th decay chains: used to calculate the environmental dose rates for 8 Kangaroo Island samples. Units are in Bq/kg^{-1} with associated 1σ uncertainties.

Sample code	U-238 Series					Th-232 Series			K-40 (Bq/kg ⁻¹)
	U-238	Ra-226	Pb-210	Ra-226: U-238	Pb-210: Ra-226	Ra-228	Th-228	Th-228: Ra-228	
	(Bq/kg ⁻¹)	(Bq/kg ⁻¹)	(Bq/kg ⁻¹)			(Bq/kg ⁻¹)	(Bq/kg ⁻¹)		
Bales#2-9	12.91 ± 0.98	12.23 ± 0.23	9.66 ± 1.13	0.95 ± 0.07	0.79 ± 0.09	4.12 ± 0.31	3.93 ± 0.21	0.95 ± 0.09	36.93 ± 2.11
PB#2-18	13.68 ± 0.79	20.45 ± 0.28	14.45 ± 0.84	1.49 ± 0.09	0.71 ± 0.04	6.16 ± 0.23	5.93 ± 0.19	0.96 ± 0.05	29.62 ± 1.23
PB#2b-3	18.43 ± 0.80	23.17 ± 0.31	16.60 ± 0.84	1.26 ± 0.06	0.72 ± 0.04	5.41 ± 0.20	5.39 ± 0.18	1.00 ± 0.05	31.77 ± 1.23
PB#2-22	13.59 ± 0.70	18.42 ± 0.24	15.14 ± 0.80	1.36 ± 0.07	0.82 ± 0.04	8.45 ± 0.21	8.19 ± 0.20	0.97 ± 0.03	33.94 ± 1.14
PB#2-x	13.95 ± 1.20	18.44 ± 0.29	13.97 ± 1.38	1.32 ± 0.12	0.76 ± 0.08	5.24 ± 0.30	6.47 ± 0.25	1.23 ± 0.09	30.49 ± 1.71
PB#2c-1	14.59 ± 0.92	22.02 ± 0.32	19.07 ± 1.04	1.51 ± 0.10	0.87 ± 0.05	6.39 ± 0.28	7.03 ± 0.24	1.10 ± 0.06	35.14 ± 1.58
PB#2b-8	18.02 ± 0.88	20.90 ± 0.29	17.03 ± 0.94	1.16 ± 0.06	0.81 ± 0.05	11.73 ± 0.30	11.70 ± 0.28	1.00 ± 0.03	47.09 ± 1.62
PB#2a-3	14.84 ± 0.75	22.34 ± 0.29	17.52 ± 0.84	1.51 ± 0.08	0.78 ± 0.04	4.96 ± 0.19	5.17 ± 0.17	1.04 ± 0.05	29.76 ± 1.11

- i) Solution and precipitation reactions (influenced by the chemistries of differing nuclides).
- ii) Gaseous diffusion of ^{222}Rn
- iii) Alpha particle recoil (the damage of mineral grains due to the recoil action of nuclei by alpha particle emission. Damaged regions can be preferentially eroded by water, allowing the removal of U isotopes. Total ejection of nuclei upon recoil can result as well) (Fleischer, 1978).

Of particular importance is process i), which primarily affects isotopes of U, and process ii), both are evident in the 8 samples from Kangaroo Island, presented in Table 7.1.

7.2.1.1 The ^{238}U decay series

Disequilibrium in the ^{238}U decay chain is represented by a deviation from unity in the $^{226}\text{Ra}/^{238}\text{U}$ ratio. The activity concentrations of ^{226}Ra exceed that of ^{238}U in all samples except Bales#2-9 (Table 7.1). The mean $^{226}\text{Ra}/^{238}\text{U}$ activity ratio for all 8 samples that underwent HRGS is 1.32 ± 0.08 . One sample (Bales#2-9) is at or near unity, another (PB#2b-8) is within 20% (between the activity ratios of 0.8 and 1.2) of equilibrium and the rest are within 50% (between 0.5-0.8 and 1.2-1.5 respectively) of secular equilibrium (Figure 7.1a). None of the samples fell outside of this range. The mean $^{210}\text{Pb}/^{226}\text{Ra}$ activity ratio for the 8 samples is 0.77 ± 0.05 . There is a deficit of ^{210}Pb compared with ^{226}Ra , indicating some ^{222}Rn loss, most likely from diffusion. However, six of the samples were within (or fell within analytical uncertainty of) 20% of secular equilibrium and two samples (PB #2-18 and PB #2b-3) were within 50% (Figure 7.1b). These results indicate that ^{222}Rn loss ranged from around 8-33% across each of the 8 samples, taking uncertainties into account.

7.2.1.2 The ^{232}Th decay series

For all of the 8 samples the ^{232}Th decay series is at or near secular equilibrium, as measured by the $^{228}\text{Th}/^{228}\text{Ra}$ activity ratio. The mean ratio is 1.03 ± 0.06 . Only one sample (PB#2-X) deviated significantly from unity at 2σ (Table 7.1 and

Figure 7.1c). However, because of the short half-life of ^{228}Ra , it is unlikely that there would be any significant effect on the final dose rate for this sample.

7.2.1.3 Implications for dose rate determinations

It is evident that there is significant disequilibrium in the ^{238}U decay series for most of the Kangaroo Island aeolianites examined here. However, the deviation from secular equilibrium was never more than 50%. For other aeolianites in the region (the South Australian mainland for example) that are rich in carbonate, and experience comparable moisture regimes, similar equilibrium conditions could be expected. The $^{210}\text{Pb}/^{226}\text{Ra}$ activity ratios indicated that there was significant ^{222}Rn loss, although disequilibrium was rarely greater than 20%. The HRGS results indicate that the ^{232}Th decay chain is at or near equilibrium for nearly all samples. Table 7.2 gives a dose rate breakdown for sample Bales#2-9, to provide a comparison of the relative contributions of the parents and daughters to the total dose rate for the Kangaroo Island samples.

Table 7.2: Relative contributions to the beta and gamma dose rate from radionuclides, for aeolianite sample Bales#2-9. Conversions from Bq/kg^{-1} were performed using the program listed in Roberts *et al.* (1993). Note: not corrected for beta attenuation or moisture content.

Radionuclides	Dose rate (Gy/ka^{-1})	Percentage total dose rate	Percentage total ^{238}U dose rate
^{238}U series			
^{238}U to ^{230}Th	0.060	14.8	28.9
^{226}Ra	0.001	0.1	0.3
^{222}Rn to ^{210}Pb	0.148	36.3	70.9
Total ^{238}U series	0.209		100
^{232}Th series			
^{228}Ra to ^{228}Th	0.074	18.0	
Potassium			
^{40}K	0.125	30.7	
Total all series	0.408	100	

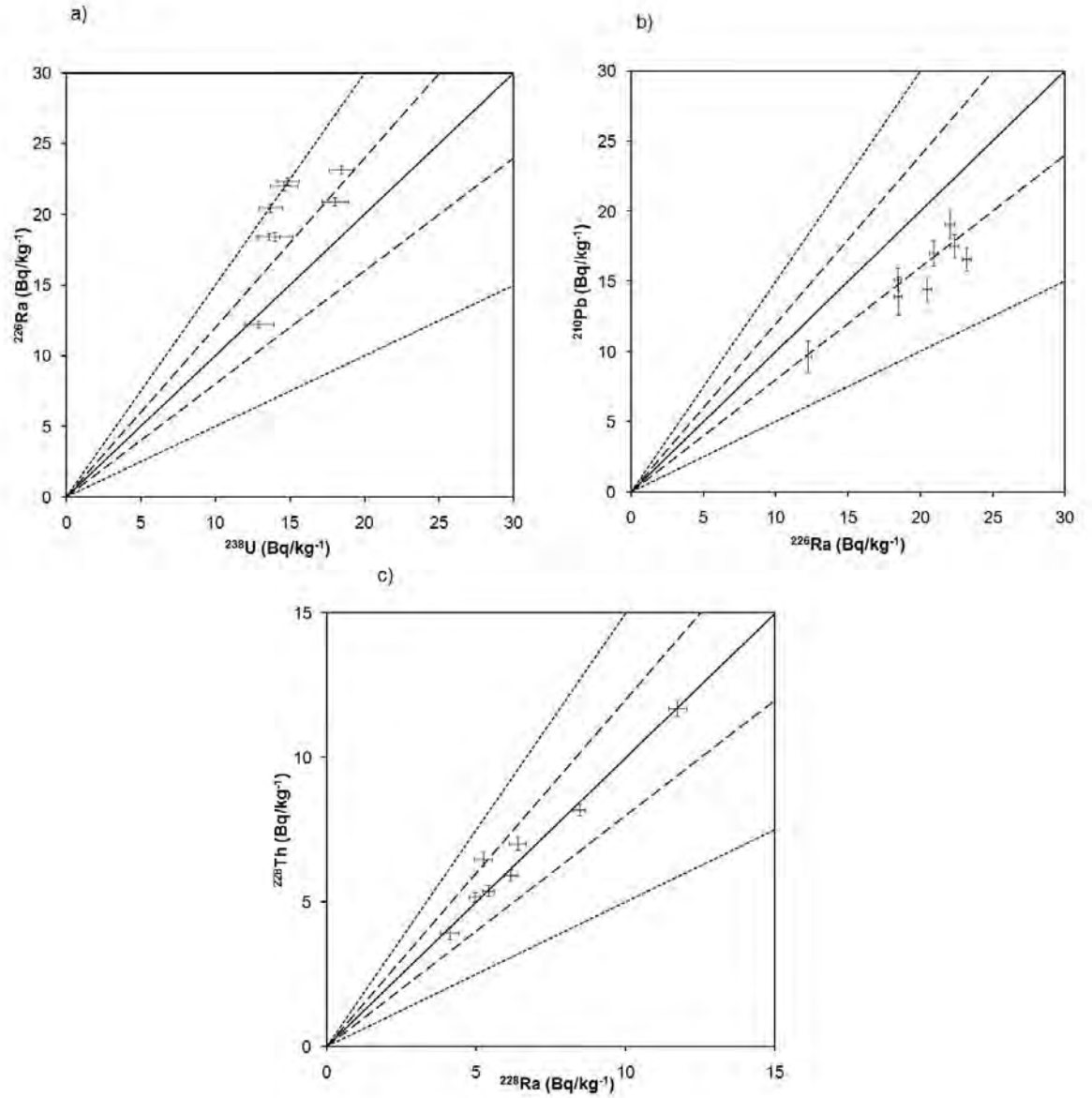


Figure 7.1: Equilibrium plots for the 8 Kangaroo Island samples that underwent HRGS analysis. The solid line represents secular equilibrium, the dashed lines represents a 20% envelope around equilibrium, and the dotted lines 50%. The plots are: a) $^{226}\text{Ra}/^{238}\text{U}$; b) $^{210}\text{Pb}/^{226}\text{Ra}$ and c) $^{228}\text{Th}/^{228}\text{Ra}$. The error bars represent 1σ uncertainty. Samples which lie in between the dashed lines are within 20% of equilibrium, and samples that lie between the dashed lines and the dotted lines are within 50% of equilibrium.

It is unlikely that the magnitude of the disequilibria shown in these 8 samples will have a significant effect on calculated ages. According to a detailed equilibrium study by Olley *et al.* (1996), undertaken on a range of fluvial samples (many of which exhibited similar levels of disequilibrium to the samples discussed here), the deviation of the calculated dose rate (at time of collection) from the “true” dose rate of a given sample will usually be relatively small (<3%). This is provided that the assumption is made that the dose rate has remained constant throughout the period of burial, the activity ratios for the sample lie within 50% of equilibrium, and that TSAC or FGS has been used to determine the concentrations of U and Th, based upon the activity ratios of the daughters (the dose rates and ages for the 8 HRGS samples, examined in this section were calculated using the program listed in Roberts *et al.* (1993); this software uses a weighted U-series to calculate the contribution of U to β and γ , and attempts to account for any disequilibrium in the ^{238}U series).

Dose rate constancy requires that the depositional environment became geochemically closed soon after the sediments were deposited. It is hard to say whether this has been the case for the Kangaroo Island samples examined here. Nevertheless, a certain amount of protection to underlying sediments could have come from the formation of the indurated surfaces (calcrete) (due to the high carbonate content of the sediment and meteoric waters) evident across most of coastal Kangaroo Island, and also internal consolidation of the sediments, particularly in the case of older aeolianites lower in the stratigraphic sequence. This should have ensured that chemical composition, and hence dose rate was relatively constant throughout the period of burial (Prescott and Hutton, 1995) (without assuming that there was, necessarily, secular equilibrium).

7.2.2 Determination of Uranium, Thorium, and Potassium via TSAC/GMBC, FGS, ICP-OES, and INAA

The concentrations of U, Th and ^{40}K were determined in 7 Kangaroo Island samples via TSAC (in combination with GMBC) (Table 7.3), and 2 samples via FGS (Table 7.4). These methods were favoured, as discussed above, if disequilibrium was suspected. The level of disequilibrium, however, cannot

really be determined. Although, comparison of independent methods can indicate if disequilibrium is present in a sample. In this instance ppm of U and Th, as determined by TSAC, FGS, and INAA (data from Tables 7.3, 7.4 and 7.5) have been plotted against each other, about unity. If no disequilibrium is present then all data points should align on or near unity. As can be seen from Figure 7.2, this is not the case for most of the U determinations; it is evident in the tabulated data as well. In the majority of cases INAA shows an excess of U in comparison to TSAC and FGS. This is puzzling with respect to the results derived from HRGS which invariably showed U in deficit for *those* samples. One would expect this to be reflected when one compares methods that derive U ppm from parents (INAA) and one that derives mostly from daughters (TSAC), from samples taken from the same areas as the HRGS samples. It is unknown at this stage why this is the case.

Regardless, before accepting or rejecting one method over the other, it was decided to check the internal consistency of the TSAC method by making a comparison between %K as determined by the combination of TSAC and GMBC (Jacobs, 2004), and %K as determined ICP-OES (Table 7.5). If there is a problem with the TSAC results then they should not be comparable.

Table 7.3: Concentrations in ppm of uranium, thorium and potassium for 7 Kangaroo Island samples; determined by TSAC (and GMBC for %K); using the methods of Aitken (1985) and Jacobs (2001).

Site	Sample code	U (ppm)	Th (ppm)	%K
Bales Beach	Bales#3-1	1.84 ± 0.04	0.53 ± 0.16	0.02 ± 0.02
Baudin Beach	BB#3-5	1.83 ± 0.08	4.64 ± 0.29	0.87 ± 0.06
Hanson Bay	HB#3-4	0.71 ± 0.03	0.82 ± 0.09	0.35 ± 0.03
Kelly Hill Caves	KH#3-1	0.23 ± 0.01	0.52 ± 0.04	0.02 ± 0.01
Pennington Bay	KPB#5-1	0.94 ± 0.03	1.02 ± 0.11	0.18 ± 0.02
Vivonne Bay	PE#3-1	0.90 ± 0.04	1.83 ± 0.15	0.19 ± 0.03
Vivonne Bay	PE#3-2	1.78 ± 0.04	0.51 ± 0.14	0.03 ± 0.02

Table 7.4: FGS results for 2 Kangaroo Island samples.

Site	Sample code	U (ppm)	Th (ppm)	K (%)	Total dry γ dose rate (Gy/ka ⁻¹)
Baudin Beach	BB#3-1	1.14 \pm 0.05	1.39 \pm 0.10	0.17 \pm 0.02	0.245 \pm 0.004
Pennington bay	PB#3-2	1.33 \pm 0.07	1.77 \pm 0.18	0.14 \pm 0.00	0.271 \pm 0.008

Table 7.5: INAA and ICP-OES analysis results of 9 Kangaroo Island dosimetry samples (INAA for U and Th; ICP-OES for K)

Site	Sample code	Uranium (ppm)	Thorium (ppm)	Potassium (%)
Bales Beach	Bales#3-1	2.80 \pm 0.08	0.90 \pm 0.03	0.08 \pm 0.003
Baudin Beach	BB#3-1	1.90 \pm 0.06	1.50 \pm 0.05	0.21 \pm 0.01
Baudin Beach	BB#3-5	1.00 \pm 0.03	7.30 \pm 0.22	0.77 \pm 0.02
Hanson Bay	HB#3-4	2.20 \pm 0.07	0.90 \pm 0.03	0.32 \pm 0.01
Kelly Hill Caves	KH#3-1	0.06 \pm 0.03	0.60 \pm 0.02	0.03 \pm 0.001
Pennington Bay	KPB#5-1	0.06 \pm 0.03	1.70 \pm 0.05	0.18 \pm 0.01
Pennington Bay	PB#3-2	3.20 \pm 0.10	2.70 \pm 0.08	0.17 \pm 0.01
Vivonne Bay	PE#3-1	1.50 \pm 0.05	1.90 \pm 0.06	0.18 \pm 0.01
Vivonne Bay	PE#3-2	2.80 \pm 0.08	1.00 \pm 0.03	0.05 \pm 0.002

Percentage K as determined by TSAC and GMBC was plotted against %K as determined by ICP-OES. The results are displayed in Figure 7.3. It should be noted that most of samples overlie unity at 1σ , and one sample lies with 20% of unity. Only one sample (Bales#3-1) failed to fall within 50% of unity. However, in this sample %K is only contributing a small amount to the total dose rate (between 3 and 12%, depending with method is used to determine %K), and if one method over another is used for %K, then it will only amount to a change of $\sim 2\%$ in the final age, and this is encompassed by the uncertainty term in any case. If these two independent methods have such excellent agreement, then it is unlikely that INAA has produced a more accurate set of results for U and Th ppm, than TSAC. For this reason and the high probability of disequilibrium in this set of samples, TSAC results were used to determine the contribution of U and Th to the β and γ dose rates in the age equation.

Since the combination and TSAC and GMBC is a subtraction method for determining %K (see Appendix E for detail), the results were derived from the more direct method, ICP-OES. In light of this the ICP-OES results were used to

determine the contribution of %K to the β and γ dose rates when calculating the OSL ages (not including the FGS samples).

7.2.3 GM Beta counting and the beta dose rate

Table 7.6 lists the GMBC results for 9 of the Kangaroo Island samples; both dry dose rates and wet and attenuated dose rates are displayed. Some of these results were used in conjunction with FGS, as the short range of β particles (~2 mm) means that the most accurate representation of the β dose comes from sampling adjacent to or from the same sample hole as the OSL sample.

Table 7.6: Beta dose rate samples from Kangaroo Island, with sample water content; dry beta dose rate, and wet and attenuated (100 μm grain size) beta dose rate. The wet and attenuated dose rate is used for the age calculation.

Sample code	Field moisture content (% dry mass) ^a	Dry β dose rate (Gy/ka^{-1})	Wet ^a and attenuated ^b (100 μm grain) β dose rate (Gy/ka^{-1})
Bales#3-1	7.9	0.295 ± 0.017	0.245 ± 0.016
BB#3-1	0.8	0.398 ± 0.021	0.359 ± 0.022
BB#3-5	5.0	1.071 ± 0.045	0.921 ± 0.047
HB#3-4	12.0	0.398 ± 0.021	0.316 ± 0.019
KH#3-1	7.3	0.066 ± 0.006	0.055 ± 0.005
KPB#5-1	13.0	0.304 ± 0.017	0.239 ± 0.015
PB#3-2	3.1	0.418 ± 0.022	0.368 ± 0.022
PE#3-1	0.8	0.332 ± 0.019	0.300 ± 0.019
PE#3-2	5.1	0.297 ± 0.017	0.255 ± 0.017

^a Water content of the sediment must be taken into account as moisture attenuates and absorbs some of the radiation. These beta dose rates are adjusted for the field water content (Aitken, 1985; 1998; Readhead, 1987).

^b Beta dose attenuation attributable to grain size; for the Kangaroo Island samples 100 μm attenuation factors were used (Mejdahl, 1979; Brennan, 2003), as the grain size range used for OSL dating was 90-125 μm .

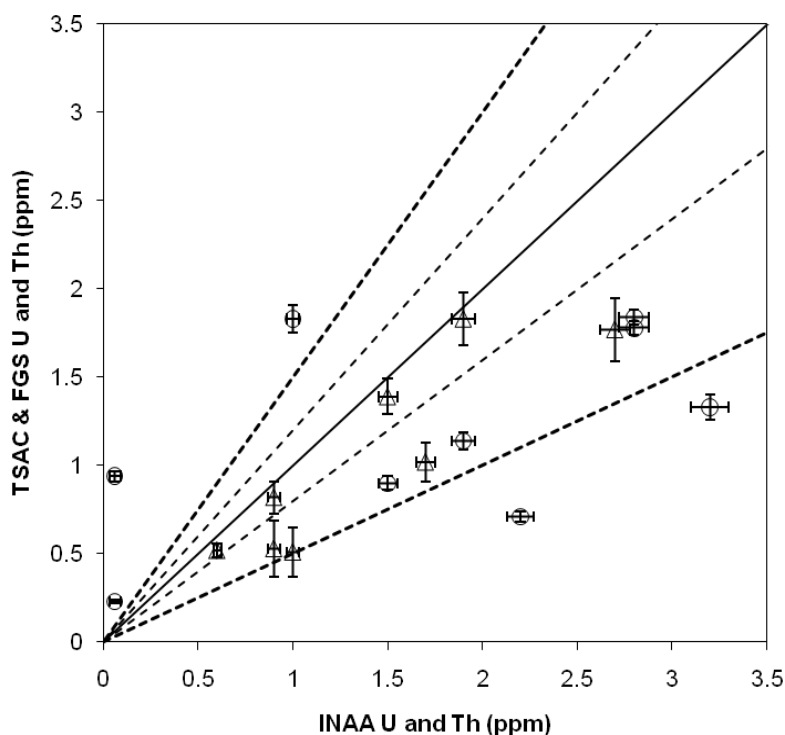


Figure 7.2: Comparison plot of the 9 Kangaroo Island samples that had U and Th ppm detected by INAA, TSAC, and FGS. Open triangles are Th and open circles are U, both with 1σ error bars. The solid line represents unity; the lighter dashed lines represent 20% around unity, and the heavy dashed lines 50%.

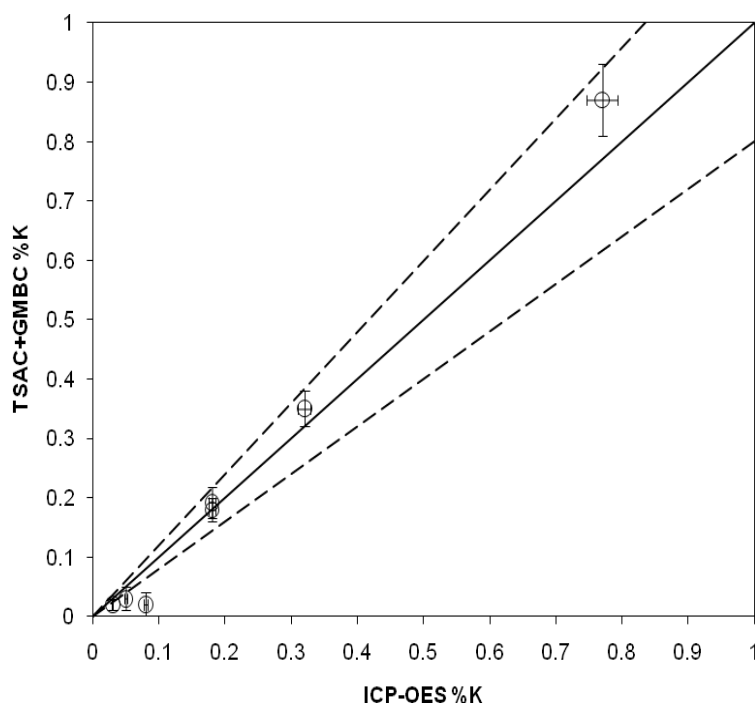


Figure 7.3: Comparison plot of %K as determined by a combination of TSAC and GMBC, and ICP-OES. The solid line is unity and the dashed lines are 20% around unity.

Table 7.7: Total dose rate data for the Kangaroo Island OSL and SARTT-OSL samples (TL dose rate data is given in Table 7.13 in Part II of this Chapter, as they were determined independently).

Sample code	Sample location (Lat. Long.)	Sample depth (m)	Field water content (% dry mass)	γ dose rate ^a (Gy/ka ⁻¹)	β dose rate ^b (Gy/ka ⁻¹)	Cosmic-ray dose rate ^c (Gy/ka ⁻¹)	Total dose rate ^{d,e} (Gy/ka ⁻¹)
Bales#2-9	S 35° 59' 37.3" E 137° 29' 47.6"	4.5	2.3	0.157 ± 0.010	0.221 ± 0.014	0.119 ± 0.012	0.528 ± 0.020
BB#3-1	S 35° 46' 35.0" E 137° 52' 06.8"	1.5	0.8	0.237 ± 0.015	0.359 ± 0.022	0.173 ± 0.017	0.799 ± 0.042
BB#3-5	S 35° 46' 24.0" E 137° 52' 28.2"	8.0	5.0	0.582 ± 0.034	0.921 ± 0.047	0.080 ± 0.008	1.613 ± 0.094
HB#3-4	S 36° 01' 02.2" E 136° 51' 22.3"	3.0	12.0	0.173 ± 0.010	0.316 ± 0.019	0.156 ± 0.016	0.675 ± 0.054
PB#2-18	S 35° 51' 07.8" E 137° 44' 50.2"	3.1	3.0	0.214 ± 0.007	0.244 ± 0.012	0.134 ± 0.013	0.622 ± 0.028
PB#2b-3	S 35° 51' 14.0" E 137° 44' 21.0"	3.4	4.6	0.223 ± 0.007	0.272 ± 0.012	0.126 ± 0.013	0.652 ± 0.030
PB#2b-8	S 35° 51' 14.1" E 137° 44' 20.6"	0.2	4.2	0.310 ± 0.008	0.345 ± 0.015	0.200 ± 0.020	0.886 ± 0.038
PB#2c-1	S 35° 51' 11.3" E 137° 45' 02.7"	2.0	5.6	0.257 ± 0.022	0.284 ± 0.017	0.155 ± 0.015	0.726 ± 0.048
PB#2-x	S 35° 51' 07.8" E 137° 44' 49.6"	5.0	4.6	0.206 ± 0.013	0.272 ± 0.013	0.110 ± 0.011	0.619 ± 0.034
PB#3-2	S 35° 51' 07.7" E 137° 44' 49.3"	5.9	3.1	0.269 ± 0.018	0.368 ± 0.022	0.141 ± 0.014	0.808 ± 0.045
PE#3-1	S 35° 59' 49.2" E 137° 11' 06.2"	1.2	0.8	0.231 ± 0.010	0.300 ± 0.019	0.179 ± 0.018	0.755 ± 0.036
Bales#3-1	S 35° 59' 40.1" E 137° 29' 36.9"	15.0	7.9	0.232 ± 0.008	0.245 ± 0.016	0.081 ± 0.005	0.589 ± 0.036
KH#3-1	S 35° 58' 51.4" E 136° 54' 25.7"	15.0	7.3	0.054 ± 0.002	0.055 ± 0.005	0.042 ± 0.004	0.182 ± 0.015
KPB#5-1	S 35° 51' 08.5" E 137° 45' 00.5"	18.0	13.0	0.173 ± 0.007	0.239 ± 0.015	0.067 ± 0.007	0.509 ± 0.041
PB#2-22	S 35° 51' 08.4" E 137° 44' 49.3"	1.6	4.3	0.245 ± 0.007	0.267 ± 0.012	0.181 ± 0.018	0.723 ± 0.033
PB#2a-3	S 35° 51' 20.1" E 137° 44' 08.8"	12.0	4.4	0.225 ± 0.007	0.258 ± 0.012	0.099 ± 0.010	0.612 ± 0.028
PE#3-2	S 35° 59' 44.7" E 137° 10' 56.5"	3.0	5.1	0.224 ± 0.008	0.255 ± 0.017	0.164 ± 0.016	0.674 ± 0.037

^a From ICP-OES, TSAC, HRGS, FGS and INAA measurements and adjusted for a field moisture content (not including FGS).

^b Corrected for beta-dose attenuation and adjusted for the field moisture content.

^c From Prescott and Hutton (1994), assigned relative uncertainties of ± 10%, and adjusted for the field moisture content. Time average equation was used: assumed steady deposition.

^d Includes an assumed internal alpha dose rate of 0.03 ± 0.01 Gy/ka⁻¹.

^e Mean ± total uncertainty (68% confidence interval), calculated as the quadratic sum of the random and systematic uncertainties.

The larger gamma sphere (300 mm) means that FGS doesn't give as accurate a representation; so GMBC was used to determine the β dose rate for the FGS samples. It was also used as a comparison to the β dose rates derived from the TSAC and ICP-OES estimation of U, Th, and K.

7.2.4 Cosmic ray dose rate

Estimation of the cosmic ray contribution to the total dose rate was calculated using the equations of Prescott and Hutton (1994). Steady deposition was assumed for the Kangaroo Island sediments in relation to the depth variable in the equations, as there may have been periods of exposure and re-burial for the sediments (rather than assuming rapid deposition with no erosion).

7.2.5 Dose rate summary and conclusions

The above sections have examined a range results derived from several different dosimetry methods. The HRGS results showed that for the carbonate rich aeolianites of Kangaroo Island disequilibrium in the ^{238}U decay series is an issue, although not one that would possibly affect the age estimations adversely. In relation to this the assumption has been made that the dose rates for all samples have prevailed since burial. The section on TSAC, FGS, INAA, and ICP-OES justified the use of TSAC over INAA, in the case of this study (through the comparison of TSAC-GMBC derived %K and ICP-OES derived %K), as the best method to determine U and Th concentrations for this set of Kangaroo Island samples (final total dose rate results are given in Table 7.7).

PART II: South coast geochronology (and introduction)

7.3 Dating results introduction

The following results utilised the dosimetry data from Part I of this Chapter, and the luminescence methods and analysis protocols described in Chapters 4 and 5, to calculate age estimates for the Kangaroo Island luminescence samples. The amino acid racemization (AAR) APK calibrations presented and evaluated in Chapter 6 were used to delineate a set of AAR age estimates, using the amino acid glutamic acid (GLX), for the Kangaroo Island whole-rock (WR) sediments, and mollusc and foraminifer (Foram) macro- and micro-fossils examined in this thesis (note: the full suite of amino acid D/L ratio results are given in Appendix E [on a digital versatile disc: DVD]). The AAR age estimates were used to compliment the OSL, SARTT-OSL, TL, and ^{14}C ages from various sites around the island. The amino acid GLX D/L ratios examined were also compiled to delineate a series of aminozones that relate to time-stratigraphic units at each site (cf. Murray-Wallace and Kimber, 1987), given in the final chapter (Chapter 8). This was accomplished by subjecting the D/L ratio datasets to statistical analysis in the form of hierarchical cluster dendrograms.

The subsequent sections will examine the derived ages on a site by site basis. The southern coastal sites will be examined first in the order Pennington Bay, Bales Beach, Point Ellen and Vivonne Bay, Kelly Hills Caves, and Hanson Bay (PART II). Then the eastern and northern coastal sites in the order American River, Rocky Point, Baudin Beach, Kingscote (PART III), North Cape, Boxing Bay, Emu Bay, Smith Bay and Stokes Bay (See Figure 7.4) (PART IV).

7.3.1 Pennington Bay

Pennington Bay is a stratigraphically complex site located on the southern coast of Kangaroo Island (Figure 7.4). There are 5 main aeolianite outcrops that were examined around the bay (PB1, PB2, PB3, PB4 and PB5: Figure 7.4); 9 stratigraphic logs were recorded, and corresponding samples were collected. Whilst the investigation of Pennington Bay was by no means exhaustive the 5 representative sites were examined in as much detail as possible, given that the upper portions of outcrop were in most cases precipitous and inaccessible. This was particularly evident at the western and eastern bounding aeolianite

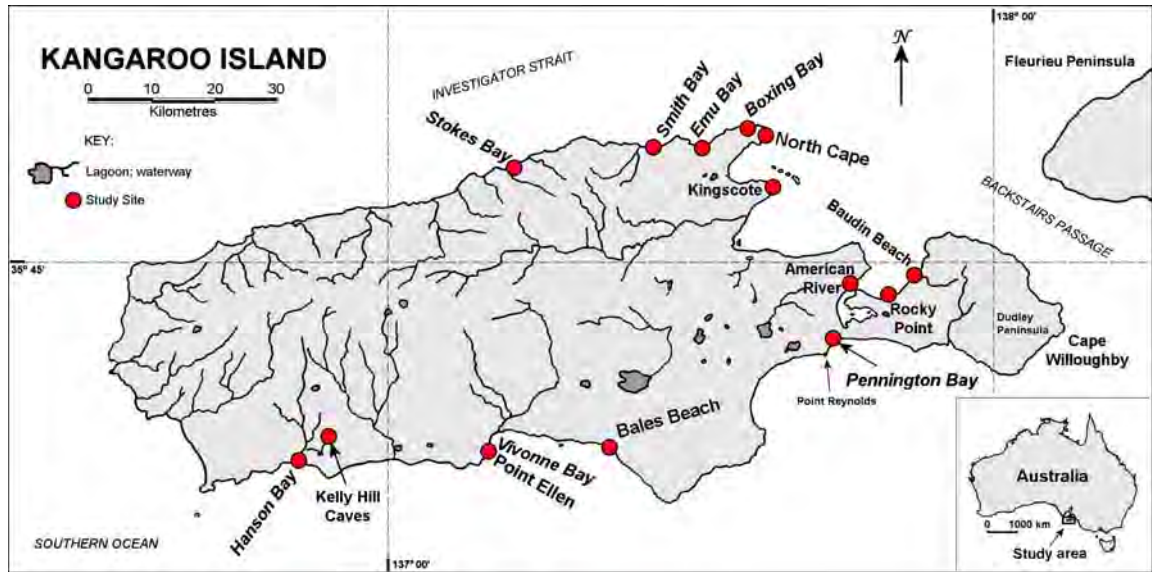


Figure 7.4: Kangaroo location map for study sites described in this chapter.

Third party source; Images redacted at request of thesis author

Figure 7.5: Morphology and location of study sites at Pennington Bay, Kangaroo Island (Google Earth, 2009). The centre inset shows the locations of the 4 sections examined at PB1.

headlands (sites PB4 and PB5: Figure 7.5), where the upper aeolianite units could not be safely accessed for sampling.

Pennington Bay was also one of the most extensively sampled sites for luminescence, in that half of the total 20 Kangaroo Island luminescence samples were removed from sedimentary units around this bay. Principally this was because the site was considered to be a representative site, and in many instances was very accessible. There was also good outcrop of aeolianite in numerous areas around the bay.

There are 4 sites around the bay where aeolianite sediments were sampled for luminescence: Site PB1, PB3, PB4 and PB5 (Figure 7.5). The Pennington Bay AAR results and calibrated AAR ages for molluscs, whole-rock (hereafter referred to as WR) sediments, and foraminifers, and the OSL, SARTT-OSL, and TL age estimates (for all Kangaroo Island sites), are presented in the following tables (Tables 7.8, 7.9, 7.10, 7.11, 7.12, 7.13, and 7.14 respectively—Table 7.8 contains the mean AAR data for all molluscs collected on Kangaroo Island [as mollusc bearing deposits were comparatively rare], although portions of this table are reproduced in Parts III and IV for conveniences sake, and Table 7.12 is a breakdown of the accepted/rejected aliquots for OSL dating). Additionally, foraminifers are not represented for every unit that was sampled; this was because it was not always possible to find suitable (or indeed any) foraminifers in some units. Even when foraminifers could be found, the D/L ratio results were sometimes all rejected on the basis of contamination (which was a problem for some of the older units examined). For many of the units that were examined both *Elphidium* spp., and *Discorbis dimidiatus* D/L ratios were combined (when both were present) for the age calculation (taking into consideration the similarity of GLX kinetics in both foraminifers: see Chapter 6).

7.3.1.1 Pennington Bay site PB1 geochronology

This site is located towards the eastern end of the bay (Figure 7.5); the outcrop forms a small embayment approximately 50 m across (see Chapter 3: section 3.5.2) (Figure 7.5). Nine stratigraphic logs were recorded around the embayment (4 at site PB1 and 2 at site PB4, and 1 each for PB2, PB3 and PB5)

Table 7.8: Kangaroo Island Pleistocene and Holocene (Holocene calibration molluscs only—American River mollusc dataset presented separately) marine and freshwater mollusc ASX and GLX AAR data, and AAR numerical ages

Lab. No.	Site	Site code / facies	Location (S Lat. E Long.)	CMAT ^a °C	Genus and species / (N) ^b	ASX D/L ratio $\pm 1\sigma^c$	Coefficient of variation (CV%)	GLX D/L ratio $\pm 1\sigma^c$	Coefficient of variation (CV%)	AAR GLX age estimate (ka) ^d $\pm 1\sigma^c$
UWGA 5835, 5098	Baudin Beach	BB2 / alluvial	35° 46' 24.8" 137° 52' 20.0"	15.4	Family Hydrobiidae (12)	0.707 \pm 0.066	9.4	0.318 \pm 0.041	12.8	101 \pm 25
UWGA 5857, 5858, 5863, 5865, 5866	Kingscote Rolls Point	KC1 / raised pebble / cobble beach	35° 39' 37.1" 137° 38' 0.24"	15.4	<i>Katelsysia scalarina</i> / (5)	0.576 \pm 0.020	3.5	0.354 \pm 0.019	5.4	129 \pm 29
UWGA 5864	Kingscote Rolls Point	KC1 / raised pebble / cobble beach	35° 39' 37.1" 137° 38' 0.24"	15.4	<i>Katelsysia scalarina</i> / (1)	0.601 \pm 0.003	0.4	0.488 \pm 0.006	1.2	264 \pm 57
UWGA 5870	Kingscote boat ramp	KC2 / raised pebble / cobble beach	35° 48' 57.2" 137° 48' 41.5"	15.4	<i>Nerita</i> (<i>Melanerita</i>) <i>atramentosa</i> / (3)	0.730 \pm 0.006	0.8	0.425 \pm 0.008	1.9	195 \pm 42
UWGA 5868	Kingscote boat ramp	KC2 / raised pebble / cobble beach	35° 48' 57.2" 137° 48' 41.5"	15.4	<i>Amesodesma angusta</i> / (7)	0.543 \pm 0.027	4.9	0.429 \pm 0.017	4.0	199 \pm 44
UWGA 7001	Rocky Point	RP / (poorly preserved) raised shelly notch deposit	35° 47' 57.7" 137° 50' 00.9"	15.4	<i>Fulvia tenuicostata</i> / (3)	0.497 \pm 0.043	8.6	0.318 \pm 0.007	2.3	101 \pm 22
UWGA 5828	Pennington Bay	PB#2e-2 / raised pebble / cobble beach	35° 51' 07.8" 137° 44' 46.5"	15.3	<i>Amesodesma angusta</i> / (8)	0.586 \pm 0.009	1.5	0.360 \pm 0.008	2.1	134 \pm 29
UWGA 5872	Vivonne Bay	PE#3-5 / raised pebble, shelly notch deposits	35° 59' 44.7" 137° 10' 56.5"	15.1	<i>Nerita</i> (<i>Melanerita</i>) <i>atramentosa</i> / (4)	0.706 \pm 0.025	3.5	0.364 \pm 0.012	3.4	(114 \pm 3)*
UWGA 5882, 5883, 5884	Hanson Bay	HB1 / raised shelly deposit	36° 01' 01.4" 136° 51' 22.8"	15.0	<i>Spisula</i> (<i>Notospisula</i>) <i>trigonella</i> / (5)	0.561 \pm 0.025	4.5	0.359 \pm 0.025	6.9	133 \pm 30
UWGA 7003	North Cape, Point Marsden	NC1 / muddy sand, tidal flat	35° 34' 39.7" 137° 37' 48.6"	15.0	<i>Anapella cycladea</i> / (2)	0.838 \pm 0.021	2.5	0.978 \pm 0.015	1.5	1.2 \pm 0.3 Ma
UWGA 7002	North Cape, Boxing Bay	NC2 / raised pebble beach	35° 34' 18.6" 137° 36' 10.6"	15.0	<i>Mactra australis</i> / (1)	0.728 \pm 0.012	1.7	0.706 \pm 0.001	0.2	590 \pm 127
UWGA 7002	North Cape, Boxing Bay	NC2 / raised pebble beach	35° 34' 18.6" 137° 36' 10.6"	15.0	<i>Tawera lagopus</i> / (1)	0.779 \pm 0.003	0.4	0.782 \pm 0.003	0.3	733 \pm 158

Table 7.8: (Cont.)

UWGA 7002	North Cape, Boxing Bay	NC2 / raised pebble beach	35° 34' 18.6" 137° 36' 10.6"	15.0	<i>Mactra australis</i> and <i>Tawera lagopus</i> / (2)	0.753 ± 0.030	4.0	0.744 ± 0.044	5.9	660 ± 148
UWGA 7016, 7017	Smith Bay	SB / raised pebble / cobble / boulder beach	35° 35' 43.1" 137° 27' 10.4"	15.0	<i>Mactra</i> spp. and <i>Irus</i> spp. / (8)	0.800 ± 0.048	6.0	0.907 ± 0.040	4.4	1.0 ± 0.2 Ma
UWGA 5886	Point Ellen	PE#1-1 / basal coquinite	35° 59' 51.2" 137° 11' 13.6"	15.1	<i>Katelysia scalarina</i> / (2)	0.788 ± 0.019	2.4	0.938 ± 0.029	3.1	1.1 ± 0.2 Ma
UWGA 5887	Point Ellen	PE#2b-2 / upper coquinite	35° 59' 56.1" 137° 11' 08.9"	15.1	<i>Katelysia</i> sp./ (4)	0.810 ± 0.019	2.3	0.946 ± 0.08	0.8	1.1 ± 0.2 Ma
UWGA 5887, 5487, 5488	Point Ellen	PE#2b-2 / upper coquinite	35° 59' 56.1" 137° 11' 08.9"	15.1	<i>Nerita milnesi</i> / (8)	0.898 ± 0.028	3.1	0.958 ± 0.016	1.7	1.1 ± 0.2 Ma
UWGA 6514, 5879	American River	AR#3-5 / coquinite	35° 47' 17.9" 137° 46' 03.3"	15.4	<i>Katelysia scalarina</i> / (1)	0.302 ± 0.013	4.5	0.137 ± 0.010	7.0	(2.5 ± 0.1) ^e
UWGA 6515, 5878	American River	AR#3-2 / coquinite	35° 47' 15.8" 137° 46' 16.1"	15.4	<i>Katelysia rhytiphora</i> / (1)	0.368 ± 0.005	1.3	0.170 ± 0.007	3.8	(5.5 ± 0.1) ^e

^a Current mean annual temperature estimated for these sites from annual temperature data via climate recording stations around Kangaroo Island (<http://www.bom.gov.au/climate/data/>)

^b Number of molluscs used for D/L ratio estimate

^c Uncertainties are 1 σ (one standard deviation—68% confidence interval)

^d Numerical age estimate from a U-series calibration (fossil coral recovered from Vivonne Bay) using an apparent parabolic model (Mitterer and Kriausakul, 1989; Murray-Wallace *et al.*, 2001); uncertainties are calculated from the square root of the sum of the squares of all error terms

^{e14}C ages used to calibrate Holocene *Katelysia* spp. from American River (also used in the Pleistocene mollusc calibration).

* U-series age of *Plesiastrea versipora*: a stony coral recovered from same unit as the marine shell *Nerita* (*Melanerita*) *atramentosa* (PE#3-5), and used to calibrate the GLX D/L ratio.

Table 7.9: Pleistocene and Holocene whole-rock (WR) sediment ASX and GLX AAR data, and AAR numerical age estimates for Pennington Bay

Lab. No.	Site	Site code / facies (N) ^c	Location (S Lat. E Long.)	CMAT ^a °C	ASX D/L ratio $\pm 1\sigma^b$	Coefficient of variation (CV%)	GLX D/L ratio $\pm 1\sigma^b$	Coefficient of variation (CV%)	AAR GLX (U-series calib.) age estimate (ka) ^d $\pm 1\sigma^b$	AAR GLX (OSL calib.) age estimate (ka) ^d $\pm 1\sigma^b$
UWGA 5094, 6550	Pennington Bay east	PB#1-4 / carbonate sand (6)	35° 51' 08.0" 137° 44' 49.7"	15.3	0.560 \pm 0.017	3.0	0.409 \pm 0.017	4.0	79 \pm 18	75 \pm 17
UWGA 6551	Pennington Bay east	PB#2c-4 / Holocene cliff-top dune (4)	35° 51' 11.3" 137° 45' 02.7"	15.3	0.427 \pm 0.008	1.8	0.279 \pm 0.003	1.2	4 \pm 1	(2.09 \pm 0.15)*
UWGA 6552	Pennington Bay middle	PB#2b-3 / aeolianite (4)	35° 51' 14.1" 137° 44' 20.6"	15.3	0.567 \pm 0.004	0.6	0.432 \pm 0.031	7.3	101 \pm 24	96 \pm 23
UWGA 6586	Pennington Bay east	PB#2-24 / aeolianite (3)	35° 51' 08.0" 137° 44' 49.7"	15.3	0.594 \pm 0.001	0.2	0.447 \pm 0.003	0.8	118 \pm 27	112 \pm 25
UWGA 6553, 6564	Pennington Bay east	PB#2-18 / aeolianite (5)	35° 51' 08.0" 137° 44' 49.7"	15.3	0.584 \pm 0.017	2.9	0.454 \pm 0.035	7.7	125 \pm 30	(122 \pm 7)*
UWGA 6466, 6546	Pennington Bay east	PB#2e-2 / raised pebble beach (6)	35° 51' 07.8" 137° 44' 46.5"	15.3	0.599 \pm 0.013	2.2	0.463 \pm 0.007	1.6	136 \pm 31	129 \pm 29
UWGA 5097, 6452, 6453	Pennington Bay east	PBTL#1-1 / aeolianite (12)	35° 51' 08.0" 137° 44' 49.7"	15.3	0.609 \pm 0.019	3.2	0.454 \pm 0.025	5.5	126 \pm 30	120 \pm 28
UWGA 6464, 6554	Pennington Bay west	PB#2a-3 / aeolianite (5)	35° 51' 20.1" 137° 44' 08.8"	15.3	0.641 \pm 0.007	1.1	0.565 \pm 0.063	11.1	288 \pm 73	274 \pm 69
UWGA 6455, 6555	Pennington Bay east	PB#2-16 / aeolianite (8)	35° 51' 08.0" 137° 44' 49.7"	15.3	0.651 \pm 0.012	1.8	0.522 \pm 0.025	4.7	217 \pm 51	207 \pm 48
UWGA 6507	Pennington Bay middle	PB#3b-1 / aeolianite (4)	35° 51' 14.1" 137° 44' 20.6"	15.3	0.595 \pm 0.004	0.7	0.524 \pm 0.013	2.4	219 \pm 51	209 \pm 47
UWGA 6502, 6556	Pennington Bay east	PB#3-2 / aeolianite (4)	35° 51' 08.0" 137° 44' 49.7"	15.3	0.657 \pm 0.004	0.6	0.530 \pm 0.002	0.4	229 \pm 53	(217 \pm 16)*
UWGA 5849	Pennington Bay east	KPB#5-2 / aeolianite (2)	35° 51' 08.5" 137° 44' 00.5"	15.3	0.614 \pm 0.001	0.1	0.530 \pm 0.004	0.8	229 \pm 53	219 \pm 49
UWGA 6451, 6558	Pennington Bay east	PB#2-22 / aeolianite (6)	35° 51' 08.0" 137° 44' 49.7"	15.3	0.676 \pm 0.010	1.5	0.551 \pm 0.046	8.4	264 \pm 64	252 \pm 60

Table 7.9: (Cont.)

UWGA 6559	Pennington Bay west	PB#2a-4 / aeolianite (2)	35° 51' 20.1" 137° 44' 08.8"	15.3	0.679 ± 0.003	0.5	0.578 ± 0.010	1.7	310 ± 71	296 ± 67
UWGA 5888, 6531, 6560	Pennington Bay east	KPB#5-1a / aeolianite (7)	35° 51' 08.5" 137° 44' 00.5"	15.3	0.676 ± 0.017	2.5	0.583 ± 0.025	4.3	321 ± 75	306 ± 70
UWGA 6561	Pennington Bay west	PB#2a-2 / aeolianite (2)	35° 51' 20.1" 137° 44' 08.8"	15.3	0.711 ± 0.001	0.07	0.645 ± 0.007	1.1	444 ± 102	424 ± 95

^a Current mean annual temperature (CMAT) estimated for these sites from annual temperature data via climate recording stations around Kangaroo Island (<http://www.bom.gov.au/climate/data/>)

^b Uncertainties are 1 σ (one standard deviation—68% confidence interval)

^c N = number of subsamples

^d Numeric age estimate from a U-series calibration (Schwebel, 1978; 1984), and an OSL calibration (this study) using an apparent parabolic model (Mitterer and Kriausakul, 1989; Murray-Wallace *et al.*, 2001); uncertainties are calculated from the square root of the sum of the squares of all uncertainty terms

* OSL age estimate of whole-rock sample used to calibrate the GLX D/L ratio.

Table 7.10: Pennington Bay Pleistocene single foraminifer ASX and GLX AAR data, and numeric AAR age estimates

Lab. No.	Site	Site code / facies	Location (S Lat. E Long.)	CMAT ^a °C	Genus and species / (N) ^b	ASX D/L ratio) ± 1σ ^c	Coefficient of variation (CV%)	GLX D/L ratio) ± 1σ ^c	Coefficient of variation (CV%)	AAR GLX age estimate (ka) ^d ± 1σ ^c
UWGA 5016, 5025, 5834, 5839, 5873	Pennington Bay east	PB#2e-1 / raised cobble / pebble beach	35° 51' 07.8" 137° 44' 46.5"	15.3	<i>Elphidium</i> sp. + <i>D.</i> <i>dimidiatus</i> / (35)	0.551 ± 0.034	6.1	0.307 ± 0.022	7.2	114 ± 34
UWGA 5084, 5834, 6562	Pennington Bay east	PBTL#1-1 / aeolianite	35° 51' 08.0" 137° 44' 49.7"	15.3	<i>Elphidium</i> sp. + <i>D.</i> <i>dimidiatus</i> / (16)	0.546 ± 0.026	4.7	0.275 ± 0.024	8.8	85 ± 26
UWGA 6562, 6563	Pennington Bay east	PB#2-18/ aeolianite	35° 51' 08.0" 137° 44' 49.7"	15.3	<i>Elphidium</i> sp. + <i>D.</i> <i>dimidiatus</i> / (19)	0.525 ± 0.031	5.8	0.281 ± 0.029	10.4	90 ± 28
UWGA 6565, 6566, 6567, 6568	Pennington Bay mid	PB#2b-3 / aeolianite	35° 51' 14.1" 137° 44' 20.6"	15.3	<i>Elphidium</i> sp. + <i>D.</i> <i>dimidiatus</i> / (30)	0.524 ± 0.027	5.1	0.268 ± 0.026	9.7	79 ± 24
UWGA 6569, 6570, 6571	Pennington Bay east	PB#3-2 / aeolianite	35° 51' 08.0" 137° 44' 49.7"	15.3	<i>Elphidium</i> sp. + <i>D.</i> <i>dimidiatus</i> / (12)	0.627 ± 0.020	3.2	0.399 ± 0.020	4.9	220 ± 74
UWGA 6572, 6573	Pennington Bay east	PB#2-16/ aeolianite	35° 51' 08.0" 137° 44' 49.7"	15.3	<i>Elphidium</i> sp. + <i>D.</i> <i>dimidiatus</i> / (11)	0.608 ± 0.026	4.3	0.373 ± 0.050	13.5	187 ± 60
UWGA 6574	Pennington Bay west	PB#2a-2 / aeolianite	35° 51' 20.1" 137° 44' 08.8"	15.3	<i>Elphidium</i> sp. / (6)	0.740 ± 0.019	2.6	0.560 ± 0.041	7.3	498 ± 149
UWGA 6575, 6576	Pennington Bay west	PB#2a-4 / aeolianite	35° 51' 20.1" 137° 44' 08.8"	15.3	<i>Elphidium</i> sp. + <i>D.</i> <i>dimidiatus</i> / (9— multiple forams per vial)	0.680 ± 0.061	8.9	0.497 ± 0.063	12.7	377 ± 119

^a Current mean annual temperature estimated for these sites from annual temperature data via climate recording stations around Kangaroo Island (<http://www.bom.gov.au/climate/data/>)

^b Number of foraminifera used for D/L ratio estimate

^c Uncertainties are 1 σ (one standard deviation—68% confidence interval)

^d Numeric age estimate from a U-series calibration (fossil coral recovered from Vivonne Bay: 114 ± 3 ka) using an apparent parabolic model (Mitterer and Kriausakul, 1989; Murray-Wallace *et al.*, 2001); uncertainties are calculated from the square root of the sum of the squares (addition in quadrature) of all uncertainty terms

Table 7.11: Conventional OSL ages for sediment samples from Kangaroo Island, together with supporting dose rate and equivalent dose data (place names in order: Bales Beach [Bales], Baudin Beach [BB], Hanson Bay [HB], Pennington Bay [PB], and Vivonne Bay [PE])

Sample code	Sample location (Lat. Long.)	Sample depth (m)	Field water content (% dry mass)	γ dose rate ^a (Gy/ka ⁻¹)	β dose rate ^b (Gy/ka ⁻¹)	Cosmic- ray dose rate ^c (Gy/ka ⁻¹)	Total dose rate ^{d,e} (Gy/ka ⁻¹)	N / σ_d (%) ^f	D _e ^g (Gy)	Age ^{e,h} (ka)
Bales#2-9	S 35° 59' 37.3" E 137° 29' 47.6"	4.5	2.3	0.157 ± 0.010	0.221 ± 0.014	0.119 ± 0.012	0.528 ± 0.020	25 / 4.4 ± 3.9	56 ± 1	107 ± 7
BB#3-1	S 35° 46' 35.0" E 137° 52' 06.8"	1.5	0.8	0.237 ± 0.015	0.359 ± 0.022	0.173 ± 0.017	0.799 ± 0.042	29 / 10.0 ± 3.4	103 ± 3	129 ± 8
BB#3-5	S 35° 46' 24.0" E 137° 52' 28.2"	8.0	5.0	0.582 ± 0.034	0.921 ± 0.047	0.080 ± 0.008	1.613 ± 0.094	13 / 15.0 ± 6.6	218 ± 15	135 ± 13
HB#3-4	S 36° 01' 02.2" E 136° 51' 22.3"	3.0	12.0	0.173 ± 0.010	0.316 ± 0.019	0.156 ± 0.016	0.675 ± 0.054	39 / 12.3 ± 2.6	96 ± 3	142 ± 12
PB#2-18	S 35° 51' 07.8" E 137° 44' 50.2"	3.1	3.0	0.214 ± 0.007	0.244 ± 0.012	0.134 ± 0.013	0.622 ± 0.028	21 / 12.0 ± 3.4	76 ± 3	122 ± 7
PB#2b-3	S 35° 51' 14.0" E 137° 44' 21.0"	3.4	4.6	0.223 ± 0.007	0.272 ± 0.012	0.126 ± 0.013	0.652 ± 0.030	39 / 15.7 ± 2.3	63 ± 2	97 ± 6
PB#2b-8	S 35° 51' 14.1" E 137° 44' 20.6"	0.2	4.2	0.310 ± 0.008	0.345 ± 0.015	0.200 ± 0.020	0.886 ± 0.038	34 / 25.9 ± 4.4	0.09 ± 0.01	0.10 ± 0.01
PB#2c-1	S 35° 51' 11.3" E 137° 45' 02.7"	2.0	5.6	0.257 ± 0.022	0.284 ± 0.017	0.155 ± 0.015	0.726 ± 0.048	24 / 5.9 ± 1.0	1.56 ± 0.02	2.09 ± 0.15
PB#2-x	S 35° 51' 07.8" E 137° 44' 49.6"	5.0	4.6	0.206 ± 0.013	0.272 ± 0.013	0.110 ± 0.011	0.619 ± 0.034	24 / 19.9 ± 3.6	96 ± 4	152 ± 11
[#] PB#3-2	S 35° 51' 07.7" E 137° 44' 49.3"	5.9	3.1	0.269 ± 0.018	0.368 ± 0.022	0.141 ± 0.014	0.808 ± 0.045	23 / 3.7 ± 14.4	175 ± 8	217 ± 16
PE#3-1	S 35° 59' 49.2" E 137° 11' 06.2"	1.2	0.8	0.231 ± 0.010	0.300 ± 0.019	0.179 ± 0.018	0.755 ± 0.036	48 / 9.5 ± 3.8	121 ± 4	163 ± 10

^a From ICP-OES, TSAC, HRGS, and FGS measurements and adjusted for a field moisture content.

^b Corrected for beta-dose attenuation and adjusted for the field moisture content.

^c From Prescott and Hutton (1994), assigned relative uncertainties of ± 10%, and adjusted for the field moisture content. Time average equation was used: assumed steady deposition.

Table 7.11: (Cont.)

^d Includes an assumed internal alpha dose rate of 0.03 ± 0.01 Gy/ka⁻¹.

^e Mean \pm total uncertainty (68% confidence interval), calculated as the quadratic sum of the random and systematic uncertainties.

^f Number of aliquots used in the final D_e estimation (N) / relative standard deviation of D_e distribution after accounting for measurement uncertainties (overdispersion, σ_d).

^g Central age model (CAM) (Galbraith *et al.*, 1999).

^h Uncertainty includes a systematic component of $\pm 2\%$ associated with laboratory beta-source calibration.

Table 7.12: Information on the number of 1 mm aliquots measured using the conventional OSL method. The table displays the rejection criteria used, associated breakdown of the rejected aliquots, and the number of accepted aliquots employed to calculate the equivalent dose (by applying the central age model). Overdispersion is also listed.

Sample	Bales#2-9	BB#3-1	BB#3-5	HB#3-4	PB#2-18	PB#2b-3	PB#2b-8	PB#2c-1	PB#3-2	PB#2-x	PE#3-1
1 mm aliquots											
Total number of aliquots measured	30	39	51	46	24	48	36	24	36	28	48
Aliquots were rejected under the following criteria:											
Poor thermal contact	1	0	0	1	0	1	0	0	0	0	0
Poor recycling ratio (>1.1 or <0.9)	1	0	0	0	0	3	0	0	0	0	0
No L_n/T_n intersection on growth curve	3	10	38	6	3	3	0	0	13	4	3
Poor IR depletion ratio (>1.1 or <0.9)	0	0	0	0	0	1	2	0	0	0	0
Poor recuperation (>5%)	0	0	0	0	0	1	0	0	0	0	0
Sum of rejected aliquots	5	10	38	7	3	9	2	0	13	4	3
No. of acceptable D_e values	25	29	13	39	21	39	34	24	23	24	45
Central D_e (Gy)	56 ± 1.3	103 ± 3	218 ± 15	96 ± 3	76 ± 3	63 ± 2	0.09 ± 0.01	1.56 ± 0.02	175 ± 8	96 ± 4	121 ± 4
Over dispersion (%)	4.4	10.0	15.0	12.3	12.0	15.7	25.9	5.9	3.7	20.0	9.5

Table 7.13: SARTT-OSL ages for sediment samples from Kangaroo Island, together with supporting dose rate and equivalent dose data (place names in order: Bales Beach [Bales], Kelly Hill Caves [KH], Pennington Bay [PB], and Vivonne Bay [PE]).

Sample code	Sample location (Lat. Long.)	Sample depth (m)	Field water content (% dry mass)	γ dose rate ^a (Gy/ka ⁻¹)	β dose rate ^b (Gy/ka ⁻¹)	Cosmic- ray dose rate ^c (Gy/ka ⁻¹)	Total dose rate ^{d,e} (Gy/ka ⁻¹)	N / σ_d (%) ^f	D _e ^g (Gy)	Age ^{e,h} (ka)
Bales#3-1	S 35° 59' 40.1" E 137° 29' 36.9"	15.0	7.9	0.232 ± 0.008	0.245 ± 0.016	0.081 ± 0.005	0.589 ± 0.036	15	212 ± 3	360 ± 24
KH#3-1	S 35° 58' 51.4" E 136° 54' 25.7"	15	7.3	0.054 ± 0.002	0.055 ± 0.005	0.042 ± 0.004	0.182 ± 0.015	12 / 8.7 ± 2.7	227 ± 7	1.3 ± 0.1 Ma
KPB#5-1	S 35° 51' 08.5" E 137° 45' 00.5"	18	13.0	0.173 ± 0.007	0.239 ± 0.015	0.067 ± 0.007	0.509 ± 0.041	15 / 3.7 ± 2.5	205 ± 4	403 ± 34
PB#2-22	S 35° 51' 08.4" E 137° 44' 49.3"	1.6	4.3	0.245 ± 0.007	0.267 ± 0.012	0.181 ± 0.018	0.723 ± 0.033	12 / 5.3 ± 2.8	172 ± 4	238 ± 13
PB#2a-3	S 35° 51' 20.1" E 137° 44' 08.8"	12.0	4.4	0.225 ± 0.007	0.258 ± 0.012	0.099 ± 0.010	0.612 ± 0.028	12 / 6.9 ± 2.6	138 ± 4	226 ± 13
PE#3-2	S 35° 59' 44.7" E 137° 10' 56.5"	3.0	5.1	0.224 ± 0.008	0.255 ± 0.017	0.164 ± 0.016	0.674 ± 0.037	12 / 1.7 ± 5.4	212 ± 4	314 ± 19

^a From ICP-OES, TSAC, HRGS, FGS and INAA measurements and adjusted for a field moisture content (not including FGS).

^b Corrected for beta-dose attenuation and adjusted for the field moisture content.

^c From Prescott and Hutton (1994), assigned relative uncertainties of ± 10%, and adjusted for the field moisture content. Time average equation was used: assumed steady deposition.

^d Includes an assumed internal alpha dose rate of 0.03 ± 0.01 Gy/ka⁻¹.

^e Mean ± total uncertainty (68% confidence interval), calculated as the quadratic sum of the random and systematic uncertainties.

^f Number of aliquots used in the final D_e estimation (N) / relative standard deviation of D_e distribution after accounting for measurement uncertainties (overdispersion, σ_d).

^g Central age model (CAM) (Galbraith *et al.*, 1999).

^h Uncertainty includes a systematic component of ± 2% associated with laboratory beta-source calibration.

Table 7.14: TL ages for sediment samples from Kangaroo Island, together with supporting dose rate and equivalent dose data (place names in order: Emu Bay [EB], Hanson Bay [HB], Pennington Bay [PB]).

Lab code	Sample code	Sample location (Lat. Long.)	Sample depth (m)	Field moisture content (% dry mass)	Cosmic- ray dose rate ^{b, c} (Gy/ka ⁻¹)	Total dose rate ^{a, c} (Gy/ka ⁻¹)	D _e ^{c, d} (Gy)	Age (ka)
W3792	EBTL#1-1	S 35° 35' 21.6" E 137° 32' 31.5"	12	3.7	0.120 ± 0.025	1.134 ± 0.058	245 ± 29	216 ± 28
W3790	HBTL#1-1	S 36° 01' 02.2" E 136° 51' 22.3"	3.0	12.0	0.147 ± 0.025	0.827 ± 0.053	120 ± 10	145 ± 15
W3791	PBTL#1-1	S 35° 51' 07.8" E 137° 44' 49.6"	5.0	5.6	0.140 ± 0.025	1.040 ± 0.027	71 ± 4	69 ± 5

^a From TSAC (Th and U) and AES (%K) measurements, and adjusted for a field moisture content.

^b From Prescott and Hutton (1994, and adjusted for the field moisture content.

^c Uncertainty levels indicated represent one standard deviation

^d D_e derived via a modified regenerative additive TL method (Shepherd and Price, 1990; Nanson *et al.*, 1991 and Price *et al.*, 1999).

and samples were collected from most of the units present. The analysis and AAR dating results, and the OSL, SARTT-OSL, and TL dating results for Pennington Bay are listed in Tables 7.8, 7.9, 7.10, 7.11, 7.13, and 7.14. Figure 7.6 illustrates the stratigraphy interpreted for the outcrop at PB1 and includes the luminescence chronology and the calculated GLX AAR ages for the units.

The OSL sample for PB#2-22 (Section 1: site PB1) was taken from the upper portion of a small aeolianite promontory that forms the western boundary of the small embayment at site PB1 (Figures 7.5, 7.6 and 7.7). The sample was taken from within a small sea-cave (under the overlying calcrete at approximately 3-4 m APSL) formed as a result of erosion during a period of higher-than-present sea-level (Figure 7.7)—given the morphostratigraphical context it most likely formed during Last Interglacial (MIS 5e, 116-132 ka). PB#2-22 was a block sample that was removed from sufficient depth into the wall of the feature to account for the γ sphere. PB#2-22 was analysed using the SARTT-OSL protocol tested in Chapter 5. Twelve 3 mm mask aliquots were run using the protocol. Given the complex nature of the signal, the only standard test used on the aliquot D_e s was the recycling ratio test. All aliquots were accepted from this analysis and the mean recycling ratio was 1.06 ± 0.09 .

The “Central Age Model” (CAM) (Galbraith *et al.*, 1999) was used to determine a weighted mean D_e of 172 ± 4 Gy (the central value) for PB#2-22, and overdispersion was very low at $5.3 \pm 2.8\%$ (Table 7.13). SARTT-OSL dose distributions are given in Figure 7.8, and it can be seen that most of the points fall within 95% of the central value. The SARTT-OSL weighted mean D_e was used in conjunction with the program listed in Roberts *et al.* (1993) to calculate an age estimate for this sample, and yielded an age of 238 ± 13 ka which is consistent with Marine Isotope Stage (MIS) 7e (Li *et al.*, 1989; Murray-Wallace, 2002). The whole-rock GLX AAR age for this unit was estimated (using the apparent parabolic kinetics method) to be 264 ± 64 ka (U-series calibration) and 252 ± 60 ka (OSL calibration), from the extent of racemization in the whole-rock (WR) sediment GLX D/L ratio: 0.551 ± 0.045 (Table 7.9). There is good agreement between these ages and the SARTT-OSL age which indicates the viability of the both the SARTT-OSL dating method developed in this thesis and

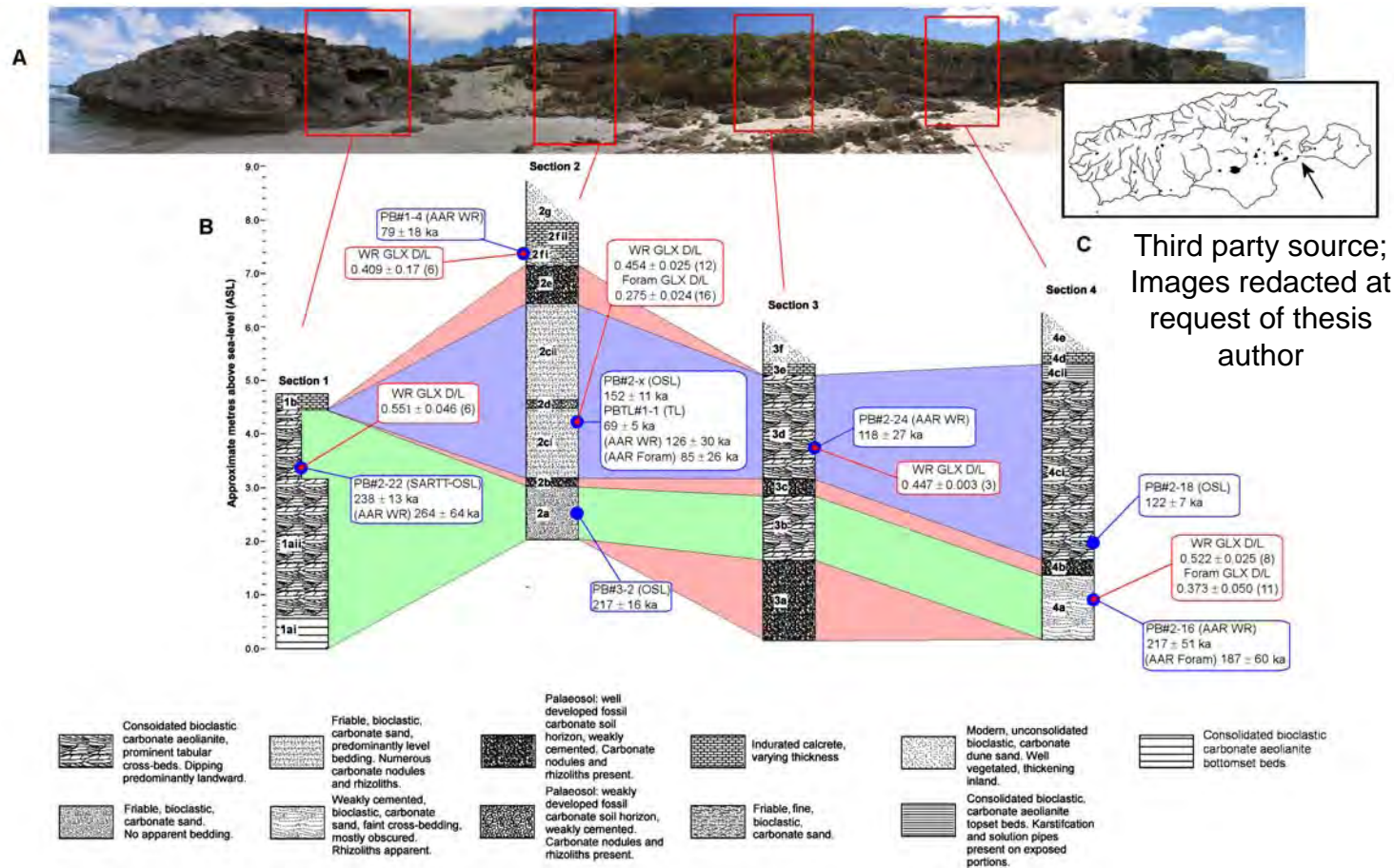


Figure 7.6: Stratigraphic logs (B) for Pennington Bay aeolianite outcrop PB1; included are the geochronological data (blue boxes) and corresponding GLX D/L ratio data (red boxes—numbers in brackets are individuals or subsamples analysed), when a GLX AAR age. The top inset (A) is a merged 180° panorama (there is some distortion towards the ends of the image) of the outcrop with boxes identifying log sections and sample areas. The RH inset (C) is a Kangaroo Island location map, with the site indicated by a black arrow, and a satellite image of the outcrop with indicated log and sample sites (modified from Google Earth, 2008). The diagram is “fenced” based upon the observed morphostratigraphical and chronostratigraphical relationships. Light-red represents the palaeosols, and light-green and light-blue represent the lower and upper aeolianite units. Note that the WR ages are from the U-series calibration.

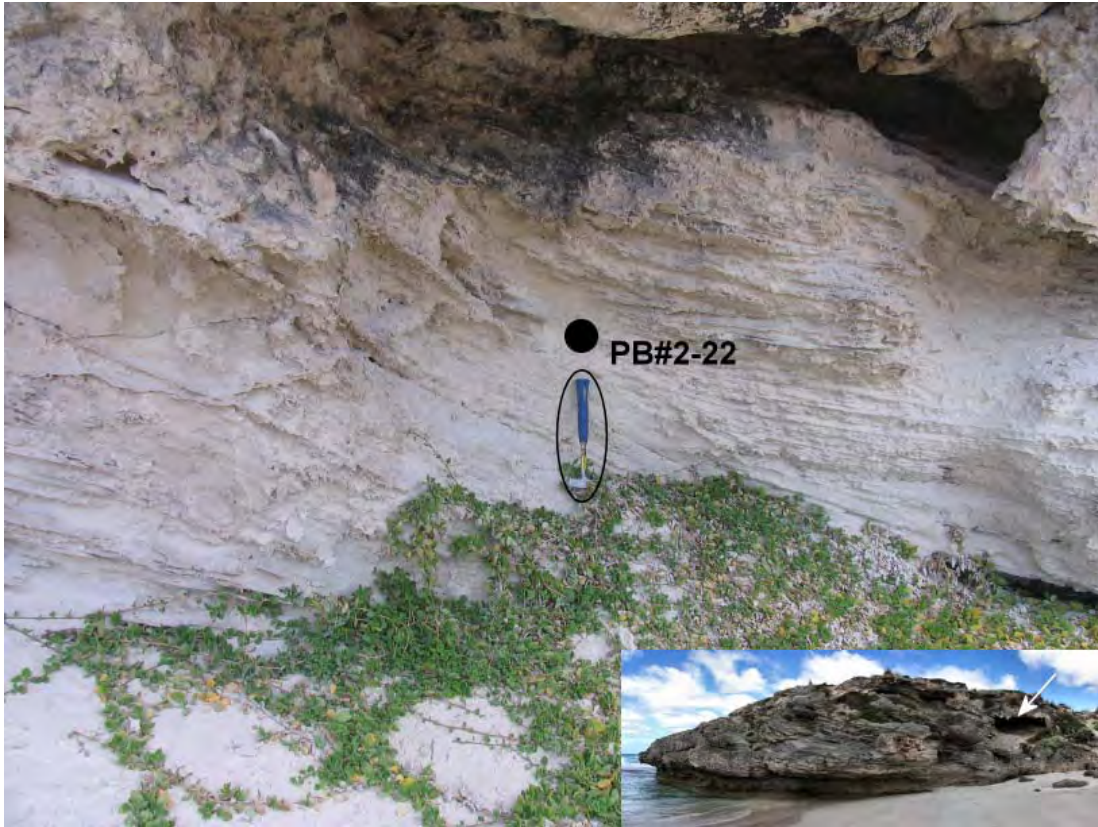


Figure 7.7: Location of PB#2-22 SARTT-OSL (also AAR) sample (black dot) at site PB1: taken from a small sea-cave set into the aeolianite promontory at this site. The open ellipse denotes the rock-hammer (33 cm) set for scale. The lower right inset shows the morphology of the promontory and the position of the cave (white arrow): note the modern wave-cut notch.

the calibration of WR GLX D/L ratios using OSL. This unit as stated above is interpreted to be early MIS 7 in age (possibly 7e). Section 2 (Figure 7.6) consists of 2 aeolianite units (2a and 2c) and intercalated palaeosols (2b, d and e); there is also a thin carbonate unit truncated by the overlying calcrete (2f). OSL and AAR Sample PB#3-2 was taken from one of the lowest units (2a) in the sequence at site PB1: section 2. There is, however, a basal calcarenite unit possibly of early Pleistocene age underlying this. Conventional OSL was used to analyse 36 aliquots of this sample (13 aliquots were rejected on the basis of no L_n/T_n intersection [Table 7.12]).

The average recycling ratio was 0.96 ± 0.03 , and the average IR depletion ratio was 1.01 ± 0.03 (full details on recycling and IR depletion ratios for all luminescence samples analysed are given in Appendix E). This sample was

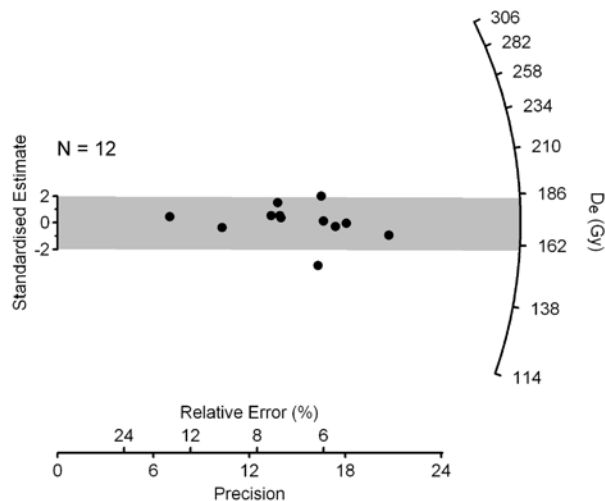


Figure 7.8: Single-aliquot (SARTT-OSL) equivalent dose (D_e) distributions for PB#2-22, displayed as a radial plot. The grey band is centred on the “Central Age Model” (CAM) (Galbraith *et al.*, 1999) estimate of sample D_e . If measurement uncertainties are sufficient to account for the scatter in D_e values, then 95% of the points should fall within the grey band. The CAM D_e for this sample is 172 ± 4 Gy.

close to saturation for conventional OSL (hence the large standard errors, and relatively low precision: Figure 7.9); although, its behaviour was very good in terms of recycling ratios and IR depletion. The weighted mean (CAM) D_e was 175 ± 8 Gy (Table 7.11). The overdispersion was $3.7 \pm 14.4\%$, and most accepted aliquots fell within 2σ of the central value (Figure 7.9). The estimated conventional OSL age for this sample was 217 ± 16 ka. This age ($\pm 1\sigma$) is consistent with MIS 7 (190 to 235 ka) (Li *et al.*, 1989; Gallup *et al.*, 1994; Bard *et al.*, 2002; Murray-Wallace, 2002; Antonioli *et al.*, 2004).

The OSL age estimate of 217 ± 16 ka obtained for the lower aeolianite (2a: sample PB#3-2, see Figure 7.10b), agrees quite well with the age of the 1a unit in section 1. The slight difference in ages may be due to different marine isotope substage deposition; although, in actuality, as the uncertainties overlap, they are essentially of the same age—stratigraphic position would indicate this also. The upper aeolianite unit (2c) at section 2 was age estimated using several methods, i.e., OSL: 146 ± 10 ka (PB#2-X: Tables 7.11 and 7.12); TL: 69 ± 5 ka (PBTL#1-1: Table 7.14); WR (U-series calibration): 126 ± 30 ka, and WR (OSL calibration): 120 ± 28 ka (GLX D/L: 0.454 ± 0.025) (the WR sediments

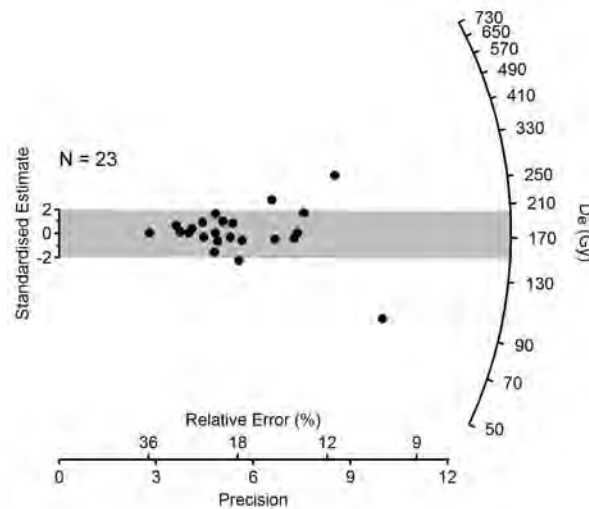


Figure 7.9: Single-aliquot (OSL) equivalent dose (D_e) distributions for PB#3-2, displayed as a radial plot. The CAM D_e for this sample is 175 ± 8 Gy.

comprising this unit were sampled from various positions within the unit to account for any inhomogeneity in the proportion of reworked carbonate grains) and Foram: 85 ± 26 ka (GLX D/L: 0.275 ± 0.024) (Tables 7.9 and 7.10). The initial Foram age estimate was derived via Ward method hierarchical multivariate analysis (explained in Chapter 3: part IV) of the foraminifer dataset ($N = 52$), which delineated GLX D/L ratio populations (in order to obtain a better representation of the “true age”) (Figure 7.10a). Three tight populations were revealed, although there was some overlap with Cluster 1 (85 ± 26 ka [$N = 16$]) and Cluster 2 (138 ± 41 ka [$N = 19$]). These two populations centre at 112 ± 35 ka (GLX D/L ratio 0.305 ± 0.034 : $N = 35$), which may be a better estimate than that derived from just Cluster 1.

OSL sample PB#2-X was removed from what was apparently a middle aeolianite, under a thin palaeosol (Figure 7.10b). Twenty eight 1 mm aliquots of this sample were analysed and 4 were rejected on the basis of saturation (no L_n/T_n intersection) (Table 7.12). The average recycling ratio and IR depletion ratio for the accepted aliquots was 0.95 ± 0.03 and 1.00 ± 0.03 , respectively. Prior to the dating run, 12 aliquots were subjected to a dose recovery test, using the modified SAR protocol, as in Chapter 7, section 3.1.1.1.

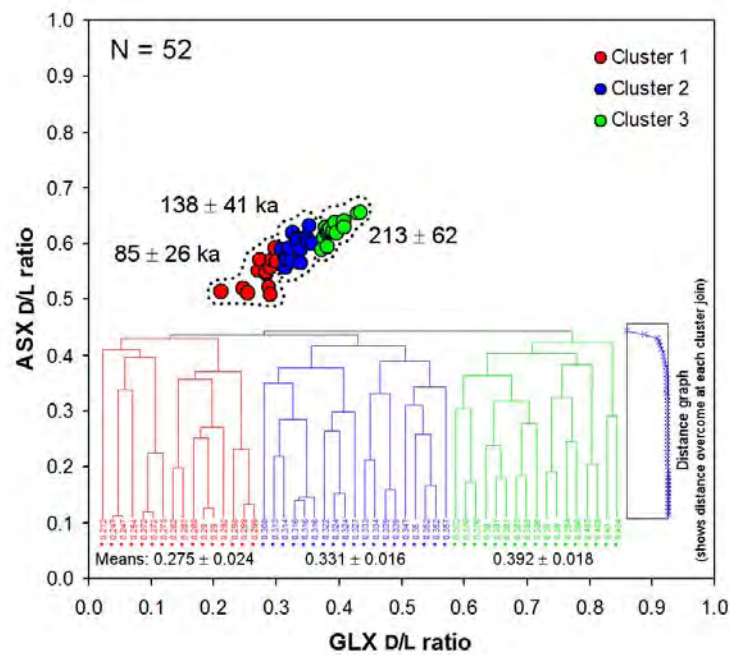


Figure 7.10a: Ward method hierarchical multivariate (cluster) analysis of the single foraminifer GLX D/L ratio data from Unit 2c (site PB1 section 2 aeolianite), inset within a bivariate plot (ASX vs. GLX). Three age populations are identified. The lowest set of D/L ratios is assumed to be representative of the “true” age.

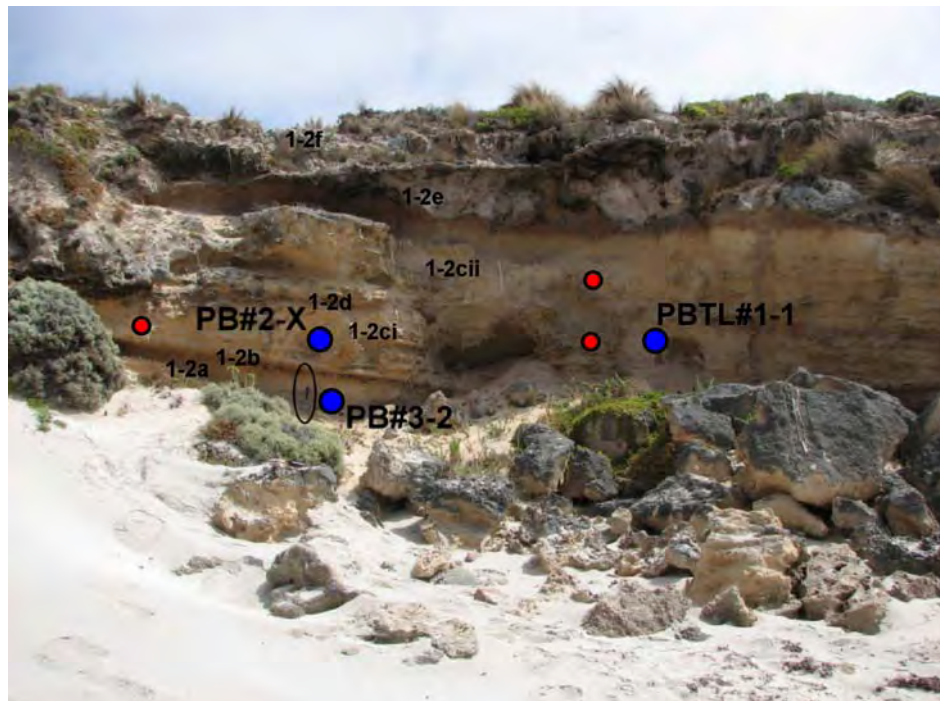


Figure 7.10b: Location of PB#2-X and PB#3-2 OSL (and AAR) samples, and the PBTL#1-1 TL sample (blue dots) at site PB1, and stratigraphic designations for section 2 at site PB1, Pennington Bay (the prefix represents the site number, i.e., PB1). PB#2-X is taken from an apparent middle aeolianite at this site; the unit immediately below is a thin palaeosol. PB#3-2 was sampled from the aeolianite below this palaeosol. The open ellipse denotes a rock-hammer (33 cm) set for scale. The red circles denote alternate AAR sample points for unit 1-2c.

The mean recovered dose was 48 ± 1 Gy, and all aliquots fell within 2σ of the laboratory dose (50 Gy) (full details on dose recovery, and IR depletion tests for all OSL samples are given in Appendix F). The remaining 24 usable aliquots were subjected to the CAM, yielding a weighted mean D_e of 92 ± 3 Gy for PB#2-X (Table 7.11 and 7.12). The overdispersion was $9 \pm 3\%$, and the distribution of the equivalent doses is displayed in Figure 7.11. The age estimate was calculated as above yielding an age of 146 ± 10 ka. At $\pm 2\sigma$ this would indicate an early MIS 5 (Li *et al.*, 1989) to MIS 6 deposition (cf. Siddall *et al.*, 2007). However, the AAR age estimates would suggest MIS 5 rather than the MIS 6 glacial.

The OSL and the WR and Foram AAR methods all agree well with each other; however, the TL age is significantly different, this may be due to an error in the TL dose rate calculation for this sample (PBTL#1-1). The TL dose rate

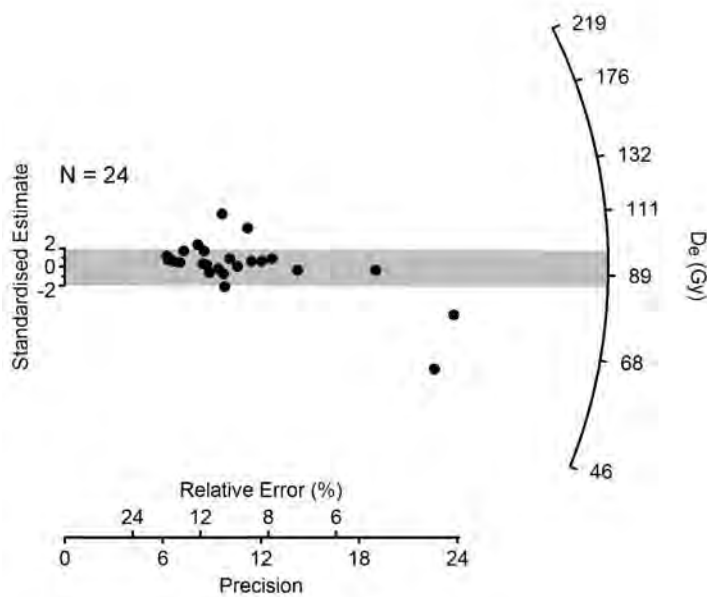


Figure 7.11: Single-aliquot (OSL) equivalent dose (D_e) distributions for PB#2-X, displayed as a radial plot. The CAM D_e for this sample is 92 ± 3 Gy.



Figure 7.12: Location of WR AAR sample PB#2-24, and stratigraphic designations for section 3 at site PB1, Pennington Bay (the prefix represents the site number, i.e., PB1).

calculated for this sample (see Table 7.14 and 7.11) was significantly higher than that calculated for the OSL sample; additionally the TL dose rate was uncharacteristically high in comparison to other dose rates from around the island (Table 7.11 and 7.13). In light of the overlap in ages (and the concurrence between the WR and Foram AAR calibrated ages) this unit is interpreted to be early MIS 5 in age; possibly being deposited during the Last Interglacial. The position of the unit in relation to shoreline proximity and current sea-level, however, would imply either deposition just prior to the Last Interglacial during the transgression, or just after during the regression (the OSL age would suggest prior deposition). This unit has a bisecting, thin, weakly developed palaeosol (2d), which indicates a short depositional hiatus, possibly during a MIS 5 stadial.

The uppermost truncated carbonate unit (Figure 7.6: unit 2fi, a fine carbonate sand) was dated (using WR AAR), at 79 ± 18 ka (U-series calibration) and 75 ± 17 ka (OSL calibration) (GLX D/L: 0.409 ± 0.017) (Table 7.9) indicating a

possible late MIS 5 (5d?) or MIS 4 deposition. This unit seems to be isolated, and may indeed be part of the overlying calcrete unit.

Section 3 (Figures 7.6 and 7.12) consists of 2 aeolianite units (3b and 3d) with intercalated palaeosols (3a and 3c), and is essentially the same as section 2; although somewhat less complex. The upper aeolianite (3d) was estimated to be 118 ± 27 ka (U-series calibration) and 112 ± 25 ka (OSL calibration) (GLX D/L: 0.447 ± 0.003) in age, using WR AAR (this agrees with the ages for 2c in section 2: see Figure 7.6) (Table 7.9). The lower aeolianite unit (3b) was not sampled; however, stratigraphic position would suggest its depositional relationship to both 2a and 1a. The large well-developed palaeosol lens (3a) apparently underlies the lowest aeolianite units at site PB1 and may represent a depositional hiatus that took place prior to MIS 7 (possibly MIS 8).

There are 2 aeolianite units (4a and 4c) at section 4 (Figure 7.6 and 7.13); the sediment at 4a was age estimated using WR AAR and Foram AAR. This yielded GLX AAR numerical age estimates of 217 ± 51 ka (U-series calibration) and 207 ± 48 ka (OSL calibration) (WR GLX D/L: 0.522 ± 0.025), and 172 ± 59 ka (Foram GLX D/L: 0.361 ± 0.035), respectively (Tables 7.9 and 7.10). These are in good agreement with the ages derived for the aeolianite units 1a, and 2a, which indicate MIS 7 deposition.

A conventional OSL sample (PB#2-18—this sample was also used in many of the SARTT-OSL experiments presented in Chapter 5) (Figure 7.13) was taken from the uppermost aeolianite at this section, which is unconformably overlain by a blocky calcrete of varying thickness. Twenty four 1 mm mask aliquots of this sample were run; 3 were rejected (Table 7.12). The sample yielded a D_e of 76 ± 3 Gy with an overdispersion of $12.0 \pm 3.4\%$ (Table 7.11), calculated using the CAM. Equivalent dose distributions are illustrated in Figure 7.14. The low overdispersion (Table 7.11 and 7.12) indicates that this is primarily a single dose population and that either grain mixing through bioturbation or partial bleaching of the quartz grains is not significant. Due to the sample location and the homogeneous nature of the sediment it is assumed that dose rate inhomogeneities are negligible also. The weighted mean D_e (from CAM) was

used in conjunction with the program listed in Roberts *et al.* (1993) to calculate an age estimate for this sample. The conventional OSL age estimate for sample PB#2-18 is 122 ± 7 ka (the WR AAR and Foram AAR ages were 125 ± 30 and 90 ± 28 ka, respectively [Table 7.9 and 7.10]).

This would indicate that the aeolianite unit that sample PB#2-18 was removed from was deposited at a time during peak sea-level (+2 to +4 m) of the Last Interglacial (Marine Isotope Stage 5e [MIS 5e: 132-116 ka]) (Lambeck and Chappell, 2001; Siddall *et al.*, 2007)). Although, the position of the unit, in relation to a +2 to +4 m sea-level, and the distance from the current shoreline (~10 m), would indicate deposition during a lower sea-level than at peak MIS 5e (i.e. slightly before, or sometime after, as the sequence is undercut and collapsed). This, in the context of the OSL age, suggests either deposition during the transgression towards MIS 5e or the regression after termination, and either erosion during the highstand (if deposited during the transgression), or the Holocene.

Standard tests performed on this sample indicate that the modified protocol outlined in Chapter 4 (section 4.3.4.3, Figure 4.11) is adequate, i.e. the mean recycling ratio is 0.94 ± 0.03 . Also, the sample does not have significant feldspathic contamination (with a mean IR depletion ratio of 1.01 ± 0.03), or recuperation (mean of $0.9 \pm 0.05\%$) problems.

Before undertaking the dating analysis for this sample a short dose recovery test was performed on 6 sunlight bleached (24 hr) 1 mm aliquots of the sample. The aliquots were given a 50 Gy laboratory dose and subjected to the modified SAR protocol (Chapter 4). The mean recovered dose was 47 ± 3 Gy; and all aliquots fell within 2σ of the given dose; although, several aliquots slightly underestimated.

OSL was used to derive an age estimate for the upper aeolianite unit (4c); the resulting estimate, 122 ± 7 ka, is statistically similar (at 2σ) to the OSL age for unit 2c in section 2, and the AAR age estimates for units 2c and 3d (section 3) at 1σ . The OSL age estimate for unit 4c indicates a reasonably good correlation to the LIG (116-132 ka: from a variety of sources listed in Siddall *et al.* [2007]).



Figure 7.13: Location of PB#2-18 OSL (and AAR) sample (blue circle) at site PB1 (also shown are sample points for PB#2-24 and PB#2-16: red circles): taken from the uppermost aeolianite at this site. The open ellipse denotes a rock-hammer (33 cm) set for scale. The unit immediately below the OSL sample is a palaeosol (4b, and also 3c).

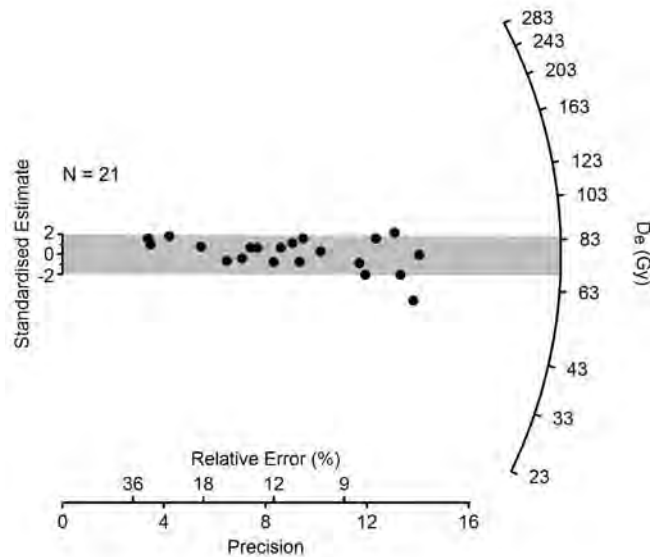
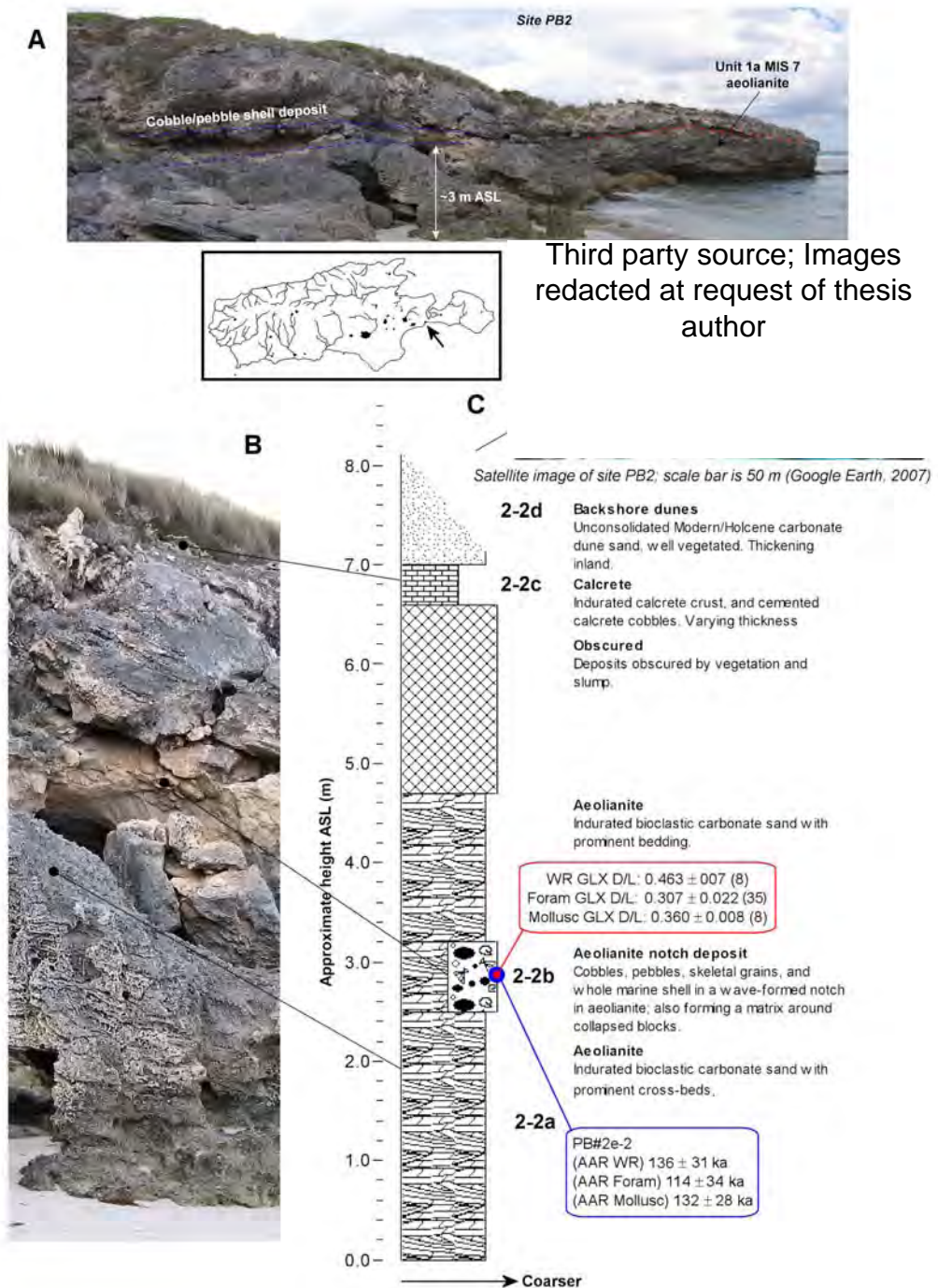


Figure 7.14: Single-aliquot (OSL) equivalent dose (D_e) distributions for PB#2-18, displayed as a radial plot. The CAM D_e for this sample is 76 ± 3 Gy.



Third party source; Images redacted at request of thesis author

Figure 7.15: Pennington Bay Glanville Formation equivalent, site PB2. Stratigraphic log (B) for the PB2 aeolianite outcrop; included are the geochronological data (blue boxes) and corresponding GLX D/L ratio data (red boxes—numbers in brackets are individuals or subsamples analysed), when a GLX AAR age. The top inset (A) is a merged 180° panorama (there is some distortion towards the ends of the image) of the outcrop. The RH inset (C) is a Kangaroo Island location map, with the site indicated by a black arrow, and a satellite image of the outcrop with indicated log and sample site (modified from Google Earth, 2007).

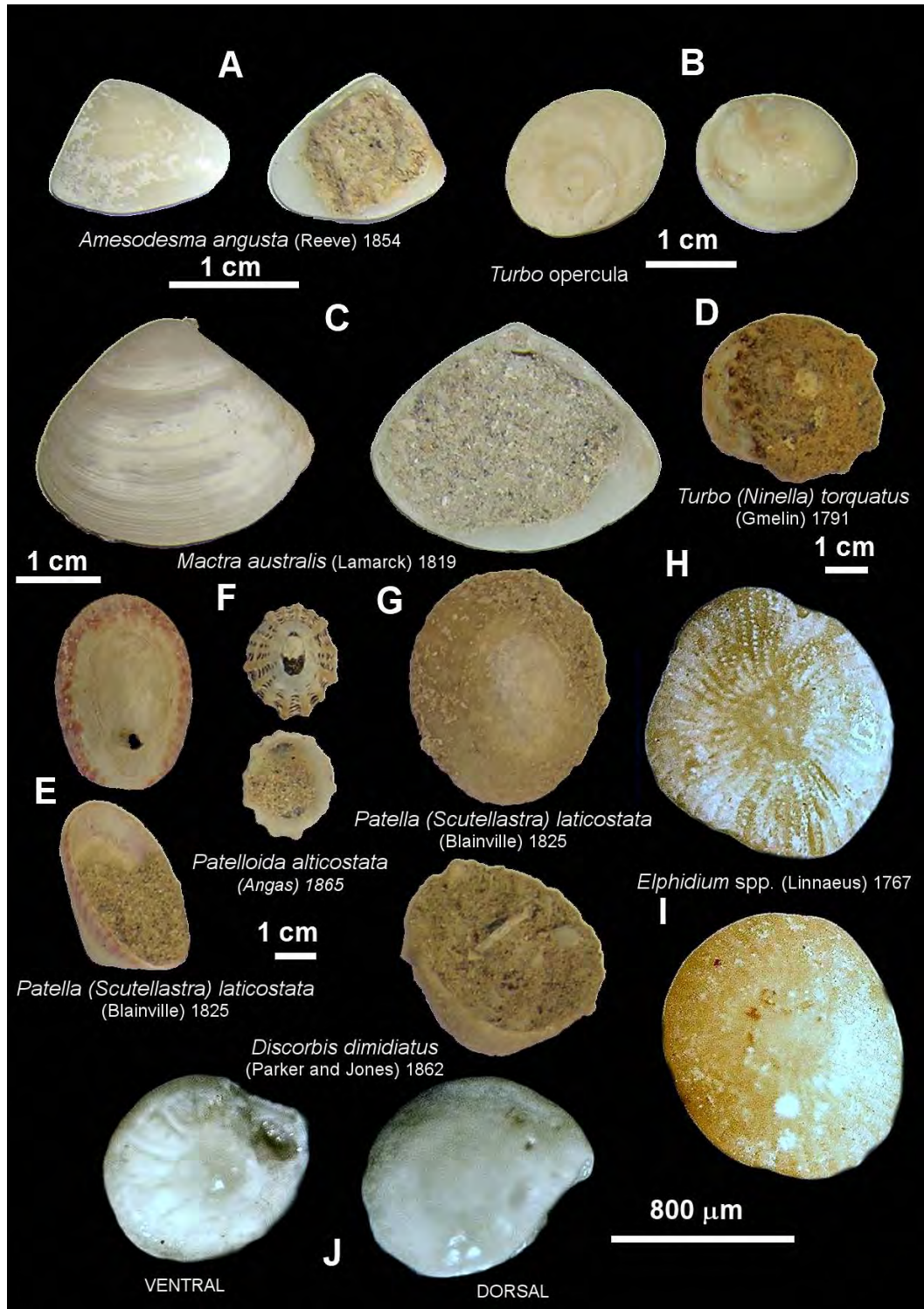


Figure 7.16: Common fossil fauna from the Pennington Bay cobble/pebble beach deposit at site PB2. The molluscan assemblage is mixed, with representatives from rocky coast (*Turbo*, *Patella*, and *Patelloida*) and sandy shore (*Amesodesma*, and *Mactra*) habitats. Modern analogues of both habitats are present at Pennington Bay.



Figure 7.17a: Site PB2 showing position of cobble/pebble shell unit (dashed blue lines), and sample positions (red circles)

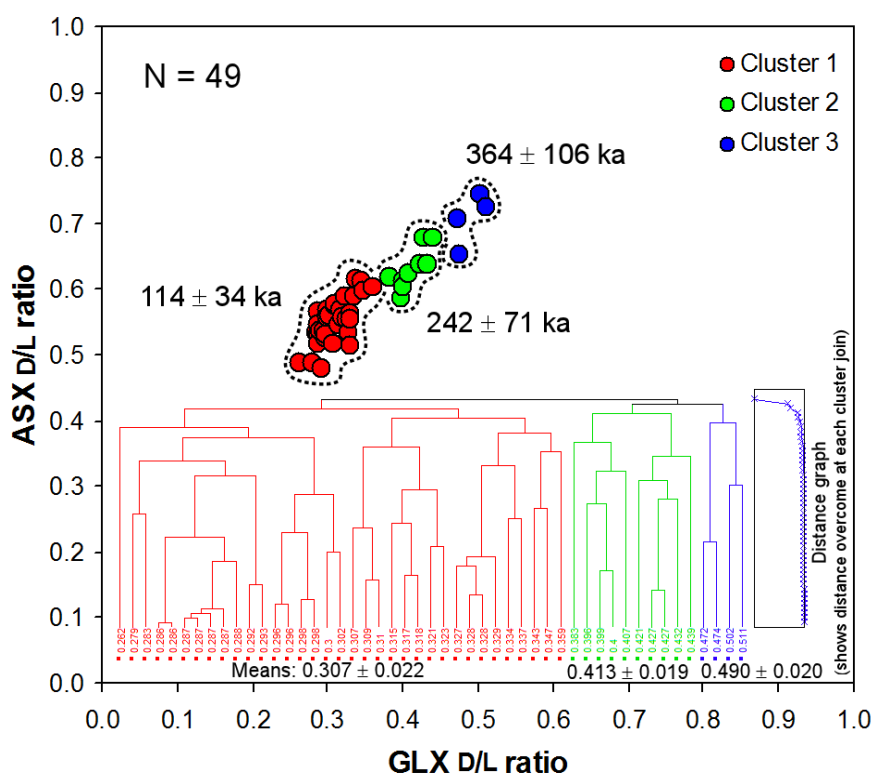


Figure 7.17b: Ward method hierarchical multivariate (cluster) analysis of the single foraminifer GLX D/L ratio data from PB#2e-2 (site PB2 raised shell/pebble notch deposits), inset within a bivariate plot (ASX vs. GLX). Three age populations are identified. The lowest set of D/L ratios is assumed to be representative of the “true” age.

7.3.1.2 Pennington Bay site PB2 geochronology

This site hosts a cobble/pebble beach notch deposit (Figure 7.15) that is rich in molluscan fauna and foraminifers (principally *Turbo* sp. and their opercula, *Macra australis*, *Amesodesma angusta* [this species of bivalve was the most abundant], limpets such as *Patella* and *Patelloida*, and *Elphidium* spp., and *Discorbis dimidiatus*—see Figure 7.16). The deposit has been cemented into a notch that was eroded out during a period of higher sea-level than the present. The notch is clearly visible in Figure 7.15 (A and B) and 7.17a, and is approximately 3.2 m APSL (to the top of the deposit), which suggests a highstand depositional event (see Chapter 3, section 3.5.2.2 for more detail) (i.e. a cobble beach at this level during MIS 5e). The unit into which the notch is cut is the same aeolianite as in section 1a at site PB1 (deposited during MIS 7). Cobbles, pebbles, marine shell and foraminifers are plastered into the notch and cemented in a carbonate matrix; the notch has a lateral extent of approximately 80 m; although the shelly cobble/pebble deposits are only present in a small section of this.

A range of marine shell, foraminifers, and whole-rock sediment was collected from the deposit for AAR analysis. The marine bivalve *Amesodesma angusta* was the most abundant shell found, thus several of these were analysed, as were a number of *Elphidium* spp., and *D. dimidiatus* foraminifers (Figure 7.16) for amino acid D- and L-enantiomers. AAR ages were estimated for the notch deposit using the three materials (molluscs, whole-rock sediments, and foraminifers); as follows (see Tables 7.8, 7.9, and 7.10, Figure 7.15, and 7.17a): 136 ± 31 ka (U-series calibration) and 129 ± 29 ka (OSL calibration) for WR AAR (GLX D/L: 0.463 ± 0.007), 114 ± 34 ka for Foram AAR (GLX D/L: 0.307 ± 0.022), and 132 ± 28 ka for Mollusc AAR (GLX D/L: 0.360 ± 0.008).

The Foram age estimate of 114 ± 34 ka ($N = 35$) was calculated from the mean of the lowest GLX D/L ratio population, delineated via Ward method hierarchical multivariate analysis of the GLX D/L ratio dataset ($N = 49$) (Figure 7.17b).

These ages in conjunction with the position of the deposit (which suggests a beach at this level in the past) supports a Last Interglacial (MIS 5e) age for the

deposit. This deposit can be equated with the Last Interglacial Glanville Formation shell-beds of the South Australian coastline (cf. Firman, 1967; Cann, 1978; Belperio *et al.*, 1983, 1984; Hails *et al.*, 1984; Murray-Wallace *et al.*, 1988; Murray-Wallace and Belperio, 1991). If any possible neotectonic uplift is disregarded then this deposit places the Last Interglacial (MIS 5e) sea-level on the southern coast of Kangaroo Island at around +3 m APSL; this agrees well with the +2 to +3 m APSL estimate of Murray-Wallace and Belperio (1991) for South Australia, and the +2 to +4 m APSL estimate of Stirling *et al.* (1998) for Western Australia.

7.3.1.3 Pennington Bay site PB3 geochronology

Site PB3 lies at the approximate centre of Pennington Bay (Figure 7.5) and consists of a series of 3 aeolianites and 2 palaeosols (Figure 7.18 and 7.19). The lowest aeolianite (3a) outcrops further west from the main site, and is apparently under the lowest palaeosol. This aeolianite unit was dated at 219 ± 51 (U-series calibration) and 209 ± 48 ka (OSL calibration) (GLX D/L: 0.524 ± 0.013), using the extent of whole-rock GLX AAR (see Table 7.9). This is in keeping with the other lower-level aeolianites at site PB1, and most likely represents a MIS 7 deposition.

The middle aeolianite unit is apparently separated from the lower unit by a thick well developed palaeosol, and was sampled for both OSL and AAR analysis. OSL sample PB#2b-3 was taken from this unit, and 48 1 mm mask aliquots were subjected to the modified SAR protocol (Chapter 4, section 4.3.4.3). Several aliquots were rejected on the basis of behaviour (see Table 7.12 for details), and the remaining aliquots (39) were analysed using the CAM. These yielded a D_e of 63 ± 2 Gy, with an overdispersion $15.7 \pm 2.3\%$ indicating a primarily single-dose population (Table 7.11 and 7.12). The equivalent dose distributions are displayed in Figure 7.20, and the average recycling and IR depletion ratios for this sample were 0.96 ± 0.03 , and 1.02 ± 0.03 , respectively. Recuperation was also negligible. A dose recovery experiment was also performed on this sample: 6 sunlight bleached aliquots were given a 50 Gy β -dose, and were subject to the modified SAR protocol. The mean recovered dose for the 6 aliquots was 50 ± 1 Gy (see Appendix E, for details).

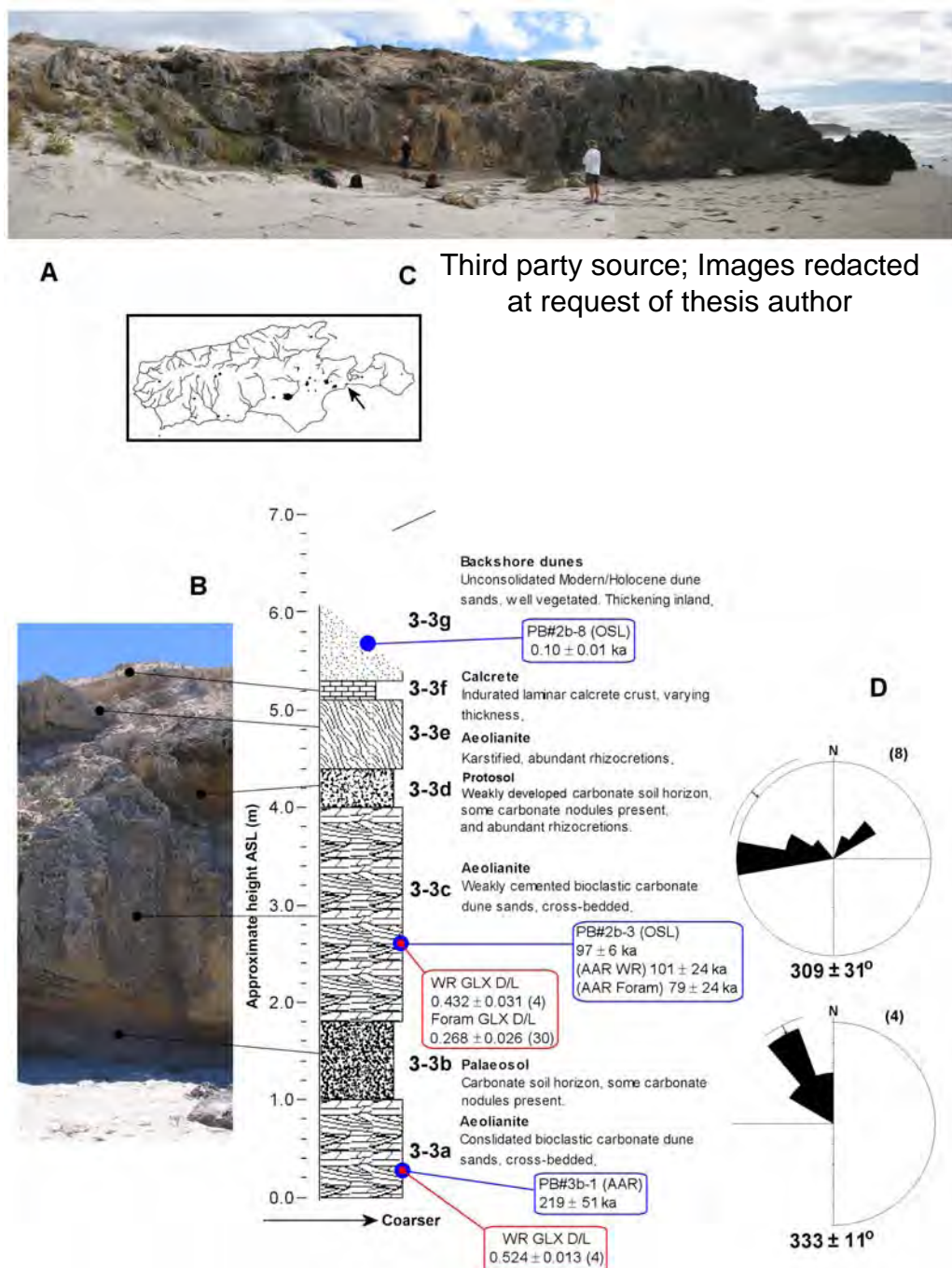


Figure 7.18: Pennington Bay site PB3 stratigraphic log (B), for the aeolianite outcrop in the centre of the bay; included are the geochronological data (blue boxes) and corresponding GLX D/L ratio data (red boxes—numbers in brackets are individuals or subsamples analysed), when a GLX AAR age. The top inset (A) is a merged 180° panorama (there is some distortion towards the ends of the image) of the outcrop. The RH inset (C) is a Kangaroo Island location map, with the site indicated by a black arrow, and a satellite image of the outcrop with indicated log and sample site (from Google Earth, 2010). The lower RH inset (D) is a set of bedding orientation rose diagrams (explained in Chapter 3: section 3.5.2.3), for the bottom and middle aeolianite units.

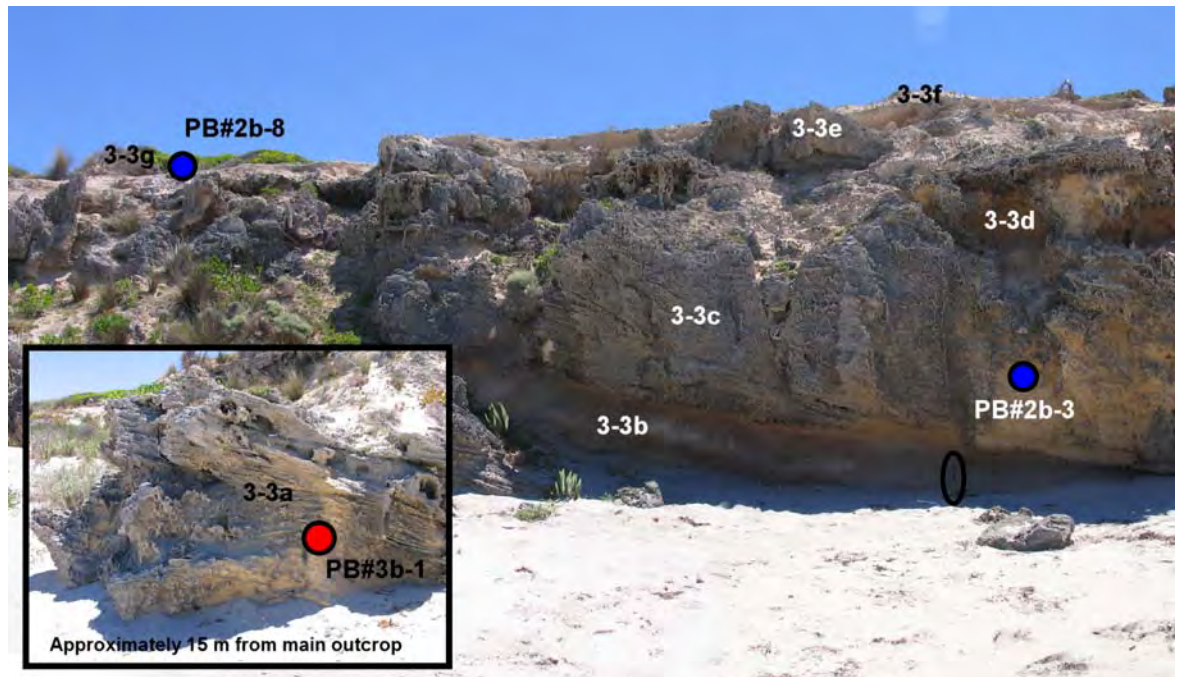


Figure 7.19: Site PB3 showing OSL (blue) and AAR (red) sample points (AAR samples were also taken from the same holes as the OSL samples) and unit designations. The open ellipse denotes a rock-hammer (33 cm) set for scale.

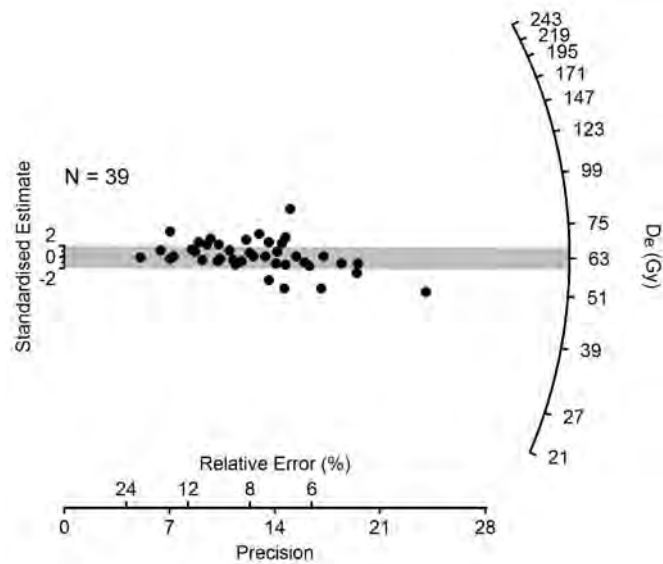


Figure 7.20: Single-aliquot (OSL) equivalent dose (D_e) distributions for PB#2b-3, displayed as a radial plot. The CAM D_e for this sample is 63 ± 2 Gy.

The OSL age estimate for this unit is 97 ± 6 ka. It was also dated using WR AAR: 101 ± 24 ka (U-series calibration) and 96 ± 23 ka (OSL calibration) (GLX D/L: 0.432 ± 0.031), and Foram AAR: 79 ± 24 ka (GLX D/L: 0.268 ± 0.026). These age estimates all agree well with each other, and would suggest deposition during late MIS 5, possibly 5a, b or c; however, given the more precise OSL age, MIS 5c seems more probable (Potter *et al.*, 2004). In terms of the OSL age it is significantly younger than what was originally thought to be an equivalent aeolianite at site PB1 (units 2c, 3d and 4c—see Figure 7.6).

Unfortunately the uppermost aeolianite was not sampled as a suitable sample point could not be located. This unit was extremely karstified and was thickly threaded by rhizocretions, and may have been deposited during MIS 4, 3 or 2, although this remains as speculative until suitable samples can be collected and analysed.

The modern backshore dunes overlying the sequence were dated using OSL. The OSL sample PB#2b-8 was taken from these overlying dunes, and 36 aliquots (1 mm mask size) of this sample were analysed using the modified protocol. Two aliquots were rejected on the basis of recycling and a central D_e of 0.09 ± 0.01 Gy, for the remaining 34 was determined using the CAM (Table 7.11 and 7.12). Overdispersion was high at $26.0 \pm 4.4\%$, indicating some possible grain mixing or partial bleaching effects; however, the uncertainty term overlaps what could be expected for a single-dose population. The mean recycling and IR depletion ratios were 1.0 ± 0.1 and 1.0 ± 0.2 , respectively, and the equivalent dose distributions are displayed in Figure 7.21. The D_e of 0.09 ± 0.01 Gy returned an age estimate of 0.10 ± 0.01 ka for the overlying modern dunes at this site (Table 7.11). A standard dose recovery test was also undertaken on 6 sunlight bleached aliquots of PB#2b-8. A 50 Gy β -dose was given to the aliquots, and a mean 47.4 ± 1.3 Gy dose was recovered using the modified SAR protocol.

This young age for the backshore dunes at site PB3 testifies to rapid aeolian dune formation from the modern beach material. The GLX D/L ratios of modern beach material and backshore dunes at Pennington Bay are very similar, e.g.,

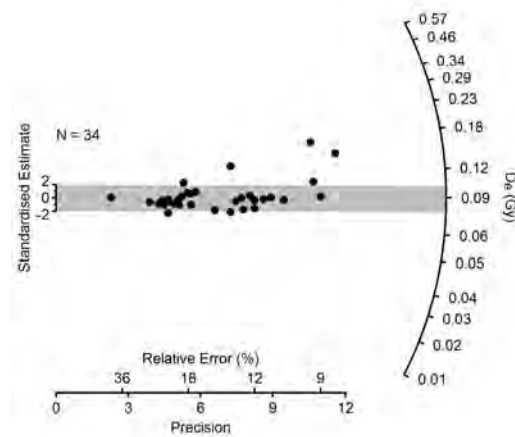


Figure 7.21: Single-aliquot (OSL) equivalent dose (D_e) distributions for PB#2b-8, displayed as a radial plot. The CAM D_e for this sample is 0.09 ± 0.01 Gy.

GLX D/L 0.314 ± 0.014 for the modern backshore dune at PB3, and GLX D/L 0.279 ± 0.003 for the modern beach.

The palaeosol 3b may not really overlie the aeolianite unit 3a (this palaeosol is interpreted to be equivalent to the thick, lower palaeosol [section 3, unit 1-3a] at site PB1), as 3-3a lies a further ~15 m west from the main site and protrudes through the modern beach sand—the palaeosol, then, may be an infilling lense in a dune saddle as it is at site PB1, rather than a continuous unit. Unit 3a at site PB3 in this case may be an isolated remnant of a small headland similar to section 1, site PB1 (Figure 7.6).

Site PB3 exhibits at least 3 periods of aeolianite deposition: MIS 7, late MIS 5 (possibly 5c), and a younger karstified aeolianite overlying this; interspersed with hiatuses represented by palaeosols (unit 3d is too weakly developed to be called a palaeosol; it is better defined as a protosol). These units broadly correlate with those at site PB1.

7.3.1.4 Pennington Bay site PB4 geochronology

PB4 is a broad headland at the western end of Pennington Bay; it is an older sequence than those previously examined. Two logs were recorded at this site: PB4-2 on the eastern side and PB4-1 on the western side (a detailed description is given in Chapter 3, section 3.5.2.4). The site was difficult to

sample, and only the lower portions could be easily accessed, which was unfortunate as it is a complicated site comparatively. The upper units were totally inaccessible and it was difficult to see structures such as palaeosol layers and calcretes; however, some aeolianite bedding was prominent enough to allow bedding orientations to be observed. Regardless, the lower units that could be accessed were sampled for either SARTT-OSL dating or AAR dating (see Tables 7.9, 7.10 and 7.13, and Figure 7.22 and 7.23).

At site PB4-1 the lower aeolianite (4-1b) was dated at 444 ± 102 ka (apparent parabolic kinetics calibration, using the U-series age of Schwebel [1978, 1984]) and 424 ± 96 ka (OSL calibration) using WR AAR (GLX D/L: 0.645 ± 0.007) and 498 ± 149 ka using Foram AAR (GLX D/L: 0.560 ± 0.041), suggesting a mid-Pleistocene age possibly near (or between) MIS 13 or 11 (Siddall *et al.*, 2007). The base of unit exhibits a series of level beds which are interpreted to be bottomset beds; however, in hindsight the contact could also be an erosional truncation surface. The lowest unit in the sequence (4-1a) is a densely indurated, extremely hard calcarenite; this was sampled, however the material was heavily recrystallised, and the AAR results were rejected because of anomalously low D/L values, and high L-serine. This basal calcarenite is in all probability early Pleistocene in age, and at this site it is cut into an extensive set of 3 benches or platforms (Figure 7.24). The lower benches probably formed during the Holocene and the present, and the upper bench (approximately 3 m APSL) during the sea-level maximum at MIS 5e. The upper units at PB4-1 could not be reached for sampling. The site also exhibits a large, steep ($\sim 45^\circ$) sand ramp; although, it has been stable for some time as it is extensively vegetated. The cliff tops also host well-vegetated Holocene dunes that overlie a blocky calcrete.

Another log (Figure 7.26) was recorded on the eastern side of site PB4: PB4-2; here SARTT-OSL and AAR methods were used to estimate ages for lower and middle aeolianite units. OSL sample PB#2a-3 was recovered from unit 4-2b. Twelve 3 mm mask size aliquots of this sample were analysed using the SARTT-OSL protocol (Chapter 5), and a central D_e of 138 ± 4 Gy (Table 7.13) was determined using the CAM (equivalent dose distributions are given in

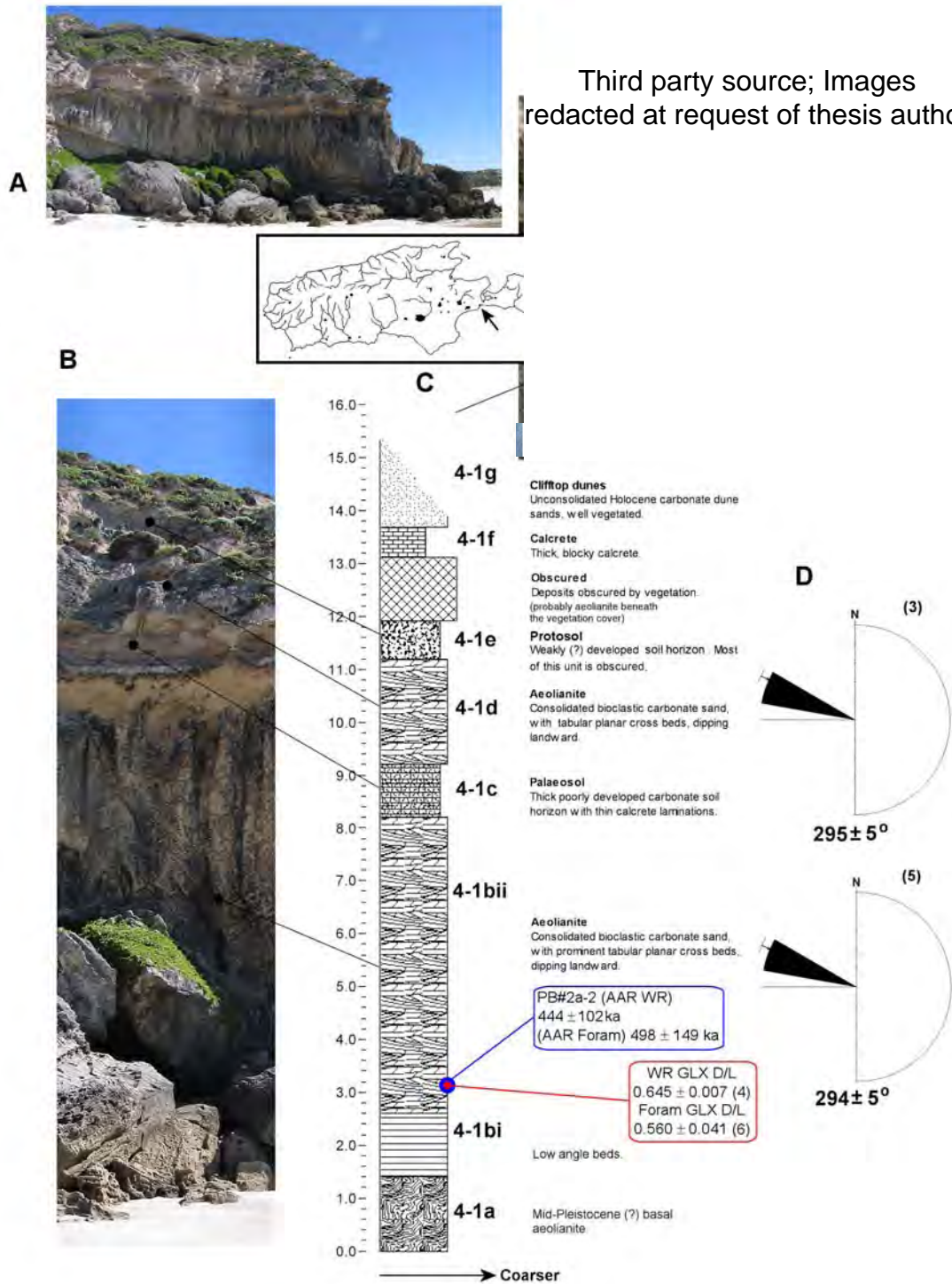


Figure 7.22: Pennington Bay site PB4-1 stratigraphic log (B) for the aeolianite outcrop towards the western end of the bay; included are the geochronological data (blue boxes) and corresponding GLX D/L ratio data (red boxes—numbers in brackets are individuals or subsamples analysed). The top inset (A) is a merged panorama (there is some distortion towards the ends of the image) of the outcrop. The RH inset (C) is a Kangaroo Island location map, with the site indicated by a black arrow, and a satellite image of the outcrop with indicated log and sample site (modified from Google Earth, 2007). The lower RH inset (D) is a set of bedding orientation rose diagrams (explained in Chapter 3: section 3.5.2.4), for the bottom and middle aeolianite units.

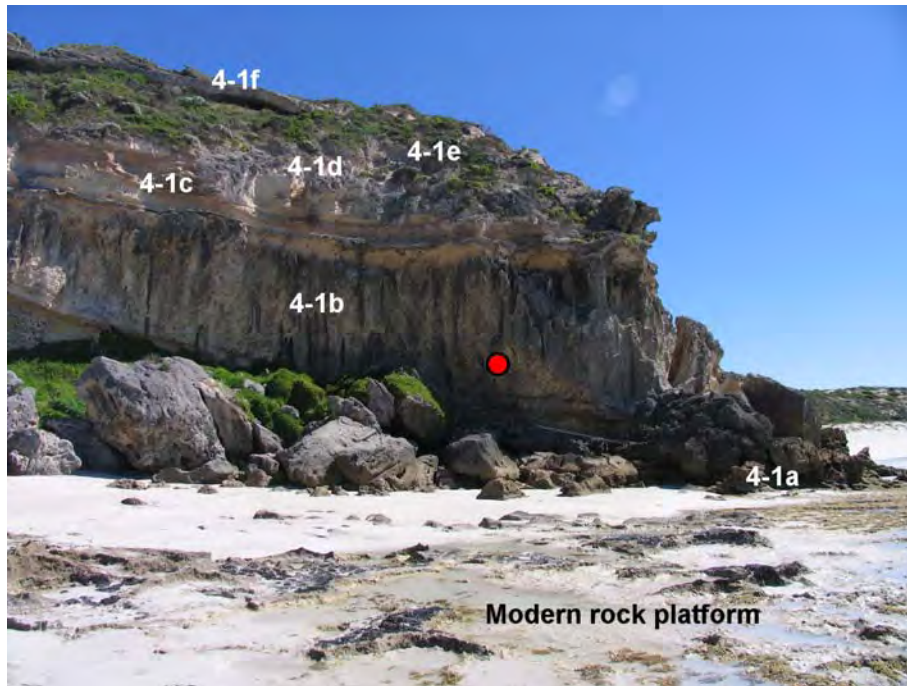


Figure 7.23: Site PB4-1 showing AAR (red) sample point and unit designations. Note the broken blocks of aeolianite and the modern rock platform.



Figure 7.24: Wave-cut benches at site PB4, western Pennington Bay. Bench 1 is modern, bench 2 most likely formed during a slightly higher than present Holocene sea-level, and bench 3, at approximately +3 m APSL, possibly formed during the Last Interglacial.

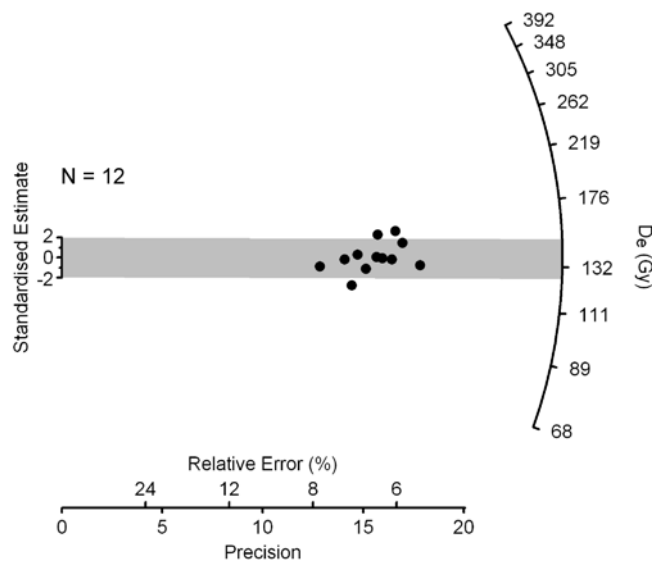


Figure 7.25: Single-aliquot (SARTT-OSL) equivalent dose (D_e) distributions for sample PB#2a-3, displayed as a radial plot. The CAM D_e for this sample is 138 ± 4 Gy.

Figure 7.25). The overdispersion was low at $6.9 \pm 2.6\%$, and the mean recycling ratio was 0.99 ± 0.08 . An age estimate of 226 ± 13 ka was determined from the central D_e using the program listed in Roberts *et al.* (1993).

The age for the lower aeolianite is much younger than that estimated for the middle unit (4-2d), using AAR. This is difficult to explain. However, it is possible that the section of the lower unit (4-2b) that was dated using SARTT-OSL (226 ± 13 ka) was actually a dislodged block of aeolianite from an upper unit (possibly the topmost unit (4-2f)—rather than actually being part of the lower aeolianite) (see Figure 7.26 and 7.27). This offers a plausible explanation as the area *is* strewn with large broken blocks of aeolianite, and the sample area could have been confused with one of these blocks. It is also possible that the middle unit (4-2d) contains a higher proportion of reworked grains; hence, a higher D/L ratio is derived and a greater age is calculated. However, the D/L ratio scatter in multiple batches of single foraminifer grains is reasonably consistent (Figure 7.28)—multiple foraminifers were hydrolysed in each RP-HPLC vial to boost amino acid concentrations. Although only a small number of usable grains could be recovered for analysis, a higher proportion of lower D/L ratios would be expected if the deposit was “contaminated” with a large reworked component. A

discrepancy between the Foram AAR age (377 ± 119 ka), and the WR AAR ages (310 ± 71 ka [U-series calibration] and 296 ± 67 ka [OSL calibration]) is noted (which could indicate a reworked component as a major contributor to a higher D/L, if by chance only older grains were sampled for single grain AAR analysis); however, all ages still overlap at 1σ .

The lower aeolianite at section PB4-1b can be traced around the headland to PB4-2b; hence, it is definitely the same unit. Given this, if the sampled section (PB4-2b) was derived from the same unit then the WR D/L ratios would be expected to match, which they do not, i.e., PB4-1b: GLX D/L: 0.645 ± 0.007 , and PB4-2b: GLX D/L: 0.531 ± 0.060 . Nevertheless, further work is needed to offer a better, alternative, explanation for this discrepancy in superposition. The units described at PB4-2 conform generally to those at PB4-1; even though they are at somewhat different heights, and some are obscured. It must be remembered that this is a very broad headland at around 80-100 m at the widest point; therefore some undulation in units can be expected.

Site PB4 requires more geochronological work to clarify the relationships between the units on the western side and eastern side of the headland; sampling of the upper portions of the site would be required for this.

Despite the discrepancies the chronology is interpreted to indicate a period of aeolian deposition during the middle-Pleistocene at MIS 13-11 (possibly MIS 11), and another during MIS 11-9 (possibly MIS 9). The upper units were not sampled as stated previously; however if the lower unit sampled (PB4-2b) on the eastern side of the headland is indeed a dislodged block from the uppermost aeolianite; then these units may have been deposited during MIS 7. This would imply that the younger MIS 5 aeolianites prevalent at sites PB1 and PB3, are absent from this sequence, or at least hidden from view given the height of the site and obscuring vegetation.

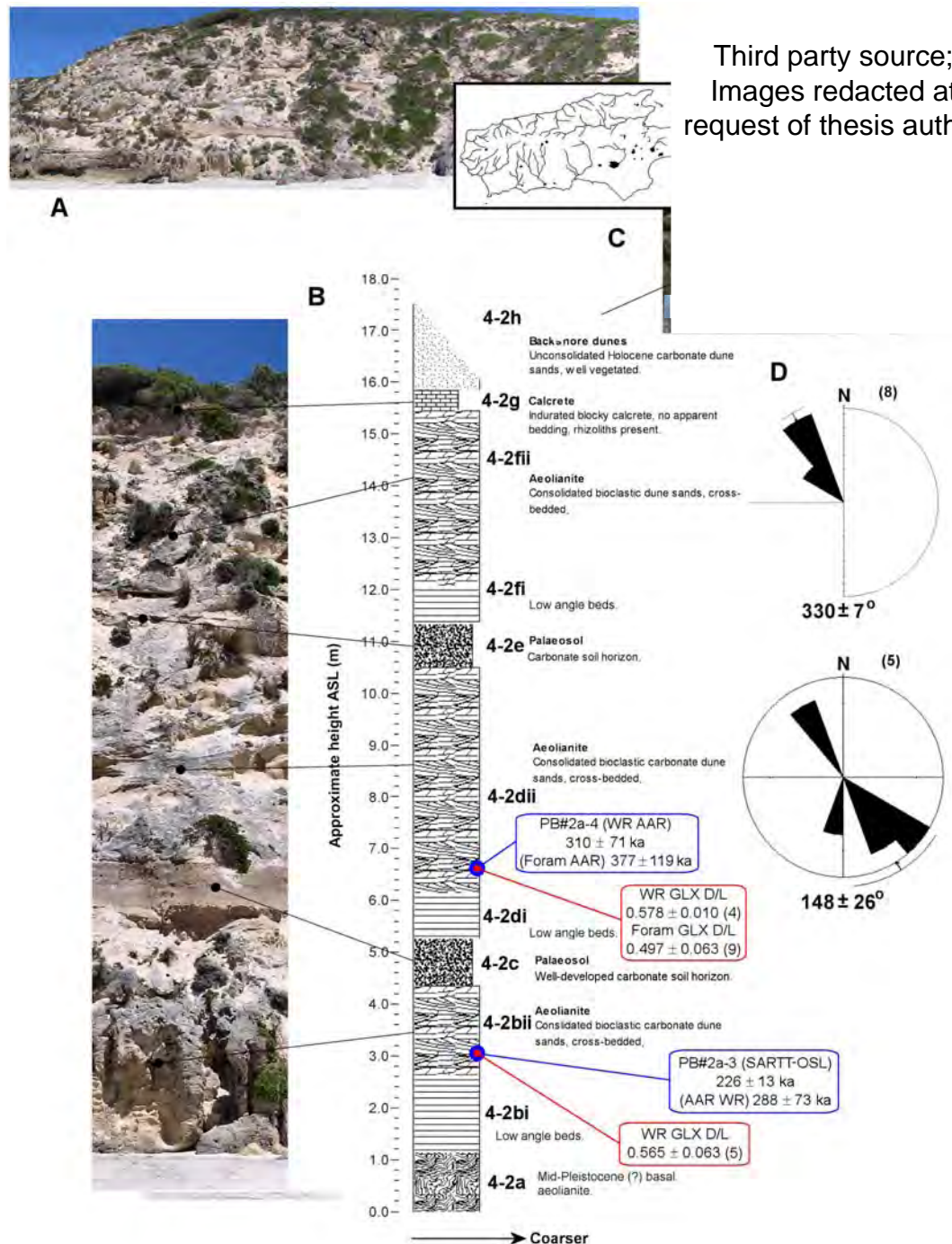


Figure 7.26: Pennington Bay site PB4-2 stratigraphic log (B) for the aeolianite outcrop towards the western end of the bay; included are the geochronological data (blue boxes) and corresponding GLX D/L ratio data (red boxes—numbers in brackets are individuals or subsamples analysed). The top inset (A) is a merged panorama (there is some distortion towards the ends of the image) of the outcrop. The RH inset (C) is a Kangaroo Island location map, with the site indicated by a black arrow, and a satellite image of the outcrop with indicated log and sample site (from Google Earth, 2007). The lower RH inset (D) is a set of bedding orientation rose diagrams (explained in Chapter 3: section 3.5.2.4), for the middle and upper aeolianite units.

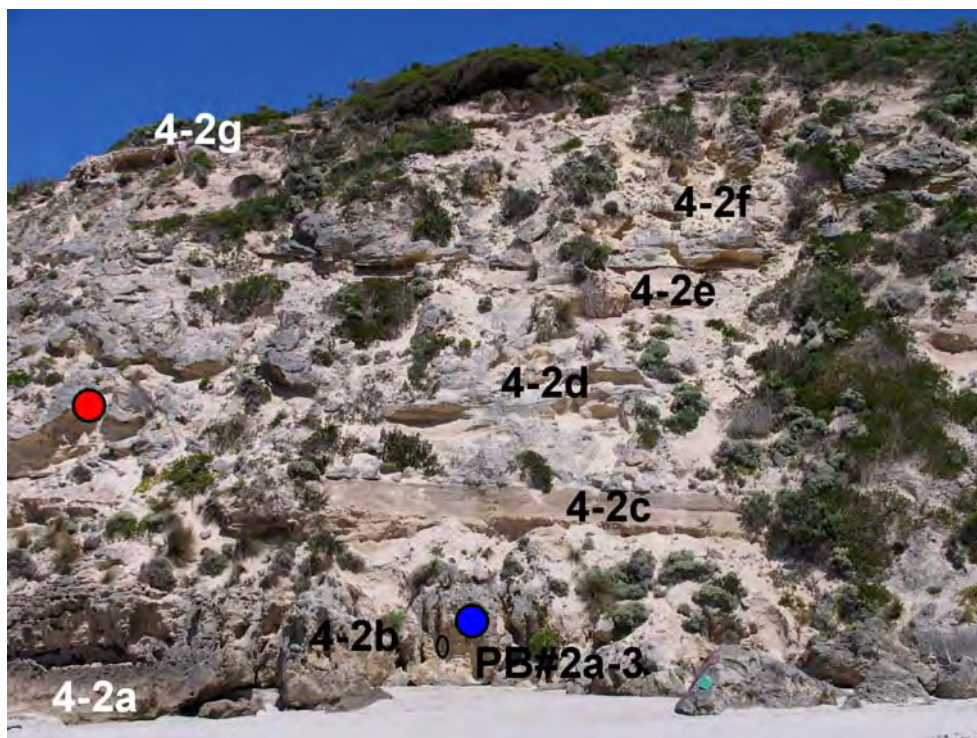


Figure 7.27: Site PB4-2 showing OSL (blue) and AAR (red) sample points (AAR samples were also taken from the same hole as the OSL sample) and unit designations. The open ellipse below the OSL sample point denotes a rock-hammer (33 cm) set for scale.

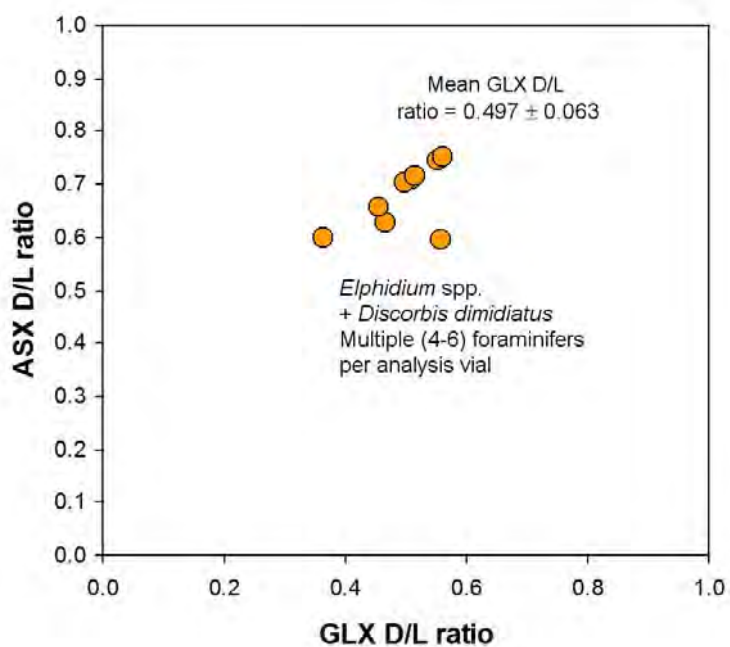


Figure 7.28: Bivariate plot of *Elphidium* spp. and *D. dimidiatus* D/L ratios, from site PB4, unit PB4-2d, Pennington Bay. Each point on the plot represents multiple foraminifers.

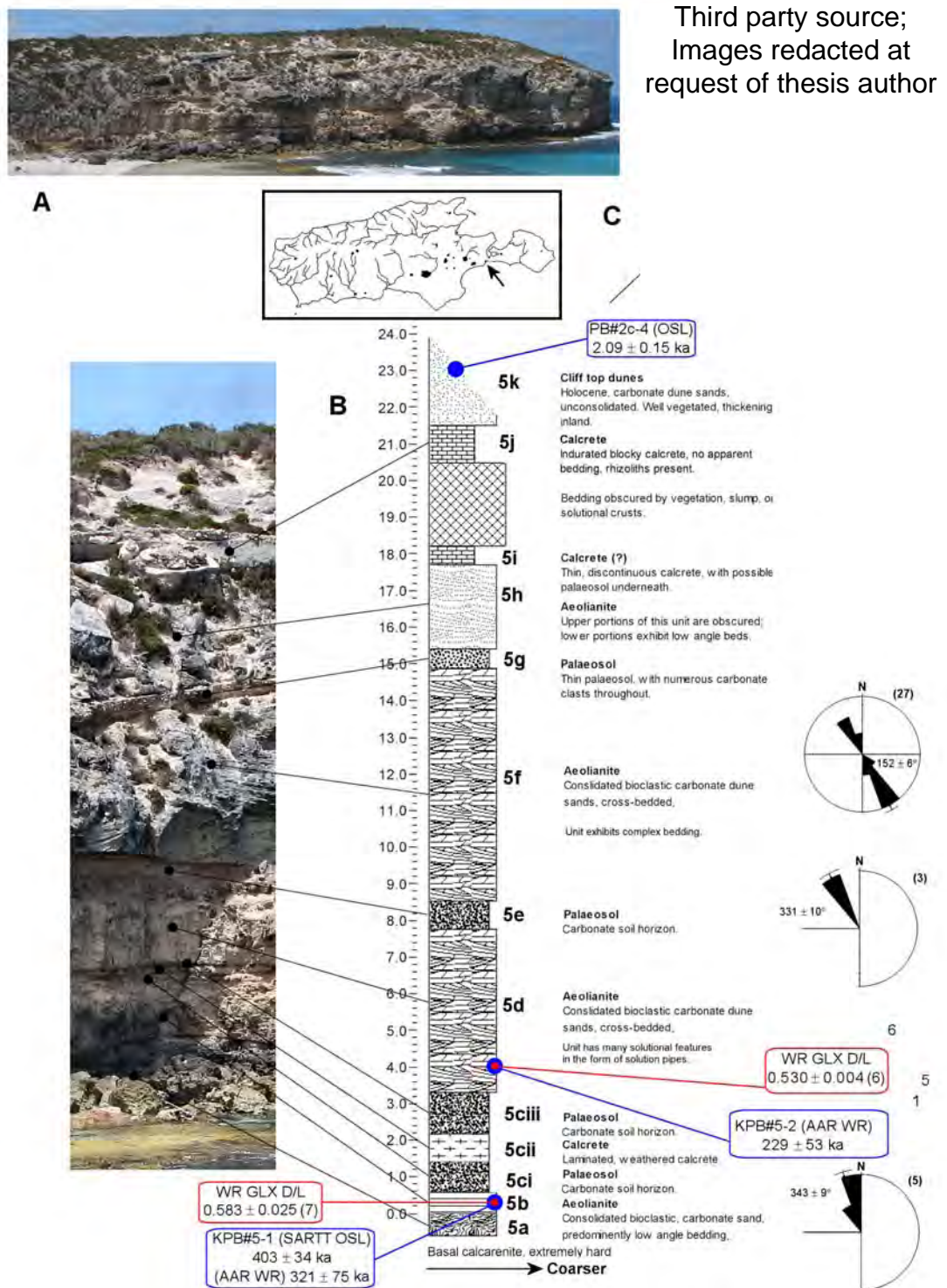


Figure 7.29: Pennington Bay site PB5 stratigraphic log (B) for the aeolianite outcrop towards the western end of the bay; included are the geochronological data (blue boxes) and corresponding GLX D/L ratio data (red boxes—numbers in brackets are individuals or subsamples analysed). The top inset (A) is a merged panorama (there is some distortion towards the ends of the image) of the outcrop. The RH inset (C) is a Kangaroo Island location map, with the site indicated by a black arrow, and a satellite image of the outcrop with indicated log and sample site (modified from Google Earth, 2007). The lower RH inset (D) is a set of bedding orientation rose diagrams (explained in Chapter 3: section 3.5.2.4), for the middle and upper aeolianite units.

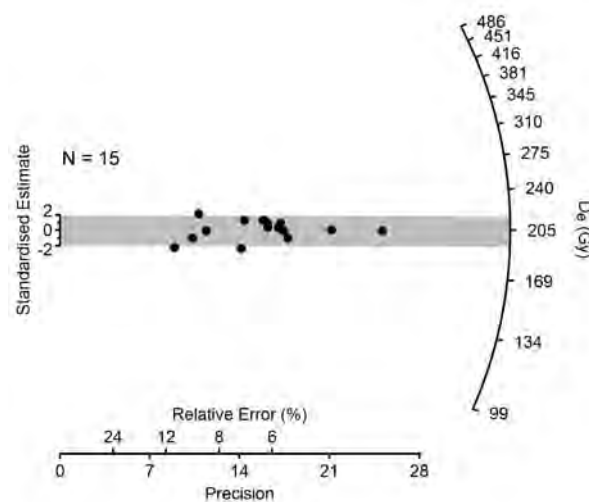


Figure 7.30: Single-aliquot (SARTT-OSL) equivalent dose (D_e) distributions for sample KPB#5-1, displayed as a radial plot. The CAM D_e for this sample is 205 ± 4 Gy.

7.3.1.5 Pennington Bay site PB5 geochronology

Site PB5 is located on the main bounding headland at the eastern end of Pennington Bay (Figure 7.5). PB5 is the most complicated outcrop in the bay, and exhibits 5 (exposed) aeolianite units (Figure 7.29). Unfortunately only the lower units could be accessed for sampling as the site was too precipitous for safe access. The lower aeolianite unit (5b) which conformably overlies the early (possibly middle) Pleistocene basal calcarenite (5a) was sampled for both SARTT-OSL and AAR dating purposes. The SARTT-OSL sample (KPB#5-1) was removed from Unit 5b, and 15 aliquots (3 mm mask size) of the sample were subjected to the SARTT-OSL protocol (Chapter 5), yielding a central D_e of 205 ± 4 Gy (using the CAM) (see Figure 7.30 for equivalent dose distributions). The overdispersion was low at $3.7 \pm 2.5\%$, and the mean recycling ratio was 1.06 ± 0.08 —no aliquots were rejected. A SARTT-OSL age estimate was derived from the central D_e giving an age of 403 ± 34 ka (Table 7.13), which coincides with MIS 11 (see Huntley *et al.* [1993, 1994], Siddall *et al.* [2007], and Murray-Wallace [2002]). AAR analysis of GLX D/L ratios using whole-rock sediment, and the apparent parabolic kinetics model for calibration, gave AAR ages of 321 ± 75 ka (U-series calibration) and 306 ± 70 ka (OSL calibration).

(GLX D/L: 0.583 ± 0.025) for this unit (see Table 7.9). These luminescence and AAR ages bracket a MIS 11 age quite adequately for the lower unit. The apparently younger ages (even though all of the ages overlap at 1σ) derived using AAR may be explained by leaching of more racemized lower molecular weight organic residues, allowing higher molecular weight less racemized residues to exert greater influence on the D/L ratio. Contamination as the cause can be discounted as L-SER values were comparatively low for the sample set.

The next aeolianite unit in the sequence was unit 5d which overlies a complex palaeosol profile. This unit was sampled for AAR dating only as it was difficult to sample for luminescence due to the precarious position. The AAR age estimates, based upon WR sediments were 229 ± 53 ka (U-series calibration) and 219 ± 49 ka (OSL calibration). The age estimates suggest a MIS 7 deposition for this unit (possibly also MIS 8 or 9); although, stratigraphic position better supports an MIS 9 age for 5d. The upper 2 (or 3) aeolianite units could not be reached to sample. The cliff top dunes, however, could be easily accessed, and these were dated using OSL. Sample PB#2c-1 was collected for OSL analysis from these dunes, and 24 aliquots (1 mm mask size) were analysed using the modified SAR protocol. All aliquots were accepted and the central D_e (calculated using the CAM) was 1.56 ± 0.02 Gy, with an overdispersion of $5.9 \pm 1.1\%$ (equivalent dose distributions are given in Figure 7.31). Recycling and IR depletion ratios all conformed to unity with mean ratios of 1.00 ± 0.03 and 1.01 ± 0.03 , respectively. An age estimate of 2.09 ± 0.15 ka was derived from the central D_e , using the program listed in Roberts *et al.* (1993). This indicates a late Holocene deposition for these deeply dissected dunes.

The units that could not be reached for sampling (units 5f and 5h) most likely represent—if highstand deposition of aeolianites follows, which seems likely given the luminescence chronology for other sites around the bay—MIS 7 and MIS 5.

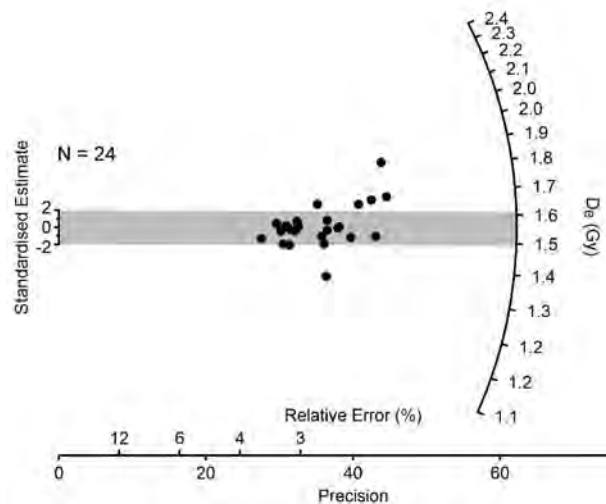


Figure 7.31: Single-aliquot (OSL) equivalent dose (D_e) distributions for sample PB#2c-1, displayed as a radial plot. The CAM D_e for this sample is 1.56 ± 0.02 Gy.

7.3.1.6 Discussion of the Pennington Bay geochronology

The amino acid GLX D/L ratio results calibrated using independently dated materials enabled the derivation of a series of AAR age estimates which were used to compliment the luminescence chronology of selected sites comprising Bridgewater Formation aeolianites and associated facies around Pennington Bay.

The chronology reveals several periods of aeolianite deposition that essentially coincide with highstands of sea-level that occurred during interglacial periods. The sequences around Pennington Bay exhibit units that range in age from modern to middle Pleistocene time; with the oldest series being present on bounding headlands at the western and eastern ends of the embayment. These older sequences may have been the walls of a sea-way that bisected the neck of the Dudley Peninsula (see Figure 7.5) connecting Pelican Lagoon and American River to the ocean during periods of higher-than-present sea-level. The presence of a sea-way would also explain the lack of older units in the lower topography towards the centre of the bay. Generally the aeolianites are coupled with an overlying unconformity, usually a palaeosol, which indicates a hiatus in deposition. It is hypothesized that the unconformity represents a halt in

carbonate deposition that occurs during a glacial period; where the continental shelf is exposed (terminating carbonate production), due to a lowering of sea-level. The exposed shelf is consequently vegetated. The hiatus allows the formation of soils (and calcretes), and subsequent de-vegetation and deflation exposes the pedogenetically modified B-horizon. When carbonate deposition restarts this horizon is buried; hence, the couplet relationship between aeolianite and palaeosol. At Pennington Bay there are apparently 3 main palaeosol units, indicating 3 hiatuses, some of which are not continuous around the bay, there are also some minor, thin palaeosols / calcretes (often running through thick aeolianite units) which are thought to represent short breaks in deposition, probably corresponding to stadials. The morphostratigraphical and chronostratigraphical interpretations of Pennington Bay sediments are explored in Figures 7.32 and 7.33.

There are 4 (MIS 11, 9, 7 and 5), possibly 5 (MIS 3) distinct aeolianite units present at Pennington Bay, one of which can be traced all of the way around the bay (MIS 7), and another that can be traced most of the way (MIS 5). These units are interpreted, on the basis of the luminescence and AAR chronology, to be associated with periods of high sea-level (not necessarily as high as [or higher] than present); as would be experienced during an interglaciation. Indeed the position and morphology of many of the outcrops suggests that deposition occurred when sea-level was lower—some outcrops extend below current sea-level, and strandline-parallel cliff morphology implies erosion from high sea-level. Nevertheless much of the dating aligns the aeolianite units at Pennington Bay with interglacial periods. It is possible that deposition of carbonate sediments is initiated during the transgression and prior to maximum sea-level, or during a regression, which may also mobilise onshore deposition of carbonate shelf sediments. It is difficult to say which the case is; indeed both circumstances may occur.

The large uncertainty associated with the AAR ages means that (particularly for older deposits) it is difficult to directly associate the age with an interglacial period, as the large uncertainties make the age imprecise. However, as many of

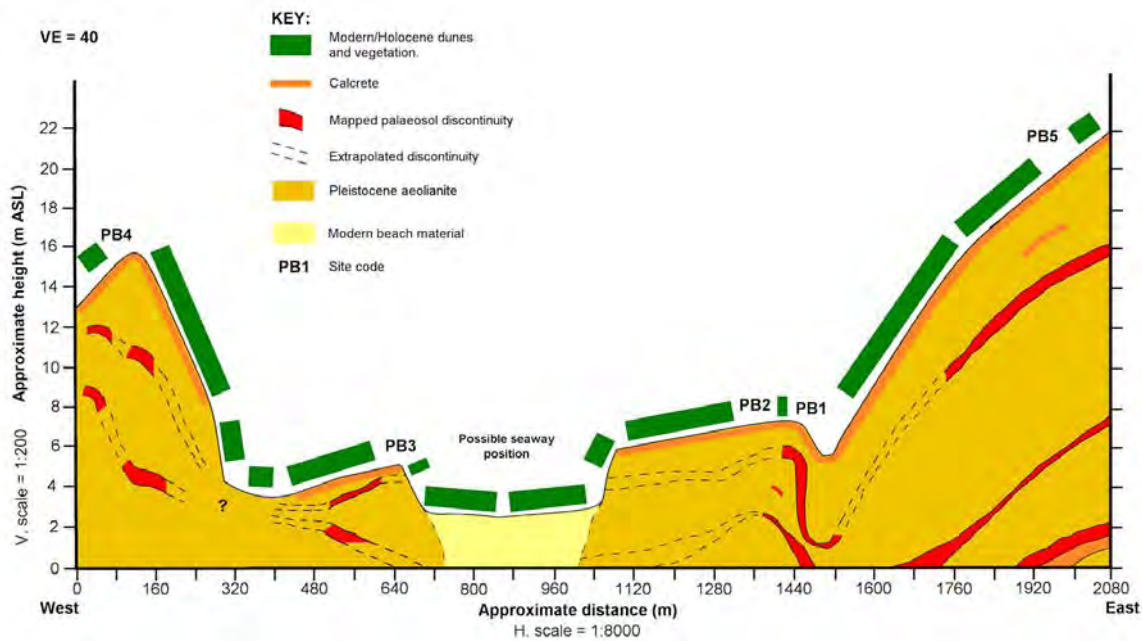


Figure 7.32: Morphostratigraphical interpretation of the Pennington Bay sites based upon recorded logs. The cross-section has a vertical exaggeration of 40, a vertical scale of 1:200, and a horizontal scale of 1:8000.

the younger OSL ages have relatively small uncertainties, a direct connection to a given interglacial MIS stage or even substage is rendered reasonably unambiguous. Thus, the precision (and alignment) in the OSL ages allows the construction of a more plausible interpretation of the less precise AAR ages.

To summarise: aeolian deposition of carbonate marine sediments at Pennington Bay (as components of the Pleistocene Bridgewater Formation) is interpreted here to have occurred during periods of high sea-level associated with interglacial periods. The basal calcarenite which underlies much of the outcropping sediment is most likely a remnant of an early Pleistocene aeolianite which has possibly acted as a “keystone” for subsequent deposition. The two major headlands at the western and eastern ends of the bay are the oldest sequences; the lowest units at both sites corresponding to MIS 11 deposition (not including the basal calcarenite); the provenance issue with unit PB4-2b notwithstanding. Also represented at these sites is an aeolianite that broadly correlates to MIS 9. The most common aeolianite units can be unambiguously associated with MIS 7 and MIS 5 (MIS 5e and 5c, b or a). The MIS 7 unit underlies all of the younger more central-to-the-bay outcrops (also forming small headlands), and is probably present in the upper portions of the older

Third party source; Images
redacted at request of thesis
author

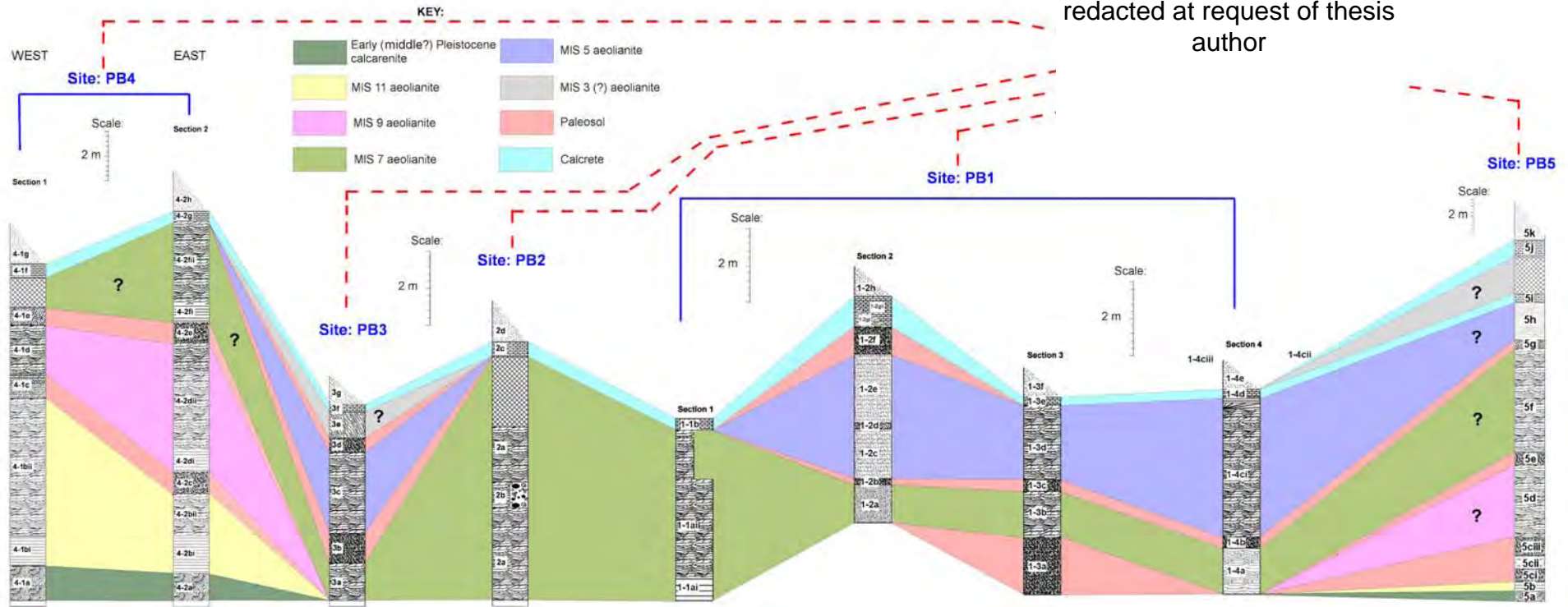


Figure 7.33: Chronostratigraphical interpretation of the Pennington Bay sites, based upon the derived AAR, and luminescence chronologies. The scales are different for some logs, therefore the heights are not directly comparable in this sense; however, this does not detract from the presentation.

sequences in the west and east—although this is yet to be geochronologically established. The MIS 5 units are found in the more central outcrops, and are probably present as the upper units at site PB5, although they may be absent or obscured at site PB4. A younger aeolianite may also be present at site PB3 that is possibly MIS 3 (or 4) in age. The outcrops at all sites examined are unconformably overlain by a calcrete that is most likely of the same age at all sites. This in turn is covered (although the calcrete is exposed at the precipice) by either late Holocene cliff top dunes at the bounding headlands, or modern backshore dunes in the central portion of the bay, although further inland from the shore the parabolic dunes may be Holocene in age (a chronostratigraphic interpretation of the Pennington Bay sites is given in Figure 7.33).

7.3.2 Bales Beach

Bales Beach lies on the south-coast of Kangaroo Island, approximately 38 km straight-line distance west from Pennington Bay (Figure 7.4), in the Seal Bay Conservation Park. This site is similar to Pennington Bay hosting strandline-parallel aeolianite / palaeosol couplets, and high headland outcrops. Two sections were examined at Bales Beach (Figure 7.34):

- i) a length of low, scarped, complex aeolianite / palaeosol units that run parallel to the shoreline; which may represent a single MIS deposition: Bales1
- ii) a large, high headland at the western end of the bay: Bales2

The amino acid data and calculated AAR ages for the Bales Beach sites are presented in Tables 7.15 and 7.16.

7.3.2.1 Bales Beach site Bales1 geochronology

Bales1 is a series of aeolianite / palaeosol couplets that grade at around 6° towards the east until the calcrete mantle enters the modern beach sand below

Third party source; Images redacted at request of thesis author

Figure 7.34: Satellite image of Bales Beach sites (Google Earth, 2008).

sea-level. The aeolianite scarp in this area of the bay is complex and the presented stratigraphic log (E) in Figure 7.35 is a composite of three large sections along the scarp. This deposit according to the AAR and luminescence chronology is representative of a single marine isotope stage, in this case MIS 5. Thirty aliquots (1 mm mask size) of sample Bales#2-9 (taken from the upper aeolianite unit [1e]) were analysed for OSL (5 aliquots were rejected, see Table 7.11 for details), and yielded a central D_e of 56 ± 1 Gy (using the CAM) with an overdispersion of $4.5 \pm 3.9\%$ (equivalent dose distributions are displayed in Figure 7.36). The recycling and IR depletion ratios were 0.95 ± 0.04 and 1.03 ± 0.03 , respectively. The remaining aliquots were dated using the program listed in Roberts *et al* (1993), yielding an OSL age of 107 ± 7 ka. This corresponds to a late MIS 5 deposition most likely 5c, b or a. The aeolianite unit that is below 1e (1c) was dated using a combination of WR AAR and Foram AAR, giving ages of 126 ± 29 ka (U-series calibration) and 120 ± 27 ka (OSL calibration) (GLX D/L: 0.455 ± 0.008), and 160 ± 50 ka (GLX D/L: 0.350 ± 0.040) respectively (Tables 7.15 and 7.16). These ages would indicate that this middle unit was the result of aeolian deposition during MIS 5; however, the large uncertainties preclude aligning the ages with a particular substage. The lowest

Table 7.15: Pleistocene and Holocene whole-rock sediment ASX and GLX AAR data, and GLX AAR numerical ages for Bales Beach

Lab. No.	Site	Site code / facies / (N) ^a	Location (S Lat. E Long.)	CMAT ^b °C	ASX D/L ratio $\pm 1\sigma^c$	Coefficient of variation (CV%)	GLX D/L ratio $\pm 1\sigma^c$	Coefficient of variation (CV%)	AAR GLX (U-series calib.) age estimate (ka) ^d $\pm 1\sigma^b$	AAR GLX (OSL calib.) age estimate (ka) ^d $\pm 1\sigma^b$
UWGA 6579	Bales Beach east	Bales#2-10 / backshore dunes (4)	35° 59' 37.3" 137° 20' 47.6"	15.3	0.411 \pm 0.020	4.8	0.257 \pm 0.015	5.7	1.02 \pm 0.24	0.98 \pm 23
UWGA 6578	Bales Beach east	Bales#2-9 / aeolianite (4)	35° 59' 37.3" 137° 20' 47.6"	15.3	0.604 \pm 0.003	2.7	0.439 \pm 0.007	5.9	109 \pm 25	(105 \pm 7)*
UWGA 6577	Bales Beach east	Bales#2-7 / aeolianite (4)	35° 59' 37.3" 137° 20' 47.6"	15.3	0.625 \pm 0.014	2.2	0.455 \pm 0.008	1.8	126 \pm 29	120 \pm 27
UWGA 6580	Bales Beach east	Bales#2-3 / aeolianite (4)	35° 59' 37.3" 137° 20' 47.6"	15.3	0.611 \pm 0.015	2.5	0.464 \pm 0.006	1.4	137 \pm 31	131 \pm 29
UWGA 5843	Bales Beach west	Bales#3-1a / aeolianite (4)	35° 59' 40.1" 137° 20' 36.9"	15.3	0.730 \pm 0.003	0.3	0.667 \pm 0.001	0.1	495 \pm 114	473 \pm 106

^a N = number of subsamples

^b Current mean annual temperature (CMAT) estimated for these sites from annual temperature data via climate recording stations around Kangaroo Island

(<http://www.bom.gov.au/climate/data>)

^c Uncertainties are 1 σ (one standard deviation—68% confidence interval)

^d Numeric age estimate from a U-series calibration (Schwebel, 1978; 1984), and an OSL calibration (this study) using an apparent parabolic model (Mitterer and Kriaušakul, 1989; Murray-Wallace *et al.*, 2001); uncertainties are calculated from the square root of the sum of the squares of all uncertainty terms

* OSL age estimate of whole-rock sample used to calibrate the GLX D/L ratio.

Table 7.16: Bales Beach Pleistocene single foraminifer ASX and GLX AAR data, and numeric AAR age estimates

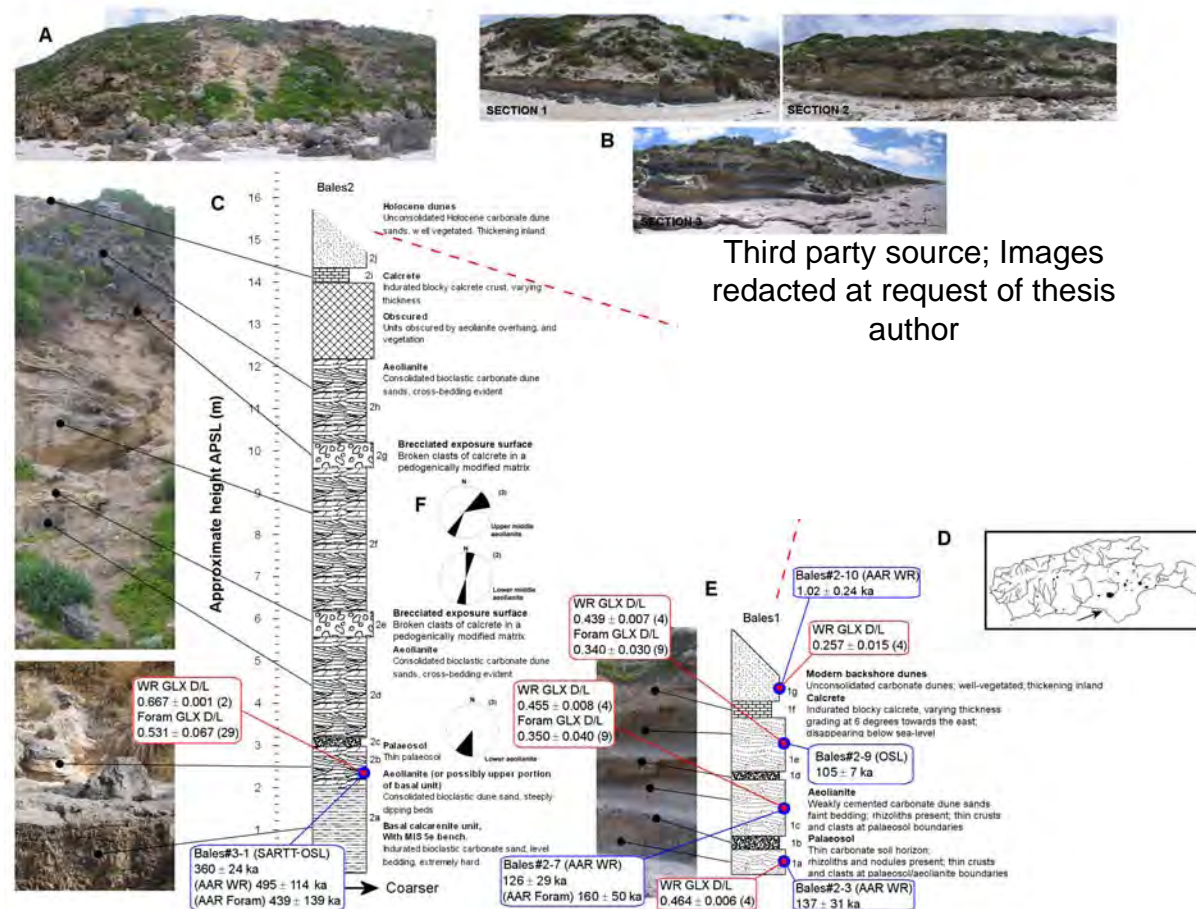
Lab. No.	Site	Site code / facies	Location (S Lat. E Long.)	CMAT ^a °C	Genus and species / (N) ^b	ASX D/L ratio) ± 1σ ^c	Coefficient of variation (CV%)	GLX D/L ratio) ± 1σ ^c	Coefficient of variation (CV%)	AAR GLX age estimate (ka) ^d ± 1σ ^c
UWGA 6581, 6582	Bales Beach	Bales#2-9 / aeolianite	35° 59' 37.3" 137° 20' 47.6"	15.3	<i>Elphidium</i> sp. + <i>D.</i> <i>dimidiatus</i> / (9)	0.582 ± 0.018	3.1	0.340 ± 0.030	8.7	149 ± 45
UWGA 5822	Bales Beach	Bales#2-7 / aeolianite	35° 59' 37.3" 137° 20' 47.6"	15.3	<i>Elphidium</i> sp. + <i>D.</i> <i>dimidiatus</i> / (6)	0.537 ± 0.059	11.0	0.350 ± 0.040	11.3	160 ± 50
UWGA 5814, 5819, 6583, 6584, 6585	Bales Beach	Bales#3-1a / aeolianite	35° 59' 40.1" 137° 20' 36.9"	15.3	<i>Elphidium</i> sp. + <i>D.</i> <i>dimidiatus</i> / (39)	0.699 ± 0.039	5.5	0.531 ± 0.067	12.6	439 ± 139

^a Current mean annual temperature estimated for these sites from annual temperature data via climate recording stations around Kangaroo Island
(<http://www.bom.gov.au/climate/data>)

^b Number of foraminifera used for D/L ratio estimate

^c Uncertainties are 1 σ (one standard deviation—68% confidence interval)

^d Numeric age estimate from a U-series calibration (fossil coral recovered from Vivonne Bay) using an apparent parabolic kinetics model (Mitterer and Kriaušakul, 1989; Murray-Wallace *et al.*, 2001); uncertainties are calculated from the square root of the sum of the squares (addition in quadrature) of all uncertainty terms



Third party source; Images redacted at request of thesis author

Figure 7.35: Bales Beach sites Bales1 and 2 (stratigraphic logs E and C) for the aeolianite outcrops towards the western end of the bay; included are the geochronological data (blue boxes) and corresponding GLX D/L ratio data (red boxes—numbers in brackets are individuals or subsamples analysed). The top RH inset (A) is a merged panorama for the Bales2 (there is some distortion towards the ends of the image) outcrop. The top RH inset panoramas (B) show the 3 sections comprising log E. The lower RH inset (D) is a Kangaroo Island location map, with the site indicated by a black arrow, and a satellite image of the outcrop with indicated log and sample sites (from Google Earth, 2007). The lower RH inset (F) is a set of bedding orientation rose diagrams (explained in Chapter 3: section 3.5.2), for the lower, lower middle and upper middle aeolianite units.

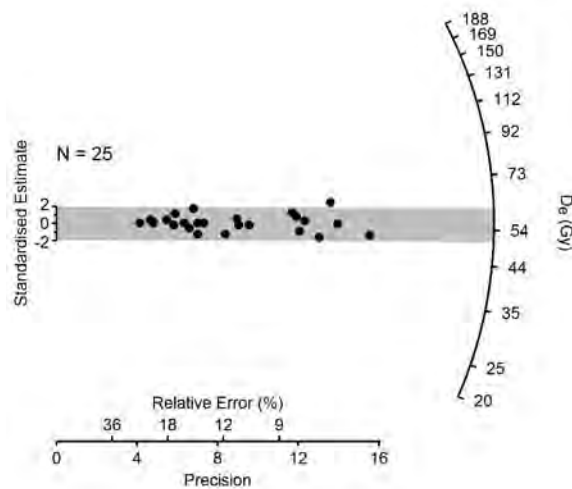


Figure 7.36: Single-aliquot (OSL) equivalent dose (D_e) distributions for sample Bales#2-9, displayed as a radial plot. The CAM D_e for this sample is 56 ± 1 Gy.

unit in the sequence (1a) dates at 137 ± 31 ka (U-series calibration) and 131 ± 29 ka (OSL calibration), using WR AAR (GLX D-L: 0.464 ± 0.006). Again this would allude to MIS 5 deposition (Table 7.15). All of the aeolianite units are separated by relatively thin palaeosols (1b and 1d) which may be indicators of stadial hiatuses in carbonate deposition, given that the dating indicates that the sequence may represent a single MIS. In this instance then it may be possible to suppose the following history for the sequence: MIS 5e deposition for unit 1a, MIS 5c for unit 1c, and MIS 5a for unit 1e. This is following the premise of aeolianite deposition during highstands (or transgressions/regressions) related to interglacials, and interstadials (as discussed in Chapter 2: section 2.4.2).

The units are mantled by a blocky calcrete and the entire sequence dips or grades towards the east at approximately 6° . All units, including the mantle, disappear beneath the modern beach sediment. Modern dunes overlying the calcrete surface were age estimated using the extent of whole-rock sediment AAR giving an age of 1.02 ± 0.24 ka; the extent of racemization in these dunes is similar to that from the Pennington Bay modern backshore dunes (i.e. GLX D-L 0.314 ± 0.014 for Pennington Bay modern dunes, and 0.257 ± 0.015 for Bales Beach modern dunes). Because the y-intercept in the apparent parabolic kinetics calibration is based upon the mean of a series of modern beach samples, the actual age of the modern dunes dated using WR AAR is difficult to determine. However, if the Pennington Bay OSL age of 0.10 ± 0.01 ka is used

to compare the GLX D-L ratios, the age for the Bales Beach modern dunes is similar.

7.3.2.2 Bales Beach site Bales2 geochronology

As with the Pennington Bay western and eastern headlands the Bales2 site is a high, complex sequence of aeolianites, and palaeosols, and also brecciated exposure surfaces. This site lies at the western end of the Bales Beach bay and forms the beginning of a high cliffed section of coast. The basal portion of the sequence is an extremely hard indurated calcarenite (unit 2a), most likely of the same or similar antiquity (early or perhaps middle Pleistocene in age) to that found as the lowest unit at the Pennington Bay headland outcrops. A bench has formed in the unit at approximately +2 m APSL, suggesting erosion during a higher sea-level, probably the Last Interglacial. Site Bales2 was largely inaccessible and only the lower aeolianite was able to be sampled (unit 2b). Sample Bales#3-1 was taken from this unit and analysed using the SARTT-OSL protocol, as it was expected to be beyond the conventional OSL method given its stratigraphic position. Fifteen 3 mm mask size aliquots were analysed (none were rejected) yielding a CAM D_e of 212 ± 3 (in this case overdispersion was too low to be calculated by the model), and a mean recycling ratio of 1.03 ± 0.08 . The age estimate derived from the central D_e was 360 ± 24 ka (equivalent dose distributions are shown in Figure 7.37). This age is reasonably consistent with MIS 11. Calculated AAR ages using both whole-rock and foraminifers are older (although not significantly so) with respect to the SARTT-OSL age. The WR AAR ages for this unit are 495 ± 114 ka and 473 ± 106 ka, respectively, for the U-series and OSL calibrations. The Foram AAR age estimate is 439 ± 139 ka. These ages, even though the uncertainties are large, would suggest MIS 11 to 13.

A younger GLX D-L ratio population was isolated using hierarchical clustering (Ward method), and the population mean yielded a Foram AAR estimate of 301 ± 90 ka (rather than 439 ± 139 ka which was derived from the total mean) (Figure 7.38). This is in better agreement with the SARTT-OSL age of 360 ± 24 ka, and would suggest either MIS 9 or MIS 11 deposition. It is difficult to

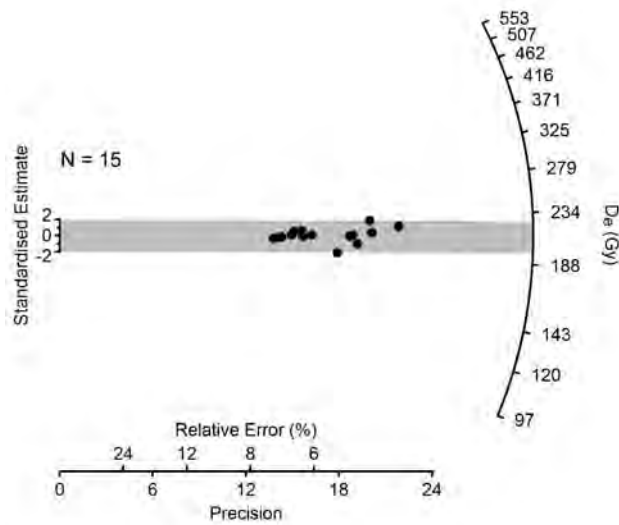


Figure 7.37: Single-aliquot (SARTT-OSL) equivalent dose (D_e) distributions for sample Bales#3-1, displayed as a radial plot. The CAM D_e for this sample is 212 ± 3 Gy.

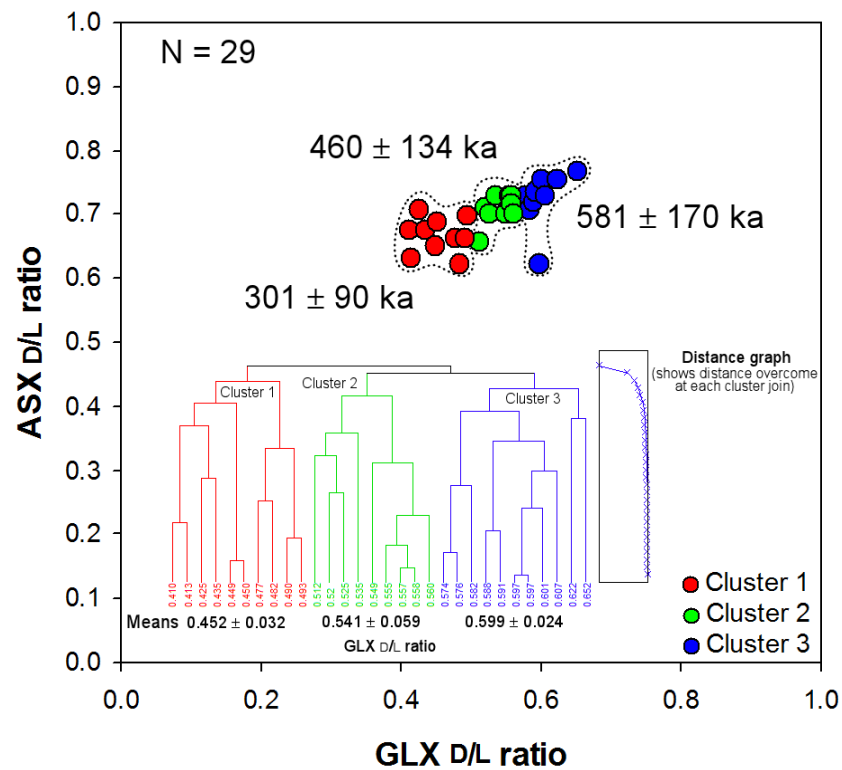


Figure 7.38: Bivariate plot of Bales#3-1 foraminifer (*Elphidium* spp. + *Discorbis dimidiatus*) D-L ratio data. Here a hierarchical clustering dendrogram (lower inset) was used to delineate three D-L ratio populations within the group. The mean of each cluster was subjected to the Foram calibration to estimate three ages: 301 ± 90 ka, 460 ± 134 ka, and 581 ± 170 ka. These older clusters represent reworked grain populations.

estimate the age of this unit (2b) on the basis of the AAR and luminescence chronology. However, it would certainly appear to have been deposited sometime near or between MIS 9 and MIS 11, rather than MIS 13 (given that the WR AAR ages may have been influenced by older reworked grains—see Figure 7.38).

7.3.2.3 Discussion of the Bales Beach geochronology

Since the chronology is limited at the Bales Beach site little can be concluded concerning the upper units at Bales2 (Figure 7.34); however, if a *MIS 11* age is given to unit 2b then a MIS 9, MIS 7 and MIS 5 age may be assigned to the upper aeolianites (2d, 2f, and 2h), respectively (Figure 7.34). Unusually, the aeolianite units at Bales2 are intercalated with brecciated exposure surfaces (except the unconformity overlying 2b) (i.e. irregularly shaped cobbles of calcrete in a pedogenetically modified matrix), rather than relatively featureless palaeosols. This would imply different diagenetic processes being in operation at Bales Beach compared to Pennington Bay, during the Pleistocene. The units at Bales1 appear to represent a single marine isotope stage, i.e., MIS 5. This is similar to Pennington Bay where only relatively young units are found towards the middle of the embayment. At Bales Beach the central portions of the bay can be characterised by modern and Holocene parabolic dunes with no older material being present.

7.3.3 Point Ellen and Vivonne Bay

Point Ellen and Vivonne Bay lie on the southern coast of Kangaroo Island approximately 15 km straight-line distance west from Bales Beach (Figure 7.4). Point Ellen hosts the type section of the early Pleistocene Point Ellen Formation (Ludbrook, 1983; 1984; Milnes *et al.*, 1983). As discussed in Chapter 3, the Point Ellen Formation is a richly fossiliferous marine (primarily gastropods and bivalves) deposit that infills a large irregular basin in the Cambrian Kanmantoo Group bedrock at the site. The formation has lateral extent of approximately 240 m at Point Ellen, and ranges from up to ~2 to ~4 m in thickness (thicker than originally reported in Milnes *et al.*, 1983). It can be characterised by 2 discrete shelly units found at the base and at the top of the Formation.

The Point Ellen Formation, first defined by Milnes *et al.* (1983), crops out to a limited extent at 'Table Rock' Point Reynolds, near Pennington Bay and at Cape Willoughby (Figure 7.39: upper LH inset). However, the largest and most extensive outcrop is at Point Ellen (Figure 7.40). The Point Ellen Formation is also present on the mainland at Cape Jervis and Naracoorte (Ludbrook, 1983; 1984). A strontium isotope ($^{87}\text{Sr}/^{86}\text{Sr}$) age of 1.2 Ma (no uncertainty was reported) was obtained for the upper portion of the formation (+3 m APSL) at Point Reynolds, Pennington Bay by Belperio (1995), supporting the Early Pleistocene age assigned to the formation.

Third party source; Images redacted at request of thesis author

Figure 7.39: Location of sites around Vivonne Bay, and Point Ellen. The upper right inset shows the geographical location of the bay (small black arrow); the red spots are mapped areas, and the numbered blue spots (inset) are the locations of 1) the Point Ellen type section for the Point Ellen Formation, 2) the Point Ellen Formation at Point Reynolds, Pennington Bay, and 3) the Point Ellen Formation at Cape Willoughby (image courtesy of Google Earth, 2008).

Three other sites were examined along the south-western portion of the bay, PE2, PE3 and PE4 (Figure 7.39). PE2 is located on the south-western edge of Vivonne Bay, and hosts an extensive (approximately 270-300 m) single aeolianite (much bedding is obliterated), capped by a laminar/blocky calcrete. The outcrop is cliffed, as with most of these sites, indicating failure in the upper units due to undercutting at higher sea-level. The base of the outcrop is strewn with broken boulders of aeolianite and calcrete derived from the upper units. PE3 is also located on the south-western margin of Vivonne Bay, approximately 330 m north-west of site PE2. At this site the aeolian facies from PE2 are

absent. There are 5 discrete units found along outcrop: the basal calcarenite, a cemented cobble and shell layer, collapsed large scale aeolianite blocks cemented *in situ*, a calcrete gravel unit, and a calcrete mantle.

Third party source; Images redacted at request of thesis author

Figure 7.40: Approximate extent (red line) of the Point Ellen Formation outcrop (~240 m laterally).

Site PE4 is approximately 450 m north-west from PE3 (Figure 7.39). This site consists of an isolated aeolianite unit outcropping at sea-level (forming a small promontory) that is mantled by a thin calcrete (~0.3 m), and extensive well-vegetated Holocene/modern backshore dunes. The height of the outcrop, not including the overlying dunes is approximately 6.5 m APSL; large-scale crossbedding is plainly visible.

The following sections will detail the chronology and aminostratigraphy of these 4 sites at Point Ellen and Vivonne Bay.

7.3.3.1 Point Ellen site PE1 geochronology

Two points along the Point Ellen Formation outcrop were logged: PE1A and PE1B, approximately 220 m from each other, i.e., representing the eastern and western most extents of the outcrop. Luminescence dating was not used at these sites, although the main fossiliferous units were sampled for AAR dating purposes. Marine molluscs and whole-rock sediment samples were removed for

analysis from both the upper shell unit and the basal shell unit in the Formation (Figure 7.41).

Three types of samples were removed from the basal shell bed (at site PE1A): whole-rock matrix sediment, marine bivalves (*Katelsia scalarina*: see Figure 7.42), and foraminifers (*Elphidium rotatum*: see Figure 7.41), for amino acid dating purposes. The results of the AAR analyses are given in Tables 7.17, 7.8, and 7.18, respectively.

Only 2 useful bivalves were recovered from the samples collected (from the basal shell unit—see Figure 7.41 and 7.43), and these were analysed and age estimated using an apparent parabolic calibration, yielding an AAR age of 1.1 ± 0.2 Ma (GLX D-L ratio: 0.938 ± 0.029) (Table 7.8). The whole-rock analyses were in good agreement with this age, i.e., 1.2 ± 0.3 Ma (U-series calibration) and 1.1 ± 0.3 Ma (OSL calibration). Ten single foraminifers (*Elphidium rotatum*) were also picked from the whole-rock matrix sediment, giving an AAR age estimate (based upon the mean GLX D-L ratio value: 0.853 ± 0.068) of 1.3 ± 0.4 Ma.

The upper shell (at site PE1B) (see Tables 7.8, 7.17, and 7.18, and Figure 7.41 and 7.43) yielded a similar set of results: marine shell (*Nerita milnesi* and *Katelsia* sp.: see Figure 7.42) gave an AAR age of 1.1 ± 0.2 Ma (GLX D-L ratios: 0.958 ± 0.016 and 0.946 ± 0.08 respectively) whole-rock matrix sediment an AAR age of 745 ± 171 ka (U-series calibration) and 711 ± 160 ka (OSL calibration) (GLX D-L ratio: 0.765 ± 0.008), and foraminifers (10 x *Elphidium rotatum*) and AAR age of 1.3 ± 0.4 Ma (GLX D-L ratio: 0.854 ± 0.052).

Table 7.17: Pleistocene whole-rock (WR) sediment ASX and GLX AAR data, and AAR numerical age estimates for Point Ellen and Vivonne Bay.

Lab. No.	Site	Site code / facies (N) ^c	Location (S Lat. E Long.)	CMAT ^a °C	Mean ASX D-L ratio $\pm 1\sigma^b$	Coefficient of variation (CV%)	Mean GLX D-L ratio $\pm 1\sigma^b$	Coefficient of variation (CV%)	AAR GLX (U-series calib.) age estimate (ka) ^d $\pm 1\sigma^b$	AAR GLX (OSL calib.) age estimate (ka) ^d $\pm 1\sigma^b$
UWGA 6545, 6432	Point Ellen east	PE#1-2b / coquinite: basal (12)	35° 59' 56.1" 137° 11' 08.9"	15.1	0.808 \pm 0.019	2.4	0.897 \pm 0.036	4.0	1.2 \pm 0.3 Ma	1.1 \pm 0.3 Ma
UWGA 6591, 6592	Point Ellen west	PE#2b-2 / coquinite: upper (4)	35° 59' 56.1" 137° 11' 08.9"	15.1	0.771 \pm 0.002	0.2	0.765 \pm 0.008	1.1	745 \pm 171	711 \pm 160
UWGA 5844, 6505, 6593, 6594	Vivonne Bay east	PE#3-1 / aeolianite (8)	35° 59' 49.2" 137° 11' 06.2"	15.1	0.626 \pm 0.003	0.5	0.487 \pm 0.005	0.9	166 \pm 38	159 \pm 36
UWGA 5845, 6506, 6537	Vivonne Bay west	PE#3-2 / aeolianite (5)	35° 59' 44.7" 137° 10' 56.5"	15.1	0.729 \pm 0.007	1.0	0.614 \pm 0.011	1.8	380 \pm 87	363 \pm 82
UWGA 6597, 6598	Vivonne Bay west (beach)	KVIV#3-1 / aeolianite (4)	35° 59' 29.4" 137° 10' 45.1"	15.1	0.558 \pm 0.002	0.4	0.426 \pm 0.006	1.5	95 \pm 22	90 \pm 20

^a Current mean annual temperature (CMAT) estimated for these sites from annual temperature data via climate recording stations around Kangaroo Island (<http://www.bom.gov.au/climate/data/>)

^b Uncertainties are 1 σ (one standard deviation—68% confidence interval)

^c N = number of subsamples

^d Numeric age estimate from a U-series calibration (Schwebel, 1978; 1984), and an OSL calibration (this study) using an apparent parabolic model (Mitterer and Kriausakul, 1989; Murray-Wallace *et al.*, 2001); uncertainties are calculated from the square root of the sum of the squares of all uncertainty terms

* OSL age estimate of whole-rock sample used to calibrate the GLX D-L ratio.

Table 7.18: Point Ellen and Vivonne Bay Pleistocene single foraminifer ASX and GLX AAR data, and numeric AAR age estimates

Lab. No.	Site	Site code / facies	Location (S Lat. E Long.)	CMAT ^a °C	Genus and species / (N) ^b	Mean ASX D-L ratio) $\pm 1\sigma^c$	Coefficient of variation (CV%)	Mean GLX D-L ratio) $\pm 1\sigma^c$	Coefficient of variation (CV%)	AAR GLX age estimate (ka) ^d $\pm 1\sigma^c$
UWGA 5142	Point Ellen east	PE#1-2b / coquinite: basal	35° 59' 51.2" 137° 11' 13.6"	15.1	<i>Elphidium rotatum</i> (10)	0.817 \pm 0.047	5.8	0.853 \pm 0.068	7.9	1.3 \pm 0.4 Ma
UWGA 6589	Point Ellen west	PE#2b-2 / coquinite: upper	35° 59' 56.1" 137° 11' 08.9"	15.1	<i>Elphidium rotatum</i> (10)	0.972 \pm 0.066	6.8	0.854 \pm 0.052	6.1	1.3 \pm 0.4 Ma
UWGA 5831, 5833	Vivonne Bay east	PE#3-1 / aeolianite	35° 59' 49.2" 137° 11' 06.2"	15.1	<i>Elphidium</i> sp. + <i>D. dimidiatus</i> / (13)	0.567 \pm 0.034	6.0	0.314 \pm 0.046	14.6	121 \pm 39
UWGA 5871, 6587, 6588	Vivonne Bay west	PE#3-4 / raised pebble, shelly notch deposits	35° 59' 43.7" 137° 10' 53.9"	15.1	<i>Elphidium</i> sp. + <i>D. dimidiatus</i> / (11)	0.545 \pm 0.027	5.0	0.308 \pm 0.025	8.3	(114 \pm 3)*
UWGA 6589, 6590	Vivonne Bay west	PB#3-2 / aeolianite	35° 59' 44.7" 137° 10' 56.5"	15.1	<i>Elphidium</i> sp. + <i>D. dimidiatus</i> / (9)	0.696 \pm 0.040	5.7	0.445 \pm 0.027	6.1	290 \pm 86
UWGA 6595, 6596	Vivonne Bay west (beach)	KVIV#3-1 / aeolianite	35° 59' 29.4" 137° 10' 45.1"	15.1	<i>Elphidium</i> sp. + <i>D. dimidiatus</i> / (6)	0.567 \pm 0.040	7.0	0.333 \pm 0.019	5.7	141 \pm 42

^a Current mean annual temperature estimated for these sites from annual temperature data via climate recording stations around Kangaroo Island

(<http://www.bom.gov.au/climate/data/>)

^b Number of foraminifera used for D-L ratio estimate

^c Uncertainties are 1 σ (one standard deviation—68% confidence interval)

^d Numeric age estimate from a U-series calibration (fossil coral recovered from Vivonne Bay: 114 \pm 3 ka*) using an apparent parabolic model (Mitterer and Kriausakul, 1989; Murray-Wallace *et al.*, 2001); uncertainties are calculated from the square root of the sum of the squares (addition in quadrature) of all uncertainty terms

* U-series age of *Plesiastrea versipora*: a stony coral recovered from same unit as the foraminifers *Elphidium* spp. and *Discorbis dimidiatus* (PE#3-4), and used to calibrate the GLX D-L ratio

Third party source;
Images redacted
at request of thesis
author

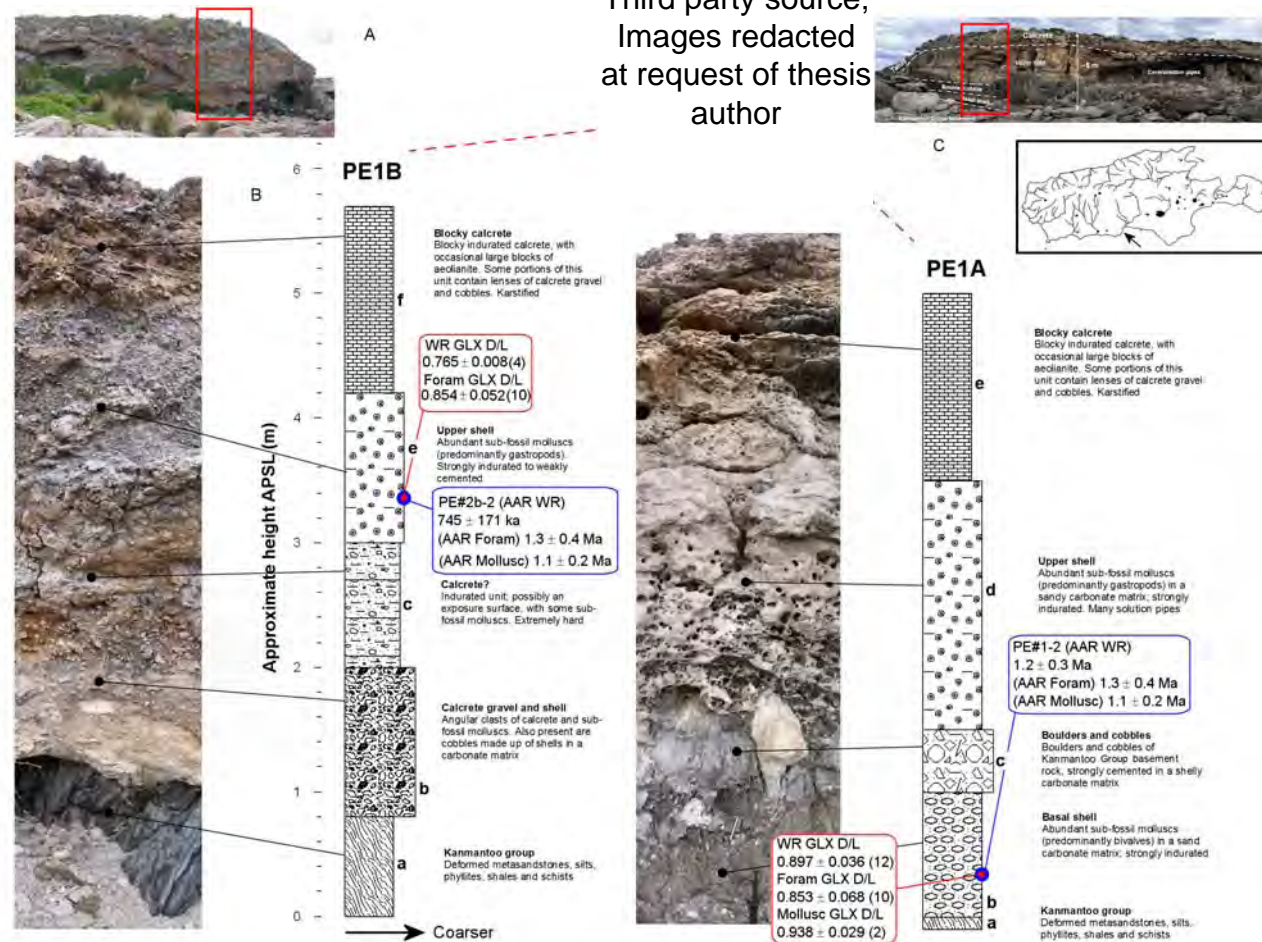


Figure 7.41: Point Ellen sites PE1A and PE1B (stratigraphic logs) for the Point Ellen Formation outcrops in the eastern and western portions of the point. Included are the geochronological data (blue boxes) and corresponding GLX D-L ratio data (red boxes—numbers in brackets are individuals or subsamples analysed). The top RH inset (A) is a merged panorama for the PE1B (there is some distortion towards the ends of the image) outcrop. The top RH inset (C) comprises a panorama for PE1A, a Kangaroo Island location map (with the site location indicated by a black arrow), and a satellite image of the outcrop with indicated log and sample sites (from Google Earth, 2007).

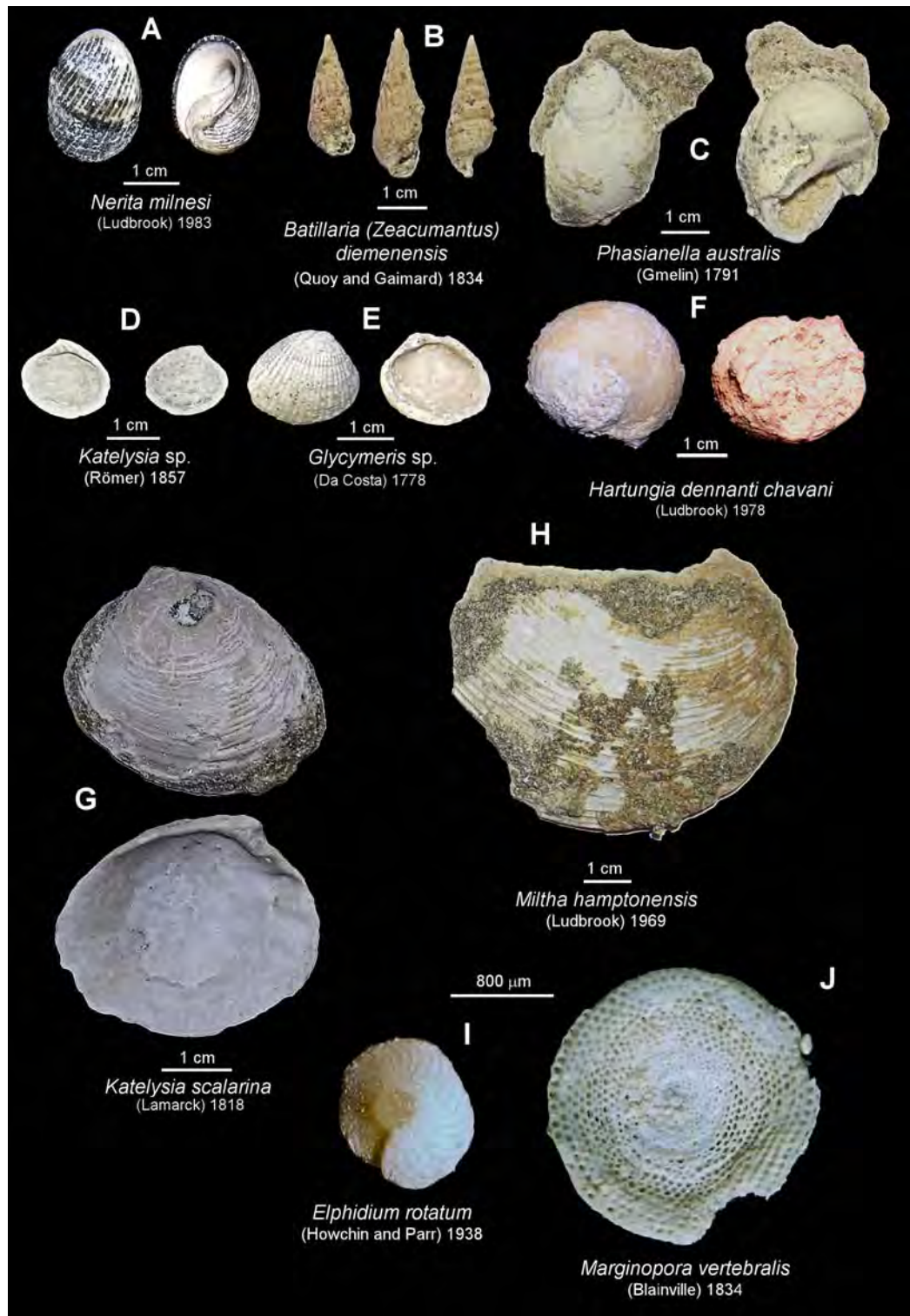


Figure 7.42: Examples of marine molluscs and foraminifers found in the upper and basal portions of the Point Ellen Formation.

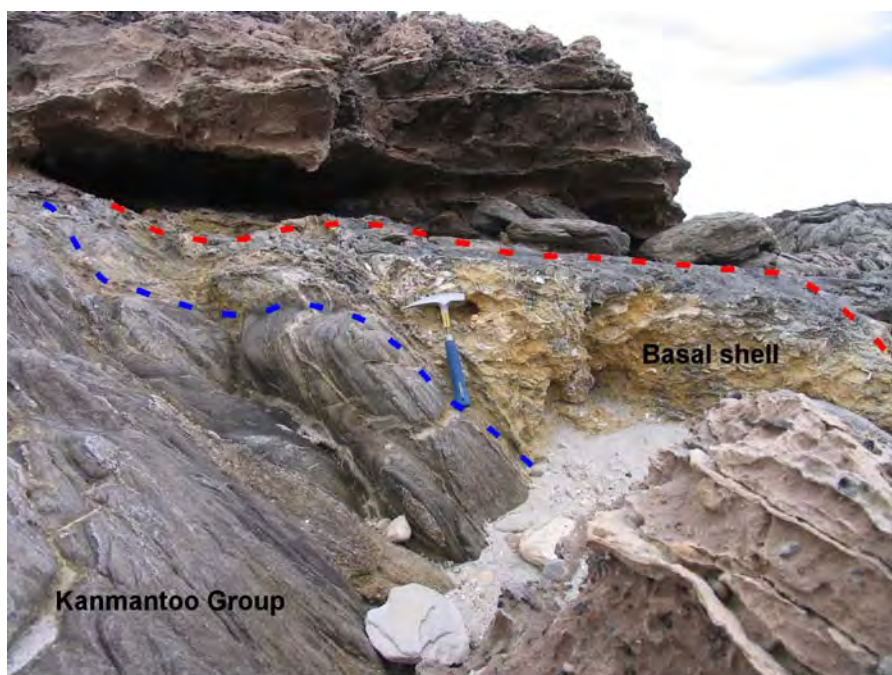


Figure 7.43: Sample area at Point Ellen site PE1A. Several specimens of *Katelsysia scalarina* were recovered from this patch of the basal shell horizon overlying and infilling the irregular surface of the Kanmantoo Group bedrock (at ~sea-level). Whole-rock sediment was also sampled. Note the palaeosol block (upper LH), with thin carbonate laminations (and lower RH broken block of the same material), overlying this part of the basal shell (rock-hammer for scale: 33 cm).



Figure 7.44: Sample area at Point Ellen site PE1B (see lower LH inset for detail). Several specimens of *Nerita milnesi* and *Katelsysia* sp. were recovered from this part of the upper shell horizon (red circle). Whole-rock sediment was also sampled. Note the small cave at approximately +3 m APSL.

The WR estimates suggest a younger age for the upper shell unit, although the ages all generally overlap at 1σ .

This set of amino acid results supports the previous early Pleistocene interpretation of the Point Ellen Formation by Ludbrook (1983; 1984) and Milnes *et al.* (1983) (and also the strontium isotope age of Belperio [1995]), and would exclude a Late Pliocene interpretation for the Formation.

7.3.3.2 Vivonne Bay site PE2 geochronology

As described above this site is apparently a single aeolianite unit that overlies a basal calcarenite that is possibly early Pleistocene in age (this may be the same unit that underlies the middle and late Pleistocene sequences at Pennington Bay and Bales Beach). The unit was sampled for both OSL and AAR analysis. OSL sample PE#3-1 was removed from the upper portion of the aeolianite unit just underneath the calcrete unit (Figure 7.45 and 7.46).

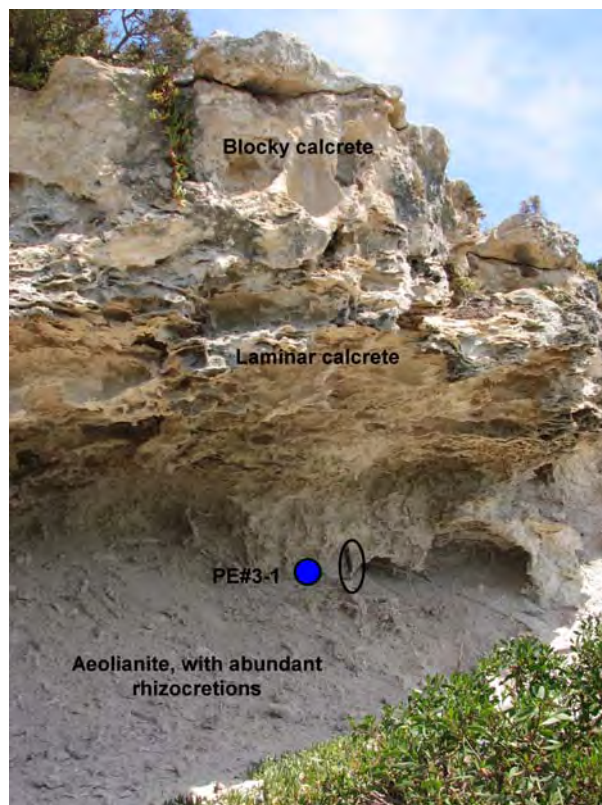


Figure 7.45: Location of PE#3-1 OSL sample (site PE2). Note that the sample was removed far enough from the calcrete contact to account for the gamma sphere. Also note the prominent calcrete visor. The black ellipse denotes a rock-hammer (33 cm) set for scale.

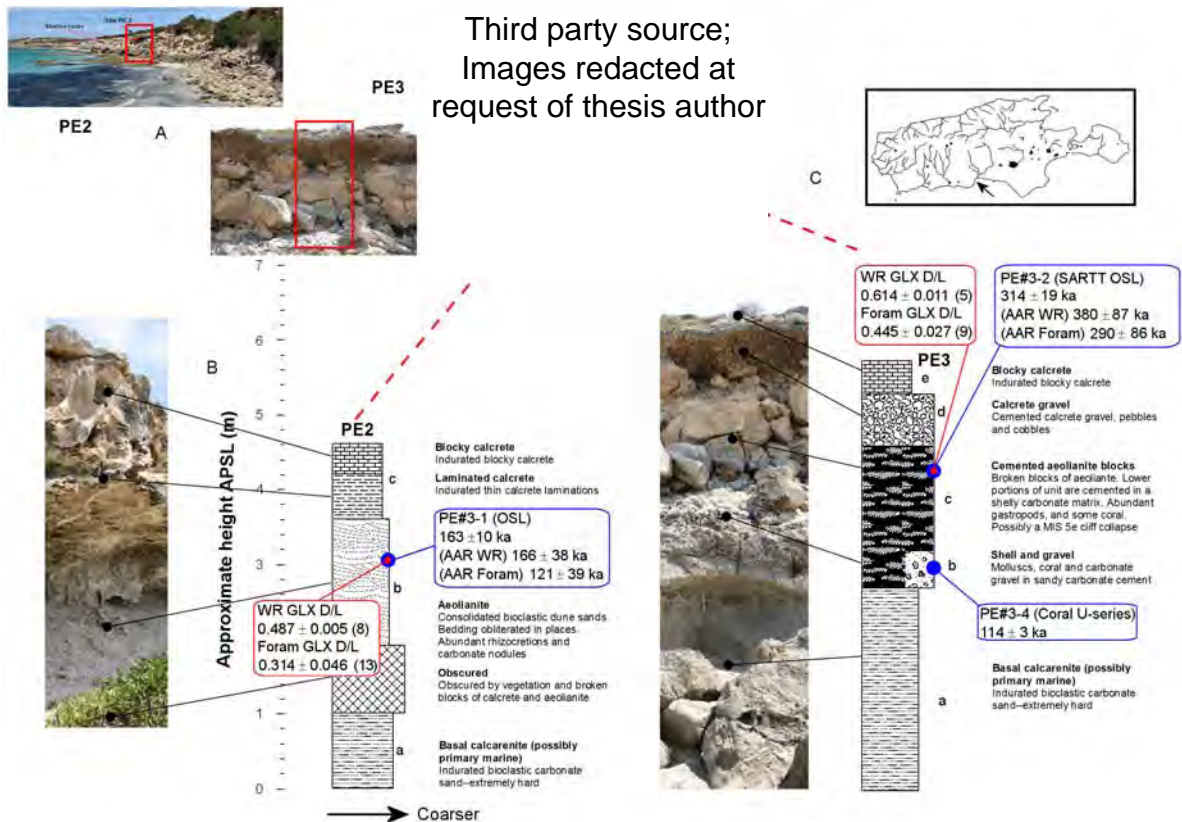


Figure 7.46: Vivonne Bay sites PE2 and PE3: stratigraphic logs for the aeolianite outcrops towards the southern end of the bay. Included are the geochronological data (blue boxes) and corresponding GLX D-L ratio data (red boxes—numbers in brackets are individuals or subsamples analysed). The top RH inset (A) is a merged panorama for the PE2 and PE3 sites (there is some distortion towards the ends of the image) outcrop. The top RH inset (C) comprises a satellite image (Google Earth, 2007) showing indicated log and sample sites, and a Kangaroo Island location map (with the site indicated by a black arrow).

Forty eight aliquots (1 mm mask size) of this sample were analysed using the modified SAR protocol (Chapter 4); 3 aliquots were rejected on the basis of no L_n/T_n dose response curve intersection (Table 7.12). A D_e of 121 ± 4 Gy was calculated from the remaining 45 aliquots using the CAM, with an overdispersion of $9.5 \pm 3.2\%$ (indicating a single dose population). The recycling and IR depletion ratios were 0.98 ± 0.03 and 1.02 ± 0.03 respectively, showing excellent test-dose sensitivity correction and negligible IR depletion of the OSL signal (i.e. little feldspathic contamination of the quartz) (Table 7.11 and 7.12). The CAM D_e was used to calculate an OSL age of 163 ± 10 ka—the equivalent dose distributions are illustrated in Figure 7.47.

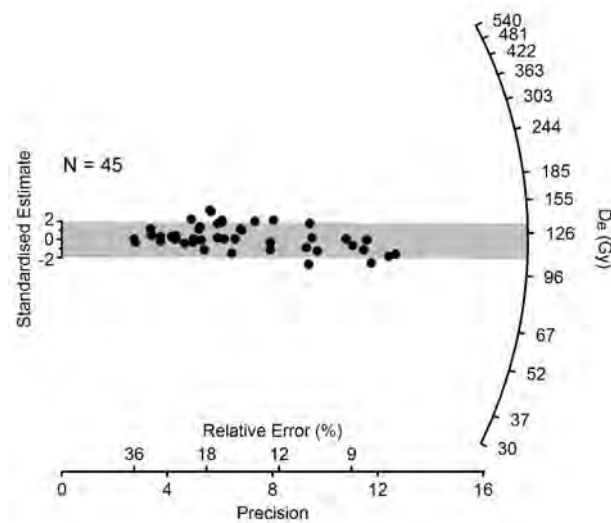


Figure 7.47: Single-aliquot (OSL) equivalent dose (D_e) distributions for sample PE#3-1, displayed as a radial plot. The CAM D_e for this sample is 121 ± 4 Gy.

This sample was expected to be of MIS 5 age; however, the OSL age estimate would indicate that it is significantly older than this, placing it during the MIS 6 glacial. The whole-rock AAR age estimate of 166 ± 38 ka (U-series calibration) and 159 ± 36 ka (OSL calibration) also agree quite well with the OSL age. However, the age estimate of 121 ± 39 ka for foraminifers (GLX D-L ratio: 0.314 ± 0.046) extracted from the unit would suggest an MIS 5 deposition (Tables 7.17 and 7.18). It is difficult to account for the difference, although the greater age for the WR could be explained by a high proportion of older reworked grains. Nevertheless, the WR and Foram ages still overlap at 1σ , therefore the difference is not significant. It must be noted that the presence of erosional features (sea-caves) at +3 m APSL (cut into this sequence just below the calcrete) all along this outcrop (Figure 7.48), would suggest deposition of the aeolianite (and formation of the calcrete) prior to the Last Interglacial.

7.3.3.3 Vivonne Bay site PE3 geochronology

Site PE3 hosts a complex profile that extends for approximately 600 m north-west from the Vivonne Bay jetty (Figure 7.39 and 7.40). OSL and AAR samples were taken from the middle unit (c) and a shell / pebble notch

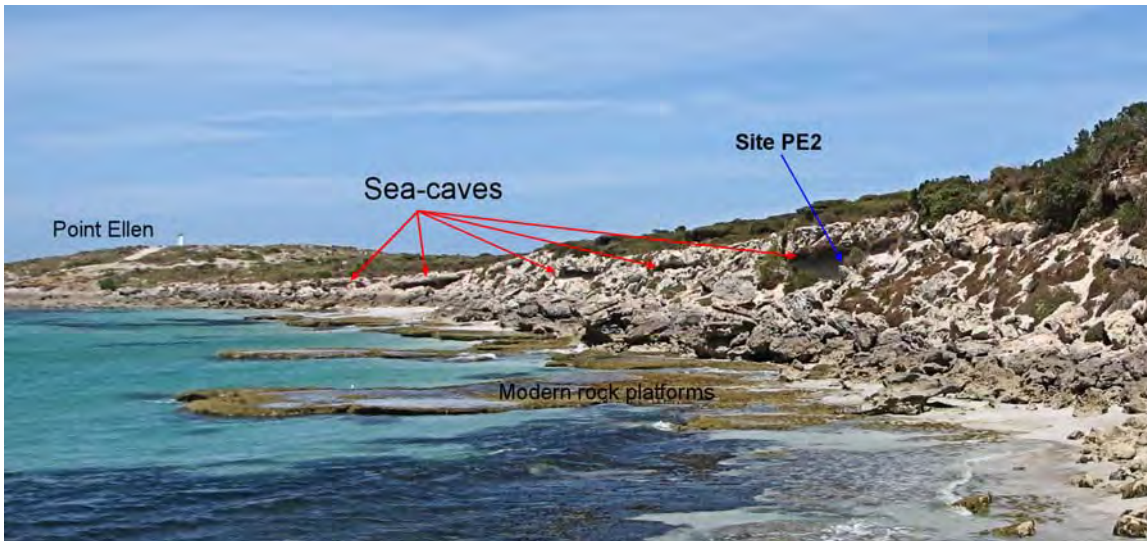


Figure 7.48: Panorama looking east from Vivonne Bay, showing the location of PE2 and a series of Last Interglacial sea-caves.

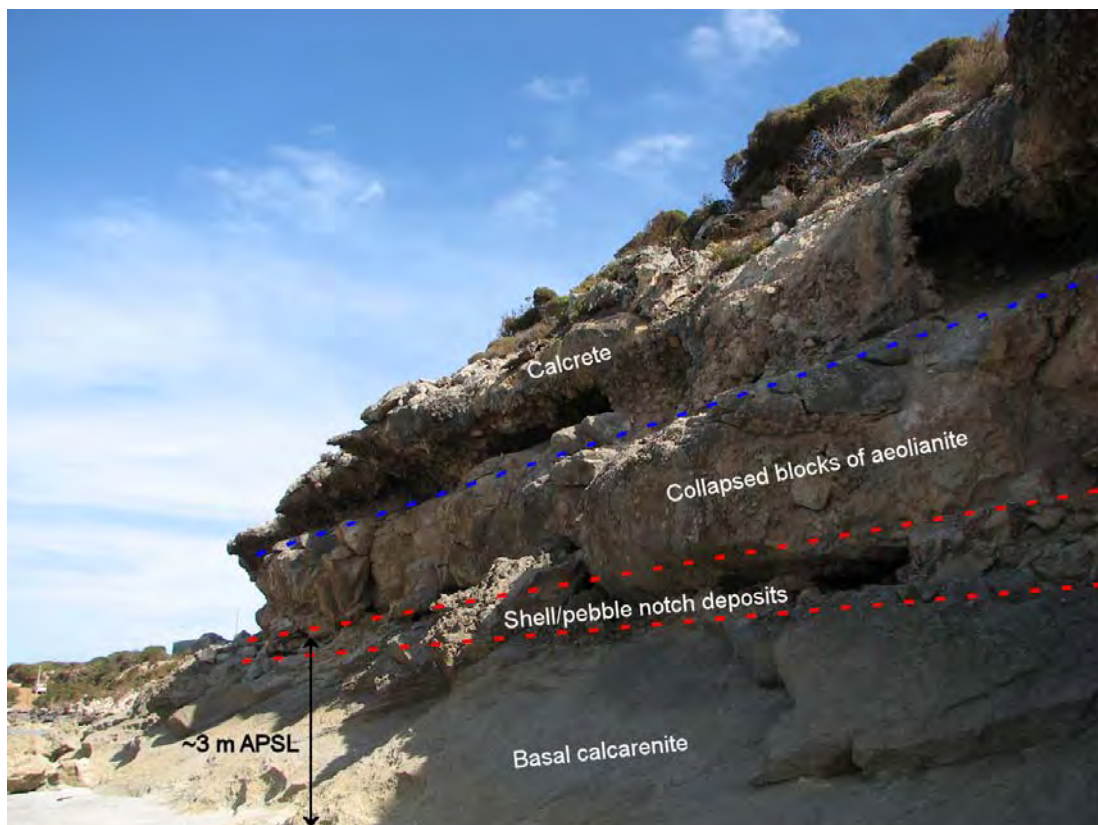


Figure 7.49: View south-east from Vivonne Bay site PE3, showing positions of units.

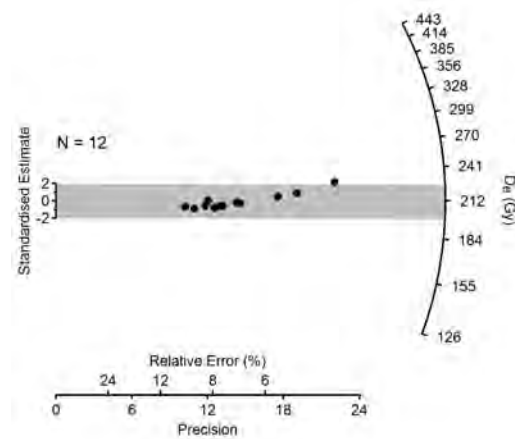


Figure 7.50: Single-aliquot (SARTT-OSL) equivalent dose (D_e) distributions for sample PE#3-2, displayed as a radial plot. The CAM D_e for this sample is 212 ± 4 Gy.

deposit (b) in the lower portions of the unit (Figure 7.46). The middle unit is a series of collapsed blocks of aeolianite in matrix cement, the lower parts of the blocks have been eroded during a period of higher sea-level, and marine shell, coral, skeletal carbonate, and pebbles have been cemented into the notches (the tops of the notches are approximately +3 m APSL) (Figure 7.49). These represent the remnants of an extensive raised pebble beach in this section of the embayment. This unit overlies a basal calcarenite (as with PE2). Some of the notches are quite large and are more analogous to sea-caves. Stringers of the raised beach material can be seen plastered to the ceilings of the caves. The upper units consist of an angular calcrete gravel layer, cemented in a matrix, and a blocky calcrete mantle (Figure 7.49).

OSL sample PE#3-2 was removed from one of the collapsed blocks of aeolianite in unit c (PE3), and given the morphostratigraphy it was assumed that the age of the unit would be beyond the range of conventional OSL. Therefore the OSL sample PE#3-2 was analysed using the SARTT-OSL protocol. Twelve aliquots (3 mm mask size) were analysed and a central D_e of 212 ± 4 Gy was determined using the CAM (Table 7.13). The overdispersion for this set of aliquots was $1.7 \pm 5.4\%$, and the recycling ratio was 1.05 ± 0.09 .

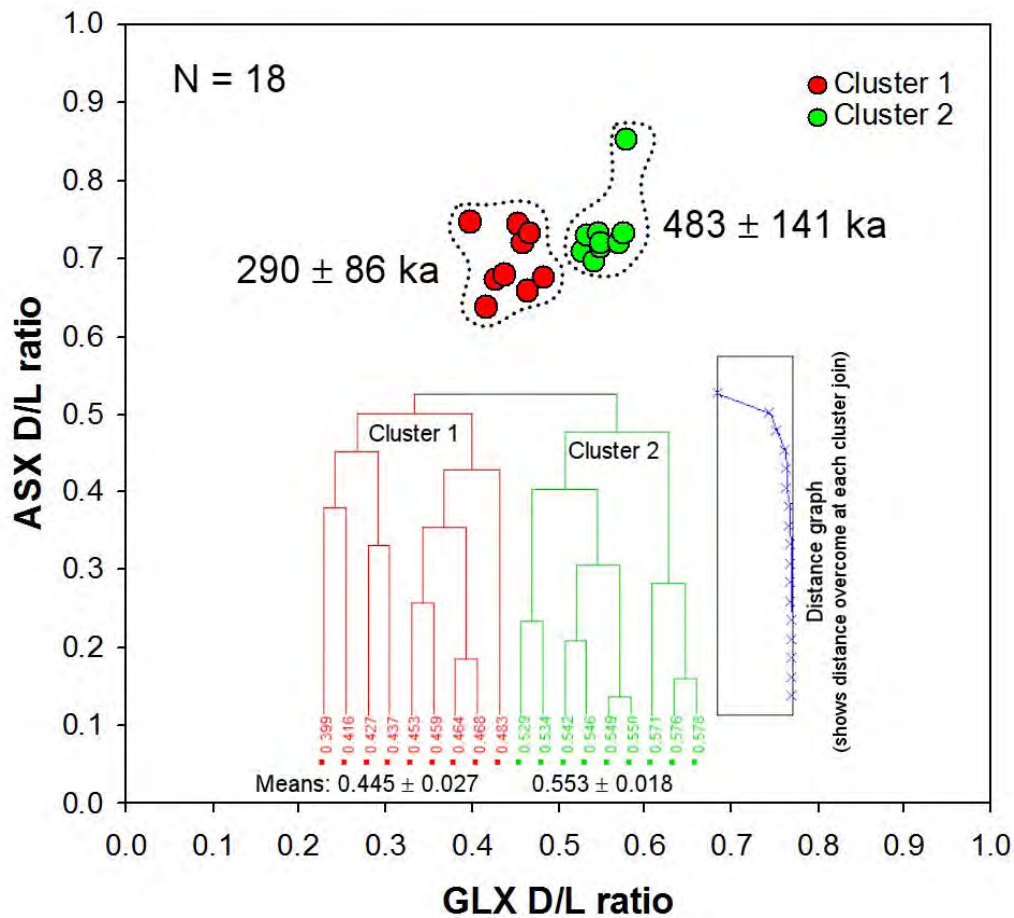


Figure 7.51: Ward method hierarchical multivariate (cluster) analysis of the single foraminifer GLX D-L ratio data from PE#3-2 (site PE3), inset within a bivariate plot (ASX vs. GLX). Two age populations are identified.

A SARTT-OSL age estimate of 314 ± 19 ka was determined from the central D_e value (equivalent dose distributions are displayed in Figure 7.50). This age agrees quite well with a MIS 9c (324 ± 3 ka to 318 ± 3 ka) (Stirling *et al.*, 2001) deposition. Whole-rock and foraminifers were also used to estimate AAR ages for the unit (Tables 7.17 and 7.18). The calculated WR age estimates were 380 ± 87 ka (U-series calibration) and 363 ± 82 ka (OSL calibration) (GLX D-L ratio: 0.614 ± 0.011), the overestimation while not significant alluded to the influence of a large proportion of reworked grains. Hence, the group of 18 single foraminifer (recovered from PE#3-2 whole-rock sediment) GLX D-L ratios was subjected to Ward method hierarchical multivariate (cluster) analysis. This delineated two age populations within the group (see Figure 7.51). The younger (lower D-L) population was assumed to be representative of the “true” age. This group (cluster 1) had a mean GLX D-L ratio of 0.445 ± 0.027 , which gave a

Foram AAR age estimation of 290 ± 86 ka (Table 7.18). This age is in better agreement with the SARTT-OSL age than that derived from a total mean of all 18 single foraminifers (i.e. 380 ± 119 ka). The older population (cluster 2) had an age of 483 ± 141 ka (based upon the mean GLX D-L ratio of the cluster).

The lower portions of this unit have been eroded (at approximately +3 m APSL) and deposits of shell, coral, and pebbles in a carbonate matrix have been plastered into the gaps. Several specimens of *Nerita (Melanerita) atramentosa* (a marine gastropod characteristic of rock-platforms), and 1 specimen of a stony coral (*Plesiastrea versipora*) were recovered from the notch deposits (Figure 7.53). Samples of the matrix (sample PE#3-4, 3-5, and 3-6) were also taken for whole-rock and single foraminifer AAR analysis. The coral was U-series dated at 114 ± 3 ka (see Table 7.19) which corresponds to the Last Interglacial (132-116 ka: Siddall *et al.* [2007]). The WR AAR analyses yielded an age estimate of 250 ± 57 ka (U-series calibration) and 239 ± 54 ka (OSL calibration) (GLX D-L ratio: 0.543 ± 0.006) (Table 7.17).

The older WR ages would suggest that either the U-series age for the coral is inaccurate or (more likely) there were a high proportion of reworked older grains in the whole-rock sediment. To test this a large number (45 grains—some were rejected on the basis of high L-SER, i.e., very low SER D-L ratios) of single foraminifer grains (*Elphidium* spp. and *Discorbis dimidiatus*) were analysed from the matrix cement. The ASX and GLX D-L ratios were then graphed in a bivariate plot and it was immediately obvious that there were several age populations of grains within the group. Ward method hierarchical multivariate (cluster) analysis of the GLX D-L ratios enabled the delineation of 5 possible age populations—the bivariate plot and cluster analysis are illustrated in Figure 7.52. The youngest population was assumed to represent the “true” age, and was used to provide the corresponding GLX D-L ratio (0.308 ± 0.025) for the Foram U-series calibration (using the U-series age for the stony coral: 114 ± 3 ka) (Table 7.17 and 7.18). As a point of interest the other age populations for PE#3-4, 3-5, and 3-6 were age estimated (using the GLX D-L ratio means of each cluster), and it is noteworthy that two of the older populations (clusters 3 and 4) overlap the populations described for PE#3-2 (clusters 1 and 2: Figure

7.51). This revealed that the overlying broken blocks of aeolianite (unit c, PE3) were the primary source for the reworked foraminifer grains. There were also some younger (176 ± 51 ka—cluster 2) and older (641 ± 186 ka—cluster 5) grains in the group (Figure 7.52).

The U-series age derived for a coral extracted from the shell/pebble raised notch deposits (unit b, PE3) indicate a Last Interglacial deposition. The top of the notch deposits at +3 m APSL also indicate the sea-level at the time of deposition. This is comparable to Last Interglacial Glanville Formation sites on the South Australia mainland (palaeosea-levels at +2 to +3 m APSL) (e.g. Eyre Peninsula, Spencer Gulf, Port Wakefield, Port Adelaide) (cf. Belperio *et al.*, 1984; Murray-Wallace, 1987; Murray-Wallace *et al.*, 1988), and the raised cobble beach deposit at Pennington Bay (see section 7.7.1.2 of this Chapter). In this respect the Vivonne Bay shell/pebble notch deposits can also be considered as a Glanville Formation equivalent.

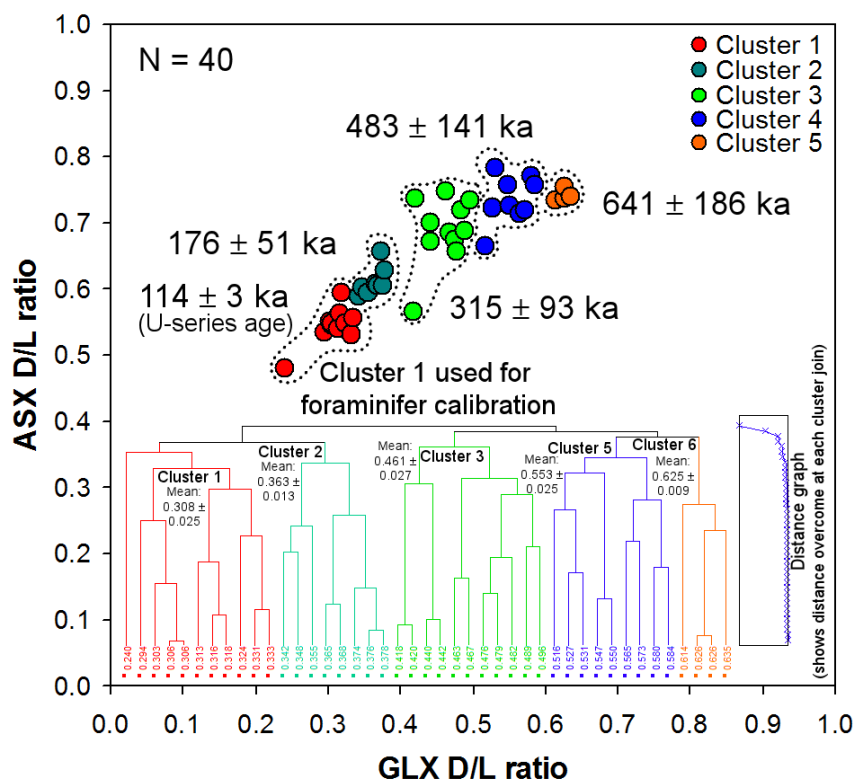


Figure 7.52: Ward method hierarchical multivariate (cluster) analysis of the single foraminifer GLX D-L ratio data from PE#3-4, 3-5 and 3-6 (site PE3 shell/pebble notch deposits), inset within a bivariate plot (ASX vs. GLX). Five age populations are identified. The lowest set of D-L ratios provided the corresponding mean D-L for the U-series age used in the foraminifer calibration.

Table 7.19: Uranium series analyses data (Australian National University geochronology), and calculated U-series age estimate for the stony coral *Plesiastrea versipora* (sample PE#3-4), recovered from unit b site PE3, Vivonne Bay.

Th(U) + U data							Uncorrected for detrital or water column initial ^{230}Th						
Lab code	Weight (g)	U ppm	^{230}Th ppt	^{232}Th ppb	Delta ^{234}U	\pm Delta ^{234}U	$[\text{^{230}Th}/\text{^{238}U}]$	$\pm [\text{^{230}Th}/\text{^{238}U}]$	$[\text{^{230}Th}/\text{^{232}Th}]$	Age (ka)	$\pm 1\sigma$ (ka)	Initial Delta ^{234}U	\pm Initial Delta ^{234}U
TU235	0.22	0.05	0.6	0.806	142.5	6.9	0.75789	0.00663	143	114.6	2.2	197.0	8.7
TU236	0.21	0.06	0.7	0.771	141.6	6.5	0.75507	0.00622	175	114.0	2.1	196.0	8.2
Mean age										114.3	3.0		

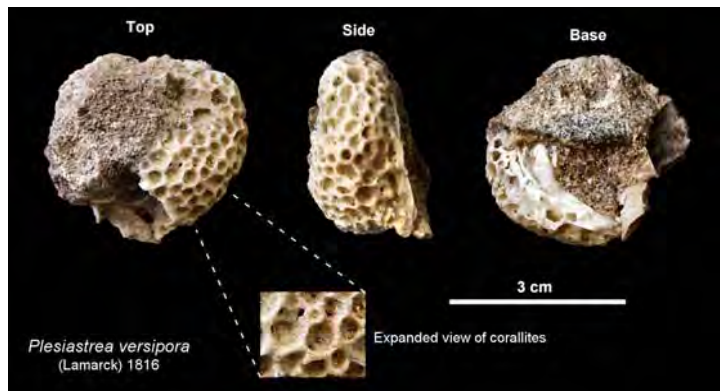


Figure 7.53: The stony coral *Plesiastrea versipora* (sample PE#3-4), recovered from unit b site PE3, Vivonne Bay, Kangaroo Island.

Because of the large proportion of reworked grains in the shell/pebble matrix the whole-rock sediment mean GLX D-L ratio could not be used in the calibration. Hence the use of the Woakwine I U-series age (Schwebel, 1978; 1984) and the OSL ages for whole-rock sediment calibration purposes. In this instance the modern beach does not adequately reflect the grain mix characteristics of this Last Interglacial deposit.

7.3.3.4 Vivonne Bay site PE4 geochronology

PE4 is an isolated outcrop of aeolianite on the south-western side of Vivonne Bay approximately half way between Point Ellen and the Harriet River (Figure 7.39). This is a single unit of aeolianite with a calcrete mantle, and overlying Holocene/modern dunes. Samples were collected near the base of the unit for amino acid dating purposes (see Figure 7.54). Whole-rock AAR analysis gave an age estimate of 95 ± 22 ka (U-series calibration) and 90 ± 20 ka (OSL calibration) (GLX D-L ratio: 0.426 ± 0.006), indicating a MIS 5 deposition. The foraminifer AAR age estimate was 141 ± 42 ka (GLX D-L: 0.333 ± 0.019). These ages bracket MIS 5 quite adequately.

7.3.3.5 Discussion of the Point Ellen and Vivonne Bay geochronology

The Point Ellen and Vivonne Bay area have a greater variety of facies when compared to Pennington and Bales Beach; ranging from richly fossiliferous marine deposits, to large-scale aeolianite block collapses, and calcrete breccias.

The Point Ellen Formation is confirmed here to be early Pleistocene in age using calibrated whole-rock sediment, mollusc, and foraminifer D-L ratios. Unfortunately, the precision in the ages is not adequate to delineate an age difference between the basal and upper shell layers of the Formation. Point Ellen Formation molluscs, foraminifers, and other skeletal particles were likely to have been deposited within the irregular bedrock basin between 900 ka and 1.3 Ma, as suggested by the molluscan AAR age estimates.

The south Vivonne Bay area hosts an extensive aeolianite deposit (site PE2) characterised by several sea-caves formed by wave erosion during a

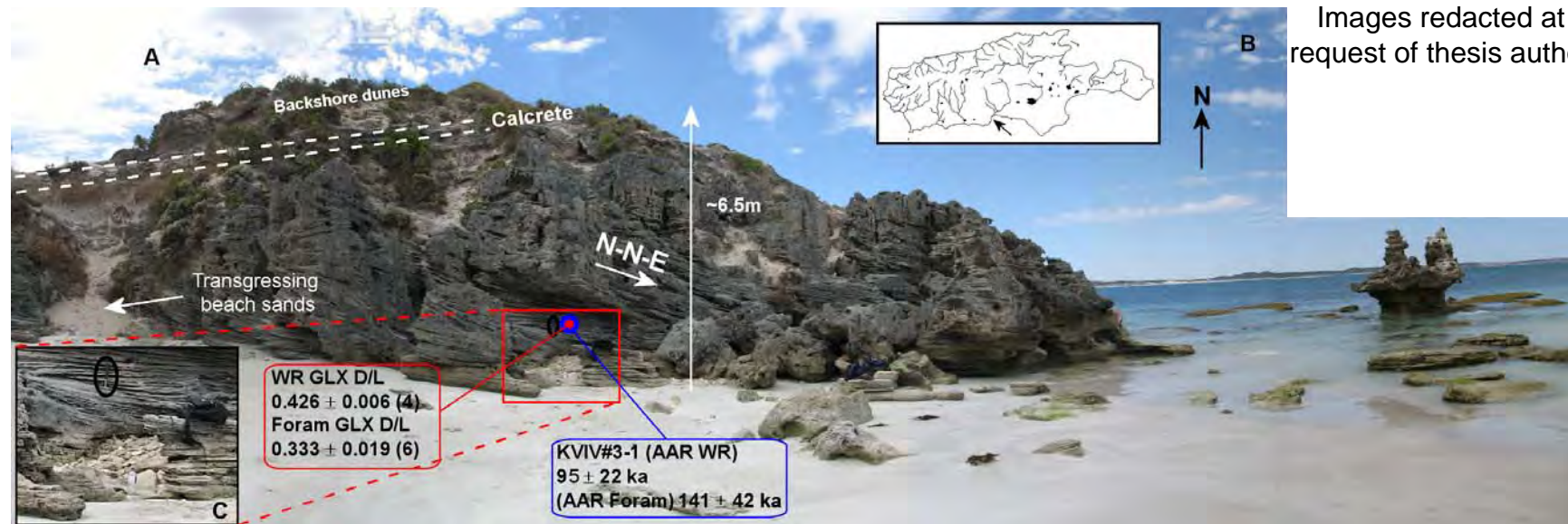


Figure 7.54: Vivonne Bay site PE4, an aeolianite outcrop towards the centre of the bay. Included are the geochronological data (blue boxes) and corresponding GLX D-L ratio data (red boxes—numbers in brackets are individuals or subsamples analysed). The top RH inset (B) comprises a Kangaroo Island location map (with the site indicated by a black arrow), and a satellite image (Google Earth, 2007) showing indicated sample site. The bottom LH inset (C) is an expanded view of the bottom set beds, and the sample area. The black ellipses indicate a rock-hammer placed for scale (33 cm).

period of higher-than-present sea-level. The sequence grades upwards towards the north-west, from around 3 m to 6 m APSL. According to the geochronology this aeolianite was deposited before the Last Interglacial, in all probability during the MIS 6 glacial. The presence of sea-caves at approximately +3 m APSL would support this, i.e., the aeolianite was deposited prior to the period of higher sea-level. Further north-west from PE2 is another extensive outcrop (PE3) in which the PE2 aeolianite facies are apparently absent. This outcrop is characterised by large-scale collapsed blocks of aeolianite, of MIS 9 age, cemented in the upper portions by a carbonate matrix derived from solutional weathering of the overlying calcrete, and by Last Interglacial sediments in the lower portions at approximately +3 m APSL. The lower portions of this unit are undercut and caved in various places and shells, coral and skeletal carbonate of Last Interglacial age, and pebbles (in a carbonate cement), are plastered into the gaps, notches and cavities. This is a major collapse that most likely took place during the peak sea-level at MIS 5e. Site PE4 is an isolated aeolianite outcrop of MIS 5 age, characterised by prominent large-scale cross-bedding.

7.3.4 Hanson Bay

Hanson Bay lies on the south coast of Kangaroo Island, between Cape Younghusband and Cape Bouguer, at approximately 30 km straight-line distance west from Point Ellen and Vivonne Bay (Figure 7.55).

Hanson Bay is around 8 km wide and is broken up into a series of smaller embayments, with moderate to high-energy beaches, by small headlands; similar to Pennington Bay. The beaches can be characterised for the most part by unconsolidated, skeletal carbonate, long-walled, parabolic backshore dunes (Holocene), and actively eroding calcarenite cliffs (Pleistocene).

The study sites are found in a small embayment towards the centre of the main bay. They lie west and east of the entrance to South West River; at the rear of aeolianite headlands.

As discussed in Chapter 3, the first study site (HB1) is a series of deposits overlying an old calcarenite platform. The basal portion of the platform consists

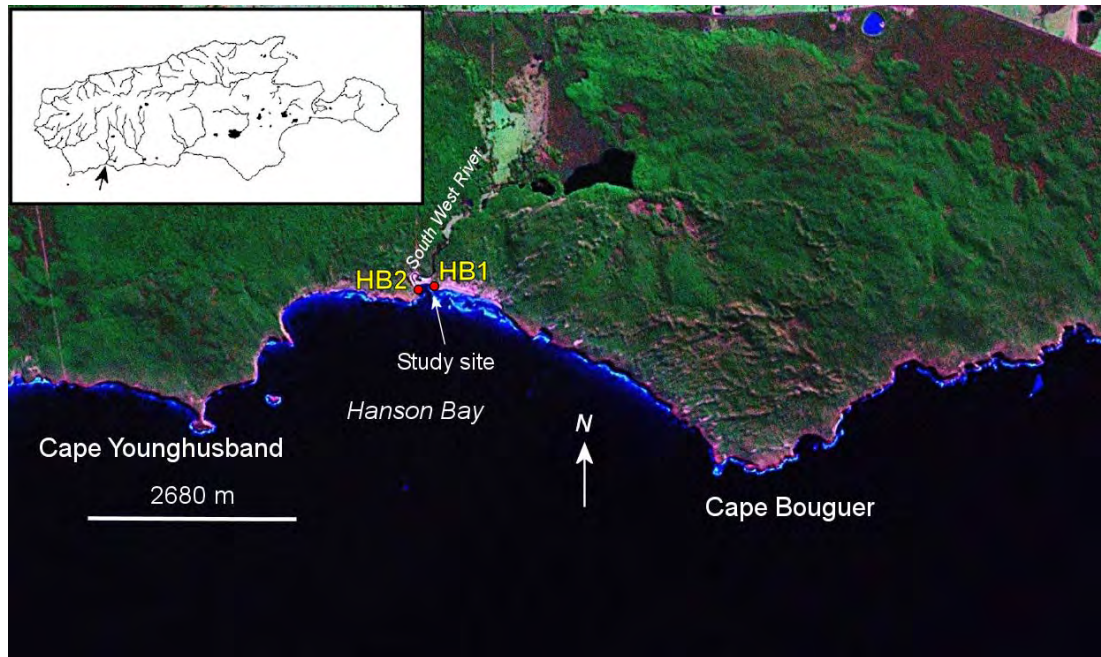


Figure 7.55: Hanson Bay satellite image showing the location of the study sites (HB1 and HB2) and bay morphology (main image is a Landsat ETM: NASA Landsat program, 2001).

of outcropping aeolianite of unknown age extending offshore—although it is possibly early to middle-Pleistocene in age. The platform hosts a sub-aerial exposure surface which shows evidence of scouring. The exposure surface is an indurated calcrete/palaeosol much of which has been removed, and there are now only thin patches remaining scattered around the platform. It is reasonable to assume that much of this surface was scoured during sea-level highstands, when and if sea-level was high enough for wave action to cause erosion. Some of these patches are overlain by remnants of what is apparently a shelly washover or sublittoral deposit—the main part of this unit is on the eastern portion of the platform (Figure 7.56 illustrates common fossil marine molluscs and foraminifers found in the deposit). Evidence of higher sea-level can be seen on some of the washover patches in the form of small notch and visor structures. Most of this unit too, barring that on the eastern part of the platform, was removed as well. Overlying all units at this site are a calcrete and thick Holocene dunes. The washover/sublittoral deposit appears to truncate a set of what have been interpreted here to be back-barrier estuarine lagoon sediments.

The deposits of interest extend from the aeolianite platform inland for approximately 10 metres, where they vanish into overlying Holocene dunes.

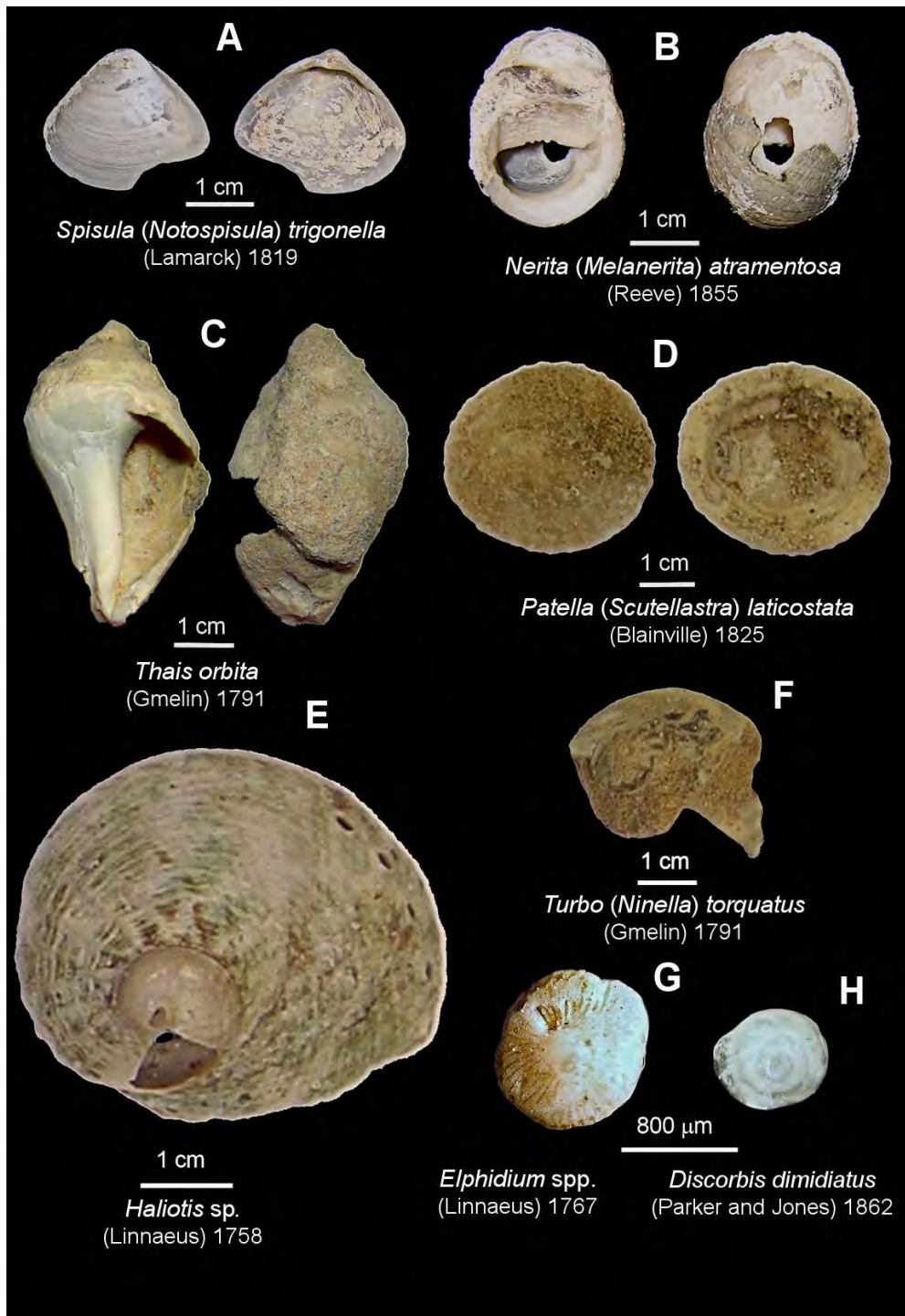


Figure 7.56: Common fossil fauna from the Hanson Bay shelly facies at site HB1. The molluscan assemblage is mixed, with representatives from rocky coast (F: *Turbo* [*Ninella*] *torquatus*, B: *Nerita* [*Melanerita*] *atramentosa*, and D: *Patella* [*Scutellastra*] *laticostata*), littoral zone (C: *Thais orbita*) and estuarine habitats (A: *Spisula* [*Notospisula*] *trigonella*). This is consistent with modern analogues of these habitats present at Hanson Bay.

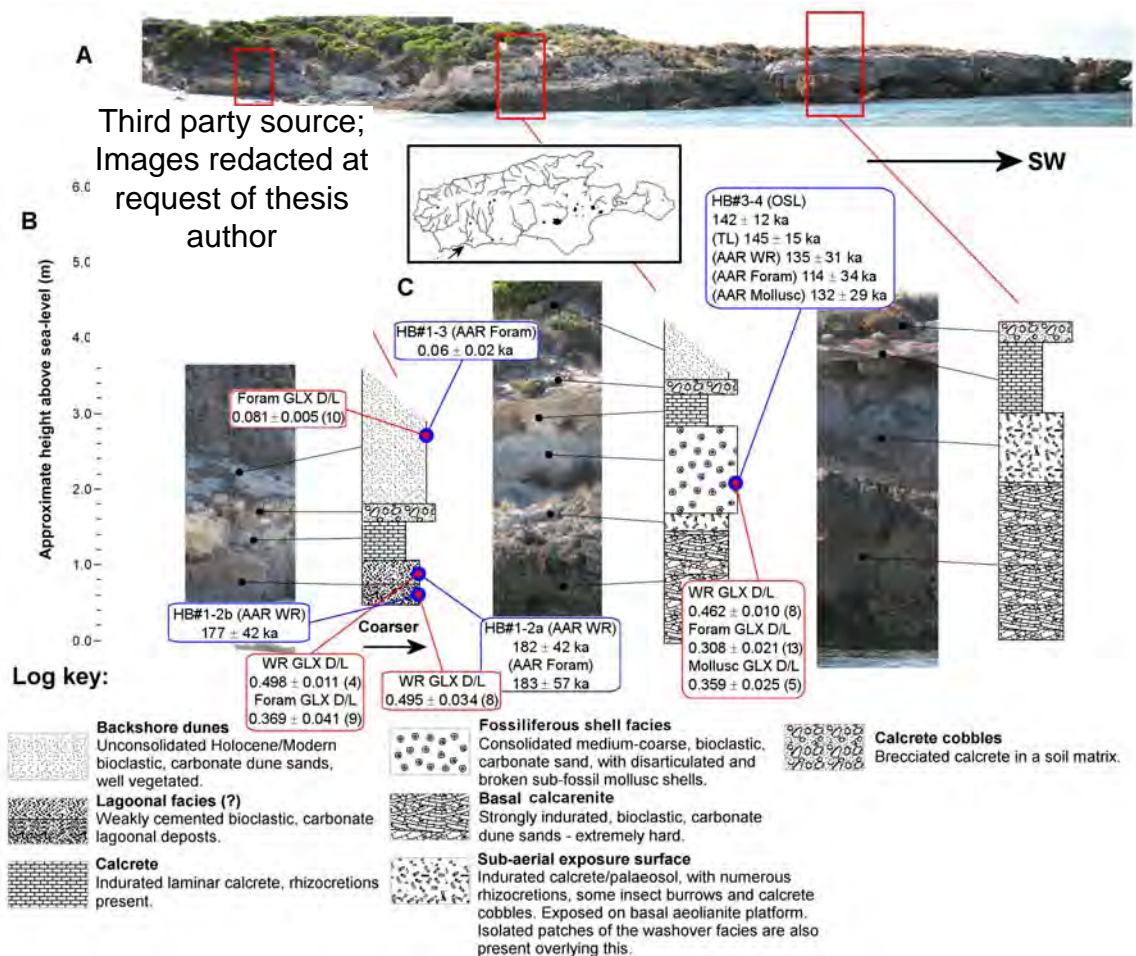


Figure 7.57: Hanson Bay stratigraphic logs for the sedimentary outcrops towards the eastern end of the beach (HB1). Included are the geochronological data (blue boxes) and corresponding GLX D-L ratio data (red boxes—numbers in brackets are individuals or subsamples analysed). The top inset (A) is a merged panorama of the site (there is some distortion towards the ends of the image) outcrop. The middle LH inset (B) comprises a satellite image (Google Earth, 2007) showing indicated log and sample sites, and a Kangaroo Island location map (with the site indicated by a black arrow).

The second study site (HB2) is a calcarenite platform on the western side of the bay. Here a sample of the basal calcarenite (thought to be of early/middle Pleistocene in age) was taken for whole-rock sediment AAR dating purposes.

The following sections will present the geochronological results for the deposits at the Hanson Bay study site.

7.3.4.1 Hanson Bay site HB1 geochronology

This outcrop extends laterally northward for approximately 100 m, before disappearing under modern beach sands at the shoreface. The basal calcarenite was not sampled at this site (as it was very hard and recrystallised—

similar to that found at Vivonne Bay, Bales Beach and Pennington Bay). However, it was sampled at site HB2, on the western side of the beach (discussed in the next section). The lagoonal facies, shell deposit, and overlying modern dunes were sampled (see Figure 7.57 for sedimentary logs). The shell deposit was sampled for OSL and TL from a less shelly region of the deposit (and also for whole-rock and marine molluscs), and the lagoonal facies and dunes were sampled for AAR dating (i.e. whole-rock and foraminifers). Sample HBTL#1-1 was removed from the lower portions of the shelly facies, and this sample yielded a TL age estimate of 145 ± 15 ka (see Table 7.14). This is slightly older than was expected for this deposit, given its morphostratigraphical position (i.e. approximately +3 m APSL), and the fossiliferous nature of the deposit, it was expected to be Last Interglacial in age. Although, the TL age still falls within range of the Last Interglacial (116-132 ka: Siddall *et al.* [2007]) at 1σ (see Figure 7.58 for TL and OSL sample area) .

Forty six aliquots (1 mm mask size) of OSL sample HB#3-4 were run using the modified OSL SAR protocol (Chapter 4). This gave a central D_e value of 96 ± 3 Gy, calculated using the CAM—the equivalent dose distributions are illustrated in Figure 7.59.

Several aliquots were rejected; details are given in Table 7.12. The mean recycling and IR depletion ratios were 1.00 ± 0.03 and 1.02 ± 0.03 respectively, indicating excellent test dose correction and insignificant feldspathic contamination. A 50 Gy dose recovery test was also run on sample HB#3-4 using 10 (1 mm mask) 24 hr sunlight bleached aliquots; this test yielded a mean dose recovery ratio of 1.03 ± 0.10 , which also indicates adequate performance of the modified protocol (full details of all OSL tests are given in Appendix E).

The OSL age estimate of 142 ± 12 ka was calculated using the weighted mean D_e , the dose rate data in Table 7.10 and the program listed in Roberts *et al.* (1993). The calculated age estimate is in good agreement with TL age, and overlaps with the Last Interglacial at 1σ .

A Last Interglacial age for the shell facies is also supported by the calculated whole-rock, foraminifer, and mollusc age estimates. Whole-rock analysis gave

an age of 135 ± 31 ka (U-series calibration) and 129 ± 29 ka (OSL calibration) (mean GLX D-L ratio: 0.462 ± 0.010) (Table 7.20). Ward method hierarchical (cluster) analysis was used on the foraminifer dataset (*Elphidium* spp. and *Discorbis dimidiatus*—see Figure 7.56) as it was apparent upon observation of the bivariate plot (ASX vs. GLX) that there were multiple populations of D-L ratios in the group. The cluster analysis delineated 3 discrete populations (see Figure 7.60), and the lowest (or “youngest”) D-L population was assumed to be representative of the “true” age. The population mean (cluster 1) upon calibration with using the apparent parabolic kinetics model yielded an age estimate of 114 ± 34 ka (mean GLX D-L ratio: 0.308 ± 0.021) (Table 7.21). This age too is consistent with the Last Interglacial. Other age population clusters (Figure 7.60) possibly represent reworked grains from previous periods of carbonate accumulation (perhaps during MIS 7 or MIS 9).



Figure 7.58: OSL sample point (blue circle) (TL sample was removed adjacent to this), and various facies at HB1, Hanson Bay (black ellipse denotes rock-hammer set for scale—33 cm). Top of shell rich unit is approximately +3 m APSL.

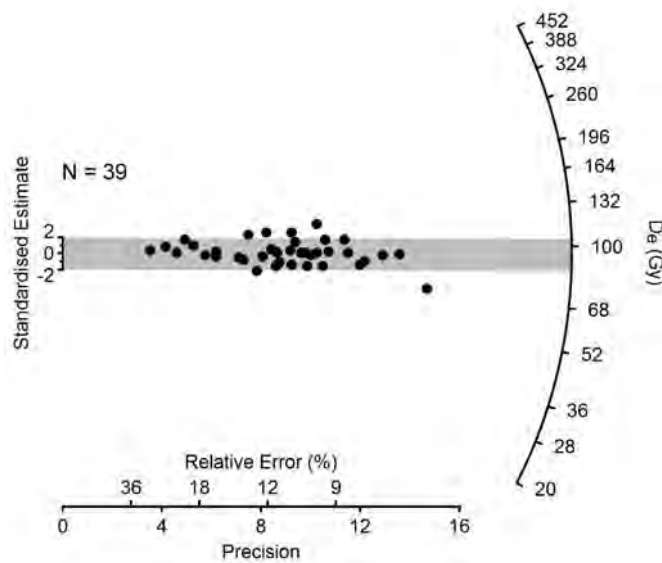


Figure 7.59: Single-aliquot (OSL) equivalent dose (D_e) distributions for sample HB#3-4, displayed as a radial plot. The CAM D_e for this sample is 96 ± 3 Gy.

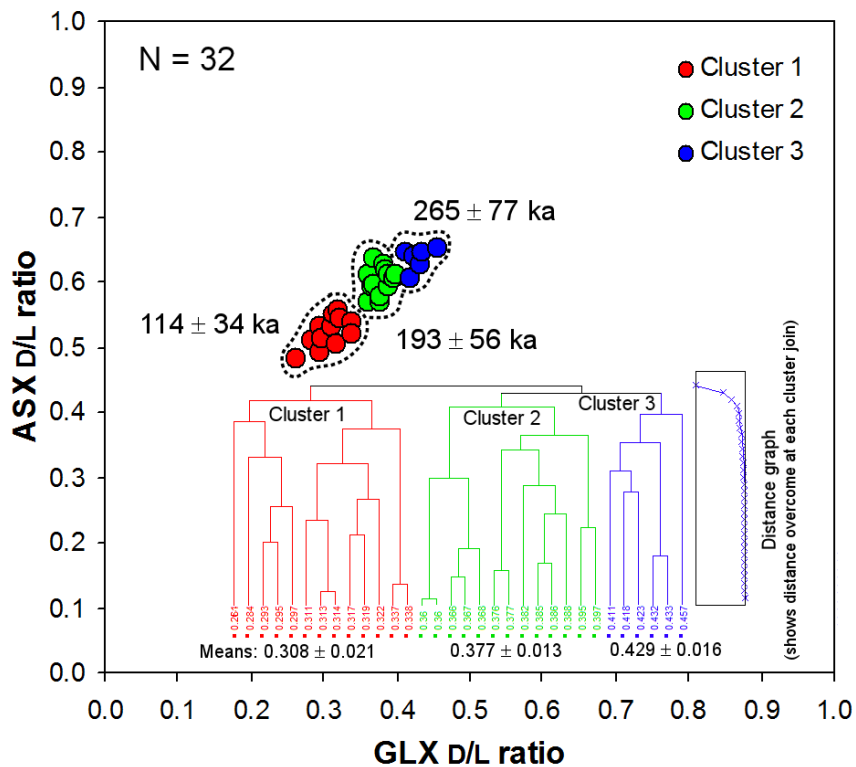


Figure 7.60: Ward method hierarchical multivariate (cluster) analysis of the single foraminifer GLX D/L ratio data from the shell facies at HB1, inset within a bivariate plot (ASX vs. GLX). Three age populations are identified. The mean of the lowest set of D/L ratios was used to calculate the Foram AAR estimate for this unit.

Table 7.20: Pleistocene whole-rock (WR) sediment ASX and GLX AAR data, and AAR numerical age estimates for Hanson Bay.

Lab. No.	Site	Site code / facies (N) ^c	Location (S Lat. E Long.)	CMAT ^a °C	Mean ASX D-L ratio $\pm 1\sigma^b$	Coefficient of variation (CV%)	Mean GLX D-L ratio $\pm 1\sigma^b$	Coefficient of variation (CV%)	AAR GLX (U-series calib.) age estimate (ka) ^d $\pm 1\sigma^b$	AAR GLX (OSL calib.) age estimate (ka) ^d $\pm 1\sigma^b$
UWGA 5850, 6504, 6599	Hanson Bay east	HB#3-4 / raised shelly deposit (6)	36° 01' 01.4" 136° 51' 22.8"	15.0	0.622 \pm 0.006	0.9	0.462 \pm 0.010	2.1	135 \pm 31	129 \pm 29
UWGA 5874	Hanson Bay east	HB#1-2a / lagoonal (4)	36° 01' 01.4" 136° 51' 22.8"	15.0	0.640 \pm 0.004	0.6	0.498 \pm 0.011	2.2	182 \pm 42	173 \pm 39
UWGA 5092, 5875	Hanson Bay east	HB#1-2b / lagoonal (8)	36° 01' 01.4" 136° 51' 22.8"	15.0	0.621 \pm 0.022	3.6	0.495 \pm 0.034	6.9	177 \pm 42	169 \pm 40
UWGA 6544, 7000	Hanson Bay west	KHa#1 / aeolianite (6)	36° 01' 03.8" 136° 51' 11.0"	15.0	0.741 \pm 0.023	3.1	0.722 \pm 0.018	2.5	630 \pm 145	601 \pm 136

^a Current mean annual temperature (CMAT) estimated for these sites from annual temperature data via climate recording stations around Kangaroo Island (<http://www.bom.gov.au/climate/data/>)

^b Uncertainties are 1 σ (one standard deviation—68% confidence interval)

^c N = number of subsamples analysed

^d Numeric age estimate from a U-series calibration (Schwebel, 1978; 1984), and an OSL calibration (this study) using an apparent parabolic model (Mitterer and Kriausakul, 1989; Murray-Wallace *et al.*, 2001); uncertainties are calculated from the square root of the sum of the squares of all uncertainty terms

Table 7.21: Hanson Bay Pleistocene single foraminifer ASX and GLX AAR data, and numeric AAR age estimates

Lab. No.	Site	Site code / facies	Location (S Lat. E Long.)	CMAT ^a °C	Genus and species / (N) ^b	Mean ASX D- L ratio) $\pm 1\sigma^c$	Coefficient of variation (CV%)	Mean GLX D- L ratio) $\pm 1\sigma^c$	Coefficient of variation (CV%)	AAR GLX age estimate (ka) ^d $\pm 1\sigma^c$
UWGA 5029, 5030, 5035, 5036, 5048, 5049	Hanson Bay east	HB#1-3 / Modern dune	36° 01' 01.4" 136° 51' 22.8"	15.0	<i>Elphidium</i> sp. + <i>Discorbis</i> <i>dimidiatus</i> / (10)	0.195 \pm 0.019	9.9	0.081 \pm 0.005	6.6	0.06 \pm 0.02
UWGA 5043, 5050, 5832	Hanson Bay east	HB#3-4 / raised shelly deposit	36° 01' 01.4" 136° 51' 22.8"	15.0	<i>Elphidium</i> sp. + <i>D.</i> <i>dimidiatus</i> / (13)	0.526 \pm 0.023	4.5	0.308 \pm 0.021	7.0	114 \pm 34
UWGA 5877	Hanson Bay east	HB#1-2a / lagoonal	36° 01' 01.4" 136° 51' 22.8"	15.0	<i>Elphidium</i> sp. + <i>D.</i> <i>dimidiatus</i> / (9)	0.605 \pm 0.038	6.3	0.369 \pm 0.041	11.2	183 \pm 57

^a Current mean annual temperature estimated for these sites from annual temperature data via climate recording stations around Kangaroo Island (<http://www.bom.gov.au/climate/data/>)

^b Number of foraminifera used for GLX D-L ratio estimate

^c Uncertainties are 1 σ (one standard deviation—68% confidence interval)

^d Numeric age estimate from a U-series calibration (fossil coral recovered from Vivonne Bay: 114 \pm 3 ka*) using an apparent parabolic model (Mitterer and Kriauasakul, 1989; Murray-Wallace *et al.*, 2001); uncertainties are calculated from the square root of the sum of the squares (addition in quadrature) of all uncertainty terms

* U-series age of *Plesiastrea versipora*: a stony (scleractinian) coral recovered from same unit as the foraminifers *Elphidium* spp. and *Discorbis dimidiatus* (PE#3-4), and used to calibrate the GLX D-L ratio



Figure 7.61: Close view of shell facies at HB1, note that most shells in this photo are broken; it was difficult to find reasonably whole shell for AAR analyses in this unit. RH inset shows a closer view of the section outlined by the red rectangle (rock-hammer set for scale—33 cm).

Several molluscs (5 x *Spisula* [*Notospisula*] *trigonella*) (see Figure 7.56 and Table 7.8) were also analysed and an AAR age estimate of 132 ± 29 ka was calculated from the mean GLX D-L ratio (0.359 ± 0.025). All of these ages are reasonably consistent with a Last Interglacial deposition for this shell rich deposit; this is further supported by the morphostratigraphical position of the unit, i.e. approximately +3 m APSL at top contact.

HB1 also exhibits a truncated lagoonal unit at the rear of the calcarenite platform (See Figure 7.57 and 7.62). Two whole rock samples were removed from this unit (HB#1-2a and 1-2b). Both samples were dated using the whole-rock calibrations; however, foraminifers were only recovered from sample HB#1-2a. Whole-rock AAR age estimates of 182 ± 42 ka (U-series calibration) and 173 ± 39 ka (OSL calibration) were determined for sample HB#1-2a (mean

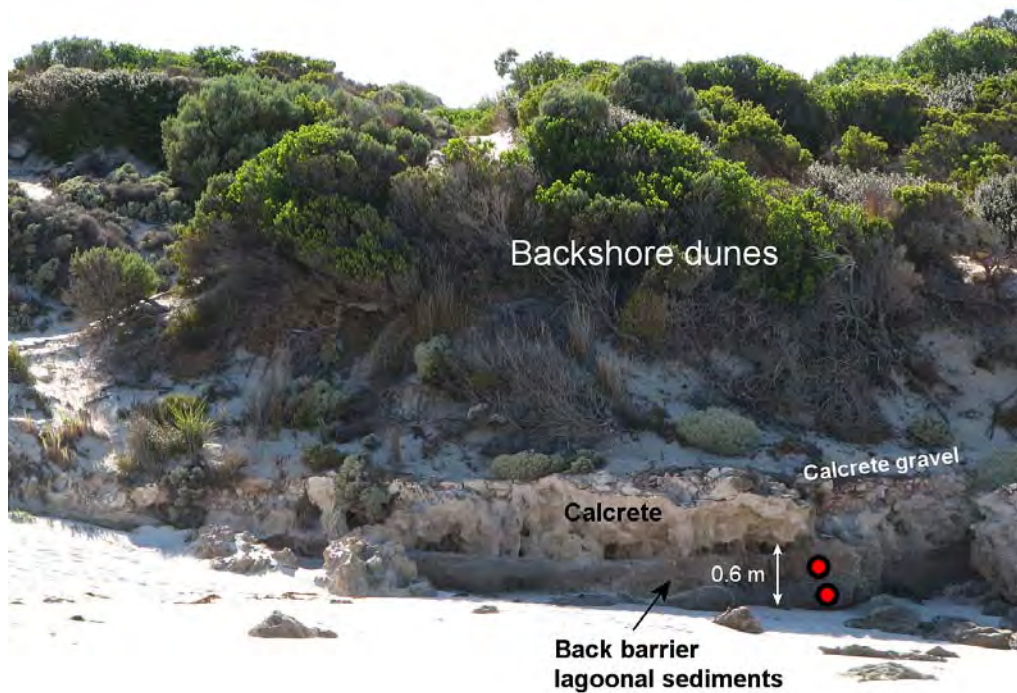


Figure 7.62: Morphology of the lagoonal unit at site HB1. The red circles show the position of the whole-rock sediment AAR dating samples. Note: base of lagoonal sediments is ~ 0.5 m APSL (see also stratigraphic log: Figure 7.57).

GLX D-L ratio: 0.498 ± 0.011) (Table 7.20). Foraminifers extracted from this sediment yielded an age of 183 ± 57 ka (mean GLX D-L ratio: 0.369 ± 0.041) (Table 7.21). The AAR WR sample was also age estimated yielding an AAR ages of 177 ± 42 ka (U-series calibration) and 169 ± 40 ka (OSL calibration) (mean GLX D-L ratio: 0.495 ± 0.034). The position of this unit seems to suggest that a back-barrier lagoon existed in this area of the embayment at a period of slightly higher sea-level than present (although not as high as in MIS 5e). The ages (even though some are consistent with the upper age range for MIS 5e, i.e., 132 ka) all suggest deposition before the Last Interglacial, if the position of the units in relation to an MIS 5e sea-level is taken into account. Sea-levels during MIS 7a (190-201 ka: Gallup *et al.* [1994]; Bard *et al.* [2002]; Antonioli *et al.* [2004]) were estimated to have been -5 to -15 m APSL (Siddall *et al.*, 2007: various studies from Italy, Barbados, and the Bahamas). Murray-Wallace (2002) estimated MIS 7a sea-levels for the Coorong

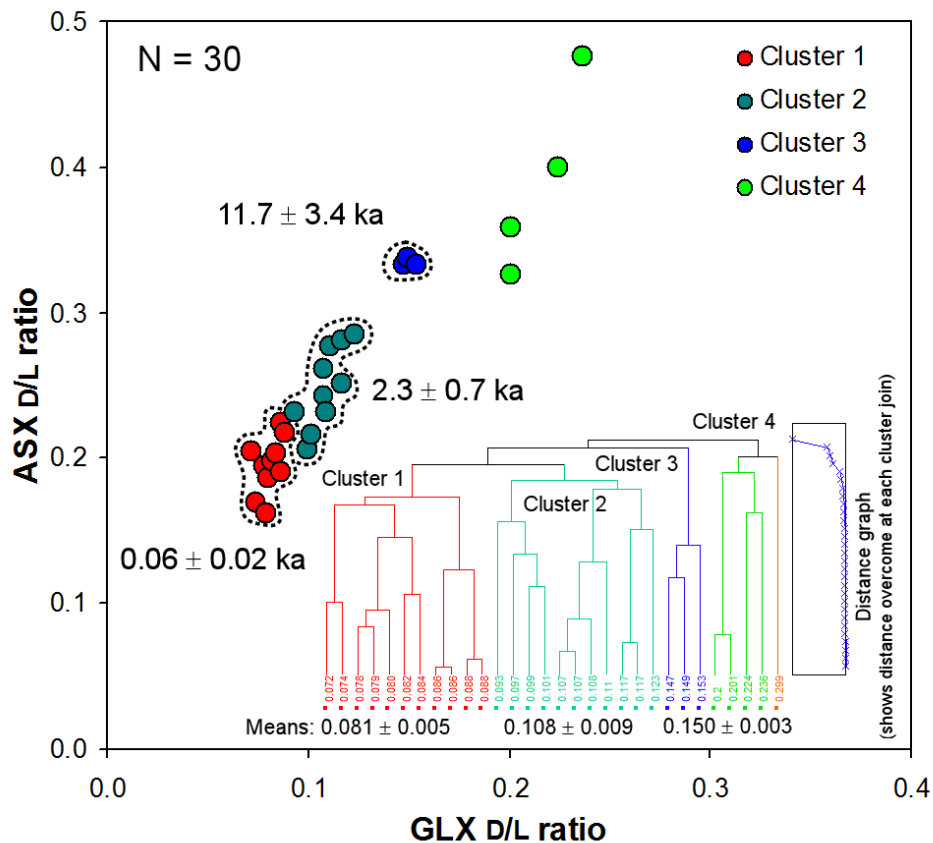


Figure 7.63: Ward method hierarchical multivariate (cluster) analysis of the single foraminifer GLX D-L ratio data from the modern backshore dunes at HB1, inset within a bivariate plot (ASX vs. GLX). Three age populations are identified. The mean of the lowest set of D-L ratios was used to calculate the Foram AAR estimate for this unit.

coastal region, South Australia, to be approximately -6 m APSL. Thus, even though the chronology of the lagoonal units relates more agreeably to a MIS 7a age, it is difficult to reconcile this with the position of the units, unless gentle uplift is invoked. It is also possible that the units were deposited just prior to the MIS 5e highstand, if the AAR ages are considered to be overestimated.

The overlying backshore dunes (see Figure 7.58 and 7.62) were dated using single foraminifers (*Elphidium* spp. and *Discorbis dimidiatus*). A bivariate plot (ASX vs. GLX) revealed a level of grain mixing in these comparatively young sediments, although more grains would need to be analysed to strengthen this conclusion. Nevertheless, the 30 GLX D-L ratio results derived from the single foraminifers were subjected to Ward method hierarchical (cluster) analysis, and at least 3 age (D-L) clusters were delineated (Figure 7.63). The lowest D-L

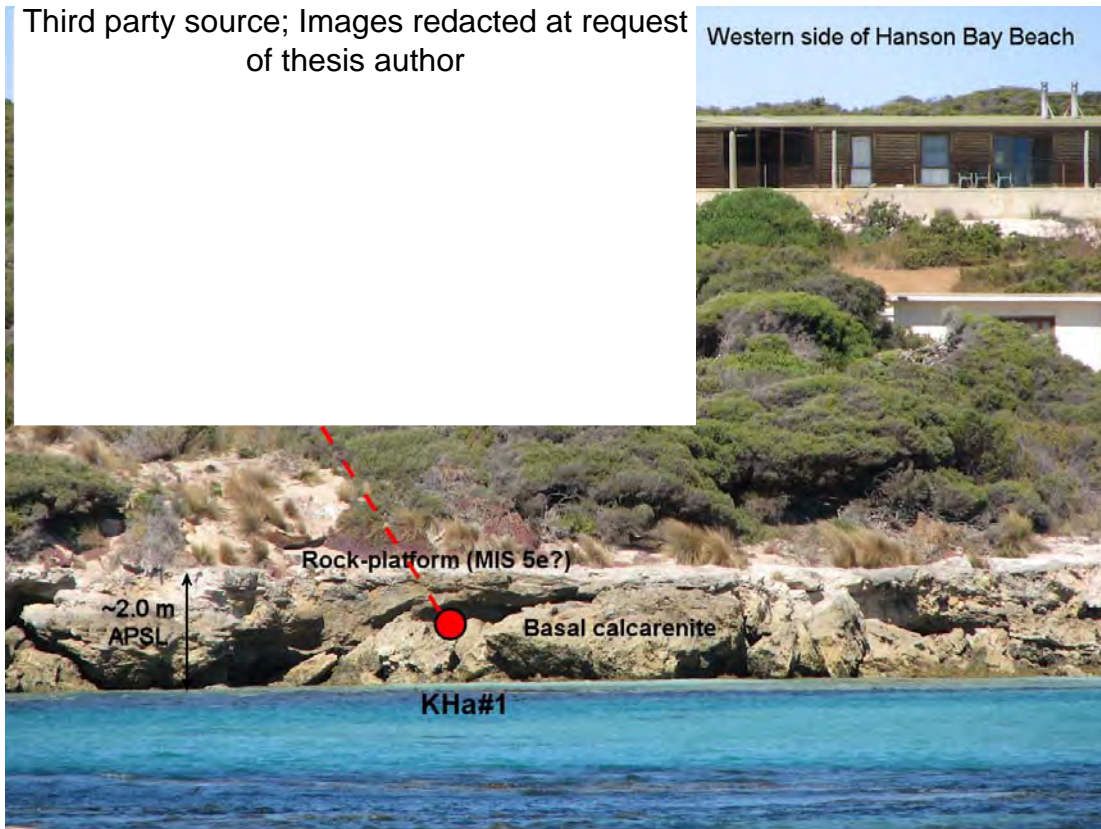


Figure 7.64: Location of sample KHa#1 at site HB2, on the western end of Hanson Bay Beach (upper LH inset image Google Earth, 2009).

population (mean GLX D-L ratio: 0.081 ± 0.005 was used to estimate an AAR age 0.06 ± 0.02 ka for the dunes. This age is consistent (at 2σ) with the OSL age (0.10 ± 0.01 ka) obtained for the Pennington Bay backshore dunes at site PB3. There are two other clusters that relate well with the late and early Holocene (Figure 7.63). If a mean was taken without identification of the “true” age (D-L) population the calculated AAR age would be overestimated by several thousand years.

The age for these dunes alludes to rapid deposition of modern beach sand into backshore dune structures.

7.3.4.2 Hanson Bay site HB2 geochronology

The basal calcarenite was sampled on the western side of the beach, as it was softer and more easily sampled than the unit on the eastern side of the beach (which was strongly cemented and recrystallised—see Chapter 3) (Figure 7.64). The whole-rock sample (KHa#1) was analysed as whole-rock only, and WR age estimates of 630 ± 145 ka (U-series calibration) and 601 ± 136 ka (OSL

calibration) (mean GLX D-L ratio: 0.722 ± 0.018) (Table 7.20) were determined using calibrations based upon apparent parabolic kinetics. This implies an early/middle Pleistocene age for the basal calcarenite unit.

7.3.4.3 Discussion of the Hanson Bay geochronology

This small beach site at Hanson Bay, Kangaroo Island, hosts two small rock platforms constructed of early to middle Pleistocene calcarenite. This basal calcarenite is unconformably overlain at the eastern platform by a pedogenetically modified exposure surface, much of which has been removed by scouring. The age of this unit is unknown, although it is certainly older than MIS 5. Overlying this in turn is a thick shell facies (up to 1 m), that may be a sublittoral shell-bed, a washover facies, or possibly a shelly deflation deposit (see Chapter 3). The unit was dated using several methods, the ages of which converge on the Last Interglacial (MIS 5e). A thick calcrete horizon unconformably overlies the shell unit (and the lagoonal facies). The upper portion of the calcrete unit is brecciated in places, where irregular fragments of calcrete are in a soil matrix. The shell unit truncates the lagoonal facies, at the rear of the platform, which submerge beneath the beach sand, moving landward. This unit was dated using WR and Foram AAR, and although the age is uncertain, a late MIS 7 age is consistent with both the amino- and morphostratigraphy. Overlying the calcrete are backshore dunes estimated to be modern in age (consistent with OSL dated dunes at Pennington Bay). The backshore dunes at Bales Beach (dated using WR AAR) appear to be older; however, this could also be due to the influence of reworked biomineral components, as was shown to be the case with the Hanson Bay dunes.

7.3.5 Kelly Hill Caves

The age of the Kelly Hill Caves on Kangaroo Island, really the depositional ages of the dune calcarenites (aeolianites) that the caves are formed within, is estimated to range between the Miocene and Pleistocene (Sprigg, 1954; Bauer, 1959; Milnes *et al.*, 1983; Belperio, 1995; Twidale and Bourne, 2002). Calcarenite samples collected in Kelly Hill Caves by Major and Vitols (1973) for example may be as early as Miocene in age, as suggested by Milnes *et al.* (1983), based upon the presence of the foraminifera *Pararotalia* sp., *Elphidium*

chapmani and *Crespinella umbonifera*; although all three of these species are extant into the Early Pliocene. There is also the possibility that these foraminifers were reworked from older material.

7.3.5.1 Kelly Hill Caves geochronology

As a part of this thesis a re-examination of the age of the Kelly Hill Caves site by undertaking luminescence geochronology on quartz extracted from calcarenite in the main cavern, using the experimental OSL method: SARTT-OSL (Chapter 5), and whole-rock sediment amino acid racemisation (AAR).

As discussed in Chapter 3, there are numerous underground drainage features on Kangaroo Island with at least two large systems, the largest and most extensive being Kelly Hill caves (Bauer, 1959). The Kelly Hill Cave system is

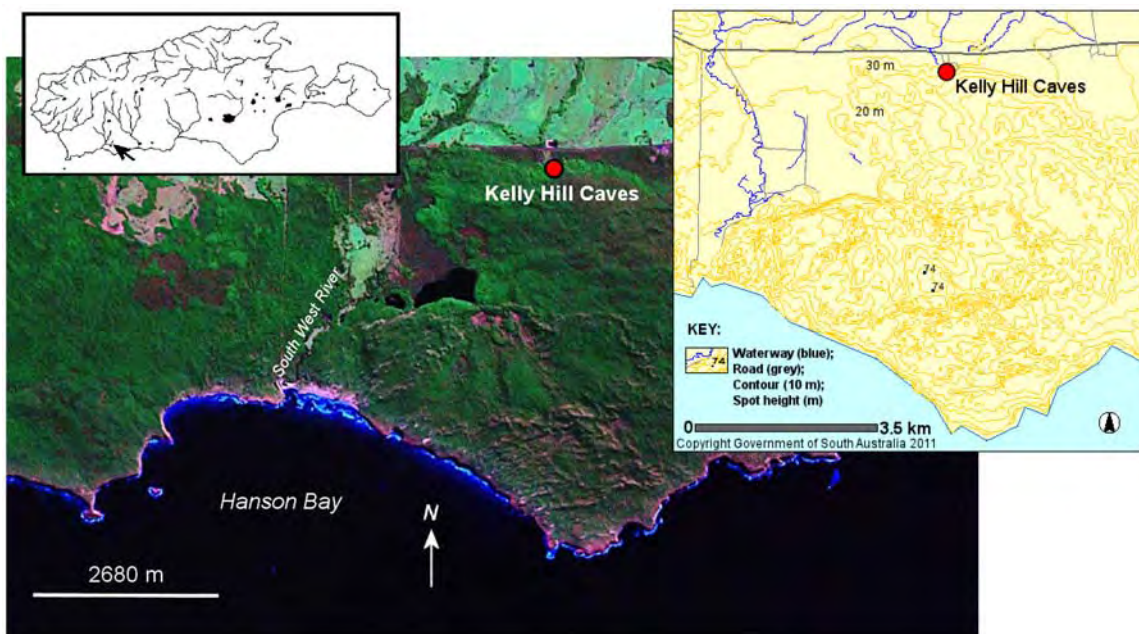


Figure 7.65: Location of Kelly Hill caves on the southern coast of Kangaroo Island. Upper LH inset shows the location on a regional map (black arrow) (main image is a Landsat ETM: NASA Landsat program, 2001). The upper RH inset illustrates the topography of the area. The cave complex is located between the 30 m and 40 m contour lines (modified from the online atlas of South Australia [2011]).

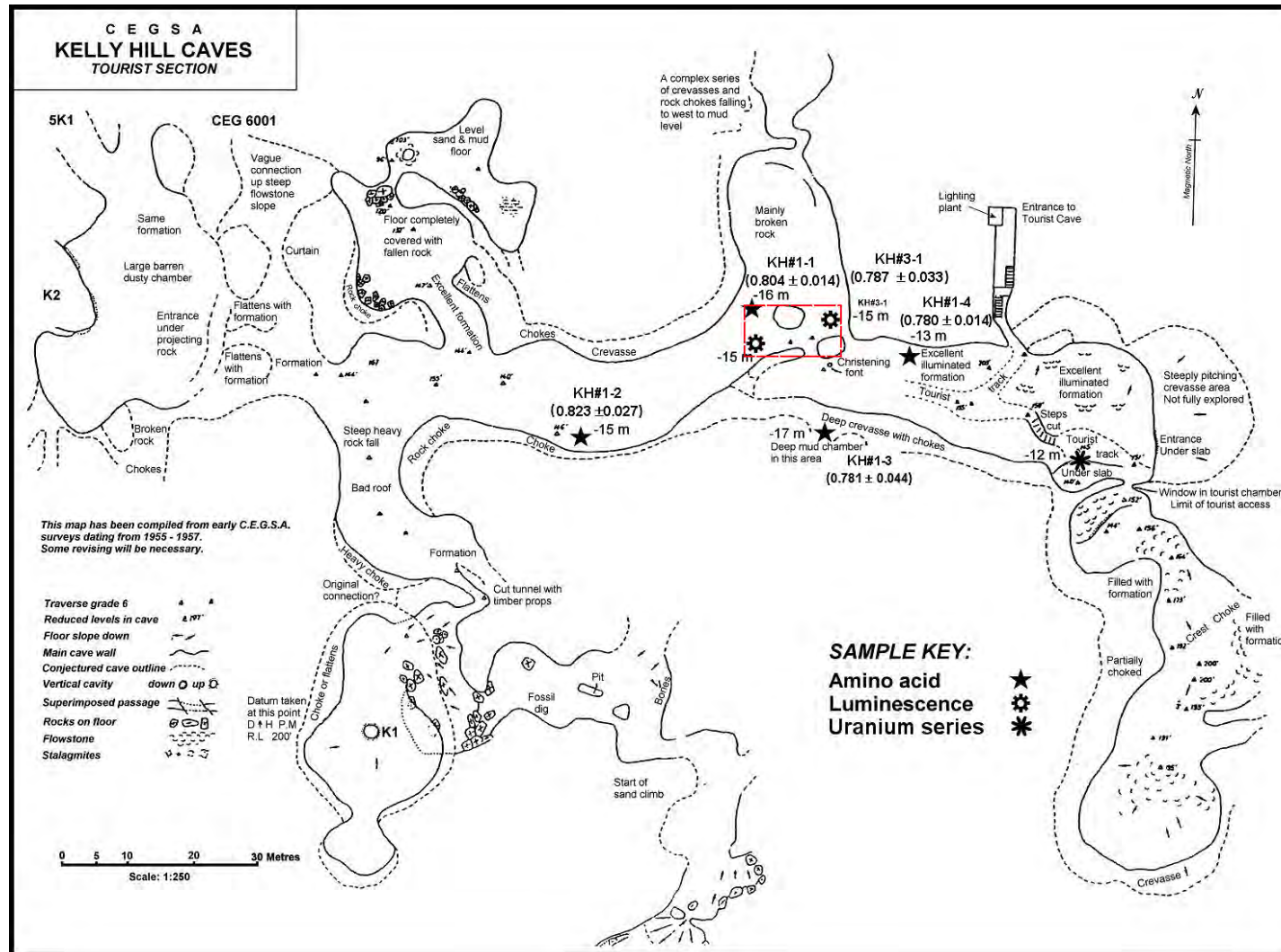


Figure 7.66: Map of main cavern at Kelly Hill, showing locations of various sample points. Cave map (modified) courtesy of G. Gartrell, P. Horne, and G. Pilkington of CEGSA (Cave exploration group of South Australia) (2007). Numbers in brackets are GLX D-L ratio means for AAR samples.

located on the southern portion of Kangaroo Island approximately 6 kilometres from the coast (Figure 7.4 and Figure 7.65). The caves are formed in calcarenite that may be between Miocene and Late Pleistocene in age. Bauer (1959) surmised that the basal calcarenite was of Pliocene age and may have been covered by Pleistocene calcarenites, as the surface topography around the caves region was precisely the same as along the southern coast. The caverns formed by solutional weathering as groundwater flowed through and into the basal portions of the deposits; chambers becoming larger as there was an upward migration of cavern roofs due to mass collapse (Bauer, 1959; Hill, 1957). Hill (1957) in an unpublished draft also discusses the origin of the cave system, and Bauer (1959) supported Hill's speculations on the formation of the caves. Other researchers have sampled from the caves, for example Major and Vitols (1973) collected samples from within the caves, and Milnes *et al.* (1983) included a small section in their Cainozoic study of the island discussing these samples with regard to the depositional age of the Kelly Hill Caves calcarenite. They preferred a Miocene age on the basis of the foraminifera found, as iterated above. Belperio (1995) suggested rather that the Kelly Hill caves were formed in Pleistocene calcarenites; similar to karst features found on the west coast of the Eyre Peninsula, and the south-western end of the Yorke Peninsula. In 1996 P. Marianelli of the Australian National University (Heath, pers. comm., 2007) undertook some Uranium-series dating analyses on a 1.2 m thick flowstone sequence at 12 metres depth, approximately 25 metres southeast of the cave entrance (Figure 7.66). The top of the sequence dated at 3.8 ± 0.2 ka, and the base of the sequence dated to >500 ka, beyond the range of the Uranium-series method.

Two luminescence samples (KH#3-1 [only KH#3-1 was analysed], and KH#3-2) were collected near the Christening Font, either side of two supporting pillars (see Figure 7.66—red dashed rectangle for location) from fresh collapse material. Twelve aliquots of KH#3-1 (3 mm mask size) were analysed using the SARTT-OSL protocol. A central D_e of 227 ± 7 Gy ($8.7 \pm 2.7\%$ overdispersion) was calculated using the CAM (equivalent dose distributions are given in Figure 7.67).

Table 7.22: Pleistocene whole-rock (WR) sediment ASX and GLX AAR data, and AAR numerical age estimates for Kelly Hill Caves.

Lab. No.	Site	Site code / facies (N) ^c	Location (S Lat. E Long.)	CMAT ^a °C	Mean ASX D-L ratio $\pm 1\sigma$ ^b	Coefficient of variation (CV%)	Mean GLX D-L ratio $\pm 1\sigma$ ^b	Coefficient of variation (CV%)	AAR GLX (U-series calib.) age estimate (ka) ^d $\pm 1\sigma$ ^b	AAR GLX (OSL calib.) age estimate (ka) ^d $\pm 1\sigma$ ^b
UWGA 6498, 6499, 6500, 6501, 6535	Kelly Hill Caves	KH / aeolianite cave system (19)	35° 58' 44.6" 136° 54' 16.6"	15.0	0.694 \pm 0.015	2.2	0.795 \pm 0.031	3.8	835 \pm 194	796 \pm 181

^a Current mean annual temperature (CMAT) estimated for these sites from annual temperature data via climate recording stations around Kangaroo Island

(<http://www.bom.gov.au/climate/data/>)

^b Uncertainties are 1 σ (one standard deviation—68% confidence interval)

^c N = number of subsamples analysed

^d Numeric age estimate from a U-series calibration (Schwebel, 1978; 1984), and an OSL calibration (this study) using an apparent parabolic model (Mitterer and Kriausakul, 1989; Murray-Wallace *et al.*, 2001); uncertainties are calculated from the square root of the sum of the squares of all uncertainty terms

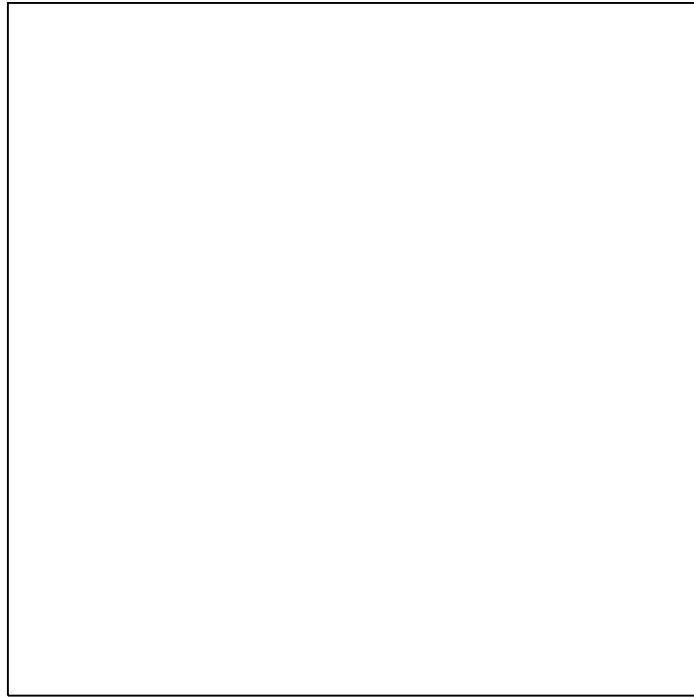


Figure 7.67: Single-aliquot (SARTT-OSL) equivalent dose (D_e) distributions for sample KH#3-1, displayed as a radial plot. The CAM D_e for this sample is 227 ± 7 Gy.



Figure 7.68: Location of AAR WR sample KH#1-1. See also Figure 7.64. Sample was removed from ~200 mm deep into relatively weakly cemented calcarenite.

The equivalent doses exhibited a mean recycling ratio of 1.05 ± 0.11 . The dose rate data for KH#3-1 (Table 7.13) was then combined with the central equivalent dose to yield a SARTT-OSL age estimate (using the program listed in Roberts *et al.* [1993]) of 1.3 ± 0.1 Ma. It must be noted here that the overall dose rate for KH#3-1 was very low (0.182 ± 0.015 Gy/ka⁻¹; Table 7.13), and the OSL age calculation uses an assumed internal alpha dose rate of 0.030 ± 0.01 Gy/ka⁻¹. Normally this internal alpha contribution is insignificant when compared to the gamma and beta dose rates. In the case of the Kelly Hill cave sediments it is of comparable magnitude. Regarding this some caution should be exercised when interpreting the age. Nevertheless, if the “true” internal alpha dose rate was 50% larger or smaller (i.e. between 0.045 and 0.015 Gy/ka⁻¹) than the assumed value the “true” age would still only differ from the calculated age by <10% (\pm).

Whole-rock samples (for AAR analysis) of the cave parent sediment were collected from fresh collapses and crevasse walls at various places within the main cave. Five samples were collected in all (see Figure 7.66 for locations, and Figure 7.68 for an example sample area [KH#1-1]), and 4 subsamples were analysed for WR amino acid enantiomers from each sample (suitable foraminifers could not be recovered for single grain AAR analysis). This gave 20 total D-L ratio results (1 result was rejected on the basis of laboratory contamination). The means for each sample are given in Figure 7.66; although the total mean for the remaining 19 results was used in the AAR age estimate (Table 7.22).

The mean GLX D-L ratio for all KH samples was 0.795 ± 0.031 . This was calibrated using the U-series AAR calibration and the OSL AAR calibration, yielding age estimates of 835 ± 194 ka and 796 ± 181 respectively (Table 7.22). These ages are significantly different to the SARTT-OSL age estimate at 1σ , although they all overlap at 2σ . The apparently younger WR AAR age is possibly due to leaching of lower molecular weight more highly racemized macromolecules and free amino acids. This would allow higher molecular weight, less racemized macromolecules (upon analysis) to have a greater

contribution to the final values of the D-L ratios; therefore yielding lower than expected D-L ratios.

7.3.5.2 Discussion of the Kelly Hill Caves geochronology

Regardless of some *potential* problems with the results, the SARTT-OSL and WR AAR ages suggest an early Pleistocene deposition for the parent calcarenite of the Kelly Hill Caves system. This supports the view of Belperio (1995) that the caves formed in Pleistocene sediments similar to cave systems on the South Australian mainland. The formation of the Kelly Hill cave system itself can only be estimated to have occurred sometime after ~1.4 Ma to sometime before 500 ka (Marianelli U-series estimate).

PART III: Dudley Peninsula and east coast geochronology

7.3.6 Rocky Point

As discussed in Chapter 3, Rocky Point lies on the northern coast of the neck of Dudley Peninsula, in Eastern Cove (see Figure 7.4 and 7.69). The site is a wave eroded notch in an aeolianite outcrop which forms a small headland. The aeolianite is capped by a blocky calcrete that has been undercut resulting in quantities of broken blocks scattered about the site. The calcrete has lenses of diagenetically modified sediments (indicated by a pinkish hue) characterised by pebble-sized angular clasts of carbonised (black in colour) calcrete in a strongly cemented matrix. These lenses may represent sediments and clasts washed into dune swales after bushfires (i.e. palaeofires; hence the carbonisation).

Towards the rear of the headland at approximately +2 m APSL is a wave eroded notch filled with poorly preserved (chalky) fossiliferous carbonate sediment (see Figure 7.70). The sediment comprises primarily molluscan fragments and some rare whole shell, in a skeletal carbonate matrix. Few shells could be recovered that were in suitable condition for amino acid analysis.

Third party source; Images
redacted at request of thesis
author

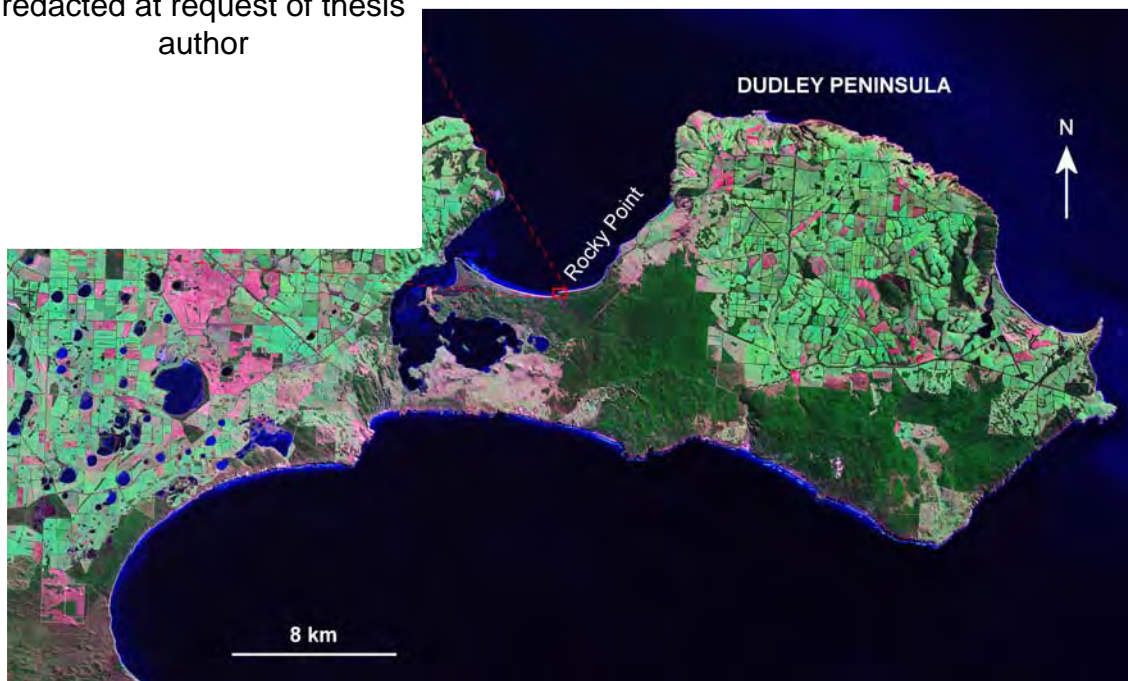


Figure 7.69: Location of Rocky Point site (red circle upper LH inset) on the neck of the Dudley Peninsula (upper LH inset from Google Earth, 2009) (main image is a Landsat ETM: NASA Landsat program, 2001).

Figure 7.70: Rocky Point stratigraphic log (C) for the sedimentary outcrops at the rear of the aeolianite headland. Included are the geochronological data (blue boxes) and corresponding GLX D-L ratio data (red boxes—numbers in brackets are individuals or subsamples analysed). The top inset (A) is a merged panorama of the site outcrop. The middle LH inset (B) comprises a satellite image (Google Earth, 2007) showing indicated log and sample sites, and a Kangaroo Island location map (with the site indicated by a black arrow).

Common foraminifers found in the deposit were *Elphidium* spp. and *Discorbis dimidiatus*, and also fragments of *Marginopora vertebralis*.

7.3.6.1 Rocky Point geochronology

Three specimens of *Fulvia tenuicostata* (see Figure 7.71) were recovered from the Rocky Point notch sediments for AAR analysis (see Table 7.8 and Figure 7.72). These shells yielded a mean GLX D-L ratio of 0.318 ± 0.007 that when calibrated gave an age estimate of 100 ± 21 ka. This age when considered in conjunction with the raised position of the bed (approximately +2 m APSL) is consistent with the Last Interglacial (MIS 5e).

Whole-rock sediment was also analysed. Here 4 subsamples of the sediment gave age estimates of 71 ± 16 ka (U-series calibration) and 68 ± 15 ka (OSL calibration) (Mean GLX D-L: 0.401 ± 0.005) (Table 7.23). This is significantly younger than the mollusc age, however, this may be explained by the leaching of highly racemized lower molecular weight macromolecules and free amino acids, in these poorly preserved sediments.

Some foraminifers were also recovered for analysis, although they were rare and generally in poor condition. Eleven foraminifers were analysed (*Elphidium* spp. and *Discorbis dimidiatus*), yielding a mean GLX D-L ratio of 0.358 ± 0.088 (Table 7.24). There was a large amount of scatter in the data, and the age estimate of 169 ± 64 ka may have been influenced by the presence of reworked grains. There were generally too few grains, and too much scatter to utilise cluster analysis on this group of foraminifers (Figure 7.73).

7.3.6.2 Discussion of Rocky Point geochronology

Given the doubtful integrity of the molluscan carbonate matrix, the shell AAR results represent the most reliable age for the Rocky Point notch deposit. It is expected then that this fossiliferous sediment was deposited in a notch formed in an older aeolianite (possibly MIS 7) during the Last Interglacial. This is in keeping with the presence of *Marginopora vertebralis*, and the morphostratigraphy of the deposit.

Table 7.23: Rocky Point Pleistocene whole-rock (WR) sediment ASX and GLX AAR data, and AAR numerical age estimates.

Lab. No.	Site	Site code / facies (N) ^c	Location (S Lat. E Long.)	CMAT ^a °C	Mean ASX D-L ratio $\pm 1\sigma^b$	Coefficient of variation (CV%)	Mean GLX D-L ratio $\pm 1\sigma^b$	Coefficient of variation (CV%)	AAR GLX (U-series calib.) age estimate (ka) ^d $\pm 1\sigma^b$	AAR GLX (OSL calib.) age estimate (ka) ^d $\pm 1\sigma^b$
UWGA 6436	Rocky Point	RP / shelly notch deposit (4)	35° 47' 57.7" 137° 50' 00.9"	15.4	0.597 \pm 0.005	0.8	0.401 \pm 0.005	1.4	71 \pm 16	68 \pm 15

^a Current mean annual temperature (CMAT) estimated for these sites from annual temperature data via climate recording stations around Kangaroo Island (<http://www.bom.gov.au/climate/data/>)

^b Uncertainties are 1 σ (one standard deviation—68% confidence interval)

^c N = number of subsamples analysed

^d Numeric age estimate from a U-series calibration (Schwebel, 1978; 1984), and an OSL calibration (this study) using an apparent parabolic model (Mitterer and Kriausakul, 1989; Murray-Wallace *et al.*, 2001); uncertainties are calculated from the square root of the sum of the squares of all uncertainty terms

Table 7.24: Rocky Point Pleistocene single foraminifer ASX and GLX AAR data, and numeric AAR age estimates

Lab. No.	Site	Site code / facies	Location (S Lat. E Long.)	CMAT ^a °C	Genus and species / (N) ^b	Mean ASX D-L ratio) $\pm 1\sigma^c$	Coefficient of variation (CV%)	Mean GLX D-L ratio) $\pm 1\sigma^c$	Coefficient of variation (CV%)	AAR GLX age estimate (ka) ^d $\pm 1\sigma^c$
UWGA 5853	Rocky Point	RP / shelly notch deposit	35° 47' 57.7" 137° 50' 00.9"	15.4	<i>Elphidium</i> sp. + <i>Discorbis dimidiatus</i> / (11)	0.583 \pm 0.087	15.0	0.358 \pm 0.088	24.5	169 \pm 64

^a Current mean annual temperature estimated for these sites from annual temperature data via climate recording stations around Kangaroo Island (<http://www.bom.gov.au/climate/data/>)

^b Number of foraminifera used for GLX D-L ratio estimate

^c Uncertainties are 1 σ (one standard deviation—68% confidence interval)

^d Numeric age estimate from a U-series calibration (fossil coral recovered from Vivonne Bay: 114 \pm 3 ka*) using an apparent parabolic model (Mitterer and Kriausakul, 1989; Murray-Wallace *et al.*, 2001); uncertainties are calculated from the square root of the sum of the squares (addition in quadrature) of all uncertainty terms

* U-series age of *Plesiastrea versipora*: a stony (scleractinian) coral recovered from same unit as the foraminifers *Elphidium* spp. and *Discorbis dimidiatus* (PE#3-4), and used to calibrate the GLX D-L ratio



Figure 7.71: Examples of marine shell recovered from the Rocky Point notch deposit. Found in the deposit are representatives from shallow water sand dwelling species (*Fulvia*), sublittoral rock dwelling species (*Conus*), and rocky coast species (*Diloma* and *Nerita*).



Figure 7.72: Sample site location (red circle) at Rocky Point. Note the large broken calcrete block RH mid-ground, with carbonised calcrete clasts. Dashed lines denote limits of the shell bed, and the black ellipse shows the location of a rock-hammer set for scale (33 cm).

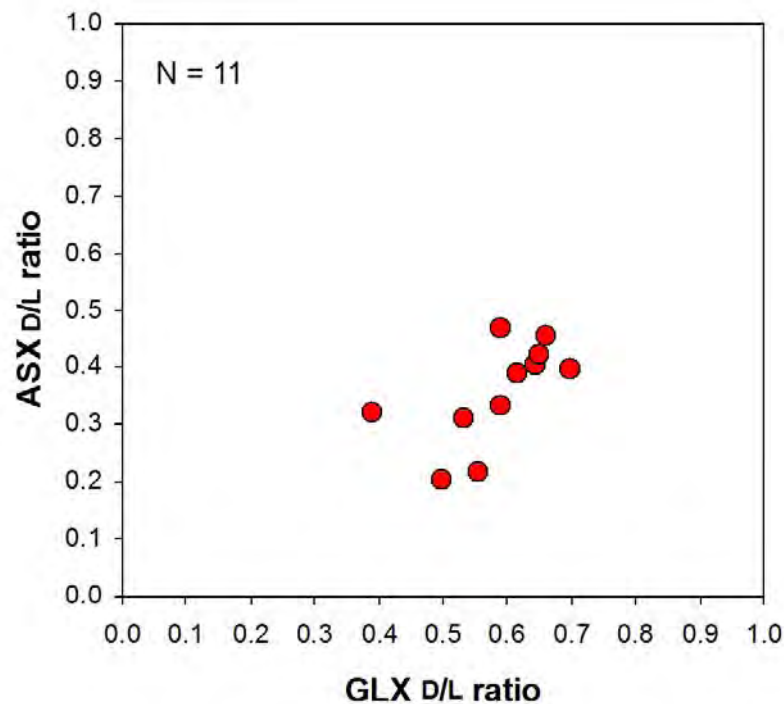


Figure 7.73: Foraminifer (*Elphidium* spp. and *Discorbis dimidiatus*) bivariate plot for Rocky Point. Note the scatter in the D-L ratios.

7.3.7 Baudin Beach

As discussed in Chapter 3, Baudin Beach is located on the western side of the Dudley peninsula (Figure 7.4 and 7.74), and the entire sequence examined here extends for approximately 2 km along a north-east/south-west line. The morphology of the sites can be characterised by low aeolianite cliffs (approximately 7 m high) with narrow carbonate sand beaches (low energy) dominated by broken (often jagged) blocks of calcrete and indurated palaeosol of various sizes (i.e. cobbles to large boulders) (Figure 7.75). The blocks are derived from cliff collapses caused by wave undercutting during periods of higher sea-level (i.e. during a storm surge for example) (the aeolianite units are only weakly cemented hence any subsequent collapse is soon removed—only calcrete remains). The overlying calcrete hardpan grades below sea-level at site BB1 (Figure 7.76).

Third party source;
Images redacted at
request of thesis author

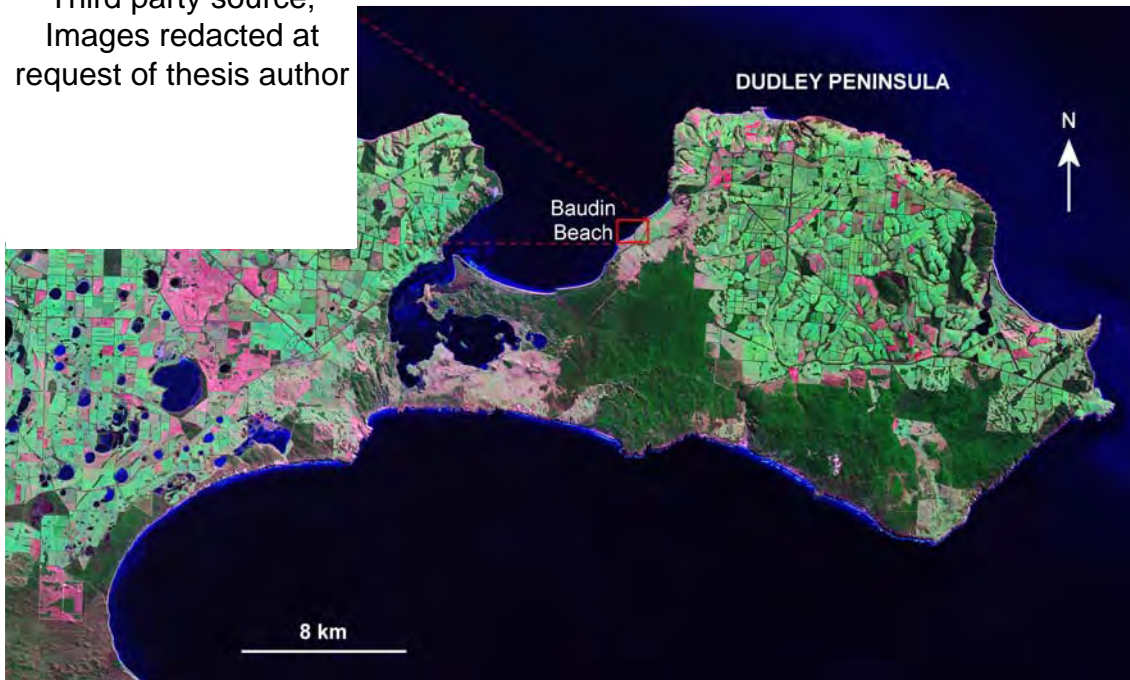


Figure 7.74: Location of Baudin Beach sites (red circles upper LH inset) on the western side of the Dudley Peninsula (upper LH inset from Google Earth, 2009) (main image is a Landsat ETM: NASA Landsat program, 2001).



Figure 7.75: Collapsed calcrete/palaeosol blocks at site BB1, Baudin Beach, Kangaroo Island.



Figure 7.76: Calcrete hardpan grading below sea-level (red dashed line) at site BB1, Baudin Beach, Kangaroo Island.

This is where the south-western portion of the Pleistocene sequence terminates. Modern/Holocene dunes dominate from this point on (until Rocky Point).

The Pleistocene aeolian units are truncated by a large alluvial fan deposit (equivalent to the South Australian Pooraka Formation: Firman, 1967; Milnes and Hutton, 1983; Bourman *et al.*, 1997; Bourman *et al.*, 2010) at site BB2 (Figure 7.74 and 7.77), and alluvial sediment that is apparently a constituent of this large fan underlies the upper Pleistocene aeolianite at site BB3. There are two alluvial units (see Figure 7.78 for details of the stratigraphy and chronology at each log site):

- i) A lower unit (BB2b and BB3c), which is of course older, truncates the lower aeolianite (BB3a and BB2a) at BB2 and overlies it at BB3; this is in turn overlain at BB3 by the upper aeolianite unit (BB3d).
- ii) A younger upper alluvial unit (BB2d) which overlies the upper aeolianite (BB3d).



Figure 7.77: Panorama near site BB3 showing the upper aeolianite and the alluvial fan sediments. The blue dashed line (middle background) demarks two apparently different alluvial units, and also the smooth contact between the alluvial sediments and the upper aeolianite (LH midground).

7.3.7.1 Baudin Beach site BB1 geochronology

Site BB1 hosts a single aeolianite unit mantled by a thick calcrete/palaeosol. OSL sample BB#3-1 was taken from this unit and analysed using the modified SAR protocol (Chapter 4). Thirty nine 1 mm mask aliquots were analysed and the resultant equivalent doses were subjected to the CAM. A central D_e of 103 ± 3 Gy was determined (overdispersion was $10.0 \pm 3.4\%$: Table 7.12) from 29 of the aliquots, as 10 were rejected on the basis of no L_n/T_n intersection (D_e distributions are given in Figure 7.79). Recycling, IR depletion, and dose recovery (50 Gy) ratios were 0.96 ± 0.03 , 0.99 ± 0.03 and 1.13 ± 0.11 , respectively. The central D_e in conjunction with the dose rate data in Table 7.11 and the program listed in Roberts *et al.* (1993) yielded an age estimate of 129 ± 8 ka, which is consistent with a Last Interglacial (MIS 5e) deposition.

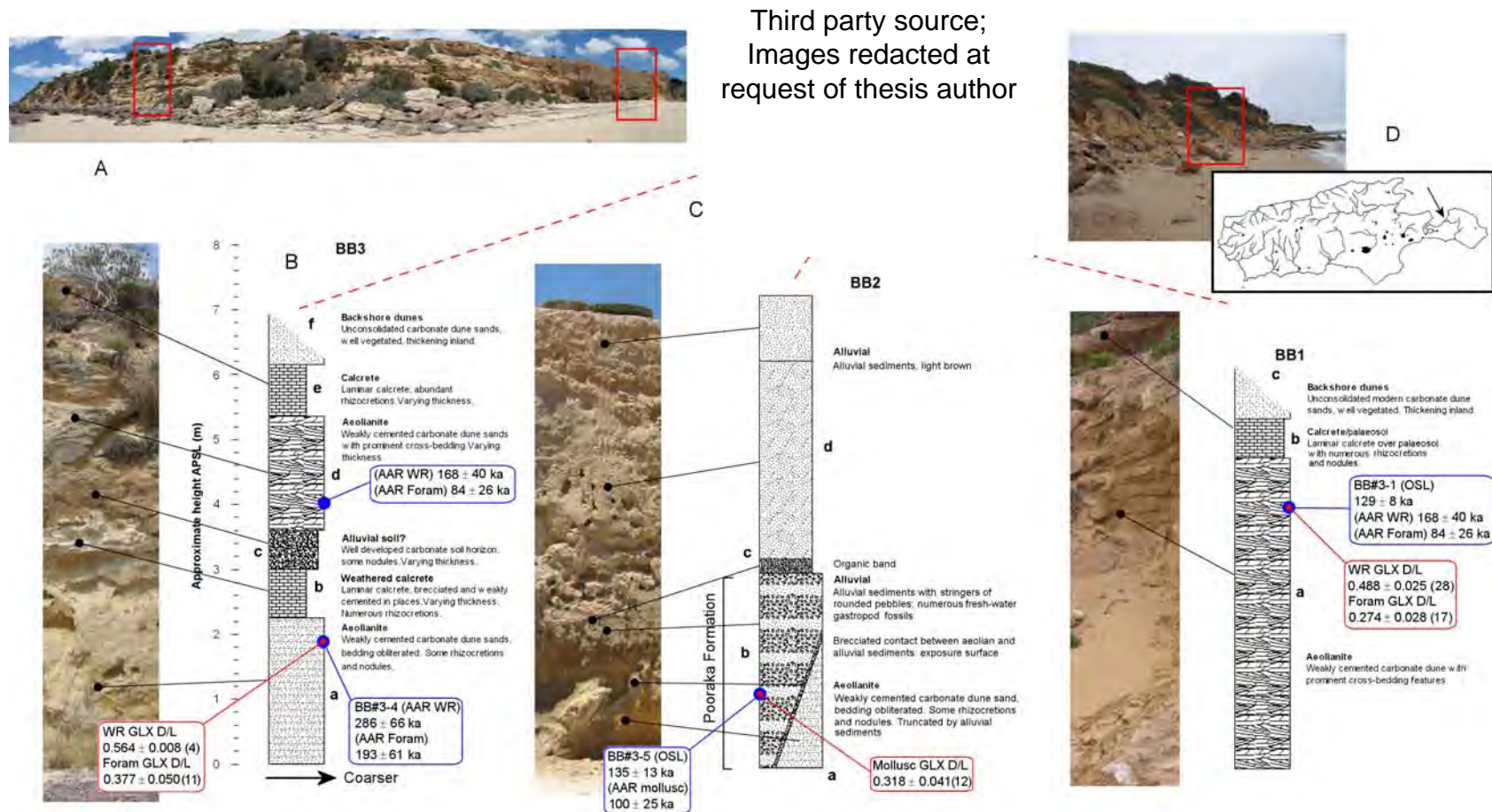


Figure 7.78: Baudin Beach stratigraphic logs (B) for the sedimentary outcrops along a section of the north-west coast of the Dudley Peninsula. Included are the geochronological data (blue boxes) and corresponding GLX D-L ratio data (red boxes—numbers in brackets are individuals or subsamples analysed). The top LH inset (A) is a merged panorama (there is some distortion towards the ends of the image) of the BB2 and BB3 site outcrop. The middle top inset (C) comprises a satellite image (Google Earth, 2010) showing indicated log and sample sites, and the RH top inset (D) is a panorama of site BB1 outcrop, and a Kangaroo Island location map (with the site indicated by a black arrow).

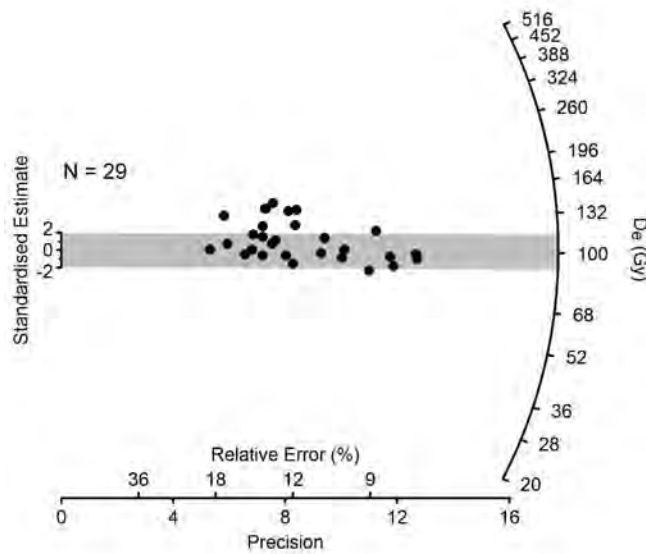


Figure 7.79: Single-aliquot (OSL) equivalent dose (D_e) distributions for sample BB#3-1, displayed as a radial plot. The CAM D_e for this sample is 103 ± 3 Gy.

This unit was also dated by WR and Foram AAR giving age estimates of 168 ± 40 ka (U-series calibration), 161 ± 37 ka (OSL calibration) (mean GLX D-L ratio: 0.488 ± 0.025), and 84 ± 26 ka (mean GLX D-L ratio: 0.274 ± 0.028 (Table 7.25 and 7.26). Note the difference in the WR and Foram ages, this may be due to the influence of reworked older components in the sediment not adequately accounted for by the empirical correction (i.e. $WR \text{ mean } [D-L]_{unknown} = WR \text{ mean } [D-L]_{modern \text{ beach}} = WR [D-L]_{corrected}$). The Foram age is based upon the lowest D-L population ($N = 17$: cluster 1) in 24 single tests of *Discorbis dimidiatus* (Table 7.26) from the upper aeolianite (BB1a and BB3d) (Figure 7.78 and 7.80), determined by Ward method multivariate (cluster) analysis. A portion of these tests may be derived (through reworking) from the lower aeolianite (BB3a). This can be seen in Figure 7.81, where the BB3a foraminifers overlie the higher D-L ratio population (cluster 2: Figure 7.80) derived from the upper aeolianite (BB1a and BB3d) at sites BB1 and BB3.

Table 7.25: Baudin Beach Pleistocene whole-rock (WR) sediment ASX and GLX AAR data, and AAR numerical age estimates.

Lab. No.	Site	Site code / facies (N) ^c	Location (S Lat. E Long.)	CMAT ^a °C	Mean ASX D-L ratio $\pm 1\sigma$ ^b	Coefficient of variation (CV%)	Mean GLX D-L ratio $\pm 1\sigma$ ^b	Coefficient of variation (CV%)	AAR GLX (U-series calib.) age estimate (ka) ^d $\pm 1\sigma$ ^b	AAR GLX (OSL calib.) age estimate (ka) ^d $\pm 1\sigma$ ^b
UWGA 5851, 6467, 6468, 6469, 6530, 7002, 7003, 7004, 7005, 7006	Baudin Beach south	BB1b, BB3d / aeolianite (28)	35° 46' 35.0" 137° 52' 06.8"	15.4	0.626 \pm 0.011	1.8	0.488 \pm 0.025	5.2	168 \pm 40	161 \pm 37
UWGA 5848	Baudin Beach north	BB3a / aeolianite (4)	35° 46' 21.7" 137° 52' 29.8"	15.4	0.682 \pm 0.006	0.8	0.564 \pm 0.008	1.4	286 \pm 66	273 \pm 61

^a Current mean annual temperature (CMAT) estimated for these sites from annual temperature data via climate recording stations around Kangaroo Island (<http://www.bom.gov.au/climate/data/>)

^b Uncertainties are 1 σ (one standard deviation—68% confidence interval)

^c N = number of subsamples analysed

^d Numeric age estimate from a U-series calibration (Schwebel, 1978; 1984), and an OSL calibration (this study) using an apparent parabolic model (Mitterer and Kriausakul, 1989; Murray-Wallace *et al.*, 2001); uncertainties are calculated from the square root of the sum of the squares of all uncertainty terms

Table 7.26: Baudin Beach Pleistocene single foraminifer ASX and GLX AAR data, and numeric AAR age estimates

Lab. No.	Site	Site code / facies	Location (S Lat. E Long.)	CMAT ^a °C	Genus and species / (N) ^b	Mean ASX D- L ratio) $\pm 1\sigma^c$	Coefficient of variation (CV%)	Mean GLX D- L ratio) $\pm 1\sigma^c$	Coefficient of variation (CV%)	AAR GLX age estimate (ka) ^d $\pm 1\sigma^c$
UWGA 5816, 5821, 5823, 7007	Baudin Beach south	BB1b, BB3d / aeolianite	35° 46' 35.0" 137° 52' 06.8"	15.4	<i>Discorbis</i> <i>dimidiatus</i> / (17)	0.528 \pm 0.025	4.7	0.274 \pm 0.028	10.3	84 \pm 26
UWGA 5853	Baudin Beach north	BB3a / aeolianite	35° 46' 21.7" 137° 52' 29.8"	15.4	<i>Elphidium</i> sp. + <i>Discorbis</i> <i>dimidiatus</i> / (11)	0.625 \pm 0.039	6.2	0.377 \pm 0.050	13.2	193 \pm 61

^a Current mean annual temperature estimated for these sites from annual temperature data via climate recording stations around Kangaroo Island

(<http://www.bom.gov.au/climate/data/>)

^b Number of foraminifera used for GLX D-L ratio estimate

^c Uncertainties are 1 σ (one standard deviation—68% confidence interval)

^d Numeric age estimate from a U-series calibration (fossil coral recovered from Vivonne Bay: 114 \pm 3 ka*) using an apparent parabolic model (Mitterer and Kriauasakul, 1989; Murray-Wallace *et al.*, 2001); uncertainties are calculated from the square root of the sum of the squares (addition in quadrature) of all uncertainty terms

* U-series age of *Plesiastrea versipora*: a stony (scleractinian) coral recovered from same unit as the foraminifers *Elphidium* spp. and *Discorbis dimidiatus* (Site PE3, sample PE#3-4), and used to calibrate the GLX D-L ratio

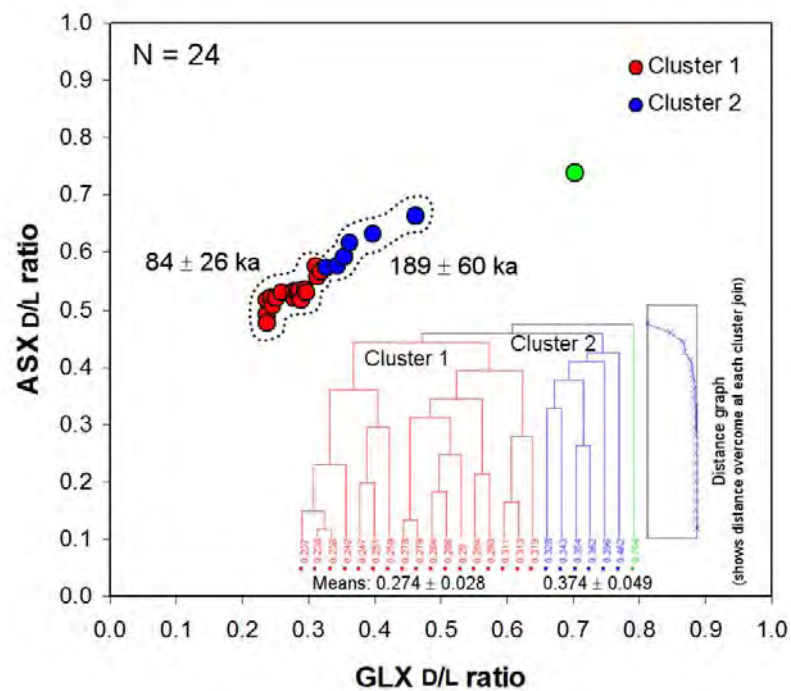


Figure 7.80: Ward method hierarchical multivariate (cluster) analysis of the single foraminifer GLX D-L ratio data from the upper aeolianite at site BB1 and BB3, inset within a bivariate plot (ASX vs. GLX). Two age populations are identified. The mean of the lowest set of D-L ratios was used to calculate the Foram AAR age estimate for this unit.

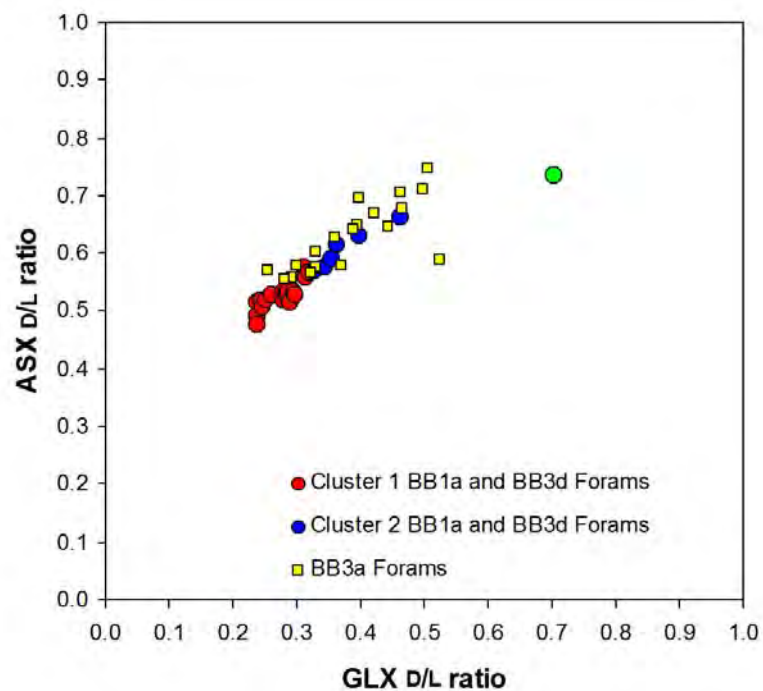


Figure 7.81: Overlay of BB3a foraminifer D-L ratios (ASX vs. GLX) onto the BB1a and BB3d data. Note how the BB3a population overlies the higher D-L population from BB1a and BB3d.

The Foram age suggests a later time of deposition than MIS 5e for the upper aeolianite than the OSL or WR ages. It is difficult to reconcile this difference, although it may indicate a tendency for the foraminiferal data to underestimate ages. At this stage it is uncertain whether this tendency is related to the foraminifer calibration, or an aspect of the D-L ratio data itself (i.e. a diagenetic effect). Nevertheless, the Foram age is still consistent with the OSL age at 2σ .

7.3.7.2 Baudin Beach site BB2 geochronology

At site BB2 the alluvial sediments (the lower deposit is classified here as an equivalent to the South Australian mainland Pooraka Formation—see also Chapter 3) were logged where they truncate the lower aeolianite (BB2a and BB3a). OSL sample BB#3-5 was removed from the lower alluvial unit (Pooraka Formation—BB2b: Figure 7.78) which underlies the aeolianite unit BB3d. Fifty one aliquots (1 mm mask size) of this sample were analysed using the modified SAR protocol (most were rejected on the basis of no L_n/T_n intersection—see Table 7.12 for details). The remaining aliquot equivalent doses (13) were subjected to the CAM, yielding a central D_e of 218 ± 15 Gy (overdispersion was $15.0 \pm 6.6\%$ and D_e distributions are given in Figure 7.82) (see also Table 7.11 for OSL sample details). This sample was close to saturation for conventional OSL, hence the large number of rejected aliquots. SARTT-OSL analysis could have been employed, however, due to the nature of the sediments being analysed it was not used (i.e. the alluvial sediments may not have received adequate sunlight exposure to ensure complete erosion of any pre-existing SARTT-OSL signal [the SARTT-OSL method is better suited to aeolian sediments]—see Chapter 5).

The recycling and IR depletion ratios (at 0.92 ± 0.03 and 1.05 ± 0.03) indicated satisfactory performance of the protocol, and insignificant feldspathic contamination of the quartz. The central D_e value in conjunction with the dose rate data in Table 7.11 and the program listed in Roberts *et al.* (1993) gave an age estimate of 135 ± 13 ka which (as with OSL sample BB#3-1) is consistent

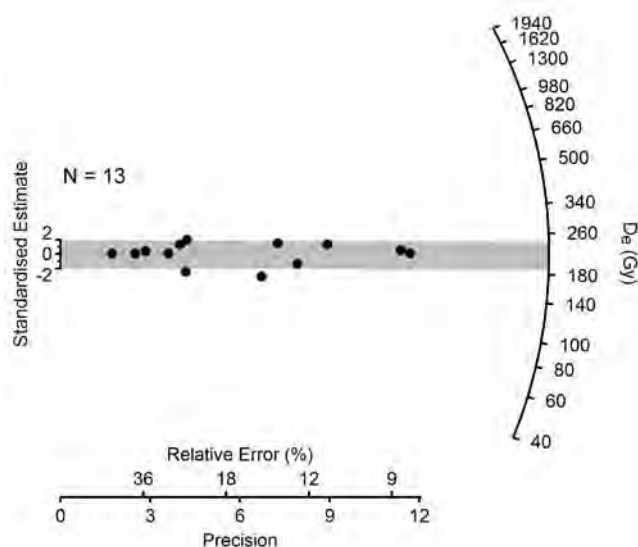


Figure 7.82: Single-aliquot (OSL) equivalent dose (D_e) distributions for sample BB#3-5, displayed as a radial plot. The CAM D_e for this sample is 218 ± 15 Gy.

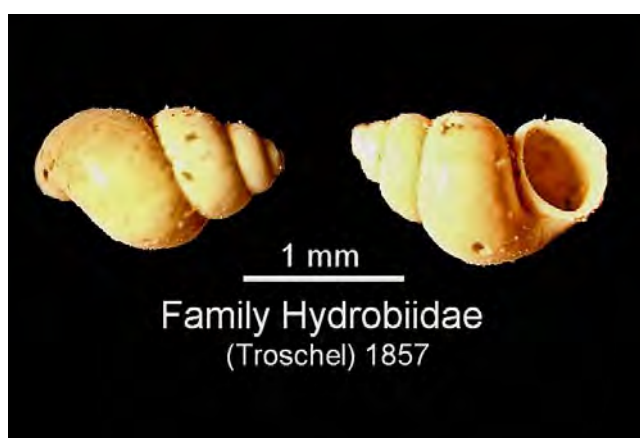


Figure 7.83: Freshwater gastropods (Family Hydrobiidae) extracted from the Pooraka Formation sediments at site BB2, Baudin Beach.

with the Last Interglacial as the time of deposition. The OSL age determined here also agrees quite well with the TL and GLSL (green light stimulated luminescence) ages of Bourman *et al.* (1997) and the OSL ages of Bourman *et al.* (2010) for the Pooraka Formation, i.e., 126 ± 29 ka, 116 ± 6 ka and 105 ± 22 ka, and 138 ± 18 ka, 118 ± 9 ka and 122 ± 17 ka respectively.

The Pooraka Formation sediments were also dated using the extent of GLX AAR in freshwater gastropods (these were disseminated throughout) extracted

from the formation. The Mollusc AAR age estimate for the Pooraka Formation sediments is based upon the mean GLX D-L ratio (0.318 ± 0.041) of 12 freshwater gastropods (Family Hydrobiidae) (see Figure 7.83). Using the Mollusc calibration this ratio produced an age estimate of 100 ± 25 ka (Table 7.8). This age is consistent with the OSL age and the Last Interglacial (MIS 5e).

7.3.7.3 Baudin Beach site BB3 geochronology

The lowest aeolianite unit (BB2a and BB3a) present at sites BB2 and BB3 was dated using both whole-rock sediment AAR and foraminifer AAR methods. Multivariate cluster analysis was not employed on the foraminifer D-L ratio data as it was too evenly scattered (Figure 7.81). A simple mean was used instead (using the criteria described in Chapter 6, section 6.4.7.2). The estimated WR ages and Foram ages were 286 ± 66 ka (U-series calibration) and 273 ± 61 ka (OSL calibration) (mean GLX D-L ratio: 0.564 ± 0.008), and 193 ± 61 ka (mean GLX D-L ratio: 0.377 ± 0.050) respectively. These ages would suggest deposition between MIS 5e and MIS 10 (taking 1σ uncertainties into account). Although a MIS 5e deposition is unlikely given the position of the unit, the calcrete unconformity (unit BB3b: suggesting an extensive hiatus), and the ages of the overlying alluvial (Pooraka Formation) and aeolianite units (i.e. Last Interglacial: MIS 5e). The Foram age and the spread in the Foram D-L ratio data (Figure 7.81) infers that the BB3a whole-rock sediment comprises a proportion of older reworked grains that have influenced the WR age. It seems in this respect that a MIS 7, or more broadly speaking, a later middle-Pleistocene deposition is more probable for this lower aeolianite unit.

7.3.7.4 Discussion of the Baudin Beach geochronology

The units at Baudin Beach represent a (late) middle to late Pleistocene sequence overlain in places by modern/Holocene dunes. The middle Pleistocene aeolianite (BB2a and BB3a) is truncated at site BB2 by sediments of the Pooraka Formation (BB2b and BB2d). Further north, at site BB3, the middle Pleistocene aeolianite and a calcrete unconformity (BB3b) are overlain by the (BB2b and BB3c) same sediments. Both the Pooraka Formation sediments (BB2b and BB3c) and the upper aeolianite (BB1a and BB3d) were

estimated to be of Last Interglacial age. The upper alluvial unit (BB2d) was not dated, however, it overlies the upper aeolianite unit and the corresponding calcrete/palaeosol unconformity (BB1b and BB3e) near site BB2 (Figure 7.84).



Figure 7.84: Location of units near site BB2. Note position of upper alluvial sediments in relation to the upper aeolianite unit (BB1a and BB3d) and calcrete (BB1b and BB3e). See person midfield for scale (~2 m).

In light of this its age must be younger than MIS 5e or, depending upon the time of calcrete formation (if the view of depositional hiatuses being aligned with glacial or stadial periods is taken), possibly younger than MIS 4. Bourman *et al.* (2010) described a “sub-pluvial” alluvial unit (at Burra Creek, South Australia) aligned with MIS 3 that overlies the Pooraka Formation. This unit, which contains *Diprotodon* bones, was dated at 43 ± 3 ka using OSL. The thick alluvial unit (~4 m) overlying the Pooraka Formation at Baudin Beach may be equivalent to this sub-pluvial unit (other similar units [although undated] can be found at Sellicks Creek, Redbanks, and River Glenn Marina in South Australia, and also at Redbanks near Hallet Cove, on Kangaroo Island [Bourman *et al.*, 2010]).

The upper aeolianite at sites BB1 and BB3 was deposited during the Last Interglacial (MIS 5e). This unit is equivalent to similar units at Pennington Bay and Bales Beach (sites PB1 and Bales1) also deposited during this period.

Figure 7.85 presents a chronostratigraphical and morphostratigraphical interpretation of the units at Baudin Beach. A Last Interglacial age was determined for the Pooraka Formation alluvial units (BB2b and BB3c), and the upper aeolianite (BB1a and BB3d), however, the upper aeolianite clearly overlies the Pooraka Formation at site BB3 (Figure 7.77, 7.78 and 7.85). This would indicate that the Pooraka Formation is older than the upper aeolianite. How much older is difficult to determine, although the clean contact (with little diagenetic alteration: see Figure 7.86) between the underlying Pooraka Formation and the overlying aeolianite would suggest a relatively short period between the successive depositions. Indeed the aeolianite deposition and formation may have occurred during the regressive phase just after MIS 5e. The lateral extent of the Pooraka Formation at Baudin Beach was not fully mapped due to time constraints. However, it does extend far northward beyond site BB3 at varying thicknesses, infilling eroded surfaces of the underlying calcrete and aeolianite (see Figure 7.87 for a long view of the Pooraka Formation), having a distinctively level upper surface.

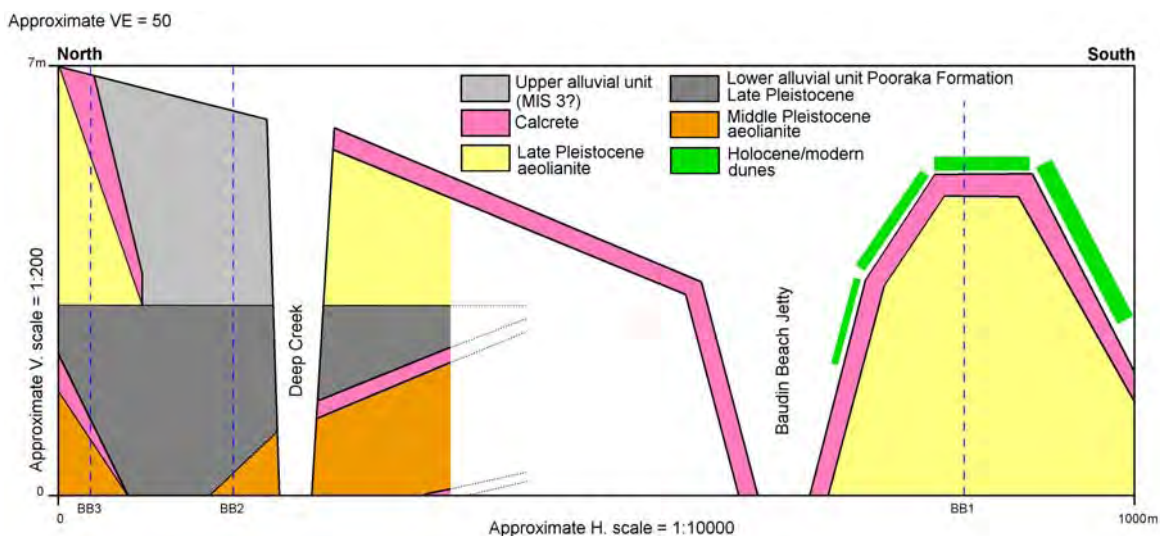


Figure 7.85: Schematic representation of the units present along a 1000 m section of Baudin Beach encompassing the 3 examined sites (BB1, BB2 and BB3).

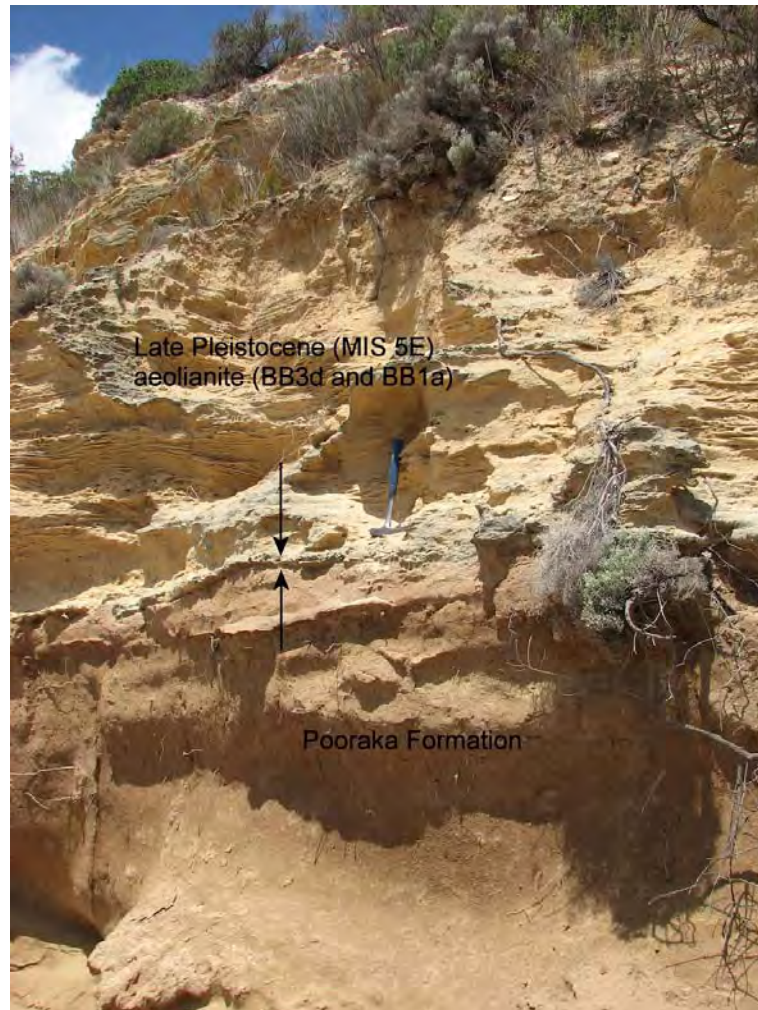


Figure 7.86: Pooraka Formation and overlying aeolianite near site BB3. Note clean contact (arrows) (Rock-hammer set for scale: 33 cm).

7.3.8 American River

This site is an extensive Holocene marine shell deposit on the shores of American River, south-west of Buicks Point, on Kangaroo Island. Examined in this section are the amino acid racemization results of *Katelsysia scalarina*, *Katelsysia peronii*, and *Katelsysia rhytiphora* shells, and the AMS ^{14}C results of a single *Katelsysia scalarina* and *Katelsysia rhytiphora*, sampled from the two sites (the AMS ^{14}C samples were taken not to date particular shell beds, but to calibrate GXL D-L ratio data for the sites) (Figure 7.88). The sites consist of a series of extensive unconsolidated coquina beds, characterized by a hash of whole shells, comminuted shell, and other skeletal fragments in a loose, primarily carbonate, matrix (although not including foraminifers).



Figure 7.87: Long view looking north from Baudin Beach Jetty (near site BB1), showing the sequence at sites BB2 and BB3. Note the level upper surface (lower blue dotted line) of the Pooraka Formation that extends for many hundreds of metres. Also note the position of the upper alluvial sediments in relation to the underlying aeolianite. The vertical black dotted lines show the location of the BB3 and BB2 site logs. The lower aeolianite (BB3a and BB2a) exists sporadically under the Pooraka Formation, having been eroded completely away in places by the palaeodrainage-channels of a more extensive Pleistocene Deep Creek delta.

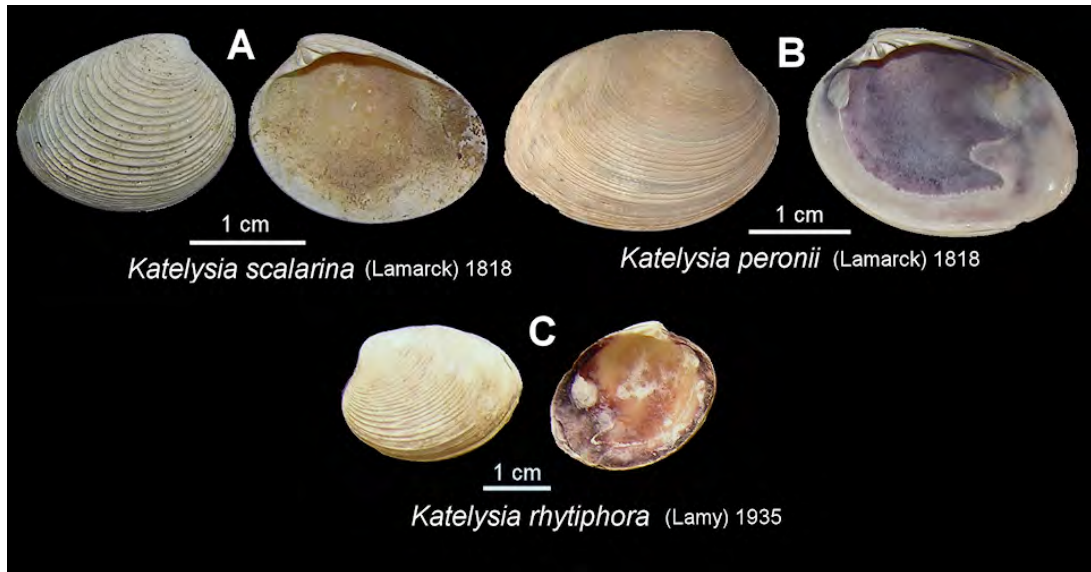


Figure 7.88: Examples of marine molluscs analysed from sites AR1 and AR2 at American River.

American River is a large channel that almost bisects the Dudley Peninsula (Figure 7.89), and broadens to form Pelican Lagoon. In the past the channel may have formed a seaway that isolated the Peninsula from the rest of the island (see section 7.7.1.6). The study site is an extensive tidal flat deposit consisting of densely packed unconsolidated shell layers overlying Tapanappa Formation metasandstones of the Kanmantoo Group (these outcrop extensively north of Buicks Point—see Figure 7.90).

The sediment contains numerous species of bivalves, and gastropods, typical of lagoonal, tidal flat, sand flat and estuarine contexts. The deposits cover a large area, and are characterised by low arcuate features which have similar morphology to beach ridges.

7.3.8.1 American River geochronology

Marine bivalves (although not foraminifers as they were so rare) were sampled from two sites at American River, designated AR1 and AR2. AR1 is approximately 320 meters from AR2, bearing 80 degrees east (Figure 7.89). The AR1 sample site (Figure 7.89) is a pit excavated into the samphire tidal flat sediment down to sea-level (water level); the mollusc samples were removed at +0.4 to +0.5 m above sea-level (APSL), and at sea-level. Figure 7.91 gives further sample site details.

Third party source;
Images redacted at
request of thesis author

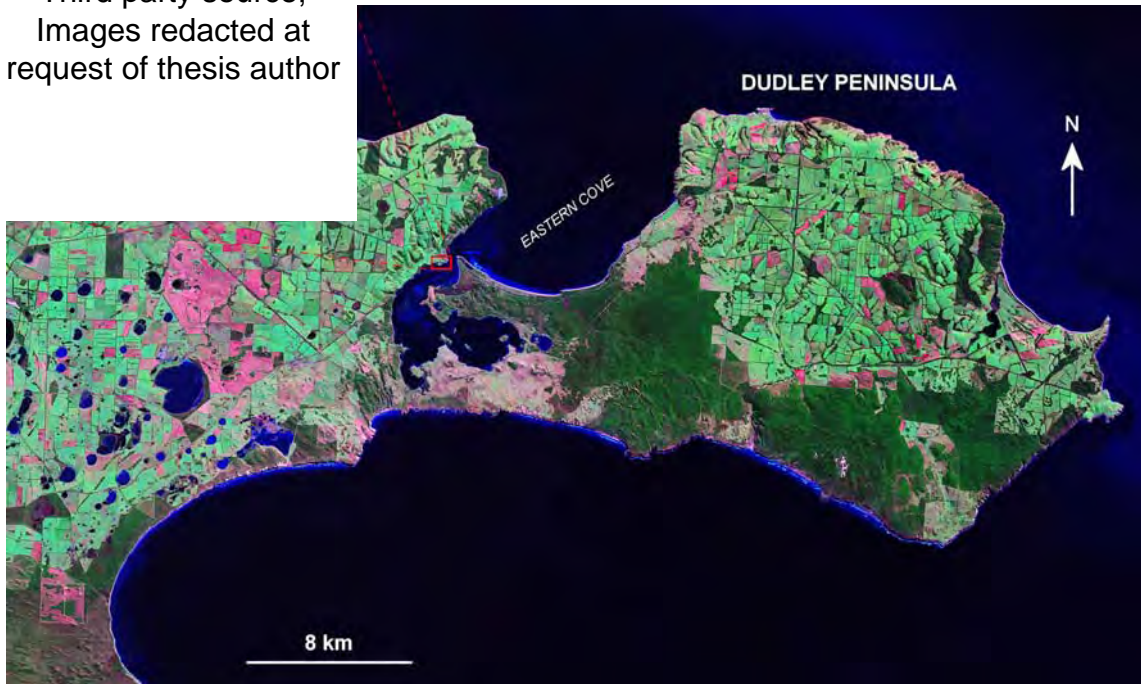


Figure 7.89: Location of American River sites (red circles upper LH inset) on the western side of the Dudley Peninsula (upper LH image from Google Earth, 2010) (main image is a Landsat ETM: NASA Landsat program, 2001).



Figure 7.90: Cambrian Tapanappa Formation outcropping at American River, north from Buicks Point.

AR2 is a higher site, and marine shell was removed for analysis from a wave-cut beach ridge. The tidal wash sediments were excavated from the face of the exposure and marine shell was collected at +0.7 m APSL and +1.2 m APSL (Figure 7.91).

An AMS ^{14}C shell sub-sample (AR#3-2AMS from sample AR#3-2) was extracted from site AR1 at the +0.4 to +0.5 level. One half of the marine shell (*Katelysia rhytiphora*) was submitted to Waikato Radiocarbon Dating Laboratory (Waikato University, New Zealand: Dr. A. Hogg) for AMS ^{14}C dating. The remaining shell was sub-sampled from the umbo region (4 small sections from the umbo taken for analysis) and subsequently analysed for amino acid D- and L-enantiomers.

The derived radiocarbon age (5154 ± 45 a BP [Wk-21538]) was calibrated by means of OxCal version 3.10 (Bronk Ramsey, 2005) and the marine curve of Hughen *et al.* (2004) (corrected for the marine reservoir effect using a ΔR value of 62 ± 63). The calibrated AMS ^{14}C age for AR#3-2AMS was 5455 ± 105 a BP (1σ), and the corresponding mean GLX D-L ratio for the shell was 0.179 ± 0.011 (Table 7.27). Figure 7.92 gives the OxCal calibration for sample AR#3-2AMS.

Table 7.27: AMS ^{14}C ages and sample details for American River mollusc samples.

Lab. No. ^a	Sample code	Location / (S. Lat. E. Long.)	Genus / species (N) ^b	GLX D-L ratio $\pm 1\sigma$	Uncalibrated radiocarbon age (a BP) $\pm 1\sigma^c$	Calibrated radiocarbon age (a BP) ^d $\pm 1\sigma^c$
Wk-21538	AR#3-2AMS	American River / 35° 47' 17.9" 137° 46' 03.3"	<i>Katelysia rhytiphora</i> (4)	0.179 ± 0.011	5154 ± 45	5455 ± 105
Wk-21537	AR#3-5AMS	American River / 35° 47' 15.8" 137° 46' 16.1"	<i>Katelysia scalarina</i> (4)	0.137 ± 0.010	2833 ± 32	2495 ± 115

^a Waikato Radiocarbon Dating lab code

^b N = number of subsamples (portions of umbo) analysed from individual mollusc

^c Uncertainties are 1σ (one standard deviation: 68% confidence interval)

^d Marine data from Hughen *et al.* (2004); ΔR 62 ± 63 ; calibrated using OxCal v3.10 Bronk Ramsey (2005); cub r:5 sd:12 prob usp [chron]

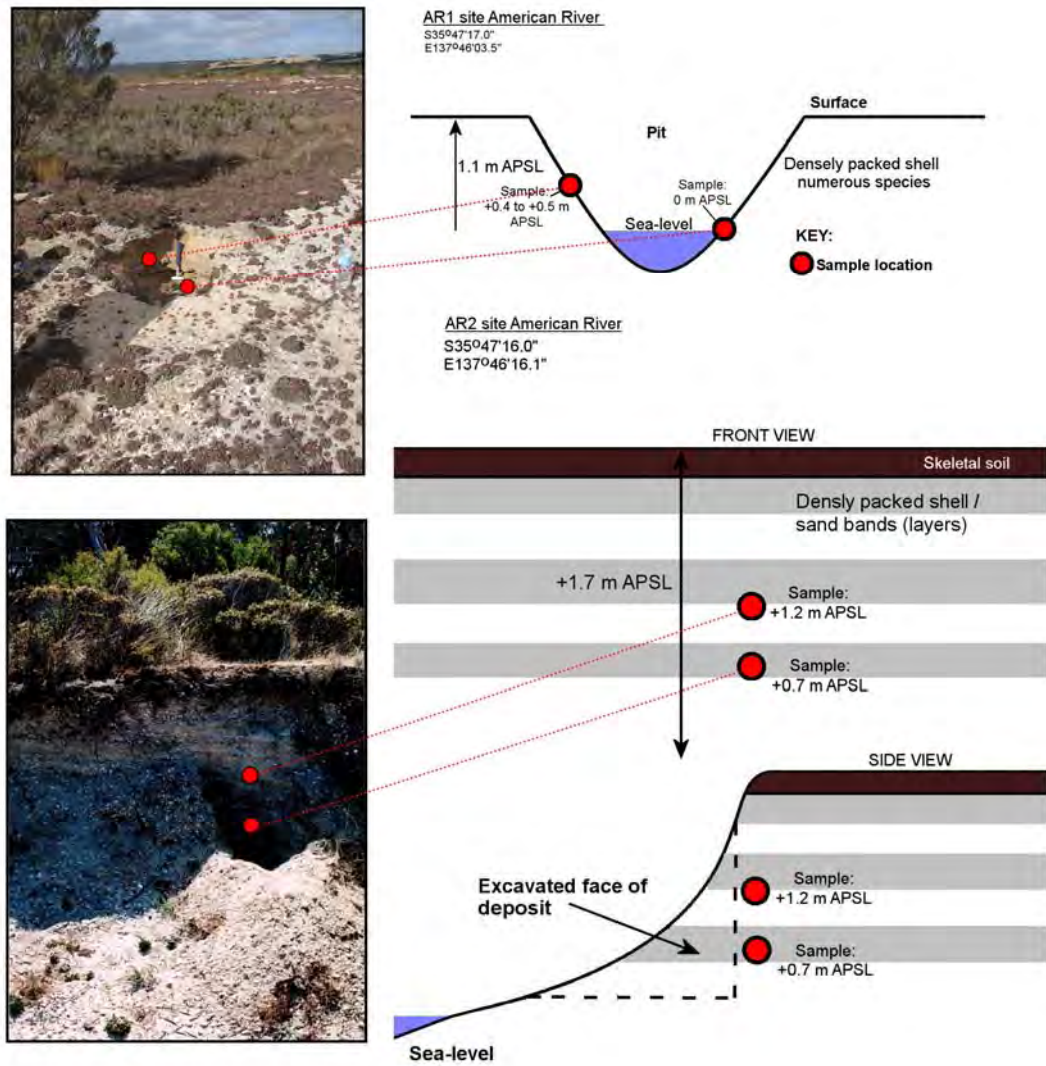


Figure 7.91: AR1 and AR 2 sites at American River, with sample locations (red circles). The schematics are not to scale.

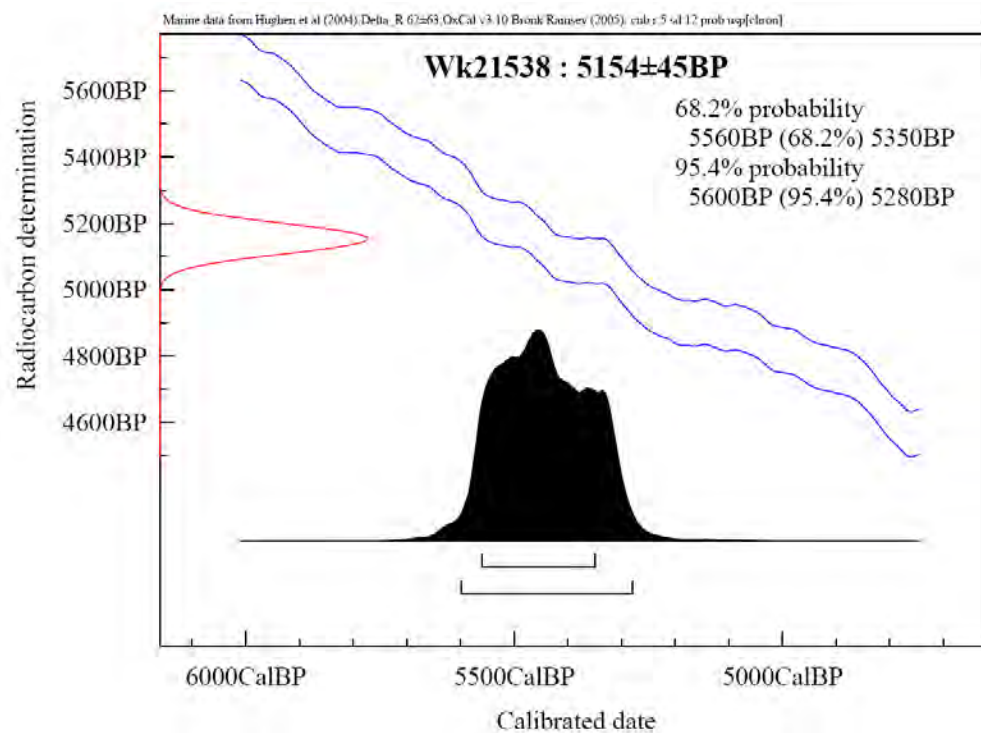


Figure 7.92: OxCal (V. 3.10) calibration plot for American River AMS ^{14}C sample AR#3-2AMS.

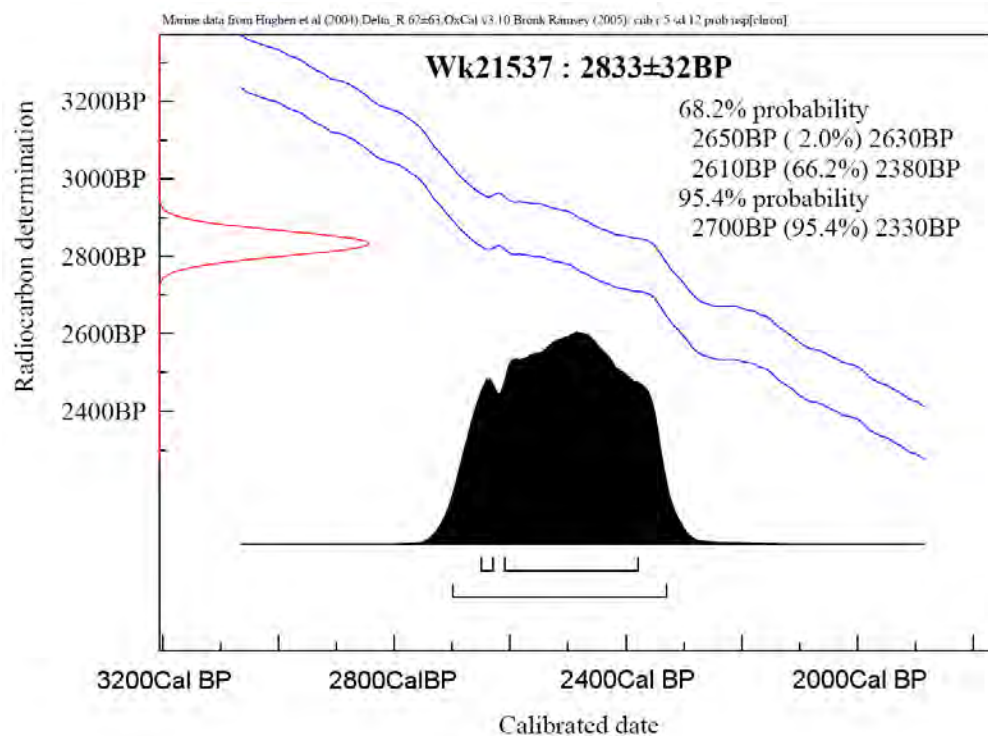


Figure 7.93: OxCal (V. 3.10) calibration plot for American River AMS ^{14}C sample AR#3-5AMS.

As above a single shell (*Katelysia scalarina*: AR#3-5AMS) was extracted from sample AR#3-5 (site AR2 at 1.2 m ASPL) for AMS ^{14}C dating. The same procedure was used as with AR#3-2AMS. The radiocarbon age (2833 ± 32 a BP [Wk-21537]) was calibrated as above, and an AMS ^{14}C age estimate of 2495 ± 115 a BP (using the 66.2% probability range: see Figure 7.93) was derived (the corresponding GLX D-L ratio was 0.137 ± 0.010) (Table 7.27). These ages were used to calibrate GLX D-L ratio data for unknown age Holocene marine mollusc samples (see Chapter 6, section 6.6.4.1). The ages were also used in the Pleistocene mollusc calibration (see Chapter 6, section 6.6.4.1).

High resolution sampling of molluscs was not undertaken at either of the sites at American River. Only two samples were removed from each site, from shell bands near the centre of the deposits and near the bases—samples were also removed from the tops of the deposits, however, these were not analysed for AAR as the greater diagenetic temperature variation experienced by near-surface shells (because of the lack of insulating overburden) would affect the D-L ratios. The shells beds represent thanatocenose rather than biocenose faunal assemblages, as no articulated individuals were found, and many shells were broken. Even during the early stage of this research it was deemed likely that both sites comprised shell material that was greatly reworked.

Thirty individual shells (*Katelysia scalarina* and *Katelysia peronii*) were analysed using AAR methods from the +0.4 to +0.5 m APSL level of the pit at site AR1 (sample AR#3-2). The ASX and GLX D-L ratio results when plotted (bivariate) formed a tight cluster with a mean GLX D-L ratio of 0.088 ± 0.008 (see Figure 7.94). The age estimate for this mean was 0.52 ± 0.10 ka (Table 7.28). The lower (sea-level) sample (AR#3-3, 5 shells analysed: *Katelysia rhytiphora* and *Katelysia peronii*) had a higher set of D-L ratios. Four shells clustered with a GLX mean D-L ratio of 0.148 ± 0.009 , and 1 shell was much higher with a GLX D-L ratio of 0.215 ± 0.003 (Figure 7.94). These gave AAR age estimates of 3.19 ± 0.58 ka and 8.84 ± 1.50 ka, respectively (Table 7.28).

Table 7.28: Holocene American River marine mollusc ASX and GLX AAR data, and AAR numerical ages

Lab. No.	Location: site (position)	Site code / facies / AMINOCLUSTER*	Location (S Lat. E Long.)	CMA T ^a °C	Genus and species / (N) ^b	ASX D-L ratio $\pm 1\sigma^c$	Coefficient of variation (CV%)	GLX D-L ratio $\pm 1\sigma^c$	Coefficient of variation (CV%)	AAR GLX age estimate (ka) ^d $\pm 1\sigma^c$
UWGA 5394, 5513, 6509	American River: AR1 (+0.40 to +0.50 m APSL)	AR#3-2 / unconsolidated shell beds / AMINOCLUSTER 1	35° 47' 17.9" 137° 46' 03.3"	15.4	<i>Katelsysia scalarina</i> and <i>Katelsysia peronii</i> (30)	0.204 \pm 0.010	4.7	0.088 \pm 0.008	8.6	0.52 \pm 0.10
UWGA 6510	American River: AR1 (sea-level)	AR#3-3 / unconsolidated shell beds / AMINOCLUSTER 2	35° 47' 17.9" 137° 46' 03.3"	15.4	<i>Katelsysia rhytiphora</i> and <i>Katelsysia peronii</i> / (5)	0.308 \pm 0.011	3.4	0.148 \pm 0.009	6.3	3.19 \pm 0.58
UWGA 6510	American River: AR1 (sea-level)	AR#3-3 / unconsolidated shell beds / AMINOCLUSTER 4	35° 47' 17.9" 137° 46' 03.3"	15.4	<i>Katelsysia rhytiphora</i> / (1)	0.392 \pm 0.006	1.6	0.215 \pm 0.003	1.6	8.84 \pm 1.50
UWGA 5509-5512, 5518-5522, 6512, 6513	American River: AR2(+0.70 and +1.2 m APSL)	AR#3-5, 3-6 / unconsolidated shell beds / AMINOCLUSTER 2	35° 47' 15.8" 137° 46' 16.1"	15.4	<i>Katelsysia scalarina</i> , <i>Katelsysia rhytiphora</i> and <i>Katelsysia peronii</i> / (27)	0.310 \pm 0.015	5.0	0.141 \pm 0.009	6.7	2.75 \pm 0.50
UWGA 5509-5512, 5518-5522, 6512, 6513	American River: AR2(+0.70 and +1.2 m APSL)	AR#3-5, 3-6 / unconsolidated shell beds / AMINOCLUSTER 3	35° 47' 15.8" 137° 46' 16.1"	15.4	<i>Katelsysia scalarina</i> , <i>Katelsysia rhytiphora</i> and <i>Katelsysia peronii</i> / (11)	0.360 \pm 0.008	2.1	0.166 \pm 0.012	7.2	4.48 \pm 0.82
UWGA 5509-5512, 5518-5522, 6512, 6513	American River: AR2(+0.70 and +1.2 m APSL)	AR#3-5, 3-6 / unconsolidated shell beds / AMINOCLUSTER 4	35° 47' 15.8" 137° 46' 16.1"	15.4	<i>Katelsysia scalarina</i> , <i>Katelsysia rhytiphora</i> and <i>Katelsysia peronii</i> / (4)	0.421 \pm 0.010	2.4	0.204 \pm 0.015	7.2	7.77 \pm 1.43

^a Current mean annual temperature estimated for these sites from annual temperature data via climate recording stations around Kangaroo Island (<http://www.bom.gov.au/climate/data/>)

^b Number of molluscs used for D-L ratio estimate

^c Uncertainties are 1 σ (one standard deviation—68% confidence interval)

^d Numerical age estimate from an AMS ¹⁴C calibration (*Katelsysia* spp. from American River) using an apparent parabolic kinetics model (Mitterer and Kriausakul, 1989; Murray-Wallace *et al.*, 2001); uncertainties are calculated from the square root of the sum of the squares of all error terms

*Group of amino acid D-L ratios delineated via multivariate analysis

At site AR2 D-L ratios determined for marine shell from both levels in the pit (+0.7 m APSL and +1.2 m APSL) overlaid each other revealing 3 distinct populations (Figure 7.95). As each population had representatives in each sample position (i.e. +0.7 m and +1.2 m APSL) the implication was that the shells in the profile at site AR2 (at least between 0.7 m and 1.2 m) were reworked. Multivariate cluster analysis was used to define the clusters (using ASX D-L ratios rather than GLX, as the faster racemizing ASX allowed for better differentiation in the clusters—multivariate analysis was not used on the AR1 data as the clusters were easily defined by eye, i.e., see Figure 7.94).

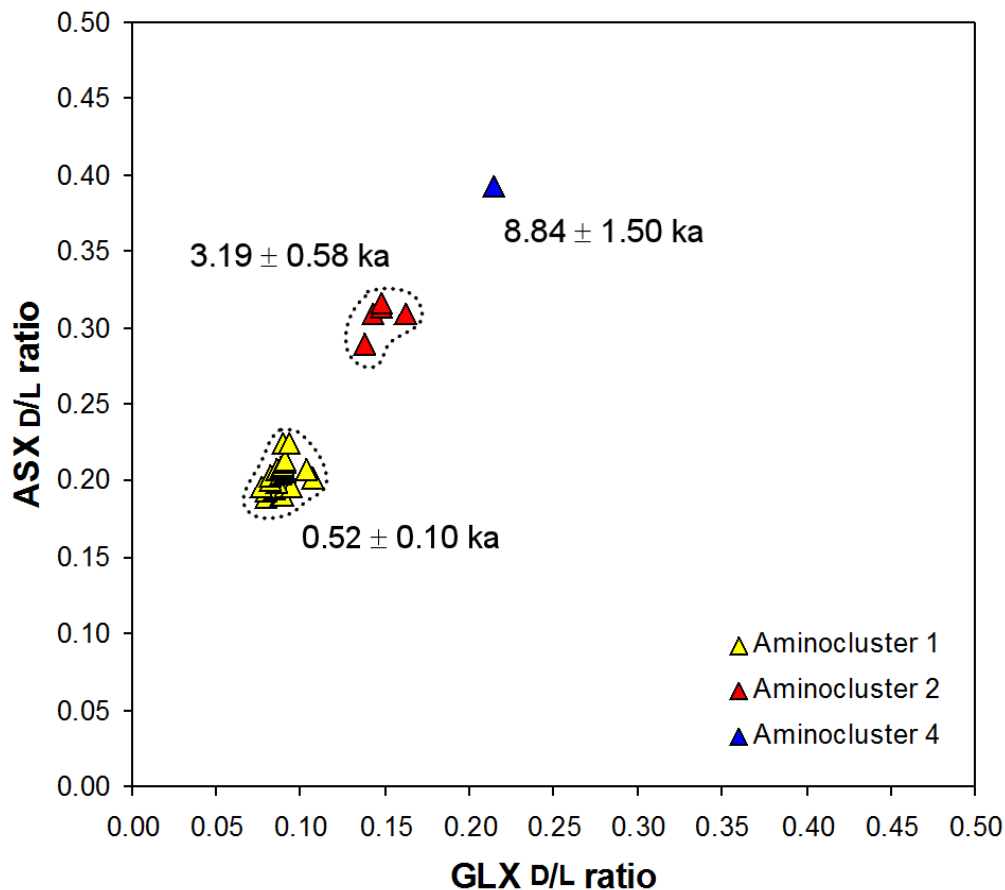


Figure 7.94: Bivariate plot of ASX vs. GLX for AR1 site marine molluscs (*Katelysia scalarina*, *Katelysia peronii* and *Katelysia rhytiphora*). Cluster 1 represents a group of shells from +0.4 to +0.5 m APSL, cluster 2 from sea level, and cluster 4 from sea level (cluster 3 is present at site AR2) (see Table 7.26 for D-L ratios).

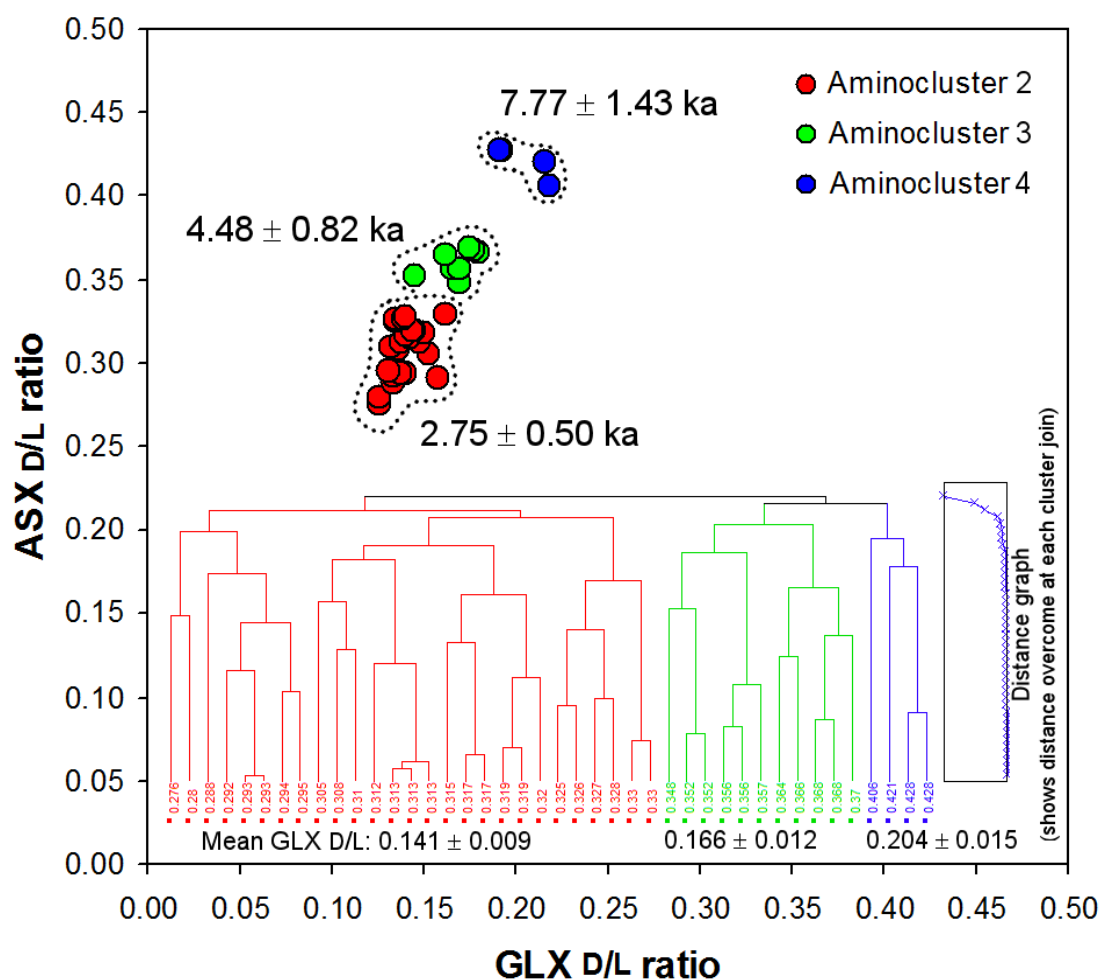


Figure 7.95: Bivariate plot of ASX vs. GLX for AR2 site marine molluscs (*Katelsia scalarina*, *Katelsia peronii* and *Katelsia rhytiphora*). Inset is the Ward method multivariate plot used to differentiate the clusters.

In light of the reworking of marine shell, the distinctive shell bands observable at site AR2 (see Figure 7.96) can not really be dated via amino acid racemization, i.e., the depositional timing of the bands themselves. A method of age determination (such as OSL: provided there is sufficient quartz), that delineates time of deposition would be better suited. The amino acid results, however, do allow the determination of periods of carbonate production, and patterns of reworking. The ages for the clusters at AR2 are 2.75 ± 0.50 ka, 4.48 ± 0.83 ka and 7.77 ± 1.43 ka (Figure 7.95 and Table 7.28). Clusters 2 and 4 are also represented at site AR1 (Figure 7.94).

7.3.8.2 Discussion of the American River geochronology

Figure 7.97 presents all of the American River data (AR1 and AR2) and it can be seen that the older aminoclusters from AR1 (triangles) overlie the same



Figure 7.96: Shell and sandy bands (layers) at site AR2, American River.

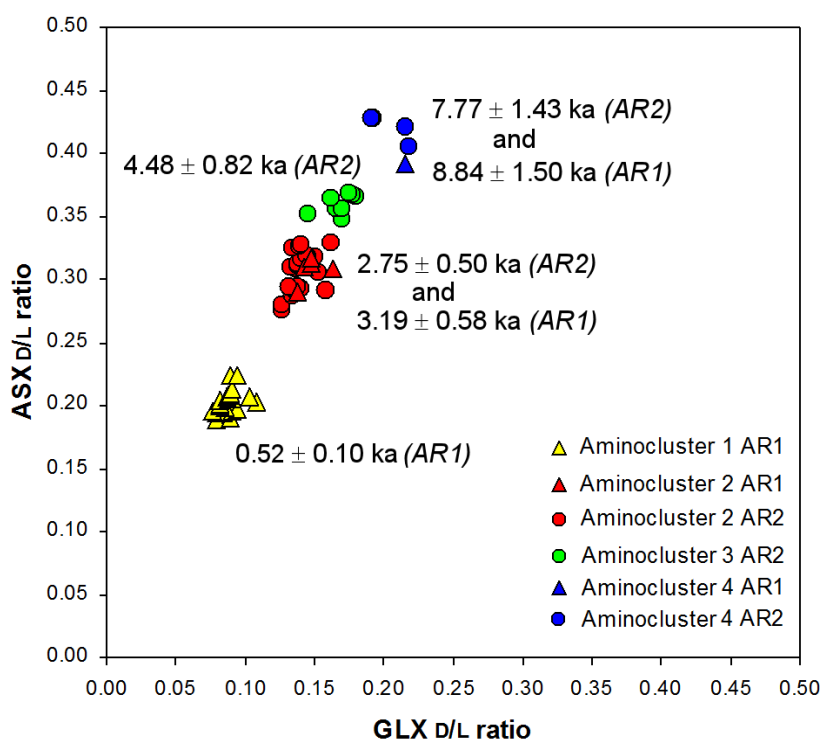


Figure 7.97: Bivariate plot of ASX vs. GLX for all shells analysed at American River. The ages were determined using a mean GLX D-L value (determined by Ward method multivariate clustering in ASX D-L ratios) for each cluster, using an apparent parabolic kinetics model (calibrated using the AMS ^{14}C ages—above). Triangles designate site AR1 and circles AR2.

clusters at AR2. Aminocluster 1 is not apparent at site AR2, even though these shells were sampled close to the same level as AR2. The lower elevation of the AR1 site has allowed for the deposition of younger sediments. The older ages (~8 ka: aminocluster 4) may reflect the onset of marine carbonate production at American River during the later stages of the post-glacial marine transgression (10 ka to 7ka), where sea-level was approaching its present position (reaching a level of circa +1 m at approximately 7 to 6 ka in southern Australia) (Belperio *et al.*, 2002).

The other aminoclusters (3 and 2) may represent pulses of carbonate production related to climatic optima and oscillating sea-levels that occurred through the middle to late Holocene (cf. Lewis *et al.*, 2008: centennial scale pulses of higher than present sea-level at approximately 4.6 ka and at 2.8 ka [circa +0.3 to +1 m sea-level]).

The shell beds at AR2 were deposited sometime after approximately 3 ka, apparently at times of slightly higher-than-present sea-level, i.e., the banding of shelly and sandy layers may specify periods of higher and lower sea-level (the finer sandy bands indicating hiatuses in marine deposition). Conversely, the banding may also have occurred as a result of seasonal fluctuations in depositional conditions, i.e. high (stormy?) to low energy conditions. Regardless, in order to determine the precise nature of the banding high resolution OSL dating of the less shelly bands would be required.

The age estimate for aminocluster 1 at site AR1 points to a period of carbonate production at approximately 0.5 ka (Figure 7.97). The sediment banding at site AR2 is not evident here, perhaps indicating a shorter depositional period.

Given the AMS ^{14}C and AAR age determinations the sites at American River are considered to host intertidal and tidal flat sediments of the Holocene St. Kilda Formation (cf. Firman, 1966).

7.3.9 Kingscote Conglomerate

As discussed in Chapter 3, the Kingscote study site is an extensive raised (+3.5 to +3.0 m APSL—top of unit) basalt cobble/pebble (Jurassic Wisanger Basalt is the most common cobble, with occasional limestone and quartz cobbles)

conglomerate beach deposit, strongly cemented in a fine carbonate matrix, with relatively abundant whole and broken shell. The thickness of the unit varies in conjunction with the undulations in the karstified underlying Kingscote Limestone (Late Eocene to early Late Oligocene: Milnes *et al.* [1983]); it ranges from a few 10s of cm to over 1 m in thickness. The lateral extent exposed sporadically in outcrop is approximately 680 m (Figure 7.4 and 7.98). The unit is usually unconformably overlain by a thin calcrete, and soil mantle, although the conglomerate is sometimes exposed on the surface (Figure 7.99). Clay pot Karst features are also present.

Good outcrop of the unit can be found south of Beare Point, near Rolls Point (see Figure 7.98, 7.100, 7.101 and 7.103) and there is a small unconsolidated and pedogenically modified exposure near the boat ramp south-east of “The Bluff” (Figure 7.98, 7.102 and 7.10). Here the matrix is soft and unconsolidated (light brown colouring: Munsell 10YR 8/4), with flat basalt pebbles and marine shell falling out of the exposure. The unit is overlain by a massive, thick red-brown soil, which is possibly alluvial in origin.

The Kingscote Conglomerate unit was first described by Howchin (1899) who regarded it as a Recent coastline deposit. Bauer (1959) suggested a Pleistocene age based upon molluscs found in the unit. Further examination of the molluscan and foraminiferal assemblages led Milnes *et al.* (1983) to consider a Late Pleistocene age, equating the conglomerate with the south Australian Glanville Formation (cf. Firman, 1967; Cann, 1978; Belperio *et al.*, 1983, 1984; Hails *et al.*, 1984; Murray-Wallace *et al.*, 1988; Murray-Wallace and Belperio, 1991). The AAR dating work completed (in this thesis) on the Kingscote conglomerate agrees with Milnes *et al.* (1983) chronological interpretation.

7.3.9.1 Kingscote Conglomerate geochronology

Amino acid racemization analyses were undertaken on marine shell, and foraminifers recovered from the conglomerate near Rolls Point (site KC1) and the boat ramp exposure (site KC2) (Figure 7.98). Six specimens of *Katelsysia scalarina* were recovered from the KC1, although very few usable foraminifers could be found (3 only of *Discorbis dimidiatus* that were suitable for



Figure 7.98: Extent in outcrop of the Kingscote Conglomerate, at sites KC1 and KC2, Kingscote, Kangaroo Island (Landsat ETM image: NASA Landsat program, 2001).



Figure 7.99: Kingscote Conglomerate exposed at surface, near Rolls Point (site KC1), Kingscote.



Figure 7.100: Kingscote Conglomerate near Rolls Point (site KC1). Note solution pipe middle background (knapsack for scale: 50 cm)

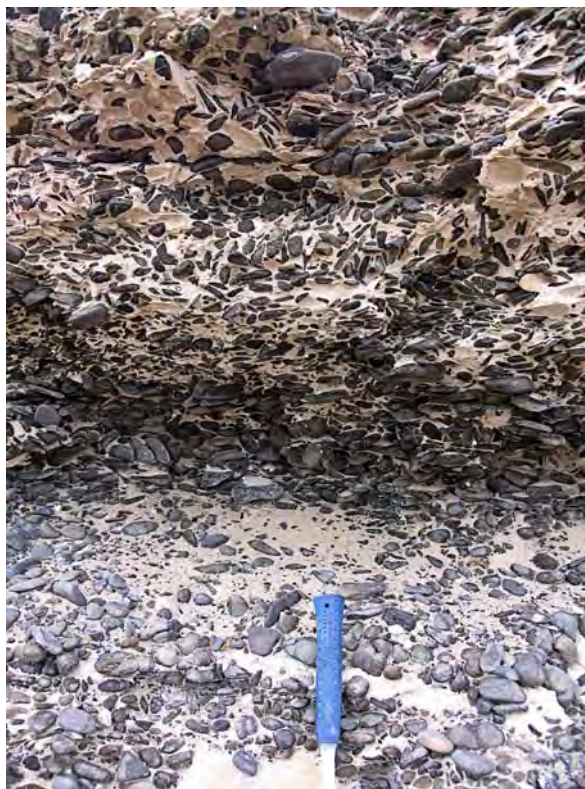


Figure 7.101: Close-up of the Kingscote Conglomerate unit (near Rolls Point). Note abundant basalt clasts (rock-hammer handle for scale: 20 cm).

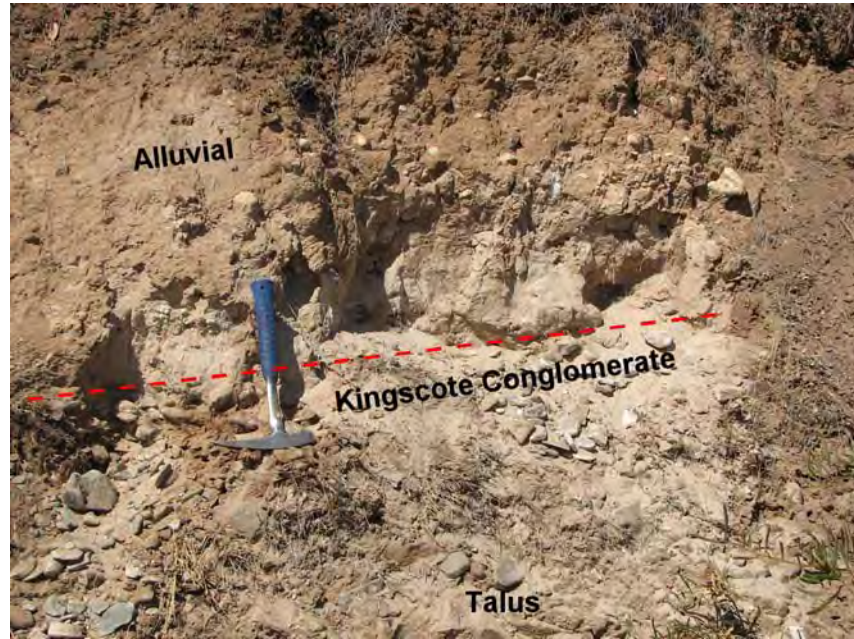


Figure 7.102: Kingscote Conglomerate at site KC2. Red dashed line shows approximate position of the unit (uppermost) (rock-hammer for scale: 33 cm)

Third party source; Images redacted at request of thesis author



Figure 7.103: Location of Kingscote study site. The upper LH inset shows GPS data points (yellow points) for extent in outcrop of the Kingscote Late Pleistocene raised basalt conglomerate. The unit is most extensive south of Beare Point near, and south-west of, Rolls Point. There is also a small unconsolidated and pedogenically modified exposure at the rear of the boat ramp south-east from “The Bluff” (upper LH inset, from Google Earth [2010]) (main image is a Landsat ETM: NASA Landsat program, 2001).

Table 7.29: Kingscote Conglomerate Pleistocene marine mollusc ASX and GLX AAR data, and AAR numerical ages

Lab. No.	Site	Site code / facies	Location (S Lat. E Long.)	CMAT ^a °C	Genus and species / (N) ^b	ASX D-L ratio ± 1σ ^c	Coefficient of variation (CV%)	GLX D-L ratio ± 1σ ^c	Coefficient of variation (CV%)	AAR GLX age estimate (ka) ^d ± 1σ ^c
UWGA 5857, 5858, 5863, 5865, 5866	Kingscote Rolls Point	KC1 / raised pebble / cobble beach	35° 39' 37.1" 137° 38' 0.24"	15.4	<i>Katelysia</i> <i>scalarina</i> / (5)	0.576 ± 0.020	3.5	0.354 ± 0.019	5.4	129 ± 29
UWGA 5864	Kingscote Rolls Point	KC1 / raised pebble / cobble beach	35° 39' 37.1" 137° 38' 0.24"	15.4	<i>Katelysia</i> <i>scalarina</i> / (1)	0.601 ± 0.003	0.4	0.488 ± 0.006	1.2	264 ± 57
UWGA 5870	Kingscote boat ramp	KC2 / raised pebble / cobble beach	35° 48' 57.2" 137° 48' 41.5"	15.4	<i>Nerita</i> (<i>Melanerita</i>) <i>atramentosa</i> / (3)	0.730 ± 0.006	0.8	0.425 ± 0.008	1.9	195 ± 42
UWGA 5868	Kingscote boat ramp	KC2 / raised pebble / cobble beach	35° 48' 57.2" 137° 48' 41.5"	15.4	<i>Amesodesma</i> <i>angusta</i> / (7)	0.543 ± 0.027	4.9	0.429 ± 0.017	4.0	199 ± 44

^a Current mean annual temperature estimated for these sites from annual temperature data via climate recording stations around Kangaroo Island

(<http://www.bom.gov.au/climate/data/>)

^b Number of molluscs used for D-L ratio estimate

^c Uncertainties are 1 σ (one standard deviation—68% confidence interval)

^d Numerical age estimate from a U-series AMS ¹⁴C calibration (fossil coral recovered from Vivonne Bay and fossil shell from American River) using an apparent parabolic model (Mitterer and Kriausakul, 1989; Murray-Wallace *et al.*, 2001); uncertainties are calculated from the square root of the sum of the squares of all error terms (U-series age of *Plesiastrea versipora*: a stony coral recovered from same unit as the marine shell *Nerita (Melanerita) atramentosa* (PE#3-5), and used to calibrate the GLX D-L ratio. ¹⁴C ages used to calibrate Holocene *Katelysia* spp. from American River).

Table 7.30: Kingscote Conglomerate Pleistocene single foraminifer ASX and GLX AAR data, and numeric AAR age estimates

Lab. No.	Site	Site code / facies	Location (S Lat. E Long.)	CMAT ^a °C	Genus and species / (N) ^b	ASX D-L ratio) $\pm 1\sigma^c$	Coefficient of variation (CV%)	GLX D-L ratio) $\pm 1\sigma^c$	Coefficient of variation (CV%)	AAR GLX age estimate (ka) ^d $\pm 1\sigma^c$
UWGA 7010	Kingscote Rolls Point	KC1 / raised pebble / cobble beach	35° 39' 37.1" 137° 38' 0.24"	15.4	<i>Discorbis dimidiatus</i> / (3)	0.536 \pm 0.100	18.6	0.325 \pm 0.053	16.3	132 \pm 44
UWGA 7011, 7012	Kingscote boat ramp	KC2 / raised pebble / cobble beach	35° 48' 57.2" 137° 48' 41.5"	15.4	<i>Discorbis dimidiatus</i> and <i>Elphidium sp.</i> / (6)	0.534 \pm 0.029	5.4	0.323 \pm 0.028	8.6	130 \pm 39

^a Current mean annual temperature estimated for these sites from annual temperature data via climate recording stations around Kangaroo Island (<http://www.bom.gov.au/climate/data/>)

^b Number of foraminifera used for D-L ratio estimate

^c Uncertainties are 1 σ (one standard deviation—68% confidence interval)

^d Numeric age estimate from a U-series calibration (fossil coral recovered from Vivonne Bay: 114 \pm 3 ka) using an apparent parabolic model (Mitterer and Kriaušakul, 1989; Murray-Wallace *et al.*, 2001); uncertainties are calculated from the square root of the sum of the squares (addition in quadrature) of all uncertainty terms



Figure 7.104: Mollusc species analysed for AAR D-L enantiomers, from the Kingscote Conglomerate, Kingscote, Kangaroo Island.

AAR analysis—several *Marginopora vertebralis* were also found, although these were not analysed). The molluscs were clustered at two GLX D-L ratio means: 0.354 ± 0.019 ($N = 5$) and 0.488 ± 0.006 ($N = 1$) (see Figure 7.103 and 7.104 and Table 7.29). The higher D-L ratio most likely represents a reworked shell (the shell, however, was not taphonomically dissimilar to the shells with lower D-Ls). These means were calibrated using the apparent parabolic kinetics mollusc calibration (Chapter 6, section 6.6.4.1), yielding age estimates of 129 ± 29 ka and 264 ± 57 ka (Table 7.29). The lowest set of GLX D-L ratios is representative of the “true” age of the deposit. Here a Last Interglacial age (MIS 5e) is probable given the extent of racemization in the marine molluscs and the morphostratigraphical position of the unit (approximately +3.0 m APSL) (see Figure 7.106). Only 3 useable foraminifers could be recovered from the sediments sampled at KC1, and these gave a Foram AAR age (foraminifer calibration: Chapter 6, section 6.6.4.2) of 132 ± 44 ka (mean GLX D-L ratio: 0.325 ± 0.053 —the data were scattered resulting in a large uncertainty) (Table 7.30). This age, even though based upon few data, agrees quite well with the Mollusc AAR age.

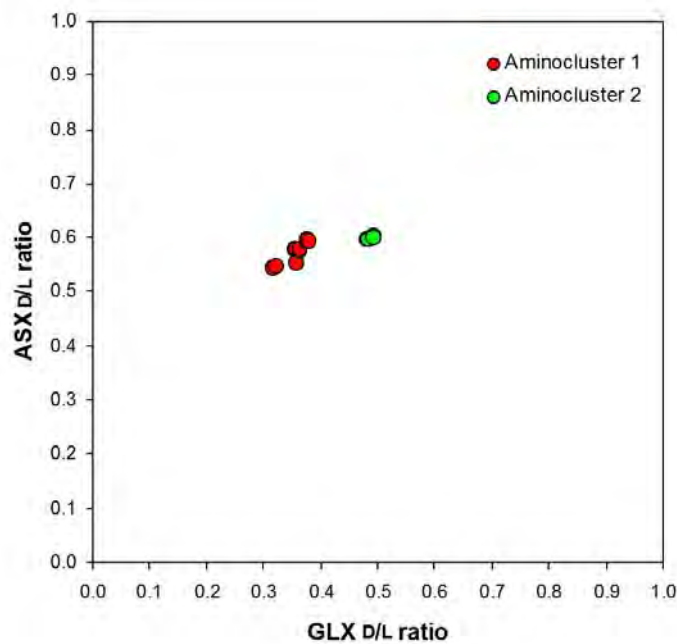


Figure 7.105: Amino acid D-L ratio bivariate plot for *Katelaysia scalarina* (N = 6) extracted from the Kingscote conglomerate (site KC1). The lower GLX D-L ratio population was used to determine the AAR age.

At site KC2 10 molluscs were recovered for analysis (7 *Amesodesma angusta*, and 3 *Nerita* [*Melanerita*] *atramentosa*) (Figure 7.104). The mean of the ages (see Table 7.27) derived for these two genera is 197 ± 43 ka (mean GLX D-L ratios: 0.429 ± 0.017 and 0.425 ± 0.008) (see Figure 7.106 and Table 7.29). This is older than expected, in comparison to the age at site KC1. It is possible that the shells analysed were part of a reworked population. It is also possible that the sediments were subaerially exposed for a period of their history (or were buried at a shallow depth, i.e., <1 m), which could have increased overall racemization rate, as a result of exposure to greater diagenetic temperature flux (Murray-Wallace and Bourman, 2002). This can result in higher than expected amino acid D-L ratios upon analysis. Shallow burial depth of a Last Interglacial raised beach deposit at Sellicks Beach, South Australia (examined in a study undertaken by Murray-Wallace and Bourman [2002]), resulted in higher than expected D-L ratios (ranging from 0.549 to 0.789 for GLX) for a range of marine mollusc genera recovered from the unit. Murray-Wallace and Bourman (2002) concluded that the elevated enantiomeric ratios (in comparison to marine shell recovered from other Last Interglacial sites) were related to a higher integrated diagenetic temperature rather than age variation in the shell.

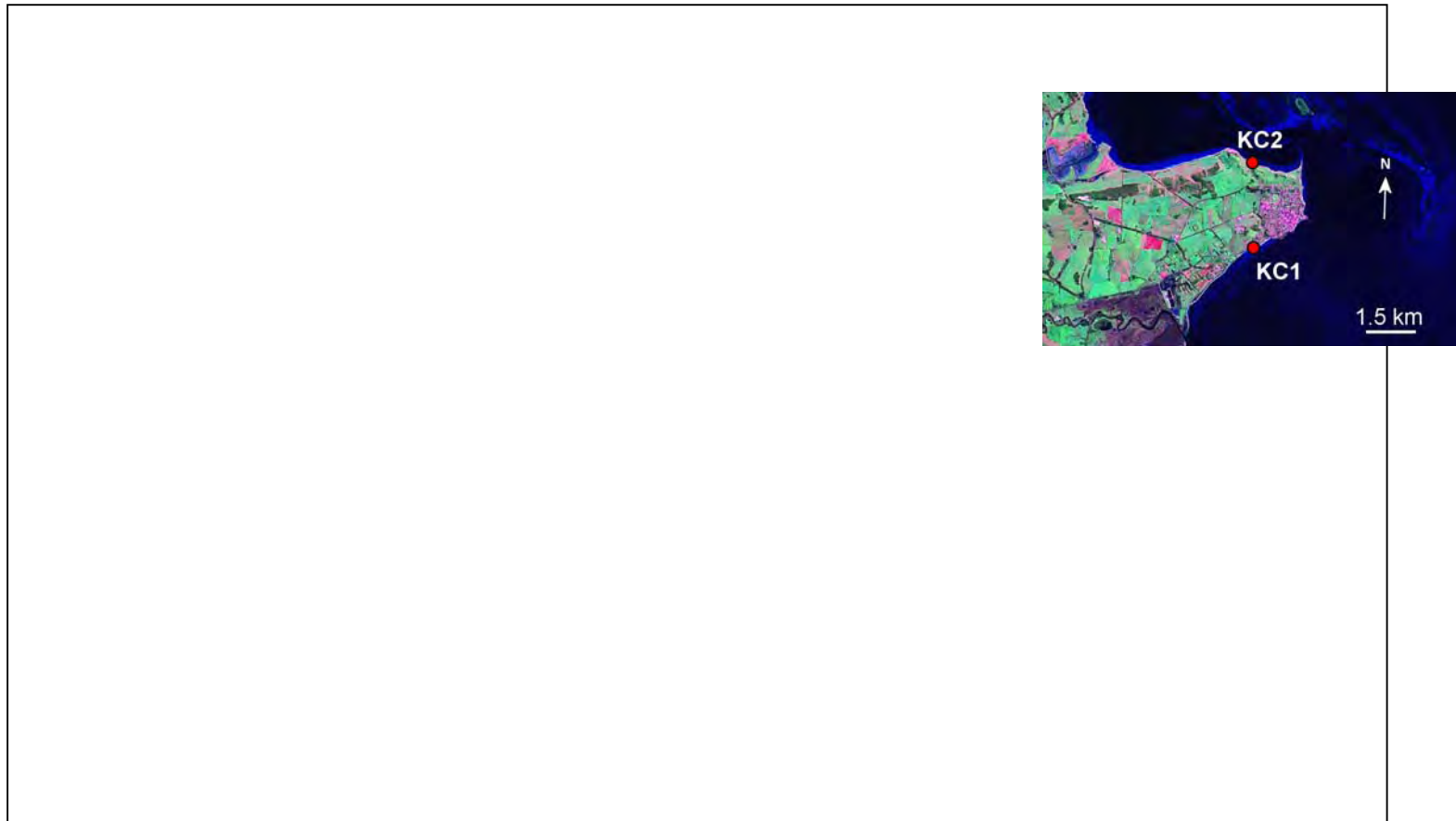


Figure 7.106: Kingscote stratigraphic logs for the sedimentary outcrops near Rolls Point (KC1), and near “The Bluff” (KC2). Included are the geochronological data (blue boxes) and corresponding GLX D-L ratio data (red boxes—numbers in brackets are individuals or subsamples analysed). The top LH insets (A) are panoramas of site KC1 and site KC2 example outcrops. The middle inset (B) is a Kangaroo Island location map (with the location indicated by a black arrow). The site logs are C, and LH inset D comprises a satellite image (Landsat ETM: NASA Landsat program, 2001) showing indicated log and sample sites.

However, AAR analysis on a group of 6 foraminifers extracted from the KC2 matrix sediment did not show similar elevated GLX D-L ratios. The KC2 D-L ratios were almost identical to those of the foraminifers recovered from KC1 (see Table 7.30). The Foram AAR age estimate for KC2 was 130 ± 39 ka (mean GLX D-L ratio: 0.323 ± 0.028), which is in excellent agreement with the ages determined using both molluscs and foraminifers for KC1. In the context of the foraminifer D-L ratio data it seems that the higher ratios for marine shell extracted from the KC2 unit suggest reworking, rather than diagenesis, as a basis for the elevated ages.

7.3.9.2 Discussion of the Kingscote Conglomerate geochronology

The Kingscote conglomerate is confirmed here, using AAR geochronology, to be of Last Interglacial age (mean AAR age ~130 ka: MIS 5e). AAR analyses of marine shell and foraminifers recovered from site KC1 and foraminifers from KC2 yielded several ages that overlap the range of the Last Interglacial highstand (116-132 ka: from sources listed in Siddall *et al.* [2007], i.e., Chen *et al.* [1991]; Gallup *et al.* [1994]; Stirling *et al.* [1998]). The unit itself is a relatively unambiguous indicator of higher-than-present sea-level at time of deposition. The height of the unit (from current sea-level to the top of the unit) averaged at approximately +3.0 m along outcrop. Cobble/pebble beaches are deposited close to sea-level, and generally, clast size decreases up-beach, as a morphological response to landward reduction in wave energy. Smith Bay on the northern coast of Kangaroo Island hosts a modern example of a cobble beach (see Chapter 3), although clast sizes are larger (up to boulder size, however, some of these are erratics eroded from the local Permian till) as the coastal area is less protected than Kingscote Beach, and is therefore higher energy. The Kingscote modern beach itself is also morphologically similar to the raised conglomerate, in places (see Figure 7.107).

The geochronological and morphological data from the Kingscote Conglomerate is also in good agreement with other, similar, sites on the east and south coasts of Kangaroo Island, i.e., Rocky Point, Hanson Bay, Vivonne Bay, and Pennington Bay (see Table 7.31).



Figure 7.107: Cobbles and pebbles (limestone, basalt, and quartz) on Kingscote Beach at the mid-tide level, south of Rolls Point.

Table 7.31: Height data (APSL) for Last Interglacial (MIS 5e) raised beach deposits, and raised shelly deposits on Kangaroo Island.

Location	Site code	Approximate height top of unit (+m APSL) ^a	Depositional age estimate*
Kingscote	KC1 and KC2	3.0-3.5	Last Interglacial (MIS 5e)
Pennington Bay	PB2	3.2	Last Interglacial (MIS 5e)
Vivonne Bay	PE3	3.0	Last Interglacial (MIS 5e)
Hanson Bay	HB1	3.0	Last Interglacial (MIS 5e)
Rocky Point	RP1	2.0	Last Interglacial (MIS 5e)

^a Mean ($\pm 1\sigma$) $+3.0 \pm 0.5$ m APSL

* Based on AAR age estimates (calibrated using luminescence and U-series)

PART IV: North coast geochronology (and Chapter summary)

7.3.10 North Cape

Two sites were examined on North Cape, Kangaroo Island: site NC1, south of Point Marsden, and site NC2, situated in Boxing Bay. The sites are located on the North Cape, a large cape on the northern coast of Kangaroo Island (Figure 7.108).

As discussed in Chapter 3, the coast along NC1 is characterised by broad tidal flats (~100 m wide) and sandy/cobble high-tide beaches. The beach at the study site is bordered by low cliffs cut into Early Pleistocene calcareous sediments, the base of the cliff is strewn with broken blocks of calcrete, and the upper sediments are undercut. These sediments form a large platform (above the cliff-line) that grades towards the north at ~3° of dip, and to the east. The top of the cliff-line near the shore is approximately +4 m APSL. This site has what are probably 2 discrete units: a weakly cemented muddy or clayey sand with *in situ* marine shell (predominantly the marine bivalve *Anapella cycladea*), and an overlying calcrete mantle. These units were informally designated as the North Cape Beds in Chapter 3.

The beach at NC2, in Boxing Bay, is of moderate wave energy, and is characterised by a sandy beach with some storm deposited cobbles and boulders at the landward margin of the berm. The backshore of the beach hosts high calcarenite cliffs (~8 m APSL) that overlie cemented shelly sands and a cemented cobble/pebble beach. The cobble/pebble beach extends to below sea-level at the eastern end of the bay. This would indicate that the cobble/pebble beach was of much greater extent in the past and was subsequently eroded sometime after deposition and cementation. The cobble/pebble beach and thin shelly sands were informally designated as the Boxing Bay Conglomerate in Chapter 3 (this should not be confused with the conglomerate facies associated with the Cambrian Boxing Bay Formation [cf. Daily *et al.*, 1980], which are located further east and west near Point Marsden and White Point [see Figure 7.108])

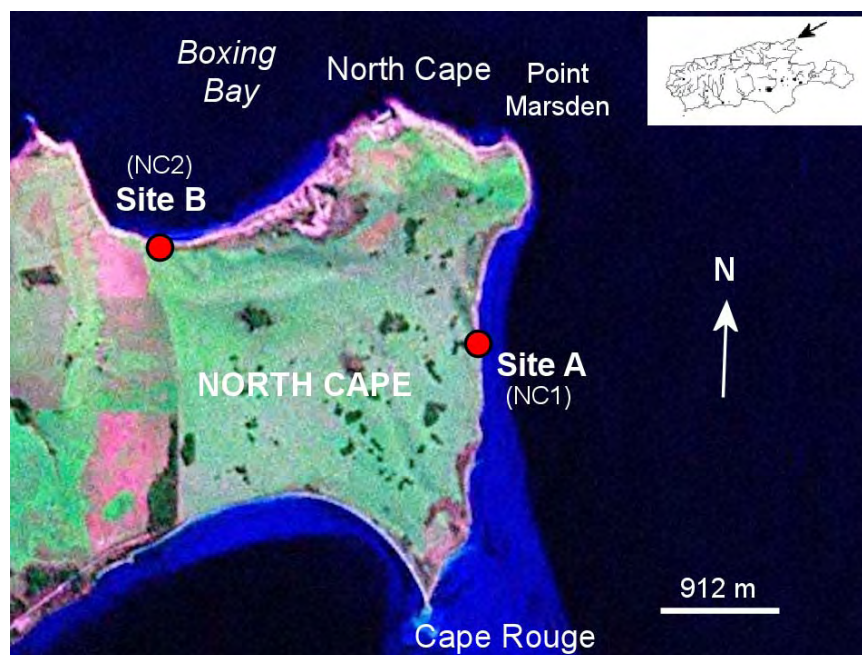


Figure 7.108: Locations for study sites on North Cape, Kangaroo Island. The general locations of sites NC1 and NC2 are designated with red circles (image is a Landsat ETM: NASA Landsat program, 2001). Upper RH inset shows Kangaroo Island location (black arrow).

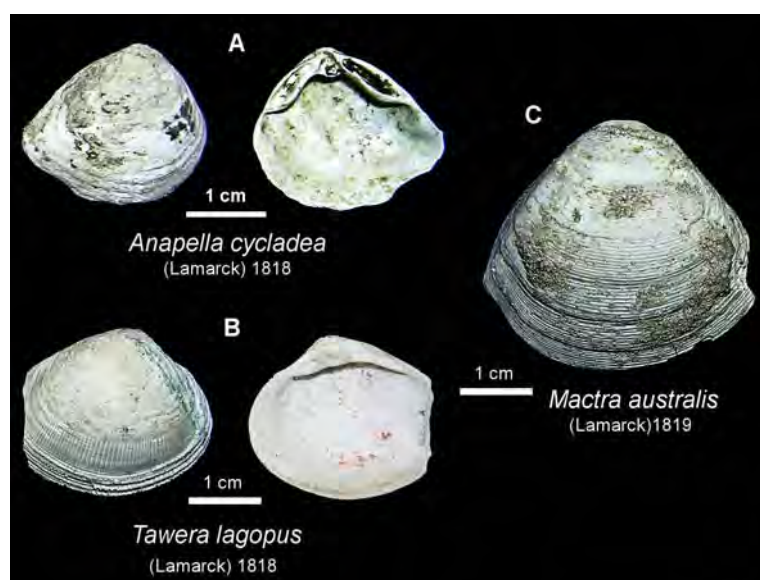


Figure 1.109: Marine shell analysed for amino acid enantiomers. (A) *Anapella cycladea*, from site NC1, characteristic of tidal inlets, estuarine contexts and tidal flats. (B) *Tawera lagopus* and *Mactra australis*, from site NC2, characteristic of moderate to high energy beaches in shallow, sandy contexts.

7.3.10.1 North Cape site NC1 geochronology

Two marine shells (*Anapella cycladea*: see Figure 7.109) were analysed for amino acid enantiomers from the muddy sand unit (aii) at site NC1 (see Figure 7.108, 7.110 and 7.112). One was articulated and the other was a single valve.

Neither whole-rock analysis nor single foraminifer analysis was undertaken at this site as the sediments contained very low concentrations of amino acids, and no foraminifera were visible. The molluscs yielded a near racemic mean GLX D-L ratio of 0.978 ± 0.015 (see Table 7.31). When this was calibrated using the apparent parabolic kinetics Mollusc calibration (Chapter 6), an amino acid age estimate of 1.2 ± 0.3 Ma was derived (Table 7.31). On the basis of the extent of GLX racemization and the U-series Mollusc calibration the muddy sand unit (aii) of the North Cape Beds was deposited during the early



Figure 7.109: Muddy sand unit (aii) at site NC1, near Point Marsden. Note rock-hammer for scale (33cm) (black ellipse).

Table 7.31: North Cape Pleistocene marine mollusc ASX and GLX AAR data, and AAR numerical ages

Lab. No.	Site	Site code / facies	Location (S Lat. E Long.)	CMAT ^a °C	Genus and species / (N) ^b	ASX D-L ratio $\pm 1\sigma^c$	Coefficient of variation (CV%)	GLX D-L ratio $\pm 1\sigma^c$	Coefficient of variation (CV%)	AAR GLX age estimate (ka) ^d $\pm 1\sigma^c$
UWGA 7003	North Cape, Point Marsden	NC1 / muddy sand, tidal flat	35° 34' 39.7" S 137° 37' 48.6" E	15.0	<i>Anapella cycladea</i> / (2)	0.838 \pm 0.021	2.5	0.978 \pm 0.015	1.5	1.2 \pm 0.3 Ma
UWGA 7002	North Cape, Boxing Bay	NC2 / raised pebble beach	35° 34' 18.6" S 137° 36' 10.6" E	15.0	<i>Mactra australis</i> / (1)	0.728 \pm 0.012	1.7	0.706 \pm 0.001	0.2	590 \pm 127
UWGA 7002	North Cape, Boxing Bay	NC2 / raised pebble beach	35° 34' 18.6" S 137° 36' 10.6" E	15.0	<i>Tawera lagopus</i> / (1)	0.779 \pm 0.003	0.4	0.782 \pm 0.003	0.3	733 \pm 158
UWGA 7002	North Cape, Boxing Bay	NC2 / raised pebble beach	35° 34' 18.6" S 137° 36' 10.6" E	15.0	<i>Mactra australis</i> and <i>Tawera lagopus</i> / (2)	0.753 \pm 0.030	4.0	0.744 \pm 0.044	5.9	660 \pm 148

^a Current mean annual temperature estimated for these sites from annual temperature data via climate recording stations around Kangaroo Island

(<http://www.bom.gov.au/climate/data/>)

^b Number of molluscs used for D-L ratio estimate

^c Uncertainties are 1 σ (one standard deviation—68% confidence interval)

^d Numerical age estimate from a U-series AMS ¹⁴C calibration (fossil coral recovered from Vivonne Bay and fossil shell from American River) using an apparent parabolic model (Mitterer and Kriaušakul, 1989; Murray-Wallace *et al.*, 2001); uncertainties are calculated from the square root of the sum of the squares of all error terms (U-series age of *Plesiastrea versipora*: a stony coral recovered from same unit as the marine shell *Nerita* (*Melanerita*) *atramentosa* (PE#3-5), and used to calibrate the GLX D-L ratio. ¹⁴C ages used to calibrate Holocene *Katelysia* spp. from American River).

Table 7.32: North Cape Pleistocene single foraminifer ASX and GLX AAR data, and numeric AAR age estimates

Lab. No.	Site	Site code / facies	Location (S Lat. E Long.)	CMAT ^a °C	Genus and species / (N) ^b	ASX D-L ratio) $\pm 1\sigma^c$	Coefficient of variation (CV%)	GLX D-L ratio) $\pm 1\sigma^c$	Coefficient of variation (CV%)	AAR GLX age estimate (ka) ^d $\pm 1\sigma^c$
UWGA 7013	North Cape, Boxing Bay	NC2 / raised pebble beach	35° 34' 18.6" 137° 36' 10.6"	15.0	<i>Elphidium</i> sp. / (5)	0.783 \pm 0.020	2.6	0.725 \pm 0.019	2.7	894 \pm 260

^a Current mean annual temperature estimated for these sites from annual temperature data via climate recording stations around Kangaroo Island (<http://www.bom.gov.au/climate/data/>)

^b Number of foraminifera used for D-L ratio estimate

^c Uncertainties are 1 σ (one standard deviation—68% confidence interval)

^d Numeric age estimate from a U-series calibration (fossil coral recovered from Vivonne Bay: 114 \pm 3 ka) using an apparent parabolic model (Mitterer and Kriauasakul, 1989; Murray-Wallace *et al.*, 2001); uncertainties are calculated from the square root of the sum of the squares (addition in quadrature) of all uncertainty terms

Table 7.33: Pleistocene (WR) sediment ASX and GLX AAR data, and AAR numerical age estimates for North Cape.

Lab. No.	Site	Site code / facies (N) ^c	Location (S Lat. E Long.)	CMAT ^a °C	ASX D-L ratio $\pm 1\sigma^b$	Coefficient of variation (CV%)	GLX D-L ratio $\pm 1\sigma^b$	Coefficient of variation (CV%)	AAR GLX (U-series calib.) age estimate (ka) ^d $\pm 1\sigma^b$	AAR GLX (OSL calib.) age estimate (ka) ^d $\pm 1\sigma^b$
UWGA 7014	North Cape, Boxing Bay	NC2 / raised pebble beach (4)	35° 34' 18.6" 137° 36' 10.6"	15.0	0.765 \pm 0.010	1.2	0.788 \pm 0.020	2.5	812 \pm 187	775 \pm 175
UWGA 5846, 6534, 7015	North Cape, Boxing Bay	NC2 / raised beach facies (6)	35° 34' 18.6" 137° 36' 10.6"	15.0	0.762 \pm 0.002	0.3	0.823 \pm 0.008	1.0	920 \pm 211	878 \pm 197

^a Current mean annual temperature (CMAT) estimated for these sites from annual temperature data via climate recording stations around Kangaroo Island (<http://www.bom.gov.au/climate/data/>)

^b Uncertainties are 1 σ (one standard deviation—68% confidence interval)

^c N = number of subsamples

^d Numeric age estimate from an OSL alignment using an apparent parabolic model (Mitterer and Kriauasakul, 1989; Murray-Wallace *et al.*, 2001); uncertainties are calculated from the square root of the sum of the squares of all uncertainty terms

* OSL age estimate of whole-rock sample used to calibrate the GLX D-L ratio.

Pleistocene, similar to the Point Ellen Formation. However, given the uncertainty in the AAR age it is difficult to speculate that unit aii at site NC1 is contemporaneous with the Point Ellen Formation.

7.3.10.2 North Cape site NC2 geochronology

Marine shell was also recovered from the consolidated, thin, shelly sand covering and infilling the cobble/pebble beach (subunits ai and aii) at site NC2 (see Figure 7.108, 7.112) (The Boxing Bay Conglomerate). It was difficult to recover good specimens from the hard sediment. Because of this only 2 shells could be sampled intact, and in relatively good condition. Both were marine bivalves (*Mactra australis* and *Tawera lagopus*) characteristic of shallow water, sandy, near shore, medium to high energy environments (Figure 7.109).

The amino acid analyses of both shells yielded a mean GLX D-L ratio of 0.744 ± 0.044 (Table 7.31). The AAR age estimate derived from this D-L ratio was 660 ± 148 ka which suggests an early / middle Pleistocene deposition for these sediments. Whole-rock sediment and foraminifers were also analysed from the Boxing Bay Conglomerate.

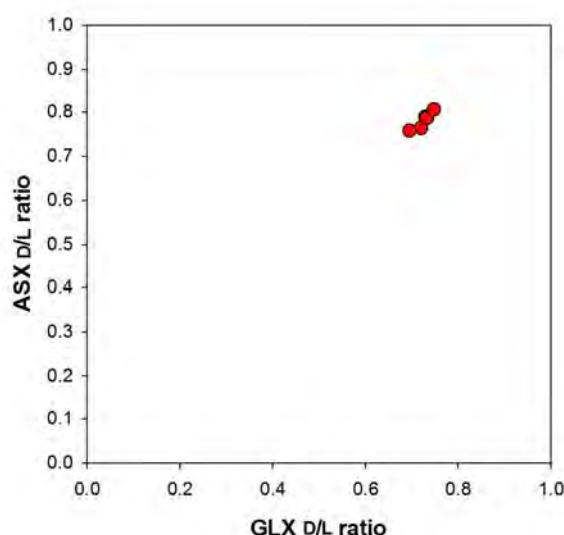


Figure 7.111: Foraminifer bivariate plot (ASX vs. GLX) of *Elphidium* sp. recovered from the Boxing Bay Conglomerate. Note D-L ratio clustering in the highly racemized foraminifers.

Third party source; Images
redacted at request of
thesis author

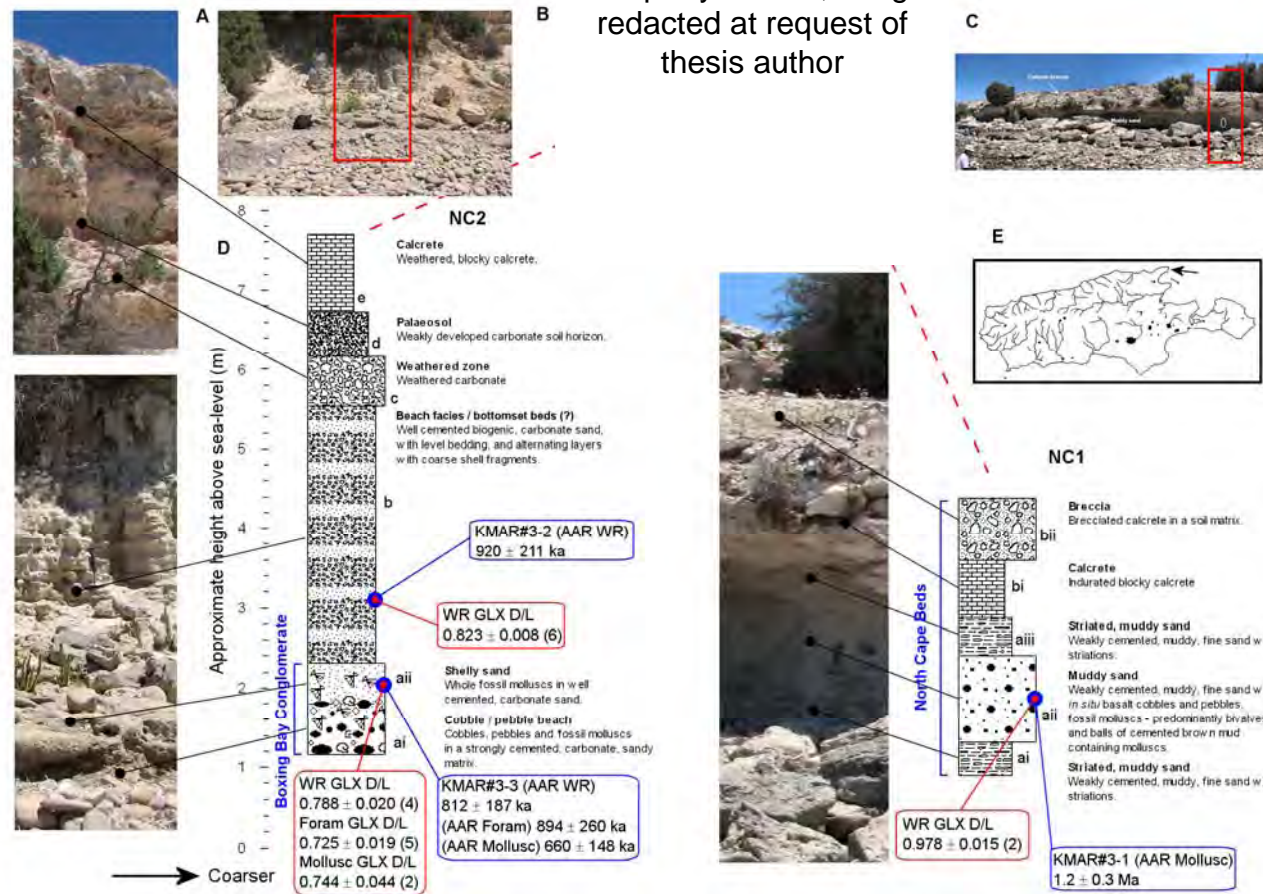


Figure 7.112: North Cape stratigraphic logs for the sedimentary outcrops near Point Marsden (NC1), and Boxing Bay (NC2). Included are the geochronological data (blue boxes) and corresponding GLX D-L ratio data (red boxes—numbers in brackets are individuals or subsamples analysed). The top LH and RH insets (A and C) are panoramas of site NC2 and site NC1 example outcrops. The middle inset (B) is a satellite image (courtesy of Google Earth, 2010) showing indicated log and sample sites. E is a Kangaroo Island location map (with the location indicated by a black arrow). The site logs for NC1 and NC2 are D.



Figure 7.113: The Boxing Bay Conglomerate and beach facies (these could also be the bottomset beds of an aeolianite deposit (rock-hammer set for scale [black ellipse]: 33 cm).

These yielded mean GLX D-L ratios of 0.788 ± 0.020 and 0.725 ± 0.019 , respectively (Table 7.32 and 7.33). The foraminifers showed good bivariate clustering (ASX vs. GLX) (Figure 7.111), even though relatively few were suitable for analysis. The calculated AAR age estimates for the whole-rock sediments and the foraminifers recovered from the Boxing Bay Conglomerate were 812 ± 187 ka (U-series calibration) and 775 ± 175 ka (OSL calibration), and 894 ± 260 ka, respectively (Table 7.32 and 7.33). These ages are all in broad agreement with the Mollusc AAR age, indicating again an early / middle Pleistocene age for the Conglomerate.

Overlying the early / middle Pleistocene Boxing Bay Conglomerate is a thick (~ 4m) carbonate sand unit with level bedding (unit b) (Figure 7.112, 7.113, and



Figure 7.114: Closer view of the level bedded unit (b) overlying the Boxing Bay Conglomerate.



Figure 7.115: Closer view of the Boxing Bay Conglomerate, and thin sand layer (knapsack is 50 cm high).



Figure 7.116: Long view east from site NC2 of a Boxing Bay Conglomerate patch with a wave-cut Holocene (?) platform (blue dashed line). Note the large cemented boulders at the shoreface. This unit was originally much larger in extent, and this entire bay beach may have been predominantly shingled cobbles and boulders during the early / middle Pleistocene.

7.114). It was initially thought that these may have been a beach facies. However, the scale of the level beds is probably too large for this designation. It is more likely that the bedding is attributable to dune bottomsets.

Whole-rock sediment samples recovered from these beds were analysed for amino acid enantiomers, and a mean GLX D-L ratio of 0.823 ± 0.008 was calculated from 6 analyses. Using the whole-rock calibration (Chapter 6 section 6666) AAR age estimates of 920 ± 211 ka (U-series calibration) and 878 ± 197 ka (OSL calibration) were derived. Due to large uncertainties the age difference between the deposition of the Boxing Bay Conglomerate and the overlying level beds is unknown. Nevertheless the overlapping age estimates suggest a *relatively* short period of time. The presence of a weathered zone and palaeosol at the top of the unit (Figure 7.113) implies a period of subaerial exposure, and pedogenesis. The blocky calcrete at the top of the sequence may be the remnant 'B' horizon from a middle or late Pleistocene dune unit.

7.3.10.3 Discussion of the North Cape geochronology

The sequence at site NC1 is early Pleistocene in age and the muddy sand unit (a) may represent a tidal flat formed during a period of higher sea-level, possibly +2.0 to +2.5 m APSL (possibly as high as [or higher than] +4.0 m APSL). The presence of *Anapella cycladea* would support the tidal flat interpretation.

The expansive platformal surface formed by the upper sediments too may be part of the original tidal flat deposit, where subaerial exposure, pedogenesis and deflation of the carbonaceous muddy sand has formed a thick calcrete mantle (which has preserved the underlying sediment), possibly during the middle Pleistocene.

The Boxing Bay Conglomerate at site NC2 (Figure 7.115) was most likely deposited at a sea-level of approximately +2.0 m APSL, during the early / middle Pleistocene. The conglomerate is also present along the eastern section of Boxing Bay in broad patches. Some of these patches grade down to below current sea-

level, forming large Holocene platforms (see Figure 7.116). This is testament to a much thicker and more extensive original deposit.

The overlying units at NC2 (Figure 7.112) are probably representative of aeolian deposition of skeletal carbonate sediments during the early to middle Pleistocene, the upper units having undergone pedogenesis and deflation. The characteristic middle and late Pleistocene aeolianite sequences of the southern coast of Kangaroo Island are not apparent here.

7.3.11 Emu Bay

Emu Bay is a large embayment on the northern coast of Kangaroo Island, at the neck of the North Cape isthmus (see Figure 7.117). The study site (EB) is an isolated outcropping of an aeolianite sequence located towards the eastern end of the embayment. The outcrop extends to sea-level forming a small headland, similar to those at Pennington Bay. The beach is of moderate energy and most of the embayment is dominated by well-vegetated modern and Holocene backshore dunes.

The sequence (see Figure 7.118) consists of 2 aeolianite units (a and c) separated by a palaeosol unconformity (b), and capped by a calcrete mantle (d) and cliff-top dunes (e). Both of the aeolianite units were sampled for AAR analysis, although no foraminifer results are reported because of overall low amino acid concentrations and relatively high L-SER concentrations (i.e. very low SER D-L ratios: <0.050 in many cases), in every single-grain analysis. This was taken to indicate contamination with younger organic residues. While not excessive contamination, the lowered concentrations of indigenous amino acids means that adsorbed non-indigenous organic material may have a greater influence on the final D-L ratios (effectively lowering the final D-L) (see Chapter 6).

7.3.11.1 Emu Bay geochronology

A thermoluminescence sample (EBTL#1-1) was removed from the basal aeolianite unit (a) at site EB (see Figure 7.118 and 7.119). This was analysed at

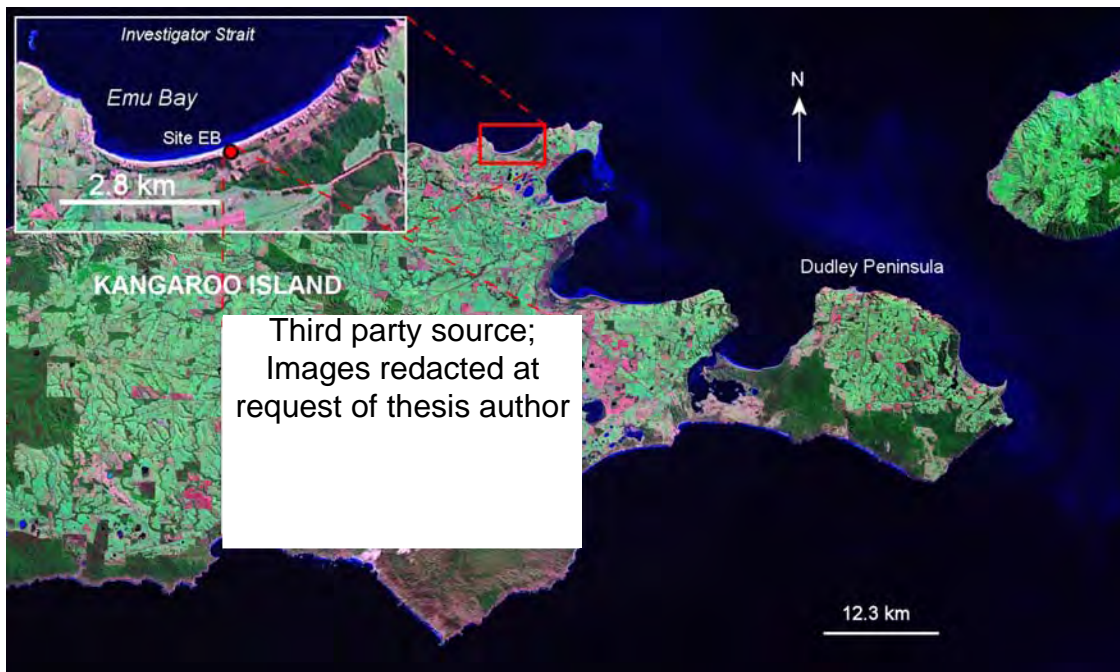


Figure 7.117: Location map (Landsat ETM image: NASA Landsat program, 2001) for study site on Emu Bay, Kangaroo Island. Inset (upper LH) shows the general location of site EB (red circle). The lower RH inset is a closer view of the EB study site; the red arrows indicate sample positions (Google Earth, 2010).

the University of Wollongong Thermoluminescence Dating Laboratory, by D. Price, and a TL age estimate of 216 ± 28 ka was derived (see Table 7.14). This age suggests that the deposition of this lower unit took place during MIS 7, and although resolution does not allow for a particular substage, the TL age does centre over MIS 7c (212-220 ka: Li *et al.*, 1989).

Several (4: each was subsampled twice, and analysed) whole-rock samples were also taken along the basal aeolianite unit (a) at site EB (see Figure 7.118 and 7.119). These were analysed for amino acid enantiomers, and a mean GLX D-L ratio of 0.548 ± 0.045 was derived (Table 7.34). Upon calibration, using the whole-rock sediment U-series and OSL calibrations (Chapter 6 section, 6666), age estimates of 258 ± 63 ka and 246 ± 59 ka were calculated (Table 7.34). These ages agree quite well with the TL date at 1σ .

An AAR sample was also removed from the upper aeolianite at site EB (Figure 7.118 and 7.119). The whole rock analysis gave a mean GLX D-L ratio of 0.595

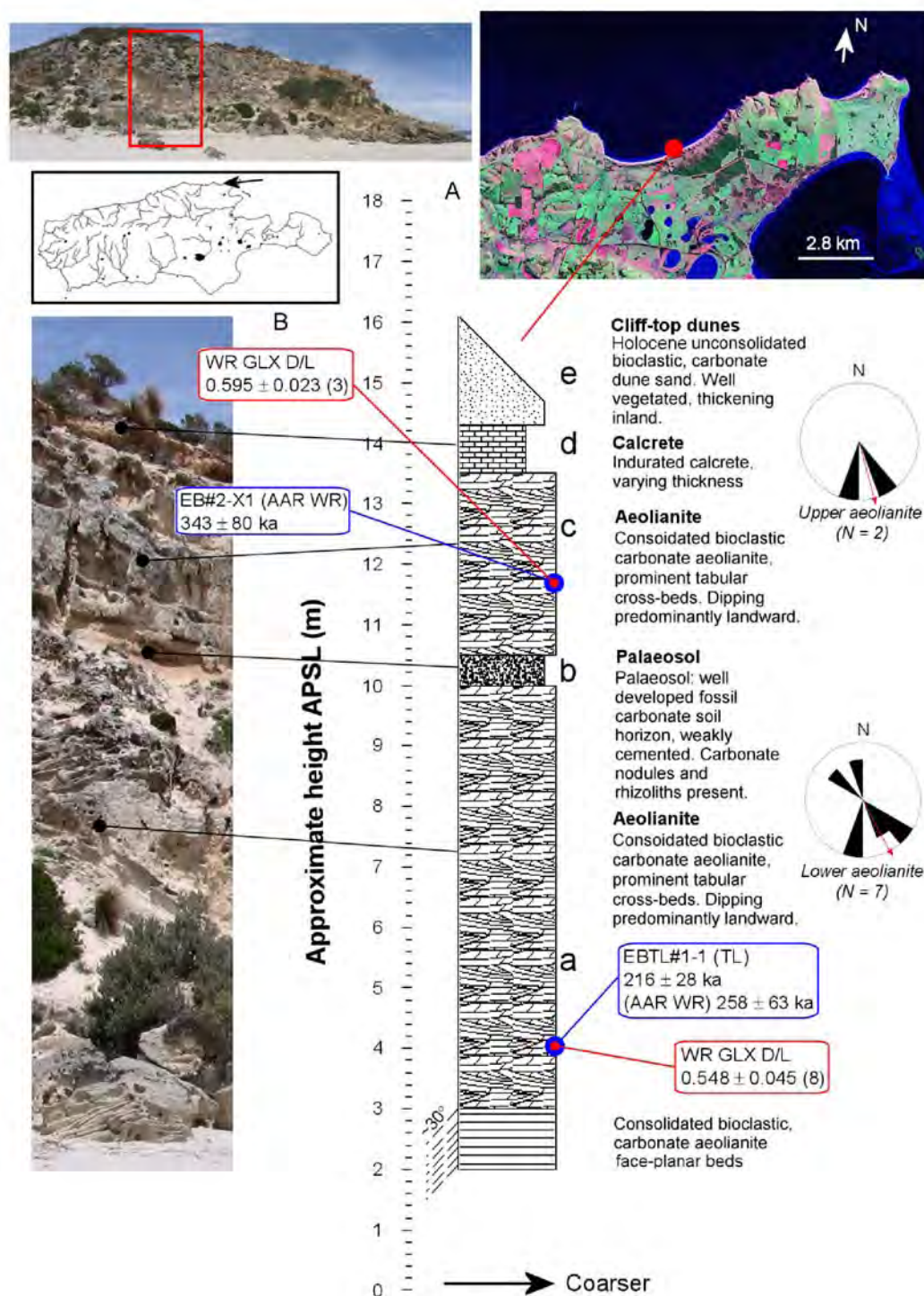


Figure 7.118: Stratigraphic log (B) for the sedimentary outcrop at Emu Bay (EB). Included are the geochronological data (blue boxes) and corresponding GLX D-L ratio data (red boxes—numbers in brackets are individuals or subsamples analysed). The top LH, lower LH, and RH insets (A) are a panorama of site EB outcrop, a satellite image (Landsat ETM: NASA Landsat program, 2001) showing indicated log and sample sites, and a Kangaroo Island location map (with the location indicated by a black arrow). Rose diagrams are given for the upper and lower aeolianite units, showing bedding orientations attributable to wind vector.

Table 7.34: Pleistocene whole-rock (WR) sediment ASX and GLX AAR data, and AAR numerical age estimates for Emu Bay.

Lab. No.	Site	Site code / facies (N) ^c	Location (S Lat. E Long.)	CMAT ^a °C	ASX D-L ratio $\pm 1\sigma^b$	Coefficient of variation (CV%)	GLX D-L ratio $\pm 1\sigma^b$	Coefficient of variation (CV%)	AAR GLX (U-series calib.) age estimate (ka) ^d $\pm 1\sigma^b$	AAR GLX (OSL calib.) age estimate (ka) ^d $\pm 1\sigma^b$
UWGA 7014	Emu Bay east	EB / lower aeolianite (8)	35° 35' 21.6" 137° 32' 28.6"	15.0	0.656 \pm 0.023	3.5	0.548 \pm 0.045	8.2	258 \pm 63	246 \pm 59
UWGA 5846, 6534, 7015	Emu Bay west	EB / upper aeolianite (3)	35° 35' 21.2" 137° 32' 28.6"	15.0	0.693 \pm 0.008	1.2	0.595 \pm 0.023	3.9	343 \pm 80	327 \pm 75

^a Current mean annual temperature (CMAT) estimated for these sites from annual temperature data via climate recording stations around Kangaroo Island (<http://www.bom.gov.au/climate/data/>)

^b Uncertainties are 1 σ (one standard deviation—68% confidence interval)

^c N = number of subsamples

^d Numeric age estimate from an OSL alignment using an apparent parabolic model (Mitterer and Kriausakul, 1989; Murray-Wallace *et al.*, 2001); uncertainties are calculated from the square root of the sum of the squares of all uncertainty terms

* OSL age estimate of whole-rock sample used to calibrate the GLX D-L ratio.

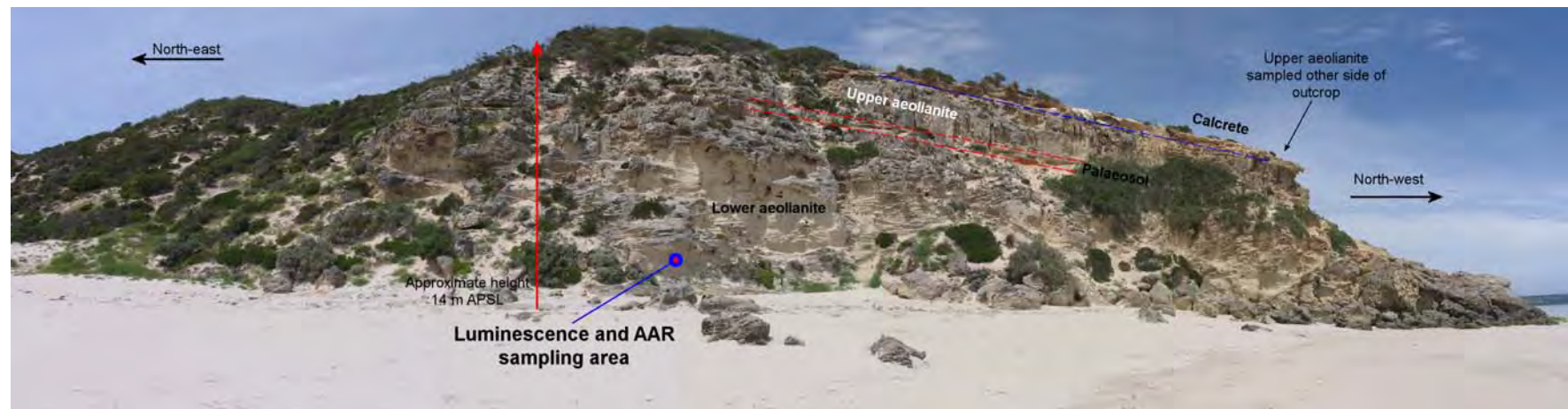


Figure 7.119: Panorama of the Emu Bay site, showing sample locations, height of the sequence (~14 m APSL), orientation of the site, and location of the stratigraphic units.

± 0.023 (Table 7.34). This was higher than that derived for the lower aeolianite unit, although not significantly so. U-series and OSL calibrations yielded AAR age estimates of 343 ± 80 ka and 327 ± 75 ka (Table 7.34). It would be expected that the D-L ratios would be lower (in terms of stratigraphic position) for the upper aeolianite unit. The reason that the AAR data for the upper and lower aeolianite can be superimposed may be due to reworking of older materials, or the age differences cannot be resolved using the AAR method at this site, i.e., the times of deposition for the lower and upper units were relatively close to each other (or a combination of both factors). Also, it is possible that upper aeolianite sample may have been exposed to greater diagenetic temperature flux.

This sequence may represent deposition during a single marine isotope stage, in this case MIS 7. The thin palaeosol (unit b) may have formed during the hiatus in carbonate deposition at MIS 7d.

7.3.11.2 Discussion of the Emu Bay geochronology

Limited geochronological analyses were undertaken at this site, and there were inherent problems in the utilization of single-grain AAR data. The luminescence chronology suggests an MIS 7 deposition for the lower aeolianite, as does the AAR chronology. The lower unit in the sequence was most likely deposited at the same time as the aeolianite that makes up the small headlands towards the centre of Pennington Bay (at sites PB1 and PB3).

The upper aeolianite was only analysed for AAR, and because of possible reworking of constituent carbonate materials and/or relatively short differences in depositional timing, the AAR data were not significantly different to that derived for the lower unit. Luminescence dating of the upper aeolianite unit would be required to resolve this issue. Regardless, the sequence at Emu Bay may be the result of deposition during a single marine isotope stage (MIS 7), or alternately, it could also be equally likely that the upper unit is from a later marine isotope stage, possibly MIS 5 (given the sequence stratigraphy at other sites on the southern coast, i.e., MIS7 aeolianite>Palaeosol>MIS5 aeolianite).

7.3.12 Smith Bay

Smith Bay is located on the northern coast of Kangaroo Island, approximately 8 km straight line distance west of Emu Bay. The study site at Smith Bay hosts an uplifted pebble / cobble / boulder beach that rests unconformably on Permian glaciogene sediments. This unit was informally designated in this study as the early Pleistocene Smith Bay Conglomerate in Chapter 3.

Smith Bay is a wide (~4 km) shallow bay (in terms of coastal morphology, not water depth—Figure 7.120). The embayment can be characterised by high-angled shingled cobble/boulder beaches with a sandy margin at the shore, resting on Cambrian Kangaroo Island Group platformal sediments (in this case the Smith Bay Shale [Chapter 1, section 1.4.1.1]).

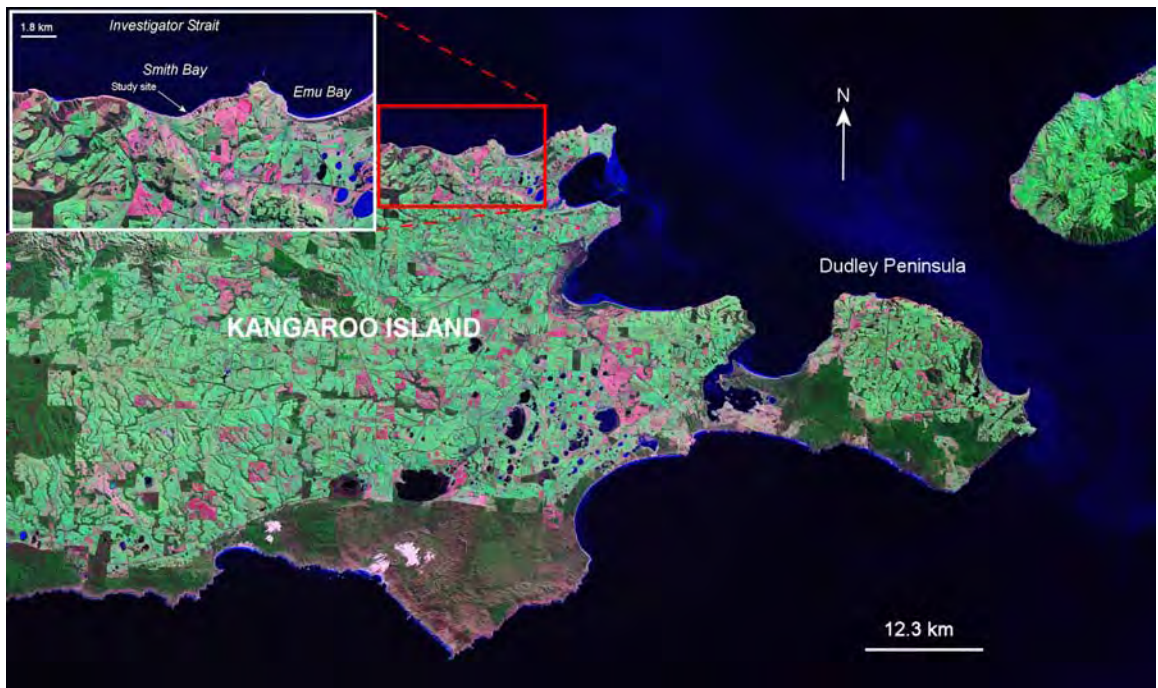


Figure 7.120: Location map for study site at Smith Bay, Kangaroo Island. Inset (upper LH) shows the general location of site SB. The white arrow indicates sample site (Landsat ETM: NASA Landsat program, 2001).

The cobble beach unit is located near the top of a broad headland towards the eastern side of the embayment (Figure 7.120). The base of the unit is approximately +18 m APSL, and ranges up to ~2 m thick. It is overlain by a blocky, weathered calcrete; the upper surface of the calcrete over the entire ridgeline is broken and dissected, and strewn with calcrete rubble. Thin soil infills the broken surface and the lower portions of the calcrete are often powdery (limey) and loose.

The Smith Bay Conglomerate (Figure 7.121, 7.122 and 7.123) overlies ~18 m of Permian glacial till. The conglomerate was briefly described by Bourman and Alley (1999), and was interpreted to be of Pleistocene age. The pebbles, cobbles and boulders that make up the beach are strongly cemented and the matrix is composed primarily of unidentifiable carbonate bioclasts, rare foraminifers and calcareous algae, and a high proportion of subordinate quartz grains. Also cemented in the matrix were marine molluscs although these were rare, in poor condition, and difficult to remove. None were found that were unbroken unfortunately. Nevertheless, some fragments of shell were large enough to permit identification to the genus level, although only two genera were identified, these were: *Macra* spp. (Linnaeus, 1767) and *Irus* spp. (Linnaeus, 1758). Both genera have species that live in a range of environments, from sandy beaches to tidal inlets and mangrove swamps (Ludbrook, 1984).

This beach (the Smith Bay Conglomerate) probably formed under similar conditions to that of its modern counterpart.

7.3.12.1 Smith Bay geochronology

AAR geochronology was limited at Smith Bay, as finding suitable material to analyse was difficult, given the preservation state of marine mollusc shell material. All shell recovered from the Smith Bay Conglomerate was fragmented and in most cases the fragments were in a poor state of preservation (outer surfaces were very chalky, and powdery, indicating recrystallization). However,



Figure 7.121: The early Pleistocene Smith Bay Conglomerate, overlying Permian till at Smith Bay, Kangaroo Island.

several fragments were recovered that, after cleaning and surface treatments, were suitable for AAR dating purposes. Here 3 *Macra* spp. and 5 *Irus* spp. (marine bivalves) fragments were analysed for amino acid enantiomers. Whole-rock material was also analysed, however, results were rejected on the basis of overall low concentrations of amino acids. Unfortunately suitable foraminifers could not be recovered from the sediment.

The combined marine shell data yielded a near racemic mean GLX D-L ratio of 0.907 ± 0.040 (Table 7.35). This was calibrated using the Mollusc calibration (Chapter 6), giving an AAR age estimate of 1.0 ± 0.2 Ma. This confirms the initial interpretation of an early Pleistocene age for the deposit (Chapter 3).

Table 7.35: Smith Bay Conglomerate early Pleistocene marine mollusc ASX and GLX AAR data, and AAR numerical ages

Lab. No.	Site	Site code / facies	Location (S Lat. E Long.)	CMAT ^a °C	Genus and species / (N) ^b	ASX D-L ratio $\pm 1\sigma^c$	Coefficient of variation (CV%)	GLX D-L ratio $\pm 1\sigma^c$	Coefficient of variation (CV%)	AAR GLX age estimate (Ma) ^d $\pm 1\sigma^c$
UWGA 7016, 7017	Smith Bay	SB / raised pebble / cobble / boulder beach	35° 35' 43.1" 137° 27' 10.4"	15.0	<i>Macra</i> spp. and <i>Irus</i> spp. / (8)	0.800 ± 0.048	6.0	0.907 ± 0.040	4.4	1.0 ± 0.2

^a Current mean annual temperature estimated for these sites from annual temperature data via climate recording stations around Kangaroo Island

(<http://www.bom.gov.au/climate/data/>)

^b Number of molluscs used for D-L ratio estimate

^c Uncertainties are 1σ (one standard deviation—68% confidence interval)

^d Numerical age estimate from a U-series and AMS ^{14}C calibration (fossil coral recovered from Vivonne Bay and fossil shell from American River) using an apparent parabolic model (Mitterer and Kriauasakul, 1989; Murray-Wallace *et al.*, 2001); uncertainties are calculated from the square root of the sum of the squares of all error terms (U-series age of *Plesiastrea versipora*: a stony coral recovered from same unit as the marine shell *Nerita* (*Melanerita*) *atramentosa* (PE#3-5), and used to calibrate the GLX D-L ratio. ^{14}C ages used to calibrate Holocene *Kataysia* spp. from American River).

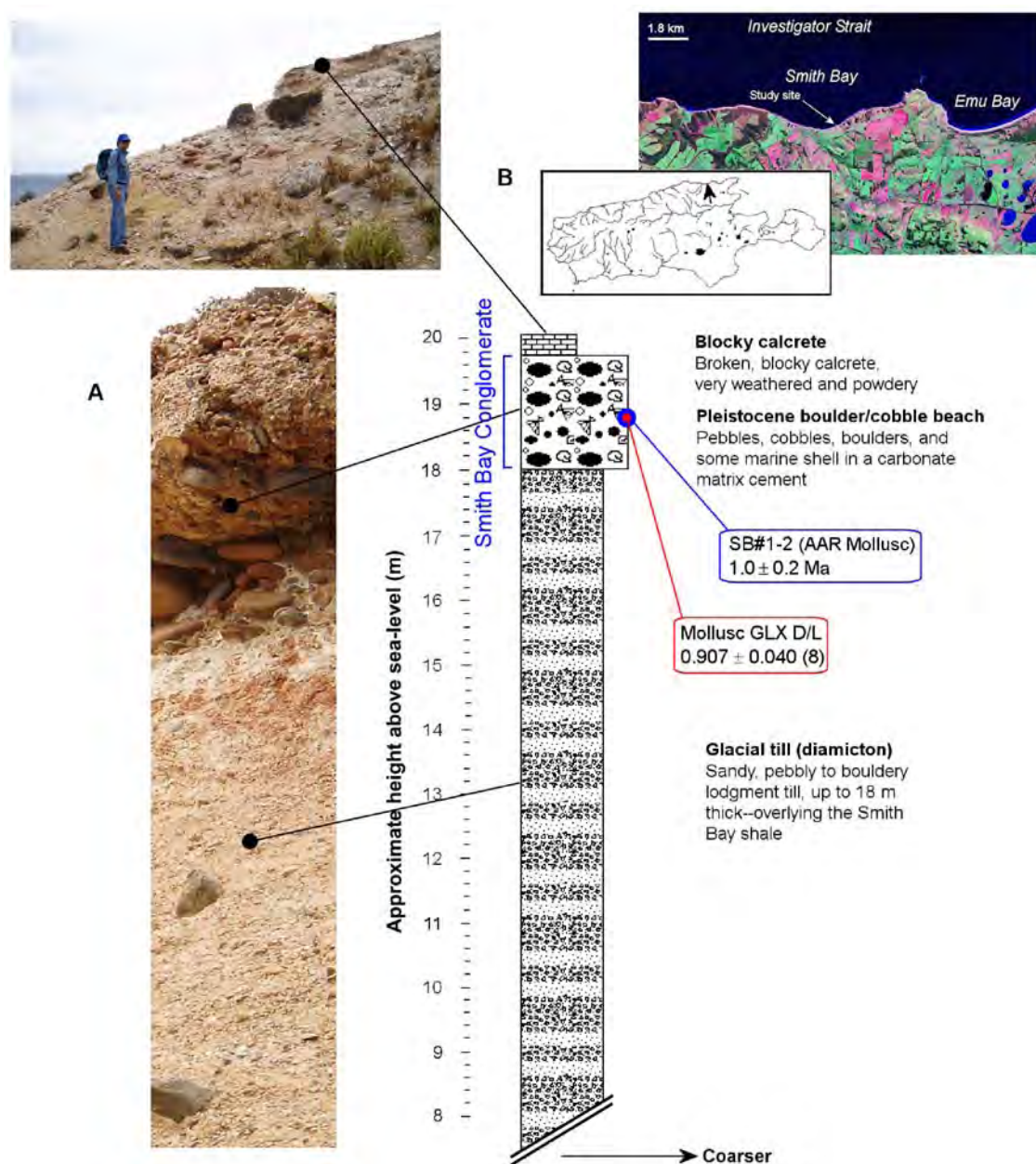


Figure 7.122: Stratigraphic log (A) for the sedimentary outcrop at Smith Bay (SB). Included are the geochronological data (blue boxes) and corresponding GLX D-L ratio data (red boxes—numbers in brackets are individuals or subsamples analysed). The top LH, top middle, and top RH insets (B) are a panorama of site SB outcrop, a Kangaroo Island location map (with the location indicated by a black arrow), and a satellite image (Landsat ETM: NASA Landsat program, 2001) showing indicated log and sample sites.



Figure 7.123: Wider view of the early Pleistocene Smith Bay Conglomerate (red dashed lines), overlying Permian till at Smith Bay, Kangaroo Island. Note upper calcrete and talus slope over the Conglomerate.

7.3.12.2 Discussion of the Smith Bay geochronological results

This unit was initially interpreted to be of early Pleistocene age, given its morphostratigraphical position. In this case then the height of the beach unit implies that tectonic uplift must have taken place later in the Pleistocene. Given the AAR age estimate it is assumed that the Smith Bay Conglomerate is of similar antiquity to the Point Ellen Formation, which implied a sea-level of around +3.0 to +4.0 m APSL during deposition (see Chapter 3) then the Smith Bay Conglomerate may have been uplifted by as much as +15 m. Neotectonic uplift must be considered as according to the oxygen isotope record (Lisiecki and Raymo, 2005) it is unlikely that any instances of interglacial sea-levels reached the current height of the unit during the Quaternary period. Indeed, according to Siddall *et al.* (2007) interglacial sea-levels prior to MIS 11 were similar to or lower than present. It is, however, difficult to reconcile probable uplift at this site (unless the uplift was

localised in the Smith Bay area) when another site of similar antiquity (site NC1 [the North Cape Beds] at North Cape) is at near current sea-level.

7.3.13 Stokes Bay

Stokes bay is a small embayment located on the northern coast of Kangaroo Island, approximately 22 km west of Smith Bay. The bay hosts a sandy moderate energy beach backed by ~8 m high aeolianite cliffs, with scree slopes and large dislodged blocks of aeolianite and calcrete at the base.

The study site is the bounding western calcarenite headland (see Figure 7.124). The headland is a single aeolianite unit, overlain by a blocky calcrete that is weathered and brecciated. The aeolianite is karstified, very weathered and leached, and although the sediment is indurated it is quite friable and “foamy” (of low density) in places. Most of the bedding is obliterated, although some is visible in patches along the outcrop. The unit was initially interpreted to be of early Pleistocene age, and this was based on the appearance of the sediments, in terms of the weathered and leached facade.

7.3.13.1 Stokes Bay Geochronology

Two whole-rock sediment samples were recovered from the lower portions of the aeolianite unit (Figure 7.125, 7.126 and 7.127) (foraminifers were not readily identifiable in the sediment), these were analysed several times (7) to derive a mean GLX D-L ratio of 0.779 ± 0.010 (Table 7.36). This ratio was calibrated using the U-series and OSL apparent parabolic kinetics calibration to yield WR AAR ages of 786 ± 181 ka and 750 ± 169 ka, respectively (Table 7.35).

These age estimates support the initial early Pleistocene interpretation to a degree (Chapter 3), however, the estimates would also suggest an early / middle Pleistocene age for deposition.

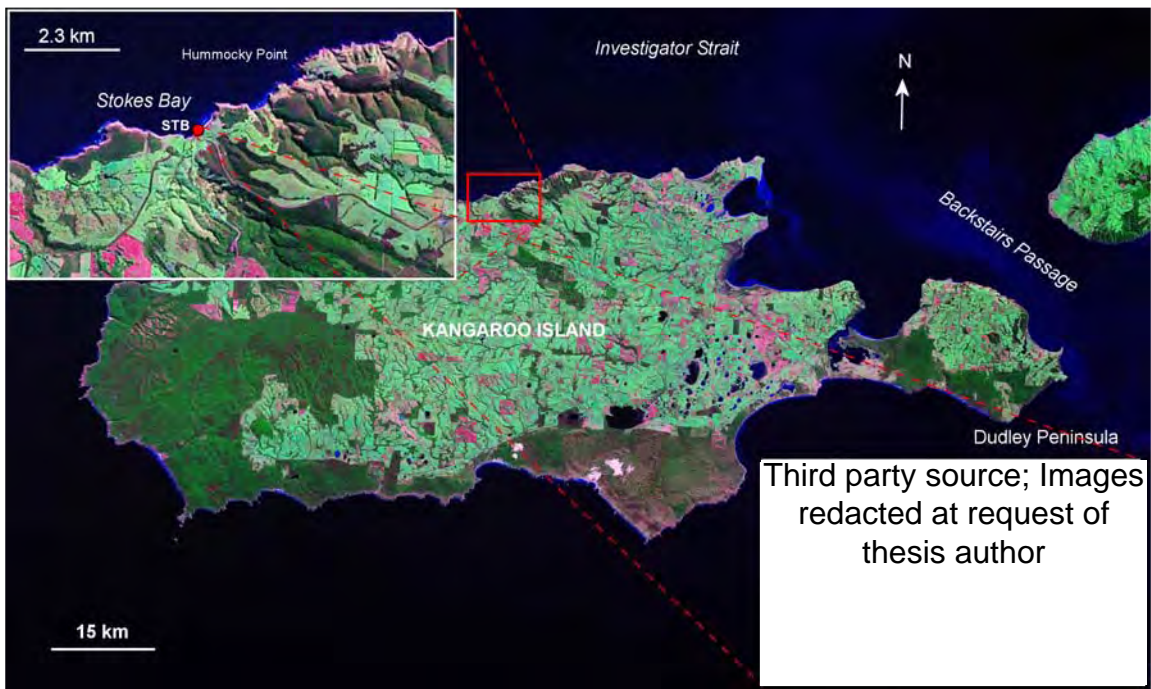


Figure 7.124: Location map (Landsat ETM image: NASA Landsat program, 2001) for study site at Stokes Bay, Kangaroo Island. Inset (upper LH) shows the general location of site STB (red circle). The lower middle inset is a closer view of the STB study site; the red arrow indicates sample positions (from Google Earth, 2009).



Figure 7.125: Aeolianite at Stokes Bay. Note weathered condition of the calcarenite (Rock-hammer set for scale: 33 cm)

Table 7.36: Pleistocene whole-rock (WR) sediment ASX and GLX AAR data, and AAR numerical age estimates for Stokes Bay.

Lab. No.	Site	Site code / facies (N) ^c	Location (S Lat. E Long.)	CMAT ^a °C	ASX D-L ratio $\pm 1\sigma^b$	Coefficient of variation (CV%)	GLX D-L ratio $\pm 1\sigma^b$	Coefficient of variation (CV%)	AAR GLX (U-series calib.) age estimate (ka) ^d $\pm 1\sigma^b$	AAR GLX (OSL calib.) age estimate (ka) ^d $\pm 1\sigma^b$
UWGA 5847, 6533, 7018, 7019	Stokes Bay	STB / aeolianite (7)	35° 37' 21.8" 137° 12' 26.9"	15.0	0.718 \pm 0.011	1.5	0.779 \pm 0.010	1.3	786 \pm 181	750 \pm 169

^a Current mean annual temperature (CMAT) estimated for these sites from annual temperature data via climate recording stations around Kangaroo Island (<http://www.bom.gov.au/climate/data/>)

^b Uncertainties are 1 σ (one standard deviation—68% confidence interval)

^c N = number of subsamples

^d Numeric age estimate from an OSL alignment using an apparent parabolic model (Mitterer and Kriausakul, 1989; Murray-Wallace *et al.*, 2001); uncertainties are calculated from the square root of the sum of the squares of all uncertainty terms

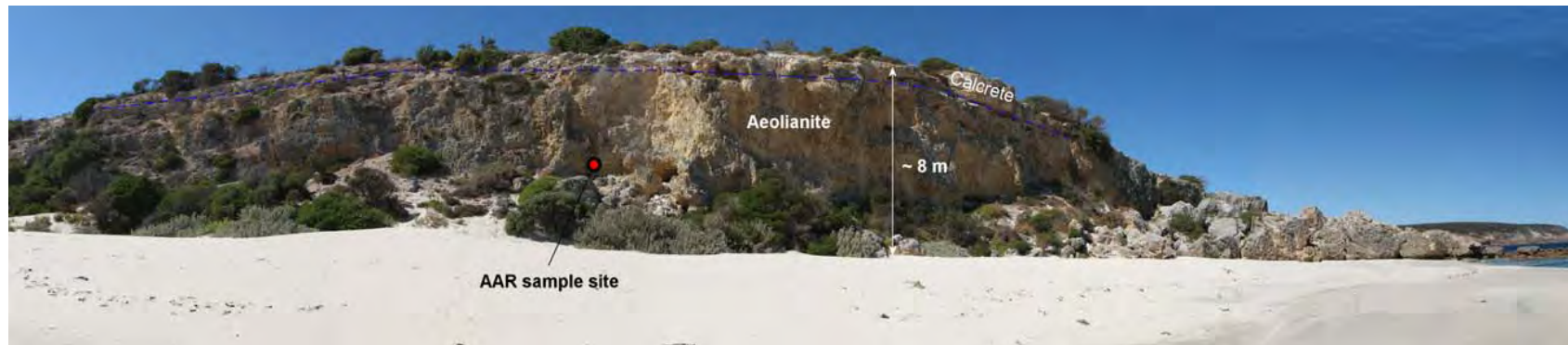


Figure 7.126: Panorama of Stokes Bay outcrop (site STB), showing sample area, position of calcrete and height of the units. Note the large collapsed blocks of aeolianite and calcrete at the seaward margin of the headland.

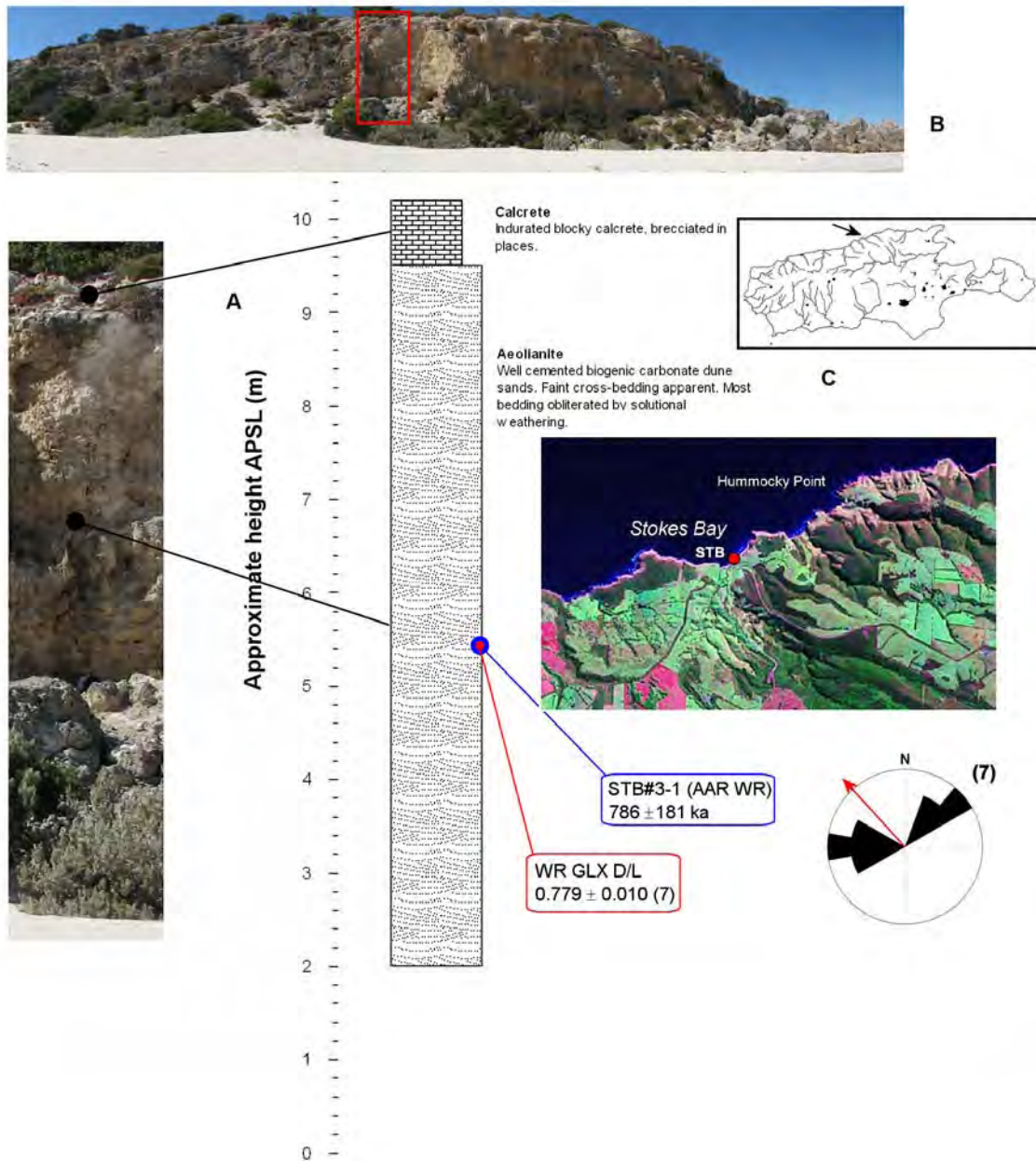


Figure 7.127: Stratigraphic log (A) for the sedimentary outcrop at Stokes Bay (STB). Included are the geochronological data (blue boxes) and corresponding GLX D-L ratio data (red boxes—umber in brackets is the subsample analysed). The top inset (B) is a panorama of site STB outcrop. Left (C) is a Kangaroo Island location map (with the location indicated by a black arrow), and a satellite image (Landsat ETM: NASA Landsat program, 2001) showing indicated log and sample sites. A rose diagram is given for aeolianite unit, showing bedding orientations attributable to wind vector (this is evaluated in Chapter 3).

7.3.13.1 Discussion of the Stokes Bay Geochronological results

This is apparently an old aeolianite site, and the younger sequences evident on the southern coastal regions of Kangaroo Island are absent at Stokes Bay, i.e., there is no Last Interglacial sequence for example. Why this is the case is difficult to say, however, carbonate deposition along the north coast was undoubtedly restricted because of the pre-Quaternary geology that forms much of this precipitous northern coastline (this is evidenced by the distinct lack of widespread outcrop of Bridgewater Formation aeolianites along the north coast). Keeping this in mind, the existence of extensive high cliffs of older Pleistocene aeolianite may have precluded a late Pleistocene imprint at Stokes Bay.

7.4 Summary of dating results

Analysis of the Kangaroo Island dosimetry samples ($N = 8$) using HRGS, uncovered disequilibrium in the ^{238}U decay series. Fortunately this disequilibrium was not more than 50% and was occasionally within 20% of unity. Essentially this meant that any deviation from the “true” dose rate of a given sample would be relatively small, i.e., <3% (provided an assumption of secular equilibrium was not made, and TSAC, FGS, or HRGS was used to determine U and Th concentrations). TSAC, GMBC, FGS, and ICP-OES, were also successfully used to determine dose rates for the other 9 luminescence samples.

Pennington Bay was the most extensively studied site on the south coast of Kangaroo Island. Morphostratigraphical and aminostratigraphical correlation revealed 4 (possibly 5) distinct Bridgewater Formation aeolianite units that were present around the embayment. The depositional timing of these units was determined by a combination of luminescence and calibrated AAR dating methods. The age estimates generally aligned the deposition of the aeolianite units with interglacial periods, although in the case of large uncertainties associated with AAR ages, alignment to a particular marine isotope substage was not really possible (unless there were other chronostratigraphical, morphostratigraphical, and

biostratigraphical forms of evidence, i.e., if the units had similar D-L ratios to luminescence dated deposits, or they were raised pebble beach deposits, with signature macro- or microfossils). A range of materials were analysed for amino acids from Pennington Bay: whole-rock sediment, marine molluscs, and single foraminifers. These different materials commonly yielded similar AAR age estimates, the exceptions being when there were a large proportion of reworked skeletal grains present in the sediment. In most cases this could be accounted for by empirically correcting the GLX D-L ratio of the unknown by subtracting the mean extent of GLX racemization in modern beach sediments (in the case of whole-rock sediment), or by selection of the lowest GLX D-L ratio population (assumed representative of the “true” age) via a statistical method (i.e. hierarchical cluster analysis) (in the case of foraminifers). This aside, the AAR data were often sufficient to delineate to the marine isotope stage level, although this correlation was sometimes broad.

Underlying all outcrops (sometimes only visible as shoreface patches) was a dense recrystallised basal calcarenite. Although this was not dated, it was interpreted to be early/middle Pleistocene in age (given its morphostratigraphical position and level of induration), and probably represents the oldest Quaternary unit found around the embayment. The oldest sequences were only present on the major bounding headlands of the bay, and the oldest units (not including the basal calcarenite) were estimated to be MIS 11 in age. The bounding discontinuities overlying this MIS 11 aeolianite at each of the headlands separated a MIS 9 aeolianite. However, there is less certainty that the unit in the eastern headland is of this age.

The upper units at the Pennington Bay headland sites remain undated due to inaccessibility; their ages are an assumption based upon stratigraphic correlation with younger, dated aeolianite units located towards the centre of the embayment. These units ranged from MIS 7 (forming small low headlands, and underlying younger MIS 5 aeolianites) to MIS 4 or 3 in age. MIS 7 and MIS 5 aeolianites were

the most common. The calcretised surface on top of the headlands and cliffs around Pennington Bay hosts extensive vegetated unconsolidated dunes of both modern and Holocene age. The centre of the bay is characterised by low backshore dune topography, and the absence of significantly aged deposits (i.e. no consolidated aeolianites). It is hypothesized that this may have once been the mouth of a sea-way (formed during periods of high sea-level) connecting Pelican Lagoon and American River to the sea, and bisecting Dudley Peninsula from the main body of Kangaroo Island (effectively forming “Dudley Island”). This may have been the case during the Last Interglacial (MIS 5e). Site PB2 hosts a cobble beach deposit in a MIS 7 aeolianite notch. The top of the notch is +3.2 m APSL, and this deposit was age estimated at MIS 5e, using Mollusc, Foram, and WR AAR. This suggested an approximate +3.0 m sea-level during the Last Interglacial (MIS 5e).

The study sites at Bales Beach have (particularly the high western headland site: Bales2) limited geochronology. It was difficult to resolve an age for the lower aeolianite unit at Bales2 (overlying a basal calcarenite—as at Pennington Bay), although the SARTT-OSL and AAR age estimates suggested a MIS 11 age (which would be in keeping with Pennington Bay). Aeolianite units (stacked in a low sequence of 3 aeolianites and 2 intercalated, thin, palaeosols) east of Bales2 (site Bales1) were much lower topographically, and possibly reflected a single MIS deposition, here MIS 5 (ranging between 168 to 100 ka [taking uncertainties into account]—OSL and AAR ages). It is hypothesized that the sequence may represent (on the basis of the OSL and AAR geochronology) a MIS 5e deposition for unit 1a, MIS 5c for unit 1c, and MIS 5a for unit 1e (Figure 7.35, Part II) (following highstand deposition of aeolianites). Similar to Pennington Bay the calcretised upper surface of the sequences are overlain by modern and Holocene well-vegetated, unconsolidated dunes.

Point Ellen and Vivonne Bay exhibited a diverse range of deposits (when compared with the previous 2 study areas). The Point Ellen Formation is confirmed here to be of early Pleistocene age (ranging between 0.9 Ma to 1.7 Ma, on the

basis of Foram and Mollusc AAR dating [taking uncertainties into account]). This formation may be equated with the fossiliferous Plio/Pleistocene Jandakot Member (Yoganup Formation, Perth Basin, Western Australia), and the (early Pleistocene [minimum]) Roe Calcarene (Great Australian Bight) (Murray-Wallace and Kimber, 1989; James *et al.*, 2006).

Sites PE2 and PE3 host a penultimate glacial and a MIS 9 aeolianite, respectively. The MIS 9 aeolianite at PE3 is also notched at approximately +3.0 m APSL. The notch deposit (containing marine shell, coral, and foraminifers) was dated to MIS 5e using U-series methods. As with the Pennington Bay notch deposit (at PB2) a +3.0 m sea-level is inferred for the Last Interglacial. North-west of these deposits is an isolated outcrop of a MIS 5 aeolianite (overlain by a calcrete and unconsolidated dunes), which forms a small headland. Older and younger aeolianite units are absent; although south of this (approximately 300 m) there is a patch of early/middle Pleistocene basal calcarenite.

The Hanson Bay sites comprise unconsolidated Holocene dunes that overlie a shell rich carbonate deposit (with calcretised upper surface)—this in turn overlies an early/middle Pleistocene basal calcarenite and an exposure surface. The shell unit truncates a set of what are apparently lagoonal deposits (from micro-fossil abundance). The shell unit is thought to be either a sub-littoral deposit, or a washover facies (see Chapter 3). This unit correlates with an MIS 5 deposition. The lagoonal facies at the rear of the platform were apparently deposited during late MIS 7. The position of these facies would be in keeping with global estimates of a -5 m to -15 m MIS 7a sea-level (cf. Li *et al.*, 1989; Lundberg and Ford 1994; Toscano and Lundberg, 1999; Antonioli *et al.*, 2004) (given the location of the 20 m isobath and the presence of the South-West River).

Luminescence and AAR dating suggest an early Pleistocene age for the Kelly Hill Caves parent calcarenite. Cave formation is thought to have occurred sometime

between ~1.4 Ma and 500 ka (on the basis of SARTT-OSL and U-series ages estimates).

The shell unit at Rocky Point is consistent with a Last Interglacial raised beach deposit. Even though its elevation is lower (+2.0 m rather than +3.0 m) than other Last Interglacial units of this type (i.e. at Pennington Bay, Vivonne Bay, and Hanson Bay), the Mollusc AAR ages and the *Marginopora vertebralis* biostratigraphical indicator support this interpretation.

Baudin Beach hosts a sequence of aeolianites that is interspersed with alluvial deposits, palaeosols and calcretes. The oldest unit in the sequence is a weathered aeolianite that is of probable MIS 7 age. This is truncated and removed in places along outcrop being displaced or overlain by alluvial sediment correlated with the Last Interglacial South Australia Pooraka Formation. The upper portion of the sequence is an aeolianite unit equated with MIS 5, this overlain by a calcrete/palaeosol and modern/Holocene dunes.

Amino acid racemization analysis of a series of 78 marine shells (*Katelysia* spp.) from a large shelly deposit at American river revealed patterns of reworking and periods of carbonate production during the Holocene (via hierarchical cluster analysis of the D-L ratio data). The amino acid geochronology suggested the onset of carbonate production at ~10.3 ka to ~6.3 ka during the post-glacial marine transgression, when sea-level was approaching its present position. Pulses of production were also evident between ~5.3 ka to ~3.7 ka, ~2.3 to ~3.8 ka, and ~0.6 to ~0.4 ka (these age ranges are based upon the means of D-L ratio clusters), possibly related to optimal climatic conditions and higher sea-level. Because of reworking there was no real relationship between D-L ratio and profile depth. Hence, in order to determine the actual timing of deposition of the shelly bands high-resolution OSL dating would be required. These shell deposits were equated with the Holocene St. Kilda Formation.

The Kingscote Conglomerate at Kingscote Beach, is another example (although very extensive in outcrop) of a Last Interglacial raised beach deposit. This interpretation is supported by the Mollusc and Foram AAR age estimates, and morphostratigraphical and biostratigraphical evidence (i.e. the presence of the indicator fossil *Marginopora vertebralis*) recovered from the study sites. The average height of the unit indicated a Last Interglacial sea-level of approximately +3.0 m (this agrees with palaeosea-levels from Pennington Bay, Vivonne Bay, Hanson Bay and Rocky Point [to a degree]).

Two study sites were examined at North Cape. Site NC1, near Marsden Point, was a large carbonate platform, of early Pleistocene age. The sediments are the remnants of an early Pleistocene sand/mud flat, which accumulated under a palaeosea-level of between +2.0 m to +4.0 m. The age estimate for the sediments (1.2 ± 0.3 Ma) was derived from AAR analysis of the marine shell *Anapella cycladea* (characteristic of tidal inlets, estuarine contexts and tidal flats [Ludbrook, 1984]). Site NC2 is located on the northern side of the cape in Boxing Bay, and hosts an extensive beach conglomerate (the Boxing Bay Conglomerate) that outcrops at +2.0 m APSL down to present sea-level. AAR analysis of marine shell, whole-rock sediments and foraminifers recovered from the conglomerate allowed the assignment of an early/middle Pleistocene age. Overlying the conglomerate are consolidated dune sands of similar antiquity.

Emu Bay hosts an isolated aeolianite unit, located towards the eastern side of the embayment. The sequence consists of two aeolianite units, separated by a palaeosol. The lower unit was dated using TL and WR AAR, yielding a MIS 7 age for deposition. The upper unit was also analysed using AAR, however, the age derived was not significantly different at 1σ to that of the lower unit. This implied two things:

- i) the sediment was deposited during a later MIS, however, a significant reworked component was not compensated for by the empirical

correction (i.e. subtraction of the racemization extent of modern beach sediment)

- ii) or the units were deposited during a single marine isotope stage, and the age difference between the two aeolianite units was not resolvable by the method.

Luminescence dating of the upper aeolianite unit would be required to resolve this issue.

An extensive raised cobble/boulder beach is present at Smith Bay (the Smith Bay Conglomerate) on the north coast of the island. The beach is approximately +18 m APSL and rests unconformably on a thick deposit of Permian glaciogene sediments. An AAR age estimate of 1.0 ± 0.2 Ma was derived using marine molluscs (*Macra* spp. and *Irus* spp.), indicating an early Pleistocene deposition. The site is interesting not only for its probable antiquity, but also for the neotectonic implications of its current height above sea-level.

Stokes Bay, the final site examined on the north coast of Kangaroo Island, hosts an extensive aeolianite outcrop that consists of a single unit unconformably overlain by a blocky, weathered calcrete. The aeolianite yielded an age of 786 ± 181 ka and 750 ± 169 ka using WR AAR (useable foraminifers were unavailable), aligning it with the early/middle Pleistocene. It must be noted that the aeolianite sediment at Stokes Bay was in generally poor condition, and it is very likely that there may have been extensive leaching of lower molecular weight, more highly racemized peptide residues and free amino acids—leading to lower than expected D-L ratios upon analysis. This could mean that the aeolianite may be older than the calculated age estimate suggests.

The results presented here, and insights gained in previous chapters that examined aeolianite deposition, global sea-level change, and the stratigraphy and petrology of Bridgewater Formation deposits is evaluated and discussed in the next

and final Chapter: Chapter 8. Following the discussion a set of conclusions will be presented.

Chapter 8: Kangaroo Island near-coastal Quaternary carbonate sediments: a synthesis

8.1 Introduction

This final chapter discusses the evolution of the Kangaroo Island near coastal sediments, at the sites examined in this thesis, in the context of the AAR and luminescence chronologies.

The chronostratigraphical relationships of the sediment deposits from the north, east, and south coast study sites on Kangaroo Island are explored first, followed by aeolianite landform evolution and sea-level controls on sediment deposition (i.e. aeolianite and raised beach deposits). This will be followed by a brief comparison with other near coastal carbonate sediment chronologies from the southern and northern hemispheres. A set of thesis conclusions, and a statement of further research concludes this final chapter.

8.2 Chronostratigraphical relationships of the Bridgewater Formation aeolianite sequences and other near-coastal carbonate sediment deposits around Kangaroo Island

While many sites were explored, and numerous samples were taken, this study has focused primarily on the Quaternary evolution of coastal carbonate sedimentation on Kangaroo Island. The south coast of Kangaroo Island in particular is a stratigraphically complex region. Aeolianites on the south-western portion (i.e. between Hanson Bay and Cape du Couedic) of this coast form very high (>120 m in places) and extremely precipitous cliffs which are a challenge to sample—this is disappointing as the sediments here probably form the oldest aeolianite sequences on the island. More work is required; however, this initial broad study provides a basis for any future investigations on Kangaroo Island.

8.2.1 Age determination methods

This study predominantly used calibrated amino acid racemization (AAR) dating techniques, and luminescence dating techniques to generate age estimates for a range of Kangaroo Island carbonate sediments (aeolianite, raised beach

sediments, calcrete, Holocene dunes, modern dunes, coquinite, and lagoonal sediments). Also, a small number (2) of U-series and AMS ^{14}C (2) age determinations with corresponding AAR D-L (GLX) ratios were used to establish calibration points for the AAR data (see Chapter 6 for the whole-rock sediment, foraminifer, and mollusc calibrations: section 6.6.4). Luminescence techniques (OSL, TL, and an experimental single aliquot TT-OSL [termed SARTT-OSL] technique developed in this study) were used to directly date some aeolianite units, and OSL ages were also used in conjunction with corresponding AAR D-L (GLX) ratios to provide a luminescence calibration. Numerical AAR ages produced from this calibration were comparable (generally within experimental uncertainty) to those derived using a U-series calibration, even though OSL and U-series are dating two different events—to reiterate:

- i) OSL dates the time since burial of an inorganic mineral grain (i.e. quartz, or feldspar). Sunlight exposure or high temperature empties traps in the crystal matrix of these grains. When the grain is buried the traps act as natural dosimeters, collecting electrons as a response to the energy supplied from exposure to the natural radiation flux of the surrounding sediment. Simplified, the amount of electrons in these traps records the time since the grain was last exposed to either sunlight or heating.
- ii) U-series dates the time since cessation of ^{238}U uptake during precipitation of an organisms (e.g. coral) carbonate skeleton. This cessation can equate with death or the termination of skeletal growth in the organism. U-series can also be used to date pedogenic, and speleogenic carbonates.

Radiocarbon dating is similar to U-series as what is being dated is the cessation in uptake of a particular isotope; here ^{14}C . When the organism dies ^{14}C is no longer replenished through the carbon cycle, and so what is remaining in the organic matrix begins to decay to ^{14}N .

AAR, conversely, is a time and temperature dependant *chemical reaction* where optical isomers of amino acids reversibly convert from the L-configuration to the D-configuration (see Chapter 6, section 6.2.1). L-amino acids are metabolically

supported when an organism is alive; hence D-amino acids are generally not present. When the organism dies, however, there is no longer metabolic support and D-amino acids begin to accumulate until equilibrium is reached. The D-L ratio in this instance can be used to estimate the time of protein metabolism cessation (in short-lived organisms this is statistically indistinguishable from death). With regards to similarities, however, the geochronological methods of U-series, ^{14}C , and AAR all endeavour to estimate time since the termination of some metabolic process (respiration, protein production, skeletal precipitation) that can often be associated with the death of the organism (or in the case of U-series, also the cessation of pedogenic, or speleogenic precipitation of carbonate).

In light of these differences in the characteristics of luminescence, U-series, ^{14}C , and AAR dating, it is important to realise that potential complexities may arise, particularly in relation to whole-rock sediment AAR age estimates. For example continental shelf, sublittoral, subtidal and near-shore residence times experienced by sediments may conflict with dating methods such as TL, OSL, or SARTT-OSL that record time since deposition. Potentially, skeletal grains (e.g. foraminifers), and molluscan shells may have been dead for a significant period of time prior to deposition, or they may have been reworked from older deposits. This is particularly important in dynamic depositional environments, such as those that exist on the coasts of Kangaroo Island and mainland South Australia, where reworking of older sediments into younger, later phase sediments occurs. It would be expected then that there may be some disparity between ages derived from luminescence and ages derived from an AAR calibration.

Nevertheless, the separate AAR and luminescence chronologies developed in this thesis agree favourably. The large uncertainties related to the AAR numerical ages did mean that the possible magnitudes of age-offsets (because of residence times) were accounted for within the range of uncertainty (and also because of the use of an empirical correction of the whole-rock sediment D-L ratio: see Chapter 6. section 6.6.4). Rejection criteria and the use of a statistical method (Ward [1963] hierarchical clustering dendrograms) to identify clusters of D-L ratio populations within groups of foraminifers from a single stratigraphical

unit, allowed the reduction of the level of uncertainty. This method also allowed the identification of patterns of reworking within populations of single grains, and the identification of superimposed reworking “source signals” from nearby, although chronostratigraphically different, units (see Chapter 6, section 6.6.4 and Chapter 7). AAR numerical dating—despite these potential complexities—has still provided relatively good age control for stratigraphic units around Kangaroo Island. The technique has also confirmed ages for units and formations described in the literature (e.g. the Kingscote Conglomerate, the Point Ellen Formation, and the Pooraka Formation—see Chapter 7). Although the ages derived using the various calibrations often have large uncertainties (particularly in foraminifer samples and samples of early and middle Pleistocene age), they are still useful in providing the basis of a chronostratigraphical framework for carbonate deposition on Kangaroo Island.

8.2.2 Time-stratigraphical relationships between Kangaroo Island study sites: aminozones

Relative to the size of Kangaroo Island only a few areas were mapped in detail. Regardless, it was found that there are time-stratigraphical correlations between sites for a number of different facies types. Raised pebble/cobble beach deposits, raised shelly deposits, and shelly notch deposits that were sampled from around the island (Pennington Bay, Vivonne Bay, Hanson Bay, Kingscote Beach, and Rocky Point) were shown to have not only similar morpho- and biostratigraphical characteristics (i.e. 2 m to 3.5 m APSL [see Table 7.31, Chapter 7, section 7.3.9.2], and exhibiting MIS 5e marker foraminifers [*Marginopora vertebralis*]), but are also similar in terms of the GLX D-L ratios derived from whole-rock sediments, single foraminifers and marine gastropod and bivalve fossils. Table 8.1 demonstrates these similarities. Calibration of these ratios yielded a series of ages that corresponded with the timing of the Last Interglacial highstand (cf. Siddall *et al.*, 2007) (the mean and standard deviation of all GLX AAR ages derived for these deposits is 125 ± 22 ka [not including propagation of individual uncertainties]), and the upper limits of these units (m APSL) allowed the estimation of a mean sea-level for the Last Interglacial shoreline on Kangaroo Island: $+3.0 \pm 0.5$ m (see Chapter 7, section 7.3.9.2).

Table 8.1: GLX D-L ratio data (whole-rock sediment, mollusc, and foraminifer) for Last Interglacial raised deposits for Kangaroo Island Sites Pennington Bay, Vivonne Bay, Hanson Bay, Rocky Point and Kingscote.

Location	*Sample code / facies	Genus / species	N	GLX D-L \pm 1 σ
Pennington Bay	PB#2e-2 / raised pebble beach	Whole-rock	6	0.463 \pm 0.007
Rocky Point	RP / shelly notch deposit	Whole-rock	4	0.401 \pm 0.005
Hanson Bay	HB#3-4 / raised shelly deposit	Whole-rock	6	0.462 \pm 0.010
Kingscote	KC1 / raised pebble / cobble beach	<i>Kataysia scalarina</i>	5	0.354 \pm 0.019
Rocky Point	RP / (poorly preserved) raised shelly notch deposit	<i>Fulvia tenuicostata</i>	3	0.318 \pm 0.007
Pennington Bay	PB#2e-2 / raised pebble / cobble beach	<i>Amesodesma angusta</i>	8	0.360 \pm 0.008
Vivonne Bay	PE#3-5 / raised pebble, shelly notch deposits	<i>Nerita (Melanerita) atramentosa</i>	4	0.364 \pm 0.012
Hanson Bay	HB1 / raised shelly deposit	<i>Spisula (Notospisula) trigonella</i>	5	0.359 \pm 0.025
Pennington Bay	PB#2e-1 / raised cobble / pebble beach	<i>Elphidium</i> sp. + <i>Discorbis dimidiatus</i>	35	0.307 \pm 0.022
Vivonne Bay	PE#3-4 / raised pebble, shelly notch deposits	<i>Elphidium</i> sp. + <i>Discorbis dimidiatus</i>	11	0.308 \pm 0.025
Hanson Bay	HB#3-4 / raised shelly deposit	<i>Elphidium</i> sp. + <i>Discorbis dimidiatus</i>	13	0.308 \pm 0.021
Rocky Point	RP / shelly notch deposit	<i>Elphidium</i> sp. + <i>Discorbis dimidiatus</i>	11	0.358 \pm 0.088
Kingscote	KC1 / raised pebble / cobble beach	<i>Discorbis dimidiatus</i>	3	0.325 \pm 0.053
Kingscote	KC2 / raised pebble / cobble beach	<i>Elphidium</i> sp. + <i>Discorbis dimidiatus</i>	6	0.323 \pm 0.028

* PB = Pennington Bay; RP = Rocky Point; HB = Hanson Bay; KC1 = Kingscote Beach; PE = Point Ellen and Vivonne Bay; KC2 = Kingscote Boat Ramp

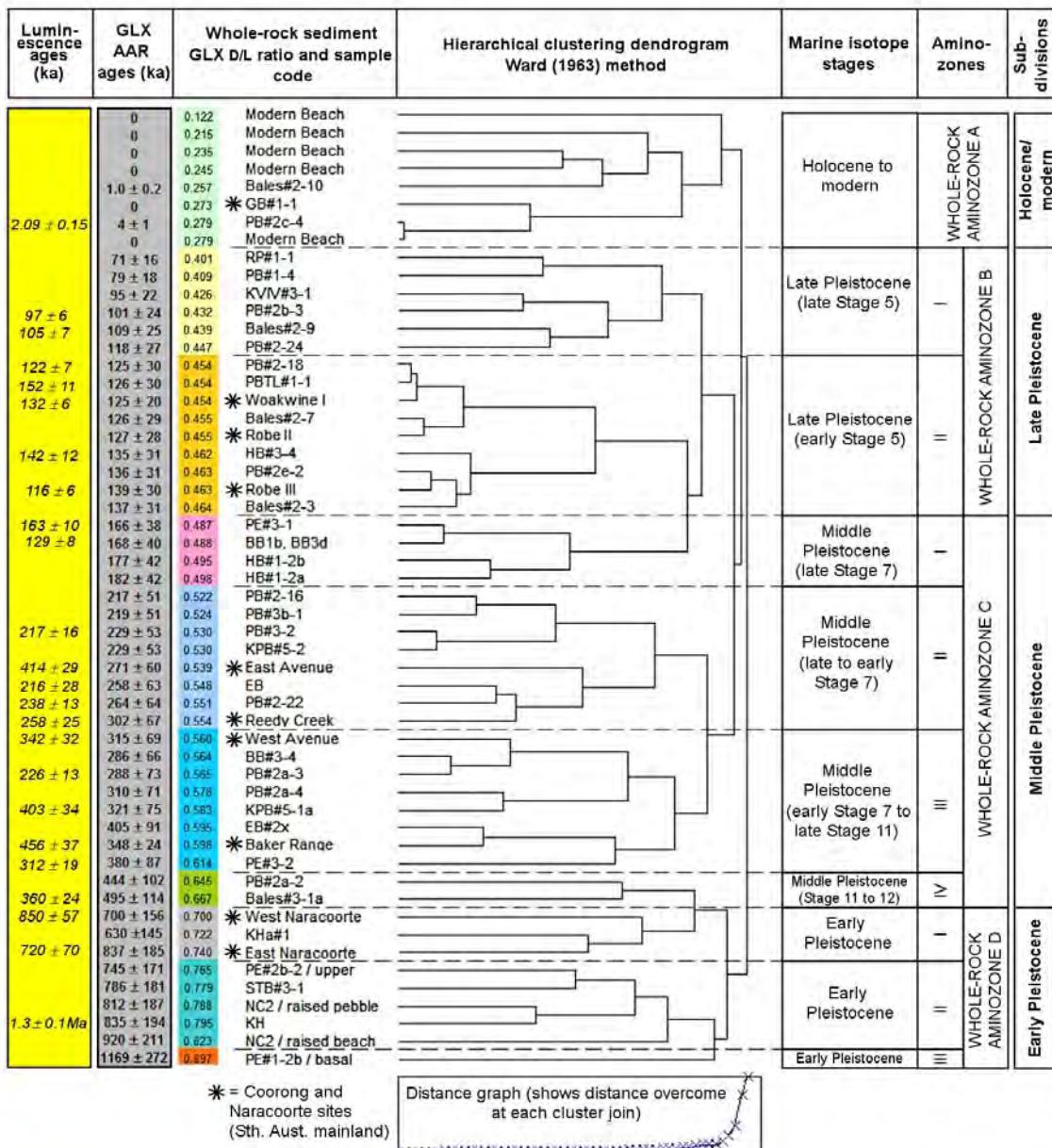


Figure 8.1: Ward (1963) method hierarchical clustering dendrogram (constructed in SAS JMP) of whole-rock sediment GLX D-L ratio data from Kangaroo Island, and Coorong and Naracoorte on the southeast South Australia mainland (indicated by asterisk); accompanied by the luminescence chronology (including the TL ages of Huntley *et al.*, 1993, 1994), and AAR chronology, and amino zones defined on the basis of 10 clusters. Amino acid D-L ratios are mean data (not including uncertainties); coloured overlays are for definition purposes—colours are arbitrary. The dashed lines represent software selected cluster sections (Bales = Bales Beach; GB = Guichen Bay; PB = Pennington Bay; RP = Rocky Point; KVIV = Vivonne Bay; Woakwine = Woakwine Range; Robe = Robe Range; PE = Point Ellen and Vivonne Bay; BB = Baudin Beach; HB = Hanson Bay; KPB = Pennington Bay; East Avenue = East Avenue Range; EB = Emu Bay; Reedy Creek = Reedy Creek Range; West Avenue = West Avenue Range; West Naracoorte = West Naracoorte Range; KHa = Hanson Bay; East Naracoorte = East Naracoorte Range; STB = Stokes Bay; NC2 = Boxing Bay; KH = Kelly Hill Caves).

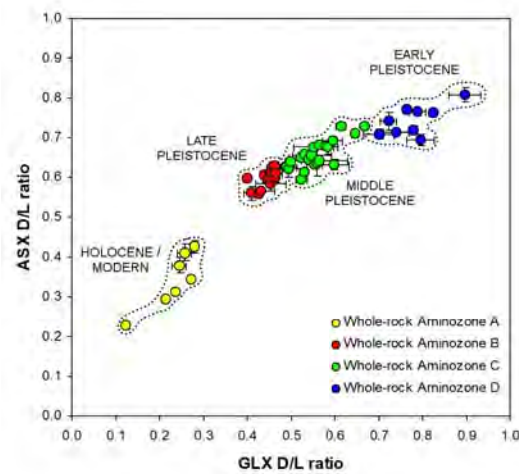


Figure 8.2: Bivariate plot of mean whole-rock sediment AAR data from the Kangaroo Island sites clustered using Ward (1963) method hierarchical dendrograms.

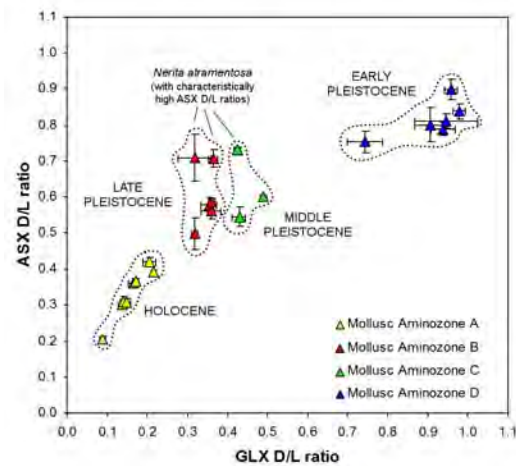


Figure 8.3: Bivariate plot of mean mollusc AAR data from the Kangaroo Island sites clustered using Ward (1963) method hierarchical dendrograms.

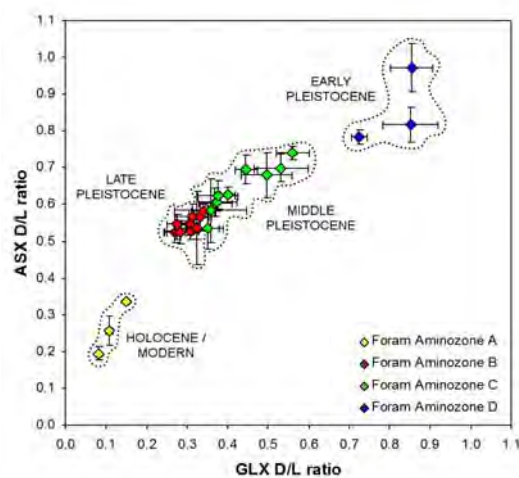


Figure 8.4: Bivariate plot of mean foraminifer AAR data from the Kangaroo Island sites clustered using Ward (1963) method hierarchical dendrograms.

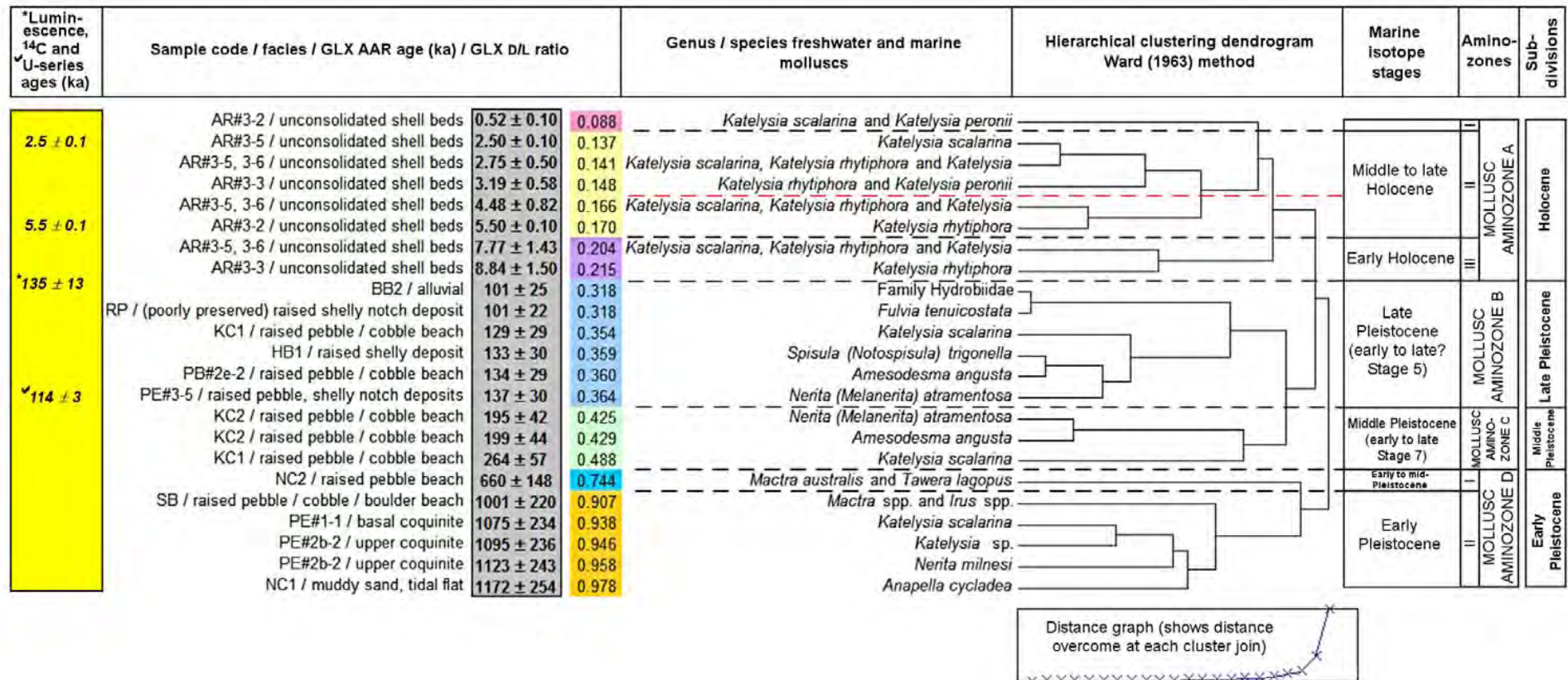


Figure 8.5: Ward (1963) method hierarchical clustering dendrogram (constructed in SAS JMP) of molluscan GLX D-L ratio data from Kangaroo Island; accompanied by the ¹⁴C and U-series chronology and amino zones defined on the basis of 7 clusters. Amino acid D-L ratios are mean data (not including uncertainties); coloured overlays are for definition purposes—colours are arbitrary. The dashed lines represent software selected cluster sections (AR = American River; BB = Baudin Beach; RP = Rocky Point; KC1 = Kingscote Beach; HB = Hanson Bay; PB = Pennington Bay; PE = Point Ellen and Vivonne Bay; KC2 = Kingscote Boat Ramp; NC2 = Boxing Bay; SB = Smith Bay; NC1 = North Cape).

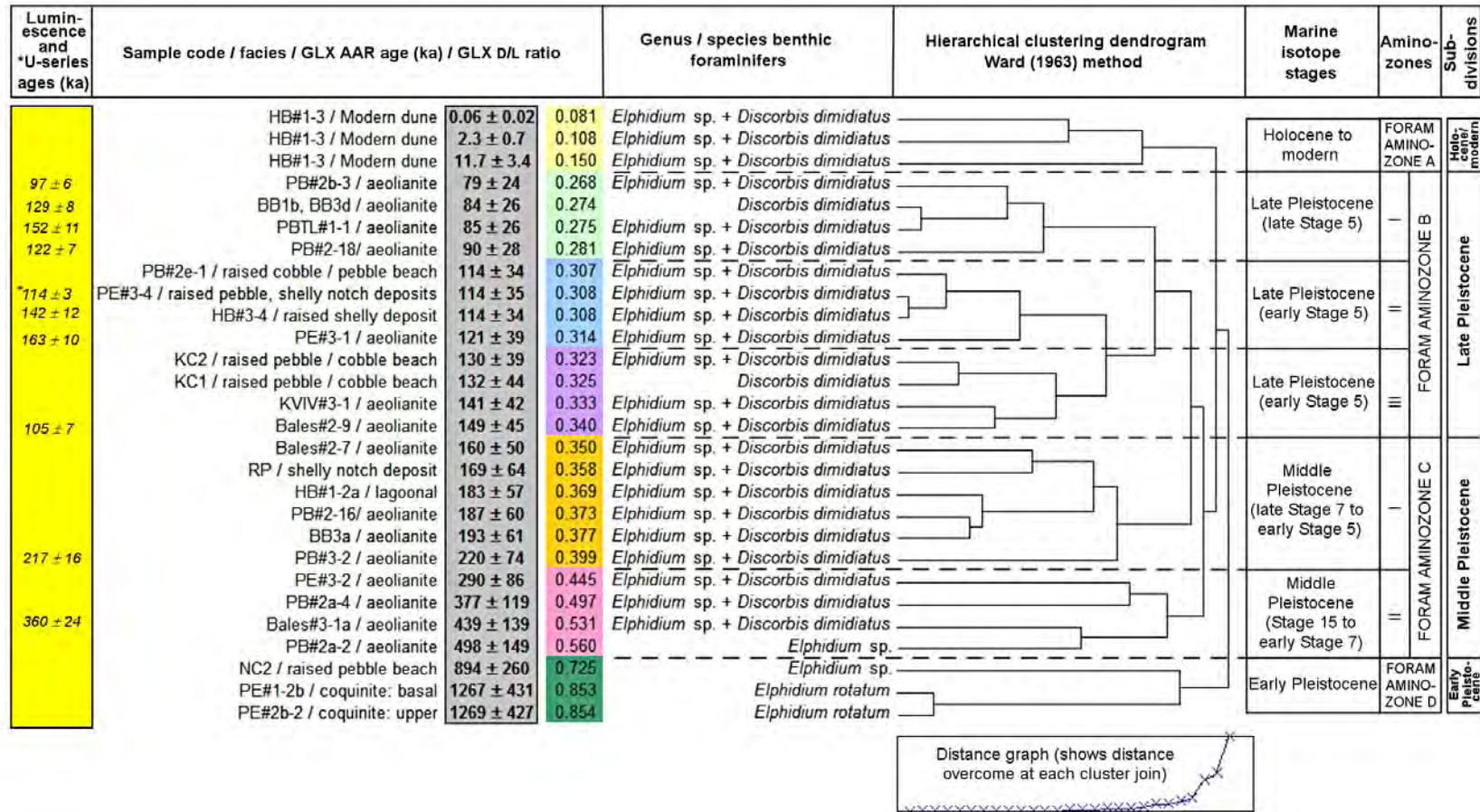


Figure 8.6: Ward (1963) method hierarchical clustering dendrogram (constructed in SAS JMP) of foraminifer GLX D-L ratio data from Kangaroo Island; accompanied by the luminescence and U-series chronology and amino zones defined on the basis of 7 clusters. Amino acid D-L ratios are mean data (not including uncertainties); coloured overlays are for definition purposes—colours are arbitrary. The dashed lines represent software selected cluster sections (HB = Hanson Bay; PB = Pennington Bay; BB = Baudin Beach; PE = Point Ellen and Vivonne Bay; KC2 = Kingscote Boat Ramp; KC1 = Kingscote Beach; KVIV = Vivonne Bay; Bales = Bales Beach; RP = Rocky Point; NC2 = Boxing Bay).

These raised beach units correspond with a Late Pleistocene GLX aminozone (the limits of which were defined by cluster analysis of the GLX D-L ratio datasets): designated Aminozone B (for whole-rock sediment [Figure 8.1 and 8.2]; Molluscs [Figure 8.3 and 8.5]; Forams [Figure 8.4 and 8.6]), that also encompasses a series of upper aeolianite units on the southern and eastern coasts of Kangaroo Island (Pennington Bay, Bales, Beach, Vivonne Bay, and Baudin Beach), and aeolianite dunes on the south-east South Australia mainland (i.e. Woakwine I, Robe II and III on the Coorong coastal plain) (see Figure 8.1). The limits of the aminozones for whole-rock sediment, mollusc, and foraminifers were defined using the Ward (1963) method of hierarchical cluster analysis (explained in Chapter 6, section 6.4.7) of each GLX D-L ratio dataset. The age span of each aminozone was defined using the corresponding AAR ages. The AAR ages broadly agree with the luminescence chronologies, although there are significant differences with some AAR ages—this may be attributable to (particularly for the whole-rock and foraminifer datasets) the contribution (to the D-L ratio) of older reworked materials, or diagenetic factors (for example leaching of more highly racemized lower molecular weight residues).

Some aminozones also comprise a series of “subzones” (designated by roman numerals in Figures 8.1, 8.5, and 8.6) which may correspond with particular marine isotope stages (MIS), substages, and even subdivisions in the Holocene (depending upon the level of uncertainty in the GLX D-L ratio derived ages)—see Figure 8.5: Aminozone A, for example. Here precision was great enough in the ^{14}C calibrated GLX D-L ratio data (marine molluscs recovered from American River) to differentiate pulses of carbonate production through the Holocene (see Chapter 7, section 7.3.8). Figure 8.7 displays a Holocene sea-level curve (modified from Belperio *et al.*, 2002) generated from Holocene coastal sites in southern Australia. This curve is overlain by the Kangaroo Island Holocene geochronological data. The Holocene (to modern) aminozone (A) also includes modern beach sediments, and backshore and cliff-top dunes.

The upper limits of each aminozone may vary between material type (i.e. whole-rock, foraminifer, and mollusc) due to the range of D-L ratios in each dataset (for example the whole-rock aminozones are more comprehensive because of the

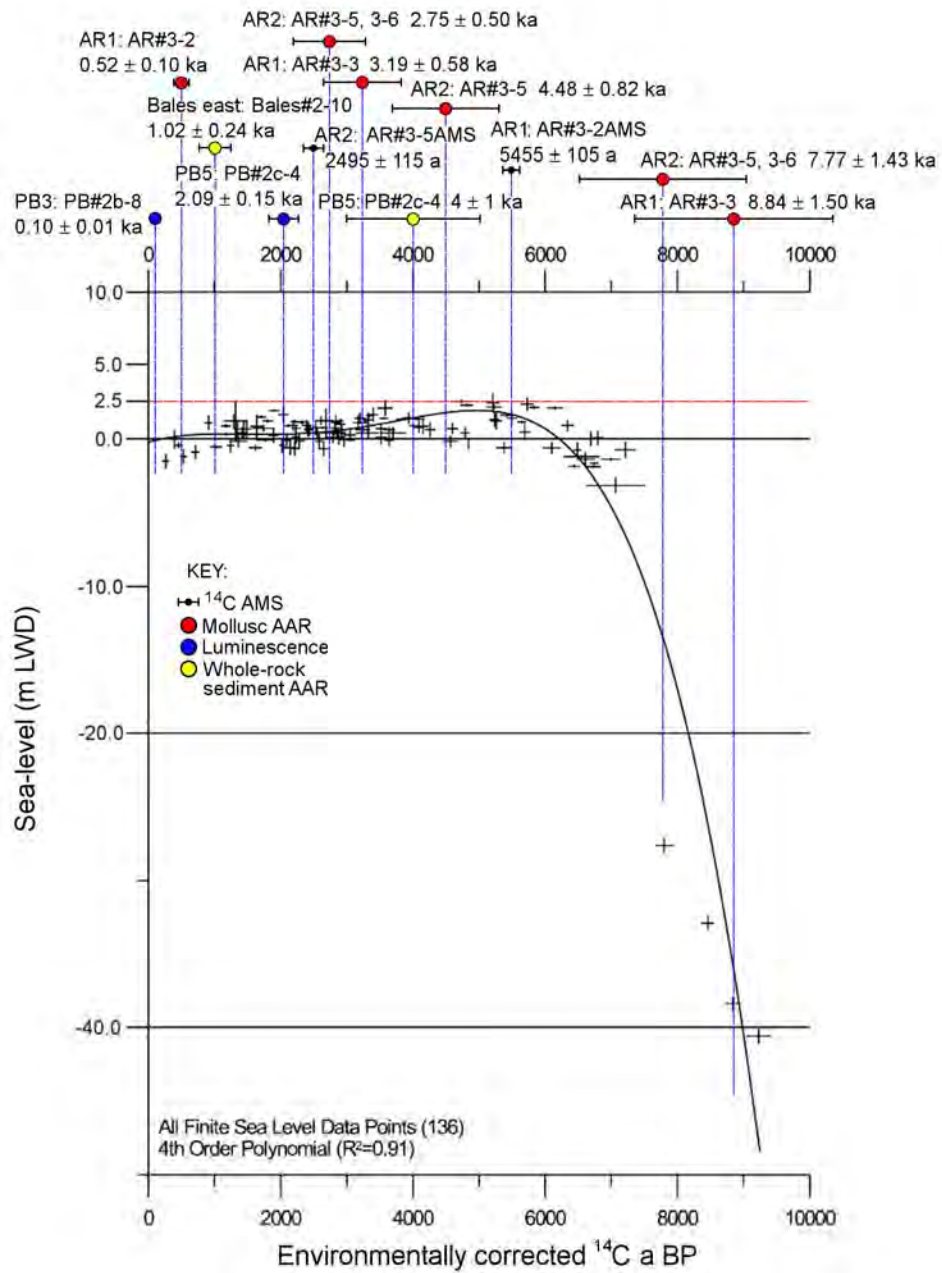


Figure 8.7: Holocene sea-level curve generated from 136 finite sea-level data points (compiled from southern Australia sites) fitted with a fourth-order polynomial. The sea-level curve is relative to present Low Water Datum (m LWD) (figure modified from Belperio *et al.*, 2002). The curve is overlain with GLX AAR ages, luminescence ages, and ^{14}C ages from this study. The blue dashed lines give the age intersections on the sea-level curve, and the red dashed line represents a +2.5 m sea-level, for reference purposes.

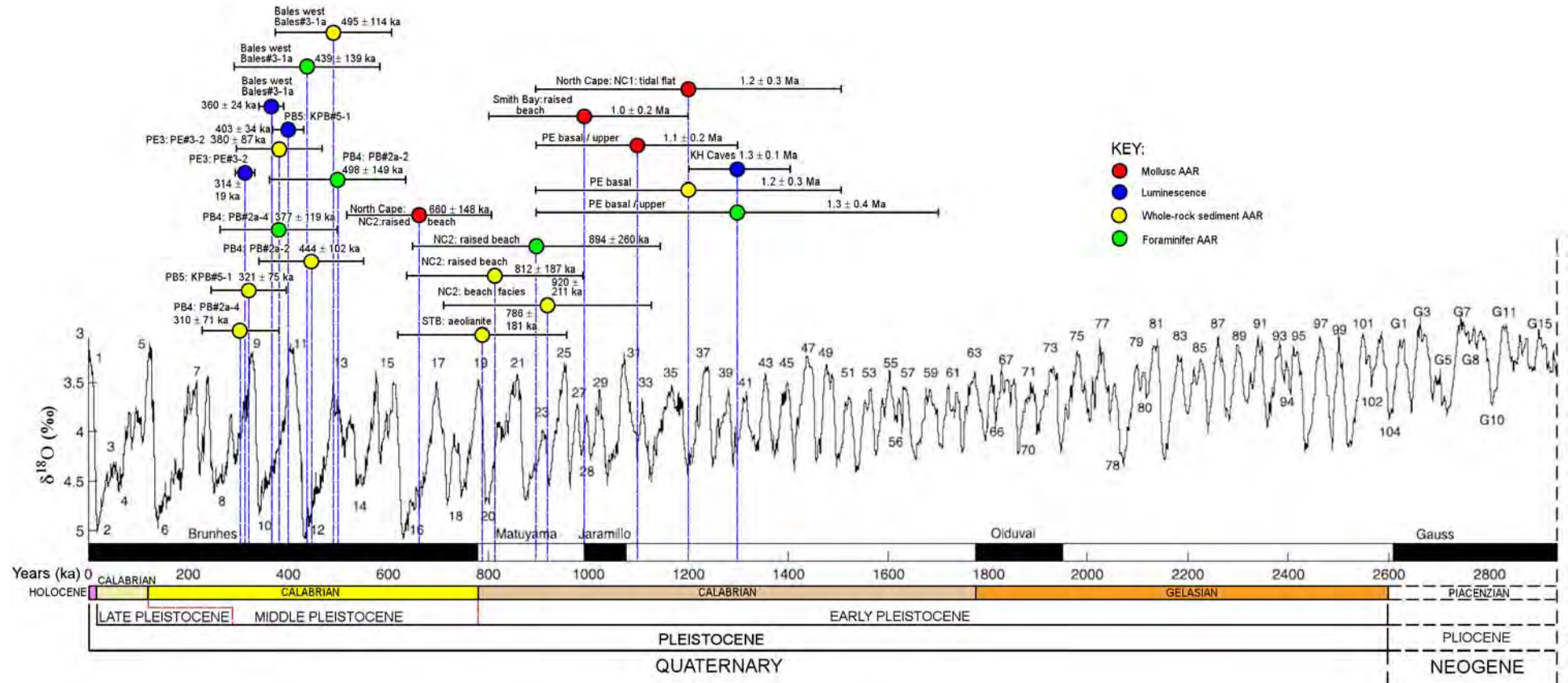


Figure 8.8: Quaternary oxygen isotope curve (modified from the Quaternary section of the Lisiecki and Raymo [2005] LR04 stack) with luminescence (SARTT-OSL), and amino acid racemization (AAR) chronologies, from this study, overlain. Note: only early Pleistocene and (early) middle Pleistocene ages are shown (for the sake of resolution younger ages are given on higher resolution sea-level curves: Figure 8.7 [Holocene] and 8.9 [late middle Pleistocene to late Pleistocene]) (age point y-axis locations are arbitrary; uncertainty bars are 1σ).

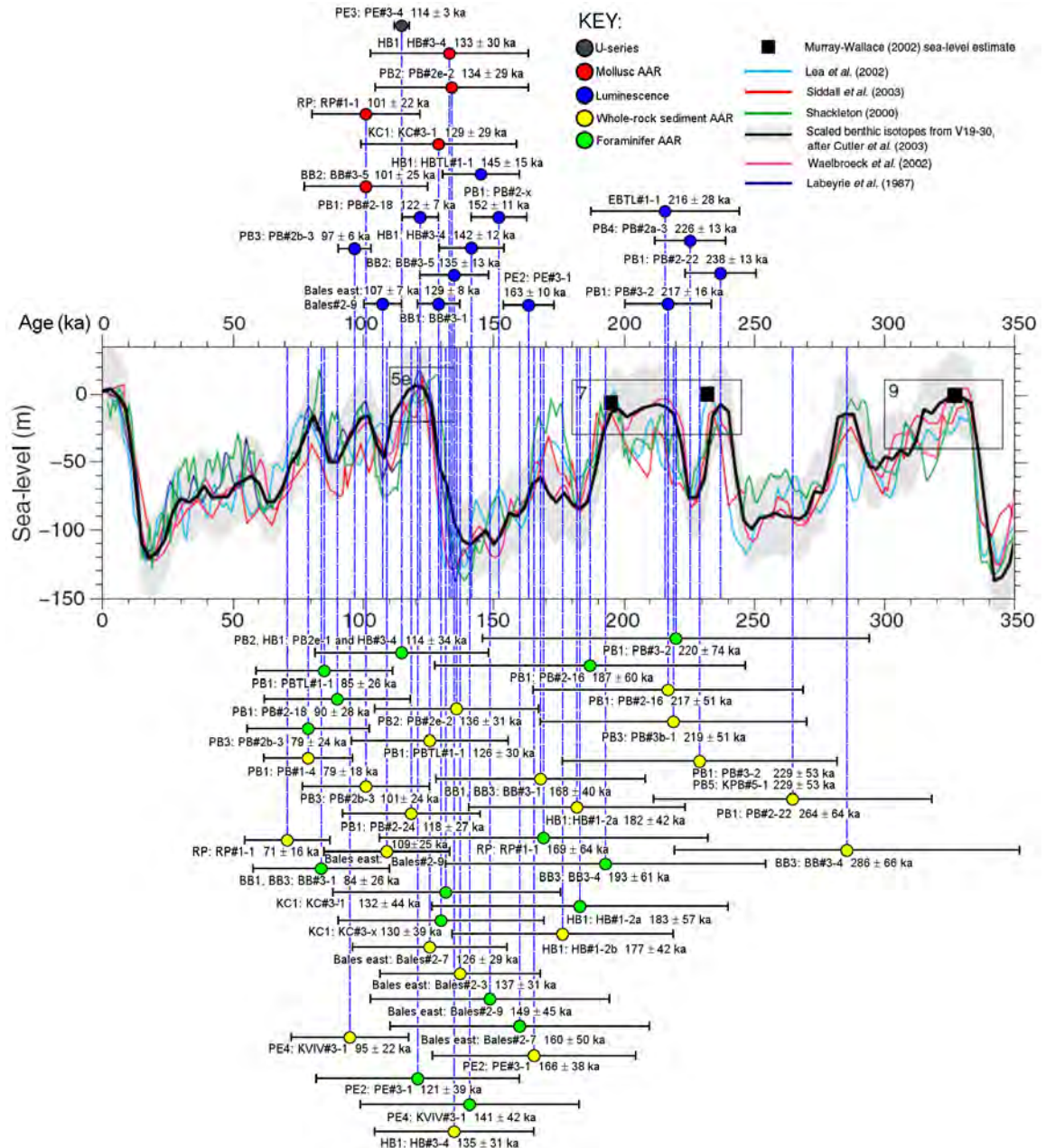


Figure 8.9: Continuous sea-level estimates on the SPECMAP timescale (up to MIS 9) from a range of sources (coupled with other sea-level indicators), and compared with the benthonic oxygen isotope record of core V19-30 (Shackleton and Pisias, 1985) from the east equatorial Pacific (scaled after Cutler *et al.*, 2003) (figure modified from Siddall *et al.*, 2007). The luminescence (OSL, SARTT-OSL and TL) and AAR ages from Kangaroo Island are overlaid onto the sea-level curves (the y-axis positions of the age points are arbitrary and do not relate to a scale; uncertainties are 1σ) and the blue dashed lines give the age intersections with the sea-level curves. This is a complex diagram; however, more simply it serves to show where the greatest concentrations of ages are during the middle to late Pleistocene, i.e., the highest densities of ages (and hence blue dashed lines) are at MIS 7 and MIS 5e. Luminescence (blue) (and the U-series age [grey] from Vivonne Bay), and mollusc AAR ages (red) are at the top of the diagram, and whole-rock sediment (yellow) and foraminifer AAR ages (green) are at the bottom.

larger more extensive dataset)—in this sense the amino “subzones” of each material type are only broadly compatible in some instances (although each is more compatible at the Quaternary subdivision level [see Figures 8.1, 8.4, and 8.5]). It must also be noted that the boundaries between aminozones are not sharp (as suggested in Figures 8.1, 8.5 and 8.6); there are overlaps because of uncertainties in the GLX ages and GLX D-L ratio means used to define the zones. There are also gaps in the data (in terms of D-L ratios), particularly for molluscs and to a smaller degree foraminifers, and most noticeably between the A and B, and C and D aminozones, where the GLX D-L jumps from ~0.2 to ~0.3 and ~0.5 to ~0.8 (see Figure 8.5). For molluscs the reason for this is the lack of shelly deposits at these ranges of antiquity on Kangaroo Island, which is most likely attributable to a paucity of high sea-level events close to or higher than the present (sea-level) during the time periods represented by the gaps, and also their preservation potential in the longer-term stratigraphic record. The gaps are more artificial for foraminifers and are often due to poor preservation of tests in older (middle-early Pleistocene) deposits, and the absence of tests of suitable size in younger, finer sediments (e.g. in fine grained backshore and cliff-top Holocene dunes). The gap between the Holocene and the latter part of the late Pleistocene is present in the whole-rock sediment data too (perhaps pertaining to marine isotope stages 4, 3 and 2) (preliminary AAR work on the large-scale unconsolidated dunes at Little Sahara, and Prospect Hill may partially fill this gap though). Gaps are generally not seen in the older whole-rock sediment data, where the transitions are relatively even; this perhaps reflects consistent cycles of aeolian sedimentation, and a smoothing effect attributable to a reworking “signal”.

As explained above prior to the late Pleistocene and during the middle Pleistocene there is a conspicuous absence of shelly / cobble / pebble beach deposits. Even though a middle Pleistocene mollusc aminozone is defined (Figure 8.5: aminozone C), it is based upon a few reworked shells recovered from the MIS 5e Kingscote Boat Ramp site (see Chapter 7 section 7.3.9). These shells were most likely reworked from an MIS 7 shell bed located just off the coast at Kingscote during the Last Interglacial. The lack of an older shell bed presence then may be attributable to deposition at lower-than-present-sea-

levels (at peak interglacial highstands) during this period, i.e., any such deposits would now lie off the coast, and be concealed by onlapped younger sediments, or even be eroded completely away. However, during the early Pleistocene, near the latter portion of the early Pleistocene (i.e. ~1.3 Ma) and towards the middle / early Pleistocene boundary (~780 ka), several possibly higher-than-present sea-level events were recorded as dense shell deposits (the early Pleistocene Point Ellen Formation), shelly cobble beach deposits (the Smith Bay Conglomerate and the Boxing Bay Conglomerate), and shelly tidal flat facies (the North Cape Beds). It is also possible that this was a single event recorded, as uncertainties on the AAR ages overlap. Nonetheless, the Boxing Bay Conglomerate most likely does represent a younger event than the others as the whole-rock, foraminifer, and mollusc AAR ages tended to cluster together (see Figure 8.8). The Point Ellen Formation, Smith Bay Conglomerate, and North Cape Beds may be contemporaries however. Although, it is difficult to reconcile the position of the Smith Bay Conglomerate in comparison (i.e. approximately +20 m APSL as opposed to +2 to +4 m APSL for the North Cape Beds and the Point Ellen Formation). As suggested in Chapter 7, section 7.3.12, it is possible that the Smith Bay Conglomerate (and the underlying glacial till, and bedrock) was uplifted by a local tectonic event sometime after deposition—the site requires further study to ascertain if this is likely. The GLX D-L ratios for whole-rock sediments, foraminifers and molluscs recovered from these conglomerates and shell beds, along with GLX D-L ratios for whole-rock sediments and foraminifers from aeolianite units at Boxing Bay and Stokes Bay (and the calcarenite in which Kelly Hill Caves was formed), define the oldest aminozone on Kangaroo Island: the early Pleistocene Aminozone D (see Figures 8.1, 8.5 and 8.6). The east and west Naracoorte dunes, based upon their respective whole-rock sediment GLX D-L ratios, fall within this aminozone as well (Figure 8.1).

Aminozone B (pertaining mainly to the early part of the late Pleistocene, i.e., subzone II, which relates most likely to MIS 5) and aminozone C (pertaining mainly to subzone I and II: possibly MIS 7c and 7a) aeolianite sediments form the bulk of sediments sampled on Kangaroo Island. This is also evident in

Figure 8.9 which clearly shows that these are the greatest age densities located on the OI curve.

8.2.3 Chronostratigraphy of south coast Kangaroo Island near-coastal carbonate sediments

The sediments examined along the south coast of Kangaroo Island were of predominantly Holocene, Last Interglacial, and MIS 7 age, with older aeolianite sequences forming large bounding headlands. The most extensive examinations were undertaken at Pennington Bay revealing successions of aeolianites overlying a basal calcarenite of probable early Pleistocene age.

Third party source; Images redacted at request of thesis author

Figure 8.10: Oblique view (200 m altitude) of Pennington Bay, facing north-east. Note position of small inner-bay headlands (centre and right mid-ground) (image is vertically exaggerated by 3— image and DEM from Google Earth, 2010). The high peak in the rear mid-ground is Prospect Hill (a vegetated, unconsolidated, large-scale dune).

The following chronostratigraphies will mainly refer to the whole-rock aminozone scheme (Figure 8.1) when comparing sites, because it is more comprehensive.

8.2.3.1 Pennington Bay

The Pennington Bay successions are in outcrop as low cliffs towards the middle of the embayment, bounded by small headlands, with higher headlands forming the north-eastern and south-western boundaries of the bay (see Figure 8.10).

The low cliffs are formed in a sequence of aeolianite / palaeosol or aeolianite / calcrete couplets. The lowest unit is thick, *terra rossa* palaeosol, which crops out intermittently around the embayment (as lenses that probably formed in dune swales) and underlies an MIS 7 aeolianite unit. The age of this palaeosol is speculative; however, it seems likely that it formed during the MIS 8 glaciation, given its position under a MIS 7 dated unit. The MIS 7 (whole-rock Aminozone C, subzone II) aeolianite unit is present as discrete calcrete-capped headlands in the middle sections of the bay, and is also present as the lowest aeolianite unit (not including the basal calcarenite) in the low-cliffed areas, and as an upper unit in major bounding headlands (see section 7.3.1 in Chapter 7). This unit was sampled several times around the embayment (PB#2a-3, PB#2-22, PB#3-2, PB#2-16, and PB#3b-1) and has a grand mean GLX D-L ratio of 0.538 ± 0.039 for whole-rock sediment. This gives an average WR AAR age estimate of 242 ± 58 ka for outcrops of this unit around the bay; foraminifers, where available, yielded a similar age. The unit was also dated several times using OSL and SARTT-OSL at 217 ± 16 ka, 238 ± 13 ka, and 226 ± 13 ka. At site PB2 wave action during a period of higher sea-level (interpreted as peak MIS 5e) has cut a notch into the MIS 7 aeolianite at approximately 3.0 m APSL. The notch is packed with the remnants of a shelly, cobble / pebble beach deposit, which has been dated at MIS 5e using various methods (i.e. 136 ± 31 ka [WR AAR], 134 ± 29 ka [Mollusc AAR], and 114 ± 34 ka [Foram AAR], morphostratigraphical position and marker foraminifers).

The MIS 7 unit is unconformably overlain by a palaeosol that varies in thickness at different outcrops. The unit above this is a thick MIS 5 aeolianite unit (whole-rock Aminozone B, subzones I and II) that consists of sediment that was deposited during substages 5e and 5c-d. This unit dated at 125 ± 30 ka (WR AAR), 122 ± 7 ka (OSL), 152 ± 11 ka (OSL), and 90 ± 28 ka (Foram AAR), at site PB1, and 101 ± 24 ka (WR AAR), 97 ± 6 ka (OSL), and 79 ± 24 ka (Foram AAR) at site PB3 (see section 7.3.1, in Chapter 7, and Figure 8.11) (hence the interpretation of MIS 5c-d for the unit at site PB3). Unconformably overlying the MIS 5 aeolianite is a calcrete / palaeosol which varies in thickness and character around the embayment. The calcrete drapes the landscape on a regional basis, and a large proportion of the sheet may be of one age. A sample

was taken for WR AAR analysis at PB1; although it was recovered near the surface and the AAR rates may have been adversely affected by diagenetic temperature flux. Regardless, AAR ages of 79 ± 18 ka (WR) and 137 ± 50 ka (Foram) was calculated, suggesting MIS 3 to 5 deposition of the components (this may be very overestimated however). Modern backshore dunes and Holocene dunes cover the calcrete intermittently along the coast, although, the calcrete is commonly bare at cliff-tops. These dunes along with the modern beach sediments form whole-rock Aminozone A. The whole-rock GLX D-L ratios vary greatly depending upon the relative proportions of reworked component skeletal grains in the sediments; however, they were never recorded as being >0.320 .

The main bounding headlands (PB4 and PB5) hosted stacked sequences of greater age than that found towards the central part of the bay. The lowest aeolianite units (not including the basal calcarenite unit) are of possibly MIS 12-9 in age (whole-rock Aminozone C, subzones III and IV) (see section 7.3.1, in Chapter 7, and Figure 8.1, and 8.11). WR and Foram AAR ages were between 321 ± 75 ka and 498 ± 149 ka. The SART-OSL age (403 ± 34 ka) for this unit at site PB5 is more precise and does centre on MIS 11. The next unit in the sequence, was dated at both sites using WR and Foram AAR, yielding ages of between 229 ± 53 ka and 377 ± 119 ka: MIS 7 to 11 (whole-rock aminozone C, substages II and III). Given the stratigraphical position of this unit a MIS 9 age was preferred (see section 7.3.1 in Chapter 7, and Figure 8.1, and 8.11). The upper units in these sequences could not be safely sampled. However, based upon superposition the upper aeolianite units at the PB5 sequence appear to represent MIS 7 to 5, although at PB4 the MIS 5 aeolianite may be missing.

8.2.3.2 Bales Beach

Similar to Pennington Bay the Bales Beach sediments crop out as low cliffs and major headlands (see Figure 8.12). The low aeolianite cliffs were sampled at Bales1 (see Figure 8.11) (sampling took place at a range of lateral positions along outcrop). This outcrop apparently represents a single MIS: MIS 5 (see section 7.3.2 in Chapter 7 for more detail); WR and Foram ages range from 109 ± 25 ka (WR) to 160 ± 50 ka (Foram) (i.e. whole-rock aminozone B, subzones I

Third party source; Images redacted at request of thesis author

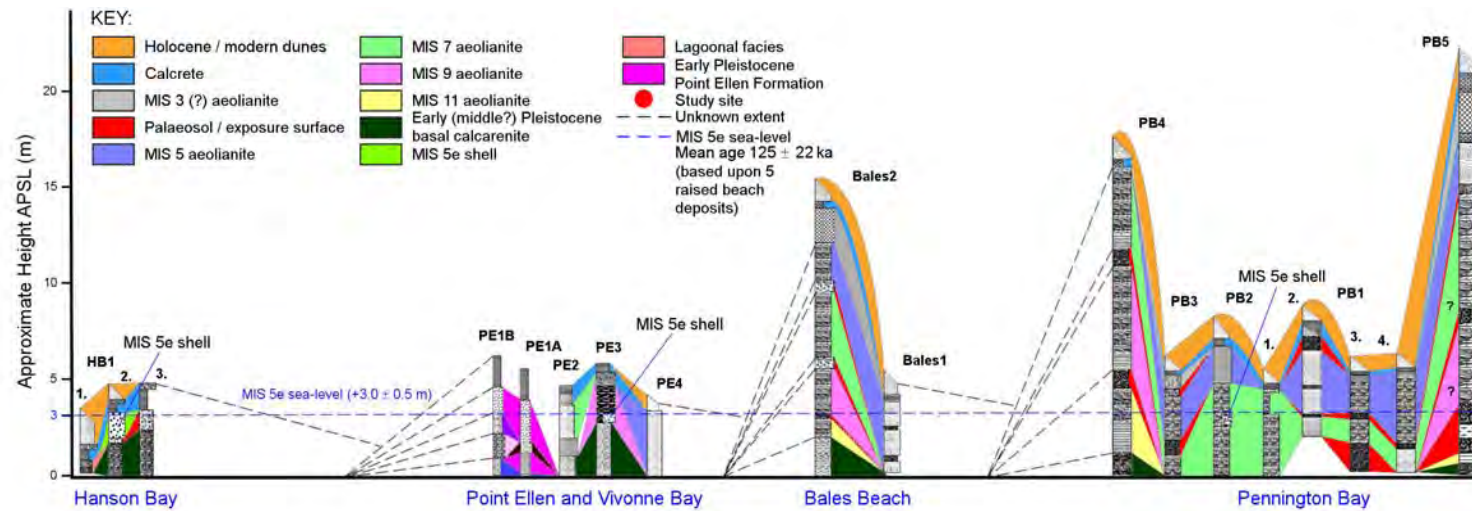


Figure 8.11: Proposed chronostratigraphy for the south coast of Kangaroo Island based upon the luminescence and AAR chronologies. The y-axis and logs are to scale, however the x-axis is not (top image is a Landsat ETM: NASA Landsat project, 2001).

Third party source; Images redacted at request of thesis author

Figure 8.12: Oblique view (241 m altitude) of Bales Beach, facing north-east (image is vertically exaggerated by 3—image and DEM from Google Earth, 2010).

and II)—the Foram ages, however, are not as consistent as the WR ages. The upper aeolianite unit was also dated using OSL, giving an age estimate of 105 ± 7 ka, which is in excellent agreement with the WR age for this sediment. These ages are also in good agreement with MIS 5 sediments at Pennington Bay sites PB1 and particularly site PB3. The large north-western headland (Bales2) is an older sequence, and the lower aeolianite unit dated at 360 ± 24 ka (OSL), 495 ± 114 ka (WR) and 439 ± 139 ka (Foram): these ages are reasonably consistent with MIS 11 (whole-rock aminozone C, subzones III and IV), and are comparable to the lower units at Pennington Bay sites PB4 and PB5. The upper parts of the sequence could not be reached for sampling, however, and it was assumed that the aeolianite units would follow as MIS 9, MIS 7 and MIS 5.

8.2.3.3 Point Ellen and Vivonne Bay

The early Pleistocene Point Ellen Formation (sites PE1A and 1B) crops out as a thick coquinite in a bedrock basin, located on the south-western headland of Vivonne Bay (see Figure 8.13). The early Pleistocene age of the deposit was confirmed using WR, Foram and Mollusc AAR dating calibrations. These calibrations gave ages between 745 ± 171 ka (WR) and 1.3 ± 0.4 Ma (Foram) for the upper Point Ellen Formation and between 1.1 ± 0.2 Ma (Mollusc) and 1.3

Third party source; Images redacted at request of thesis author

Figure 8.13: Oblique view (452 m altitude) of Point Ellen and Vivonne Bay, facing north-west (image is vertically exaggerated by 3—image and DEM from Google Earth, 2010).

± 0.4 Ma (Foram) for the basal Point Ellen Formation (see section 7.3.3 in Chapter 7). A long (laterally) sequence of aeolianite (site PE2 and PE3) outcrops west of Point Ellen consisting of a basal calcarenite (similar to that found at Pennington Bay and Bales Beach), overlain by a series of collapsed aeolianite blocks cemented by a thin matrix of pebbles and shell at approximately 3 m APSL (site PE2) (Figure 8.11). The blocks date between MIS 7 and 11, using SARTT-OSL (312 ± 19 ka), WR AAR (380 ± 87 ka), and Foram AAR (290 ± 86 ka); however the more precise SARTT-OSL age would suggest a MIS 9 deposition (equating this unit with the 4-1d, 4-2d and 5d units at Pennington Bay, and the 2d unit at Bales Beach). Overlying or perhaps truncating this unit is a MIS 5-7 (whole-rock aminozone C, subzone I) aeolianite (site PE1) dated at 163 ± 10 ka (OSL), 166 ± 38 (WR AAR), and 121 ± 39 (Foram AAR). The OSL and WR ages would suggest a MIS 6 deposition.

The shelly matrix at ~ 3.0 m APSL surrounding the MIS 9 aeolianite blocks was dated using U-series (114 ± 3 ka), WR AAR (137 ± 30 ka), and Foram AAR (114 ± 35 ka). These ages (also considering morphostratigraphical position and marker foraminifers) equate the deposit with MIS 5e, revealing that this deposit is a correlative of the PB2 MIS 5e notch deposit at Pennington Bay.

Further north-west around Vivonne Bay is an isolated single aeolianite (capped with calcrete and overlying Holocene dunes) of possible MIS 5 age; it was age estimated using WR AAR (95 ± 22 ka) and Foram AAR (141 ± 42 ka). The unit in all probability equates with the MIS 5 aeolianite units at Pennington Bay and Bales Beach (i.e. whole-rock aminozone B).

8.2.3.4 Kelly Hill Caves

Calcarenate sediment was recovered from ~15 m depth in Kelly Hill Caves for AAR and luminescence analysis. The material was dated at 1.3 ± 0.1 Ma using SARTT-OSL and 835 ± 194 ka, using WR AAR (see section 7.3.5 in Chapter 7). It is possible that this early Pleistocene (whole-rock Aminozone D) calcarenite is contemporaneous with the Point Ellen Formation; however, in view of the large uncertainty in all terms, this is rendered as supposition. At this stage in the research the potential age equivalence shall be viewed with caution.

Third party source; Images redacted at request of thesis author

Figure 8.14: Oblique view (107 m altitude) of Hanson Bay section, facing north-east (image is vertically exaggerated by 3—image and DEM from Google Earth, 2010).

8.2.3.5 Hanson Bay

The Hanson Bay site (Figure 8.14) consists of a basal calcarenite (dated to 630 ± 145 ka using WR AAR, at site HB2) which is overlain by a MIS 6 to 7 lagoonal facies (site HB1) (dated at 177 ± 42 to 183 ± 57 ka using WR AAR and Foram

AAR: whole-rock Aminozone C, subzones I and II) (Figure 8.1). The lagoonal facies is truncated by a MIS 5 consolidated, shelly, medium grained sand deposit (possibly a sub-littoral or washover facies). The shell layer is ~3.0 m APSL, and was dated at 142 ± 12 ka (OSL), 135 ± 31 ka (WR AAR), 133 ± 30 ka (Mollusc AAR), and 114 ± 34 ka (Foram AAR). This layer is equated with MIS 5e (whole-rock aminozone B, subzone II) and is therefore contemporaneous with other raised shelly sediments located at Vivonne Bay and Pennington Bay (at sites PE3 and PB2) Formation (see section 7.3.4, in Chapter 7, and Figure 8.11).

The shelly sand is unconformably overlain by a blocky calcrete and modern backshore dunes—the dunes based upon Foram AAR are probably less than a century old (age determination from the lowest GLX D-L ratio cluster in the population).

8.2.4 Chronostratigraphy of east coast Kangaroo Island and Dudley Peninsula near-coastal carbonate sediments

Four sites were examined on the eastern portion of the island: Rocky Point, Baudin Beach, American River and Kingscote. Only Baudin Beach has an aeolianite sequence; American River, Rocky Point and Kingscote comprise a Holocene shell hash, and MIS 5 raised shelly cobble beach deposits, respectively.

8.2.4.1 Rocky Point

Rocky Point lies on the northern coast of the neck of Dudley Peninsula, in Eastern Cove (see Chapter 7, section 7.3.6). The site is a wave eroded notch in an aeolianite outcrop which forms a small headland. The aeolianite is capped by a blocky calcrete. Shells, foraminifers and whole-rock sediment were used to date the deposit at 101 ± 22 ka, 169 ± 64 ka and 71 ± 16 ka. Given the poor state of preservation of the deposit, the mollusc AAR age probably represents the best estimate for the “true” age of the site. This deposit is thought to be a contemporary with other similar raised deposits on the south coast of Kangaroo Island (at Pennington Bay, Vivonne Bay and Hanson Bay), and relating to

whole-rock Aminozone B (see Figure 8.1). The sediments were most likely deposited during the Last Interglacial (MIS 5e).

Third party source; Images redacted at request of thesis author

Figure 8.15: Oblique view (155 m altitude) of Baudin Beach sections, facing south-west (image is vertically exaggerated by 3—image and DEM from Google Earth, 2010).

8.2.4.2 Baudin Beach

Baudin Beach is located on the western side of the Dudley peninsula (see Chapter 7, section 7.3.7), and the entire sequence examined extends for approximately 2 km along a north-east/south-west line (see Figure 8.15). The sequence consists of a lower sand unit that is weakly cemented (most of the bedding has been obliterated) which is most probably an aeolianite. This unit (BB3a sample BB#3-4) is of probable MIS 7 age (whole-rock aminozone C, substage II and III: Figure 8.1) and was dated to 286 ± 66 ka using WR AAR, and 193 ± 61 ka using Foram AAR. This unit can be equated with the MIS 7 aeolianite common around Pennington Bay.

This aeolianite is overlain (and truncated further south-west at BB2) by an alluvial soil, rich in freshwater gastropod fossils. The alluvial soil has been equated with the South Australian Pooraka Formation, and has been age estimated using OSL (135 ± 13 ka) and Mollusc AAR (101 ± 25 ka), it is likely to be of MIS 5 age, possibly MIS 5e. The alluvial deposit is in turn overlain by an

aeolianite that is of probable MIS 5 age also. This unit (at BB3 and BB1) has been dated at 129 ± 8 ka using OSL, 168 ± 40 ka using WR AAR, and 84 ± 26 ka using Foram AAR; the OSL age would indicate an MIS 5e deposition (whole-rock Aminozone B). However this deposit must be younger than the underlying alluvial unit—the clean contact between the two units would indicate a relatively short period between the two depositional events. This aeolianite, even though it has a different character, is in all likelihood a contemporary of the MIS 5 aeolianites at Pennington Bay, and Bales Beach.

The uppermost aeolianite is unconformably overlain by a blocky calcrete that is rich in rhizcretions, and is palaeosol-like (has reddish pedogenic colouring) intermittently along outcrop, in its lower portions. Modern backshore dunes are common in the south-west part of the outcrop (BB1).

8.2.4.3 American River

This site is an extensive Holocene marine shell deposit on the shores of American River, south-west of Buicks Point (see Chapter 7, section 7.3.8). The study site is an extensive deposit consisting of densely packed unconsolidated shell layers that form large flat near sea-level areas and arcuate beach ridge formations. The site was extensively dated using mainly calibrated Mollusc AAR and some AMS ^{14}C . The AAR ages were consistent with a range of episodes from the early, middle and late Holocene (whole-rock Aminozone A, and mollusc Aminozone A, subzones I, II and III: Figure 8.5). This type of deposit was unique to American River and Pelican Lagoon.

Given the AMS ^{14}C and AAR age determinations the sites at American River are considered to host intertidal and tidal flat sediments of the Holocene St. Kilda Formation (cf. Firman, 1966) (whole-rock Aminozone A: Figure 8.1).

8.2.4.4 Kingscote

The Kingscote study site is an extensive raised (+3.5 to +3.0 m APSL—top of unit) basalt cobble/pebble (Jurassic Wisanger Basalt is the most common cobble, with occasional limestone and quartz cobbles) conglomerate beach deposit, strongly cemented in a fine carbonate matrix, with relatively abundant whole and broken shell. The thickness of the unit varies in conjunction with the

undulations in the karstified underlying Kingscote Limestone (Late Eocene to early Late Oligocene: Milnes *et al.* [1983]); it ranges from a few 10s of cm to over 1 m in thickness. The lateral extent exposed sporadically in outcrop is approximately 680 m (see Chapter 7, section 7.3.9 for details). The unit is usually unconformably overlain by a thin calcrete, and soil mantle, although the conglomerate is sometimes exposed on the surface. The Kingscote Conglomerate was dated here using Mollusc AAR (129 ± 29 ka) and Foram AAR (132 ± 44 ka). Also, given the morphostratigraphical position of the unit and the presence of marker foraminifers—fragments of *Marginopora vertebralis*—it has been associated with a Last Interglacial deposition (Glanville Formation, MIS 5e: mollusc Aminozone B). This unit is a contemporary of similar raised deposits at Rocky Point and on the south coast of Kangaroo Island (at Pennington Bay, Vivonne Bay and Hanson Bay).

8.2.5 Chronostratigraphy of north coast Kangaroo Island near-coastal carbonate sediments

This section examines the chronostratigraphy of the sites at North Cape (NC1: near Point Marsden and NC2: Boxing Bay), Emu Bay, Smith Bay, and Stokes Bay. These sites all host units that are of middle to early Pleistocene age.

8.2.5.1 North Cape

Two sites were examined on North Cape, Kangaroo Island: site NC1, south of Point Marsden, and site NC2, situated in Boxing Bay. The sites are located on the North Cape, a large cape on the northern coast of Kangaroo Island (see Chapter 7, section 7.3.10). The coast along NC1 (see Figure 8.16) is characterised by broad tidal flats (~100 m wide) and sandy/cobble high-tide beaches. The beach at the study site is bordered by low cliffs cut into Early Pleistocene calcareous sediments, the base of the cliff is strewn with broken blocks of calcrete, and the upper sediments are undercut. These sediments form a large platform (above the cliff-line) that grades towards the north and to the east. The top of the cliff-line near the shore is approximately +4 m APSL. This site has what are probably 2 discrete units: a weakly cemented muddy or clayey sand with *in situ* marine shell (predominantly the marine bivalve *Anapella*

cycladea), and an overlying calcrete mantle. These units were informally designated as the North Cape Beds in Chapter 3.

Marine shell recovered from the muddy sand unit (NC1aii) was analysed for amino acids, and a Mollusc AAR age was calculated at 1.2 ± 0.3 Ma. The shells were highly racemized having a mean GLX D-L ratio of 0.978 ± 0.015 . This unit is part of the mollusc Aminozone D, subzone II (Figure 8.5), and may be a correlative of the Point Ellen Formation on the south coast, however the large uncertainties preclude this being a certainty (although they still may be equated to the same aminozone) (see Figure 8.5).

Third party source; Images redacted at request of thesis author

Figure 8.16: Oblique view (144 m altitude) of North Cape site NC1, near Point Marsden, facing north-west (image is vertically exaggerated by 3—image and DEM from Google Earth, 2010).

The beach at NC2 (Figure 8.17), in Boxing Bay, is of moderate wave energy, and is characterised by a sandy beach with some storm deposited cobbles and boulders at the rear of the berm (these cobbles and boulders may have been sourced from the local Permian glacial till [i.e. erratics]). The backshore of the beach hosts high calcarenite cliffs (~8 m APSL) that overlie cemented shelly sands and a cemented cobble/pebble beach. The cobble/pebble beach extends to below sea-level at the eastern end of the bay. This would indicate that the cobble/pebble beach was of much greater extent in the past and was subsequently eroded sometime after deposition and cementation. The

cobble/pebble beach and thin shelly sands were informally designated as the Boxing Bay Conglomerate in Chapter 3 (this should not be confused with the conglomerate facies associated with the Cambrian Boxing Bay Formation [cf. Daily *et al.*, 1980], which are located further east and west near Point Marsden and White Point [see Chapter 7, section 7.3.10 for more detail).

Third party source; Images redacted at request of thesis author

Figure 8.17: Oblique view (163 m altitude) of North Cape site NC2, in Boxing Bay, facing south-west (image is vertically exaggerated by 3—image and DEM from Google Earth, 2010).

The Boxing Bay Conglomerate was sampled for molluscs, whole-rock sediment, and foraminifers, and give age estimates of between 660 ± 148 ka to 894 ± 260 ka. The ages (taking into account the large uncertainties) would suggest middle to early Pleistocene age (Aminozone C-D: Figure 8.1, 8.5 and 8.6). This unit should be considered to be a younger deposit than the North Cape Beds, or the Point Ellen Formation on the south coast.

8.2.5.2 Emu Bay

Emu Bay is a large embayment on the northern coast of Kangaroo Island, at the neck of the North Cape isthmus. The study site (EB) is an isolated outcrop of an aeolianite sequence located towards the eastern end of the embayment. The outcrop extends to sea-level forming a small headland, similar to those at Pennington Bay. The beach is of moderate energy and most of the embayment is dominated by well-vegetated modern and Holocene backshore dunes. The

sequence consists of 2 aeolianite units separated by a palaeosol unconformity, and capped by a calcrete mantle and Holocene cliff-top dunes (see Chapter 7, section 7.3.11 for detail).

The lower aeolianite unit was dated using TL (216 ± 28 ka), and WR AAR (258 ± 63 ka); these ages would suggest an MIS 7 deposition (whole-rock Aminozone C, subzone II). The upper aeolianite was dated at 343 ± 80 ka using WR AAR, apparently older in age than the lower aeolianite in the sequence. There are two possibilities: i) the upper unit was deposited during MIS 7 as well, and the age difference between the upper and lower aeolianite is too small to resolve using the method, or ii) there is a problem with the D-L ratio determinations for the upper unit (i.e., a very high proportion of reworked grains in the sediment giving higher than expected ratios), hence, the unit may be of MIS 5 age. Regardless, the lower unit can be equated with the other MIS 7 units at Baudin Beach, and Pennington Bay.

8.2.5.3 Smith Bay

Smith Bay is located on the northern coast of Kangaroo Island, approximately 8 km straight line distance west of Emu Bay. The study site at Smith Bay hosts an uplifted pebble / cobble / boulder beach that rests unconformably on Permian glaciogene sediments (see Chapter 7, section 7.3.12 for more detail). This unit was informally designated as the early Pleistocene Smith Bay Conglomerate in Chapter 3. Smith Bay is a wide (~4 km) shallow bay (in terms of coastal morphology, not water depth). The embayment can be characterised by high-angled shingled cobble/boulder beaches with a sandy margin at the shore, resting on Cambrian Kangaroo Island Group platformal sediments (in this case the Smith Bay Shale [Chapter 1 section 1.4.1.1]).

The cobble beach unit is located near the top of a broad headland towards the eastern side of the embayment. The base of the unit is approximately +18 m APSL, and ranges up to ~2 m thick. It is overlain by a blocky, weathered calcrete; the upper surface of the calcrete over the entire ridgeline is broken and

dissected, and strewn with calcrete rubble. Thin soil infills the broken surface and the lower portions of the calcrete are commonly powdery (limey) and loose.

Third party source; Images redacted at request of thesis author

Figure 8.18: Oblique view (188 m altitude) of the Smith Bay site SB, facing south-west (image is vertically exaggerated by 3—image and DEM from Google Earth, 2010).

The Smith Bay Conglomerate overlies ~18 m of Permian glacial till. The conglomerate was briefly described by Bourman and Alley (1999), and was interpreted to be of Pleistocene age. Calibrated Mollusc AAR dating was used to date the uplifted deposit. Here a Mollusc AAR age of 1.0 ± 0.2 Ma (mollusc Aminozone D, subzone II: Figure 8.5) was determined from the mean GLX D-L ratio of 0.907 ± 0.040 from 9 shell fragments. It is possible (though speculative given the uncertainties) that this uplifted unit is contemporaneous with the south coast early Pleistocene Point Ellen Formation, and the early Pleistocene North Cape Beds.

8.2.5.4 Stokes Bay

Stokes bay is a small embayment located on the northern coast of Kangaroo Island, approximately 22 km west of Smith Bay. The bay hosts a sandy moderate energy beach backed by ~8 m high aeolianite cliffs, with scree slopes and large dislodged blocks of aeolianite and calcrete at the base.

The study site is the bounding western calcarenite headland. The headland is a single aeolianite unit, overlain by a blocky calcrete that is weathered and brecciated. The aeolianite is karstified, very weathered and leached, and although the sediment is indurated it is quite friable and “foamy” (of low density) in places. Most of the bedding is obliterated, although some is visible in patches along the outcrop. The unit was initially interpreted to be of early Pleistocene age, and this was based on the appearance of the sediments, in terms of the weathered and leached façade (see Chapter 7, section 7.3.13 for more detail).

Third party source; Images redacted at request of thesis author

Figure 8.19: Oblique view (472 m altitude) of the Stokes Bay site STB, facing south-east (image is vertically exaggerated by 3—image and DEM from Google Earth, 2010).

Two whole-rock sediment samples were recovered from the lower portions of the aeolianite unit (foraminifers were not readily identifiable in the sediment), these were analysed several times (7) to derive a mean GLX D-L ratio of 0.779 ± 0.010 (Table 7.35). This ratio was calibrated using the U-series apparent parabolic kinetics calibration to yield a WR AAR ages of 786 ± 181 ka. This age estimate supports the initial early Pleistocene interpretation to a degree; although, the estimate would also suggest an early / middle Pleistocene age for deposition. Nevertheless, the GLX D-L ratio for this WR sample is similar to those of the Boxing Bay Conglomerate, the upper Point Ellen Formation, and

the Kelly Hill Caves calcarenite, so an early Pleistocene (whole-rock Aminozone D, subzone I to II) interpretation is valid (see Figure 8.1).

8.2.5.5 Summary and conclusions

The chronostratigraphy discussed above shows that aeolianite deposition has been occurring on Kangaroo Island since at least early Pleistocene time. Aeolianites have been recorded from the early part of the middle Pleistocene, and from MIS 11 and 9, although it is difficult to establish the exact timing (particularly for these older deposits) because of large uncertainties in both the luminescence and AAR ages. Aeolianites of MIS 7 and MIS 5 formed the bulk of the aeolianites studied, and could be more confidently assigned to the respective marine isotope stage. MIS 7 and MIS 5 units were prevalent on the south coast of Kangaroo Island and on the west coast of Dudley Peninsula; although no MIS 5 units were located on the northern coast. These units form part of the whole-rock aminozone B (MIS 5: subzones I and II) and C (MIS 7: subzones I and II).

During the early Pleistocene (from 1.0 ± 0.2 Ma to 1.2 ± 0.3 Ma [mollusc AAR ages]) an event occurred (or events) (i.e. interglacial highstands) where sea-level was around +2 m to +4 m, and deposition of dense shell beds, shelly cobble / pebble beach units, and shelly tidal flat facies transpired. This higher sea-level event (or events) was recorded at Point Ellen, North Cape, and possibly Smith Bay (although the Smith Bay site could have been uplifted sometime after deposition, and the Boxing Bay site at North Cape may represent a later early Pleistocene event).

The Last Interglacial sea-level highstand was recorded around Kangaroo Island in the form of raised notch deposits (remnants of a previous cobble / pebble beach sediments preserved in aeolianite notches [Pennington Bay site PB2]), as a matrix (Vivonne Bay site PE3), or as a large extensive deposit (i.e. the Kingscote Conglomerate). At Hanson Bay and Rocky Point the highstand was recorded as a shelly sand deposit. These sites were dated using mainly calibrated marine mollusc and foraminifer GLX D-L ratios. The grand mean AAR age (at 1σ) for these deposits is 125 ± 22 ka. The height of the deposits above

mean sea-level allowed the estimation of a $+3.0 \pm 0.5$ m sea-level for the Last Interglacial on Kangaroo Island.

A comprehensive sampling of the intercalated palaeosols associated with aeolianite units on Kangaroo Island was undertaken; unfortunately, none of the units sampled exhibited useful macrofossils, e.g. terrestrial gastropods, which could be used for AAR dating purposes. Extensive AAR analysis of palaeosol whole-rock samples was completed; however, the results are not presented in this thesis as they may not be suitable for developing a chronology, at this stage. Nevertheless, an aminostratigraphy may be developed to explore the aminostratigraphical relationships between different palaeosol units; this, however, will be the subject of further work.

8.3 Sea-level controls on the evolution of the Bridgewater Formation aeolianite sequences and other near-coastal carbonate sediment deposits on Kangaroo Island

Studies from other locations around the world, most notably from the western Mediterranean (Brückner, 1986; Engelmann *et al*, 2001) the Caribbean (Land *et al*, 1967; Harmon *et al* 1981; Hearty *et al*, 1992; Vacher *et al*, 1995; Hearty, 2002), Lord Howe Island (Brooke *et al.*, 2003), and the Coorong coastal plain of south-eastern Australia (Murray-Wallace *et al*, 2001), support the premise of sea-level highstand deposition of aeolianites. Other studies, from South Africa, have shown that aeolian deposition may be related to transgressive and regressive phases prior to and just after an interglacial period (Bateman *et al.*, 2004; Butzer, 2004; Carr *et al.*, 2010). According to Bateman *et al.* (2004) aeolianite deposition is a 2 part process governed firstly by large-scale entrainment and deposition of skeletal carbonate sands, and secondly by subaerial conditions appropriate for cementation. Bateman *et al.* (2004) cites rapid sea-level change (particularly in the Late Pleistocene) occurring post-interglacial, during interstadials, as the driving force for the mobilisation of carbonate sediments onshore.

Conversely there are some sites examined where aeolianite deposition apparently occurred during glacial lowstands. There are various studies of

aeolianites in the Mediterranean (Porat and Wintle, 1995; Frechen *et al*, 2001) and some Californian islands (Johnson, 1977) as well as some sites in Africa (Coetzee, 1975) and Australia (Zhou *et al.*, 1994; Price *et al*, 2001) that suggest that the aeolianites were, at times, deposited during sea-level lowstands. According to Brooke (2001) these glacial age deposits are most likely the result of aeolian reworking of carbonate that was deposited on the shelf or shoreline during an interglacial.

Figures 8.20 and 8.21 explore the position of sea-level, and possible depositional regimes operating over time at two sites on the south coast (Pennington Bay and Vivonne Bay). The model proposes 4 depositional regimes:

A: erosion of existing shorelines, and deposition of barrier dunes, and inland dunes—sea-level highstands (for example, MIS 1, MIS 5e, also possibly MIS 9 and 11)

B: Inner shelf deposition, and inland dune deposition—during transgressive and regressive phases of interglacial periods, and interstadials (formation of aeolianites?)

C: Middle shelf deposition—low sea-level events (for example late MIS 3 or MIS 4, or MIS 7d), where dune deposits would be later inundated or eroded (during higher sea-level).

D: Inner and middle shelf subaerial exposure (palaeosol, and calcrete formation)—extreme low sea-level events (for example MIS 2, MIS 6, MIS 8, MIS 10). Vegetation colonization of shelf (cf. Barwis and Tankard, 1983), stabilisation and formation of palaeosols and calcretes on inland dunes or older coastal barriers.

The Kangaroo Island sites from an initial morphological standpoint reflect the conclusions of Bateman *et al.* (2004) and Carr *et al.* (2010) of transgressive and regressive phase onshore carbonate accretion, and as proposed in the above model. For example, the position of Kangaroo Island aeolianite sequences in relation to the current shoreline i.e., the present day erosion and formation of aeolianite cliff-faces, the offshore location of small aeolianite “stacks” (~2 to 5 m

Third party source; Images
redacted at request of thesis
author

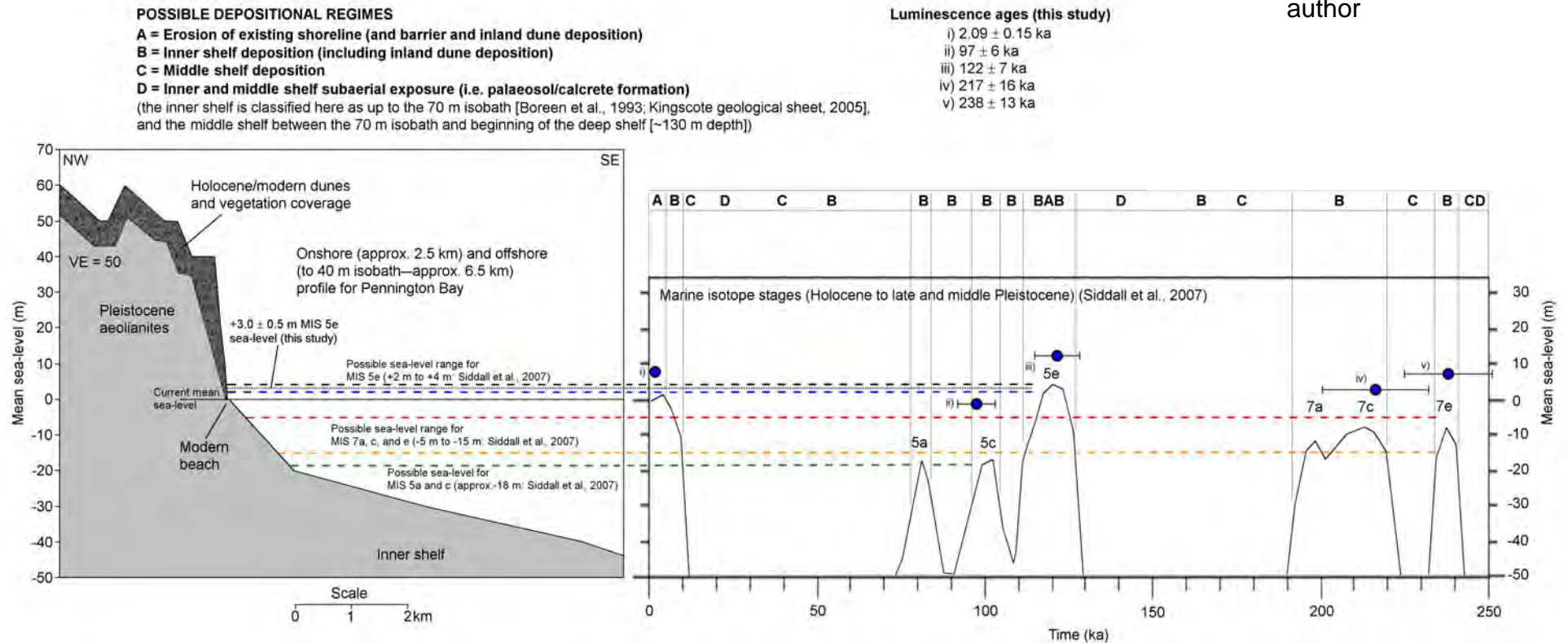


Figure 8.20: Onshore and offshore profile for Pennington Bay (LH inset): upper RH inset shows orientation of the cross-section (image from Google earth, 2010), and the lower RH inset is a section of the scaled benthic oxygen isotope curve of Cutler *et al.* (2003), from Siddall *et al.* (2007). The OI curve is tuned to y-axis scale on the cross-section. The dashed lines show the probable position of sea-level at various times during the (late) middle Pleistocene to late Pleistocene and Holocene. A proposed depositional model is also overlain onto the OI curve. See upper LH inset for model key. Middle inset shows luminescence ages for some of the aeolianites at Pennington Bay; the blue circles are the ages aligned with the x-axis time scale (ka). Elevation and isobath data from the Kingscote geological sheet (2005) 1:100,000, and the Destrees (6426-3) topographical map (1986) 1:50,000.

Third party source; Images redacted at request of thesis author

Figure 8.21: Onshore and offshore profile for Vivonne Bay (LH inset): upper RH inset shows orientation of the cross-section (image from Google earth, 2010), and the lower RH inset is a section of the scaled benthic oxygen isotope curve of Cutler *et al.* (2003), from Siddall *et al.* (2007). The OI curve is tuned to y-axis scale on the cross-section. The dashed lines show the probable position of sea-level at various times during the (late) middle Pleistocene to late Pleistocene and Holocene. A proposed depositional model is also overlain onto the OI curve. See upper LH inset for model key. Middle inset shows a luminescence age and a U-series age for an aeolianite and a MIS 5e sediment at Vivonne Bay; the blue and pink circles are the ages aligned with the x-axis time scale (ka). Elevation and isobath data from the Kingscote geological sheet (2005) 1:100,000, and the Vivonne (6326-3) topographical map (1988) 1:50,000.

high), and aeolianite headlands that protrude offshore well below current sea-level. These morphological characteristics all point to aeolianite deposition during periods of slightly lower sea-level than at present. In terms of the luminescence chronology age precision while quite good, it is still not precise enough to really resolve this issue.

However, even though only few Last Interglacial (MIS 5e) raised, cemented shelly notch deposits were found on Kangaroo Island, none of these were located filling notches within Late Pleistocene sediments. They were all located in wave-cut notches in—or as a matrix around (collapsed blocks)—Middle Pleistocene sediments (i.e. Rocky Point, Pennington Bay [site PB2], and Vivonne Bay [site PE3]). The implication is that the Late Pleistocene aeolianites were *not* present during the Last Interglacial highstand. Effectively this implies that the sediments were *not* deposited during the transgression prior to MIS 5e, or during peak sea-level. It is more likely that they formed during the regressive phase *after* MIS 5e, as sea-level was falling, and sediment was mobilised onshore. South coast sea-caves at around +3.0 m APSL (morphologically associated with MIS 5e) moreover were only found in sediments apparently older than MIS 5 (i.e. MIS 7 at Pennington Bay, MIS 6 and 9 at Vivonne Bay, and early Pleistocene at Point Ellen).

Figure 8.22 outlines a model for aeolianite deposition and evolution in a headland bound embayment, similar to Pennington Bay. The age for the basal calcarenite in time-slice A is based upon the WR AAR age for the calcarenite at Hanson Bay (630 ± 145 ka) (the bedrock consists of Kanmantoo Formation metasandstones on the south coast). The units in time-slice B relate to MIS 11, 9, and 7 aeolianites and intercalated palaeosols. The proposal is that the basal calcarenite was planed during high sea-level forming a broad platform on which later dune successions were deposited. These aeolianites may have in turn have been shaped into platforms on which sheet-like palaeosols and laminar calcretes formed, or the planar morphology may be due to the position of the watertable during evolution. Time-slice C proposes a major phase of dune deposition (and erosion of existing successions at peak sea-level) during the early part of the late Pleistocene (i.e. near MIS 5e), possibly occurring during the transgression just prior to peak sea-level, or more likely just after during the

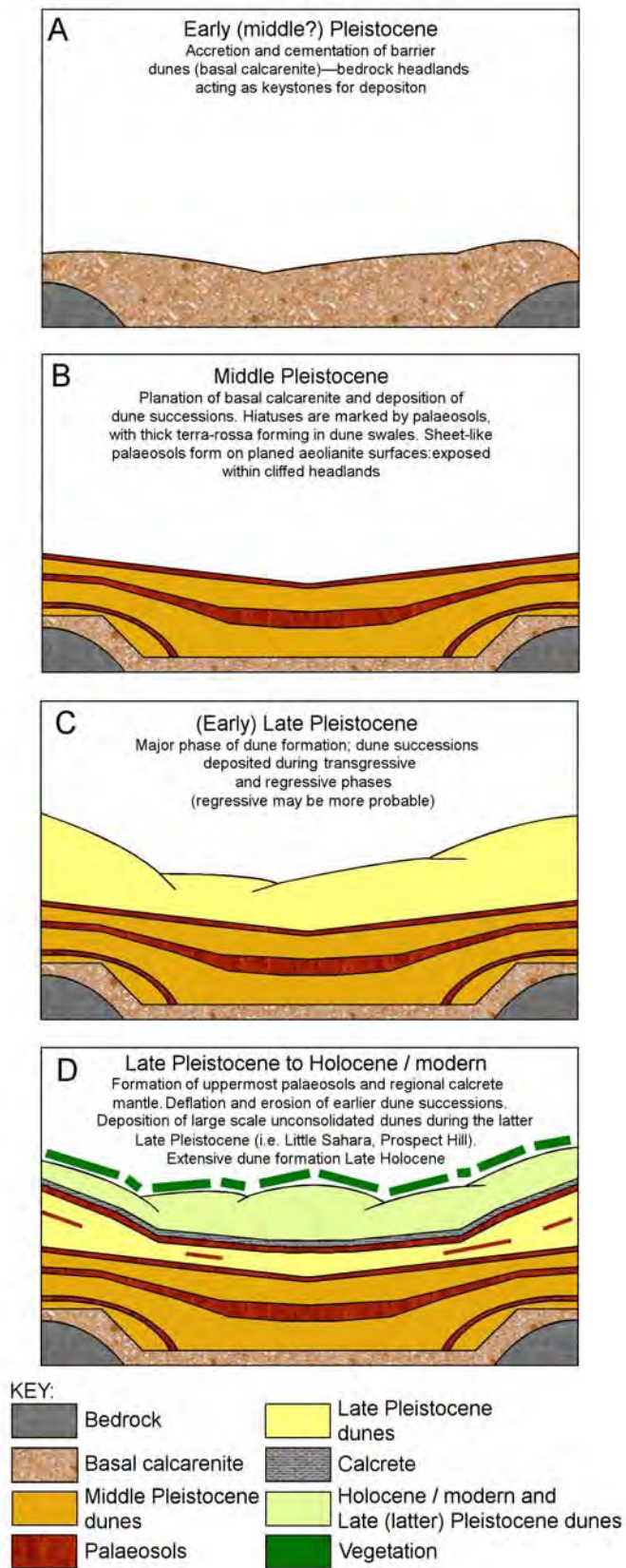


Figure 8.22: Proposed model for aeolianite dune deposition, from the early Pleistocene to the Late Pleistocene and Holocene, in a headland bound embayment (similar to Pennington Bay).

regression (for the reasons explained above) (this hypothesis disagrees somewhat with the proposed highstand timing of aeolianite deposition on the South Australian mainland—the Coorong region). Formation of intermediate minor palaeosols and calcretes occurs during the early part of time-slice D; formation of large scale, unconsolidated inland dunes (e.g. Little Sahara, and Prospect Hill) takes place during the latter late Pleistocene (~MIS 3). Formation of upper palaeosol units and calcretes (and deflation) may have occurred during MIS 2, although the WR and Foram AAR ages for the top calcrete at Pennington Bay suggested MIS 3-5 (this sample was taken close to the surface, hence it may have been affected by diagenetic temperature flux, i.e., experienced periods of increased racemization rate). Major erosion of previously deposited coastal successions occurs during the Holocene, as well as emplacement of backshore dunes and cliff top dunes.

8.4 Comparisons with other near-coastal carbonate sediment chronologies from the southern and northern hemispheres

A large database of glutamic acid D-L ratios (at the appropriate CMAT) does not exist in the literature (particularly for whole-rock sediment and foraminifers), as many users have utilised aspartic acid, valine, leucine, and alloseleucine for dating purposes. However, there are a number of relatively recent studies from South Australia, and South Africa, which have used GLX and are comparable in terms of the CMAT (~16-15 °C) at the sites. Table 8.2 compares GLX D-L ratios from MIS 5 (and MIS 5e) samples (whole-rock sediment and marine mollusc) from Kangaroo Island, the South Australia mainland and South Africa.

Upon examination it can be seen that, generally speaking, the GLX D-L ratio data from these equivalent sites is in reasonable agreement, particularly when comparing molluscs from Kangaroo Island with those of the South Australia mainland. Although, the molluscan dataset from South Africa is small and agreement is poor. Conversely, the whole-rock sediment data from South Africa, however, agrees reasonably well with the Kangaroo Island data. The whole-rock sediment data from the South Australian samples is quite variable; this may be attributable to different grain mixing characteristics (i.e. variable proportions of reworked skeletal grains) at each of the study sites.

Table 8.2: Mollusc and whole-rock sediment GLX D-L ratio data for selected, predominantly Last Interglacial, sites on Kangaroo Island (this study), the South Australia mainland, and the cape region of South Africa

Kangaroo Island				
Location	*Sample code / facies	Genus / species	N	GLX D-L \pm 1 σ
Pennington Bay	PB#2e-2 / raised pebble beach	Whole-rock	6	0.463 \pm 0.007
Rocky Point	RP / shelly notch deposit	Whole-rock	4	0.401 \pm 0.005
Hanson Bay	HB#3-4 / raised shelly deposit	Whole-rock	6	0.462 \pm 0.010
Kingscote	KC1 / raised pebble / cobble beach	<i>Katelysia scalarina</i>	5	0.354 \pm 0.019
Rocky Point	RP / (poorly preserved) raised shelly notch deposit	<i>Fulvia tenuicostata</i>	3	0.318 \pm 0.007
Pennington Bay	PB#2e-2 / raised pebble / cobble beach	<i>Amesodesma angusta</i>	8	0.360 \pm 0.008
Vivonne Bay	PE#3-5 / raised pebble, shelly notch deposits	<i>Nerita (Melanerita) atramentosa</i>	4	0.364 \pm 0.012
Hanson Bay	HB1 / raised shelly deposit	<i>Spisula (Notospisula) trigonella</i>	5	0.359 \pm 0.025
South Australian mainland				
Pondalowie Bay ^a	DK04-20A / Glanville Formation	<i>Katelysia scalarina</i>	10	0.375 \pm 0.015
Mark Point ^b	Foreshore facies	<i>Donax (Plebidonax) deltoides</i>	?	0.340 \pm 0.001
McCourt's Cutting ^b	Lagoon facies, Woakwine Range	<i>Katelysia rhytiphora</i>	?	0.340 \pm 0.002
West Dairy range ^b	Lagoon facies	<i>Anadara trapezia</i>	?	0.370 \pm 0.01
Lake Hawdon ^b	Lagoon facies	<i>Katelysia scalarina</i>	?	0.310 \pm 0.03
Surfer Beach ^c	5548A-F / aeolianite	Whole-rock	6	0.471 \pm 0.013
Knight Beach ^c	5547A-F / aeolianite	Whole-rock	6	0.614 \pm 0.007
Hindmarsh Island ^c	5549A-F / aeolianite	Whole-rock	6	0.586 \pm 0.027
Narrung Peninsula ^c	5389A-E / aeolianite	Whole-rock	5	0.328 \pm 0.032
Hindmarsh Island ^c	5380A-F / Glanville Formation	<i>Mactra rufescens</i>	6	0.305 \pm 0.034
Hindmarsh Island ^c	5381A-B / Glanville Formation	<i>Spisula (Notospisula) trigonella</i>	2	0.388 \pm 0.024
Hindmarsh Island ^c	5627A-E / Glanville Formation	<i>Spisula (Notospisula) trigonella</i>	5	0.373 \pm 0.032
Hindmarsh Island ^c	5628A-B / Glanville Formation	<i>Katelysia scalarina</i>	2	0.394 \pm 0.020
Hindmarsh Island ^c	5629A-E / Glanville Formation	<i>Mactra australis</i>	5	0.382 \pm 0.018
Normanville ^c	5661A-T / Glanville Formation	<i>Katelysia rhytiphora</i>	20	0.366 \pm 0.035
Normanville ^c	5660A-Z / Glanville Formation	<i>Mactra australis</i>	26	0.342 \pm 0.043

Table 8.2: (Continued)

Woakwine ^c	5645A-E / Glanville Formation	<i>Katelsysia rhytiphora</i>	4	0.407 ± 0.024
South Africa (cape region)				
False Bay ^d	5953A-E / Aeolianite	Whole-rock	5	0.419 ± 0.014
Cape Aghulas ^d	5233A-C / raised beach	<i>Turbo cidaris</i> (operculum)	3	0.413 ± 0.012
Cape Aghulas ^e	5232A-F / raised gravel beach	<i>Turbo</i> sp.	6	0.461 ± 0.036
Still Bay ^f	5400A-C / aeolianite	Whole-rock	3	0.485 ± 0.004
Still Bay ^f	5399A-B / aeolianite	Whole-rock	2	0.475 ± 0.001
Still Bay ^f	5398A-C / basal aeolianite	Whole-rock	3	0.493 ± 0.016

^a Kaufman, unpublished data (2005)

^b Murray-Wallace *et al.* (1999)

^c Murray-Wallace *et al.* (2009)

^d Roberts *et al.* (2008a)

^e Carr *et al.* (2010)

^f Roberts *et al.* (2008b)

In order to evaluate the Kangaroo Island chronology on a wider global basis, the Kangaroo Island luminescence data was compared on a latitudinal scale against the scaled benthic oxygen isotope curve of Cutler *et al.* (2003), from Siddall *et al.* (2007), and a range of other luminescence ages. Over 280 individual luminescence ages (with some ¹⁴C and U-series) from 13 aeolianite sites around the world (including Australia) were compared with the Kangaroo Island aeolianite luminescence chronology: the Arabian Peninsula (Preusser, 2009), East Africa (Armitage *et al.*, 2006), the east Atlantic (Goodfriend *et al.*, 1996), Brazil (Giannini *et al.*, 2007), Egypt (El-Asmar and Wood, 2000), Israel (Engelmann *et al.*, 2001; Frechen *et al.*, 2004; Sivan and Porat, 2004), Italy (Theil *et al.*, 2010), Cancun (Mexico) (McLaren and Gardner, 2000), Sardinia (Andreucci *et al.*, 2010), South Africa (Bateman *et al.*, 2004; Carr *et al.*, 2006; Bateman *et al.*, 2010; Carr *et al.*, 2010), Spain (Forno *et al.*, 2009), Turkey (Kiyak and Erginal, 2010), Lord Howe (Price *et al.*, 2001), Victoria (Australia) (Gardner *et al.*, 2006), Western Australia (Price *et al.*, 2001), South Australia (see Figure 8.23) (Huntley *et al.*, 1993, 1994; Murray-Wallace *et al.*, 2010), the Bahamas (Hearty *et al.*, 2007), Hawaii (Muhs *et al.*, 2002; Hearty *et al.*, 2007), Bermuda (Land *et al.*, 1967; Hearty *et al.*, 1992; Kindler and Hearty, 2000;

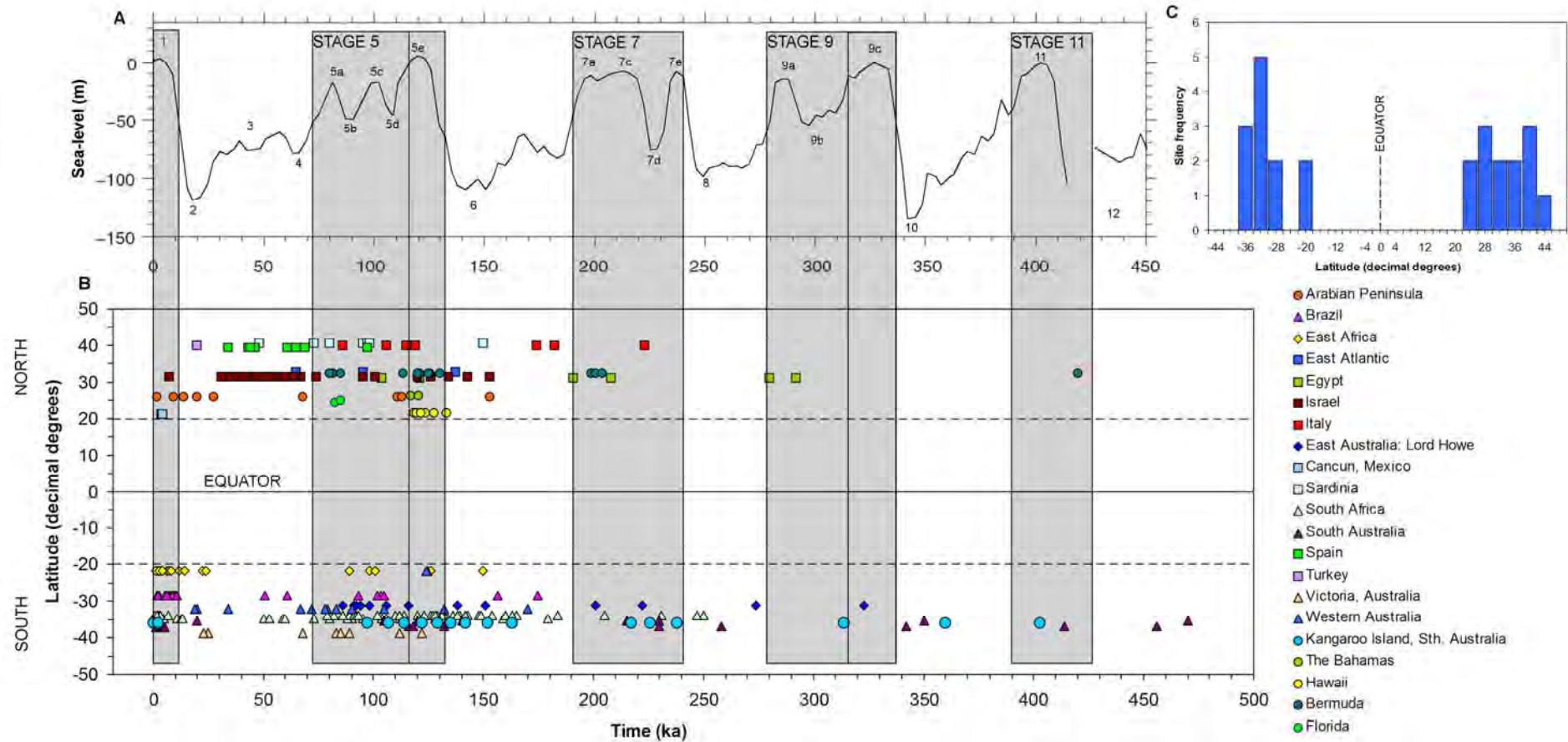


Figure 8.23: Luminescence (some U-series and ^{14}C) ages from sites around the world, along with the Kangaroo Island ages, compared latitudinally and tuned to the scaled benthic oxygen isotope curve of Cutler *et al.* (2003), from Siddall *et al.* (2007). Uncertainties were not included in the plot in order to preserve the visual integrity. However, uncertainties (which generally increase with age) for the Arabian Peninsula sites ranged from 1-10%, Brazil 5-37%, East Africa 5-16%, East Atlantic 7-17%, Egypt 5-28%, Israel 5-24%, Italy 5-10%, Lord Howe 9-55%, Cancun 12-13%, Sardinia 6-8%, South Africa 4-14%, South Australia 4-22%, Spain 9-12%, Turkey ~2%, Victoria 7-12%, Western Australia 4-16%, Kangaroo Island 3-10%, the Bahamas 0.4-6%, Hawaii 0.4-0.7%, Bermuda 0.5-12% and Florida 0.6-2%. The grey bands highlight interglacial periods (timing from Siddall *et al.*, 2007). The upper RH inset is a frequency histogram, which shows the frequency of sites at particular latitudes. The South Australia and Kangaroo Island records do proceed past 500 ka; however, for the purposes of this comparison the extra time-depth was not required.

Muhs et al., 2002; Hearty et al., 2007), and Florida (Toscano and Lundberg, 1999).

The comparison in Figure 8.23 shows that the Kangaroo Island chronology (light-blue circles) is particularly compatible with the South African (light-green squares), South Australian (dark-red triangles), Lord Howe (blue diamonds), the Bahamian (light-green circles), and Bermuda records (dark-green circles). The ages tend to align with interglacial periods; this alignment is especially evident in MIS 1, MIS 5 and MIS 7, predominantly in the southern hemisphere (it should be noted that the bulk of the observations are in the southern hemisphere also). The upper right-hand inset in Figure 8.23 is a frequency histogram that shows the frequency of sites occurring at particular latitudes.

In the Bahamas and Bermuda, in particular, aeolianite deposition is aligned tightly with MIS 5e and MIS 7; the African and Australian records, however, are more widely dispersed particularly between MIS 5 and 6. This may indicate that some deposition was occurring during glacial periods (this interpretation is subject to the size of the relative uncertainties for the given ages, as many of these ages, in this regard, overlap MIS 5e).

Here it is shown that aeolianites are most common between approximately 25° and 40° north and south latitude; as Brooke (2001) suggested, this alludes to the global nature of the environmental controls that influence aeolianite formation. The aeolianites of Kangaroo Island fall within the upper part of the south latitude range.

8.6 Conclusions of this study, and recommendations for further research

This thesis has used luminescence, U-series, ^{14}C , and independently calibrated amino acid racemization dating (for the first time using the amino acid GLX) to establish an aminostratigraphical and chronostratigraphical framework for carbonate deposition on Kangaroo Island. In order to do this a new long-range, single aliquot, luminescence dating method (SARTT-OSL) was developed and more comprehensive preparation treatments for amino acid racemization samples were established (to better isolate indigenous amino acids). A novel

approach for the analysis of single grain AAR results was developed through the use of a statistical method (Ward [1963] hierarchical cluster analysis). This allowed the identification of the youngest age population in a group of foraminifers (from the same sample) (for aminostratigraphical purposes) and also the identification of clusters of reworked tests within the sample. Amino acid racemization kinetic experiments were performed on molluscs, foraminifers, and (for the first time) whole-rock carbonate rich sediment, in order to compare the racemization forward rates of various amino acids (GLX in particular) and the changes in the individual amino acid rates across material types, i.e., molluscs, foraminifers, and whole-rock. Here GLX was identified as the amino acid with the most utility (in terms of range, stability, and concentration). It was also revealed that for the Kangaroo Island samples the amino acid GLX was the most compatible (in terms of racemization rate) across many genera of molluscs (i.e. *Nerita*, *Kataysia*, *Amesodesma*, *Fulvia*, and *Spisula*), and at least two genera of foraminifers (i.e. *Elphidium*, and *Discorbis*).

The AAR chronology and morphostratigraphical position of raised shelly / cobble/ pebble beach deposits allowed the estimation of a Last Interglacial (MIS 5e) sea-level for Kangaroo Island, which supports similar sea-level estimates from the mainland (cf. Murray-Wallace and Belperio, 1991; Stirling *et al.*, 1998). The GLX D-L ratios for Last Interglacial marine molluscs, where available, were similar to those found on the South Australia mainland, in Glanville Formation shell-beds (cf. Firman, 1967; Cann, 1978; Belperio *et al.*, 1983, 1984; Hails *et al.*, 1984; Murray-Wallace *et al.*, 1988; Murray-Wallace and Belperio, 1991; Murray-Wallace *et al.*, 2010).

Aeolianite deposition has taken place on Kangaroo Island since at least the latter part of the Early Pleistocene (and in all likelihood some time before this), with the oldest aeolianites recorded (WR AAR age 786 ± 181 ka: whole rock Aminozone D, subzone II) being from Stokes Bay on the north coast of the island, and Kelly Hill Caves (WR AAR age 835 ± 194 ka, and SARTT-OSL 1.3 ± 0.1 Ma: whole-rock Aminozone D, subzone II) on the south coast. The predominant aeolianites were of MIS 7 (Emu Bay, Pennington Bay, Baudin Beach) and MIS 5 (Pennington Bay, Bales Beach, Vivonne Bay, and Baudin Beach) age, with older aeolianites (MIS 11 and 9) being located on the

bounding headlands of embayments (particularly on the south coast: Bales Beach and Pennington Bay). The location of the older sediments on headlands is hypothesized to be due to underlying geology acting as keystones or anchors for deposition, allowing the older sediments to build-up to the stage where younger sediments could begin to accrete in the lower topography in the central portions of embayments.

The indirect evidence of Last Interglacial (MIS 5e) raised beach deposits only being located within sediments older than the late Pleistocene points to regressive phase deposition rather than transgressive or highstand deposition of aeolianites (at least for late Pleistocene aeolianites). It is probable in this respect that late Pleistocene aeolianites were being deposited during the regressive phase just after MIS 5e (ca. 116 ka), and the regressive phases after MIS 5c (at Bales Beach ca. 97 ka—OSL age) and 5a.

In summary the major conclusions and contributions of this thesis are:

- i) Glutamic acid is a stable, relatively slowly racemizing amino acid that has proven (in this thesis) to be a useful tool for the age estimation of skeletal carbonate deposits. It has been shown to have geochronological utility across a range of ages, from the early Pleistocene to the Holocene, and provides relatively robust APK independent age calibrations. As such this thesis has provided further support for the use of independent age calibration (using APK) of amino acid D-L ratios as a dating tool, and demonstrated (for the first time) the successful use of the amino acid GLX for this purpose (rather than ASX, VAL, LEU or A/I).
- ii) Kinetic experiments (see Chapter 6), and cross-genera D-L ratio comparisons of same-age molluscs, have empirically shown the stability and similarity of GLX AAR rates across different genera. This shows that it is possible to use different genera for dating purposes provided that a series of experiments is undertaken to demonstrate stability and rate similarity.
- iii) This thesis has developed a new, experimental, single aliquot, long-range thermally transferred OSL dating method (SARTT-OSL)—based

upon the MAR TTOSL method of Wang *et al.* (2006a). This new method was implemented to date very old aeolianite deposits on Kangaroo Island (up to 1.3 ± 0.1 Ma) and, in its initial testing, the West Naracoorte dune (SESA145: 850 ± 57 ka) on the South Australia mainland.

- iv) This thesis has demonstrated the application of independent age calibration (using ^{14}C , U-series, and OSL) of the amino acid GLX to the dating of Kangaroo Island carbonate sediments, marine molluscs, freshwater molluscs, and foraminifers; successfully building an aminostratigraphy for the coastal carbonate deposits. Continental shelf residence times for carbonate sediments were also estimated (i.e. between 7 ka and 51 ka).
- v) Ward (1963) method cluster analysis can be successfully used to isolate the “true age” of a sediment on the basis of identifying the youngest cluster of D-L ratios in a large group of marine shells or foraminifers (from the same sample), or identify clusters of reworked shells or foraminifers in a large group. This is a novel use of this statistical method.
- vi) This thesis has established a broad chronostratigraphy for Kangaroo Island near-coastal carbonate sediments, based upon predominantly luminescence ages (some ^{14}C , and U-series ages), and the calibrated extent of GLX racemization in whole-rock sediment, molluscs, and foraminifers. AAR dating and luminescence dating have shown that aeolianite deposition and formation has been occurring at least since the early Pleistocene (i.e. Stokes Bay). Aeolianite units have also been identified that were deposited during MIS 11, 9, 7, and 5. This thesis has provided 20 new luminescence ages, and over 100 new AAR ages for the region.
- vii) This thesis has demonstrated a possible correlation of dune deposition with regressive phases of interglacials and interstadials (at least for the Last Interglacial—MIS 5e), on Kangaroo Island.
- viii) This thesis has provided an estimation of a $+3.0 \pm 0.5$ m Last Interglacial (MIS 5e) sea-level for Kangaroo Island. Based upon the identification,

height mAPSL, and AAR dating of raised shelly deposits (i.e. cobble / pebble beach, notch, and matrix).

- ix) Identification of a possible early Pleistocene high sea-level(s) recorded as dense shell deposits, shelly tidal flat facies, and cobble / pebble deposits (recorded not only at Point Ellen, but also at North Cape [Point Marsden and possibly Boxing Bay], and Smith Bay).

8.6.1 Further research

As previously stated, this thesis, while comprehensive in its methodology, has only initiated a “first step” in understanding the complexities of carbonate deposition on Kangaroo Island, its relevance to the broader issues of aeolianite development, and the nuances of deriving time frameworks for their formation. However, this thesis will provide the basic framework for future investigations. Further work required would be:

- i) A more comprehensive and wider range of sampling for luminescence dating, in order to refine the chronology.
- ii) Further refinement of the SARTT-OSL method for long-range luminescence dating.
- iii) Further refinement of existing amino acid analysis methods. Exploitation of the intra-crystalline amino acid fraction for dating purposes.
- iv) Further investigation into the kinetic behaviour of glutamic acid across a wider range of genera. Establishment of a rate order for glutamic acid (in relation to amino acid position).
- v) Location and identification of more Last Interglacial raised beach deposits, also with regard to the age of the host sediment (i.e. if a notch or matrix deposit)—further evidence for regressive phase deposition of aeolianites on Kangaroo Island.
- vi) Location and identification of more early Pleistocene deposits on Kangaroo Island to explore further the possibility contemporaneous

relationships (acknowledging the difficulty of identifying such deposits for the morphostratigraphy).

- vii) A detailed investigation of the Smith Bay Conglomerate and surrounds to establish the occurrence of local tectonic uplift.
- viii) Investigation of additional sites not exploited in this thesis (i.e. D'Estrees Bay, the south coast of Dudley Peninsula, the west coast of the island, and the far north coast.

This concludes the thesis.

References

- Abelson, P. H. (1954). Organic constituents of fossils. Ann. Rept. of Dir. of Geophys. Lab., Carnegie Inst., 97-101. Wash., Paper No. 1235: pp 97-101
- Activation Laboratories Ltd. (2006). INAA, ICP-OES.
<http://www.actlabs.com/page.aspx?menu=72&app=239&cat1=602&tp=2&lk=no>
- Adamiec, G., Aitken, M. J. (1998). Dose-rate conversion factors: update. *Ancient TL* 16: 37–50
- Agassiz, A. (1894). A Visit to the Bermudas in March, 1894. *Bulletin of the Museum of Comparative Zoology at Harvard College* 26(2): 207-279
- Aitken, M. J. (1985). *Thermoluminescence Dating*. Academic Press, London 359 pp
- Aitken, M. J. (1990). *Science-based Dating in Archaeology*. Longman, England
- Aitken, M. J. (1998). *An Introduction to Optical Dating*. Oxford University Press. London 267 pp
- Ajje, H., Kaplan, I. R., Slota, P. J. Jr., Taylor, R. E. (1990). AMS radiocarbon dating of bone osteocalcin. In: Yiou, F., and G.M. Raisbeck (Editors). *Proceedings of the 5th International Symposium on Accelerator Mass Spectrometry*. Nuclear Instruments and Methods, B52 (3,4): 433-437
- Alexeenko, V. V., Khaerdinov, N. S., Lidvansky, A. S., Petkov, V. B. (2002). Transient variations of secondary cosmic rays due to atmospheric electric fields and evidence for pre-lightning particle acceleration. *Phys. Lett. A* 301, 299-306
- Allen, J. R. L. (1982a). *Sedimentary Structures, Their Character and Physical Basis*. Elsevier, Amsterdam. Volume 1, 611 pp
- Allen, J. R. L. (1982b). *Sedimentary Structures, Their Character and Physical Basis*. Elsevier, Amsterdam. Volume 2, 679 pp
- Andreucci, S., Clemmensen, L. B., Murray, A. S., Pascucci, V. (2010). Middle to late Pleistocene coastal deposits of Alghero, northwest Sardinia (Italy): Chronology and evolution. *Quaternary International* 222: 3-16
- Ankjærgaard, C., Murray, A. S. (2007). Total beta and gamma dose rates in trapped charge dating based on beta counting. *Radiation Measurements* 42: 352-359
- Antonioli, F., Bard, E., Potter, E.-K., Silenzi, S., Improta, S. (2004). 215-ka History of sealevel oscillations from marine and continental layers in Argenterola Cave speleothems (Italy). *Global and Planetary Change* 43(1-2): 57-78
- Armitage, S. J., Botha, G. A., Duller, G. A. T., Wintle, A. G. (2006). The formation and evolution of the barrier islands of Inhaca and Bazaruto, Mozambique. *Geomorphology* 82: 295-308
- Atlas of South Australia (2011) (online). Kangaroo Island 1:250000, and 1:50000 digital topographic maps. <http://www.atlas.sa.gov.au>
- Bada, J. L. (1972). The dating of fossil bones using the racemization of isoleucine. *Earth and Planetary Science Letters* 15: 223-231
- Bada J. L. (1981). Racemization of amino acids in fossil bones and teeth from the Olduvai Gorge Region, Tanzania, East Africa. *Earth Planet. Sci. Lett.* 55: 292-298
- Bada, J. L. (1985). Racemization of amino acids. In: Barrett, G.C. (Editor). *Chemistry and Biochemistry of the Amino Acids*. Chapman & Hall, London pp 399–414
- Bada, J. L., Luyendyk, B. P., Maynard, J. B. (1970). Marine sediments: dating by the racemization of amino acids. *Science* 170: 730–732

- Bada, J. L., Protsch, R. (1973). Racemization reaction of aspartic acid and its use in dating fossil bones. *Proceedings of the National Academy of Science* 70: 1331-1334
- Bada, J. L., Shou, M.-Y., Man, E. H., Schroeder, R. A. (1978). Decomposition of hydroxy amino acids in foraminiferal tests: kinetics, mechanism and geochronological implications. *Earth and Planetary Science Letters* 41: 67-76
- Bagnold, R. A. (1941). *The physics of blown sand and desert dunes*. London: Methuen, 265 pp
- Bailey, R. M. (2004). Paper I—simulation of dose absorption in quartz over geological timescales and its implications for the precision and accuracy of optical dating. *Radiation Measurements* 38: 299-310
- Bailey, R. M., Armitage, S. J., Stokes, S. (2003). An investigation of pulsed-irradiation regeneration of quartz OSL and its implications for the precision and accuracy of optical dating (Paper II). *Radiation Measurements* 39: 347-359
- Bailey, R. M., Armitage, S. J., Stokes, S. (2005). An investigation of pulsed-irradiation regeneration of quartz OSL and its implications for the precision and accuracy of optical dating (Paper II). *Radiation Measurements* 39: 347-359
- Ball, D., (1998). *Kangaroo Island Vegetation Mapping*. Edited by S. Carruthers. Information and Data Analysis Branch, Planning SA
- Banerjee, D., Hildebrand, A. N., Murray-Wallace, C. V., Bourman, R. P., Brooke, B. P., Blair, M. (2003). New quartz SAR-OSL ages from the stranded beach dune sequence in south-east South Australia. *Quaternary Science Reviews* 22: 1019-1025
- Banner, J. L. (2004). Radiogenic isotopes: systematics and applications to earth surface processes and chemical stratigraphy. *Earth-Science Reviews* 65: 141-194
- Bard, E., Arnold, M., Fairbanks, R. G., Hamelin, B. (1993). ^{230}Th - ^{234}U and ^{14}C Ages obtained by Mass Spectrometry on corals. *Radiocarbon* 35 (1): 191-99
- Bard, E., Antonioli, F., Silenzi S. (2002). Sea-level during the penultimate interglacial period based on a submerged stalagmite from Argenterola Cave, Italy. *Earth and Planetary Science Letters* 196: 135-146
- Barnes, R., Hughes, R. (1999). *An Introduction to Marine Ecology*; Third Edition. Malden, MA: Blackwell Science, Inc. 117-141
- Barwis, J. H., Tankard, A. J. (1983). Pleistocene shoreline deposition and sea-level history at Swartklip, South Africa. *Journal of Sedimentary Petrology* 53: 1281–1294
- Bateman, L. P. (1987). *Stratigraphy of the Quaternary sequence in south-west Yorke Peninsula, South Australia*. Flinders University (South Australia). B.Sc. (Hons) thesis (unpublished)
- Bateman, M. D., Holmes, P. J., Carr, A. S., Horton, B. P., Jaiswal, M. K. (2004). Eolianite and barrier dune construction spanning the last two glacial–interglacial cycles from the southern Cape coast, South Africa. *Quaternary Science Reviews* 23: 1681-1698
- Bateman, M. D., Carr, A. S., Dunajko, A. C., Holmes, P. J., Roberts, D. L., McLaren S. J., Bryant, R. G., Marker. M. E., Murray-Wallace, C. V. (2011). The evolution of coastal barrier systems: a case study of the Middle-Late Pleistocene Wilderness barriers, South Africa. *Quaternary Science Reviews* 30: 63-81
- Bateman. M. D., Nash, D. J., Bullard, J. E., Latorre, C. (2010). Quaternary aeolianite development in a tectonically active coastal setting: a case study from the Atacama Desert of northern Chile. Quaternary Research Association (QRA)—Annual Discussion Meeting, January, 2010. Applebey lecture theatre, Geography Department, Durham University, UK
- Bauer, F. J., (1959). *The regional geography of Kangaroo Island, South Australia*. Australian National University, Canberra. PhD thesis (unpublished)

Belperio, A. P. (1983). Terrigenous sedimentation in the central Great Barrier Reef Lagoon: a model from the Burdekin region. *BMR Journal of Australian Geology and Geophysics* 8: 179-190

Belperio, A. P. (1988). Fowlers Bay rotary drilling report and revision of the Quaternary geology around Fowlers Bay. South Australia. Department of Mines and Energy. Report Book 88/93.

Belperio A. P. (1995). Quaternary. In: Drexel J. F. & Preiss W. V. (Editors). *The Geology of South Australia, Vol. 2. The Phanerozoic: 218-280*. Geological Survey of South Australia. Bulletin 54

Belperio, A. P., Harvey, N., Bourman, R. P. (2002). Spatial and temporal variability in the Holocene sea-level record of the South Australian coastline. *Sedimentary Geology* 150: 153-169

Belperio A. P., Fairclough M. C. & Randabel J. P. J. (2000). Kingscote Map Sheet, Geological Atlas, 1:250 000 Series (Preliminary edition). Geological Survey of South Australia, Adelaide

Belperio, A. P., Flint, R. B. (1999). Geomorphology and geology. In: Robinson, A. C., Armstrong, D. M. (Editors). *A Biological Survey of Kangaroo Island, South Australia, 19-28*. Endeavour Press, Adelaide.

Belperio, A. P., Harvey, N., Bourman, R. P. (2002) Spatial and temporal variability in the Holocene sea-level record of the South Australian coastline. *Sedimentary Geology* 150: 153-169

Belperio, A. P., Murray-Wallace, C. V., Cann, J. H. (1995). The Last Interglacial shoreline in southern Australia: morphostratigraphic variations in a temperate carbonate setting. *Quaternary International* 26: 7-19

Belperio, A. P., Preiss, W.V., Fairclough, M.C., Gatehouse C.G, Gum, J., Hough, J. Burt, A. (1998). Tectonic and metallogenic framework of the Cambrian Stansbury Basin—Kanmantoo Trough, South Australia. *AGSO Journal of Australian Geology & Geophysics* 17(3): 183-200

Belperio, A. P., Flint T. B. (1992). The geological and geomorphological framework of Kangaroo Island SA. Dept. Mines and Energy Report Book 92/1

Belperio, A. P., Smith. B. w., Polach, H. A., Nittrouer, C. A., De Master, D. J., Prescott, J. R, Hails, J. R., Gostin, V. A. (1984). Chronological studies of Quaternary marine sediments of northern Spencer Gulf. *Marine Geology* 61: 265-296

Betts, D. S., Couturier, L., Khyarat, A. H., Luff, B. J., Townsend, P. D. (1993). Temperature distribution in thermoluminescence experiments---I. Experimental results. *Journal of Physics D* 26: 843-848

Betts, D. S., Townsend P. D. (1993). Some calculation models. *Journal of Physics D* 26, 849-857

Berger, R., Horney, A. G., and Libby, W. F. (1964). Radiocarbon dating of bone and shell from their organic components. *Science* 144:999-1001

Boardman, M. R., McCartney, R. F., and Eaton, M. R. (1995). Bahamian Paleosols: Origin, relation to paleoclimate and stratigraphic significance. In: Curran, H.A., and White, B. *Terrestrial and Shallow Marine Geology of the Bahamas and Bermuda: Boulder, CO, Geological Society of America Special Paper* 300

Bøtter-Jensen, L., Mejdahl V. (1988). Assessment of beta dose-rate using a GM multiscaler system. *Nuclear Tracks and Radiation Measurements* 14(1-2): 187-191

Bourman, R. P. (1993). Perennial problems in the study of laterite: A review. *Australian Journal of Earth Sciences*, 40 (4): 387-401

- Bourman, R.P. Alley, N.F. (1999). Permian glaciated bedrock surfaces and associated sediments on Kangaroo Island, South Australia: implications for local Gondwanan ice-mass dynamics. *Australian Journal of Earth Sciences* 46: 523-531
- Bourman R. P., Martinaitis P., Prescott J. R., Belperio A. P. (1997). The age of the Pooraka Formation and its implications, with some preliminary results from luminescence dating. *Transactions of the Royal Society of South Australia* 121: 83-94
- Bourman, R. P. , Prescott, J. R. , Banerjee, D. , Alley, N. F. and Buckman, S. (2010). Age and origin of alluvial sediments within and flanking the Mt Lofty Ranges, southern South Australia: a Late Quaternary archive of climate and environmental change', *Australian Journal of Earth Sciences*, 57 (2): 175-192
- Boutakoff, N. (1963). The Geology and Geomorphology of the Portland Area. Geological Survey of Victoria, Memoir No. 22
- Boutakoff, N., Sprigg, R. C. (1953). Summary report on the petroleum possibilities of the Mount Gambier sunken lands. *Mining and Geological journal of Victoria* 5: 28–42
- Bowdler, S. (1995). Offshore Islands and maritime explorations in Australian Prehistory. *Antiquity* 69: 946-958
- Bowler, J. M., Johnston, H., Olley, J. M., Prescott, J. R., Roberts, R. G., Shawcross, W., Spooner, N. A. (2003). New ages for human occupation and climatic change at Lake Mungo, Australia. *Nature* 421: 837-840
- Bretz, J. H. (1960). Bermuda: a partially drowned late mature Pleistocene karst. *Geological Society of America Bulletin* 71: 1729–1754
- Bronk Ramsey C. (2005) OxCal v3.10: a program designed for the analysis of chronological information. Oxford University. <http://c14.arch.ox.ac.uk/embed.php?File=oxcal.html>
- Brooke, B. P. (1999). Quaternary stratigraphy and evolution of eolianite on Lord Howe Island. PhD Thesis (Unpublished). School of Geosciences, University of Wollongong, Australia
- Brooke, B. (2001). The Distribution of Carbonate Eolianite. *Earth-Science Reviews* 55: 135-164
- Brooke, B. P., Woodroffe, C. D., Murray-Wallace, C. V., Heijnis, H. and Jones, B. G. (2003). Quaternary calcarenite stratigraphy on Lord Howe Island, southwestern Pacific Ocean and the record of coastal carbonate deposition. *Quaternary Science Reviews* 22: 859-880
- Brückner, H. (1986). Stratigraphy, evolution and age of Quaternary marine terraces in Morocco and Spain. *Zeitschrift für Geomorphologie* 62: 83-101
- Brückner, H., Wittner, R., Godel, H. (1991) Fully automated high-performance liquid chromatographic separation of DL-amino acids derivatised with o-phthalaldehyde together with N-isobutryl-cysteine, application to food samples. *Chromatographia* 32: 383-388
- Bureau of Meteorology (2007). Climate averages. <http://www.bom.gov.au/climate/averages/>
- Burgess, S. N., McCulloch, M. T., Gagan, M. K., Ward, T. M. (2006) Long-term anthropogenic change in South Australian gulfs recorded by the faiid coral *Plesiastrea versipora*. *Goldschmidt Conference Abstracts 2006*.06.251 p A74
- Butzer, K. W. (2004). Coastal eolian sands, paleosols, and Pleistocene geoarchaeology of the Southwestern Cape, South Africa. *Journal of Archaeological Science* 31: 1743–1781
- Buzas, Martin A., Douglass, Raymond C., and Smith, Charles C. (1987). Kingdom Protista; in, *Fossil Invertebrates*, R. S. Boardman, A. H. Cheetham, and A. J. Rowell, eds.: Boston, Blackwell Scientific Publications, p. 67-106
- Campbell. C. V. (1966). Truncated wave-ripple laminae: *Journal of Sedimentary Petrology* 36: 825-828

- Campbell, C. V. (1971). Depositional model Upper Cretaceous Gallup beach shoreline. Ship Rock area. Northwestern New Mexico. *Journal of Sedimentary Petrology* 41: 395-409
- Cann J. H. (1978). An exposed reference section for the Glanville Formation. South Australia Geological Survey. *Quarterly Geological Notes* 65: 2-4
- Cann, J. H., Clarke, J. A. D. (1993). The significance of *Marginopora vertebralis* (Foraminifera) in surficial sediments at Esperance, Western Australia and in last interglacial sediments in northern Spencer Gulf. *Marine Geology* 111: 171–187
- Cann, J. H., Harvey, N., Barnett, E. J., Belperio, A. P., Bourman, R. P. (2002). Foraminiferal biofacies eco-succession and Holocene sealevels, Port Pirie, South Australia. *Marine Micropaleontology* 44: 31-55
- Cann, J. H., Murray-Wallace, C. V., Belperio, A. P., Brenchley, A. J. (1999). Evolution of Holocene coastal environments near Robe, southeastern South Australia. *Quaternary International* 56: 81-97
- Carew, J. L., Mylroie, J. E. (1995). Depositional model and stratigraphy for the Quaternary Geology of the Bahama Islands. In: Curran, H.A., White, B. (Editors). *Terrestrial and Shallow Marine Geology of the Bahamas and Bermuda*, Special Paper 300. Geological Society of America, Boulder, CO. pp. 5–32
- Carew, J. L., Mylroie, J. E., (1997). Geology of the Bahamas. In: Vacher, H. L., Quinn, T. (Editors) *Geology and Hydrogeology of Carbonate Islands*. *Developments in Sedimentology* 54: 91–139. Elsevier Science, Amsterdam
- Carr, A. S., Bateman, M. D., Roberts, D. L., Murray-Wallace, C. V., Jacobs, Z., Holmes, P. J. (2010). The last interglacial sea-level high stand on the southern Cape coastline of South Africa. *Quaternary Research* 73: 351–363
- Carr, A. S., Thomas, D. S. G, Bateman, M. D. (2006). Climatic and sea level controls on Late Quaternary eolian activity on the Agulhas Plain, South Africa. *Quaternary Research* 65: 252-263
- Chave, K. E. (1967). Recent carbonate sediments—an unconventional view. *Journal of Geological Education* 15: 200–204
- Chivas, A. R., García, A., van der Kaars, S., Couapel, M. J. J., Holt, S., Reeves, J. M., Wheeler, D. J., Switzer, A. D., Murray-Wallace, C. V., Banerjee, D., Price, D. M., Wang, S. X., Pearson, G., Edgar, N. T., Beaufort, L., De Deckker, P., Lawson, E., Cecil, C. B. (2001). Sea-level and environmental changes since the last interglacial in the Gulf of Carpentaria, Australia: an overview. *Quaternary International* 83-85: 19-46
- Choquette, P. W., Pray L. C. (1970). Geologic Nomenclature and Classification of Porosity in Sedimentary Carbonates. *AAPG Bulletin* 54 (2): 207 – 250
- Clarke, P.A. (1996). Early European Interaction with Aboriginal Hunters and Gatherers on Kangaroo Island, South Australia. *Aboriginal History* 20: 51-81
- Clarke, S. J., Murray-Wallace, C. V. (2006). Mathematical expressions used in amino acid racemisation geochronology—a review. *Quaternary Geochronology* 1: 261–278
- Coetzee, F. (1975). Coastal aeolianites at Black Rock, Northern Zululand. *Transactions of the Geological Society of South Africa* 78: 313-322
- Collins, M. J., Riley, M. S. (2000). Amino acid racemization in biominerals, the impact of protein degradation and loss. In: *Perspectives in Amino Acid and Protein Geochemistry*, Goodfriend, G. A., Collins, M. J., Fogel, M. L., Macko, S. A., Wehmiller, J. F. (Editors). Oxford University Press: Oxford: 120–142
- Collinson, J. D., Thompson, D. B. (1989) *Sedimentary Structures* (2nd edition): Academic Division of Unwin Hyman Ltd, Winchester, MA

Croll, J. (1875). *Climate and Time in their Geological Relations: a Theory of Secular Changes of the Earth's Climate*. Edward Stanford, London, 577 pp

CSIRO, (2007). Monthly sea surface temperature and ocean current images <http://www.cmar.csiro.au/remotesensing/oceancurrents/Adelaide/index.html>

Cullen, P., Bird, E. (1980). *The Management of Coastal Sand Dunes in South Australia*, Prepared for the Coast Protection Board, June 1980

Cumpston, J.S. (1970). *Kangaroo Island 1800-1836*. Roebuck Society Publishers, Canberra

Curran, H. A., White, B. (1991). Trace fossils of shallow subtidal to dunal ichnofacies in Bahamian Quaternary carbonates. *Palaos* 6 (5): 498-510

Cutler, K.B., Edwards, R. L., Taylor, F. W., Cheng, H., Adkins, J., Gallup, C. D., Cutler, P. M., Burr, G. S., Bloom, A. L. (2003). Rapid sea-level fall and deep-ocean temperature change since the last interglacial period. *Earth and Planetary Science Letters* 206: 253-271

Daily, B., Milnes, A.R., Twidale, C.R., and Bourne, J.A. (1979). *Geology and Geomorphology*. In: Tyler, M.J., Twidale, C.R. and Ling, J.K. Editors. *Natural history of Kangaroo Island*. Royal Society of South Australia, Adelaide: 1-38

Daily, B., Moore, P. S., Rust, B. R. (1980). Terrestrial-marine transition in the Cambrian rocks of Kangaroo Island, South Australia. *Sedimentology* 27: 379-399

Daily, B., Twidale, C. R. Milnes, A.R. (1974). The Age of the Lateritized Summit Surface on Kangaroo Island and Adjacent Areas of South Australia. *Journal of the Geological Society of Australia* 21(4): 387-392

Daly, R. A. (1927). The geology of Saint Helena Island. *Proceedings of the American Academy of Arts and Sciences* 62 (2): 31-98

Darwin, C. R. (1844). *Geological Observations on the Volcanic Islands, Visited During the Voyage of the H.M.S. Beagle*. Together with some brief notes on the geology of Australia and the Cape of Good Hope. In: Barrett, P. H., and Freeman, R. B., Editors, (1986). *The Works of Charles Darwin*. Volume 8. *The Geology of the Voyage of H.M.S. Beagle*. Part II: *Geological Observations on the Volcanic Islands*. William Pickering, London. pp 117

Davies, R. J. P. (1982). *The Conservation of major plant associations in South Australia*. Adelaide: Conservation Council of South Australia Inc.

Davies, W. D., and Treloar, F. E. (1977). The application of racemization dating in archaeology—a critical review. *The Artefact* 2: 63-95

Davis, R. A. Jr. (1985). *Coastal sedimentary environments*. New York, Springer-Verlag

Dobberstein, R. C., Huppertz, J., von Wurmb-Schwark, N. & Ritz-Timme, S. (2008) Degradation of biomolecules in artificially and naturally aged teeth: implications for age estimation based on aspartic acid racemization and DNA analysis. *Forensic Science International* 179: 181-191

Dodson, J. R. (1998). Timing and response of vegetation change to Milankovitch forcing in temperate Australia and New Zealand. *Global and Planetary Change* 18: 161-174

Domingues, C.M. (2006). *Kinematics and Heat Budget of the Leeuwin Current*. Flinders University, South Australia. Unpublished PhD Thesis

Dravis, J. J. (1996). Rapidity of freshwater calcite cementation—implications for carbonate diagenesis and sequence stratigraphy *Sedimentary Geology* 107 (1-2): 1-10

Dudley, E. (1995) *Map Maker version 3.5*. GIS software. Map Maker Ltd. Scotland

Duller, G. A. T. (1995). Luminescence dating using single aliquots: Methods and applications. *Radiation Measurements* 24: 217-226

- Duller, G. A. T. (2003). Distinguishing quartz and feldspar in single grain luminescence measurements. *Radiation Measurements* 37: 161–165
- Duller, G. A. T., Bøtter-Jensen, L. (1993). Luminescence from potassium feldspars stimulated by infrared and green light. *Radiation Protection Dosimetry* 47: 683-688
- Eberl, D. D. (2003). User's guide to RockJock—a program for determining quantitative mineralogy from powder x-ray diffraction data. U.S. Department of the Interior, U.S. Geological Survey Open-File Report 03-78
- Edwards, G. (1987). Kangaroo Island Coast Protection District Study Report, Prepared for the Coast Protection Board
- El-Asmar, H. M., Wood, P. (2000). Quaternary shoreline development: the northwestern coast of Egypt. *Quaternary Science Reviews* 19: 1137-1149
- Engelmann, A., Neber, A., Frechen, M., Boenigk, W., Ronen, A., (2001). Luminescence chronology of upper Pleistocene and Holocene aeolianites from Netaya South—Sharon Coastal Plain, Israel. *Quaternary Science Reviews (Quaternary Geochronology)* 20: 799–804
- Eppley, R. W., Peterson, B. J. (1979). Particulate organic matter flux and planktonic new production in the deep ocean. *Nature* 282: 677-680
- Fairbridge, R. W. (1948). Notes on the geomorphology of the Pelsart Group of the Houtman's Abrolhos Islands. *Journal of the Royal Society of Western Australia* 33: 1-36
- Fairbridge, R. W. (1950). The geology and geomorphology of Point Peron, Western Australia. *Journal of the Royal Society of Western Australia* 34: 35-72
- Fairbridge, R. W. and Johnson, D.L. (1978). Eolianite. In: R.W Fairbridge and J. Bourgeois, Editors. *The Encyclopedia of Sedimentology*. Dowden, Hutchinson and Ross, Stroudsburg (PA), 279-282
- Fairbridge, R. W., Teichert, C. (1953). Soil horizons and marine sands in the coastal limestones of Western Australia. *Proceedings of the Royal Society of New South Wales* 86: 68-87
- Farrell, J. W., Clemens, S. C., Gromet, L. P. (1995). Improved chronostratigraphic reference curve of Late Neogene seawater $^{87}\text{Sr}/^{86}\text{Sr}$. *Geology* 23: 403-406.
- Finkel, R. C., Suter, M. (1993). AMS in the Earth Sciences: Technique and Applications, *Advances in Analytical Geochemistry* 1: 1-114.
- Firman, J. B., (1966). Stratigraphic units of Late Cainozoic age in the St Vincent Basin, South Australia. South Australia. Geological Survey. *Quarterly Geological Notes* 17: 6-9
- Firman, J. B. (1967). Stratigraphy of Late Cainozoic deposits in South Australia. *Royal Society of South Australia. Transactions* 91: 165-180
- Fleming, S. (1979). Thermoluminescence techniques in archaeology. Clarendon Press, Oxford
- Flottmann, T., Haines, P., Jago, J., P. James, Belperio, A, Gum, J. (1998). Formation and reactivation of the Cambrian Kanmantoo Trough, SE Australia: implications for early Palaeozoic tectonics at eastern Gondwana's plate margin. *Journal of the Geological Society* 155: 525-539
- Flottmann, T., James, P. (1997). Influence of basin architecture on the style of inversion and fold-thrust belt tectonics—the southern Adelaide Fold-Thrust Belt. *South Australia Journal of Structural Geology* 19(8): 1093-1110
- Flottmann, T., James, P., Menpes, R., Cesare, P., Twining, M., Fairclough, M., Randabel, J. Marshak, S. (1995). The structure of Kangaroo Island, South Australia: strain and kinematic partitioning during Delamerian basin and platform reactivation. *Australian Journal of Earth Sciences* 42: 35-49

- Flügel, E. (2004). *Microfacies of Carbonate Rocks: analysis, interpretation and application*. Springer, Berlin Heidelberg New York
- Foden, J. D., Elburg, M. A., Turner, S. P., Sandiford, M., O'Callaghan, J., Mitchell, S. (2002). Granite production in the Delamerian Orogen, South Australia. *Journal of the Geological Society Annual* 159 (5): 557-576
- Forman, S. L., Pierson, J. and Lepper, K. (2000). *Luminescence Geochronology*. In: Noller, J. S., Sowers, J. M., and Lettis, W. R. (Editors). *AGU Reference Shelf 4. Quaternary Geochronology: Methods and Applications*. American Geophysical Union, Washington DC, USA. 157-176
- Fornos, J. J., Clemmensen, L. B., Pujol, L. G., Murray, A. S. (2009). Late Pleistocene carbonate aeolianites on Mallorca, Western Mediterranean: a luminescence chronology. *Quaternary Science Reviews* 28: 2697-2709
- Fragoulis, D. V., Readhead, M. L. (1991). Feldspar inclusions and the enhancement of thermoluminescence in quartz grains. *Nuclear Tracks and Radiation Measurements* 18 (3): 291-296
- Frechen, M., Dermann, B., Beonigk, W., Ronen, A. (2001). Luminescence chronology of aeolianites from the section Givat Olga – coastal plain of Israel. *Quaternary Science Reviews (Quaternary Geochronology)* 20: 805-809
- Frechen, M., Neber, A., Tsatskin, A., Boenigk, W., Ronen, A. (2004). Chronology of Pleistocene sedimentary cycles in the Carmel Coastal Plain of Israel. *Quaternary International* 121: 41-52
- Fuller, M. K., Bone, Y., Gostin, V. A., Von der Borch, C. C. (1994). Holocene cool-water carbonate and terrigenous sediments from southern Spencer Gulf, South Australia. *Australian Journal of Earth Sciences* 41: 353-363
- Funder, S. (1989). Quaternary geology of the ice-free area and adjacent shelves of Greenland. In: R. J. Fulton (Editor), *Quaternary geology of Canada and Greenland*. Geological Survey of Canada, Geology of Canada, No. 1 (also Geological Society of America, *The Geology of North America*, vol. K-1)
- Funder, S., Hjort, C. H., Landvik, I. Y. (1991). Quaternary stratigraphy of Jameson Land - a first approximation. - In: P. Möller; Ch. Hjort, O. Ingolfssoneds., *The last interglacial-glacial cycle: preliminary report on the PONAM fieldwork in Jameson Land and Scoresby Sund, East Greenland*. *Lundqua Reports* 33: 171-176, Lund
- Galbraith, R.F., Roberts, R.G., Laslett, G.M., Yoshida, H., Olley, J.M. 1999. Optical dating of single and multiple grains of quartz from Jinmium rock shelter, northern Australia: Part I, experimental design and statistical models. *Archaeometry* 41: 339-364
- Gallup, C. D., Edwards, R. L., Johnson, R. G. (1994). The timing of high sealevels over the past 200,000 years. *Science* 263: 796-800.
- Gardner, T. W., Webb, J., Davis A. G., Cassel, E. J., Pezzia C., Merritts D. J., Smith, B. (2006). Late Pleistocene landscape response to climate change: eolian and alluvial fan deposition, Cape Liptrap, southeastern Australia. *Quaternary Science Reviews* 25: 1552–1569
- Garrett, P., Gould, S. J. (1984). *Geology of New Providence Island, Bahamas*. Geological Society of America Bulletin 95: 209-220
- Giannini, P. C. F., Sawakuchi, A. O., Martinho, C. T., Tatum, S. H. (2007). Eolian depositional episodes controlled by Late Quaternary relative sea level changes on the Imbituba–Laguna coast (southern Brazil). *Marine Geology* 237: 143-168
- Gillespie, R., Hedges, R. E. M., Wand, O. J. (1984). Radiocarbon dating of bone by Accelerator Mass Spectrometry. *Journal of Archaeological Science* 11: 165-170

- Goodfriend G. A. (1991). Patterns of racemization and epimerization of amino acids in land snail shells over the course of the Holocene. *Geochim. Cosmochim. Acta*. 55: 293-302
- Goodfriend, G. A., Brigham-Grette, J., Miller, G. H. (1996). Enhanced age resolution of the marine Quaternary record in the arctic using aspartic acid racemization dating of bivalve shells. *Quaternary Research* 45: 176-187
- Goodfriend, G. A., Cameron, R. A. D., Cook, L. M., Courty, M., Fedoroff, N., Livett, E., Tallis, J. (1996). The Quaternary eolian sequence of Madeira: stratigraphy, chronology, and paleoenvironmental interpretation. *Palaeogeography, Palaeoclimatology, Palaeoecology* 120: 195-234
- Goodfriend, G.A., Collins, M.J., Fogel, M.L., Macko, S.A., Wehmiller, J.F. (Editors). (2000). *Perspectives in Amino Acid and Protein Geochemistry*. Oxford University Press, New York pp 320-330
- Goodfriend G., Weidman C. (2001). Ontogenetic trends in aspartic acid racemization and amino acid composition within modern and fossil shells of the bivalve *Arctica*. *Geochim Cosmochim Acta* 65: 1921-1932
- Google Earth. (2005-2010). Images of Kangaroo Island, South Australia: various locations. Visual data from: Geoeye; Cnes; Spot; TerraMetrics; SIO; NOAA; US Navy; NGA; GEBCO and Digital Globe. [Accessed 2005-2010].
- Gostin, V. A., Belperio, A. P., Cann, J. H. (1988). The Holocene non-tropical coastal and shelf carbonate province of south Australia. *Sedimentary Geology* 60: 51-70
- Gove, H. E. (1998). *From Hiroshima to the Iceman: The Development and Applications of Accelerator Mass Spectrometry*. Institute of Physics Publication
- Haines, P. W., Jago, J. B., Gum, J. C. (2001). Turbidite deposition in the Cambrian Kanmantoo Group, South Australia. *Australian Journal of Earth Sciences* 48: 465-478.
- Haines, P.W., Jago, J.B, Gum, J.C. (2001). Turbidite deposition in the Cambrian Kanmantoo Group, South Australia. *Australian Journal of Earth Sciences* 48: 465-478
- Hails, J. R., Belperio, A. P., Gostin, V. A. (1984a). Quaternary sea levels, northern Spencer Gulf, Australia. *Marine Geology* 61: 373-389.
- Hails, J. R., Belperio, A. P., Gostin, V. A, Sargent, G. E. G. (1984b). Submarine Quaternary stratigraphy of northern Spencer Gulf, South Australia. *Marine Geology* 61: 345-372
- Hancock, G., Pietsch, T. (2008) Sediment tracing and dating techniques employed at CSIRO Land and Water, CSIRO Land and Water Science Report 64/08
- Hare, P. E. (1962) The amino acid composition of the organic matrix of some west coast species of *Mytilus*: (PhD Dissertation) Pasadena, California Institute of Technology pp 109
- Hare, P. E. (1969). Geochemistry of proteins, peptides, and amino acids, in Eglinton, G. and Murphy, M. J. T., (Editors). *Organic Geochemistry, Methods and Results*: New York, Springer Verlag, p. 438-463
- Hare, P. E., Brooks, A. S., Kokis, J. E., Kumin, K. (1984). Aminostratigraphy: the use of ostrich eggshell in dating the middle stone age at #Gi, Botswana: *Geological Society of America Abstracts with Programs* 16: p A529
- Harmon, R. S., Land, L. S., Mitterer, R. M., Garrett, P., Schwarcz, H. P., Larson, G. J. (1981). Bermuda sea level during the last interglacial. *Nature* 289: 481-483
- Hearty, P. J. (1998). The geology of Eleuthera island, Bahamas: a Rosetta Stone of Quaternary stratigraphy and sea-level history. *Quaternary Science Reviews* 17: 333-355

- Hearty, P. J. (2002). Revision of the late Pleistocene stratigraphy of Bermuda. *Sedimentary Geology* 153: 1-21
- Hearty, P. J. (2003). Stratigraphy and timing of eolianite deposition on Rottnest Island, Western Australia. *Quaternary Research* 60: 211-222
- Hearty, P.J., Hollin, J. T., Neumann, A. C., O'Leary, M. J., McCulloch, M. (2007). Global sea-level fluctuations during the Last Interglaciation (MIS 5e). *Quaternary Science Reviews* 26: 2090–2112
- Hearty, P. J., Kaufman, D. S. (2000). Whole-Rock Aminostratigraphy and Quaternary Sea-Level History of the Bahamas. *Quaternary Research* 54: 163–173
- Hearty, P. J., Kindler, P. (1993). New Perspectives on Bahamian Geology: San Salvador Island, Bahamas. *Journal of Coastal Research* 9 (2): 577–594
- Hearty, P. J., Kindler, P. (1997). The stratigraphy and surficial geology of New Providence and surrounding islands, Bahamas. *Journal of Coastal Research* 13 (3): 798-812
- Hearty, P. J., Neumann, A. C. (2001). Rapid sea level and climate change at the close of the Last Interglaciation (MIS 5e): evidence from the Bahama Islands. *Quaternary Science Reviews* 20: 1881-1895
- Hearty, P. J., O'Leary, M. J. (2008). Carbonate eolianites, quartz sands, and Quaternary sea-level cycles, Western Australia: A chronostratigraphic approach. *Quaternary Geochronology* 3: 26–55
- Hearty, P. J., O'Leary, M. J., Kaufman, D. S., Page, M. C., Bright, J. (2004). Amino acid geochronology of individual foraminifer (*Pulleniatina obliquiloculata*) tests, north Queensland margin, Australia: a new approach to correlating and dating Quaternary tropical marine sediment cores. *Paleoceanography* 19: PA4022
- Hearty, P. J., Vacher, H. L. (1994). Quaternary stratigraphy of Bermuda: a high-resolution pre-Sangamonian rock record. *Quaternary Science Revision* 13: 685-697
- Hearty, P. J., Vacher, H. L. and Mitterer, R. M. (1992). Aminostratigraphy and ages of Pleistocene limestones of Bermuda. *Geological Society of America Bulletin* 104: 471-480
- Heath, N. (2007) Personal Communication. Ranger at Kelly Hill Caves Conservation Park.
- Heilprin, A. (1888). Contributions to the natural history of the Bermuda Islands. *Proceedings of the Academy of Natural Sciences of Philadelphia* 40: 302-328
- Henshilwood, C. S., d'Errico, F., Yates, R., Jacobs, Z., Tribolo, C., Duller, G. A. T., Mercier, N., Sealy, J. C., Vallada, H., Watts, I., Wintle, A. G. (2002). Emergence of modern human behavior: middle stone age engravings from South Africa. *Science* 295: 1278–1280
- Hill, A. L. (1957). The origin of the Kelly Hill Caves, Kangaroo Island. Cave exploration group of South Australia (CEGSA). Unpublished draft
- Hocking, R. M., Mory, A. J. (2006). Geology of the Kalbarri area—a field guide. Geological survey of western Australia. Department of Industry and Resources
- Hodell, D. A., Mueller, P. A., Garrido, J. R. (1991). Variations in the strontium isotopic composition of seawater during the Neogene. *Geology* 19: 24-27
- Holail, H., Rashed, M. (1992). Stable isotopic composition of carbonate-cemented recent beachrock along the Mediterranean and the Red Sea coasts of Egypt. *Marine Geology* 106: 141–148
- Howe, S. A., Marshall, A. T. (2002). Temperature effects on calcification rate and skeletal deposition in the temperate coral *Plesiastrea versipora* (Lamarck). *Journal of Experimental Marine Biology and Ecology* 275: 63–81

Hughen, K. A., Baillie, M. G. L., Bard, E., Beck, J. W., Bertrand, C. J. H., Blackwell, P. G., Buck, C. E., Burr, G. S., Cutler, K. B., Damon, P. E., Edwards, R. L., Fairbanks, R. G., Friedrich, M., Guilderson, T. P., Kromer, B., McCormac, G., Manning, S., Bronk Ramsey, C., Reimer, P. J., Reimer, R. W., Remmele, S., Southon, J. R., Stuiver, M., Talamo, S., Taylor, F. W., van der Plicht, J., Weyhenmeyer, C. E. (2004). Marine04 marine radiocarbon age calibration, 0-26 cal kyr BP. *Radiocarbon* 46 (3): 1059-1086.

Huntley, D. J., Godfrey-Smith, D. I., Thewalt, M. L. W. (1985). Optical dating of sediments. *Nature* 313: 105-107

Huntley, D. J., Hutton, J. T., Prescott, J. R. (1993). The stranded beach-dune sequence of south-east Australia: a test of the thermoluminescence dating, 0–800 ka. *Quaternary Science Reviews* 12: 1–20.

Huntley, D. J., Hutton, J. T., Prescott, J. R. (1994). Further thermoluminescence dates from the dune sequence in the southeast of South Australia. *Quaternary Science Reviews* 13: 201–207.

Huntley, D. J., Prescott, J. R. (2001). Improved methodology and new thermoluminescence ages for the dune sequence in south-east Australia. *Quaternary Geochronology. Quaternary Science Reviews* 20: 687–699.

Huntley, D. J., Wintle, A. G. (1981). The use of alpha scintillation counting for measuring Th-230 and P-231 contents of ocean sediments: *Canadian Journal of Earth Science* 18: 419-432

Illenberger, W. K., Verhagen, B. T. (1990). Environmental history and dating of coastal Dunefields. *South African Journal of Science* 86: 311–314.

Illenberger, W., Rust, I., Vogel, J. (1997). Luminescence dating of coastal dunes of the southern Cape. XIII Biennial Conference of the Southern African Society for Quaternary Research Abstracts of Papers 6-7

Imbrie, J., Imbrie, J. Z. (1980). Modelling the climatic response to orbital variations. *Science* 207: 942-953

Imbrie, J., Imbrie, K. P. (1979). *Ice Ages, Solving the Mystery*. Enslow, New Jersey

Jacobs, Z. (2004). Development of luminescence techniques for dating Middle Stone Age sites in South Africa. Unpublished Ph.D. thesis, University of Wales, Aberystwyth

Jacobs, Z., Wintle, A. G., Duller, G. A. T. (2003). Optical dating of dune sand from Blombos Cave, South Africa: I—multiple grain data. *Journal of Human Evolution* 44: 599-612

Jacobs, Z., Wintle, A. G., Duller, G. A. T. (2006). Evaluation of SAR procedures for De determination using single aliquots of quartz from two archaeological sites in South Africa. *Radiation Measurements* 41: 520-533

Jacobs, Z. (2008). Luminescence chronologies for coastal and marine sediments. *Boreas* 37: 508-535

Jain, M., Duller, G. A. T., Wintle, A. G. (2007). Dose response, thermal stability and optical bleaching of the 310 °C isothermal TL signal in quartz. *Radiation Measurements* 42: 1285-1293

Jain, M., Murray, A. S., Bøtter-Jensen, L. (2003). Characterisation of blue light stimulated luminescence components in different quartz samples: implications for dose measurement. *Radiation Measurements* 37: 441-449

Jain, M., Singhvi, A. K. (2001). Limits to Depletion of Blue-green Light Stimulated Luminescence in Feldspars: Implications for Quartz Dating. *Radiation Measurements* 33 (6): 883-892

James, N. P. (1997) The cool-water carbonate depositional realm. In: James, N. P., Clarke, J. A. D. (Editors). *Cool-Water Carbonates*, SEPM Special Publication No. 56. Society for Sedimentary Geology, Tulsa, OK: 1–21

James, N. P., Bone, Y., Carter, R. M., Murray-Wallace, C. V. (2006). Origin of the Late Neogene Roe Plains and their calcarenite veneer: implications for sedimentology and tectonics in the Great Australian Bight. *Australian Journal of Earth Sciences* 53: 407-419

James, N. P., and Choquette, P. W. (1989). Diagenesis 5. In: Scholle, P. A., James, N. P., Read, J. F. Editors. *Short Course in Geology: Volume 4. Carbonate Sedimentology and Petrology*: 41-79. American Geophysical Union, Washington, D. C.

James, N. P., and Choquette, P. W. (1989). Diagenesis 9. In: Scholle, P. A., James, N. P., Read, J. F. Editors. *Short Course in Geology: Volume 4. Carbonate Sedimentology and Petrology*: 41-79. American Geophysical Union, Washington, D. C.

James, N. P., Bone, Y. (2011). *Neritic Carbonate Sediments in a Temperate Realm: Southern Australia*. Springer Dordrecht Heidelberg London New York. 204p

James, N. P., Bone, Y., Carter, R. M., Murray-Wallace, C. V. (2006). Origin of the Late Neogene Roe Plains and their calcarenite veneer: implications for sedimentology and tectonics in the Great Australian Bight. *Australian Journal of Earth Sciences* 53: 407– 419

James, N. P., Collins, L., Bone, Y., Hallock, P. (1999). Subtropical carbonates in a temperate realm: modern sediments on the southwest Australian shelf. *Journal of sedimentary research* 69 (6): 1297–1321

James, P. R., Clarke, I. F. (2002). Geology. In: Davies, M., Twidale, C. R., Tyler, M. J., (Editors). *Natural history of Kangaroo Island. Occasional publications of the Royal Society of South Australia* 2. Royal Society of South Australia, Adelaide

Johnson, D. L. (1977). The Late Quaternary climate of coastal California: evidence for an Ice Age refugium. *Quaternary Research* 8: 154-179

Kaufman, D. S. (2000). Amino acid racemization in ostracods. In: Goodfriend, G.A., Collins, M.J., Fogel, M.L., Macko, S.A., Wehmiller, J.F. (Editors). *Perspectives in Amino Acid and Protein Geochemistry*. Oxford University Press, New York pp 145–161

Kaufman, D. S., Manley, W. F. (1998). A new procedure for determining enantiomeric (D/L) amino acid ratios in fossils using reverse phase liquid chromatography. *Quaternary Science Reviews* 17: 987–1000

Kimber, R. W. L., Griffin, C. C., Milnes, A. R. (1986). Amino acid racemization dating: evidence of apparent reversal in aspartic acid racemization with time in shells of *Ostrea*. *Geochimica et Cosmochimica Acta* 50: 1159-1161

Kimber, R. W. L., Griffin, C. V. (1987). Further evidence of the complexity of the racemization process in fossil shells with implications for amino acid racemization dating. *Geochimica et Cosmochimica Acta* 51: 839-846

Kindler, P. (1995). New data on the Holocene stratigraphy of Lee Stocking Island (Bahamas) and its relation to sea-level history. In: Curran, H. A., White, B. (Editors). *Terrestrial and Shallow Marine Geology of the Bahamas and Bermuda Special Paper 300*. Geological Society of America, Boulder, CO, pp. 105-116

Kindler, P., Hearty, P. J. (1996). Carbonate petrology as an indicator of climate and sea-level changes: new data from Bahamian Quaternary units. *Sedimentology* 43: 381-399

Kindler, P., Hearty, P. J. (1997). Geology of the Bahamas: architecture of Bahamian Islands. In: Vacher, H.L., Quinn, T. (Editors). *Geology and Hydrogeology of Carbonate Islands, Developments in Sedimentology*, Vol. 54. Elsevier, Amsterdam, pp. 141–160

Kindler, P., Hearty, P. J. (2000). Elevated marine terraces from Eleuthera (Bahamas) and Bermuda: sedimentological, petrographic and geochronological evidence for important deglaciation events during the middle Pleistocene. *Global and Planetary Change* 24: 41–58

- Kindler, P. and Mazzolini, D. (2001). Sedimentology and petrography of dredged carbonate sands from Stocking Island (Bahamas). Implications for meteoric diagenesis and aeolianite formation. *Palaeogeography Palaeoclimatology Palaeoecology* 175: 369-379
- Kiyak, Erginal (2010). Optical Stimulated Luminescence Dating Study of Eolianite on the Island of Bozcaada, Turkey: Preliminary Results. *Journal of Coastal Research* 26 (4): 673-680
- Kneale, K., Viles, H. A. (2000). Beach cement: incipient CaCO_3 -cemented beachrock development in the upper intertidal zone, North Uist, Scotland. *Sedimentary Geology* 132 (3-4): 165-170
- Knoerich, A. C., Mutti, M. (2003). Controls of facies and sediment composition on the diagenetic pathway of shallow-water heterozoan carbonates: the Oligocene of the Maltese Islands. *International Journal of Earth Science* 92: 494-510
- Koch, P. L., Tuross, N., Fogel, M. L. (1997). The effects of sample treatment and diagenesis on the isotopic integrity of carbonate in biogenic hydroxylapatite. *Journal of Archaeological Science* 24: 417-429
- Kosnik, M.A., and D.S. Kaufman. (2008). Identifying outliers and assessing the accuracy of amino acid racemization measurements for use in geochronology: II. Data screening. *Quaternary Geochronology* 3(4): 328-341.
- Kriausakul, N., Mitterer, R. M. (1978). Isoleucine epimerization in peptides and proteins: kinetic factors and application to fossil proteins. *Science* 201: 1011-1014
- Kriausakul, N., Mitterer, R. M. (1983). Epimerization of COOH-terminal isoleucine in fossil dipeptides. *Geochimica et Cosmochimica Acta* 47: 963-966
- Ku, T. L. (2000). Uranium-series methods. In: Noller, J. S., Sowers, J. M., Lettis, W. R. (Editors). *AGU Reference Shelf 4. Quaternary Geochronology: Methods and Applications*. American Geophysical Union, Washington, USA. 101-114
- Kvenvolden, K. A. (1975). Advances in the geochemistry of amino acids. *Annu. Rev. Earth Planet. Sci.* 3: 183-212
- Kvenvolden, K. A., Blunt, D. J. (1978). Amino acid dating of *Saxidomus giganteus* at Willapa Bay, Washington, by racemization of glutamic acid In: Hare, P. E., Hoering, T. C., King, Jr., K. (Editors). *Biogeochemistry of Amino Acids*. Wiley, New York pp 393-401
- Laabs, B. J. C., Kaufman, D. S. (2003). Quaternary highstands in Bear Lake Valley, Utah and Idaho. *Geological Society of America Bulletin* 115: 463-478
- Lambeck, K., Chappell, J. (2001). Sea Level Change Through the Last Glacial Cycle. *Science* 292 (5517): 679-686
- Lajoie, K., J. F. Wehmiller, and G. L. Kennedy (1980) Inter- and intra-generic trends in apparent racemization kinetics of amino acids in Quaternary mollusks. In: Hare, P. E., Hoering, T. C., and King, K., Jr. (eds.), *Biogeochemistry of Amino Acids*, John Wiley, New York, pp. 305-340.
- Lajoie, K. R. (1986). Coastal Tectonics. In: *Active Tectonics*. Geophysics Research Forum (U.S.). Geophysics Study Committee. National Academy Press, Washington DC: 95-125
- Lambeck, K., Chappell, J. (2001). Sea Level Change Through the Last Glacial Cycle. *Science* 292: 679-685
- Lampert, R. (1981). The great Kartan mystery. *Terra Australis* 5. Canberra: Prehistory Department Research, School of Pacific studies. Australian National University
- Land, L. S., Mackenzie, F. T., Gould, S. J. (1967). Pleistocene History of Bermuda. *Geological Society of America Bulletin* 78 (8): 993-1006

- Lees, A. (1975). Possible influences of salinity and temperature on modern shelf carbonate sedimentation. *Marine Geology* 19: 159–198.
- Lees, A., Buller, A. T. (1972). Modern temperate water and warm water shelf carbonate sediments contrasted. *Marine Geology* 13: 1767–1773
- Lewis, S. E. Wüst, R. A. J. Webster, J. M. Shields, G.A. (2008). Mid-late Holocene sea-level variability in eastern Australia. *Terra Nova* 20: 74–81
- Li, W.-X., Lundberg, J., Dickin, A. P., Ford, D. C., Schwarz, H. P., McNutt, R., Williams, D. (1989). High-precision mass-spectrometric uranium series dating of cave deposits and implications for paleoclimate studies. *Nature* 339: 534–536
- Li, Q., James, N. P., McGowran, B., Bone, Y., Cann, J. H. (1998). Synergetic influence of water masses and Kangaroo Island barrier on foraminiferal distribution, Lincoln and Lacedpede shelves, South Australia: a synthesis. *Alcheringa* 22, 153–176
- Lindroth, P. Mopper, K. (1979). High Performance Liquid Chromatographic Determination of Subpicomole Amounts of Amino Acids by Precolumn Fluorescence Derivatisation with *o*-Phthaldialdehyde. *Analytical Chemistry* 51: (11) 1667–1674
- Lisiecki, L. E., Raymo, M. E. (2005). A Pliocene-Pleistocene stack of 57 globally distributed benthic $\delta^{18}\text{O}$ records, *Paleoceanography* 20, PA1003, doi:10.1029/2004PA001071
- Longman, M. W. (1982). Carbonate Diagenesis as a Control on Stratigraphic Traps (with Examples from the Williston Basin). American Association of Petroleum Geologists. Education Course Note Series No. 21
- Lowenstam, H. A. and Weiner, S. (1989). *On Biomineralization*. Oxford University Press, New York
- Ludbrook, N. H. (1973) Distribution and Stratigraphic Utility of Cenozoic Molluscan Faunas in Southern Australia. *Tohoku Univ., Sci. Rep., 2nd ser. (Geol.), Special Volume, no. 6 (Hatai Memorial Volume)*: 241–261
- Ludbrook, N. H. (1978). Quaternary molluscs of the western part of the Eucla Basin. *Bulletin of the Geological Survey of Western Australia* 125: 1–286
- Ludbrook, N. H. (1983). Molluscan fauna from the Early Pleistocene Point Ellen Formation & Burnham Limestone, South Australia. *Transactions of the Royal Society of South Australia* 107: 37–50
- Ludbrook, N.H. (1983). Molluscan faunas of the early Pleistocene Point Ellen Formation and Burnham Limestone, South Australia. *Transactions of the Royal Society of South Australia* 107(1/2): 37–49
- Luly, J. G., Blair, D., Parsons, J. G., Fox, S., Van Der Wal, J. (2010). Last Glacial Maximum habitat change and its effects on the grey-headed flying fox (*Pteropus poliocephalus*, Temminck, 1825). In: Haberle, S., Stevenson, J., Prebble, M. (Editors). *Altered Ecologies: Fire, climate and human influence on terrestrial landscapes*. *Terra Australis* 32: 83–100
- Machel, H. G. (1999). Effects of groundwater flow on mineral diagenesis, with emphasis on carbonate aquifers. *Hydrogeology Journal* 7: 94–107
- Mackenzie, F. T. (1964). Bermuda Pleistocene eolianites and paleowinds. *Sedimentology* 3: 52–64
- Major, R. B., and Vitols, V. (1973). The geology of the Vennachar and Borda 1:50 000 Map areas, Kangaroo Island. *Mineral Resources Review of South Australia* 134: 38–51
- Malan, J. A. (1987). The Bredasdorp Group in the area between Gans Bay and Mossel Bay. *South African Journal of Science* 83: 506–507

- Malan, J. A. (1990). The stratigraphy and sedimentology of the Bredasdorp Group, southern Cape Province. Unpublished MSc thesis, University of Cape Town
- Mangerud, J. (1972). Radiocarbon dating of marine shells, including a discussion of apparent age of recent shells from Norway. *Boreas* 1: 143-172
- Manley, W. F., Miller, G. H., Czywczynski, J. (2000). Kinetics of aspartic acid racemization in *Mya* and *Hiatella*: modelling age and paleotemperature of high-latitude Quaternary mollusks. In: Goodfriend, G.A., Collins, M.J., Fogel, M.L., Macko, S.A., Wehmiller, J.F. (Editors). *Perspectives in Amino Acid and Protein Geochemistry*. Oxford University Press, New York pp 202–219
- Margolis, S., Rex, R. W. (1971). Endolithic Algae and Micrite Envelope Formation in Bahamian Oölites as Revealed by Scanning Electron Microscopy. *Geological Society of America Bulletin* 82 (4): 843-852
- Marin, F., Luquet, G. (2004). Molluscan shell proteins. *C. R. Palevol.* 3: 469-492
- Marshall, J. F. (1980). Continental Shelf Sediments: Southern Queensland and Northern New South Wales, Bureau of Mineral Resources, Canberra
- Marshall, J. F., Davies, P. J. (1978). Skeletal carbonate variation on the continental shelf of eastern Australia. *BMR Journal of Australian Geology and Geophysics* 3: 85–92
- Marshak, S., Flottnann, T. (1996). Structure and origin of the Fleurieu and Nackara Arcs in the Adelaide fold-thrust belt, South Australia: salient and recess development in the Delamerian Orogen. *Journal of Structural Geology* 18(7): 891-908
- McArthur, J. M., Howarth, R. J., Bailey, T. R. (2001). Strontium Isotope Stratigraphy: LOWESS Version 3. Best-fit line to the marine Sr-isotope for 0-509 Ma and accompanying look-up table for deriving numerical age, *Journal of Geology* 109: 155-169
- McCulloch, M. T., Mortimer, G. E. (2008) Applications of the ^{238}U – ^{230}Th decay series to dating of fossil and modern corals using MC-ICPMS. *Australian Journal of Earth Science* 55 (6): 955-965
- McGowran, B., Li, Q., Cann, J., Padley, D. McKirdy, D.M., Shafik, S. (1997). Biogeographic impact of the Leeuwin Current in southern Australia since the late middle Eocene. *Palaeogeography, Palaeoclimatology, Palaeoecology* 136:19-40
- McIlreath, I., and Morrow, D. (Editors) (1990), *Diagenesis*: Geological Society of Canada, Geoscience Canada Reprint Series 4
- McKee, E. D. and Ward, W.C. (1983). Eolian environment. In: Scholle, P. A., Bebout, D. G., and Moore, C. H., (Editors). *Carbonate Depositional Environments*. American Association of Petroleum Geologists. Memoir 33: 131-170
- McKinney, M .L. (1984) Suwannee Channel of the Paleogene coastal plain: Support for the carbonate suppression model of basin formation: *Geology* 12: 343–345
- McLaren, S.J. (1993). Use of cement types in the palaeoenvironmental interpretation of coastal aeolianite sequences. In: Pye, K. (editor). *The Dynamics and Environmental Context of Aeolian Sedimentary Systems*. Special publications of the Geological Society, London (72). 235–244
- McLaren, S., Gardner, R. (2000). New radiocarbon dates from a Holocene aeolianite, Isla Cancun, Quintana Roo, Mexico. *The Holocene* 10 (6): 757-761
- Meyers, J.H. (1987). Marine vadose beachrock cementation by cryptocrystalline magnesian calcite—Maui, Hawaii. *Journal of Sedimentary Petrology* 57, 558–570
- Milankovitch, M. (1941). Kanon der Erdbestrahlung und sei Eiszeitenproblem. Acad. R. Serbe (Beleggrade), ed. Spec. 133 Sect. Sci. Math. Naturales. 633. (Canon of Insolation and the Ice Age Problem: translated by the Israel Program for Scientific Translations. Jerusalem, 1970)

- Miller, G. H., Brigham-Grette, J. (1989). Amino acid geochronology: resolution and precision in carbonate fossils. *Quaternary International* 1: 111–128
- Miller, G. H., Hart, C. P., Roark, E. B., Johnson, B. J. (2000). Isoleucine epimerization in eggshells of the flightless Australian birds *Genyornis* and *Dromaius*. In: Goodfriend, G.A., Collins, M.J., Fogel, M.L., Macko, S.A., Wehmiller, J.F. (Editors). *Perspectives in Amino Acid and Protein Geochemistry*. Oxford University Press, New York pp 161–182
- Miller, J. (1988). Microscopical techniques: I. Slices, slides, stains and peels. In: Tucker, M. editor. *Techniques in Sedimentology*. Blackwell, Oxford, London, Edinburgh, Boston, Palo Alto, Melbourne
- Miller, G. H., Brigham-Grette, J. (1989). Amino acid geochronology: resolution and precision in carbonate fossils. *Quaternary International* 1: 111–128
- Miller, G. H., Clarke, S. J. (2007). Amino acid Dating. In: *Encyclopedia of Quaternary Sciences*, Elsevier pp 41-52
- Miller, G. H., Hare, P. E. (1980). Amino acid chronology: integrity of the carbonate matrix and potential of molluscan fossils. In: Hare, P. E., Hoering, T. C., King, Jr., K. (Editors). *Biogeochemistry of Amino Acids*. Wiley, New York pp 415-443
- Miller, G. H., Mangerud, J. (1985). Aminostratigraphy of European marine interglacial deposits. *Quaternary Science Reviews* 4: 215-278
- Milnes, A. R., Hutton, J. T. (1983). Calcretes in Australia. In: *Soils, an Australian viewpoint*. CSIRO, Melbourne pp 119-162
- Milnes, A. R., Ludbrook, N. H., Lindsay, J. M., Cooper, B. J. (1983). The succession of Cainozoic marine sediments on Kangaroo Island, South Australia. *Transactions of the Royal Society of South Australia* 107: 11-35
- Milnes, A. R., Ludbrook, N.H., Lindsay, J.M., Cooper, B.J. (1983). The succession of Cainozoic marine sediments on Kangaroo Island, South Australia. *Transactions of the Royal Society of South Australia* 107(1/2): 1-35
- Milnes, A. R., Cooper, B.J., Cooper, J. A. (1982). The Jurassic Wisanger Basalt of Kangaroo Island, South Australia. *Transactions of the Royal Society of South Australia* 106 (1): 1-13
- Mitterer, R. M., Kriaušakul, N. (1989). Calculation of amino acid racemization ages based on apparent parabolic kinetics. *Quaternary Science Reviews* 8: 353-357
- Moore, C. H. (1973). Intertidal carbonate cementation Grand Cayman, West Indies. *Journal of Sedimentary Petrology* 43: 591–602
- Moorhouse, W. W. (1959). *The study of rocks in thin section*. Harper & Row. New York, Evanston and London and John Weatherhill Inc. Tokyo
- Mount J. F. (1984). Mixing of siliciclastic and carbonate sediments in shallow shelf environments. *Geology* 12: 432-435
- Muhs, D. R., Simmons, K. R., Steinke, B. (2002). Timing and warmth of the Last Interglacial period: new U/Th evidence from Hawaii and Bermuda and a new fossil compilation for North America. *Quaternary Sciences Reviews* 21: 1355-1383
- Munyikwa K. (2000). Cosmic ray contribution to environmental dose rates with varying overburden thickness. *Ancient TL* 18: 27-34
- Murray, A. S., Roberts, R. G. and Wintle, A. G. (1997). Equivalent dose measurement using a single aliquot of quartz. *Radiation Measurements* 27: 171-181
- Murray, A. S., Roberts, R.G. (1998). Measurement of the equivalent dose in quartz using a regenerative-dose single-aliquot protocol. *Radiation Measurements* 29 (5): 503-515

- Murray, A. S., Wintle, A. G. (2000). Luminescence dating of quartz using an improved single-aliquot regenerative-dose protocol. *Radiation Measurements* 32: 57-73
- Murray A. S., Wintle, A. G., (2003). The single-aliquot regenerative-dose protocol: potential for improvements in reliability. *Radiation Measurements* 37: 377-381
- Murray-Wallace, C. V. (1995). Aminostratigraphy of Quaternary coastal sequences in southern Australia—an overview. *Quaternary International* 26: 69–86
- Murray-Wallace, C. V. (2000). Quaternary coastal aminostratigraphy—Australian data in a global context. In: Goodfriend, G.A., Collins, M.J., Fogel, M.L., Macko, S.A., Wehmiller, J.F. (Editors). *Perspectives in Amino Acid and Protein Geochemistry*. Oxford University Press, New York pp 279–300
- Murray-Wallace, C. V. (2002). Pleistocene coastal stratigraphy, sea-level highstands and neotectonism of the southern Australian passive continental margin—a review. *Journal of Quaternary Science* 17(5-6): 469-489
- Murray-Wallace, C. V., Belperio, A. P. (1991). The Last Interglacial shoreline in Australia—a review. *Quaternary Science Reviews* 10: 441-461
- Murray-Wallace, C. V., Bourman, R. (1990). Direct radiocarbon calibration for amino acid racemization dating *Australian Journal of Earth Sciences*, Volume 37 (3): 365-367
- Murray-Wallace, C. V., Bourman, R. (2002). Amino Acid Racemisation Dating of a raised gravel beach deposit, Sellicks Beach, South Australia. *Transactions of the Royal Society of South Australia: Incorporated* 126: 21-28
- Murray-Wallace, C. V., Belperio, A. P., Cann, J. H., Huntly, D. J., Prescott, J. R. (1996). Late Quaternary uplift history, Mount Gambier region, South Australia. *Zeitschrift für Geomorphologie Supplement Band* 106: 41–56.
- Murray-Wallace, C. V., Belperio, A. P., Bourman, R. P., Cann, J. H., Price, D. M. (1999). Facies architecture of a last interglacial barrier: a model for Quaternary barrier development from the Coorong to Mount Gambier Coastal Plain, southeastern Australia. *Marine Geology* 158: 177–195
- Murray-Wallace, C. V., Belperio, A. P., Cann, J. H. (1998). Quaternary neotectonism and intra-plate volcanism: the Coorong to Mount Gambier Coastal Plain, southeastern Australia: a review. *Geological Society, London, Special Publications* 146: 255-267
- Murray-Wallace, C. V., Beu, A. G., Kendrick, G. W., Brown, L. J., Belperio, A. P., Sherwood, J. E. (2000). Palaeoclimatic implications of the occurrence of the arcoid bivalve *Anadara trapezia* (Deshayes) in the Quaternary of Australasia. *Quaternary Science Reviews* 19: 559–590.
- Murray-Wallace, C. V., Bourman, R. P., Prescott, J. R., Williams, F., Price, D. M., Belperio, A. P. (2010). Aminostratigraphy and thermoluminescence dating of coastal aeolianites and the later Quaternary history of a failed delta: The River Murray mouth region, South Australia. *Quaternary Geochronology* 5 (1): 28-49
- Murray-Wallace, C. V., Brooke, B. P., Cann, J. H., Belperio, A. P. and Bourman, R. P. (2001). Whole-rock aminostratigraphy of the Coorong Coastal Plain, South Australia: towards a 1 million year record of sea-level highstands. *Journal of the Geological Society, London* 158: 111-124
- Murray-Wallace, C. V., Kimber, R. W. L (1987). Evaluation of the amino acid racemization reaction in studies of Quaternary marine sediments in South Australia *Australian Journal of Earth Sciences* 34: 279-292
- Murray-Wallace, C. V., Kimber, R. W. L. (1989) Quaternary marine aminostratigraphy: Perth Basin, Western Australia., *Australian Journal of Earth Sciences* 36 (4): 553-568

- Murray-Wallace, C. V., Kimber, R. W. L., Belperio, A. P., Gostin, V. A. (1988). Aminostratigraphy of the Last Interglacial in southern Australia. *Search* 19: 33-36
- Myers J. S., Hocking R. M. (1998). Geological Map of Western Australia, 1:2 500 000 (13th edition). Geological Survey of Western Australian, Perth
- NASA Landsat program. (2001) Landsat enhanced thematic mapper (ETM+ mosaics) image, Kangaroo Island, Australia, scene S-53-35_2000, UTM 53, USGS, 18/09/2001.
- Nelson, R. J. (1837). On the geology of the Bermudas. *Geological Society of London Transactions* 5: 103-123
- Nanson, G. C., Price, D. M., Short, S. A., Young, R. W., Jones, B. G. (1991). Comparative uranium-thorium and thermoluminescence dating of weathered Quaternary alluvium in the tropics of northern Australia. *Quaternary Research* 35: 347-366
- Noller, J. S., Sowers, J. M., Lettis, W. R. (2000). Quaternary Geochronology. Methods and Applications. American Geophysical Union Monograph 582 pp
- Nordstrom, K., Psuty, N., Carter, B. (1990). Coastal dunes: form and process. Chichester (England); New York: Wiley
- North American Commission for Stratigraphic Nomenclature (2005). North American Stratigraphic Code: AAPG Bulletin 89 (11):1547-1591
- Northcote, K.H. (2002). Soils. In: Davies, M., Twidale, C. R. & Tyler, M. J., Editors. Natural history of Kangaroo Island. Occasional publications of the Royal Society of South Australia, 2. Royal Society of South Australia, Adelaide
- Olley, J. M., Caitcheon, G. G., Roberts, R.G. (1999). The origin of dose distributions in fluvial sediments, and the prospect of dating single grains of quartz from fluvial deposits using optically stimulated luminescence. *Radiation Measurements* 30: 207-217
- Olley, J. M., Murray, A. S., Roberts, R. G. (1996). The effects of disequilibria in the uranium and thorium decay chains on burial dose rates in fluvial sediments. *Quaternary Science Reviews* 15: 751-760
- Olley, J. M., Roberts, R. G., Murray, A. S. (1997). Disequilibria in the uranium decay series in sedimentary deposits at Allen's Cave, Nullarbor Plain, Australia: implications for dose rate determinations. *Radiation Measurements* 27: 433-443
- Oslick, J. S., Miller, K. G., Feigenson, M. D., Wright, J. D. (1994). Oligocene—Miocene strontium isotopes: stratigraphic revisions and correlations to an inferred glacioeustatic record, *Paleoceanography* 9 (3): 427-443
- Otvos, E. G. (2000) Beach ridges—definitions and significance. *Geomorphology* 32: 83-108
- Péron, F. (1817). *Voyage de Découvertes aux Terres Australes, exécuté sur les Corvettes le Géographe, le naturaliste, et la Goëlette le Casuarina*, Paris : De l'Imprimerie Imperiale vol. II
- Penkman, K. E. H. (2005). Amino acid geochronology: a closed system approach to test and refine the UK model. Unpublished PhD thesis, University of Newcastle
- Penkman, K. E. H., Preece, R. C., Keen, D. H., Maddy, D., Schreve, D. C., Collins, M. (2007). Testing the aminostratigraphy of fluvial archives: the evidence from intracrystalline proteins within freshwater shells. *Quaternary Science Reviews* 26: 2958-2969
- Penkman, K. E. H., Kaufman, D. S., Maddy, D., Collins, M. J. (2008). Closed-system behaviour of the intra-crystalline fraction of amino acids in mollusc shells. *Quaternary Geochronology* 3: 2-25
- Perry, C. T., Smithers, S. G., Palmer, S. E., Larcombe, P., Johnson, K. G. (2008). 1200 year paleoecological record of coral community development from the terrigenous inner shelf of the Great Barrier Reef. *Geology* 36: 691–694

- Pillans, B., Chappell, J., Naish, T. R. (1998). A review of the Milankovitch climatic beat: template for Plio–Pleistocene sea-level changes and sequence stratigraphy. *Sedimentary Geology* 122: 5–21
- Pizzarello S., Huang Y., Alexandre M. R. (2008). Molecular asymmetry in extraterrestrial chemistry: Insights from a pristine meteorite. *Proceedings of the National Academy of Sciences* 105: 3700–3704
- Playford, P. E. (1988). *Guidebook to the Geology of Rottnest Island*. Geological Society of Australia, Perth.
- Playford, P. E. (1990). Geology of the Shark Bay area, Western Australia. In: Berry, P. F., Bradshaw, S. D., Wilson, B. R. (Editors). *Research in Shark Bay, Report of the France–Australie Bicentenary Expedition Committee*. Western Australian Museum, Perth. 13–31 pp
- Playford, P. E. (1997). Geology and hydrogeology of Rottnest Island, Western Australia. In: Vacher, L. H., Quinn, T. M. (Editors). *Geology and Hydrogeology of Carbonate Islands. Developments in Sedimentology* 54. Elsevier, Amsterdam. 783–810.
- Playford, P. E., Cockbain, A. E., Lowe, G. H. (1976). Geology of the Perth Basin, Western Australia. *Western Australia Geological Society Bulletin* 124: 298.
- Porat, N., Wintle, A. G. (1995). IRSL dating of aeolianites from the Late Pleistocene kurkar ridge. Israel. INQUA 14th International Conference. Alfred Wegner Stiftung, Berlin
- Potter, E. K., Esat, T. M., Schellmann, G., Radtke, U., Lambeck, K., McCulloch, M. T. (2004). Suborbital-period sea-level oscillations during marine isotope substages 5a and 5c. *Earth and Planetary Science Letters* 225: 191–204
- Prescott J. R., and Hutton J. T. (1994). Cosmic ray contributions to dose rates for luminescence and ESR dating: large depths and long term variations. *Radiation Measurements* 23, 497–500
- Prescott J. R., and Hutton J. T. (1995). Environmental dose rates and radioactive disequilibrium from some Australian luminescence dating sites. *Quaternary Science Reviews* 14: 439–48
- Preusser, F. (2009). Chronology of the impact of Quaternary climate change on continental environments in the Arabian Peninsula. *C. R. Geoscience* 341: 621–632
- Price, D. M., Bryant, E. A., Young, R. W. (1999). Thermoluminescence evidence for the deposition of coastal sediments by tsunami wave action. *Quaternary International* 56: 123–128
- Price, D. M., Brooke, B. P., Woodroffe, C. D. (2001). Thermoluminescence dating of aeolianites from Lord Howe Island and South-West Western Australia. *Quaternary Science Reviews* 20: 841–846
- Pye, K., Tsoar, H. (1990). *Aeolian Sand and Sand Dunes*. Unwin Hyman, London
- Ramsay, P. J., Cooper, J. A. G. (2002). Late Quaternary sea-level change in South Africa. *Quaternary Research* 57: 82–90.
- Rao, C. P. (1996). *Modern Carbonates Tropical, Temperate, Polar: Introduction to Sedimentology and Geochemistry*. University of Tasmania, Hobart
- Reimer, P. J., Reimer, R. (2001). A marine reservoir correction database and on-line interface. *Radiocarbon* 43: 461–463.
- Reineck H. E., Singh I. B. (1980). *Depositional sedimentary environments with reference to terrigenous clastics*. Springer-Verlag, Berlin
- Richardson, L., Mathews, E., Heap, A. (2005). *Geomorphology and Sedimentology of the South Western Planning Area of Australia: Review and synthesis of relevant literature in support of Regional Marine Planning*. Geoscience Australia Record 2005/17

- Ridky, J., Travnicek, P., DELPHI collaboration (2003). Detection of muon bundles from cosmic ray showers at medium depth underground. *Nuclear Physics A* Volume 722: C444-C448
- Roberts, D. L., Bateman, M. D., Murray-Wallace, C. V., Carr, A. S., Holmes, P. J. (2009). West coast dune plumes: Climate driven contrasts in dunefield morphogenesis along the western and southern South African coasts. *Palaeogeography, Palaeoclimatology, Palaeoecology* 271 (1-2): 24-38
- Roberts, D. L., Bateman, M. D., Murray-Wallace, C. V., Carr, A. S., Holmes, P. J. (2008). Last Interglacial fossil elephant trackways dated by OSL/AAR in coastal aeolianites, Still Bay, South Africa. *Palaeogeography, Palaeoclimatology, Palaeoecology* 257: 261–279
- Roberts, D., Berger, L. (1997). Last Interglacial (c. 117 kyr) human footprints from South Africa. *South African Journal of Science* 93: 349–354
- Roberts, H. M., Duller, G. A. T. (2004). Standardised growth curves for optical dating of sediment using multiple-grain aliquots. *Radiation Measurements* 38: 241 – 252
- Robert, R. G., Uren, C. J., Murray, A. S. (1993). Thermoluminescence dating techniques at the Alligator Rivers region Research Institute. Supervising scientist for the Alligator Rivers region. Technical memorandum 41. Australian Government Publishing Service, Canberra
- Robins, J., Jones, M., Matisoo-Smith, E., (2001). Amino Acid Racemization Dating in New Zealand: An Overview, Auckland University Private Bag 92019, Auckland: 1- 45
- Roduit, N. (2008). JMicroVision (a software toolbox for measuring and quantifying high-definition image components). Department of Geology, University of Geneva
- Ruddiman, W. F. (2003). Orbital insolation, ice volume, and greenhouse gases. *Quaternary Science Reviews* 22: 1597–1629
- Saenko, O. A., Weaver, A. J. (2003). Southern Ocean upwelling and eddies: sensitivity of the global overturning to the surface density range. *Tellus* 55A: 106-111
- Sayles, R. W. (1931). Bermuda during the ice age. *Proceedings of the American Academy of Arts and Sciences* 66: 380-467
- Saxena, S., Betzler, C. (2003). Genetic sequence stratigraphy of cool water slope carbonates (Pleistocene Eucla Shelf, southern Australia). *International Journal of Earth Sciences (Geologische Rundschau)* 92: 482–493
- Scholle, P. (1978). *Am. Assoc Petrol Geol Memoir* 27, (Editor). University of Vermont, 2005-03-16
- Schroeder, R. A., Bada, J. L. (1976). A review of the geochemical applications of the amino acid racemization reaction. *Earth Science Reviews* 12: 347–391
- Schuhmacher, H., Zibrowius, H. (1985). What is hermatypic? *Coral Reefs* 4 (1): 1-9
- Schwebel, D. A. (1978). Quaternary Stratigraphy of the Southeast of South Australia. Ph.D. Thesis, Flinders University of South Australia (Unpublished).
- Schwebel, D. A., (1984). Quaternary stratigraphy and sea-level variation in the southeast of South Australia. In: Thom, B.G. (Editor) *Coastal Geomorphology in Australia*. Academic Press, Sydney. 291–311
- Schwebel, D. A. (1983). Quaternary dune systems. In: Tyler, M.J., Twidale, C.R, Ling, J. K., Holmes, J. W. (Editors). *Natural history of the South East*. Royal Society of South Australia. Occasional Publications 3: 15-24.
- Schwerdtfeger, P. (2002). Climate. In: Davies, M., Twidale, C. R. & Tyler, M. J., Editors. *Natural history of Kangaroo Island*. Occasional publications of the Royal Society of South Australia, 2. Royal Society of South Australia, Adelaide

- Seppälä, M. (1995). Deflation and redeposition of sand dunes in Finnish Lapland. *Quaternary Science Reviews* 14: 799-809
- Siesser, W. G., Rogers, J. (1970). An investigation of the suitability of four methods used in routine carbonate analysis of marine sediments. *Deep Sea Research* 18: 135-139
- Singarayer, J., Bailey, R. M., Rhodes, E. J. (2000). Potential of the slow component of quartz OSL for the age determination of sedimentary samples. *Radiation Measurements* 32: 873-880
- Shaw, A. E., Holmes, P. J., Rogers, J. (2001). Depositional landforms and environmental change in the headward vicinity of Dias Beach, Cape Point. *South African Journal of Geology* 104: 101-114
- Shepherd, M. J., Price, D. M. (1990). Thermoluminescence dating of late Quaternary dune sand, Manawata/Horowhenua area, New Zealand: a comparison with ¹⁴C age determinations. *New Zealand Journal of Geology and Geophysics* 33: 535-539
- Short, A. D. (2006). *Beaches of the South Australian Coast and Kangaroo Island. A guide to their nature, characteristics, surf and safety.* Coastal Studies Unit, School of Geosciences, University of Sydney. Sydney University Press
- Short, A.D., Fotheringham, D.G. (1986). Coastal Morphodynamics and Holocene Evolution of the Kangaroo Island Coast, South Australia. Coastal Studies Unit Technical Report No. 86/1. University of Sydney
- Siddall, M., Chappell, J., Potter, E. (2007). Eustatic sea level during past interglacials. In: *Developments in Quaternary Science* 7: 75-92
- Singarayer, J. S., Bailey, R. M., Rhodes, E. J. (2000). Potential of the slow component of quartz OSL for age determination of sedimentary samples. *Radiation Measurements* 32: 873-880
- Sivan, D., Porat, N. (2004). Evidence from luminescence for Late Pleistocene formation of calcareous aeolianite (kurkar) and paleosol (hamra) in the Carmel Coast, Israel. *Palaeogeography, Palaeoclimatology, Palaeoecology* 211: 95-106
- Skinner, H. C. W., Jahren, A. H. (2007). Biomineralization. In: Schlesinger, W.H. (Editor). *Biogeochemistry, Volume 8: Treatise on Geochemistry: Oxford, Elsevier-Pergamon, Chapter 4, Pages 1-69*
- Sloss, C. R., Murray-Wallace, C. V., Jones, B. G., Wallin, T. (2004). Aspartic acid racemisation dating of mid-Holocene to recent estuarine sedimentation in New South Wales, Australia: a pilot study. *Marine Geology* 212: 45-59
- Specht, R. L. (1972). *The vegetation of South Australia.* (2nd edition). Government Printer, Adelaide
- Sprigg, R. C. (1952). The geology of the South-East province, South Australia, with special reference to Quaternary coast-line migrations and modern beach developments. *South Australia. Geological Survey, Bulletin*, 29
- Sprigg, R. C. (1954). Geology of Kangaroo Island. In: Sprigg, R. C. Campana, B and King, D. Kingscote map sheet. *Geological Atlas of South Australia 4-mile series.* Geological Survey of South Australia, Adelaide
- Sprigg, R. C. (1955). The Point Marsden Cambrian Beds, Kangaroo Island, South Australia. *Transactions of the Royal Society of South Australia* 78: 165-168
- Sprigg, R. C. (1959). Stranded sea beaches and associated sand accumulations of the upper Southeast. *Transactions of the Royal Society of South Australia* 82: 183-193
- Sprigg, R. C. (1979). Stranded and submerged sea-beach systems of Southeast South Australia and the aeolian desert cycles. *Sedimentary Geology* 22: 53-96.

- Staines, H. R. E. (1985). Field geologist's guide to lithostratigraphic nomenclature in Australia. *Australian Journal of Earth Sciences* 32: 83-106
- Stirling, C. H., Esat, T. M., Lambeck, K., McCulloch, M. T. (1998). Timing and duration of the last interglacial: evidence for a restricted interval of widespread coral reef growth. *Earth and Planetary Science Letters* 160: 745-762
- Stride, A. H., Wilson, J. B., and Curry, D. (1999). Accumulation of late Pleistocene and Holocene biogenic sands and gravels on the continental shelf between northern Scotland and western France. *Marine Geology* 159: 273-285.
- Stuiver, M., Braziunas, T. F. (1993). Modeling atmospheric ^{14}C influences and ^{14}C ages of marine samples to 10,000 BC. *Radiocarbon* 35: 137-189
- Stuiver, M., Pearson, G., Braziunas, T. (1986). Radiocarbon age calibration of marine samples back to 9000 CAL YR BP. *Radiocarbon* 28: 980-1021
- Sykes, G. A., Collins, M. J., Walton, D. I. (1995). The significance of a geochemically isolated intracrystalline fraction within biominerals. *Organic Geochemistry* 23: 1059-1065
- Tate, R. (1883). The Botany of Kangaroo Island. *Transactions of the Royal Society of South Australia* 6: 116-171
- Taylor, R. (2000). Savages or Saviours?—The Australian Sealers and Aboriginal Tasmanian Survival. *Journal of Australian Studies* 66: 73-84
- Taylor, R. E., Aitken, M. J. (1997). *Chronometric dating in archaeology*. Plenum, New York
- Teichert, C. (1947). Contributions to the geology of Houtman's Abrolhos. *Proceedings of the Linnean Society of Western Australia*. New South Wales 71: 145-196
- Teichert, C. (1950). Late Quaternary changes of sea level at Rottneest Island, Western Australia. *Royal Society of Victoria Proceedings* 59: 63-9
- Thiel, C., Coltorti, M., Tsukamoto, S., Frechen, M. (2010). Geochronology for some key sites along the coast of Sardinia (Italy). *Quaternary International* 222: 36-47
- Thomsen, K. J., Jain, M., Murray, A. S., Denby, P. M., Roy, N., Bøtter-Jensen, L. (2008). Minimizing feldspar OSL contamination in quartz UV-OSL using pulsed blue stimulation. *Radiation Measurements* 43: 752 -757
- Thompson, C. W. (1873). Geological peculiarities of the Bermudas. *Nature* 13: 266-267
- Thorne, A., Grün, R., Mortimer, G., Spooner, N. A., Simpson, J. J., McCulloch, M. T., Taylor, L., Curnoe, D. (1999). Australia's oldest human remains: age of the Lake Mungo 3 skeleton. *Journal of Human Evolution* 36: 591-612
- Torres, T., Llamas, F.J., Canoira, L., Garcí'a-Alonso, P., Garcí'a-Corte's, A., Mansilla, H. (1997). Amino acid chronology of the Lower Pleistocene deposits of Venta Micena (Orce, Granada, Andalusia, Spain). *Organic Geochemistry* 26: 85-97
- Torres, T., Llamas, J., Canoira, L., Coello, F. J., Garcí'a-Alonso, P., Ortiz, J.E . (2000). Aminostratigraphy of two Pleistocene marine sequences from the Mediterranean Coast of Spain: Cabo de Huertas (Alicante) and Garrucha (Almería). In: Goodfriend, G. A., Collins, M. J., Fogel, M. L., Macko, S. A., Wehmiller, J. F. (Editors). *Perspectives in Amino Acids and Protein Geochemistry*. Oxford University Press, New York pp 263-278
- Toscano, M. A., Lundberg, J. (1999). Submerged Late Pleistocene reefs on the tectonically stable S.E. Florida margin: high-precision geochronology, stratigraphy, resolution of Substage5a sea-level elevation, and orbital forcing. *Quaternary Science Reviews* 18: 753-767
- Trenhaile, A. S. (1997). *Coastal dynamics and landforms*. Oxford: Oxford University Press

- Trumbore, S. E., (2000). Radiocarbon Geochronology. In: Noller, J. S., Sowers, J. M., Lettis, W. R. (Editors). AGU Reference Shelf 4. Quaternary Geochronology: Methods and Applications. American Geophysical Union, Washington, USA. 41–60
- Tucker, M. E. (1990). Diagenetic processes, products and environments. In: Tucker, M. E. and Wright, V. P. (Editors). Carbonate Sedimentology. Blackwell Scientific Publications. Oxford, London, Edinburgh, Boston, Melbourne: 314-365
- Tucker, M. E. and Wright, V. P. (1990). Carbonate Sedimentology. Blackwell Scientific Publications. Oxford, London, Edinburgh, Boston, Melbourne
- Tuniz, C., Bird, J. R., Fink, D., Herzog, G. F. (1998). Accelerator mass spectrometry: Ultrasensitive analysis for global science: Boca Raton, Florida, CRC Press 371 pp
- Twidale, C.R, Bourne, J.A. (2002). The Land Surface. In: Davies, M., Twidale, C. R. & Tyler, M. J., Editors., Natural history of Kangaroo Island. Occasional publications of the Royal Society of South Australia, 2. Royal Society of South Australia, Adelaide
- Twidale, C.R. (2000). Early Mesozoic (?Triassic) Landscapes in Australia: Evidence, Argument, and Implications. *Journal of Geology* 108 (5): 537-552
- Vacher, H. L. Hearty, P. J., Rowe, M. P. (1995). Stratigraphy of Bermuda: nomenclature, concepts, and status of multiple systems of classification. In: Curran, H. A., White, B., Editors. Terrestrial and Shallow Marine Geology of the Bahamas and Bermuda. Geological Society of America Special Paper 300. Geological Society of America. Boulder, CO. 271-294
- Vacher, H. L., and Rowe, M. P. (1997). Geology and hydrogeology of Bermuda. In: Vacher, H. L., Quinn, T. M. (Editors). Geology and Hydrogeology of Carbonate Islands. Elsevier, Amsterdam p 35-90
- Van Duin, A. C. T., Collins, M. J. (1998). The effects of conformational constraints on aspartic acid racemization. *Org. Geochem.* 29: 1227-1232
- Vogel, J. C., Wintle, A. G., Woodbourne, S. M. (1999). Luminescence dating of coastal sands: overcoming changes in environmental dose rate. *Journal of Archaeological Science* 26: 729-733
- Vollbrecht, R., Meischner, D. (1996). Diagenesis in coastal carbonates related to Pleistocene sea-level, Bermuda platform. *Journal of Sedimentary Research* 66: 243-258
- Wallinga, J., Murray, A. S., Bøtter-Jensen, L. (2002). Measurement of the dose in quartz in the presence of feldspar contamination. *Radiation Protection Dosimetry* 101 (1): 367-370
- Walter, L. M., Bischof, S. A., Patterson, W. P., and Lyons, T. W. (1993). Dissolution and recrystallization in modern shelf carbonates: evidence from pore water and solid phase chemistry. *Philosophical Transactions of Royal Society London A*, 344: 27–36
- Walton, D. (1998). Degradation of intracrystalline proteins and amino acids in fossil brachiopods. *Organic Geochemistry* 28 (6): 389-410
- Wang, X. L., Lu, Y. C., Wintle, A. G. (2006a). Recuperated OSL dating of fine-grained quartz in Chinese Loess. *Quaternary Geochronology* 1: 89-100
- Wang, X. L., Wintle, A. G., Lu, Y. C. (2006b). Thermally transferred luminescence in fine-grained quartz from Chinese loess: Basic observations. *Radiation Measurements* 41: 649-658
- Wang, X. L., Wintle, A. G., Lu, Y. C. (2007). Testing a single-aliquot protocol for recuperated OSL dating. *Radiation Measurements* 42: 380-391
- Ward, C. W. (1973). Influence of Climate on the Early Diagenesis of Carbonate Eolianites. *Geology* 1 (4): 171-174

- Ward, J. H. (1963). Hierarchical grouping to optimize an objective function. *Journal of the American Statistical Association* 58 (301): 236-244
- Ward, W. C. (1973). Influence of climate on the early diagenesis of carbonate aeolianites. *Geology* 1: 171-174
- Ward, S., Stokes, S., Bailey, R., Singarayer, J., Goudie, A., Bray, H. (2003). Optical dating of quartz from young samples and the effects of pre-heat temperature. *Radiation Measurements* 37: 401-407
- Warren, S. E. (1978). Thermoluminescence dating of pottery: an assessment of the dose-rate from rubidium. *Archaeometry* 20: 71-72
- Weiner, S., Talmon, Y., Traub, W. (1983). Electron diffraction of mollusc shell organic matrices and their relationship to the mineral phase. *Int. J. Biol. Macromol.* 5: 325-328.
- Wehmiller, J. F. and P. E. Hare (1971). Racemization of amino acids in marine sediments. *Science* 173, 907-911.
- Wehmiller, J. F. (1982). A review of amino acid racemization studies in Quaternary mollusks: stratigraphic and chronologic applications in coastal and interglacial sites, Pacific and Atlantic coasts, United States, United Kingdom, Baffin Island, and Tropical Islands. *Quaternary Science Reviews* 1, 83-120.
- Wehmiller, J. F. (1984a). Interlaboratory comparison of amino acid enantiomeric ratios in fossil mollusks. *Quaternary Research* 22: 109-120
- Wehmiller J. F. (1984b). Relative and absolute dating of Quaternary molluscs with amino acid racemization: evaluation, applications and questions. In: Mahaney, W. C. editor. *Quaternary Dating Methods*: 171-193. Elsevier, Amsterdam
- Wehmiller, J. F., D. F. Belknap, B. S. Boutin, J. E. Mirecki, S. D. Rahaim, and L. L. York. (1988). A Review of the Aminostratigraphy of Quaternary Mollusks from United States Atlantic Coastal Plain Sites. *Geol. Soc. Amer. Special Paper* 227, *Dating Quaternary Sediments*, D. L. Easterbrook (ed.), pp. 69-110.
- Wehmiller, J. F., Miller, G. (2000). Aminostratigraphic dating methods in Quaternary geology. In: Noller, J. S., Sowers, J.M., Lettis, W.R. (Editors), *Quaternary Geochronology: Methods and Applications*. American Geophysical Union Books Board, Washington, DC, pp. 187-222
- Wehmiller, J. F., H. A. Stecher III, L. L. York, and I. Friedman (2000). The thermal environment of fossils: effective ground temperatures (1994-1998) at aminostratigraphic sites, U.S. Atlantic coastal plain. *Perspectives on Amino Acid and Protein Geochemistry*, G.A. Goodfriend et al., (eds).
- Wells, P., Okada, H. (1996). Holocene and Pleistocene glacial palaeoceanography off southeastern Australia, based on foraminifers and nannofossils in Vema cored hole V18-222. *Australian Journal of Earth Sciences* 43: 509-523
- Williams, K.M., and Smith, G.G. (1977). A critical evaluation of the application of amino acid racemization to geochronology and geothermometry. *Origins of Life* 8: 91-144
- Williams, M., Prescott, J. R., Chappell, J., Adamson, D., Cock, B., Walker, K., Gell, P. (2001). The enigma of a late Pleistocene wetland in the Flinders Ranges, South Australia. *Quaternary International* 83-85: 129-144
- Williams, M., Cook, E., van der Kaars, S., Barrows, T., Shulmeister, J., Kershaw, P. (2009). Glacial and deglacial climatic patterns in Australia and surrounding regions from 35000 to 10000 years ago reconstructed from terrestrial and near-shore proxy data. *Quaternary Science Reviews* 28: 2398-2419
- Wilson, C. C. (1991). Geology of the Quaternary Bridgewater Formation of southwest and central South Australia. Flinders University (South Australia). Ph.D. thesis (unpublished)

- Wintle, A. G. (1997). Luminescence dating: laboratory procedures and protocols. *Radiation Measurements* 27: 769-817
- Wintle, A. G., Murray, A. S. (2006). A review of quartz optically stimulated luminescence characteristics and their relevance in single-aliquot regeneration dating protocols. *Radiation Measurements* 41: 369-391
- Wolf, K. H. (1965). "Grain-diminution" of algal colonies to micrite. *Journal of Sedimentary Petrology* 35 (2): 420-427
- Woodroffe, C. D. (2002). *Coasts: form, process and evolution*. Cambridge University Press, Cambridge
- Wright, V. P. (1990). Carbonate sediments and limestones: constituents. In: Tucker, M. E. and Wright, V. P. (Editors). *Carbonate Sedimentology*. Blackwell Scientific Publications. Oxford, London, Edinburgh, Boston, Melbourne: 314-365
- Yassini, I., Jones, B. G. (1995). *Foraminifera and Ostracoda from estuarine and shelf environments on the southeastern coast of Australia*. University of Wollongong Press, Wollongong 484 pp
- Yokoyama, Y., De Deckker, P., Lambeck, K., Johnston, P., Fifield, L. K. (2001). Sea-level at the Last Glacial Maximum: evidence from northwestern Australia to constrain ice volumes for oxygen isotope stage 2. *Palaeogeography, Palaeoclimatology, Palaeoecology* 165: 281-297
- Yokoyama, Y., Lambeck, K., De Deckker, P., Johnston, P., Fifield, L. K. (2000). Timing of the Last Glacial Maximum from observed sea-level minima. *Nature* 406: 713-716
- Yokoyama, Y., Purcell, A., Lambeck, K., Johnston, P. (2001). Shore-line reconstruction around Australia during the Last Glacial Maximum and Late Glacial Stage. *Quaternary International* 83-85: 9-18
- Yoshida, H., Roberts, R. G., Olley, J. M., Laslett, G. M., Galbraith, R. F. (2000) Extending the age range of optical dating using single 'supergrains' of quartz. *Radiation Measurements* 32: 439-446
- Yoshida, H., Roberts, R. G., Olley, J. M. (2003). Progress towards single grain optical dating of fossil mud-wasp nests and associated rock art in northern Australia. *Quaternary Science Reviews* 22: 1273-1278
- Zhang, J. F., Zhou, L. P. (2007). Optimization of the 'double SAR' procedure for polymineral fine grains. *Radiation Measurements* 42: 1475-1482
- Zhou, L. P., Williams, M. A. J., and Peterson, J. A. (1994). Late Quaternary Aeolianites, Paleosols and Depositional Environments on the Nepean Peninsula, Victoria, Australia. *Quaternary Science Reviews* 13 (3): 225-239

- Wintle, A. G. (1997). Luminescence dating: laboratory procedures and protocols. *Radiation Measurements* 27: 769-817
- Wintle, A. G., Murray, A. S. (2006). A review of quartz optically stimulated luminescence characteristics and their relevance in single-aliquot regeneration dating protocols. *Radiation Measurements* 41: 369-391
- Wolf, K. H. (1965). "Grain-diminution" of algal colonies to micrite. *Journal of Sedimentary Petrology* 35 (2): 420-427
- Woodroffe, C. D. (2002). *Coasts: form, process and evolution*. Cambridge University Press, Cambridge
- Wright, V. P. (1990). Carbonate sediments and limestones: constituents. In: Tucker, M. E. and Wright, V. P. (Editors). *Carbonate Sedimentology*. Blackwell Scientific Publications. Oxford, London, Edinburgh, Boston, Melbourne: 314-365
- Yassini, I., Jones, B. G. (1995). *Foraminifera and Ostracoda from estuarine and shelf environments on the southeastern coast of Australia*. University of Wollongong Press, Wollongong 484 pp
- Yokoyama, Y., De Deckker, P., Lambeck, K., Johnston, P., Fifield, L. K. (2001). Sea-level at the Last Glacial Maximum: evidence from northwestern Australia to constrain ice volumes for oxygen isotope stage 2. *Palaeogeography, Palaeoclimatology, Palaeoecology* 165: 281-297
- Yokoyama, Y., Lambeck, K., De Deckker, P., Johnston, P., Fifield, L. K. (2000). Timing of the Last Glacial Maximum from observed sea-level minima. *Nature* 406: 713-716
- Yokoyama, Y., Purcell, A., Lambeck, K., Johnston, P. (2001). Shore-line reconstruction around Australia during the Last Glacial Maximum and Late Glacial Stage. *Quaternary International* 83-85: 9-18
- Yoshida, H., Roberts, R. G., Olley, J. M., Laslett, G. M., Galbraith, R. F. (2000) Extending the age range of optical dating using single 'supergrains' of quartz. *Radiation Measurements* 32: 439-446
- Yoshida, H., Roberts, R. G., Olley, J. M. (2003). Progress towards single grain optical dating of fossil mud-wasp nests and associated rock art in northern Australia. *Quaternary Science Reviews* 22: 1273-1278
- Zhang, J. F., Zhou, L. P. (2007). Optimization of the 'double SAR' procedure for polymineral fine grains. *Radiation Measurements* 42: 1475-1482
- Zhou, L. P., Williams, M. A. J., and Peterson, J. A. (1994). Late Quaternary Aeolianites, Paleosols and Depositional Environments on the Nepean Peninsula, Victoria, Australia. *Quaternary Science Reviews* 13 (3): 225-239

APPENDIX A: Stratigraphical methods

A.1 Stratigraphical field methods

The recording of stratigraphical characteristics was restricted to site areas that were easily accessible. Cluffed sites and perpendicular headlands were preferred as this allowed not only a cutaway view of the deposits, but also access to the internal geometry of the sedimentary units (i.e. bedding plane angles, and orientation, for example). However, often these sites could not be easily or safely accessed because of height, steep gradients, or instability.

A1.1 Identifying units and recording sedimentary sequences

Units were identified and described in the field using information given in a variety of sources (e.g. McKee and Ward, 1983; Graham, 1988; Tucker, 2003). Stratigraphic terminology used to describe some types of units is given in Table 3.1 (Chapter 3: Part I).

Units were recorded in a field notebook as stratigraphical logs, and notes were taken listing the thickness, character and colour of each logged unit, and the overall height of the sequences. When possible, long, lateral, sedimentary sequences were logged as fence diagrams on graph paper, in order to capture a more comprehensive representation of the successions at a given site.

Along with this a series of high resolution photographs were also taken to contextualise each site. Where possible the thickness of units and heights of sequences were measured using a measuring tape. If the sequences were too high (or inaccessible) for this, a Brunton field compass and TANGENT tables were used to estimate both.

Sketches of site morphology were also recorded, and each site and unit was extensively photographed. Area photographs were also taken to provide a regional context for each site.

Bedding dip and orientation data were also collected at each site, where possible, using a Brunton field compass. Locations were recorded using a global positioning system (GPS).

APPENDIX B: Petrology: grain characteristics

B1.1 Microstructural and diagnostic features of biogenic carbonate grains

Aeolianite and marine sediments are comprised of a range of skeletal grain types; this appendix describes the criteria used to classify the main biogenic grain types found in the thin sections of Kangaroo Island carbonate deposits.

B1.1.2 Foraminifers

Foraminifer grains (tests) can range from 50 μm to >1000 μm (Flügel, 2004); being present as either whole or fragmented grains in thin section. They are distinctively multichambered and have varied morphology and mineralogy. The most common foraminifers found in the Kangaroo Island thin sections were of the order Rotaliida, which have tests constructed of calcite or aragonite fibres with, generally, lamellar walls (Yassini and Jones, 1995). These are usually translucent light-brown in colour under plane-polarized light; the chambers sometimes filled with sparry calcite.

Agglutinated tests (order Textulariida) have walls constructed of a variety of mineral particles (e.g. quartz granules, mica flakes, sponge spicules, shell fragments, etc.), 'glued' together with a variety of cement types (i.e. both mineral and organic), secreted by the organism itself (Yassini and Jones, 1995).

Miliolid (order Miliolida) and Fusulinid (order Fusulinida) tests are composed of microgranular calcite (closely packed, small subspherical granules of calcite, cemented with calcium carbonate) (Horowitz and Potter, 1971; Yassini and Jones, 1995), and have a brown colouring under plane-polarized light. Fusulinids may exhibit a spiral structure in cross-section (Scholle, 1978; Buzas *et al.*, 1987).

B1.1.3 Molluscs

Molluscs grains under thin section have a wide range of morphologies, from elongate, arcuate, cross-sectional bivalve fragments to chambered gastropods. The shell structure in molluscs consists of either entirely calcite, or entirely aragonite, or both aragonite and calcite in alternating layers (Flügel, 2004). In thin section, under plane-polarized light, molluscan grains exhibit a translucent

yellow to dark brown colouring (depending upon diagenetic maturity), and consist of long crystals (several μm) of calcite or aragonite. These crystal structures become less distinct with diagenetic alteration.

Commonly, mollusc grains under thin section exhibit distinctive, prismatic, cross-lamellar structures, oriented normal or inclined to the outer surface (Flügel, 2004). These diagnostic structures were used to identify molluscan grains when morphology was indeterminate (e.g. when arcuate morphology was disrupted by fragmentation).

B1.1.4 Echinoderms

Echinoid spines are relatively common constituents in marine or aeolian carbonate facies. In thin section, cross-sections of echinoid spines exhibit a characteristic internal radial structure (the structure is very regular and quite distinctive; the radial elements are wedge-shaped, and widen towards the periphery of the spine: Flügel, 2004, p. 556), and are either circular or elliptical in shape. Echinoderm plates are characterised by a polygonal shape, and a speckled (porous) surface, with a net-like microstructure. Under plane-polarized light they show a yellow-brown colouring. Mineralogy is generally high-Mg calcite (Tucker and Wright, 1990; Flügel, 2004).

B1.1.5 Bryozoans

Bryozoans are colonial suspension feeders that are formed of interconnected individuals (zooids). Bryozoan colonies (zoarium) can range in size from 1 mm to several cm, and are constructed of tube or box-like calcareous chambers, in which the zooids live. The morphologies of these colonies range from being massive or encrusting, to stick-like or delicate branching networks (Flügel, 2004: p. 514). Skeletal mineralogy is generally low-Mg calcite. In thin section bryozoans can show as elongate (several μm) chambered structures, dendroidal frameworks, or fenestrate mesh-like structures. They can be characterised by laminar, fibrous or granular microstructures—thick lamellar walls are particularly characteristic (Flügel, 2004: p. 516). Under plane-polarized light they exhibit a light-brown to brown colouring.

B1.1.6 Calcareous (Coralline) red algae

Corallinacean algae of the Rhodophyta Group are the most calcareous of the red algae (Flügel, 2004: p. 412), and were one of the more common components of the Kangaroo Island thin sections. The grains are constructed of micritic Mg calcite, and under plane-polarized light have a distinctive red-brown colouring. The cross-section of a coralline algae grain (in thin section) can be found in two forms: a simple form where the hypothallus layers are stacked, and arc up to the perithallus, and a coaxial form where the hypothallus layers are arranged concentrically, perpendicular to the perithallus (Flügel, 2004: p. 413)). These characteristics give the algal grain a distinctive curved, fine, mesh-like structure in thin section.

B1.1.7 Micritic grains

Micritic grains can be produced through a variety of diagenetic processes. Faecal pellets often contribute as a significant component of a micritic grain mix; also, processes such as weathering and microbial (algae; cyanobacteria) activity can micritise skeletal grains. Grain alteration through recrystallisation, reworking of micrite and carbonate muds, and also the rasping activities of some organisms can produce micritic grains (Flügel, 2004: p. 112).

Micritic grains (in thin section) have a characteristic dark-brown colour under plane-polarized light. They are usually a solid colour, with little or no internal structure. Micritic grains derived from the diagenesis of skeletal carbonate have an irregular shape, whereas those that have a faecal origin, or are derived from rasping activities, are generally elliptical or circular in shape, or have a scoop shape, respectively.

B1.1.8 Lithoclasts

Lithoclastic grains occurred infrequently in the Kangaroo Island thin sections, although they are very distinctive. They are typically large aggregates (usually >250 μm) (derived from reworked sediments) of foraminifer, red algal, molluscan, and micritic grains, in a calcitic cement. The lithoclasts are generally a deep, translucent brown under plane-polarized light, and a lighter, more yellow, brown under cross-polarized light.

APPENDIX C: Optically stimulated luminescence (OSL) and dosimetry sample preparation

C.1 OSL sample preparation

Standard procedures for isolating the quartz (sand-sized) fractions from a sedimentary (luminescence) sample (e.g. Stokes, 1992; Wintle, 1997) have generally been used in this study. Sample preparation was undertaken at the University of Wollongong OSL wet laboratory. All OSL samples were prepared under subdued red-light conditions, as exposure to white-light removes the stored OSL signal.

C.1.1 Sample removal

OSL samples were taken as either tube samples (a hollow steel or plastic tube is hammered into the face of the sedimentary unit [i.e. unconsolidated sand dune sand]—the sample is captured within, and then the tube is dug out of the unit and sealed with caps at either end), or block samples (a block of indurated sediment was removed from the unit by chopping out a section with a rock hammer) (i.e. consolidated aeolianite). Before preparation the sample must be ‘trimmed’ to ensure that any surface sediment that may have been exposed to sunlight during sampling is *not* included in the preparation. This was undertaken as follows:

- i) Tube samples were uncapped, and the first 2-3 cm of material at either end of the tube was discarded (or used as a dosimetry / water content sample) . The sample was then placed into a 2 L beaker for further treatment.
- ii) Block samples were exposed to a bath of hydrochloric acid (32%), and the outer 1-2 cm of material was etched away (i.e. the carbonate cement is dissolved by the HCl) leaving a core of unexposed consolidated sediment. Or a layer 1-2 cm thick was shaved away using a hammer and chisel. The etch method was preferentially used. Once etched or shaved the remaining sample block was placed into a 2 L or 5 L beaker (depending upon the size of the block) for further treatment.

C.1.2 Sample reduction in hydrochloric acid (removal of carbonates)

Subsequently, the samples (tube or block) were digested in 10% hydrochloric acid (HCl), to remove carbonates. Acid was added to the sample incrementally until all reaction (effervescence) had ceased; the length of time required for this varied, depending upon carbonate content. For the Kangaroo Island aeolianite samples generally a day of this treatment was sufficient to reduce all of the carbonate content, yielding a mixture of inorganic minerals.

The sample was then drained (care was taken not to decant any sand-sized sediment; very fine suspended material was discarded) and then washed in several volumes of water (3-4 times or until the water was reasonably clear) to remove any remaining HCl, salt solution, and free organic material (e.g. rootlets, insect cases, humus, etc.). Distilled water was used for the final rinse of the remaining sediment.

C.1.3 Sample oxidation in hydrogen peroxide (removal of organics)

After the HCl treatment the sample was then oxidised in a 10% hydrogen peroxide (H_2O_2) solution to remove the organic fraction. The length of time required for this step varied from sample to sample, for most of the Kangaroo Island samples 3-4 days was sufficient for the oxidation reaction to cease, after incremental addition of H_2O_2 .

The sample was then washed again in water, several times (3-4 times) (to remove dissolved residues and excess H_2O_2 (with a final rinse of distilled water). The sample was then placed in a 50 °C oven to dry overnight, or left under the fume hood to air-dry.

C.1.4 Sample sieving and heavy liquid separation

The remaining sediment (now comprised predominantly of quartz, feldspar, and heavy mineral grains) was wet sieved in a sieve stack comprising 300 μm , 212 μm , 180 μm , 125 μm , and 90 μm sieves. The grain-size fractions were collected in small beakers and either air-dried under the fume hood, or in a 50 °C oven overnight.

The size fractions of 90-125 μm and 180-212 μm were then heavy-liquid separated into the heavy mineral (e.g. zircons, rutile, ilmenite etc.), quartz, and feldspar (potassium and sodium) fractions, by immersion in a sodium polytungstate solution—adjusted to densities of 2.70 g/cm^3 (quartz + feldspars float and heavy minerals sink) and 2.62 g/cm^3 (feldspars float and quartz sinks), respectively.

After separation from the heavy minerals and feldspars, the quartz fraction was retained in filter paper, washed 3-4 times in distilled water and either air dried under the fume hood or in a 50 °C oven overnight.

C.1.5 Hydrofluoric (HF) acid etching

Prior to optical analysis, the refined sample quartz grains were etched for 45 min in cold (room temperature) 40% hydrofluoric acid, to remove the alpha irradiated outer portion of the quartz grain (the 'rind'), and any remaining feldspars. The HF was drained off and the refined quartz was then soaked in 32% HCl for 45 min, and washed 4 times in distilled water, to remove any HF residue and precipitated fluorides. The quartz was then air or oven (50 °C) dried, and then sieved again into its original size fractions (i.e. 90-125 μm or 180-212 μm). These fractions were then analysed in the Risø dating machines. In this study the 90-125 μm quartz fraction was commonly used in single aliquot analysis.

C.1.6 Single aliquot disc preparation

The quartz sample material (either 90-125 μm or 180-212 μm) was mounted on stainless steel sample discs (9.8 mm diameter) prior to analysis in the Risø dating machines. The sample was applied as a monolayer to the discs using a viscous silicone oil (Silkospray)—the viscous oil retains the quartz grains. Silicone oil is sprayed onto the discs using a variety of mask sizes; in this study a 1 mm mask size was generally used for conventional OSL analysis (5 mm mask size was used for SARTT-OSL samples).

The disc was then applied to the quartz sample and a 1 mm diameter monolayer, of approximately 80 (90-125 μm) grains, will adhere to the silicone

oil on the disc. The discs (usually 24 or 48 were prepared from a given sample) were then placed on a sample carousel and analysed in the Risø dating machines.

C.2 Dosimetry sample preparation

Dosimetry samples require no pre-treatment, other than drying, and being ground to a fine powder prior to analysis—see below.

Mass of sample pre-drying was recorded, as was mass of sample post-drying. The difference between the two masses was used to calculate the percentage water content by dry mass. This is used as part of the age calculation (to correct for beta-dose attenuation attributable to sediment field water content).

C.2.1 Thick source alpha counting (TSAC)

Thick source alpha counting (TSAC) samples are recovered from the same sample holes as the OSL samples. The TSAC sample is dried for several days (3-5 days, depending upon the volume and consistency of the sample) (at 100 °C), and is then milled to a fine powder (<20µm—a flour-like consistency) in a Retsch ball mill. The samples were left for several weeks to allow progeny ingrowth, prior to counting in a Daybreak 583 TSAC.

C.2.2 Geiger-Müller beta counting (GMBC)

The sampling and preparation protocol for Geiger-Müller beta counting samples is the same as for TSAC. The sample was then counted in a Geiger-Müller multi-counter, Risø model GM-25–5.

APPENDIX D: Amino acid racemization (AAR) sample preparation

D.1 Preparation of samples for AAR analysis

D.1.1 Marine molluscs

Fossil marine molluscs were first selected for analysis on the basis of best preservation. Shells that were oxidised or showed evidence of extensive

weathering, or recrystallisation (i.e. powdery or chalky surfaces) were rejected for preparation and analysis.

D.1.1.1 Cleaning of shells

Marine mollusc shells were first thoroughly washed in purified (Millipore) water, then placed in a sonic bath for several minutes to help disaggregate any adhering sediments. They were then mechanically cleaned to remove any remaining sediments, cements, patches of weathered material, or recrystallised carbonate. This was done by either grinding or scraping (rotary grinding tool, dental drill, or probe). Marine and freshwater gastropods are more problematic than bivalves, as sediment can be trapped within the axial whorls that make up the interior of the shell. If this material is not removed it may lead to contamination. To solve this problem gastropod shells are sampled for analysis from the aperture. However, with small gastropods (<200 mg) the whole shell can be analysed; in this case the shell was carefully broken into two or three parts (this was done by covering with a layer of Pergamon paper and gently tapping with forceps), so any sediment trapped within the axial chambers could be easily removed.

The cleaned shell (small shells were not mechanically cleaned, other than that described above, they were, however, sonically cleaned) was then subjected to another sonic bath for up to 10 minutes. This thoroughly cleaned the shell of any particulates left over from the mechanical cleaning. The shell was rinsed in 3 to 5 volumes of purified (Millipore) water then air dried on Kimwipes or in sterile plastic dishes. After this the dried shell was accurately weighed then acid etched in 2 M hydrochloric acid (HCl), where 0.0033 mL of 2 M HCl was added for every 1 mg of shell:

For example: a shell specimen weighs 45 mg

2 M HCl to add = 0.0033 mL x 45 mg

= 0.1485 mL 2 M HCl

The shell was placed in a culture tube or beaker and covered with purified (Millipore) water and then the appropriate amount of acid was added. It is

important to note that the solution should be kept mobile to ensure that acid reaches every surface of the shell equally—this can be done by adding a mixing bar and placing on a magnetic mixer, or by agitating the solution from time to time by hand. This treatment removes approximately 33% (by dry mass) of the outer layers of the shell. This is done to ensure that any outer shell surfaces, which may have been contaminated by non-indigenous amino acids or leached of more highly racemized, low molecular weight macromolecules, are removed.

After the reaction stops the specimen is rinsed in 3 to 5 volumes of purified (Millipore) water. As a final cleaning step, the specimen is immersed in excess 3% hydrogen peroxide (H_2O_2) for 2 hours. However, if shell sample is limited and extensive contamination is suspected, or if the shell specimen is considered to be extremely old (e.g. early Pleistocene) (in this case concentrations of indigenous amino acids may be low; allowing any contaminating non-indigenous amino acids to have a significant influence on the D/L ratio), a 24 hr soak in excess 12.5% sodium hypochlorite (NaOCl —bleach) is used as an alternative to the 2 hr H_2O_2 soak. Both of these steps remove contaminating (adsorbed) organic material by oxidation; however, NaOCl is a more effective oxidiser and as such it can *also* remove *indigenous* amino acids that are within the inter-crystalline fraction of the shell carbonate. This is not problematic *per se* for whole shell (as opposed to powdered shell), due to the structural integrity of the molluscan carbonate matrix. Nevertheless, NaOCl should still be used with caution.

The shell is then rinsed thoroughly (4-5 washes) in purified (Millipore) water and left to air-dry on Kimwipes or in sterile plastic dishes (if a NaOCl soak was used the shell is also rinsed once in 100% methanol to remove any remaining bleach). After drying it is weighed in preparation for hydrolysis. It should be noted that the shell is now considered sterile and should not be directly handled except with sterile forceps.

D.1.1.2 Protein Hydrolysis

If the shell is large, then a only a portion is sampled for hydrolysis—in the case of a bivalve the hinge area is sampled or in the case of a gastropod the aperture area is sampled. Normally these sections of the shell would be sampled prior to

the cleaning treatments to minimise handling. If shells are small (< 200 mg) then the whole shell can be hydrolysed.

Hydrolysis involves the denaturing of proteins and peptides into their component amino acids via heating at 110 °C and exposure to an aqueous strong acid for 22 hours—in this case 8 M HCl. The acid first releases these macromolecules, peptides, and ‘free’ amino acids by dissolution of the shell carbonate, as they are bound in the inter- and intra-crystalline matrices of the shell carbonate. The products of hydrolysis are an assortment of α -aminocarboxylic acids in both L- and D-configurations. The amino acid utilised as a geochronological and stratigraphic tool in this study is glutamic acid (GLX).

The 8 M HCl acid is added in excess (although the volume added is calculated to optimise concentration of amino acids in the final solution), so that once digestion of the shell calcium carbonate is complete the solution is still highly acidic; in this case the final concentration of HCl is 7 M.

The following formula is used to derive the volume to be added:

0.02 mL 8 M HCl x mass (mg) specimen = X mL 8 M HCl to add to sample.

For example: 0.02 mL x 45 mg = 0.9 mL 8 M HCl to add

Generally samples are reacted and hydrolysed in the same vessel—here 4 mL glass vials with screw caps are used—as it is possible for higher molecular weight molecules to adsorb onto glass surfaces (note: glassware used in amino acid preparation and analysis was either purchased as sterile items [i.e. disposable, borosilicate culture tubes, and Pasteur pipettes] or was sterilized in an electric muffle furnace at 450 °C for 4 hours prior to use). Therefore, if separate vessels are used for dissolution and hydrolysis, there may be some loss of these less racemized molecules; however, this has not been directly observed in this study.

After digestion of the shell carbonate is complete, a flow of nitrogen (N₂) gas is directed into the vial for approximately 10 seconds; the vial is then quickly capped. Nitrogen gas replaces the air in the vial and prevents oxidation of

amino acids during hydrolysis. The sample vial is then placed in an oven set to 110 °C, and left for 22 hours.

After hydrolysis the sample is either freeze dried *in vacuo* using liquid nitrogen, or two 50 µL sub-samples are taken and are dried in a vacuum desiccator. The dried sample is then re-hydrated. The samples are re-hydrated using a solution composed of 0.01 mM L-HomoArginine + 0.01 M HCl + 0.77 mM sodium azide—the L-HomoArginine acts as an internal standard, whereby the concentrations of sample amino acids can be calculated. The volume of re-hydration solution added is the same as the volume of acid added for hydrolysis, or if a sub-sample was taken then 50 µL is added. Occasionally these volumes were reduced to improve amino acid peak resolution in older samples.

Once re-hydrated the sample is ready for analysis in the reverse phase high pressure liquid chromatograph (RP-HPLC).

D1.2 Benthic foraminifers

Foraminifera are generally selected on the basis of preservation; where only the largest and best preserved are used in analysis. However, when the intention is to examine distributions of D/L ratios within a sample, rather than chronology or stratigraphy, care was taken to select individuals of a particular species without bias; taphonomy was also recorded. One of the advantages of using the RP-HPLC to analyse foraminifera is its capability to resolve amino acids in the pico mole range, from sub-milligram samples. This means essentially that individual particles of sediment can be analysed for amino acids; in this case D- and L-amino acids are extracted from individual foraminifers.

D1.2.1 Cleaning of foraminifers

Before picking foraminifera from the sediment sample, the whole-rock sample itself is first washed in 3-4 volumes of purified (Millipore) water then placed in an ultra-sonic bath for several minutes. It is subsequently washed again several times, and the sediment is air dried. This step helps to break-up and clean the sediment thoroughly; silt, clay, organic particles, and interstitial cements (if any)

can be washed away without difficulty. This makes it easier to identify and pick the foraminifera that will be used in analysis.

Occasionally the sample that the foraminifers are to be picked from is indurated and will not readily disaggregate. In this instance the sample is broken into fragments and then lightly ground in a mortar and pestle. If care is taken to gently roll the concretions of sediment, without pressure, the sediment will readily disaggregate into constituent grains. Interstitial cements are then sieved out, and the sample can be cleaned as above in preparation for picking.

Generally foraminifera are not subjected to the acid etch cleaning step. Often they are very small ($<100\ \mu\text{m}$), and not enough are picked to amount to a significant mass—in terms of calculating the volume of 2 M HCl to add. However, from time to time, a sediment sample will yield large (500-1000 μm) specimens of foraminifera. These can be weighed as a group, placed in a culture tube together, covered with purified (Millipore) water and the appropriate amount of 2 M HCl acid can be added for etching. The procedure for this is the same as for marine molluscs, although a mixing bar is not used. If the foraminifers are too small, then after picking, a second ultrasonic treatment and rinse is used. Foraminifers are also treated with H_2O_2 as in section A.1.1.1, and then the tests are air dried in sterile plastic dishes.

D.1.2.2 Protein Hydrolysis

Once dry the foraminifers are subjected to the same hydrolysis procedure outlined in section D.1.1.2 and are dried in a vacuum desiccator; although, hydrolysis volumes are not calculated, and a different HCl acid is used (the reasons are outlined below).

The aim here is too examine the D/L ratios of individual tests, in light of this aim; single tests are placed in separate 100 μl vials for hydrolysis and subsequent analysis. However, since, in most cases, individual foraminifers are too small to register on the balance used in this laboratory, they are all hydrolysed with the same volume of HCl acid. For foraminifers 5 μL of 6 M HCl acid is used. The 6 M HCl used is purchased in 2 mL ampoules and is of extremely high purity. The 8 M acid used in section A1.1.2 is prepared from 32% w/w laboratory grade HCl

which is not a high purity reagent; however, it is adequate when processing large mollusc samples with high concentrations of amino acids. However, for smaller samples such as individual foraminifers where even though concentrations of amino acids are (due to the small hydrolysis volume) relatively high, the extremely small volume of HCl acid used renders any contamination a potential disaster. Therefore, a high purity hydrolysis medium is desirable to reduce, at least, the reagent pathway of contamination.

Re-hydration and analysis is performed as in section D1.1.2.

D1.3 “Whole-rock” sediment samples

The initial processing of whole-rock samples (these steps applied in particular to those samples that were consolidated) requires a series of steps, in order to reduce grain aggregates to individual grains and strip away much of the interstitial and rind cements. This is outlined below:

- i) If consolidated sediment, break off an appropriately sized piece (several 10s of grams) and crush gently in a mortar and pestle.
- ii) Sieve through 1000 μm , 500 μm , and 250 μm sieves. Collect the 250-500 μm and 500-1000 μm fraction.
- iii) Grind both fractions in a mortar and pestle, gently, no pressure; roll the grains.
- iv) Sieve through a 500 μm and 250 μm sieve stack. Check grains for aggregate (repeat iii and iv, if any present). Collect the 250-500 μm fraction.
- v) Grind the 250-500 μm fraction in a mortar and pestle, gently, no pressure, roll the grains. Check grains for aggregate, repeat if any present
- vi) When no aggregates are visible, sieve then sample the 250-500 μm fraction (you must also determine % carbonate of this fraction for estimating the appropriate amount of 2 M and 8 M HCl to add for etching and hydrolysis.

After this treatment the 250-500 μm fraction was washed in 3-4 volumes of purified (Millipore) water then placed in an ultra-sonic bath for several minutes.

It was subsequently washed again several times (3-4), and the sediment air dried. This step helps to clean the sediment thoroughly of any silt, clay, organic particles, or remaining interstitial cements.

As iterated above each sample of whole-rock will contain a varying amount of carbonate; the percentage by mass of this carbonate must be determined if the correct amount of acid for etching and hydrolysis is to be added. In short this is determined by placing a known mass of the 250-500 μm fraction into a beaker of known mass; then 8 M HCl acid is added in increments until the reaction stops. The sample is carefully washed to remove unreacted acid and salts, and then the beaker is placed in a 110 °C oven overnight to dry. Once dry the beaker plus sample is weighed (and the mass of the beaker is subtracted); hence, the net weight loss is the amount of carbonate contained in the fraction.

After the above processes are complete, preparation and analysis of the whole-rock sediment sample (taking into account % carbonate) is performed as in sections D1.1.1 and D1.1.2.

APPENDIX E: AAR and OSL raw data and spreadsheets DVD